

---

# **NANOWIRES - FUNDAMENTAL RESEARCH**

---

Edited by **Abbass Hashim**

**INTECHWEB.ORG**

## **Nanowires - Fundamental Research**

Edited by Abbass Hashim

### **Published by InTech**

Janeza Trdine 9, 51000 Rijeka, Croatia

### **Copyright © 2011 InTech**

All chapters are Open Access articles distributed under the Creative Commons Non Commercial Share Alike Attribution 3.0 license, which permits to copy, distribute, transmit, and adapt the work in any medium, so long as the original work is properly cited. After this work has been published by InTech, authors have the right to republish it, in whole or part, in any publication of which they are the author, and to make other personal use of the work. Any republication, referencing or personal use of the work must explicitly identify the original source.

Statements and opinions expressed in the chapters are these of the individual contributors and not necessarily those of the editors or publisher. No responsibility is accepted for the accuracy of information contained in the published articles. The publisher assumes no responsibility for any damage or injury to persons or property arising out of the use of any materials, instructions, methods or ideas contained in the book.

**Publishing Process Manager** Viktorija Zgela

**Technical Editor** Teodora Smiljanic

**Cover Designer** Jan Hyrat

**Image Copyright** Vlue, 2010. Used under license from Shutterstock.com

First published July, 2011

Printed in Croatia

A free online edition of this book is available at [www.intechopen.com](http://www.intechopen.com)  
Additional hard copies can be obtained from [orders@intechweb.org](mailto:orders@intechweb.org)

Nanowires - Fundamental Research, Edited by Abbass Hashim

p. cm.

ISBN 978-953-307-327-9

**INTECH** OPEN ACCESS  
PUBLISHER

**INTECH** open

**free** online editions of InTech  
Books and Journals can be found at  
**[www.intechopen.com](http://www.intechopen.com)**



---

# Contents

---

## **Preface IX**

### **Part 1 Silicon Nanowires 1**

- Chapter 1 **Silicon Nanowire Waveguides and Their Applications in Planar Wavelength Division Multiplexers/Demultiplexers 3**  
Jun Song and Jinfei Ding
- Chapter 2 **Four-Wave Mixing in Silicon Nanowire Waveguides and its Applications in Wavelength Conversion 25**  
Shiming Gao and Sailing He
- Chapter 3 **Wet - Chemically Etched Silicon Nanowire Architectures: Formation and Properties 45**  
Vladimir Sivakov, Felix Voigt, Björn Hoffmann, Viktor Gerliz and Silke Christiansen
- Chapter 4 **First Principles Study of Si/Ge Core-Shell Nanowires - *Structural and Electronic Properties* 81**  
Xihong Peng, Fu Tang and Paul Logan
- Chapter 5 **Nanowire Applications: Thermoelectric Cooling and Energy Harvesting 101**  
Gang Zhang
- Chapter 6 **Silicide Nanowires from Coordination Compound Precursors 123**  
John Philip
- ### **Part 2 Oxide Nanowires 139**
- Chapter 7 **The Anisotropic Growth of Perovskite Oxide Nanowires 141**  
Yongming Hu, Haoshuang Gu and Zhao Wang

- Chapter 8 **Junction Properties and Applications of ZnO Single Nanowire Based Schottky Diode** 161  
Sachindra Nath Das, Jyoti Prakash Kar and Jae-Min Myoung
- Chapter 9 **Metal Oxide Nanowires – Structural and Mechanical Properties** 183  
L. Dai, C.H. Sow, C.T. Lim and V.B.C. Tan
- Part 3 Metal Alloy Nanowires** 203
- Chapter 10 **Synthesis of Pt – Containing Metals Alloy and Hybrid Nanowires and Investigation of Electronic Structure Using Synchrotron-Based X-Ray Absorption Techniques** 205  
Xiaowei Teng, Wenxin Du and Qi Wang
- Chapter 11 **GaN Nanowires Fabricated by Magnetron Sputtering Deposition** 225  
Feng Shi
- Chapter 12 **Fabrication, Characterization and Thermal Properties of Nanowires** 263  
Yang-Yuan Chen, Cheng-Lung Chen, Ping-Chung Lee and Min-Nan Ou
- Chapter 13 **Role of Intrinsic Defects in Nanowires** 285  
Usha Philipose
- Part 4 Metal Nanowires** 307
- Chapter 14 **Gold and Silver Nanowires for Fluorescence Enhancement** 309  
Krystyna Drozdowicz-Tomsia and Ewa M. Goldys
- Chapter 15 **On the Behavior of Ni Magnetic Nanowires as Studied by FMR and the Effect of “Blocking”** 333  
Carlos A. Ramos, Ettore C. Vassallo Brigneti, Emilio De Biasi and Manuel Vázquez
- Chapter 16 **Growth of Germanium Nanowires on a Flexible Organic Substrate** 357  
Lauren A. Klein, Daniel D. T. Mastrogiovanni, Aurelien Du Pasquier, Tong Wang, Alan S. Wan and Eric Garfunkel
- Chapter 17 **Thermoelectric and Magnetic Nanowires** 371  
Yu-Biao Liu and Shao-Min Zhou

- Chapter 18 **Nanowire Formation under Femtosecond Laser Radiation in Liquid** 395  
Yasuhiko Shimotsuma, Kiyotaka Miura and Kazuyuki Hirao
- Chapter 19 **High-bias Instability of Atomic and Molecular Junctions** 439  
Akira Sakai
- Chapter 20 **Electron Diffraction and HRTEM Structure Analysis of Nanowires** 461  
José Reyes-Gasga, David Romeu, Alfredo Gómez-Rodríguez
- Chapter 21 **Charge and Spin Transport Charge and Spin Transport** 485  
N. Sedlmayr, J. Berakdar,  
M. A. N. Araújo, V.K. Dugaev and J. Barna's
- Part 5 Organic and Inorganic Nanowires** 507
- Chapter 22 **Nanowires of Molecule-Based Charge-Transfer Salts** 509  
De Caro Dominique
- Chapter 23 **Novel Pressure - Induced Structural Transformations of Inorganic Nanowires** 527  
Yang Song and Zhaohui Dong



---

# Preface

---

During the last 20 years the nanotechnology has been a demand of the worldwide technology. In the early 1990s the microscale technology was almost fully understood and the scientists tried to find a solution how to miniturize electronic devices and engineering applications to a microscale level. At that time they already had the evidence that this is possible particularly due to fast development of microscope test equipments and facilities. Advanced miniaturization was a key thrust area to enable new science and exploration missions.

NASA's nanotechnology attempt started in 1996 and it resulted in the founding of the Centre for Nanotechnology. Apart from this centre, the research has been focused on the experimental research and development in computational nanoelectronics and computational optoelectronics.

IBM's Nanotechnology Research Centre is one of the best centres in Europe which has won considerable number of Nobel prizes. They are developing novel concepts in nanotechnology for future needs of electronics, computing, sensors, and advanced miniaturization of many systems.

Ultrasmall sensors, power sources, communication, navigation, and other systems with very low mass, volume and power consumption are needed. A part of processing of the ultrasmall system is a nanowire. Nanowire is the functional part in these application systems individually, which improves them.

The nanowires research presents a whole new spectrum of opportunities to build device components and systems for entirely new space architectures.

Understanding and building up the foundation of nanowire concept is a high requirement and a bridge to new technologies. Any attempt in such direction is considered as one step forward in the challenge of advanced nanotechnology.

In the last few years, InTech scientific publisher has been taking the initiative of helping worldwide scientists to share and improve the methods and the nanowire technology.

This book is one of InTech's attempts to contribute to the promotion of the nanowire technology. The book contains 23 chapters divided into five sections.

Silicon is the most important semiconducting material in microelectronics and silicon-based devices. Silicon has played a dominant role in many components. Generally, the semiconductor device consisting of nanowire arrays of p–n junction may provide a solution for the design and optimization of this device. In the first section (Silicon Nanowires), we focus only on the silicon materials for system application. The section contains six updatig silicon technology chapters. The chapters are framed to throw the light on the current silicon nanotechnology.

Section two (Oxide Nanowires) is putting the stress on the growth of oxide nanowires: Perovskite Oxide, compound, oxides (e.g., TiO<sub>2</sub>, ZnO), and their alloys. This section, containing three chapters, is focusing on the growth methods, structural properties and morphology of oxide nanowires.

Metal alloy as a unique generation semiconductor material (III-V), has shown great adaptation in the applications of light-emitting devices (LEDs), short wavelength devices (UV), microwave devices and high-power semiconductor devices, due to its exclusive physical properties such as a high thermal conductivity, wide band-gap (3.39 eV direct gap at room temperature), high electron saturated mobility, high thermal stability, and so on. Section three is comprised of four chapters describing the advanced technology of metal alloy nanowires.

Section four (eight chapters) is considering the development of more powerful electronics that depend on the progress in miniaturizing the components. However, the laws of quantum mechanics, the limitations of fabrication techniques, and the cost of the fabrication facilities may provide us with more information on the further scaling down of the conventional metal technology. The alternative technologies have stimulated a surge of interest in nanometer-scale materials and devices in recent years. Metal nanowires are one of the most attractive materials because of their unique properties that may lead to a variety of applications.

Currently we are approaching the physical limits of conventional silicon-based electronics and there is a clear need for new types of materials that can deliver considerably smaller devices with very individual characteristics. A strong candidate in this field and of a great technological importance is the organic nanowire. The last section in this book contains two chapters. One of them is studying the challenge of organic nanowires.

Finally I would like to express my great gratitude to InTech publisher and to all authors for their own hard and individual work. Myself, as an editor, and the authors would like to use this opportunity to share our research interest with every researcher in the world and we hope that this book will be useful to them.

**Dr. Abbass Hashim**  
Material and Engineering Research Institute  
Sheffield Hallam University  
UK





# **Part 1**

## **Silicon Nanowires**



# Silicon Nanowire Waveguides and Their Applications in Planar Wavelength Division Multiplexers/Demultiplexers

Jun Song and Jinfei Ding

*Institute of Optoelectronics, Key Lab of Optoelectronics Devices and Systems of Ministry of Education/Guangdong Province, Shenzhen University, Shenzhen, China*

## 1. Introduction

In the middle of last century, with the development of the first semiconductor transistor, the age of micro-electronics has started. Since then, electronic circuits keep developing rapidly, according to Moore's famed law. Nowadays, in a very large scale integration chip (VLSI), length is typically several tens of nanometers. Millions of such transistors can be integrated in a single square millimetre area. With the maturing of the fabrication technology, the idea of systems on chips has been brought up. People have successfully integrated the whole system consisting of different functional modules, e.g., analytical circuits, radio frequency modules, micro control units, digital signal processing modules, memories, micro electro-mechanical systems, etc., in a single chip.

Photonics is the technology associated with signal generation, processing, transmission, and detection where the signal is carried by photons (i.e., light). Photonics is a rapidly expanding technology with applications in a large number of areas. One hitherto dominating sector has been telecommunication, but photonics is much broader than that. Nowadays, besides telecommunication, applications of photonics include consumption equipment, medicine, industrial manufacturing, construction, aviation, military, entertainment, metrology, photonic computing, etc. However, as compared to electronics, photonics is about several tens of years behind in maturity. In order to compete with electronics in our modern life, photonics has to follow the same development dynamics as electronics. Recently, Moore's law in photonics has been concluded by several researchers (Thylén et al., 2006). They showed us very promising perspectives that the development of photonics is actually faster than that of electronics, and the VLSI of photonics will be realized in the next twenty years.

As we have discussed above, the major issue in the development of photonics is to reduce the dimension of devices, i.e., to increase the integration density. In the present chapter, we will consider planar wavelength division multiplexers/demultiplexers as examples to show the effective application of silicon nanowire technology in the modern photonics.

Fibre-optic communication is growing extensively in recent years. Nowadays a great number of optical fibres are laid on all parts of the world, which dramatically increases the capacity and the quality of telecommunications. However, traditional optical fibres are still

inadequate to carry the heavy traffic resulted from the exponential increase of the bandwidth demand. Fortunately, the wavelength division multiplexing (WDM) technique provides an effective and low-cost way to increase the capacity tens or hundreds of times in an optical transmission system.

WDM is a kind of frequency division multiplexing technique for fibre-optic cable in which multiple optical carrier signals on a single optical fibre by using different wavelengths (colours) of laser light to carry different signals. These channels are also called lambda circuits. Think of each wavelength as a different colour of light in the infrared range that can carry data.

Optical multiplexers and demultiplexers are the key components in the WDM fibre-optical communication system. Multiplexers splice the different signal wavelengths together at the input to the system and demultiplexers split apart the different signal wavelengths at the output of the system. Currently, commercially available components are mainly based on thin film interference filters, fibre Bragg gratings or micro-optic techniques. A cost-effective scheme for carrying more information is implemented by inserting them on both sides of a fibre link. Arrayed waveguide gratings (AWGs) (Smit & Dam, 1996) and etched diffraction gratings (EDGs) (Cremer et al., 1991) are two typical multiplexers/demultiplexers based on planar integrated optical waveguides. They take the advantages of mature semiconductor manufacturing process and can offer more than 40 channels of dense wavelength division multiplexing (DWDM).

Different technologies based on different materials have been introduced to support planar optical devices. Silica-on-silicon technology has been widely adopted for fabrications of WDM devices in commercial systems, due to the material refractive index which matches that of optical fibres. A common drawback of the silica-based photonic integrated devices is the overall size of components, mostly limited by the large bending radius. This limitation is dictated by a low refractive index difference between the core and the cladding. The size of a typical device, e.g., a multi-channel EDG demultiplexer, is several cm<sup>2</sup> and the integration of more complex structures is often difficult on a single wafer. To increase the integration density for future WDM systems a considerable size reduction is necessary. III-V semiconductor technology is another promising technology due to its ability to integrate some optoelectronic or active devices (Cremer et al., 1991), e.g., high-quality lasers, high-speed modulators, etc. It can also help to decrease the size of, e.g., an A WG to a few mm<sup>2</sup> based on the common ridge waveguide, but this is at the expense of higher loss, higher material cost, and more complex fabrication technology. To stay with silicon, as it is the most popular material for modern micro-electronics, Si based nanowire waveguides were introduced (Bogaerts et al., 2005), formed as silicon strips on a silica layer. A very high contrast of refractive index in all directions and high light confinement allow for a very high integration grade.

Due to the compatibility of the fabrication technology with micro-electronics, silicon photonics has attracted a lot of interests. Both A WGs and EDGs based on Si have been studied in the recent years. However to maintain single mode propagation along such a silicon nanowire waveguide the cross section of the waveguide becomes very small. The performance of such sub-micrometer sized devices strongly depends on the fabrication accuracy. For a passive component, when the feature size shrinks down to sub-micron or nano scales, the most challenging issues are the scattering loss due to sidewall roughness and the coupling efficiency from fibre. By optimizing the technology or employing a

roughness reduction procedure (Lee et al., 2001), the propagation loss of a typical Si nanowire waveguide has reached  $\sim 0.2\text{dB/mm}$ . The coupling efficiency can also be improved significantly with a spot size converter ( $\sim 0.5\text{dB}$  loss per connection) (Fukuda et al., 2005). With these improvements, the high-index-contrast material structures for photonic devices have been intensively studied during these years, since their ability to achieve planar integration, and their compatible fabrication technology with micro-electronics.

## 2. Silicon nanowires in photonics: designs and fabrications

Due to the compatibility of the fabrication technology with micro-electronics, silicon photonics has attracted a lot of interests. A search for the high-index contrast waveguide led us to the Si-channel waveguides that consist of a Si core with an extremely small cross section and have a surrounding cladding of  $\text{SiO}_2$  materials or air. Their basic characteristics have been investigated, and many functional devices have been demonstrated by using these waveguide structures. Various compact components based on Si nanowires, e.g., filters (Yamada et al., 2003), multiplexers (Chu et al., 2006), photonics crystals (Rue et al., 2006), as well as a number of active devices like lasers (Rong et al., 2005), modulators (Hattori et al., 2010), and switches (Belotti et al., 2010), were studied in the recent years.

### 2.1 Designs of silicon nanowire waveguide

First, the properties of the Si nanowire waveguide were studied. The typical structure of a Si nanowire waveguide based on a Si substrate is shown in Figure 1 (a). The silica buffer layer should be thick enough ( $\sim 5\ \mu\text{m}$ ) to ensure a low leaky loss. For a typical photonics application, the thickness  $h=250\text{nm}$  is fixed here, and the width  $w=500\ \text{nm}$  is chosen, which lies in the single mode region. The intensity profile of the propagating electric field is simulated for the channel wire waveguides (see Figure 1(b)).

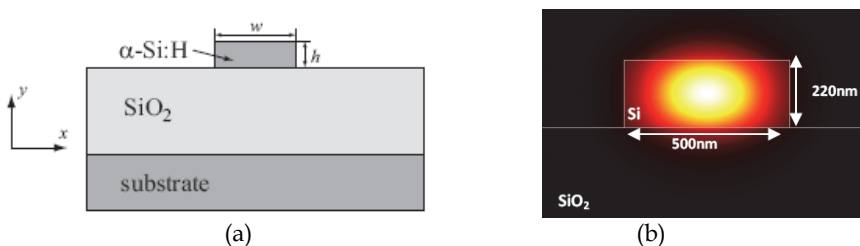


Fig. 1. Sketch of  $\alpha\text{-Si}$  nanowire waveguide (a) and the simulated intensity profile of the light in the silicon waveguide (b).

Since the structure is asymmetric along the  $y$  direction (see Figure 1 (a)), there exists a cut-off width for each of the modes. Figure 2 shows the propagation constants of some waveguide modes with different structural parameters. The single mode condition can be easily drawn from this figure. It is worthwhile to note that at  $w=275\text{nm}$  the propagation constants of  $\text{TE}_{00}$  mode and  $\text{TM}_{00}$  mode are equal. At this point, the birefringence in this Si nanowire waveguide disappears. This might be used for building polarization independent devices. Another interesting phenomenon here is the mode mixing between  $\text{TM}_{00}$  mode and  $\text{TE}_{10}$  mode around  $w=700\text{nm}$ , which results in a gap between the corresponding curves. This

is because of the fact that these two modes have the same symmetry along the x direction (Pavesi & Lockwood, 2004).

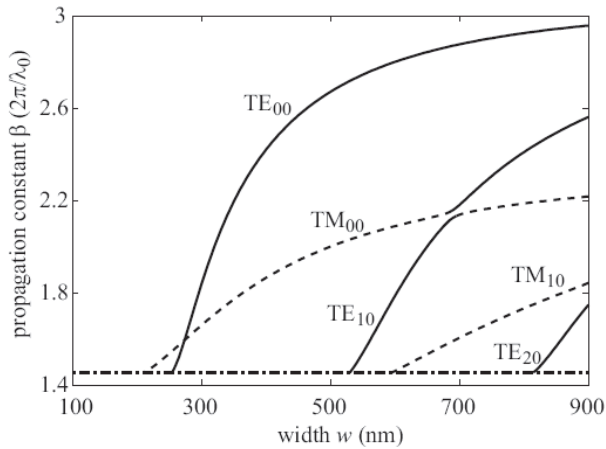


Fig. 2. Propagation constants of different modes in Si nanowire waveguides. Here,  $\lambda_0=1550$  nm,  $h=250$  nm,  $n_{\text{Si}}=3.63$ , and  $n_{\text{SiO}_2}=1.455$ . The solid lines are for TE modes, and the dashed lines are for TM modes. The dash-dotted line denotes  $n_{\text{SiO}_2}$ . Below this line, modes become leaky.

Propagation losses in straight silicon nanowires arise from different sources, these includes bulk and nonlinear absorptions, substrate leakage, and Rayleigh and sidewall roughness scattering. The Bulk Si has a negligibly low absorption around 1650 nm. The nonlinear absorption arises from high power interaction. If the power used is small, nonlinear effect is not considered, equally for the Rayleigh scattering.

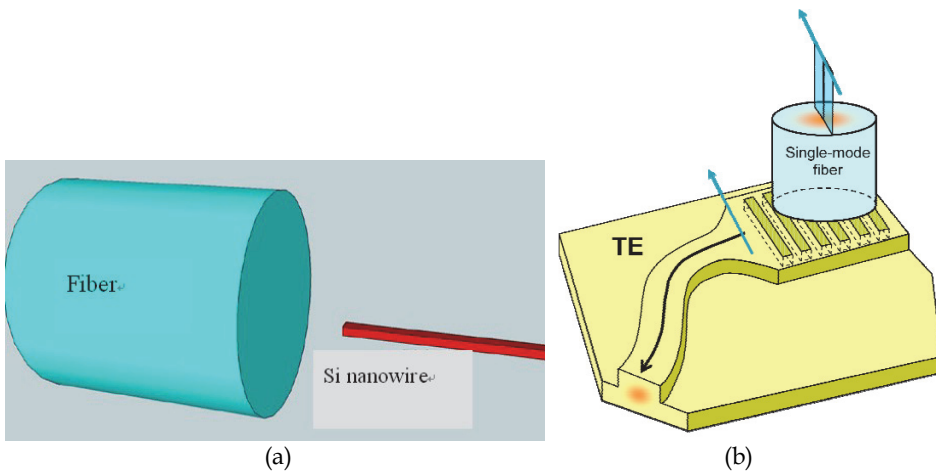


Fig. 3. Fibre butt coupling to Si nanowire waveguide (a); Schematic vertical coupler used to couple light from the fibre into the Si nanowire and vice versa (Taillaert, 2004) (b)

The coupling efficiency from fibre to silicon nanowire waveguide is also very crucial for photonics applications. One wants to couple the biggest amount of light into the waveguide. Some research has shown an efficient way to couple light from the fibre into the nanowire and vice versa, by using grating couplers (see Figure 3), no lenses or focusing gratings are needed, and indeed 38% of coupling efficiency can be achieved (Taillaert, 2004).

## 2.2 Fabrications of silicon nanowire waveguide

High-index contrast and highly integrated photonics requires a suitable fabrication technology. The silicon nanowire waveguide fabricated and discussed in this chapter consists of a 220 nm thick Si waveguide layer on top of 5  $\mu\text{m}$  thick buried oxide layer on a Silicon substrate. By etching completely through the silicon waveguide layer, we obtain a very high refractive index contrast leading to a strong confinement of the light. For silicon nanowires of photonics applications, main fabrication processes are as follows.

### 2.2.1 Film deposition

To create thin films of the desired materials on a substrate is the beginning step of the device of silicon nanowires fabrication. As shown in Figure 1,  $\sim 5 \mu\text{m}$  silica buffer layer and 250 nm  $\alpha\text{-Si:H}$  core layer will be successively deposited on a silicon wafer. A uniform, smooth, and defect-free film is always expected. Usually, the plasma enhanced chemical vapour deposition (PECVD) technology is employed for hydrogenated amorphous silicon ( $\alpha\text{-Si:H}$ ) and silica depositions.

Parameters	$\text{SiO}_2$	$\alpha\text{-Si:H}$
$\text{SiH}_4$ flow rate	20 sccm	60 sccm
$\text{N}_2\text{O}$ flow rate	2000 sccm	0 sccm
pressure	300 mTorr	270 mTorr
RF power	800 W	5 W
RF frequency	380 kHz	13.56 MHz
temperature of showerhead	300 $^\circ\text{C}$	300 $^\circ\text{C}$
temperature of platen	250 $^\circ\text{C}$	250 $^\circ\text{C}$
deposition rate	$\sim 160 \text{ nm/min}$	$\sim 8 \text{ nm/min}$

Table 1. Process parameters for depositing some films with PECVD

A full description of this deposition process is extremely complex; please refer to the book (Schul & Pearton, 2004) for detailed discussions. Generally speaking, the chamber is first evacuated, then gases with the required species are filled in the chamber through the showerhead. RF energy at a desired frequency (380 kHz or 13.56 MHz) is capacitively coupled in through a matching unit. Plasma is started between the showerhead and the bottom electrodes, which are both usually heated around 250  $^\circ\text{C}$ . The highly energized electrons in this plasma cause the dissociation of the gas precursors into free radicals. These radicals arrive at the substrate by diffusion, and react with each other to establish chemical bonds, then to form the film. The most critical parameters for this deposition process include the gas composition, the process pressure, the RF power and frequency, the temperature of the platen and showerhead. All of these parameters have been optimized for 5  $\mu\text{m}$  silica buffer layer and 250 nm  $\alpha\text{-Si:H}$  core layer (see Table 1).

### 2.2.2 Pattern generation

After thin film deposited, the wafer was then cleaved into small samples. Then a process of pattern generation will be carried out. Lithography technology with high resolution and accuracy is required for patterning the photonic components on the desired material. When pushing the lateral dimension of a silicon nanowire waveguide down below half micron, the resolution of conventional I-Line (365nm) steppers is not sufficient. Deep ultra-violet (248nm) lithography has been adopted for fabrication of silicon nanowire waveguides (Bogaerts et al., 2005). The electron beam lithography (EBL) can also be employed, since its low running cost and ability to push the resolution further down to ~50nm. We ever use the Raith 150 EBL system for creating the patterns of Si nanowires. To increase the coupling efficiency, the width of each input waveguide can be tapered from 500 nm to 2  $\mu\text{m}$  through a 25  $\mu\text{m}$  long linear taper. Another write-field with size of 100 $\mu\text{m}$  is employed for these 2  $\mu\text{m}$  wide access waveguides.

E-beam resists are the recording and transfer media for EBL [8]. We can categorize them into two types, positive resists and negative resists. Now, a negative resist (ma-N 2405) is chosen and spined onto samples. The process for a resist is as follows:

Spinning at 3000 rpm-6000 rpm to obtain 500 nm-300 nm thin films;

Soft-bake on 90 °C for 3 minutes to drive out the solvent, and consolidate the film;

Exposure at 25kV with 120 $\mu\text{C}/\text{cm}^2$ ;

Developing with ma-D 532 for 3.5 minutes to form the pattern;

Stripping under O<sub>2</sub> plasma or acetone.

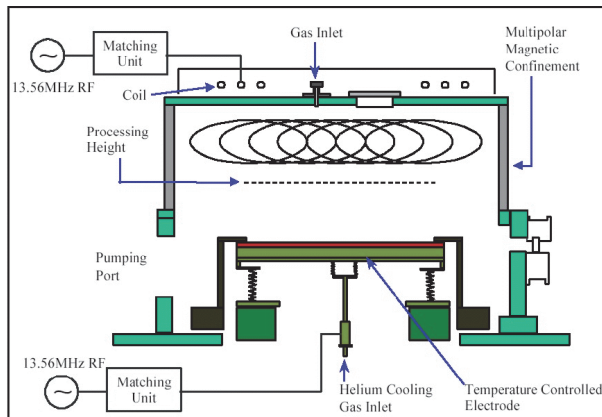


Fig. 4. Sketch of a ICP-RIE system

### 2.2.3 Pattern transfer

We always need to transfer the pattern from the resist onto the target silicon films. This can be achieved usually by etching technique. Reactive ion etching (RIE) technology has been widely adopted for etching semiconductors, dielectrics, and metals, due to its ability to achieve anisotropic, high-selectivity, and high-aspect-ratio etching. However, for the capacitively coupled systems of conventional RIE, the plasma density and energy of ions bombarding the substrate are correlated. By employing an inductively coupled plasma (ICP)-RIE system (see Figure 4), they can be adjusted separately. In this system, the RF

power on the coil is mainly responsible for the plasma density, while that on the platen controls the ion energy. In this thesis work, the samples were etched using ICP-RIE technology with the SF<sub>6</sub> and C<sub>4</sub>F<sub>8</sub> gas mixture, where C<sub>4</sub>F<sub>8</sub> is responsible for the carbon-fluorine polymer deposition to protect the sidewalls, and SF<sub>6</sub> is the main etching gas providing reactive F radicals. The corresponding process parameters are as follows: coil power is 500 W, platen power is 20 W, platen temperature is 20°C, pressure is 20 mTorr, and the flow rates of SF<sub>6</sub> and C<sub>4</sub>F<sub>8</sub> gas are 10 and 15 sccm, respectively. Then, a Si etching rate of ~220nm/min is obtained. After the etching process, the samples were baked at 110 °C for 30min in an oven just before etching. This helped to reduce the sidewall roughness.

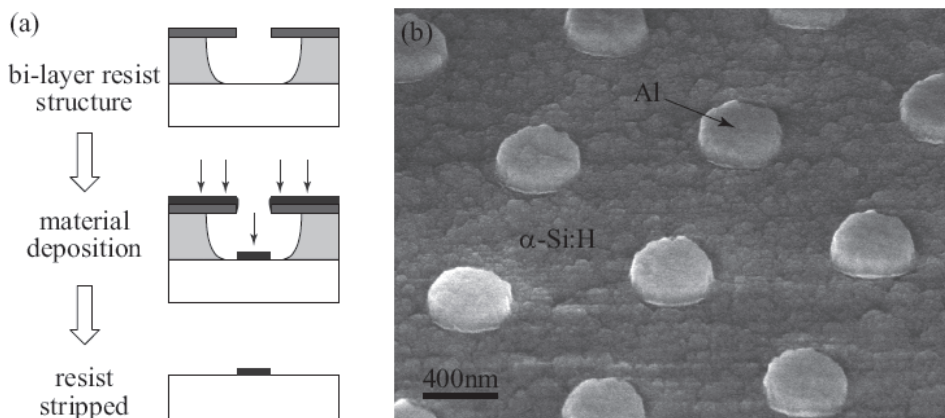


Fig. 5. Flow of the the lift-off process (a) and Fabricated structure of an Al hard mask on Si (b)

Depending on the material and some other aspects, several transfer steps might be needed (e.g., first transfer to a metal layer with lift-off, and then perform silicon etching). Figure 5 shows the typical flow of a lift-off process. A material is deposited onto the substrate usually with evaporation because of the high directivity of the incoming molecules. With the benefit of the undercut profile of the bi-layer resist structure, the material which is deposited on the substrate and on the resist is well separated. Then, the resist is washed away in a solvent, e.g., acetone or Remover 1165, usually with the aid of ultrasonic agitation. The material deposited on the resist is “lifted-off” from the substrate, while that deposited directly on the substrate remains. Note that the polarity of a pattern is also reversed (e.g., from a positive image to a negative image) in this case. Figure 5 (b) shows a fabricated structure with the lift-off process, where the pattern has been transfer to an Al layer, which will be used as a hard mask for the subsequent Si etching.

### 2.2.4 Measurements

Fabricated silicon-nanowire devices have to be carefully detected using a end-fire coupling setup. A typical end-fire coupling setup is mainly employed to test silicon photonic components as shown in Figure 6. An amplified spontaneous emission (ASE) source gives a broadband unpolarized light with spectral range 1530nm–1610nm. This unpolarized light is butt-coupled to the input waveguide of a component through a focusing gradient index

(GRIN) lens. The output light is collected with a microscope objective and split into two beams, one to an infrared (IR) camera, and the other to an optical spectrum analyzer (OSA) through a multi-mode fibre. Polarizers are inserted in front of the IR camera and the multi-mode fibre in order to separate the two polarizations.

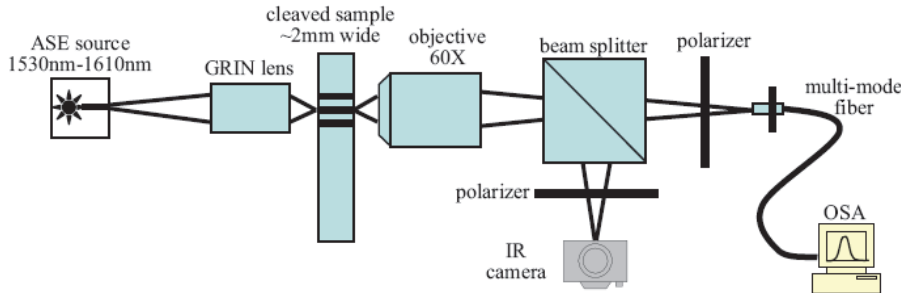


Fig. 6. Sketch of the end-fire characterization setup

### 3. Planar wavelength division multiplexers/demultiplexers based on silicon nanowires

As one of typical applications of silicon nanowire platforms, the chapter will review the recent progress of planar waveguide multiplexers/demultiplexers using Si-nanowire waveguides, including different improved designs and their effective applications in optical networks.

#### 3.1 Filter-type multiplexers/demultiplexers using silicon nanowire platforms

Several different approaches have been reported for wavelength multiplexer and demultiplexer on silicon platform. For a 1:  $N$  multiplexer or demultiplexer, if the channel number is not large (e.g.,  $N$  equals to 2, 4 and 8), planar filter including Mach-Zehnder interferometer (MZI) based interleaver and cascaded ring add/drop filters using high index contrast Si waveguide have the potential to make very compact multiplexer/demultiplexers with desirable optical performance. On the other hand, multiplexers based on AWG and EDG devices are typically large in size but low insertion loss, more desirable for multiple channel applications (e.g.,  $N$  equals to 16, 64 and 128). MZI filters with flat-top filter responses can contribute to large tolerances to fabricated waveguide width, operated laser wavelength and temperature deviations. Ultra-compact ring resonators based add/drop filters have the small pass band and large channel isolation.

##### 3.1.1 Multiplexers based on MZI filters

A typical MZI is shown in Figure 7(a). Two waveguides with a length difference of  $L$  connects  $L/8$ -long directional couplers, where  $L$  is the total length of the directional coupler in the MZI. The longer unbalanced interferometer arm consists of four curved and two straight sections. The shorter interferometer arm consists of four curved sections and one straight section. The same radius of curvature  $R$  and the same directional angle change  $\Theta$  are used for all curved waveguides. The length difference  $L$  is generated in the straight waveguide sections.

Four MZIs are connected to form four-stage MZI as shown in Figure 7(b). Flat-top filter responses are attained for both the cross- and bar-state wavelength bands using the four-stage MZI (Okayama et al., 2010). For a conventional planar waveguide demultiplexer, the shape of the spectral response is of Gaussian type. Therefore, the transmission efficiency is sensitive to a slight wavelength shift and the device is not suitable for high-speed modulation. These drawbacks limit the applications of planar waveguide demultiplexers of Gaussian type in WDM systems. A planar waveguide demultiplexer with a flattened spectral response is thus desirable. The calculated MZI filter response at -40 and 80 °C is shown in Figure 8. The real and dash lines mean two different beam polarizations respectively. A properly designed device can minimize the polarization sensitivity (Okayama et al., 2010).

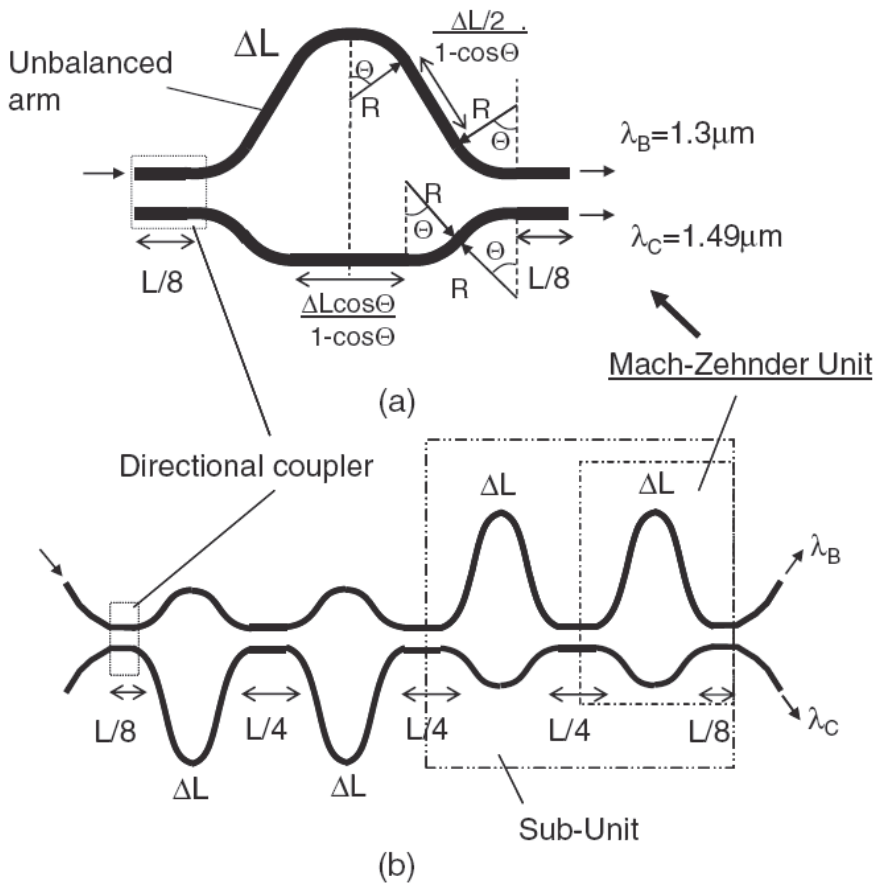


Fig. 7. Four-stage MZI filter: MZI unit (a) and four-stage filter structure constructed by cascaded MZI units (b)

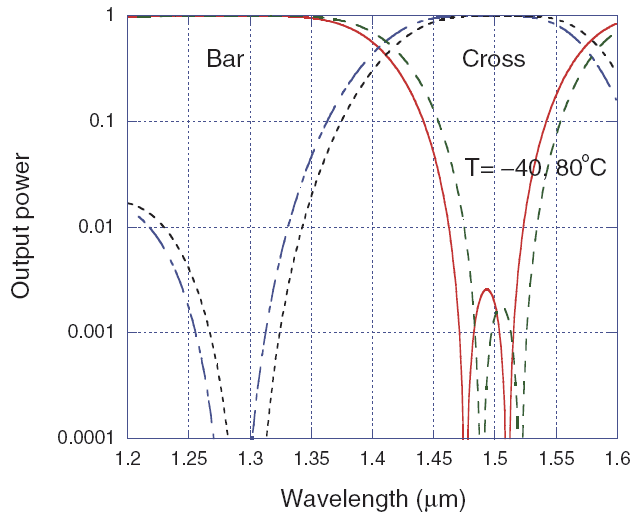


Fig. 8. Simulated spectrum response of four-stage MZI filter at different temperatures (Okayama et al., 2010)

Reconfigurable optical add-drop multiplexers (OADMs) are fundamental devices in WDM optical networks, since they can be used for dynamically wavelength routing and for replacing any failed OADM unit. MZI typed OADMs using silicon nanowires have also been proposed with Bragg-grating reflectors to tune the dropping wavelength through thermo-optic effect (Chu et al., 2006).

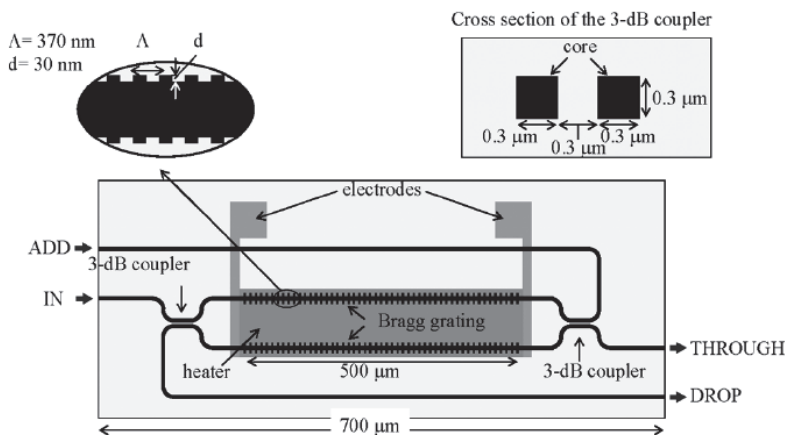


Fig. 9. Structure schematic of wavelength-tunable OADM (Chu et al., 2006)

The structure schematics of the fabricated tunable OADM are shown in Figure 9. It is composed using a MZI and two straight waveguides with Bragg-gratings-reflectors based on silicon nanowire platform. The Bragg gratings are formed by periodically making small fins ( $\sim 30$  nm size) on the side wall of the straight silicon photonic wire waveguides. Metal

thin-film heaters are arranged on the Bragg grating waveguides for thermo-optic control. By changing the heating current on the heaters, different wavelength channel can be dropped in the DROP port (see Figure 9).

### 3.1.2 Multiplexers based on ring-resonator filters

The ring resonator is one of the most suitable applications of Si nanowire waveguides with small bending radii (i.e., less than  $10\ \mu\text{m}$ ). Ring resonator coupled with two bus waveguides forms a 4-port add/drop filter device, as shown in Figure 10. For unit optical input at port 1, its through output is usually at port 2. However, the drop output can be at port 3 when the radius  $R$  of the ring waveguide has a strong resonance with the corresponding incident wavelength.

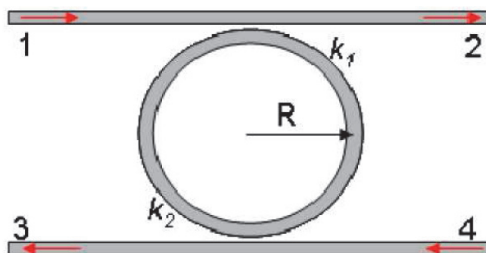


Fig. 10. Add/drop filter using ring resonator coupling with two bus waveguides

To make multi-channel multiplexers, multiple add/drop filters can be cascaded using rings slightly different in size. Figure 11 shows a four-channel wavelength add-drop filter using four ring resonators with different bend radii (6, 6.02, 6.04, and  $6.08\ \mu\text{m}$ ). However with this approach not only the resonance wavelength but also the free spectral range will vary (i.e., there is no linear relationship between the resonance wavelength and the change in radius). Therefore, the kind of multiplexers has the variable spectral band width for different channels (Bogaerts et al., 2006).

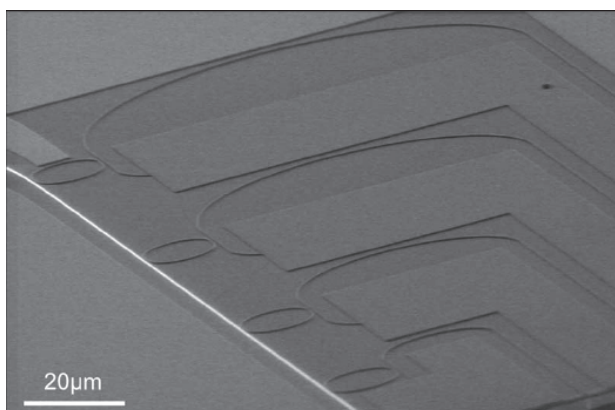


Fig. 11. Four-channel demultiplexer using ring resonators with different bend radius (Bogaerts et al., 2006)

Another fabricated 1x4 WDM multiplexer/demultiplexer with integrated thermal tuning is shown in Figure 12 (Zheng et al., 2010). Instead of using rings slightly different in size to achieve filters with different central wavelengths, identical rings with integrated thermal tuning are used. For better efficiency, the heater is directly integrated to the ring waveguide by doping part of the ring slab as doped resistor, as inset Scanning electron micrograph (SEM) picture shown in Figure 12. Injecting current to the doped resistors through the tuning pads, the ring waveguide can be heated up, and in turn the index of the waveguides are changed to shift the filter central wavelength until it's aligned with the target wavelength channel. Compared with the device shown in Figure 11, the 4-channel demultiplexer has a uniform 3dB pass band larger than 0.4 nm across all four channels.

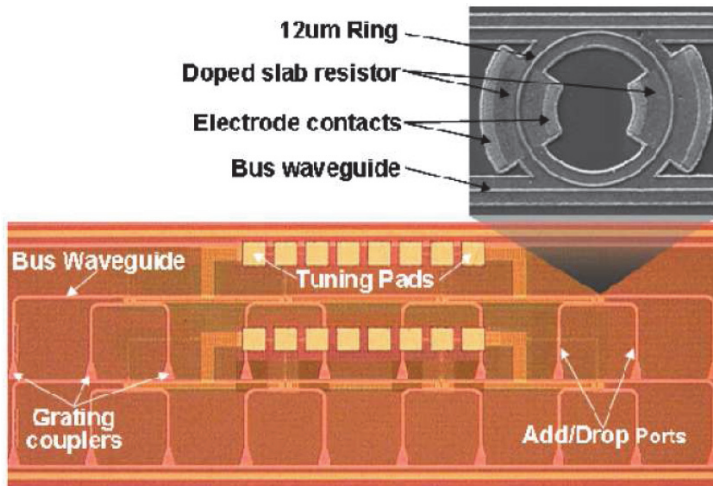


Fig. 12. Fabricated 1x4 multiplexer/demultiplexer by cascading 4 ring add/drop filters with integrated doped resistor thermal tuner (shown in the inset SEM picture) using FreeScale 130 nm CMOS process (Zheng et al., 2010)

### 3.2 Multiple-channel multiplexers/demultiplexers using silicon nanowire platform

Although planar filters are enough simple and effective for the applications of wavelength multiplexing and demultiplexing, they have to be cascaded to support multiple operated wavelength channels, which increase the insertion loss and the noise. AWGs and EDGs are two typical multiplexers/demultiplexers based on planar integrated optical waveguides, which can offer more than 40 channels of dense WDM.

#### 3.2.1 AWGs

Figure 13 shows a schematic representation of the AWG demultiplexer. The device consists of two star couplers, connected by a dispersive waveguide array. The operation principle is as follows. Light propagating in the input waveguide will be coupled into the array via the first star coupler, which is also known as free propagation region. The arrayed waveguides have different lengths. Specifically, the path length difference between adjacent waveguides is constant. The different wavelengths of the light experience different phase changes within

the arrayed waveguides. As a consequence, the field distribution at the input aperture will be reproduced at the output aperture. Therefore, at this wavelength, the light will focus in the center of the image plane (provided that the input waveguide is centered in the input plane).

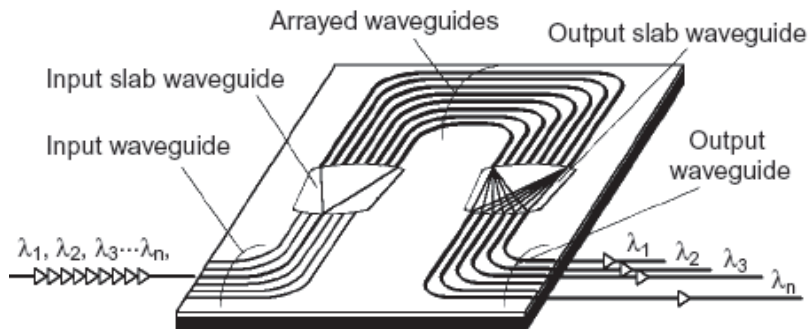


Fig. 13. Schematic configuration for an AWG demultiplexer

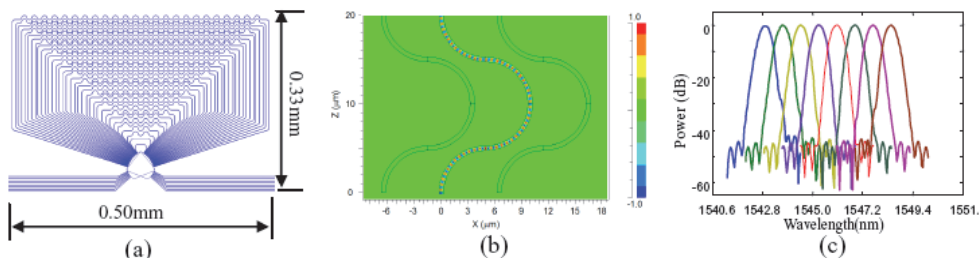


Fig. 14. AWG layout based on Si nanowire waveguides (a); light propagation in the microbends (b); the calculated spectral response (c) (Dai & He, 2006a)

As a design example, a design layout is shown in Figure 14 (a) based on Si nanowire waveguides, where the two free propagation regions are overlapped and a series of microbends are inserted at the middle of arrayed waveguides (Dai & He, 2006a). With such a microbend design the device size is minimized to only about 0.165mm<sup>2</sup>. Figure 14 (b) shows the light propagation in the microbends of the arrayed waveguides. From this figure, one sees that the coupling between arrayed waveguides is negligible even when the adjacent arrayed waveguides are placed very closely. This is due to the decoupling separation of Si nanowires is at the order of 2 μm. Figure 14 (c) shows the calculated spectral response (which does not include the coupling loss between the input/output waveguides and the fibres). From Figure 14(c), one sees that the calculated crosstalk is smaller than -30dB. The excess loss due to the inserted microbends in the arrayed waveguides is very small when the bending radius is large enough.

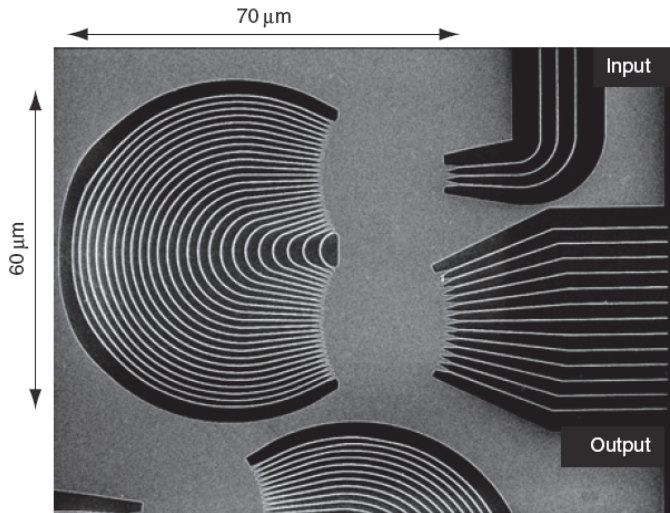


Fig. 15. SEM picture of a fabricated AWG based on Si nanowire platform (Sasaki et al., 2005)

Figure 15 shows a SEM picture of a fabricated AWG chip with only  $70 \times 60 \mu\text{m}^2$  size (Sasaki et al., 2005). The clear Gaussian spectrum is obtained with a channel spacing of 11 nm, a loss of less than 1 dB, adjacent channel crosstalk of  $\sim 13$  dB, and an oscillation by the Fabry-Perot resonance of 0.9 dB. In addition, the free spectral range is measured to be 92 nm, which is close to the theoretical value. The dimension of the Si nanowire AWG is 2-3 orders of magnitude smaller than conventional silica based AWG devices. However, the channel crosstalk is too large to satisfy a practical WDM application for the present silicon nanowire AWGs.

An improved design to reduce the channel crosstalk has been proposed by inserting a parabolic taper to expand the guided light beam without exciting higher-order modes (Ohno et al., 2006). Figure 16 shows the modal profile in the slab waveguide, provided that the taper length is  $3 \mu\text{m}$  and the taper width is taken as a parameter. Here, the profile is observed on an arc showing the best fit to the wavefront of the expanded beam. The best Gaussian-like beam is observed for taper width equals to  $1.48 \mu\text{m}$ , as shown in Figure 16. With the optimal design, the channel crosstalk can be reduced to -22 dB in the best spectrum.

For Si nanowire devices, owing to the difference in the propagation constants of the transverse electric (TE) and transverse magnetic (TM) modes in planar waveguides, the polarization sensitivity occurs in the spectral responses, which results in a shift in the spectral response peak of each wavelength channel. This wavelength shift is sensitive to the design of the planar waveguide, and can range from a few tenths of nanometers to a few nanometers. As WDM systems move toward closer and closer channel spacing, even a small polarization dependent wavelength shift becomes a severe problem.

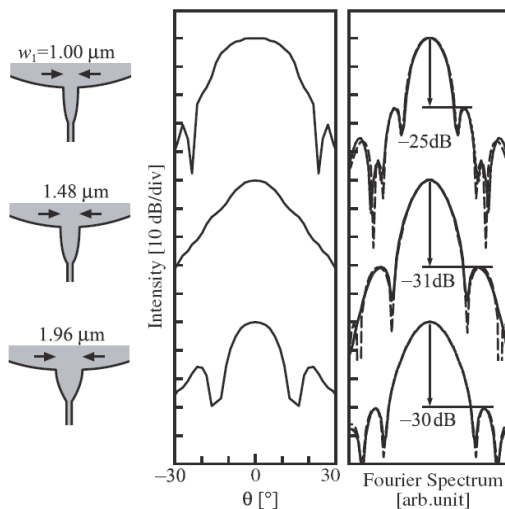


Fig. 16. Improved input waveguide to reduce the channel crosstalk of Si nanowire AWGs (Ohno et al., 2006)

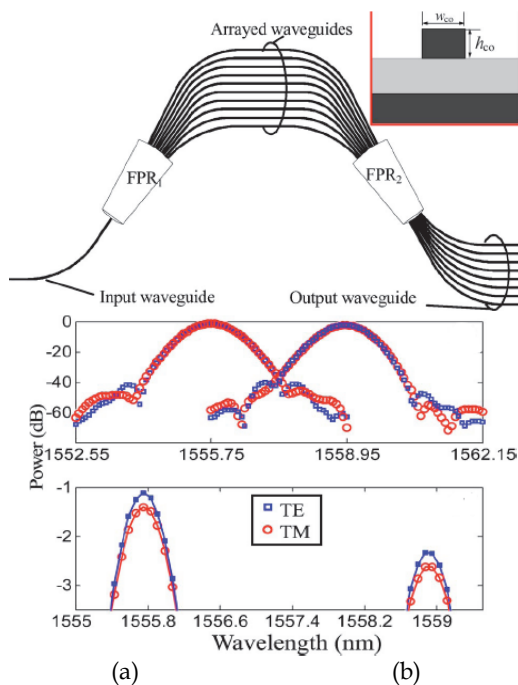


Fig. 17. Design of a polarization insensitive AWG demultiplexer based on silicon photonic wires: Schematic configuration for an AWG demultiplexer (a) and simulated spectral responses (TE and TM polarizations) of the designed low AWG for the central and edge channels (top figure), and enlarged view (bottom figure) (b) (Dai & He, 2006b)

A polarization insensitive design of AWG demultiplexers based on Si photonic wires has been presented (Dai & He, 2006b). By optimizing the height and width of the arrayed waveguides, the channel spacing becomes polarization insensitive. To reduce polarization dependent wavelength shift, different diffraction orders for the TE and TM polarizations are chosen. A non-central input has been used to eliminate the shift. The Si photonic wire with an air cladding is considered as an example, and the cross section is shown in the inset of Figure 17(a). When one chooses  $w_{co}=297$  nm and  $h_{co}=362$  nm, a maximal fabrication tolerance for the core width is obtained. By selecting different diffraction order for both polarizations ( $m_{TE}=61$  and  $m_{TM}=72$ ), one can obtain a low polarization shift. The simulated spectral responses are shown in Figure 17 (b), from which one sees that the peaks of the spectral responses for the TE and TM polarizations are almost the same. This indicates that both the channel spacing and channel wavelengths are polarization insensitive, as predicted.

### 3.2.2 EDGs

EDG demultiplexers, which integrate the function of a flat grating and a focal lens, can image the input field while dispersing the wavelengths. The Rowland circle structure for a concave grating is one of the most popular configurations for a spectrometer, and has been adopted in an EDG demultiplexer for DWDM applications. Although an EDG demultiplexer is more difficult to fabricate (mainly in the deep etching of the grating facets), it is more compact than an AWG and potentially has a higher spectral finesse (since the total number of the grating facets of an EDG can be much greater than the total number of the arrayed waveguides in an AWG with the modern semiconductor fabrication technology). Unlike in a conventional AWG, the input and output waveguides in an EDG can be arranged at the same side facing the grating, and this allows a low-cost single-side packaging of the chip.

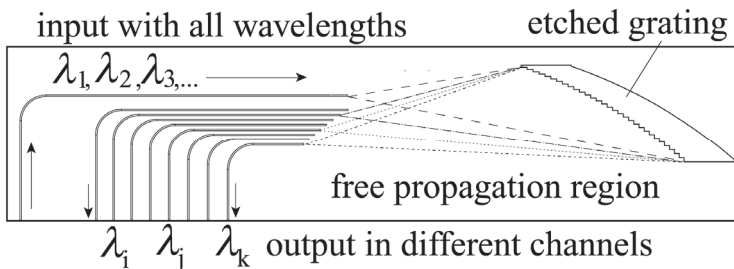


Fig. 18. Schematic diagram of an EDG demultiplexer

An EDG based on a Rowland mounting is illustrated in Figure 18. The field propagating from an input waveguide to the free propagation region is diffracted by each grating facet. It is then refocused onto an imaging curve and guided into the corresponding output waveguides according to the wavelengths. The grating of an EDG demultiplexer is usually coated with a metal (e.g., Au) at the backside in order to enhance the reflection efficiency. In order to reduce reflection loss without the additional processing steps required to coat the back of the grating facets with a reflecting metal coating, a retro-reflecting V-shaped facet was used at each grating tooth. A SEM photograph of the etched grating based on silicon nanowire platforms is shown in Figure 19. In this design light hits each grating facet at about  $45^\circ$  incidences producing total internal reflection (Song & Ding, 2009).

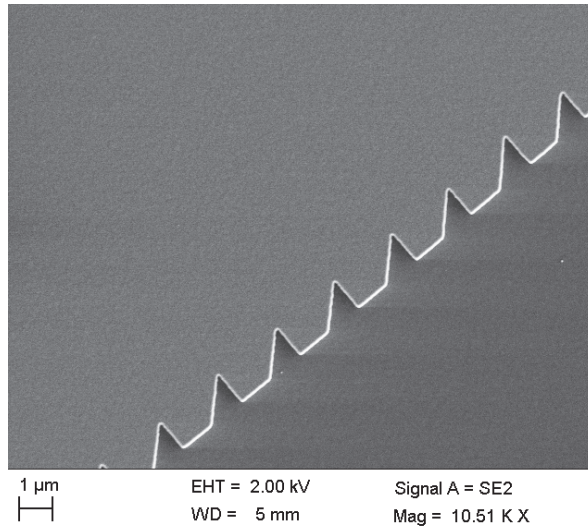


Fig. 19. SEM photograph of a section of the etched grating showing the retro-reflecting V-shaped facets (Song & Ding, 2009)

An EDG demultiplexer based on commercially available silicon-on-insulator (SOI) wafer was recently studied with good performances (Brouckaert et al., 2010). Figure 20 shows the fabricated demultiplexer on a nanophotonic SOI platform using standard wafer scale CMOS processes including deep-UV lithography. The device has four wavelength channels with a channel spacing of 20 nm and a record-small footprint of  $280 \times 150 \mu\text{m}^2$ .

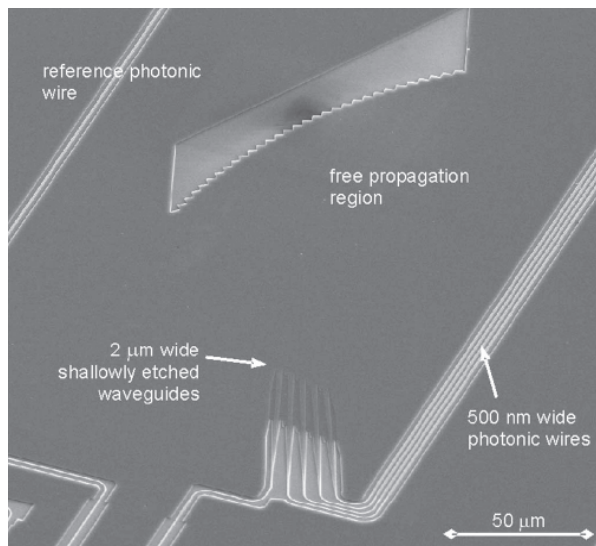


Fig. 20. SEM picture of  $1 \times 4$  EDG demultiplexer using nanophotonic SOI platform (Brouckaert et al., 2010)

Except the commercial SOI platform, the amorphous-Si ( $\alpha$ -Si) is the other important material for nanowire waveguide devices. Although the loss is larger due to the large scattering loss of  $\alpha$ -Si waveguides than commercial a SOI wafer, this technology is more versatile since thickness and refractive indices can be adjusted in some range to fit some special requirements and designs. The fabrication process can also be optimized to obtain high quality and high precision. Figure 21 shows a fabricated EDG picture based on  $\alpha$ -Si-on-SiO<sub>2</sub> instead of commercial SOI wafers (Song & Ding, 2010a).

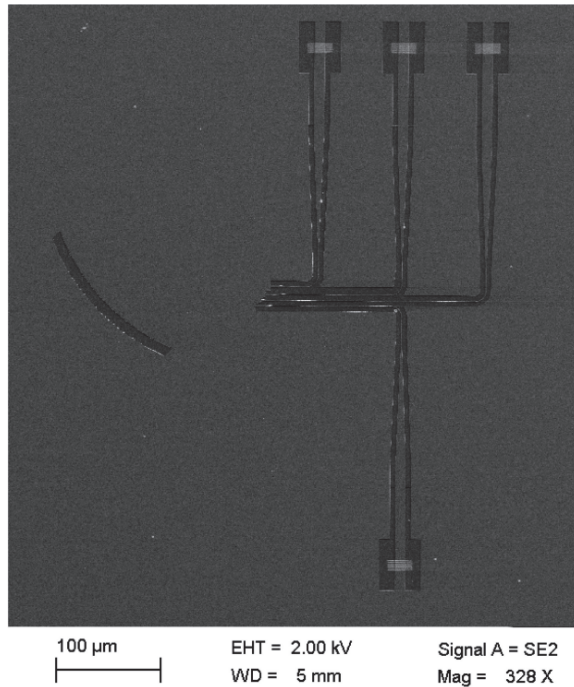


Fig. 21. SEM picture of an EDG demultiplexer using nanophotonic amorphous-Si platform (Song & Ding, 2010a)

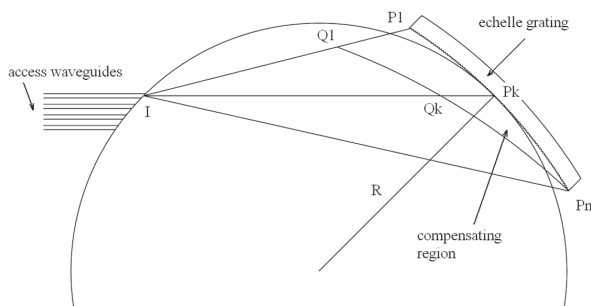


Fig. 22. A schematic show of an EDG, the polarization compensation region is  $Q_1P_1P_n$ , where  $n$  is the total number of the grating facets,  $I$  is the incident point (Zhu et al., 2008).

The performances of multiplexers based on both silicon nanowire materials are influenced by the large polarization dependent wavelength shift. The method shown in Figure 22 has effectively been used for the polarization compensation of AWGs. However, the same method can not be used for the case of EDGs. For an EDG demultiplexer, there exists a simple free propagation region (a 2D-slab). No other design freedom can be used to compensate the birefringence in the only free propagation region. Recently, by integrating a prism-like polarization compensator in the slab waveguide region adjacent to the grating, one can also obtain a low polarization sensitivity of the design for EDG demultiplexers (Zhu et al., 2008). The same method is also effective for an AWG case. A schematic of the polarization compensated waveguide demultiplexer based on an etched diffraction grating is presented in Figure 22. The polarization compensator consists of a prism-shaped region, which has different effective indexes (for both TE and TM modes) from those of the slab waveguide surrounding it. It can be realized by shallow etching in the same process step as that used to define the single mode ridge waveguides. Thus, no additional processing steps are required. The shape of this area can be optimized to compensate the birefringence in the large free propagation region.

EDG demultiplexers based on conventional waveguide platforms have usually large grating facets, which are advantageous to lowering the manufacturing difficulty. Therefore, we can easily obtain a lower than 30 dB sidelobe level for conventional fabricated EDGs. However, all fabricated EDG demultiplexers using silicon nanowire technology have the sidelobe level from 10 dB to 15 dB due to their sub-wavelength facet size, which leads too high noise floors to satisfy practical WDM requirements. A low sidelobe design has been proposed using Fourier analysis to lightly modulate the size and structure of each retro-reflecting V-shaped facet (Song & Ding, 2010b).

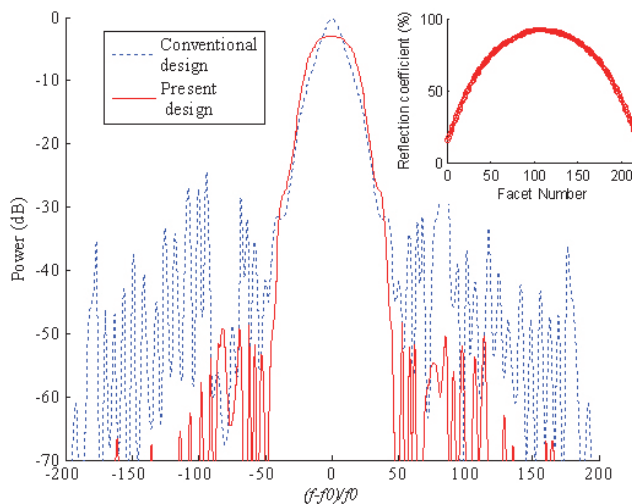


Fig. 23. Spectral responses at the central channel using the conventional and improved design (Song & Ding, 2010b)

Figure 23 shows the spectral responses of the central channel using both the conventional and improved design. Final reflection coefficient for each facet is also shown in the upper-right corner in Figure 23. Due to the effect of the concave grating using the conventional design, the image field distribution near each output waveguide will expand larger sidelobes into the two adjacent waveguides, which results in a large noise floor for the spectral response (see Figure 23). Suppressing crosstalk as small as 30 dB is usually considered inside specifications for telecommunication. In the fabrication process, some technical factors (e.g., writing resolution of photomasks) will also deteriorate the crosstalk performance for an EDG demultiplexer. Therefore, it is of necessity that suppressing crosstalk to less than 50 dB in theory to give an enough space for some fabrication errors. From Figure 23, one can see that the sidelobes using the design by modulating the transfer function into a Gaussian distribution can keep to less than -50 dB. However, the present design also results in an extra loss for the operational spectrum. For the central channel, the additional loss using the low noise floor design is about 2.6 dB. As shown in the upper-right corner in Figure 23, the additional loss results from the process of Gaussian apodization. Therefore, it is possible to reduce significantly the loss with a slightly more generous sidelobe suppression requirement.

#### 4. Conclusion

This chapter has reviewed the recent progress of silicon nanowire waveguide devices and its applications in planar waveguide multiplexers/demultiplexers, including main structures and their different improved designs. The characteristics of Si photonic wire waveguides and ultrasmall optical devices fabricated with this waveguide structure have been described. As application examples, very compact wavelength-selective functions in silicon nanowire platforms have been demonstrated. These include MZI filters, ring resonators, AWGs and EDGs. A few MZI filters are cascaded to attain a flat-top filter response. Micro-ring resonators are easily used to design reconfigurable optical add-drop multiplexer with low-power-consumption, highly flexible and ultra-compact size. AWGs and EDGs are two types of the key components for constructing flexible and large capacity optical networks. We have described their operation principle. Some design examples for Si-nanowire-base AWGs have also been introduced to meet the urgent demand of the size-reduction and increase the scale of planar devices. Some designs for achieving low crosstalk and polarization independence have been reviewed in detail in this chapter.

#### 5. Acknowledgment

Parts of works in the chapter are supported by National Natural Science Foundation of China (No. 61007032); Natural Science Foundation of Guangdong Province, China (No. 10451806001005352) and Special Foundation for Young Scientists of Guangdong Province, China (No. LYM10115).

The section of the fabrication of silicon nanowires is carried out at the Department of Microelectronics and Applied Physics, Royal Institute of Technology (Sweden).

#### 6. References

Belotti M.; Galli M.; Gerace D.; Andreani L.C.; Guizzetti G.; Zain A.R.M.; Johnson N.P.; Sorel M. & De la Rue R.M. (2010). All-optical switching in silicon-on-insulator photonic

- wire nano-cavities. *Opt. Express*, Vol.18, No.2, (January 2010), pp. 1450-1461, ISSN 1094-4087
- Bogaerts W.; Baets R.; Dumon P.; Wiaux V.; Beckx S.; Taillaert D.; Luyseart B.; Van Campenhout J.; Bienstman P. & Van Thourhout D. (2005). Nanophotonic waveguides in silicon-on-insulator fabricated with CMOS technology. *J. Lightwave Technol.*, Vol.23, No.1, (January 2005), pp. 401-412, ISSN 0733-8724
- Bogaerts W.; Dumon P.; Thourhout D.V.; Taillaert D.; Jaenen P.; Wouters J.; Beckx S.; Wiaux V. & Baets R.G. (2006). Compact wavelength-selective functions in silicon-on-insulator photonic wires. *IEEE J. Select. Topics in Quantum Electron.*, Vol.12, No.6, (November 2006), pp. 1394-1401, ISSN 1077-260X
- Brouckaert J. B.; Bogaerts W.; Dumon P.; Thourhout D. V. & Baets R. (2007). Planar concave grating demultiplexer fabricated on a nanophotonic silicon-on-insulator platform. *IEEE Photon. Technol. Lett.*, Vol.19, No.5, (March 2007), pp. 1269-1271, ISSN 1041-1135
- Chu T.; Yamada H.; Ishida S. & Arakawa Y. (2006). Tunable optical add-drop multiplexer based on silicon photonic wire waveguides. *IEEE Photon. Technol. Lett.*, Vol.18, No.13, (July 2006), pp. 1409-1411, ISSN 1041-1135
- Cremer C.; Ebbinghaus G.; Heise G.; Muller-Nawrath R.; Schienle M. & Stoll L. (1996). Grating spectrograph in InGaAsP/InP for dense wavelength division multiplexing. *Appl. Phys. Lett.*, Vol.59, No.6, (August 1991), pp. 627-629, ISSN 0034-6748
- Dai D.X. & He S. (2006a). Novel ultracompact Si-nanowire-based arrayed waveguide grating with microbends. *Opt. Express*, Vol.14, No.12, (June 2006), pp. 5260-5265, ISSN 1094-4087
- Dai D.X. & He S. (2006b). Design of a polarization-insensitive arrayed waveguide grating demultiplexer based on silicon photonic wires. *Opt. Lett.*, Vol.31, No.13, (July 2001), pp. 1988-1990, ISSN 0146-9592
- Fukuda H.; Watanabe T.; Takahashi J.; Takahashi M.; Shoji T.; Tamechika E.; Itabashi S.; Tsuchizawa T.; Yamada K. & Morita H. (2005). Microphotonic devices based on silicon microfabrication technology. *IEEE J. Select. Topics in Quantum Electron.*, Vol.11, No.1, (January 2005), pp. 232-240, ISSN 1077-260X
- Hattori J.; Uno S.; Nakazato K. & Mori N. (2010). Scaling consideration and compact model of electron scattering enhancement due to acoustic phonon modulation in an ultrafine free-standing cylindrical semiconductor nanowire. *J. of Applied Physics*, Vol.107, No.3, (February 2010), pp. 033712 1-7, ISSN 0021-8979
- Lee K. K.; Lim D. R. & Kimerling L. C. (2001). Fabrication of ultralow-loss Si/SiO<sub>2</sub> waveguides by roughness reduction. *Opt. Lett.*, Vol.26, No.23, (December 2001), pp. 1888-1890, ISSN 0146-9592
- Ohno F.; Sasaki K.; Motegi A. & Baba T. (2006). Reduction in sidelobe level in ultracompact arrayed waveguide grating demultiplexer based on Si wire waveguide. *Jpn. J. Appl. Phys.*, Vol.45, No.8A, (August 2006), pp. 6126-6131, ISSN 0021-4922
- Okayama H.; Kotani K.; Maeno Y.; Shimura D.; Yaegashi H. & Ogawa Y. (2010). Design of polarization-independent Si-wire-waveguide wavelength demultiplexer for optical network unit. *Jpn. J. Appl. Phys.*, Vol.49, No.4, (April 2010), pp. 04DG19-1-5, ISSN 0021-4922
- Pavesi L. & Lockwood D. J. (2004). *Silicon Photonics*, Springer, ISBN 978-3-540-21022-1, Berlin, Germany

- Rong H.; Liu A.; Jones R.; Cohen O.; Hak D.; Nicolaescu R.; Fang A. & Paniccia M. (2005). An all-silicon Raman laser. *Nature*, Vol.433, No.2, (January 2005), pp. 292-294, ISSN 0028-0836
- Rue R. D. L.; Chong H., Gnan M.; Johnson N.; Ntaklis I.; Pottier P.; Sorel M.; Zain A. M.; Zhang H.; Camargo E.; Jin C.; Armenise M. & Ciminelli G. (2006). Photonic crystal and photonic wire nano-photonics based on silicon-on-insulator. *New J. Phys.*, Vol.8, No.10, (October 2006), pp. 256-262, ISSN 1367-2630
- Sasaki K.; Ohno F.; Motegi A. & Baba T. (2005). Arrayed waveguide grating of  $70 \times 60 \mu\text{m}^2$  size based on Si photonic wire waveguides. *Electron. Lett.*, Vol.41, No.14, (July 2005), pp. 1514-1515, ISSN 0013-5194
- Schul R. J. and Pearton S. J. (2000). *Handbook of advanced Plasma Processing Techniques*, Springer, ISBN 978-3-540-66772-8, Berlin, Germany
- Smit M. K. & Dam C. V. (1996). Phasar-based WDM-devices: principles, design and applications. *IEEE J. Select. Topics in Quantum Electron.*, Vol.2, No.2, (June 1996), pp. 236-250, ISSN 1077-260X
- Song J. & Ding J. (2009). Amorphous-Si based planar grating demultiplexers with total internal reflection grooves. *Electron. Lett.*, Vol.45, No.17, (July 2009), pp. 905-906, ISSN 0013-5194
- Song J. & Ding J. (2010a). Ultra-compact planar grating multiplexers using silicon platforms. *Fiber and Integrated Optics*, Vol.29, No.5, (September 2010), pp. 431-440, ISSN 0146-8030
- Song J. & Ding J. (2010b). Analytical design of total-internal-reflection grating demultiplexers with a low noise floor. *IEEE Photon. Technol. Lett.*, Vol.22, No.16, (August 2010), pp. 1229-1231, ISSN 1041-1135
- Taillaert D. (2004). *Grating couplers as Interface between Optical Fibres and Nanophotonic Waveguides*, PhD Thesis, (June 2004), Ghent University, Belgium
- Thylén L., He S. ; Wosinski L. & Dai D. (2006). Moore's law for photonic integrated circuits. *J. Zhejiang Univ. SCI.*, Vol.7, No.12, (December 2006), pp. 1961-1967, ISSN 1673-1581
- Yamada K.; Shoji T.; Tsuchizawa T.; Watanabe T.; Takahashi J. & Itabashi S. (2003). Silicon-wire-based ultrasmall lattice filters with wide free spectral ranges. *Opt. Lett.*, Vol.28, No.18, (September 2003), pp. 1663-1664, ISSN 0146-9592
- Zheng X.; Shubin I.; Li G.; Pinguet T.; Mekis A.; Yao J.; Thacker H.; Luo Y.; Costa J.; Raj K.; Cunningham J.E. & Krishnamoorthy A.U. (2010). A tunable  $1 \times 4$  silicon CMOS photonic wavelength multiplexer/demultiplexer for dense optical interconnects. *Opt. Express*, Vol.18, No.5, (March 2010), pp. 5151-5160, ISSN 1094-4087
- Zhu N.; Song J.; Wosinski L. & He S. (2008). Design of a polarization insensitive echelle grating demultiplexer based on silicon nanophotonic wires. *IEEE Photon. Technol. Lett.*, Vol.20, No.10, (May 2008), pp. 860-862, ISSN 1041-1135

# Four-Wave Mixing in Silicon Nanowire Waveguides and Its Applications in Wavelength Conversion

Shiming Gao and Sailing He  
*Centre for Optical and Electromagnetic Research,  
State Key Laboratory of Modern Optical Instrumentation,  
Zhejiang University, Hangzhou,  
China*

## 1. Introduction

In recent years, silicon photonics has been considered as a new promising technology platform for low-cost optical communications and interconnects. Silicon photonic devices can be fabricated using existing semiconductor techniques. It has the possibility to integrate optical and electronic components onto a single microchip since silicon is already used as the substrate for most integrated circuits. Silicon nanowire waveguides based on silicon-on-insulator techniques have exhibited the high-density integration of optical circuits due to the strong light confinement from its high refractive-index contrast. Nowadays, the silicon nanowire waveguides can be easily fabricated with the accuracy of nanometer and the power density is higher than that of the conventional single-mode fiber by a factor of about 1000 (Fukuda et al., 2005). Therefore, nonlinear optical effects will easily occur although a low input power is used. On the other hand, the nonlinear Kerr coefficient of silicon is still high, which strengthens the nonlinear ability of silicon nanowire waveguides. Many kinds of nonlinear effects, such as self-phase modulation, cross-phase modulation, stimulated Raman scattering, two-photon absorption (TPA), and four-wave mixing (FWM), have been observed in silicon nanowire waveguides, and have been used to realize silicon Raman lasers (Boyraz & Jalali, 2004), Raman amplifiers (Liang & Tsang, 2004), all-optical switches (Almeida et al., 2004), logical gates (Liang et al., 2006), parametric amplifiers (Foster et al., 2006), and wavelength converters (Rong et al., 2006).

In particular, wavelength conversion is an essential operation in wavelength-routing wavelength division multiplexing networks and FWM in silicon nanowire waveguides has been regarded as a promising alternative due to the all-optical and strictly transparent characteristics, etc. Wavelength conversion has been realized in silicon nanowire waveguides using coherent anti-Stokes Raman scattering (Raghunathan et al., 2005) or nonresonant electronic response FWM (Lin et al., 2006). For a real-life wavelength converter, conversion efficiency and bandwidth are two important figures of merit. In addition, polarization dependency will also influence the performance of wavelength converters. Different from the wavelength conversion in optical fibers, the nonlinear losses due to TPA and TPA-induced free-carrier absorption (FCA) will greatly affect the conversion efficiency in silicon nanowire waveguides (Sang & Boyraz, 2008), especially where the FCA effect is quadratically proportional to the incident power.

In this chapter, the theoretical model of FWM in silicon nanowire waveguides will be introduced by taking into account all the factors including self-phase modulation, cross-phase modulation, TPA, and TPA-induced FCA. The progresses on the bandwidth enhancement will be reviewed by engineering the dispersion profile of the silicon nanowire waveguide through changing the waveguide geometry or designing special waveguide structures, as the phase-matching condition of the FWM effect is tightly dominated by the waveguide dispersion. Also, the bandwidth can be enhanced by introducing two-pump regimes and realizing wavelength conversion via nondegenerate FWM. FWM based wavelength conversion is tightly related to the state of polarization (SOP) of the input signal with respect to the pump. In particular, no converted signal can be generated if they are polarized orthogonally to each other. The realization of polarization independency of wavelength conversion in silicon nanowire waveguides will also be reviewed to eliminate the influence of the polarization of the input signal wave.

## 2. Theoretical model of FWM in silicon nanowire waveguides

FWM in silicon nanowire waveguides can be classified as degenerate and nondegenerate FWMs according to the number of the incident pumps. Degenerate FWM efficiently occurs when a single pump wave  $\lambda_p$  is injected into a silicon nanowire waveguide together with a signal wave  $\lambda_s$  when the phase-matching condition is well satisfied. A converted wave  $\lambda_c$  is generated under the energy conservation condition  $1/\lambda_c = 2/\lambda_p - 1/\lambda_s$ . By taking the linear propagation loss, TPA, and FCA into account, the coupled equations for the FWM process under the continuous wave or quasi-continuous wave assumption can be expressed as (Zhang et al., 2009)

$$\frac{dA_p}{dz} = -\frac{1}{2}(\alpha_p + \alpha_{TPAp} + \alpha_{FCAp})A_p + j\gamma_p \left[ |A_p|^2 + 2|A_s|^2 + 2|A_c|^2 \right] A_p + 2j\gamma_p A_p^* A_s A_c \exp(j\Delta\beta z) \quad (1)$$

$$\frac{dA_s}{dz} = -\frac{1}{2}(\alpha_s + \alpha_{TPAs} + \alpha_{FCA_s})A_s + j\gamma_s \left[ 2|A_p|^2 + |A_s|^2 + 2|A_c|^2 \right] A_s + j\gamma_s A_s^* A_p^2 \exp(-j\Delta\beta z) \quad (2)$$

$$\frac{dA_c}{dz} = -\frac{1}{2}(\alpha_c + \alpha_{TPAc} + \alpha_{FCAc})A_c + j\gamma_c \left[ 2|A_p|^2 + 2|A_s|^2 + |A_c|^2 \right] A_c + j\gamma_c A_s^* A_p^2 \exp(-j\Delta\beta z) \quad (3)$$

For the nondegenerate FWM, two pumps  $\lambda_{p1}$  and  $\lambda_{p2}$  are injected into the silicon nanowire waveguide together with the signal  $\lambda_s$ . A converted wave  $\lambda_c$  is generated at  $1/\lambda_c = 1/\lambda_{p1} + 1/\lambda_{p2} - 1/\lambda_s$ . The coupled equations can be expressed as (Gao et al., 2010)

$$\begin{aligned} \frac{dA_{p1}}{dz} = & -\frac{1}{2}(\alpha_{p1} + \alpha_{TPAp1} + \alpha_{FCAp1})A_{p1} + j\gamma_{p1} \left[ |A_{p1}|^2 + 2|A_{p2}|^2 + 2|A_s|^2 + 2|A_c|^2 \right] A_{p1} \\ & + 2j\gamma_{p1} A_{p2}^* A_s A_c \exp(j\Delta\beta z) \end{aligned} \quad (4)$$

$$\begin{aligned} \frac{dA_{p2}}{dz} = & -\frac{1}{2}(\alpha_{p2} + \alpha_{TPAp2} + \alpha_{FCAp2})A_{p2} + j\gamma_{p2} \left[ 2|A_{p1}|^2 + |A_{p2}|^2 + 2|A_s|^2 + 2|A_c|^2 \right] A_{p2} \\ & + 2j\gamma_{p2} A_{p1}^* A_s A_c \exp(j\Delta\beta z) \end{aligned} \quad (5)$$

$$\frac{dA_s}{dz} = -\frac{1}{2}(\alpha_s + \alpha_{TPAs} + \alpha_{FCAs})A_s + j\gamma_s \left[ 2|A_{p1}|^2 + 2|A_{p2}|^2 + |A_s|^2 + 2|A_c|^2 \right] A_s + 2j\gamma_s A_c^* A_{p1} A_{p2} \exp(-j\Delta\beta z) \quad (6)$$

$$\frac{dA_c}{dz} = -\frac{1}{2}(\alpha_c + \alpha_{TPAc} + \alpha_{FCAc})A_c + j\gamma_c \left[ 2|A_{p1}|^2 + 2|A_{p2}|^2 + 2|A_s|^2 + |A_c|^2 \right] A_c + 2j\gamma_c A_s^* A_{p1} A_{p2} \exp(-j\Delta\beta z) \quad (7)$$

In Eqs. (1)-(7),  $A_{p,p1,p2,s,c}(z)$  are the amplitudes of the pumps, the signal, and the converted waves,  $\gamma_{p,p1,p2,s,c}$  are the nonlinear coefficients,  $\Delta\beta$  is the linear phase mismatch,  $a_{p,p1,p2,s,c}$  are the linear-loss coefficients,  $a_{TPAp,p1,p2,s,c}$  and  $a_{FCAp,p1,p2,s,c}$  are the nonlinear-loss coefficients caused by the TPA and FCA effects. Mathematically the loss coefficients induced by TPA and FCA can be expressed as

$$\alpha_{TPAi} = \frac{\beta_{TPA}}{A_{eff}} \left( |A_i|^2 + 2 \sum_{m \neq i} |A_m|^2 \right),$$

$$(i, m = p, s, c \text{ for single-pump FWM}; i, m = p1, p2, s, c \text{ for two-pump FWM}) \quad (8)$$

$$\alpha_{FCAi} = \frac{\sigma_i \beta_{TPA} \tau}{2hc A_{eff}^2} \left( \sum_m \lambda_m |A_m|^4 + 4 \sum_{m \neq n} \frac{\lambda_m \lambda_n |A_m|^2 |A_n|^2}{\lambda_m + \lambda_n} \right),$$

$$(i, m = p, s, c \text{ for single-pump FWM}; i, m = p1, p2, s, c \text{ for two-pump FWM}) \quad (9)$$

where  $\sigma_{p,p1,p2,s,c}$  are the FCA cross sections.

Denoting the nonlinear index coefficient of silicon as  $n_2$ , the nonlinear coefficients for the involved waves can be calculated as

$$\gamma_i = 2\pi n_2 / \lambda_i A_{eff}, \quad (i = p, p1, p2, s, c) \quad (10)$$

Since all the involved waves are in the same wavelength region, it is reasonable to consider  $a_{p,p1,p2,s,c} = a$ ,  $\sigma_{p,p1,p2,s,c} = \sigma$ , and  $\gamma_{p,p1,p2,s,c} = \gamma$ . Supposing  $P_{p,p1,p2,s,c} = |A_{p,p1,p2,s,c}|^2$  the phase mismatch can be reduced to a simple expression for single-pump FWM (Foster et al., 2007):

$$\kappa_d = \Delta\beta + 2\gamma P_p = \beta_s + \beta_c - 2\beta_p + 2\gamma P_p \quad (11)$$

And for the two-pump FWM:

$$\kappa_{nd} = \Delta\beta + \gamma(P_{p1} + P_{p2}) = \beta_s + \beta_c - \beta_{p1} - \beta_{p2} + \gamma(P_{p1} + P_{p2}) \quad (12)$$

where  $\beta_{p,p1,p2,s,c}$  are the wave numbers of the interacting waves.

In lossy cases and saturation regimes only numerical solutions are available for Eqs. (1)-(3) or Eqs. (4)-(7). In particular the solution to Eq. (3) or Eq. (7) leads to the definition of the conversion efficiency and the conversion bandwidth. The calculation of conversion efficiency, which is defined as

$$\eta(\text{dB}) = 10 \log_{10} [P_c(z) / P_s(0)] \quad (13)$$

provides an easy solution to the determination of the conversion bandwidth after solving the coupled equations numerically.

### 3. Wavelength conversion based on FWM in silicon nanowire waveguides

FWM is considered to be an effective way to realize all-optical and strictly transparent wavelength conversion. In this section, the applications of FWM in silicon nanowire waveguides on wavelength conversion will be introduced, including bandwidth enhancement, efficiency improvement, and polarization independency.

#### 3.1 Bandwidth enhancement and efficiency improvement of FWM-based wavelength conversion

Conversion bandwidth and efficiency are two important performances for wavelength conversion in dense wavelength division multiplexing systems. For FWM-based wavelength conversion, the conversion bandwidth is dominated by the phase-matching condition. Since the phase mismatch is effectively changed by the dispersion profile and the pump wavelength setting, it is reasonable to realize broadband wavelength conversion through dispersion engineering or two-pump regime.

##### 3.1.1 Optimization of waveguide geometry

The conversion bandwidth is dominated by the dispersion property of the waveguide since it determines the linear phase mismatch of the involved waves. The linear phase mismatch can be considered as the contribution of two parts: one is the material dispersion, which is large and normal within the telecommunication wavelength range; and the other is the waveguide dispersion, which can vary from anomalous to normal by adjusting the waveguide dimensions (Turner et al., 2006). Considering a silicon channel waveguide, Fig. 1 shows the values of the zero-dispersion wavelength (ZDW) corresponding to different waveguide sizes. Generally, there are two ZDWs in the entire wavelength region and both of them shift to the long wavelength for TE mode as the waveguide dimensions increase. For TM mode, the left ZDW shifts first to the short and then to the long wavelength and the right ZDW keeps increasing as the waveguide dimensions increase. Figures 1(a) and 1(b) show the distribution of the left and the right ZDWs for TE mode in terms of the waveguide dimensions, respectively. Figures 1(c) and 1(d) are for TM mode. The available wavelength range is considered from 1300 to 2000 nm (shown as the colorful zone in Fig. 1). The white zone in Fig. 1 indicates that there is no ZDW within this wavelength range.

In order to avoid the influence of higher-order modes on the FWM process, the nanowire waveguide is required to be of single mode. The single-mode condition for the waveguides at a specific wavelength of 1550 nm is numerically analyzed by using the semi-vectorial beam propagation method. To obtain the single-mode condition, one can scan the height and width of the silicon nanowire waveguide and judge whether higher-order modes exist. For a fixed height we reduce the width with a step of 5 nm until all the higher-order modes disappear. The calculated results are also shown in Fig. 1. The solid curves indicate the critical boundaries of single mode for TE mode in Figs. 1(a) and 1(b), and the curves are for TM mode in Figs. 1(c) and 1(d). The single-mode region is on the left-bottom side of the curve and the multi-mode region is on the right-top side in each figure.

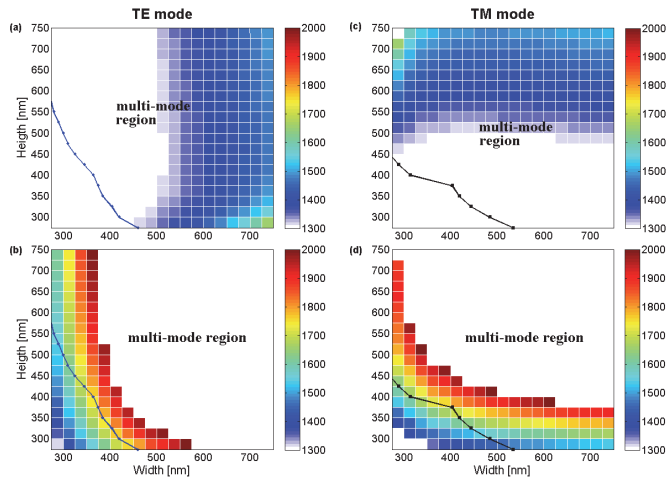


Fig. 1. Distribution of the ZDWs for the TE and TM modes. (a) the left ZDW for TE mode; (b) the right ZDW for TE mode; (c) the left ZDW for TM mode; (d) the right ZDW for TM mode. The solid lines in (a)-(d) denote the single-mode conditions for TE or TM modes. (Zhang et al., 2009 ; © 2009 The Electromagnetics Academy)

The dispersion profile of the silicon channel waveguide is directly determined by the waveguide geometry. By selecting suitable waveguide height and width, the ZDW can be shifted to the 1550-nm region and the dispersion can be flattened. Figure 2 shows the dispersion versus the wavelength for some waveguides whose ZDWs are all around 1555 nm. For the TE mode, the dispersion slope increases as the waveguide height increases. The situation is reversed for the TM mode. The flatter the curve is, the broader the conversion bandwidth is since the phase mismatch of the involved waves maintains small values within a wide wavelength range. After comparing the dispersion slopes of these waveguides, the waveguide cross section is optimized as 400 nm × 269 nm (height × width) for the TM mode in order to obtain the smallest dispersion slope corresponding to the broadest conversion bandwidth.

Figure 3(a) shows the conversion efficiency versus the wavelength detuning for different pump wavelengths in the anomalous region in the optimized waveguide of 400 nm × 269 nm with a fixed input power of 200 mW,  $\alpha = 2.5$  dB/cm,  $\sigma = 1.45 \times 10^{-17}$  cm<sup>2</sup>,  $\beta_{TPA} = 0.3$  cm/GW, and  $\tau = 1$  ns. When the pump is tuned away from the ZDW, the appearance of a second pair of conversion efficiency peaks farther from the pump, which is introduced by the location shift and increased number of the perfect phase-matching wavelengths, increases the 3-dB bandwidth. The maximum conversion bandwidth is achieved when the pump is at 1538.7 nm with the assumption of a 200-mW input pump power and a 2-cm-long interaction length. Figure 3(b) simulates the conversion response for the optimized 400 nm × 269 nm waveguide for TM polarization together with two other waveguides with the dimensions of 275 nm × 351 nm for TE polarization and 375 nm × 287 nm for TM polarization. These results are obtained in a 2-cm-long waveguide with a 200-mW pump wave at 1538.7 nm. The 3-dB bandwidth is over 280 nm for the optimized waveguide and the bandwidths of 275 nm × 351 nm and 375 nm × 287 nm waveguides are 77 nm and 112 nm.

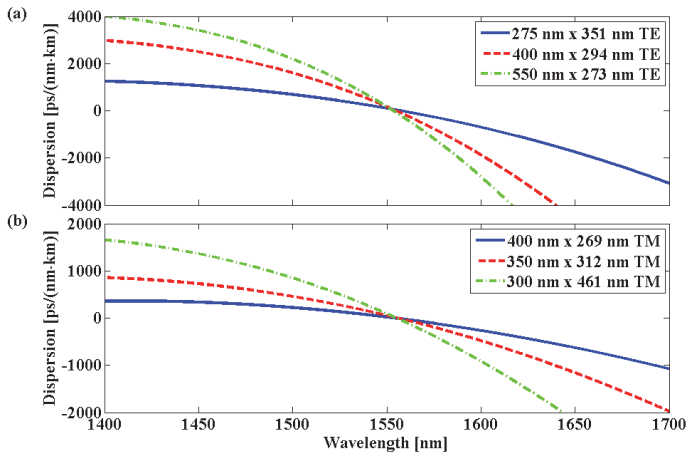


Fig. 2. Dispersion as a function of the wavelength for (a) TE and (b) TM modes. (Zhang et al., 2009 ; © 2009 The Electromagnetics Academy)

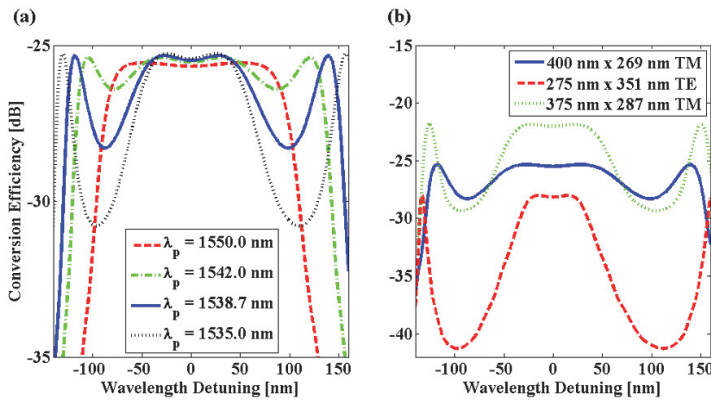


Fig. 3. (a) Conversion efficiency versus the wavelength detuning for different pump wavelengths in the optimized  $400 \text{ nm} \times 269 \text{ nm}$  waveguide. (b) Conversion response comparison of the  $400 \text{ nm} \times 269 \text{ nm}$ ,  $275 \text{ nm} \times 351 \text{ nm}$ , and  $375 \text{ nm} \times 287 \text{ nm}$  waveguides with the optimized pump wavelength. (Zhang et al., 2009 ; © 2009 The Electromagnetics Academy)

### 3.1.2 Design of slot waveguide structure

The efficiency of FWM is tightly related to the nonlinear coefficient of the silicon nanowire waveguide. If the field is effectively confined to decrease the effective mode area, the nonlinear coefficient can be increased (Liu et al., 2011). Figure 4(a) shows a schematic description of the silicon slot waveguide filled with silicon nanocrystals (Si-nc's). This kind of Si-nc material has a high Kerr coefficient at telecommunication wavelengths and its fabrication is compatible with the conventional semiconductor technologies (Martínez et al., 2010). By assuming that the Si-nc's have a silicon excess of 0.08 and a linear refractive index

of 1.6, a typical transverse electric (TE) mode distribution is shown in Fig. 4(b), where the slot width is assumed to be  $W_s = 50$  nm, the silicon slab width is  $W_h = 310$  nm, and the waveguide height is  $h = 305$  nm. From Fig. 4(b) one can find that the field is strongly confined in the low index nonlinear material due to the high index contrast in the horizontal direction. The effective mode area is calculated to be  $0.042 \mu\text{m}^2$  at 1550 nm. By using the definition in Eq. (10), the corresponding nonlinear coefficient is calculated to be  $\gamma = 3.86 \times 10^6 \text{ W}^{-1}\text{km}^{-1}$ . For comparison, the mode area and nonlinear coefficient are calculated to be  $0.15 \mu\text{m}^2$  and  $1.53 \times 10^5 \text{ W}^{-1}\text{km}^{-1}$  for a  $305 \text{ nm} \times 670 \text{ nm}$  silicon channel waveguide, which has approximately the same dimensions as the slot waveguide above. The nonlinear coefficient of the slot waveguide is roughly 19 times larger than that of the channel waveguide, which means higher conversion efficiency, due to both the high confinement of the light in the slot structure and the high nonlinearity of Si-nc's.

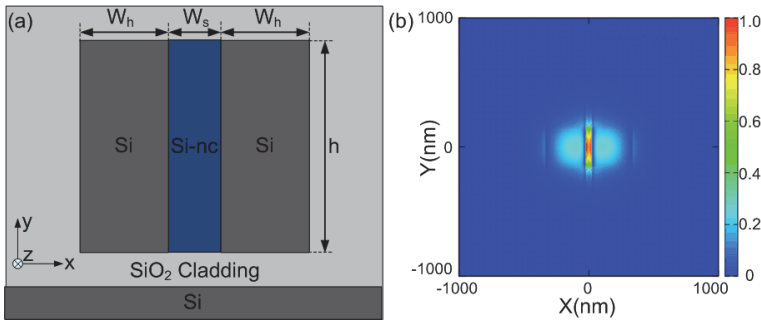


Fig. 4. (a) Schematic configuration of a slot waveguide, (b) Mode profile of the slot waveguide structure calculated by the beam propagation method. (Liu et al., 2011; © 2011 OSA)

As shown in Eq. (11), the phase-matching condition is a dominating factor of the bandwidth in a FWM-based wavelength conversion and the linear phase mismatch  $\Delta\beta$  is determined by the dispersion profile of the used waveguide. By expanding  $\beta_{s,c}$  as the Taylor series to the fourth-order around the pump frequency  $\omega_p$  and omitting the higher-order items, the linear phase mismatch can be rewritten as (Foster et al., 2007):

$$\begin{aligned} \Delta\beta &= \beta_2(\omega_p)\Omega^2 + \frac{1}{12}\beta_4(\omega_p)\Omega^4 \\ &= -\frac{1}{2\pi c}\lambda_p^2 D(\lambda_p)\Omega^2 - \frac{\lambda_p^4}{(2\pi c)^3} \left[ \frac{1}{2}D(\lambda_p) + \frac{1}{2}\lambda_p D'(\lambda_p) + \frac{1}{12}\lambda_p^2 D''(\lambda_p) \right] \Omega^4 \end{aligned} \quad (14)$$

where  $\Omega = \omega_s - \omega_p$  is the frequency difference between the signal and pump waves. The linear phase mismatch is approximately determined by the dispersion and its first- and second-order derivatives at the pump wavelength. It is expected to realize the optimal bandwidth by scanning the waveguide parameters to acquire a minimal phase mismatch with a given frequency difference. Since the slot width  $W_s$  has very slight influence, it is reasonable to consider a fixed slot width to simplify the optimization. Here the slot width is chosen to be  $W_s = 50$  nm (considering the limit of the fabrication technology). Figure 5(a) shows the variation of the linear phase mismatch in terms of  $h$  and  $W_h$  when the slot width is fixed to 50 nm. Here the pump and signal wavelengths are set to be 1550 and 1450 nm,

respectively. A set of zero points can be obtained for different waveguide heights  $h$  ranging from 200 to 400 nm when the slab width  $W_h$  is carefully chosen. For comparison, Fig. 5(b) shows the dispersion values at 1550 nm versus the waveguide dimensions. By comparing Fig. 5(a) with Fig. 5(b), one can find that the minimum absolute value of the linear phase mismatch agrees well with the ZDWs in the 1550-nm region for different waveguide dimensions, which means that the conversion bandwidth can be broadened further near the ZDW in the slot waveguide as long as the dispersion is flat enough. Among the designs with a minimum absolute value of the linear phase mismatch as well as a ZDW at 1550 nm in Fig. 5, an optimized waveguide configuration with  $W_h = 310$  nm and  $h = 305$  nm is found. The Si-nc slot waveguide with a 310-nm slab width, a 305-nm height, and a 50-nm slot width, whose mode area is about  $0.042 \mu\text{m}^2$ , can be considered as an optimized structure to enhance the bandwidth of FWM-based wavelength conversion in 1550-nm wavelength window since it has smaller and flatter dispersion to satisfy the phase-matching condition.

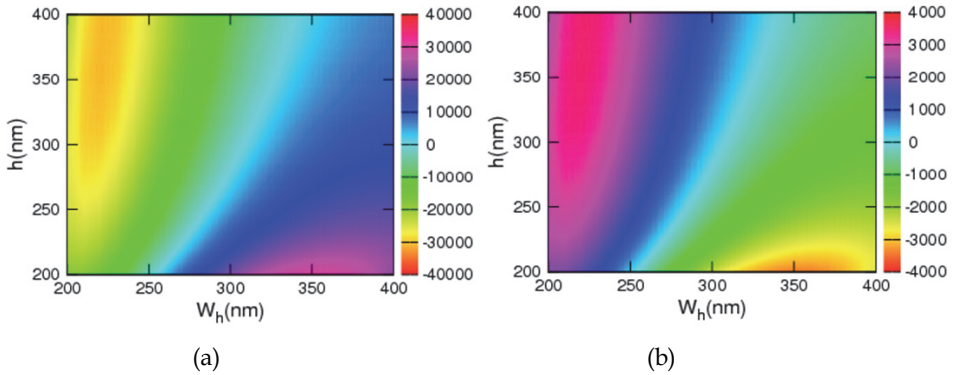


Fig. 5. (a) Linear phase mismatch (in units of  $\text{m}^{-1}$ ) as a function of  $h$  and  $W_h$  with  $W_s = 50$  nm, (b) the dispersion value (in units of  $\text{ps/km/nm}$ ) at 1550 nm as a function of  $h$  and  $W_h$  with  $W_s = 50$  nm. (Liu et al., 2011; © 2011 OSA)

After optimizing the dispersion of the Si-nc slot waveguide, the performance of FWM-based wavelength conversion is evaluated in such a waveguide by comparing with some traditional silicon nanowire waveguides. Assuming that all the pump, signal, and idler waves are polarized along the TE-axis, the coupled equations for the single-pump FWM process can be expressed using Eqs. (1)-(3). Assuming that the parameter values are as follows:  $n_2 = 4 \times 10^{-17} \text{ m}^2/\text{W}$ ,  $\beta_{TPA} = 5 \times 10^{-11} \text{ m/W}$ ,  $\tau_{\text{eff}} = 1 \text{ ns}$ ,  $\alpha_{p,s,i} = 6 \text{ dB/cm}$ , and  $\sigma_{p,s,i} = 3.5 \times 10^{-22} \text{ m}^2$ , one can obtain the conversion efficiency by numerically solving these coupled equations. When a continuous-wave (cw) pump with a power of 150 mW and a signal with a power of 15 mW are used, Fig. 6(a) shows the linear phase mismatch as a function of the signal wavelength for three different pump wavelengths including 1536, 1556, and 1576 nm in a 6-mm-long optimized Si-nc slot waveguide ( $W_h = 310$  nm,  $W_s = 50$  nm, and  $h = 305$  nm). The phase mismatch is tightly connected to the pump wavelength and it can be effectively controlled within a small value by setting the pump in the anomalous dispersion region near the ZDW (1550 nm). Correspondingly, the conversion responses for the three different pumps are simulated in Fig. 6(b) in the 6-mm-long slot waveguide. The two side peaks on conversion efficiency correspond

to the two zero points far away from the ZDW, where the phase-matching condition is also satisfied. From Fig. 6(b), the conversion bandwidth can be read out to be 87, 390, and 250 nm for the 1536-, 1556-, and 1576-nm pumps, respectively. The conversion bandwidth reaches its maximum with the 1556-nm pump.

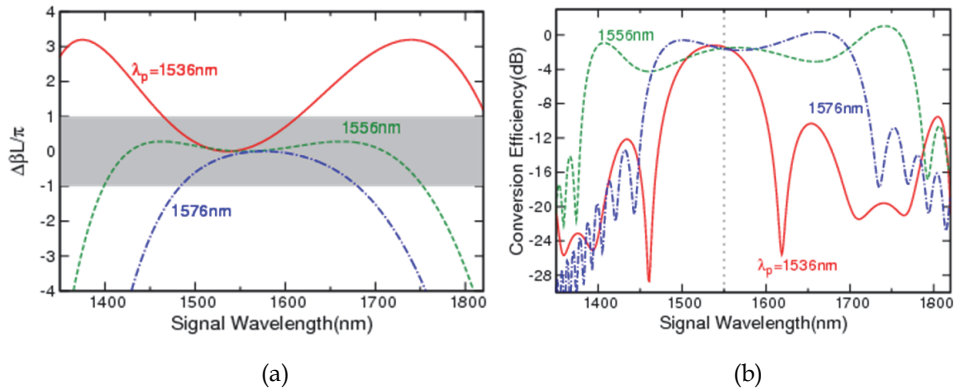


Fig. 6. (a) Linear phase mismatch and (b) conversion efficiency as the signal wavelength varies for three pumps at 1536, 1556, and 1576 nm in a 6-mm-long waveguide. (Liu et al., 2011; © 2011 OSA)

The conversion bandwidth will reduce as the waveguide length increases since the accumulated phase mismatch is proportional to the waveguide length. Also, the conversion efficiency is influenced by the waveguide length. Figure 7 simultaneously shows the conversion bandwidth and the efficiency as functions of the waveguide length for the slot waveguide as well as for a traditional silicon channel waveguide (280 nm  $\times$  342 nm), which also has an optimized dispersion profile with ZDW at 1550 nm. The pump and signal powers are assumed to be 150 and 15 mW and the pump wavelengths of the slot and channel waveguide are set to be 1556 and 1535 nm to obtain broader conversion bandwidths. For both waveguides, the conversion bandwidth remarkably drops as the waveguide becomes longer. The bandwidth decreases from 407 to 83 nm for the slot waveguide or from 271 to 101 nm for a silicon channel waveguide when the waveguide length increases from 4 to 20 mm. The two discontinuities in the bandwidth curves of these two waveguides are caused by the two concavities beside the pump wavelength in the conversion efficiency curves (Zhang et al., 2009). The conversion bandwidth of a slot waveguide is greatly broader than a traditional channel waveguide when the waveguide is short while it is a little narrower when the waveguide length increases. However, the conversion efficiency of the slot waveguide is much higher than that of the traditional channel waveguide, which reaches -1.46 dB when the waveguide is 7 mm long. The conversion efficiency for the silicon channel waveguide can reach -16.6 dB in the 20-mm-long waveguide, which is nearly 15 dB lower than the slot waveguide under the same incident condition. As shown in Fig. 7, a 3-dB conversion bandwidth of over 400 nm incorporating a conversion efficiency of -2.38 dB can be achieved in a 4-mm-long slot waveguide.

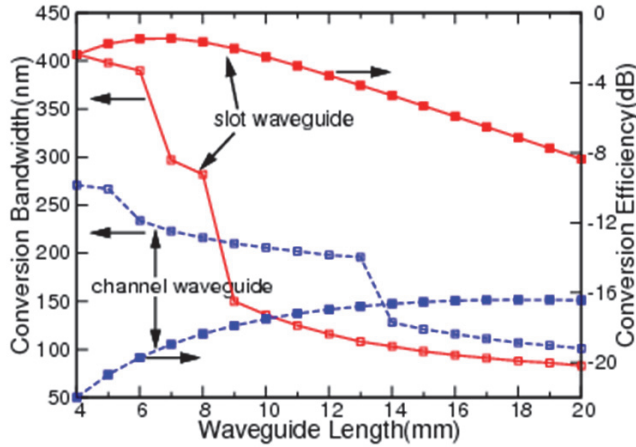


Fig. 7. Conversion bandwidth and efficiency as the waveguide length varies for the slot waveguide and the silicon channel waveguide. (Liu et al., 2011; © 2011 OSA)

### 3.1.3 Usage of two-pump FWM

According to Eq. (12), the phase-matching condition of FWM can be freely controlled by the pump spacing when a two-pump regime is used and the bandwidth may be enhanced by setting the pumps. Preliminary calculations are performed in a 1.5-cm-long  $300 \text{ nm} \times 650 \text{ nm}$  silicon nanowire waveguide that corresponds to a  $0.12158 \mu\text{m}^2$  effective mode area. The zero-dispersion wavelength is at  $1456 \text{ nm}$ . Since the pump power attenuates along the propagation length, the phase mismatch will vary with respect to the distance even though the signal wavelength is fixed. For the single-pump FWM-based wavelength conversion, Fig. 8(a) and 8(b) simulate the phase mismatches for the pump powers of  $100 \text{ mW}$  and  $1000 \text{ mW}$  in the above waveguide and the pump wave is assumed to be set at  $1550 \text{ nm}$ . In our calculation, the linear propagation loss coefficient is assumed to be  $\alpha = 2.5 \text{ dB/cm}$ , the TPA coefficient is  $\beta_{\text{TPA}} = 0.8 \text{ cm/GW}$  for both degenerate and nondegenerate absorptions, the FCA cross section is  $\sigma = 1.45 \times 10^{-17} \text{ cm}^2$ , the effective free-carrier lifetime of carriers is  $\tau = 2 \text{ ns}$ , and the nonlinear index coefficient is  $n_2 = 9 \times 10^{-18} \text{ m}^2/\text{W}$ . One can see that the exact phase-matching curves in Figs. 8(a) and 8(b) are quite similar particularly after propagating  $0.5 \text{ cm}$  in the silicon nanowire waveguide, although the incident pump powers are dramatically different. This effect results in the nonlinear loss due to TPA and FCA, especially where FCA is quadratically proportional to the pump powers. A high incident power will be attenuated rapidly to a relatively low level. As a result, the phase mismatch is slightly changed by the pump power. Figure 8(c) shows the conversion responses for the two cases corresponding to Figs. 8(a) and 8(b) with a signal power of  $1 \text{ mW}$ . The 3-dB conversion bandwidths are  $71.5$  and  $77.2 \text{ nm}$  when  $100\text{-mW}$  and  $1000\text{-mW}$  pumps are adopted. The bandwidth enhancement is very limited by changing the pump power.

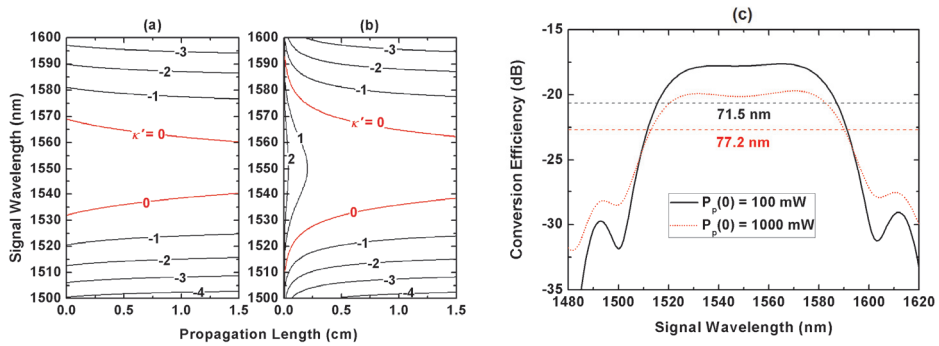


Fig. 8. Phase mismatch (in the units of  $\text{cm}^{-1}$ ) of the single-pump FWM as a function of the signal wavelength and the propagation length with the pump power of (a) 100 mW or (b) 1000 mW. (c) Single-pump conversion efficiency as the signal wavelength for the pump power of 100 mW or 1000 mW. (Gao et al., 2010; © 2010 IEEE)

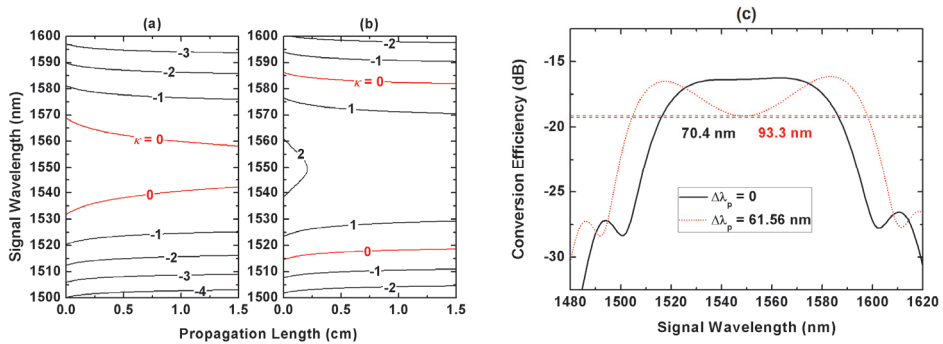


Fig. 9. Phase mismatch (in the units of  $\text{cm}^{-1}$ ) of the two-pump FWM as a function of the signal wavelength and the propagation length when the wavelength spacing between the two pumps is (a) 0 and (b) 61.56 nm. (c) Two-pump conversion efficiency as the signal wavelength varies for the pump wavelength spacing of 0 or 61.56 nm. (Gao et al., 2010; © 2010 IEEE)

In contrast, the phase mismatch is greatly dependent on the two pump wavelengths in the two-pump FWM scheme. When the mean pump wavelength is fixed at 1550 nm, the phase mismatch is calculated by using Eq. (12) with a pump spacing of 0 and 61.56 nm, as shown in Figs. 9(a) and 9(b), in which the pump powers are fixed at 100 mW. The linear phase mismatch  $\Delta\beta$  is directly determined by the pump wave numbers, that is, the pump wavelengths. One can find that the total phase mismatch is sensitive to the pump wavelength spacing and the perfect phase-matching curves ( $\kappa = 0$ ) are separated from each other in the contour map as the pump spacing increases, which results in the enhancement of bandwidth. The simulation results of the conversion responses are shown in Fig. 9(c). The 3-dB bandwidth is 70.4 nm when the two pumps are very close, which is quite similar to the single-pump FWM. When the two pumps are separated from each other, the bandwidth is enhanced gradually. For the pump wavelength spacing of 61.56 nm, the bandwidth reaches 93.3 nm, which is enhanced by 22.9 nm (33%) compared to the case when the two pumps are put closely.

The nonuniformity of the conversion response is also concomitantly enhanced as the pump spacing of the two-pump FWM increases since the central signals suffer from larger phase mismatch, which means a lower conversion efficiency. For the sake of convenience, we define the efficiency difference between the maximum efficiency and the central minimum efficiency as the response nonuniformity. With both pump powers of 100 mW, the conversion bandwidth and the corresponding response nonuniformity are quantitatively simulated as the pump wavelength spacing varies, as shown in Fig. 10. One can see that the response nonuniformity is also enhanced together with the conversion bandwidth by separating the two pumps. The response nonuniformity reaches 3 dB for a 61.56-nm wavelength spacing. Further increasing the pump spacing results in a response nonuniformity of more than 3 dB and the 3-dB bandwidth is divided into two regions. Also, the conversion bandwidth will decrease as the pump spacing increases, which is not beneficial to the wavelength conversion function. The maximum 3-dB bandwidth of 93.3 nm can be achieved just when the response nonuniformity is 3 dB.

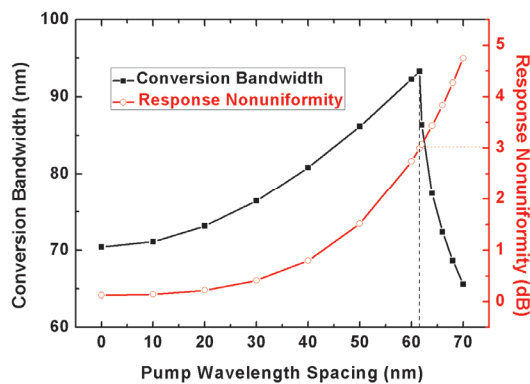


Fig. 10. Conversion bandwidth and the corresponding response nonuniformity as the pump wavelength spacing varies. (Gao et al., 2010; © 2010 IEEE)

The bandwidth enhancement based on two-pump FWM is experimentally demonstrated, as shown in Fig. 11. The two pumps are provided by two cw tunable lasers (Santec ECL-200) whose wavelengths are set at 1549.9 and 1564.8 nm. They are coupled through a 50/50 coupler and amplified using a high-power erbium-doped fiber amplifier (Amonics AEDFA-C-33-R), whose saturation power is around 23 dBm. The two pumps are filtered out through a demultiplexer whose central wavelength is at 1550 nm and a tunable band-pass filter, which is tuned to about 1565 nm. Another cw tunable laser (ECL-210) serves as the signal, whose output power is about 11 dBm. The pumps and signal are coupled into a 1.7-cm-long silicon waveguide with a cross section of  $3 \mu\text{m} \times 3 \mu\text{m}$  (the effective mode area is about  $5 \mu\text{m}^2$ ) via a 70/30 coupler. After this coupler, the powers of the two pumps and the signal are estimated to be around 13.2, 19.8, and 6.1 dBm, respectively. The coupling loss between the fiber and the waveguide is about 1.5 dB. In the silicon waveguide, FWM occurs among the two pumps and the signal, and an idler is generated. The FWM spectrum is observed using an optical spectrum analyzer (Ando AQ6317B).

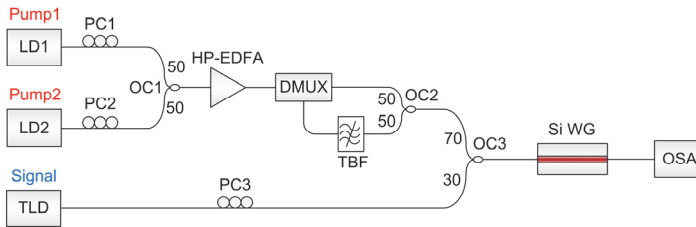


Fig. 11. Experimental setup for the wavelength conversion based on two-pump FWM. TLD: tunable laser diode, PC: polarization controller, EDFA: erbium-doped fiber amplifier, TBF: tunable bandwidth filter, OC: optical coupler, and OSA: optical spectrum analyzer. (Gao et al., 2010; © 2010 OSA)

Figure 12(a) shows the measured optical spectrum of the two-pump wavelength conversion using the experimental setup in Fig. 11. Here the signal is set at 1561.4 nm and the idler is generated at 1553.2 nm, which is enlarged and shown in the inset. From Fig. 12(a), one can find that the extinction ratio of the generated idler, which is defined as the difference between peak power and the noise floor, is about 10 dB with a measured resolution of 0.01 nm. For comparison, the FWM with a single pump is also experimentally demonstrated. Here Pump1 is turned off and Pump2 is tuned to 1557.7 nm, almost equal to the central wavelength of the two pumps in the two-pump FWM. As shown in Fig. 12(b), a signal at 1561.5 nm is converted to 1553.9 nm pumped by the single Pump2.

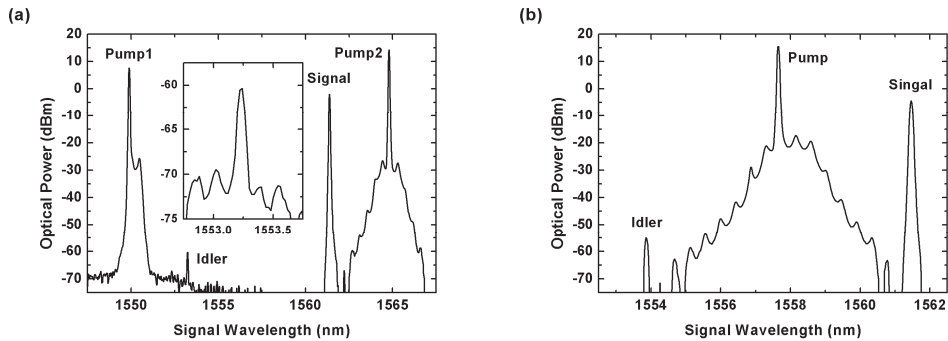


Fig. 12. (a) Optical spectrum of the FWM pumped by two cw pumps at 1549.9 nm and 1564.8 nm. The inset is the enlarged description of the generated idler. (b) Optical spectrum of the FWM pumped by a single cw pump at 1557.7 nm. (Gao et al., 2010; © 2010 OSA)

By scanning the signal wavelength, the response of conversion efficiency can be obtained from a series of measured FWM spectra, as shown in Fig. 13. It is known that the efficiency is tightly related to the pump powers, i.e.,  $\eta_{nd} \propto P_{p1}P_{p2}$  and  $\eta_d \propto P_p^2$ . In the experiments, the gains in the EDFA will be different for the two-pump and single-pump cases. For comparison, unit conversion efficiency is introduced by eliminating the influence of the pump powers (i.e.,  $\eta_{nd-unit} = \eta_{nd}/P_{p1}P_{p2}$  and  $\eta_{d-unit} = \eta_d/P_p^2$ ). By fitting the measured conversion efficiencies, the experimental bandwidths are calculated from Fig. 13. The bandwidth of the single-pump FWM is 29.8 nm, while it is enhanced to 37.4 nm for the two-pump FWM. The bandwidth is improved by 25% through introducing the two-pump FWM regime.

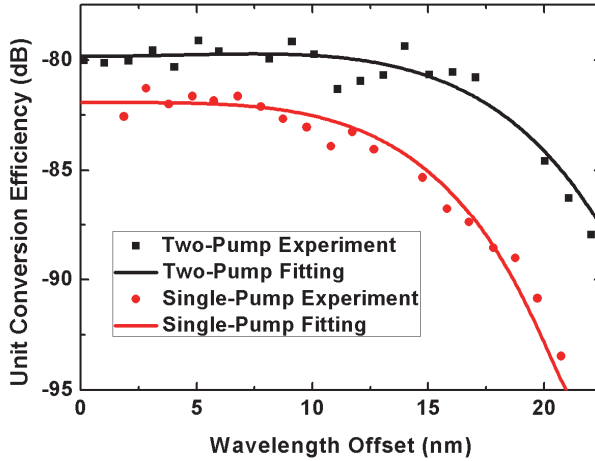


Fig. 13. Measured unit conversion efficiencies and the fitting curves for the two-pump and single-pump wavelength conversions. (Gao et al., 2010; © 2010 OSA)

### 3.2 Polarization independency

In a silicon nanowire waveguide, both the pump wave  $\lambda_p$  and the signal wave  $\lambda_s$  coupled into the waveguide can be decomposed to the TE and TM modes. FWM occurs only among these waves with the same polarization mode (Inoue, 1992). Under the law of energy conservation, the converted wave  $\lambda_c$  satisfies the relationship  $1/\lambda_c = 2/\lambda_p - 1/\lambda_s$  for both TE- and TM-mode FWMs. By ignoring the pump and signal power transforms due to FWM and simplifying the coupled equations in Eqs. (1)-(3), the converted wave of TE or TM mode follows:

$$\frac{dA_{c-TE, TM}(z)}{dz} = -\frac{\alpha_{c-TE, TM}}{2} A_{c-TE, TM}(z) + j\gamma_{TE, TM} A_{p-TE, TM}^2(0) A_{s-TE, TM}^*(0) \times \exp\left[-\left(\alpha_{p-TE, TM} + \frac{\alpha_{s-TE, TM}}{2} + j\kappa_{TE, TM}\right)z\right] \quad (15)$$

where  $A_{p,s,c-TE, TM}(z)$  are the amplitudes of the TE or TM mode of the pump, signal, and converted waves in the waveguide. Denoting the polarization angle of the incident pump or signal against the TE-axis as  $\theta_{p,s}$ , as shown in Fig. 14, the pump and signal fields coupled into the waveguide satisfy

$$|A_{p,s-TE}(0)| = \sqrt{C_{TE}} |A_{p0,s0}| \cos\theta_{p,s} \quad (16)$$

$$|A_{p,s-TM}(0)| = \sqrt{C_{TM}} |A_{p0,s0}| \sin\theta_{p,s} \quad (17)$$

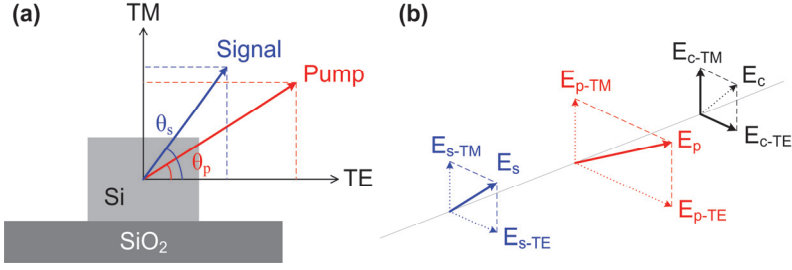


Fig. 14. Principle of the polarization-independent wavelength conversion based on FWM with an angled-polarization pump in a silicon nanowire waveguide. (a) Schematic description of the incident pump and signal; (b) FWM processes in the silicon nanowire waveguide. (Gao et al., 2010; © 2010 IEEE)

where  $A_{p0,s0}$  are the amplitudes of the TE or TM mode of the incident pump and signal waves and  $C_{TE, TM}$  is the relative coupling efficiency of the TE or TM mode. Assuming the incident pump and signal powers  $P_{p0,s0} = |A_{p0,s0}|^2$ , the coupled powers can also be written as

$$P_{p0,s0-TE} = C_{TE} P_{p0,s0} \cos^2 \theta_{p,s} \quad (18)$$

$$P_{p0,s0-TM} = C_{TM} P_{p0,s0} \sin^2 \theta_{p,s} \quad (19)$$

In Eq. (15),  $\gamma_{TE, TM}$  is the nonlinear coefficient,  $\kappa_{TE, TM}$  is the phase mismatch of the FWM process, and  $a_{p,s,c-TE, TM}$  are the total losses of the pump, signal, and converted waves in the silicon nanowire waveguide, which are expressed as

$$\alpha_{p-TE, TM} = \alpha_{Lin-TE, TM} + \alpha_{TPA-TE, TM} + \alpha_{FCA-TE, TM} \quad (20)$$

$$\alpha_{s-TE, TM} = \alpha_{Lin-TE, TM} + 2\alpha_{TPA-TE, TM} + \alpha_{FCA-TE, TM} \quad (21)$$

$$\alpha_{c-TE, TM} = \alpha_{Lin-TE, TM} + 2\alpha_{TPA-TE, TM} + \alpha_{FCA-TE, TM} \quad (22)$$

Here  $\alpha_{Lin-TE, TM}$  is the linear loss coefficient of the TE or TM mode in the waveguide, and the TPA- and FCA-induced nonlinear loss coefficients are

$$\alpha_{TPA-TE, TM} = \beta_{TPA} P_{p0} (C_{TE} \cos^2 \theta_p + C_{TM} \sin^2 \theta_p) / A_{eff-TE, TM} \quad (23)$$

$$\alpha_{FCA-TE, TM} = \sigma \beta_{TPA} \tau_{eff} \lambda_p P_{p0}^2 (C_{TE} \cos^2 \theta_p + C_{TM} \sin^2 \theta_p)^2 / 2hc A_{eff-TE, TM}^2 \quad (24)$$

where  $\beta_{TPA}$  is the TPA coefficient,  $\sigma$  is the FCA cross section,  $\tau_{eff}$  is the effective lifetime,  $h$  is the Planck's constant, and  $A_{eff-TE, TM}$  is the effective mode areas for the TE or TM mode.

The nonlinear coefficient  $\gamma_{TE, TM}$  is expressed as

$$\gamma_{TE, TM} = 2\pi n_2 / \lambda_c A_{eff-TE, TM} \quad (25)$$

where  $n_2$  is the nonlinear index coefficient. In the coupled equation, the TE- or TM-mode phase mismatch is

$$\kappa_{TE, TM} = \Delta\beta_{TE, TM} + 2\gamma_{TE, TM} \left[ P_{p0-TE, TM} + \frac{2}{3} P_{p0-TM, TE} \right] \quad (26)$$

Denoting the wave numbers of the interaction waves as  $\beta_{p,s,c}$  which can be calculated via the corresponding effective refractive indices  $n_{p,s,c}$  in a silicon nanowire waveguide, the linear phase mismatch in Eq. (26) can be expressed as

$$\begin{aligned} \Delta\beta_{TE, TM} &= \beta_{s-TE, TM} + \beta_{c-TE, TM} - 2\beta_{p-TE, TM} \\ &= 2\pi \left( n_{s-TE, TM} / \lambda_s + n_{c-TE, TM} / \lambda_c - 2n_{p-TE, TM} / \lambda_p \right) \end{aligned} \quad (27)$$

The linear phase mismatch in Eq. (27) can also be rewritten using the dispersion values. Expanding  $\beta_{p,s,c}$  in a Taylor series to the fourth-order around the pump wavelength  $\lambda_p$ , one obtains

$$\begin{aligned} \Delta\beta_{TE, TM} &= -\frac{1}{2\pi c} (\omega_s - \omega_p)^2 \lambda_p^2 D'_{TE, TM}(\lambda_p) - \frac{1}{(2\pi c)^3} (\omega_s - \omega_p)^4 \\ &\quad \times \left[ \frac{1}{2} \lambda_p^4 D''_{TE, TM}(\lambda_p) + \frac{1}{2} \lambda_p^5 D'''_{TE, TM}(\lambda_p) + \frac{1}{12} \lambda_p^6 D^{(4)}_{TE, TM}(\lambda_p) \right] \end{aligned} \quad (28)$$

where  $D(\lambda_p)$  is the dispersion parameter at  $\lambda_p$ ,  $D'(\lambda_p)$  and  $D''(\lambda_p)$  are the first- and second-order derivatives, respectively.

Solving Eq. (15) analytically, one obtains the generated converted wave:

$$\begin{aligned} A_{c-TE, TM}(L) &= j\gamma_{TE, TM} A_{p-TE, TM}^2(0) A_{s-TE, TM}^*(0) \\ &\quad \times \exp\left(-\frac{\alpha_{c-TE, TM} L}{2}\right) \frac{1 - \exp\left[(-j\kappa_{TE, TM} - \alpha_{p-TE, TM})L\right]}{j\kappa_{TE, TM} + \alpha_{p-TE, TM}} \end{aligned} \quad (29)$$

The output converted power at the end of the waveguide can be expressed as

$$\begin{aligned} P_c(L) &= |A_{c-TE}(L)|^2 + |A_{c-TM}(L)|^2 \\ &= \gamma_{TE}^2 C_{TE}^3 P_{p0}^2 P_{s0} \exp(-\alpha_{c-TE} L) \left| \frac{1 - \exp\left[(-j\kappa_{TE} - \alpha_{p-TE})L\right]}{j\kappa_{TE} + \alpha_{p-TE}} \right|^2 \cos^4 \theta_p \cos^2 \theta_s \\ &\quad + \gamma_{TM}^2 C_{TM}^3 P_{p0}^2 P_{s0} \exp(-\alpha_{c-TM} L) \left| \frac{1 - \exp\left[(-j\kappa_{TM} - \alpha_{p-TM})L\right]}{j\kappa_{TM} + \alpha_{p-TM}} \right|^2 \sin^4 \theta_p \sin^2 \theta_s \end{aligned} \quad (30)$$

From Eq. (30) one sees that the converted wave power will be polarization-independent (i.e., independent of the SOP of the incident signal) when the following relationship is satisfied:

$$\left| \frac{1 - \exp\left[(-j\kappa_{TE} - \alpha_{p-TE})L\right]}{j\kappa_{TE} + \alpha_{p-TE}} \right| = \frac{\gamma_{TM} C_{TM}^{3/2}}{\gamma_{TE} C_{TE}^{3/2}} \tan^2 \theta_p \quad (31)$$

$$\times \exp\left[ \frac{(\alpha_{c-TE} - \alpha_{c-TM})L}{2} \right] \left| \frac{1 - \exp\left[(-j\kappa_{TM} - \alpha_{p-TM})L\right]}{j\kappa_{TM} + \alpha_{p-TM}} \right|$$

The incident pump polarization angle can be obtained by solving Eq. (31). Since the TE and TM phase mismatches and losses are also functions of the incident pump polarization angle, Eq. (31) can only be solved numerically. Substituting the solved pump polarization angle into Eq. (30), one can obtain the converted wave power for an arbitrary incident signal polarization angle and verify the polarization-independent characteristic.

Since the phase mismatch varies with the signal wavelength, the required pump polarization angle changes for different signal waves. Therefore, the polarization independence can be exactly realized only for one or several signal wavelengths once the pump polarization angle is determined, and the conversion efficiencies for the other signals will fluctuate slightly as the signal SOP varies. We take a  $300 \text{ nm} \times 500 \text{ nm}$  silicon nanowire waveguide as an example. The TE- and TM-polarization effective mode areas are  $A_{eff-TE} = 9.484 \times 10^{-2} \mu\text{m}^2$  and  $A_{eff-TM} = 9.838 \times 10^{-2} \mu\text{m}^2$ . For convenience, the relative coupling efficiency of the TM mode is simplified as  $C_{TM} = 1$ , and the coupling efficiency ratio of the TE to TM mode is calculated to be  $C_{TE}/C_{TM} = 0.473$  through mode field overlapping integral method. This simplification does not affect the polarization-independent characteristic of the proposed wavelength conversion scheme. The linear propagation losses are considered as  $\alpha_{Lin-TE} = 2.5 \text{ dB/cm}$  and  $\alpha_{Lin-TM} = 2 \text{ dB/cm}$  for the TE and TM modes, the TPA coefficient is  $\beta_{TPA} = 0.5 \text{ cm/GW}$ , the FCA cross section is  $\sigma = 1.45 \times 10^{-17} \text{ cm}^2$ , the effective lifetime of carriers is  $\tau_{eff} = 2.5 \text{ ns}$ , the nonlinear index coefficient is  $n_2 = 9 \times 10^{-18} \text{ m}^2/\text{W}$ , and the waveguide length is  $L = 0.8 \text{ cm}$ . According to Eq. (31), the required pump polarization angle is related to the losses and the phase mismatches of the TE and TM modes. Assuming the incident pump power is  $P_{p0} = 100 \text{ mW}$  at wavelength  $\lambda_p = 1550 \text{ nm}$ , the required pump polarization angle for each signal wavelength to realize exact polarization-independent wavelength conversion is obtained by substituting Eqs. (20)-(22) and (26) into Eq. (31), as shown in Fig. 15. It is noticeable that for a wide signal wavelength range the required pump polarization angles are almost the same. The inset shows the enlarged illustration in the range from 1530 to 1570 nm. The peak-to-peak fluctuation of the required pump polarization angles (for signals around the pump) is only  $0.004^\circ$  in the inset and the optimal pump polarization angle (averaged) is calculated to be  $28.844^\circ$ . One can use the average pump polarization angle in this region as the optimized value. This is of great convenience for the angled-polarization pump operation.

Figure 16(a) illustrates the conversion efficiency versus the signal wavelength. Here the shadowed region is used to illustrate the conversion efficiency fluctuation when changing the incident signal SOP arbitrarily, and the efficiency fluctuation is quantitatively described in Fig. 16(b). The enlarged description in the range from 1530 to 1570 nm is shown in the inset of Fig. 16(b), where one can find that four exact zero-fluctuation signal wavelengths exist, because the pump polarization angle we used here is exactly the solution of Eq. (31) for these signal wavelengths. In Fig. 16(b), one sees that the 1-dB polarization-independent bandwidth is 61 nm and the efficiency fluctuation is less than 0.04 dB for the signals in the

30-nm range around the 1550-nm pump. The wavelength conversion scheme we presented exhibits excellent polarization-independent characteristic in the entire C-band (the most significant telecommunication band) and thus is quite suitable for use in dense wavelength division multiplexing systems.

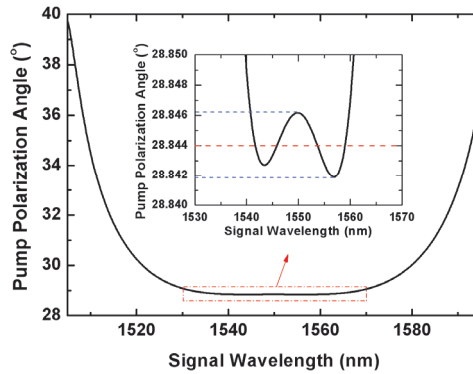


Fig. 15. Incident pump polarization angle required to realize exact polarization independence versus the signal wavelength in the  $300 \text{ nm} \times 500 \text{ nm}$  waveguide with a pump at 1550 nm. The inset shows the enlarged illustration in the range of 1530-1570 nm. (Gao et al., 2010; © 2010 IEEE)

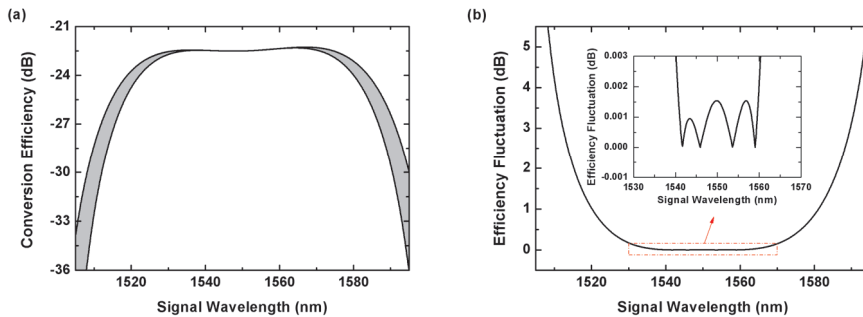


Fig. 16. (a) Conversion efficiency region and (b) the corresponding fluctuation value versus the signal wavelength. The inset in (b) shows the enlarged illustration in the range of 1530-1570 nm. (Gao et al., 2010; © 2010 IEEE)

For our proposed wavelength conversion scheme in silicon nanowire waveguides, the bandwidth is determined mainly by the TE- and TM-mode phase-matching conditions, which are related to the dispersions. The edges of these conversion efficiency regions in Fig. 16(a) are just the conversion efficiencies of the TE- and TM-polarization signals. Therefore, the polarization-independent bandwidth is limited by the larger one of the TE- and TM-mode phase mismatches, and the polarization-independent bandwidth is no more than the narrower one of the TE- and TM-mode bandwidths. If both the TE- and TM-mode

dispersion values in the 1550-nm band are reduced and flattened further by designing special waveguide structures and dimensions, larger polarization-independent bandwidth can be expected.

#### 4. Summary and prospects

In this chapter, the FWM effect in silicon nanowire waveguides has been investigated and its applications in wavelength conversion have been introduced. The theoretical model of the FWM effect has been established. The conversion bandwidth and efficiency have been tried to improve by optimizing the waveguide geometry or designing special structure. Also, the improvement based on two-pump regime has been presented and demonstrated. The polarization independency of the wavelength conversion has been avoided by using an angled-polarization pump. Wavelength conversion based on silicon nanowire waveguides has been considered as a promising solution for the next generation integrated optical communication systems.

#### 5. References

- Fukuda, H. et al. (2005). Four-wave mixing in silicon wire waveguides. *Optics Express*, Vol.13, No.12, (June 2005), pp. 4629-4637, ISSN 1094-4087
- Boyraz, O. & Jalali, B. (2004). Demonstration of a silicon Raman laser. *Optics Express*, Vol.12, No.21, (October 2004), pp. 5269-5273, ISSN 1094-4087
- Liang, T. K. & Tsang, H. K. (2004). Efficient Raman amplification in silicon-on-insulator waveguides. *Applied Physics Letters*, Vol.85, No.16, (October 2004), pp. 3343-3345, ISSN 0003-6951
- Almeida, V. R. et al. (2004). All-optical control of light on a silicon chip. *Nature*, Vol.431, No.7012, (October 2004), pp. 1081-1084, ISSN 0028-0836
- Liang, T. K. et al. (2006). High speed logic gate using two-photon absorption in silicon waveguides. *Optics Communications*, Vol.265, No.1, (September 2006), pp. 171-174, ISSN 0030-4018
- Foster, M. A. et al. (2006). Broad-band optical parametric gain on a silicon photonic chip. *Nature*, Vol.441, No.7096, (June 2006), pp. 960-963, ISSN 0028-0836
- Rong, H. et al. (2006). High efficiency wavelength conversion of 10 Gb/s data in silicon waveguides. *Optics Express*, Vol.14, No.3, (February 2006), pp. 1182-1188, ISSN 1094-4087
- Raghunathan, V. et al. (2005). Parametric Raman wavelength conversion in scaled silicon waveguides. *Journal of Lightwave Technology*, Vol.23, No.6, (June 2005), pp. 2094-2102, ISSN 0733-8724
- Lin, Q. et al. (2006). Ultrabroadband parametric generation and wavelength conversion in silicon waveguides. *Optics Express*, Vol.14, No.11, (May 2006), pp. 4786-4799, ISSN 1094-4087
- Sang, X. & Boyraz, O. (2008). Gain and noise characteristics of high-bit-rate silicon parametric amplifiers. *Optics Express*, Vol.16, No.17, (August 2008), pp. 13122-13132, ISSN 1094-4087
- Zhang, X. et al. (2009). Optimal design of a silicon-on-insulator nanowire waveguide for broadband wavelength conversion. *Progress In Electromagnetics Research*, Vol.89, (January 2009), pp. 183-198, ISSN 1559-8985

- Gao, S. et al. (2010). Performance Evaluation of Nondegenerate Wavelength Conversion in a Silicon Nanowire Waveguide. *Journal of Lightwave Technology*, Vol.28, No.21, (November 2010), pp. 3079-3085, ISSN 0733-8724
- Foster, M. A. et al. (2007). Broad-band continuous-wave parametric wavelength conversion in silicon nanowaveguides. *Optics Express*, Vol.15, No.20, (September 2007), pp. 12949-12958, ISSN 1094-4087
- Turner, A. C. et al. (2006). Tailored anomalous group-velocity dispersion in silicon channel waveguides. *Optics Express*, Vol.14, No.10, (May 2006), pp. 4357-4362, ISSN 1094-4087
- Liu, Q. et al. (2011). Dispersion engineering of a silicon nanocrystal-based slot waveguide for broadband wavelength conversion. *Applied Optics*, in press, ISSN 1559-128X
- Martínez, A. et al. (2010). Ultrafast all-optical switching in a silicon-nanocrystal-based silicon slot waveguide at telecom wavelengths. *Nano Letters*, Vol.10, No.4, (March 2010) pp. 1506-1511, ISSN 1530-6984
- Gao, S. et al. (2010). Experimental demonstration of bandwidth enhancement based on two-pump wavelength conversion in a silicon waveguide. *Optics Express*, Vol.18, No. 26, (December 2010), pp. 27885-27890, ISSN 1094-4087
- Inoue, K. (1992). Polarization effect on four-wave mixing efficiency in a single-mode fiber. *IEEE Journal of Quantum Electronics*, Vol.28, No.4, (April 1992), pp. 883-894, ISSN 0018-9197
- Gao, S. et al. (2010). Polarization-independent wavelength conversion using an angled-polarization pump in a silicon nanowire waveguide. *IEEE Journal of Selected Topics in Quantum Electronics*, Vol.16, No.1, (January-February 2010), pp. 250-256, ISSN 1077-260X

# Wet - Chemically Etched Silicon Nanowire Architectures: Formation and Properties

Vladimir Sivakov<sup>1</sup>, Felix Voigt<sup>1,2</sup>, Björn Hoffmann<sup>1</sup>,  
Viktor Gerliz<sup>2</sup> and Silke Christiansen<sup>1,3</sup>

<sup>1</sup>*Institute of Photonic Technology, Jena,*

<sup>2</sup>*University of Oldenburg, Institute of Physics, Oldenburg,*

<sup>3</sup>*Max Planck Institut für die Physik des Lichts, Erlangen,  
Germany*

## 1. Introduction

In the last years, there is an enormously growing interest in the research and development of silicon nanowires (SiNWs) for various applications in the fields of optoelectronics, photonics and photovoltaics as well as in the sensor field (Cui, 2001; Ross, 2005; Hochbaum, 2005; Schmidt, 2005; Duan, 2001; Kelzenberg, 2008; Stelzner, 2008). The silicon based approaches are certainly favoured because of material abundance and non-toxicity at a high level of materials control and understanding together with a huge industrial infrastructure to account for low production/processing costs and high production yields. The bottom-up fabrication of SiNWs is based on either metal catalyzed growth, known as vapor-liquid-solid (VLS) growth (Givargizov, 1975; Wagner@Ellis, 1964) where metal nanoparticles that form a low temperature eutectic with silicon, such as gold, are liquefied so that they form nanoscale droplets that can be supersaturated from the gas phase with silicon containing species by e.g. chemical vapour deposition (CVD) (Wang, 2006) or physical vapour deposition methods such as laser ablation (Eisenhawer, 2011), molecular beam epitaxy (MBE) (Fuhrmann, 2005; Oh, 2008) or electron beam evaporation (EBE) (Sivakov, 2006, 2007). The growth is carried out with gold (Au) or other metal (Al, Ga, In etc.) (Sunkara, 2001; Civale, 2004) nanoparticles to catalyze the preferred selective axial NW growth at temperatures sufficiently high to form a liquid eutectic with the growth species (Wagner@Ellis, 1964; Lieber, 2003). The first VLS studies were carried out in the 1960s where NW diameters from 100 nm to 100  $\mu$ m were realized (Givargizov, 1975; Wagner@Ellis, 1964). Today, NWs show diameters in the range between few nanometers up to micrometer scale, with the diameter being determined by the diameter of the metal catalyst nanoparticle (Kamins, 2001; Heath, 1993; Hanrath, 2002; Zhang, 2000; Lauhon, 2002; Xia, 2003; Wagner@Ellis, 1965; Wu, 2000). The schematic representation, shown in Figure 1, illustrates the VLS growth process as it occurs when a particle beam provides the growth species. Vaporized growth species (e.g. silicon atoms or silane (SiH<sub>4</sub>) molecules) reach the substrate surface that is covered with metal nanoparticles. The substrate temperature is held above the eutectic temperature of the alloy (here: Au-Si at 373 °C) so that the liquid gold droplet can be supersaturated with silicon atoms. Under the influence of a concentration gradient between the droplet surface and the droplet/nanowire interface, the silicon atoms diffuse to the interface to be incorporated into the silicon nanowire crystal.

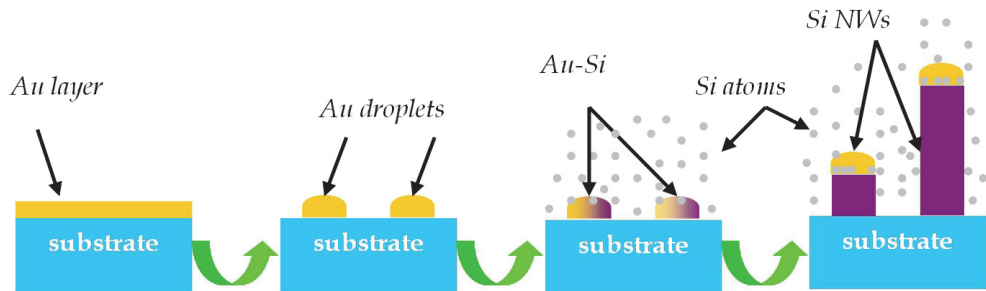


Fig. 1. Schematic drawing of the VLS process as it takes place in a PVD or CVD deposition experiment; first two steps yield the formation of gold droplets by heating of a continuous gold layer on a silicon substrate; third step shows Si atoms to reach the substrate and to be incorporated into the liquid Au-Si droplet above the eutectic temperature (Au-Si: 373°C); and in the last one supersaturation of the Au-Si droplet with Si leads to growth of the SiNW at a higher growth velocity than the continuous silicon layer in between the droplets takes place.

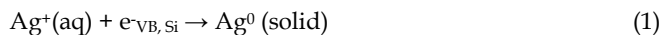
For all device concepts based on SiNWs, the crystal structure, geometry (alignment of SiNW with respect to the substrate), interfacial properties between the SiNW and the substrate as well as the Si core and the shell of the SiNW (either native or thermally grown oxide or a passivating layer like amorphous hydrogenated silicon or silicon nitride), dopant concentrations and impurity levels are of key importance for functioning of the devices. For VLS (bottom-up) grown SiNWs the additional important question arises where and how much metal catalyst (mostly, gold) from the catalyst particle, that initiates the VLS wire growth, resides in the SiNW. However, the enormous impact that even smallest concentrations of Au atoms as a dopant in silicon have a strong influence on optoelectronic properties of the SiNWs makes it essential to understand the extent to which Au atoms diffuse in the SiNW and Si(111) substrate and stay incorporated there and on the SiNW surfaces (Ostwald, 1900). Essentially after it has been shown that the Au from the catalyst is very mobile and diffuses all over the SiNW surfaces and between SiNWs at temperatures as low as 600°C, leading to Ostwald ripening process of Au nanoparticles at the NW sidewalls or even of the NW top Au droplet itself (Allen, 2008; Wagner, 1961; Lifschitz@Slyozov, 1961; Hannon, 2006). VLS approach gives high quality NWs but requires the use of hazardous silane gases at high temperature. Alternatively silicon nanowires can be formed by wet chemical etching method. Metal assisted etching (MAE) has gained an enormous interest in the last time. The technique is based on selective electrochemical etching using catalytic metal and can give ordered and densely packed arrays of high aspect ratio single crystal SiNWs with uniform crystallographic orientations. In a subsequent step, the formation of highly parallel SiNWs with desired lengths, at diameters of the order of few ten nanometers up to a few hundred nanometers could easily be obtained by an aqueous electroless chemical etching of single crystalline silicon wafers (Peng, 2002, 2005, 2006, 2007; Huang, 2008; Qiu, 2005). In this paper we will discuss on the wet chemical etching of SiNWs into a thin silicon layer on glass or single crystal silicon wafer substrates and their optical, optoelectronic and photovoltaic properties.

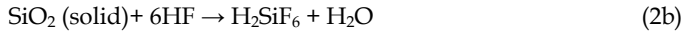
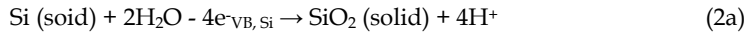
## 2. Metal Assisted Wet Chemical Etching (MAWCE)

A catalyst free SiNWs can be realized by electroless wet chemical etching or electrochemical etching into bulk Si wafers or even thin silicon layers (they can be single-, multi-, nano-crystalline or even amorphous) on substrates such as glass (Sivakov, 2009). Engineering flexibility in doping characters of silicon nanowires (SiNWs) is highly desirable to widen the range of their potential applications. Metal assisted wet chemical etching (MAWCE) is a simple and low-cost approach to fabricate SiNWs with designable doping nature. In general, MAWCE can be classified into two types, involving one-step (MAWCE-I) and two-step (MAWCE-II) reactions. In MAWCE, SiNWs are fabricated through non-uniform etching on silicon substrates in aqueous acid solutions, which is catalyzed by electroless deposition of metal nanoparticles on the substrate surfaces (Peng, 2002). This is a simple technique involving only wet chemical processing under the near ambient conditions, leading to a low-cost operation. Note that semiconductor and crystallographic characters of the as generated SiNWs are duplicated from the source substrates by MAWCE. As a result, it may be substantially achievable in MAWCE the flexible engineering of electronic and optical properties in SiNWs. In principle, MAWCE composes of two processes: metal nucleation on silicon substrates by electroless deposition or physical vapor deposition (for example, sputtering), followed by electroless etching of silicon catalyzed by the metal particles. In MAWCE-I only the second step processes consequently occur in an aqueous acid solution containing hydrofluoric acid and hydrogen peroxide. As for MAWCE-II, the metal nucleation is firstly operated in an active aqueous solution for a short period of time, and then the metal deposited silicon surfaces are transferred to another etching solution for SiNW fabrication.

### 2.1 MAWCE-I

Although MAWCE-I contains only one-step reaction, it is a complex metal catalyzed electrochemical process, involving various critical determinants, such as a concentration of metal ions and etchants, ambient temperature, reaction duration, and nature of source silicon substrates for etching (with relevance to doping character, crystallinity, and crystallographic orientation). The generation of SiNWs using MAWCE-I is involved in simultaneous reduction of metal ions, and oxidation and dissolution of silicon. For instance, aqueous hydrofluoric acid (HF) solution containing silver nitrate ( $\text{AgNO}_3$ ) is appropriately selected for etching, and the reaction mechanism has been well studied as following (Peng, 2006). An  $\text{Ag}^+$  in the vicinity of the Si substrate captures an electron from Si (eq. 1), causing  $\text{Ag}^0$  nucleation on the substrate surface. The electron transfer from Si to  $\text{Ag}^+$  is thermodynamically preferential owing to the energy level of the  $\text{Ag}^+/\text{Ag}^0$  system lying below that of the Si valence band (VB) edges. Accompanying, silicon underneath the  $\text{Ag}^0$  nucleus is oxidized into  $\text{SiO}_2$  (eq. 2a), which is dissolved by HF (eq. 2b). The dissolution of the electrochemically generated  $\text{SiO}_2$  creates a pit underneath the  $\text{Ag}^0$  nucleus, and then the nucleus falls into the pit. The excess oxidation causes accumulation of electrons on the surface of  $\text{Ag}^0$  nuclei, which attracts  $\text{Ag}^+$  in the solution to the vicinity of the nuclei, and the consequent reduction leads to the growth of Ag particles immobilized in the pits on the substrate surfaces. The corresponding reactions can be outlined by (Peng, 2005; Hochbaum, 2009)





A large amount of  $\text{Ag}^+$  in the aqueous solution and Si in the bulk substrate force these reactions occur repeatedly and continuously. As a result, successive deposition of Ag produces a dendrite layer covering the Si substrate, and vertically aligned SiNW arrays are created on the substrate. The vertical alignment is contributed to the longitudinal falling-down of the Ag particles from the surface to the bulk of Si substrates, along with continuous dissolution of Si in the vicinity of Ag particles. The lateral etching along the walls of the generated pores in the bulk Si does not readily take place, because of the longer electron diffusion pathway from the wall to Ag particle comparing to that from the pore bottom underneath the particle. Ag particles play a significant role in catalyzing the cathodic reaction (eq. 1) by effectively lowering the electrochemical reaction barrier. The length of silicon nanowires etched in MAWCE-I is limited to 50  $\mu\text{m}$  at atmospheric conditions (RT, 1 atm), but in the autoclave a length over 50  $\mu\text{m}$  can be reached (Hochbaum, 2008).

## 2.2 MAWCE-II

Compared to MAWCE-I, the nucleation and electroless etching are operated in two different aqueous solutions in MAWCE-II (Peng, 2005, 2006). The Ag nucleation in MAWCE-II takes place in a  $\text{HF}/\text{AgNO}_3$  aqueous solution, identical to MAWCE-I, followed by etching in a  $\text{HF}/\text{Fe}(\text{NO}_3)_3$  aqueous solution.  $\text{Fe}^{3+}$  is more electronegative than silicon, leading to a cathodic reaction described as



This cathodic reaction occurs in the vicinity of the electron-excessive surfaces of Ag particles catalyzed by the particles. The Si underneath the Ag particles is longitudinally dissolved by HF (through eq. 2a and 2b), and continuous occurrence of these reactions produces the vertically aligned SiNW arrays. Note that Ag particles will not dissolved by exchanging electrons with the  $\text{Fe}^{3+}/\text{Fe}^{2+}$  system, contributed from the energy level of the  $\text{Ag}^+/\text{Ag}^0$  system lying below that of the  $\text{Fe}^{3+}/\text{Fe}^{2+}$  system. The matching in the energy levels effectively facilitates the catalysis of the electroless etching by the Ag particles. Due to the lack of  $\text{Ag}^+$  in the electroless etching process, there is no dendrite layer generated on the Si substrates. Electroless etching can be also carried out in a  $\text{HF}/\text{H}_2\text{O}_2$  aqueous solution, with the cathodic reaction given by (Peng, 2007; Zhang, 2008)



The substitution of  $\text{Fe}^{3+}/\text{Fe}^{2+}$  with  $\text{H}_2\text{O}_2/\text{H}_2\text{O}$  to promote the electroless etching is based on the fact that the energy level of the  $\text{H}_2\text{O}_2/\text{H}_2\text{O}$  system lies far below that of the Si VB edges. Our chemical etching method to produce SiNWs is based on a two step process, as presented in Figure 2d (Sivakov, 2010). In the first step, Ag nanoparticles were deposited on silicon wafer surfaces by immersing the wafers in aqueous solution of silver nitrate ( $\text{AgNO}_3$ ) and hydrofluoric acid (HF) in the volume ratio 1:1 (solution I) for short time. The morphology of the forming Ag nanoparticle deposits is strongly depending on the immersion time. In the second step, silicon wafers covered with Ag nanoparticles of different morphology were immersed in a second etching solution containing HF and 30%  $\text{H}_2\text{O}_2$  in the volume ratio 10:1 (solution II) for defined time at room temperature.

We show wet chemical etching of silicon wafers involving Ag nanoparticles, HF and H<sub>2</sub>O<sub>2</sub> to realize SiNWs of different morphologies depending on processing details, e.g. Ag nanoparticle morphology, silicon wafer orientation (Si(111) and Si(100)). With this control over morphologies at hand we can realize different optical properties of the material to be custom made for optical/photonic devices such as e.g. solar cells. The different SiNW morphologies were investigated using scanning electron microscopy (SEM) as shown in Fig. 2a-c. SiNWs of different regularity and with different orientations could be obtained.

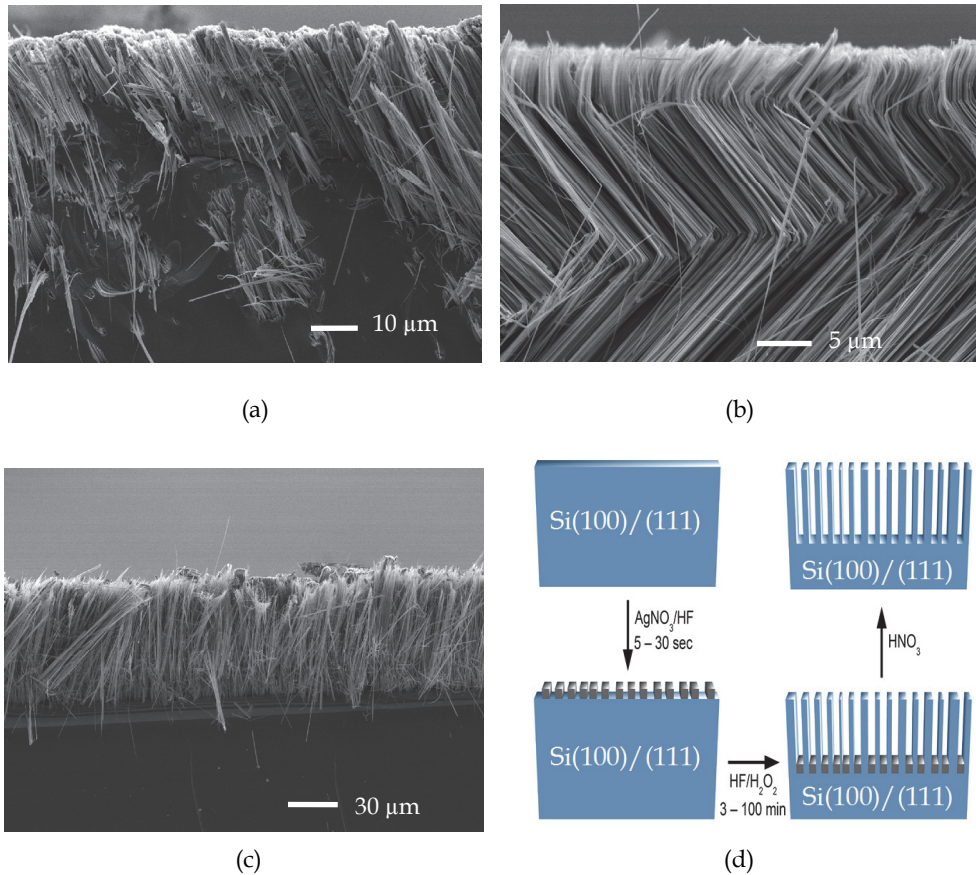


Fig. 2. SEM cross sectional micrographs of SiNW arrays formed *via* wet chemical treatment of Si(111) surfaces at: (a) 15s, solution I; 1h, solution II; (b) 60s, solution I; 1h, solution II; (c) 30s, solution I; 1h, solution II. All etching experiments were performed using initial treatment in the 0.02M AgNO<sub>3</sub> and 5M HF (solution I) followed by 1h treatment in the second etching agent contained 30% H<sub>2</sub>O<sub>2</sub> and 5M HF in the volume ratio of 1:10 (solution II); (d) schematic illustration of the etching process of silicon wafers using a sequence of two solutions; solution I is based on AgNO<sub>3</sub>/HF and solution II is based on H<sub>2</sub>O<sub>2</sub>/HF. After solution I treatment, a quasi continuous Ag layer forms on the silicon surface consisting of densely aligning polycrystalline Ag nanoparticles (Sivakov, 2010).

Homogeneous etching profiles and thus regular SiNWs were observed for samples with thicker layers of silver nanoparticles, which form as a result of longer treatment in the  $\text{AgNO}_3/\text{HF}$  solution (solution I). Based on these micrographs, it becomes obvious, that the silicon etching homogeneity is strongly depending on the morphology of the Ag nanoparticles/Ag layer. This finding is supported by TEM studies (presented in (Sivakov, 2010)) that show how Ag nanoparticles/Ag layers reside on the silicon wafer surfaces after solution I treatment, prior to solution II etching of SiNWs and also gives information about Ag/Si interface and crystallographic structure.

Our results strongly compared with existing literature data we can state the following: Chen et al. showed wet chemical etching to create SiNWs (Chen, 2008) using Si(100) and Si(110) wafers and some of their results resemble our findings, i.e. they found preferential etching along [100] directions and for changing peculiarities of the etching conditions the Si(111) wafers could also etch along [111] directions, i.e. Si(111) wafers can either be etched perpendicular to the wafer surface along [111] direction or pyramidal along [100] direction. We could show etching of Si(111) wafers for which we can realize straight etching along [111] directions or transition of [111] to [100] directions so that zig-zag architecture in SiNWs forms. To prove the varying etching directions we used electron backscatter diffraction (EBSD) in a SEM. Results of EBSD studies are shown in Fig. 3 and Fig. 4. Due to its excellent spatial resolution of a few 10 nm even over large probed areas, EBSD enables orientation analysis of SiNW with emphasis on grain size (or single crystallinity), grain distribution and SiNW orientations. Fig. 3 proves single crystallinity over the full SiNW length, as given by

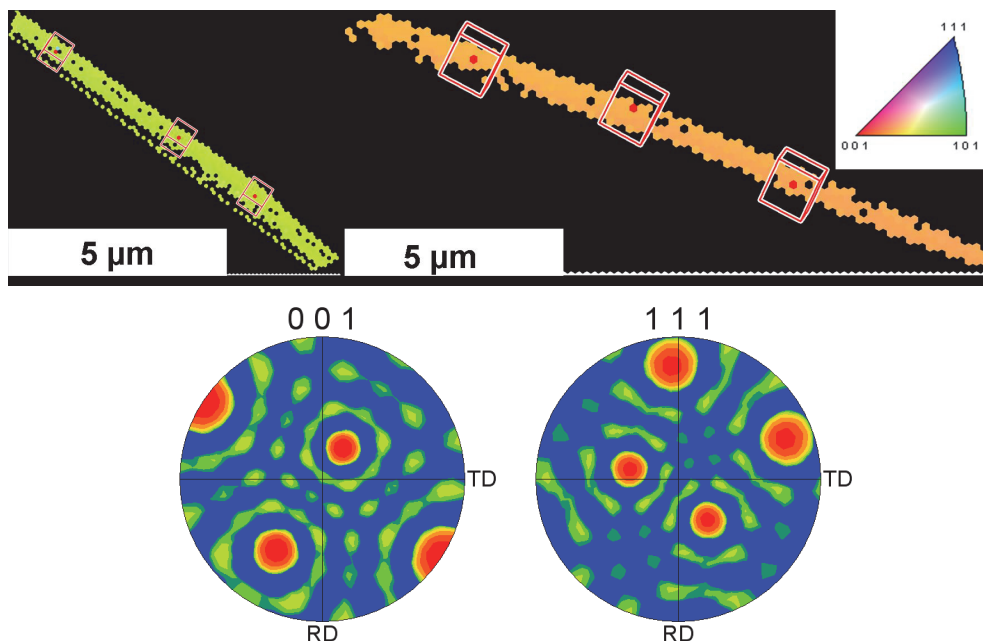


Fig. 3. EBSD analysis (inverse pole figure representation) of two silicon nanorods (SiNRs) fragments etched into a Si(111) wafer. The orientation cubes for both SiNRs show etching direction (parallel to the long axis of the SiNR) to be parallel to [100] direction.

the single colour, coding the SiNW. In contrast to the common use of pole figures for orientation representation in the following the present crystal orientation will be illustrated by orientation cubes showing the orientation of the unit cell with respect to the sample surface. Here every orientation cube belongs to an individual point of the EBSD scan and thus provides only information for the particular point. According to that the determination of small deviations between different points could not be visualized and no statistic about the entire scan could. Nevertheless it provides a direct visualisation of the present crystal orientation and enables an intuitive access to the etching direction. Here it could be shown that etching SiNW from Si(100) wafer results in wires with a long axis almost parallel to the [100] direction. The result of which is displayed by the colour coding of the SiNW surface normal which is a less important number since it shows only how the SiNW is lying on the TEM grid; thus, two SiNWs show different surface normal colour coding in Fig. 3, but identical [100] etching direction as well as the orientation cube that clearly shows the SiNW etching direction to be almost parallel to the [100] direction. In case of vertically etched SiNWs from Si(111) wafers the obtained etching direction is almost parallel to the [111] direction with uniform orientation as shown in Fig. 4.. The overlaid orientation cube for this SiNW shows the etching direction to be close to [111]. Small deviations of the expected crystal directions could result from non planar positioning of the SiNW with respect to the TEM grid support.

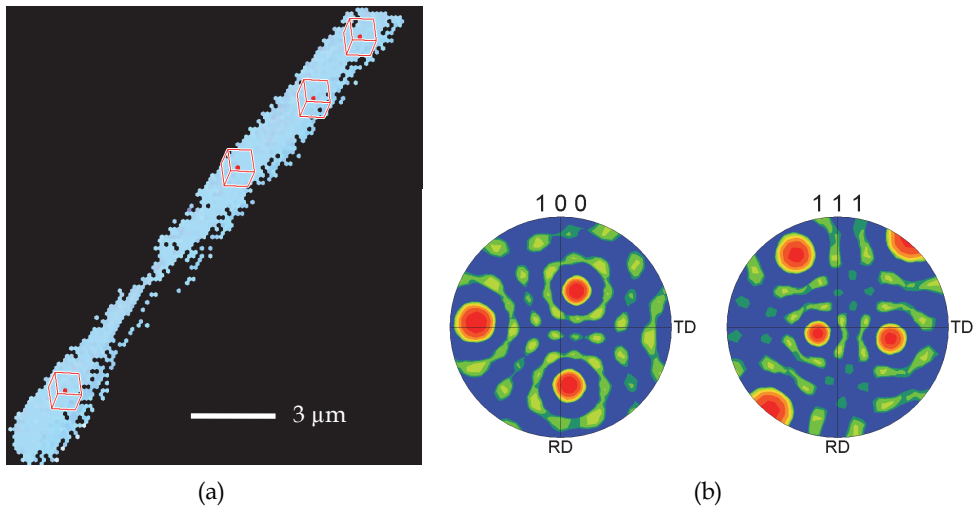


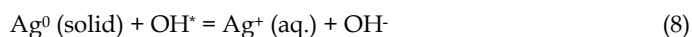
Fig. 4. (a) EBSD analysis one SiNW fragment of such a wafer; (b) colour coded inverse pole figure representation; the orientation cubes for this SiNW indicate etching direction (parallel to the long axis of the SiNW) to be parallel to the [111] direction.

To support the understanding of the differences in etching morphologies that could be observed we carried out thermodynamic considerations of the different processes. An interesting side effect of the solution I and solution II etching of silicon wafers was, that the processes substantially lead to a heating of the etching solutions from initially room temperature to strongly elevated temperatures of 85°C and above (depending on the used volumes of the solution). Our experiments show that in the first 10 minutes of etching in

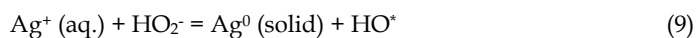
solution II (100 ml) the temperature of the solution reached 85°C, after further 15 minutes of reaction time the temperature slowly decreased again reaching room temperature again after 1h. One of the possible explanations of the energy release during the etching procedure in solution II is that a catalytic decomposition of H<sub>2</sub>O<sub>2</sub> takes place (Sivakov, 2010). Haber and Weiss (Haber@Weiss, 1935) have investigated the catalytic decomposition of H<sub>2</sub>O<sub>2</sub> in homogeneous systems, where the H<sub>2</sub>O<sub>2</sub> is primarily attacked monovalently, yielding the active radicals OH<sup>\*</sup> or HO<sub>2</sub><sup>\*</sup> (O<sub>2</sub><sup>-</sup>) which may further give rise to the chain reactions as shown in Eqs. 5, 6:



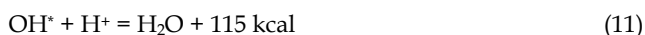
The catalytic decomposition of H<sub>2</sub>O<sub>2</sub> on Ag nanoparticles has also been studied by McIntosh [McIntosh, 1902] and Wiegel. (Wiegel, 1930). These groups have investigated the catalytic decomposition of H<sub>2</sub>O<sub>2</sub> in the presence of colloidal Ag. The colloidal Ag partly dissolves in H<sub>2</sub>O<sub>2</sub> without appreciable formation of gaseous components according to Eqs. 7, 8:



H<sub>2</sub>O<sub>2</sub> is acting as an oxidizing agent in such an environment. Initially, the Ag surface is oxidized, but finally elemental Ag is formed again according to Eq. 9.



This reaction can take place to a considerable extent, so that elemental Ag and HO<sub>2</sub><sup>\*</sup> radicals are produced. The latter starts the chain reactions of Eqs. 5 and 6 and give rise to a strong catalytic decomposition of the H<sub>2</sub>O<sub>2</sub>. As we pointed out in the experimental part, the etching process takes place in an acidic atmosphere by adding 5M HF to the solution. In the case of decomposition in an acidic solution a smaller or greater part of the H<sub>2</sub>O<sub>2</sub> is reduced to water without the formation of any gas, according to the equations taken from reference (Weiss, 1935):



As clearly see from Eqs. 10 and 11 during catalytic decomposition of H<sub>2</sub>O<sub>2</sub> on Ag nanoparticle surfaces in acidic atmosphere we have a strong exothermal reaction with substantial release of energy that can very well explain the heating of solution II in the first 10-15 minutes of the reaction followed by cooling back to room temperature once the H<sub>2</sub>O<sub>2</sub> concentration decreases with reaction time. The substantial temperature rise in the initial 10-15 min of the process may very well influence the preferred etching directions.

In conclusion, we have demonstrated that we can realize homogeneously and reproducibly over large areas SiNW ensembles by wet chemical etching of Si wafers. Different SiNW architectures can be obtained by varying Si wafer orientation and processing peculiarities. Thus, we obtain SiNWs that can either be straight and perpendicular to the wafer surface with a preferred [100] direction of the SiNWs when

using Si(100) starting wafers or zig-zag with orientations varying between [111] and [100] directions when using Si(111) starting wafers. The etching process in acidic atmosphere is a strongly exothermic process thereby heating the etching solution substantially. This process inherent temperature rise is most probably responsible for the change in etching directions with time, thereby allowing the self-organized formation of zig-zag SiNWs. The stabilization and control of straight and zig-zag SiNW formation is very promising to be applied in optical/photonic applications.

### 3. Absorption, reflectance and transmission

It appears to be obvious that straight and zig-zag SiNWs show different optical properties such as scattering, absorption and transmission of light. As reported before, wet chemically etched SiNWs exhibit a very intense optical absorption (Sivakov, 2009; Tsakalakos, 2007). These wet chemically etched microcrystalline silicon (mc-Si) surfaces show also very low reflectance compared to Si thin layers or wafers (Stelzner, 2008; Andrä, 2007, 2008). This low reflectance is potentially interesting for photovoltaic applications where enough absorption of solar light in an as thin as possible Si layer is desired and a combination of light trapping structures and antireflective coatings have usually to be applied (Peng, Xu, 2005; Kaynes, 2005; Tsakalakos, Balch, 2007). The SiNWs themselves have shown to absorb solar light very satisfactorily and can therefore be used as the solar cell absorber (Tsakalakos, 2007; Tsakalakos, Balch, 2007; Koynov, 2006). The optical reflectance spectra of MAWCE SiNWs etched mc-Si surface on glass and single crystalline wafers as reference are shown in Fig. 5a. The average reflectance of SiNWs realized by wet chemical etching is less than 5% within a range of wavelengths between 300 nm and 1000 nm. The reflectance values (R) are much smaller than those of a polished Si wafer (that shows an R of more than 30%).

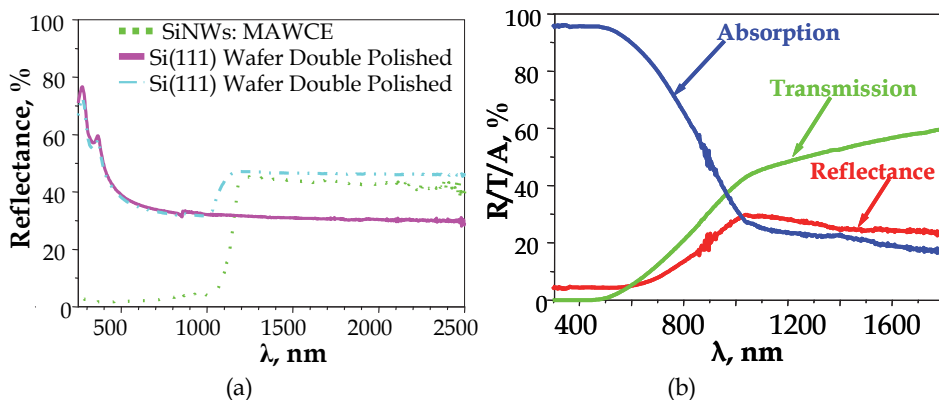


Fig. 5. (a) Reflectance spectra (Sivakov, 2009) of SiNWs prepared via  $\text{AgNO}_3/\text{HF}$  etching of mc-Si layers on glass; as a reference, single or double side polished single crystalline silicon wafers were used; (b) optical transmission (T), reflectance (R) and absorption ( $A=1-T-R$ ) of SiNWs prepared by etching of mc-Si layers on glass.

The absorption (A) of SiNWs on glass was determined from the optical reflectance (R) and transmission (T) measurements as shown in Fig. 5b. The SiNWs show a very low

reflectance as was also pointed out in Fig. 5a. In the last years, in many reports shown that Si nanostructures can be used as antireflective coatings in solar cells (Tsakalacos, 2007; Andr a, 2007; Tsakalacos, Balch, 2007; Koynov, 2006). Our observation shows the same tendency. On the other hand, it has to be stated that the SiNWs do not transmit light in the range between 300 and 550 nm. This transmission would however be important to use them as antireflection coating on top of a processed solar cell. Moreover, the absorption of mc-Si layers with etched nanowire structures at wavelength > 550 nm was observed to be higher than that of a Si layer of the same thickness. These optical phenomena are selling propositions for the realization of efficient solar cells based on etched SiNWs.

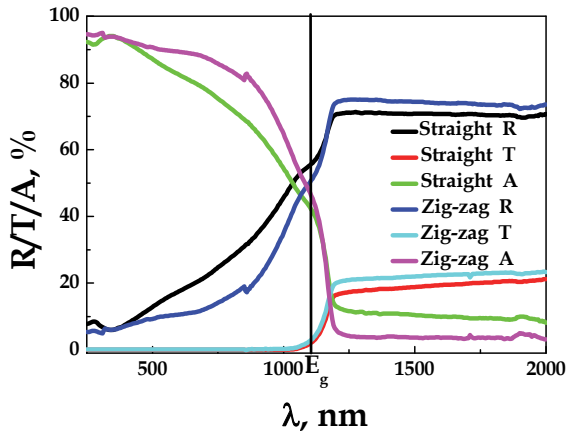


Fig. 6. Reflectance, transmission and absorption spectra of SiNW ensembles with straight and zig-zag SiNWs architecture. The solid line ( $E_g$ ) indicates the wavelength that corresponds to the Si band gap energy.

Figure 6 shows the comparison results of optical properties of samples with straight and zig-zag SiNWs using an integrating sphere. In the short wavelength range below 1100 nm the reflectance of etched SiNWs is in general low and depends on the morphology of SiNWs, i.e. zig-zag SiNWs and perpendicular SiNWs behave differently as visible from the curves in Fig. 6. The transmission spectra show for short wavelengths (<1100nm) very limited transmission for zig-zag SiNWs and straight, perpendicular to the surface SiNWs. Transmission values increase at higher wavelengths (>1100nm) for both types of SiNWs architectures. The transmission behaviour is important for the use of these SiNWs in antireflection coating applications or absorber layers both to be used e.g. for solar cells. The amount of absorbed light is significantly increased in the zig-zag SiNW material, being important for the aforementioned absorber layer application. As we observed, the absorption of silicon material with zig-zag architecture close to 1100 nm is over 60% and is thus higher than the absorption in the straight SiNWs as shown in Fig. 6.

A significant light absorption was observed in MAWCE-II SiNWs wrapped with aluminium doped zinc oxide (AZO) as shown in Fig. 7. The reflection between two phases with refractive indices  $n_0$  and  $n_s$  can be minimized by a thin layer with a refractive index of  $\sqrt{n_0 \cdot n_{Si}}$  which gives with  $n_0 \approx 1.0$  and  $n_{Si} = 3.5$  (Jellison@Modine, 1982) an ideal refractive

index of  $n_1 = 1.87$ , a value close to the value of the deposited AZO (1.85 – 1.90). Furthermore, the AZO surface is not smooth but rough, as shown in Figure 22b, from crystallites that assume the shape of half-spheres. This roughness introduces a kind of moth-eye-effect (Wilson@Huntley, 1982) and thus leads to even increased absorption. Due to the metallic back contact the solar cells do not show any transmission in the investigated wavelength area from 300 to 1500 nm, therefore the absorption  $A$  is calculated by  $A=1-R$ . The average reflectance of wet-chemically etched SiNWs wrapped with AZO is less than 10% within a range of wavelengths between 300 nm and 1050 nm. Such silicon nanostructures show over 90% absorption in the range between 300nm and 1050 nm. We have also demonstrated that lowly and heavily doped SiNWs from wet chemical etching of single crystalline silicon wafers can strongly emit visible photoluminescence at room temperature (Sivakov, Voigt, 2010). These optical phenomena are selling propositions for the realization of efficient solar cells based on etched SiNWs.

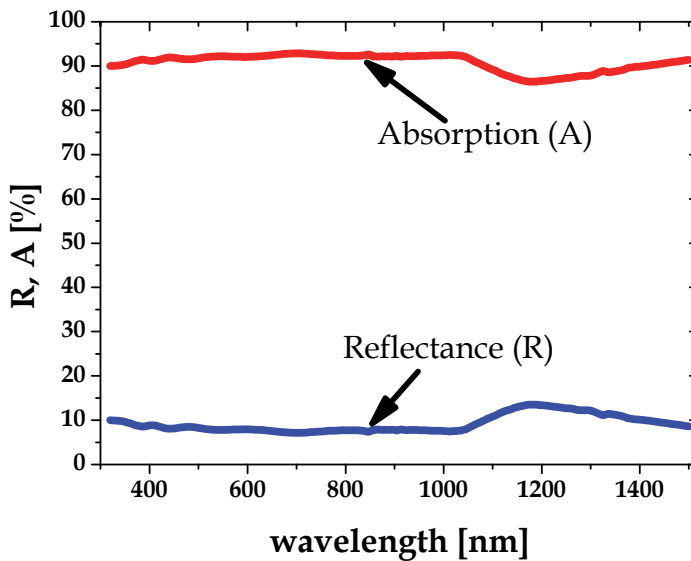


Fig. 7. Optical reflectance ( $R$ ) and absorption ( $A=1-R$ ) of semiconductor-insulator-semiconductor (SIS) solar cells based on wet chemically etched SiNWs.

## 4. Room temperature photoluminescence

### 4.1 Photoluminescence background

Enormous interest of the scientific community in the photoluminescence (PL) of Si based nanostructured silicon started, after the formation of porous silicon was realized and strong visible PL was observed (Canham, 1990). The material was obtained by anodic oxidation of crystalline Si wafers in diluted hydrofluoric acid (HF). It involves an electrochemical process, where the Si wafer serves as anode and another material is immersed as cathode within the solution. First reports of anodically etched porous silicon (AE-PSi) were

published by Uhlir (Uhlir, 1956). This publication concentrated on electrolytic shaping of Ge and Si and especially on the formation of etch pits, but did so far not mention the strong visible PL of AE-PSi, which at a later date, highly excited the scientific community. Only after the next step in porous silicon (PSi) history - the report of the discovery of strong visible PL of AE-PSi (Canham, 1990) - a real drive in the exploration of optoelectronic properties of AE-PSi started. Canham et al. attributed the PL emission at super band gap energies to the formation of quantum wires within the etched Si layer. For crystalline silicon (c-Si) the room temperature (RT) band gap amounts to  $E_{g,c-Si} = 1.12$  eV. The PL light emission in the visible range of the spectrum highly excited scientists in the field of semiconductor physics, because with this discovery one goal in the direction of building a visible range silicon LED was reached, a device which was still missing. Overall practical aim mentioned in Canham's above cited publication was the reduction of the extremely large intrinsic radiative lifetime of c-Si in order to make it feasible for light emitting devices and the followed approach for realization was the introduction of quantum confined states in silicon by anodic etching. But, so far no microscopic evidence of the hypothesis of quantum confined states as source of the found PL in the photon energy range 1.4 eV to 1.6 eV had been given by Canham, the existence of quantum confined states in AE-PSi was still a working thesis.

Contemporaneously, Lehmann and Gösele (Lehmann, 1990) published a similar hypothesis about the presence of quantum wires, resulting in quantum confinement effects in AE-PSi. But, in contrary, they concluded this result from optical transmission measurements on the etched layers, and not from PL measurements. Further strong hints to support their hypothesis were drawn from comparison of AE-PSi produced from degenerate initial Si wafer material with non-degenerate p-type silicon. For degenerate wafers, larger structures with dimensions in the range of the depletion width in the Si material - when forming a junction with the surrounding HF etchant - were found by transmission electron microscopy (TEM) and smaller structures were detected for AE-PSi obtained from p-type, non-degenerate wafers. The diameter ranges observed were further affirmed by gas adsorption measurements, by means of which the porosity of the material was estimated. The formation of wires with different diameters was explained by a model, assuming that for degenerate wafers complete depletion of the pore walls stops the etching process, whereas for p-type, non-degenerate wafers a self-limiting process occurs, which is due to quantum wire formations including band gap energy shifts. And band gap energy shifts related to quantum confinement happen at much smaller wire diameters than the depletion width inside degenerate wafers. These observations of wire diameters in complementation with investigations of absorption on AE-PSi formed from different types of initial wafers were again in agreement with the quantum confinement hypothesis in the wires. It was found that AE-PSi formed from degenerate wafers does not show quantum confinement related features in absorption measurements, whereas material formed from p-type, non-degenerate wafers did.

In the following years this initial hypothesis of quantum wire PL in AE-PSi was critically challenged and other hypotheses for the origin of the high energy PL in the material arose. These hypotheses can roughly be summarized as follows:

A Quantum confinement effects within quantum wires

B Quantum confinement effects within quantum dots (nanocrystals)

C Surface and interface effects, e.g. in the Si/SiO<sub>x</sub> boundary interfaces or more generally in the surface region

Models A and B both belong to the quantum confinement hypothesis, applied to 1D and 0D structures, respectively. Model C implies a large number of possibilities, because surfaces and interfaces of nanostructured silicon very sensitively depend on the method of preparation. There are a lot of possibilities of SiO<sub>x</sub> compounds and structures, which can lead to PL in the visible range of the spectrum. Overall, one can conclude from publications and review articles on this field, that all three hypotheses (A, B, C) are appropriate, but which one applies in each case depends on the exact microscopic and nanoscopic structure of the AE-PSi sample under investigation. For the hypothesis A and B more detailed specification of the models is not necessary here, they are sufficiently well defined by the sentences above and sketched in Figures 8a, b. There exist many publications on methods to prepare precisely defined single silicon nanowires (SiNWs) (e.g. Peng, 2002; Hochbaum, 2009; Qu, 2009; Sivakov, 2009; Stelzner, 2008) or silicon nanocrystals (Si-NCs) (e.g. Ehbrecht, 1995) and also a lot of publications about PL originating from single SiNWs (e.g. Walavalkar, 2010) or Si-NCs (Huisken, 2002; Ledoux, 2002). Basis of most of the PL studies on these low dimensional single structures is mostly a quantum confinement effect, which induces an energy shift of the emission peak with respect of the RT band gap of silicon.

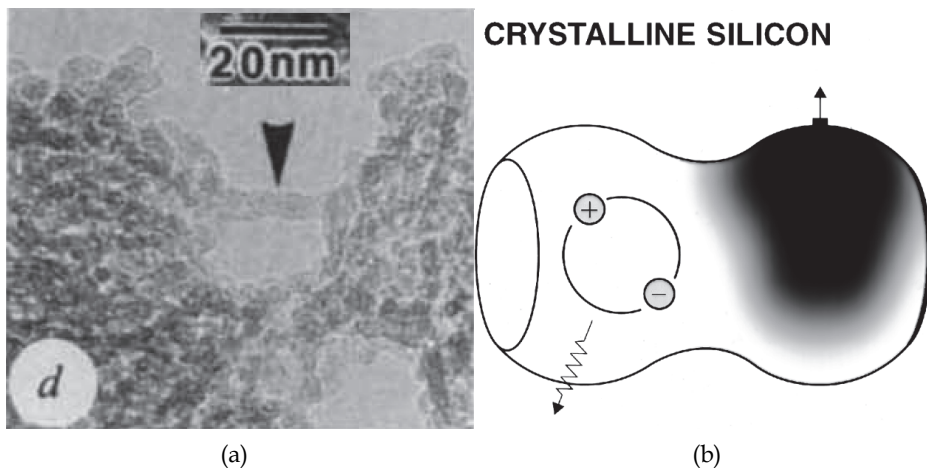


Fig. 8. PL generation in nanostructured Si due to quantum confinement effects. (a) Quantum wire as seen by TEM in an AE-PSi sample, referring to hypothesis A; Reprinted by permission from Macmillan Publishers Ltd: nature (Cullis, 1991), copyright 1991. (b) Nanocrystals or homomorphous, near 0-dimensional structures, referring to hypothesis B; reprinted with permission from (Cullis, 1997). Copyright 1997, American Institute of Physics.

There have been proposed numerous models for the origin of visible PL, belonging to hypothesis C. Many of them were summarized in the review article (Cullis, 1997). We will further roughly follow this review article in order to discuss the main issues thereof. Fig. 9 shows four possible sources of PL origin as discussed in (Cullis, 1997), which we will discuss in the following paragraphs.

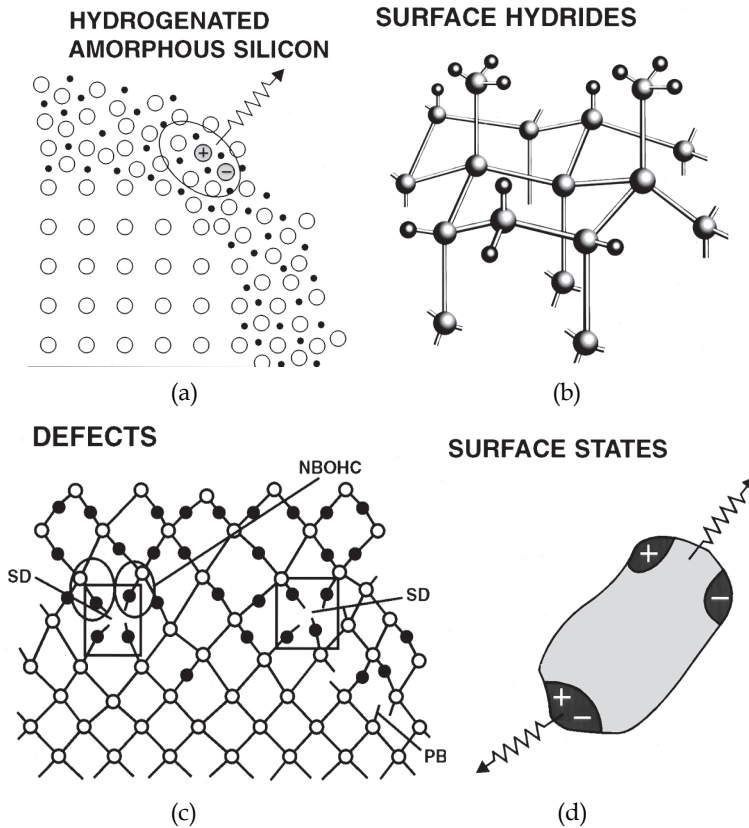


Fig. 9. Four models of PL origin belonging to hypothesis C. Reprinted with permission from (Cullis, 1997). Copyright 1997, American Institute of Physics. Part (d) was initially adopted from (Koch, 1993) and is reproduced with permission by Cambridge University Press. 4.1.1 Hydrogenated amorphous silicon

Hydrogenated amorphous silicon (a-Si:H) can be formed on the surfaces of the porous material (Street, 1991). In the transition region between the crystalline cores of the porous material and the surface, nonstoichiometric silicon oxide ( $\text{SiO}_x$ ) is formed. This region usually is of amorphous structure, and in the presence of hydrogen atoms during the preparation process, also incorporates H-atoms. The presence of H-atoms is true in the case of AE-PSi, as the Si surfaces immediately after removal from the dilute hydrofluoric acid are known to be hydrogen terminated (Kolasinski, 2009). It is known that a-Si:H possesses a PL band with peaks in the photon energy at 1.3 to 1.4 eV (Carius, 2000). In the following, if we speak about energy ranges in PL emission, always the ranges of the peak positions are denoted. Furthermore, PL emission range can be tuned by variation of hydrogen and also oxygen content within the material. Variations of oxygen content in a-SiO<sub>x</sub>:H films were reported to result in photon energy emission ranges as large as from 1.3 to 1.7 eV (Carius, 2000). The different ranges of PL emission due to several possible origins of PL are also summarized by Voigt et al.

### 4.1.2 Surface hydrides

Surface  $-\text{SiH}_2$  species were found to be essential to the visible PL of AE-PSi (Tsai, 1991) and proposed as possible origin of PL of AE-PSi (Wolford, 1983). However, this hypothesis in the course of research was falsified. Main knock-out criterion were observations by FTIR studies, which showed that PL can be quenched for AE-PSi samples, while only a small fraction of surface hydrides is removed from the sample by thermal desorption, but the main part of the hydrides still remain on the samples surface. Hence, there is “no direct correlation between the PL and the silicon hydrogen surface species” (Robinson, 1993). The passivation quality of the surface hydrides rather seem to imply a PL, and not the hydrides themselves are a source of PL. Similar PL can be obtained by AE-PSi either passivated by hydrides – as it is known to naturally be the case for freshly prepared samples – or passivated by a high quality surface oxide. Also, recently methoxy ( $-\text{OCH}_3$ ) group passivation of the surfaces of porous silicon appear to have a similar passivation effect as hydrides or well grown oxygen. In summary, surface hydrides have been shown not to be direct source of the main part of visible PL in AE-PSi.

### 4.1.3 Defects

Several possibilities of carrier location at distortions of stoichiometrically built crystal lattices can be accounted to the category of defects. These defects can be either localized within the c-Si cores of AE-PSi, or are found near the boundaries of the crystalline cores within the AE-PSi samples. Near the oxide of the c-Si cores, defects are formed more often, because only there the elemental ratios show up gradients, dependent on the surface treatment of the samples after preparation. For the case of oxidized samples the material composition shows a transit from c-Si to  $\text{SiO}_2$ , where one has to keep in mind that additionally hydrogen can be incorporated due to initial hydrogen termination of the surfaces immediately after preparation. Known defects of this kind are three types of non bridging oxygen centers (NBOCs). These defects consist in trapped holes located at an oxygen atom owing a bond only to one neighbour atom. The first kind of this defect is an “isolated” Si-O, the second one is stabilized with a hydrogen bond Si-O ... H-O, the third type is the least understood and is likely to be caused by the strain of bonding configurations or density (Prokes, 1996). NBOCs emit light in with peaks around 1.9 eV and FWHM of 0.1 to 0.3 eV – depending on which types of the various forms of NBOCs are present in the material (Skuja, 1979; Hibino, 1985; Munekuni, 1990; Nishikawa, 1991).

Most important support for the relevance of defect states in the luminescence of AE-PSi was derived from electron spin resonance (ESR) measurements. We therefore introduce the relevant ESR specific nomenclature, following (Prokes, 1996), see Fig. 10: Oxygen shallow donors (SDs) have been described as oxygen clusters at a silicon vacancy, in AE-PSi they occur near the sample surfaces and consist of a cluster of NBOCs. Furthermore, dangling bonds exist at silicon surfaces, if they are not entirely passivated by hydrogen or other species; they are called  $P_b$  centres in ESR nomenclature. After oxidation of freshly prepared AE-PSi a new type of defect appears in ESR measurements, called EX center. According to Stesmans et al. (Stesmans, 1994) EX centers consist of NBOC clusters, sharing a delocalised electron. These three types of Si-O related defect centres are suggestively sketched in Fig. 3. A major pro argument for the hypothesis that defects play a considerable role in the PL of AE-PSi was the observation that at low temperature annealing the  $P_b$  signal increased together with the SD signal and at the same time PL became more intense (Prokes, 1996). This experimental result cannot be explained by the non-radiative recombination channel,

which is opened by  $P_b$  centers, because PL would have to decrease with increasing  $P_b$  signal. Thus, the variation in PL intensity is not controlled solely by a change in surface passivation, but must have other reasons. An evident explanation is that the increase of SD signal - and therefore an increase in NBOC density - accounts for the higher PL yield.

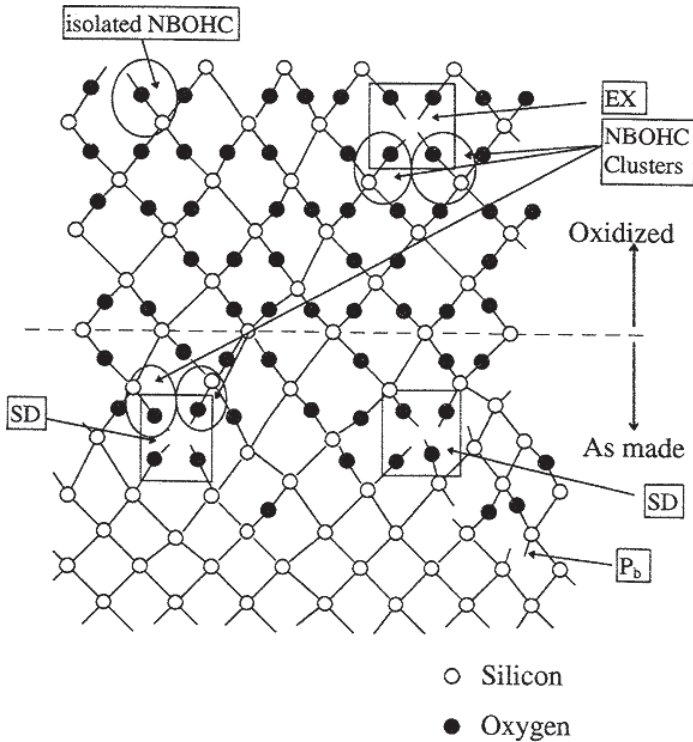


Fig. 10. Detailed model sketch of Si-O based NBOC defects; Reprinted with permission from (Prokes, 1995). Copyright 1995, American Institute of Physics.

A more elaborate model of how defects in the silicon oxide/silicon interface could act as luminescent centers within porous material was discussed by Sacilotti et al. in (Sacilotti, 1993). It is based on the idea of type II semiconductor interface PL, which was inspired from the case of a AlAs/GaAlAs/AlAs heterostructure.

At this point we clearly state that different sources of PL can be present in differently prepared and differently surface treated AE-PSi. Further, the author believes that this point of view is helpful in understanding the PL of AE-PSi and of other kind of nanostructured silicon derivatives, because there probably are a variety of existing PL mechanisms in complicatedly micro and nanostructured samples, and it is only a matter of knowing which PL channel prevails in each case, to appropriately explain the main PL mechanism.

#### 4.1.4 Surface states

Reason for the presumption that surface states may play a role in PL of porous silicon structures was the consideration that the internal surface of porous silicon is very large.

There have been proposed 2 types of surface states for AE-PSi, one being energetically deep states, the other one shallow states (see Fig. 9d). Experimental evidence for the existence of non-quantum-confined states consisted in the observation of a large energy difference between absorption and PL peak in samples of AE-PSi (Lockwood, 1994). This energy difference was attributed to the existence of surface states, in which excited carriers relax after being absorbed in the crystalline parts of the material.

## **4.2 Photoluminescence in metal assisted wet chemically etched silicon**

### **4.2.1 Introduction**

Our main interest in PL on MAWCE-II silicon nanowire (SiNW) structures is to explore the origin of PL in each material produced with specific preparation parameters, which is a scientific basic research concern. In addition, the view on application of such obtained classes of materials is very challenging. As it is said in the credo of the semiconductor industry that “if it can be done in silicon, it will be done in silicon” (Vetterl, 2000), also light emitting devices will be built from silicon if sufficiently strong and fast emitters will be feasible. It’s this respect, which the applied side of development aims to building a “silicon diode” or even better, constructing a “silicon laser”. In this respect it is essential to overcome two main shortcomings of bulk c-Si.

A The band gap in the infrared regime of the spectrum

B The long PL lifetimes, which are related to the indirect nature of the silicon band gap

Shortcoming A was already solved by emission of visible PL of AE-PSi and this feature is still maintained by the material obtained by MAWCE-II. Shortcoming B is more complicated to be eliminated. Many approaches have been followed so far, but the final goal has not been reached yet, as one can see from the observation that no “silicon laser” with silicon or silicon compounds as active part of the device is available on the market to the best of the author’s knowledge. Nevertheless, silicon based light emitting devices (LEDs) with c-Si as the light emitting source already exist in laboratories. Green et al. (Green, 2001) introduced a c-Si based device, similar to a high efficiency solar cell, but this LED emits in the infrared region with photon energies near 1.1 eV and therefore does not overcome drawback A. Presti et al. (Presti, 2006) published an article about electroluminescence of a Si quantum dot based LED in combination with a photonic crystal structure. This device emits light in the visible range of the spectrum, however to the best of the author’s knowledge, they are not available on the market. And devices based on silicon nanocrystals (Si-NCs) do – as far as the author knows – not overcome drawback B. In Si nanocrystals the nature of the band gap is still predominantly indirect (Guillois, 2004). This issue is especially important, because long radiative lifetimes imply low emission decay rates, lead to low quantum yields at high excitation and finally hinder the design of a Si laser.

Solar cells built from AE-PSi or material produced by MAWCE follow a similar track, with the difference that shortcoming B is not so relevant in this case. For solar cells, the desired output is electric energy and not radiative emission. The negative nature of B for solar cells is only that absorption for indirect band gap semiconductors is very low as compared to direct band gap semiconductors.

### **4.2.2 Samples prepared from heavily doped and from weakly doped c-Si wafers**

Fascinating feature of samples prepared from heavily doped wafers by MAWCE-II is their shiny bright visible PL emitted in the orange-red spectral range (Fig. 11b). This strong

visible light emission is only observed for samples prepared from heavily doped silicon wafers (by about  $10^{20} \text{ cm}^{-3}$ ), whereas samples from weakly doped wafers (about  $10^{16} \text{ cm}^{-3}$ ) show considerably weaker light emission (see Fig. 13). We observed that this trend does not, or only marginally, depend on the type of doping, on whether it is n-type or p-type. All PL measurements presented in this section were performed on a setup as described in our previous work (Sivakov, Voigt, 2010).

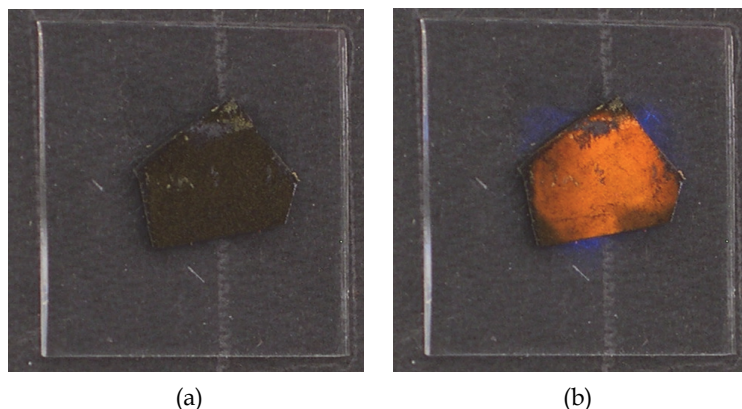


Fig. 11. Bright visible orange-red PL as seen from a heavily doped sample prepared by MAWCE-II. (a) Sample as seen under exposure to white light; (b) the same sample additionally irradiated by laser light at wavelength of 337 nm. Blue luminescence is due to the glass substrate whereon sample was mounted. Reprinted from (Voigt, 2011).

Complementarily, structural investigations by SEM have shown that MAWCE-II samples prepared from heavily doped wafers own a mainly porous nanostructure (see Fig. 12a), whereas samples prepared from weakly doped wafers for certain preparation conditions are composed of SiNWs standing on the substrate like grass on an English yard's garden (conf. Fig. 2c). If one looks at the porous-like structure of the heavily doped samples in more detail, one observes that they also show up longish, wire-like features (Fig. 12b). These features might, however, not be of crystalline type, but again porous themselves as we observed in TEM measurements (not shown in this publication) and as (Qu, 2009) also pointed out for similarly prepared samples.

As the strong visible PL of the porous-like, heavily doped MAWCE-II samples reminds of the PL observed from high porosity AE-PSi - obtained by heavily doped, but non-degenerate p-type wafer material (Lehmann, 1991) - this implies that the nanostructure of the MAWCE-II samples might be very similar to the one of highly porous AE-PSi samples. In comparison to AE-PSi samples, we conclude that

- the large PL yield of heavily doped MAWCE-II samples in the visible range reminds of similar PL observed for highly porous AE-PSi.
- the microstructure of weakly doped MAWCE-II samples shows up SiNWs, in best case similar to Fig. 2c.
- the microstructure of heavily doped MAWCE-II samples resembles that of highly porous AE-PSi, with the difference that in highly doped MAWCE-II samples also wire-like structures are seen, but these are probably porous themselves again.

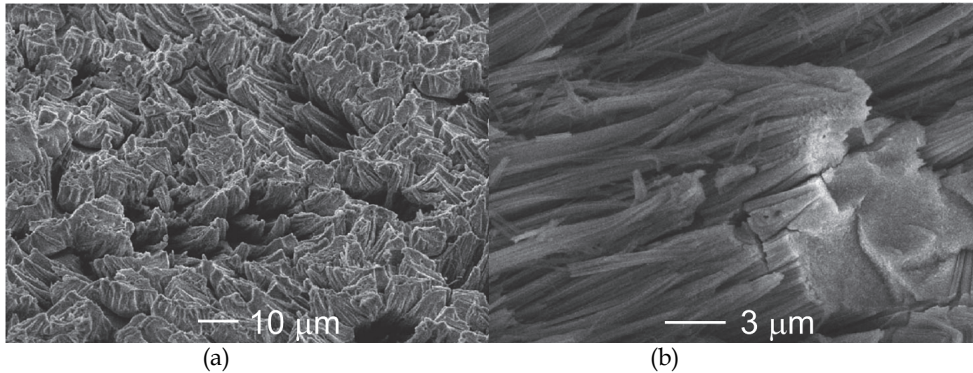


Fig. 12. SEM microstructure studies of heavily doped ( $10^{20} \text{ cm}^{-3}$ ) MAWCE-II silicon surfaces (Voigt, 2011). (a) Unordered, porous-like structure seen in top view; (b) in side view and larger magnification it becomes visible that also in this material wire-like features are present.

One has to bear in mind that as well by anodic etching as by MAWCE-II a large variety of microstructures can be achieved, sensitively depending on the initial wafer type and the following etching conditions. With this respect it is illustrative to especially examine the overall influence of the initial wafer's doping density on the nanostructure and the PL spectra. Fig. 13 shows PL spectra, which were obtained from various samples, prepared by MAWCE-II.

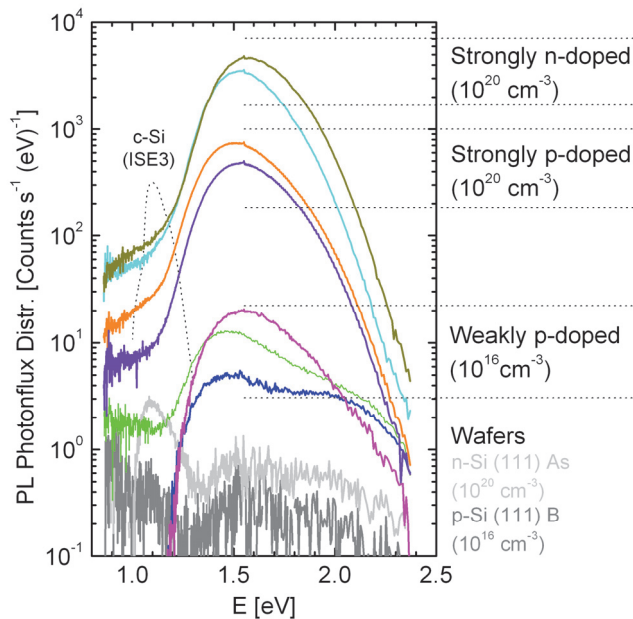


Fig. 13. PL spectra of differently doped as-prepared, oxidized samples, prepared by MAWCE-II. Dotted line and solid grey lines denote PL of crystalline Si wafers, showed for comparison.

Main trends in the yield of the different samples can be related to the initial wafers' different grades of doping. The higher the doping density is, the higher quantum PL yield will be gained. It became evident from more extensive measurement series that for MAWCE prepared samples this relation holds, independently whether n-type or p-type initial wafers are used (not shown in this publication). The type of doping plays a minor role and does not disturb the main general trend. Additionally, we performed measurements of PL spectra after an etch in dilute HF (dashed lines), which will be treated in the following subsection.

#### 4.2.3 Influence of subsequent HF treatment to MAWCE samples

What is interesting in the observation of PL prior and posterior to HF treatment of the already oxidized MAWCE produced samples, is the ability to distinguish between PL sources, which are due to the oxide-free part of the sample and sources which lie in the oxide or the oxide/silicon interface. This is possible because an etch in dilute HF strips off the oxide from the sample and after removal from the etchant the surface of the nanowire-like or porous material is still passivated by hydrogen atoms (Ikeda, 1995; Kolasinski, 2009). According to our experience this passivation sufficiently holds for duration of about 5 to 10 min, in order not to perturb spectral PL measurements. Fig. 14a shows measurements of PL before and after etching in diluted HF (2.5%) for duration of 3 min. After the HF bath, the samples were rinsed by deionized (DI) water and blown dry by ambient air. The sample under investigation for re-oxidation investigations (Fig. 14b) was prepared from an n-type c-Si (111) wafer, doped by arsenic As with a density of  $10^{20} \text{ cm}^{-3}$ . It was prepared by a MAWCE-II process and is of highly porous type rather than nanowire containing. One clearly sees that

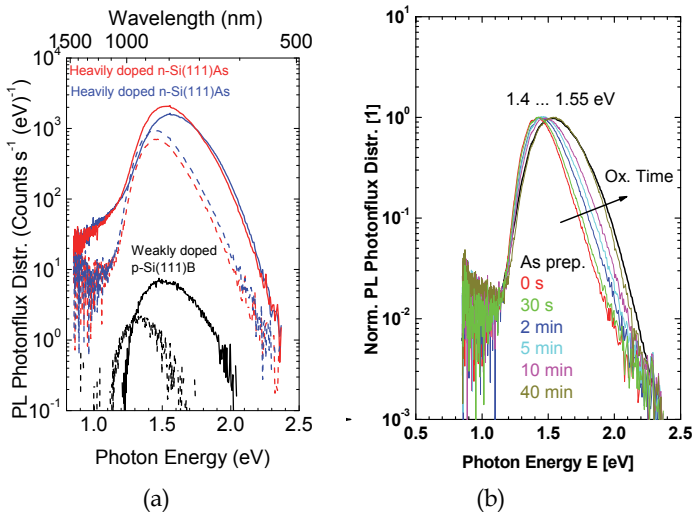


Fig. 14. Spectrally resolved PL of samples prepared by MAWCE (Sivakov, Voigt 2010). (a) PL measurements before (solid line) and after (dashed line) HF treatment on the as-prepared, already oxidized samples of different doping; (b) re-oxidation of an HF treated porous sample. All curves are normalized to obtain the value 1 in the maximum. Also indicated is the PL measurement on the as prepared, oxidized sample. Oxidization times after the first measurement are listed in the legend.

PL of all samples shrinks by the HF treatment and the peak shifts from higher to lower photon energies (Fig. 14a). We attribute this to a loss in energy states, which were due to the silicon oxide film or the Si/SiO<sub>x</sub> interface. These hypothetical energy states must be located in high energy range with photon energies around 1.6 eV, whereas the remaining PL is centred around 1.4 eV. The remainder of PL at all after etching is a strong hint to the existence of quantum confined states within the material. Quantum confined states giving rise to a PL emission with peak at 1.4 eV can be attributed to silicon nanocrystals with mean diameter of approximately 6 nm, if one follows the equation

$$\frac{d}{\text{nm}} = \left( \frac{3.73 \text{ eV}}{E_{PL} - E_{g,\text{Si}}} \right)^{1/1.39} \quad (12)$$

where  $d$ ,  $E_{PL}$ ,  $E_{g,\text{c-Si}} = 1.12 \text{ eV}$  mean the nanocrystal diameter, PL peak energy and silicon RT band gap, respectively. Eq. 12 can be derived by simple reorganization of formulae given in (Delerue, 1993) and (Ledoux, 2000).

#### 4.2.4 Re-oxidization of HF treated sample

By observation of the re-oxidation of HF treated samples, further insight in the PL mechanism and sources of PL is gained. The advantage of measurements during reoxidation as compared to the previously discussed observation of the effect of HF treatment is that a process is monitored and not only initial and final states are observed. Normalized PL spectra, recorded during this process are shown in Fig. 14b. The black line designates the as-prepared, oxidized sample. After removing the sample from the HF etchant, rinsing it by DI water and blowing it dry by air, we had to wait for < 3 min until the first PL measurement could be performed, for transfer and sample mounting reasons. The measurement performed directly after this time is labelled by "0 s". We assume that no or very little effect of re-oxidation in ambient air happens during the transfer time. The results show that the initial state of the as-prepared sample was nearly reached after 40 min of re-oxidation.

#### 4.2.5 Models

Various models have been proposed in order to describe PL arising from AE-PSi; examples have been enumerated and explained in Section 4.1. Here, we want do discuss in more detail about models appropriate to explain the main features observed during RT PL experiments on MAWCE-II prepared samples, as described in Sections 4.2.1 to 4.2.7.

##### *2-media model comprising localized confinement*

We start with a simple 2-media model sketched in Fig. 15a, which can be applied to SiNW containing samples of this kind. The black "stalk" in the middle of Figs. 15a and b symbolizes the crystalline core of the nanowire. Small nanocrystals are located within the SiO<sub>x</sub> layer surrounding the SiNW. They are isolated from each other and from the SiNW stalk by SiO<sub>x</sub>. As the PL contribution due to the crystalline SiNWs can be neglected if their diameters are large enough, main parts of the PL spectrum will stem either from quantum confined states or SiO<sub>x</sub>-related states. Because of the assumption of only 2 PL active sources within the material, we call the model a 2-media model. PL from the medium of Si-NCs in this model corresponds to light emission from quantum confined states. PL from the

medium of  $\text{SiO}_x$  can be attributed to amorphous  $\text{SiO}_x$  (see Subsec. 4.1.1 and Carius, 2000), to Si-O related defects (see Subsec. 4.1.3) or to surface states localized at the Si/ $\text{SiO}_x$  boundary (see Subsec. 4.1.4).

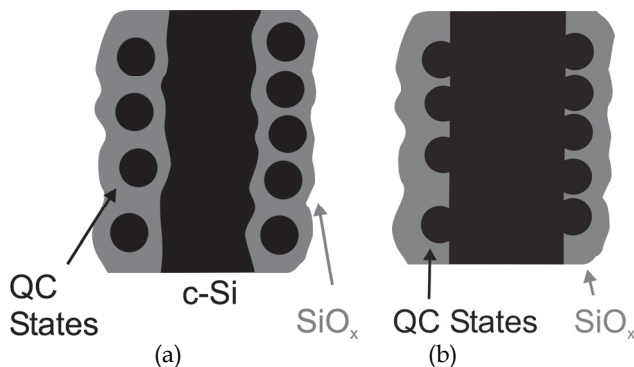


Fig. 15. Two-media models for SiNWs containing samples prepared by MAWCE. The dark part in the middle of the figures symbolizes a single crystalline SiNW. (a) Model of localized confinement of charge carriers in isolated Si-NCs within a matrix of amorphous  $\text{SiO}_x$ . (b) Model of semilocalized confinement of charge carriers within Si-NCs, being still attached to the crystalline core of a SiNW.

#### *“Millet gruel” model*

The 2-media model of localized confinement shown in Fig. 15a can account for PL measurements on MAWCE-II silicon, which really show crystalline-core SiNWs within the material. However, under certain deposition conditions no SiNWs are found inside the etched part of the wafer and another model has to be considered. For some MAWCE-II silicon a model holds, which we call the “millet gruel” model. The millet seeds within the gruel symbolize the Si-NCs within the porous matrix and the milk-starch-mixture surrounding the seeds symbolizes the oxide layers (see Fig. 16). Although there are no wire-like or more extended structures present within the millet gruel, it looks similar to a SEM



Fig. 16. The “millet gruel” model of porous silicon. It can be appropriate for AE-PSi as well as for MAWCE samples, while strongly depending on preparation parameters. The millet seeds symbolize single silicon nanocrystals, which are interconnected by milk-starch-mixture mush, symbolizing the  $\text{SiO}_x$  regions of porous Si.

micrograph of AE-PSi, shown in Fig. 12a. Also in the millet gruel wire-like features are formed, but they do not consist in longish seeds, but in seeds bonded together by an adhesive medium. Likewise, in highly porous AE-Psi as in samples belonging to Fig. 12a there may not be any SiNWs present and the longish structure to be seen in the figure might only be a chain of Si-NCs glued together by SiO<sub>x</sub>. In this case, and only in this case, the “millet gruel” model is appropriate. In comparison to the 2-media model of localized confinement, this model only lacks the interface between the crystalline SiNWs and the SiO<sub>x</sub>, and the SiNW cores themselves.

#### *2-media model comprising semi-localized confinement*

The 2-media model comprising semi-localized confinement resembles the one assuming localized confinement. In both cases crystalline SiNWs are present within the regarded material. The only difference between the models is that in the semi-localized case the Si-NCs are still attached to the crystalline SiNW core, forming kind of protuberances at a rough Si-NW surface. Actually, by TEM investigations, SiNWs with very rough surfaces have been found in weakly doped MAWCE-II silicon (Sivakov, Voigt 2010). The corresponding peak to valley height of the sidewall roughness was found to lie in the range between 2.5 to 3.5 nm. In order to understand, how a shift of PL emission peak energies can be explained by the model of semi-localized confinement, one has to regard 3 items:

- Confinement within the Si-NC-like protuberances will only occur, if one of the two charge carriers – either the electron or the hole – is trapped at some surface part of the protuberance. Two quasi-freely existing charge carriers of opposite electrical charge, or more precisely an exciton, would not move into a protuberance, where the total energy will be increased due to quantum confinement.
- Several energy contributions have to be taken into account, if one wants to calculate the energy of the finally emitted photon. These are
  - the Coulomb-attraction between the electron and hole,  $\Delta E_{Coul}$
  - the energy decrease of the exciton due to localization of one charge carrier in a trap,  $\Delta E_{trap}$
  - the energy increase of the system due to (semi)confinement,  $\Delta E_{conf}$
- The state achieved as semi-localized state (one carrier trapped at surface of protuberance) must be of stable or metastable type. I.e., an energy barrier must exist for the electron hole pair to diffuse into the bulk of the SiNW and form a free (if the SiNW diameter is large) or a wire-confined state (if the SiNW diameter is small).

In summary, the energy  $E_{Phot}$  of the emitted photon can be calculated as

$$E_{Phot} = E_g + \Delta E_{conf} - \Delta E_{Coul} - \Delta E_{trap} \pm E_{Phon}, \quad (13)$$

where  $E_g$  and  $E_{Phon}$  denote the semiconductor band gap and the energy of an emitted or absorbed phonon.

A similar model as the one of semi-localized confinement has already been proposed to explain the process of electroluminescence (EL) generation of AE-PSi by (Billat, 1996). The latter model is sketched in Fig. 17. Additionally to the kind of “semi-localized Si-NCs” to be seen at the boundary region of the material, the model does also incorporate the development of the material’s surface structure by the process of electrochemical oxidation within the electrolytic environment during the EL emission (oxidation process steps in Figs. 17a-c). The proposed oxidation leads to a decrease of the Si-NC like structures’

diameters, which is in accord with the observation of a shift of the PL peak to higher photon emission energies with time. As higher photon energies correspond to lower diameters in the framework of quantum confinement models, the observation of shift together with the proposed model are strongly supporting the hypothesis of the possibility of semi-localized quantum confinement within Si-NC-like protuberance.

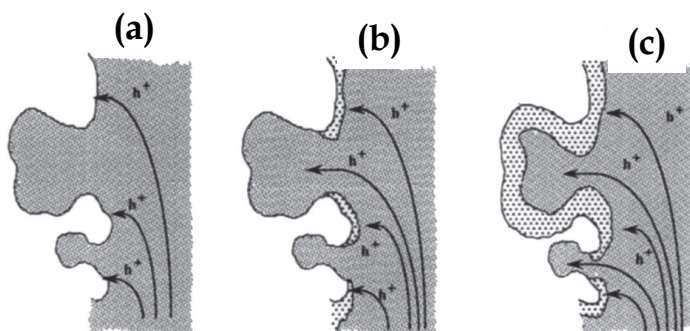


Fig. 17. Sketches of a model designed to explain the electroluminescence (EL) of AE-PSi. Image from (Billat, 1996). Reproduced by permission of ECS – The Electrochemical Society. Single Si-NC-like protuberances are seen at the boundary of the bulk Si part. Steps (a), (b), (c) symbolize the evolution of the material due to oxidation in electrolytic environment during EL measurements.

#### *Model of self-trapped exciton (STE)*

The model of semi-localized confinement can be complemented by the model of self-trapped excitons (STEs), described by Delerue et al. (Delerue, 2004 in Sec. 6.4). In the latter model it is assumed that under certain circumstances an electron hole-pair can be localized on a single covalent bond. If the implicated lattice displacements of the two corresponding atoms are large enough, the separation between the anti-bonding and the bonding state will decrease much, leading to a large energy shift between the photon absorption in the bulk part and the photon emission, due to the exciton localized on the bond (Stokes-shift). A large Stokes-shift of about 1 eV has actually been observed for a sample of oxidized AE-PSi with crystallite diameters of about 1.5 nm (Lockwood, 1994), as was already mentioned in Subsec. 4.1.4, dealing about surface states. The model of STEs was accompanied by calculations of various kind (Delerue, 2004), hence it can be regarded as theoretically funded.

### **4.3 Discussion and conclusions**

We focused on spectral RT measurements of PL on MAWCE-II silicon in this section, including investigations on

1. the dependence of spectral PL on doping grade of the samples,
2. surface treatment by HF and
3. re-creation of PL due to reoxidation.

Samples can be either of SiNW-like type – corresponding to weakly doped initial wafers – or of porous type, resembling AE-PSi – corresponding to heavily doped initial wafers. SiNW-like samples usually show up low PL emission, whereas samples of porous types emit

strong visible PL in the red-orange spectral range. After treatment by dilute HF the high-energy part of PL vanishes – as well for SiNW-like as for porous samples. Interestingly the disappearance takes place not in the total spectral range, but significant PL contributions remain centred around the peak energy at about 1.4 eV. We conclude that different sources of PL are present in the MAWCE-II processed samples. This is evident from PL measurements before and after HF treatment of the as-prepared, already oxidized samples and from the process of re-oxidation. We explain these observations by the following models, which categorize different parts of the PL spectrum to different structural features or regions, corresponding to the sources of PL as discussed for AE-PSi in Subsec. 4.1.

- i. The 2-media model of **localized** Si-NCs within a matrix of  $\text{SiO}_x$  surrounding the SiNWs in MAWCE-prepared samples (Fig. 15a) sufficiently explains the origin of PL prior and posterior to HF treatment. The crystalline silicon core of the nanowires plays with respect to PL emission no role, hence this model can also be applied to highly porous structures, where only Si-NC-like features are present embedded in an amorphous matrix of  $\text{SiO}_x$ . In this regard the 2-media model of localized confinement can for highly porous samples better be changed to the “millet gruel” model (see Fig. 16). By means of this model also the development of PL after HF etching and during the process of re-oxidation can be interpreted. After the HF etch, the oxide around the Si-NCs and the SiNW is entirely removed. Therefore only PL from quantum confined states within the Si-NCs remains (being centered at about 1.4 eV as seen in Fig. 15a, b). During the process of re-oxidation two processes occur simultaneously. Firstly, the  $\text{SiO}_x$  layer is built up again, leading to steadily increasing  $\text{SiO}_x$ -related PL. Secondly, the diameters of the Si-NCs shrink, which increases the confinement energy according to eq.12, hence the confinement part of the PL shifts to higher energies. The first process is readily seen in Fig. 4b, process 2 plays a minor role and its effect is only visible after application of successive HF etch steps.
- ii. The “**millet gruel**” model is a submodel of the 2-media model of **localized** confinement, the only difference being the leave-out of the crystalline SiNW cores. This model applies for highly porous Si material.
- iii. Another 2-media model featuring **semi-localized** Si-NCs within the matrix of  $\text{SiO}_x$  was introduced (Fig. 15b). It can explain PL emanating from SiNWs with rough surfaces, without assuming the existence of isolated Si-NCs within the  $\text{SiO}_x$  matrix. However, this model currently lacks direct experimental support and theoretical foundation and is therefore speculative.

another model was cited in Subsec. 4.2.5, which explains the PL of porous Si with very small diameters around 1.5 nm as a result of self trapped excitons (STE), being localized at the boundary of small Si-NCs (see ref. Delerue, 2004). This model resembles the 2-media model of **semi-localized** confinement, but in contrast to semi-localized confinement, which was proposed to explain PL emission from rough surfaces of large-diameter SiNWs, the STE model in silicon was applied to explain PL emission of very small diameter Si-NCs.

Surely, more detailed, more extended experimental PL investigations on the MAWCE-II silicon are sensible (as well as reviews on already published results). To name some of them:

- Time dependent PL measurements, like PL decay
- Temperature dependent PL
- PL excitation measurements

There are many other, especially micro-, and nano-scopic, experimental approaches, which either already exist or still have to be found, which can be applied to materials obtained by MAWCE-II and give further insight into PL mechanisms and responsible sources of photoluminescence. Especially, scanning optical near field (SNOM) measurements on single, isolated SiNWs produced by MAWCE-II or even more simple micro-PL measurements – can give insight and either verify or falsify the model of the PL by semi-localized Si-NCs within an SiO<sub>x</sub> matrix (see Fig. 15b). In summary, the PL of MAWCE-II samples is a very exciting, buzzing field of investigation and it's likely that a lot of insights and relations still wait to be discovered.

## 5. Solar cell architectures based on wet chemically etched silicon nanowires

Among various sources of energy, sunlight is the most abundant and cleanest natural energy resource. In principle, photovoltaics (PVs) hold a great promise to exploit the sunlight to generate clean energy to accommodate the ever-increasing energy demands [Barnham, 2006; Crabtree, 2007; Alsema; 2000]. Photovoltaics is the field of technology and research related to the application of solar cells for energy generation by converting solar energy directly into electricity. Electrical production with solar cells is continuously increasing. Solar cells are particularly useful as power generators in distant and terrestrial places like weather stations and satellites. Solar cells are used in small devices like watches and calculators, but mostly they are used to produce electricity either in large-scale power plants or by being incorporated into walls and rooftops. The function of solar cells essentially involves the presence of a p-n junction close to its surface in order to create potential difference in the bulk. A transport of photogenerated charge carriers across the junction to lower its potential energy is harnessed to execute work. About 90% of solar photovoltaic modules are silicon-based [Miles, 2007], but in recent years increased demand for silicon solar cells has inflated the price of solar-grade silicon. The price of Si accounts for about half of the price of solar cells. The grid parity of electricity produced by solar cells is close to 1 USD/Watt assuming a 20-year lifetime of the cells [Gunawan, 2009], but the price is currently four times higher. One obvious way to lower the cost is to reduce the amount of silicon in the cells. By using thin film technology, the thickness of the silicon can be reduced from 200–300 μm to 0.2–5 μm. Another way to cut down production cost is to use low-grade Si instead of ultra-pure Si currently being used. However, this lower-grade material is less efficient. It is presumed that the grid parity of solar cells will be reached by using thin film technology or a new design that is most-likely based on nanotechnology.

### 5.1 Axial p-n junction in MAWCE SiNWs

Wet chemically etched microcrystalline silicon (mc-Si) surfaces show very low reflectance compared to Si thin layers or wafers [Stelzner, 2008; Andrä, 2007, 2008]. This low reflectance is potentially interesting for photovoltaic applications where enough absorption of solar light in an as thin as possible Si layer is desired and a combination of light trapping structures and antireflective coatings have usually to be applied [Tsakalakos, 2007; Peng, Xu, 2005]. The SiNWs themselves have shown to absorb solar light very satisfactorily and can therefore be used as the solar cell absorber [Tsakalakos, Balch, 2007; Kaynes, 2005; Koynov, 2006].

In this part we will show how the wet chemical etching into a thin silicon layer on glass substrate to be useful to serve a solar cell absorber in a thin film solar cell concept on glass. Fig. 18 shows a schematic representation of the multicrystalline silicon layer stack on glass before wet chemical etching. Fig. 19 shows scanning electron microscopy (SEM) micrographs of the SiNWs after wet chemical etching into the mc-Si layers on glass. Fig. 19a shows an SEM micrograph of SiNWs in cross section. The etching profile is homogeneous and the etching depth approximately is  $2\ \mu\text{m}$  from the top surface. Fig. 19b shows a SEM micrograph of SiNWs from the top surface. A difference in the SiNW orientation is discernible for starting grains of different orientation prior to wet chemical etching. The diameter of the SiNWs varies from 50 nm to 150 nm with an average of approximately 100 nm.

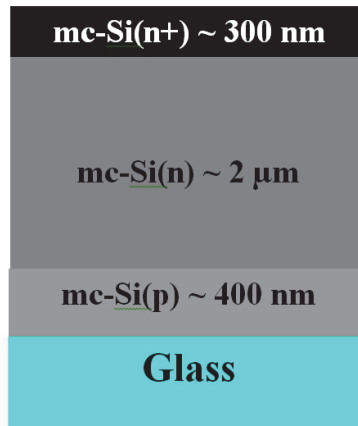


Fig. 18. Schematic cross sectional view of the mc-Si p-n junction layer stack on a glass substrate.

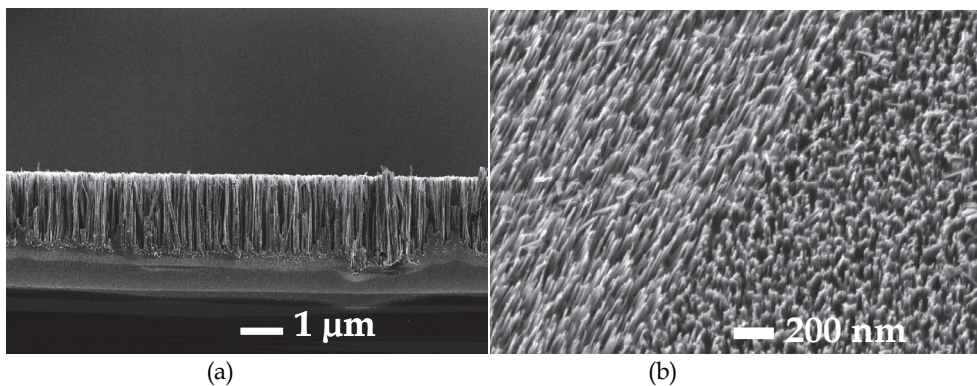


Fig. 19. (a) Cross sectional SEM micrograph of the  $\text{AgNO}_3/\text{HF}$  etched mc-Si layer on glass; (b) planar SEM micrograph of SiNWs etched into grains of different orientation; the grain boundary in the starting mc-Si layer is clearly discernible (Sivakov, 2009).

SiNWs have been contacted by metallic tips for the characterization of the optoelectronic properties. The samples were illuminated through the glass substrate (superstrate configuration) using well defined AM1.5 illumination conditions. I-V-curves are shown in Fig. 20. The four different curves were obtained at four positions within a single sample. While in all cases the open circuit voltage ( $V_{oc}$ ) is rather similar lying in the range of 410 - 450 mV, the short circuit current ( $I_{sc}$ ) values differ appreciably. This may be due to the point contacting with gold needles which allows either to contact a higher or lower number of SiNWs just depending on position. Therefore, it is not simple to give a reliable current density. The short circuit current densities,  $j_{sc}$  in Fig. 20 ranging from 13.4 mA/cm<sup>2</sup> to 40.3 mA/cm<sup>2</sup> were calculated. The shunting is responsible for the deviation of the I-V-curve parallel to the x-axis; a large series resistance is responsible for a deviation of the curve parallel to the y-axis. Shunting may be due to the large unpassivated surface of the SiNWs or even due to surface currents along the SiNW surfaces. High series resistance and shunting lead to a low fill factor FF of about 30%. From the measured values an energy conversion efficiency ( $\eta$ ) of 1.7% to 4.4 % follows. The highest power conversion efficiency of SiNWs based solar cell on glass was 4.4 % which shows potential for low cost solar cells with such design. The high current density of about 40 mA/cm<sup>2</sup> requires complete light absorption and high quantum efficiency. Moreover, to increase the power conversion efficiency for such nanostructures, the shunting should be minimized and all production steps must be optimized for such solar cell architecture.

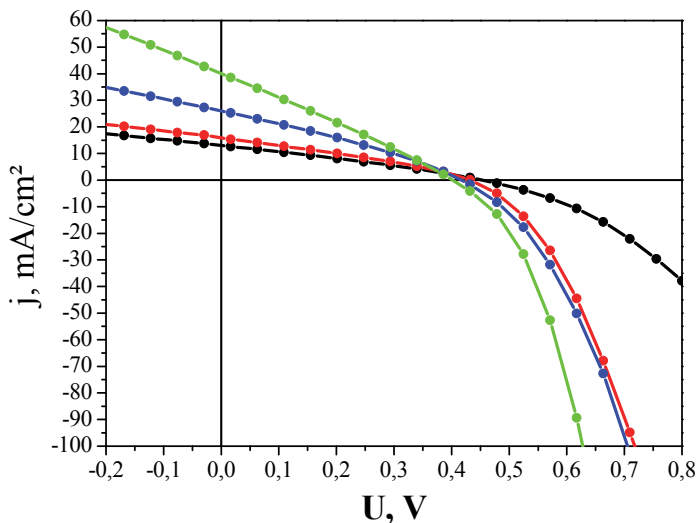


Fig. 20. Illuminated (AM1.5) I-V curves of SiNWs etched into a mc-Si layer on glass. SiNW are irradiated through the glass substrate (super-state configuration) and contacted by metal tips at four different sample positions (Sivakov, 2009).

### 5.2 n-SiNWs/Al<sub>2</sub>O<sub>3</sub>/AZO semiconductor-insulator-semiconductor isotype heterojunction

In this part we will present a semiconductor-insulator-semiconductor (SIS) concept based on very efficiently light absorbing wet-chemically etched SiNWs as presented in Fig. 21.

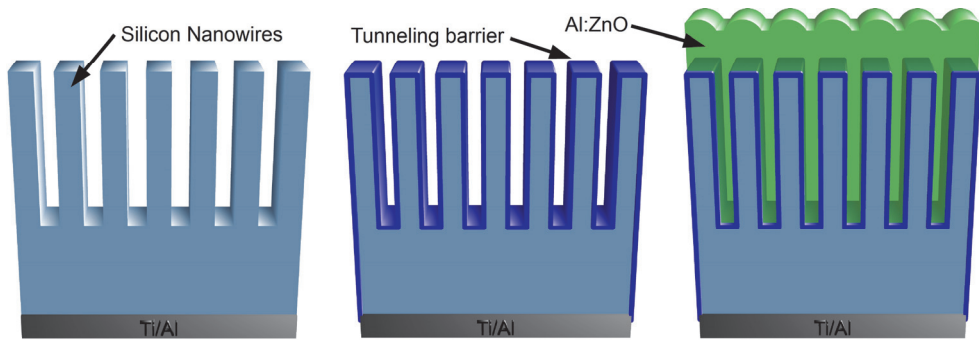


Fig. 21. Schematic cross sectional view of the formation of semiconductor-insulator-semiconductor solar cell based on wet chemically etched silicon nanowires.

Fig. 22 shows cross sectional SEM micrographs of the SiNWs after wet chemical etching of single crystalline n-Si(100) wafers and the same sample after atomic layer deposition (ALD) of alumina ( $\text{Al}_2\text{O}_3$ ) as a tunnelling oxide and aluminium doped zinc oxide (AZO) as a front contact. The etching profile (Fig. 22a) is homogeneous and the etching depth is approximately  $2\ \mu\text{m}$  from the original wafer surface. Fig. 22b shows the homogeneous filling of the gaps between the SiNWs with  $\text{Al}_2\text{O}_3$ /AZO.

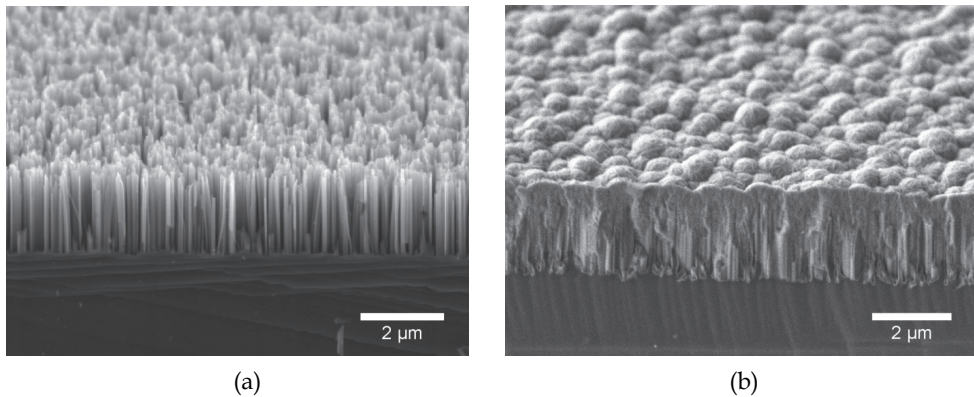


Fig. 22. Cross sectional SEM micrographs of (a) as prepared wet chemically etched SiNWs; (b) the complete layer stack of an SIS solar cell with  $\text{Al}_2\text{O}_3$  wrapped insulating as well as wrapped AZO films.

Illuminated and dark I-V-curves are shown in Fig. 23. The highest observed open current voltage ( $V_{\text{OC, max}}$ ), short current density ( $J_{\text{SC, max}}$ ) and fill factor (FF) under AM1.5 ( $1000\text{W}/\text{m}^2$ ) illumination were  $470\ \text{mV}$ ,  $33\ \text{mA}/\text{cm}^2$  and  $61\%$ , respectively. The solar cell with the best  $8.6\%$  efficiency is shown in Fig. 23.

In conclusion we have demonstrated a semiconductor-insulator-semiconductor (SIS) solar cell based on wet chemically etched silicon nanowires (SiNWs) and aluminium oxide ( $\text{Al}_2\text{O}_3$ ) as a tunnelling barrier grown by atomic layer deposition (ALD). The highest power

conversion efficiency of SiNWs based SIS solar cell was 8.6 % which shows potential for low cost solar cells with such a design. The most promising and important factor is the improvement of the  $V_{oc}$  which can be tuned by the SiNW dominated surface structure. We see a real potential for further improvement of solar cell parameters such as  $V_{oc}$  to 600-700 mV and a power conversion efficiency of >15%.

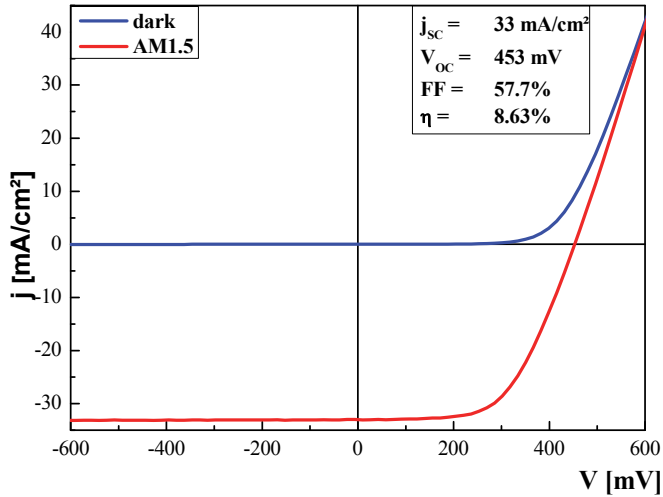


Fig. 23. Non illuminated and illuminated (AM1.5) I-V curves of an SIS solar cell with a 11 Å  $Al_2O_3$  tunneling barrier layer and optimized SiNW structure. The SIS cell is contacted by metal tips, one on the rear wafer surface which is contacted by a Ti/Al layer and one on the front AZO layer surface.

## 6. Acknowledgments

The authors are gratefully acknowledged to Mr. H. Köbe and Mrs. A. Dellith (Institute of Photonic Technology, Jena/Germany) for the scanning electron microscopy investigations and to Mrs. S. Hopfe (Max-Planck-Institute of Microstructure Physics, Halle/Germany) for the preparation of the TEM samples. Prof. Gottfried H. Bauer is acknowledged for his great help by discussing the model of semi-localized quantum confinement. The authors gratefully acknowledge financial support by European Commission in part the European Project in the framework of FP7, "ROD-SOL" as well as by the Max Planck Society in the framework of the "NANOSTRESS" project.

## 7. References

- [Allen, 2008] J.E. Allen, E.R. Hemesath, D.E. Perea, J.L. Lensch-Falk, Z.Y. Li, F. Yin, M.H. Gass, P. Wang, A.L. Bleloch, R.E. Palmer, L.J. Lauhon. High-resolution detection of Au catalyst atoms in Si nanowires. *Nature Nanotechnology* 3, 168 - 73 (2008).
- [Alsema, 2000] E.A. Alsema. Energy pay-back time and CO<sub>2</sub> emissions of PV systems. *Prog. Photovoltaics* 8, 17 - 25 (2000).

- [Andrä, 2007] G. Andrä, M. Pietsch, Th. Stelzner, F. Falk, S.H. Christiansen, A. Scheffel, S. Grimm. Proceedings 22nd European Photovoltaic Solar Energy Conference and Exhibition, Milan, Italy, September 3–7, 481 (2007).
- [Andrä, 2008] G. Andrä, M. Pietsch, V. Sivakov, Th. Stelzner, A. Gawlik, S. Christiansen, F. Falk, Proceedings 23rd European Photovoltaic Solar Energy Conference and Exhibition, Valencia, Spain, September 1–5, 163 (2008).
- [Barnham, 2006] K.W.J. Barnham, M. Mazzer, B. Clive. Resolving the energy crisis: nuclear or photovoltaics? *Nature Materials* 5, 161 - 64 (2006).
- [Billat, 1996] S. Billat. Electroluminescence of heavily doped p-type porous silicon under electrochemical oxidation in galvanostatic regime. *J. Electrochem. Soc.* 143, 1055 - 61 (1996).
- [Canham, 1990] L.T. Canham. Silicon quantum wire array fabrication by electrochemical and chemical dissolution of wafers. *Appl. Phys. Lett.* 57, 1046 (1990).
- [Carius, 2000] R. Carius. Optical gap and photoluminescence properties of amorphous silicon alloys. *Philos. Mag. B* 80, 741–53 (2000).
- [Civale, 2004] Y. Civale, L.K. Nanver, P. Hadley, E.J.G. Goudena. Aspects of silicon nanowire synthesis by aluminum-catalyzed vapor-liquid-solid mechanism. Proceedings of 7th Annual Workshop on Semiconductor Advances for Future Electronics (SAFE 2004), November 25–26, 2004, Veldhoven, The Netherlands, Publ. STW, ISBN 90-73461-43-X, 692-96 (2004).
- [Chen, 2008] C.-Y. Chen, C.-S. Wu, C.-J. Chou, T.-J. Yen. Morphological control of single-crystalline silicon nanowire arrays near room temperature. *Adv. Mater.* 20, 3811 - 15 (2008).
- [Crabtree, 2007] G.W. Crabtree, N. S. Lewis. Solar energy conversion. *Phys. Today* 60, 37 - 42 (2007).
- [Cui, 2001] Y. Cui, L.J. Lauhon, M.S. Gudiksen, J. Wang, C.M. Lieber. Diameter-controlled synthesis of single crystal silicon nanowires. *Appl. Phys. Lett.* 78, 2214 (2001).
- [Cullis, 1991] A.G. Cullis, L.T. Canham. Visible light emission due to quantum size effects in highly porous crystalline silicon. *Nature* 353, 335 - 38 (1991).
- [Cullis, 1997] A.G. Cullis, L.T. Canham, P.D.J. Calcott. The structural and luminescence properties of porous silicon. *J. Appl. Phys.* 82, 909 - 65 (1997).
- [Delerue, 1993] C. Delerue, G. Allan, M. Lannoo. Theoretical aspects of the luminescence of porous silicon. *Phys. Rev. B* 48, 11024 (1993).
- [Delerue, 2004] C. Delerue, M. Lannoo. Nanostructures : theory and modeling. Berlin - New York : Springer (2004).
- [Duan, 2001] X. Duan, Y. Huang, Y. Cui, J. Wang, C.M. Lieber. Indium phosphide nanowires as building blocks for nanoscale electronic and optoelectronic devices. *Nature* 409, 66 - 69 (2001).
- [Ehbrecht, 1995] M. Ehbrecht, H. Ferkel, V. V. Smirnov, O. M. Stelmakh, W. Zhang, F. Huisken. Laser-driven flow reactor as a cluster beam source. *Rev. Sci. Instrum.* 66, 3833 (1995).
- [Eisenhauer, 2011] B. Eisenhauer, D. Zhang, R. Clavel, A. Berger, J. Michler and S. Christiansen. Growth of doped silicon nanowires by pulsed laser deposition and their analysis by electron beam induced current imaging. *Nanotechnology* 22, 075706 (2011).

- [Fuhrmann, 2005] B. Fuhrmann, H.S. Leipner, H.-R. Höche, L. Schubert, P. Werner, U. Gösele. Ordered arrays of silicon nanowires produced by nanosphere lithography and molecular beam epitaxy. *Nano Letters* 5, 2524 - 27 (2005).
- [Givargizov, 1975] E.I. Givargizov. Fundamental aspects of VLS growth. *J. Cryst. Growth* 31, 20 - 30 (1975).
- [Green, 2001] M.A. Green, J. Zhao, A. Wang, P.J. Reece, M. Gal. Efficient silicon light-emitting diodes. *Nature* 412, 805 - 08 (2001).
- [Guillois, 2004] O. Guillois, N. Herlin-Boime, C. Reynaud, G. Ledoux, F. Huisken. Photoluminescence decay dynamics of noninteracting silicon nanocrystals. *J. Appl. Phys.* 95, 3677 - 82 (2004).
- [Gunawan, 2009] O. Gunawan, S. Guha. Characteristics of vapor-liquid-solid grown silicon nanowire solar cells. *Solar Energy Materials and Solar Cells* 93, 1388 - 93 (2009).
- [Haber@Weiss, 1935] F. Haber, J. Weiss. The catalytic decomposition of hydrogen peroxide by iron salts. *Proc. Roy. Soc.*, 147A, 332 - 51 (1935).
- [Hannon, 2006] J.B. Hannon, S. Kodambaka F.M. Ross, R.M. Tromp. The influence of the surface migration of gold on the growth of silicon nanowires. *Nature* 440, 69 - 71(2006).
- [Hanrath, 2002] T. Hanrath, B.A. Korgel. Nucleation and growth of germanium nanowires seeded by organic monolayer-coated gold nanocrystals. *J. Am. Chem. Soc.* 124, 1424 - 29 (2002).
- [Heath, 1993] J.R. Heath, F.K. LeGoues. A liquid solution synthesis of single crystal germanium quantum wires. *Chem. Phys. Lett.* 208, 263 - 68 (1993).
- [Hibino, 1985] Y. Hibino, H. Hanafusa, S. Sakaguchi. Drawing condition dependences of optical absorption and photoluminescence in pure silica optical fibers. *Appl. Phys. Lett.* 47, 1157-59 (1985).
- [Hochbaum, 2005] A.I. Hochbaum, R. Fan, R. He, P. Yang. Controlled growth of Si nanowire arrays for device integration. *Nano Letters* 5, 457 - 60 (2005).
- [Hochbaum, 2008] A.I. Hochbaum, R. Chen, R. Diaz Delgado, W. Liang, E.C. Garnett, M. Najarian, A. Majumdar, P. Yang. Enhanced thermoelectric performance of rough silicon nanowires. *Nature* 451, 163 - 67 (2008).
- [Hochbaum, 2009] A.I. Hochbaum, D. Gargas, Y. J. Hwang, P. Yang. Single crystalline mesoporous silicon nanowires. *Nano Letters* 9, 3550 - 54 (2009).
- [Huang, 2008] Z. Huang, X. Zhang, M. Reiche, L. Liu, W. Lee, T. Shimizu, S. Senz, U. Gösele. Extended arrays of vertically aligned sub-10 nm diameter [100] Si nanowires by metal-assisted chemical etching. *Nano Letters* 8, 3046 - 51 (2008).
- [Huisken, 2002] F. Huisken, G. Ledoux, O. Guillois, C. Reynaud. Light-emitting silicon nanocrystals from laser pyrolysis. *Adv. Mater.* 14, 1861 - 65 (2002).
- [Ikeda, 1995] H. Ikeda, K. Hotta, T. Yamada, S. Zaima, H. Iwano, Y. Yasuda. Oxidation of H-terminated Si(100) surfaces studied by high-resolution electron-energy-loss spectroscopy. *J. Appl. Phys.* 77, 5125 (1995).
- [Jellison@Modine, 1982] G. Jellison, F. Modine. Optical constants for silicon at 300 and 10 K determined from 1.64 to 4.73 eV by ellipsometry. *J. Appl. Phys.* 53, 3745 (1982).
- [Kamins, 2001] T.I. Kamins, R.S. Williams, D.P. Basile, T. Hesjedal, J.S. Harris. Ti-catalyzed Si nanowires by chemical vapor deposition: microscopy and growth mechanisms. *J. Appl. Phys.* 89, 1008 (2001).

- [Kayes, 2005] B.M. Kayes, N.S. Lewis, H.A. Atwater. Comparison of the device physics principles of planar and radial *p-n* junction nanorod solar cells. *J. Appl. Phys.* 97, 114302 (2005).
- [Kelzenberg, 2008] M.D. Kelzenberg, D.B. Turner-Evans, B.M. Kayes, M.A. Filler, M.C. Putnam, N.S. Lewis, H.A. Atwater. Photovoltaic measurements in single-nanowire silicon solar cells. *Nano Letters* 8, 710 - 14 (2008).
- [Koch, 1993] F. Koch, V. Petrova-Koch, T. Muschik, A. Nikolov, V. Gavrilenko. Some perspectives on the luminescence mechanism via surface-confined states of porous Si. *Mat. Res. Soc. Symp. Proc.* 283, 197 (1993).
- [Kolasinski, 2009] K. W. Kolasinski. Etching of silicon in fluoride solutions. *Surface Science* 603, 1904-11 (2009).
- [Koynov, 2006] S. Koynov, M.S. Brandt, M. Stutzmann. Black nonreflecting silicon surfaces for solar cells. *Appl. Phys. Lett.* 88, 203107 (2006).
- [Lauhon, 2002] L.J. Lauhon, M.S. Gudiksen, D. Wang, C.M. Lieber. Epitaxial core-shell and core-multishell nanowire heterostructures. *Nature* 420, 57 -61 (2002).
- [Ledoux, 2000] G. Ledoux, O. Guillois, D. Porterat, C. Reynaud, F. Huisken and B. Kohn, V. Paillard. Photoluminescence properties of silicon nanocrystals as a function of their size. *Phys. Rev. B* 62, 15942 (2000).
- [Ledoux, 2002] G. Ledoux, J. Gong, and F. Huisken, O. Guillois and C. Reynaud. Photoluminescence of size separated silicon nanocrystals: Confirmation of quantum confinement. *Appl. Phys. Lett.* 80, 4834 - 36 (2002).
- [Lehmann, 1991] V. Lehmann, U. Gösele. Porous silicon formation: a quantum wire effect. *Appl. Phys. Lett.* 58, 856 (1991).
- [Lockwood, 1994] D. J. Lockwood. Optical-properties of porous silicon. *Solid State Communications* 92, 101 (1994).
- [Lieber, 2003] C.M. Lieber. Nanoscale science and technology: Building a big future from small things. *MRS Bull.* 28, 486 - 91 (2003).
- [Lifschitz@Slyozov, 1961] I.M. Lifschitz, V.V. Slyozov. The kinetics of precipitation from supersaturated solid solutions. *J. Phys. Chem. Solids* 19, 35 - 50 (1961).
- [McIntosh, 1902] D. McIntosh. Inorganic Ferments. *J. Phys. Chem.* 6, 15 - 44 (1902).
- [Miles, 2007] R.W. Miles, G. Zoppia, I. Forbes. Inorganic photovoltaic cells. *Materials Today* 10, 20 - 27 (2007).
- [Munekuni, 1990] S. Munekuni, T. Yamanaka, Y. Shimogaichi, R. Tohmon, Y. Ohki, K. Nagasawa, Y. Hama. Various types of nonbridging oxygen hole center in high-purity silica glass. *J. Appl. Phys.* 68, 1212 (1990).
- [Nishikawa, 1991] H. Nishikawa, R. Nakamura, K. Nagasawa, Y. Ohki, Y. Hama. Proceedings of the 3rd Internat. Conf. on Properties and Applications of Dielectric Materials Vol. 1-2, pp. 1032-35 (1991).
- [Oh, 2008] S.H. Oh, K. van Benthem, S.I. Molina, A.Y. Borisevich, W. Luo, P. Werner, N.D. Zakharov, D. Kumar, S.T. Pantelides, S.J. Pennycook. Point defect configurations of supersaturated atoms inside Si nanowires. *Nano Letters* 8, 1016 - 19 (2008).
- [Ostwald, 1900] W. Ostwald. Über die vermeintliche Isomerie des roten und gelben Quecksilberoxyds und die Oberflächenspannung fester Körper. *Z. Phys. Chem.* 34, 495 (1900).
- [Peng, 2002] K.-Q. Peng, Y.-J. Yan, S.-P. Gao, J. Zhu. Synthesis of large-area silicon nanowire arrays via self assembling nanoelectrochemistry. *Adv. Mater.* 14, 1164 - 67 (2002).

- [Peng, 2005] K. Peng, Y. Wu, H. Fang, X. Zhong, Y. Xu, J. Zhu. Uniform, Axial-orientation alignment of one- dimensional single-crystal silicon nanostructure arrays. *Angew. Chem. Int. Edn.* 44, 2797 – 2802 (2005).
- [Peng, Xu 2005] K. Peng, Y. Xu, Y. Wu, Y. Yan, S.-T. Lee, J. Zhu. Aligned single-crystalline Si nanowire arrays for photovoltaic applications. *Small* 1, 1062 (2005).
- [Peng, 2006] K.Q. Peng, J.J. Hu, Y.J. Yan, H. Fang, Y. Xu, S.T. Lee, J. Zhu. Fabrication of single crystalline silicon nanowires by scratching a silicon surface with catalytic metal particles. *Adv. Funct. Mater.* 16, 387 – 94 (2006).
- [Peng, 2007] K. Peng, M. Zhang, A. Lu, N.B. Wong, R. Zhang, S.T. Lee. Ordered silicon nanowire arrays via nanosphere lithography and metal-induced etching. *Appl. Phys. Lett.* 90, 163123 (2007).
- [Presti, 2006] C.D. Presti, A. Irrera, G. Franzò, I. Crupi, F. Priolo, F. Iacona, G. Di Stefano, A. Piana, D. Sanfilippo, P. G. Fallica. Photonic-crystal silicon-nanocluster light-emitting device. *Appl. Phys. Lett.* 88, 033501 (2006).
- [Prokes, 1995] S.M. Prokes, W.E. Carlos. Oxygen defect center red room temperature photoluminescence from freshly etched and oxidized porous silicon. *J. Appl. Phys.* 78, 2671 (1995).
- [Prokes, 1996] S.M. Prokes. Surface and optical properties of porous silicon. *J. Mater. Res.* 11, 305 – 20 (1996).
- [Qin, 1993] G.G. Qin, Y.Q. Jia. Mechanism of the visible luminescence in porous silicon. *Solid State Comm.* 86, 559 – 63, (1993).
- [Qiu, 2005] T. Qiu, X.L. Wu, X. Yang, G.S. Huang, Z.Y. Zhang. Self-assembled growth and optical emission of silver-capped silicon nanowires. *Appl. Phys. Lett.* 84, 3867 (2005).
- [Qu, 2009] Y. Qu, L. Liao, Y. Li, H. Zhang, Y. Huang, X. Duan. Electrically conductive and optically active porous silicon nanowires. *Nano Lett.* 9, 4539 – 43 (2009).
- [Robinson, 1993] M. B. Robinson, A. C. Dillon, and S. M. George. Porous silicon photoluminescence versus HF etching: No correlation with surface hydrogen species. *Appl. Phys. Lett.* 62, 1493 – 95 (1993).
- [Ross, 2005] F. M. Ross, J. Tersoff, M. C. Reuter. Sawtooth faceting in silicon nanowires. *Phys. Rev. Lett.* 95, 146104 (2005).
- [Sacilotti, 1993] M. Sacilotti, P. Abraham, B. Champagnon, Y. Monteil, J. Bouix. Porous silicon photoluminescence: type II-like recombination mechanism. *Electr. Lett.* 29, 790 – 91 (1993).
- [Schmidt, 2005] V. Schmidt, S. Senz, U. Gösele. Diameter-dependent growth direction of epitaxial silicon nanowires. *Nano Letters* 5, 931 - 35 (2005).
- [Sivakov, 2006] V. Sivakov, G. Andrä, C. Himcinschi, U. Gösele, D.R.T. Zahn, S.H. Christiansen. Growth peculiarities during vapor-liquid-solid growth of silicon nanowhiskers by electron-beam evaporation. *Appl. Phys. A* 85, 311 - 15 (2006).
- [Sivakov, 2007] V. Sivakov, F. Heyroth, F. Falk, G. Andrä, S.H. Christiansen. Silicon nanowire growth by electron beam evaporation: Kinetic and energetic contributions to the growth morphology. *J. Cryst. Growth* 300, 288 – 93 (2007).
- [Sivakov, 2009] V. Sivakov, G. Andrä, A. Gawlik, A. Berger, J. Plentz, F. Falk, S.H. Christiansen. Silicon nanowire based solar cells on glass: synthesis, optical properties, and cell parameters. *Nano Letters* 9, 1549 – 54 (2009).

- [Sivakov, 2010] V.A. Sivakov, G. Brönstrup, B. Pecz, A. Berger, G.Z. Radnoczi, M. Krause, S.H. Christiansen. Realization of vertical and zigzag single crystalline silicon nanowire architectures. *J. Phys. Chem. C* 114, 3798 – 3803 (2010).
- [Sivakov, Voigt, 2010] V.A. Sivakov, F. Voigt, A. Berger, G. Bauer, S.H. Christiansen. Roughness of silicon nanowire sidewalls and room temperature photoluminescence. *Phys. Rev. B* 82, 125446 (2010).
- [Skuja, 1979] L.N. Skuja, A.R. Silin. Optical properties and energetic structure of non-bridging oxygen centers in vitreous SiO<sub>2</sub>. *Physica Status Solidi A* 56, K11-K13 (1979).
- [Stelzner, 2008] Th. Stelzner, M. Pietsch, G. Andrä, F. Falk, E. Ose, S.H. Christiansen. Silicon nanowire-based solar cells. *Nanotechnology* 19, 295203 (2008).
- [Stesmans, 1994] A. Stesmans, F. Scheerlinck. Natural intrinsic EX center in thermal SiO<sub>2</sub> on Si: <sup>17</sup>O hyperfine interaction. *Physical Review B* 50, 5204-5212 (1994).
- [Street, 1991] R.A. Street. Hydrogenated amorphous silicon. Cambridge: Cambridge University Press (1991).
- [Sunkara, 2001] M.K. Sunkara, S. Sharma, and R. Miranda. Bulk synthesis of silicon nanowires using a low temperature vapor-liquid-solid method. *Appl. Phys. Lett.* 79, 1546 (2001).
- [Tsai, 1991] C. Tsai, K.-H. Li, J. Sarathy, S. Shih, and J. C. Campbell, B. K. Hance, J.M. White. Thermal treatment studies of the photoluminescence intensity of porous silicon. *Appl. Phys. Lett.* 59, 2814 – 16 (1991).
- [Tsakalacos, 2007] L. Tsakalacos, J. Balch, J. Fronheiser, M. Shih, S. LeBoeuf, M. Pietrzykowski, P. Codella, B. Korevaar, O. Sulima, J. Rand & others. Strong broadband optical absorption in silicon nanowire films. *J. Nanophotonic* 1, 013552 (2007).
- [Tsakalacos, Balch, 2007] L. Tsakalacos, J. Balch, J. Fronheiser, A. Korevaar, O. Sulima, J. Rand. Silicon nanowire solar cells. *Appl. Phys. Lett.* 91, 233117 (2007).
- [Uhlir, 1956] A. Uhlir. Electrolytic shaping of germanium and silicon. *Bell. Syst. Tech. J.* 35, 333 (1956).
- [Vetterl, 2000] O. Vetterl, F. Finger, R. Carius, P. Hapke, L. Houben, O. Kluth, A. Lambertz, A. Mück, B. Rech, H. Wagner. Intrinsic microcrystalline silicon: A new material for photovoltaics. *Solar Energy Materials and Solar Cells* 62, 97-108 (2000).
- [Voigt, 2011] F. Voigt, V. Sivakov, V. Gerliz, G. H. Bauer, B. Hoffmann, G. Z. Radnoczi, B. Pecz, S. Christiansen. Photoluminescence of samples produced by electroless wet chemical etching: Between silicon nanowires and porous structures. *Physica Status Solidi A* 208, 893 (2011).
- [Wagner, 1961] C. Wagner. Theorie der Alterung von Niederschlägen durch Umlösen (Ostwald-Reifung). *Z. Elektrochem.* 65, 581 - 91 (1961).
- [Wagner@Ellis, 1964] R. S. Wagner, W. C. Ellis. Vapor-solid-liquid mechanism of single crystal growth. *Appl. Phys. Lett.* 4, 89 (1964).
- [Wagner@Ellis, 1965] R. S. Wagner, W. C. Ellis. The vapor-liquid-solid mechanism of crystal growth and its application to silicon. *Trans. Metall. Soc. AIME* 233, 1053 - 64 (1965).
- [Walavalkar, 2010] S. S. Walavalkar, C. E. Hofmann, A. P. Homyk, M. D. Henry, H. A. Atwater, A. Scherer. Tunable visible and near-IR emission from sub-10 nm etched single-crystal Si nanopillars. *Nano Lett.* 10, 442328 (2010).
- [Wang, 2006] Y. Wang, V. Schmidt, S. Senz, U. Gösele. Epitaxial growth of silicon nanowires using an aluminium catalyst. *Nature Nanotechnology* 1, 186 - 189 (2006).

- [Weiss, 1935] J. Weiss. The catalytic decomposition of hydrogen peroxide on different metals. *Trans. Faraday Soc.* 31, 1547- 57 (1935).
- [Wiegel, 1930] E. Wiegel. Über Farbe und Teilchengröße von kolloidem Silber, insbesondere der neuen Wasserstoffperoxydsilbersole *Colloid & Polymer Science* 53, 96-101 (1930).
- [Wilson@Hutley, 1982] S. Wilson, M. Hutley. The optical properties of 'Moth Eye' antireflection surfaces. *J. Modern Opt.* 29, 993 - 1009 (1982).
- [Wolford, 1983] D. J. Wolford, B. A. Scott, J. A. Reimer, J. A. Bradley. Efficient visible luminescence from hydrogenated amorphous silicon. *Physica B+C* 117-118, 920-22 (1983).
- [Wu, 2000] Y. Wu, P. Yang. Germanium nanowire growth via simple vapor transport. *Chem. Mater.* 12, 605 - 07 (2000).
- [Xia, 2003] Y. Xia, P. Yang, Y. Sun, Y. Wu, B. Mayers, B. Gates, Y. Yin, F. Kim, H. Yan. One-dimensional nanostructures: Synthesis, characterization, and applications. *Adv. Mater.* 15, 353 - 89 (2003).
- [Zhang, 2000] Y. F. Zhang, Y. H. Tang, N. Wang, C. S. Lee, I. Bello, S. T. Lee. Germanium nanowires sheathed with an oxide layer. *Phys. Rev. B* 61, 4518 - 21 (2000).
- [Zhang, 2008] M.-L. Zhang, K.-Q. Peng, X. Fan, J.-S. Jie, R.-Q. Zhang, S.-T. Lee, N.-B. Wong. Preparation of large area uniform silicon nanowires arrays through metal-assisted chemical etching. *J. Phys. Chem. C* 112, 4444 - 50 (2008).

# First Principles Study of Si/Ge Core-Shell Nanowires - *Structural and Electronic Properties*

Xihong Peng<sup>1</sup>, Fu Tang<sup>2</sup> and Paul Logan<sup>2</sup>

<sup>1</sup>*Department of Applied Sciences and Mathematics, Arizona State University, Mesa,*

<sup>2</sup>*Department of Physics, Arizona State University, Tempe,  
USA*

## 1. Introduction

One-dimensional semiconductor nanostructures, such as Si and Ge nanowires, have attracted extensive research efforts over the past decades (B. Y-K Hu & Das Sarma, 1992; Hirschman et al., 1996; Morales & Lieber, 1998; Holmes et al., 2000; Cui & Lieber, 2001; Cui et al., 2001, 2003; Koo et al., 2004; Audoit et al., 2005; X. Y. Wu et al., 2008; Dailey & Drucker, 2009). They are expected to play important roles as both interconnects and functional components in future nanoscale electronic and optical devices, such as light-emitting diodes (LEDs) (Hirschman et al., 1996; Cui & Lieber, 2001), ballistic field-effect transistors (FETs) (Cui et al., 2003; Koo et al., 2004), inverters (Cui & Lieber, 2001), and nanoscale sensors (Cui et al., 2001; Hahm & Lieber, 2004). Experimental and theoretical investigations showed that in these nanoscale structures charge carriers are confined in the lateral direction of the wires, thus quantum confinement effect is expected to play an important role on the electronic properties. This confinement effect has been observed, for example, in photoluminescence studies, by exhibiting substantial blue-shift of emission with reduction of the nanowire diameter (Z. Wu et al., 2008; Beckman et al., 2006; Bruno et al., 2005). Researchers also found that the band gap of Si and Ge nanowires depends on several factors, such as size (Beckman et al., 2006; Bruno et al., 2005; Arantes & Fazio, 2007), crystalline orientation (Bruno et al., 2005; Arantes & Fazio, 2007; Medaboina et al., 2007), surface chemistry (Medaboina et al., 2007; Kagimura et al., 2007), and doping (Medaboina et al., 2007; Peelaers et al., 2007).

Recently, particular attention has been given to Si/Ge core-shell nanowires, in which factors, such as heterostructure composition and interface geometry, can be further manipulated to tune the electronic properties of nanowires (Kagimura et al., 2007; Lauhon et al., 2002; Y. Y. Wu et al., 2002; Lu et al., 2005; Trammell et al., 2008; J. Q. Hu et al., 2009; Peng & Logan, 2010; Peng et al., 2011b). Compared to pure Si and Ge wires, the core-shell structure has some greater properties. For instance, a better conductance and higher mobility of charge carries can be obtained, due to the conduction and valence band offsets in the core-shell nanowires (Kagimura et al., 2007; Goldthorpe et al., 2008; L. Yang et al., 2008). The band offsets also offer the heterostructure a wide range of applications in solar cells (Tian et al., 2007) and high-switching speed transistors (Y. J. Hu et al., 2008).

Experimentally, Yang and colleagues (J. E. Yang et al. 2006) grew crystalline  $\text{Si}_{1-x}\text{Ge}_x$  nanowires by an Au catalyst-assisted chemical vapor synthesis, and showed that the energy gap of the  $\text{Si}_{1-x}\text{Ge}_x$  nanowires can be tuned in the range from near-infrared to visible regions. In addition, Varahramyan and co-worker (Varahramyan et al., 2009) used ultrahigh vacuum chemical vapor deposition to grow  $\text{Si}_x\text{Ge}_{1-x}$  epitaxial core-shell nanowires, and the Si/Ge shell content can be tuned to enable radial band and strain engineering in these heterostructures.

In addition to the experimental studies, several theoretical calculations were performed to study the quantum confinement effect in Si/Ge core-shell nanowires (Amato et al., 2009; Musin & Wang, 2005, 2006; L. Yang et al., 2008). In these calculations, the band gap and near-gap electronic states are particularly investigated as a function of hetero-composition. For example, Wang's group (Musin & Wang, 2005, 2006) reported the band gap of Si/Ge core-shell nanowires as a function of composition for wires with diameter up to 3 nm; Migas & Borisenko (Migas & Borisenko, 2007) studied the electronic properties of Si/Ge core-shell nanowire along the [100] direction with a diameter of 1.5 nm; Yang et al. (L. Yang et al., 2008) investigated the near-gap electronic states with the core and shell regions along [110] and [111] directions with diameter up to 4 nm.

Our group (Peng & Logan, 2010; Peng et al., 2011b), in particular, explored the effect of intrinsic and external strain on the band structures of Si/Ge core-shell nanowires along the [110] direction with the wire diameter up to 5 nm. It is known that strain is used as a routine parameter in industry to engineer electronic properties, such as the band gap, of semiconductors. In the Si/Ge core-shell nanowires, there is an intrinsic strain in the core-shell interface, due to the lattice mismatch between Si and Ge (Hahm & Lieber, 2004). In addition, external strain can be also applied to engineer the band structures. There are a few limited experimental studies in synthesis, strain relaxation, and equilibrium strain-energy analysis of coherently strained Si/Ge core-shell nanowires (Goldthorpe et al., 2008; Trammell et al., 2008). Here, we reported a detailed theoretical study of the effects of both intrinsic and external strains on the structural, mechanical, and electronic properties of Si/Ge core-shell nanowires.

We found that the intrinsic strain in the core-shell nanowires has significantly countered the quantum confinement effect and reduced the band gap of the core-shell nanowires. In addition, external uniaxial strain can further modulate the bands structure of the core-shell nanowires. Therefore, electronic properties, such as the gap, effective masses of charge carriers and work function, are substantially tuned by the strain.

## 2. Methods

First principles density-functional theory (DFT) (Kohn & Sham, 1965) calculations were performed to study Si/Ge core-shell nanowires. The simulations were done using local density approximation (LDA) implemented in Vienna Ab-initio Simulation Package (Kresse & Furthmuller, 1996a, 1996b). A pseudo-potential plane wave method was used and the plane wave energy cutoff for the wave-function basis is set to be 200.0 eV. Core electrons were described using ultra-soft Vanderbilt pseudo-potentials (Vanderbilt, 1990). Reciprocal space was sampled at  $1 \times 1 \times 4$  K-points using Monkhorst Pack mesh. A larger plane wave energy cutoff of 350.0 eV and a K-points mesh of  $1 \times 1 \times 9$  were used to check the calculations. No significant difference was found in the results using those parameters and the current setting. In the band structure calculations, 21 K-points were scanned along the reciprocal direction from  $\Gamma$  to X.

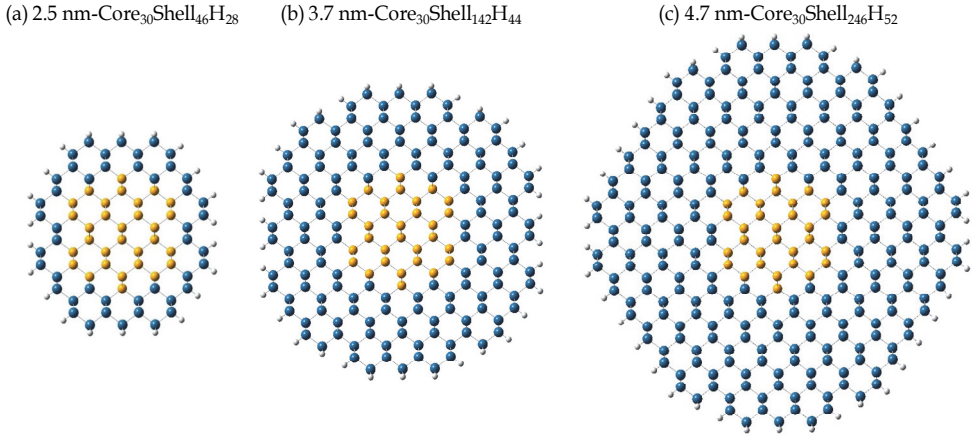


Fig. 1. Snapshots of Si/Ge core-shell nanowires viewed from the cross section. The core atoms can be Si (Ge), thus the shell will be Ge(Si). White dots on the surface are H atoms.

Dangling Si and Ge bonds on the wire surface were saturated by hydrogen atoms with the initial bond lengths 1.47 Å (Si-H), and 1.51 Å (Ge-H), respectively. Those Si-H and Ge-H bonds were allowed to relax during structure optimization. In the studied Si/Ge core-shell nanowires, the core contains 30 atoms and the thickness of the shell varies, as shown in Fig. 1. If the shell composition is Si, the initial axial lattice constant of the core-shell nanowire was set to be 0.3862 nm, taken from the lattice constant of bulk Si 0.5461 nm according to the following equation,

$$a_{\text{initial}[110]} = a_{\text{bulk}[110]} = a_{\text{bulk}} / \sqrt{2} \quad (1)$$

If the shell is Ge, the axial lattice constant was initially set to be 0.3977 nm, derived from the lattice constant of bulk Ge 0.5625 nm. We chose the initial lattice constant from the bulk shell composition since the nanowires generally have more shell atoms than core atoms (see Fig. 1). In the lateral direction of the nanowires, the vacuum distance between the wire and its mirror images (due to periodic boundary conditions) is greater than 1.0 nm, in order to eliminate the interaction between wires. The axial lattice constants of all core-shell nanowires were fully optimized through the technique of energy minimization. Atoms were fully relaxed until the forces were less than 0.02 eV/Å.

Electronic properties of a wire, such as band structure, energy gap, effective masses of charge carrier, and work function, were then calculated by solving the Kohn-Sham equation within the frame of DFT. The band gap is defined by the energy difference between the conduction band edge (CBE) and the valance band edge (VBE). The effective masses of the electron and hole can be readily calculated through parabolic fitting from the band edges according to the following formula,

$$m^* = \hbar^2 \cdot \left( \frac{d^2E}{dk^2} \right)^{-1} \quad (2)$$

The studied Si/Ge core-shell nanowires are listed in Table 1.  $D$  is the diameter of a nanowire in unit of nanometers, defined as the longest distance between two outer shell atoms in the cross-section of the wire;  $N(\text{core})/N(\text{shell})$  is the number of the core/shell atoms in a given wire;  $N(\text{H})$  is the number of H atoms needed to passivate the surface dangling bonds. Fig. 1 gives the snapshots of three core-shell nanowires with the diameters of 2.5 nm, 3.7 nm, and 4.7 nm, respectively. The diameter of the core in the nanowires is roughly 1.5 nm. The core and shell atoms could be either Si or Ge.

<b>D (nm)</b>	<b>N(core)</b>	<b>N(shell)</b>	<b>N(H)</b>
2.5	30	46	28
3.0	30	80	32
3.7	30	142	44
4.7	30	246	52

Table 1. A list of Si/Ge core-shell nanowires along the [110] direction studied in present work.  $D$  is the diameter of a wire.

Based upon the geometrically optimized wire, uniaxial tensile/compressive strain was applied by scaling the axial lattice constant. For instance, a tensile strain of 2% means that the axial lattice and the  $z$  coordinates of the atoms were rescaled to 102% of their original values, while a compressive strain of 2% implies the axial lattice and the  $z$  coordinates were rescaled to 98% of their original values. The positive values of strain refer to uniaxial expansion, while negative corresponds to compression. For each strained wire, the lateral  $x$  and  $y$  coordinates are further relaxed through energy minimization. Our study showed that the band structure of a wire is significantly modulated by strain.

## 2. Results and discussion

### 2.1 Geometrical structures of Si/Ge core-shell nanowires

The lattice constants in bulk Si and Ge are 0.357 nm and 0.357 nm, respectively, based on the simulation parameters mentioned above. The optimized axial lattice constants  $a$  for the Si/Ge core-shell nanowires were obtained through energy minimization. With those relaxed lattice constants, the axial stress in the wires is also minimal. The optimized lattice constants  $a$  were reported in Table 2 and Fig. 2. It shows that in the Si-core/Ge-shell nanowires,  $a$  generally increases with the diameter of the wire, from 0.3917 nm for the 2.5 nm wire to 0.3944 nm for the 4.7 nm wire. In addition, these lattice constants are smaller than 0.3977 nm (derived from bulk Ge), but larger than 0.3862 nm (derived from bulk Si), as shown in Fig. 2. These results are expected since a larger Si-core/Ge-shell wire contains more Ge atoms in the shell, thus the lattice constant generally increases with size. On the other hand, the lattice constant of the Ge-core/Si-shell nanowires decreases with the diameter of the wire, from 0.3985 nm to 0.3900 nm. It is interesting to note that the lattice constant for the smallest Ge-core/Si-shell wire with a diameter of 2.5 nm is even larger than 0.3977 nm from bulk Ge (see Fig. 2). This is consistent with the findings in pure Si and Ge nanowires with H passivation (Logan & Peng, 2009; Peng et al., 2009), in which small Si or Ge nanowires along the [110] direction were expanded, comparing to their bulk lattices.

	D (nm)	a (nm)	$\epsilon_{\text{intrinsic}}$ to core (%)	$\epsilon_{\text{intrinsic}}$ to shell (%)	Y (GPa)
Si-core/Ge-shell	2.5	0.3917	1.5	-1.5	67.2
	3.0	0.3945	2.2	-0.8	62.6
	3.7	0.3965	2.7	-0.3	62.3
	4.7	0.3944	2.1	-0.8	62.2
Ge-core/Si-shell	2.5	0.3985	0.2	3.2	59.2
	3.0	0.3950	-0.7	2.3	65.3
	3.7	0.3931	-1.2	1.8	67.2
	4.7	0.3900	-1.9	1.0	82.2

Table 2. The calculated structural properties in the geometrically optimized Si/Ge core-shell nanowires.

With these optimized lattice constants, an intrinsic strain was produced in the core-shell nanowires. This intrinsic strain  $\epsilon_{\text{intrinsic}}$  was calculated according to the formula,

$$\epsilon_{\text{intrinsic}} = (a - a_{\text{bulk}[110]}) / a_{\text{bulk}[110]} \quad (3)$$

where  $a$  is the relaxed lattice constant of the nanowire, and the  $a_{\text{bulk}[110]}$  is the lattice constant of bulk Si or Ge along the [110] direction. The calculated intrinsic strain was reported in Table 2. In general, the Si composition is in a tensile strain (i.e. positive strain), while the Ge composition is in a compressive strain (i.e. negative strain). This intrinsic strain brings an effect in the band gap, significantly countering the quantum confinement effect, as discussed later.

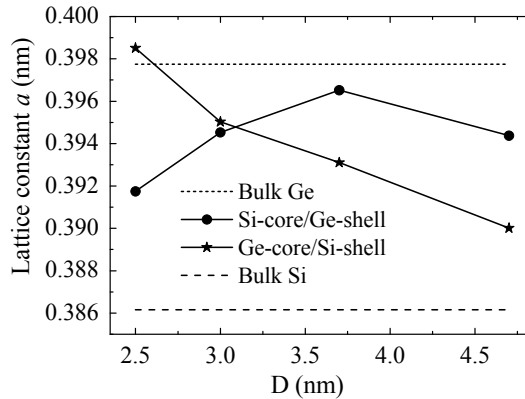


Fig. 2. The optimized axial lattice constant of Si/Ge core-shell nanowires as a function of the wire diameter.

As mentioned before, external uniaxial strain has also been applied to the geometrically relaxed nanowires. Strain energy  $SE$  of the nanowires is defined as the difference in the total energy between the strained and relaxed wires,

$$SE = E(total)_{strained} - E(total)_{relaxed} \quad (4)$$

The strain energy is plotted as a function of strain in Fig. 3. From both Fig. 3(a) and 3(b), at a given value of uniaxial strain, the strain energy is greater for larger wires. For example, under -2% compression, the strain energy for the 3.0 nm Si-core/Ge-shell wire is 0.5 eV, while it is 1.3 eV for the 4.7 nm wire. Similarly, under 2% tensile strain, the strain energy for the 3.0 nm Ge-core/Si-shell wire is 0.3 eV, while it is 1.8 eV for the 4.7 nm wire. Greater strain energy in larger wires is primarily resulting from the fact that more bonds being placed under strain in the larger wires.

Young's modulus is defined as the ratio between the stress and the strain. Young's modulus of a nanostructure is dependent on its geometry, size, composition, and orientation (Xu et al., 2005; Chen et al., 2006; Lee & Rudd, 2007a, 2007b; Kulkarni et al., 2005; Liu et al., 2008). Young's modulus  $Y$  of a nanowire can be calculated from the formula,

$$Y = \frac{1}{V_0} \left( \frac{\partial^2 E}{\partial \varepsilon^2} \right) \Bigg|_{\varepsilon=0} \quad (5)$$

where  $V_0$  is the volume of the relaxed nanowire defined as the product of the axial lattice constant  $a$  and the cross-section area  $A = \pi D^2/4$ ,  $E$  is the total energy, and  $\varepsilon$  is the external uniaxial strain.

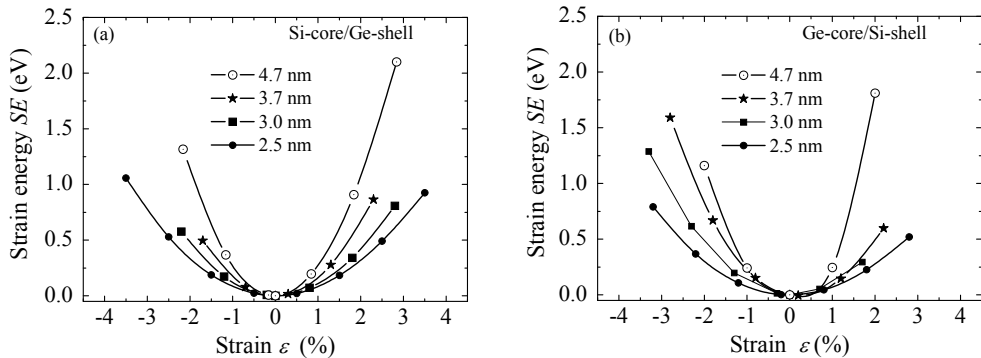


Fig. 3. The strain energies of the Si/Ge core-shell nanowires plotted as a function of strain.

The calculated modulus  $Y$  is reported in Table 2. Generally, for the Si-core/Ge-shell nanowires, the predicted Young's modulus decreases when increasing the diameter of the wire, from 67.2 GPa in the 2.5 nm wire to 62.2 GPa in the 4.7 nm wire. On the other hand, for the Ge-core/Si-shell nanowires, the Young's modulus increases with the wire diameter, from 59.2 GPa in the 2.5 nm wire to 82.2 GPa in the 4.7 nm wire. These general trends can be understood from the composition of the core-shell nanowires. Note that the Young's modulus in bulk Ge is smaller than that in bulk Si. Larger Si-core/Ge-shell nanowires contains more Ge atoms, thus a smaller modulus is expected. Similarly, larger Ge-core/Si-shell nanowires contain more Si atoms, and therefore display a larger modulus.

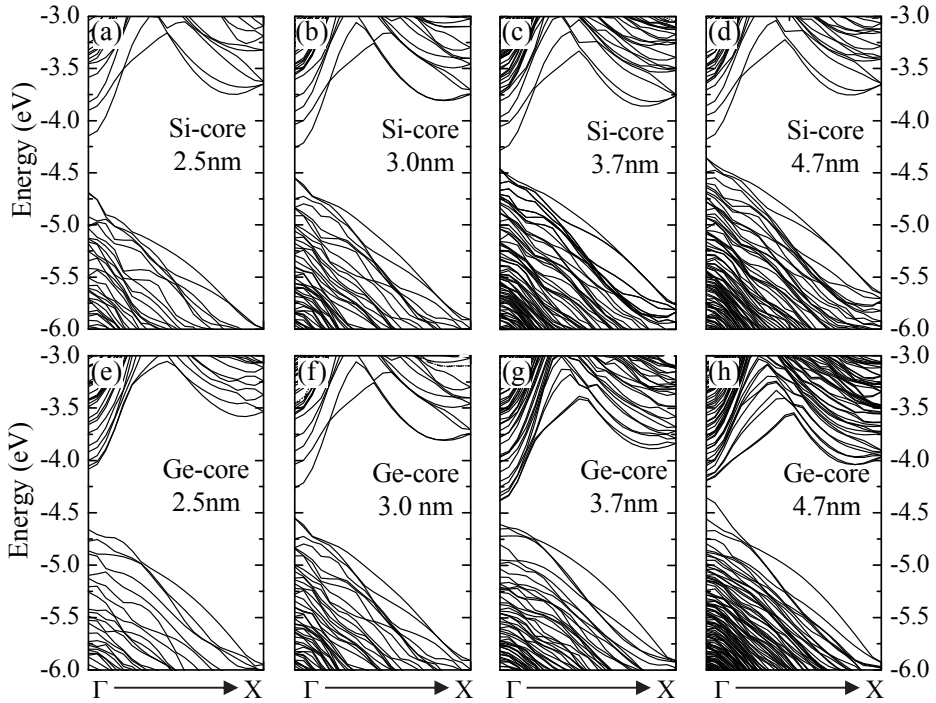


Fig. 4. The band structures of Si/Ge core-shell nanowires. The energies are referenced to the vacuum level.

## 3.2 Band structures

### 3.2.1 Band structure for relaxed Si/Ge core-shell nanowires

Bulk Si and Ge are indirect band gap materials. However, the Si/Ge core-shell and the pure Si and Ge nanowires with H passivation along the [110] direction demonstrate a direct band gap at  $\Gamma$  (Beckman et al., 2006; Arantes & Fazzio, 2007; Medaboina et al., 2007; L. Yang et al., 2008, Peng et al., 2009, Peng & Logan, 2010, Peng et al., 2011b). The band structures for the relaxed Si/Ge core-shell nanowires are presented in Fig. 4. In particular, the CBE and VBE were further examined, since both determine the band gap. The contour plots of charge density of CBE and VBE confirms that the band lineup in the Si/Ge core-shell nanowires is type II band offset. As an example, Fig. 5 shows the isovalue surfaces of the charge density of VBE and CBE in the nanowires with diameters of 2.5 nm and 3.7 nm. From the figures viewed in the cross sections (i.e. in the  $xy$  plane), the charge of VBE in the Si-core/Ge-shell wires is mainly distributed in the Ge shell, while the charge of CBE is mainly located in the Si core, as shown in Fig. 5(a) and 5(b). On the other hand, the charge of VBE in the Ge-core/Si-shell wires is primarily in the Ge core, while the charge of CBE is distributed in the Si shell, shown in Fig. 5(c) and 5(d). In conclusion, the VBE charge is in the Ge composition while the CBE charge is in the Si composition, regardless of whether the nanowire is of a Si-core/Ge-shell or Ge-core/Si-shell structure (L. Yang et al. 2008; Peng et al., 2011b).

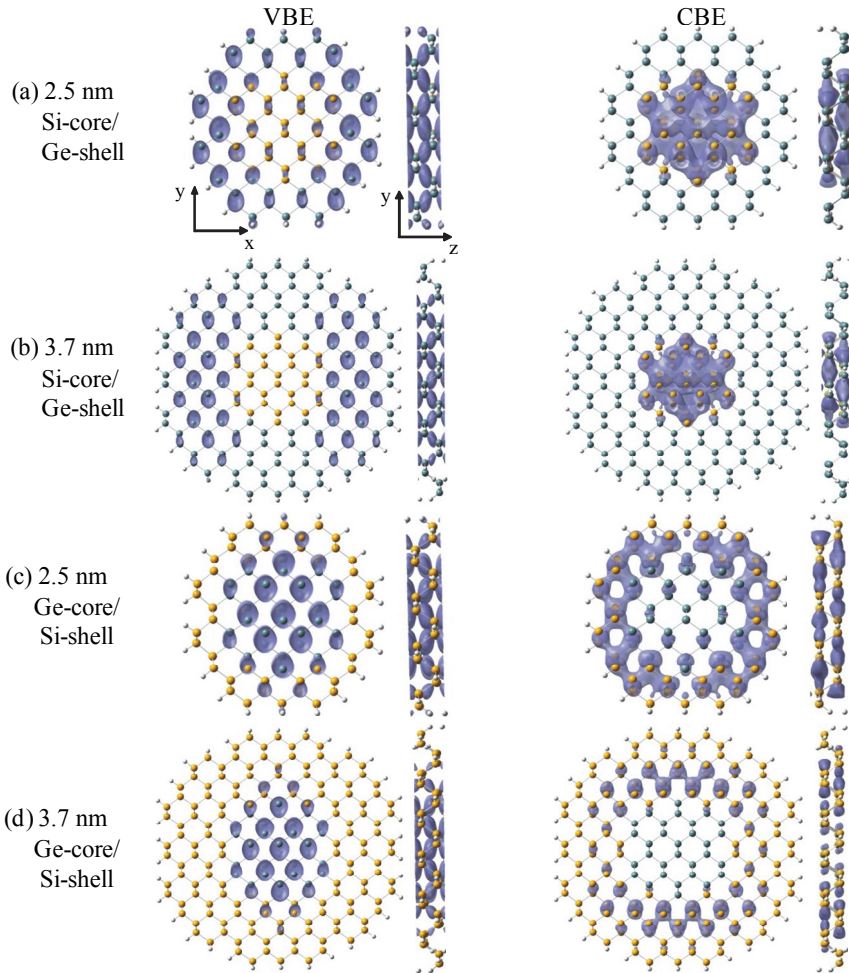


Fig. 5. The isovalue surfaces of the charge density of the valence/conduction band edges in Si/Ge core-shell nanowires. The yellow, blue and white dots represents Si, Ge, and H atoms, respectively.

This band lineup is also implied in the band structures. Examining the band edges at  $\Gamma$  in Fig. 4, one can notice that for the Si-core/Ge-shell wires, as shown in Fig. 4(a) – 4(d), the valence and lower occupied bands at  $\Gamma$  are generally close to each other, while the conduction band and higher unoccupied bands are considerably discrete. The discrete energies of the conduction band (contributed by Si composition) and neighbored unoccupied bands at  $\Gamma$  result from the fact that the Si atoms in the core are more significantly quantum confined compared to the Ge atoms in the shell. On the other hand, for the Ge-core/Si-shell wires in Fig. 4(e) – 4(h), the space of the energy levels in the valence band (contributed by Ge composition) and neighbored occupied bands are larger than that of conduction bands, mainly due to the fact that the Ge atoms in the core are more significantly quantum confined.

### 3.2.2 Band structure for strained Si/Ge core-shell nanowires

External strain shows a significant effect on the band structures of the core-shell nanowires. As an example, the band structure of 2.5 nm Ge-core/Si-shell nanowires under different values of uniaxial strain is plotted in Fig. 6(a) – 6(e). Examining the band edges, one can find that the energies of both CBE and VBE are decreased with tensile strain, while they are increased under compression. Interestingly, tensile strain shows a dramatic effect in the VBE. In Fig. 6(d) and 6(e), the VBE is no longer located at  $\Gamma$ , implying an indirect band gap in the nanowire. This effect and direct-to-indirect band gap transition will be discussed in detail in the following section of effective masses.

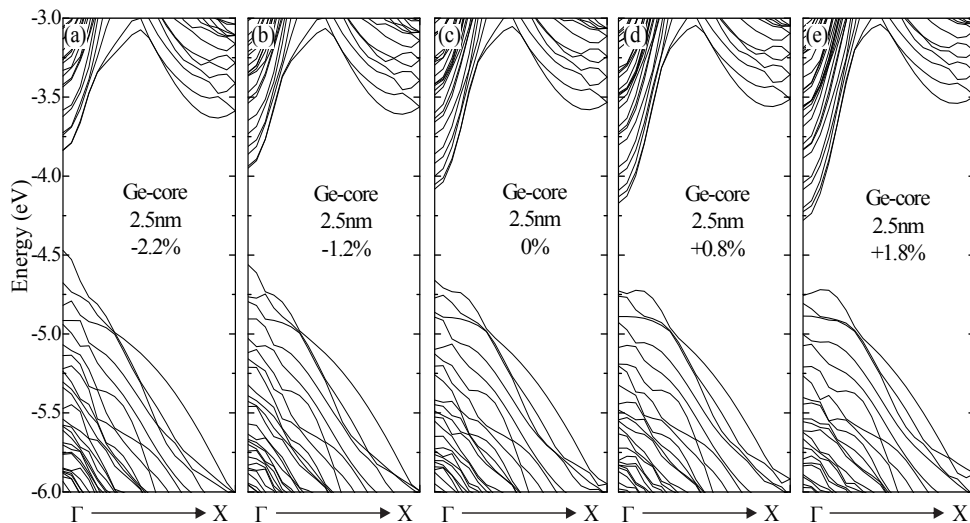


Fig. 6. The band structure of 2.5 nm Ge-core/Si-shell nanowire under different values of uniaxial strain. The energies are referenced to vacuum level.

### 3.3 Band gaps

#### 3.3.1 Band gap for relaxed Si/Ge core-shell nanowires

As mentioned earlier, the band gap of the Si/Ge core-shell wire is defined by the energy difference between CBE and VBE. DFT predicted band gaps for the Si/Ge core-shell wires are given in Table 3 and Fig. 7(a). It is known that DFT underestimates the band gap of semiconductors, and an advanced GW method (Hedin, 1965; Faleev et al., 2004; Bruneval et al., 2005) can provide improved predictions. However, for the size of the nanowires investigated in the present work, GW is not applicable due to its extremely high computing cost. The present work is mainly focused on the variation of electronic properties under factors such as external strain and size. Previous studies (Peng et al., 2006) on Si nanoclusters showed that the energy gap calculated by DFT obeys a similar strain-dependency as the optical gap predicted by advanced configuration interaction (CI) method and the quasi-particle gap (defined as the difference of ionization potential and electron affinity). In addition, DFT gap predicts a similar size-dependency as the optical gap obtained using GW and quantum Monte Carlo methods (Puzder et al., 2002; Zhao et al.,

2004). Therefore, the band gap calculated by DFT should qualitatively predict the correct trends both with varying size and strain.

As shown in Fig. 7(a), the band gap of the core-shell nanowires increases with reducing wire size, which is mainly due to the quantum confinement effect. The band gaps of pure Si and Ge nanowires with H passivation are also plotted in Fig. 7(a). It is interesting to note that the band gap of the core-shell nanowires is smaller than that of both pure Si and Ge nanowires, at a given diameter. For example, the DFT gap for Si and Ge wires with the diameter 2.5 nm are 1.02 eV and 0.73 eV (Peng et al., 2009; Logan & Peng, 2009), respectively. However the gap for the Si/Ge core-shell wires are 0.58 eV(Ge-core) and 0.54 eV (Si-core), respectively, which are both smaller than that of Si and Ge wires. Similar trends are also observed for the larger wires.

	D (nm)	$E_g$ (eV)	$m_e^*$ ( $m_e$ )	$m_h^*$ ( $m_e$ )	$\phi$ (eV)
Si-core/Ge-shell	2.5	0.54	0.13	0.16	4.64
	3.0	0.29	0.13	0.21	4.55
	3.7	0.18	0.14	0.32	4.46
	4.7	0.13	0.14	0.26	4.38
Ge-core/Si-shell	2.5	0.58	0.14	0.21	4.66
	3.0	0.31	0.13	0.17	4.58
	3.7	0.23	0.14	0.74	4.61
	4.7	0.18	0.14	0.36	4.36

Table 3. The electronic properties in the geometrically optimized Si/Ge core-shell nanowires.  $E_g$  is the band gap;  $m_e^*$  and  $m_h^*$  are the effective masses of the electron and hole in unit of free electron mass;  $\phi$  is the work function.

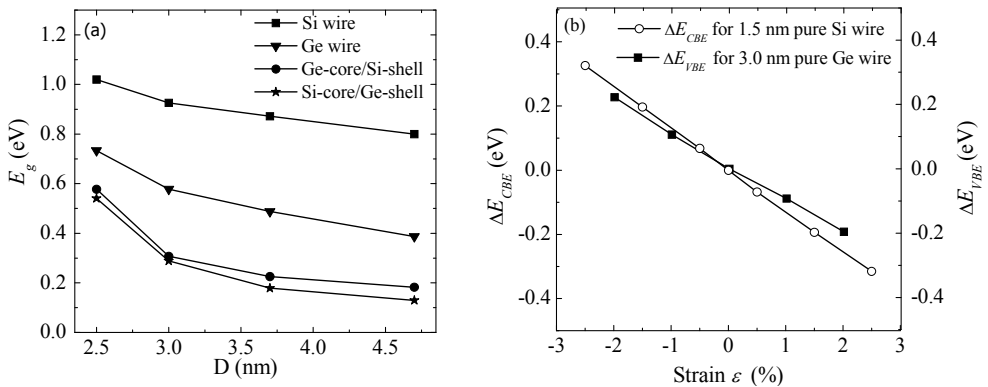


Fig. 7. (a) The band gap of Si/Ge core-shell and pure wires as a function of the wire diameter; (b) the energy variation of CBE (for 1.5 nm pure Si wire) and VBE (for 3.0 nm pure Ge wire) with strain.

In order to understand this reduced gap in the core-shell wires, the 3.0 nm Si-core/Ge-shell nanowire was examined as an example. The gap of the wire was reduced by 0.3 eV, compared to the pure 3.0 nm Ge wire. From the lattice constant and intrinsic strain reported in Table 2, the Si-core in the 3.0 nm Si-core/Ge-shell nanowire experiences a 2.2% tensile strain while the Ge-shell is contracted with a 0.8% compressive strain. Since the CBE/VBE states in the core-shell wire are primarily contributed by Si/Ge composition, we examined the CBE energy variation with strain in the pure Si nanowire of a diameter of 1.5 nm (represents the core) and the VBE energy variation with strain in the pure Ge nanowire of a diameter of 3.0 nm. The energy variations of CBE and VBE with strain is defined as,

$$\begin{aligned}\Delta E_{CBE} &= E_{CBE}(\varepsilon) - E_{CBE}(0) \\ \Delta E_{VBE} &= E_{VBE}(\varepsilon) - E_{VBE}(0)\end{aligned}\quad (6)$$

where  $E_{VBE}(\varepsilon)/E_{CBE}(\varepsilon)$  and  $E_{VBE}(0)/E_{CBE}(0)$  are energies of VBE/CBE with and without strain, respectively. The results are shown in Fig. 7(b). The CBE of the 1.5 nm Si wire is decreased by  $\sim 0.28$  eV under a 2.2% tensile strain. However, the VBE energy in the 3.0 nm Ge wire is increased about 0.8 eV with a 0.8% compressive strain. This implies that the band gap in the 3.0 nm Si-core/Ge-shell nanowire will be reduced by 0.36 eV, compared to the pure 3.0 nm Ge wire. This estimated reduction in the band gap (0.36 eV) is close to the actual calculation ( $\sim 0.3$  eV). Similar qualitative behaviors are also observed in the Ge-core/Si-shell nanowires.

From the above analysis, one can see that the reduced band gap is closely related to the intrinsic strain of the core-shell wires. Amato and colleagues (Amato et al., 2009) also observed a reduced band gap in Si/Ge hetero nanowires, which form an explicit interface between Si and Ge regions. The authors explained the gap reduction using quantum confinement effects in the band edges. The quantum confinement effect may be able to explain the results in their wires with diameters up to 1.6 nm. However, it is not able to explain our larger wires with a diameter up to 5 nm, where the quantum confinement is weaker. We argue that the reduction of the band gap in the Si/Ge core-shell nanowires is mainly due to the intrinsic strain in the Si/Ge composition.

### 3.3.2 Band gap for strained Si/Ge core-shell nanowires

The band gap of the Si/Ge core-shell nanowires can also be notably modulated by external strain. The variation of the band gap with strain is calculated as the difference in the band gap between the strained and relaxed wires,

$$\Delta E_g = E_g(\varepsilon) - E_g(0) \quad (7)$$

where  $E_g(\varepsilon)$  and  $E_g(0)$  are the band gap of the wire with and without strain, respectively. Fig. 8 plots  $\Delta E_g$  as a function of uniaxial strain for the core-shell nanowires. It is clear that strain can modify the band gap. Generally, the band gap in Si/Ge core-shell nanowires decreases evidently under tensile strain, while it only slightly varies with compression. As mentioned earlier, the nanowires demonstrate a transition from a direct to indirect band gap under a sufficient tensile strain. In Fig. 8, the data points representing an indirect band gap are indicated by arrows.

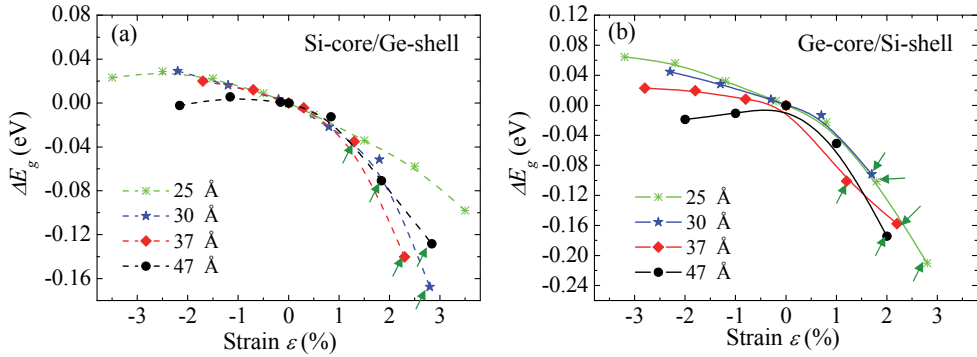


Fig. 8. The variation of the band gap in the Si/Ge core-shell wires with uniaxial strain.

In order to explain the general trends presented in Fig. 8 (i.e. the gap reducing with the uniaxial tensile strain), the energies of both CBE and VBE were further examined. The energy variation of CBE/VBE with strain is calculated as the energy difference in CBE/VBE between the strained and relaxed wires according to the equation (6). As an example, Fig. 9 shows the energy variations of CBE and VBE with strain in the 2.5 nm Si-core/Ge-shell nanowire. Note that a similar behavior is also observed for other wires. From Fig. 9, the energies of CBE and VBE both decrease nearly linearly with strain. In addition, the CBE curve has a slightly larger slope in tensile strain, compared to that of the VBE curve (thus giving a reduced gap under tensile strain).

The physical origin of the curves of the 2.5 nm Si-core/Ge-shell wire in Fig. 9 may be understandable from the wave-function character of CBE and VBE. The wave-function of various electronic states including CBE and VBE has been projected onto spherical harmonics within spheres of a radius of 1.2 Å around each Si and Ge ion. The decomposed contributions/coefficients of  $s$ ,  $p$ ,  $d$  orbitals are listed in Table 4. The VBE (i. e. VB at  $\Gamma$ ) is dominated by a  $p_z$  character, which suggests that the nodal surfaces of the positive and negative values of the wave-function are perpendicular to the axis of the wire (Leu et al., 2008; Z. G. Wu et al., 2009). Under a tensile strain, the distance between the nodal surfaces increases, and the kinetic energy associated with the electron transportation between atoms reduces (Z. G. Wu et al., 2009). The same holds true for the VBE energy. For the CBE (i. e. CB at  $\Gamma$ ), the projected wave-function includes a significant  $d_{z^2}$  character, which is consistent with literature (Richard et al., 2003; Ren et al., 1998; Filonov et al., 1995) that the  $d$  character defines the orbitals of the conduction band in a crystal. Similar to the  $p_z$  character, the  $d_{z^2}$  orbit also produces the nodal surfaces perpendicular to the axis of the wire. Therefore, the CBE energy reduces when the nanowire is under a tensile strain.

From the charge distribution of CBE and VBE shown in Fig. 5(a), one can see that the charge of VBE and CBE of the 2.5 nm Si-core/Ge-shell nanowire are mainly located in the Ge-shell and Si-core, respectively. The confined distributions of the electron charge in VBE and CBE give a clue to why the CBE curve in Fig. 9 has a larger slope compared to that of VBE curve. For the relaxed 2.5 nm Si-core/Ge-shell nanowire (i.e. no external strain applied), the intrinsic strain in the Si-core and the Ge-shell are +1.5% and -1.5%, respectively, due to the lattice mismatch of Si and Ge (Peng & Logan, 2010). If a +2% external tensile strain is applied to the wire, the resulting strain in the Si-core and Ge-shell are approximately +3.5%

and +0.5%, compared to their bulk lattice. Therefore, one expects the Si atoms in the core are more effectively expanded compared to those of the Ge atoms in the shell. Since the charge of CBE is mainly located in the Si-core while the electron of VBE is in the Ge-shell, the energy of CBE will have a larger reduction compared to that of VBE under expansion.

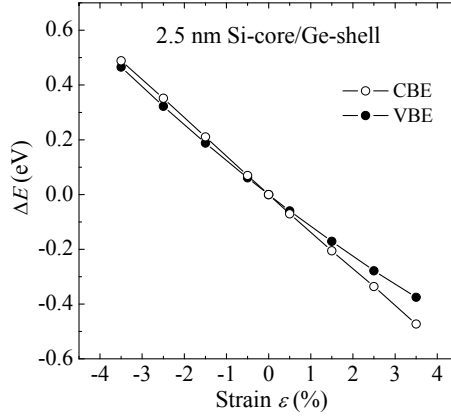


Fig. 9. The energy variation of CBE and VBE with the external strain in the Si-core/Ge-shell nanowire with the diameter of 2.5 nm. The vertical axis  $\Delta E$  is defined as the energy difference of CBE/VBE between the strained and the relaxed wire.

wire	state	$ s\rangle$	$ p_x\rangle$	$ p_y\rangle$	$ p_z\rangle$	$ d_{xy}\rangle$	$ d_{yz}\rangle$	$ d_{z^2}\rangle$	$ d_{xz}\rangle$	$ d_{yz}\rangle$
2.5 nm	VB at $\Gamma$	0.014	0.000	0.000	0.995	0.000	0.099	0.000	0.002	0.000
Si-core	VB at $0.2\cdot 2\pi/a$	0.045	0.967	0.212	0.098	0.095	0.008	0.011	0.003	0.005
/Ge-shell	CB at $\Gamma$	0.596	0.022	0.585	0.000	0.000	0.000	0.547	0.000	0.044
	CB at $0.2\cdot 2\pi/a$	0.603	0.155	0.532	0.054	0.012	0.006	0.066	0.006	0.567
2.5 nm	VB at $\Gamma$	0.008	0.000	0.000	0.995	0.000	0.097	0.000	0.002	0.000
Ge-core	VB at $0.2\cdot 2\pi/a$	0.059	0.991	0.073	0.018	0.089	0.002	0.005	0.005	0.002
/Si-shell	CB at $\Gamma$	0.588	0.022	0.669	0.000	0.005	0.000	0.452	0.000	0.044
	CB at $0.2\cdot 2\pi/a$	0.646	0.152	0.545	0.108	0.038	0.025	0.063	0.013	0.494

Table 4. Projections of the valence band (VB) and conduction band (CB) onto the  $s$ ,  $p$ , and  $d$  states in the 2.5 nm Si/Ge core-shell nanowires.

### 3.4 Effective masses of electron and hole

#### 3.4.1 Effective masses of electron and hole for relaxed Si/Ge core-shell nanowires

The effective masses of the electron and hole can be obtained from the band structure of the nanowires according to equation (2) through parabolic fitting the band edges. The calculated effective masses of the electron and hole for the relaxed Si/Ge core-shell nanowires are reported in Table 3, where  $m_e^*$  represents the effective mass of the electron, while  $m_h^*$  is the effective mass of the hole, in unit of free electron mass  $m_e$ . The effective mass of the electron are  $0.13 m_e$  or  $0.14 m_e$ , having a negligible change with size and the core-shell composition. In contrast, the effective mass of the hole is dependent on the wire size and composition.

### 3.4.2 Effective masses of electron and hole for the strained Si/Ge core-shell nanowires

The strain effect on the effective masses of the electron and hole were further studied. Taking the 2.5 nm Ge-core/Si-shell wire as an example, the dispersion relation with the K vector in the range of  $\pm 0.2 \cdot b$ , where  $b = 2\pi/a$ , is plotted under different values of strain in Fig. 10(a). It shows that strain has a dominant effect on the band structure at  $\Gamma$  - the energies are evidently shifted (Peng et al., 2011b). However, the strain has a negligible effect on the bands with K vectors away from  $\Gamma$  ( $K > 0.15 \cdot b$  or  $K < -0.15 \cdot b$ ). These strain effects may be understandable from a simple tight-binding model discussed in the reference (Logan & Peng, 2009). For an in-depth understanding, a detailed analysis of the wave-function character is reported in Table 4. For the valence/conduction band at  $\Gamma$ , there is a significant portion of  $p_z/d_z^2$  character. Therefore, the energy of the valence/conduction band at  $\Gamma$  decreases with an external tensile strain (see details discussion on Fig. 9). However, for the wave-functions at  $K = 0.20 \cdot b$ , the portion of  $p_z/d_z^2$  character is largely reduced, while the  $p_x/p_y$  character dominates. With the  $p_x/p_y$  character, the nodal surfaces of the wave-functions are parallel to the axis of the nanowire and the distance between the nodal surfaces is negligibly changed by a uniaxial strain. Therefore, the kinetic energy associated with the electron transportation stays the same, giving a minimal energy shift with strain (Z. G. Wu et al., 2009).

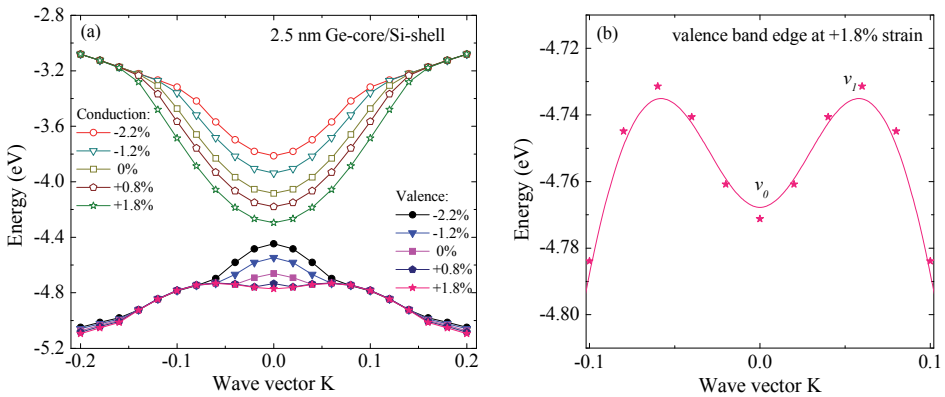


Fig. 10. The conduction and valence band of a Ge-core/Si-shell wire with a diameter of 2.5 nm at the near region of  $\Gamma$  under different values of uniaxial strain. The curve of valence band under +1.8% strain has been enlarged in (b), indicating an indirect band gap with valence band edge located at state  $v_1$  rather than  $v_0$ .

From Fig. 10(a), the CBE is located at  $\Gamma$ , regardless of the values of uniaxial strain. However, the VBE shows an interesting transition - it is no longer located at  $\Gamma$  for a large tensile strain (+1.8%), implying an indirect band gap. An enlarged graph of the VBE under +1.8% strain is presented in Fig. 10(b). The nature of the band gap (direct or indirect) is determined by the energies of the two states labeled as  $v_0$  at  $\Gamma$  and  $v_1$  at  $K = 0.05 \cdot b$ . Without strain, the energy of  $v_0$  is higher than that of  $v_1$ , as shown in Fig. 10(a), resulting in a direct band gap. With +1.8% tensile strain, the energy of  $v_1$  is higher than that of  $v_0$ , giving an indirect band gap. This direct-to-indirect gap transition with strain is clearly demonstrated in Fig. 10. In Fig. 10(a), the energy of the valence band at  $\Gamma$  ( $K = 0.0$ ) is noticeably decreased with tensile

strain, where the energy shift of the valence band at K vectors away from  $\Gamma$  (i.e.  $K > 0.05 \cdot b$ ) is negligible with strain. Therefore, with a sufficient tensile strain, the energy of the valence band at  $\Gamma$  can be reduced to an extent so that it is lower than the energy at  $K = 0.05 \cdot b$ . The reason for the different band energy shifts at  $\Gamma$  and other K vectors with strain stems from their different  $s, p, d$  orbital projection. (See the above section for detailed discussion).

The strain effects on the effective masses of the electron and hole are reported in Fig. 11. The variation of the effective mass of the electron with strain for three wires with a diameter of 2.5 nm, 3.0 nm and 3.7 nm are minimal, as shown in Fig. 11(a) and 11(b). For the wire with a diameter of 4.7 nm, the effective mass of the electron slightly increases with the compressive strain. In contrast, the change in the effective mass of the hole is dramatic, as shown in Fig. 11(c) and 11(d). Taking the 2.5 nm Ge-core/Si-shell wire as an example, the effective mass of the hole decreases from 0.21  $m_e$  (no strain) to 0.15  $m_e$  (-2.2% strain), which is indicated by the dispersion relations in Fig. 10(a) shown by the curves with solid dots and squares, respectively. In the case of the 3.0 nm Ge-core/Si-shell wire, the effective mass of the hole decreases slightly from 0.166  $m_e$  without strain to 0.145  $m_e$  at -2.3% strain (decreased by 13%), while it dramatically increases to 0.728  $m_e$  at 0.7% tensile strain (increased  $\sim 300\%$ ). When a +1.7% tensile strain is applied, the VBE of the wire shifts from  $\Gamma$  to the K vector at  $0.04 \cdot b$ . The effective mass of the hole was reduced back to 0.453  $m_e$  by a parabolic fitting of the dispersion relation near this new K vector. Similar behavior is also observed for other wires, as shown in Fig. 11(c) and 11(d).

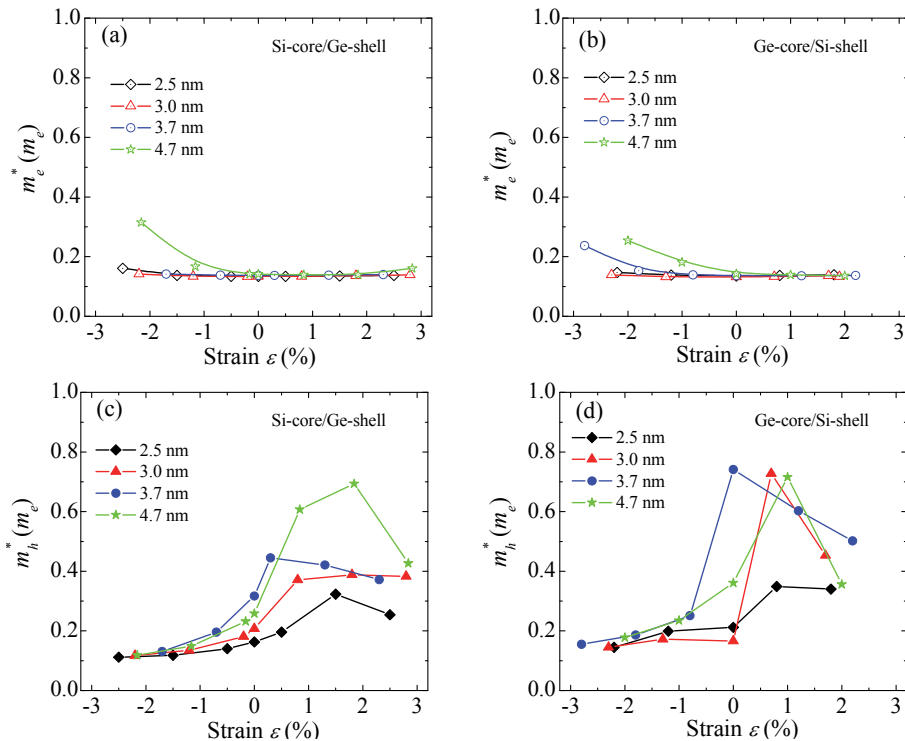


Fig. 11. The effective masses of the electron and hole as a function of strain for Si/Ge core-shell nanowires at different size and composition.

It is concluded that the effective mass of the hole in the Si/Ge core-shell nanowires is much more sensitive to strain, compared to that of the electron. This is also implied in Fig. 10(a), in which the curvature of the conduction band around  $\Gamma$  is not sensitive to strain. However, the shape of the valence band is dramatically changed with strain.

### 3.5 Work function

#### 3.5.1 Work function of the relaxed Si/Ge core-shell nanowires

It is of great importance to predict work function of semiconducting nanowires, since it affects band alignment in nanowire/metal interfaces and displays impact in device performance (Leu et al., 2008). The work function of a nanowire is defined as the energy difference between Fermi and vacuum levels,

$$\phi = V_{vacuum} - E_{Fermi} \quad (8)$$

Usually in first principles DFT calculations, the Fermi level is set to be the energy level of the highest occupied state, i. e. VBE. Since all electronic energies in present calculations are referenced to the vacuum, the work function  $\phi$  is simply,

$$\phi = -E_{VBE} \quad (9)$$

The calculated work functions  $\phi$  for the Si/Ge core-shell nanowires are reported in Table 3. The work function is in the range of 4.4 ~ 4.6 eV, consistent with the reported work function of H-passivated Si nanowires along the [110] direction (Ng et al., 2010; Leu et al., 2008). In general, the work function of the nanowire decreases with increasing size. For example, the work function of the Si-core/Ge-shell nanowires reduces from 4.64 eV for the 2.5 nm wire to 4.38 eV for the 4.7 nm. For the Ge-core/Si-shell wires, it decreases from 4.66 eV in 2.5 nm wire to 4.36 eV in 4.7 nm wire. This general trend is also demonstrated in the band structures in Fig. 4. Since the band energies in Fig. 4 are reference to vacuum level, the energy of VBE reflects the work function (with opposite sign). With increasing nanowire size, the VBE energies increase, implying that the work function decreases. This size-dependence of the work function is also consistent with that of Si nanowires (Ng et al., 2010; Leu et al., 2008).

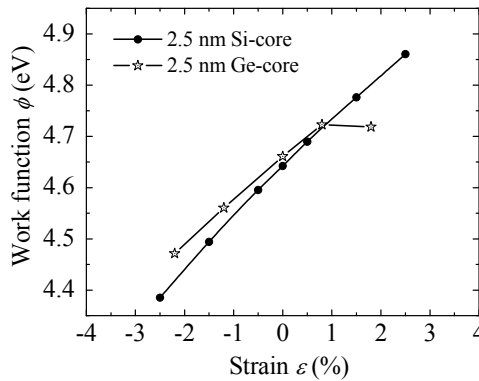


Fig. 12. The work function of the 2.5 nm Si/Ge core-shell nanowires as a function of external uniaxial strain.

### 3.5.2 Work function of the strained Si/Ge core-shell nanowires

It was also found that the work function of the Si/Ge core-shell nanowires can be modulated by external uniaxial strain. As an example, Fig. 12 presents the variation of the work function with strain in the 2.5 nm Si/Ge core-shell nanowires. In general, the work function for both wires increases with tensile strain, while reduces under compression. The effect was discussed in details in the above section for Fig. 10 and Fig. 7(b), where the energy of VBE is decreasing with tensile strain (note that the change of the potential of vacuum level is negligible with strain). This general trend is consistent with that in Si nanowires (Leu et al., 2008) and graphene nanoribbons (Peng et al., 2011a). In addition, it is interesting to note that the work function of the Si-core/Ge-shell wire increases nearly linearly, whereas for the Ge-core/Si-shell wire it saturates at a value on the tensile strain (shown in Fig. 12). This is due to the fact that with the tensile strain, the VBE of the Ge-core/Si-shell nanowires is located at  $K = 0.075\cdot b$ , rather than at  $\Gamma$  and shifts negligible with strain (see Fig. 6 and Fig. 10).

## 4. Conclusion & future work

In summary, first principles DFT calculations were performed to study the structural, mechanical and electronic properties of Si/Ge core-shell nanowires with the diameter up to 5 nm. Firstly, it was found that an intrinsic strain was produced in the core-shell nanowires. The intrinsic strain shows a dramatic effect in reduction of the band gap in the core-shell structure, significantly countering the quantum confinement effect. Secondly, the band structure can be greatly modified by external uniaxial strain, therefore the electronic properties, such as the band gap, effective masses of the electron and hole, work function, can be modulated by the strain.

The Si/Ge core-shell nanowires were demonstrated with a type II band alignment, where the valence band is contributed by Ge composition, while the conduction band is contributed by Si composition. In this case, electrons and holes are separated into core and shell regions, respectively. This offers an opportunity to employ the core-shell structure for novel device applications. To fulfill the purpose, an appropriate doping strategy has to be developed. We propose to theoretically investigate the effects of defects and surface functionality on the electronic properties of core-shell nanowires. Particularly, the shallow states introduced near VBE/CBE need be thoroughly studied, which potentially serve as the donor/acceptor centers. In addition, a dispersed/alloyed Si and Ge nanowire is also of great interest to study, bridging the knowledge of pure and core-shell nanowires. The dispersed/alloyed nanowires yield a maximum Si/Ge interface, where novel electronic properties could occur.

## 5. Acknowledgement

This work is supported by the Start-Up Fund from Arizona State University (ASU) to Peng. We thank the computational resources provided by ASU High Performance Computing Initiative Saguaro Cluster, National Center for Supercomputing Applications (NCSA) Abe Cluster, and Pittsburgh Supercomputing Center (PSC). Andrew Copple is acknowledged for reviewing the manuscript.

## 6. References

Amato M, Palumbo M & Ossicini S, (2009) Reduced quantum confinement effect and electron-hole separation in SiGe nanowires, *Phys. Rev. B* 79 201302- 201305

- Arantes J T & Fazio A, (2007) Theoretical investigations of Ge nanowires grown along the [110] and [111] directions, *Nanotechnology* 18 295706-295710
- Audoit G, Ni Mhuirheartaigh T, Lipson S M, Morris M A, Blau W J & Holmes J D, (2005) Strain induced photoluminescence from silicon and germanium nanowire arrays, *J. Mater. Chem.* 15 4809-4815
- Beckman S P, Han J & Chelikowsky J R, (2006) Quantum confinement effects in Ge [110] nanowires, *Phys. Rev. B* 74 165314-165318
- Bruneval F, Sottile F, Olevano V, Del Sole R & Reining L, (2005) Many-body perturbation theory using the density-functional concept: Beyond the GW approximation, *Phys. Rev. Lett.* 94 186402-186405
- Bruno M, Palummo M, Marini A, Del Sole R, Olevano V, Kholod A N & Ossicini S, (2005) Excitons in germanium nanowires: Quantum confinement, orientation, and anisotropy effects within a first-principles approach, *Phys. Rev. B* 72 153310-153313
- Chen C Q, Shi Y, Zhang Y S, Zhu J & Yan Y J, (2006) Size Dependence of Young's Modulus in ZnO Nanowires, *Phys. Rev. Lett.* 96 075505
- Cui Y & Lieber C M, (2001) Functional nanoscale electronic devices assembled using silicon nanowire building blocks, *Science* 291 851-853
- Cui Y, Wei Q Q, Park H K & Lieber C M, (2001) Nanowire nanosensors for highly sensitive and selective detection of biological and chemical species, *Science* 293 1289-1292
- Cui Y, Zhong Z H, Wang D L, Wang W U & Lieber C M, (2003) High performance silicon nanowire field effect transistors, *Nano Lett.* 3 149-152
- Dailey E & Drucker J, (2009) "Seedless" vapor-liquid-solid growth of Si and Ge nanowires: The origin of bimodal diameter distributions, *J. Appl. Phys.* 105 064317-064321
- Faleev S V, van Schilfhaarde M & Kotani T, (2004) All-electron self-consistent GW approximation: Application to Si, MnO, and NiO, *Phys. Rev. Lett.* 93 126406-126409
- Filonov A B, Tralle I E, Petrov G V & Borisenko V E, (1995) Silicon band-structure calculations by the self-consistent crystalline orbital method *Modell. Simul. Mater. Sci. Eng* 3 45-52
- Goldthorpe I A, Marshall A F & McIntyre P C, (2008) Synthesis and strain relaxation of Ge-core/Si-shell nanowire arrays, *Nano Lett.* 8 4081-4086
- Hahm J & Lieber C M, (2004) Direct ultrasensitive electrical detection of DNA and DNA sequence variations using nanowire nanosensors, *Nano Lett.* 4 51-54
- Hedin L, (1965) New method for calculating the one-particle Green's function with application to the electron-gas problem, *Phys. Rev.* 139 A796-A823
- Hirschman K D, Tsybeskov L, Duttagupta S P & Fauchet P M, (1996) Silicon-based visible light-emitting devices integrated into microelectronic circuits, *Nature* 384 338-341
- Holmes J D, Johnston K P, Doty R C & Korgel B A, (2000) Control of thickness and orientation of solution-grown silicon nanowires, *Science* 287 1471-1473
- Hu B Y-K & Das Sarma S, (1992) Many-body properties of a quasi-one-dimensional semiconductor quantum wire, *Phys. Rev. Lett.* 68 1750-1753
- Hu J Q, Bando Y & Golberg D, (2009) Novel semiconducting nanowire heterostructures: Synthesis, properties and applications, *J. Mater. Chem.* 19 330-343
- Hu Y J, Xiang J, Liang G C, Yan H & Lieber C M, (2008) Sub-100 nanometer channel length Ge/Si nanowire transistors with potential for 2 THz switching speed, *Nano Lett.* 8 925-930

- Kagimura R, Nunes R W & Chacham H, (2007) Surface dangling-bond states and band lineups in hydrogen-terminated Si, Ge, and Ge/Si nanowires, *Phys. Rev. Lett.* 98 026801- 026805
- Kohn W & Sham L J, (1965) Self-consistent equations including exchange and correlation effects, *Phys. Rev.* 140 1133-1138
- Koo S M, Fujiwara A, Han J P, Vogel E M, Richter C A & Bonevich J E, (2004) High inversion current in silicon nanowire field effect transistors, *Nano Lett.* 4 2197-2201
- Kresse G & Furthmuller J, (1996) Efficiency of ab-initio total energy calculations for metals and semiconductors using a plane-wave basis set, *Comput. Mater. Sci.* 6 15-50
- Kresse G & Furthmuller J, (1996) Efficient iterative schemes for ab initio total-energy calculations using a plane-wave basis set, *Phys. Rev. B* 54 11169-11186
- Kulkarni A J, Zhou M & Ke F J, (2005) Orientation and size dependence of the elastic properties of zinc oxide nanobelts, *Nanotechnology* 16 2749-2756
- Lauhon L J, Gudixsen M S, Wang C L & Lieber C M, (2002) Epitaxial core-shell and core-multishell nanowire heterostructures, *Nature* 420 57-61
- Lee B & Rudd R E, (2007) First-principles calculation of mechanical properties of Si<001> nanowires and comparison to nanomechanical theory, *Phys. Rev. B* 75 195328-195340
- Lee B & Rudd R E, (2007) First-principles study of the Young's modulus of Si<001> nanowires, *Phys. Rev. B* 75 041305-041308
- Leu P W, Svizhenko A & Cho K, (2008) Ab initio calculations of the mechanical and electronic properties of strained Si nanowires, *Phys. Rev. B* 77 235305-235318
- Liu X W, Hu J & Pan B C, (2008) The composition-dependent mechanical properties of Ge/Si core-shell nanowires, *Physica E: Low-dimensional Systems and Nanostructures* 40 3042-3048
- Logan P & Peng X H, (2009) Strain-modulated electronic properties of Ge nanowires: A first-principles study, *Phys. Rev. B* 80 115322-115328
- Lu W, Xiang J, Timko B P, Wu Y & Lieber C M, (2005) One-dimensional hole gas in germanium/silicon nanowire heterostructures, *Proc. Natl. Acad. Sci. U. S. A.* 102 10046-10051
- Medaboina D, Gade V, Patil S K R & Khare S V, (2007) Effect of structure, surface passivation, and doping on the electronic properties of Ge nanowires: A first-principles study, *Phys. Rev. B* 76 205327-2053213
- Migas D B & Borisenko V E, (2007) Structural, electronic, and optical properties of <001>-oriented SiGe nanowires, *Phys. Rev. B* 76 035440-035448
- Morales A M & Lieber C M, (1998) A laser ablation method for the synthesis of crystalline semiconductor nanowires, *Science* 279 208-211
- Musin R N & Wang X Q, (2005) Structural and electronic properties of epitaxial core-shell nanowire heterostructures, *Phys. Rev. B* 71 155318-155321
- Musin R N & Wang X Q, (2006) Quantum size effect in core-shell structured silicon-germanium nanowires, *Phys. Rev. B* 74 165308-165312
- Ng M F, Sim L Y, Da H X, Jin H M, Lim K H & Yang S W, (2010) Modulation of the work function of silicon nanowire by chemical surface passivation: a DFT study, *Theoretical Chemistry Accounts* 127 689-695
- Peelaers H, Partoens B & Peeters F M, (2007) Properties of B and P doped Ge nanowires, *Appl. Phys. Lett.* 90 263103-263105

- Peng X H, Alizadeh A, Kumar S K & Nayak S K, (2009) Ab-initio study of size and strain effects on the electronic properties of Si nanowires, *Int. J. of Applied Mechanics* 1 483-499
- Peng X H, Ganti S, Alizadeh A, Sharma P, Kumar S K & Nayak S K, (2006) Strain-engineered photoluminescence of silicon nanoclusters, *Phys. Rev. B* 74 035339-035343
- Peng X H & Logan P, (2010) Electronic properties of strained Si/Ge core-shell nanowires, *Appl. Phys. Lett.* 96 143119-143121
- Peng X H, Tang F & Copple A, (2011) Work function of armchair graphene nanoribbons, (unpublished)
- Peng X H, Tang F & Logan P, (2011) Band structure of Si/Ge core-shell nanowires along [110] direction modulated by external uniaxial strain, *J. Phys. Condens. Matter* 23, 115502-115509
- Puzder A, Williamson A J, Grossman J C & Galli G, (2002) Surface chemistry of silicon nanoclusters, *Phys. Rev. Lett.* 88 097401-097404
- Ren S Y, Chen X & Dow J D, (1998) Tight-binding  $sp^3d^5$  Hamiltonian for Si, *J. Phys. Chem. Solids* 59 403-410
- Richard S, Aniel F, Fishman G & Cavassilas N, (2003) Energy-band structure in strained silicon: A 20-band k-p and Bir-Pikus Hamiltonian model, *J. Appl. Phys.* 94 1795-1799
- Tian B Z, Zheng X L, Kempa T J, Fang Y, Yu N F, Yu G H, Huang J L & Lieber C M, (2007) Coaxial silicon nanowires as solar cells and nanoelectronic power sources, *Nature* 449 885-889
- Trammell T E, Zhang X, Li Y L, Chen L Q & Dickey E C, (2008) Equilibrium strain-energy analysis of coherently strained core-shell nanowires, *J. Cryst. Growth* 310 3084-3092
- Vanderbilt D, (1990) Soft self-consistent pseudopotentials in a generalized eigenvalue formalism, *Phys. Rev. B* 41 7892-7895
- Varahramyan K M, Ferrer D, Tutuc E & Banerjee S K, (2009) Band engineered epitaxial  $Ge_xSi_{1-x}$  core-shell nanowire heterostructures, *Appl. Phys. Lett.* 95 033101-033103
- Wu X Y, Kulkarni J S, Collins G, Petkov N, Almecija D, Boland J J, Erts D & Holmes J D, (2008) Synthesis and electrical and mechanical properties of silicon and germanium nanowires, *Chem. Mat.* 20 5954-5967
- Wu Y Y, Fan R & Yang P D, (2002) Block-by-block growth of single-crystalline Si/SiGe superlattice nanowires, *Nano Lett.* 2 83-86
- Wu Z, Neaton J B & Grossman J C, (2008) Quantum confinement and electronic properties of tapered silicon nanowires, *Phys. Rev. Lett.* 100 246804-246807
- Wu Z G, Neaton J B & Grossman J C, (2009) Charge separation via strain in silicon nanowires, *Nano Lett.* 9 2418-2422
- Xu B, Lu A J, Pan B C & Yu Q X, (2005) Atomic structures and mechanical properties of single-crystal GaN nanotubes, *Phys. Rev. B* 71 125434-125439
- Yang J E, Jin C B, Kim C J & Jo M H, (2006) Band-gap modulation in single-crystalline  $Si_{1-x}Ge_x$  nanowires, *Nano Lett.* 6 2679-2684
- Yang L, Musin R N, Wang X Q & Chou M Y, (2008) Quantum confinement effect in Si/Ge core-shell nanowires: First-principles calculations, *Phys. Rev. B* 77 195325-195329
- Zhao X, Wei C M, Yang L & Chou M Y, (2004) Quantum confinement and electronic properties of silicon nanowires, *Phys. Rev. Lett.* 92 236805-236808

# Nanowire Applications: Thermoelectric Cooling and Energy Harvesting

Gang Zhang

*Key Laboratory for the Physics and Chemistry of Nanodevices and  
Department of Electronics, Peking University  
China*

## 1. Introduction

Recently, thermoelectric materials have attracted extensive attention again. This is primarily due to the increasing awareness of the deleterious effect of global warming on the planet's environment, a renewed requirement for long-life electrical power sources, and the increasing miniaturization of electronic circuits and sensors. Thermoelectrics is able to make a contribution to meet the requirements of all the above activities. Moreover, the advent of nanotechnology has had a dramatic effect on thermoelectric material development and has resulted in the syntheses of nanostructured materials whose thermoelectric properties surpass the best performance of its bulk counter, such as Silicon nanowires (SiNWs). (Boukai et al., 2008; Hochbaum et al., 2008) SiNWs are appealing choice in the novel nano-scale TE materials because of their small sizes and ideal interface compatibility with conventional Si-based technology. For a good thermoelectric material, the material must have a high figure of merit ( $ZT$ ), which is proportional to the Seebeck coefficient ( $S$ ), electrical conductivity, and absolute temperature, but inversely proportional to thermal conductivity. In order to make materials that are competitive for (commercial) thermoelectric application, the  $ZT$  of the material must be larger than three. There are several ways to do this. The first approach is to increase the Seebeck coefficient  $S$ . However, for general materials, simply increase  $S$  will lead to a simultaneous decrease in electrical conductivity. The second approach is to increase the electrical conductivity. This has also proven to be ineffective, because electrons are also carriers of heat and an increase in electrical conductivity will also lead to an increase in the thermal conductivity. The ideal case is to reduce the thermal conductivity without affecting the electrical conductivity. It is possible to achieve this in SiNWs. In SiNWs, the electrical conductivity and electron contribution to Seebeck coefficient are similar to those of bulk silicon, but exhibit 100-fold reduction in thermal conductivity, showing that the electrical and thermal conductivities are decoupled. Recent experiments have provided direct evidence that an approximately 100-fold improvement of the  $ZT$  values over bulk Si are achieved in SiNW over a broad temperature range. (Boukai et al., 2008; Hochbaum et al., 2008) This large increase of  $ZT$  is contributed by the decrease of thermal conductivity. SiNWs have attracted broad interests in recently years due to their fascinating potential applications. Extensive investigations have been carried out on the synthesis, properties and applications of SiNWs. Experimental

technology has been developed to control the growth of SiNWs not only in various growth orientations, but also with various shapes of transverse cross section including rectangle (square), hexagon (rough circle), and triangle. A large number of theoretical and experimental works have been done to explore the properties and applications of these nano wires. Due to the limit of space, here we only address the most fundamental aspects of thermoelectric in nanowires. For the comprehensive review of nanoscale thermal conductivity, please refer to these articles (Cahill et al., 2002; G. Zhang & B. Li, 2010). However, to be self-consistent, we will also give a brief summary about the anomalous thermal conduction and diffusion in one-dimensional nano materials. These results are helpful in understanding the phonon transport in nanowires. In this chapter, it provides an update of recent developments and serves both as an authoritative reference text on thermoelectric property of nanowires for the professional scientist and engineer, and as a source of general information on thermoelectric application for the well-informed layman. This chapter is review type and arranged in eight sections, entitled Introduction; Thermal Conduction in Low-Dimensional Systems; Impact of doping on thermal conductivity of NWs; Effect of surface roughness on phonon transport; Reduction of thermal conductivity by surface scattering; Thermoelectric Property of SiNWs; Realization of SiNW based On-Chip Coolers and Conclusion.

## **2. Thermal conduction in low-dimensional systems**

In recent years, different models and theories have been proposed to study the phonon transport mechanism in low dimensional system. The physical connection between energy diffusion and thermal conductivity has been demonstrated theoretically. (B. Li et al., 2005) For instance, when phonon transports diffusively, which is what we have in bulk material, the thermal conductivity is a size-independent constant. However, in the ballistic transport region, the thermal conductivity of the system increases with the system size, which is the case for ideal One-Dimensional harmonic lattice. Low dimensional nanostructures such as nanowires and nanotubes provide a test bed for these new theories.

Regardless of the specific application, it is obvious that the systematic applications of nano materials will be greatly accelerated by a detailed understanding of their material property. Thermal property in nanostructures differs significantly from that in macrostructures because the characteristic length scales of phonon are comparable to the characteristic length of nanostructures. In bulk materials, the optical phonon modes contribute little to heat flux. However, in nano system, optical phonon (short wavelength) also plays a major role to the heat flux.

A large variety of studies on thermal conductivity of nano materials have been undertaken in the past decade, and quite unexpected phenomena have been observed. This chapter is to address the most important aspects of thermal conduction and thermoelectric property in low dimensional nano materials, of particular focus on semiconducting nanowires. For a comprehensive review of nanoscale thermal conductivity, please refer to these articles. (Cahill et al., 2002; G. Zhang & B. Li, 2010)

### **2.1 Thermal conduction in nanotubes**

Carbon nanotube (CNT) is one of the promising nanoscale materials discovered in 1990's. (Iijima, 1991) It has many exceptional physical and chemical properties. Depending on its

chirality and diameter, the nanotube can be either metallic or semiconducting. At room temperature, the electronic resistivity is about  $10^{-4}$ – $10^{-3}$   $\Omega$  cm for the metallic nanotubes, while the resistivity is about 10  $\Omega$  cm for semiconducting tubes. By combining metallic and semiconducting CNTs, the whole span of electronic components can be embodied in nanotubes. Actually, CNTs are ranked among the best electron field emitters that are now available.

In the past few years, there has been some experimental works on the heat conduction of CNTs. The thermal conductivity of a single CNT was found to be larger than 3000 W/mK at room temperature. (Kim et al., 2001) In addition to the experimental activity, there are also many theoretical studies on heat conduction of CNTs. It was found that at room temperature, thermal conductivity of CNTs is about 6600 W/mK. (Berber et al., 2000) Yamamoto *et al.* have demonstrated that even for the metallic nanotubes, the electrons give some but limited contributions to thermal conductivity at very low temperature (close to 0 K), and this part decreases quickly with temperature increasing. (Yamamoto et al., 2004) More important, it is found that thermal conductivity of CNT  $\kappa$  diverges with length as a power law:  $\kappa \propto L^\beta$ , with the exponents  $\beta$  is between 0.12 to 0.4 (G. Zhang & B. Li, 2005) and between 0.11 to 0.32 (Maruyama, 2002). This length dependent thermal conductivity can be understood from the vibrational energy diffusion in SWNT.

## 2.2 Thermal conduction in nanowires

In addition to CNTs, Silicon nanowires (SiNWs) have attracted a great attention in recent years because of their potential applications in many areas including biosensor (Cui et al., 2001), electronic device (Xiang et al., 2006) and solar PVs (J. Li et al., 2009). SiNWs are appealing choice because of their ideal interface compatibility with conventional Si-based devices.

Due to the size effect and high surface to volume ratio, the thermal conduction properties of silicon nanostructures differ substantially from those of bulk materials. Volz and Chen (Volz & G. Chen, 1999; 2000) have found that the thermal conductivity of individual silicon nanowires is more than 2 orders of magnitude lower than the bulk value. Li *et al.* (D. Li et al., 2003) have also reported a significant reduction of thermal conductivity in silicon nanowires compared to the thermal conductivity in bulk silicon experimentally. The reduction in thermal conductivity is due to the following two factors. Firstly, the low frequency phonons, whose wave lengths are longer than the scale of nanowire, cannot survive in nanowire. Therefore, the low frequency contribution to thermal conductivity is largely reduced. Secondly, because of the large surface to volume ratio, the boundary scattering in NW is greatly significant.

More experimental and theoretical activities have been inspired to do further in this direction, including the theoretical prediction of thermal conductivity of Ge nanowires, molecular dynamics simulation of SiGe NWs, and experimental growth of the isotopic doped SiNWs. The low temperature (<2K) thermal conductance of individual suspended SiNWs was measured by Bourgeois *et al.* (Bourgeois et al., 2007) And the pure phonon confinement effect has been observed in germanium nanowires by measurement of Raman spectra. (X, Wang et al., 2007)

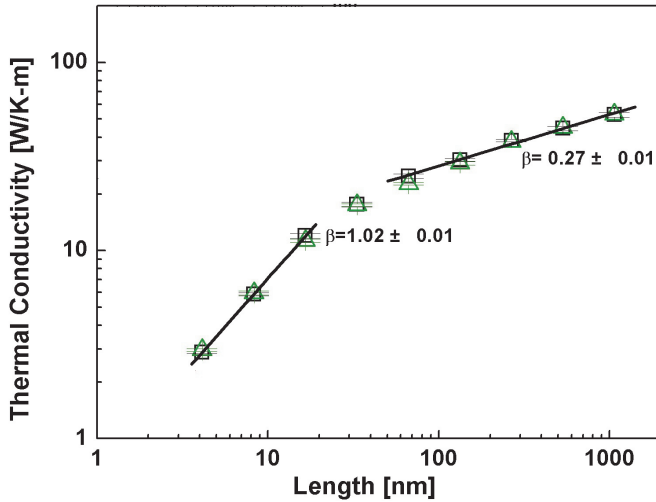


Fig. 1. The thermal conductivity of SiNWs vs longitude length

The similar length dependent thermal conductivity was also observed in SiNWs by using NEMD simulation. (N. Yang et al., 2010) As shown in Fig. 1, it is obvious that the thermal conductivity increases with the length as,  $\kappa \propto L^\beta$ , even when the wire length is as long as 1.1  $\mu\text{m}$ . By using the phonon relaxation time ( $\sim 10$  ps) in SiNWs (Volz & G. Chen, 1999), and the group velocity of phonon as 6400 m/s (N. Yang et al., 2010), the mean free path  $\lambda$  is about 60nm. The maximum SiNW length (1.1  $\mu\text{m}$ ) in Fig. 1 is obviously much longer than the phonon mean free path of SiNW. Traditionally, it is well known that in macroscopic systems, the thermal conductivity is a constant when system scale  $L \gg \lambda$ . However, the NEMD results demonstrated that in SiNWs, thermal conductivity is no longer a constant even when the length is obviously longer than the traditionally mean free path.

Moreover, it is obvious that the length dependence of thermal conductivity is different in different length regimes. At room temperature, when SiNW length is less than mean free path (about 60 nm), the thermal conductivity increases with the length linearly ( $\beta \approx 1$ ). For the longer wire ( $L > 60$  nm), the diverged exponent  $\beta$  reduces to about 0.27. The dependence of  $\beta$  on NW length can be understood from the picture of phonon coupling. There is weak interaction among phonons when the length of SiNW is shorter than mean free path. So the phonons transport ballistically, and  $\beta \approx 1$ . However, when the length of SiNW is longer than the mean free path, phonon-phonon scattering dominates the process of phonon transport and the phonon cannot flow ballistically. Thus the diverged exponent  $\beta$  reduces from 1 to 0.27.

Then let us turn to the energy diffusion process in SiNWs. To study the energy diffusion process, the SiNW is first thermalized to a temperature  $T$ , then a heat pulse (a packet of energy) is excited in the middle of the wire and its spreads along the wire was recorded. To suppress statistical fluctuations, an average over  $10^3$  realizations is performed. The details of the numerical calculation can be found in (N. Yang et al., 2010). Based on billiard gas

channel models, Li and Wang (B. Li & J. Wang, 2003) proposed a phenomenologically formula that connect anomalous heat conduction with the anomalous diffusion of heat carrier, namely,  $\beta = 2 - 2/\alpha$ . This connection indicates that only when the heat carrier undergoes normal diffusion like in the bulk material, the thermal conductivity is independent of system size. In super-diffusion case,  $\alpha > 1$ , the exponent  $\beta > 0$ , which means that thermal conductivity diverges with system size, this is the case observed in thermal conductivity of CNTs and SiNWs. In Fig. 2 we show  $\langle \sigma^2(t) \rangle$  versus time in double logarithmic scale, so that the slope of the curve gives the value of  $\alpha$ . For the NWs of length of 140 nm, it was obtained  $\alpha = 1.15$  at 300 K. With the value of diffusion exponent ( $\alpha = 1.15$  at 300 K), one can obtain  $\beta = 0.26$  at 300 K, which are very close to those values (0.27) calculated directly from NEMD simulation. These results demonstrate that the super diffusion is responsible for the length dependent thermal conductivity of SiNWs.

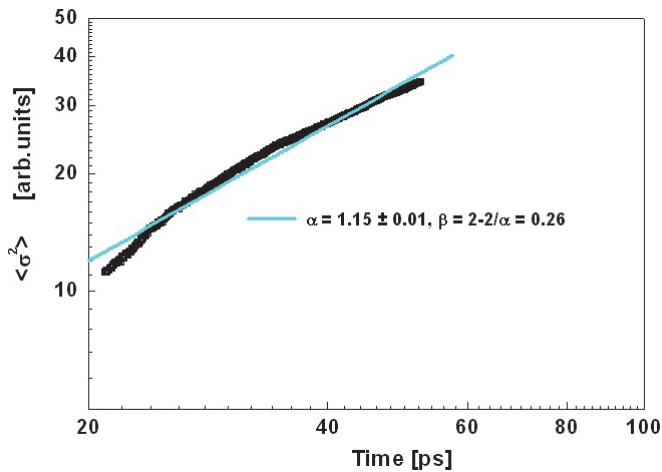


Fig. 2. The behavior of energy diffusion in SiNW at room temperature. The length of SiNW is 140 nm.

### 3. Impact of doping on thermal conductivity of NWs

Although the thermal conductivity of SiNWs is lower than that of the bulk silicon, it is still larger than the reported ultralow thermal conductivity (0.05 W/m-K) found in layered materials. So it is indispensable to reduce the thermal conductivity of SiNWs further in order to achieve higher thermoelectric performance. Actually, real materials can have natural defects and doping in the process of fabrication. The doping of isotope and/or other atoms have played key roles in some of the most important problems of materials, such as elastic, and field emission properties. Since the phonon frequency depends on mass, the isotopic doping can lead to increased phonon scattering. Thus, natural SiNW always contain a significant number of scattering centers leading to localization of some phonon modes and reduces thermal conductivity. By using molecular dynamics simulations, Yang *et al.* (N. Yang et al., 2008) have proposed one approach which is to dope SiNWs with isotope

impurity randomly for reduction of thermal conductivity of SiNWs. In silicon isotopes,  $^{28}\text{Si}$  is with the highest natural abundance (92%), then  $^{29}\text{Si}$  and  $^{30}\text{Si}$  with 5% and 3% respectively. Here the effect of doping  $^{29}\text{Si}$  to  $^{28}\text{Si}$  NWs are shown.

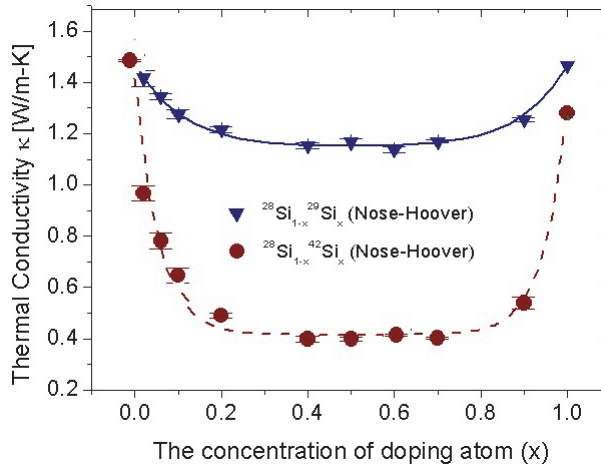


Fig. 3. Thermal conductivity of SiNWs versus the percentage of randomly doping isotope atoms ( $^{42}\text{Si}$  and  $^{29}\text{Si}$ ) at 300K.

The curve of thermal conductivity first reach a minimum and then increases as the percentage of isotope impurity atoms changes from 0 to 100%. At low isotopic percentage, the small ratio of impurity atoms can induce large reduction on conductivity. Contrast to the high sensitivity at the two ends, the thermal conductivity versus isotopic concentration curves are almost flat at the center part as show in Fig. 3, where the value of thermal conductivity is only 77% ( $^{29}\text{Si}$  doping) of that of pure  $^{28}\text{Si}$  NW. The calculated thermal conductivity of SiNW with natural isotopic abundance, 5%  $^{29}\text{Si}$  and 3%  $^{30}\text{Si}$  is around 86% of pure  $^{28}\text{Si}$  NW, which reduction (14%) is higher than the experimental results in bulk Si, which is about 10% reduction.

In addition to the disorder doping, it has been shown that superlattices are efficient structures to get ultra low thermal conductivity. The isotopic-superlattice (IS) is a good one to reduce the thermal conductivity without destroying the stability. The thermal conductivity of IS structured NWs which consists of alternating  $^{28}\text{Si}/^{29}\text{Si}$  layers along the longitudinal direction are shown in Fig. 4. As expected, the thermal conductivity decreases as the period length decreases, which means the number of interface increases. The thermal conductivity reaches a minimum when the period length is 1.09 nm. This is consistent with the fact that increasing number of interface will enhance the interface scattering, and results to the reduction of the thermal conductivity. With the period length smaller than 1.09 nm, the thermal conductivity increases rapidly as the period length decreases. This anomalous superlattice dependence of thermal conductivity can be understood from the phonon density of states (DOS). When period length is 2.17 nm, there is an obvious mismatch in the DOS spectra, both at low frequency band and high frequency band, results in very low thermal conductivity. On the contrary, the DOS spectra overlap perfectly for IS structured

SiNW whose period length is 0.27 nm. The good match in the DOS comes from the collective vibrations of different mass layers which is harder to be built in longer superlattice period structures. The match/mismatch of the DOS spectra between the different mass layers controls the heat current.

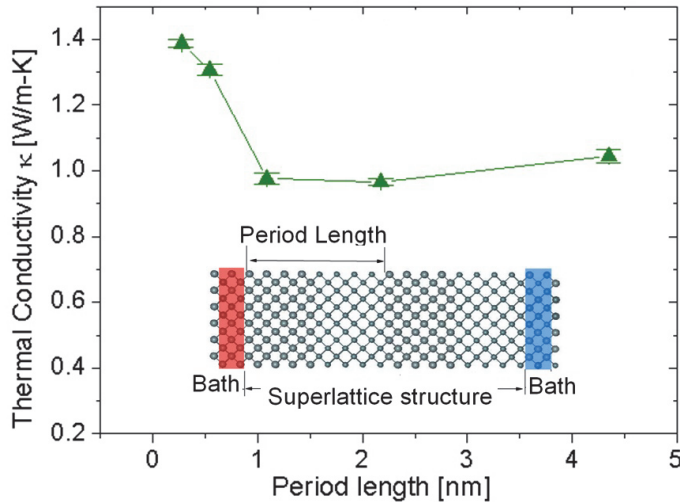


Fig. 4. Thermal conductivity of the superlattice SiNWs versus the period length at 300 K.

It is worth to point out that the growth of isotopically controlled silicon nanowires by the vapor-liquid-solid mechanism has been done recently. (Moutanabbir et al., 2009) The growth is accomplished by using silane precursors  $^{28}\text{SiH}_4$ ,  $^{29}\text{SiH}_4$  and  $^{30}\text{SiH}_4$  synthesized from  $\text{SiF}_4$  isotopically enriched in a centrifugal setup. And the effect of isotope doping on Si-Si LO phonon has also been investigated. The corresponding experimental measurement of thermal conductivity is on-going.

Moreover, Silicon and Germanium can form a continuous series of substitutional solid,  $\text{Si}_{1-x}\text{Ge}_x$  over the entire compositional range of  $0 \leq x \leq 1$ . These semiconductor alloys offer a continuously variable system with a wide range of crystal lattices and band gaps, leading to various electrical property. Single crystalline  $\text{Si}_{1-x}\text{Ge}_x$  NWs have been successfully grown. (J-E. Yang et al., 2006) Those composite nanocrystals constitute a new class of semiconductor materials with unique chemical and physical properties which are not possible in single-component compounds. The tenability of those properties makes this kind of semiconductor systems very attractive for industrial application. In spite of an increasing number of works devoted to the electronic and optical properties, very little has done for thermal conductivity of  $\text{Si}_{1-x}\text{Ge}_x$  NW.

Here we address the non-equilibrium molecular dynamics (NEMD) calculated thermal conductivity of  $\text{Si}_{1-x}\text{Ge}_x$  NWs with  $x$  changing from 0 to 1. (J. Chen et al., 2009) In NEMD, to derive the force term, Stillinger-Weber (SW) potential (Stillinger & Weber, 1985) is used for Si and Ge. SW potential consists of a two-body term and a three-body term that can stabilize the diamond structure of silicon and germanium. The two-body interaction can be described as:

$$v_2(r_{ij}) = \varepsilon f_2(r_{ij} / \sigma), \quad (1)$$

$$f_2(r) = A(Br^{-p} - r^{-q})\exp[(r - a)^{-1}], (r < a) \quad (2)$$

where  $r_{ij}$  is the inter atomic distance,  $A$ ,  $B$ ,  $p$ ,  $q$ ,  $\varepsilon$  and  $\sigma$  are potential parameters, and  $a$  is the potential cutoff distance above which no interaction occurs. The three-body interaction is:

$$v_3(\mathbf{r}_i, \mathbf{r}_j, \mathbf{r}_k) = \varepsilon f_3(\mathbf{r}_i / \sigma, \mathbf{r}_j / \sigma, \mathbf{r}_k / \sigma),$$

$$f_3(\mathbf{r}_i, \mathbf{r}_j, \mathbf{r}_k) = h(r_{ij}, r_{ik}, \theta_{jik}) + h(r_{ji}, r_{jk}, \theta_{ijk}) + h(r_{ki}, r_{kj}, \theta_{ikj}), \quad (3)$$

$$h(r_{ij}, r_{ik}, \theta_{jik}) = \lambda \exp[\gamma(r_{ij} - a)^{-1} + \gamma(r_{ik} - a)^{-1}] \times (\cos\theta_{jik} + 1/3)^2,$$

where  $\lambda$  and  $\gamma$  are potential parameters, and  $\theta_{jik}$  is the angle between  $r_{ij}$  and  $r_{ik}$ . The parameters of Si-Ge interactions are taken to be the arithmetic average of Si and Ge parameters for  $\sigma_{\text{Si-Ge}}$ , and the geometric average for  $\lambda_{\text{Si-Ge}}$  and  $\varepsilon_{\text{Si-Ge}}$ .

According to the Boltzmann distribution, the temperature  $T_{MD}$  in MD simulation, is calculated from the kinetic energy of atoms as:

$$\langle E_k \rangle = \frac{1}{2} \sum_{i=1}^N m_i v_i^2 = \frac{3}{2} N k_B T_{MD}, \quad (4)$$

where  $\langle E_k \rangle$  is the mean kinetic energy,  $v_i$  is the velocity of atom  $i$ ,  $m$  is the atomic mass,  $N$  is the number of particles in the systems, and  $k_B$  is the Boltzmann constant. However, Eq. (4) is valid only when  $T \gg T_D$ , where  $T_D$  is the Debye temperature. Therefore, if the system is simulated at a MD temperature below the Debye temperature ( $T_D = 645\text{K}$  for Si), a quantum correction to both MD temperature and thermal conductivity should be carried out. According to the equipartition theorem, the system energy is twice the kinetic energy. So we can write the equality of phonon energy as:

$$3Nk_B T_{MD} = \int_0^{\omega_D} D(\omega) n(\omega, T) \hbar \omega d\omega, \quad (5)$$

where  $\omega$  is the phonon frequency,  $D(\omega)$  is the density of states,  $n(\omega, T)$  is the phonon occupation number given by the Bose-Einstein distribution, and  $\omega_D$  is the Debye frequency. The real temperature  $T$  can be deduced from the MD temperature  $T_{MD}$  by this relation. Correspondingly, the "real" thermal conductivity is rescaled by

$$k = k_{MD} \frac{|\nabla T_{MD}|}{|\nabla T|} = k_{MD} \frac{\partial T_{MD}}{\partial T}. \quad (6)$$

When  $T_{MD}$  is at room temperature, 300K, the rescale rate ( $\alpha = \partial T_{MD} / \partial T$ )  $\alpha = 0.91$  for silicon, which gives a quite small quantum correction effect on thermal conductivity.

Figure 5 shows the thermal conductivity  $\kappa$  versus Ge content  $x$  at room temperature. The thermal conductivity of pure SiNW calculated is 3.18W/m-K. The lowest  $\kappa$  is 0.59W/m-K, which is 18% of that of pure SiNW. At the two ends of the curves, the thermal conductivity

shows a very sensitive dependence on  $x$  and follows an exponential decay, which is caused by the localization of high frequency phonons by the impurity. It is quite interesting that with only 5% Ge atoms ( $\text{Si}_{0.95}\text{Ge}_{0.05}$  NW), its thermal conductivity can be reduced 50%.

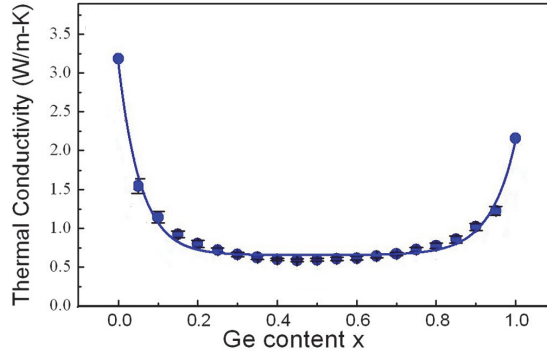


Fig. 5. The thermal conductivity  $\kappa$  versus  $x$  at  $T=300\text{K}$ . The blue circles are the average values of the simulation results, and the solid curve is the best fitting to the formula  $\kappa = A_1e^{-x/B_1} + A_2e^{-(1-x)/B_2} + C$ .

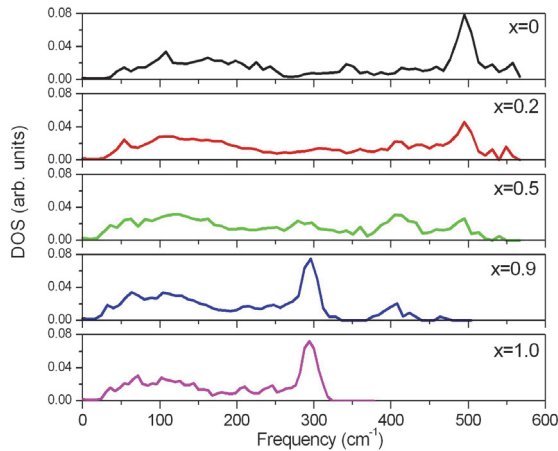


Fig. 6. The representative PDOS for  $\text{Si}_{1-x}\text{Ge}_x$  NWs with  $0 \leq x \leq 1$ .

To understand the compositional dependence of thermal conductivity, we show representative phonon density of states (PDOS) of the  $\text{Si}_{1-x}\text{Ge}_x$  NWs in Figure 6. There is significant difference between nano and bulk material in the PDOS, in particular in the high frequency regime. In bulk materials, the optical modes contribute little to heat flux. However, in nano scale system, optical phonon (high frequency) also plays a major contribution to heat flux. For both pure Si NW and pure Ge NW, a significant PDOS peak appears at high frequency range, indicating the main contribution of optical modes to heat flux. However, in the  $\text{Si}_{1-x}\text{Ge}_x$  NWs ( $0 < x < 1$ ), as the introduction of disorder scattering, the main PDOS peak at

high frequency range weakens and vanishes with the impurity concentration increasing. In contrast to the strong dependence of high frequency PDOS on  $x$ , the low frequency PDOS are almost independent on the composition change. This is consistent with the idea that in nano materials, the high frequency phonons are more sensitivity to the impurity than low frequency phonons (which have long wavelength) do, and the reduction in thermal conductivity mainly comes from the suppressing of high frequency modes. (Che et al., 2000)

#### 4. Effect of surface roughness on phonon transport

It is well known that the thermal conductivity of NW decreases with wire diameter. To calculate the diameter dependent thermal conductivity quantitatively, an analytical formula including the surface scattering and the size confinement effects of phonon transport is proposed by Liang and Li (Liang & B. Li, 2006) to describe the size dependence of thermal conductivity in NWs and other nanoscale structures. In their approach, the phonon-phonon interaction is assumed to increase with size reduction due to the confinement, which causes the decrease of heat conduction. On the other hand, as the size decreases and the surface-volume ratio increases, the large surface/interface scattering, corresponding to certain boundary conditions, has great influence on the transport. Considering the nonequilibrium phonon distribution due to boundary scattering, the effect of the surface roughness with the boundary scattering shows an exponential suppression in the distribution and the conduction. Then, the quantitative formula for the size-dependent thermal conductivity of SiNW is obtained (Liang & B. Li, 2006):

$$\frac{\kappa}{\kappa_b} = p \exp\left(-\frac{d_0}{D}\right) \left[ \exp\left(\frac{-(\alpha-1)}{D/\lambda-1}\right) \right]^{3/2} \quad (7)$$

Here  $\kappa$  is the thermal conductivity of SiNW,  $\kappa_b$  is the thermal conductivity of bulk silicon. The details about this formula can be found in (Liang & B. Li, 2006). This empirical formula gives a quantitative prediction for the size-dependent thermal conductivity. The larger value of  $p$  corresponds to the smaller roughness, thus the more probability of specular scattering. Thermal conductivity of Si nanowires from the experiments and the comparison with theoretical predictions from Eq. (7) with suitable parameters  $p$  are shown in Fig. 7. The predictions are in good agreements with the experimental results. (D. Li et al., 2003) It is obvious that the phonon thermal conductivity increases with diameter increases remarkably until the diameter is larger than about hundreds nms. This reflects the fact that scattering at the surface introduces diffuse phonon relaxation in the transverse cross section. After the diameter reaches large values, the portion of phonons experiencing boundary scattering becomes much smaller, as a result, the thermal conductivity tends to be constant and is close to the value of bulk silicon. For Si nanowires with diameter of 20-100 nm,  $p=0.4$ , reflecting the larger surface roughness of the nanowires in the sample fabrication. This is consistent with the experimental image. (Hochbaum et al., 2008)

Donadio and Galli (Donadio & Galli, 2009) also studied heat transport in SiNWs systematically, by using molecular dynamics simulation, lattice dynamics, and Boltzmann transport equation calculations. It was demonstrated that the disordered surfaces, nonpropagating modes analogous to heat carriers, together with decreased lifetimes of propagating modes are responsible for the reduction of thermal conductivity in SiNWs.

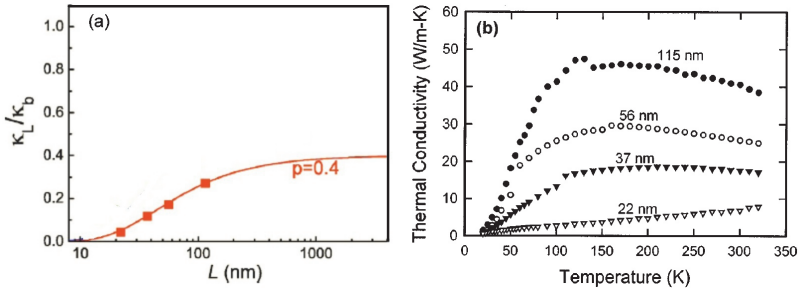


Fig. 7. Size-dependent thermal conductivity of Si nanowires.(a) Comparison of thermal conductivity between theoretical prediction and experimental measurements. The curve is prediction from Eq. 7 and the symbols are experimental results from(D. Li et al., 2003). (b) The experimental temperature dependent thermal conductivity from (D. Li et al., 2003).

### 5. Reduction of thermal conductivity by surface scattering

Very recently, another mechanism to reduce thermal conductivity by introducing more surface scattering: making SiNWs hollow to create inner surface, i.e. silicon nanotubes (SiNTs) was proposed. (J. Chen et al., 2010) Fig. 8 shows the thermal conductivity of SiNWs and SiNTs versus cross section area at 300K. It is interesting to find that even with a very small hole, the thermal conductivity decreases obviously, from  $\kappa_{NW}=12.2\pm 1.4$  W/mK to  $\kappa_{NT}=8.0\pm 1.1$  W/mK. In this case, only a 1% reduction in cross section area induces the reduction of thermal conductivity of 35%. Moreover, with increasing of size of the hole, a linear dependence of thermal conductivity on cross section area is observed. It is clear that for SiNW, thermal conductivity decreases with cross section area decreases. This is because with the increase of size, more and more phonons are excited, which results in the increase of thermal conductivity. So the decrease of cross section area is one origin for the low thermal conductivity of SiNT but not the sole one. We can see that with the same cross section area, thermal conductivity of SiNTs is only about 33% of that of SiNWs. This additional reduction is due to the localization of phonon states on the surface.

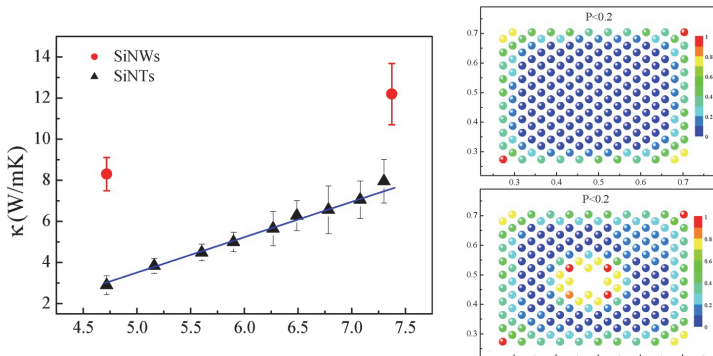


Fig. 8. Left: Thermal conductivity of SiNWs and SiNTs versus cross section area at 300K. Right: Normalized energy distribution on the cross section plane for SiNWs and SiNTs. Here are energy distribution for modes with  $P < 0.2$ .

To understand the underlying physical mechanism of thermal conductivity reduction in SiNTs, a vibrational eigen-mode analysis on SiNWs and SiNTs was carried out. Mode localization can be quantitatively characterized by the participation ratio  $P_\lambda$  which measures the fraction of atoms participating in a given mode, and effectively indicates the localized modes with  $O(1/N)$  and delocalized modes with  $O(1)$ . Fig. 8 shows the normalized energy distribution on the cross section plane for SiNWs and SiNTs at 300K. The positions of the circles denote different locations on plane. For those localized modes with p-ratio less than 0.2, it is clearly shown that the intensity of localized modes is almost zero in the centre of NW, while with finite value at the boundary. This demonstrates that the localization modes in SiNWs are distributed on the boundary of cross section plane, which corresponds to the outer surface of SiNWs. In addition, due to inner-surface introduced in SiNTs, energy localization also shows up around the hollow region. These results provide direct numerical evidence that localization takes place on the surface region.

Compared with SiNWs, SiNTs have a larger surface area, which corresponds to a higher SVR. As a result, there are more modes localized on the surface, which increases the percentage of the localized modes to the total number of modes. In heat transport, the contribution to thermal conductivity mainly comes from the delocalized modes rather than the localized modes. Due to the enhanced SVR in SiNTs which induces more localized modes, the percentage of delocalized modes decreases, leads to a reduction of thermal conductivity in SiNTs compared with SiNWs. Very recently, the similar SiNT structures have been fabricated experimentally by reductive decomposition of a silicon precursor in an alumina template and etching (Park et al., 2009). Thus SiNTs is a promising thermoelectric material by using reliable fabrication technology.

## 6. Thermoelectric property of SiNWs

From above sections, it is well established that reduction of thermal conductivity, such as by isotopic doping, is an efficient way to increase the figure of merit  $ZT$ .  $ZT$  depends on both the phonon and electron transport properties. Thus to maximize the performance of SiNW thermoelectric cooler, it is indispensable to have a comprehensive understanding of the above factors. In this section, we will discuss systematically the impacts of size, isotope concentration and alloy effect on thermoelectric property of SiNW.

By using the density functional derived tight-binding method (DFTB), Shi et al. (L. Shi et al., 2009) have studied the size effect on thermoelectric power factor. The DFTB has high computational efficiency and allows the simulation of bigger systems than conventional density functional theory (DFT) at a reasonable computational time and with similar accuracy. Here the cross section area is ranging from  $1 \text{ nm}^2$  to about  $18 \text{ nm}^2$ . The corresponding diameter  $D$  is from 1.7 to 6.1 nm.

It has been shown that electron transport is diffusive in SiNWs longer than 1.4 nm. (Gilbert et al., 2005) Therefore,  $\sigma$ ,  $S$  and  $\kappa_e$  are evaluated by only elastic scattering processes. The electrical conductivity  $\sigma$ , the electron thermal conductivity  $\kappa_e$ , and the Seebeck coefficient  $S$ , are obtained from the electronic structure with the solution of 1-Dimensional Boltzmann transport equation as:

$$\begin{aligned}\sigma &= \Lambda^{(0)} \\ \kappa_e &= \frac{1}{e^2 T} [\Lambda^{(2)} - \Lambda^{(1)} (\Lambda^{(0)})^{-1} \Lambda^{(1)}] \\ S &= \frac{1}{e T} (\Lambda^{(0)})^{-1} \Lambda^{(1)} \\ A^{(n)} &= e^2 \tau \frac{2}{m^*} \sum_{E_k} \Delta E \left[ \frac{\beta \exp(\beta(E_k - \mu))}{(1 + \exp(\beta(E_k - \mu)))^2} \right] D(E_k) E_k (E_k - \mu)^n\end{aligned}\quad (8)$$

Here  $e$  is the charge of carriers,  $T$  is the temperature,  $E_k$  is the electron energy,  $\tau$  is the relaxation time,  $m^*$  is the effective mass of the charge carrier,  $\mu$  is the electron chemical potential and  $D(E_k)$  is the density of states. The relaxation time  $\tau$ , is obtained by fitting the calculated mobility to measured electrical conductivity data of SiNW.

The carrier concentration is defined as:

$$n = \int D(E - \mu) \times f(E - \mu) \times dE, \quad (9)$$

where  $f(E)$  is the Fermi distribution function. In this model,  $n$  corresponds to the concentration of charge in a system that is artificially doped by varying the chemical potential while assuming a fixed band structure. With the change in  $\mu$ , the carrier concentration changes, and induces the corresponding modification in thermoelectric property.

Figure 9(a) and 9(b) show the size effects on  $\sigma$  and  $S$  with different electron concentration. The size dependence arises from quantum confinement effect on the electronic band structure of SiNWs. It is obvious that the larger the dimension of the wire the smaller the band gap due to quantum confinement. In contrast to the weak size dependence of electronic conductivity, Seebeck coefficient  $S$  decreases with increasing of size remarkably.

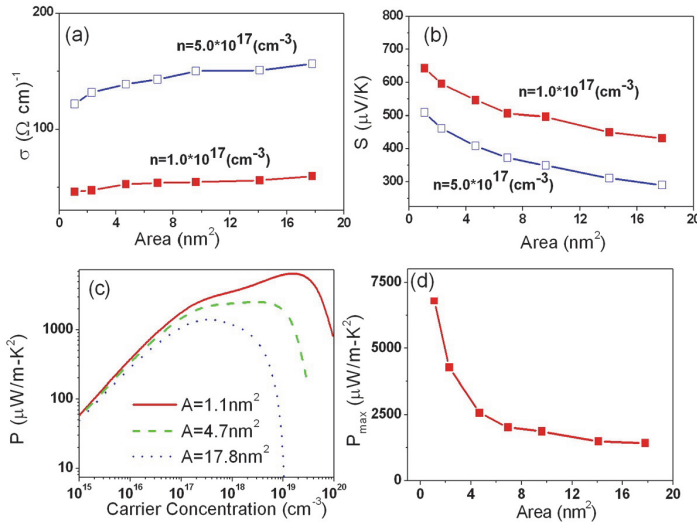


Fig. 9. (a) and (b) Electrical conductivity and  $S$  vs cross sectional area with different carrier concentration. (c) Thermal power factor of SiNW vs carrier concentration. (d) Maximum power factor vs cross sectional area.

Besides the electronic band gap, Seebeck coefficient  $S$  also depends on the detailed band structure, in which narrow DOS distribution is preferred. (R. Y. Wang et al., 2008) In a bulk material, the continue electron energy levels give a wide distribution of carrier energies. However, the DOS of SiNW differs dramatically from that of bulk silicon. The large numbers of electronic states in narrow energy ranges can lead to large  $S$ . With the transverse dimension increases, the sharp DOS peaks widen and reduces  $S$ . The increase in transverse dimension has two effects on band structure: reduce the band gap; and widen the sharp DOS peaks, both have negative impacts on Seebeck coefficient. So the Seebeck coefficient decreases quickly with transverse size increasing.

In thermoelectric application, the power factor  $P$ , which is defined as  $P = S^2\sigma$ , is an important factor influencing the thermoelectric performance directly. Figure 9 (c) shows the power factor versus carrier concentration for SiNWs with different cross sectional areas. The power factor increases with carrier concentration increases, and there is an optimal carrier concentration  $N_{Max}$  yielding the maximum attainable value of  $P_{Max}$ . Above  $N_{Max}$ , the power factor decreases with increasing carrier concentration. This phenomenon can be understood as below. Increasing carrier concentration has two effects on power factor. On the one hand, the increase of carrier concentration will increase the electrical conductivity. On the other hand, the increase of carrier concentration will suppress the Seebeck coefficient  $S$ . The power factor is determined by these two effects that compete with each other. Therefore, there exists an optimal carrier concentration  $N_{Max}$ . With SiNW diameter increases, the maximum attainable power factor  $P_{Max}$  decreases (as shown in figure 9(c)), due to the slow increase of  $\sigma$  is offset by obvious decreasing in  $S$  ( $P \sim S^2$ ). Figure 9 (d) shows the maximum power factor  $P_{Max}$  versus the cross section area of SiNWs. With the area increases from about 1 nm<sup>2</sup> to 18 nm<sup>2</sup>, the maximum power factor decreases from about 6800 to 1400  $\mu\text{W}/\text{m}\cdot\text{K}^2$ . At small size, the small increases of cross section area can induce large reduction on power factor. For example, with the cross section area increases from 1.1 to 4.7 nm<sup>2</sup>, the power factor decreases with about 4300  $\mu\text{W}/\text{m}\cdot\text{K}^2$ . In contrast to the high sensitivity at the small size range, the power factor versus cross section area curves are almost flat at the large wire range, where the power factor is almost constant when cross section area increases from 14.1 to 17.8 nm<sup>2</sup>.

In the calculation of  $ZT$ , both electron and phonon contribute to the total thermal conductivity. It is clear that electron thermal conductivity increases with diameter as it is proportional to electronic conductivity. For SiNWs with length in  $\mu\text{m}$  scale, the phonon thermal conductivity increases with diameter increases remarkably until the diameter is larger than about hundreds nms. (Liang & B. Li, 2006) As both the electron and phonon contributions to thermal conductivity increase as transverse size increasing, it is obvious that the total thermal conductivity increases with transverse dimension. Combine the size dependence of the power factor as shown in figure 9(d), we can conclude that  $ZT$  will decrease when the NW diameter increases.

As we discussed above, the isotope doping is an important method to modulate the thermal conductivity of nano materials. Now we focus on the isotope doping effect on  $ZT$  of SiNW ( $^{28}\text{Si}_{1-x}\text{Si}_x$  NWs) with fixed cross section area of 2.3 nm<sup>2</sup>. Here we use the phonon thermal conductivity value calculated in (Yang et al., 2008) with cross section area of 2.6 nm<sup>2</sup>. It is obvious that within the moderate carrier concentration, the thermal conductivity from phonons is much larger than that from electrons. Using the calculated  $S$ ,  $\sigma$ , electron thermal conductivity and the phonon thermal conductivity, the dependence of maximum attainable

value of  $ZT_{Max}$  on doping concentration is shown in figure 10(a). The  $ZT_{Max}$  values increase with  $^{29}\text{Si}$  concentration, reach a maximum and then decreases. This phenomenon is from the isotope doping effect on lattice thermal conductivity. (Yang et al., 2008) At low isotopic percentage, the small ratio of isotope atoms can induce large increase in  $ZT_{Max}$ . For instance, in the case of  $^{28}\text{Si}_{0.8}^{29}\text{Si}_{0.2}$  NW, its  $ZT_{Max}$  increases with 15% from that of pure  $^{28}\text{Si}$  NW. And with 50%  $^{29}\text{Si}$  doping, the  $ZT_{Max}$  can increase with 31%.

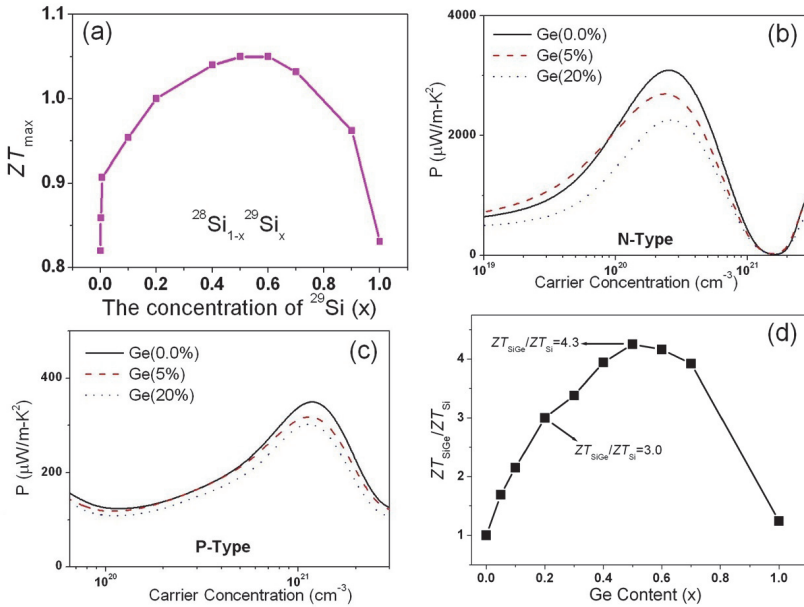


Fig. 10. (a)  $ZT_{Max}$  vs the concentration of  $^{29}\text{Si}$  atom. Thermal power factors of  $\text{Si}_{1-x}\text{Ge}_x$  NWs versus carrier concentration for n-type wires (b) and p-type wires (c). (d)  $ZT_{\text{SiGe}}/ZT_{\text{Si}}$  versus the Ge content  $x$  for n-type  $\text{Si}_{1-x}\text{Ge}_x$  wires.

Besides SiNW, it has also been demonstrated that  $\text{Si}_{1-x}\text{Ge}_x$  NW is a promising candidate for high-performance thermoelectric application since its thermal conductivity can be tuned by the Ge contents (J. Chen et al., 2009). It has been observed experimentally that when the Ge content in the  $\text{Si}_{1-x}\text{Ge}_x$  nanocomposites increases from 5% to 20%, the thermal conductivity decreases obviously. (G. H. Zhu et al., 2009) However, at the same time, the power factor also decreases, and induces uncertainty in the change of figure of merit  $ZT$ . The composition dependence of the thermoelectric properties in  $\text{Si}_{1-x}\text{Ge}_x$  NWs have been investigated systematically by Shi et al. (L. Shi et al. 2010) Figure 10 (b) and Figure 10(c) show the power factor versus carrier concentration for n-type and p-type wires. The power factor of p-type wire is much smaller (only about 15%) than that in its n-type counterpart because of the reduced charge mobility in p-type wires. As different doping (p-type or n-type) only have various changes on the electronic property, but the same impact on the lattice vibration, so the phonon thermal conductivity of p-type nanowire should be close to that of n-type wire. Combine the calculated power factor, it is obvious that  $ZT$  of n-type wire is about 6-7 times

of that of p-type nanowire. In the next, we only show the Ge content dependent  $ZT$  of n-type NW. Using the calculated  $S$ , and  $\sigma$  and the relative phonon thermal conductivity ( $k_{SiGe}/k_{Si}$ , here  $k_{Si}$  and  $k_{SiGe}$  are thermal conductivities of SiNW and  $Si_{1-x}Ge_x$  NW, respectively) calculated by using molecular dynamics method from (J. Chen et al., 2009), the dependence of  $ZT_{Si_{1-x}Ge_x}/ZT_{Si}$  on Ge content  $x$  is shown in figure 10(d). The  $ZT_{Si_{1-x}Ge_x}/ZT_{Si}$  values increase with Ge content, reach a maximum and then decreases. It is worth pointing out that the calculated  $ZT$  of pure Ge NW is only 1.3 times of that of pure SiNW, which is far less than the 9-fold increase in the respective bulk materials. The remarkable difference in the increased factor of  $ZT$  between the respective bulk and nanowires is due to the similarity of the thermal conductivity and electronic property in the nano scale. Moreover, at low Ge content, the small ratio of Ge atoms can induce large increase in  $ZT$ . For instance, in the case of  $Si_{0.8}Ge_{0.2}$  NW, namely, 20% Ge,  $ZT_{Si_{1-x}Ge_x}/ZT_{Si}$  is about 3. And with 50% Ge atoms ( $Si_{0.5}Ge_{0.5}$  NW), the  $ZT_{Si_{1-x}Ge_x}/ZT_{Si}$  can be as high as 4.3. Combine with the experimental measured  $ZT$  of n-type SiNW which is about 0.6-1.0, it is exciting that we may obtain high  $ZT$  value of about 2.5-4.0 in n-type  $Si_{1-x}Ge_x$  NW.

## 7. Realization of SiNW based on-chip coolers

Typical integrated circuit (IC) chips have millions or even billions of transistors, which can generate huge heat fluxes in very small areas which is called as hot-spot. The hot spot removal is a key for future generations of IC chips. Circulated liquid cooling is one of current available cooling technologies, which moves heat sink away from the processors by increasing the surface area. However, reliability is a big concern if the liquid hose is leaking. Moreover, this and other conventional cooling techniques are used to cool the whole package temperature and none of them addresses the hot spots cooling. The hot spots in microprocessors are normally in the order of 300-400  $\mu\text{m}$  in diameter, thus even the smallest commercial cooling module is still too large for spot cooling. In addition, as the three-dimensional (3D) chips are investigated, this can create smaller and hotter spots. The current cooling technologies are fast reaching their limits. High efficiency and nano scale cooler is a key enabler to remove small hot spots in IC chips and for the future improvements of IC thermal management. To solve the hot spot issue, one way is to use thermoelectric (TE) materials to cool the hot spot. In above of this chapter, we have discussed the thermal and thermoelectric properties of NWs. A natural question comes promptly: if a cooler is built from SiNW, then how cool we can achieve? And what are the cooling power and efficiency? In this section, we will show the answers to these questions.

By using finite element simulation, Zhang et al. (G. Zhang et al., 2009a) studied the the cooling temperature, cooling power density and coefficient of performance of SiNW based on-chip cooler. The size of SiNW is 50 nm  $\times$  50 nm  $\times$  2.5  $\mu\text{m}$ . Upon electrical current flow through, electrons absorb thermal energy from lattice at one junction and transport it to another junction (Peltier effect), creating a cold and hot side. Here the assumed hot spot is in contact with the cold side and the hot side is fixed at 300 K. Besides this positive cooling effect, the back-flow of heat from hot end to cold end and Joule heat will weaken the cooling efficiency. So heat flux is the sum of Seebeck (Peltier) effect, Fourier effects, and the Joule heat. For SiNW with 50 nm diameter, 20 W/m-K is observed for vapour-liquid-solid grown SiNW (VLS-SiNWs), while 1.6 W/m-K is found for aqueous electroless-etching grown wire (EE-SiNWs). (Hochbaum et al., 2008) The large

discrepancy in thermal conductivity lies from the surface scattering of phonons. Both thermal conductivity values are used to explore the importance of thermal conductivity on thermoelectric performance. Natural convection and radiation as the heat transfer mechanism between the system and the surrounding air are established. The surrounding environment is assumed to be stationary air at atmospheric pressure. From the finite element simulation, it was found that for nanoscale systems such as SiNWs, the contribution of natural convection and radiation are very low in the total heat transfer, while thermal conduction is the major contribution. (G. Zhang et al., 2009a)

Figure 11(a) shows the cooling temperature versus electrical current. For both EE-wire and VLS-wire, the cooling temperature increases with supplied current increases, and there is a maximum at about  $I_M=3.5-4.0 \mu\text{A}$ . Above  $I_M$ , cooling temperature decreases with increasing current. This phenomenon can be understood as below. Increasing electrical current has two effects on cooling. On the one hand, the increase of electrical current will absorb more thermal energy from one end and transport it to another end. We call this effect the "positive" effect. On the other hand, the increase of electrical current will also increase Joule heating that in turn will increase the heat flux to the cool end, thus suppress cooling. We call it the "negative" effect. The cooling temperature is determined by these two effects that compete with each other. And as demonstrated in Figure 11(a), the maximum cooling temperature of EE-wire is much larger than that of VLS-wire, although they are with the same dependence characteristic on electrical current.

In the cooling temperature analysis above, the hot spot is a non-source device. If the device (hot spot) generates heat, the maximum cooling temperature will depend on the dissipation power, and we can predict the maximum cooling power that SiNW cooler can arrive. Fig. 11(b) shows the relation between the cooling temperature with the power dissipation density from the device for both EE- and VLS-SiNWs with electrical current of  $4 \mu\text{A}$ . The maximum cooling power is defined as the heat load power that makes the device's maximum cooling temperature equal to zero. The maximum cooling power density is about  $6.6 \times 10^3 \text{ W/cm}^2$  here, and is independent on the special thermal conductivity. The independence of maximum cooling power density on thermal conductivity is due to the maximum cooling power is arrived when the temperature difference between the two ends is zero and no Fourier heat flux. The maximum cooling power density,  $6.6 \times 10^3 \text{ W/cm}^2$  for SiNW, is about six times larger than that of SiGeC/Si superlattice coolers (X. Fan et al., 2001), ten times larger than that of Si/Si<sub>x</sub>Ge<sub>1-x</sub> thin film cooler (Y. Zhang et al., 2006), and six hundred times larger than that of commercial TE module. (Rowe 2006)

The performance of any thermoelectric material is in general expressed by its coefficient of performance (COP). This is defined as the actual cooling power divided by the total rate at which electrical energy is supplied. The electrical power consumption of SiNW cooler is used to generate the Joule heat and overcome the Seebeck effect, which generates power due to the temperature difference between the two junctions of the wire. However, the maximum cooling power is the heat load power that makes the device's maximum cooling temperature equal to zero, so here the electrical power consumption is equal to the Joule heat. From Figure. 11, we can obtain the COP for both EE and VLS nanowires are 61%. This is larger than that of Si/Si<sub>x</sub>Ge<sub>1-x</sub> thin film cooler (Y. Zhang et al., 2006) which is 36%, and larger than that of commercial TE module which is only 0.1%. (Rowe 2006)

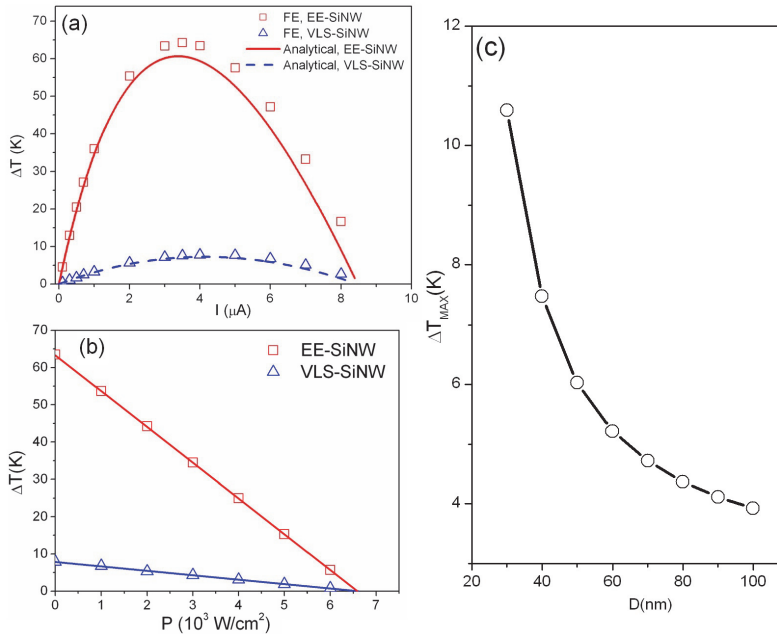


Fig. 11. (a) Dependences of cooling temperature on thermal conductivity and applied electrical current. (b) Cooling temperature versus heat load power density. (c) Maximum cooling temperature vs diameter of SiNW.

From the analytical expression of cooling temperature, we can provide a prediction of the transverse size effect on the cooling temperature. For SiNWs with length in  $\mu\text{m}$  scale, the thermal conductivity increases with diameter increases remarkably until the diameter is larger than about hundreds nm. (Liang and B. Li, 2006) Using the quantitative formula for the size-dependent thermal conductivity from Eq. 7, Figure 11(c) shows the maximum cooling temperature vs diameters of SiNWs. It is obvious that cooling temperature decreases as diameter increases. When the diameter increases to 100 nm, the maximum cooling temperature is only about 4K. So to keep high cooling temperature, SiNW with small diameter is preferred.

In the following, we will discuss time dependent cooling performance of SiNWs, (G. Zhang et al., 2009b) including the cooling response time, and the impact of number of SiNWs in the bundle. Figure 12(a) shows the time dependent temperature of the hot spot. Upon current flow through the SiNW, the temperature of the island decreases exponentially initially and then converges to a constant temperature  $T_C$  which is much lower than the environment temperature  $T_0$ . The cooling temperature  $\Delta T = T_0 - T_C$ . From the best fitting of the time dependent temperature curves, the cooling response time  $t_0$  can be calculated. Figure 12(b) shows that  $t_0$  decreases as applied electrical current increases monotonously. From Figure 12 (a), the maximum cooling temperature can be achieved with about 3-4  $\mu\text{A}$  electrical current, which corresponds to 0.05-0.06 s response time. This demonstrates that SiNW is a fast response cooler.

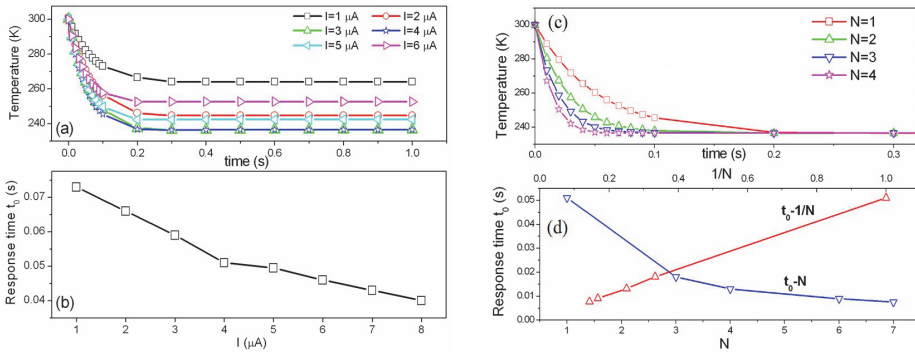


Fig. 12. (a) Time dependent temperature of the hot spot for different applied electrical current. (b) Dependences of cooling response time on applied electrical current. (c) The time dependent temperature for different number of SiNWs  $N$ . (d) The cooling response time  $t_0$  for different number of SiNWs  $N$ . Here the electrical current is  $4 \mu\text{A}$ .

In practical application, a bundle of SiNWs will be used, which can be realized by top-down method on SOI wafers. Figure 12 (c) shows the time dependent temperature of the silicon island with a number of SiNWs  $N$  ( $>1$ ). With increase in  $N$ , the cooling process becomes faster. However, the maximum  $\Delta T$  does not change with  $N$ . Figure 12 (d) shows the  $N$  dependent response time. It is obvious that in practical applications, increasing of  $N$  is an efficient approach to speed the cooling process.

## 8. Conclusions

The present article tries to give an overview of the thermal and thermoelectric property of semiconducting nanowires. Here we use Silicon nanowires as examples, however, the physics addressed in this article is not limited to silicon system. The thermal transport in low dimensional system has attracted wide research interests in last decade. Silicon Nanowires are promising platforms to verify fundamental phonon transport theories. Moreover, the study of thermal property of SiNWs is also important for potential application, such as waste heat energy harvesting and on-chip cooling. Compared with ten years ago, we have a comprehensive understanding of the impacts of doping, surface scattering and alloy effect on thermal conductance and thermoelectric property of nanowires. However, further experimental and theoretical studies on fundamental mechanism will be greatly helpful to advance the field.

## 9. Acknowledgment

The authors wish to thank Prof. Baowen Li, Dr. Nuo Yang, Dr. Jie Chen and Dr. Lihong Shi for long time collaboration and support. And acknowledge the support by the Ministry of Science and Technology of China (Grant Nos. 2011CB933001).

## 10. References

Berber, S.; Kwon, Y.-K. & Tománek, D. (2000) Unusually High Thermal Conductivity of Carbon Nanotubes. *Phys. Rev. Lett.*, Vol. 84, No. 20 (May 2000) pp.4613.

- Boukai, A. I.; Bunimovich, Y.; Kheli, J. T.; Yu, J.-K.; Goddard III, W. A. & Heath, J. R. (2008) Silicon nanowires as efficient thermoelectric materials. *Nature*, Vol. 451, No.7175, (January 2008), pp. 168-172.
- Bourgeois, O.; Fourniew, T. & Chaussy, J. (2007), Measurement of the thermal conductance of silicon nanowires at low temperature. *Journal of Applied Physics*, Vol. 101, No. 1 (January 2007) pp. 016104-016106.
- Cahill, D. G.; Ford, W. K.; Goodson, K. E. *et al.* (2002) Nanoscale thermal transport, *J. Appl. Phys.*, Vol. 93, No. 2, (August 2002), pp. 793-818.
- Che, J.; Cagin, Tahir; Deng, W. & Goddard III, W.A. (2000) Thermal conductivity of diamond and related materials from molecular dynamics simulations, *J. Chemical Physics*, Vol. 113, No. 16 (July 2000) pp.6888-6900.
- Chen, J.; Zhang, G. & Li, B., (2009), Tunable Thermal Conductivity of Si<sub>1-x</sub>Ge<sub>x</sub> Nanowires, *Appl. Phys. Lett.* Vol. 95, No. 7 (August 2009), pp. 073117.
- Cui, Y.; Wei, Q.; Park, H. & Lieber, C. M. (2001) Nanowire Nanosensors for Highly Sensitive and Selective Detection of Biological and Chemical Species, *Science*, Vol. 293, (August 2001), pp. 1289-1292.
- Donadio, D. & G. Galli, (2009) Atomistic Simulations of Heat Transport in Silicon Nanowires, *Phys. Rev. Lett.*, Vol. 102, No. 19 (May 2009) pp. 195901.
- Fan, X.; Zeng, G.; Labounty, C.; Bowers, J. E.; Croke, E.; Ahn, C. C.; Huxtable, S.; Majumdar, A. & Shakouri, A. (2001) SiGeC/Si superlattice microcoolers, *Appl. Phys. Lett.* Vol. 78, No. 11 (January 2001) pp. 1580.
- Gilbert, M. J.; Akis, R. & Ferry, D. K. (2005), Phonon-assisted ballistic to diffusive crossover in silicon nanowire transistors, *J. Appl. Phys.*, Vol. 98, No. 9, (November 2005) pp. 094303-094310.
- Hochbaum, A. I.; Chen, R.; Delgado, R. D.; Liang, W.; Garnett, E. C.; Najarian, M.; Majumdar, A. & Yang, P. (2008) Enhanced thermoelectric performance of rough silicon nanowires, *Nature*, Vol. 451, No. 7175, (January 2008), pp. 163-168.
- Iijima, S. (1991) Helical microtubules of graphitic carbon. *Nature* Vol. 354, No. 6345 (November 1991) pp. 56 - 58.
- Kim, P.; Shi, L.; Majumdar, A. & McEuen, P. L. (2001) Thermal Transport Measurements of Individual Multiwalled Nanotubes. *Phys. Rev. Lett.*, Vol. 87, No. 21 (October 2001), pp. 215502.
- Li, B. & Wang, J. (2003), Anomalous Heat Conduction and Anomalous Diffusion in One-Dimensional Systems, *Phys. Rev. Lett.* Vol. 91, No. 4 (July 2003) pp. 044301.
- Li, B.; Wang, J.; Wang, L. & Zhang, G. (2005) Anomalous heat conduction and anomalous diffusion in nonlinear lattices, single wall nanotubes, and billiard gas channels. *Chaos*, Vol. 15, No. 1, (April, 2005), pp. 015121
- Li, D.; Wu, Y.; Kim, P.; Shi, L.; Yang, P. & Majumdar, A. (2003) Thermal conductivity of individual silicon nanowires, *Appl. Phys. Lett.*, Vol.83, No. 14 (August 2003) pp. 2934.
- Li, J.; Yu, H.; Wong, S.; Li, X.; Zhang, G.; Lo, G-Q & Kwong, D.-L., (2009) Design guidelines of periodic Si nanowire arrays for solar cell application. *Appl. Phys. Lett.*, Vol. 95, No. 24 (December 2009) pp. 243113.
- Liang, L. H. & Li, B. (2006) Size-dependent thermal conductivity of nanoscale semiconducting systems, *Phys. Rev. B*, Vol. 73, No. 15, (April 2006) pp. 153303.

- Maruyama, S. (2002) A Molecular Dynamics Simulation of Heat Conduction of Finite Length SWNTs, *Physica B*, Vol. 323, No. 1-4 (October 2002), pp. 193-195.
- Moutanabbir, O.; Senz, S.; Zhang, Z. & Gösele, Ulrich (2009), Synthesis of isotopically controlled metal-catalyzed silicon nanowires. *Nano Today*, Vol. 4, No. 5 (August 2009), pp. 393-398.
- Park, M.; Kim, M.; Joo, J.; Kim, K.; Kim, J.; Ahn, S.; Cui, Y. & Cho, J. (2009) Silicon Nanotube Battery Anodes, *Nano Lett.*, Vol. 9, No. 11 (November 2009) pp. 3844-3847.
- Rowe, D. M. (2006). *Thermoelectrics Handbook Macro to Nano*, Taylor & Francis Group, France.
- Shi, L.; Yao, D.; Zhang, G. & Li, B. (2009) Size Dependent Thermoelectric Properties of Silicon Nanowires, *Appl. Phys. Lett.*, Vol. 95, No. 6 (August 2009) pp. 063102.
- Shi, L.; Yao, D.; Zhang, G. & Li, B. (2010) Large Thermoelectric Figure of Merit In  $\text{Si}_{1-x}\text{Ge}_x$  Nanowires, *Appl. Phys. Lett.*, Vol. 96, No. 17 (April 2010) pp. 173108.
- Stillinger, F. H. & Weber, T. A. (1985) Computer simulation of local order in condensed phases of silicon. *Phys. Rev. B*, Vol. 31, No. 8, (April 1985) pp. 5262-5271.
- Volz, S. G. & Chen, G., (1999) Molecular dynamics simulation of thermal conductivity of silicon nanowires, *Appl. Phys. Lett.*, Vol. 75, No. 14 (August 1999) pp. 2056.
- Volz, S. G. & Chen, G. (2000), Molecular-dynamics simulation of thermal conductivity of silicon crystals, *Phys. Rev. B*, Vol. 61, No. 4 (January 2000) pp. 2651-2656.
- Wang, R. Y.; Feser, J. P.; Lee, J-S; Talapin, D. V.; Segalman, R. & Mujumdar, A. (2008) Enhanced Thermopower in PbSe Nanocrystal Quantum Dot Superlattices, *Nano Lett.*, Vol. 8, No. 8 (August 2008) pp. 2283-2288.
- Wang, X.; Shakouri, A.; Yu, B.; Sun, X. & Meyyappan, M. (2007) Study of phonon modes in germanium nanowires, *Journal of Applied Physics*, Vol. 102, No. 1 (July 2007), pp. 014304-014309.
- Xiang, J.; Lu, W.; Hu, Y.; Wu, Y.; Yan, H. & Lieber, C. M. (2006), Ge/Si nanowire heterostructures as high-performance field-effect transistors. *Nature*, Vol. 441, No. 7092, (May, 2006) pp. 489-494.
- Yamamoto, T.; Watanabe, S. & Watanabe, K. (2004), Universal Features of Quantized Thermal Conductance of Carbon Nanotubes. *Phys. Rev. Lett.*, Vol. 92, No. 7 (February 2004), pp. 075502.
- Yang, J-E.; Jin, C-B.; Kim, C-J. & Jo, M-H. (2006), Band-Gap Modulation in Single-Crystalline  $\text{Si}_{1-x}\text{Ge}_x$  Nanowires, *Nano Lett.*, Vol. 6, No. 12 (December 2006) pp. 2679-2684.
- Yang, N.; Zhang, G. & Li, B. (2008), Ultralow Thermal Conductivity of Isotope-Doped Silicon Nanowires. *Nano Letters*, Vol. 8, No. 1 (January, 2008) pp. 276-280.
- Yang, N.; Zhang, G. & Li, B. (2010), Violation of Fourier's Law and Anomalous Heat Diffusion in Silicon Nanowires. *Nano Today*, Vol. 5, No. 2 (March 2010) pp. 85-90.
- Zhang, G. & Li, B. (2005) Thermal conductivity of nanotubes revisited: Effects of chirality, isotope impurity, tube length, and temperature. *J. Chem. Phys.*, Vol. 123, No. 114714. (September 2005), pp. 114714.
- Zhang, G.; Zhang, Q. X.; Bui, C.-T.; Lo, G.-Q. & Li, B. (2009) Thermoelectric Performance of Silicon Nanowires, *Appl. Phys. Lett.*, Vol. 94, No. 21 (May 2009) pp. 213108.
- Zhang, G.; Zhang, Q.-X.; Kavitha, D. & Lo, G.-Q. (2009) Time Dependent Thermoelectric Performance of A Bundle of Silicon Nanowires For On-Chip Cooler Applications, *Appl. Phys. Lett.*, Vol. 95, No. 24, (December 2009) pp. 243104.
- Zhang, G. & Li, B. (2010), Impacts of Doping On Thermal And Thermoelectric Properties of Nanomaterials. *NanoScale*, Vol. 2, No. 7 (July 2010), pp. 1058-1068.

- Zhang, Y.; Christofferson, J.; Shakouri, A.; Zeng, G.; Bowers, J. E. & Croke, E. T. (2006) On-chip high speed localized cooling using superlattice microrefrigerators, *IEEE Transactions on Components and Packaging Technologies*, Vol. 29, No. 2, (June 2006). pp. 395-401.
- Zhu, G. H.; Lee, H.; Lan, Y.C.; Wang, X.W.; Joshi, G.; Wang, D.Z.; Yang, J.; Vashaee, D.; Guilbert, H.; Pillitteri, A.; Dresselhaus, M.S.; Chen, G. & Ren, Z.F. (2009) Increased Phonon Scattering by Nanograins and Point Defects in Nanostructured Silicon with a Low Concentration of Germanium. *Phys. Rev. Lett.*, Vol. 102, No. 19 (May 2009) pp. 196803.

# Silicide Nanowires from Coordination Compound Precursors

John Philip  
*The Catholic University of America*  
USA

## 1. Introduction

In the last two decades there has been a great interest in the synthesis and characterization of one-dimensional materials. A variety of inorganic materials have been prepared in the form of nanowires and nanobelts with a diameter of a few nanometer and lengths going up to several hundreds of microns (Xia et al., 2003). The two main techniques used for nanowire growth are vapor-assisted (Wagner, 1964) and solution-based growth (Stejny, 1981; Stejny, 1979; Kruyt & Arkel, 1923; Gates et al., 2002; Mayers & Xia, 2002; Messer et al., 2000; Song et al., 2001) processes. Nanowires, nanorods and nanobelts constitute an important class of 1D nanostructures, which provide models to study the relationship between electrical transport, optical, magnetic and combined properties such as electro-optic and magneto-electronic properties with dimensionality and size confinement.

In recent decades strong interest has been drawn to explore silicides (Murarka, 1983; Miglio & d'Heurle, 2000), which are chemical compounds of silicon with different metals. Considerable amount of studies are carried out on transition metal silicides such as  $\text{CoSi}_2$ ,  $\text{NiSi}$ ,  $\text{MnSi}$ ,  $\text{CrSi}_2$ ,  $\text{FeSi}$  (Maex & Rossum, 1995). The magnetic properties of  $\text{MnSi}$  and  $\text{FeSi}$  are studied extensively.  $\text{MnSi}$  has a helical spin structure at low fields below 29 K and it is paramagnetic above that temperature (Ishikawa et al., 1976; Belitz, 1999).  $\text{CrSi}$  and  $\text{NiSi}$  are either weakly paramagnetic or diamagnetic. The transition-metal monosilicides such as  $\text{MnSi}$ ,  $\text{CoSi}$  and  $\text{FeSi}$  are a group of highly correlated electron materials (Aeppli & DiTusa, 1999; Riseborough, 2000). In the case of  $\text{MnSi}$ , application of external magnetic fields results in field-induced phase transitions from the helimagnetic phase to a conical spin structure at low fields and then to a ferromagnetic state at higher magnetic fields (Ishikawa et al., 1976; Belitz, 1999). The temperature dependence of high field magnetization of field-induced ferromagnetic states of  $\text{MnSi}$  shows signatures indicating the role of both spin wave excitations and stoner band excitations related to itinerant electron ferromagnetism (Aeppli & DiTusa, 1999). In another manganese-based silicide,  $\text{Mn}_5\text{Si}_3$ , the magnetic structure has been studied for many years (Lander et al., 1967; Brown & Forsyth, 1995; Silva et al., 2002).  $\text{Mn}_5\text{Si}_3$  shows two different antiferromagnetic configurations with a low temperature highly non-collinear phase (Lander et al., 1967; Brown & Forsyth, 1995; Silva et al., 2002). It was previously reported that antiferromagnetic  $\text{Mn}_5\text{Si}_3$  can be driven into a ferromagnetic or ferrimagnetic state by insertion of carbon into the voids of Mn octahedra of the hexagonal structure (Sénateur, 1967). Thin films of  $\text{Mn}_5\text{Si}_3\text{C}_x$  with  $x = 0.8$  have a Curie temperature  $T_C = 350$  K (Sürgers, 2003) well above room temperature.  $\text{FeSi}$  is a Kondo insulator (Aeppli &

DiTusa, 1999), a class of heavy-electron compounds exhibiting Kondo lattice behavior at room temperature.

Semiconducting silicides, such as the higher manganese silicides (HMS)  $\text{MnSi}_{1.7}$ ,  $\text{CrSi}_2$  have a high potential for thermoelectric applications (Vining, 1995; Borisenko, 2000). Additionally, such semiconducting silicides  $\text{FeSi}_2$ ,  $\text{MnSi}_{1.7}$  and  $\text{Ru}_2\text{Si}_3$  are reported to have a direct band gap, which makes them attractive for optoelectronic application (Borisenko, 2000). Most of the recent investigations of semiconducting silicides have been focused on the thin films of  $\text{FeSi}_2$  and  $\text{CrSi}_2$ . Semiconducting higher manganese silicides  $\text{MnSi}_x$  with a composition  $x$  varying from 1.67 to 1.75 are the most promising candidates for understanding the fundamental physics as well as for applications such as microelectronics, spintronics and thermoelectrics. There exist a number of tetragonal HMS phases,  $\text{Mn}_4\text{Si}_7$ ,  $\text{Mn}_{11}\text{Si}_{19}$ ,  $\text{Mn}_{15}\text{Si}_{26}$ , etc., which differ slightly in their composition (Schwomma et al., 1964; Fliher et al., 1967).

Most of the studies on silicides are carried out either in bulk or in thin films. Recently several groups have explored the growth of silicide nanostructures using a variety of methods. In chemical vapor deposition (CVD) method the main precursor used is  $\text{M}(\text{SiCl}_3)_x(\text{CO})_y$ , where  $\text{M} = \text{Fe}, \text{Mn}$  or  $\text{Co}$  (Aylett & Colquhoun, 1977; Novak et al., 1997; Schmitt et al., 2010). CVD utilizes the vapor-liquid-solid (VLS) mechanism to the growth of silicide nanowires. Wagner studied the growth of millimeter-sized Si whiskers in the presence of Au particles, involving the VLS process (Wagner, 1964). According to this mechanism, the anisotropic crystal growth is promoted by the presence of the liquid alloy/solid interface. This mechanism has been widely accepted and applied for understanding the growth of various nanowires.

## 2. Growth of silicide nanowires

In this chapter, we describe the synthesis, structure and properties of nanowires of silicides with manganese as one of the components. We have grown silicide nanowires using a class of coordination compound precursors called  $\beta$ -diketone chelates. This class of precursor can be used for growing a variety of silicides, including Mn-Si-C. This chapter will be organized as follows: First we will discuss the 1) Mn-based beta-diketone chelates (Kang et al., 2009), 2) then we will describe the synthesis of  $\text{Mn}_5\text{SiC}$  nanostructures and its structural, magnetic properties (Kang et al., 2009), 3) growth of  $\text{Mn}_5\text{SiC}$  nanostructures with different boron concentration and describe their magnetic and transport properties (Kang et al., 2010) and finally 4) the growth of higher manganese silicide,  $\text{Mn}_{15}\text{Si}_{26}$  using a similar precursor. We will discuss the electrical transport properties of  $\text{Mn}_{15}\text{Si}_{26}$  nanostructures and show that for the first time we have grown semiconducting  $\text{Mn}_{15}\text{Si}_{26}$  nanostructures.

### 2.1 Coordination compound precursors

Precursors that we have used for manganese are manganese beta-diketone chelates (Walker & Li, 1965; Cotton & Holm, 1960). We have used two different Mn beta-diketone chelates (Figure 1), bis(1,1,1,5,5,5-hexafluoro-2,4-pentanedionato) manganese(II) and bis(4,4,4-trifluoro-1-phenyl-1,3-butanedionato) manganese(II) complexes. The precursor with phenyl group is used for synthesizing  $\text{Mn}_5\text{SiC}$  and the other is used for the growth of manganese silicides with varying concentrations of Mn and Si by controlling the flux of manganese and the temperature of the growth.

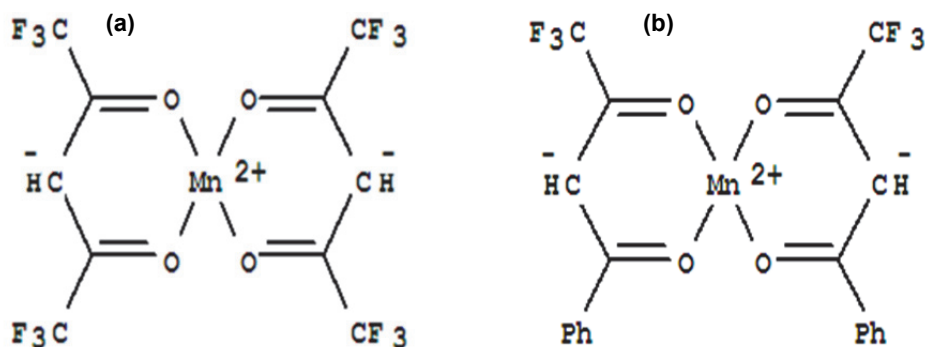


Fig. 1. (a) bis(1,1,1,5,5,5-Hexafluoro-2,4-pentanedionato) manganese(II) complex (b) bis(4,4,4-trifluoro-1-phenyl-1,3-butanedionato) manganese(II) complex.

## 2.2 Growth of $Mn_5SiC$ nanowires

We have grown  $Mn_5SiC$  nanowires using a precursor (Figure 1a) for Mn and C. Si (111) substrates were used as the Si source. A coordination complex precursor bis(4,4,4-trifluoro-1-phenyl-1,3-butanedionato) manganese(II),  $Mn(PhC(O)CHC(O)CF_3)_2$ , was used as a source for both Mn and C. The synthesis of the precursor [hereafter referred to as Mn-phenyl-complex] was carried out using the general procedure outlined in Walker & Li, 1965; Cotton & Holm, 1960. The native oxide of the Si substrate was etched away using dilute HF; a thin layer of Au nanoparticles (average size of 20 nm) was sprayed onto the etched Si surface; and the substrates were placed inside a quartz tube in a horizontal tube furnace. The system was pumped down to 10 mtorr before flowing an ultra-high purity Ar and  $H_2$  gas mixture (10 %  $H_2$ ) at a rate of 1000 standard  $cm^3$  per minute. Two heating zones with temperatures of 350 °C and 1050 °C were used for vaporization of the precursor and nanowire growth, respectively. The Si substrates were placed at the center of the furnace with the precursor at about 20 cm away. When the center of the furnace reached the set point of 1050 °C, the Mn phenyl-complex was hot (300 - 400 °C) enough to vaporize; Mn phenyl-complex is a highly volatile compound. The vapor-phase precursors were carried by the Ar- $H_2$  mixture to the center of the furnace where they reacted with silicon from the substrates. The reaction was continued under these conditions for 2 hrs before the furnace was allowed to cool to room temperature while maintaining the gas flow. Nanowires with diameters in the range of 2 - 100 nm can be grown using this method (Figure 2). Figure 3 shows the x-ray diffraction pattern of the nanowires. All of the grown nanowires exhibit orthorhombic structure with Cmc21 space group. The lattice parameters for the grown nanowires are  $a = 10.198$ ,  $b = 8.035$  and  $c = 7.630$  Å respectively. The high-resolution transmission electron microscopy (TEM) image in Figure 4(a) shows the (331) lattice planes of orthorhombic  $Mn_5SiC$  structure. The selected area electron diffraction pattern can also be indexed based on the same structure. We have measured the magnetic properties of these nanowires using a Quantum design MPMS system. These nanostructures exhibit ferromagnetic behavior (Figure 5) both at 300 and 10 K.

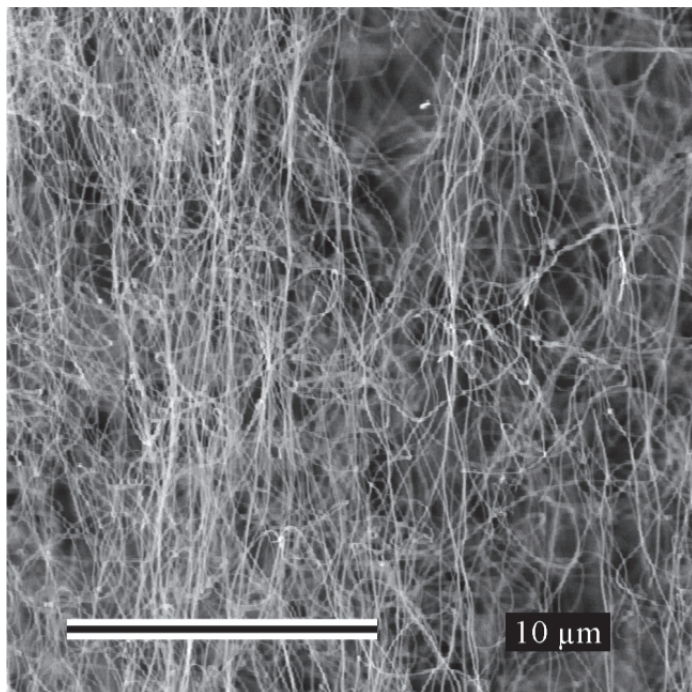


Fig. 2. Scanning electron microscopy image of Mn<sub>5</sub>SiC nanowires.

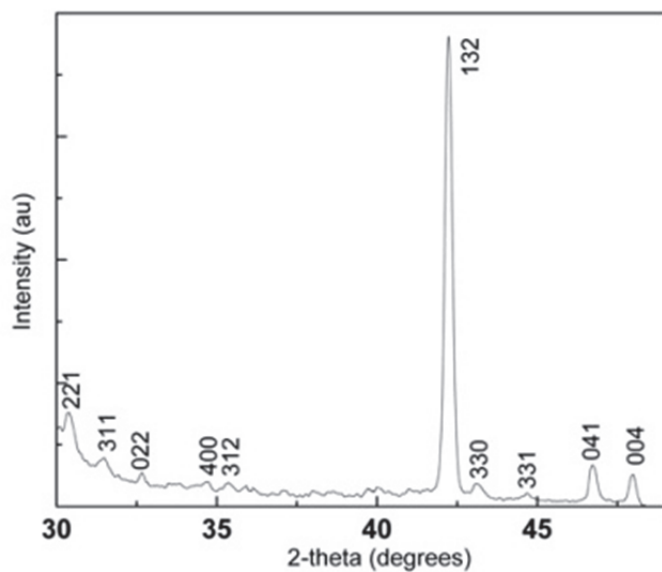


Fig. 3. X-ray diffraction pattern of as-grown Mn<sub>5</sub>SiC nanowires. The pattern is indexed based on orthorhombic Mn<sub>5</sub>SiC structure.

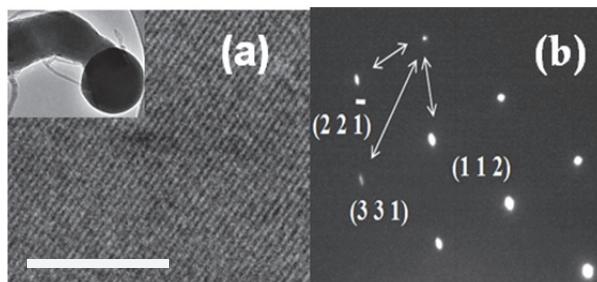


Fig. 4. (a) High resolution TEM image displays the (331) lattice planes of  $\text{Mn}_5\text{SiC}$  structure. The scale bar is 2.0 nm. Inset: TEM image showing catalyst nanoparticle at tip of the nanowire. (b) selected area electron diffraction pattern can be indexed to an orthorhombic  $\text{Mn}_5\text{SiC}$  structure.

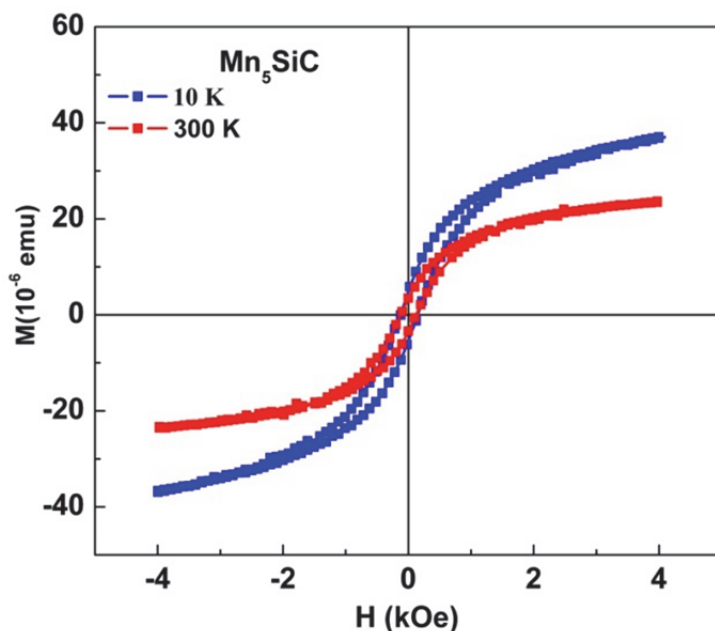


Fig. 5. Hysteresis loops of as-grown  $\text{Mn}_5\text{SiC}$  nanowire cluster at 300 and 10 K.

### 2.3 Boron-doped $\text{Mn}_5\text{SiC}$ nanowires

$\text{Mn}_5\text{SiC}$  nanowires exhibit ferromagnetic behavior and the  $T_c$  appears to be higher than 400 K. In order to clearly understand the ferromagnetic behavior and the magneto-transport properties we have grown  $\text{Mn}_5\text{SiC}$  nanostructures from differently boron-doped silicon substrates. The growth of boron-incorporated  $\text{Mn}_5\text{SiC}$  nanowires was carried out using chemical vapor deposition involving a coordination complex precursor for Mn and C. From the earlier discussion on CVD, the only difference here is in choosing the silicon substrate. We have used boron-doped silicon substrates with (100) orientation. The silicon substrate is

used as the source for silicon in boron-incorporated  $\text{Mn}_5\text{SiC}$  nanostructures. We have used silicon substrates with three different boron doping for the growth of these nanowires. The boron doping concentrations were  $2 \times 10^{17}$ ,  $5 \times 10^{18}$  and  $5 \times 10^{19} / \text{cm}^3$  respectively. The nanowires grown from these substrates will be referred to as low, medium and heavy-boron incorporated nanowires (LBNW, MBNW and HBNW) respectively. Highly dense boron-incorporated  $\text{Mn}_5\text{SiC}$  nanowires were grown as shown in Figure 6. Nanowire size ranges from 50 - 100 nm. Figure 7 illustrates the x-ray diffraction pattern of nanowires grown from three different silicon substrates. All of the grown nanowires exhibit orthorhombic structure with Cmc21 space group. The lattice parameters for the grown nanowires are  $a = 10.198$ ,  $b = 8.035$  and  $c = 7.630 \text{ \AA}$  respectively. There is no systematic shift of the peaks with boron incorporation to elucidate whether there is a lattice volume change. It would be possible that the varying size range (50 -100 nm) and the stress in the nanowires on different sets also contribute to the line width and broadening (Cullity, 1977). Gold nanoparticles (100 nm) were used as catalyst for the nanowire growth, in addition to the formation of  $\text{Mn}_5\text{SiC}$  nanowires, formation of a small fraction of  $\text{Au}_5\text{Si}_2$  particles was also observed. The peaks corresponding to the  $\text{Au}_5\text{Si}_2$  phase are marked in Figure 7. The selected area electron diffraction pattern obtained from a representative nanowire is indexed to an orthorhombic  $\text{Mn}_5\text{SiC}$  structure. The energy-dispersive x-ray analysis using high-resolution transmission electron microscopy reveals that the nanowires consist of Mn, Si and C and their ratio

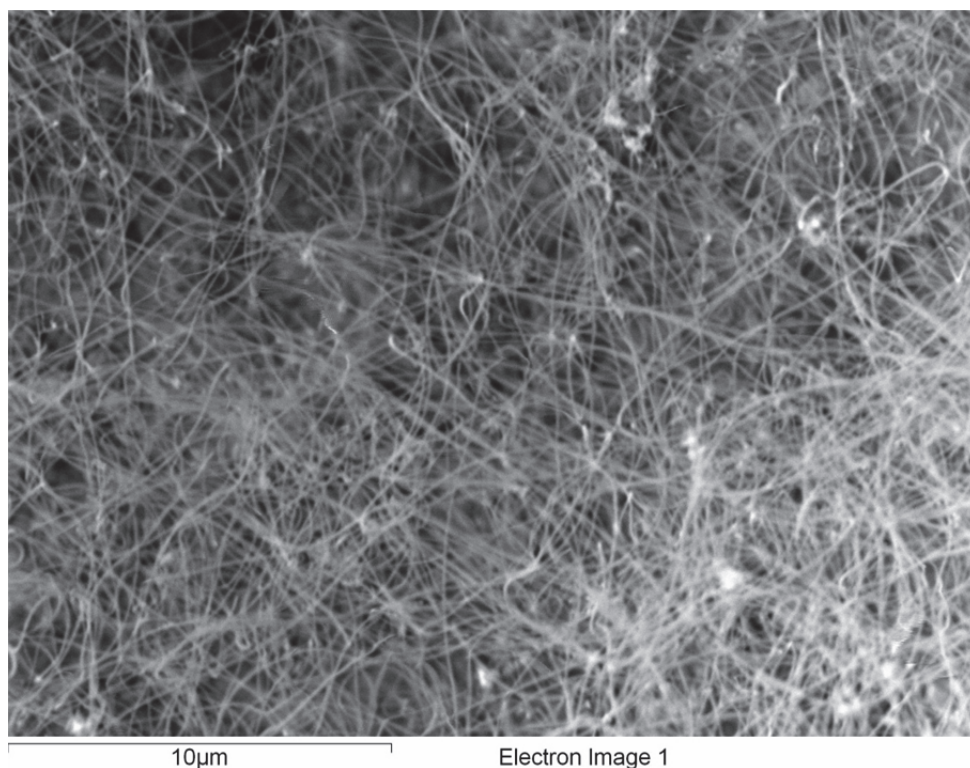


Fig. 6. Scanning electron microscopy image of boron-incorporated  $\text{Mn}_5\text{SiC}$  nanowires.

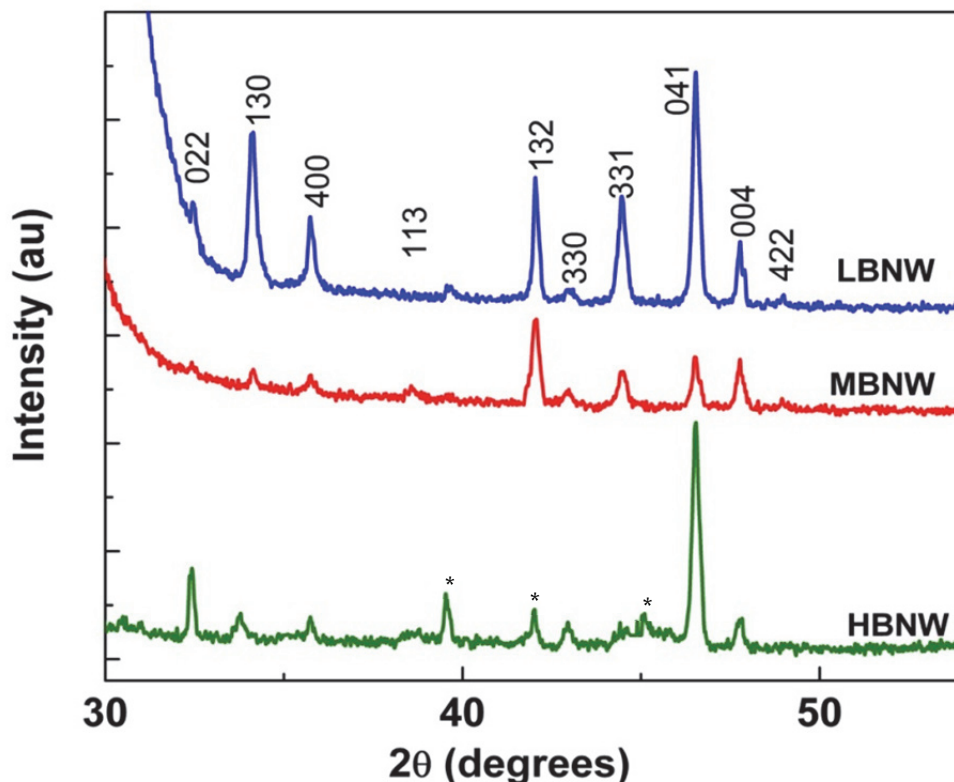


Fig. 7. X-ray diffraction patterns of boron-incorporated nanowires grown different silicon substrates (a) LBNW (b) MBNW and (c) HBNW. The peaks corresponding to  $\text{Au}_5\text{Si}_2$  phase are marked.

remained uniform over the entire length of the nanowire. In order to understand whether the boron actually goes into the nanowire, we have carried out Secondary Ion Mass Spectroscopy studies (SIMS). A cleaning procedure was carried out to make sure that the surface of the nanowires is clean of any residues. In this process, the as-grown nanowires were etched for a short time in 5% HF solution. The nanowires from the as-grown substrates are removed using sonication and are transferred to an undoped silicon substrate for SIMS analysis. The undoped substrate avoids any boron signal from the substrate as in the case of the substrates that are used for the nanowire growth. SIMS sputter profiling analysis was performed using a 100 nA, 17 keV,  $^{16}\text{O}^-$  primary beam with a square raster of 250  $\mu\text{m}$ . Figure 8 displays the SIMS data for low and heavy boron-incorporated nanowires, which clearly indicate that the boron-intensity from HBNW's is strong, compared to the other. Thus, this confirms the presence of boron in the nanowires and the signal that is detected purely arises from the highly dispersed nanowire cluster. A quantitative estimate was difficult because of the unavailability of a boron standard for this particular measurement.

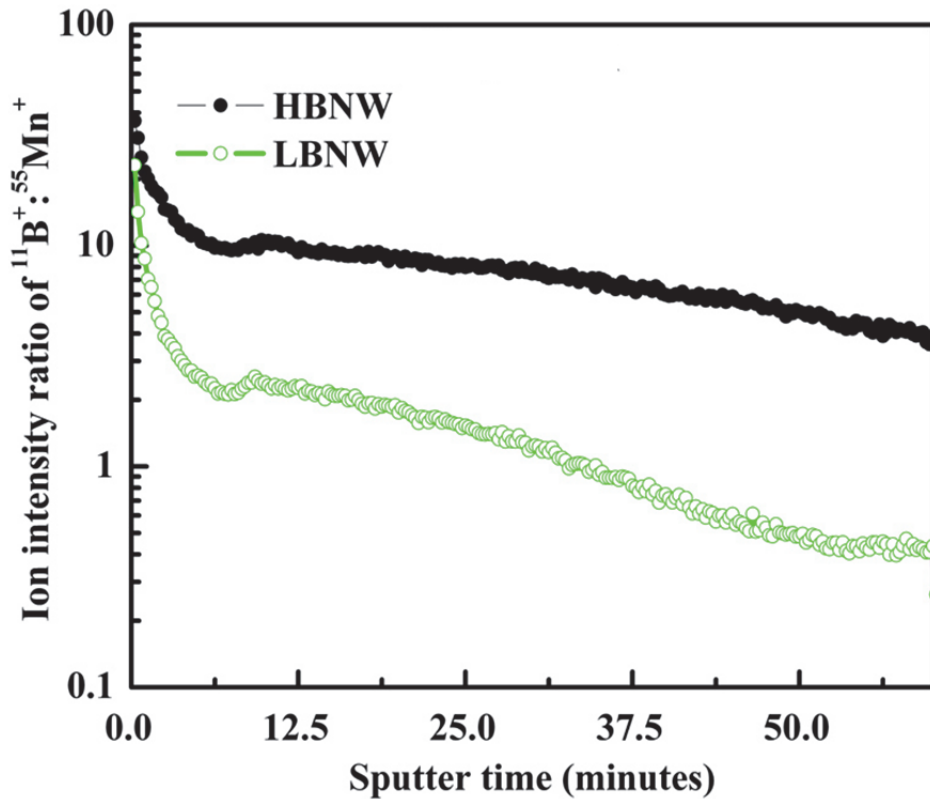


Fig. 8. SIMS data for LBNW and HBNW nanowires.

### 2.3.1 Magnetic properties

The magnetic hysteresis loops were measured using a superconducting quantum interference device (SQUID) magnetometer; the data for three different samples are displayed in Figure 9. The nanowires grown from low boron-doped silicon substrate exhibit higher saturation magnetization at room temperature. On the other hand, heavily boron-incorporated nanowires show very weak remanence; it is reduced by almost a factor of eight compared to the low-boron-incorporated nanowires. All of the three sets of nanowires exhibit magnetic hysteretic behavior at low temperature (15 K) with decreasing saturation magnetic moment as the boron incorporation increases. Thus, it is evident that the boron incorporation weakens the magnetic exchange interaction in  $\text{Mn}_5\text{Si}_3\text{C}_x$  nanostructures. We have measured the hysteresis loops up to 400 K, the low boron-doped sample exhibits clear hysteresis even at 400 K. Thus, the Curie temperature of these nanowires is higher than 400 K. Magnetic studies on thin films of  $\text{Mn}_5\text{Si}_3\text{C}_x$  has shown that they exhibit finite magnetic moments even above room temperature (Sürgers et al., 2003). There is no theoretical studies exist to compare our experimental results, most of the simulation studies are on Mn doped silicon.

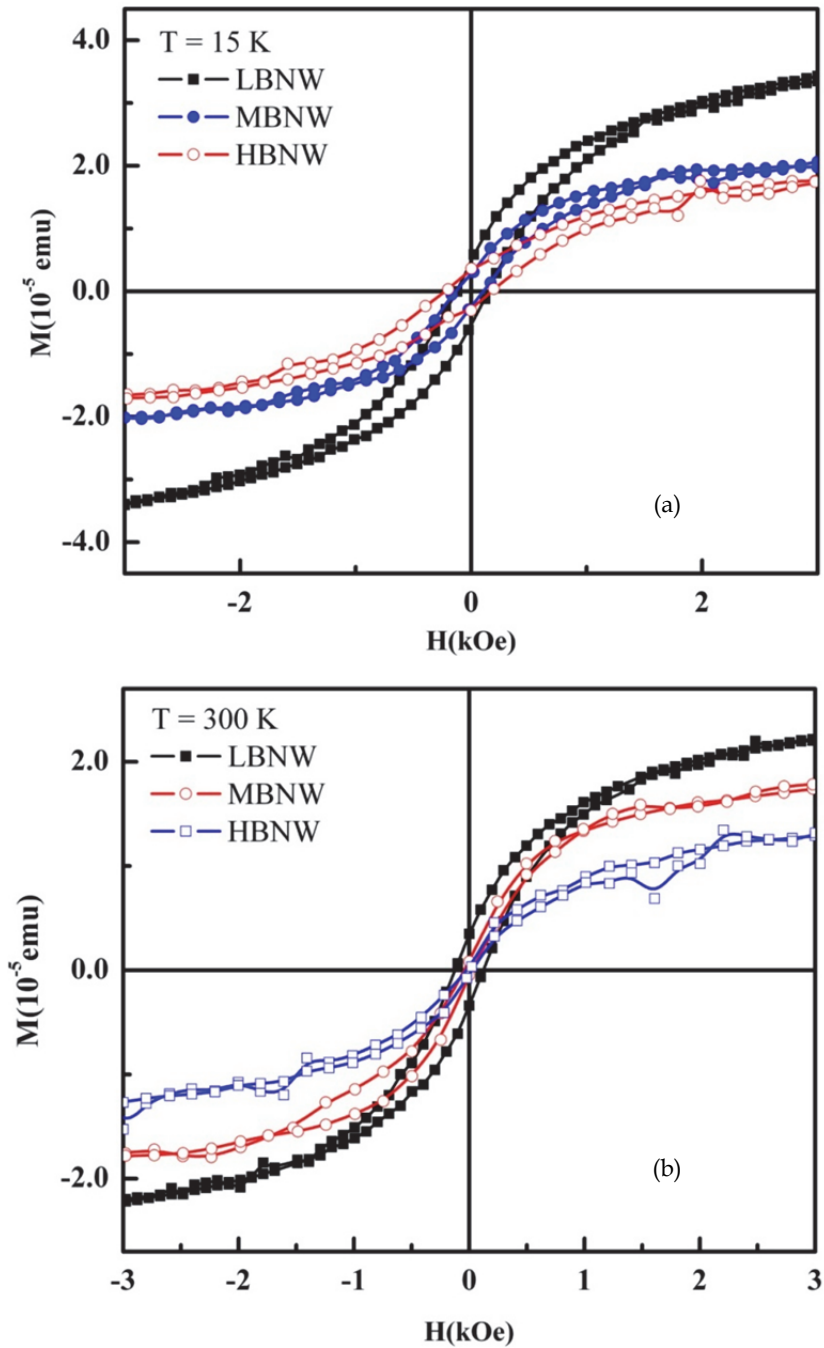


Fig. 9. The magnetic hysteresis loops of the three sets of nanowires at (a) 15 and (b) 300 K

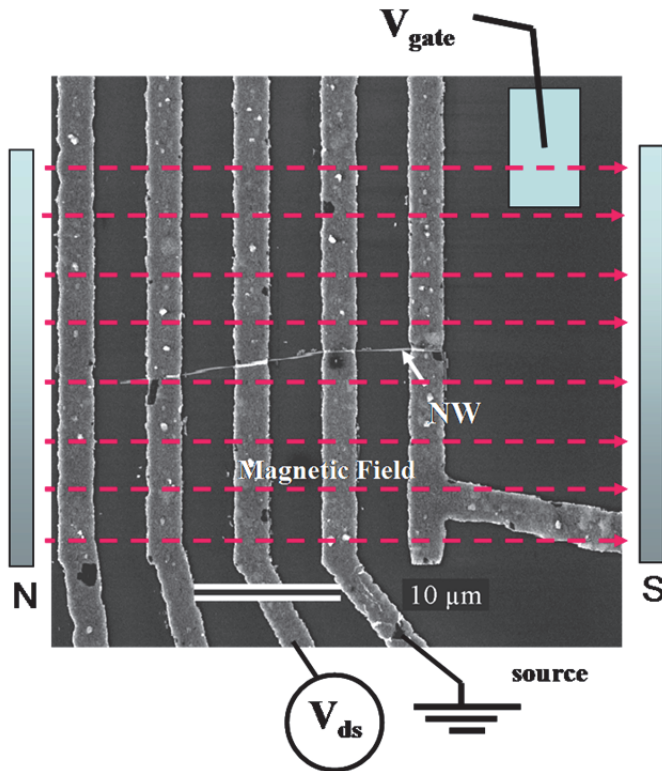


Fig. 10. SEM image of a typical nanowire device. The red lines indicate the direction of applied magnetic field. N and S denote the north and south poles of the magnet used for the measurement.

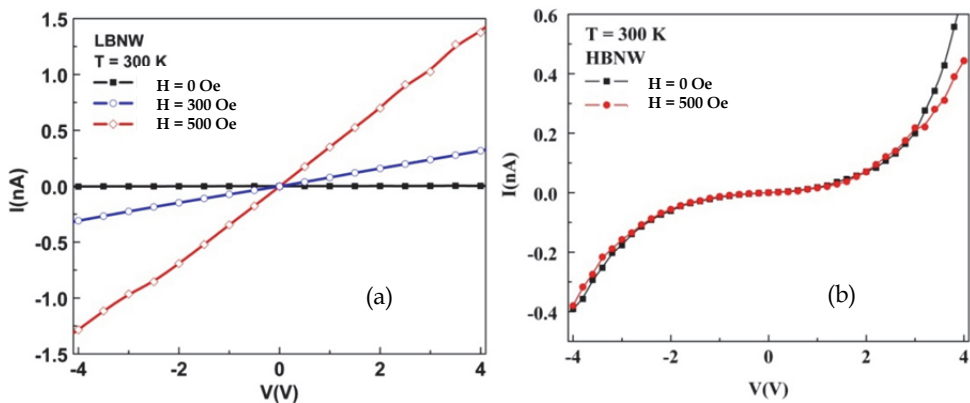


Fig. 11. Current-voltage characteristics of (a) LBNW and (b) HBNW nanowire devices with and without the presence of external magnetic fields.

### 2.3.2 Mn<sub>5</sub>SiC nanowire devices

Nanowire devices are fabricated (Figure 10) with standard electron beam lithography for electrical and magneto-transport measurements. The electrodes on the nanowire channels are layers of Al(100 nm)/Au (5 nm) evaporated using an ultra-high vacuum thin film deposition system. The current-voltage (I-V) measurements were carried out using a semiconductor parametric analyzer show metallic (linear) and semiconducting (nonlinear) behaviors for the devices fabricated with LBNW and HBNW's as displayed in Figures 11(a) and (b). This is further confirmed by measuring the resistance of the nanowire devices as a function of temperature. In the presence of small external magnetic fields applied along the axial direction of the nanowires ( $H= 300 - 1000$  Oe), there is a large change in the I-V characteristics in the case of a device fabricated with LBNW's. The change is almost two orders of magnitude, but there is an insignificant change in the case of devices with HBNW's, except for a small change at higher bias voltages. The electrical behavior, resistance of individual nanowire is measured as a function of temperature using a cryoprobe. The temperature dependence of resistance is plotted in Figure 12, it shows that the LBNW devices exhibit metallic behavior on the other hand the HBNW devices show strong semiconducting behavior. The LBNW devices display almost six orders of magnitude change in resistance. The magnetoresistance values (Figure 13) calculated from the I-V characteristics are much larger for the LBNW device and decreases for other devices as the saturation magnetization weakens. The magnetoresistance (MR) is calculated using the expression  $[(R_{H=0 \text{ Oe}} - R_{H=500 \text{ Oe}})/R_{H= 500 \text{ Oe}}]$ . The MR value is very high,  $\sim 400$  (40,000 %) for the low-boron-doped nanowire device and it is nearly negligible for the HBNW device.

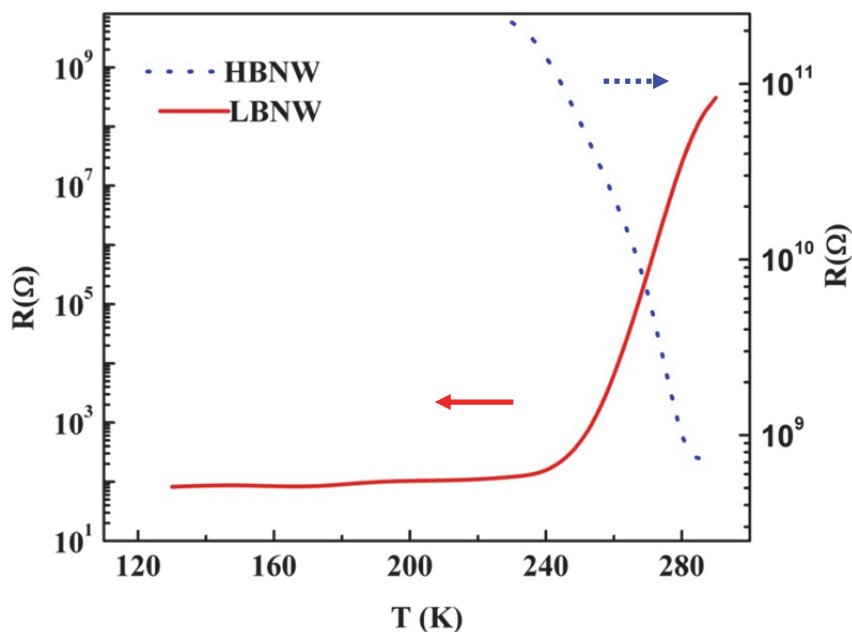


Fig. 12. Resistance vs temperature plots of the LBNW and HBNW nanowire devices exhibiting metallic and semiconducting behaviors.

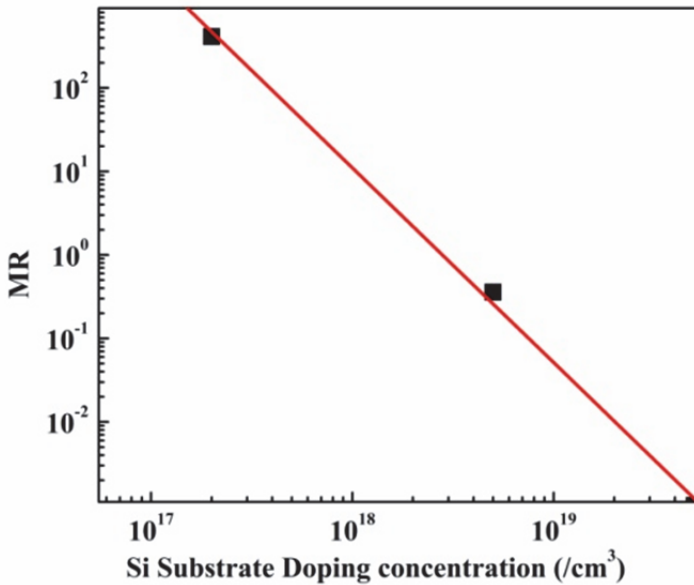


Fig. 13. MagnetoResistance of the nanowire devices decreases with the incorporation of boron. The x-axis gives the boron concentration of the silicon substrate used for the nanowire growth.

Comparing the magnetization, electrical and magneto-transport properties of the nanowires and their devices, nanowires that display strong magnetic behavior exhibit metallic behavior and huge magnetoResistance. Large incorporation of boron into the nanowires switches the electrical behavior to semiconducting, decreases the magnetic coupling and in turn considerably reduces the magnetoResistance.

#### 2.4 Higher manganese silicide nanowires

In addition to manganese monosilides and silicide carbides, another interesting class is the higher manganese silicides (HMS). There is a series of crystallographically distinct phases called as Nowotny chimney ladder (NCL) phases. NCL phases correspond to chimneys of manganese atoms with ladders of Si atoms. The four commensurate NCL phases which are reported in the literature are  $\text{Mn}_4\text{Si}_7$ ,  $\text{Mn}_{11}\text{Si}_{19}$ ,  $\text{Mn}_{15}\text{Si}_{26}$  and  $\text{Mn}_{27}\text{Si}_{47}$ . It is predicted that the electronic properties of these phases depend on the valence electron configuration and the metallic and semiconducting nature are predicted. Semiconducting higher manganese silicides are  $\text{MnSi}_{2-x}$  and  $\text{MnSi}_{1.75}$ . There are no reports about the magnetic properties of the higher manganese silicides; it is shown that they are good thermoelectric materials. Higgins et al. (Higgins et al., 2008) have synthesized  $\text{Mn}_{19}\text{Si}_{33}$  nanowires using  $\text{Mn}(\text{CO})_5\text{SiCl}_3$  precursor. These nanowires are grown using a CVD system and the mechanism of the nanowire growth is not well understood. In their CVD synthesis precursor used has a Mn/Si ratio of 1:1, but the nanowires grown have a Mn/Si ratio of 1:1.75. They have observed metallic behavior and no magnetoResistance effect for the  $\text{Mn}_{19}\text{Si}_{33}$  nanowire device.

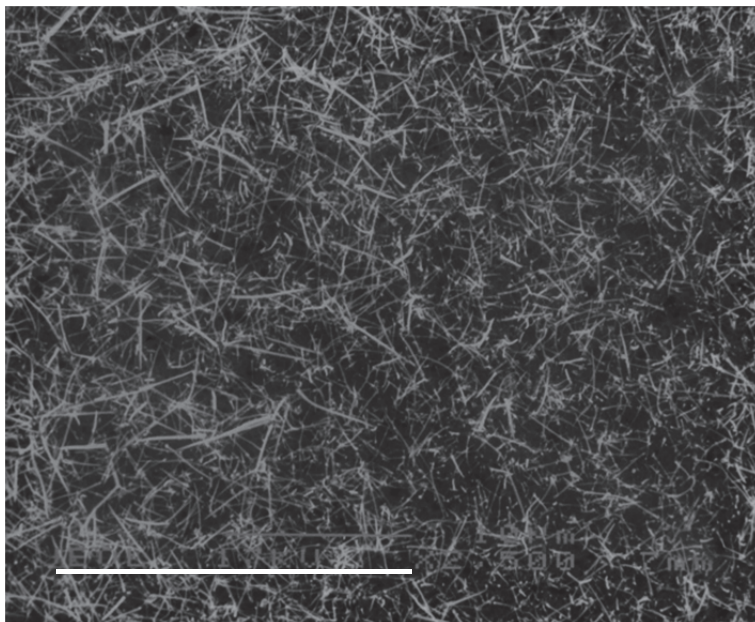


Fig. 14. Scanning electron microscopy image of  $\text{Mn}_{15}\text{Si}_{26}$  nanowires. Scale bar, 10 micrometers.

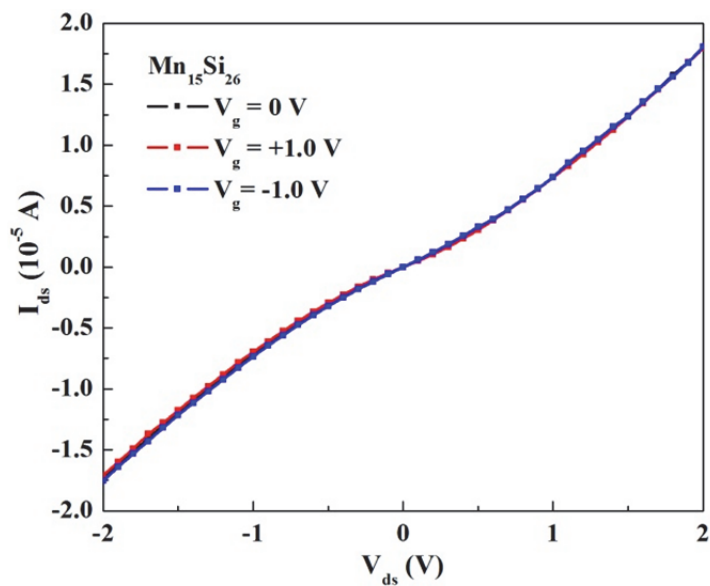


Fig. 15. Current- voltage characteristics of a typical  $\text{Mn}_{15}\text{Si}_{26}$  nanowire device. It shows p-type semiconducting behavior.

We have grown  $\text{Mn}_{15}\text{Si}_{26}$  nanowires using Mn-based beta diketone chelate precursor. The precursor is shown Fig 1(a). The growth method is similar to what is described earlier. In the CVD method we have grown the nanowires at 1050 °C for 2 hr. The wire size ranges from 80 – 200 nm and lengths up to hundreds of microns. Figure 14 shows the morphology of the wires. The x-ray diffraction analyses show that the nanowires exhibit the crystal structure of  $\text{Mn}_{15}\text{Si}_{26}$  which is also supported by the selected area diffraction pattern from transmission electron microscopy. Nanoscale devices are fabricated using electron beam lithography and we have measured the electrical transport properties as displayed in Fig 15. It clearly shows that the nanowire is semiconducting with p-type behavior. The gate-effect is not significant probably due to the degenerate character of  $\text{Mn}_{15}\text{Si}_{26}$  system.

### 3. Conclusions

Thus in conclusion, we have made use of manganese diketone chelates as precursors to grow different silicides. For the first time we have grown  $\text{Mn}_{15}\text{Si}_{26}$  nanostructures and shown that nanowires exhibit p-type semiconducting behavior as reported in the literature for bulk  $\text{Mn}_{15}\text{Si}_{26}$  system.

### 4. Acknowledgements

This work has been supported by funding from NSF under CAREER Grant No. ECCS-0845501, NSF-MRI, DMR-0922997 and VSL's startup grant. Many researchers significantly contributed to this research and the author especially thank Brewer, G. A., Kang, S, Pegg, I. L., McKeown, D. A., Buechele, A. C., Heiman, D. and Cathy. P.

### 5. References

- Aeppli, G. & DiTusa, J. F. (1999). Undoped and doped FeSi or how to make a heavy fermion metal with three of the most common elements. *Mater. Sci. Eng., B*, 63, 119–124
- Aylett, B. J. & Colquhoun, H. M. (1977). Chemical vapour deposition of transition-metal silicides by pyrolysis of silyl transition-metal carbonyl compounds. *J. Chem. Soc., Dalton Trans.*, 2058–2061
- Belitz, D.; Kirkpatrick, T. R. & Vojta, T. (1999). First Order Transitions and Multicritical Points in Weak Itinerant Ferromagnets. *Phys. Rev. Lett.* 82, 4707
- Borisenko, V. E. (2000). *Semiconducting silicides*, Springer-Verlag, ISBN 3-540-66111-5
- Brown, P. & Forsyth, J. (1995). Antiferromagnetism in  $\text{Mn}_5\text{Si}_3$ : the magnetic structure of the AF2 phase at 70 K. *J. Phys.: Condens. Matter.* 7, 7619
- Cotton, F. A. & Holm, R. H. (1960). Magnetic Investigations of Spin-Free Cobaltous Complexes. III. On the Existence of Planar Complexes. *J. Am. Chem. Soc.* 82, 2979
- Cullity, B. B. (1977). *Elements of X-Ray Diffraction*. Addison Wesley, ISBN: 0201610914, Massachusetts
- Flieher, G.; Voellenkle, H. & Nowotny, H. (1967). Mangansilicide vom Typ  $\text{Mn}_n\text{Si}_{2n-m}$ . *Monatsh. Chem.* 98, 2173–9
- Gates, B.; Mayers, B.; Cattle, B. & Xia, Y. (2002). Synthesis and Characterization of Uniform Nanowires of Trigonal Selenium. *Adv. Funct. Mater.* 12, 219–27

- Higgins, J. M.; Schmitt, A. L.; Guzei, I. A. and Jin, S. (2008). Higher Manganese Silicide Nanowires of Nowotny Chimney Ladder Phase. *J. Am. Chem. Soc.* 130, 16086-16094
- Ishikawa, Y.; Tajima, K.; Bloch, D. & Roth, M. (1976). Helical spin structure in manganese silicide MnSi. *Solid State Commun.* 19, 525
- Kang, S.; Brewer, G. A.; Battogtokh, J.; DiPietro, R.; Heiman, D.; Buechele, A. C.; McKeown, D. A.; Pegg, I. L.; Philip, J. (2009). Growth and Characterization of Mn<sub>5</sub>SiC nanowires. *Nanotech. Nanosci. Lett.* 1(2), 77
- Kang, S.; Brewer, G. A.; Jugdersuren, B.; DiPietro, R.; Heiman, D.; Buechele, A. C.; McKeown, D. A.; Pegg, I. L. & Philip, J. (2010). Magnetotransport properties of Mn-Si-C based nanostructures, *J. Appl. Phys.* 107(10), 104503
- Kruyt, H. R. & Arkel, A. E. V.; (1928). Die Ausflockungsgeschwindigkeit des Selenols. *Colloid & Polymer Science*, 32, 29-36
- Kusaka, S.; Yamamoto, K.; Komatsubara, T. & Ishikawa, Y. (1976). Ultrasonic study of magnetic phase diagram of MnSi. *Solid State Commun.* 20, 925
- Lander, G. H.; Brown, P. J. & Forsyth, J. B. (1967). The antiferromagnetic structure of Mn<sub>5</sub>Si<sub>3</sub>. *Proc. Phys. Soc. London*, 91, 332
- Maex, K. & van Rossum, M. (Eds.), (1995). *Properties of Metal Silicides*, INSPEC, ISBN-10: 0852968590, London
- Mayers, B. & Xia, Y. (2002). One-dimensional nanostructures of trigonal tellurium with various morphologies can be synthesized using a solution-phase approach. *J. Mater. Chem.* 12, 1875-81
- Messer, B.; Song, J.H.; Huang, M.; Wu, Y.; Kim, F. & Yang, P. (2000). Surfactant-Induced Mesoscopic Assemblies of Inorganic Molecular Chains. *Adv. Mater.* 12, 1526-1528
- Miglio, L. & d'Heurle, F. (2001). *Silicides: Fundamentals and Applications*, World Scientific Publishing Company, ISBN 981-02- 4452-5
- Murarka, S. P. (1983). *Silicides for VLSI Applications*, Academic Press, Inc. ISBN-10: 0125112203, Florida
- Novak, I.; Huang, W.; Luo, L.; Huang, H. H.; Ang, H. G. & Zybill, C. E. (1997). UPS Study of Compounds with Metal-Silicon Bonds: M(CO)<sub>n</sub>SiCl<sub>3</sub> (M = Co, Mn; n = 4, 5) and Fe(CO)<sub>4</sub>(SiCl<sub>3</sub>)<sub>2</sub>. *Organometallics*, 16, 1567-1572
- Pfleiderer, C.; Böni, P.; Keller, T.; Rößler, U. K. & Rosch, A. (2007). Non-Fermi Liquid Metal without Quantum Criticality. *Science*, 316, 1871
- Riseborough, P. S. (2000). Heavy fermion semiconductors. *Adv. Phys.* 49, 257-320
- Schmitt, A. L.; Higgins, J. M.; Szczech, J. R. & Song J. (2010). Synthesis and applications of metal silicide nanowires. *J. Mater. Chem.* 20, 223-235
- Schwomma, O.; Preisinger, A.; Nowotny, H. & Wittmann, A. (1964). Die Kristallstruktur von Mn<sub>17</sub>Si<sub>19</sub> und deren Zusammenhang mit Disilicid-Typen. *Monatsh. Chem.* 95, 1527-37
- Séneateur, J. P.; Bouchaud, J. -P. & Fruchart, R. (1967). Study of non- stoichiometric effects in compounds Mn<sub>5</sub>Si<sub>3</sub> and Mn<sub>3</sub>GaC<sub>1-x</sub>. *Bull. Soc. Fr. Mineral. Cristallogr.* 90, 537
- Silva, M. R.; Brown, P. J. & Forsyth, J. B. (2002). Magnetic moments and magnetic site susceptibilities in Mn<sub>5</sub>Si<sub>3</sub>. *J. Phys.: Condens. Matter* 14, 8707

- Song, J.; Messer, B.; Wu, Y.; Kind, H. & Yang, P. (2001).  $\text{MMo}_3\text{Se}_3$  ( $M = \text{Li}^+, \text{Na}^+, \text{Rb}^+, \text{Cs}^+, \text{NMe}_4^+$ ) Nanowire Formation via Cation Exchange in Organic Solution. *J. Am. Chem. Soc.* 123, 9714–9715
- Stejny, J. J.; Trinder, R.W. & Dlugosz, J. (1981). Preparation and structure of poly (sulphur nitride) whiskers. *J Mater Sci.* 16, 3161–70.
- Stejny, J. J.; Dlugosz, R.W. & Keller, A. (1979). Electron microscope diffraction characterization of the fibrous structure of poly (sulphur nitride) crystals. *J Mater Sci.* 14, 1291–300
- Stishov, S. M.; Petrova, A. E.; Khasanov, S.; Panova, G. K.; Shikov, A. A.; Lashley, J. C.; Wu, D. & Lograsso, T. A. (2007). Magnetic phase transition in the itinerant helimagnet MnSi: Thermodynamic and transport properties. *Phys. Rev. B*, 76, 052405
- Sürgers, C.; Gajdzik, M.; Fischer, G.; Löhneysen, H. v.; Welter, E. & Attenkofer, K. (2003). Preparation and structural characterization of ferromagnetic  $\text{Mn}_5\text{Si}_3\text{C}_x$  films. *Phys. Rev. B* 68, 174423
- Vining, C. B. (1995). *CRC handbook of Thermoelectrics*, Ed., D. M. Rowe, CRC Press, 277, ISBN: 0849301467
- Wagner, R. S. & Ellis, W. C. (1964). Vapor-Liquid-Solid Mechanism of Single Crystal Growth. *Appl. Phys. Lett.* 4, 89–91
- Wagner, R. S. (1970). Growth of whiskers by vapor-phase reactions, In: *Whisker technology* (ed. A. P. Levitt), ch. 2, pp. 15–119, Wiley-Interscience, ISBN 10: 0471531502, New York
- Walker, W. R; Li, N. C. (1965). 4-methyl-pyridine adducts of copper (II)  $\beta$ -diketone chelates. *J. Inorg. Nucl. Chem.* 27(10), 2255-2261
- Xia, Y.; Yang, P.; Sun, Y.; Wu, Y.; Mayers, B.; Gates, B.; Yin, Y.; Kim, F. & Yan, H. One-Dimensional Nanostructures: Synthesis, Characterization, and Applications. *Adv. Mater.* 15, (2003), 353–389

## **Part 2**

### **Oxide Nanowires**



# The Anisotropic Growth of Perovskite Oxide Nanowires

Yongming Hu, Haoshuang Gu and Zhao Wang  
*Faculty of Physics and Electronic Technology, Hubei University Wuhan,  
P R China*

## 1. Introduction

A perovskite is any material with share the same type of crystal structure as calcium titanium oxide (i.e., a structure analogous to that of the natural crystal calcium titanate, known as the “perovskite structure”), yet exhibit a broad range of interesting and excellent physical and chemical properties, which have large and potential applications in solid fuel cell, solid electrolyte, sensor, solid resistor etc for its stablized crystal structure (Bhalla et al., 2000). Their structural properties, such as phase, crystallinity and dimensional play important roles for their fundamental performances, such as optical, electric-transport, phonon vibration and ferroelectric etc. With the size of ferroelectrics decreasing, the size-dependent ferroelectric behaviors and their possible disappearance at critical size become crucial. When synthesized of ferroelectric nanomaterials via a conventional solution process, perovskite materials with cubic or pseudo-cubic symmetry of its crystal structure tends to grow uniformly along three major directions, leading to the formation of nanopowders rather than a 1D structure (Wei et al., 2007 and Lu et al., 2002).

To realize an anisotropic growth, especially no surfactant used in the hydrothermal environment, the symmetry of crystal structrue has a crucial part for the anisotropic growth of nanowires (NWs), which is very interesting for technological application in nanodevice. In the last several years, long ferroelectric NWs with perovskite structures and anistropic growth have been synthesized by different solution approach. For example, Urban *et al.* realized the creation of well-isolated NWs [001] of BaTiO<sub>3</sub> using solution-phase decomposition of bimetallic alkoxide precursors and reported its ferroelectric switching, this allows for the RT tetragonal ferroelectric phase to possess polarization along the axis of the nanowire, and recently observed the ferroelectric phase transition in a single wire of BaTiO<sub>3</sub> (Urban et al., 2002 and Spanier et al., 2006). Xu *et al.* reported the anistropic growth of tetragonal perovskite Pb(Zr<sub>0.52</sub>Ti<sub>0.48</sub>)O<sub>3</sub> (PZT) monocrystalline NWs [001] synthesized by polymer assisted hydrothermal method, showing that PZT nanorods were formed when assisted only by PVA, and PZT NWs were obtained when assisted by both PVA and PAA (Xu et al., 2005). Magrez *et al.* have realized the growth of highly uniform KNbO<sub>3</sub> NWs [011] exhibiting a narrow diameter distribution about 60 nm, the influence of the composition of the starting mixture as well as of the temperature-pressure within the hydrothermal autoclave on the product

purity and particle shape have also been identified (Magrez et al., 2006). Wang et al. reported the composite hydroxide mediated approach for the synthesis of nanostructures of complex functional oxides, including BaTiO<sub>3</sub>, BaMnO<sub>3</sub>, BaCeO<sub>3</sub> etc (Liu et al., 2006). In recent years, Rørvik *et al.* realized the anisotropic growth of PbTiO<sub>3</sub> nanorod arrays on SrTiO<sub>3</sub> substrate with different orientation grown by self-assembly of nanocrystals in template-free surfactant hydrothermal environment (Rørvik et al., 2008). Most recently, single-crystalline KTa<sub>0.25</sub>Nb<sub>0.75</sub>O<sub>3</sub> (KTN) nanorods with an orthorhombic perovskite structure were synthesized via a polymer-assisted hydrothermal method (Hu et al., 2010), the preferred crystallographic orientation of the nanorods were found to be controllable by using different types of polymers in the process; that is, [001]-oriented KTN were obtained upon the use of PVA and [110]-oriented ones were formed with the use of a combination of PAA and PVA. These NWs were produced by controlling the growth condition, and allowed for some initial insights into polarization behavior.

In this chapter, we describe the synthesis of perovskite oxide nanowires/nanorods, such as (K,Na)NbO<sub>3</sub> and Bi<sub>4</sub>Ti<sub>3</sub>O<sub>12</sub> nanowires/nanorods by hydrothermal process at low temperature (Wang et al., 2010 and Hu et al., 2009). K<sub>x</sub>Na<sub>1-x</sub>NbO<sub>3</sub> (with x=0.5) NWs and (Bi<sub>3.15</sub>Nd<sub>0.85</sub>)Ti<sub>3</sub>O<sub>12</sub> nanorods with diameters of 30~120 nm and length reaching up to several micrometers were synthesized by hydrothermal method. By the use of microstructural measurement and spectra method, the growth direction, optical properties, phonon vibrational behavior were investigated. In addition, the anisotropic growth mechanism of K<sub>x</sub>Na<sub>1-x</sub>NbO<sub>3</sub> NWs was also proposed.

## 2. Strategies for fabricating ferroelectric NWs

Well-defined ferroelectric NWs are believed to represent exciting systems to investigate fundamental issues about phase structure, intrinsic polarization, piezoelectricity and paraelectricity in one dimension. The main strategy to fabricating ferroelectric NWs is solution based method, including solution-phase decomposition, hydrothermal method, solvothermal method, and composite hydroxide mediated approach etc.

### 2.1 Solution-phase decomposition (Urban et al., 2002 and Puentes et al., 2001)

The synthesis of perovskite oxide NWs is accomplished by solution-phase decomposition of bimetallic alkoxide precursor in the presence of coordinating ligands, produces the correct product stoichiometry and avoids high-temperature treatment steps, which is similar to the method used to prepare inorganic nanocrystals and nanorods. Figure 1 shows a schematic illustration of typical solution-phase decomposition. It should be noted that rapid injection of organometallic reagents in a hot coordination solvent produces temporally discrete homogeneous nucleation. The decomposition and nucleation occurs rapidly upon injection. The lifetime of monomers in solution is short, and many small metal clusters form simultaneously.

Anisotropic nanorod growth is most likely due to precursor decomposition and crystallization in a structured inverse micelle medium formed by precursors and oleic acid under these reaction conditions. Well-isolated perovskite ferroelectric nanowires can be obtained by sonication of the reaction product followed by fractionation between water and hexane.

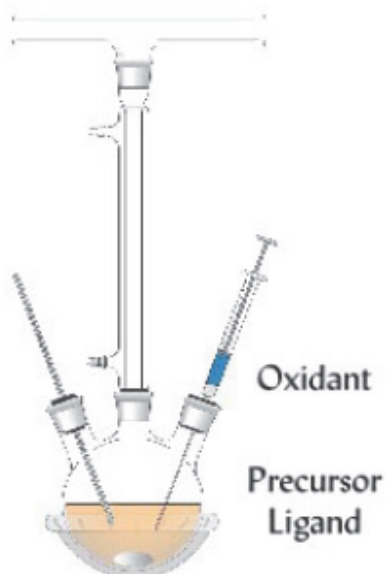


Fig. 1. A schematic illustration of a typical solution-phase decomposition (taken from reference 4).

## 2.2 Hydrothermal method (Vayssieres et al., 2001)

Hydrothermal method can be defined as a synthesis process of crystals which depends on the solubility of minerals in hot water under high pressure. The crystal growth is performed in an apparatus consisting of a steel pressure vessel called autoclave [Figure 2], in which a nutrient is supplied along with water. As an environmentally benign reaction medium, the hydrothermal method attracts much attention, which is a promising way for fabricating complex oxide nanomaterials because it can realize a low processing temperature of 200 °C or less, and can obtain products with high purity. In a typical hydrothermal method, the solubility of a solid is increased in a solvent and the reaction between the solids is sped up under pressures and temperatures above the critical point. A temperature gradient between the opposite ends of the autoclave causes the nutrients to dissolve at the hotter end and seeds to grow in the cooler end. Possible advantages of the hydrothermal method over other types of crystal growth include the ability to create crystalline phases which are not stable at the melting point, relatively low growth temperatures, and large area production at a low cost. Since most materials can be made soluble in a proper solvent by heating and pressurizing the system close to its critical point. Recently, a new synthetic method based on the hydrothermal method is used for depositing metal titanate nanowires, such as  $\text{BaTiO}_3$ ,  $\text{PbTiO}_3$  etc (Im et al., 2010). First, a  $\text{TiO}_2$  particle thin film is prepared by spray coating, and then transformed to single crystalline titanate nanowires grown on the conducting glass by hydrothermal treatment using  $\text{TiO}_2$  particles as seeds of nanowire growth.

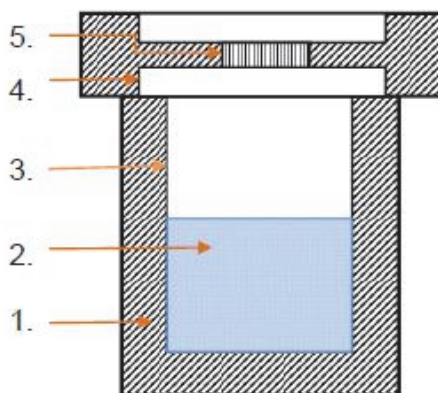


Fig. 2. A schematic illustration of a typical autoclave used in hydrothermal method, which is consist of (1) stainless steel autoclave (2) precursor solution (3) Teflon liner (4) stainless steel lid and (5) spring.

### 2.3 Solvothermal method

The solvothermal route is similar to the hydrothermal method where the synthesis is also conducted in stainless steel autoclave with the only difference is that the precursor solution is non-aqueous (eg. organic reagents). Heath and co-workers pioneered the use of solvothermal method to synthesize semiconductor nanorods (Heath & Legoues, 1993). The solvothermal method were then employed by many research groups to synthesize all sorts of nanostructures, including metal, semiconductor (Xie & Shang, 2007), graphene (Choucair et al., 2009) and complex oxide nanomaterials (Mao et al., 2005).

The shape, size, morphology and the crystallinity of nanowires can easily be altered through changing certain experimental parameters such as reaction temperature, reaction time, solvent type, surfactant type, and precursor type during a solvothermal system. However, the yield of the final products is very low, and the uniformity in size and morphology is also very poor although solution phase methods seem to be versatile in generating 1D nanostructures.

### 2.4 Composite hydroxide mediated approach (Liu et al., 2006 and Hu et al., 2009)

The composite-hydroxide-mediated (CHM) approach is based on the use of molten composite hydroxides (KOH and NaOH) as a solvent in chemical reactions at about 200 °C or even less for the synthesis of a wide range of nanostructures. The mixed hydroxides are used to not only mediate the reaction between the raw materials containing cations but also to lower the reaction temperature. Normally, the synthesis process of the CHM method is a one-step process. All of the raw materials with a certain amount of mixed hydroxides are placed within the Teflon vessel at one time. Then, the nanostructures form within the vessel after heating in a furnace at a temperature of ca. 200°C for several hours or days. The environmental appeal of this method arises from its intrinsic scalability,

generality, and facility as well as its fundamental basis on the use of hydroxides as the reaction medium.

### 3. $(K_{1-x}Na_x)NbO_3$ ferroelectric nanowires (NWs)

Nowadays, piezoelectric materials have been widely used in science and engineering, such as aerospace and medical treatments. Recently, under the requisition of the miniaturization and intergration of devices, low-dimensional piezo- & ferroelectric nanomaterials (nanowires, nanorods and nanotubes, etc.) have attracted much attention because of their potential application in nanodevices such as nanosensors and actuators, nanogenerators and nanopiezotronics (Wang et al., 2006, 2007 and Lao et al., 2007). Alkaline niobates with a perovskite structure, as a promising lead-free piezoelectric and optical material, show excellent piezoelectric, ferroelectric and electro-mechanic properties as well as good nonlinear optical and electro-optical properties (Guo et al., 2003, Saito et al., 2004 and Blomqvist et al., 2003). Potassium sodium niobate  $[(K_{1-x}Na_x)NbO_3]$ , KNN combines ferroelectrics  $KNbO_3$  and anti-ferroelectrics  $NaNbO_3$ , and have the best piezoelectric properties near the morphology phase boundary (MPB) when  $x=0.5$  in KNN ceramics (Jaeger and Egerton, 1962). However, most reports concerning about KNN materials have concentrated on KNN/KNN-based ceramics rather than KNN nanomaterials. For example, a number of methods have been developed to obtain KNN nano/micro-powders, such as solid-state route, chemical co-precipitation, sol-gel routine, micro-emulsion mediated route and molten-salt process (Villegas et al., 1999, Ravindranathan et al., 1991 and Hayashi et al., 2005). Sun *et al.* synthesized the KNN materials with  $x = 0.01, 0.24, 0.89, 0.91, 0.99$  by a hydrothermal method, but where  $x$  has a big jump from 0.24 to 0.89 in composition (Sun et al., 2009). Zhang *et al.* reported the thermodynamic evaluation of KNN material and the hydrothermal preparation (Zhang et al., 2008). So far, the synthesis, electrical or optical properties of low-dimensional KNN nanomaterials such as nanowires and nanorods has been lacking.

#### 3.1 Phase and microstructure of KNN NWs

KNN nanomaterials were synthesized by hydrothermal route using KOH, NaOH and  $Nb_2O_5$  as raw materials. There is a linear relation between the molar ratio of raw material KOH/NaOH and the atomic ratio of K/Na in the final compound, as shown in Figure 3.

Figure 4a shows the XRD patterns of the KNN samples. Sample A to C exhibit single-phase perovskite structure with orthorhombic symmetry (space group:  $Amm2$ ), which can be indexed according to JCPDS card No. 32 - 0822. Moreover, the diffraction peaks of  $K_{0.34}Na_{0.66}NbO_3$  (E) can be indexed to single-phase monoclinic perovskite structure with symmetry of space group  $Pm(6)$ , according to the JCPDS card No. 74 - 2024. However,  $K_{0.50}Na_{0.50}NbO_3$  (D) shows a main phase of orthorhombic perovskite structure as well as very weak peaks of monoclinic phases which are marked by a black dot in Figure 4a. The phase changes can be clearly proved by the symmetry changes of the (311) and (022) peaks at around  $2\theta = 56 - 57^\circ$  (Figure 4b). The lattice parameters of the as-synthesized samples (calculated by MDI JADE5) and crystal structures are listed in Table 1 as well.

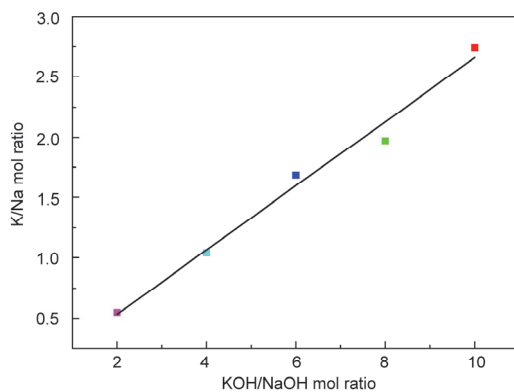


Fig. 3. The relation of molar ratio between the KOH/NaOH of the raw material and K/Na of the samples

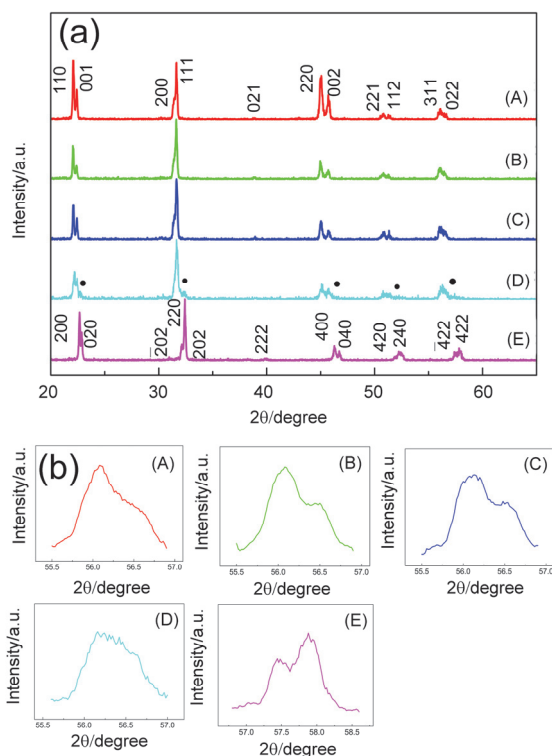


Fig. 4. (a) The XRD patterns in the  $2\theta$  range of  $20^\circ$  to  $65^\circ$  of the as-synthesized  $K_{1-x}Na_xNbO_3$  materials with different compositions; (b) The enlarged XRD patterns in the  $2\theta$  range of  $55^\circ$  to  $58^\circ$ , which suggest the phase transition by the symmetry changes of the diffraction peaks.

Sample	K/Na/Nb ratio <sup>1</sup>	Syngony	Lattice Parameters			
			<i>a</i> (Å)	<i>b</i> (Å)	<i>c</i> (Å)	(Å)
A	0.74:0.27:1	Orthorhombic	5.7075(3)	5.6845(4)	3.9689(2)	—
B	0.67:0.34:1	Orthorhombic	5.6837(7)	5.7091(3)	3.9692(0)	—
C	0.64:0.38:1	Orthorhombic	5.6846(5)	5.7039(5)	3.9649(3)	—
D	0.50:0.50:1	Orthorhombic+ Monoclinic	5.6873(8)	5.7041(9)	3.9777(6) <sup>2</sup>	—
E	0.34:0.66:1	Monoclinic	7.8451(1)	7.7719(4)	7.8439(2)	90.558

Table 1. The composition, crystalline phases and lattice parameters of the  $K_{1-x}Na_xNbO_3$ .

Figure 5 shows the FESEM images of the  $K_{0.50}Na_{0.50}NbO_3$  (D) nanowires microstructures synthesized by a hydrothermal process under 200 °C for 24 h. The morphologies are composed of two different structures which are step-like micro-scale particles (Figure 5a) and the intersectional structures of several nanorods/nanofingers (Figure 5b) of 3-5 μm in length and 300-400 nm in width. In order to characterize the detailed microstructure of the products, a single nanorod is separated from the particles shown in Figure 5b. As shown in Figure 6a, the nanowire is about 180 nm in width. The SAED pattern of the nanorod shows clear characteristic diffraction spots of crystalline  $K_{0.50}Na_{0.50}NbO_3$ , confirming that the nanorod is single-crystalline. In addition, the HRTEM (Figure 4c) show that the interplanar spacings are 3.89 and 3.98 Å, corresponding to the (020) and (002) crystal planes of monoclinic system, respectively. This proves that the monoclinic peaks in curve D of Figure 4a should be the XRD patterns of the nanowires. The results also confirm that the <010> direction is the preferred growth direction of this  $K_{0.50}Na_{0.50}NbO_3$  nanorod. Figure 7 shows the microstructure characterization of a single nanofinger taken from the particles shown in Figure 5b. The SAED pattern in Figure 7b also confirmed the single crystalline nature of the nanofinger.

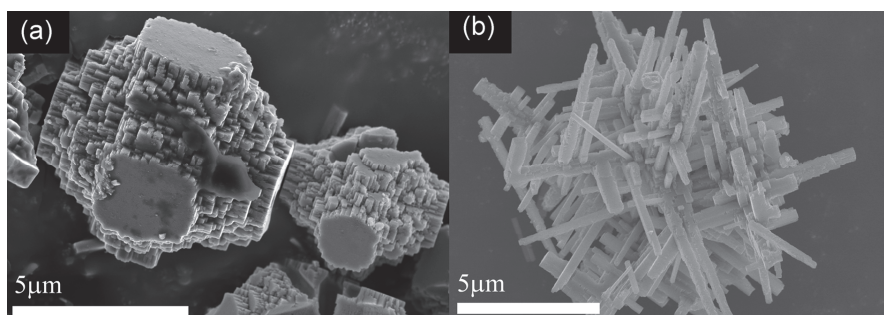


Fig. 5. FESEM images of  $K_{0.50}Na_{0.50}NbO_3$  step-like microstructures (a) and nanorods (b).

<sup>1</sup> The K/Na/Nb mol ratios were calculated from XRF results.

<sup>2</sup> The lattice parameters of sample D were calculated according to the diffraction peaks of the orthorhombic phase.

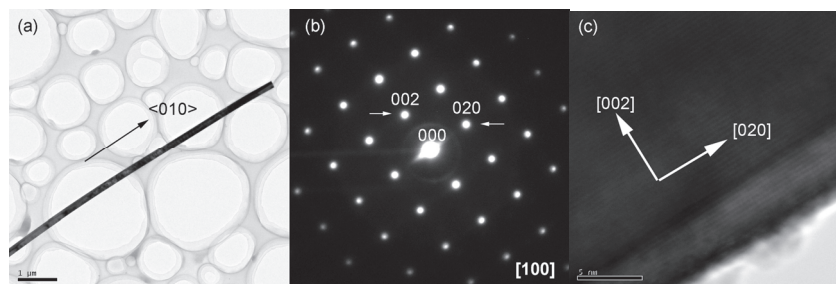


Fig. 6. The TEM results of a single  $\text{K}_{0.50}\text{Na}_{0.50}\text{NbO}_3$  nanorod. (a) TEM image; (b) SAED patterns; (c) HRTEM image.

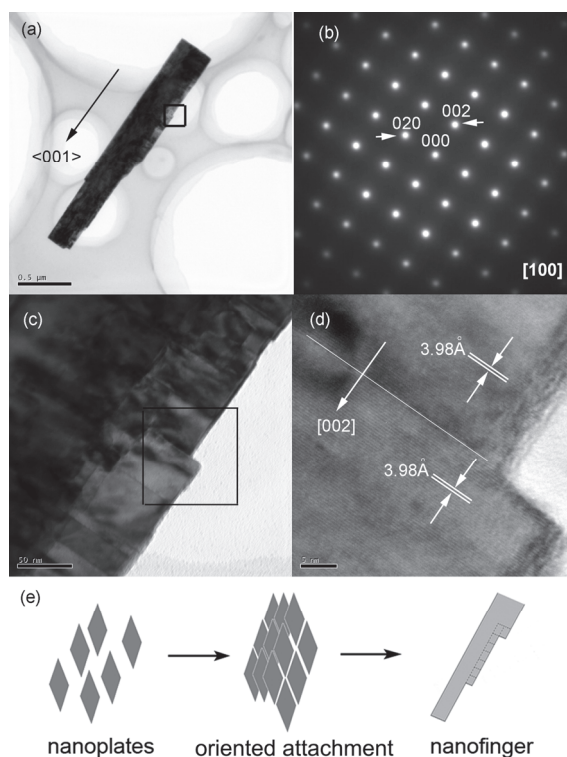


Fig. 7. The TEM results and the formation mechanism of a single  $\text{K}_{0.50}\text{Na}_{0.50}\text{NbO}_3$  nanofinger. (a) TEM image; (b) SAED patterns; (c) magnified image of the marked area in (a); (d) HRTEM image of the marked area in (c).

As shown in Figure 7c, the contrast changes at the edge of the nanofinger indicated that it was composed of several nanoplates, which should possess high surface energy and could aggregate easily at the early stage of the hydrothermal process. As shown in Figure 7d, the lattice planes of the two adjacent nanoplates are both (002) with the interplanar spacing of 3.98 Å. Therefore, it is reasonable that the formation of the nanofinger is due to

the oriented attachment growth of the small nanoplates, as illustrated in Figure 7e. The  $\text{K}_{0.50}\text{Na}_{0.50}\text{NbO}_3$  nanofinger preferentially grows along  $\langle 001 \rangle$  direction. Similar results were also found in the hydrothermal fabrication of  $\text{KTa}_{1-x}\text{Nb}_x\text{O}_3$  tower-like nanostructure (Hu et al., 2008).

### 3.2 Optical properties of KNN NWs

Raman scattering properties of the KNN nanomaterials measured at room temperature are shown in Figure 8. According to the XRD results, the structures of sample A to and D belong to the space group  $C_{2v}^{14}$  ( $Amm2$ ), which has 12 optical modes in the  $C_{2v}$  point group including  $4A_1+4B_1+3B_2+A_2$ . Among them, all the 12 modes are Raman active and also infrared IR active except the  $A_2$  mode. As shown for spectra A to D, a sharp band shows up on the low-frequency position of  $192\text{ cm}^{-1}$ . It was reported that the band at  $192\text{ cm}^{-1}$  belongs to a mixed mode of  $A_1$ ,  $B_1$  and  $B_2$  (Shen et al., 1995). Moreover, there are three bands appeared at  $261$ ,  $272$  and  $289\text{ cm}^{-1}$ , which overlap with each other and belong to the vibration mode of  $B_1(\text{TO})$ ,  $A_1(\text{TO})$  and  $A_1(\text{LO})+A_1(\text{TO})$ , respectively. Another three Raman bands show up at the range of  $300 - 800\text{ cm}^{-1}$ , including band  $430\text{ cm}^{-1}$  of mode  $A_1(\text{LO})$ ,  $537\text{ cm}^{-1}$  of mode  $B_1(\text{TO})$  and  $600\text{ cm}^{-1}$  of mode  $A_1(\text{TO})$ . In addition, another peak can be observed at  $839\text{ cm}^{-1}$ , which belongs to the mode of  $A_1(\text{LO})$ . Moreover, 11 Raman bands were observed in spectra E in the range of  $150$  to  $1000\text{ cm}^{-1}$ , which is similar to the Raman spectra of the monoclinic  $\text{NaNbO}_3$  reported by Chang et al. (Chang et al., 2009).

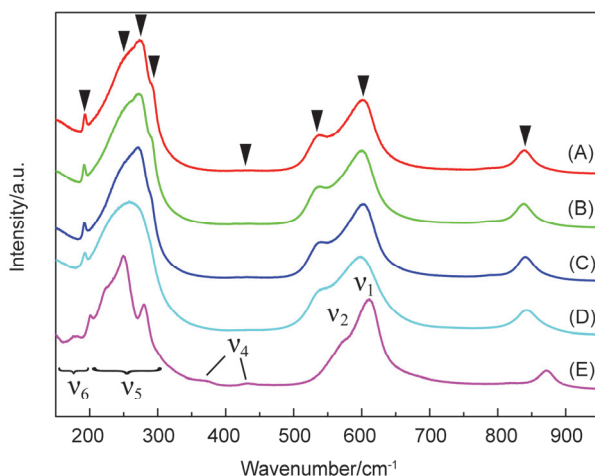


Fig. 8. The room-temperature Raman scattering spectra of the as-synthesized  $\text{K}_{1-x}\text{Na}_x\text{NbO}_3$  with different compositions derived from a hydrothermal method.

As reported, the vibration modes of  $\text{NaNbO}_3$  can be classified as internal modes of the octahedron  $\text{NbO}_6^{7-}$  anion by the model proposed by Ross (Ross et al., 1970). The vibration modes of the octahedron  $\text{NbO}_6^{7-}$  anion can be decomposed into two bond stretching vibrations of  $A_{1g}(v_1)$  and  $E_g(v_2)$ , two interbond angle bending vibrations  $v_5$  and  $v_6$  of

symmetry of  $F_{2g}$  and  $F_{2u}$ , respectively, as well as two vibrations  $\nu_3$  and  $\nu_4$  of both  $F_{1u}$  symmetry. The vibration modes of  $K_{0.34}Na_{0.66}NbO_3$  can be attributed to this explanation as well. Therefore, all Raman bands observed in spectra E can be attributed to the internal modes of octahedron  $NbO_6^{7-}$  anion, as shown in Figure 8.

Sample A			Sample E		
Freq./ ( $cm^{-1}$ )	Assign	$KNbO_3$ / ( $cm^{-1}$ )	Freq. ( $cm^{-1}$ )	Assign.	$NaNbO_3$ ( $cm^{-1}$ )
192	Mixed	196	151		153
261	$B_1(TO)$	266	177	$\nu_6$	175
272	$A_1(TO)$	280	200		201
289	$A_1(LO)+A_1(TO)$	298	224		218
430	$A_1(LO)$	435	248	$\nu_5$	247
537	$B_1(TO)$	535	280		276
600	$A_1(TO)$	597	368	$\nu_4$	378
839	$A_1(LO)$	836	431		435
			572	$\nu_2$	557
			611	$\nu_1$	602
			872	$\nu_1+\nu_5$	867

Table 2. Observed Raman bands and tentative assignments at room temperature.

The band position and corresponding assignment were also listed in Table 2, as well as that of  $KNbO_3$  and  $NaNbO_3$  (Shen et al., 1998). The transition between orthorhombic (A to D) and monoclinic (E) phase can be clearly confirmed, which is consistent with the XRD results. In addition, as shown in Figure 8 and Table 2, the lower frequency phonon modes shifted downwards from  $KNbO_3$  in Ref. 28 to Sample A, while their high frequency phonon modes (535, 597 and 836  $cm^{-1}$ ) shifted upwards. Similar phenomenon have also been observed in (Ba,Sr)TiO<sub>3</sub> materials. Because of the different ion radius, ionicity and mass of  $Na^+$  ( $Sr^{2+}$ ) from  $K^+$  ( $Ba^{2+}$ ), the introducing of  $Na^+$  ( $Sr^{2+}$ ) cations to the lattice of  $KNbO_3$  ( $BaTiO_3$ ) leads into a perturbation to the original energy levels, which causes a decrease of energy to optical phonons with lower energy and a increase of energy to optical phonons of higher energy, and finally leads to the redshift and blueshift of the low frequency and high frequency phonons, respectively. It can also be explained as a result of a dual function of lattice distortion and mass effect caused by the introducing of  $Na^+$  ( $Sr^{2+}$ ) (Katiyar et al., 2004). Moreover, 4 bands shifted to high frequency from  $K_{0.34}Na_{0.66}NbO_3$  to  $NaNbO_3$ , while others shifted downwards. It is worth noting that the blueshifted Raman band at 151, 200, 368  $cm^{-1}$  did not appear in the spectra of Sample A, together with the nearly disappeared Raman band at 430  $cm^{-1}$ . It was reported the disappearance of these Raman band in the  $KNbO_3$  Raman spectrum could be due to the vanishing of the tilting between the adjacent  $NbO_6$  octahedra. The  $NbO_6$  octahedra in an ideal  $ABO_3$  perovskite structure would be regular with the A site cations surrounded by 12 oxygens and Nb by 6 oxygens. However, such an ideal structure does not exist in the  $ANbO_3$  (A = Na and K) because of the tilting of the  $NbO_6$  octahedra and the displacements of Nb atoms from the center position which is induced by the A site cation (Na or K) and the unbalanced interatomic forces present in the perovskite

structures. These distortion depend on the size of the A cations.  $K^+$  cation with a larger size is coordinated to 12 oxygens, thus free space is unavailable for the  $NbO_6$  octahedra to tilt relative to one another. However,  $Na^+$  cation with a relatively small size is coordinated to less than 12 oxygens, and causes an  $18^\circ$  tilt angle between the adjacent  $NbO_6$  octahedra. In KNN structures, with the increasing of Na content, the  $NbO_6$  octahedra begin to tilt with one another and caused the appearance of the four bands in the Raman spectrum of sample E. The blue shift of these four Raman bands from sample E to  $NaNbO_3$  may be due to the disappearance of  $K^+$  cation which may restrain the tilting of the  $NbO_6$  octahedra. For the other Raman bands, the red shift may be due to the increasing of distortion in the  $ABO_3$  perovskite structure which leads to a stretching of the bond distance.

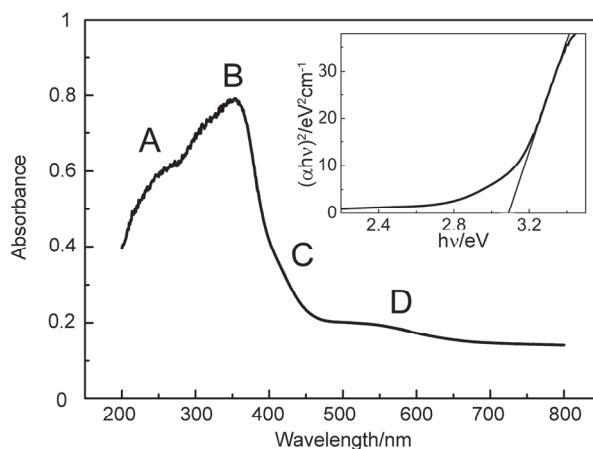


Fig. 9. The UV/Vis absorption spectra of  $K_{0.50}Na_{0.50}NbO_3$  synthesized by hydrothermal method. The inset shows the curve obtained through Tauc equation.

Figure 9 shows the UV/Vis absorption spectra of the  $K_{0.50}Na_{0.50}NbO_3$  nanowires. As shown, there are four absorption bands appearing at about A (268 nm), B (354 nm), C (411 nm) and D (533 nm). All bands can be found in the spectra of  $KNbO_3$ , indicate that there is no band attributed to  $Na^+$ . According to the results reported by Duan *et al.*, K electron states is shown in the upper part of the conduction band ( $> 8$  eV) and the lower part of the valence band ( $< -10$  eV), indicating that  $K^+$  have no influence to the absorption spectra. According to the calculated density of states (Jehng & Wachs, 1991), band A and B should be attributed to the interband transition from the  $O_{2p}$  electron states to the empty  $Nb_{4d}$  electron states. Band B originates from a transition from the top of the valence bands occupied by  $O_{2p}$  electron states to the bottom of the conduction bands dominated by the empty  $Nb_{4d}$  electron states. Band C and D can be attributed to an intraband transition in relation to the  $Nb^{5+}$  cations<sup>35</sup>. Furthermore, according to the Tauc equation, the band gaps can be estimated by absorption spectra. The relationship can be illustrated as  $(\alpha hv)^2 \propto (h\nu - E_g)$  for direct transition, where  $\alpha$  and  $h\nu$  is the absorption coefficient and photon energy, respectively. The absorption coefficient  $\alpha$  can be defined as  $\alpha = (2.303 \times 10^3 A \rho) / \delta c$ , where  $A$ ,  $\rho$ ,  $\delta$  and  $c$  is the absorbance, theoretical density, sample thickness and the concentration of solution,

respectively. As  $\rho$  and  $c$  are constants and have no relationship with the final result of band gap  $E_g$ , the equation can be simplified as  $\alpha = 2.303A / \delta$  ( $\delta$  is estimated to be 0.1 cm for the calculation). The band gap  $E_g$  of  $K_{0.50}Na_{0.50}NbO_3$  can be obtained by the curve in the inset of Figure 9 to be  $E_g = 3.09$  eV.

### 3.3 Growth mechanism of KNN NWs

As previously reported,  $KNbO_3$  nanostructures were synthesized in solution via a dissolution-precipitation process (Goh et al., 2003).  $Nb_2O_5$  is dissolved into  $Nb_6O_{19}^{8-}$  ions, and forms a octahedron of  $NbO_6^{7-}$  anions by a complex transformation, which act as elementary species to produce the precipitation of  $KNbO_3$  perovskite. Similarly, the mechanism can be applied to the formation of KNN material as well. These reactions are formulated as follows:

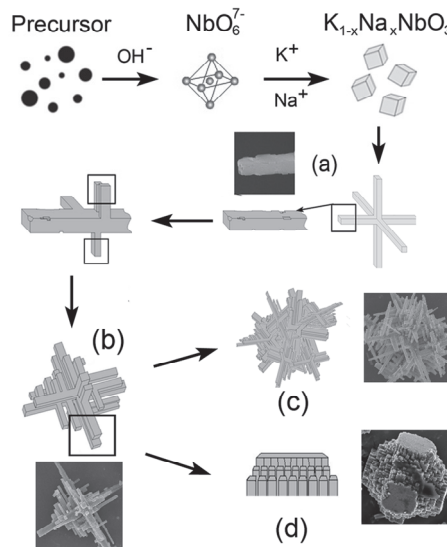
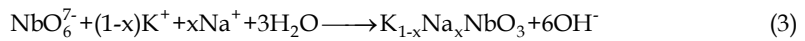
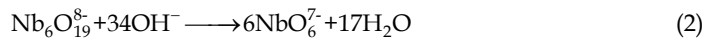
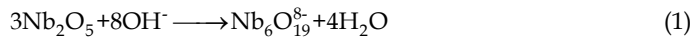


Fig. 10. The schematic illustration of the formation process of  $K_{0.50}Na_{0.50}NbO_3$  nano/micro-structures by hydrothermal process.

As described by reaction (1), the  $Nb_2O_5$  was dissolved simultaneously into the  $Nb_6O_{19}^{8-}$  ions at the initial stage of the hydrothermal reaction. Then single octahedron  $NbO_6^{7-}$  anions were formed by complex transformation occurred under higher alkaline conditions after reaction

(2). Reaction (3) referred to the tiny crystalline nucleation in a supersaturated medium followed by the crystal growth of KNN under hydrothermal conditions. The formation process of the  $K_{0.50}Na_{0.50}NbO_3$  nanostructure is illustrated in Figure 10. The reaction happened simultaneously with the crystalline nucleation due to the high supersaturation of medium at the initial stage, which promoted the continuous growth of KNN crystals, and formed several crystalline nucleuses. Once the supersaturation was reduced to a certain extent, polarization growth became a major process.

As shown in Figure 10, the {001} family of crystal planes are the polar faces of the  $NbO_6^{7-}$  structure. The dipoles exist along <001> orientation because of the  $Nb^{5+}$  and  $O^{2-}$  layers arranging alternately along this orientation. The {001} faces are therefore unstable when  $Nb^{5+}$  or  $O^{2-}$  is exposed. As a result, the crystal growth along <001> orientations are predominant in energy, along which the polarization growth occurred. Several nanorods were formed along these six directions, which formed the cross-like structures. The different growth direction shown in Figure 6a and Figure 7a could prove this supposition. Moreover, the surface of the as-formed nanorods/nanofingers served as the substrate for the latter one. Gradually, more nanorods/nanofingers would grow up while the original one grew longer. According to this tendency, the grain grew larger step by step (Figure 10b), then the grains near each other may grow together, and formed a larger structure that consisted of a number of nanorods interlacing with each other (Figure 10c). As the reaction continued, nanorods which have the same orientation and near each other gradually grew together due to the aggregation growth happened during the hydrothermal reaction process, and formed step-like particles shown in Figure 10d. Therefore, the growth of the as-prepared  $K_{0.50}Na_{0.50}NbO_3$  should be due to crystal structure of the octahedron  $NbO_6^{7-}$  anions as well as the oriented attachment and the aggregation growth mechanism.

#### 4. $Bi_4Ti_3O_{12}$ (BiT) ferroelectric NRs

To enrich the physics of ferroelectricity, especially at one dimensional nanoscale, perfectly structured polar oxide nanomaterials are the optimal samples for study. Ferroelectric bismuth layered perovskite materials, with the characteristics of fast switching speed, high fatigue resistance and good retention (Araujo et al., 1995), are currently studied extensively due to their potential in several important areas, including nonvolatile random access memories (Nv-FRAM), room temperature pyroelectric devices, electro-optic devices, and microelectro-mechanical systems etc (Scott, 1998). Among these bismuth layered ferroelectric oxides, lanthanide-modified bismuth titanate ( $Bi_{4-x}R_xTi_3O_{12}$ , R=La, Nd, Sm, etc.), especially for  $Bi_{4-x}Nd_xTi_3O_{12}$ , are regarded as one of the very important candidate for the Nv-FRAM applications because of its excellent ferroelectric properties, e.g., much improved fatigue resistance, larger remanent polarization, lead-free nature and relatively lower processing temperature in comparison to  $Pb(Zr,Ti)O_3$  (PZT) and  $SrBi_2Ta_2O_9$  (SBT) (Park et al., 1999 and Lee et al., 2006). Despite the extensive studies of  $Bi_{4-x}Nd_xTi_3O_{12}$ , however, most of these were focused on ceramics and thin films; a clear fundamental study of such low-dimensional (nanowires or nanorods) ferroelectric nanostructure has been lacking, including the phase transformation, domain structures and optical properties induced by their reduced dimensionality etc.

#### 4.1 Phase and microstructure of BiT NRs

The BNT nanorods were fabricated by hydrothermal method using bismuth nitrate pentahydrate,  $\text{Bi}(\text{NO}_3)_3 \cdot 5\text{H}_2\text{O}$ , neodymium nitrate hexahydrate,  $\text{Nd}(\text{NO}_3)_3 \cdot 6\text{H}_2\text{O}$ , tetrabutyl titanate,  $\text{Ti}(\text{OC}_4\text{H}_9)_4$  as the starting materials, NaOH served as a mineralizer and polyvinyl alcohol (PVA-124) as the additive.

Figure 11a shows the XRD pattern of BNT nanorods sample derived from hydrothermal method. As shown, all of the diffraction peaks can be indexed as the orthorhombic structure of  $\text{Bi}_{3.15}\text{Nd}_{0.85}\text{Ti}_3\text{O}_{12}$  powders with the lattice constants:  $a=5.4526\text{\AA}$ ,  $b=5.4242\text{\AA}$ ,  $c=32.0249\text{\AA}$ , agreement well with the standard literature value (JCPDS Card NO.36-1486,  $a=5.429$ ,  $b=5.405$  and  $c=32.83\text{\AA}$ ), which exhibits that the products are composed of BNT with perovskite structure and without the trace of any impurity phase. Figure 11b shows the typical FESEM images of the BNT nanorods dispersed on the silicon substrate. It can be seen that a majority of the nanorods grow into regular structure and almost all of the nanorods have smooth surface and uniform dimension. The diameters of nanorods are range of 30~120 nm and length reaching up to several micrometers, which are promising candidate for nanoscale ferroelectric sensors. In addition, it is worth noting that larger amount of small particles with unregular morphologies absorbing on the surface of BNT nanorods, which may be the PVA amorphous phase.

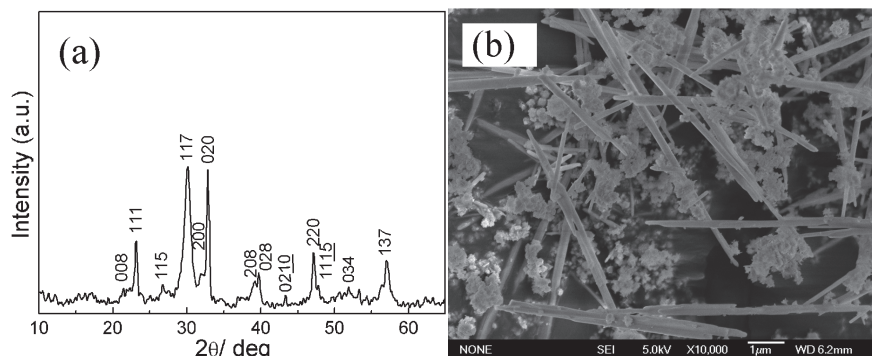


Fig. 11. (a) X-ray diffraction pattern of the as-prepared products composed of randomly oriented BNT nanorods together with small amount of particles. (b) Field emission SEM images of the BNT nanorods.

Figure 12 shows the TEM, HRTEM image, energy-dispersive X-ray analysis (EDS, inset in Figure 2a) and SAED pattern (inset in Figure 2c) of BNT single nanorods. As exhibited in Figure 12a and 2b, the as-synthesized nanorods have diameters of 30~120 nm and with smooth surface and uniform cross section along their length. And EDS shows the presence of Bi, Ti, Nd and O. The HRTEM image in Figure 12c shows the clear lattice fringes, which indicates the BNT nanorods are structurally uniform with well crystallized. The adjacent lattice spacing is 0.325 nm, which corresponds to the  $(00\bar{1}0)$  crystal planes, confirming that  $[104]$  is the preferred growth direction of the BNT nanorods. The SAED pattern shows clear diffraction spots characteristic of crystalline BNT, which confirm the single-crystalline nature of these nanorods. The SAED pattern shows clear diffraction spots characteristic of crystalline BNT obtained from the region of single nanorod, which suggests that the BNT nanorod has orthorhombic structure and single-crystalline in nature.

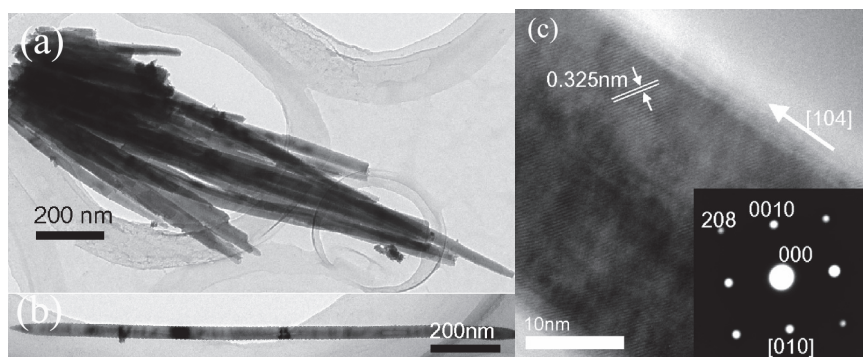


Fig. 12. (a) TEM image of the BNT nanorods; the inset is EDS spectrum of nanorods showing four elements of Bi, Ti, Nd and O. (b) The TEM image of individual BNT nanorod. (c) The HRTEM image of a single-crystal BNT nanorod and its corresponding SAED pattern (inset).

#### 4.2 Raman spectroscopy of BiT NRs

Figure 13 illustrates the Raman spectra obtained from the BNT nanorods, with a spectrum from BIT powders for comparison. One can see that ten Raman active modes (indicated by black arrows) were observed for orthorhombic phase BNT nanorods. The number of modes cannot fulfill the selection rule, which may be due to the broken symmetry, mode overdamping, and mode overlapping, making some modes unidentified (Yau et al., 2004).

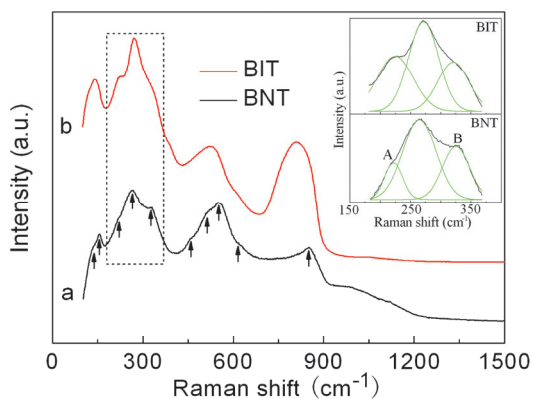


Fig. 13. Raman scattering spectrum of the BNT nanorods with the comparison of BIT samples was measured at room temperature at an excitation wavelength of 514.5 nm. The inset shows the comparison of three peaks prominently at about 220, 265 and 320  $\text{cm}^{-1}$  between BNT nanorods and BIT samples, the solid line is the original experimental data and the dashed lines are the Gaussian fitted curves.

Comparing with the Raman spectrum of BIT powders, most modes of the BNT nanorods are overdamped and highly shifted. The splitting of the mode at about 550  $\text{cm}^{-1}$  ( $B_{2g}/B_{3g}$ ) in BIT powders into two well-defined modes (510 and 552  $\text{cm}^{-1}$ ) in BNT nanorods suggests a

symmetry breaking effect. It has been reported that Raman modes from about  $121.6\text{ cm}^{-1}$  to the one above  $600\text{ cm}^{-1}$  of BIT films were all corresponding to the vibrations inside the perovskite-like slab (Yao et al., 2004). In our case, the first two modes at about  $130$  and  $155\text{ cm}^{-1}$  for BNT nanorods could be assigned to the outer vibration modes between Bi atoms and octahedron, which are upshifted and with a decrease in intensities compare to BIT. A mode at about  $220\text{ cm}^{-1}$  ( $B_{2g}+B_{3g}$ ) is due to the  $x(y)$  axis vibration of oxygen atoms, which is highly overdamped with Nd incorporated into the A site of the perovskite slab compared to that of BIT powders. The internal mode at about  $265\text{ cm}^{-1}$  ( $B_{2g}+B_{3g}$ ) is for internal angle bending vibration; the one at  $320\text{ cm}^{-1}$  ( $A_{1g}$ ) is for a combination of stretching and bending according to the literature (Kojima et al., 1994). The Gaussian fitted Raman spectra [dashed line inset of Figure 13] of the most intensive peaks in the Raman spectra gives the differences between BNT nanorods and BIT powders. Comparing to the Raman modes of BIT powders, the intensity of the shoulder peak of lower frequency (denoted by "A") decreased and the higher (denoted by "B") increased, and the full width at half maximum of these two peaks decreased as Nd doped in BIT, which may be due to the stretching of the Ti-O bonds in  $x(y)$  lattice plane according to the XRD results. In addition, the mode at about  $552\text{ cm}^{-1}$  with its shoulder ( $510\text{ cm}^{-1}$ ) and  $850\text{ cm}^{-1}$  ( $A_{1g}$ ) of BNT are corresponding to the distortion of the  $\text{TiO}_6$  octahedron of perovskite unit ( $\text{Bi}_2\text{Ti}_3\text{O}_{10}$ )<sup>2-</sup> slab (Yao et al., 2004). The internal mode at about  $615\text{ cm}^{-1}$  could derive from the stretching of the O-Ti-O-Ti-O-Ti-O octahedral chain between two  $\text{Bi}_2\text{O}_2$  layers. Nevertheless, the Raman intensity of the  $850\text{ cm}^{-1}$  mode is lower than that of BIT, which indicates that the internal vibration of  $\text{TiO}_6$  octahedrons decrease as Nd doped into BIT.

### 4.3 XPS analysis of BiT NRs

Figure 14 show the narrow scan XPS spectra of BNT nanorods. It can be seen clearly that the nanorods are consisted of four elements Bi, Ti, Nd, and O, which are agreeing with the EDS results. Figure 14a is the photoemission spectrum of  $\text{Bi}4f$  core level peak, which show two sets of spin-orbit doublet components peaking at about  $158.5$  and  $163.8\text{ eV}$ , with a typical  $\text{Bi}4f$  spin-orbit splitting of  $5.3\text{ eV}$  closed to the value of  $5.4\text{ eV}$  for BIT samples, and  $5.3\text{ eV}$  for  $\text{Bi}_{4-x}\text{La}_x\text{Ti}_3\text{O}_{12}$  (BLT) (Jovalekic et al., 1998 and Chu et al., 2002). In addition, the spin-orbit doublet with weak intensities emerge in the spectrum overlapping with the major  $\text{Bi}4f$  photoemission at the high BE side fitted by Gaussian function. The peak positions of lower BE components located at  $155.8$  and  $160.5\text{ eV}$ , show a chemical shift of  $2.7$  and  $3.3\text{ eV}$  with respect to the main peaks, respectively. These are consistent with the typical value of  $3.0\pm 0.1\text{ eV}$  between  $\text{Bi}^0$  and  $\text{Bi}_2\text{O}_3$  (Kim et al., 2003), indicated the possibility appearance of  $\text{Bi}^{+3-x}$  at the surface of BNT nanorods with only several monolayers, which may be due to a deficiency in oxygen and an enhanced concentration of oxygen vacancies in the vicinity of bismuth cations, either in the perovskite lattice structure or in the  $\text{Bi}_2\text{O}_2$  layer (Jovalekic et al., 1998). The XPS narrow scan spectrum of  $\text{Bi}4d$  and  $\text{Ti}2p$  core level is shown in Figure 14b. For BNT nanorods, the  $\text{Ti}2p_{3/2}$  photoelectron peak occurred in the XPS spectrum as a distinctively resolved feature located at a BE position of about  $457.8\text{ eV}$ , which is lower than the BLT of  $461.38\text{ eV}$ , but is very closed to the  $\text{PbTiO}_3$  ceramics of  $457.9\text{ eV}$  (Kim et al., 2003). This indicates the  $4+$  valence state of the titanium atoms within the perovskite layer of bismuth titanate, which supports our assumption about the oxygen vacancies residing inside the  $\text{Bi}_2\text{O}_2$  layer. The  $\text{Ti}2p_{1/2}$  photoemission is overlapped by the  $\text{Bi}4d_{3/2}$  core level peak located at  $465.1$  and  $465.2\text{ eV}$  respectively. The spin-orbit splitting of  $\text{Ti}2p$  is  $7.3\text{ eV}$  larger than the corresponding value of  $5.7$

eV for BLT (Chu et al., 2002), which may be due to the lattice shrinking derived from the size-effect of BNT nanorods. Figure 14c exhibits the photoemission spectrum of Nd4*d* core level peak. Only one component located at 121 eV was detected for BNT nanorods, suggests Nd-O bond is stable in the crystal. Figure 14d shows the XPS narrow scan spectrum of O1*s* core level peak. The lineshape of the O1*s* photoemission reveals three peaks fitted by Gaussian-based function. It has been reported that the oxygen atom in a stronger Ti-O bond carries a higher effective negative charge than in a weaker Bi-O bond. Hence, the first one located at 529.7 eV was assigned to the lattice oxygen of Ti-O bonds in the BNT nanorods, while the second one located at 532 eV was assigned to the oxygen of Bi-O bonds. The third one located at 533.5 eV could be ascribed to OH groups likely to be present on the surface of the grains, which are very common in samples with high surface energy.

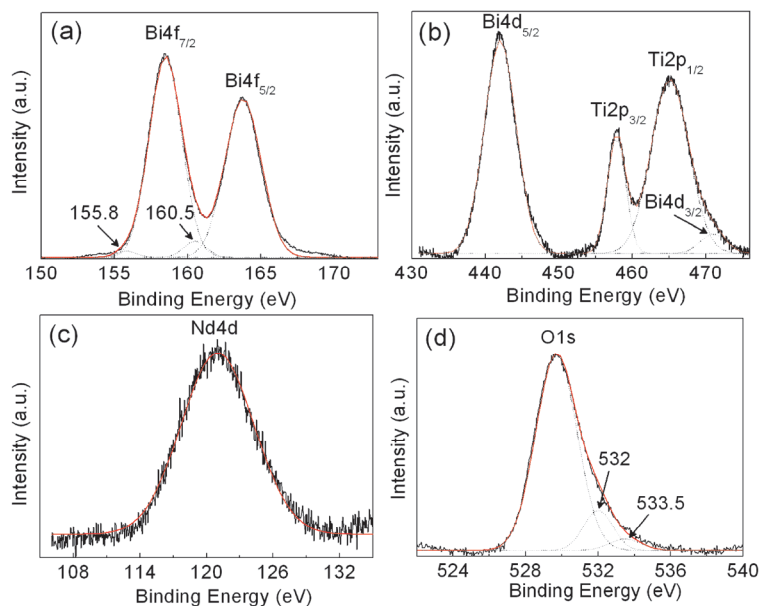


Fig. 14. Core level photoemission spectra of BNT nanorods: (a) Bi4*f*; (b) Bi4*d* and Ti2*p*; (c) Nd4*d*; (d) O1*s*, respectively.

## 5. Conclusion

1-D perovskite ferroelectric nanomaterials of (K,Na)NbO<sub>3</sub> and Bi<sub>4</sub>Ti<sub>3</sub>O<sub>12</sub> nanowires/nanorods with certain orientations were synthesized by hydrothermal approach. The anisotropic growth of (K,Na)NbO<sub>3</sub> nanowires was dependent on its tetragonal structures, while it's not the case for the growth of 1-D Bi<sub>4</sub>Ti<sub>3</sub>O<sub>12</sub> nanomaterials, which should be determined by the difference of surface energy derived from the existence of surfactants. The (K,Na)NbO<sub>3</sub> nanorods were composed of larger amounts of nanoplates with the same orientation, which indicated that the nanorods formed due to the oriented attachment growth. Moreover, the formation of the step-like particles should be due to the aggregation growth. The polarization, piezoelectricity and mechanical-electric properties are

forthcoming. These nanowires/ nanorods may be promising candidate for future nanoscale ferroelectric sensors or other functional nanodevices etc.

## 6. Acknowledgment

Financial support for this work was provided by the National Natural Science Foundation of China (Grant 90923013, 50902046 and 50872031), the Natural Science Foundation of Hubei Province of China (2009CDB085), and International Cooperation Project of Wuhan City (201070934340).

## 7. References

- Araujo, C.A.; Cuhair, J.D.; McMillan, L.D.; et al. (1995). Fatigue-free ferroelectric capacitors with platinum electrodes. *Nature* Vol.374, p. 627-629
- Bhalla, A.S.; Guo, R.; Roy, R. (2000). The perovskite structure – a review of its role in ceramic science and technology. *Materials Research Innovations*, Vol.4, No.1, p. 3-26.
- Blomqvist, M.; Khartsev, S.; Grishin, A.; et al. (2003). Optical waveguiding in magnetron-sputtered  $\text{Na}_{0.5}\text{K}_{0.5}\text{NbO}_3$  thin films on sapphire substrates. *Applied Physics Letters*, Vol.82, No.3, p. 439-441
- Choucair, M.; Thordarson, P.; Stride, J.A. (2009). Gram-scale production of graphene based on solvothermal synthesis and sonication. *Nature Nanotechnology* Vol.4, p. 30-33
- Chang, Y.F.; Yang, Z.P.; Dong, M.Y.; et al. (2009). Phase structure, morphology, and Raman characteristics of  $\text{NaNbO}_3$  particles synthesized by different methods. *Materials Research Bulletin*, Vol.44, No.3, p. 538-542
- Chu, M.W.; Ganne, M.; Galdes, M.T.; Brohan, L. (2002). X-ray photoelectron spectroscopy and high resolution electron microscopy studies of Aurivillius compounds:  $\text{Bi}_{4-x}\text{La}_x\text{Ti}_3\text{O}_{12}$  ( $x=0, 0.5, 0.75, 1.0, 1.5,$  and  $2.0$ ). *Journal of Applied Physics*, Vol.91, No.5, p. 3178-3187
- Goh, G.K.L.; Lange, F.F; Haile, S.M.; Levi, C.G.J. (2003). Hydrothermal synthesis of  $\text{KNbO}_3$  and  $\text{NaNbO}_3$  powders. *Journal of Materials Research*, Vol.18, 338-345
- Guo, Y.P.; Luo, H.S.; Ling, D.; et al. (2003). The phase transition sequence and the location of the morphotropic phase boundary region in  $(1-x)\text{PbMg}_{1/3}\text{Nb}_{2/3}\text{O}_3$ -  $x\text{PbTiO}_3$  single crystal. *Journal of Physics: Condensed Matter*, Vol.15, No.2, p.L77-L82
- Hayashi, H.; Hakuta, Y.; Kurata, Y.J. (2005). Hydrothermal synthesis of potassium niobate photocatalysts under subcritical and supercritical water conditions. *Journal of Materials Chemistry*, Vol.14, No.13, p. 2046-2051
- Heath, J.R.; Legoues, F.K. (1993). A liquid solution synthesis of single crystal germanium quantum wires. *Chemical Physics Letters*, Vol.208, No.3-4, p. 263-268
- Hu, Y.M.; Gu, H.S.; Zhou, D.; et al. (2010). Orientation-Control Synthesis of  $\text{KTA}_{0.25}\text{Nb}_{0.75}\text{O}_3$  Nanorods. *Journal of America Ceramic Society*, Vol.93, No.3, p. 609-613
- Hu, Y.M.; Gu, H.S.; Hu, Z.L.; et al. (2008). Controllable Hydrothermal Synthesis of  $\text{KTA}_{1-x}\text{Nb}_x\text{O}_3$  Nanostructures with Various Morphologies and Their Growth Mechanisms. *Crystal Growth & Design*, Vol.8, No.3, p. 832-837
- Hu, C.; Xi, Y.; Liu, H.; Wang, Z.L. (2009). Composite-hydroxide-mediated approach as a general methodology for synthesizing nanostructures. *Journal of Materials Chemistry*, Vol.19, No.7, p. 858-868

- Hu, Z.; Gu, H.; Hu, Y.; et al. (2009). Microstructural, Raman and XPS properties of single-crystalline  $\text{Bi}_{3.15}\text{Nd}_{0.85}\text{Ti}_3\text{O}_{12}$  nanorods. *Materials Chemistry and Physics*, Vol.113, No.1, p. 42-45
- Im, B.; Joshi, U.A.; Lee, K.H.; et al. (2010). Growth of single crystalline barium titanate nanowires from  $\text{TiO}_2$  seeds deposited on conducting glass. *Nanotechnology*, Vol.21, No.42, p. 425601
- Jaeger, R.E.; Egerton, L. (1962). Hot pressing of potassium-sodium niobates. *Journal of American Ceramic Society*, Vol.45, No.5, p. 209-213
- Jehng, J.M.; Wachs, I.E. (1991). Structural chemistry and Raman spectra of niobium oxides. *Chemistry of Materials*, Vol.3, No.1, p. 100-107
- Jovalekic, C.; Pavlovic, M.; Osmokrovic, P.; Atanasoska, L. (1998). X-ray photoelectron spectroscopy study of  $\text{Bi}_4\text{Ti}_3\text{O}_{12}$  ferroelectric ceramics. *Applied Physics Letters*, Vol.72, No.9, p. 1051-1053
- Kojima, S.; Imaizumi, R.; Hamazaki, S.; Takashige, M. (1994). Raman scattering study of bismuth layer-structure ferroelectric. *Japanese Journal of Applied Physics*, Vol.33, p. 5559-5564
- Katiyar, R.S.; Jain, M.; Yuzyuk, Y.I. (2004). Raman Spectroscopy of Bulk and Thin-Layer (Ba,Sr)TiO<sub>3</sub> Ferroelectrics. *Ferroelectrics*, Vol.303, p. 699-705
- Kim, J.N.; Shin, K.S.; Park, B.O.; et al. (2003). Characterization of ferroelectric ceramics using x-ray diffraction, transmission electron microscopy, and x-ray photoelectron spectroscopy. *Smart Materials Structures*, Vol.12, No.4, p. 565-569
- Lao, C.S.; Kuang, Q.; Wang, Z.L.; et al. (2007). Polymer functionalized piezoelectric-FET as humidity/ chemical nanosensors. *Applied Physics Letters*, Vol.90, p. 262107
- Lee, S.K.; Hesse, D.; Gosele, U. (2006). Growth and properties of (104)-oriented ferroelectric Nd-substituted  $\text{Bi}_4\text{Ti}_3\text{O}_{12}$  films on Si (100) using (111)-oriented  $\text{SrRuO}_3/\text{Pt}$  electrodes. *Applied Physics Letters*, Vol.88, p. 062909
- Liu, H.; Hu, C.; Wang, Z.L. (2006). Composite-Hydroxide-Mediated Approach for the Synthesis of Nanostructures of Complex Functional-Oxides. *Nano Letters*, Vol.6, No.7, p. 1535-1540
- Lu, C.H.; Lo, S.Y.; Wang, Y.L. (2002). Glycothermal preparation of potassium niobate ceramics particles under supercritical conditions. *Materials Letters*, Vol.55, No.1-2, p. 121-125
- Magrez, A.; Vasco, E.; Seo, J.W.; et al (2006). Growth of Single-Crystalline  $\text{KNbO}_3$  Nanostructures. *Journal of Physics Chemical B*, Vol.110, No.1, p. 58-61
- Mao, Y.; Park, T.J.; Wong, S.S. (2005). Synthesis of classes of ternary metal oxide nanostructures. *Chemistry Communication*, No.46, p. 5721-5735
- Park, B.H.; Kang, B.S.; Bu, S.D.; et al. (1999). Lanthanum-substituted bismuth titanate for use in non-volatile memories. *Nature*, Vol.401, p. 682-684
- Puntes, V.F.; Krishnan, K.M.; Alivisatos, A.P. (2001). Colloidal Nanocrystal Shape and Size control: The Case of Cobalt. *Science*, Vol.291, p. 2115-2117
- Ravindranathan, P.; Komarneni, S.; Bhalla, A.S.; Roy, R. (1991). Synthesis and dielectric properties of solution sol-gel derived  $0.9(\text{Mg}_{1/3}\text{Nb}_{2/3})\text{O}_3\text{-}0.1\text{PbTiO}_3$  ceramics. *Journal of American Ceramic Society*, Vol.74, No.12, p. 2996-2999
- Ross, S.D. (1970). The vibrational spectra of lithium niobate, barium sodium niobate and barium sodium tantalite. *Journal of Physics C: Solid State Physics*, Vol.3, No.8, p.1785

- Rørvik, P.M.; Almlı, Å.; Helvoort, A.T.J.; et al. (2008). PbTiO<sub>3</sub> nanorod arrays grown by self-assembly of nanocrystals. *Nanotechnology*, Vol.19, No.22, p. 225605 (1-6)
- Saito, Y.; Takao, H.; Tani, T.; et al. (2004). Lead-free piezoceramics. *Nature*, Vol.432, p. 84-87
- Scott, J.F. (1998). The physics of ferroelectric ceramic thin films for memory applications. *Ferroelectric Review*, Vol.1, p. 1-30
- Shen, Z.X.; Hu, Z.P.; Chong, T.C.; et al. (1995). Pressure-induced strong mode coupling and phase transitions in KNbO<sub>3</sub>. *Physics Review B*, Vol.52, p. 3976-3980
- Shen, Z.X.; Wang, X.B.; Kuok M.H.; Tang, S.H. (1998). Raman scattering investigations of the antiferroelectric-ferroelectric phase transition of NaNbO<sub>3</sub>. *Journal of Raman Spectroscopy*, Vol.29, No.5, p. 379-384
- Spanier, J.E.; Kolpak, A.M.; Urban, J.J.; et al. (2006). Ferroelectric Phase Transition in Individual Single-Crystalline BaTiO<sub>3</sub> NWs. *Nano Letters*, Vol.6, No.4, p. 735-739
- Sun, X.; Chen, J.; Yu, R. et al. (2009). BiScO<sub>3</sub> doped (Na<sub>0.5</sub>K<sub>0.5</sub>)NbO<sub>3</sub> lead-free piezoelectric ceramics. *Journal of American Ceramic Society*, Vol.92, No.1, p. 130-132.
- Urban, J.J.; Yun, W.S.; Gu, Q.; and Park H. (2002). Synthesis of Single-Crystalline Perovskite Nanorods Composed of Barium Titanate and Strontium Titanate. *Journal of American Chemistry Society*, Vol.124, No.7, p. 1186-1187
- Vayssieres, L.; Keis, K.S.; Lindquist, E.; and Hagfeldt, A. (2001). Purpose-bult anisotropic metal oxide material: 3D highly oriented microrod array of ZnO. *Journal of Physics Chemistry B*, Vol.105, No.17, p. 3350-3352
- Villegas, M.; Caballero, A.C.; Moure, C.; et al. (1999). Low-temperature sintering and electrical properties of chemically w-doped Bi<sub>4</sub>Ti<sub>3</sub>O<sub>12</sub> ceramics. *Journal of the European Ceramic Society*, Vol.19, No.6-7, p. 1183-1186
- Wang, X.D.; Zhou, J.; Song, J.H.; et al. (2006). Piezoelectric field effect transistor and nanoforce sensor based on a single ZnO nanowires. *Nano Letters*, Vol.6, No.12, p. 2768-2772
- Wang, X.D.; Song, J.H.; Liu, J.; Wang, Z.L. (2007). Direct-current nanogenerator driven by ultrasonic waves. *Science*, Vol.316, No.5821, p. 102-105
- Wang, Z.; Gu, H.; Hu, Y.; et al. (2010). Synthesis, growth mechanism and optical properties of (K,Na)NbO<sub>3</sub> nanostructures. *CrystEngComm*, Vol.12, p. 3157-3162
- Wei, N.; Zhang, D.M. ; Han, X.Y.; et al. (2007). Synthesis and mechanism of ferroelectric potassium tantalate niobate nanoparticles by the solvothermal and hydrothermal processes. *Journal of American Ceramics Society*, Vol.90, No.5, p. 1434-1437
- Xie, R.C.; and Shang, J.K. (2007). Morphological control in solvothermal synthesis of titanium oxide. *Jourla of Material Science* Vol.42, No.16, p. 6583-6589
- Xu, G.; Ren, Z.; Du, P.; et al. (2005). Polymer-Assisted Hydrothermal Synthesis of Single-Crystalline Tetragonal Perovskite PbZr<sub>0.52</sub>Ti<sub>0.48</sub>O<sub>3</sub> NWs. *Advanced Materials*, Vol.17, No.7, p. 907-910
- Yau, C.Y.; Palan, R.; Tran, K.; Buchanan, R.C. (2004). Raman study of Bi site-occupancy effect on orientation and polarization in Bi<sub>4</sub>Ti<sub>3</sub>O<sub>12</sub> thin films. *Applied Physics Letters*, Vol.85, No.20, p. 4714-4716
- Zhang, C.; Lv, H.J.; Guo, M.; et al. (2008). Thermodynamic evaluation and hydrothermal preparation of K<sub>x</sub>Na<sub>1-x</sub>NbO<sub>3</sub>. *Rare Metals*, Vol.27, No.4, p. 371-377

# Junction Properties and Applications of ZnO Single Nanowire Based Schottky Diode

Sachindra Nath Das<sup>1</sup>, Jyoti Prakash Kar<sup>2</sup> and Jae-Min Myoung<sup>2</sup>

<sup>1</sup>*Department of Physics, Burdwan Raj College, Burdwan, West Bengal,*

<sup>2</sup>*Department of Material Science and Engineering, Yonsei University, Seoul,*

<sup>1</sup>*India*

<sup>2</sup>*South Korea*

## 1. Introduction

Towards the beginning of 21<sup>st</sup> century, considerable interests have been paid to synthesize low-dimensional nanostructures, such as nanowires, nanorods or nanobelts because of their unique structures with large surface-to-volume ratio. Nanodevice units made from those one-dimensional nanostructures (single nanostructures as well as bunch of nanostructures) have attracted substantial research interests because they provide a unique platform for fundamental investigations. In addition, they can also serve as the building blocks for more complicated nano-systems and micro-systems, for example, sensors, diodes, solar cells, LEDs, nano-generators and transistors (Lee et al., 2010; Zhou et al., 2008). Recently, many successful attempts to develop nano-devices by using different nanostructures have already been described in scientific literatures.

There has been steady progress in demonstrating electrical components made of nanowires, such as field effect transistors, electron field emitters, switches, sensors, etc. The surface of the nanostructures has crucial role in determining the electrical and optoelectronic properties of nano-devices. As the surface-to-volume ratio is very high, the surface states also play a key role on optical absorption, gas sensing, luminescence and other properties. Thus, nanoscale electronic devices have the potential to achieve higher sensitivity and faster response than bulk material. Most of these applications require metal contact to receive and/or transmit electrical signals or to be powered by an external source. So, the devices with nanowires, nanorods or nanobelts, the electrical contacts should be scaled accordingly. Thus, the understanding of transport processes at the nanometer scale is essential for an overall improvement of the device characteristics.

Depending on the Fermi surface alignment and the nature of the interface between the metal and the semiconducting nanowires, the contacts can either be an Ohmic contact or a Schottky contact. Whether a contact is a Schottky or ohmic, depends on the work-function ( $\Phi$ ) of the metal and the semiconducting nanowire and also on the type of majority carriers (electrons or holes). For n-type semiconductor, if the work function of the metal ( $\Phi_M$ ) used for contact is higher than that of the semiconductor ( $\Phi_S$ ), a Schottky barrier will be formed. According to the Schottky-Mott theory, the barrier height ( $\Phi_B$ ) follows the rule ( $\Phi_B = \Phi_M - \chi_S$ ),

where  $\chi_s$  is electron affinity of semiconductor. But, in case of low dimensional system, the Schottky barrier height depends not only on the work functions of the metal and the semiconductor nanowire, but also on the pinning of the Fermi level by surface states, image force lowering, field penetration and the existence of an interfacial insulating layer. To a good approximation, all of these effects change only the absolute current value at very low bias regime via lowering the Schottky barrier. Thus, detailed study on Schottky nanocontacts are important because not only a great number of nanodevices are based on a metal/semiconductor Schottky contact with nanometer dimensions, but also standard electrical spectroscopies, such as deep level transient spectroscopy or photocurrent measurements, need the formation of Schottky contact. Metal/semiconductor Schottky device is also one of the most fundamental one that can be used to evaluate various semiconductor parameters including carrier density and Schottky barrier height as well as carrier density profile and bandgap discontinuity.

In this context, several semiconducting materials, such as GaN, ZnO, and AlGaN, have wide direct bandgaps which make them useful for electronic and optoelectronic applications. Among these materials, growth of vertically aligned single crystalline ZnO nanowires is easier. It is a direct wide bandgap (3.37 eV) piezoelectric material with hexagonal wurtzite structure, and has larger exciton binding energy (60 meV) than other wide bandgap semiconductor (GaN, 25 meV). Moreover, single crystalline nanowires have attracted a lot of interest for the fabrication of nanoelectronic and nanophotonic devices due to their extraordinary properties originated from their high crystallinity and large aspect ratio.

In this chapter, we have described the junction properties of ZnO nanowire based Schottky diodes with different contact metal. Also we have described the UV detection and gas sensing mechanism of single nanowire based Schottky diode which will further promote an understanding of the device physics and practical applications.

## 2. ZnO nanowire

Vertically aligned ZnO nanowires with controlled shape and ordered surface morphology have attracted considerable attentions due to their low dimensional structures and the exciting prospects for utilizing these materials in nanotechnology enabled electronic and photonic crystal device applications (Zhang et al., 2001; Chang et al. 2009). As a wide bandgap (~3.4 eV) semiconductor, ZnO has drawn a great interest for low-voltage and short wavelength optoelectronic devices (Norton et al., 2004). It is expected that in ZnO nanowires, one may eliminate some unwanted properties of bulk ZnO, such as weak exciton emission in comparison with the defect related (deep-level) visible emission, while keeping or enhancing the desirable properties such as large exciton binding energy (60 meV) (Fonoberov et al., 2006).

### 2.1 Nanowire growth

In order to control shape, aspect ratio (length/width), growth site and growth direction of the nanowires, many efforts have been directed towards the synthesis of ZnO nanostructures by aqueous, vapor-liquid-solid (VLS), metal organic chemical vapor deposition (MOCVD) and many other techniques (Kar et al., 2008; 2009; Hsu et al., 2005). However, MOCVD method is of particular interest since it has some advantages such as the

ability to fabricate nanostructures of better quality, well controllable configurations and good reproducibility. As the growth of ZnO nanowires by MOCVD is a bottom-up technique, the nature of substrates has a vital role for the dimension and alignment of the nanowires. According to lattice misfit, the most suitable substrate for ZnO growth is ScAlMgO<sub>4</sub>, which is expensive and technologically inconvenient (Ievtushenko et al., 2008). On the other hand, it is difficult to obtain well-aligned ZnO nanowires on silicon substrates, because the formation of an interfacial layer (SiO<sub>2</sub>) and large lattice misfit (Liou et al., 2005). Interestingly, C-plane sapphire overcomes some of the limitations arising from the above substrates. The ZnO nanowires, used in the experiments, were grown on *c*-plane sapphire substrates without any catalyst by using MOCVD system. Diethyl zinc and high purity oxygen (5N) were used as the Zn and O sources, respectively. The base pressure of the reactor chamber and the working pressure were kept at 10<sup>-6</sup> Torr and 3 Torr, respectively. During the growth, the nozzle-substrate spacing was 1 cm and the substrate temperature was fixed at 700 °C.

## 2.2 Micro-structural and optical property

Fig. 1(a) shows a typical FESEM image of vertically aligned ZnO nanowires (diameter~100 nm) grown on *c*-plane sapphire substrate. The appearance of a prominent (002) peak in XRD pattern (not shown here) confirms the crystalline natures of ZnO nanowires. Fig. 1(b) shows the bright field TEM image of a ZnO nanowire. The diameter of the nanowire is around 100 nm and uniform through out its length. In order to further investigate the structural characteristics of ZnO nanowire, high-resolution transmission electron microscopy (HRTEM) experiment was carried out and the magnified image is shown in the inset of Fig. 1(b). HRTEM images at different part of nanowire indicate that the nanowire is structurally uniform and do not exhibit any noticeable defects. Furthermore, the HRTEM image confirmed that the single crystalline ZnO nanowire is preferentially oriented along the *c*-axis direction with lattice spacing of 0.52 nm. The selective area electron diffraction (SAED) pattern (inset of Fig. 1(b)) also shows that the nanowire exhibits a single crystalline nature. These results are almost consistent with the FESEM observation.

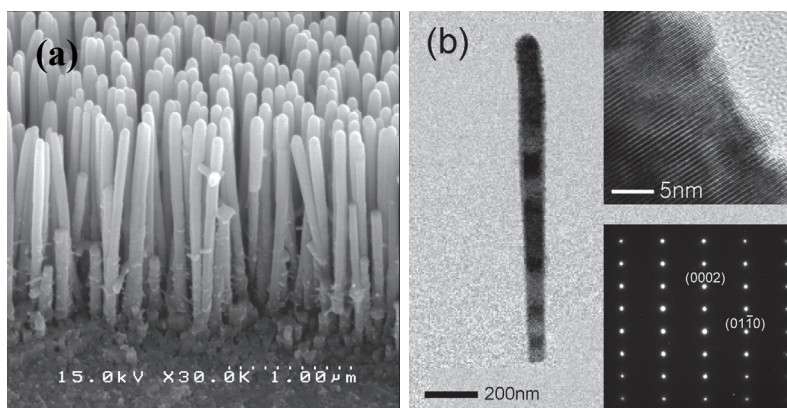


Fig. 1. (a) FESEM images and (b) TEM images of ZnO NR arrays. Inset shows the corresponding HRTEM images and diffraction pattern.

Information such as surface oxygen vacancies and other defects as well as the separation and recombination of photoinduced charge carriers can be obtained from photoluminescence (PL) measurements. Fig. 2 presents the low temperature (10 K) PL spectrum of dispersed ZnO NWs measured with 325 nm He-Cd laser. In our NWs, two strong PL peaks at 382 and 388 nm were found without any visible band emission.

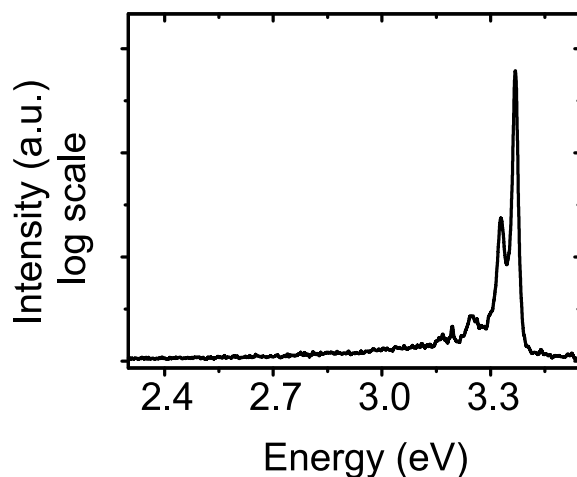


Fig. 2. Photoluminescence spectra (10 K) of ZnO nanowire arrays.

### 3. Junction properties

#### 3.1 Fabrication of single nanowire device

Electrical contacts to individual nanowires were fabricated using a procedure of lithography, metallization and lift-off technique. The nanowires were first removed from the substrate and then dispersed by sonication in isopropanol. A droplet of dispersed solution containing nanowires was then dropped on photo-lithographically pre-assigned metallic micro-pads on the substrate. Thermally oxidized (500 nm) Si wafers were used as substrates for the fabrication of Schottky diodes. The coordinates of several nanowires with respect to the pre-assigned metallic pads were then estimated by using Scanning Electron Microscope (SEM). Finally, the path of electrical connections between the pre-assigned micro-pads and the nanowires were made by e-beam lithography and lift-off techniques. All metals were deposited by Ar plasma assisted DC sputtering at a pressure of 3 mTorr. The contacts were patterned by lift-off of lithographically defined photo-resist.

To form Ohmic contact 100 nm of Ti and 200 nm of Au were successively deposited on one side of the nanowire followed by rapid thermal annealing at 550 °C for 1 min in N<sub>2</sub> atmosphere. In addition, to form Schottky contact metal with higher work function (Au, Pt or Ni) was deposited (300 nm) on the other side of the nanowire. The devices were also fabricated with homogeneous ZnO nanowire and Ti/Au contacts on both sides by using the same experimental procedures and they have shown linear current voltage (*I-V*) characteristics, confirmed the ohmic contacts with ZnO nanowire. The schematic diagram and the FESEM image of single ZnO nanowire based device are shown in Fig. 3 (a) and (b), respectively.

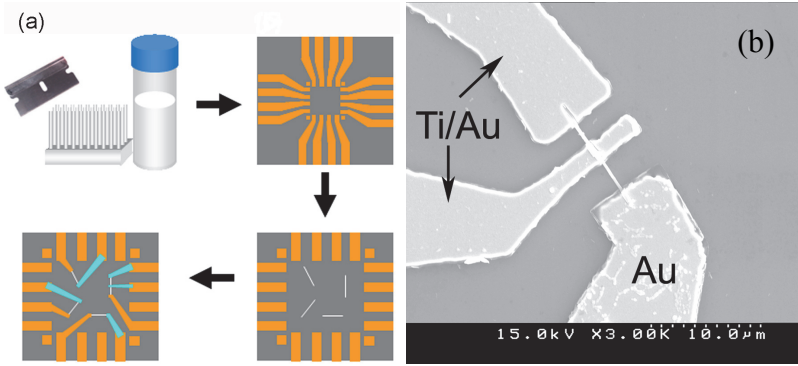


Fig. 3. (a)The schematic diagram and (b) FESEM image of single ZnO NW based device.

### 3.2 Electrical characterization

In case of low dimensional systems, the Schottky barrier height depends not only on the work functions of the metal and the semiconductor nanowire, but also on the pinning of the Fermi level by surface states, image force lowering, field penetration and the existence of an interfacial insulating layer. To a good approximation, all of these effects change only the absolute current value via lowering the Schottky barrier. The temperature dependent  $I$ - $V$  characteristics of Schottky Diodes, fabricated with Au, Pt and Ni metal were investigated and their typical characteristics are shown in Fig. 4 (a), (b) and (c), respectively. It is also found that the  $I$ - $V$  curves are nonlinear, asymmetrical and exhibit clear rectifying behavior for all the measured temperatures. The current under forward bias increases with temperature and shows typical semiconductor characteristics. The electrical characterization of Schottky diode necessitates the determination of the barrier height and the ideality factor. Generally, total current consists of both thermionic emission and tunneling component. Assuming that the thermionic emission is the most predominant mechanism, the general form of the temperature dependence of current may be expressed as (Sze, S.M. 1979):

$$I = AA^*T^2 \exp(-\beta\Phi_B) \exp\left[\frac{\beta(V - IR)}{n}\right] \quad (1)$$

where,  $\Phi_B$  is the effective barrier height,  $A$  is the junction area,  $A^* [A^* = 4\pi qm^*k^2/h^3]$  is the Richardson constant and  $m^*$  is the effective mass of the charge carriers.  $R$  is the series resistance and  $\beta = q/kT$ . For an ideal diode, the diode ideality factor ( $n$ ) should be nearly equal to unity. But in a real situation, it may increase when the effects of series resistance, leakage current etc. come into play. The main difficulty of the thermionic emission theory is that it underestimates the reverse current. But the situation is very different in a nano-system, where the measured forward current is low and is comparable to that of the reverse or leakage current. The tunneling current is therefore not negligible and indeed becomes the dominating mechanism under reverse bias. Also there are inherent difficulties when the base material would offer a considerable series resistance, which would cause a voltage drop across the junction. The current flows according to thermionic emission model only when the ideality factor ( $n$ ) is near unity. With an increase in  $n$ , the barrier height would deviate from the true value. For the large surface-to-volume ratio of the ZnO nanowire, the

surface states and the effective carrier concentration have important influence to the contact barrier. The variation of oxygen and zinc concentration during the growth of the nanowire results in the nonuniform distribution of the defects. A slight inhomogeneity of the surface states and carrier concentration at the two ends of the ZnO nanowire can result in different Schottky barriers. In such a case, generalized Norde method could be used to evaluate the effective barrier height, series resistance, and diode ideality factor ( $n$ ) from  $I$ - $V$  measurement. The values of effective barrier potential and diode ideality factor measured at different temperatures for Au/ $n$ -ZnO/Ti-Au, Ni/ $n$ -ZnO/Ti-Au and Pt/ $n$ -ZnO/Ti-Au Schottky diodes are shown graphically in Fig. 5 (a) and (b), respectively.

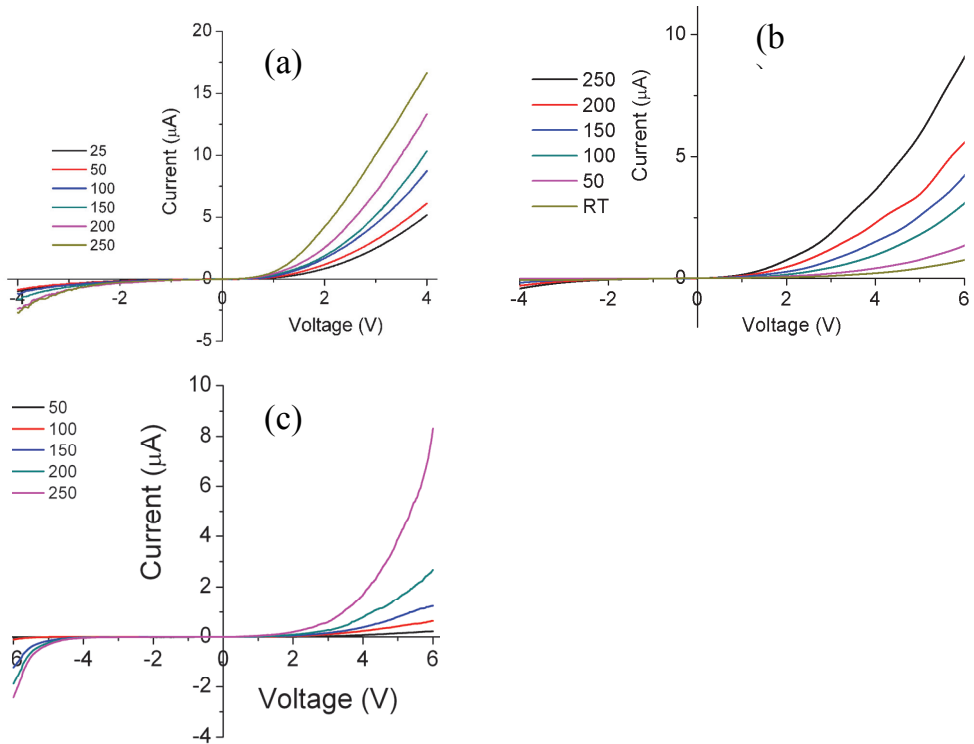


Fig. 4.  $I$ - $V$  characteristics of (a) Au/ $n$ -ZnO, Ni/ $n$ -ZnO and Pt/ $n$ -ZnO Schottky diode measured at different temperature.

The barrier height could be seen to increase with temperature (Fig. 5(a)) almost linearly. Pt offered larger barrier height than that offered by Au and Ni while Au and Ni contacts indicated nearly similar barrier heights. The increase in barrier heights with the increase in temperature from 300 K to 523 K may be associated with the increase in available charge carriers to be transported across the barrier for Fermi level equalization. It is also observed that the values of barrier heights obtained from the  $I$ - $V$  characteristics were lower than those obtained for a thin-film based Schottky diodes. Lower values of barrier height were ascribed to an enhanced electric field at the depletion region due to the small size of the nano-Schottky junction.

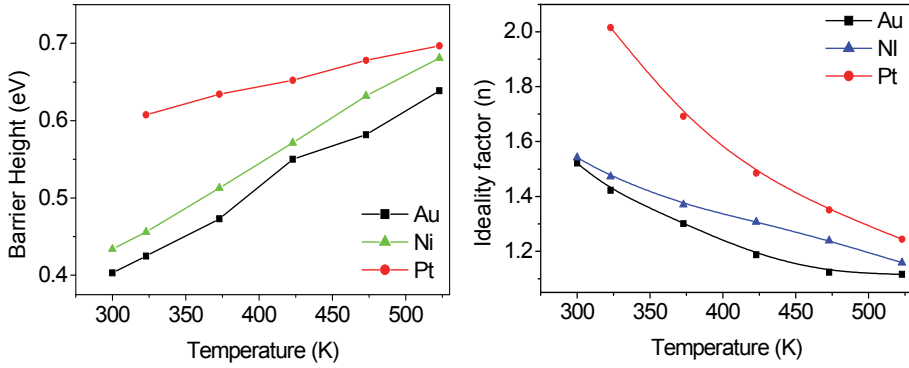


Fig. 5. Variation of (a) barrier height ( $\Phi_B$ ) and (b) ideality factor ( $n$ ) with temperature (K).

Ideality factor for the different Schottky diodes studied here varied between 1.1 and 2.0. Schottky diodes with Au Schottky contact indicated lower ideality factor ( $\sim 1.5$ ) at room temperature than that for Ni and Pt. It may be observed that the ideality factor decreased with increasing temperature. Current transport across the metal semiconductor interface is temperature dependent. Thus, the electrons at low temperature would be able to cross only the lower barriers and therefore current transport will be dominated by current passing through the lower Schottky barrier only contributing to a large ideality factor. With increasing temperature, more and more electrons would acquire significant energy to cross higher barrier. As a result, the effective barrier height will increase with the temperature and bias voltage culminating in lower ideality factor at higher temperature. This increment can be explained by taking into account of the interface state density distribution, quantum mechanical tunneling and image force lowering across the barrier of Schottky diodes.

### 3.3 XPS studies

In order to further confirm the barrier-height value of nanowire Schottky diodes, XPS is used to study the surface Fermi level position within the band gap for metallic overlayer on ZnO nanowire. Each element has a characteristic binding energy for its core electrons, and thus each element has a characteristic spectrum. Comparison of the spectrums of a bare specimen, such as ZnO, and a specimen with a thin film coating, such as ZnO/Au, can yield the barrier height of the surface. The barrier height was determined from the XPS data using the following relation (Lin, 2005)

$$q\phi_n = E_G - E_V^i + (E_{core}^i - E_{core}^{Au}) = E_G - (E_{core}^{Au} - E_{VC}) \quad (2)$$

where  $E_G$  is the bandgap of ZnO,  $E_V^i$  is the initial binding energy,  $E_{core}^i$  is the initial binding energy of the core level,  $E_{core}^{Au}$  is the binding energy of the core level with Au over layer and  $E_{VC}$  is equal to  $(E_{core}^i - E_V^i)$ . All the binding energies are compared to  $E_F$ . Fig. 6(a) shows the Zn 3d core level and the valance band spectrum of ZnO nanowires. The value of  $E_{VC}$  is calculated to be 7.53 eV. This is in good agreement with the reported value (Tsai et al. 2009). Fig. 6(b) shows the Zn 3d core level at Au/ZnO nanowire interface. The spectra determine

the Zn 3d binding energy  $E_{core}^{Au}$  (10.48 eV) relative to the  $E_F$ . Therefore, the  $q\Phi_n$  was calculated to be 0.42 eV. This is similar to the value (0.40 eV) obtained from  $I$ - $V$  measurements at 300 K.

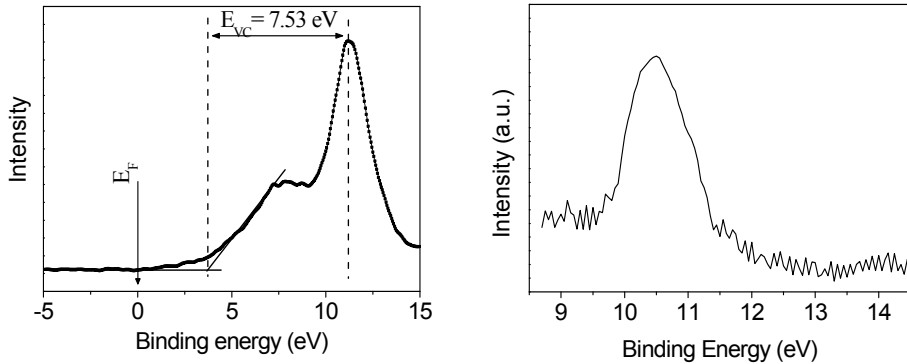


Fig. 6. (a) Zn 3d core level peak of ZnO nanowire without Au over-layer. The low energy region represents the spectrum of valance band region. A linear fit is used to determine the the energy of the valance band edge. (b) Zn 3d core level at the Au/ZnO nanowire interface.

### 3.4 Possible explanation

The deviations of diode ideality factor from unity signify the inhomogeneous nature of the Schottky diodes. Assuming the Gaussian distribution for Schottky barrier height ( $\Phi_{B0}$ ), the apparent barrier height ( $\Phi_{ap}$ ) can be written as (Werner et al., 1991; Bengi et al., 2007).

$$\Phi_{ap} = \Phi_{B0}(T = 0) - \frac{q\sigma_0^2}{2kT} \quad (3)$$

where,  $\sigma_0$  is the measure of the barrier homogeneity. The lower value of  $\sigma_0$  corresponds to more homogeneous barrier height. The value of  $\sigma_0$  obtained for temperatures for Au/ $n$ -ZnO/Ti-Au, Ni/ $n$ -ZnO/Ti-Au and Pt/ $n$ -ZnO/Ti-Au Schottky diodes are (from Fig. (7)) 0.112 V, 0.112V and 0.102 V, respectively. The values are quite low but not negligible compared to the apparent barrier height. Considering Au/ $n$ -ZnO schottky contact for details study, the calculated value of barrier height, obtained from the thermionic emission model and XPS measurement, is lower than the theoretically predicted value ( $q\Phi_B = \Phi_M - \chi_S = 1.2$  eV) and that reported for thin film based Schottky diodes ( $q\Phi_B = 0.7$ - $0.9$  eV) (Angadi et al., 2007; Coppa et al., 2003; Dhananjay et al., 2007). This discrepancy is partly due to the effects of tunneling, image force lowering on the conduction process, surface defect states, barrier height inhomogeneities and moreover Fermi level pinning in nanowires. In addition, edge leakage current due to a high electric field at the metal contact periphery or interface current due to traps at the metal semiconductor interface also affect the barrier height. Other effects due to interface oxide layer between the Ti/ZnO contacts may also contribute to such deviations.

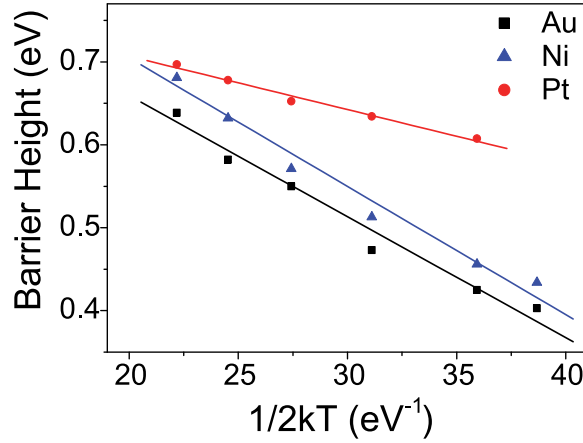


Fig. 7. Plot of  $\Phi_{np}$  versus  $1/2kT$ .

In order to understand the lowering in Schottky barrier height, we also have to know the electronic transport mechanism, which can be deduced from temperature dependent  $I$ - $V$  characteristics. In the presence of tunneling,  $I$  can be written as (Sze, S. M. 1979; Lin Y. J., 2005)

$$I = I_0 \exp\left(\frac{eV}{E_0}\right) \quad (4)$$

where the saturation current ( $I_0$ ) is given by

$$I_0 = \frac{AA^* [\pi E_{00} q (\varphi_B - V - \xi)]^{0.5}}{k_B \cosh(E_{00}/k_B T)} \exp\left(-\frac{e\xi}{k_B T} - \frac{e(\varphi_B - \xi)}{E_0}\right) \quad (5)$$

In equation (5)  $\xi$ , [=  $(E_C - E_F)/q$  = (0.2 V)] obtained from ultraviolet photoelectron spectroscopy (UPS) measurement (not shown here), is the difference between the conduction band minimum and the position of the Fermi level,  $E_0 = E_{00} \coth(E_{00}/k_B T)$  is the characteristic energy related to the tunneling probability and  $E_{00}$  is the tunneling parameter. In our case,  $E_{00}$  is 50 and 60 meV at 300 and 523 K, respectively, which is about 2 times higher than the thermal energy (25 and 43 meV at 300 and 523 K, respectively). As the temperature increases, the thermionic emission increases but the tunneling process is temperature insensitive. This result clearly supports that tunneling has a significant role at the forward current and thermionic-field emission (TFE) process is the main mechanism in Au/ZnO nanowire Schottky diode.

Although the image force lowering ( $\Delta\Phi_B$ ), ascribed for enhanced electric field at the depletion region due to small size of the nano-Schottky junction, contributes to the barrier height reduction, the tunneling effect is also significant for nanocontact. But, only the image force lowering ( $\Delta\Phi_B=0.06$  V, considering  $\epsilon_s=2\epsilon_0$  and electric field at nanocontact =  $10^4$  V/cm), inhomogeneity in barrier height ( $\Delta\Phi_B=0.11$  V) and tunneling are not enough to explain the difference between the theoretically predicted value and obtained experimental result. The

surface states play a key role on luminescence and optical absorption properties when the surface-to-volume ratio is high. The states, inside the bandgap, are formed on the ZnO surface due to Zn or O termination, dangling bonds, surface reconstruction or relaxation, structural and point defects, etc. When the diameter of nanowires becomes more than 30 nm, surface states also remain active. However, their relative contribution to the emission spectrum is small in comparison to the contribution originating from the grain volume. To explain this discrepancy, one may consider the effect of defect states at ZnO nanowire surface. But in that case, high density of defect states are required which is inconsistent with the small reverse leakage current in the device and observed photoluminescence property of our as deposited nanowire arrays (Das et al., 2009).

Generally, the band level alignment can be organized in two regimes: Fermi level pinning and vacuum level alignment (i.e. the Schottky-Mott limit). For nanowires, in absence of the metal, there is vacuum level alignment at the nanowire and air interface. But, the band alignment and Fermi level pinning at the metal/nanowire interface is markedly different when the metal over-layer is present. In presence of metal over-layer, due to pinning, the significant value of  $\Delta\Phi_B$  must be caused by some charge transfer. Bearing in mind the large charge transfer distance, the absolute magnitude of the transferred charge could be comparably small to yield the necessary shift of the levels. Thus, we propose that the interface states can be ionized by injected hot electrons which result in the emptying the interface. This ionization of interface states changes the Fermi level so that it effectively behaves like a small forward bias and hence the band bending as well as Schottky barrier height decreases. Fig. 8 shows the schematic band diagram of Au/ZnO nanowire Schottky diode under zero bias and a forward bias voltage. The experimental identification of tunneling, thermionic emission and other components for barrier height lowering predicts that the Fermi level deepening at Au-ZnO nanowire interface may originate from the ionization of interface states by injected hot electrons.

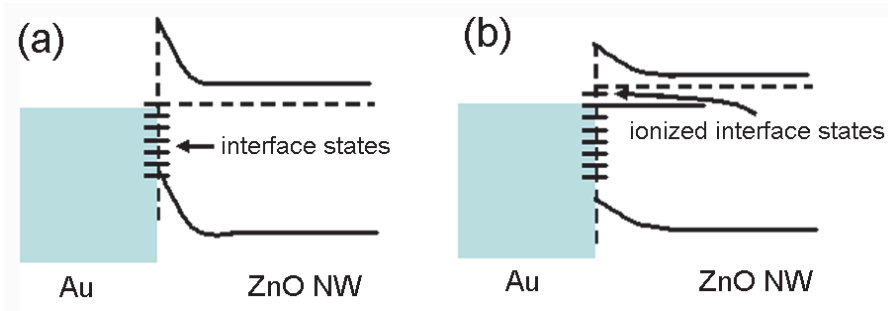


Fig. 8. Schematic band diagram of Au/ZnO NW Schottky diode (a) under zero bias and (b) with a forward bias.

## 4. Application

### 4.1 UV detector

A nanodevice unit made from single one-dimensional (1D) nanostructure, such as nanowire or nanobelt, attracts substantial research interests because it can provide a unique platform for fundamental investigations and also can serve as the building block for more

complicated device systems in nano- and microscale, for example, sensors, diodes and transistors (Lee et al., 2010; Zhou et al., 2008). Surface plays a crucial role to determine the electrical and optoelectronic properties of materials with a dimension of nanometer scale. There are several wide bandgap semiconducting materials for UV detection like GaN, ZnO, AlGaN (Munoz et al., 2001; Soci et al., 2007; Li et al., 2009). Because of their wide bandgap and high surface-to-volume ratio, nanoscale electronic devices have the potential to achieve high sensitivity and faster response for the UV detection. For a good UV detector, the growth of single crystalline ZnO nanowire is important. ZnO nanowires obtained from MOCVD technique shows a very good crystalline and optical property. As shown in Fig. (2), nanowires grown by MOCVD technique have two strong PL peaks at 382 and 388 nm, without any visible band emission. The sharp peaks presumably resulted from the excitons. Strong UV luminescence of free exciton recombination without any visible band emission is suitable for the UV laser device and visible blind UV detectors.

In past few years, enormous studies on UV detection have been conducted using ZnO nanowires, which were either fabricated with ohmic or Schottky contacts. However, most of these works are focused on the array of ZnO nanowires with few studies directed at the single nanowire (Li et al., 2009; Heo et al., 2004; Xu et al., 2006). In literature, it has been reported that single nanowires devices with both ohmic and Schottky contact have similar UV response characteristics even though the sensing mechanisms are different. The UV detection characteristics of Au/ZnO nanowire Schottky diode and the device with both side ohmic contacts were studied by measuring current-voltage ( $I$ - $V$ ) relationships with and without UV light (352 nm) (Fig. 9a). In the dark,  $I$ - $V$  curve is asymmetric for the device with Schottky contact and linear for the device with both sides ohmic contact (inset). The nonlinearity of the  $I$ - $V$  curve is caused by the Schottky barrier formed between the semiconductor and metal electrodes. For both devices,  $I$  increase with UV illumination.

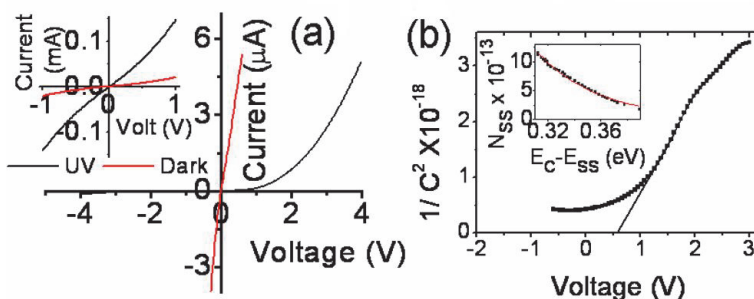


Fig. 9. (a)  $I$ - $V$  characteristics for a representative Au/ZnO nanowire Schottky diode before and after UV illumination. The inset shows the  $I$ - $V$  characteristics of a device with both side ohmic contacts. (b) Plot of  $(1/C^2)$  with  $V$  for Au/ZnO nanowires Schottky diode. The inset shows the density of interface states as a function of interface state energy ( $E_c - E_{ss}$ ).

To test the reversibility of the sensor, the device was alternatively exposed to UV light and the corresponding current at a particular voltage (0.7 V and 0.3 V for the devices with both side ohmic contact and one side Schottky contact, respectively) was measured. For high-power UV illumination (25 mW/cm<sup>2</sup>), we have observed similar characteristics (sharp rise and sharp fall) for the devices with both sides ohmic and one side Schottky contact (not

shown here). But for low-power UV illumination ( $1.5 \text{ mW/cm}^2$ ), Figs. 10 (a) and (b) show the effect of NW surface and Schottky barrier, respectively. Figure 10 (b) shows the photoresponse of the Schottky diode under the UV excitation at a forward bias of 0.3 V. The dark current was about 120 nA and the saturated photocurrent was about  $9 \mu\text{A}$  under UV excitation. On the other hand, the NW device with both side ohmic contacts has the dark and the saturated photocurrent currents about  $0.2 \mu\text{A}$  and  $0.9 \mu\text{A}$ , respectively (Fig. 10 (a)). The photocurrent/dark current ratio is 75 for Schottky diode, which is superior to single NW UV detector (4.5) with both side ohmic contacts. Upon low-power UV excitation, the conductance of the Schottky diode was increased around two orders and to 80% of its saturation value within 1 s. When the UV light is turned off, the conductance was decreased to 85% of its saturation value within 1 s and recovered to its original dark level after 3 s. On the other hand, the device with both side ohmic contacts follows sharp but an exponential rise and exponential decay. It can be noticed that the current is reached almost the same value in each cycle and fully recovered for Schottky diode. But, both the dark and the saturated photo current level for the device with both side ohmic contacts increases with repeated exposure.

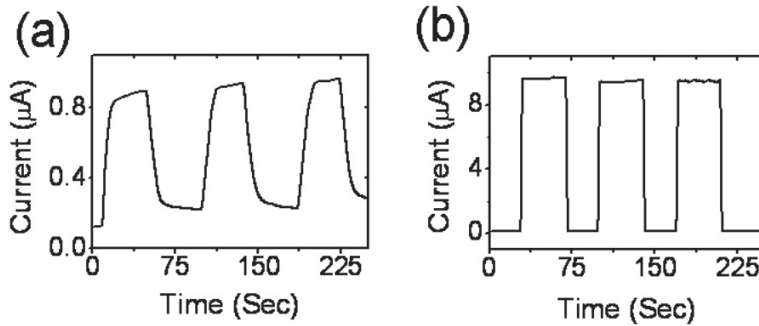


Fig. 10. UV response behaviors of the device with (a) both side ohmic contacts, (b) Schottky contact.

The interface density of states and surface states across the ZnO nanowire and Schottky contact may play a role in UV detection. To calculate the density of states at the interface of the Schottky diode, capacitance due to the depletion region was measured as a function of voltage and shown in Fig 9(b). The capacitance of a Schottky contact is related to the voltage by (Sze S. M., 1979)

$$C^{-2} = \frac{2[\Phi_{bi} - (E_C - E_F) - qV - kT]}{A^2 q \epsilon_s N_d} \quad (6)$$

where  $\Phi_{bi}$  is the barrier height,  $E_c$  is the conduction band edge,  $E_F$  is the Fermi level,  $\epsilon_s$  is the permittivity of the semiconductor,  $A$  is area of contact and  $N_d$  is the carrier concentration. By plotting  $C^{-2}$  vs  $V$  and using eq (6),  $\Phi_{bi}$  and  $N_d$  can be determined from the x-intercept and slope, respectively. The value of  $\Phi_{bi}$  and  $N_d$  was 0.56 V and  $2 \times 10^{17}/\text{cm}^3$ , respectively. The barrier width ( $W$ ) was obtained  $\sim 35 \text{ nm}$  by using 2D Schottky barrier model (Sze S. M., 1979; Rhoderick, E. H., 1988)

$$W = \sqrt{\frac{2\varepsilon_s(\Phi_{bi} + V)}{qN_D}} \quad (7)$$

The  $\Phi_{bi}$  (0.56 V) measured from  $C$ - $V$  characteristics is higher than zero bias  $\Phi_{bi}$  (0.4 V) obtained from temperature dependent  $I$ - $V$  data by using generalized Norde method (Das et al., 2009). This offset is generally attributed to the image force lowering at the interface. Another possible cause to explain this discrepancy is the presence of an interfacial insulating layer. The value of ideality factor ( $n$ ) was obtained 1.5 at 300 K. Generalized Norde's method has utilized the  $I$ - $V$  characteristics in the low voltage region for the determination of the ideality factor and barrier height (Das et al., 2009). But in practice, the  $n$  values evaluated from the  $I$ - $V$  characteristics in the forward bias region show voltage dependence. In such a case, the ideality factor  $n(V)$  is given by (Das et al., 2009)

$$n(V) = 1 + \frac{\delta}{\varepsilon_i} \left[ \frac{\varepsilon_s}{W_D} + qN_{SS}(V) \right] \quad (8)$$

where,  $W_D$  is the space charge width,  $N_{SS}$  is density of states in equilibrium,  $\delta$  is the thickness of the interfacial layer,  $\varepsilon_i$  is the permittivity of interfacial layer. The voltage-dependent ideality factors may be obtained from the slopes of  $\ln(I)$  versus  $V$  plots in the forward bias region. The calculation of the density of surface states is complicated due to interfacial layer as neither  $\varepsilon_i$  nor  $\delta$  is known. By considering  $\delta = 0.5$  nm and  $\varepsilon_i$  as that of free space,  $N_{SS}$  is calculated to be  $6 \times 10^{13}$  cm<sup>-2</sup>eV<sup>-1</sup> at 0.3 V. The energy of the interface states with respect to the bottom of the conduction band at the surface of the semiconductor is given by (Das et al., 2009):

$$E_C - E_{SS} = q(\Phi_e - V) \quad (9)$$

with

$$\Phi_e = \Phi_b + \left( 1 - \frac{1}{n(V)} \right) V \quad (10)$$

Density of interface states as a function of interface state energy ( $E_C - E_{SS}$ ) for Au /ZnO NW Schottky diode is shown in the inset of Fig. 9(b). Exponential rise in the interface state density towards the bottom of the conduction band is very apparent. Low value of interface states signifies that the surface pinning of the Schottky barrier is low. Previously it has been shown that at equilibrium, the ionization of interface state by hot electron reduced the band bending as well as the Schottky barrier height. As the Schottky barrier height changes, a characteristic asymmetric conductance change is expected. Since, the density of surface state ( $6 \times 10^{13}$  cm<sup>-2</sup>eV<sup>-1</sup> at 0.3 V) is not very high and the change in current under the UV illumination is very high, visible light may not affect so much on the current.

The experimental observations on the two types of device structures are explicitly explained using schematics of the energy band diagrams of the nanowire surface and Schottky junction in the dark and under the UV illumination (Fig. 11). In ZnO, it is well known that in the dark oxygen molecules are adsorbed at the surface and capture free electrons and a low-

conductive depletion layer is formed near the surface (Soci et al., 2007). Upon UV illumination with photon energy larger than the semiconductor bandgap, electron-hole pairs are generated; holes migrate to the surface and discharge the negatively charged adsorbed oxygen ions and leaving behind unpaired electrons. Thus, band bending occurs and conductivity of the nanowire increases (Fig. 11 (a)). This hole-trapping mechanism through oxygen adsorption and desorption in ZnO nanowires augments the high density of trap states usually found in nanowires due to the dangling bonds at the surface and thus enhances the photoresponse. In case of single nanowire device, because of the higher exposed surface compared to array of nanowires, trapping at surface states drastically affects the transport and photoconduction property. Soci et al. reported that the oxygen adsorption and desorption at the nanowire surface occur in very short time (ns), suggesting that the desorbed oxygen molecules in air remain in close proximity to the surface and can be promptly re-adsorbed (Soci et al., 2007). This indicates that the oxygen re-adsorption to the surface and consequently the lowering of the photocurrent happen quickly after switching off the UV light; however, full recovery requires longer time, due to the time required for the diffusion of oxygen molecules.

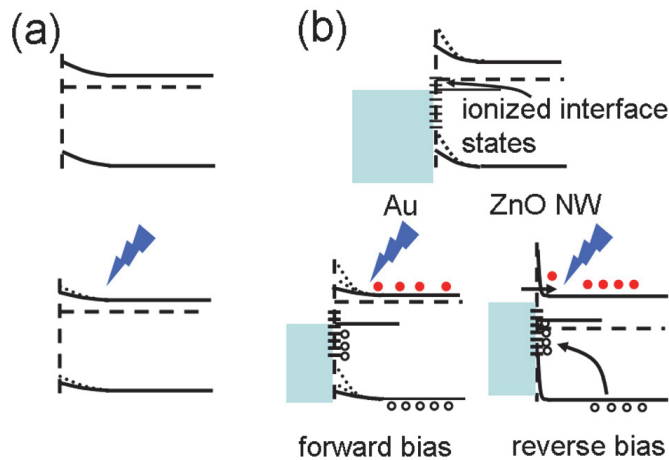


Fig. 11. Energy-level Diagram of (a) ZnO NW surface and (b) Au/ZnO NW interface.

Figure 11(b) shows the UV detection mechanism at the Schottky barrier. In Schottky device, both the forward and reverse current increase with UV exposure. It means that the photoexcited electron-hole pairs can greatly increase the concentration of majority carriers. We can therefore conclude that the barrier height is strongly modulated by the UV exposure. In forward bias, a large number of photogenerated electron-hole pair increases the majority carrier and ionizes the interface states. The ionization of interface states tends to increase the barrier height but, the large number of electron, generated due to the UV illumination, effectively reduces the barrier height under forward bias. As a result, band bending changes and current increases. Interface density of states play an important role in

reverse current. In reverse bias, holes are efficiently trapped by the interface states which shrink the depletion region and allow tunneling of electrons.

#### 4.2 Hydrogen sensor

Hydrogen is a potential source of energy, which may replace the present fossil-based transportation fuels. It is also used as an important reagent in chemical industries. However, it is highly explosive above 4 vol % due to its low flash point (-253 °C) (Christofides et al., 1989). Accordingly, hydrogen leakage detection at early stage is not only necessary but also essential for safety. Solid-state hydrogen sensors based on pure Pt, Pd or Pd-containing alloys have been thoroughly explored as the interaction with hydrogen decreases the work function and increases resistance compared to pure material (Ibanez et al., 2006). Several other materials (SnO<sub>2</sub>, InO<sub>3</sub>, WO<sub>3</sub> and CNT) are currently being investigated for the active materials of sensors (Wang et al., 2006; Li et al., 2007). However, a high operation temperature is generally required for the better performance of the above mentioned sensors. Recently, there have been an increasing number of investigations on the exploration of selective materials to make the sensor more sensitive and reliable. In this concern, tremendous attentions have been focused on ZnO as a gas sensing material due to its high mobility of conduction electrons, good chemical and thermal stability under the operating conditions of sensors (Li et al., 2007; Wan et al., 2004). In addition, single crystalline nature, high mechanical strength, high temperature stability in oxygen ambient and ease of fabrication on several substrates by various techniques (Liao et al., 2008; Wan et al., 2004) are other advantage of ZnO nanostructures.

Single nanowire-based sensors are of particular interest as they can be fabricated by using conventional lithography technique. In addition to low cost and great miniaturization potential, the large surface to volume ratio and nanoscale dimension allow quick diffusion of gases into and from the nanostructure. Thus the rate of reaction increases, which leads to achieve higher sensitivity with faster response and recovery time. Nanoscale sensors also often provide a lower limit of detection due to a larger change in their electronic properties upon surface adsorption.

In case of ZnO nanostructure-based hydrogen sensor, the surface of the nanostructures plays a vital role. In that case, the contacts at the two ends are mostly chosen to be ohmic in order to enhance the change in conductance due to surface effect of the nanostructures. The surface-adsorbed gas molecules modify the electronic surface states and vary the electron concentration which is responsible for the change in conductivity of nanosensors (Liao et al., 2007). At room temperature, electrons released due to gas exposure are very less compared to the electron concentration in nanowire. Therefore, the relative change of conductance before and after gas exposure is small. Since the interaction energy of chemisorbed oxygen atom is large (1-10 eV), metal oxide gas sensors generally require high operating temperature (above 100 °C) to overcome the energy limits and achieve high sensitivity (Fan et al., 2009). However, the high operating temperature adversely affects sensor's reliability, durability and makes the sensors expensive with many complicated heating elements.

In order to improve the sensitivity at room temperature, we deliberately introduce a nonsymmetrical Schottky contact at one end of a ZnO single nanowire based nanodevice.

Here, the surface depletion layer controls the density and mobility of electrons in the nanowire, but the contact barrier controls the transport of electrons between the nanowire and electrode. As the width of the surface depletion is significantly smaller than the diameter of the nanowire, the surface depletion has little influence on the density and mobility of the electrons in the nanowire. However, the change in potential barrier at the Schottky contact greatly modifies the current conduction. The presence of impurities, inconsistencies and asymmetry in structure may alter the effective potential barrier and inhibit the flow of charge carriers, which may change the device characteristics. To solve this problem, defect free nanowires are required. In this communication, we have studied hydrogen-sensing properties of Pt/ZnO nanowire Schottky diodes by measuring current-voltage ( $I$ - $V$ ) relationships at different temperatures.

The sensitivity tests were carried out in a test chamber, where the change in current was measured at a fixed forward voltage (4 V) due to gas exposure. A known amount of highly purified hydrogen was injected from an ampoule along with argon gas acting as a diluting agent to get the required percentage (in ppm) of hydrogen in the measuring chamber. The sensing characteristics were then recorded at different temperatures with various hydrogen concentrations.

The sensitivity is defined as

$$S = \frac{I_G - I_{Ar}}{I_{Ar}} \quad (11)$$

where  $I_G$  and  $I_{Ar}$  are the currents in hydrogen and argon ambient, respectively. The above expression can be used for both the forward and reverse current modes at a fixed voltage. Fig. 12(a) shows the variation of sensitivity with hydrogen concentration at room temperature in the forward bias mode (4 V) for a representative device. One can observe that the sensitivity increases linearly with hydrogen concentration till 2000 ppm, beyond which it increases slowly and tends to saturate.

It seems that due to the increase in hydrogen concentration, more gas molecules are available to be in contact with the device. Thus, one would expect the response to increase up to a certain limit with increase in  $H_2$  concentration as observed here. Afterwards, with the increase in concentration sensitivity tends to saturate. This may be due to a saturation of adsorption of hydrogen atoms at Pt/ZnO nanowire interface and lack of adsorbed oxygen ions at the nanowire surface to react with gas molecules. Consequently, time resolved sensitivity measurement has also been done. Fig. 12 (b) represents the variation of sensitivity with time, measured at room temperature (300 K), when the test gas (hydrogen at 2500 ppm) is introduced in the chamber. It is observed that the maximum sensitivity is obtained within 75 sec. After removal of the test gas, the sensor tends to come back to its initial state and this change is exponential. Sensitivity decreases fast for first 50 seconds and then slowly to its original state. Response time is defined as the time taken for the sensor to reach 90% of the saturation value after gas exposure. The above observation suggests that the response time in these devices is ~55 second. The response time for Pd/nano-GaN Schottky diode reported by Das *et al* (Das *et al.*, 2007) was ~12 min. On the other hand, Rout *et al*<sup>14</sup> have observed a higher response time (~300 sec) by monitoring the change in conductivity due to hydrogen exposure. Thus, the response time of the single nanowire-based Schottky diode, studied here, is superior to those reported recently by other researchers (Das *et al.*, 2007; Rout *et al.*, 2007).

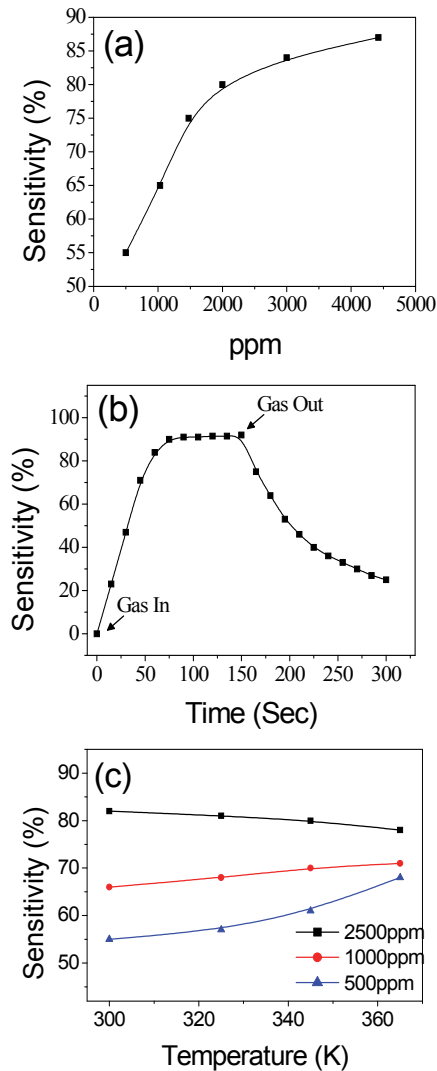


Fig. 12. (a) Variation of sensitivity with hydrogen concentration measured at room temperature in the forward current mode at 4 V. (b) Room temperature response behaviour for 2500 ppm of hydrogen. (c) Temperature dependent sensitivity for three representative hydrogen concentrations.

The contribution of ZnO nanowire surface and Pt/ZnO nanowire Schottky junction to the sensing mechanism was varied with gas concentration and temperature. In order to investigate the detail sensing mechanism, we have measured the sensitivity at different temperatures with different gas concentrations and plotted in Fig. 12(c). The measurements,

reported here, are taken at different temperatures after same interval (60 sec) of gas exposure after the equilibrium has been established. The sensitivity versus operating temperature curve shows a maximum at room temperature for 2500 ppm and decreases very slowly with increasing temperature, whereas it increases slowly but linearly with temperature for hydrogen concentration of 1000 ppm. On the other hand, for lower hydrogen concentration (500 ppm) sensitivity increases slowly up to 323 K. Beyond that appreciable change in sensitivity is observed. This can be explained by the temperature dependent adsorption and desorption process on both the nanowire surface and Schottky junction. Although individual contribution to the sensing mechanism is not distinguishable, but qualitatively one can explain the whole mechanism by considering change in band diagram in two different parts, namely ZnO nanowire surface and ZnO/Pt Schottky junction.

The hydrogen sensing mechanism, investigated in this study, is schematically shown in Fig. 13. Due to the geometry of the devices, the electric field near the junction between the ZnO nanowire and metal is much higher. As a result, the gases around the contact easily dissociate and ionized gases get adsorbed at ZnO/Pt Schottky junction even at room temperature. The change in Schottky barrier height is likely to be the most important for H<sub>2</sub> sensing but ZnO nanowire surface has also a contribution. However, this mechanism would be expected to exhibit a large dependence on the temperature and the concentration of gas around the devices. The sensing mechanism at nanowire surface can be explained in terms of the oxidizing/reducing gas effect. It is well known that the ZnO surface adsorbs oxygen species (O<sub>2</sub>, O<sup>2-</sup>, O<sup>-</sup>) from air by trapping conductive electrons and makes the nanowire more resistive. Moreover, for a ZnO nanowire, high surface to volume ratio provides large number of surface atoms, which can lead to the insufficiency of surface atomic coordination and high surface energy (Liao et al., 2008). Therefore, the surface is highly active, which promotes further adsorption of oxygen from the atmosphere. On the other hand, when the nanowire is exposed to hydrogen environment, the reductive gas decreases the concentration of oxygen species on the nanowire surface, which in fact increases the electron concentration in the nanowire. It should be noted that the chemisorbed oxygen species depend strongly on temperature. Upon exposure to H<sub>2</sub>, it is the chemisorbed surface oxygen ions that participate in the redox reaction preferably at higher temperature (Hudson J.B., 1998). The electrons, released from this process, are responsible for the change in electrical properties of ZnO nanowire through band bending. Thus, at higher temperatures, the nanowire surface will become more active for hydrogen sensing. On the other hand, the characteristic of the nanosensor is largely determined by the behavior at the Schottky junction. The electrical response comes from the variation of the Schottky barrier height and barrier width as a result of adsorption of gaseous species at the Schottky contact. The response due to adsorption can be explained from the band diagram at the metal/ nanowire contact. After the exposure to hydrogen, Pt adsorbs hydrogen by catalytic chemical adsorption. Some of the hydrogen atoms diffuse through the thin metal layer and form a dipole layer at the interface of metal-semiconductor contact, which reduces the Schottky barrier height (Schalwig et al., 2002). Although that may change the barrier width, it is the height of the barrier that matters significantly for charge transport at room temperature. As a result, both the forward and reverse current increases with the increase of the hydrogen concentration. However, the Pt surface gradually saturates with the increase in hydrogen concentration, so the rate of change of current decreases. When the gas ambient switched from hydrogen to air, the oxygen reacted with hydrogen and the resistance of the nanowires changed back to the original value. This is an attractive process for long term application of hydrogen sensor.

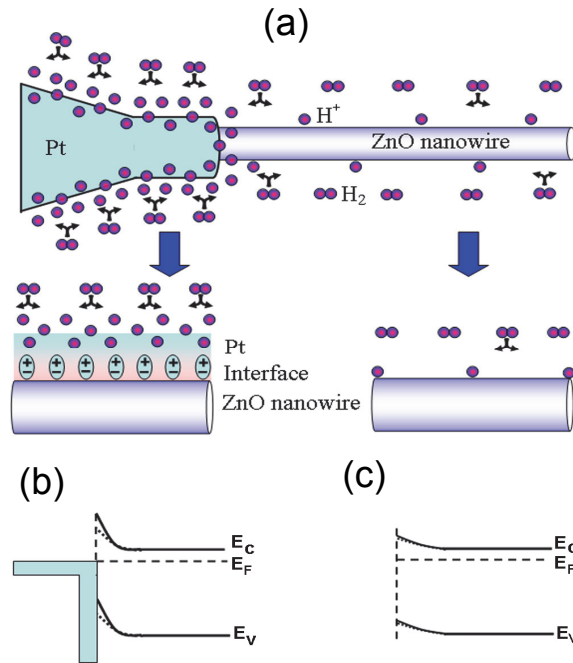


Fig. 13. (a) Schematic diagram of the Pt/ZnO single nanowire hydrogen sensing mechanism. Schematic energy level diagram of (b) Pt/ZnO nanowire interface and (c) ZnO nanowire surface.

The sensitivity depends on the combine effect of operating temperature and the hydrogen concentration. The Schottky barrier height increases with temperature, while it decreases with increase in hydrogen concentration. For higher hydrogen concentration (2500 ppm) the interface becomes saturated even at room temperature. This results a small change (decrease) in barrier height due to further adsorption of hydrogen atom with temperature, but the barrier height of the junction increases. As a result, the sensitivity decreases slowly with increase in temperature. But, for low hydrogen concentration (500 ppm), the interface does not saturate and more hydrogen can be adsorbed with increase in temperature. Thus, the sensitivity increases with increase in temperature for lower hydrogen concentration. Quick response and stability are also important characteristics of sensors. For quick response, the electron-exchange must take place rapidly so that equilibrium is established during measurement. As the Pt/nanowire interface is very small, a thin adsorbed hydrogen layer is formed quickly at the interface, which may block further electron exchange and thus equilibrium occurs. Hence, further increase in hydrogen concentration may eventually saturate the Pt/nanowire interface, which limits further electron-exchange. Thus, the interface of the Pt/ZnO nanowire Schottky device plays a significant role in quick response at room temperature hydrogen sensing.

## 5. Conclusion

In conclusion, Schottky diodes of single nanowire with different metal (Au, Ni and Pt) have been fabricated by e-beam lithography. Detailed I-V characteristics of the Schottky diodes have been investigated at different temperature. The barrier height value and ideality factor at different temperature for different Schottky diodes were obtained from I-V measurements. The calculated barrier height value using generalized Norde method is in good agreement with the value obtained from XPS measurements. However, the calculated barrier height values are lower than theoretical value obtained from Schottky-Mott theory. The effect of tunneling, Fermi level pinning and image force lowering have contribution, but not enough to explain the barrier height lowering. The ionization of interface states by the injected hot electrons result in the emptying the interface states and consequent Fermi-level deepening at metal/semiconductor interface may be the possible reason for low barrier height. The single nanowire Schottky diodes were used for UV detector (Au/ZnO nanowire) and room temperature hydrogen sensor (Pt/ZnO nanowire). The Schottky contact and ZnO surface yield unambiguous information on the UV detection mechanism, particularly in cases where the intensity of UV light is low. In case of Schottky diode, low power UV detection is significant. Hydrogen-sensing behavior of Pt/ZnO nanowire Schottky diode has suggested that it has good sensing characteristic ( $S \approx 90\%$ ) at room temperature with a response time of  $\sim 55$  s. The sensitivity shows a maximum at room temperature for  $H_2$  concentration of 2500 ppm and decreases very slowly with an increase in temperature, whereas it increases slowly with temperature for  $H_2$  concentration of 500 ppm.

## 6. References

- Angadi, B., Park, H. C., Choi, H. W., Choi, J. W. & Choi, W. K. (2007). Oxygen plasma treated epitaxial ZnO thin films for Schottky ultraviolet detection. *J. Phys. D: Appl. Phys.*, Vol.40, pp. 1422.
- Bengi, A., Altmal, S., Ozcelik, S. & Mammadov, T.S. (2007). Gaussian distribution of inhomogeneous barrier height in  $Al_{0.24}Ga_{0.76}As/GaAs$  structures. *Physica B*, Vol. 396, pp. 22.
- Chang, Y. C., Wu, H. W., Chen, H. L., Wang, W. Y. & Chen, L. J. (2009). Two-Dimensional Inverse Opal ZnO Nanorod Networks with Photonic Band Gap. *J. Phys. Chem. C*, Vol. 113, pp. 14778.
- Christofides, C. & Mandelis, A. (1989), Operating characteristics and comparison of photopyroelectric and piezoelectric sensors for trace hydrogen gas detection. I. Development of a new photopyroelectric sensor. *J. Appl. Phys.*, Vol. 66, pp. 3975
- Coppa, B. J., Davis, R. F. & Nemanich, R. J. (2003). Gold Schottky contacts on oxygen plasma-treated, n-type ZnO(0001). *Appl. Phys. Lett.*, Vol. 82, pp. 400.
- Das, S. N. & Pal, A. K. (2007), Hydrogen sensor based on thin film nanocrystalline n-GaN/Pd Schottky diode. *J. Phys. D: Appl. Phys.*, Vol. 40, pp. 7291
- Das, S. N., Sarangi, S. N., Sahu, S. N. & Pal, A. K. (2009), Metal Contacts in Nanocrystalline n-Type GaN: Schottky Diodes. *J. Nanosci. Nanotechnol.* Vol. 9, pp. 2532
- Das, S. N., Kar, J. P., Choi, J. H., Byeon, S., Jho, Y. D. & Myoung, J. M. (2009), Influence of surface morphology on the optical property of vertically aligned ZnO nanorods. *Appl. Phys. Lett.*, Vol. 95, pp. 111909.

- Dhananjay, Nagaraju, J. & Krupanidhi, S. B. (2007), Investigations on magnetron sputtered ZnO thin films and Au/ZnO Schottky diodes. *Physica B*, Vol. 391, pp. 344.
- Fan, S. W.; Srivastava, A. K. & Dravid, V. P. (2009) UV-activated room-temperature gas sensing mechanism of polycrystalline ZnO. *Appl. Phys. Lett.*, Vol. 95, pp. 142106.
- Fonoberov, V. A., Alim, K. A., Balandin, A. A., Xiu, F. & Liu, J. (2006). Photoluminescence investigation of the carrier recombination processes in ZnO quantum dots and nanocrystals. *Phys. Rev. B*, Vol.73, pp. 165317.
- Hsu, H.C., Cheng, C.S., Chang, C.C., Yang, S., Chang, C.S. & Hsieh, W.F. (2005). Orientation enhanced growth and optical properties of ZnO nanowires grown on porous silicized substrates, *Nanotechnology*, Vol. 16, pp. 297.
- Ievtushenko, A., Karpyna, V., Lashkarev, G., Lazorenko, V., Baturin, V., Karpenko, Lunika, A. M. & Danko, A. (2008). Multilayered ZnO films of improved quality deposited by magnetron sputtering, *Acta Phys. Pol. A*, Vol. 114, pp. 1131.
- Heo, Y. W., Tien, L. C., Norton, D. P., Pearson, S. J., Kang, B. S., Ren, F. & LaRoche, J. R., (2004), Pt/ZnO nanowire Schottky diodes. *Appl. Phys. Lett.* Vol. 85, pp. 3107
- Hudson, J. B. 1998 *Surface Science* (Wiley, New York).
- Ibanez, F. J. & Zamborini, F. P. (2006) Ozone- and Thermally Activated Films of Palladium Monolayer-Protected Clusters for Chemiresistive Hydrogen Sensing. *Langmuir*, Vol. 22, pp. 9789
- Kar, J.P., Lee, S.W., Lee, W. & Myoung, J.M. (2008). Effect of sputtered films on morphology of vertical aligned ZnO nanowires, *Appl. Surf. Sci.* Vol. 254, pp. 6677.
- Kar, J.P., Ham, M.H., Lee, S.W. & Myoung, J.M. (2009). Fabrication of ZnO nanostructures of various dimensions using patterned substrates, *Appl. Surf. Sci.*, Vol. 255, pp. 4087.
- Lee, T. I., Choi, W. J., Moon, K. J., Choi, J. H., Kar, J. P., Das, S. N., Kim, Y. S., Baik, H.K. & Myoung, J. M. (2010). Programmable Direct-Printing Nanowire Electronic Components. *Nano Lett.*, Vol. 10, pp. 1016.
- Li, C. C.; Du, Z. F.; Li, L. M.; Yu, H. C.; Wan Q. & Wang, T. H. (2007), Surface-depletion controlled gas sensing of ZnO nanorods grown at room temperature. *Appl. Phys. Lett.*, Vol. 91, pp. 032101.
- Li, Y., Valle, F. D., Simonnet, M., Yamada, I. & Delaunay, J. J. (2009) High-performance UV detector made of ultra-long ZnO bridging nanowires. *Nanotechnology*, Vol. 20, pp. 045501
- Liao, L.; Lu, H. B.; Li, J. C.; He, H.; Wang, D. F.; Fu, D. J.; Liu, C. & Zhang, W. F. (2007), Size Dependence of Gas Sensitivity of ZnO Nanorods *J. Phys. Chem. C*, Vol. 111, pp. 1900.
- Liao, L.; Lu, H. B.; Shuai, M.; Li, J. C.; Liu, Y. L.; Liu, C.; Shen, Z. X. & Yu, T. (2008), A novel gas sensor based on field ionization from ZnO nanowires: moderate working voltage and high stability. *Nanotechnology*, Vol. 19, pp. 175501.
- Lin, Y. J. (2005). Application of the thermionic field emission model in the study of a Schottky barrier of Ni on p-GaN from current-voltage measurements. *Appl. Phys. Lett.*, Vol. 86, pp. 122109.
- Liou, S.C., Hsiao, C.S. & Chen S.Y. (2005). Growth behavior and microstructure evolution of ZnO nanorods grown on Si in aqueous solution. *J. Cryst. Growth*, Vol. 274, pp. 438.
- Munoz, E., Monroy, E., Pau, J. L., Calle, F., Omnes, F. & Gibart, P. (2001), III nitrides and UV detection. *J. Phys.: Condens. Matter*, Vol. 13, pp. 7115

- Norton, D. P., Heo, Y. W., Ivill, M. P., Ip, K., Pearton, S. J., Chisholm, M. F. & Steiner, T. (2004). ZnO: growth, doping & processing. *Mater. Today*, Vol. 7, pp. 34, ISSN
- Rout, C. S., Kulkarni, G. U., Rao, C. N. R. (2007), Room temperature hydrogen and hydrocarbon sensors based on single nanowires of metal oxides. *J. Phys. D: Appl. Phys.*, Vol. 40, pp. 2777
- Rhoderick, E. H. & Williams, R. H. (1988), *Metal-Semiconductor Contact* (Clarendon, Oxford).
- Schalwig, J.; Muller, G.; Karrer, U.; Eickhoff, M.; Ambacher, O.; Stutzmann, M.; Gorgens, L. & Dollinger, G. (2002), Hydrogen response mechanism of Pt-GaN Schottky diodes. *Appl. Phys. Lett.*, Vol. 80, pp. 1222
- Soci, C., Zhang, A., Xiang, B., Dayeh, S. A., Aplin, D. P. R., Park, J., Bao, X. Y., Lo, Y. H. & Wang, D. (2007), ZnO Nanowire UV Photodetectors with High Internal Gain. *Nano Lett.*, Vol. 7, pp. 1003
- Sze, S. M. (1979). *Physics of Semiconductor Devices* (Wiley: New York).
- Tsai, C. L., Lin, Y. J., Chin, Y. M., Liu, W. R., Hsieh, W. F., Hsu, C. H. & Chu, J. A. (2009). Low-resistance nonalloyed ohmic contacts on undoped ZnO films grown by pulsed-laser deposition. *J. Phys. D: Appl. Phys.* Vol. 42, pp. 095108
- Wan, Q., Li, Q. H., Chen, Y. J., Wang, T. H., He, X. L., Gao, X. G. & Li, J. P. (2004), Positive temperature coefficient resistance and humidity sensing properties of Cd-doped ZnO nanowires. *Appl. Phys. Lett.* Vol. 84, pp. 3085
- Wan, Q., Li, Q. H., Chen, Y. J., Wang, T. H., He, X. L., Li, J. P. & Lin, C. L. (2004), Fabrication and ethanol sensing characteristics of ZnO nanowire gas sensors. *Appl. Phys. Lett.*, Vol. 84, pp. 3654
- Wang, C., Chu, X. & Wu, M. (2006), Detection of H<sub>2</sub>S down to ppb levels at room temperature using sensors based on ZnO nanorods. *Sensors and Actuators B*, Vol. 113, pp. 320.
- Werner, J.H. & Guttler, H.H. (1991). Barrier inhomogeneities at Schottky contacts. *J. Appl. Phys.*, Vol. 69, pp. 1522.
- Xu, Q.A., Zhang, J.W., Ju, K.R., Yang, X.D. & Hou, X. (2006), ZnO thin film photoconductive ultraviolet detector with fast photoresponse. *Journal of Crystal Growth*, Vol. 289, pp. 44
- Zhang, H. Z., Sun, X. C., Wang, R. M. & Yu, D. P. (2004). Growth and formation mechanism of c-oriented ZnO nanorod arrays deposited on glass. *J. Cryst. Growth*, Vol. 269, pp. 464.
- Zhang, J., Zhang, L. D., Wang, X. F., Liang, C. H., Peng, X. S. & Wang, Y. W. (2001). Fabrication and photoluminescence of ordered GaN nanowire arrays. *J. Chem. Phys.*, Vol. 115, pp. 5714.
- Zhou, J., Gu, Y., Fei, P., Mai, W., Gao, Y., Yang, Bao, R., G. & Wang, Z. L. (2008). Flexible Piezotronic Strain Sensor. *Nano Lett.* Vol. 8, pp. 3035.

# Metal Oxide Nanowires – Structural and Mechanical Properties

L. Dai, C.H. Sow, C.T. Lim and V.B.C. Tan  
*National University of Singapore  
Singapore*

## 1. Introduction

Metal Oxide nanowires are versatile nanostructured materials with diverse yet unique properties. Potentially, they have a wide range of applications in electrical, chemical and semiconductor technologies (Yang, Wu et al. 2002; Rao, Deepak et al. 2003; Law, Goldberger et al. 2004; Shankar and Raychaudhuri 2005; Lu, Chang et al. 2006; Lu and Lieber 2006).

Research interests in metal oxide nanowires commenced in 1990s. Up to now, there have been a considerable number of reports on success in the synthesis of 1-dimensional nanocrystalline structured nanowires of various metal oxides, such as CuO(Wang, Zhan et al. 2001; Jiang, Herricks et al. 2002), MgO(Ma and Bando 2003), ZnO(Tian, Voigt et al. 2003; Vayssieres 2003; Heo, Norton et al. 2004; Wang, Song et al. 2007; Manoharan, Desai et al. 2008), TiO<sub>2</sub>(Lakshmi, Partissi et al. 1997; Li and Wang 1999; Li and Xia 2003; Wu, Shih et al. 2005; Wu, Shih et al. 2006), Al<sub>2</sub>O<sub>3</sub>(Valcarcel, Souto et al. 1998; Xiao, Han et al. 2002), Ga<sub>2</sub>O<sub>3</sub>(Wu, Song et al. 2000), In<sub>2</sub>O<sub>3</sub>(Li, Zhang et al. 2003), SnO<sub>2</sub>(Dai, Pan et al. 2001), Sb<sub>2</sub>O<sub>5</sub>(Guo, Wu et al. 2000), V<sub>2</sub>O<sub>5</sub>(Chen, Sun et al. 2002), BaTiO<sub>3</sub>(Urban, Spanier et al. 2003), etc. The methodology of synthesis is now well developed. Reported techniques include vapor-solid phase technique(Valcarcel, Souto et al. 1998; Wu, Song et al. 2000; Jiang, Herricks et al. 2002; Ma and Bando 2003; Wu, Shih et al. 2005; Wu, Shih et al. 2006), chemical solution deposition (sol-gel) (Lakshmi, Partissi et al. 1997; Urban, Spanier et al. 2003), template etching(Xiao, Han et al. 2002), precipitation(Tian, Voigt et al. 2003; Vayssieres 2003), micro-emulsion(Guo, Wu et al. 2000), flux growth(Dai, Pan et al. 2001) and others. These are well reviewed by Shankar et al.(Shankar and Raychaudhuri 2005).

Among all the properties of metal oxide nanowires, their mechanical property is one of the most highly structure dependent and features strongly in many applications. The structural and mechanical phenomena and related mechanisms have attracted significant research interests. However, due to the difficulties in manipulating the nano-sized specimens, experimental characterizations are limited to simple mechanical tests to measure quantities like Young's modulus, strength et al. Comparatively, numerical studies, especially molecular dynamics (MD) simulations, are well suited for nanostructured materials, and have been broadly applied for investigating structural and mechanical properties. In this chapter, we will review the structural characteristics and mechanical properties of different types of metal oxides, both experimentally and numerically. Besides reviewing published literatures, we will be focusing on reporting the outputs from our research group.

## 2. Metal oxide nanowires

### 2.1 ZnO

ZnO nanocrystals possess large energy bandgap and excitation binding energy, which ensures efficient excitonic emission at room temperature. This makes it a fascinating material in potential optoelectronic applications(Wang, Song et al. 2007). Their mechanical stability is a key factor for promising working conditions, and draws significant research interest.

Experimental measurements, such as bending resonance(Bai, Gao et al. 2003; Yum, Wang et al. 2004; Chen, Shi et al. 2006; Huang, Bai et al. 2006; Ni and Li 2006; Zhou, Lao et al. 2006), bending deflection(Song, Wang et al. 2005; Manoharan, Desai et al. 2008; Wen, Sader et al. 2008), nano-indentation(Feng, Nix et al. 2006; Ni and Li 2006) and tensile stretching(Desai and Haque 2007; Hoffmann, Ostlund et al. 2007; Agrawal, Peng et al. 2008) have been carried out to measure the Young's modulus ZnO. These results deviate significantly over a wide range from 20 to 220 GPa. The lack of agreement was considered to be due to differences in degree of crystallinity, direction of loading, boundary conditions, and sample manipulations, etc. Similar scatter was also seen in hardness and ultimate tensile strength (UTS), 2.5-4.3 GPa(Feng, Nix et al. 2006) and 2.5-7.5 GPa(Hoffmann, Ostlund et al. 2007; Wen, Sader et al. 2008), respectively.

In contrast to the abundant experimental characterizations, theoretical reports on the structure and mechanical property of ZnO nanowires have not been insightful. Kulkarni et al.(Kulkarni, Zhou et al. 2005) carried out tensile simulations on ZnO nanobelt with square cross sections. It was found that the structure transformed into multi-shell structure for wires thinner than 10Å, whereas thicker nanowires maintained a crystalline structure after equilibration. The decrease in Young's modulus and UTS with increasing nanowire thickness is attributed to the high compressive internal stress induced by the free surface of the wire. In a later publication by the same group(Wang, Kulkarni et al. 2008), simulations of the wurtzite crystalline structured ZnO nanowires with hexagonal lateral geometry showed three stages of deformation when the wires were loaded in tension - wurtzite elastic stretch, phase transformation from wurtzite to body-centered-crystal (BCC) structure, and BCC elastic stretch. From the stress-strain curve, the Young's modulus was measured to be 227-299GPa for nanowires with thickness ranging from 45.5 to 19.5Å. These values are much higher than the bulk value of 140GPa. It is noted that the high stretch rate of 10-50m/s could have led to the exceptionally high stiffness and unexpectedly low toughness. In a recent literature, Agrawal et al.(Agrawal, Peng et al. 2008) reported values of 140-160GPa for the Young's modulus of 5-20Å thick [0001] oriented hexagonal ZnO nanowires, with thinner nanowires to be reportedly stiffer. The results are in agreement with bulk values and their experimental measurements.

We carried out MD simulations to model a tensile process on the ZnO nanowire at a moderate stretching rate. By presenting the structural deformation and mechanical response(Dai, Cheong et al. 2010), the mechanism behind observations were revealed.

We adopt the Buckingham potential with Kulkarni's parameters(Kulkarni, Zhou et al. 2005) to describe the atomic interactions. This potential successfully reproduces the ZnO crystalline lattice parameters. The cylindrical ZnO nanowires were built from super cells of wurtzite crystal with [0001] in the longitude direction. Atoms in the top and bottom five layers were prescribed to displace as two rigid blocks to stretch the wires while all other atoms were free of constraints. Free surface conditions were applied in all directions. The

molecular dynamics simulation was carried using the DL-POLY software ([http://www.cse.scitech.ac.uk/ccg/software/DL\\_POLY/](http://www.cse.scitech.ac.uk/ccg/software/DL_POLY/)) with time steps of 2 fs. The temperature was maintained at 300 K by scaling the atomic velocities every 1 ps. The nanowires were firstly relaxed under constant atmosphere pressure (NPT) for 1 ns to remove internal stresses, and under constant volume (NVT) for another 1 ns to reach the minimum energy state. The tensile process was carried out via displacing the top and bottom blocks of atoms in a stepwise manner. For each step, the nanowire was stretched by 1 Å and equilibrated for 500 ps, i.e., a tensile rate of 0.2 m/s. The total system energy and atomic positions were monitored to ensure the wires achieved equilibrium at the end of 500 ps. This methodology was used for all the tensile MD simulations in this chapter.

Four ZnO nanowires with lateral diameters of 7 Å, 16 Å, 25 Å and 40 Å were constructed. Their initially relaxed structures are shown in Fig.1. The thinnest 7 Å nanowire experienced a structure transformation into a totally amorphous state, due to the strong surface effect. The degree of amorphization retarded with increase in lateral size. Complete crystalline structures

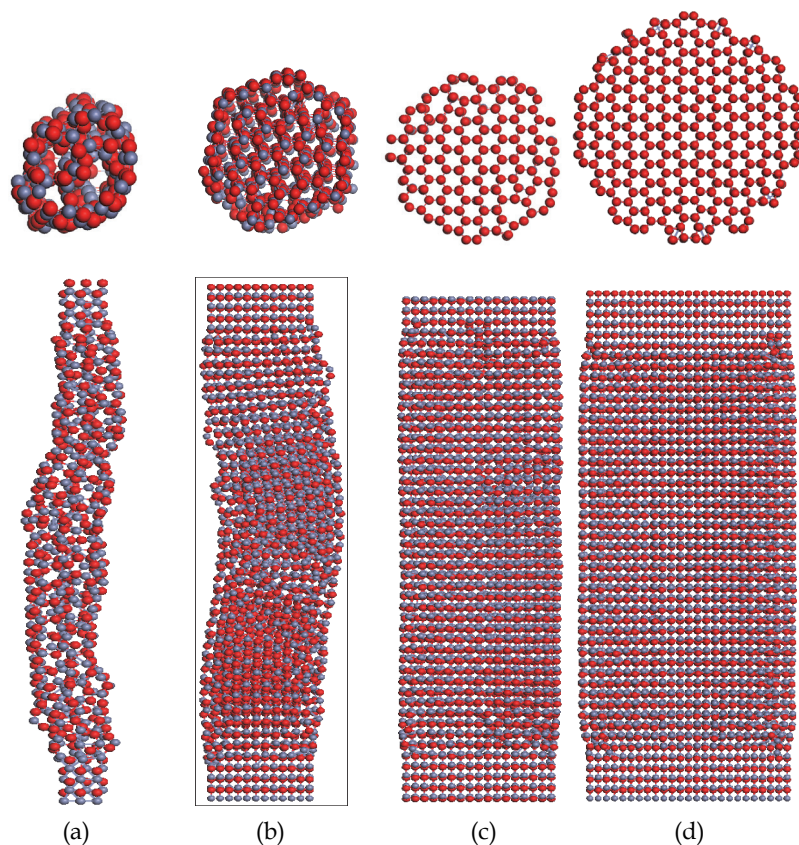


Fig. 1. Equilibrated structure of ZnO nanowires with lateral diameters of (a) 7 Å, (b) 16 Å, (c) 25 Å, and (d) 40 Å. Cross-sectional views at the nanowire center are shown at the top. Red spheres denote O atoms and grey Zn atoms.

were retained for nanowires with lateral diameter  $25\text{\AA}$  and above. A  $16\text{\AA}$  nanowire was presented as the transient state between amorphous and crystalline state. The threshold diameter for crystalline to amorphous transformation was about the length of 3-4 single crystal lattices. This empirical observation is also applicable for many other inorganic materials, such as metals, semiconductors and ceramics, in agreement with previous reports for crystals of Au(Kondo and takayanagi 2000; Wang, Yin et al. 2001), Al(Gulseren, Ercolessi et al. 1998), Pb(Gulseren, Ercolessi et al. 1998), Ti(Wang, Yin et al. 2001), SiC(Maleev, Srivastava et al. 2006).

The snapshots of tensile process for nanowires are presented for the  $7\text{\AA}$  and  $25\text{\AA}$  nanowires in Fig. 2 and Fig.3, respectively. Under tensile loading, the  $7\text{\AA}$  nanowire firstly straightened (Fig.2b), and then necked at 35.6% strain (Fig.2c). Once formed, the necked region, where stress concentrated, thinned further to a single-atom-neck chain (Fig.2d). With further stretching, more atoms were continuously pulled into the single-atom-neck, resulting in a very ductile behavior (Fig.2e, f).

The  $25\text{\AA}$  nanowire presented a novel tensile deformation process as shown in Fig.4. Initially, the original crystals in the nanowire only experienced slight and homogeneous longitude stretching without significant phase transformations. At 12.5% strain (Fig.3a, b), ZnO bond breakage occurred and structural deformation was seen at the central section (Fig.3c). This region experienced high strain and propagated quickly to create a lateral slip-deformed necking (Fig.3d). With continued stretching, the tensile process followed a three-step cycle - 1) straightening of Zn-O bonds in the necked region, 2) neck thinning, 3) relaxation of the necked region as new atoms were pulled into the neck. The nanowire was able to be extremely ductile with the iteration of the three-step plastic deformation cycle.

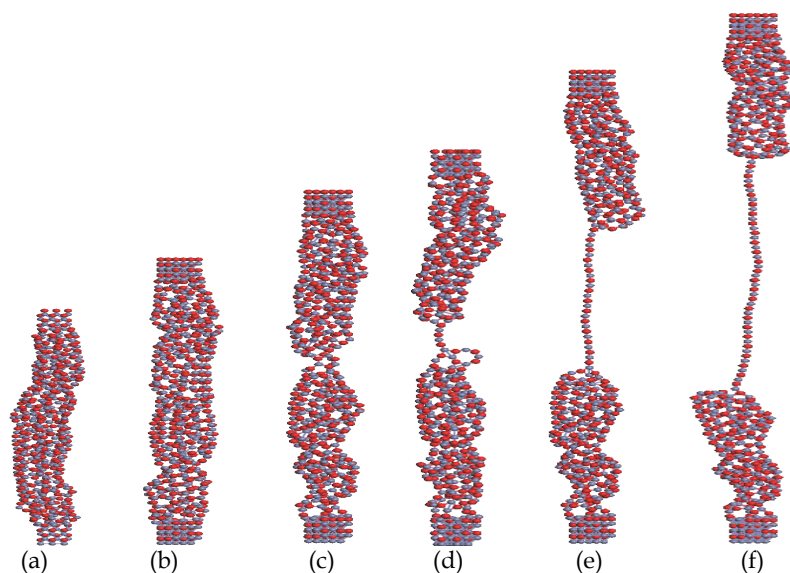


Fig. 2. Tensile stretching of  $7\text{\AA}$  diameter ZnO nanowire - (a) equilibration, (b) straightening at 16.5% strain, (c) initiation of necking at 35.6% strain, (d) formation of single-atom-neck at 41.9% strain, (e) continued growth of single-atom-neck at 77.5% strain, and (f) nanowire at 116% strain.

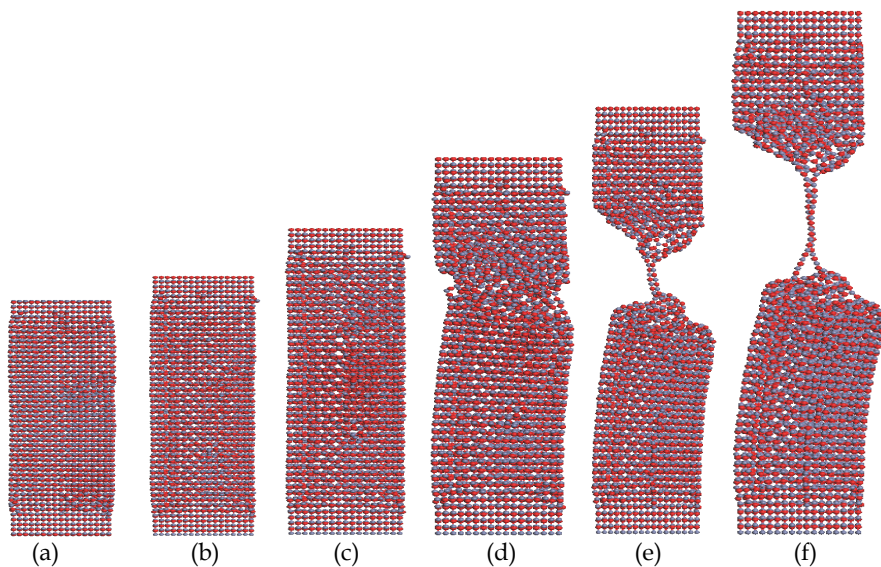


Fig. 3. Tensile stretching of 25Å diameter ZnO nanowire - (a) equilibration, (b) straightening at 12.5% strain, (c) formation of amorphous central section at 13.5% strain, (d) neck initiation at 14.4% strain, (e) neck shrinkage and formation of bi-lines at 38.5% strain, and (f) atomic neck pulling at 57.7% strain.

The displacement history of five atoms in the single-atom-neck chain (Fig.3e) is presented in Fig.4 to describe the deformation process. The five atoms were originally a twisted atomic

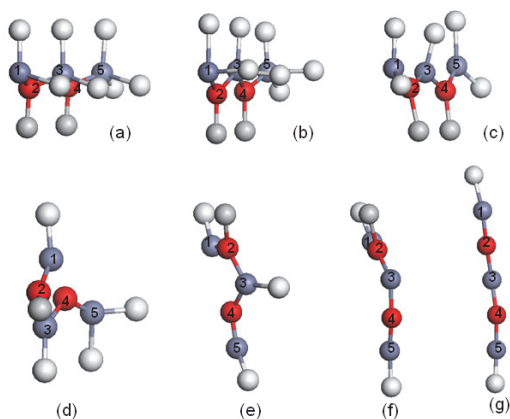


Fig. 4. Deformation process for five atoms within a single-atom-neck chain in Fig.3e. The atoms from which necking initiated are numbered 1 to 5, and the neighboring bonded atoms were shown as light grey dots. The neighbor atoms can be O or Zn atoms, which form ionic bonds with the neck atoms. The deformation process was depicted in seven snapshots (a) original lattice sites, (b) elastic stretch, (c) plastic deformation with bond breakage, (d)-(f) deformation during thinning of wire neck, and (g) formation of the single atom chain.

chain on the lattice sites of two adjacent crystals located at the nanowire surface (Fig.4a). At the initial stage of stretching, these atoms were slightly strained (Fig.4b) to take up the axial expansion. Then, bond breakage was observed for atom-3 and 5, and the atomic morphology was significantly deformed (Fig.4c), in accordance with the crystalline-to-amorphization transformation as depicted in Fig.3c. Afterwards, debonding was continuously occurring (Fig.4d-f), and each debonding relaxed the straightened atomic chain before further deformation until the formation the single-atom-neck chain (Fig.4g). This isolated atomic chain was then observed to grow via the addition of more atoms to the head and tail atoms (atoms 1 and 5 initially).

The key for the extreme ductility lies in whether an atom on the wire at the junction of the single atom chain detaches itself from the bulk to join the chain or if the chain breaks first. As shown in Fig.5, at one end of the single atom chain, atom-X is bonded to three atoms - one within the neck chain, and other two on the amorphous bulk. The forces acting on atom-X is expressed in equation-1,

$$N = \sum F_n \cos \theta_n = F_1 \cos \theta_1 + F_2 \cos \theta_2 \quad (1)$$

In equation-1, if the value of  $\cos \theta$  is less than 0.5, force vector  $F_i$  is likely to be higher than  $N$ . In the simulation models, the angle  $\theta$  was measured as  $58-74^\circ$ , thereby  $\cos \theta$  is most likely to be less than 0.5. This means the bond breakage will likely happen in the bulk, supporting the atomic neck chain to grow. After the bond breakage, atom-X joined the neck chain and the atom in the amorphous bulk that was still bonded to it, became the new connection between the neck chain and the amorphous bulk. The process was continuously repeated during the simulation process, leading to super ductility of the nanowire.

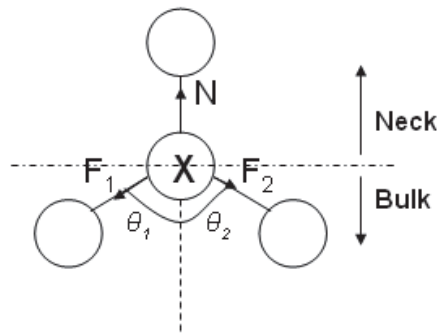


Fig. 5. Forces at the junction between the single-atom-neck chain and the amorphous bulk in the nanowire.

Fig.6 plots the stress-strain curve and change in number of Zn-O bonds (NZB) for the  $25\text{\AA}$  nanowire. Four regimes - linear (regime A), amorphization (regime B), neck shrinking (regime C) and neck chain growth (regime D) - were defined based on the deformation behavior. It gives a Young's modulus of 203 GPa and ultimate tensile strength of 8.89 GPa. Meanwhile, the  $7\text{\AA}$  diameter ZnO nanowire was much softer with 48.8 GPa Young's modulus and 2.87 GPa UTS.

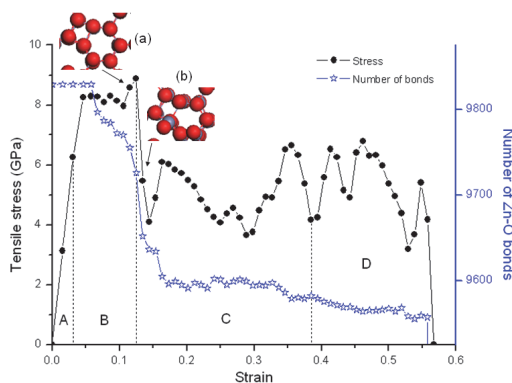


Fig. 6. Curves of tensile stress and number of Zn-O bonds for 25 Å nanowire, where four zones were defined as different deformation behavior. Charts (a) and (b) are the regional cross-section views accounting for the crystalline to amorphous transformation via the difference of atomic misfit in their top views.

## 2.2 TiO<sub>2</sub>

TiO<sub>2</sub> nanowires are often studied by experimentalists because they have wide range of applications and are suitable for many experimental techniques (Diebold 2003). Beyond experimental attractions, the theoretical studies have been carried out for analyzing nanocrystal structures, such as nanoparticles (Hallil, Tetot et al. 2006) and nanoclusters (Collins, Smith et al. 1996; Filyukov, Brodskaya et al. 2007). However, there is still a lack of literature on modeling the TiO<sub>2</sub> nanowires to present an overall understanding of the mechanism behind experimental observations.

We use Matsui and Akaogi's potential (Matsui and Akaogi 1991) for the atomic interactions, and MD simulations to study for the tensile deformation of the nanowire (Dai, Tan et al. 2009). The TiO<sub>2</sub> nanowire model was built from the most stable rutile crystal structure with the [100] direction along the wire axis. The nanowire is cylindrical, 59.18 Å in length and 27.6 Å in diameter and contains 3500 atoms. Firstly, the model was dynamically relaxed for 2 ns, resulting in an expansion of about 0.67% in volume, as shown in Fig. 7. It can be seen that the equilibration relocated the surface atoms while the core atomic arrangement remained unchanged.

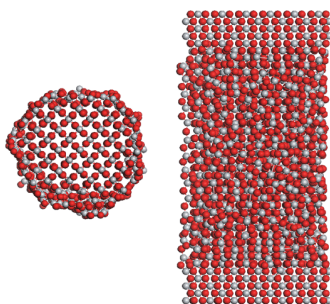


Fig. 7. Top (left) and front (right) view of equilibrated cylindrical TiO<sub>2</sub> nanowire model. The relaxed surface atoms take up about 39.4% of the total free atoms.

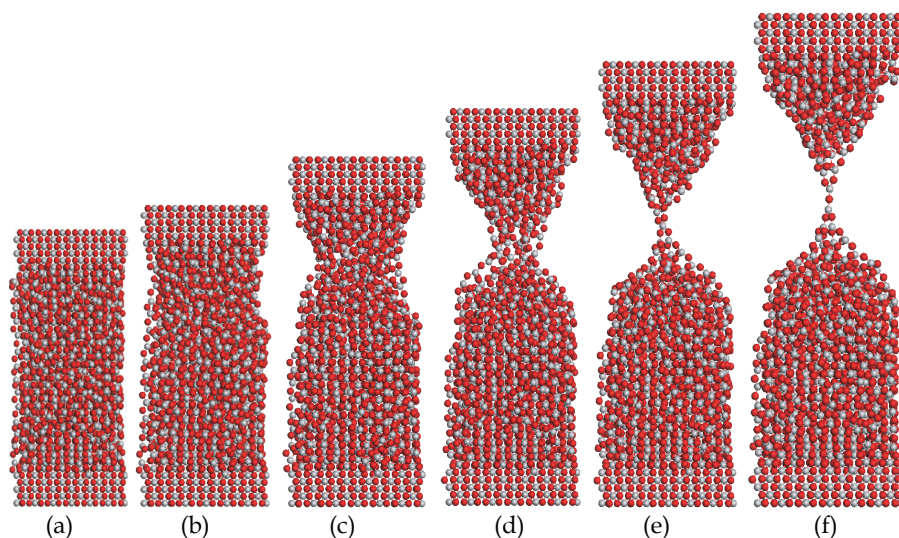


Fig. 8. Tensile process of  $\text{TiO}_2$  nanowire at different strain levels - (a) 1.6%, (b) 8.4%, (c) 20%, (d) 35.2%, (e) 43.6% and (f) 53.7%.

The snapshots of tensile process are presented in Fig.8. After a small initial linear stretching, bond breakage appeared at the surface, giving rise to the necking phenomenon. With continuous surface atom bond breaking, new surfaces were created to shrink the neck into single-atom-neck chain. In the single-atom-neck chain structure, it fails to meet the criteria of chain growth ( $\theta < 60^\circ$ ), and soon ruptured.

The tensile deformation of  $\text{TiO}_2$  nanowires was dominated by the free surface effect. Fig.9 presents the tensile induced deformation process of a group of surface atoms at five instances, namely, initial equilibration (chart a), yielding (chart b), ultimate tensile stress (UTS) (chart c) and two steps of plastic necking deformation (chart d and e). Plastic deformation was induced by the bond breakage at the surface which propagated inward resulting in new surfaces being created.

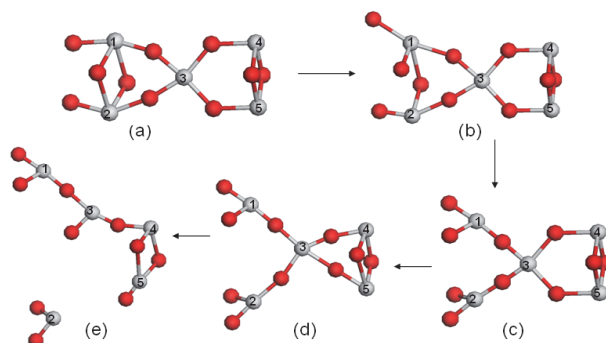


Fig. 9. Atomic re-arrangement during tensile process - (a) initial equilibration, (b) yielding, (c) UTS, (d) necking, (e) further necking. Atoms at the extreme left comprise the side surface whereas atoms 4 and 5 are connected to atoms within the core of the wire.

The bond and stress analysis are shown in Fig.10. Chart (a) shows the stress-strain curve with three additional snapshots of atomic arrangement (I to III) at yielding, UTS, and final single-atom-neck stages, individually. Fig.10 (b)-(d) show the quantitative variation of Ti-O bonds, Ti-O bond lengths, and longitudinal projections of Ti-O bond lengths, which reflect the mechanical characteristics.

These charts clearly define the bond-rotation induced elasticity, bond-breakage induced plasticity, and the continuous cycles of bond straightening – bond breakage and inner atomic distortion – neck thinning, beyond UTS until rupture.

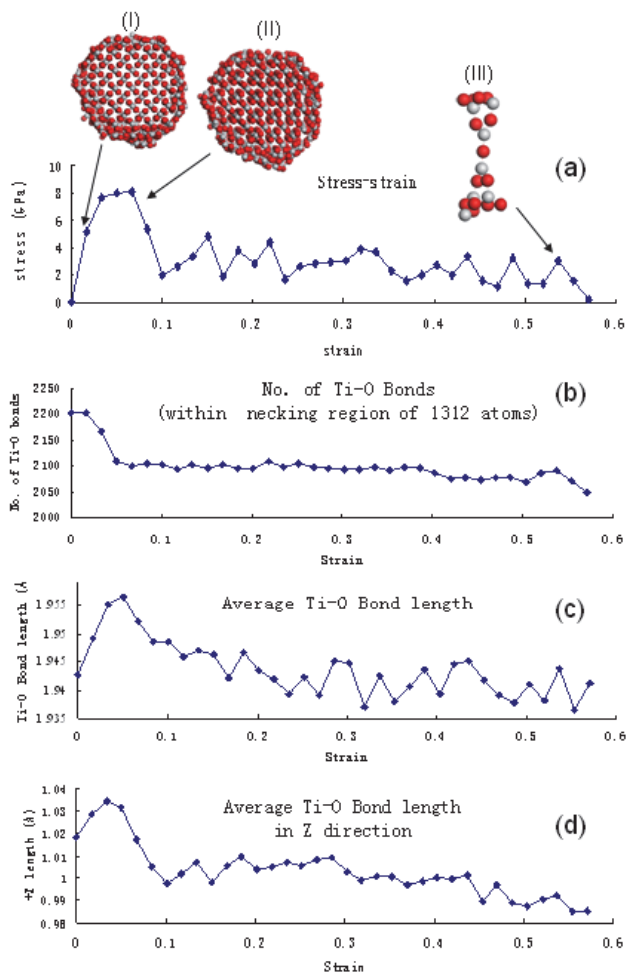


Fig. 10. Data plot of (a) Stress-strain curve (b) Number of Ti-O bonds (c) Average length of Ti-O bonds (d) Average length of Ti-O bonds projected onto the longitudinal direction. Charts (b), (c) and (d) are only for the necking region which includes 1312 atoms. In chart (a), the three insets are cross-sectional atomic arrangements at yielding, just beyond UTS and during single-atom-necking.

More TiO<sub>2</sub> nanowires with different lateral size were used for tensile simulations to investigate the size effect. These TiO<sub>2</sub> nanowires all showed similar deformation processes due to the domination of the surface effect. However, in contrast to the case of ZnO, TiO<sub>2</sub> nanowires showed enhanced stiffness and UTS with decreasing wire thickness as shown in Fig.11. The reason for the different size effects on mechanical property lies in the mechanisms of structural deformation, which will be discussed later in this chapter.

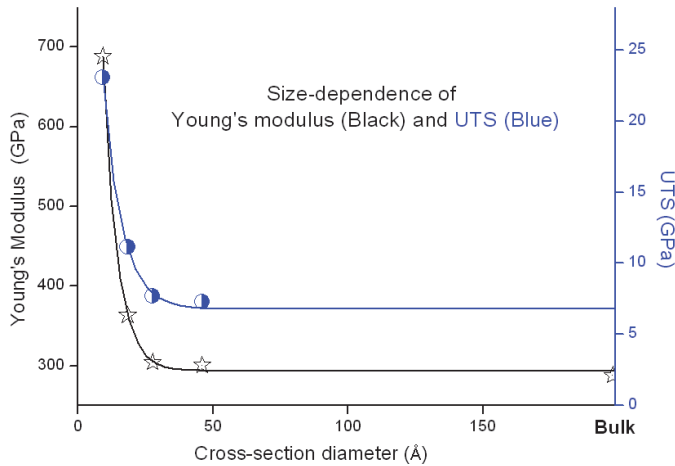


Fig. 11. Young's modulus and UTS as functions of nanowire thickness.

### 2.3 CuO

CuO plays an important role in building high temperature superconductors, and its nanowire has potential applications as an electron field emission source. Synthesis of CuO nanowires have been reported during the last decade (Wang, Zhan et al. 2001; Jiang, Herricks et al. 2002).

We used AFM and three-point bend test to measure the Young's modulus of nanowire (Tan, Zhu et al. 2007). CuO nanowires were synthesized via vapor-solid pre-action method, and deposited on the AFM calibration grid spanning across the holes, as shown in Fig.12. With one end of the nanowire fixed, a point load of up to 40-90 nN was applied to the other free end by an AFM tip. The Young's modulus could then be calculated from beam bending theory via equation-2.

$$E = \frac{FL^3}{192\delta I} \quad (2)$$

Here,  $E$  is the Young's modulus,  $F$  is the maximum force applied,  $L$  is the suspended length,  $\delta$  is the deflection of the beam at the mid-span and  $I$  is the second moment of area (where  $I = \pi D^4/64$  and  $D$  is the beam diameter).

The Young's modulus was also calculated theoretically via computing the elastic constants of CuO crystals, and the polycrystalline properties were predicted via Hashin-Shtrikman bound theory (Watt 1980). Good agreement was achieved between experimental and computational values as depicted in Fig.13.

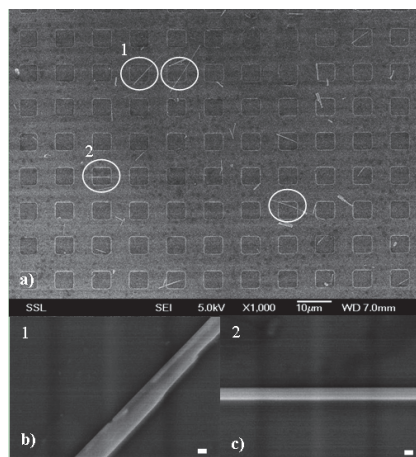


Fig. 12. Scanning electron microscopy images of CuO nanowires deposited on AFM calibration grid. (a) nanowires spanning across holes with two indicated location-1 and 2, (b) close-up image of tapered nanowire at location-1, (c) close-up image of uniform nanowire at location-2.

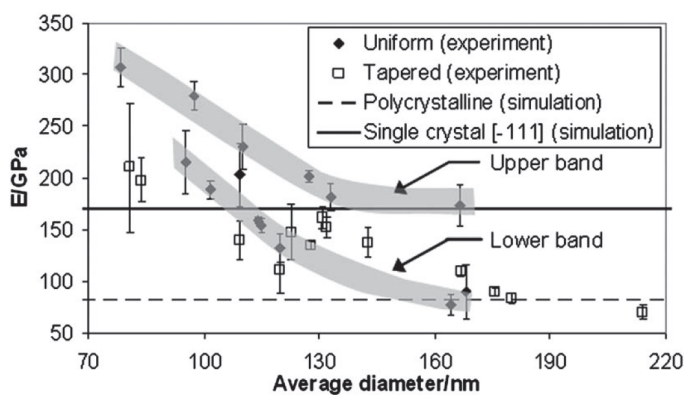


Fig. 13. Variation of Young's modulus with nanowire diameter for uniform and tapered nanowires. Theoretical values for single and polycrystalline CuO crystals are from numerical calculations.

## 2.4 $\text{Co}_x\text{O}_y$

Nanostructured  $\text{Co}_3\text{O}_4$  has excellent electrochemical reactivity and is important in applications of lithium-ion batteries, gas sensing etc. Synthesis of its crystalline structure (Petitto and Langell 2004) and nanowire (Li, Tan et al. 2006) has been reported.

In our work, the  $\text{Co}_3\text{O}_4$  nanowires were fabricated by vapor-solid method (Varghese, Teo et al. 2007) and measured via three-point-bend test. Furthermore, some  $\text{Co}_3\text{O}_4$  nanowires were converted into CoO nanowires via annealing, and tested for the mechanical properties (Fig.14).

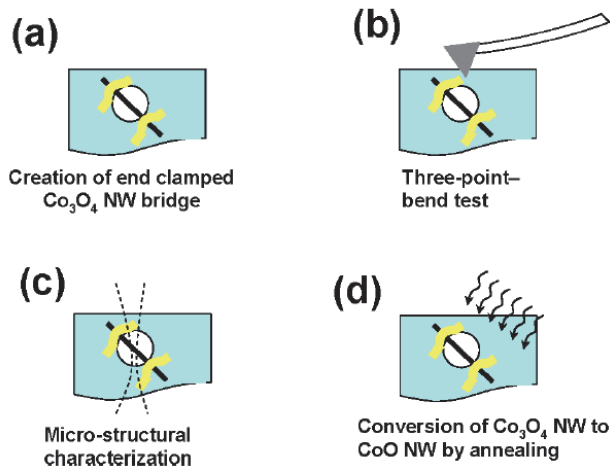


Fig. 14. Schematic of the characterization process for  $\text{Co}_3\text{O}_4$  and  $\text{CoO}$  nanowires.

The Young's modulus was also calculated theoretically and compared with our experimental values. Fig.15 clearly shows a trend of weakness with increasing of lateral diameter for  $\text{Co}_3\text{O}_4$  nanowires. Some thinner samples agree well with theoretical values, but most samples are lower than the polycrystalline value. The reason lies in the defects, impurities, and discontinuities in the specimens, especially significant for the thicker nanowires.

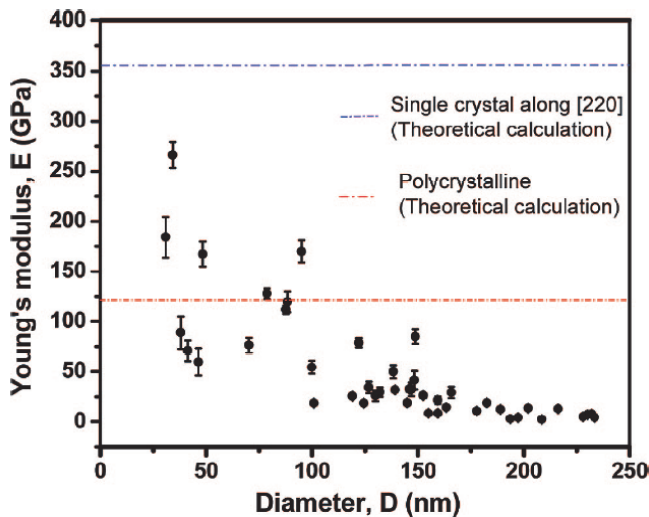


Fig. 15. Young's modulus of  $\text{Co}_3\text{O}_4$  nanowires vs lateral diameter.

The anneal  $\text{CoO}$  was also tested and the results are presented in Fig.16. After annealing, these nanowires became more brittle. Thinner nanowires become softer, but thicker ones retained similar stiffness.

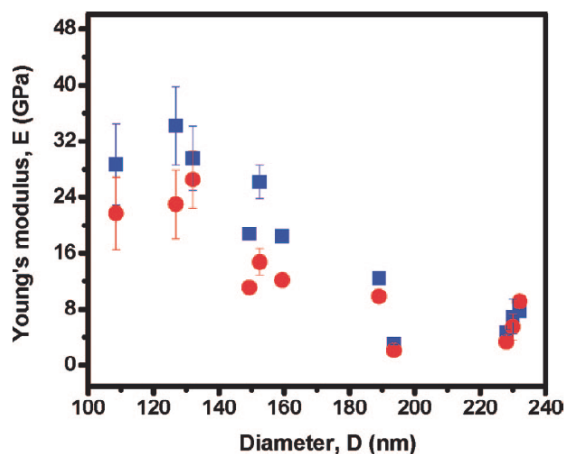


Fig. 16. Young's modulus of CoO nanowires vs lateral diameter. For comparison, the same nanowire before annealing is shown in blue.

## 2.5 $V_2O_5$

$V_2O_5$  exhibits remarkable electrochemical properties and is regarded as an ideal electrode material for Li-based battery (Lu, Chang et al. 2006). Its crystal structure shows highly anisotropic lattice morphology and mechanical stiffness.

In our work, the  $V_2O_5$  polycrystalline nanowires were fabricated via solid-vapor method, and have been measured mechanically through resonance testing (Zhu, Zhang et al. 2010). The results are presented in Fig. 17.

The as-grown nanowire was characterized as  $V_2O_5 \cdot nH_2O$ , where the  $V_2O_5$  crystals were highly randomly arranged. The measured Young's modulus showed a wide distribution from 5.6 up to 98 GPa. The stiff thin nanowires were highly anisotropic and very weak laterally. After annealing at  $450^\circ\text{C}$  in vacuum, the nanowires were converted into polycrystalline  $\alpha$ - $V_2O_5$  phase, with Young's modulus averaging around 29 GPa.

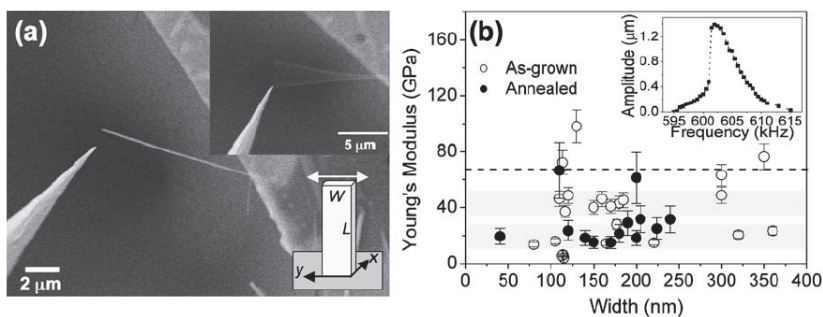


Fig. 17. (a) SEM image of a  $V_2O_5 \cdot nH_2O$  nanowire, with insets showing the image of the same nanowire under resonance (upper) and schematic vibration along the width direction. (b) Young's modulus of as-grown and annealed nanowires, with dotted lines indicating the theoretical value; the inset is a typical resonance peak.

Tensile simulation of molecular dynamics was also carried out for  $V_2O_5$  nanowires. Similar to the case of  $TiO_2$ , the deformation process was strongly dominated by the free surface effect, and resulted in brittle rupture with short single-atom-neck chain. The Young's modulus was measured to be 116 GPa, and UTS was calculated as 3.8 GPa.

## 2.6 $WO_3$

Tungsten trioxide ( $WO_3$ ) has been extensively studied because of its extraordinary electrochromic, ferroelectric and semiconductor properties (Woodward, Sleight et al. 1995; Lugovskaya, Aleshina et al. 2002; Lu, Chen et al. 2007).

We synthesized  $WO_{3-x}$  (with some oxygen starvation defects) nanowires by means of solid-vapor method (Cheong, Varghese et al. 2007). Well aligned nanowires were observed as shown in Fig.18.

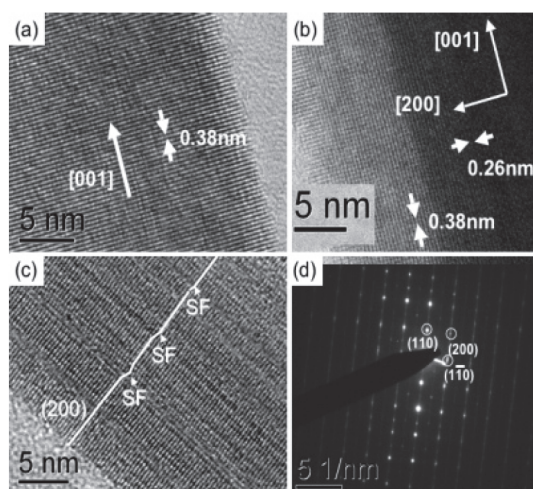


Fig. 18. HRTEM images of (a)  $WO_{3-x}$  nanowire; (b) a nanowire showing (001) and (200) lattice spacing; (c) a segment of nanowire with stacking fault ('SF' in the image) at (200) plane; (d) Electron diffraction image of a single nanowire.

From three-point bend tests, the Young's modulus of the nanowires was measured to be 10-100 GPa, lower than the theoretical perfect crystalline values of 310 GPa due to the existence of defects. Furthermore, these nanowires were found to be good field emitters with a field enhancement factor estimated to be  $9.8 \times 10^4 \text{ cm}^{-1}$ .

## 2.7 Other oxides

The reported structure-mechanical investigations for metal oxide nanowires have been very limited. Apart from Kulkarni's work on ZnO nanowires (Kulkarni, Zhou et al. 2005; Kulkarni and Zhou 2006; Wang, Kulkarni et al. 2008), MgO nanowires were reported by Xiong et al. arising molecular dynamics simulations. It was found that the MgO nanowires appear more ductile at low strain rates, and the tensile strength decreases as the cross-sectional diameter decreases or temperature increases. However, the applied strain rates of 25 and 100 m/s may have resulted in very stiff and brittle mechanical response.

A series of metal oxide nanowires (MgO, Fe<sub>2</sub>O<sub>3</sub>, MnO) together with previously mentioned ZnO, TiO<sub>2</sub> and V<sub>2</sub>O<sub>5</sub>, under tension have been simulated. Two different types of deformation processes were observed. For ZnO, MgO and MnO nanowires, the atomic bonds are highly flexible and can rotate easily. These gave rise to super ductility of the nanowire. On the other hand, the deformation of nanowires of TiO<sub>2</sub>, V<sub>2</sub>O<sub>5</sub> and Fe<sub>2</sub>O<sub>3</sub> are dominated by free surface effect which resulted in brittle fracture. All the ultra thin nanowires (lateral diameter <10Å) showed similar surface effects under tensile loading, but the ductility remained unchanged above a certain thickness.

From their stress-strain curves, the Young's moduli and UTS were obtained, and compared with theoretical polycrystalline calculations and experimental measurements, as presented in Table-1. It can be seen that the Young's modulus agree very well among the three sources of data. However, the simulation results for UTS are much higher than experimental values due to the existence of various defects in the samples.

Material	Young's modulus (GPa)			UTS (GPa)	
	Simulation	Bulk	Experiment	Simulation	Experiment
MgO	309	294(Watt 1987)	246.7(Samsonv 1982)	6.33	0.98(Samsonv 1982)
MnO	128.3	108.4(Watt 1987)	-	5.05	-
ZnO	202	140(Watt and Peselnick 1980)	100-220(Dai, Cheong et al. 2010)	8.89	2.5-7.5(Dai, Cheong et al. 2010)
TiO <sub>2</sub>	304	277(Watt 1986)	287.9(Isaak, Garnes et al. 1998)	8.15	0.054-0.068(Samsonv 1982)
Fe <sub>2</sub> O <sub>3</sub>	148.7	142.5(Watt and Peselnick 1980)	-	7.25	-
V <sub>2</sub> O <sub>5</sub>	116	68.1(Watt 1979)	-	3.8	-

Table 1. Mechanical properties of the nanowires that equilibrated with crystalline cores.

### 3. Discussion

The different mechanical responses of above mentioned metal oxide nanowires were analyzed and found to be structure related.

Fig.19 describes the atomic trajectories of six atoms that were originally located in a lateral surface of a ZnO type nanowire. It shows that the plastic deformation process was originally induced with evenly distributed longitudinal tensile bond forces, and caused selective longitude bond breaking and out-of-plane distortion of atomic planes, finally giving rise to a configuration that supports the growth of atomic neck chain and consequently leading to super ductility.

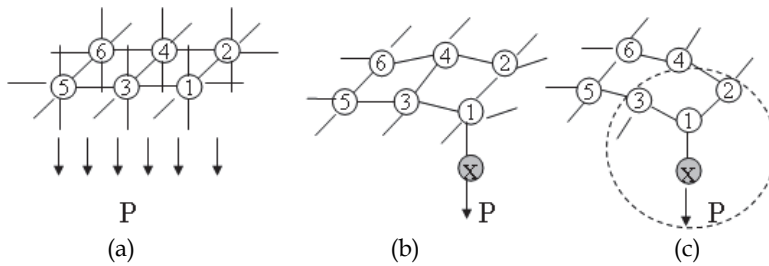


Fig. 19. Process of atomic deformation of ZnO type nanowires, from plane cleavage, plane deformation to atomic chain growth. The atomic arrangement within the dash circled region determines if a single atom chain will grow or break according to equation-1.

On the other hand, the crystal structure of TiO<sub>2</sub> type materials shows a lower symmetry of atomic distribution lattice, leading to anisotropic deformations when stress is applied. In Fig.20, which shows the displacement history of atoms originally located on a lateral surface, it is observed that bond stretching and breakage initiate from the surface (atoms 1, 4, 6 and 8 are on the surface) and propagate to the inner core. The atomic neck chain was formed at the stage shown in Fig.20c. However, the criterion for single atom chain growth of equation-1 was not satisfied and the nanowire soon ruptured.

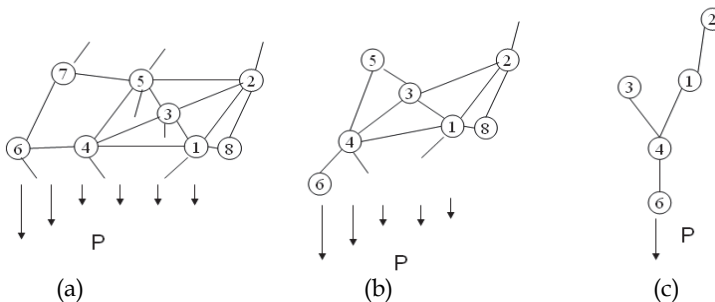


Fig. 20. Atomic deformation of TiO<sub>2</sub> type nanowires, showing a concentration of bond forces at the surface.

The stress-strain curves are presented in Fig.21. All the nanowires have similar trend in their stress-strain curves - the tensile stress jumps sharply during the elastic stage and soon reaches the ultimate tensile stress (UTS). Beyond UTS, the stresses oscillated about a considerably lower value. The tensile process reaches over 100% strain for ZnO type nanowires, but ends with rupture at around 20%-60% strain for TiO<sub>2</sub> type nanowires.

Significant differences were also predicted for how wire diameter affected the two groups of nanowires. The tensile stress was quite low for ultra thin ZnO type nanowires, and the mechanical response gradually enhanced to bulk values with size increase whereas an opposite mechanical trend of size effect was observed for TiO<sub>2</sub> type nanowires which showed that ultra thin nanowires possess superior mechanical properties. As depicted in Fig.19 and Fig.20, the atomic bonds in ZnO type structure are more flexible and are more able to rotate to accommodate the tensile stretching, whereas in TiO<sub>2</sub> type structure, tensile deformation was effected increasingly through the stretching of individual bonds as the nanowires decrease in size.

The key feature determining the difference in the mechanical behaviors between the two types of metal oxide nanowires lies in whether continuous and highly symmetrical atomic surface of the metal oxide polycrystals are formed. With a symmetrical structure, super tensile ductility can be expected. The characteristics of the two types are considered to be representative of metal oxide nanowires. Due to the large number and complex compositions of various metal oxides, there may be other structure and property characteristics that require further investigation.

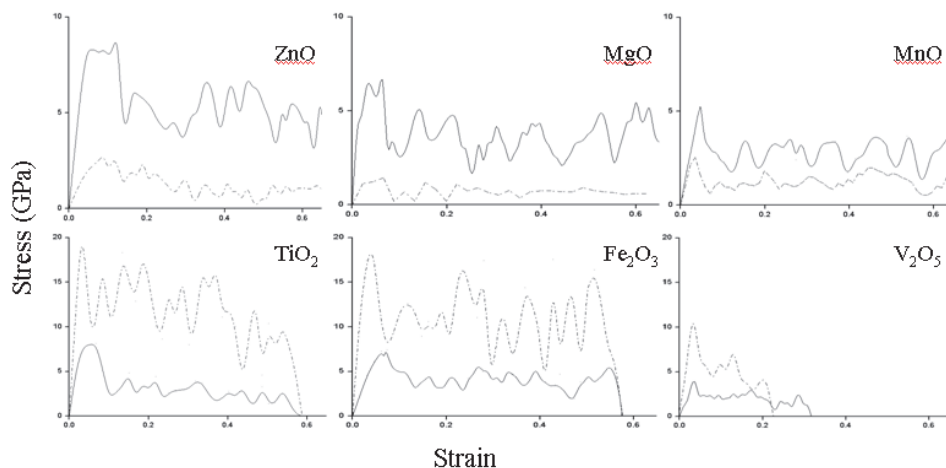


Fig. 21. Stress-strain curves for the six types of nanowire with different lateral size. Solid lines are for the nanowires of around 25 Å lateral diameter and dashed lines for the ultra thin nanowires of around 8 Å lateral diameter.

#### 4. Conclusion

In conclusion, we have reviewed published literature on the structure and mechanical properties of metal oxide nanowires. Due to their unique properties, metal oxide nanowires have been widely considered to play an important role in the next generation of materials. It is a clear trend that the experiment and simulation research activities will need to complement one another to understand their structure-mechanical property relations for the successful application of nanowires.

The development of experimental characterization and numerical simulation occurs in tandem. Simulation reveals the mechanism and predicts actual phenomena, which can help to direct the experimental process, saving time and cost. On the other hand, experimental characterizations can provide calibration data to improve the efficiency and effectiveness of simulation works.

#### 5. Acknowledgment

This work is supported by the funding from the Science and Engineering Research Council (SERC, A\*STAR) and Institute of Materials Research and Engineering (IMRE, A\*STAR), Singapore.

## 6. References

- Agrawal, R., B. Peng, et al. (2008). "Elasticity Size Effects in ZnO Nanowires-A Combined Experimental-Computational Approach." *Nano Lett.* 8: 3668.
- Bai, X. D., P. X. Gao, et al. (2003). "Dual-mode mechanical resonance of individual ZnO nanobelts." *Appl. Phys. Lett.* 82: 4806.
- Chen, C. Q., Y. Shi, et al. (2006). "Size Dependence of Young's Modulus in ZnO Nanowires." *Phys. Rev. Lett.* 96: 075505.
- Chen, X., S. M. Sun, et al. (2002). "Self-Assembling Vanadium Oxide Nanotubes by Organic Molecular Templates." *Inorg. Chem.* 41: 4524.
- Cheong, F. C., B. Varghese, et al. (2007). "WO<sub>3-x</sub> nanorods synthesized on a thermal hot plate." *J. Phys. Chem. C* 111: 17193.
- Collins, D. R., W. Smith, et al. (1996). "Molecular dynamics study of TiO<sub>2</sub> microclusters." *J. Mater. Chem* 6: 1385.
- Dai, L., W. C. D. Cheong, et al. (2010). "Molecular Dynamics Simulation of ZnO Nanowires - Size Effects, Defects and Super Ductility." *Langmuir* 26: 1165.
- Dai, L., V. B. C. Tan, et al. (2009). "Numerical Investigations into the Tensile Behavior of TiO<sub>2</sub> Nanowires : Structural Deformation, Mechanical Properties and Size Effects." *Nano Lett.* 9: 576.
- Dai, Z. R., Z. W. Pan, et al. (2001). "Ultra-long single crystalline nanoribbons of tin oxide." *Solid State Comm.* 118: 351.
- Desai, A. V. and M. A. Haque (2007). "Mechanical properties of ZnO nanowires." *Sensors and Actuators A* 134: 169.
- Diebold, U. (2003). "The surface science of titanium dioxide." *Surf. Sci. Reports* 48: 53.
- Feng, G., W. D. Nix, et al. (2006). "A study of the mechanical properties of nanowires using nanoindentation." *J. Appl. Phys.* 99: 074304.
- Filyukov, D. V., E. N. Brodskaya, et al. (2007). "Molecular-Dynamics Simulation of Nanoclusters of Crystal Modifications of Titanium Dioxide." *Russ. J. Gen. Chem.* 77: 10.
- Gulseren, O., F. Ercolessi, et al. (1998). "Noncrystalline Structures of Ultrathin Unsupported Nanowires." *Phys. Rev. Lett.* 17: 3775.
- Guo, L., Z. H. Wu, et al. (2000). "Synthesis of novel Sb O and Sb O nanorods." *Chem. Phys. Lett.* 318: 49.
- Hallil, A., R. Tetot, et al. (2006). "Use of a variable-charge interatomic potential for atomistic simulations of bulk, oxygen vacancies, and surfaces of rutile TiO<sub>2</sub>." *Phys. Rev. B* 73: 165406.
- Heo, Y. W., D. P. Norton, et al. (2004). "ZnO nanowire growth and devices." *Mater. Sci. Eng. R* 47: 1.
- Hoffmann, S., F. Ostlund, et al. (2007). "Fracture strength and Young's modulus of ZnO nanowires." *Nanotechnology* 18: 205503.
- [http://www.cse.scitech.ac.uk/ccg/software/DL\\_POLY/](http://www.cse.scitech.ac.uk/ccg/software/DL_POLY/).
- Huang, Y. H., X. D. Bai, et al. (2006). "In situ mechanical properties of individual ZnO nanowires and the mass measurement of nanoparticles." *J. Phys.: Condens. Matter* 18.
- Isaak, D. G., J. D. Garnes, et al. (1998). "Elasticity of TiO<sub>2</sub> rutile to 1800 K." *Phys. Chem. Minerals* 26: 31.
- Jiang, X. C., T. Herricks, et al. (2002). "CuO Nanowires Can Be Synthesized by Heating Copper Substrates in Air." *Nano Lett.* 2: 1333.
- Kondo, Y. and K. takayanagi (2000). "Synthesis and Characterization of Helical Multi-Shell Gold Nanowires." *science* 289: 606.

- Kulkarni, A. J. and M. Zhou (2006). "Size-dependent thermal conductivity of zinc oxide nanobelts." *Appl. Phys. Lett.* 88.
- Kulkarni, A. J., M. Zhou, et al. (2005). "Orientation and size dependence of the elastic properties of zinc oxide nanobelts." *Nanotechnology* 16: 2749.
- Lakshmi, B. B., C. J. Partissi, et al. (1997). "Sol-Gel Template Synthesis of Semiconductor Oxide Micro- and Nanostructures." *Chem. Mater.* 9: 2544.
- Law, M., J. Goldberger, et al. (2004). "Semiconductor Nanowires and Nanotubes." *Annu. Rev. Mater. Res.* 34: 83.
- Li, C., D. H. Zhang, et al. (2003). "Diameter-controlled growth of single-crystalline IN2O3 nanowires and their electronic properties." *Adv. Mater.* 2: 143.
- Li, D. and Y. N. Xia (2003). "Fabrication of Titania Nanofibers by Electrospinning." *Nano Lett.* 3: 555.
- Li, G. L. and G. H. Wang (1999). "Synthesis and characterization of rutile TiO<sub>2</sub> nanowhiskers." *J. Mater. Res.* 14: 3346.
- Li, Y. G., B. Tan, et al. (2006). "Freestanding Mesoporous Quasi-Single-Crystalline Co<sub>3</sub>O<sub>4</sub> Nanowire Arrays." *J. Am. Chem. Soc.* 128: 14258.
- Lu, D. Y., J. Chen, et al. (2007). "Raman study of thermochromic phase transition." *Appl. Phys. Lett.* 90.
- Lu, J. G., P. C. Chang, et al. (2006). "Quasi-one-dimensional metal oxide materials— Synthesis, properties and applications." *Mater. Sci. Eng. R* 52: 49.
- Lu, W. and C. M. Lieber (2006). "Semiconductor nanowires." *J. Phys. D: Appl. Phys.* 39: R387.
- Lugovskaya, L. A., L. A. Aleshina, et al. (2002). "X-ray study and structure simulation of amorphous tungsten oxide." *Acta Crystallogr. Sec. B* 58: 576-586.
- Ma, R. Z. and Y. S. Bando (2003). "Uniform MgO nanobelts formed from in situ Mg<sub>3</sub>N<sub>2</sub> precursor." *Chem. Phys. Lett.* 370: 770.
- Maleev, M. A., D. Srivastava, et al. (2006). "Silicon carbide nanowires under external loads: An atomistic simulation study." *Phys. Rev. B* 74: 165303.
- Manoharan, M. P., A. V. Desai, et al. (2008). "Synthesis and Elastic Characterization of Zinc Oxide Nanowires." *J. Nanomater.* 2008: 1.
- Matsui, M. and M. Akaogi (1991). "Molecular dynamics simulation of the structural and physical properties of the four polymorphs of TiO<sub>2</sub>." *Mol. Sim.* 6(4): 239.
- Ni, H. and X. D. Li (2006). "Young's modulus of ZnO nanobelts measured using atomic force microscopy and nanoindentation techniques." *Nanotechnology* 17: 3591.
- Petitto, S. C. and M. A. Langell (2004). "Surface composition and structure of Co<sub>3</sub>O<sub>4</sub>(110) and the effect of impurity segregation." *J. Vac. Sci. Technol. A* 22: 1690.
- Rao, C. N. R., F. L. Deepak, et al. (2003). "Inorganic nanowires." *Prog. Solid State Chem.* 31: 5-147.
- Samsonov, G. V. (1982). *The Oxide Handbook*. New York - Washington - London.
- Shankar, K. S. and A. K. Raychaudhuri (2005). "Fabrication of nanowires of multicomponent oxides: Review of recent advances." *Mater. Sci. Eng. C* 25: 738.
- Song, J. H., X. D. Wang, et al. (2005). "Elastic Property of Vertically Aligned Nanowires." *Nano Lett.* 5: 1954.
- Tan, E. P. S., Y. Zhu, et al. (2007). "Crystallinity and surface effects on Young's modulus of CuO nanowires." *Appl. Phys. Lett.* 90: 163112.
- Tian, Z. R., J. A. Voigt, et al. (2003). "Complex and oriented ZnO nanostructures." *Nature Mater.* 2: 821.
- Urban, J. J., J. E. Spanier, et al. (2003). "Single-crystalline Barium Titanate Nanowires." *Adv. Mater.* 15: 423.

- Valcarcel, V., A. Souto, et al. (1998). "Development of Single-Crystal  $\alpha$ -Al<sub>2</sub>O<sub>3</sub> Fibers by Vapor-Liquid-Solid Deposition (VLS) from Aluminum and Powdered Silica." *Adv. Mater.* 10: 138.
- Varghese, B., C. H. Teo, et al. (2007). "Co<sub>3</sub>O<sub>4</sub> Nanostructures with Different Morphologies and their Field-Emission Properties." *Adv. Funct. Mater.* 17: 1932.
- Vayssieres, L. (2003). "Growth of arrayed nanorods and nanowires of ZnO from aqueous solutions." *Adv. Mater.* 15: 464.
- Wang, B. L., S. Y. Yin, et al. (2001). "Novel Structures and Properties of Gold Nanowires." *Phys. Rev. Lett.* 86: 2046.
- Wang, B. L., S. Y. Yin, et al. (2001). "Structures and electronic properties of ultrathin titanium nanowires." *J. Phys.: Condens. Matter* 13: L403.
- Wang, J., A. J. Kulkarni, et al. (2008). "Novel mechanical behavior of ZnO nanorods." *Comput. Methods Appl. Mech. Engrg.* 197: 3182.
- Wang, W. Z., Y. J. Zhan, et al. (2001). "One-step, solid-state reaction to the synthesis of copper oxide nanorods in the presence of a suitable surfactant." *Chem. Comm.*: 727.
- Wang, X. D., J. H. Song, et al. (2007). "Nanowire and nanobelt arrays of zinc oxide from synthesis to properties and to novel devices." *J. Mater. Chem* 17: 711.
- Watt, J. P. (1979). "Hashin-Shtrikman bounds on the effective elastic moduli of polycrystals with orthorhombic symmetry." *J. Appl. Phys.* 50: 6290.
- Watt, J. P. (1980). "Hashin-Shtrikman bounds on the effective elastic moduli of polycrystals with monoclinic symmetry." *J. Appl. Phys.* 51: 1520.
- Watt, J. P. (1986). "Hashin-Shtrikman bounds on the effective elastic moduli of polycrystals with trigonal(3,-3) and tetragonal(4,-4,m) symmetry." *J. Appl. Phys.* 60: 3120.
- Watt, J. P. (1987). "POLYXSTAL: A FORTRAN PROGRAM TO CALCULATE AVERAGE ELASTIC PROPERTIES OF MINERALS FROM SINGLE-CRYSTAL." *Comput. Geosci.* 13: 441.
- Watt, J. P. and L. Peselnick (1980). "Clarification of the Hashin-Shtrikman bounds on the effective elastic moduli of polycrystals with hexagonal, trigonal and tetragonal symmetries." *J. Appl. Phys.* 51: 1525.
- Wen, B. M., J. E. Sader, et al. (2008). "Mechanical Properties of ZnO Nanowires." *Phys. Rev. Lett.* 101: 175502.
- Woodward, P. M., A. W. Sleight, et al. (1995). "Structure Refinement of Triclinic Tungsten Trioxide." *J. Phys. Chem. Solids* 56: 1305.
- Wu, J. M., H. C. Shih, et al. (2006). "Formation and photoluminescence of single-crystalline rutile TiO<sub>2</sub> nanowires synthesized by thermal evaporation." *Nanotechnology* 17: 105.
- Wu, J. M., H. C. Shih, et al. (2005). "Thermal evaporation growth and the luminescence property of TiO<sub>2</sub> nanowires." *J. Cryst. Grow.* 281: 384.
- Wu, X. C., W. H. Song, et al. (2000). "Crystalline gallium oxide nanowires: intensive blue light emitters." *Chem. Phys. Lett.* 328: 5.
- Xiao, Z. L., C. Y. Han, et al. (2002). "Fabrication of Alumina Nanotubes and Nanowires by Etching Porous Alumina Membranes." *Nano Lett.* 2: 1293.
- Yang, P. D., Y. Y. Wu, et al. (2002). "Inorganic semiconductor nanowires." *Int. J. Nanosci.* 1(1): 1.
- Yum, K. S., Z. Y. Wang, et al. (2004). "Experimental measurement and model analysis of damping effect in nanoscale mechanical beam resonators in air." *J. Appl. Phys.* 96: 3933.
- Zhou, J., C. S. Lao, et al. (2006). "Nanowire as pico-gram balance at workplace atmosphere." *Solid State Comm.* 139: 222.
- Zhu, Y. W., Y. S. Zhang, et al. (2010). "Hotplate Synthesis and Mechanical Characterization of Vanadium Oxide Nanobelts." *Acta Mater.* 58: 415.

## **Part 3**

### **Metal Alloy Nanowires**



# Synthesis of Pt – Containing Metals Alloy and Hybrid Nanowires and Investigation of Electronic Structure Using Synchrotron-Based X-Ray Absorption Techniques

Xiaowei Teng<sup>1</sup>, Wenxin Du<sup>1</sup> and Qi Wang<sup>2</sup>

<sup>1</sup>*University of New Hampshire,*

<sup>2</sup>*University of Delaware*

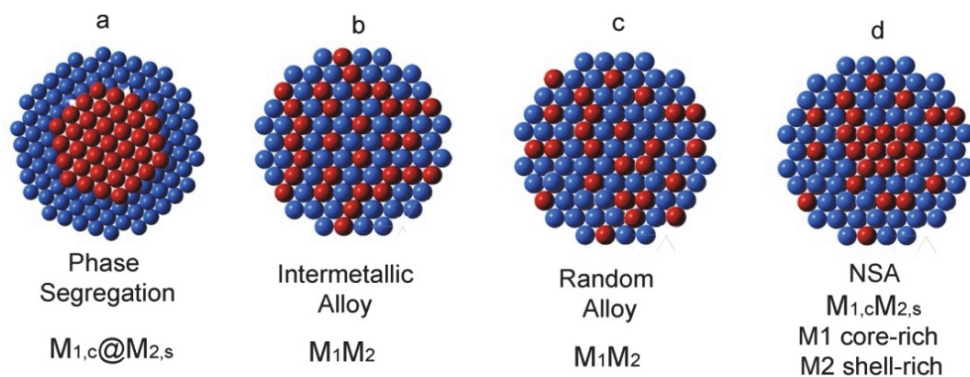
USA

## 1. Introduction

Platinum-containing bimetallic nanomaterials have shown different electronic structures from their monometallic counterparts, bringing exotic properties to various catalytic and magnetic applications. The synthesis and shape-dependent properties of bimetallic cubes, truncated cubes, dendrites, and hollow structures, have been intensively studied. One dimensional (1D) Pt-containing nanostructure has attracted special interest, although synthetic challenges in the fine control over morphology arising from unfavorable anisotropic growth of symmetric cubic lattice structures from Pt metal and alloys (Ahmadi et al., 1996; Cozzoli & Manna, 2005; Xia et al., 2003).

The electronic structure of bimetallic nanowires is associated with their heterogeneous structural diversity strongly, such as phase segregation (Zhong & Maye, 2001), intermetallic alloy (Casado-Rivera et al., 2004), random alloy (Shibata, et al., 2002) and near surface alloy (NSA) (Greeley & Mavrikakis, 2006; Knudsen, et al., 2007) (See Scheme). Therefore, detailed studies of bimetallic heterogeneous structures are essential for their applications. The structural characterization of bimetallic nanomaterials is not trivial, partly due to the complexity of heterogeneous nature imposed by nanoscale system. X-ray absorption fine spectroscopy (XAS) is a well established tool for investigating the element-resolved structure of bimetallic nanomaterials, since the local environment and electronic properties of atoms of each resonant element can be studied separately by tuning the X-ray energy to the absorbing edge of each metal. XAS has been successfully used to study bonding habit, geometry, electronic and surface structure of many bimetallic nanoparticles (e.g., Pt/Ru, Pt/Au, Pd/Au and Pt/Ir) (Nashner et al., 1997). When the short range order information extracted from XAS analysis is combined with the knowledge of the long range order and average compositional distribution obtained by complementary techniques, actual heterogeneous structure and electronic state of nanomaterials can be quantitatively analyzed.

In this chapter, we intend to focus on our recent results on the synthesis and electronic structures of ultrathin PtAu alloy nanowires, Pt/Au phase-segregated hybrid nanowires.



**Scheme** Four heterogeneous nanostructures: (a) Phase segregation (surface of metal  $M_1$  is modified by irreversibly adsorbed  $M_2$ ); (b) Intermetallic alloy (atoms  $M_1$  and  $M_2$  are mixed with definite lattice proportions); (3) Random alloy (homogeneous alloy, atoms  $M_1$  and  $M_2$  are mixed statistically in accordance with the overall concentration). (4) NSA alloy (atoms  $M_1$  are core-rich and  $M_2$  are shell-rich)

The PtAu alloy and Pt/Au hybrid nanowires with average width less than 3 nm and length over 50 nm were made from phase transfer method, in which inorganic gold and platinum precursors were transferred into an organic mixture via phase transfer agent. Subsequent injection of the reducing agent resulted in the formation of nanowires. Generally, the anisotropy of crystal structure is believed to be the main driving force for the anisotropic growth of nanostructures. However, this would not be the case accounting for formation of PtAu nanowires or Pt nanowires upon which Au particles grow to create Pt/Au hybrids, as both Pt and Au are isotropic in crystal lattice structure. Unlike the cases in quantum dots where the dipole moment was the driving force, the anisotropic growth of these Pt and PtAu nanowires is most likely due to the kinetics control of the growth rates of various facets of seeds driven by specific binding of capping agent on specific crystal surfaces. The tentative growth mechanisms to each subcategory PtAu nanowires or hybrid nanowires will be presented.

In addition to the synthesis, crystalline and electronic structure of those nanowires will be determined by various techniques, including transmission electron microscopy (TEM) and energy dispersive spectrometry (EDS), etc. The disclosure of morphology and crystalline details of those homogenous/heterogeneous bimetallic nanowires will be mainly relied on TEM and HRTEM equipped with EDS as well as EXAFS analysis. UV-vis spectroscopy is specifically used to find out the existence of Au in PtAu nanowires and possible size effect. The electronic structure, the charge transfer between the each component throughout the bimetallic nanowires in particular, will be determined by synchrotron-based X-ray absorption spectroscopy (XAS). The relationship between the heterogeneous structure and the electronic properties of the bimetallic nanowires will be studied. Our studies on the synthesis and electronic structure of Pt-containing nanowires will be highly encouraging new families of bimetallic nanowires systems. Such research may be developed to sustain the needs of emerging technologies such as renewable energy and spintronics, where there is a continuous drive to find nanomaterials with ever more exotic

electronic and catalytic properties, and where the assembly of these fundamental building blocks can lead to new types of functionality. The new electronic structure driven by enhanced charge transfer between heterogeneous atoms will continue to be our focus in the future.

## 2. Synthetic strategy of Pt-containing nanowires

There are a variety of chemical methods to be able to generate 1D nanostructures including nanowires. Although the general methods for growing 1D nanostructures still yet available, a number of strategies are readily for employ, including utilization of anisotropic crystalline structure of a material to facilitate 1D growth, introduction of a liquid-solid interface to reduce the symmetry of a seed, template-directed 1D nanostructure formation, modification of growth habit of seeds by supersaturation control, kinetic control over various facets of seeds by adding suitable capping agents, self-assembly of 0D nanostructures and size reduction of 1D microstructures. The anisotropy of crystal structure is believed to be the main driving force for the anisotropic growth of nanostructures in liquid phase synthesis. However, since both Pt and Au have symmetric cubic lattice, it is intrinsically difficult to make nanowires from these materials. In the following sections, we will show the readers our strategy to synthesize a variety of Pt and Pt/Au nanowires structures by careful selection of synthetic methods as well as manipulations of experimental conditions.

### 2.1 Synthesis of Pt nanowires

The liquid phase synthesis is commonly used for metal salt reduction, either in homogenous system or two phase systems. Here, we chose phase transfer method (Brust et al., 1994), i.e. two phase synthesis to make Pt-containing nanowires with different morphologies and electronic structures. One of the big advantages of this method is that by using relatively simple and inexpensive inorganic metal precursors, we are able to harvest nanomaterials with controllable size and shape as well as hydrophobic properties at room temperature. Typically, the metal ions are first extracted from an aqueous solution to a hydrocarbon (toluene) phase with the help of a phase-transfer agent such as tetraoctylammonium bromide (DTAB). Then further reduction occurs upon adding aqueous sodium tetrahydroborate ( $\text{NaBH}_4$ ) in the presence of an alkanethiol or alkylamine as surfactant. The nucleation and growth of these metal particles and the attachment of the thiol or amine molecules to the nanoparticles would occur simultaneously in a single step. In the synthesis of Pt nanowires, inorganic platinum chloride ( $\text{PtCl}_2$ ) or sodium hexachloroplatinate ( $\text{Na}_2\text{PtCl}_6$ ) was transferred to a mixture of surfactant octadecylamine (ODA) and toluene using phase transfer agent DTAB. Now the surfaces of metal ions were capped with ODA and DTAB as shown in Step One in Figure 1. After injection of overdosed  $\text{NaBH}_4$  in aqueous solution, platinum ions were reduced rapidly under such a highly reductive environment to form thermodynamically unstable elongated primary nanostructures (PN), which is depicted in Step Two (Figure 1). At the same time, the secondary growth of PN apparently took preferred equivalent directions also along  $\langle 111 \rangle$ , leading to the attachment growth of thread-like quasi-nanowires (Step Three, Figure 1). Considering the obvious absence of crystal structure anisotropy of Pt, the oriented attachment in these Pt nanostructures was most likely due to the selective growth driven by specific binding of capping agent on specific crystal surfaces. In general, the shape of nanomaterials is highly dependent on the

competitive growth rate along the low index crystal planes in the presence of surfactants. Alkaline seemed to preferentially adsorb on the surfaces of Pd and Pt, and facilitate the growth of PNs along  $\langle 111 \rangle$  directions.

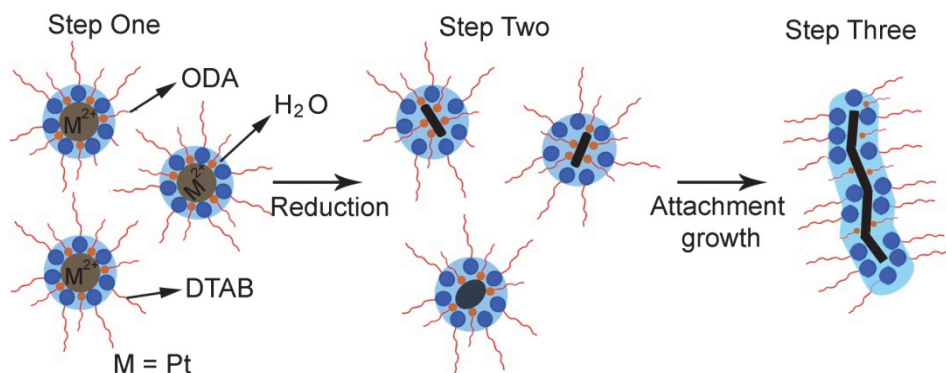


Fig. 1. Schematic diagram of the formation of Pt nanowires.

## 2.2 Synthesis of Pt/Au alloy nanowires

Similar as in the synthesis of Pt nanowire, making Pt/Au alloy nanowires also faces the same challenge to direct the unfavorable anisotropic growth due to the isotropic crystal lattice of Pt and Au. Although the reduction potential of  $\text{Au}^{3+}$  to Au is higher than that of  $\text{Pt}^{2+}$  to Pt in general, it is still possible to get Pt/Au alloy formation under highly reducing environment. Based on the successful experience of synthesis of Pt nanowires, we obtained Pt/Au nanowires via the same phase transfer method. In contrast to the synthesis of Pt nanowires, the Pt/Au alloy nanowires were made by co-reduction of two inorganic precursors, in which  $\text{AuCl}_3$  and sodium tetrachloroplatinate ( $\text{Na}_2\text{PtCl}_4$ ) were transferred into an organic mixture of octadecylamine and toluene via a phase transfer agent DTAB. Subsequent injection of the reducing agent  $\text{NaBH}_4$  aqueous solution resulted in the formation of ultrathin Pt/Au nanowires. Eventually, two alloyed ultrathin nanowires,  $\text{Pt}_{75}\text{Au}_{25}$  and  $\text{Pt}_{52}\text{Au}_{48}$ , were identified and analyzed later on.

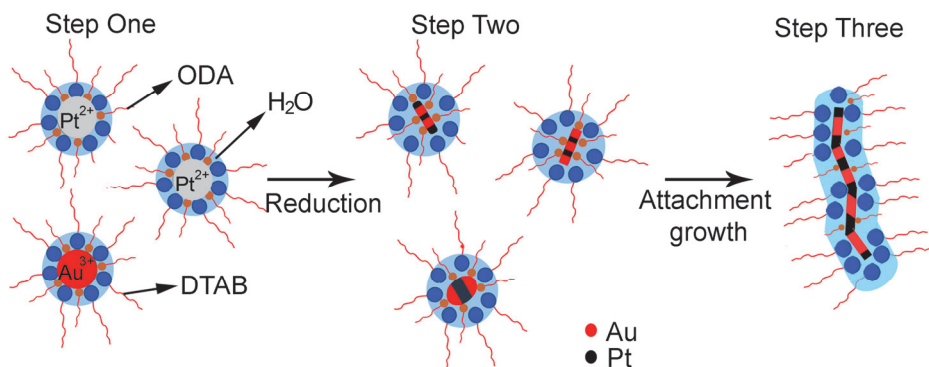


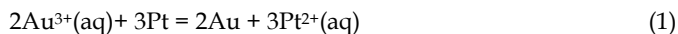
Fig. 2. Schematic diagram of the formation of Pt/Au alloy nanowires.

Compared to Pt nanowires formation, the growth mechanism of Pt/Au alloy nanowires would be similar without considering the distributions of Pt and Au atoms within the Pt/Au nanowires. Figure 2 sketches out the simplified formation process of Pt/Au alloy nanowires. In fact, the detailed Pt/Au nanowires structures exhibit stoichiometry-dependency. It is demonstrated later that Pt<sub>75</sub>Au<sub>25</sub> and Pt<sub>52</sub>Au<sub>48</sub> nanowires are alloyed structures, with the latter having homogeneous placement of Au and Pt atoms and the former a more highly ordered arrangement, with a Pt-rich shell and an Au-rich core. It is interesting to consider how the heterogeneous Pt<sub>75</sub>Au<sub>25</sub> alloy nanowires initially formed and how they subsequently evolved into homogeneous Pt<sub>52</sub>Au<sub>48</sub>. Here, we propose a growth mechanism which explains the formation of Pt/Au nanostructures with such a strong sensitivity to Pt/Au stoichiometry. In the synthesis of Pt/Au alloy nanomaterials, we believe that the standard reduction potential and surface free energy are the most important intrinsic parameters for determining the final heterogeneous nanostructures, and lead to two competing mechanisms for the distribution of Au and Pt within the growing nanowire. On the one hand, the high values of standard reduction potential of Au and Pt in solution at room temperature ( $E^\ominus(\text{Pt}^{2+}/\text{Pt}) = 1.20 \text{ V}$ ,  $E^\ominus(\text{Au}^{3+}/\text{Au}) = 1.52 \text{ V}$ ) suggest that the Au<sup>3+</sup> and Pt<sup>2+</sup> ions are reduced quickly by the addition of excess amounts of NaBH<sub>4</sub> during the synthesis. However, since the reduction potential of Au is slightly higher than that of Pt, it is plausible that Au<sup>3+</sup> would be reduced more easily during the nucleation and consequent growth stages, and would consequently be found in the core, which forms first. On the other hand, surface free energy, in fact defined by the change of the free enthalpy of the surface-creating process under an isothermal-isobaric condition, gives rise to an opposite trend for the Pt/Au atomic distribution compared to the reduction potential. The surface free energy of Au at room temperature (1.63 J/m<sup>2</sup>) is much lower than that of Pt (2.69 J/m<sup>2</sup>). This argument would then conclude that Au atoms would cluster near the surface of the product, while the Pt atoms are relegated to the sublayer or core region.

These competing growth mechanisms based on the standard reduction potential and surface free energy, are further complicated by the interaction between metal surface and capping agent. It is well known that the capping agent (surfactant) is very important in the formation of nanomaterials during solution phase synthesis. For instance, alkaline carboxylic acids, alkylamines, alkylthiols and alkylphosphines have all been used for the synthesis of transition metal/alloy and semiconductor nanomaterials with fine control over size, shape and composition. The interaction between the surfactant and the metal surface is largely dependent on the electronegativity of the metal. Electronegativity describes the power of an atom to attract electrons to it. Fluorine (the most electronegative element) is assigned a value of 4.0, while cesium and francium which are the least electronegative, have electronegativities of only 0.7. Since electronegativities of various atoms differ as following: O > N > S > Au > Pd > Pt, Pt atoms are then expected to show a relatively stronger interaction with octadecylamine (C<sub>18</sub>H<sub>36</sub>NH<sub>2</sub>) than Au atoms, following from the increased probabilities of charge transfer from Pt and Au atoms to N atoms. As a consequence of preferential binding between octadecylamine and Pt metals surfaces, we suggest that the Pt atoms will be stabilized toward the surface and Au atoms diffuse into core region, accounting for the formation of an Au<sub>c</sub>Pt<sub>s</sub> (Au-core-rich and Pt-shell-rich) heterogeneous alloy. In fact, preferential binding between alkylamine or alkylthiol with Pd atoms have previously been reported to account for the formation of Au<sub>c</sub>Pt<sub>s</sub> non-random alloy.

### 2.3 Synthesis of Pt/Au hybrids based on Pt nanowires

Considering that the standard reduction potential of Au is higher than Pt in solution at room temperature ( $E^\Phi(\text{Pt}^{2+}/\text{Pt}) = 1.20 \text{ V}$ ,  $E^\Phi(\text{Au}^{3+}/\text{Au}) = 1.52 \text{ V}$ ), it is plausible to utilize galvanic replacement reaction between  $\text{Au}^{3+}$  and Pt nanowire to obtain hybrid structures. When two metals satisfy such condition, i.e. the one with lower reduction potential exists in metallic state and the other with higher reduction potential stays as ion, the latter tends to seize electrons from the former, making itself being reduced and leaving the former metal being oxidized and thus dissolved in solution. Indeed, the Pt/Au hybrid nanowires were successfully acquired upon the galvanic replacement reaction between  $\text{AuCl}_3$  and as-made Pt nanowires as indicated by following reaction:



After fresh Pt nanowires were made,  $\text{AuCl}_3$  solution was prepared by dissolving in toluene in the presence of relatively small amount of DTAB. The different volumes (0.4, 1.0, 2.0 ml) of  $\text{AuCl}_3$  solution (40 mM) was then injected into fresh made Pt nanowire solution ( $\sim 0.06 \text{ mmol}$ ) to form 3 types of nanostructures. The galvanic replacement reaction proceeded for one hour under argon protection at room temperature.

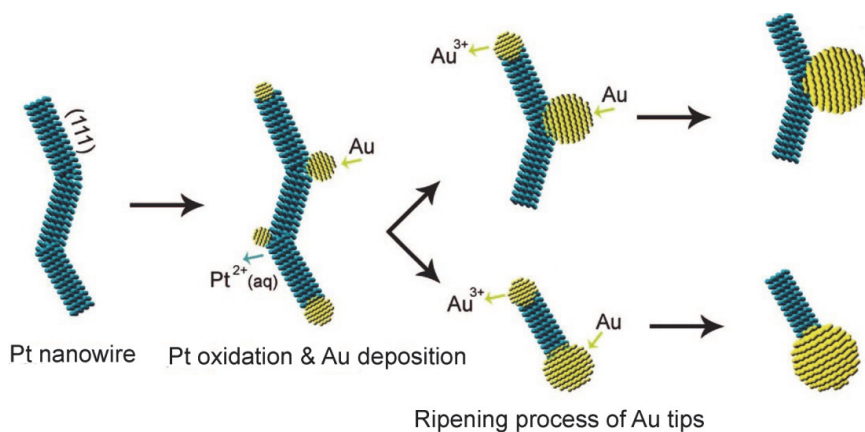


Fig. 3. Schematic drawing of the galvanic replacement reaction between Pt nanowires and  $\text{Au}^{3+}$ .

The proposed growth mechanism of Pt/Au hybrid nanowires formation is presented in Figure 3. When  $\text{AuCl}_3$  was added to the solution containing ultrathin Pt nanowires,  $\text{Au}^{3+}$  ions might preferentially attach to the certain sites along the Pt nanowires such as tips, stacking faults, and twinning boundaries, since those sites possess higher surface energy and/or relatively less passivation by surfactants due to rather sharp radius of curvature. Since the reduction potential of  $\text{Au}^{3+}$  to Au ( $E^\Phi = 1.5 \text{ V}$ ) is higher than that of  $\text{Pt}^{2+}$  to Pt ( $E^\Phi = 1.2 \text{ V}$ ), Pt nanowires were oxidized and  $\text{Au}^{3+}$  ions were then reduced by the electrons generated from the replacement reaction. As the reaction continued, the Au nanoparticles grew larger, along with the consumption and breakdown of Pt nanowires. The Ostwald ripening process may also occur during the galvanic replacement reaction, accounting for the disappearance of smaller Au components to facilitate the growth of larger Au components. The ripening of Pt nanowires, however, was not preferred as evidenced by the fact that the width of Pt nanowires did not change.

### 3. Morphology and crystalline structures of Pt-containing nanowires

To decipher the morphology and crystalline structures of Pt/Au nanowires, and electronic structures of those Pt-based nanowires, advanced characterization techniques, including transmission electron microscopy (TEM), scanning transmission electron microscopy (STEM) equipped with X-ray energy dispersive spectroscopy (EDS) or ultraviolet-visible (UV-vis) spectroscopy, and extended X-ray absorption fine structure (EXAFS) spectroscopy, were combined selectively to study these nanomaterials. In particular, the EXAFS appears as a powerful tool to provide precise crystalline details in average within the nanowires. These detailed structure information will help us obtain an insight on the exotic electronic structures in these Pt/Au nanowires.

#### 3.1 TEM and STEM-EDS analysis

The morphologies and crystalline structure of Pt nanowires can be clearly seen in Figure 4.

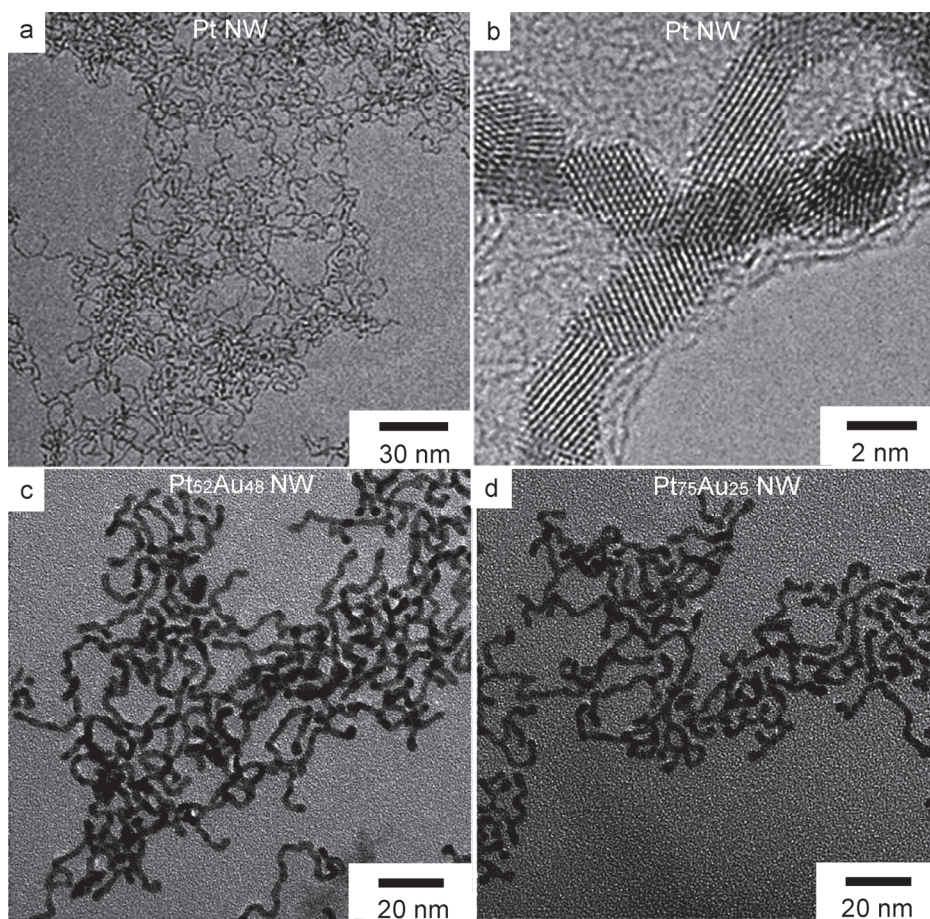


Fig. 4. TEM images of (a, b) Pt nanowires, (c) Pt<sub>52</sub>Au<sub>48</sub>, and (d) Pt<sub>75</sub>Au<sub>25</sub> nanowires.

Figure 4a shows the as-made Pt nanowires with dimension of  $2.3 \pm 0.2$  nm in width and over 30 nm in length. High-resolution TEM (HRTEM) shows Pt nanowires are polycrystalline with well-defined lattice planes, both twinning boundaries and stacking faults are observed (Figure 4b). HRTEM reveals that each nanowire is composed of several single-crystalline, elongated primary nanostructures (PNs) and the secondary growth of PNs apparently took preferred equivalent directions also along  $\langle 111 \rangle$ .

The Pt<sub>52</sub>Au<sub>48</sub> and Pt<sub>75</sub>Au<sub>25</sub> alloy nanowires which were synthesized via co-reduction of Pt and Au metal precursors, exhibited a uniform 1D morphology, with average lengths as large as 100 nm, average widths of  $2.6 \pm 0.4$  nm and  $2.5 \pm 0.3$  nm, respectively (Figure 4c, 4d). These Pt/Au nanowires appeared to be entirely crystalline, evidenced by the lattice fringes which extend across the full extent of the TEM image. Dominant lattice spacing of 2.3 Å were obtained, which corresponds to the interplanar distances of the  $\{111\}$  Pt/Au surfaces (data are not shown). In general, the shape of materials is highly dependent on competitive growth along the low index crystal planes in the present of surfactant, including (111), (110) and (100) planes. Anisotropic growth of Pt/Au nanowires is rather unexpected due to the symmetric cubic lattices of both Pt and Au metals. However, our TEM data indicate that octadecylamine might preferentially adsorb on the surfaces of Au and Pt, facilitating the growth of Pt/Au nanowires along the  $\langle 111 \rangle$  directions.

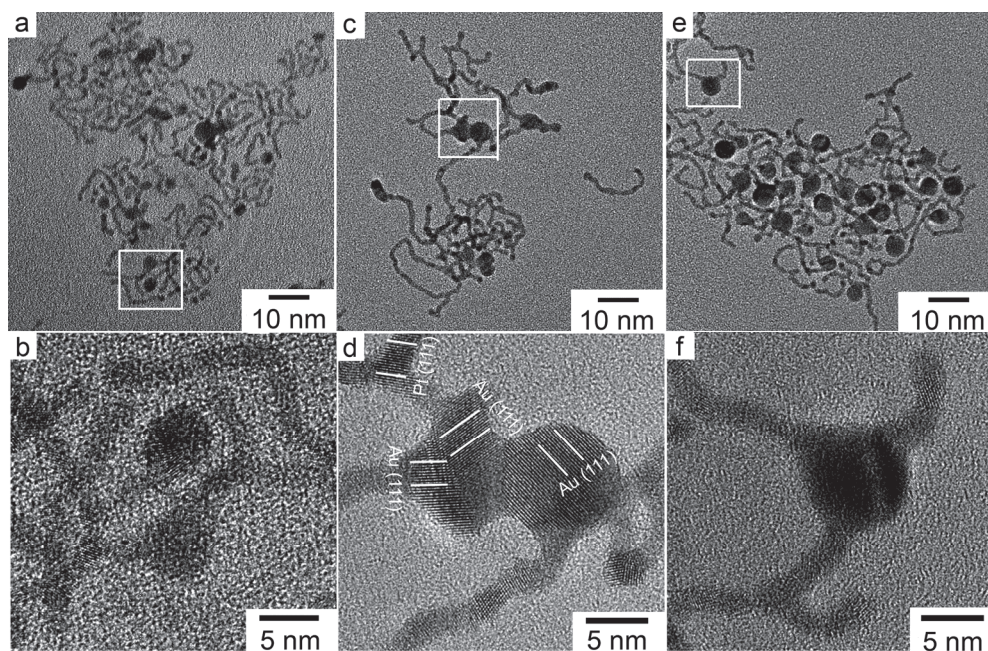


Fig. 5. TEM images of Pt/Au hybrid nanowires obtained by titrating the Pt nanowires with different volumes of 40 mM AuCl<sub>3</sub> solutions: (a, b) 0.4, (c, d) 1.0, and (e, f) 2.0 ml.

Figure 5 shows TEM images of the Pt/Au hybrid nanowires after reacting Pt nanowires with different amount of AuCl<sub>3</sub>. The galvanic replacement reaction resulted in the nucleation and deposition of Au atoms along the Pt nanowires to form an Au

nanoparticles/Pt nanowires hybrid structures. When  $\text{AuCl}_3$  was added from 0.4, 1.0 to 2.0 ml, the average size of Au components increased from  $2.7 \pm 0.9$  nm,  $4.4 \pm 0.7$  nm, to  $4.9 \pm 0.5$  nm. The HRTEM images consistently showed the lattice planes for Au and Pt with lattice spacings of 2.4 and 2.3 Å, respectively, which correspond to the {111} lattice planes in both materials (Figure 5d). Since the mismatch of the lattice constants between Pt and Au is less than 5%, Au atoms could nucleate and grow epitaxially on the Pt nanowires along the  $\langle 111 \rangle$  direction via attachment growth. Moreover, as Pearson reported, the Pt/Au phase diagram exhibits a miscibility gap: the solubility of Au in Pt is only about 4% at ambient temperature, rising to 6% at 973 K. Therefore, during the galvanic replacement reaction, reduced Au atoms display a strong tendency to form segregated Au particles on the Pt surfaces. This phenomenon also may be attributed to the low surface free energy of Au compared with that of Pt, thereby favoring the enrichment by Au on the Pt surfaces.

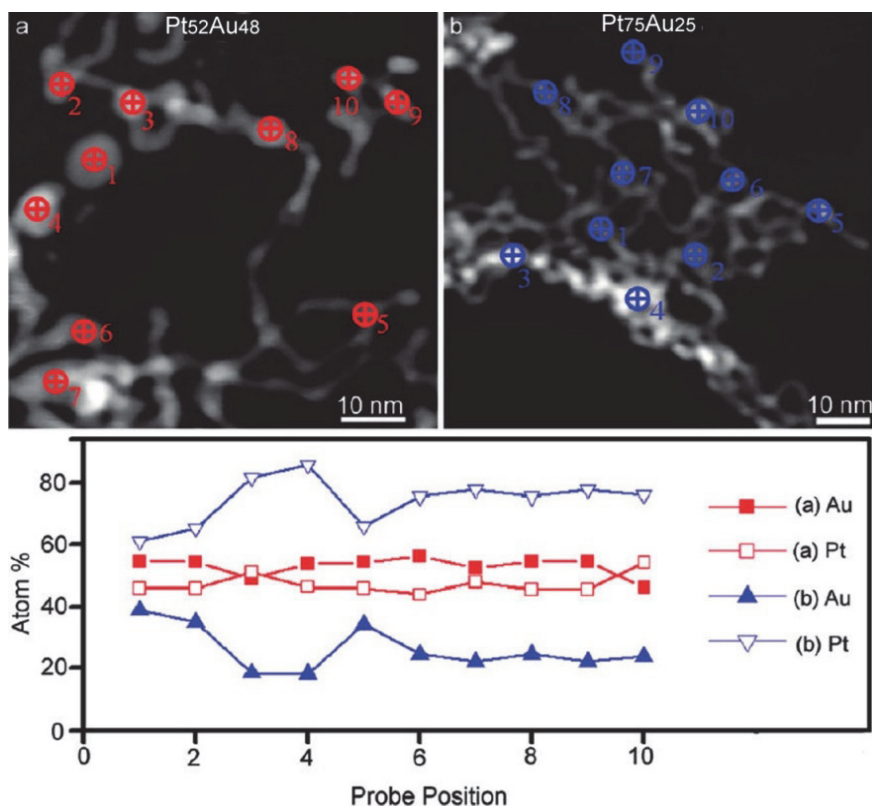


Fig. 6. The dark-field images of (a)  $\text{Pt}_{52}\text{Au}_{48}$  and (b)  $\text{Pt}_{75}\text{Au}_{25}$  nanowires, and the elements distributions along individual nanowire assessed by STEM-EDS analysis.

To explore the distributions of the Au and Pt within the Pt/Au alloy nanowires, individual  $\text{Pt}_{52}\text{Au}_{48}$  and  $\text{Pt}_{75}\text{Au}_{25}$  nanowires were assessed along the nanowire direction by the probe analysis in the STEM-EDS mode as shown in Figure 6. As illustrated, the contents of Pt and Au were determined at ten sites for either nanowire. Average chemical compositions of

$Pt_{47+3}Au_{53+3}$  and  $Pt_{74+7}Au_{26+7}$  were identified. The close correspondence of the EDS analysis results obtained from individual nanowires and from their large area assemblies, demonstrates the high degree of homogeneity in chemical composition over a large quantity of as-made  $Pt_{52}Au_{48}$  and  $Pt_{75}Au_{25}$  nanowires.

The segregation between Pt and Au in Pt/Au hybrid nanowires is evidenced by the scanning transmission electron microscopy–energy dispersive spectroscopy (STEM-EDS) measurements shown in Figure 7.

The STEM-EDS analysis revealed compositional variation along the long axis of the hybrid nanostructures. As illustrated, the contents of Pt and Au were determined for eight sites, located at the tip and along the tail. We found that, except at the site situated in the interface between the tip and tail where both Pt and Au signals were detected (2nd site), there was distinct segregation; Au was detected only at the tip region (1st site), and Pt only was recorded in the tail region, that is, the third to the eighth site.

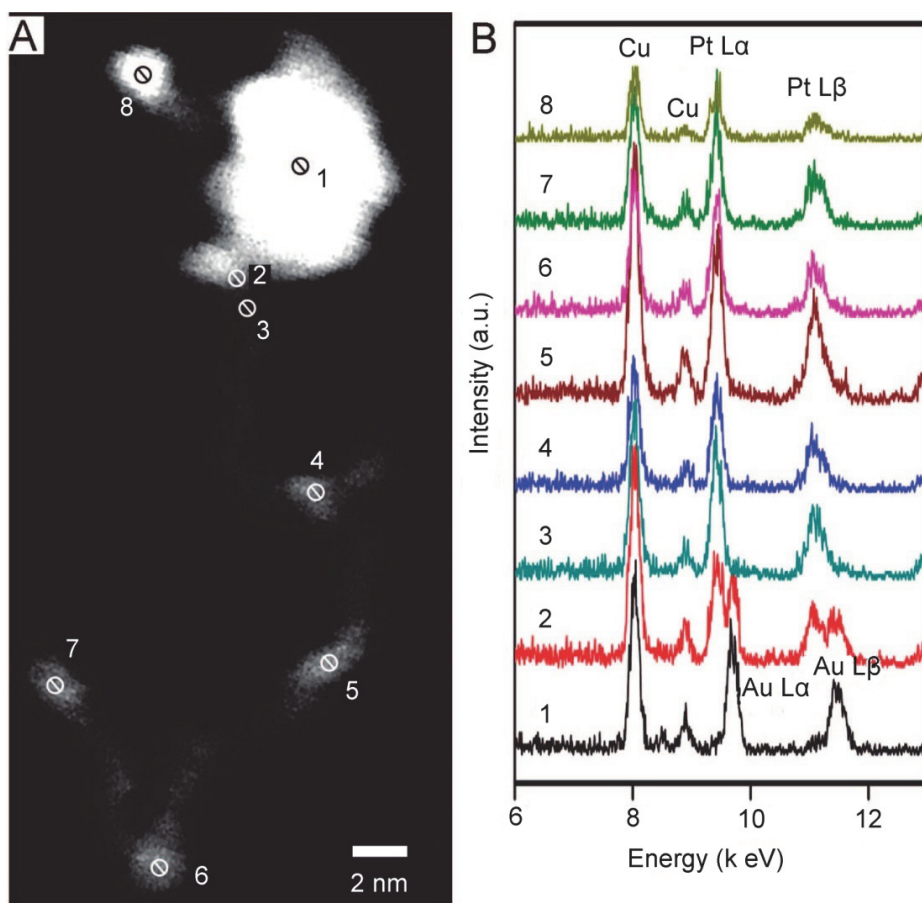


Fig. 7. (A) STEM image of a Pt/Au hybrid nanostructures obtained by titrating the Pt nanowires with 1.0 ml of 40 mM  $AuCl_3$  solutions and (B) its EDS spectra.

### 3.2 UV-vis spectroscopy analysis

The existence and size changing of Au components in Pt/Au hybrid nanowires were further evidenced from ultraviolet-visible (UV-vis) absorption studies (Figure 8a). As expected, pronounced gold characteristic peaks are obtained for these Pt/Au hybrids. With the increase in concentration of Au, the intensity of the surface plasmon resonance (SPR) peaks which characteristic of gold increased, and the SPR peak positions shifted to higher wavelength. This spectroscopic evidence further confirms the increased size of the Au components in Pt/Au hybrids as the addition of AuCl<sub>3</sub> rose.

We also performed a UV-vis absorption study of pure Pt, Pt<sub>52</sub>Au<sub>48</sub> and Pt<sub>75</sub>Au<sub>25</sub> nanowires as shown in Figure 8b. As expected, pronounced absorption peaks characteristic of gold are obtained for Pt<sub>52</sub>Au<sub>48</sub> and Pt<sub>75</sub>Au<sub>25</sub>. Moreover, the intensity of the surface plasmon resonance (SPR) peak of gold was more pronounced, and shifted to higher wavelength in the gold rich Pt<sub>52</sub>Au<sub>48</sub>. This spectroscopic evidence further confirmed the increased alloying of Au with Pt from Pt<sub>75</sub>Au<sub>25</sub> to Pt<sub>52</sub>Au<sub>48</sub>. Although we intended to synthesize Pt/Au nanowires with higher Au atomic ratios, instead a mixture of nanowires and spherical nanoparticles with various sizes was obtained. The UV-vis absorption performed on this mixture showed a broadened peak between 510 nm and 550 nm, indicating the coexistence of Pt/Au and Au nanomaterials. Because the equilibrium phase diagram is size dependent, our data obtained from PtAu nanowires which are 2~3 nm in length indicate that ~50 atomic% of Au might be the upper limit of the equilibrium concentration of Au in Pt, beyond which phase segregation occurs.

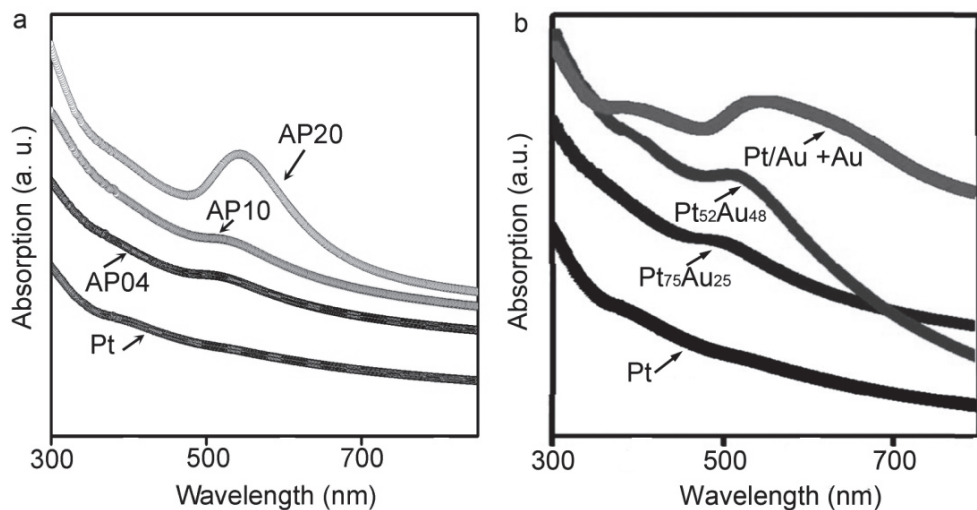


Fig. 8. (a) The UV-vis absorption spectrum of Pt nanowires and Pt/Au hybrid nanostructures obtained by titrating the Pt nanowires with different volumes of 40 mM AuCl<sub>3</sub> solutions: (AP04) 0.4, (AP10) 1.0, and (AP20) 2.0 ml; (b) UV-vis absorption spectrum of as-made Pt, Pt<sub>52</sub>Au<sub>48</sub>, Pt<sub>75</sub>Au<sub>25</sub> nanowires, and mixture of nanowires and Au nanoparticles.

### 3.3 EXAFS characterization

X-ray absorption spectroscopy (XAS) is a well-established technique which provides element specific information on the electronic and structural properties for metallic nanostructures through its two modifications, X-ray absorption near edge structure (XANES) and extended X-ray absorption fine structure (EXAFS).

The EXAFS region, defined as a spectrum region between several hundreds of eV to ~1000 eV above the absorption edge, contains the structural information for coordination environment around the absorbing element. Such parameters including ligand types, coordination numbers, bond distance and disorders can be determined by EXAFS analysis. Simultaneous analysis of EXAFS for both elements in bimetallic nanostructures supply the information of the heterogeneous as well as homogeneous metallic bondings, thus providing evidence to determine the architecture of the bimetallic materials: phase segregation, alloy or core-shell structure (Frenkel, 2007).

Although the morphology and chemical structure of Pt/Au nanowires were verified by TEM and EDS in previous sections, details of the precise crystalline structure such as the Au and Pt distribution and/or coordination inside the nanowires, which is crucial to its physical properties, has not been determined. So we conducted EXAFS studies at both Pt L<sub>3</sub> and Au L<sub>3</sub> edges. The simultaneous, multiple edge (Pt and Au) analysis was employed by fitting theoretical FEFF6 signals of first-nearest-neighbor (1NN) scatterings to the experimental data in *r*-space while properly accounting for the leakage of Pt L<sub>3</sub> to Au L<sub>3</sub> edge EXAFS. The passive electron reduction factors ( $S_0^2$ ) for both elements are fixed at the values found from fits to their respective foil standards. Several parameters describing electronic properties (e.g. Correction to the photoelectron energy origin) and local structural environment (coordination numbers (N), bond lengths (R) and their mean-squared relative deviation ( $\sigma^2$ ) around absorbing atoms are obtained from the analysis. Such multiple dataset fitting (MDS) analysis is widely applied to all types of bimetallic systems since the additional constraints derived from the association between the two component elements (e.g. Bond lengths and bond length disorders for the heterogeneous bonds are constrained to be the same as measured from either edge) significantly lower the number of fitting variables, improving the confidence levels of fitting analysis effectively.

Pt/Au bimetallic system in EXAFS analysis represents a unique case which features overlapping absorption edges. In specific, Pt L<sub>3</sub> edge (11,564 eV) and Au L<sub>3</sub> edge (11,919 eV) are so close (energy gap only 355 eV) that the Pt L<sub>3</sub> EXAFS leaks to Au L<sub>3</sub> EXAFS data. The MDS analysis of such case is performed by a simultaneous fit of both Pt L<sub>3</sub> and Au L<sub>3</sub> edges, which account three contributions: (1) the Pt EXAFS in the Au L<sub>3</sub> edge before the Au L<sub>3</sub> edge; (2) the Au EXAFS in the Au L<sub>3</sub> edge; and (3) the Pt EXAFS in the Au L<sub>3</sub> edge. Since (1) and (2) describe the same coordination environments they are strictly constrained mathematically; and a scaling factor  $F = \Delta\mu_{0,Pt} / \Delta\mu_{0,Au}$  is used as the Pt EXAFS contribution in Au EXAFS is calculated, to compensate the different magnitude of edge steps for Pt and Au L<sub>3</sub> EXAFS data. As well, a correction value (eV) at  $\Delta E_{0,Pt} - (358 + \Delta E_{0,Au})$  to threshold energy of Au L<sub>3</sub> is added for Pt L<sub>3</sub> EXAFS in Au L<sub>3</sub> edge data to correct energy grid of this contribution, where 358 eV is the difference between empirical threshold energies for Pt L<sub>3</sub> and Au L<sub>3</sub> edge, which were set at 11562 eV and 11920 eV respectively in the this analysis. Additionally, for metallic bonds, only effective structural

parameters for each element were varied: the coordination numbers ( $N_{Pt-M}$ ,  $N_{Au-M}$ ), bond lengths ( $R_{Pt-M}$ ,  $R_{Au-M}$ ) and their disorders ( $\sigma_{Pt-M}^2$ ,  $\sigma_{Au-M}^2$ ), due to the similarity of backscattering amplitudes of Pt-Pt and Pt-Au as well as Au-Au and Au-Pt pairs. Detail of this analysis approach can be found in reference.<sup>24</sup> Figure 9 depicts two examples of Pt/Au EXAFS data and their corresponding fits in r-space, along with individual contribution from each scattering path (Pt-M, Au-M, and Pt-O and Au-O) in both Pt and Au  $L_3$  edge data.

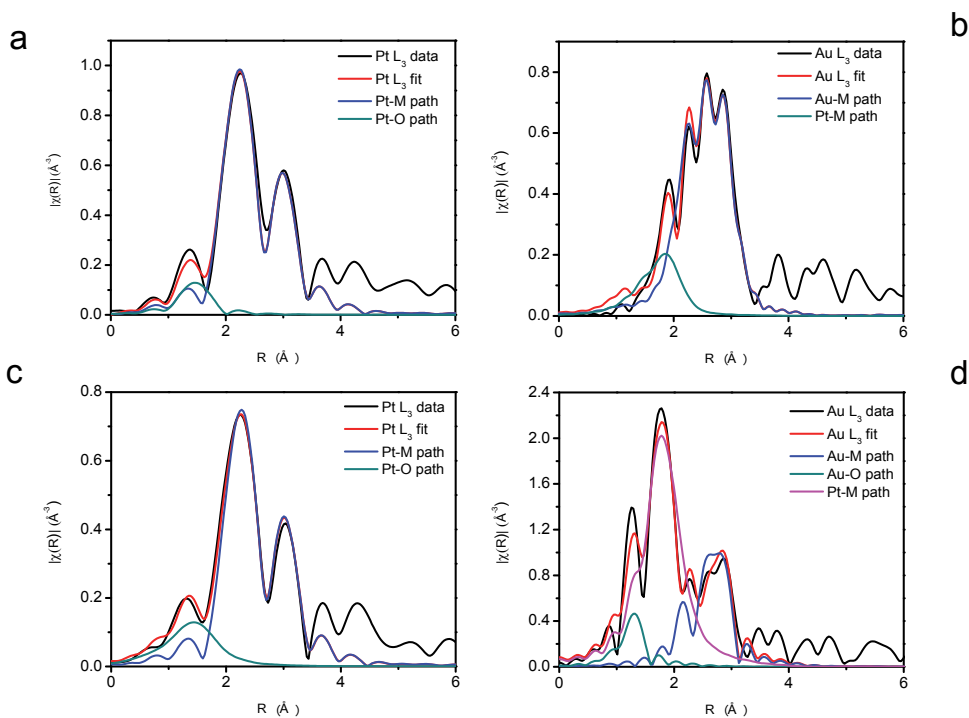


Fig. 9. Selected set of EXAFS data in R space and fits for Au/Pt bimetallic nanoparticles (a, b) AP10 and (c, d) AP04. (a, c) Pt data and fit; (b, d) Au data and fit. The comparison of Au edge EXAFS shows that Pt  $L_3$  leakage contributes much extensively in AP04 than in AP10. Also shown is that the fitting of Au data for AP04 was complicated by nonmetallic bonding to Au in addition to Pt leakage.

The best fit values of structural parameters (coordination numbers, first nearest neighbor distances and their mean squared disorders,  $\sigma^2$ ) for Pt/Au alloy nanowires and Pt/Au hybrid nanowires are listed in the Table 1 and Table 2, respectively. For  $Pt_{52}Au_{48}$  nanowires, the first-nearest-neighbor (1NN) Pt-metal coordination number ( $N_{Pt-M} \equiv N_{Pt-Au} + N_{Pt-Pt}$ ) is  $9.1 \pm 0.6$ , comparable to that of Au-metal coordination number ( $N_{Au-M} \equiv N_{Au-Au} + N_{Au-Pt} = 9.7 \pm 1.9$ ). The fact that  $N_{Pt-M} \approx N_{Au-M}$ , within the error bars, implies the formation of a homogeneous Pt/Au alloy. Thus, Au or Pt do not segregate to different macroscopic regions within the nanostructure (e.g., to the center or surface). Our measurements of  $Pt_{75}Au_{25}$

nanowires suggest a heterogeneous distribution of Au and Pt atoms inside the nanowires. The observed relationship:  $N_{\text{Pt-M}} (5.3 \pm 0.6) < N_{\text{Au-M}} (9.4 \pm 1.9)$  indicates that Au atoms tend to segregate toward the core of the  $\text{Pt}_{75}\text{Au}_{25}$  nanowires, leading to a heterogeneous nanostructure with a Au-rich and highly coordinated core and a less coordinated Pt-rich shell, since the atoms on the surface have fewer neighbors (or lower coordination number) than those in the core.

samples	Pt foil	$\text{Pt}_{75}\text{Au}_{25}$	$\text{Pt}_{52}\text{Au}_{48}$	Au foil
$N_{\text{Pt-M}}$	12 <sup>a</sup>	5.3 (6)	9.1 (6)	
$N_{\text{Au-M}}$		9.4 (1.9)	9.7 (1.9)	12 <sup>a</sup>
$N_{\text{Pt-O}}$		0.8 (7)		
$N_{\text{Au-O}}$		0.9 (5)		
$R_{\text{Pt-M}} (\text{\AA})$	2.775 (2)	2.750 (6)	2.767(5)	
$R_{\text{Au-M}} (\text{\AA})$		2.84 (1)	2.82(1)	2.877(3)
$R_{\text{Pt-O}} (\text{\AA})$		1.95 (4)		
$R_{\text{Au-O}} (\text{\AA})$		1.77 (2)		
$\sigma^2_{\text{Pt-M}} (\text{\AA}^2)$	0.0050(1)	0.0024(4)	0.0105(8)	
$\sigma^2_{\text{Au-M}} (\text{\AA}^2)$		0.0075(11)	0.0086(18)	0.0081(2)
$\sigma^2_{\text{Pt-O}} (\text{\AA}^2)$		0.0077(140)		
$\sigma^2_{\text{Au-O}} (\text{\AA}^2)$		0.0029(52)		

<sup>a</sup> 1NN coordination number was fixed at 12 for Pt and Au bulk standard analyses.

Table 1. Best Fit Results Obtained by EXAFS Analysis for Pt/Au Bimetallic Nanowires

The results from EXAFS analysis for Pt/Au hybrid bimetallic nanostructures are consistent with the elemental segregation revealed by electron microscopy. The Pt-Pt and Pt-O coordination numbers for the starting material (i.e. Pt nanowires) are  $7.2 \pm 0.4$  and  $0.28 \pm 0.2$ , respectively, which agrees with Pt nanowires of 2.3 nm in width and a small amount of oxide on the structure surface. Coordination of  $7.4 \pm 0.4$  and  $8.0 \pm 0.3$  were resulted for Pt-M in AP04 and AP10, indicating that the width of Pt nanowires did not change significantly from the starting phase when 0.4 ml and 1.0 ml  $\text{AuCl}_3$  was added. On the contrary, dramatic increase of Au-M coordination number from  $5.9 \pm 2.5$  in AP04 to  $9.8 \pm 2.1$  in AP10 was observed, which well corroborates the Au nanoparticle growth from  $2.7 \pm 0.9$  to  $4.4 \pm 0.7$  nm found from electron microscopy study. No significant change in Au-M coordination number ( $8.7 \pm 0.7$ ) was observed for AP20 compared to that of AP10, consistent with the microscopic evidence where Au particle sizes were determined to only change from  $4.4 \pm 0.7$  nm to  $4.9 \pm 0.5$  nm as  $\text{AuCl}_3$  concentration was doubled from 10 ml to 20 ml. A noticeable increase in Pt-M coordination number ( $10.5 \pm 1.1$ ) observed in AP20 relative to that in AP04 and AP10 may imply the increased Pt-Pt and Pt-Au interactions due to shortened nanowires and more Au decorations on the surface of Pt nanowire. As expected, Pt-M bonds in all hybrid samples show the contraction from bulk Pt-Pt bond, in a similar degree; while the Au-M bond in AP04 shrinks the most with the smallest size of particles. No dramatic increase in bond length disorders are shown in those Au/Pt hybrid samples compared to bulk structures, which may be explained by the non-traditional nanostructure of Pt nanowires and more complete segregation between Pt and Au in these hybrid structures.

Samples	Pt nanowires	PtAu (0.4ml)	PtAu (1.0ml)	PtAu (2.0ml)
$N_{\text{Pt-M}}$	7.2 (4)	7.4 (4)	8.0 (3)	10.5 (1.1)
$N_{\text{Pt-O}}$	0.28 (2)	1.2 (1.0)	1.1 (6)	0.3 (0.3)
$N_{\text{Au-M}}$		5.9 (2.5)	9.4 (1.9)	8.7 (7)
$N_{\text{Au-O}}$		0.6 (0.7)		
$R_{\text{Pt-M}}(\text{\AA})$	2.743 (3)	2.749 (5)	2.758 (5)	2.744 (7)
$R_{\text{Pt-O}}(\text{\AA})$	1.963 (28)	1.950 (35)	1.937 (22)	1.916 (51)
$R_{\text{Au-M}}(\text{\AA})$		2.831 (13)	2.833 (13)	2.844 (5)
$R_{\text{Au-O}}(\text{\AA})$		1.686 (36)		
$\sigma^2_{\text{Pt-M}}(\text{\AA}^2)$	0.0073 (3)	0.0053 (3)	0.0059 (2)	0.0061 (6)
$\sigma^2_{\text{Pt-O}}(\text{\AA}^2)$	0.0040 (63)	0.0260 (182)	0.0245 (166)	0.0000 (74)
$\sigma^2_{\text{Au-M}}(\text{\AA}^2)$		0.0043 (19)	0.0090 (13)	0.0085 (5)
$\sigma^2_{\text{Au-O}}(\text{\AA}^2)$		0.0000 (70)		

Table 2. Best Fit Results Obtained By EXAFS Analysis for Pt-Au hybrid Nanowires

#### 4. Electronic structure characterized by X-ray Absorption Near Edge Spectroscopy (XANES)

XANES is a powerful X-ray absorption spectroscopy technique for investigating charge transfer between distinctive elements as well as oxidation states of specific element within the nanomaterials. In contrast to EXAFS, the XANES energy range is only approximately 5~150 eV above the edge, much lower than that of EXAFS region. By analyzing these absorption signals in XANES, one can extract abundant chemical information of the studied material, like formal valence, coordination environment, the unoccupied band structure of a material, and fingerprint a mixture of sites/compounds (e.g. oxidation state determination), etc.

Since XANES is sensitive to the local electronic structure, it has been used to study the electronic redistribution or charge transfer upon alloying between various compounds. Obviously, it would also be the desirable technique to study the electronic structure of those Pt/Au hybrid nanowires. Despite the fact that Au metal with filled  $d^{10}$  orbital usually doesn't exhibit an intense white line (the first feature in the absorption edge) at  $L_3$  edge thresholds compared with unfilled  $d^9$  metals (e.g. Pt), the orbital s-p-d hybridization results in a  $5d^{10-x}6(sp)^{1+x}$  electron configuration, leading to a potentially noticeable increase of white line intensity. The changes of the number of holes in the d band reflect charge transfer between various Pt/Au hybrid nanostructures. Therefore, enhancement of the white line intensity from both Pt and Au  $L_3$  edges can thus be used as a sensor, to detect and quantify the hybrid formation. Figure 10 shows normalized Pt  $L_3$  edge XANES spectra of Pt/Au hybrids and those of Au and Pt foils for reference. It can be seen that the strength of the Au white line feature in  $L_3$  edge is noticeably lower than that of pure Au

foil as the amount of Au components decreased. Since white line features in Au  $L_3$  edge arise from  $2p_{3/2}$  to  $5d_{5/2}$  dipole transitions, the observations indicate a decrease in the number of unoccupied states of d character at the Au site upon the dilution of Au components in Pt nanowires. An opposite trend is seen at the Pt  $L_3$  edge, where the white line feature is higher than that of the pure Pt foil upon the dilution of Au concentration in Pt/Au hybrids. The data can be further interpreted in terms of the holes population above the Fermi level i.e., the d-charge depletion at the Pt site is accompanied by the d-charge gain at the Au site. The d charge gain at the Au site should be comparable to the charge loss at the Pt sites on the basis of electronic charge neutrality consideration.

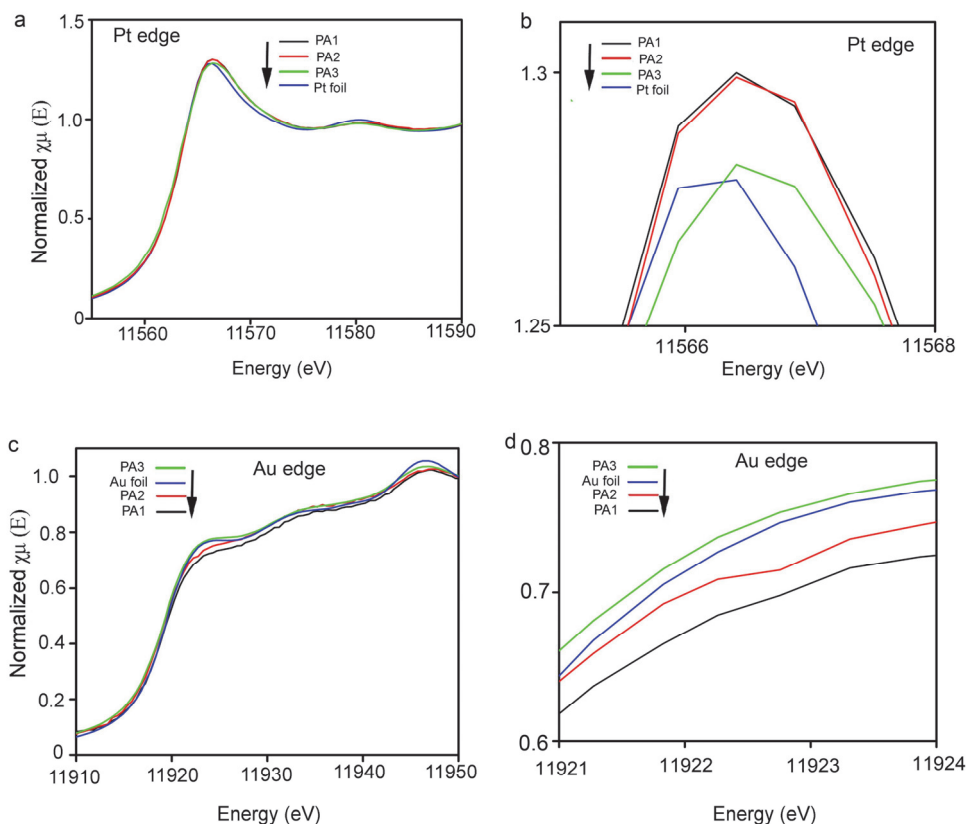


Fig. 10. Normalized XANES spectra of (a, b) Pt and (c, d) Au in the Pt/Au hybrid nanowires obtained by titrating the Pt nanowires with different volumes of 40 mM  $\text{AuCl}_3$  solutions: (AP04, black) 0.4, (AP10, red) 1.0, and (AP20, green) 2.0 ml, as well as in the Au (blue) and Pt (blue) foils.

It is important to mention that the white line intensity is known to increase as the particle size decreases. That is, the partial positive charge resulting from charge transfer is

distributed over fewer atoms (smaller particles), resulting in a greater increase in the d-hole population above the Fermi level relative to that of the larger particles. However, our data have clearly different origin as the size-effect which would cause the both Au and Pt white lines increase relative to the bulk as sizes decrease, contrary to what we observed. Moreover, the charge transfer between Pt/Au in hybrid structure seems totally different from that happened in Au bimetallic alloys such as Ag/Au, Al/Au or Ga/Au, where Au sites always lose d charges locally and therefore exhibit a more intense white line than Au foil. This unusual and interesting electronic behavior in Pt/Au hybrids is rather unexpected and deserves further investigations.

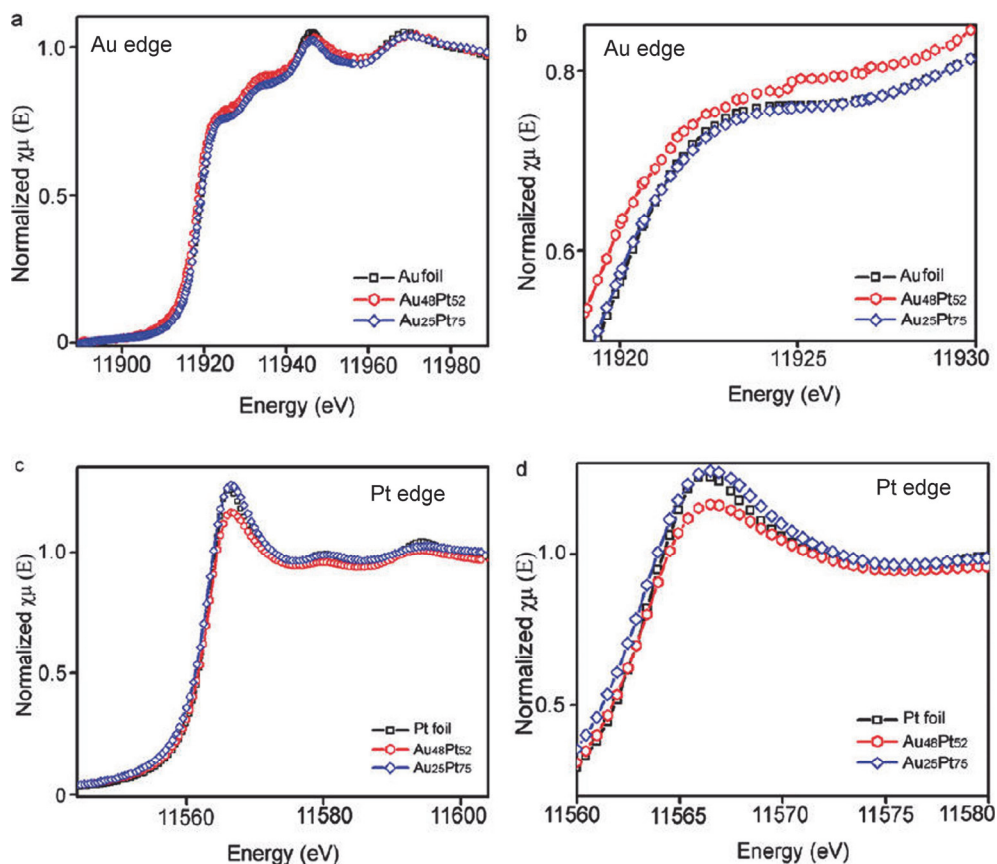


Fig. 11. XANES spectrum of (a, b) Au  $L_3$  edge and (c, d) Pt  $L_3$  edge of as-made Pt<sub>52</sub>Au<sub>48</sub> (nanowires), Pt<sub>75</sub>Au<sub>25</sub> (nanowires), Pt (foil reference), and Au (foil reference).

The XANES study of Pt/Au alloy nanowires (specifically, Pt<sub>52</sub>Au<sub>48</sub>), however, revealed a rather unexpected opposite trend of charge transfer directions compared with Pt/Au hybrids as shown in Figure 11. For Pt<sub>52</sub>Au<sub>48</sub> nanowires, the strength of the Au white line feature is noticeably higher than that of pure Au foil. Since features in the white line at the

Au  $L_3$  edge arise from  $2p_{3/2}$  to  $5d_{5/2}$  dipole transitions, our observations indicate a increase in the number of unoccupied states of d character at the Au site upon the  $Pt_{52}Au_{48}$  alloy formation. An opposite trend is seen at the Pt  $L_3$  edge, where the white line feature is lower than that of the pure Pt foil. The Pt and Au  $L_3$  edges shifted in opposite directions are the consequence of Pt/Au alloy formation. The data can be further interpreted in terms of the hole population above the Fermi level, in which sense the d-charge depletion at the Au site is accompanied by the d-charge gain at the Pt site. Electronic charge neutrality requires that the d charge gain at the Pt site should be comparable to the charge loss at the Au sites. In contrast, the Au and Pt white line features found in  $Pt_{75}Au_{25}$  nanowires are very close to those found in Au and Pt foil. The bulk-like XANES curves around the absorption edge indicate no apparent charge transfer between Au and Pt atoms, as well as between Pt/Au and octadecylamine in  $Pt_{75}Au_{25}$  nanowires. The electronic structure of PtAu alloy nanoparticles supported on the metal oxides has been studied by Van Bokhoven and coworkers, finding a charge transfer between Au and Pt similar to our results on Pt/Au free-standing nanowires (Bus & van Bokhoven, 2007). However, the charge transfer of Pt/Au hybrid phase-segregated nanostructures is totally different from that of an alloyed structure. As we discussed in earlier sections, d-charge depletion at the Pt site and d-charge gain at the Au site was found in Pt/Au hybrid with complete Au and Pt phase-segregation. We believe that the distinct electronic structures found in the two materials can be attributed to their different crystalline structures. Since Au has a higher electronegativity than Pt, in Pt/Au hybrid phase-segregated nanowires, Pt loses electrons to Au. In Pt/Au alloyed nanowires, alloying between Au and Pt drives the system towards the "covalent limit", where the d bandwidth is much larger than the energy separation of the d bands, forcing Pt and Au towards equal electron counts in the alloy (Bus & van Bokhoven, 2007). These findings dramatically highlight the intriguing structure-property relationship of nanoscaled electronic materials.

## 5. Conclusion

In summary, we synthesized Pt ultrathin nanowires, and Au/Pt alloyed and hybrid nanowires heterogeneous structures via a phase transfer wet chemistry synthetic method. Using a combination of techniques, including STEM equipped with EDS, UV-vis spectroscopy, and synchrotron-based XANES and EXAFS, we identified the stoichiometry-dependent heterogeneous crystalline structures, as well as electronic structures with respect to the charge transfer between Pt and Au within both nanowires. In particular, we observed d-charge depletion at the Au site and the d-charge gain at the Pt site in  $Au_{48}Pt_{52}$  alloyed nanowires. On the other hand, an opposite charge transfer trend was found in Au/Pt hybrid nanowires, where we observed d-charge depletion at the Pt site and the d-charge gain at the Au site. We have presented here a comprehensive study of the relationships among heterogeneous crystalline structure and electronic structure. Our studies are highly encouraging that new families of bimetallic nanosystems may be developed to sustain the needs of emerging technologies such as electronics and catalysis, where there is a continuous drive to find nanomaterials with ever more exotic electronic and catalytic properties, and where the assembly of these fundamental building blocks can lead to new types of functionality.

## 6. Acknowledgments

This work is supported by the University of New Hampshire. Dr. Wang acknowledges support by the U.S. Department of Energy grant No. DE-FG02-03ER15476. Use of the National Synchrotron Light Source, Brookhaven National Laboratory, was supported by the U.S. Department of Energy, Office of Science, Office of Basic Energy Sciences, under Contract DE-AC02-98CH10886 and beam lines X19A/X18B are partly supported by Synchrotron Catalysis Consortium under contract DE-FG02-05ER15688.

## 7. References

- Ahmadi, T. S.; Wang, Z. L.; Green, T. C.; Henglein, A.; ElSayed, M. A., (1996). Shape-controlled synthesis of colloidal platinum nanoparticles. *Science*, Vol. 272, pp 1924-1926.
- Casado-Rivera, E.; Volpe, D. J.; Alden, L.; Lind, C.; Downie, C.; Vazquez-Alvarez, T.; Angelo, A. C. D.; DiSalvo, F. J.; Abruna, H. D., (2004). Electrocatalytic activity of ordered intermetallic phases for fuel cell applications. *Journal of the American Chemical Society*, Vol. 126, pp 4043-4049.
- Cozzoli, P. D.; Manna, L., (2005). Asymmetric nanoparticles - Tips on growing nanocrystals. *Nature Materials*, Vol. 4, pp 801-802.
- Xia, Y. N.; Yang, P. D.; Sun, Y. G.; Wu, Y. Y.; Mayers, B.; Gates, B.; Yin, Y. D.; Kim, F.; Yan, Y. Q., (2003). One-dimensional nanostructures: Synthesis, characterization, and applications. *Advanced Materials*, Vol. 15, pp 353-389.
- Zhong, C. J.; Maye, M. M., (2001). Core-shell assembled nanoparticles as catalysts. *Advanced Materials*, Vol. 13, pp 1507-1511.
- Nashner, M. S.; Frenkel, A. I.; Adler, D. L.; Shapley, J. R.; Nuzzo, R. G., (1997). Structural characterization of carbon-supported platinum-ruthenium nanoparticles from the molecular cluster precursor  $\text{PtRu}_5\text{C}(\text{CO})_{16}$ . *Journal of the American Chemical Society*, Vol. 119, pp 7760-7771.
- Shibata, T.; Bunker, B. A.; Zhang, Z. Y.; Meisel, D.; Vardeman, C. F.; Gezelter, J. D., (2002). Size-dependent spontaneous alloying of Au-Ag nanoparticles. *Journal of the American Chemical Society*, Vol. 124, pp 11989-11996.
- Greeley, J.; Mavrikakis, M., (2006). Near-surface alloys for hydrogen fuel cell applications. *Catalysis Today* Vol. 111, pp 52-58.
- Knudsen, J.; Nilekar, A. U.; Vang, R. T.; Schnadt, J.; Kunkes, E. L.; Dumesic, J. A.; Mavrikakis, M.; Besenbacher, F., (2007). A Cu/Pt near-surface alloy for water-gas shift catalysis. *Journal of the American Chemical Society*, Vol. 129, pp 6485-6490.
- Brust, M.; Walker, M.; Bethell, D.; Schiffrin, D. J.; Whyman, R., (1994). Synthesis of Thiol-Derivatized Gold Nanoparticles in a 2-Phase Liquid-Liquid System. *Journal of the Chemical Society, Chemical Communications*, pp 801-802.
- Frenkel, A., (2007). Solving the 3D structure of metal nanoparticles. *Zeitschrift Fur Kristallographie*, Vol. 222, pp 605-611.

Bus, E.; van Bokhoven, J. A., (2007). Electronic and geometric structures of supported platinum, gold, and platinum - Gold catalysts. *Journal of Physical Chemistry C*, Vol. 111, pp 9761-9768

# GaN Nanowires Fabricated by Magnetron Sputtering Deposition

Feng Shi

*College of Physics & Electronics, Shandong Normal University,  
P.R.China*

## 1. Introduction

GaN, as an attractive third-generation semiconductor material (III-V), has shown great prospect in applications of short wavelength blue and ultraviolet (UV) light-emitting devices (LEDs), microwave devices and high-power semiconductor devices, due to its unique physical properties such as wide band-gap (3.39 eV direct gap at room temperature), high thermal conductivity, high electron saturated mobility, high thermal stability, and so on (Fasol, 1996; Nakamura, 1998; Morkoc & Mohammad, 1995; Han et al., 1997).

As we all know, GaN have three kinds of structure: hexagonal wurtzite ( $\alpha$ -phase), cubic blende ( $\beta$ -phase) salt mine (NaCl-type compound square structure), which are shown as Figure 1.

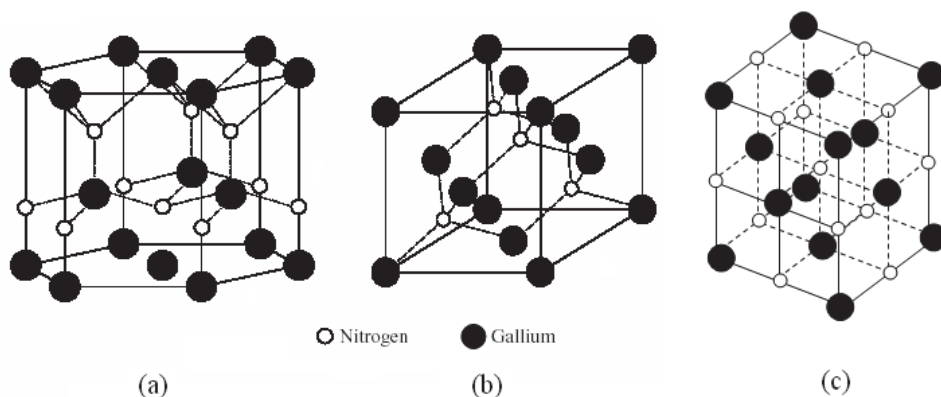


Fig. 1. The crystal structures of GaN. (a) Wurtzite Structure; (b) Blende Structure; (c) Salt Mine Structure.

In the past decades, a lot of man-powers, materials and financial resources have been put to study GaN by many countries, especially GaN nanostructures (nanowires, nanorods and nanobelts). One-dimensional GaN nanostructure has potential applications in the fields of full-color panel displays and nanometer electronic devices with high electron migration rate (Lauhon, 2002; Ham et al., 2006). However, the growth of GaN nanostructures with high

crystalline quality is the pre-condition for the fabrication of GaN-based components. Recently, several techniques have been developed to fabricate one-dimensional GaN structures such as carbon nanotube-confined reaction (Han, 1997), template-based growth method (Xu et al., 2006), direction reaction of metal Ga with  $\text{NH}_3$  (He, 2000), ammoniating  $\text{Ga}_2\text{O}_3/\text{Al}_2\text{O}_3$  films (Xue et al., 2004) and sublimation method (Li et al., 2000).

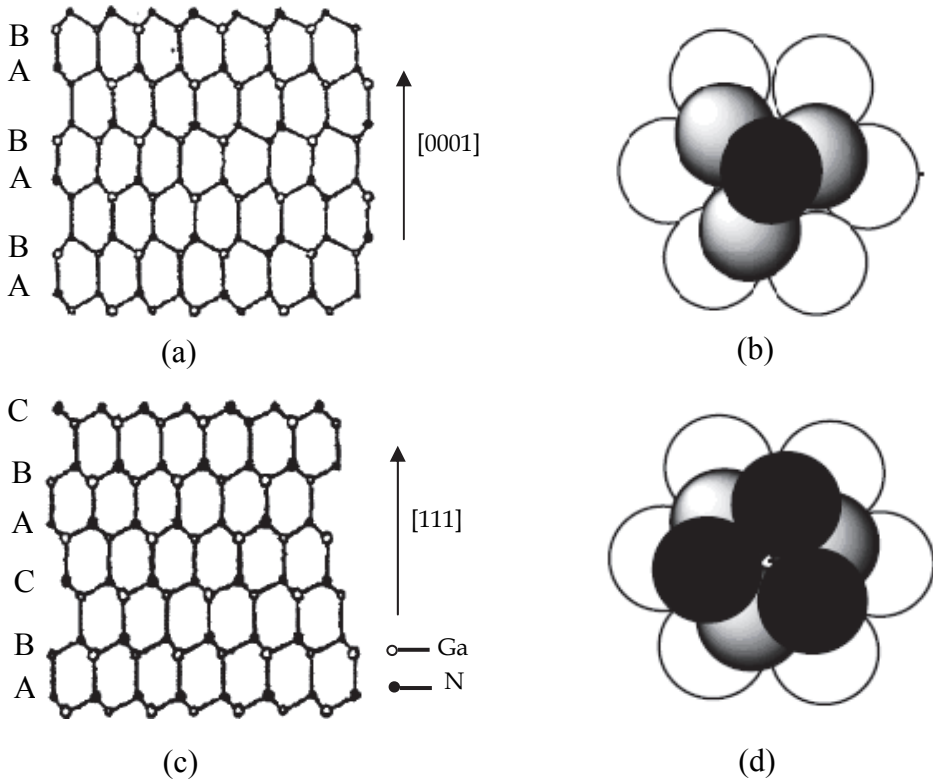


Fig. 2. Stacking Way of GaN: (a,b) Wurtzite Structure; (c,d) Blende Structure.

Of these methods, the metal catalyst-assisted growth is the most successful approach used popularly. According to our previous experimental results (Shi, 2010a, 2010b) the intermediate layer between Si substrates and  $\text{Ga}_2\text{O}_3$  had great influence on the modality and characteristics of the GaN nanostructures. Therefore, we attempted a novel route via Tb as the intermediate layer and synthesized unexpectedly large-scale GaN nanowires by ammoniation radio frequency (RF) magnetron sputtering method, *i.e.*, the transition metals of Ti, V, Cr, Co, Nb, Mo, Ta, and Tb (short for  $M_e$ ) are employed as catalyst materials forming the intermediate layer between Si substrate and  $\text{Ga}_2\text{O}_3$  film to grow unexpectedly large-scale GaN nanowires by ammoniation radio frequency (RF) magnetron sputtering method. That is, Ti, V, Cr, Co, Nb, Mo, Ta, and Tb ( $M_e$ ), the elements of transition metals, are employed as catalyst materials forming the intermediate layer between Si substrate and

Ga<sub>2</sub>O<sub>3</sub> films to growth one-dimensional GaN nanowires. In this chapter, high-quality GaN nanostructures, especially, nanowires, catalyzed by Ti, V, Cr, Co, Nb, Mo, Ta, and Tb have been fabricated on Si (111) substrate by ammoniating Ga<sub>2</sub>O<sub>3</sub> thin films. The fabrication condition, microstructure, morphology and photoluminescence (PL) optical properties were analyzed and the growth mechanism of GaN nanowires is further discussed. One-dimensional GaN nanowires are also fabricated by using MgO, TiO<sub>2</sub>, Al<sub>2</sub>O<sub>3</sub>, SiC, BN, and ZnO (short for C<sub>m</sub>) as intermediate layers. Through ammoniating Ga<sub>2</sub>O<sub>3</sub> films doped with Mg, high-quality P-typed GaN nanowires have been synthesized on Si(111) substrates. The growth mechanism of GaN nanowires are analyzed in detail.

The high-quality single GaN nanowires have also been fabricated by NiCl<sub>2</sub> Catalyzed Chemical vapor deposition and the growth mechanism of GaN nanowires are also analyzed in particular.

## 2. GaN nanowires fabricated by RF magnetron sputtering method

### 2.1 Catalyzed by transition metals of M<sub>e</sub>

#### 2.1.1 Experimental procedures

The growth method catalyzed by metallic M<sub>e</sub> is simple in fabrication progress and easy to control the size of the GaN nanostructures. Therefore, in our experiment, metallic M<sub>e</sub> and Ga<sub>2</sub>O<sub>3</sub> were deposited on the polished n-type Si(111) substrates in turn to form Ga<sub>2</sub>O<sub>3</sub>/M<sub>e</sub> films by sputtering the M<sub>e</sub> targets of 99.95 % purity and the sintered Ga<sub>2</sub>O<sub>3</sub> target of 99.99 % purity in a JCK-500A magnetron sputtering system. The sputtering time of M<sub>e</sub> and Ga<sub>2</sub>O<sub>3</sub> was 2 s ~ 5 s and 90 min with the thickness of 5 ~ 20 nm and 500 nm, respectively. The working conditions were, 150-Wand RF sputtering power of 13.56 MHz ; 20-Wand DC sputtering power; background pressure of 1.0×10<sup>-3</sup> Pa; and pure Ar (≥ 99.99%) as the working at a working pressure of 1~3 Pa. The distance between the target and the substrate was 8 cm. The sputtering progress was maintained at room temperature by the cooling system. After sputtering, the samples were ammoniated in a conventional tube furnace at atmosphere of pure NH<sub>3</sub> gas with purity of 99.999% under the temperatures of 800 °C ~ 1000 °C for 10~20 min. After being ammoniated, the samples were taken out for characterization.

The microstructure, composition, morphology and optical properties of the samples were studied using X-ray diffraction (XRD, Rigaku D/max-rB,Cu, K<sub>α</sub>, λ=1.54178 Å), FT-IR spectrophotometer with Mg X-ray source (FTIR, Bruker TENSOR27), X-ray photoelectron spectroscopy (XPS, Microlab MKII), scanning electron microscope (SEM, Hitachi S-570), high-resolution transmission electron microscope (HRTEM, Philips TECNAI-20), and photoluminescence spectroscopy (PL, LS50-fluorescence spectrophotometer).

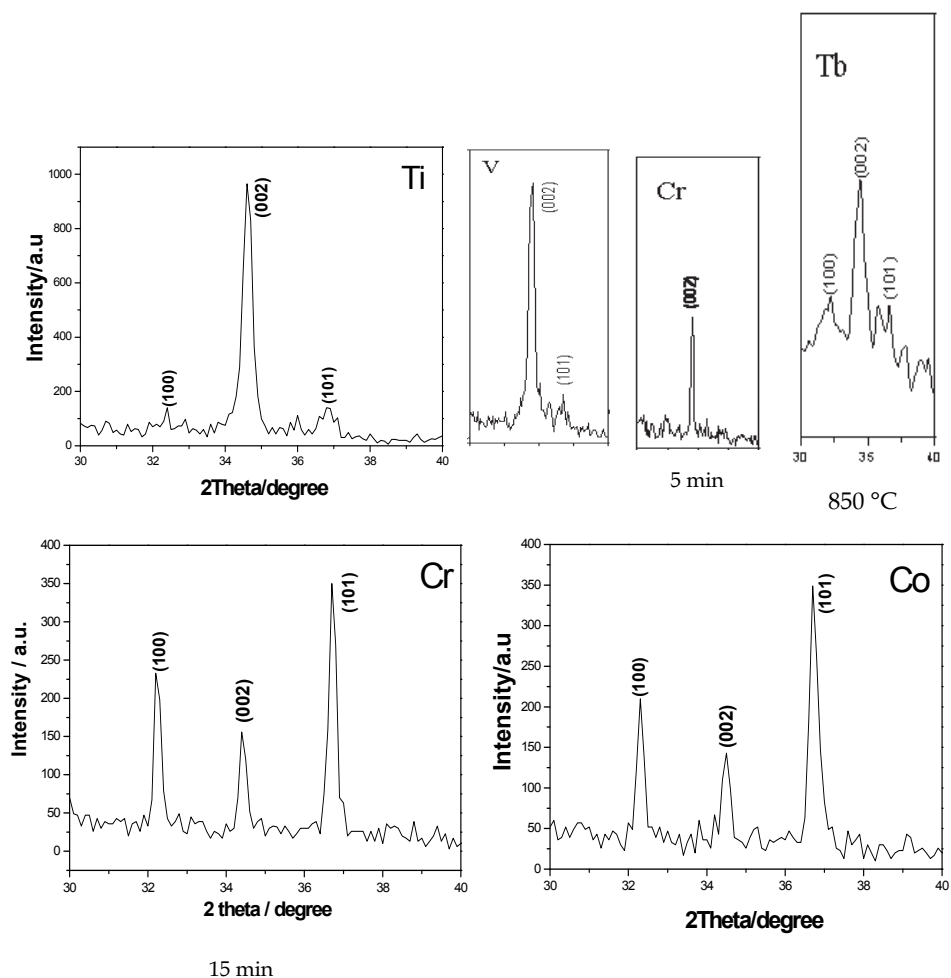
#### 2.1.2 Results and discussion

Figure 3 show the X-ray diffraction pattern of the samples grown at different temperatures with different transition metals.

As shown in Figure 3, the samples after ammoniation are hexagonal wurtzite GaN with lattice constant of  $a = 0.3186$  nm and  $c = 0.5178$  nm, and the diffraction peaks located at about  $2\theta=32.3^\circ$ ,  $34.5^\circ$ , and  $36.7^\circ$  correspond to (100), (002) and (101) planes, which are consistent with the reported values for bulk GaN (Perlin,1992). No peak of Ga<sub>2</sub>O<sub>3</sub>, M<sub>e</sub> or M<sub>e</sub>O is observed, indicating that neither Ga<sub>2</sub>O<sub>3</sub>, M<sub>e</sub> metal nor M<sub>e</sub>O coats the sample surface,

which indicates that these transitional elements take great catalytic action for the growth of GaN nanostructures.

Figure 3 tells us that at special conditions, the GaN nanostructures can grow along preferred (002) plane catalyzed by transitional elements of Ti, V, Cr, and rare-earth of Tb. While the GaN nanostructures can't grow along preferred plane by transitional elements of Nb, Mo, Co, and Ta. That is, the GaN nanostructures can grow along preferred (002) plane catalyzed by the first elements of the II, III, IV subgroups on the Periodic Table of chemical elements, except the other elements. This is a noticed phenomenon deserved further study. Ammoniating times and temperatures have great influence on the crystalline quality of the samples. The sample catalyzed by Cr can form preferred (002) plane ammoniated for 5 min, and the sample catalyzed by Tb can form preferred (002) plane ammoniated at 850 °C, which can be shown as Figure 4.



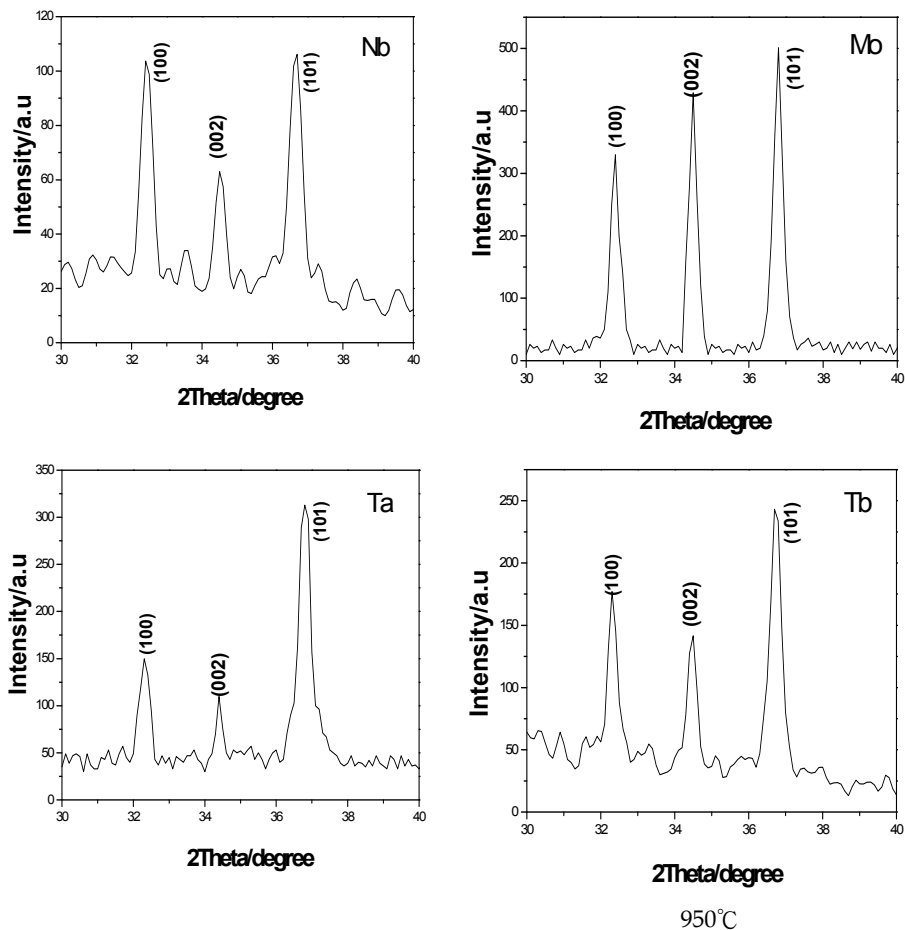


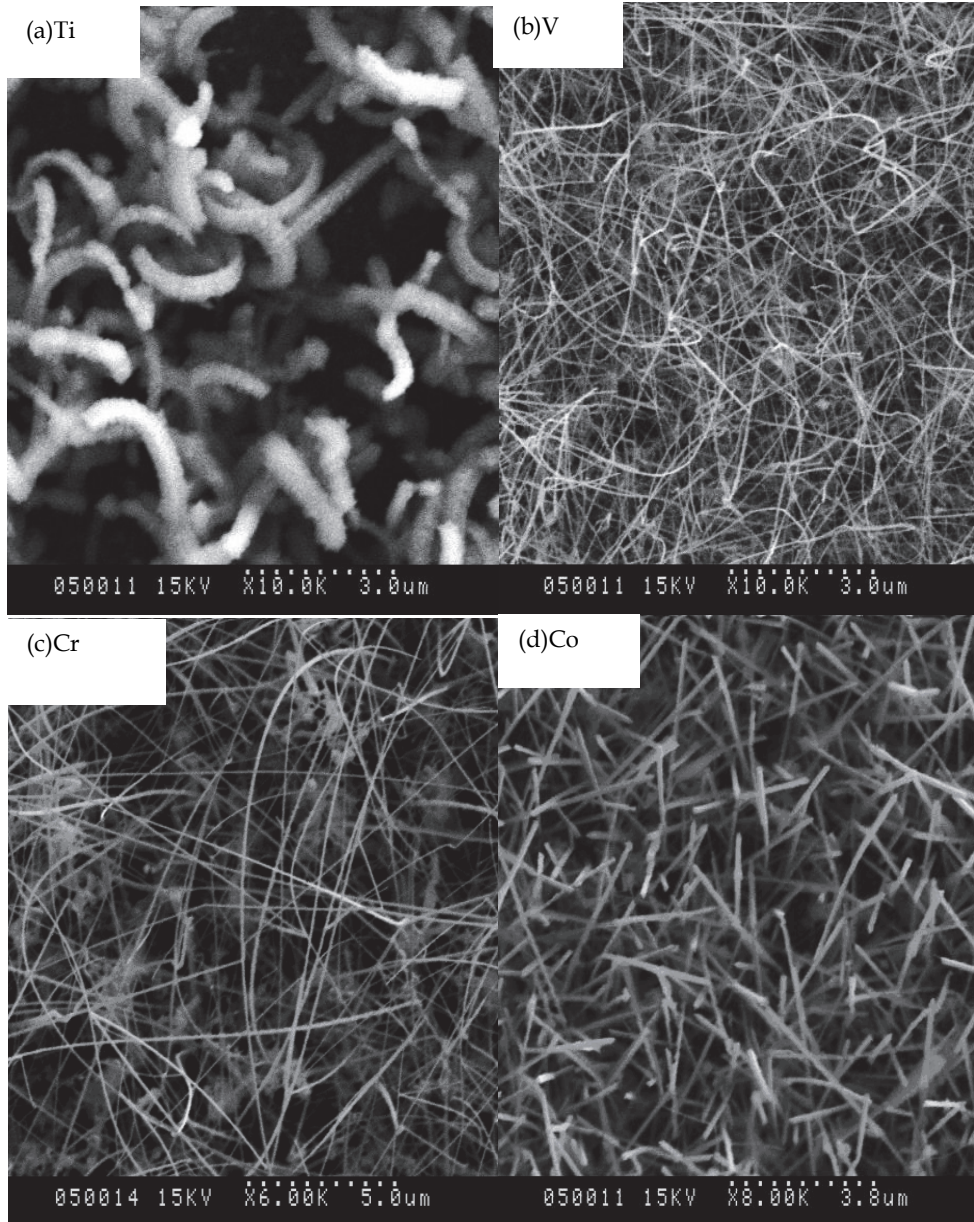
Fig. 3. X-ray diffraction pattern of the samples grown at different temperatures with different transition metals.

As shown from Figure 4, a large amount of one-dimensional nanowires distribute on the sample surfaces with high crystalline quality after catalyzed by V, Cr, Co, Nb, Mo, Ta, and Tb except catalyzed by Ti. Most of them are straight and smooth of uniform thickness along the spindle direction, and interlace with each other disorderly, having the size of about 50 ~100 nm in diameter and several tens of microns in length.

The diameters increase with the number of the protons, for example, the samples can form GaN nanowires when catalyzed by Ti, V, and Cr, however, with the increase in the protons, nanorods can be formed, such as the sample catalyzed by Co, as shown in Figure 4d. For Cr, and Co, the comparison is the most obvious.

As for V, Nb, and Ta, which are of the same sub-group, nanowires can be formed catalyzed by V, however, nanorods can be formed when catalyzed by Nb and Ta. Cr and Mo are of the same subgroup, the sample catalyzed by Cr can form nanowires, while after catalyzing by Mo, nanorods can be formed.

In short, the catalytic action increases with the increase in the number of the protons at the same line of the Periodic Table of chemical elements, and the morphology become obvious. And the same law exists in the same row.



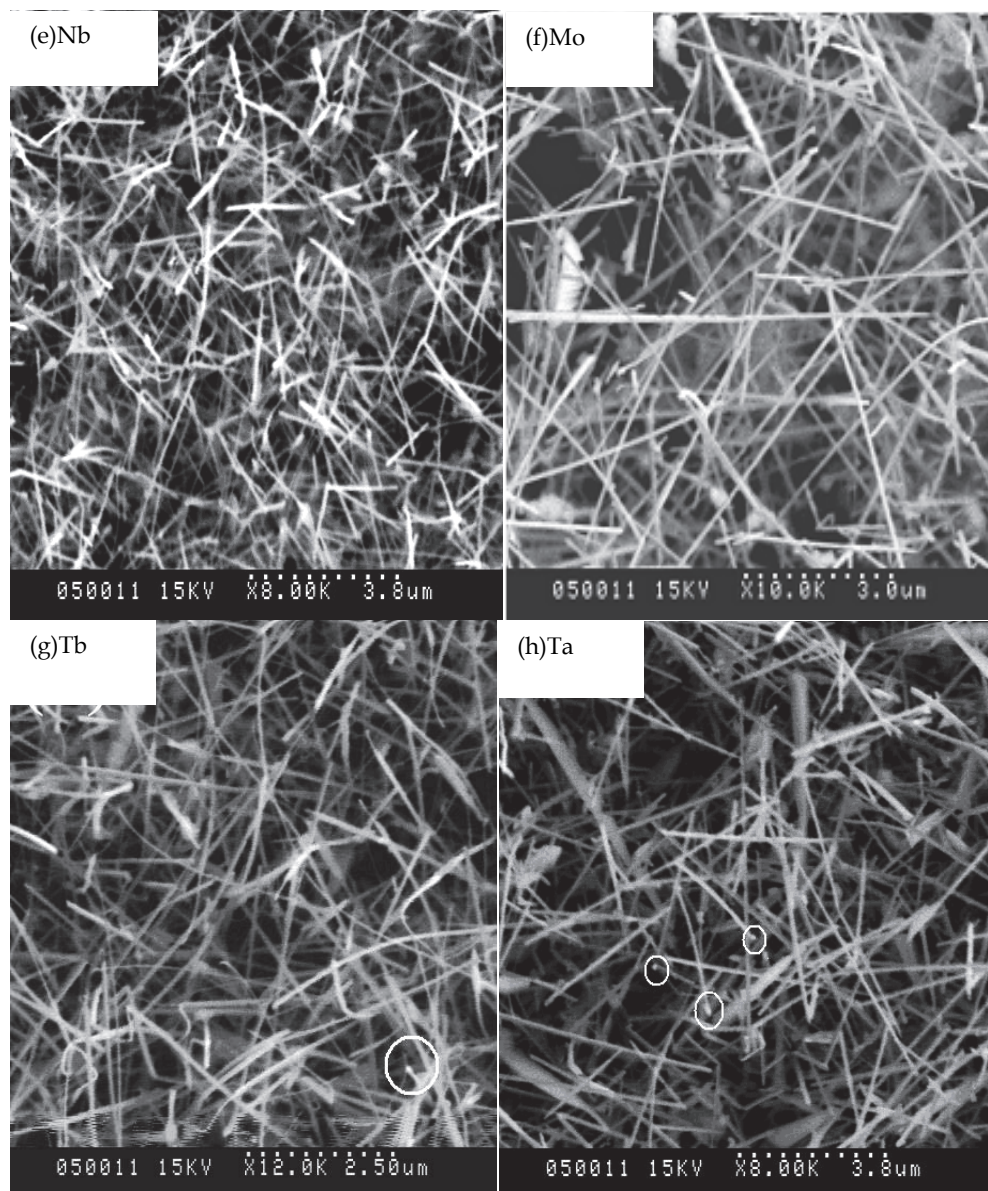


Fig. 4. SEM images of the samples catalyzed by different transition metals.

Ammoniating temperatures have great influence on the morphology of the sample catalyzed by Cr, which are shown in Figure 4c and Figure 5. In Figure 4c, nanowires are formed in the sample ammoniated at 950 °C, however, nanorods are formed ammoniated at 1000 °C, as shown in Figure 5.

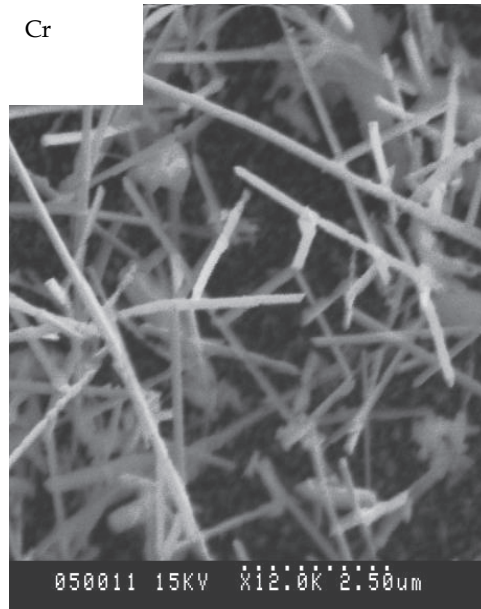


Fig. 5. SEM image of the sample grown at 1000 °C catalyzed by Cr.

Figure 6 show the TEM, selected area electron diffraction (SAED) and HRTEM images of an individual GaN nanowire. (a) TEM and SAED images,(b) HRTEM image.

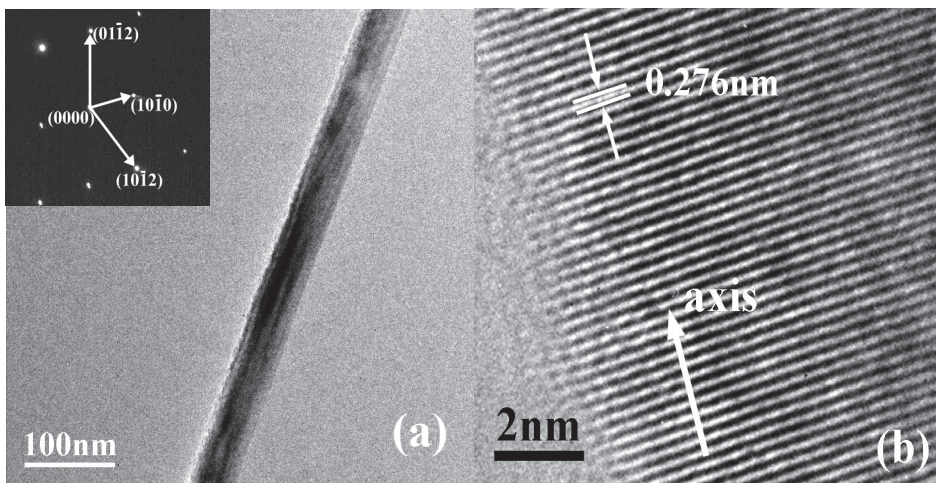


Fig. 6. TEM, selected area electron diffraction (SAED) and HRTEM images of an individual GaN nanowire. (a) TEM and SAED images,(b) HRTEM image.

As seen in Figure 6a, the nanowire is straight and smooth with uniform thickness in diameter and the diameter of nanowire is about 30 nm. Meanwhile, it shows the GaN nanowire is solid structure while not hollow tubular structure. Diffraction spots from

SAED are regular which shows GaN nanowire is monocrystal with hexagonal wurtzite structure. Seen from Figure 6b, HRTEM lattice image of straight GaN nanowire, the well-spaced lattice fringes in the image indicate a single crystal structure of GaN nanowires with high crystalline quality. The crystal plane spacing of nanowire is about 0.276 nm, which corresponds to (100) crystal plane spacing (0.276 nm) of hexagonal GaN single crystal.

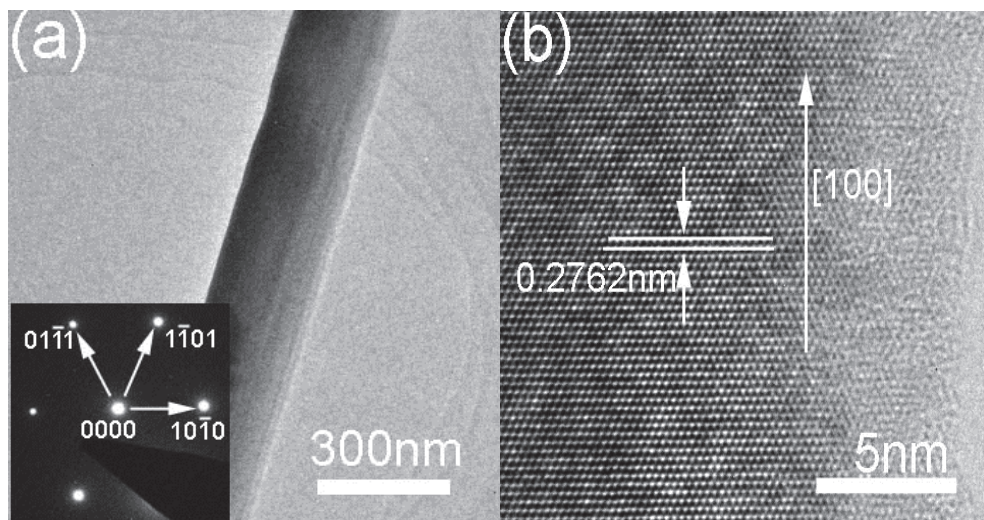


Fig. 7. TEM, selected area electron diffraction (SAED) and HRTEM images of an individual GaN nanorod. (a) TEM and SAED images, (b) HRTEM image.

Figure 7a shows that the nanorod is straight and smooth, of 150 nm in diameter. As seen from Figure 7b, HRTEM lattice image of the straight GaN nanorod, the well-spaced lattice fringe in the image indicates that the GaN nanorods have high crystalline quality with less dislocations and defects. The crystal plane spacing of the nanorod is about 0.2762 nm, which is less than that of (100) crystal plane spacing (0.276 nm) of hexagonal GaN single crystal (Monemar, 1974). The growth direction of this nanorod is parallel to [100] orientation. Diffraction spots from SAED (the inset in Figure 7a) are regular and corresponding to the diffraction direction of  $1\bar{2}1\bar{3}$ , which shows the GaN nanorod is monocrystal with hexagonal wurtzite structure.

We used different  $M_e$  elements to catalyze GaN samples and they were ammoniated at different temperatures and different times, nanowires and nanorods can be observed with clear surface, and we take the Mo as an example. Figure 8. FTIR patterns of the sample catalyzed by Mo after ammoniation at 950 °C for different times.

As seen in Figure 8, there are three well-defined prominent absorption bands, located at 564.07  $\text{cm}^{-1}$ , 608.94  $\text{cm}^{-1}$ , and 1102.31  $\text{cm}^{-1}$ . The band located at 564.07  $\text{cm}^{-1}$  corresponds to Ga-N stretching vibration ( $E_1(\text{TO})$  mode) in hexagonal type GaN crystal (Yang, 2002), and the other two bands are related to the Si substrate. The band located at 608.94  $\text{cm}^{-1}$  is associated with the local vibration of substituted carbon in the Si crystal lattice (Ai et al, 2007), whereas the band located at 1102.31  $\text{cm}^{-1}$  is attributed to the Si-O-Si asymmetric

stretching vibration because of the oxygenation of Si substrate (Sun,1998). There is no Ga-O bond and other absorption band in the spectrum (Demichelis, 1994), therefore,  $\text{Ga}_2\text{O}_3$  films react with  $\text{NH}_3$  completely at  $950^\circ\text{C}$  for 15 min and form hexagonal type GaN crystal, which is the same as the results of the XRD. The Ga-N bond intensity of the sample whose ammoniating time is 20 min is stronger than those of the other two samples, which proves the sample has the highest crystalline quality, and is also the same as the results of the XRD.

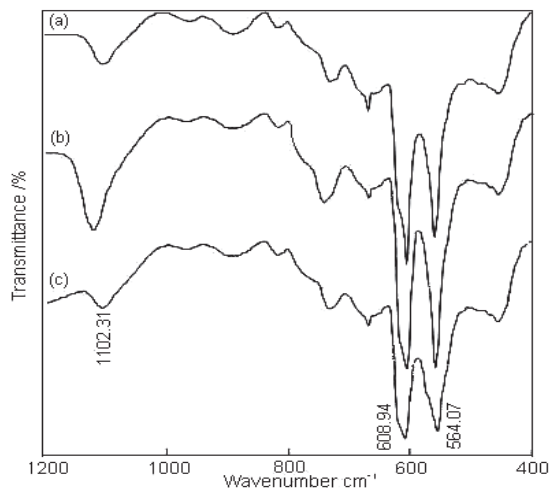


Fig. 8. FTIR patterns of the sample catalyzed by Mo after ammoniation at  $950^\circ\text{C}$  for different times. (a) 15 min; (b) 20 min; (c) 25 min.

We have tested other samples which were ammoniated by other  $M_e$  elements, the composition can be observed clearly by FTIR, and only GaN exists. In short, catalyzed by  $M_e$ , the ammoniation reaction was complete and  $\text{Ga}_2\text{O}_3$  has turned to GaN completely.

Figure 9 shows the XPS images of N1s, Ga2p, Ga3d, and O1s for GaN synthesized at the ammoniating temperature of  $950^\circ\text{C}$ , respectively.

Figure 9a shows the general scan in the binding energy ranging from 0 eV to 600 eV and the main components are Ga, C, N, and O with XPS peaks at the location of  $\text{Ga}2p_{3/2}$  (1177.16 eV),  $\text{Ga}2p_{1/2}$  (1144.10 eV), Ga3d (20.2 eV), N1s (396.1 eV) and O1s (530.3 eV).

The core level of Ga has a positive shift from elemental Ga, as shown in Figure 9b. This shift in the binding energies of Ga and N confirms the bonding between Ga and N and the absence of elemental gallium. As seen in Figure 9c, the binding energies of  $\text{Ga}2p_{3/2}$  and  $\text{Ga}2p_{1/2}$  are 1117.8 eV and 1144.5 eV, respectively, which are consistent with the results of Wei (Wei et al., 2005) whereas the banding energies of Ga element are 1116.6 eV (Elkashef et al., 1998) · 1118.5 eV (Kingsley et al., 1995) and 1119.2 eV (Sasaki et al.,1998). No bond formation is observed between Ga and O as the Ga3d spectrum does not show any satellite peak corresponding to  $\beta$ -Ga (Ishikawa et al., 1997) shows the Ga atom existing only as combined GaN, not  $\text{Ga}_2\text{O}_3$ . Quantification of the peaks shows that the atomic ratio of Ga to N is approximately 1:1.

As observed, the energy peak for N1s shown in Figure 9d is centered at 396.1eV, instead of 399 eV (binding energy of N element existing as atomic style), similar to the results of

Li (397.4 eV) (Li et al., 1997) and Veal (397.6 eV) (Veal et al., 2004), i.e., N atom exists as a nitride. The width and slight asymmetry of the N1s peak are attributed to N-H2 and N-H3 formation due to the interaction between N2 and NH3 at the GaN film surface (King,1999).

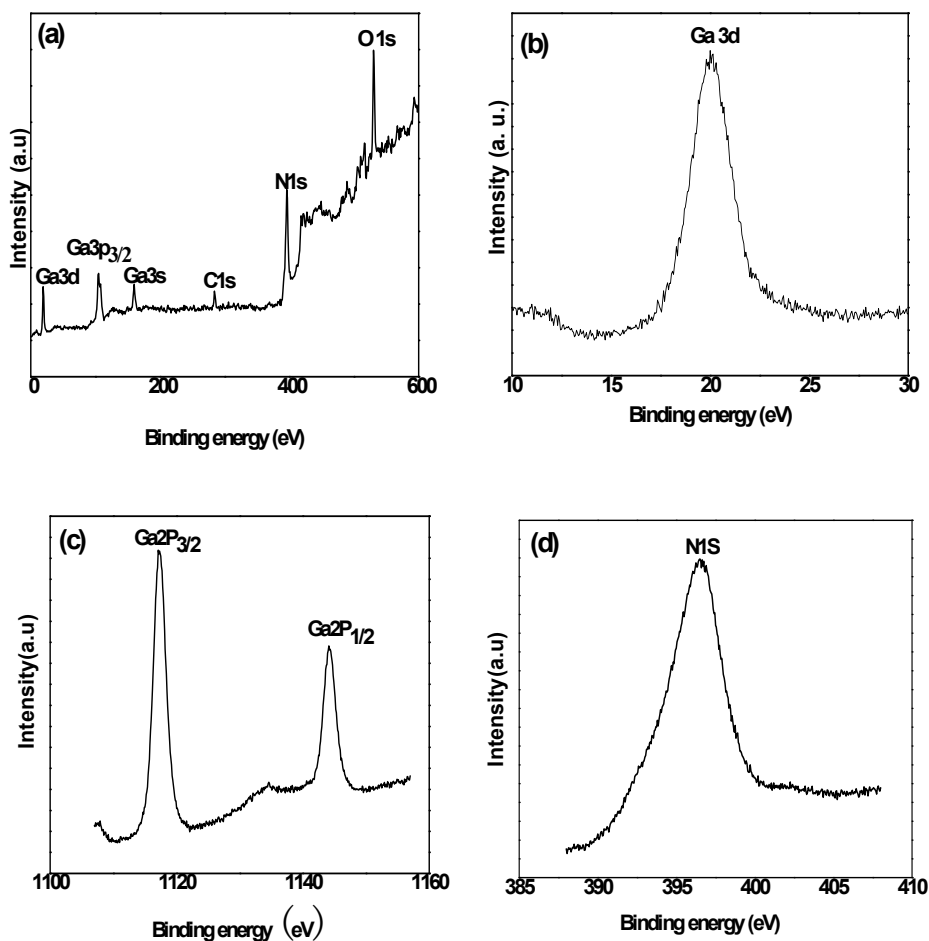


Fig. 9. XPS spectra of the sample after ammoniation at 950 °C for 15 min (Cr). (a) general scan spectrum; (b) Ga3d band; (c) Ga2p<sub>1/2</sub> and Ga2p<sub>3/2</sub> bands; (d) N1s band.

The elements of C and O arise from the surface pollution of the sample (Monemar,1974) . The O1s peak centered at 530.7 eV. According to Amanullah et al (Amanullah et al., 1998), generally, the O1s peak had been observed in the binding energy region of 529-535 eV, and the peak around 529-530 eV is ascribed to lattice oxygen. For chemisorbed O<sub>2</sub> on the surface the binding energy ranged from 530.0 eV to 530.9 eV. Therefore, the O1s peak in the present work is part of chemisorbed oxygen.

In short, XPS analysis shows that  $\text{Ga}_2\text{O}_3$  reacts with  $\text{NH}_3$  completely and forms GaN after ammoniation at  $950^\circ\text{C}$  for 15 min, similar to the results of the XRD and FITR analysis.

Figure 10 is the photoluminescence spectrum of the samples grown at different temperatures for 15 min (Tb).

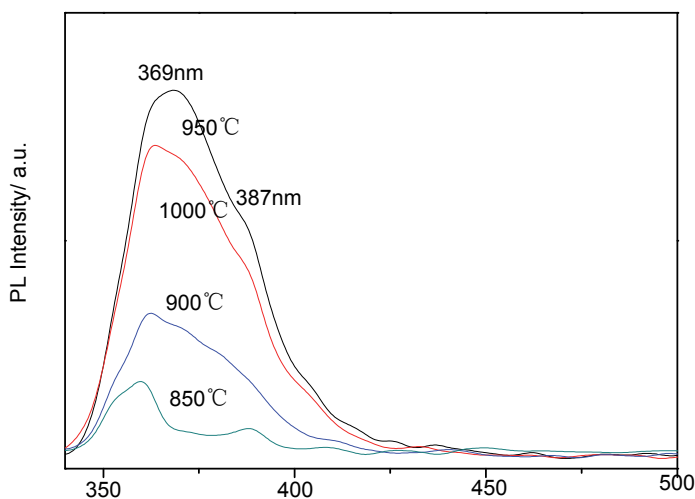


Fig. 10. Photoluminescence spectrum of the samples grown at different temperatures for 15 min (Tb). (a)  $850^\circ\text{C}$ , (b)  $1000^\circ\text{C}$ , (c)  $900^\circ\text{C}$ , (d)  $950^\circ\text{C}$ .

Figure 10 shows there is a strong UV emission peak centered at 369 nm corresponding to near band-edge emission of hexagonal GaN (Xiao et al., 2005). Because the diameter of the nanorod is much larger than the Bohr exciton radius (11 nm), beyond the work scope of quantum confinement effects, no blue-shift is discerned when compared with bulk GaN, but a small red-shift has occurred when compared with 365 nm reported by reference (Monemar, 1974). The reason of red-shift is probably related with band gap change caused by the tensile stress of one-dimensional GaN nanomaterials along the axial direction (Bae et al., 2003). The corresponding binding energy (eV) is 3.36 eV and thus it is smaller than binding energy of bulk GaN with 3.39 eV. Meanwhile, a weak light emission band centered at 387 nm can be observed, too, which is due to the excitons bound to surface or other structure defects (Schlager, 2006). The luminescence properties have been affected by more probabilities of defects and surface states due to larger surface area, comparing with the GaN epitaxial layer. The locations of the two emission peaks do not change but the intensity of the emission peaks changes obviously with the variation of the ammoniating temperature, which indicates the optical properties are closely related with the ammoniating temperature. The luminous intensity of GaN nanostructures is at its highest at  $950^\circ\text{C}$ .

Figure 11 shows the photoluminescence spectra of the samples (Cr) nitridized at  $950^\circ\text{C}$  for different nitridation times.

Figure 11 shows there is only one strong ultraviolet emission peak centered at 362 nm, which is close to the result of 365 nm reported by reference (Monemar, 1974). A blue-shift

occurs, which is attribute to quantum confinement effect (Chen et al., 2001; Liu et al., 2001). The site of the strong emission peak does not change but the intensities of the emission peak changes obviously with the viriation of nitridation time. The intensity of the emission peak reaches its best after nitridation for 15 mins, which shows that the optical properties of GaN nanowire structures significantly depend on ammoniating times.

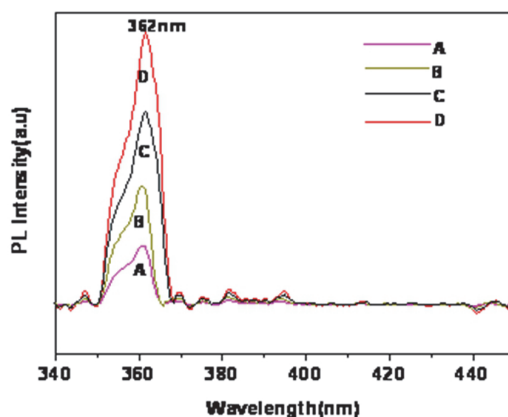


Fig. 11. The photoluminescence spectra of the samples (Cr) nitridized at 950 °C for different nitridation times of (a) 20 mins; (b) 5 mins; (c) 10 mins; (d) 15 mins.

Different metallics have great influence on the optical properties of GaN nanowires. We summarized the data after testing all the samples catalyzed by Ti, V, Cr, Co, Nb, Mo, and Ta, which are listed in Table 1.

Ti 364nm	V 368.2nm	Cr 362nm	Co 370nm
	Nb 367.5nm	Mo 370.5nm	
	Ta 364nm		

Table 1. Wavelengths of strong UV emission peaks for the samples catalyzed by different  $M_e$ .

Table 1 shows that with the increase in the number of protons, the wavelength of the samples catalyzed by different elements can change their sites, i.e., blue-shift, red-shift, and then blue-shift, red-shift. In short, wavelength shifts to long wave, i.e., red-shift, with the increase in the number of the protons at the same line of the Periodic Table of chemical elements. While as for the same subgroup elements, from V to Nb to Ta, wavelength decreases, i.e, blue-shift.

Note: Cr is an exception, and the reason is unknown.

### 2.1.3 Growth mechanism

There are several growth mechanisms for one-dimension nanowires, One is vapor-liquid-solid (VLS) process(Sun et al., 2002), in which nanoparticles as catalysts are formed on the tip of nanowires. The other is VS mechanism (Wang et al., 2004), in which nanowires are

fabricated from the vapor of precursor directly, without a liquid state. For the GaN nanowires synthesized in our cases, VLS mechanism is dominant but not enough to explain the growth of the GaN nanowires.

The growth of one-dimensional nanowires are closely related to the defect energies because there are more broken bonds at defect sites with lower chemical potential and nanowires can grow from these defects. Less nanowires can form when GaN films were deposited on the single crystal Si substrate by MBE or MOCVD because there are less defects on the Si substrate surface and the surface energies are too low to provide enough energy for the growth of one-dimensional nanowires. One-dimensional nanowires can form after the intermediate layer is deposited on the Si substrate. The defects originating from the intermediate layer can change the energy distribution on the substrate surface and provide more energies for the growth of nanowires.

Figure 12 show the typical images of GaN nanostructures.

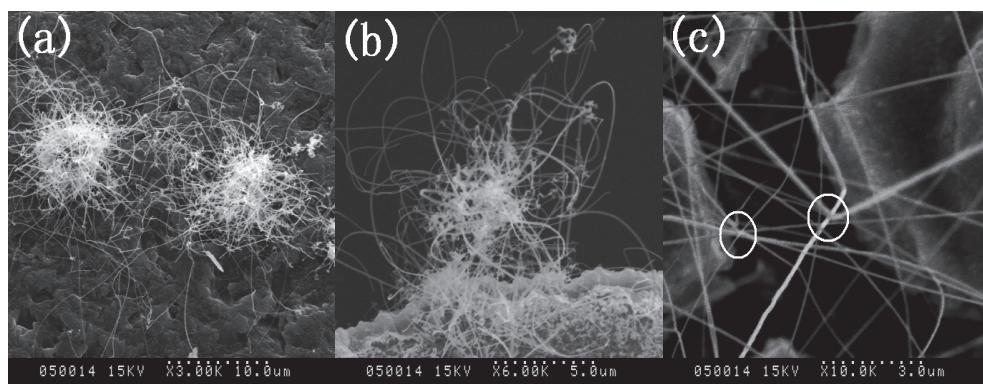


Fig. 12. (a) Cluster growth of one-dimensional GaN nanostructure; (b) Magnification of local area in image (a); (c) SEM image of single nanowire with nanoparticle on the tip.

During our experiments, we found that these nanowires grew as clusters-like structure, as shown in Figure 12a and Figure 12b, and distributed on the substrate surface scarcely. In Figure 12, there exist cluster-like nanowires and nanowires grow radially outward from the central nuclei. As identified in Figure 12c and Figure 4g, and 4h, there are nanoparticles on the tips of nanowires, which is the most noteworthy feature of the vapor-liquid-solid (VLS) mechanism. Therefore, we infer that metallic  $M_e$  forms the central nuclei during ammoniation on the substrate surface and GaN nanowires occur from these nanoparticles. That is,  $M_e$  intermediate layers provide nucleation points for the formation of GaN crystalline nuclei and play an important role for the formation of GaN nanowires.

The growth procedure of nanowires is inferred and clarified as follows. Cr nanoparticles form and distribute on the substrate surface at ammoniation temperature (Ohno et al., 2005) and thus many defects occur on the single crystal Si substrate surface, which has less defects originally. These defects energies have changed the energy distribution on the substrate surface. The broken bonds on the defect sites absorb dissociative gaseous state Ga and N atoms and form Cr-Ga-N structures continuously (as shown in Figure 13). We name this explanation as "defect energies confinement theory" (Shi et al., 2010c).

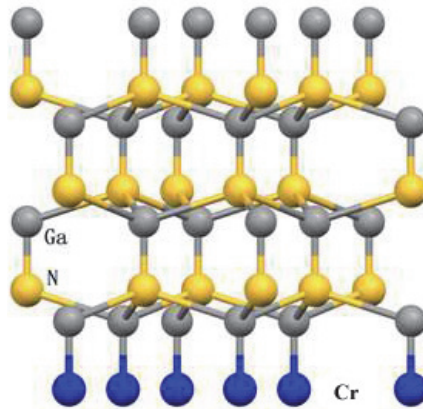
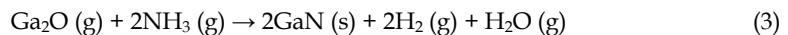
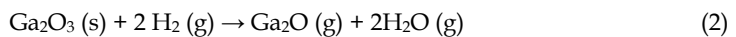


Fig. 13. Cr-Ga-N structures during the formation of GaN nanowires.

On the other hand,  $\text{NH}_3$  decomposes to  $\text{NH}_2$ ,  $\text{NH}$ ,  $\text{H}_2$  and  $\text{N}$  gradually when temperature reaches  $850^\circ\text{C}$  (Tang et al., 2000; Xue et al., 2005)  $\text{Ga}_2\text{O}_3$  particles are deoxidized to gaseous  $\text{Ga}_2\text{O}$  by  $\text{H}_2$  and next GaN molecules are synthesized through the reaction of  $\text{Ga}_2\text{O}$  and ammonia. GaN molecules occur by the reaction of gaseous  $\text{Ga}_2\text{O}$  and  $\text{NH}_3$  gases diffuse and move to the substrates, forming GaN crystalline nuclei. When GaN molecules carried by gas flow meet GaN crystallite nuclei, they can combine together immediately, therefore, GaN crystallite nuclei grow up gradually and single-crystal nanowires come into being. During the whole process, there are broken bonds on the nanowires surface and thus defect energies accumulate and absorb Ga- and N atoms from the surrounding saturated gas. When the concentration of gas reduces or when the defect energies of the nanowires fall to an insufficient level and can't absorb GaN nanowires, the growth of nanowires ends. From a macro perspective, the GaN nanowires formation on the substrate surface includes absorption, migration, nucleus formation, converging to islands, growth and desorption before they are formed into GaN nanowires.

The reaction formula are as follows:



We deposited  $\text{Ga}_2\text{O}_3$  on the silicon substrate without Cr intermediate layer under the same conditions but no nanowires were generated. Therefore, Cr is thought to be a nucleation point of the GaN nanowires and plays an important role as catalyst. The process of growth follows the vapor-liquid-solid (VLS) mechanism.

In short, both VLS and defects energy theory can explain the formation of the GaN nanowires.

### 2.1.4 Summary

Large-scale GaN nanowires can be formed and the predominant phase of samples fabricated by magnetron sputtering method catalyzed by metallics of  $M_c$  is the hexagonal wurtzite

GaN crystal identified by XRD analysis; the existence of the Ga-N bond is established by the FTIR spectrum and N atom exists as nitride by XPS.

The GaN nanowires are single crystal with straight, smooth surface and uniform thickness along spindle direction, have the size of 30-80 nm in diameter and several tens of microns in length with high-quality crystalline.

At special conditions, the GaN nanostructures can grow along preferred (002) plane catalyzed by transitional elements of Ti, V, Cr, and rare-earth of Tb. While the GaN nanostructures can't grow along preferred plane by transitional elements of Nb, Mo, Co, and Ta. That is, the GaN nanostructures can grow along preferred (002) plane catalyzed by the first elements of the II, III, IV subgroups on the Periodic Table of chemical elements, except the other elements. This is a noticed phenomenon deserved further study.

Ammoniating times and temperatures have great influence on the crystalline quality of the samples. The sample catalyzed by Cr can form preferred (002) plane ammoniated for 5 min, and the sample catalyzed by Tb can form preferred (002) plane ammoniated at 850 °C.

The diameters increase with the number of the protons, for example, the samples can form GaN nanowires when catalyzed by Ti, V, and Cr, however, with the increase in the protons, nanorods can be formed, such as the sample catalyzed by Co. As for V, Nb, and Ta, which are of the same sub-group, nanowires can be formed catalyzed by V, however, nanorods can be formed when catalyzed by Nb and Ta. Cr and Mo are of the same subgroup, the sample catalyzed by Cr can form nanowires, while after catalyzing by Mo, nanorods can be formed. That is, the catalytic action increases with the increase in the number of the protons at the same line of the Periodic Table of chemical elements, with the morphology becoming obvious. And the same law exists in the same row.

Ammoniating temperatures have great influence on the morphology of the sample catalyzed by Cr, nanowires are formed in the sample ammoniated at 950 °C, however, nanorods are formed ammoniated at 1000 °C.

GaN nanowires have good optical properties, which can be tested by PL spectra. The optical properties of GaN nanowires greatly depend on the ammoniating temperatures and times. With the increase in the number of protons, the wavelength of the samples catalyzed by different elements can change their sites, i.e., blue-shift, red-shift, and then blue-shift, red-shift. In short, wavelength shifts to long wave, i.e., red-shift, with the increase in the number of the protons at the same line of the Periodic Table of chemical elements. While as for the same subgroup elements, from V to Nb to Ta, wavelength decreases, i.e., blue-shift. However, Cr is an exception, and the reason is unknown.

The growth procedure follows the VLS mechanism, and  $M_e$  acts as the nucleation point for GaN crystalline nuclei and plays an important role as catalyst during ammoniation process. Defect energies confinement theory can also be applied to explain the formation of GaN nanostructures.

## 2.2 GaN Nanowires catalyzed by intermediate layer of $C_m$

### 2.2.1 Experimental procedures

The experimental procedure is the same as the second section, i.e., GaN Nanowires Catalyzed by Transition Metallic of  $M_e$ , and the only difference between them lies in that the  $C_m$  and  $Ga_2O_3$  films were sputtered on Si (111) substrates by RF magnetron sputtering method, with the  $C_m$  (MgO,  $TiO_2$ ,  $Al_2O_3$ , SiC, BN, and ZnO) target of 99.99% purity and the sintered  $Ga_2O_3$  target of 99.999% purity. The thicknesses of the intermediate layers are of 10 nm ~ 200 nm.

The other conditions are the same as that stated in the second section of "GaN Nanowires Catalyzed by Transaction Metallic of  $M_e$ ".

### 2.2.2 Results and discussion

Figure 14 show the X-ray diffraction patterns of the samples grown at different temperatures with different intermediate layer of  $C_m$ .

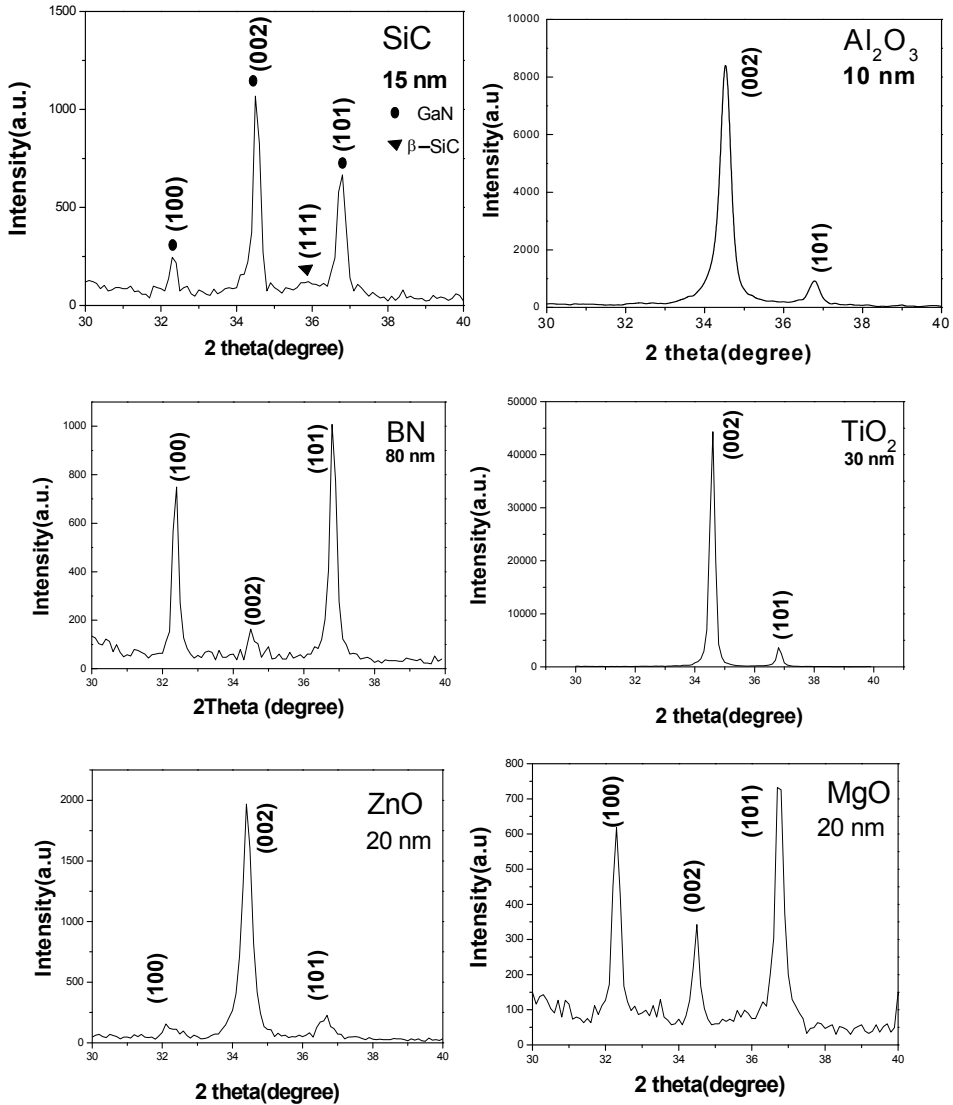
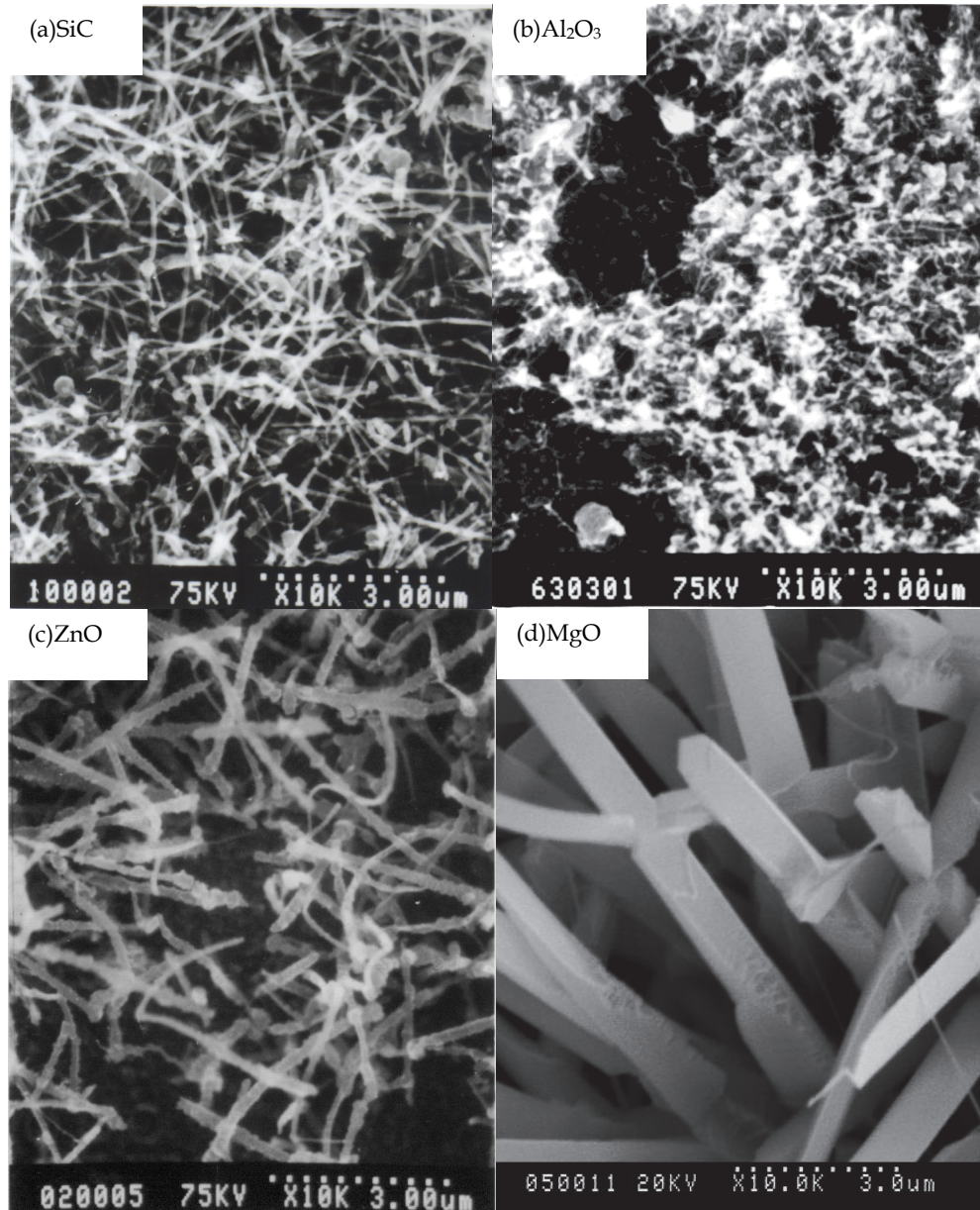


Fig. 14. X-ray diffraction pattern of the samples grown at different temperatures with different intermediate layer of  $C_m$ .

Figure 14 shows that GaN can grow along preferred (002) planes catalyzed by  $\text{Al}_2\text{O}_3$  (10 nm), ZnO (20 nm), and  $\text{TiO}_2$  (30 nm), which were fabricated at the optimal conditions. However, other samples can't grow along preferred (002) planes.

Figure 15 show the SEM images of the samples catalyzed by different intermediate layers of  $\text{C}_m$ .



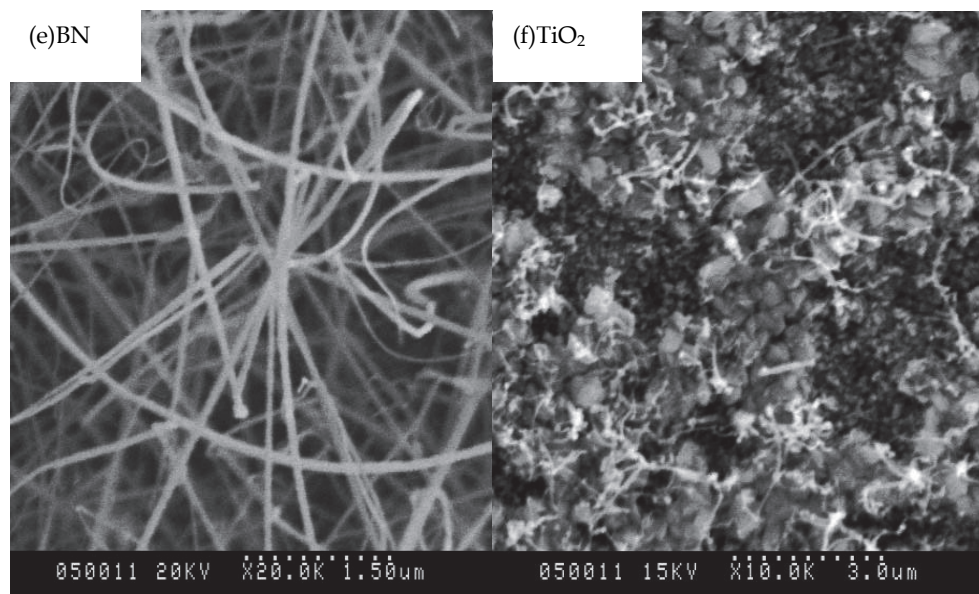


Fig. 15. SEM images of the samples catalyzed by different intermediate layers of C<sub>m</sub>.

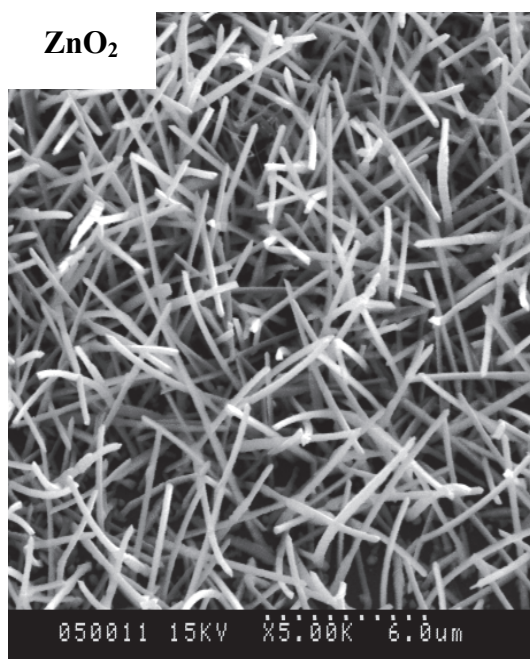


Fig. 16. SEM image of the sample catalyzed by 200 nm ZnO thin film as intermediate layer.

Figure 15 show that pure and clear GaN nanostructures can be formed with ZnO, MgO, and BN as intermediate layers. While as for the samples using SiC, Al<sub>2</sub>O<sub>3</sub>, and TiO<sub>2</sub> as intermediate layers, GaN nanostructures are vague. GaN nanowires are formed with ZnO, and BN as intermediate layers, and nanobelts are formed with MgO, as intermediate layers. When the thickness of ZnO increases form 20 nm to 200 nm, the sample can turn from GaN nanowires to nanorods, which is shown as Figure 16.

Figure 17. SEM images of the sample catalyzed by 20 nm MgO thin film as intermediate layer and ammoniated at different temperatures.

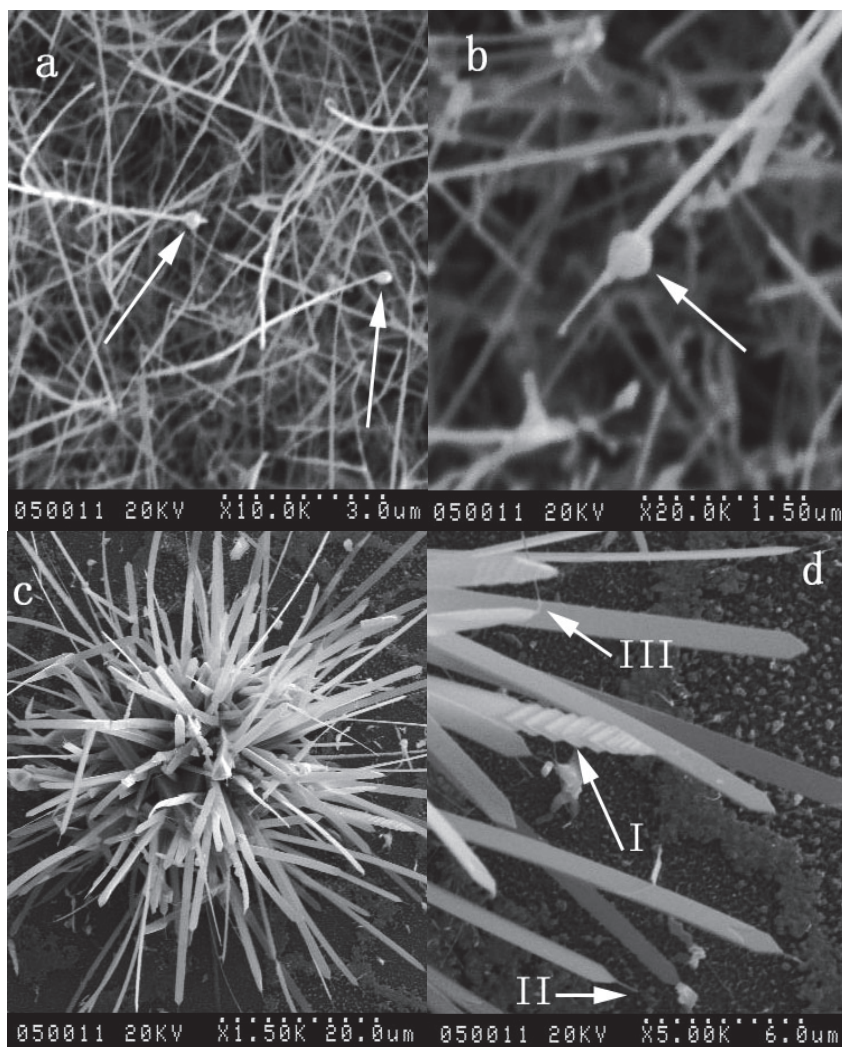


Fig. 17. SEM images of the sample catalyzed by 20 nm MgO thin film as intermediate layer and ammoniated at different temperatures. a, 950 °C; b, 1000 °C; c, 1050°C; d, enlarged picture at the limbic part of c.

As shown as Figure 17, nanoparticles exist on the tips of the GaN nanowires, which shows that the growth mechanism complies with vapor-liquid-solid (VLS) process. Grown at 950 °C, nanowires occur, grown at 1000 °C, nanorods exist, and when the ammoniating temperature increase to 1050 °C, nanobelts appear. That is, the ammoniating temperatures can affect the morphology of the GaN samples deeply.

Figure 18 show HRTEM and SAED images of an individual nanowire with MgO as intermediate layer.

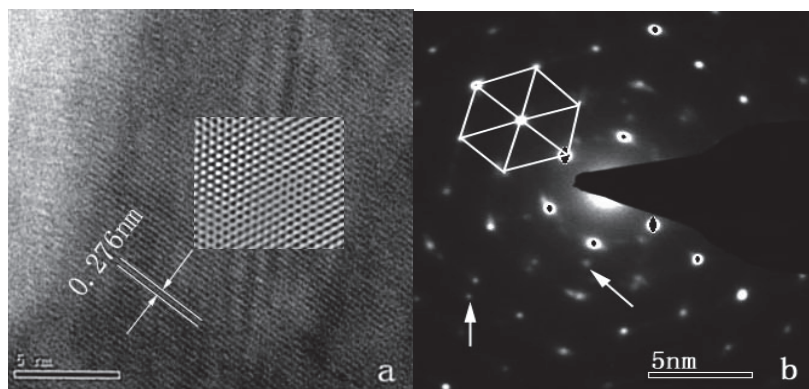


Fig. 18. (a) HRTEM, (b) SAED images of an individual nanowire with MgO as intermediate layer. The inset picture in HRTEM is a two-dimensional crystals space picture from rapid Fourier inverse transformation of image a.

Figure 18 indicate that GaN nanowire can form when MgO was used as intermediate layer with high crystalline quality. The crystal plane spacing of nanowire is about 0.276 nm, which corresponds to (100) crystal plane spacing (0.276 nm) of hexagonal GaN single crystal. No defects are observed.

Different compounds ( $C_m$ ) have great influence on the optical properties of GaN nanowires. We summarized the data after testing all the samples catalyzed by  $Al_2O_3$ , ZnO, SiC, and BN, which are listed in Table 2.

$Al_2O_3$	ZnO	SiC	BN
347 nm	344 nm	371 nm	373 nm

Table 2. Wavelengths of strong UV emission peaks for the samples catalyzed by different  $C_m$ .

As shown in Table 2, the wavelengths could be shorten when oxidizing materials were used as intermediate layers, i.e., blue-shift, while when carbide and nitride were used as intermediate layers, the wavelengths could increase, i.e., red-shift.

### 2.2.3 Summary

GaN can grow along preferred (002) planes catalyzed by  $Al_2O_3$  (10 nm), ZnO (20 nm), and  $TiO_2$  (30 nm), which were fabricated at the optimal conditions. However, other samples can't grow along preferred (002) planes.

Pure and clear GaN nanostructures can be formed with ZnO, MgO, and BN as intermediate layers. GaN nanowires are formed with ZnO, and BN as intermediate layers, and nanobelts

are formed with MgO, as intermediate layers. When the thickness of ZnO increases from 20 nm to 200 nm, the sample can turn from GaN nanowires to nanorods. The ammoniating temperatures can affect the morphology of the GaN samples deeply. Nanowires occur at 950 °C, nanorods exist at 1000 °C, nanobelts appear at 1050 °C.

The wavelengths (PL spectra data) could be shortened when oxidizing materials were used as intermediate layers, i.e., blue-shift, while when carbide and nitride were used as intermediate layers, the wavelengths could increase, i.e., red-shift.

### 2.3 Mg-Doped GaN nanowires

To improve the progress in GaN-based nano-photoelectric device and to enhance photoelectric performance of nano-devices, proper doping is very necessary. P-type doping and p-n junctions are great significance in fabricating nanowires (Fasol,1996; Nakamura,1998) and the formation of p-typed GaN films is the key technology in developing these devices and p-doping of GaN nanostructures with Mg as dopant is more effective in practice than with other dopants, because the ionic radius of Mg (0.65Å) is only slightly greater than that of Ga (0.62Å), and the gallium positions can be easily substituted by Mg under certain conditions. In this work, Mg-doped GaN nanowires were synthesized by a technique resembling the delta-doping method, and the concentration of Mg in GaN nanowires was varied to study its influence on the surface morphology, crystallinity, and optical properties of Mg-doped GaN nanowires (Shi et al., 2010a; Zhang et al., 2009).

#### 2.3.1 Experimental procedures

Mg-doped GaN nanowires have been fabricated using ammoniating Ga<sub>2</sub>O<sub>3</sub> films doped with Mg under flowing ammonia atmosphere. First, the Mg doped Ga<sub>2</sub>O<sub>3</sub> films were grown on Si (111) substrates by sputtering the Mg target of 99.99% purity and the sintered Ga<sub>2</sub>O<sub>3</sub> target of 99.999% purity in a JCK-500A radio frequency magnetron sputtering system. Both the Mg target and Ga<sub>2</sub>O<sub>3</sub> target were subjected to direct-current (DC) and radio-frequency (RF) magnetron sputtering, respectively. Next 30 cycles of this process were performed for a total deposition time of about 100 min, after which the total thickness of the Mg-doped Ga<sub>2</sub>O<sub>3</sub> films was about 630 ~ 850 nm. In a single sputtering cycle, first an undoped Ga<sub>2</sub>O<sub>3</sub> layer of 6 ~ 30 nm in thickness was deposited, followed by an approximately 5 nm Mg buffer layer. Figure 19 shows the growth sketch of the Ga<sub>2</sub>O<sub>3</sub> films.

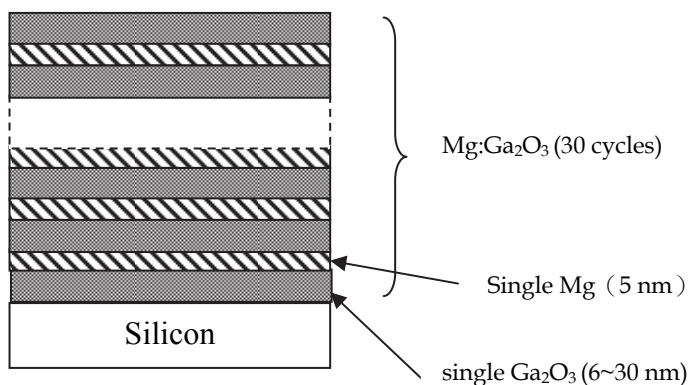


Fig. 19. The growth sketch of the Mg doped Ga<sub>2</sub>O<sub>3</sub> films.

Second, the  $\text{Ga}_2\text{O}_3$  thin films as deposited were ammoniated at  $\text{NH}_3$  atmosphere in a conventional tube furnace at 850 °C, 900 °C, and 950 °C for 5 min, 10 min, 15 min, and 20 min, respectively. The working conditions were, 150-Watt RF sputtering power of 13.56 MHz ; 20-Watt DC sputtering power; background pressure of  $0.9 \times 10^{-3}$  Pa; and pure Ar ( $\geq 99.99\%$ ) as the working at a working pressure of 2 Pa.

### 2.3.2 Results and discussion

Figure 20, and 21 show the X-ray diffraction patterns of the samples grown at 850 °C, 900 °C, and 950 °C for 15 min.

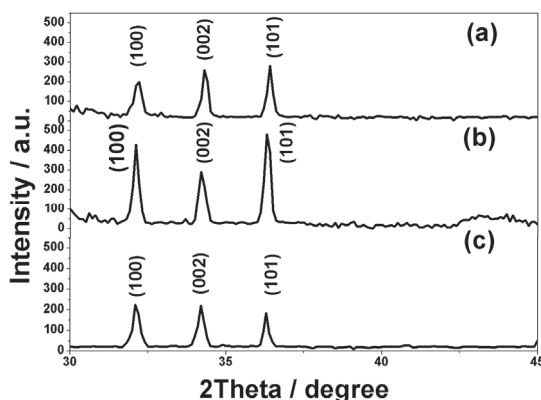


Fig. 20. X-ray diffraction patterns of samples at different temperature for 15 min, (a) 850 °C; (b) 900 °C; (c) 950 °C.

As shown in Figure 20, the samples following ammoniation are hexagonal wurtzite GaN (JCPDS card No.65-3410, International Center for Diffraction Data, 2002) with lattice constant of  $a = 0.3186$  nm and  $c = 0.5178$  nm, with the diffraction peaks located at  $2\theta = 32.1^\circ$ ,  $34.2^\circ$  and  $36.4^\circ$  corresponding to (100), (002) and (101) planes, which are consistent with the reported values for bulk GaN. No peak of  $\text{Ga}_2\text{O}_3$ , Mg or MgO is observed, indicating that neither  $\text{Ga}_2\text{O}_3$ , Mg metal nor MgO coats the nanowire surface.

The intensity of the sample shown in Figure 20b is stronger than that of the samples ammoniated at 850 °C and 950 °C, which shows the highest crystalline quality of this sample. The diffraction peak intensities decrease when the ammoniation temperature is lower or higher than 900 °C, which is probably caused by incomplete growth of GaN grains at lower temperature and decomposition or sublimation of GaN grains at higher temperature (Yang et al., 2002).

Figure 21 show the X-ray diffraction patterns of the samples grown at 900 °C for 5 min, 10 min, 15 min, and 20 min, respectively.

As seen in Figure 21, the main phase of samples following ammoniation are hexagonal wurtzite GaN with lattice constant  $a = 0.3186$  nm and  $c = 0.5178$  nm, with the diffraction peaks located at  $2\theta = 32.1^\circ$ ,  $34.2^\circ$ , and  $36.4^\circ$  corresponding to (100), (002) and (101) planes, which are consistent with the reported values for bulk GaN. No peak of  $\text{Ga}_2\text{O}_3$ , Mg or MgO is observed, indicating that neither  $\text{Ga}_2\text{O}_3$ , Mg metal nor MgO coats the nanowire surface.

Crystalline increases gradually with the increase of ammoniating time from 5 min to 15 min, and reaches the strongest intensity for the diffraction peak at 15 min, then decreases at 20 min, which is probably caused by incomplete reaction at less time and decomposition or sublimation at more time.

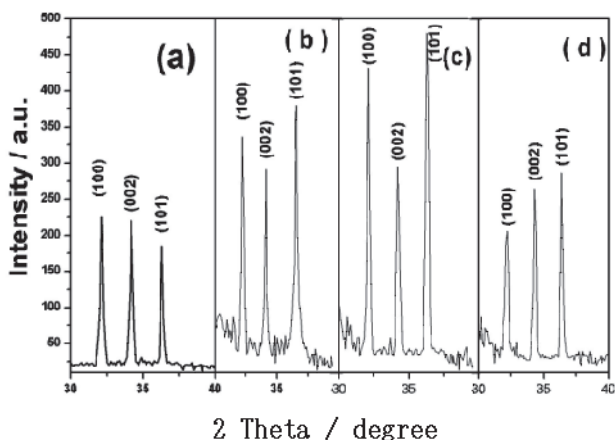


Fig. 21. X-ray diffraction patterns of samples at 900 °C for different time, (a) 5 min; (b) 10 min; (c) 15 min; (d) 20 min.

To further analyze the components of the GaN sample, FT-IR test was carried out for the sample after ammoniated at 900 °C for 15 min, as shown in Figure 22.

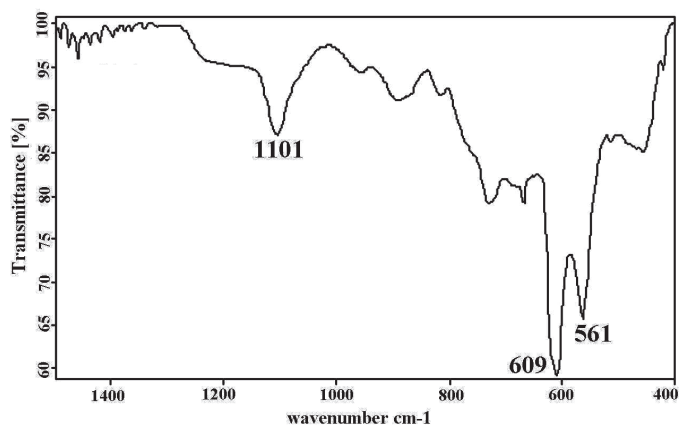


Fig. 22. FTIR pattern of the sample ammoniated at 900 °C for 15 min.

As seen in Figure 22, there are three well-defined prominent absorption bands, located at 561 cm⁻¹, 609 cm⁻¹, and 1101 cm⁻¹. The band at 561 cm⁻¹ corresponds to Ga-N stretching vibration in hexagonal type GaN crystal, and the other bands correlate to the Si substrate. The peak at 609 cm⁻¹ is associated with the local vibration of substituted carbon in the Si crystal lattice (Sun et al., 1998) whereas the band at 1101 cm⁻¹ is attributed to the Si-O-Si

asymmetric stretching vibration because of the oxygenation of the Si substrate. There is no Ga-O bond or other absorption band in the spectrum); therefore,  $\text{Ga}_2\text{O}_3$  films react with  $\text{NH}_3$  completely at  $900^\circ\text{C}$  and form the hexagonal-type GaN crystal, which is the same as the results of the XRD.

The sample was also characterized by XPS as shown in Figure 23.

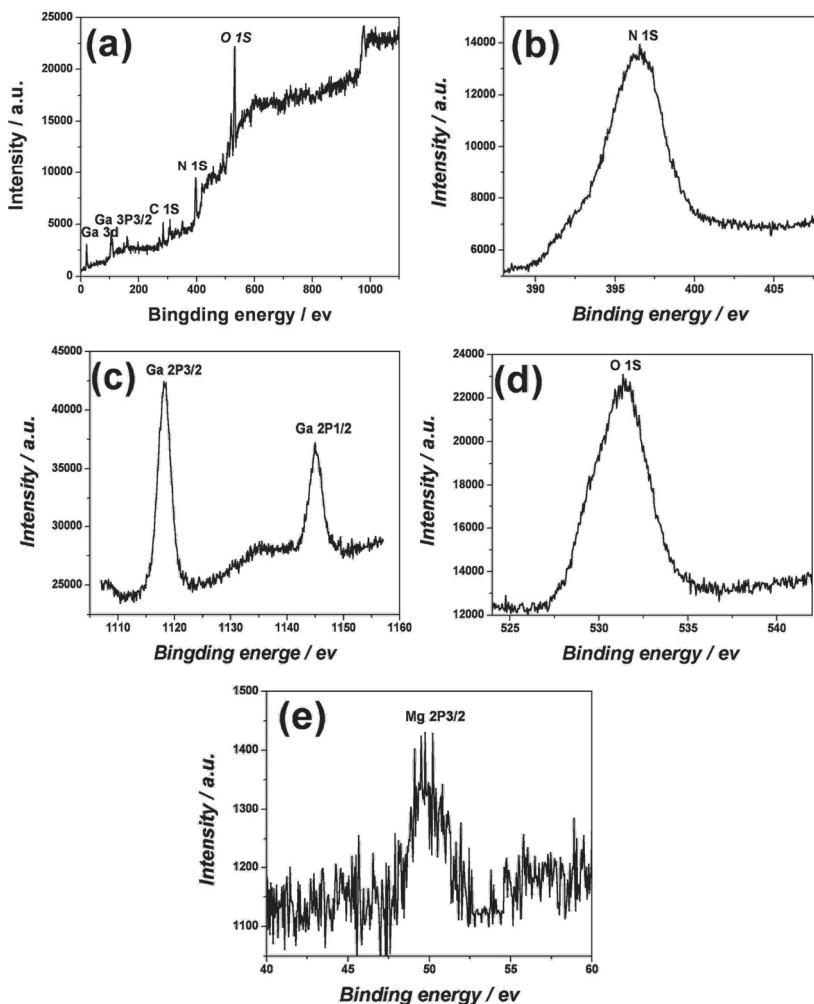


Fig. 23. XPS spectrum of the sample ammoniated at  $900^\circ\text{C}$  for 15 min, (a) general scan spectrum; (b) N1s band; (c) Ga2p<sub>1/2</sub> and Ga2p<sub>3/2</sub> band; (d) O1s band; (e) Mg2p<sub>3/2</sub> band.

Figure 23a shows the XPS images of N1s, Ga2p, Ga3d, and O1s for GaN synthesized at the ammoniating temperature of  $900^\circ\text{C}$ , respectively. Figure 23a shows the general scan in the binding energy, ranging from 0 eV to 1100 eV with the main components being Ga, C, N, and O, with XPS peaks at the location of Ga3d (20.1 eV), Ga3p (109.1 eV), Ga3s (167.3 eV),

C1s (288.3 eV), N1s (397.6 eV) and O1s (534.3 eV). The strong peak at the site of 189.6 eV is LMM Auger peak of Ga element. C and O arise from the surface pollution of the sample. As observed, the energy peak for N1s shown in Figure 23b is centered at 397.6 eV, instead of 399 eV (binding energy of N element existing as atomic style), similar to the results of Li (397.4 eV) and Veal (397.6 eV), that is, the N atom exists as a nitride. The width and slight asymmetry of the N1s peak are attributed to N-H<sub>2</sub> and N-H<sub>3</sub> formation due to the interaction between N<sub>2</sub> and NH<sub>3</sub> at the GaN film<sup>[18]</sup> surface.

As seen in Figure 23c, the core level of Ga has a positive shift from elemental Ga. This shift in the binding energies of Ga and N confirms the bonding between Ga and N and the absence of elemental gallium. The binding energies of Ga2p<sub>1/2</sub> and Ga2p<sub>3/2</sub> are 1145.0 eV and 1118.1 eV, respectively, which are consistent with the results reported by different references of Ga2p<sub>3/2</sub> (1117.4 eV) (Elkashef et al., 1998), Ga2p<sub>1/2</sub> (1144.8 eV) (Kingsley et al., 1995), and Ga2p<sub>1/2</sub> (1144.3 eV) (Sasaki et al., 1998). No bond formation is observed between Ga and O as the Ga3d spectrum does not show any satellite peak corresponding to β-Ga<sup>[21]</sup>, but shows the Ga atom existing only as combined GaN, not Ga<sub>2</sub>O<sub>3</sub>.

The percentage of elements is calculated according to the formula (Choi et al., 1998) as follows.

$$X\% = \left( \frac{A_x}{S_x} \right) / \sum_{i=1}^N \frac{A_i}{S_i}$$

A<sub>x</sub> (A<sub>i</sub>) indicates the peak area of element, x (i); S<sub>x</sub> (S<sub>i</sub>) is the atomic sensitivity factor of x (i) element; N is the number of the total elements. The values of the atomic sensitivity factors of Ga and N atoms are 6.9 and 0.38, respectively. Therefore, quantification of the peaks shows that the atomic ratio of Ga to N is approximately 1:1.09.

As shown in Figure 23d, the O1s peak is centered at 530.9 eV. According to Amanullah *et al.*, generally, the O1s peak had been observed in the binding energy region of 529-535 eV, and the peak around 529 - 530 eV is ascribed to lattice oxygen. For chemisorbed O<sub>2</sub> on the surface, the binding energy ranged from 530.0 eV to 530.9 eV. Therefore, the O1s peak in the present work is part of chemisorbed oxygen.

Figure 23e indicates the Mg2P<sub>3/2</sub> peak is at the site of 49.3 eV, with the bonding energy of Mg (Zhang et al., 2009). The XPS results show that the sample is Mg-doped GaN, similar to that of the XRD (Zhang et al., 2009).

Figure 24 shows the typical SEM images of the samples grown at different temperatures.

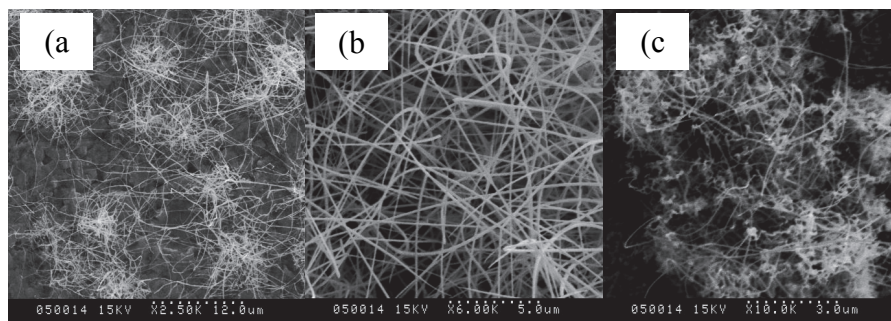


Fig. 24. SEM images of the samples grown at different temperatures, (a) 850 °C (b) 900 °C (c) 950 °C.

Figure 24a shows many cluster-like nanowires distributed on the sample surface, each of which grows radially outward, from the same point on the substrate. These nanowires are thin in diameter but rough on the surface, which are of 35 nm in diameter and 10-20  $\mu\text{m}$  in length. Figure 24b shows the sample comprises several one-dimensional nanowires distributed evenly on the substrate. As compared with the nanowires shown in Figure 24a, these one-dimensional nanowires have cleaner surfaces and are of greater quantity. Most of which are straight and smooth, uniformly thick along the spindle direction, and they intertwine with each other, possessing a thicker diameter of 50 nm and a longer length of several tens of microns. In Figure 24c, a large number of gossypine nanostructures are clearly observed, because of decomposition or sublimation of GaN grains at higher temperature, however, the amount of the GaN nanowires decrease, comparing with the sample shown in Figure 22b.

Ammoniating temperature has great influence on the morphology of the GaN nanowires and with the increase in ammoniating temperature from 850  $^{\circ}\text{C}$  to 900  $^{\circ}\text{C}$  (Shi et al., 2011), the diameter, the length, and the quantity increase but their quantity and crystallinity decrease when the ammoniating temperature rises to 950  $^{\circ}\text{C}$ . The GaN grains can't crystallize completely at lower temperature of 850  $^{\circ}\text{C}$ , however, the samples can decomposition or sublimation at higher temperature of 950  $^{\circ}\text{C}$ . In short, the crystalline is at its best after ammoniation at 900  $^{\circ}\text{C}$ , from the observation shown in Figure 24.

Figure 25 shows the typical SEM images of the samples at 900  $^{\circ}\text{C}$  for different times.

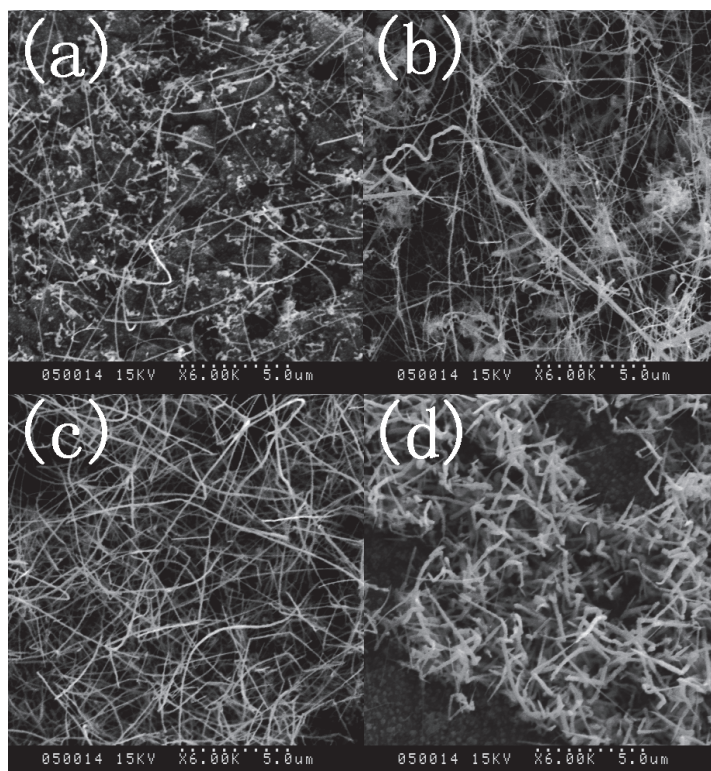


Fig. 25. Typical SEM images of the samples at 900  $^{\circ}\text{C}$  for 5 min, 10 min, 15 min, 20 min.

As shown in Figure 25a, most  $\text{Ga}_2\text{O}_3$  thin film has been ammoniated after ammoniated at 5 min. There are many irregular nanoparticles covered on the substrate surface with a small amount of nanowires. These nanowires intertwine with each other and distribute on the surface randomly having the size of 35 nm in diameter and less than ten microns in length. Clear variation occurs on the surface of the samples, observed from Figure 25b, Figure 25c and Figure 25d. When ammoniated at 10 min, substrate surface is covered by nanowires completely but they are uneven thickness with 10-20 microns. Figure 25c shows nanowires become smooth and clean with even diameter of about 50 nm and 20 microns in length, while in Figure 25d, the nanowires become shorter and thicker with coarse surface, which is because of recrystallization of GaN. The results are consistent with XRD analysis. Ammoniating time has great influence on the morphology of the GaN nanowires and the nanowires become more in number, longer in length, and thicker in diameter with the increase of ammoniating time. The GaN grains can't crystallize completely at shorter time of 5 min and 10 min, however, the samples can recrystallize at longer time of 20 min. In short, the crystalline is at its best after ammoniation for 15 min from the observation of Figure 25.

Figure 26 shows the TEM, SAED, HRTEM and EDX images of an individual nanowire grown at 900 °C for 15 min.

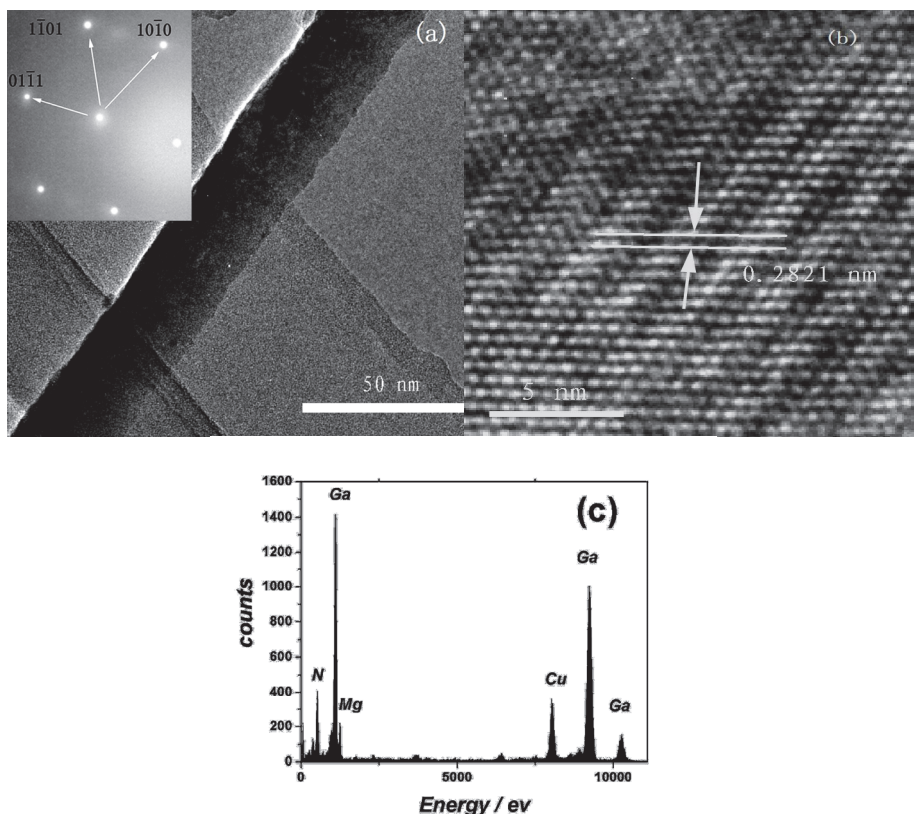


Fig. 26. TEM, SAED, HRTEM and EDX images of individual nanowire.

Figure 26a shows that the nanowire is 35 nm in diameter with a coarse surface. The reason for the coarse surface is attributed to the decreased mass transportation of Ga affected by the rich N atmosphere and Mg doping during growth<sup>[26]</sup>. Diffraction spots from SAED (the inset in Figure 26a) are regular and correspond to the diffraction zone axis of  $[\bar{1}2\bar{1}3]$ , which reveals the GaN nanowire is monocrystal with a hexagonal wurtzite structure. Seen from Figure 26b, the HRTEM lattice image of the straight GaN nanowire and the well-spaced lattice fringe in the image indicate the single crystal structure of GaN nanowires with high crystalline quality but with less dislocations and defects. The crystal plane spacing of nanowires is about 0.2821 nm, which is larger than that of (100) crystal plane spacing (0.2757 nm) of the hexagonal GaN single crystal. Mg doping slightly changes the lattice constant of GaN. The growth direction of this nanowire is parallel to  $[100]$  the orientation. Figure 26c shows the EDX image of this nanowire and reveals its composition as follows, 47% Ga, 48.5% N and 3% Mg (mole fraction), which is similar to that of the XPS (Shi et al., 2010a). Figure 27 is the photoluminescence spectrum of samples ammoniated at 900°C for different time, detected with He-Cd laser used as the excitation source (with a wave length of 325 nm) at room temperature.

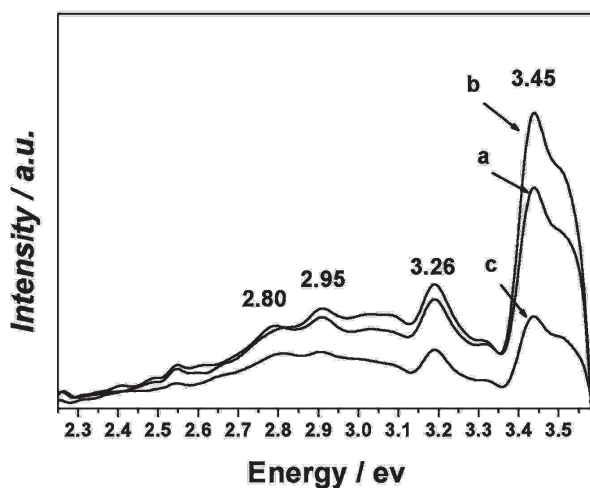


Fig. 27. Photoluminescence spectrum of samples ammoniated at 900°C for different times; (a) 10 min; (b) 15 min; (c) 20 min.

According to Figure 27, the nanowires show four emission peaks, their corresponding  $E_v$  are 3.45 eV, 3.26 eV, 2.95 eV, and 2.80 eV, respectively. A clear blueshift of the band-gap emission has occurred, from 3.39 eV for bulk GaN<sup>†</sup> to 3.45 eV for Mg-doped GaN. When GaN is doped with Mg, the excess carriers generated enter to the conduction band of GaN and effectively hinder the transition of electrons at the bottom of GaN conduction band, thereby increase the energy from the conduction band to the valence band when electrons excited. This leads to a blueshift in the optical band-to-band transitions. This is consistent with the Burstein-Moss effect (Zhou et al., 2004). As for the emission peak at 3.26 eV, it is caused by the transition of electrons from the bottom of GaN conduction band to shallow acceptor level of Mg (acceptor level of Mg is at the site of 200 meV above valence band). The

emission bands at the site of 2.95 eV and 2.80 eV are caused by deep acceptor level of Mg doping. This observation consists with the results of Zolper et al (Zolper et al., 1996). The sites of the four emission peaks do not change but the strength of the emission peaks changes obviously with the increase of ammoniating time. Ammoniating time has great influence on the optical properties and the best condition is 15 min.

Figure 28 is the photoluminescence spectrum of samples ammoniated at different temperatures for 15 min, detected with He-Cd laser used as the excitation source (with a wave length of 325 nm) at room temperature.

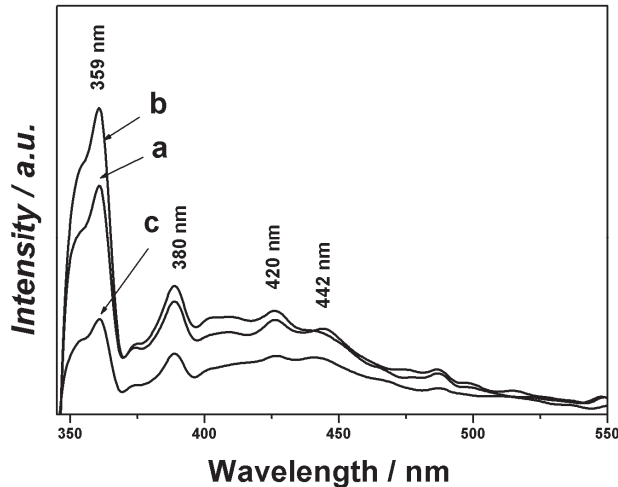


Fig. 28. Photoluminescence spectrum of samples ammoniated at different temperatures for 15 min. (a) 850 °C; (b) 900 °C; (c) 950 °C.

The nanowires show four emission peaks, at 359 nm, 380 nm, 420 nm, and 442 nm. Bulk GaN shows photoluminescence at 365 nm at room temperature. According to the equation  $E_v/eV=1240/\lambda$ , the peak at 359 nm corresponds to  $E_v=3.45$  eV. Thus, a clear blueshift of the band-gap emission has occurred, too. The reason is just like what has stated above. The other three peaks located at 380 nm, 420 nm, and 442 nm correspond to 3.26 eV, 2.95 eV, and 2.80 eV, respectively, and can be explained the same as that in Figure 10. The sites of the four emission peaks do not change but the strength of the emission peaks changes obviously with the variation of ammoniating temperature, which indicates the optical properties are closely related to ammoniating temperature. The luminous intensity of GaN nanostructures is at its best at 900°C.

### 2.3.3 Growth mechanism

During the nanowire growth process, higher surface energy exist on the nanowire's tip, but lower surface energy exist on their sides. The sides of the nanowires play a significant role during the growth process as a path to provide materials. The main aim of GaN molecules, Ga atoms, and N atoms is to find a position with higher surface energy and to grow there so as to decrease the surface energy.

Mg metal and Si element can react and form silico-magnesium alloys, which exist as a dissociative phase. The silico-magnesium alloys can not only promote the growth of the GaN nanowires and the chemical reaction, but also inevitably lead to the uneven distribution of the energy on the substrate surface, i.e., some positions have high surface energy and the energy can aggregate around the defects, thus providing nucleation points for the GaN nanowires (Shi et al., 2010c).

Cluster-like GaN nanowires are seen on the Si substrate surface, as identified in Figure 29.

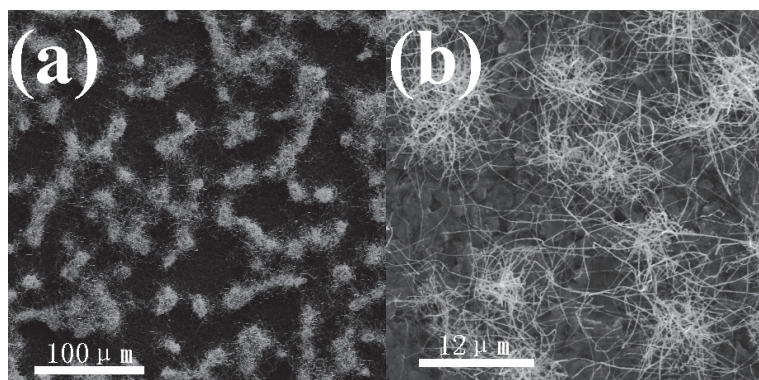


Fig. 29. SEM images of the cluster-like nanowires distributed on Si substrate surface, an ordinary area of substrate and (b) the amplified image of sample (a).

More defects exist on the Si substrate surface, i.e., aggregation of the defect energy, which have more broken bonds and lower chemical power. Therefore, the GaN nanowires will grow at the sites of the defects, the aggregation sites of the defect energy become the nucleation points for the GaN nanowires, as shown in Figure 30.

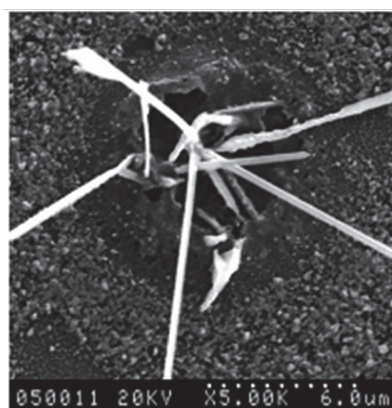


Fig. 30. SEM image of a defect on the Si substrate surface and the nanostructure growth from this position with more energy aggregated.

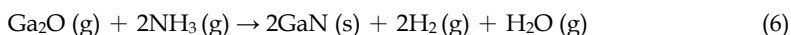
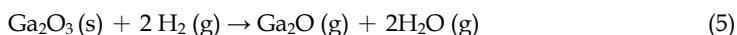
In the sputtering process, a multilayer structure of Mg-doping  $\text{Ga}_2\text{O}_3$  films is obtained. Thus, Mg has greater opportunity to substitute Ga, and then leads to more defects. In the

annealing process,  $\text{NH}_3$  decomposes into  $\text{NH}_2$ ,  $\text{NH}$ ,  $\text{H}_2$ , and  $\text{N}$ , when the ammoniating temperature reaches  $850^\circ\text{C}$ . The Ga atoms can combine with the N atoms, and  $\text{Ga}_2\text{O}$  can react with  $\text{NH}_3$  to form GaN molecules, and finally form GaN microcrystallites. These microcrystallites become the seed crystals for the GaN nanowires growth.

GaN molecules carried by air flow would combine with the GaN microcrystallites and induce the GaN microcrystallites' growth. There are broken bonds on the GaN nanostructure surfaces, and the defect energy can aggregate together so that the Ga atoms and N atoms can be absorbed from the surrounding saturated gas by the broken bonds of the defects to form a Ni-Ga-N structure. The absorbed Ga and N atoms could also generate broken bonds, therefore, the absorption process could carry on continuously. However, when the concentration of gas reduces or when the defect energy of the nanowires falls to a level that is insufficient to absorb Ga- and N atoms, the growth of the GaN nanowires can stop at last.

As seen from a macro-perspective, the formation of the GaN nanowires included absorption, migration, nucleus formation, aggregation, growth and desorption before they turn to GaN nanowires. Meanwhile, Mg is doped into the GaN cells to occupy the Ga vacancies because the ion radius of Mg (0.065 nm) is similar to that of Ga (0.062 nm). Mg doping can distort the GaN cell, which can introduce more defects, so the defect energy increases, which promotes the growth of the GaN nanowires. This theory can be called "defect energy confinement theory" (Shi et al., 2010c).

The reaction formula of  $\text{Ga}_2\text{O}_3$  becoming GaN are as follows:



Therefore, we think that the H atoms decomposed from  $\text{NH}_3$  can promote the decomposition of  $\text{Ga}_2\text{O}_3$  to generate more Ga atoms and  $\text{Ga}_2\text{O}$  molecules; then Ga atoms and  $\text{Ga}_2\text{O}$  molecules can react with N atoms to form GaN, which is decomposed from  $\text{NH}_3$ . That is, the growth mechanism complies with vapor-liquid-solid (VLS) process and the aggregation of the defect energy accelerates this growth of the GaN nanowires.

### 2.3.4 Summary

The predominant phase of the samples fabricated by the magnetron sputtering method is the hexagonal wurtzite GaN crystal identified by the XRD analysis. The best condition to fabricate the GaN nanowires is at  $900^\circ\text{C}$  for 15 min, the highest crystalline quality can be obtained at this condition. The presence of the Ga-N bond is established by the FTIR spectrum and the N atom exists as a nitride by XPS and quantification of the peaks reveals that the atomic ratio of Ga to N is approximately 1:1.09.

Ammoniating temperatures and ammoniating times greatly influence the GaN nanowires morphology. The GaN nanowires grown at  $900^\circ\text{C}$  for 15 min are straight and smooth with uniform thickness along the spindle direction, 50 nm in diameter and several tens of microns in length, with high crystalline quality. The growth direction of this GaN nanowire is parallel to [100] orientation.

PL spectra show that GaN nanowires after ammoniation at  $900^\circ\text{C}$  for 15 min possess good optical properties and have a strong emission peak at 359 nm. The optical properties of the

GaN nanowires are closely related to the ammoniating temperature and ammoniating time, because the strength of the emission peak changes with the variation in temperature and time, whereas its site does not change accordingly.

The aggregation of the defect energy is used to explain the growth mechanism of the GaN nanowires. Mg doping causes the distortion of the GaN cell and introduces more defects in the crystal cell so that the defect energy are added, which promotes the growth of the GaN nanowires. The growth mechanism mainly follows the VLS process, and the aggregation of the defect energy accelerates this growth of the GaN nanowires.

### 3. Conclusion

#### 3.1 Catalyzed by $M_e$

We have been fabricated large-scale single-crystalline GaN nanowires with high-quality by RF magnetron sputtering method using Ti, V, Cr, Co, Nb, Mo, Ta, and Tb ( $M_e$ ) as catalysts.

The diameters increase with the number of the protons, for example, the samples can form GaN nanowires when catalyzed by Ti, V, and Cr, however, with the increase in the protons, nanorods can be formed, such as the sample catalyzed by Co. As for V, Nb, and Ta, which are of the same sub-group, nanowires can be formed catalyzed by V, however, nanorods can be formed when catalyzed by Nb and Ta. Cr and Mo are of the same subgroup, the sample catalyzed by Cr can form nanowires, while after catalyzing by Mo, nanorods can be formed. That is, the catalytic action increases with the increase in the number of the protons at the same line of the Periodic Table of chemical elements, with the morphology becoming obvious. And the same law exists in the same row.

GaN nanowires have good optical properties, which can be tested by PL spectra. The optical properties of GaN nanowires greatly depend on the ammoniating temperatures and times. With the increase in the number of protons, the wavelength of the samples catalyzed by different elements can change their sites, i.e., blue-shift, red-shift, and then blue-shift, red-shift. In short, wavelength shifts to long wave, i.e., red-shift, with the increase in the number of the protons at the same line of the Periodic Table of chemical elements. While as for the same subgroup elements, from V to Nb to Ta, wavelength decreases, i.e., blue-shift. However, Cr is an exception, and the reason is unknown.

The growth procedure follows the VLS mechanism, and  $M_e$  acts as the nucleation point for GaN crystalline nuclei and plays an important role as catalyst during ammoniation process. Defect energies confinement theory can also be applied to explain the formation of GaN nanostructures.

#### 3.2 Catalyzed by $C_m$

We have been fabricated large-scale single-crystalline GaN nanowires with high-quality by RF magnetron sputtering method using MgO, TiO<sub>2</sub>, Al<sub>2</sub>O<sub>3</sub>, SiC, BN, and ZnO (short for  $C_m$ ) as intermediate layers. GaN can grow along preferred (002) planes catalyzed by Al<sub>2</sub>O<sub>3</sub> (10 nm), ZnO (20 nm), and TiO<sub>2</sub> (30 nm), which were fabricated at the optimal conditions. However, other samples can't grow along preferred (002) planes.

Pure and clear GaN nanostructures can be formed with ZnO, MgO, and BN as intermediate layers. GaN nanowires are formed with ZnO, and BN as intermediate layers, and nanobelts are formed with MgO, as intermediate layers. When the thickness of ZnO increases from 20

nm to 200 nm, the sample can turn from GaN nanowires to nanorods. The ammoniating temperatures can affect the morphology of the GaN samples deeply. Nanowires occur at 950 °C, nanorods exist at 1000 °C, nanobelts appear at 1050 °C.

The wavelengths (PL spectra data) could be shortened when oxidizing materials were used as intermediate layers, i.e., blue-shift, while when carbide and nitride were used as intermediate layers, the wavelengths could increase, i.e., red-shift.

### 3.3 Doped with Mg

Mg-doped GaN nanowires have been successfully grown on Si (111) substrates by magnetron sputtering through ammoniating Ga<sub>2</sub>O<sub>3</sub>/Mg thin films.

The aggregation of the defect energy is used to explain the growth mechanism of the GaN nanowires. Mg doping causes the distortion of the GaN cell and introduces more defects in the crystal cell so that the defect energy is added, which promotes the growth of the GaN nanowires. The growth mechanism mainly follows the VLS process, and the aggregation of the defect energy accelerates this growth of the GaN nanowires.

## 4. Acknowledgements

This project was supported by the Key Research Program of the National Natural Science Foundation of China (No.90201025) and the National Natural Science Foundation of China (No. 90301002). I also thank Prof. Cehngshan Xue for his great contribution to this project.

## 5. References

- Fasol, G. (1996). Room-Temperature Laser Diode Nitride Blue Gallium, *Science*, Vol. 272, No. 5269, (June 1996), pp. 1751-1752, ISBN 0036-8075
- Nakamura, S. (1998). The roles of structural imperfections in InGaN-Based blue light-emitting diodes and laser diodes, *Science*, Vol. 281, No. 5379, (August 1998), pp. 956-961, ISBN 0036-8075
- Morkoç, H.; Mohammad S.N. (1995). High-Luminosity Blue and Blue-Green Gallium Nitride Light-Emitting Diodes, *Science*, Vol. 267, No. 5194, (January 1995), pp. 51-55, ISBN 0036-8075
- Han, W.Q.; Fan, S.S.; Li, Q.Q. & Hu, Y.D. (1997). Synthesis of Gallium Nitride Nanorods Through a Carbon Nanotube-Confined Reaction, *Science*, Vol. 277, No. 5194, (August 1997), pp. 1287-1289, ISBN 0036-8075
- Lauhon, L.J.; Gudiksen, M.S.; Wang, D. & Lieber, C.M. (2002). Epitaxial core-shell and core-multishell nanowire heterostructures, *Nature*, Vol. 420, No. 6911, (November 2002), pp. 57-61, ISBN 0028-0836
- Ham, M.H.; Choi, J.H.; Hwang, W.; Park, C.; Lee, W.Y. & Myoung, J.M. (2006). Contact characteristics in GaN nanowire devices, *Nanotechnology*, Vol. 17, No. 9, (May 2006), pp. 2203-2206, ISBN 0957-4484
- Xu, B.S.; Zhai, L.Y.; Liang, J.; Ma, S.F.; Ja, H.S. & Liu, X.G. (2006). Synthesis and characterization of high purity GaN nanowires, *Journal of Crystal Growth*, Vol. 291, No. 1, (May 2006), pp. 34-39, ISBN 0022-0248

- He, M.; Minus, I.; Zhou, P.; Mohammed, S. N.; Halpern, J. B.; Jacobs, R.; Sarney, W. L.; Salamanca-Riba, L.; & Vispute, R. D. (2000). Growth of large-scale GaN nanowires and tubes by direct reaction of Ga with  $\text{NH}_3$ , *Applied Physics Letter*, Vol. 77, No.23, (December 2006), pp. 3731-3733, ISBN 0003-6951
- Xue, C.S.; Wei, Q.Q.; Sun, Z.C.; Dong, Z.H.; Sun, H.B. & Shi, L.W. (2004). Fabrication of GaN nanowires by ammoniating  $\text{Ga}_2\text{O}_3/\text{Al}_2\text{O}_3$  thin films deposited on Si(111) with radio frequency magnetron sputtering, *Nanotechnology*, Vol. 77, No.23, (July 2004), pp. 724-726, ISBN 0957-4484
- Li, J. Y.; Chen, X. L.; Qiao, Z.Y.; Cao, Y.G. & Lan, Y.C. (2000). Formation of GaN nanorods by a sublimation method, *Journal of Crystal Growth*, Vol. 213, No. 3-4, (June 2000), pp. 408-410, ISBN 0022-0248
- Shi, F.; Zhang, D.D. & C.S.Xue. (2010). Influence of Ammoniating Time on the Microstructure of Mg-Doped GaN Nanowires, *Materials Science and Engineerin: B*, Vol. 167, No. 1, (May 2010), pp. 80-84, ISBN 0921-5107
- Shi, F.; Li, H. & Xue, C.S. (2010). Fabrication of GaN nanowires and nanorods catalyzed with tantalum, *Journal of Materials Science: Materials in Electronics*, Vol. 21, No. 12, (December 2010), pp. 1249-1254, ISBN 0957-4522
- Perlin, P.; Jauberthie-Carillon, C.; Itie, J.P.; Miguel, A. S.; Grzegory, I. & Polian, A. (1992). Raman scattering and x-ray-absorption spectroscopy in gallium nitride under high pressure, *Physical Review B*, Vol. 45, No. 1, (January 1992), pp.83-89, ISBN 0163-1829
- Monemar, B. (1974). Fundamental energy gap of GaN from photoluminescence excitation spectra, *Physical Review B*, Vol. B10, No. 1, (July 1974), pp. 676-681, ISBN 1098-0121
- Yang, Y.G.; Ma, H.L.; Xue C.S., Zhuang, H.Z.; Hao, X.T.; Ma, J. & Teng, S.Y. (2002). Preparation and structural properties for GaN films grown on Si (111) by annealing, *Applied Surface Science*, Vol. 193, No. 1-4, (June 2002), pp. 254-260, ISBN 0169-4332
- Ai, Y.J.; Xue, C.S.; Sun, C.W.; Sun, L.L.; Zhuang, H.Z.; Wang, F.X.; Li, H. & Chen, J.H. (2007). Synthesis of GaN nanowires through  $\text{Ga}_2\text{O}_3$  films' reaction with ammonia, *Materials Letter*, Vol. 61, No. 13, (May 2007), pp. 2833-2836, ISBN 0167-577X
- Sun, Y.; Miyasato, T. S. & Nobuo. (1998). Outdiffusion of the excess carbon in SiC films into Si substrate during film growth, *Journal of Applied Physics*, Vol. 84, No. 11, (December 1998), pp. 6451-6453, ISBN 0021-8979
- Demichelis, F.; Crovini, G.; Pirri, C.F.; Tressoa, E.; Amatob, G.; Cosciac, U.; Ambrosonec, G. & Ravad, P. (1994). Optimization of a-Si<sub>1-x</sub>C<sub>x</sub>: H films prepared by ultrahigh vacuum plasma enhanced chemical vapour deposition for electroluminescent devices, *Thin Solid Films*, Vol. 241, No. 1-2, (April 1994), pp. 274-277 , ISBN 0040-6090
- Wei, Q.Q.; Xue, C.S.; Sun, Z.C.; Cao, W.T.; & Zhuang, H.Z. (2005). Formation of GaN Film by Ammoniating  $\text{Ga}_2\text{O}_3/\text{Al}_2\text{O}_3$  Deposited on Si(111) Substrate, *Rare Metal Materials and Engineering*, Vol. 34, No.2, (February 1994), pp. 312-315, ISBN 1002-185X

- Elkashaf, N.; Srinivasa, R.S.; Major, S. Sabharwal, S. C. & Muthec, K. P. (1998). Sputter deposition of gallium nitride films using a GaAs target, *Thin Solid Films*, Vol. 333, No.1-2, (November 1998), pp. 9-12, ISBN 0040-6090
- Kingsley, C.R.; Whitaker, T.J.; Wee, A.T.S.; Jackman, R. B. & Foord, J. S. (1995). Development of chemical beam epitaxy for the deposition of gallium nitride, *Materials Science and Engineering B*, Vol. 29, No.1-3, (January 1995) , pp. 78-82, ISBN 0921-5107
- Sasaki, T. & Matsuoka, T. (1988). Substrate-polarity dependence of metal-organic vapor-phase epitaxy-grown GaN on SiC, *Journal of Applied Physics*, Vol. 64, No.9, (November 1988), pp. 4531-4535, ISBN 0021-8979
- Ishikawa, H.; Kobayashi, S.; Koide, Y.; Yamasaki,S.; Nagai, S.; Umezaki, J.; Koike, M.; & Murakami,M. (1997). Effects of surface treatments and metal work functions on electrical properties at *p*-GaN/metal interfaces, *Journal of Applied Physics*, Vol. 81, No.3, (February 1997), pp. 1315-1322, ISBN 0021-8979
- Li, D.; Sumiya, M.; Fuke, S. Yang, D.R.; Que, D.L.; Suzuki, Y. & Fukuda, Y. (2001). Selective etching of GaN polar surface in potassium hydroxide solution studied by x-ray photoelectron spectroscopy, *Journal of Applied Physics*, Vol. 90, No.8, (October 2001), pp. 4219-4223, ISBN 0021-8979
- Veal, T. D.; Mahboob, I.; Piper, L.F.J.; McConville, C. F. & Hopkinson, M. (2004). Core-level photoemission spectroscopy of nitrogen bonding in GaNAs alloys, *Applied Physics Letters*, Vol. 85, No.9, (August 2004),pp.1550-1552, ISBN 0003-6951
- King, S.W.; Carlson, E.P.; Therrien, R.J. Christman, J.A.; Nemanich, R. J. & Davis, R.F. (1999). X-ray photoelectron spectroscopy analysis of GaN/(0001) AlN and AlN/(0001) GaN growth mechanisms, *Journal of Applied Physics*, Vol. 86, No.10, (November 1999), pp. 5584-5593, ISBN 0021-8979
- Amanullah, F.M.; Pratap, K.J. & Hari, V.B. (1998). Compositional analysis and depth profile studies on undoped and doped tin oxide films prepared by spray technique, *Materials Science and Engineering B*, Vol. 52, No.2-3, (April 1998), pp.93-98, ISBN 0921-5107
- Xiao, H.D.; Ma, H.L.; Xue, C.S.; Hu, W.R.; Ma, J.; Zong, F.J.; Zhang, X.J. & Ji, F. (2005). Synthesis and structural properties of GaN particles from GaO<sub>2</sub>H powders, *Diamond and Related Materials*, Vol.14, No.10, (October 2005), pp.1730-1734, ISBN 0925-9635
- Bae, S.Y.; Seo, H.W.; Park,J.; Yang, H. & Kim, B. (2003). Porous GaN nanowires synthesized using thermal chemical vapor deposition, *Chemical Physics Letters*, Vol. 376, No.3-4, (July 2003), pp.445-451, ISBN 0009-2614
- Schlager, J.B.; Sanford N.A.; Bertness, K. A.; Barker, J. M.; Roshko, A. & Blanchard, P. T. (2006). Polarization-resolved photoluminescence study of individual GaN nanowires grown by catalyst-free molecular beam epitaxy, *Applied Physics Letters*, Vol. 88, No.21, (May 2006), pp.213106-213108, ISBN 0003-6951
- Chen, C.C.; Yeh, C.C.; Chen, C.H.; Yu, M.Y.; Liu, H.L.; Chen, K.H.; Chen, L.C.; Peng, J.Y. & Chen, Y.F. (2001). Catalytic Growth and Characterization of Gallium Nitride Nanowires, *Journal of the American Chemical Society*, Vol.123, No. 12, (February 2001), pp.2791-2798, ISBN 0161-4940

- Liu, H.L.; Chen, C.C.; Chia, C.T.; Yeh, C.C.; Chen, C.H.; Yu, M.Y.; Keller, S. & Nbaars, S. (2001). Infrared and Raman-scattering studies in single-crystalline GaN nanowires; *Chemical Physics Letters*, Vol.345, No.3-4, (September 2001), pp.245-251, ISBN 0009-2614
- Sun, Y.L.; Zhang, X.B.; Ning, Y.S.; Kong, F.Z. & Liu, F. (2002), CVD Method to Synthesize Carbon Nanotubes on a Large Scale, *Journal of Inorganic Materials*, Vol.17, No.2, (April 2002), pp.337-342, ISBN 1000-324X
- Wang, M.X.; Yang, L. & Wang, C.M.; (2004). Synthesis of One-Dimensional GaN Nanowires by Ammoniating, *Rare Metal Materials and Engineering*, Vol.33, No.6, (December 2004), pp.670-672, ISBN 1002-185X
- Ohno, Y.; Shirahama, T.; Takeda, S.; Ishizumi, A. & Kanemitsu, Y. (2005), Fe-catalytic growth of ZnSe nanowires on a ZnSe (001) surface at low temperatures by molecular-beam epitaxy, *Applied Physics Letters*, Vol. 87, No.4, (July 2005), pp. 043105-043107, ISBN 0003-6951
- Shi, F.; Wang, Z.P. & Xue, C.S. (2010). Synthesis and Characterization of GaN Nanowires through Ammoniating Ga<sub>2</sub>O<sub>3</sub>/Cr Thin Films Deposited on Si(111) Substrates, *Applied Surface Science*, Vol.256, No.16, (June 2010), pp.4483-4487, ISBN 0169-4332
- Tang, C.C.; Fan, S.S.; Dang, H.Y. ; Li, P. & Liu, Y. M.; (2000). Simple and high-yield method for synthesizing single-crystal GaN nanowires, *Applied Physics Letters*, Vol. 77, No.13, (September 2000), pp. 1961-1963, ISBN 0003-6951
- Xue, C.S.; Wu, Y.X.; Zhuang, H.Z.; Tian, D.H.; Liu, Y.-A.; Zhang, X.K., Ai, Y.J., Sun, L.L. & Wang, F.X. (2005). Growth and characterization of high-quality GaN nanowires by ammonification technique, *Physica E*, Vol. 30, No. 1-2, (December 2005), pp.179-181, ISBN 1386-9477
- Shi, F., Zhang, D.D. Xue, C.S. (2010). Influence of Ammoniating Time on the Microstructure of Mg-Doped GaN Nanowires, *Materials Science and Engineering B*, Vol.167, No.2, (May 2010), pp.80-84, ISBN 0921-5107
- Zhang, D.D.; Xue, C.S.; Zhuang, H.Z., Sun, H.B., Cao, Y.P., Huang, Y.L., Wang, Z.P. & Wang, Y. (2009). Influence of Mg Doping on GaN Nanowires, *Chemphyschem*, Vol.10, No.3, (February 2009), pp571-575, ISBN 1439-4235
- Choi, W.F.; Song, T.Y. & Tan, L.S. (1998), Infrared and X-ray photoelectron studies of as-prepared and furnace-annealed radio-frequency sputtered amorphous silicon carbide films, *Journal of Applied Physics*, Vol. 83, No.9, (May 1998), pp. 4968-4973, ISBN 0021-8979
- Shi F., Zhang, D.D. & Xue, C.S. (2011). Effect of ammoniating temperature on microstructure and optical properties of one-dimensional GaN nanowires doped with magnesium, *Journal of Alloys and Compounds*, Vol. 509, No.4, (January 2011), pp.1294-1300, ISBN 0925-8388
- Zhou, S.M.; Zhang, X.H.; Meng, X.M.; Zou, K.; Fan, X.; Wu, S.K. & Lee, S.T. (2004). The fabrication and optical properties of highly crystalline ultra-long Cu-doped ZnO nanowires, *Nanotechnology*, Vol. 15, No.9, (September 2004), pp.1152-1155, ISBN 0957-4484

Zolper, J.C.; Crawford, M.H.; Howard, A.J.; Ramer, J. & Hersee S.D. (1996). Morphology and photoluminescence improvements from high-temperature rapid thermal annealing of GaN, *Applied Physics Letters*, Vol. 68, No.2, (September 2000), pp. 200-202, ISBN 0003-6951

# Fabrication, Characterization and Thermal Properties of Nanowires

Yang-Yuan Chen, Cheng-Lung Chen, Ping-Chung Lee and Min-Nan Ou  
*Institute of Physics, Academia Sinica,  
Taiwan*

## 1. Introduction

The physical properties of nanomaterials are novel and completely different from those in conventional bulk materials. The new discovered properties of nanomaterials not only reflected in electronic transports but also exhibited in optics and magnetism. For past decades, intensive and broad studies on nanoscience and nanotechnology were initialized all over the world. Nanoparticles (or quantum dots) are the first candidate of nanomaterials for such a study. In past the most important findings in nanoparticles are phonon softening, electronic energy level splitting and red shift etc. However due to their small size and dispersed characteristic, only few limited applications have been developed, the examples are the quantum dots in matrix for opto-electronics, dispersed nanoparticles for drug carries and thermal therapy of cancers etc. For above reasons, the study of nanowires (NWs) stimulates a great interest in their fundamental scientific researches and potential applications. The size effects, in general, have two aspects: one is the Quantum Size Effect (QSE), which originates from the variation of electronic density-of-states in nanostructure. QSE can thus derive a drastic change of transport and thermodynamic properties from those of the bulks. In contrast to Quantum Size Effect (QSE), the physical properties changed due to vast surface atoms, grain boundaries and structural deficiency are categorized to Non-Quantum Size Effect (NQSE), with no doubt this also inevitably plays an important role in the novel properties of nanowires. For examples, thermal and electrical conductivity of nanowires are significantly reduced as a result of electron/phonon scatterings occurring at grain boundaries of nanoscale crystallization. One of the most important characteristics of nanowire is its substantial small thermal conductivity. Thus, from manipulated materials to low-dimensional nanowires, it provides an innovative strategy to improve heat-electricity conversion efficiency for thermoelectric materials.

In the content of this chapter, two main sections will be included, the first section is the fabrication and characterization of nanowires, and the second section is the measurement techniques and setups for Seebeck coefficient, electrical conductivity and thermal conductivity.

For nanowire fabrication, two categories of fabrication method will be included. The first category is called the Bottom-up method, in which the nanowires were formed self-assembly. The second category of nanowire fabrication is the Top-down method, in which many patterning and etching processes are required for forming individual nanowires.

After nanowires are fabricated, the details of morphology, microstructures and crystallization of nanowires will be characterized and analyzed by various instruments such as scanning electron microscope (SEM), transmission electron microscope (TEM), X-ray diffraction (XRD) and energy dispersive X-ray (EDX).

At the end of this chapter, the introduction to techniques of physical property measurements for Seebeck coefficient, electrical conductivity and thermal conductivity on either nanowires array or a single nanowire will be described thoroughly. Several examples mentioned in this chapter are related to thermoelectric nanowires, the reason is that manipulating and optimizing the thermoelectric properties for sustainable energy applications has become a main stream of nanowire researches. Thermoelectric materials (TE) can be used either as a power generator based on the Seebeck effect, or a thermocooler based on the Peltier effect. The efficiency of a thermoelectric material is evaluated by its dimensionless figure of merit,  $ZT = \sigma S^2 T / \kappa$ , where  $T$ ,  $S$ ,  $\sigma$ , and  $\kappa$  are respectively the absolute temperature, Seebeck coefficient, electrical conductivity, and thermal conductivity (Rowe, 1995). Accordingly, the low thermal conductivity is a crucial factor for a material being a superior TE material. In the past few decades, bismuth telluride,  $\text{Bi}_2\text{Te}_3$ , has been recognized as the best TE material with  $ZT \sim 1$  near 300 K (Tritt, 1999). However, to fit in future applications, further enhancement of  $ZT$  is essential for the next generation TE materials. In this respect, reduction of dimensionality is a seemingly viable approach. For example, size-dependent behavior on thermal transport in nanowires has been studied by Li and his co-workers (Li et al., 2003). They found that the thermal conductivity of nanowires is much lower than the bulk value, and suggested that heat conduction in confined systems seems to be greatly influenced by phonon-boundary scattering. The same principle also works on  $\text{Bi}_2\text{Te}_3/\text{Sb}_2\text{Te}_3$  superlattice thin films reported by Venkatasubramanian et al (Venkatasubramanian et al., 2001). Such phonon-blocking and electron-transmitting phenomena are indeed helpful in enhancing  $ZT$ . Much higher values were even predicted theoretically by Hicks and Dresselhaus for nanowires, based on the change of electronic density-of-states and increased phonon surface scattering (Hicks & Dresselhaus, 1993).

## 2. Fabrications and characterizations of nanowires

In general, nanowire fabrication methods can be categorized to two types. The first one is called the Bottom-up method, in which the nanowires are formed by self-assembly (Self-Assembly Method, SAM). The nanowires grown in the nano-porous template of anodic alumina oxide (AAO) by chemical electrodeposition are belonged to this category. Another method of nanowire fabrication, which is very similar to chemical vapor deposition, will also be introduced. By this method nanowires can be grown from deposited film through thermal annealing based on the stress generated from thermal expansion mismatching between the film and its substrate. The second category of nanowire fabrication is named the Top-down method. This method involves a lot of patterning and etching processes such as Optical Lithography (OL), Electron Beam Lithography (EBL), and etching techniques. Nanowires of Bi,  $\text{Bi}_2\text{Te}_3$ , and  $\text{Sb}_2\text{Te}_3$  fabricated by this method will be illustrated. The control parameters of the growing conditions for the composition, size (or diameter) and crystallization of nanowires will also be involved. After the section of nanowire fabrication, the details of morphology, microstructures and crystallization of nanowires characterized by SEM, TEM, XRD and EDX will be followed.

## 2.1 Electrodeposition techniques and Anodic Alumina oxide (AAO) for the fabrication of Fe, Ni, Bi<sub>2</sub>Te<sub>3</sub>, and Sb<sub>2</sub>Te<sub>3</sub> nanowires

### Preparation of Anodic Alumina oxide (AAO)

Electrodeposition is an economic processing for depositing thin films and nanostructures due to its low-cost setup, high-yield production, and low energy consumption. Its capability for generating multifarious and high aspect ratio features is another advantage. So far, the method has been widely applied in the microelectronic industry for interconnects and magnetic storage (Andricacos et al., 1998; Osaka, 1999). Furthermore, the electrodeposition of metallic or semiconducting materials into nanoporous membranes such as AAO is considered as a conceptually simple and alternative way to fabricate nanowires, as shown in Fig. 1. In contrast to other deposition methods like thermal evaporation or chemical vapor deposition, the growth of nanowires in this technique can start from the pore bottom and continues in the pore direction to form nanowires array and is rather promising in various device applications. The following sections simply review the preparations and characterizations of magnetic and thermoelectric nanowires.

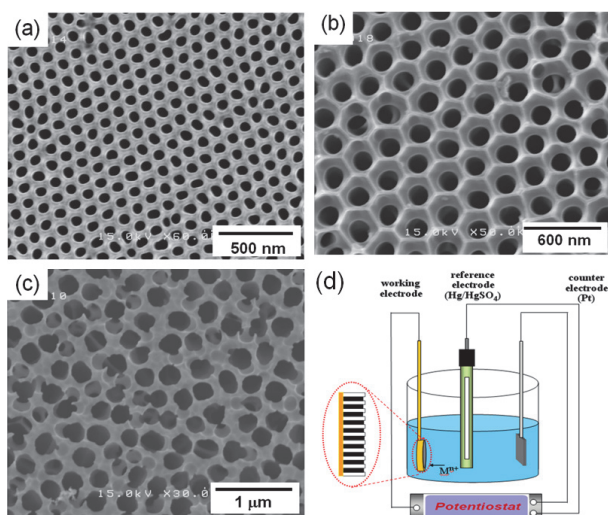


Fig. 1. Scanning electron micrographs of AAO templates with different pore sizes of approximately: (a) 60 nm, (b) 120 nm, (Reproduced with permission from Chen C. L. et al., *J. Phys. Chem. C*, 114, 3385-3389. Copyright ©2010 from American Chemical Society), (c) 200 nm, (d) The schematic arrangement of experimental electrodeposition setup. The deposition process is carried out in a conventional three-electrode cell with a saturated calomel electrode as the reference and a platinum sheet as the counter electrode. The AAO is attached to the working negative electrode for filling the chosen material through electrodeposition.

### Fabrication of Fe and Ni nanowires in AAO templates

Nanostructured ferromagnetic materials are of interest in either theoretical studies or practical applications due to their anisotropic magnetism and magnetoresistance. These unique properties have great potential applications for high density magnetic storage

media, high sensitivity magnetic sensor and biologic technology (Liu et al., 1995; Reich et al., 2003). For example, perpendicular magnetic recording (PMR) of nanowires array could overcome the thermal instability limitation of superparamagnetism. Modern magnetic storage devices made by these materials can have bit densities in excess of 100 Gbit/in<sup>2</sup> (Weller & Moser, 1999). In preparation of Fe nanowires array, iron can be potentiostatically electrodeposited into a porous membrane by applying a voltage of -1.2 V, and the electrolyte solution consisting of FeSO<sub>4</sub> · 7H<sub>2</sub>O (0.43 M) and boric acid (0.72 M) with pH~3 at room temperature (Ou et al., 2009). After the deposition, a mechanical polishing process was carried out to remove the overgrown thick iron layer on the top surface of AAO. The shiny surface on the top of iron nanowires array indicates that the oxidation of the materials is negligible. Subsequently, an electrodeposition of gold is performed to form a thin layer on the surface of the nanowire arrays to protect NWs from oxidation and serves as the contact electrode for electrical resistivity measurement. Fig. 2 shows the X-ray diffraction, morphologies, and structures of iron-filled nanowires array (Ou et al., 2009). The diffraction peaks of deposited films and 200 nm- nanowires array can be identified to be the (110), (200), and (211) planes of  $\alpha$ -Fe; whereas 60 nm- Fe nanowires array shows a strong preferred orientation along the [110].

Besides the finite growth space has an obvious influence on the crystalline structures of nanowires, the magnetic properties of Fe nanowires array also greatly depend on the diameter of nanowires. The hysteresis loops for the Fe nanowires array with different sizes at 300 K are shown in Fig. 3. It is clear that 60 nm- Fe nanowire array shows a relatively strong hysteresis and anisotropic behavior than that of 200 nm- nanowires array. This intriguing feature can be attributed to the fact that the magnetic easy axis is along the longitudinal direction of nanowires, and which probably derives from the line shape anisotropy in nanowires.

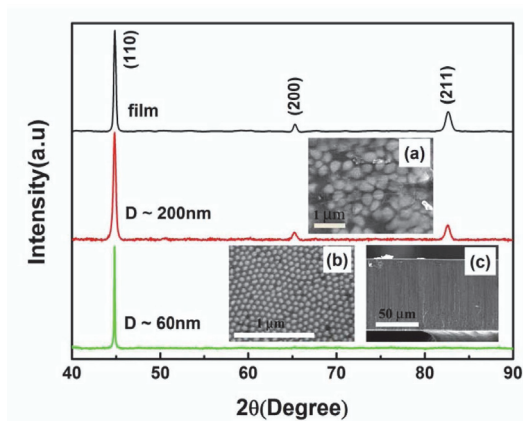


Fig. 2. X-ray diffraction patterns of the electrodeposited film, 200 nm-, and 60 nm- nanowires array. Insets (a) and (b) are the top views of the 200 nm- and 60 nm- nanowires, respectively. In these two images, white spots represent the alpha-Fe phase nanowires embedded in the template. (c) Side view of the home-made empty template (Reproduced with permission from Ou M. N. et al., *Chin. J. Phys.*, 47, 848-853. Copyright ©2009 from PSROC).

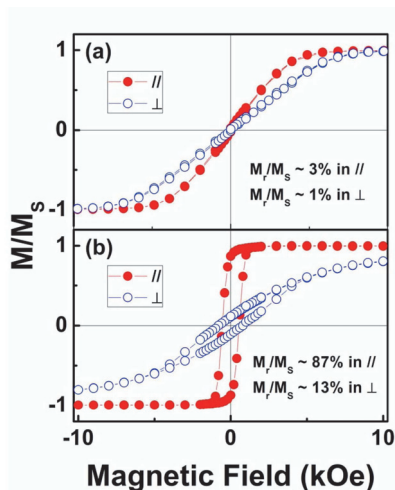


Fig. 3. Hysteresis loops of the Fe nanowires array with applied magnetic field parallel ( $\parallel$ ) and perpendicular ( $\perp$ ) to the longitudinal axis of the nanowires array: (a) 200 nm- and (b) 60 nm- NWs. The coercive fields in the easy axis are  $\sim 100$  Oe and  $\sim 600$  Oe for the 200 nm- and 60 nm- NWs, respectively. The ratios of the remanence ( $M_r$ ) to the saturation magnetization ( $M_s$ ) for different orientations are also presented. (Reproduced with permission from Ou M. N. et al., *Chin. J. Phys.*, 47, 848-853. Copyright ©2009 from PSROC).

#### *Fabrication of $\text{Bi}_2\text{Te}_3$ and $\text{Sb}_2\text{Te}_3$ nanowires in AAO templates*

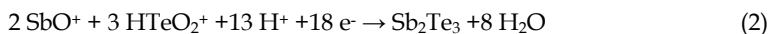
$\text{Bi}_2\text{Te}_3$  is a narrow band gap semiconductor with an energy band gap of about 0.18 eV at 300K, and which can be either n- or p-type depending on the doping (Rowe, 1995). The electrodeposition of  $\text{Bi}_2\text{Te}_3$  nanowires is mostly performed in nitric acid baths. The deposited crystal structures and their correlating compositions are highly dependent on the deposition potential, temperature, and the electrolyte concentration (Michel et al., 2006). In this respect, Martin-Gonzalez et al. proposed a Pourbaix-type diagram for the electrodeposition of Bi, Te, and their related deposits, and showed the thermodynamic stability of the dominant species as a function of pH value and potentials (Martin-Gonzalez et al., 2002). As the deposited potential is altered to more negative value, Bi-rich deposits are obtained. Detailed investigations on the cyclic voltammetry of Bi, Te, and Bi/Te dissolved in 1 M  $\text{HNO}_3$  revealed two different underlying processes. First process involves the reduction of  $\text{HTeO}_2^+$  to  $\text{Te}^0$  and forming  $\text{Bi}_2\text{Te}_3$  through a subsequent interaction between  $\text{Bi}^{3+}$  and reduced  $\text{Te}^0$ . The second process occurring at more negative reduction potentials involves reduction of  $\text{HTeO}_2^+$  to  $\text{H}_2\text{Te}$  followed by the chemical interaction with  $\text{Bi}^{3+}$ . The crystalline  $\text{Bi}_2\text{Te}_3$  probably resulted from these two processes. This work indeed offers insights into the deposited mechanism of  $\text{Bi}_2\text{Te}_3$ . The overall chemical reaction can be described as:



According to the above conclusions, a series of  $\text{Bi}_2\text{Te}_3$  nanowires were electrodeposited potentiostatically at -150 mV by filling nanoporous membrane in 1 M  $\text{HNO}_3$  solution containing different Bi/ Te ratio to find the optimal deposition condition (Chen et al., 2010). These deposits were thus characterized by measuring their corresponding Seebeck

coefficients. Interestingly, all nanowires were *n*-type, and the optimal condition is about 0.008 M [Bi<sup>3+</sup>] and 0.014 M [HTeO<sub>2</sub><sup>+</sup>], corresponding to 65 μV/K. Once deviated from this electrolyte concentration, the measured Seebeck coefficients of the nanowires decrease to very small values. This event is understandable from the plot of Seebeck coefficient versus composition percentage for bulk Bi<sub>2</sub>Te<sub>3</sub> (Rowe, 1995). Therefore, this parameter was selected for the preparation of Bi<sub>2</sub>Te<sub>3</sub> nanowires. Through filling different sizes of template, the Bi<sub>2</sub>Te<sub>3</sub> nanowires array with different diameter were fabricated, shown in Fig. 4. The filling ratio of these templates is higher than 80 %, and comparable to the best samples of this kind ever reported (Borca-Tasciuc et al., 2004). Judging from EDX analysis, only elements present in these nanowires are Bi and Te – in the ratio of 0.37 ± 0.02/ 0.63 ± 0.03 corresponding to Te-rich *n*-type Bi<sub>2</sub>Te<sub>3</sub>. Extra Te may be situated as substitution to Bi sites or at interstitial sites. They may also be in grain boundaries, but not enough to be observed in XRD as impurity phase (Chen et al., 2010). Meanwhile, all the XRD patterns of these nanowires array can be indexed to rhombohedral structure, and confirming their single-phase purity. The strong (110) peak also suggests that the wires are highly textured in the [110] direction. This conclusion can be verified by the high-resolution transmission electron microscopy (HRTEM) result, shown in Fig. 5(b). In our experience, although annealing process can lower electrical resistivity of as-prepared film as expected, the annealing-induced thermal shock seems to have critical influence on the continuity of nanowires and leads to extremely high electrical resistance in nanowires embedded in AAO.

As for antimony telluride (Sb<sub>2</sub>Te<sub>3</sub>), it has the same crystal structure as Bi<sub>2</sub>Te<sub>3</sub> with Sb atoms occupying Bi lattice sites. However, only a few efforts have been conducted on the electrodeposition of Sb<sub>2</sub>Te<sub>3</sub> films and nanowires due to obstacles in the preparations of electrolytes. Recently, some limited studies have been reported. For example, Leimkuhler *et al.* developed an electroplating process for Sb<sub>2</sub>Te<sub>3</sub> thin films on an indium tin oxide (ITO) substrate from an acid solution containing SbO<sup>+</sup> and HTeO<sub>2</sub><sup>+</sup> ions. In their investigations, the pH value, bath temperature, deposited potential, and composition ratio of the electrolyte significantly influenced the crystal structure and morphology of the film (Leimkuhler et al., 2002). Through controlling Sb/Te ratio in the electrolyte, the deposit composition could be adjusted to stoichiometry. Later, Jin et al. used a simple direct current electrodeposition process to synthesize Sb<sub>2</sub>Te<sub>3</sub> nanowire array embedded in alumina templates (Jin et al., 2005). These conclusions demonstrate the possibility in electrodepositing Sb<sub>2</sub>Te<sub>3</sub> films and nanowires; however, there is a lack of systematic studies for characterizing the physical properties of the deposits. According to the above conclusions, Sb<sub>2</sub>Te<sub>3</sub> films were electrodeposited potentiostatically at -500 mV onto an ITO glass substrate from 1 M HNO<sub>3</sub> solution containing different Sb/Te ratios (at 5~8 °C). In order to obtain well dissolved SbCl<sub>3</sub> in aqueous solution, 0.3 M of sodium citrate/ citric acid are suggested, which acting as complexing agents for Sb(III) ions (Huang et al., 2008). A conventional three-electrode cell was used for potentiostatic electrodeposition at room temperature. A platinum sheet was used as the counter electrode and a saturated calomel electrode (SCE) as reference. The working electrode is an ITO substrate, for the growth of films. In such condition, Sb and Te were in the form of SbO<sup>+</sup> and HTeO<sub>2</sub><sup>+</sup>, respectively. The chemical reaction of these cations is described as (Leimkuhler et al., 2002):



With regard to the growth of Sb<sub>2</sub>Te<sub>3</sub> nanowires, the working electrode was changed to AAO template, on which the evaporated gold/chromium (3000 Å/100 Å thick) film served as the

conducting layer. The nanowire arrays were synthesized via filling the AAO template under similar growth condition. Since the crystallization temperature of  $\text{Sb}_2\text{Te}_3$  is slightly above room temperature (Huang et al., 2008; Baily & Emin, 2006), it is easy to prepare crystallized near stoichiometric  $\text{Sb}_2\text{Te}_3$  nanowires by post-annealing treatment at 500 K in high vacuum ( $2 \times 10^{-6}$  torr) for several hours. Figs. 6(b) and (e) are mechanically polished top view of AAO templates after being deposited with  $\text{Sb}_2\text{Te}_3$ . Obviously, the filling ratio can be higher than 80 %, and the elements present in the nanowires are Sb and Te— in the ratio of  $0.39 \pm 0.02 / 0.61 \pm 0.03$ , corresponding to nearly stoichiometric  $\text{Sb}_2\text{Te}_3$ . The TEM images of 60 nm-  $\text{Sb}_2\text{Te}_3$  nanowire are given in Figs. 5(c) and (d). From Fig. 6(g), most XRD peaks of these nanowires can be indexed to rhombohedral structure (standard ICCD PDF card 71-0393); however, the peak marked with an asterisk is indexed to a  $\text{Sb}_{0.405}\text{Te}_{0.595}$  structure (monoclinic, ICCD PDF card 45-1229). That means the crystal structures of the prepared nanowires probably contained two phases: rhombohedral and monoclinic.

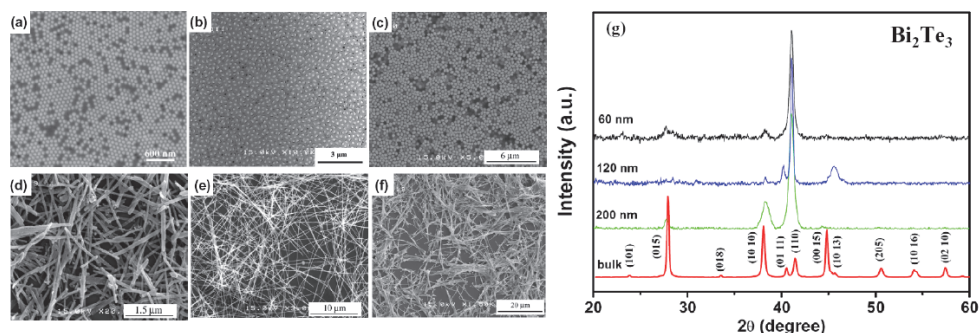


Fig. 4. SEM micrographs and XRD patterns of  $\text{Bi}_2\text{Te}_3$  nanowires array. Surface view: (a) 60 nm, (b) 120 nm, (c) 200 nm. Separated nanowires after AAO being dissolved: (d) 60 nm, (e) 120 nm, (e) 200 nm. (g) XRD patterns of  $\text{Bi}_2\text{Te}_3$  bulk, and as-prepared nanowire array of different diameters (60, 120, and 200 nm). (Reproduced with permission from Chen C. L. et al., *J. Phys. Chem. C*, 114, 3385-3389. Copyright ©2010 from American Chemical Society).

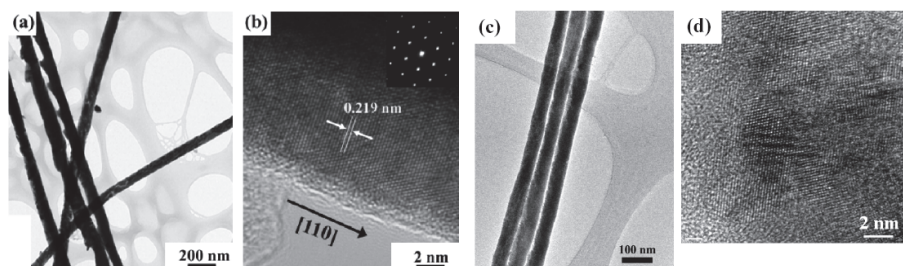


Fig. 5. TEM images of  $\text{Bi}_2\text{Te}_3$  and  $\text{Sb}_2\text{Te}_3$  nanowires. (a) The uniform profile of  $\text{Bi}_2\text{Te}_3$  nanowires with a diameter of 120 nm. (b) HRTEM image of a single  $\text{Bi}_2\text{Te}_3$  nanowire. Inset: Diffraction patterns of a selected area. (c) TEM images of  $\text{Sb}_2\text{Te}_3$  nanowires with a diameter of 60 nm. (d) High resolution image of a single  $\text{Sb}_2\text{Te}_3$  nanowire. (Reproduced with permission from Chen C. L. et al., *J. Phys. Chem. C*, 114, 3385-3389. Copyright ©2010 from American Chemical Society).

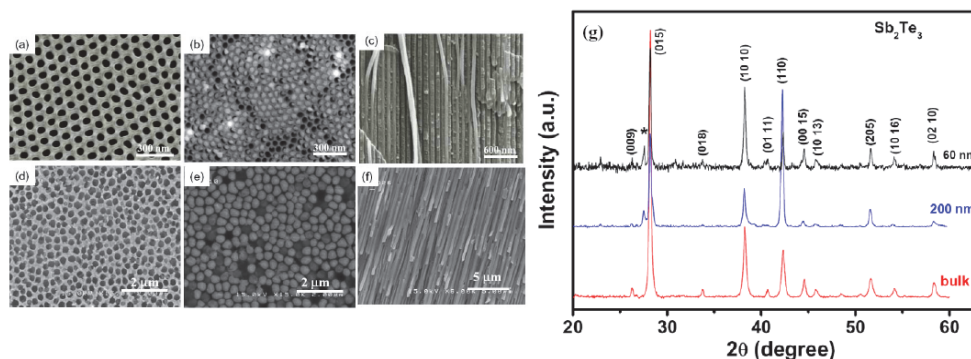


Fig. 6. SEM micrographs and XRD patterns of  $\text{Sb}_2\text{Te}_3$  nanowires array. Top view images: (a) to (c)  $d \sim 60$  nm; (d) to (f)  $d \sim 200$  nm. Figures (c) and (f) are cross-sectional views, and the others are surface views. (g) XRD patterns for  $\text{Sb}_2\text{Te}_3$  bulk and nanowires array of different diameters. The peak marked with an asterisk is indexed to a  $\text{Sb}_{0.405}\text{Te}_{0.595}$  structure (monoclinic, ICDD PDF card 45-1229).

## 2.2 Fabrication of Bi, $\text{Bi}_2\text{Te}_3$ nanowires by stress-induced method

More recently, Shim and Ham *et al.* (Shim *et al.*, 2009; Ham *et al.*, 2009) proposed the fabrication of single crystalline Bi and  $\text{Bi}_2\text{Te}_3$  NWs based on a mechanism in which the mismatch of the thermal expansion between the substrate and the film can drive the mass flow along grain boundaries to grow nanowires during thermal annealing temperature. Such growth process of nanowires is a kind of releasing the compressive stress by means of atomic diffusion. Although the inspiration of this interesting growth idea of the author comes from the formation of whiskers or hillocks in metal films (Au, Sn, Zn, In) in electronic packaging process, in fact this mechanism is entirely different from the above (Tu, 1996). In a typical procedure, the chosen material is initially deposited onto a thermally oxidized silicon substrate. Then the film is heated up to optimal annealing temperature, for example, 270 °C for Bi, and 350 °C for  $\text{Bi}_2\text{Te}_3$ . The length of nanowire is proportional to the annealing time, and the diameter of the wire is tunable by controlling the mean grain size of the deposited film. In the case of Bi nanowires, the nanowires were found to grow along the [001] direction, and was defect-free, single crystalline. The relationship between growth direction of nanowires and orientations of grains in the film is not clear. Interestingly, the  $\text{Bi}_2\text{Te}_3$  nanowires can be also grown by the same mechanism to exhibit single crystallinity with growth direction along [110], and the chemical composition of the nanowire is close to stoichiometry. To further understand the thermoelectric properties of nanowires prepared by following method, we have followed the same growth mechanism to prepare  $\text{Bi}_2\text{Te}_3$  nanowires, and successfully obtained the single crystalline nanowires, shown in Fig. 7. The detailed electrical and thermoelectric properties will be discussed in the next section. The development of this method definitely provides researchers an alternative route to prepare nanowires, and also promotes the application possibility by utilizing Bi and  $\text{Bi}_2\text{Te}_3$  nanowires in thermoelectric devices.

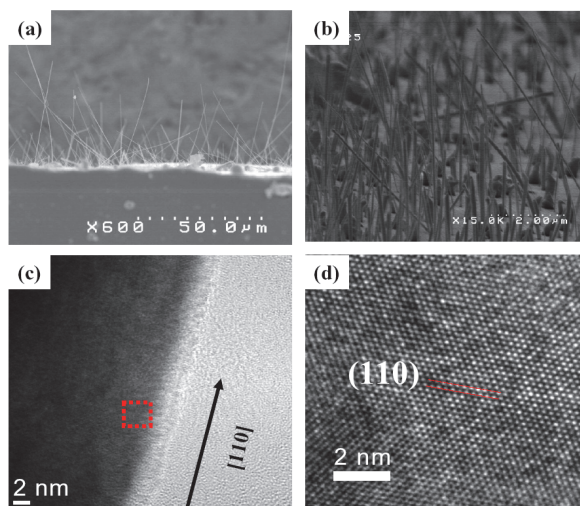


Fig. 7. SEM and TEM images of the prepared  $\text{Bi}_2\text{Te}_3$  nanowires. (a) The side view image clearly shows that all nanowires grow from the surface of the deposited film. (b) The image reveals very dense and uniform nanowires with several micrometers in length. (c) A low-magnification TEM image of a  $\text{Bi}_2\text{Te}_3$  nanowire, and (d) A HRTEM image taken from selected area marked in (c) of the  $\text{Bi}_2\text{Te}_3$  nanowire indicates that the growth direction of the nanowire is [110].

### 2.3 Fabrication of individual nanowires of Ni, $\text{Bi}_2\text{Te}_3$ and $\text{Sb}_2\text{Te}_3$ using lithographically patterned method

#### *Lithography*

In general, the lithography is a series of processes of photoresist coating, e-beam writing or mask-light exposure and photoresist removing. The series of progresses can be repeated many times and depend on the complexity of the pattern designed. We defined a pattern by transfer a predesigned pattern with an energetic source in a moveable photoresist layer, then remove the useless parts of the pattern by various etching techniques. Typically, the energetic source can be a light beam or electron beam, which used to transfer predesigned patterns by either projecting or masking to define a two-dimensional shape for devices over an entire surface simultaneously. The pattern formed by this method is named optical or electron-beam lithography that is up to the kind of beam source adapted. The remaining parts of photoresist would be a protecting layer for etching process.

#### *Optical lithography (OL) and Electron Beam Lithography (EBL)*

Optical lithography is also called Photolithography is a process to remove parts of a thin film. Usually, it applies ultraviolet light to transfer a pattern from a mask to a light-sensitive photoresist on the substrate. The processes are consisting of wafer cleaning, baking, exposure and development. The schematic steps are shown in figure 8 for a typical pattern on a silicon substrate. After Si substrate is cleaned, a uniform metal layer is deposited on it, and followed by a subsequent photoresist coating. Only the selected parts defined by a patterned mask are exposed to illumination of ultraviolet light, the photoresist exposed to

illumination can be easily removed in developer bath. In principle, the resolution can be increased by using shorter wavelengths such as X-ray. Instead of light illumination, electron beam can be used for electron resist, like PMMA (poly-methyl metacrylate). For positive resist, the electron beam breaks the bonds between the monomers with increased solubility results. For negative photoresist, on the other hand, the electron beam generates inter-chain cross linking and decreases its solubility. For EBL, a focused electron beam is scanned in a predefined pattern. In contrast to optical lithography one time exposure of illumination, this is a much slower process. However the structure with size resolution smaller than 50 nm can be made. Using high energy electron beam, usually larger than 30 keV, an extremely small spot of about 1 nm can be achieved. However the expose resolution is much worse than spot size of electron beam, the backscattered secondary electrons from the substrate actually expand the exposure size of resist. The secondary exposure to the resist causes an undercut profile. The undercut is often improved by coating a two-layer electron beam resist. By these techniques, the various materials like nickel,  $\text{BiTe}_x$ , and  $\text{SbTe}_x$  were produced successfully with the wire size around 100 nm, as shown in Figs. 8 (c), (d), and (e). In principle, the fine tune of e-beam exposure could reduce the width of wire-like pattern down to 30 nm.

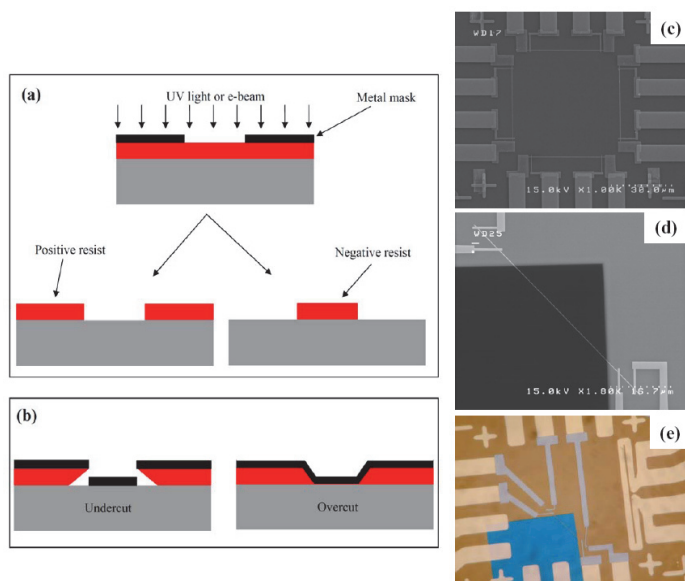


Fig. 8. The selected resists and exposure devices may change the pattern resolution by the typical sequences of process steps. (a) The resist cross section of positive and negative resist. The solubility of the exposed areas increases for a positive resist while it decreases in negative resist. (b) The resist profile of different resists. (c), (d), and (e) are micrographs of nickel,  $\text{BiTe}_x$ , and  $\text{SbTe}_x$  nanowires, respectively.

#### *Fabricating a sagging nickel nanowire*

The details of optical and e-beam lithography methods are described below. The key steps of fabrication process for the sagging single nickel nanowire (Ni-NW) are shown in Fig. 9(a).

(Ou et al., 2008). In order to measure thermal conductivity and specific heat of an individual nanowire by  $3\omega$  method which will be described below, there are some requisitions. With no doubt, the primary part of the wire should be separated from substrate to minimize heat leakage in measurement. For example, the heat could leak to substrate and environments by direct heat-contact and radiation. Furthermore, the two ends of sample should have well thermal contact to substrate to satisfy the requirement that two ends of wire have same temperature as that of substrate. How to fabricate a sagging single nickel nanowire to meet the criterion mentioned above will be described below.

The primary substrate is p-type silicon wafer coated by a 200 nm thickness silicon-nitride ( $\text{Si}_3\text{N}_4/\text{Si}$ ) with [100] out-plane orientation. Meanwhile, a photoresist layer was uniformly deposited to protect the silicon under silicon-nitride from the etching of KOH aqua. The desired pattern was defined with focused electron beam (E-Beam) on a clear and polymethyl methacrylate (PMMA)-coated primitive chip. This pattern includes four wires for four-probe measurement. The configuration of the chip is consist of one nano-ditch, two thin leads for signal pick up and two wide leads for current injection. The designed nano-ditch is 35  $\mu\text{m}$  in length and 150 nm in width (Fig. 9(b)). To minimize the joule heating generated at the interfaces and current leads, the width of leading wires are about 50 times of the nano-ditch. Furthermore, also the nano-ditch takes about 8  $\mu\text{m}$  away from the junction to reduce the temperature fluctuation at the two end parts of nanowire.

In the next step, a 100 nm thickness film of nickel was deposited on the exposed and developed chip by thermal evaporator in vacuum chamber with a base pressure less than  $1 \times 10^{-6}$  torr. The followed lift-off process would take off the resist and the nickel above. Finally a single Ni nanowire with four electrodes was fabricated. The resistance of the nanowire was measured by four-probe method with resistance about 750  $\Omega$ . This patterning process was repeated again to form an etching window allowing  $\text{CF}_4$  to etch out the  $\text{Si}_3\text{N}_4$  with a "V" shape groove around the nanowire by reactive-ion etching (RIE) (Fig. 9(b)). The formed sagging nickel nanowire is about 35  $\mu\text{m}$  in length and 180 nm in width, shown in Figs. 10(a), (b), and (c). This junction-free nanowire with lead electrodes prevents undesired heating at joints during measurements. Although this sample went through all the measurements processes, its resistance is kept around 750  $\Omega$ . This consequence implies that the stability of the specimen with no visible surface oxidation.

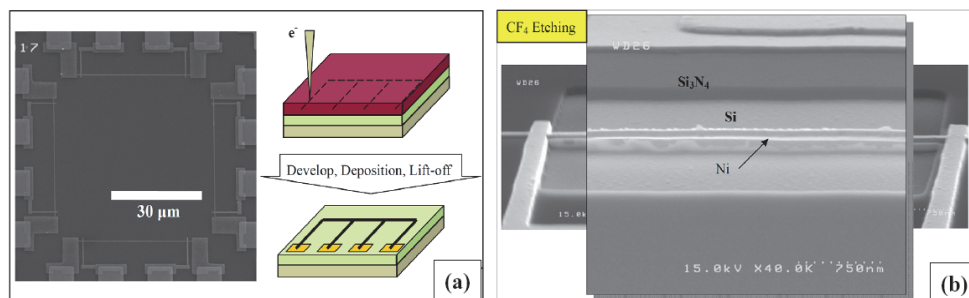


Fig. 9. The defined pattern and etching results. Inset (a) shows the sequence of e-beam exposure, developed and deposition, and lift-off. Inset (b) shows the magnification of the single nanowire.

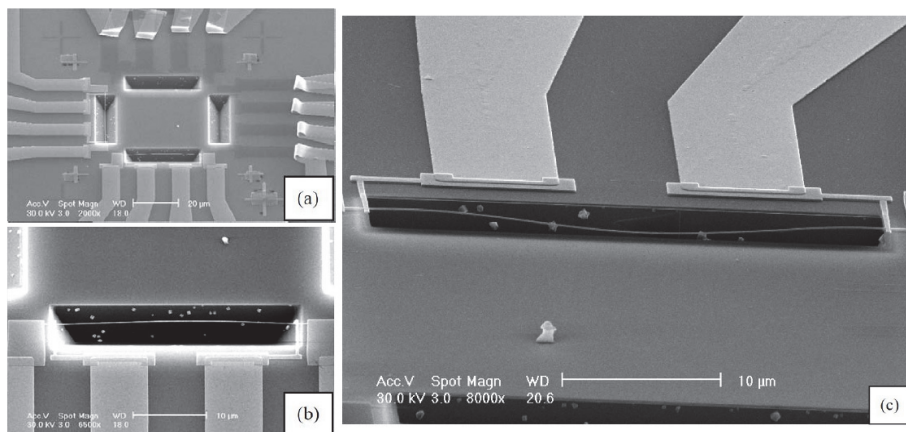


Fig. 10. The SEM images of the sagging Ni-NW. Inset (a) and (b) are the top view with different magnifications. Inset (c) is the image with 45 degree tilt angle. (Reproduced with permission from Ou M. N. et al., *Appl. Phys. Lett.*, 92, 063101-063103. Copyright ©2008 from American Institute of Physics).

### 3. Measurement techniques of transport and thermal properties

In this section, the techniques for measurements of Seebeck coefficient, electrical conductivity and thermal conductivity for either nanowires array or a single nanowire will be illustrated thoroughly. Basically the measurement techniques for physical properties of nanowire are very similar to those for bulk, except a couple of issues which have to be taken into account in the measurements for nanoscale specimens. The first one is how to place or prepare the nanowire sample in a measurement platform; the second one is how to narrow down the size of measurement probes and their configuration which is comparable to the size of nanowire. For nanowires array sample, like AAO templates, their sizes are usually down to a few to a hundred micrometers that are in the same order as measuring probes and lead contacts, for example, thermocouple dips and electrodes respectively. To obtain correct result, reducing the size of the measurement probes and their contacts are inevitable. For measurement of a single nanowire, there are a couple of tools available to solve the problem. Below, we demonstrate the procedures for nanowire array measurement and two approaches to prepare and measure a single nanowire specimen.

#### 3.1 Measurement principle and setup

##### *Measurement platform fabrication for nanowires array*

A longitudinal DC steady-state set-up for bulk specimens is employed to measure the temperature gradient,  $\Delta T$ , and generated thermo-emf (EMF),  $\Delta V$ , across the nanowire specimen and thus the derivation of the Seebeck coefficient  $S (= \Delta V / \Delta T)$ . Two pairs of thermocouples with 25  $\mu\text{m}$  diameter were served as the temperature probe and electric leading wires for EMF measurement. The silver paste is used to assist better thermal and electrical contact. The four wires of thermocouples can also be employed for electrical conductivity measurement of semi-four probe method. The schematic setup is shown in Fig.

11 (Chen et al., 2010). For thermal conductivity measurements, as the specimen size is larger than 6 mm in diameter, then it generally can be accomplished using laser flash setup of thermal diffusivity and calorimeter of specific heat.

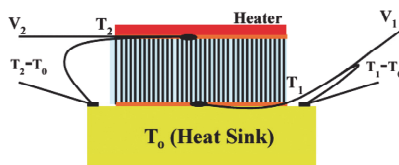


Fig. 11. Schematic setup for Seebeck coefficient measurements on nanowires array of AAO. (Reproduced with permission from Chen C. L. et al., *J. Phys. Chem. C*, 114, 3385-3389. Copyright ©2010 from American Chemical Society).

#### *Measurement platform fabrication for a single nanowire*

The method is to transfer a pre-fabricated nanowire to a silicon wafer which will be further processed to a measurement platform using lithography procedures. There are a couple of methods to achieve this goal. One is by directly attaching the sample substrate, on which nanowires were grown, to a blank silicon wafer (Fig. 12). Or alternatively, you can dip a drop of liquid containing nanowires to the silicon wafer.

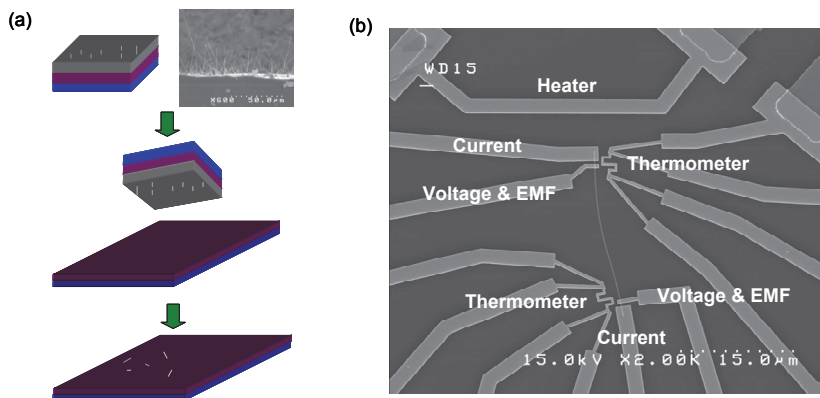


Fig. 12. (a) The processes of transferring nanowires to the working silicon wafer. (b) The SEM picture of a  $\text{Bi}_2\text{Te}_3$  nanowire specimen and configuration of electrical leads, heaters and temperature thermometers.

For more precise sample control and manipulation, four nano-manipulation probes integrated into an SEM can be employed to select and pick up a nanowire and lay it down to a specific region of a well prepared template (Fig. 13(a)). This template has a  $\text{SiN}_x$  membrane in the center with underneath been etched away. After nanowire was placed, EDX and SEM were applied to analyze the configuration and morphology of the nanowire, and mark the position of nanowire simultaneously. Followed by photolithograph and e-beam lithography processes, patterning of leading wires, thermometers and heaters can be accomplished. For suspending the nanowire, the  $\text{SiN}_x$  membrane can be removed by various etching processes. Now the suspended nanowire is ready for all kinds of measurements of Seebeck coefficient, electrical conductivity and thermal conductivity (Fig. 13(b)).

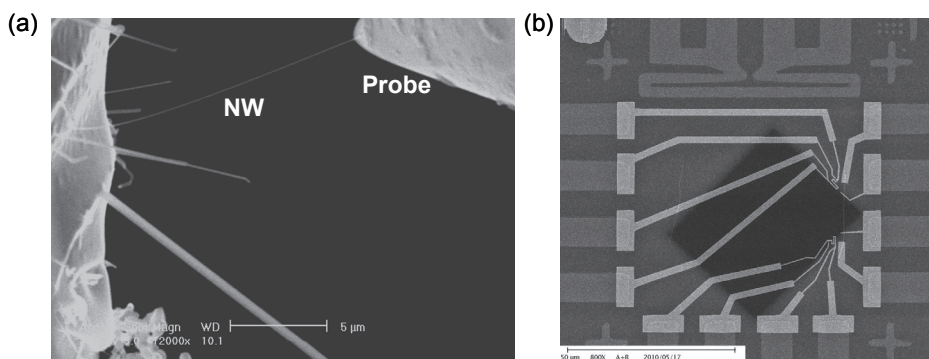


Fig. 13. (a) Shows the controllable probe in SEM attached a  $\text{Bi}_2\text{Te}_3$  nanowire grown on the silicon substrate. (b) The SEM picture of the measurement platform for  $\text{Bi}_2\text{Te}_3$  nanowire sample.

### 3.2 Measurements of Seebeck coefficient

The Seebeck coefficient ( $S$ ) is defined as:

$$S = -\frac{\Delta V}{\Delta T} \quad (3)$$

$\Delta T$  is the temperature gradient of the sample, and  $\Delta V$  is the generated EMF. A traditional Seebeck coefficient measurement setup for bulk sample is shown in Fig. 14(a). However for nanowire specimen, the setup and design are completely different, as shown in Fig. 14(b).

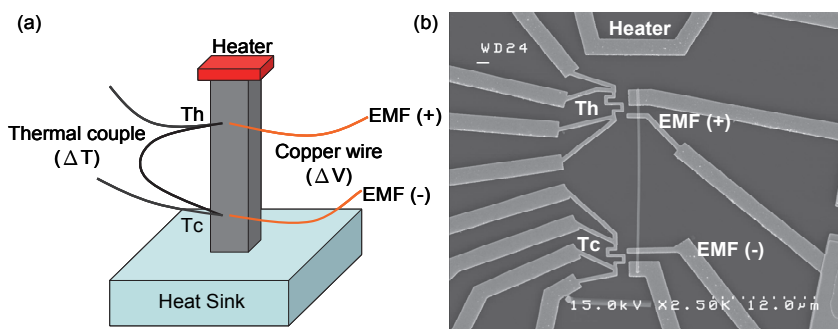


Fig. 14. (a) A traditional Seebeck coefficient measurement setup for bulk specimens. (b) The setup for a single  $\text{Bi}_2\text{Te}_3$  nanowire specimen.

In Seebeck coefficient measurement, the main issue is how to reduce the measurement error of temperature gradient across the specimen. The error of temperature measurement mainly comes from two sources, the thermometer size and the non-common position of the thermometer and EMF probe. For bulk sample, in general, typical size of thermal couples is small enough for the pinpoint of the exact position of temperature measured. For nanowire measurement, the size of traditional thermocouples is no longer applicable in nanoscale. For

nanowire measurement, the resistive metal wires are served as thermometers but narrowed down to nanometer scale. In Fig. 15, an example measurement of Seebeck coefficient measurements for a  $\text{Bi}_2\text{Te}_3$  nanowire at 180 K is shown. The Seebeck coefficient about  $-5 \mu\text{V}/\text{K}$  is obtained by the linear fit to the data of  $\Delta V$  versus  $\Delta T$ .

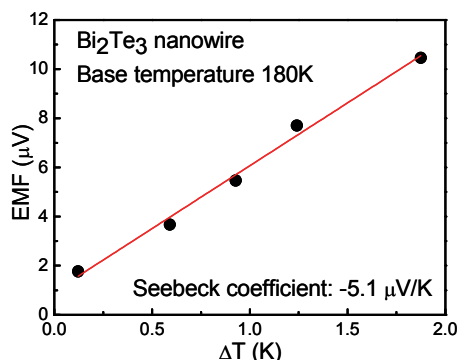


Fig. 15. The Seebeck coefficient measurement of a single  $\text{Bi}_2\text{Te}_3$  nanowire at 180 K.

### 3.3 Measurements of electrical and thermal conductivities of a nanowire

#### *Electrical conductivity measurements*

The arrangement of measuring circuit diagram for electrical conductivity of Ni nanowire is shown in Fig. 16. An AC current was injected through two outside electrodes ( $L_5$  and  $L_6$ ), and voltage drop was picked up by two inner electrodes ( $L_2$  and  $L_3$ ). A measured current dependence of voltage is shown in Fig. 17. Within the current range from 1 to 50  $\mu\text{A}$ , a linear dependence of voltage versus current is exhibited, indicating the resistivity of Ni nanowire follows Ohmic law. The measurement of electrical conductivity was excited by an alternating current described by a sine wave  $I_0\sin(\omega t)$  with frequency  $f = 15.3 \text{ Hz}$ . The corresponding in-phase voltage signal of the same frequency was picked up by a lock-in amplifier.

The data of resistivity  $\rho$  of the nickel nanowire (Ni-NW) in the temperature region of 0.5- 300 K is showed in Fig. 18. The temperature dependence of resistivity is metallic and similar to that of the bulk but with a larger magnitude of resistivity. The relative ratio of resistivity,  $\rho(300 \text{ K})/\rho(4.2 \text{ K}) = 2$ , is much smaller as compared to the value of 47 for the bulk. Since the wire dimensions are much larger than the mean free path of Ni ( $\sim 14 \text{ nm}$ ) (Reale, 1974), the increase in resistivity is conjectured to be the predominant effect of the grain-boundary scattering. The temperature coefficient of resistivity (TCR) is positive in the entire temperature range, indicating that the Ni-NW is weakly disordered. At low temperatures  $T < 10 \text{ K}$ , the temperature dependence of resistivity can be formulated as  $\rho = \rho_0 + T^n$ , with the power  $n \sim 2$  (inset in Fig. 18). The consequence is similar to that of the bulk (Zhang et al., 2001), except the magnitude of residual resistivity  $\rho_0 = 17.6 \mu\Omega\text{-cm}$  is five times of bulk Ni. The huge residual resistivity indicates an enhanced electronic scattering on boundaries and defects.

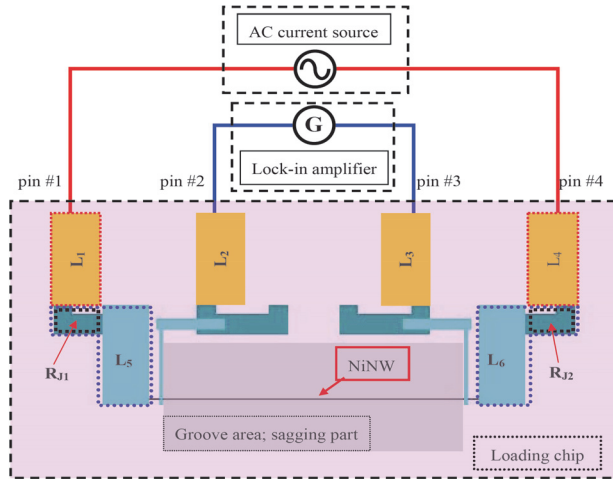


Fig. 16. The schematic diagram of the nanowire specimen and electrode leads for both electrical and thermal conductivity measurements. Nanowire ( $100\text{ nm}\times 180\text{ nm}\times 35\text{ }\mu\text{m}$ ) and electrode pads were fabricated from a piece of thermally deposited Ni film using photolithography and e-beam writer, thus there is no junction between nanowire and electrode pads.  $L_1$ ,  $L_2$ ,  $L_3$  and  $L_4$  are the gold electrode pads.

It is noted that the  $\rho(T)$  curve of Ni-NW is well fitted to the modified Bloch-Gruneisen formula by Wilson (White & Wood, 1959) for transition metals with Debye temperature  $\theta_D$  and constant  $d$  as the two adjustable fitting parameters. As a result of the fitting, we obtained the smaller value of  $\theta_D = 440\text{ K}$  than that of the bulk ( $\theta_D = 557\text{ K}$ ) at fixed  $d$ . The reduction of the Debye temperature presumably reflects the phonon softening due to the enhanced disorders in nanowires. The consequence was previously observed in other nanowires and disordered systems (Bid et al., 2006; Fultz et al., 1997; Frase & Fultz, 1998).

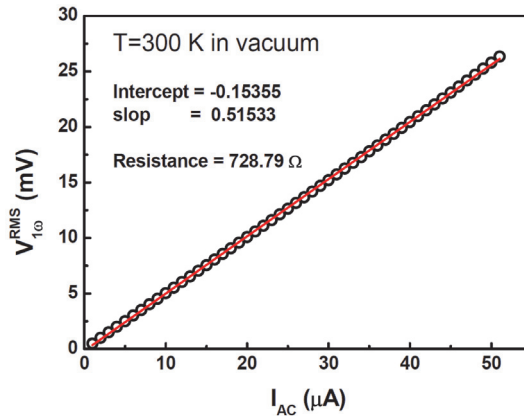


Fig. 17. The current dependence of voltage signal. Experimental data represented by open circles are fit to a solid line.

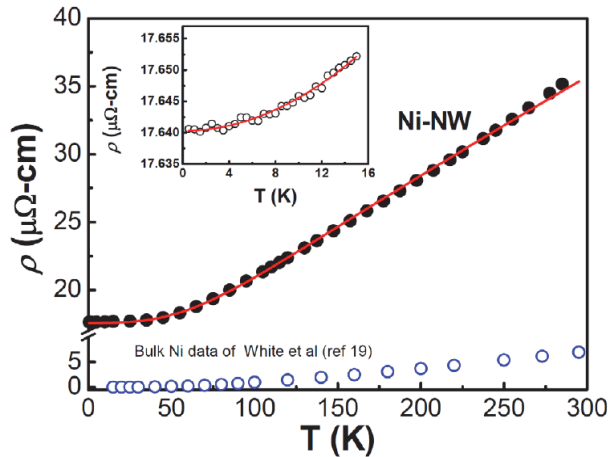


Fig. 18. The resistivity  $\rho(T)$  of the Ni-NW (solid circles) and the bulk (open circles) from White et al. The solid line is the fitting results using Bloch-Gruneisen formula (Bid et al., 2006). The inset: the resistivity in low temperature range is in good agreement with the curve of  $T^2$  dependence. (Reproduced with permission from Ou M. N. et al., *Appl. Phys. Lett.*, 92, 063101-063103. Copyright ©2008 from American Institute of Physics).

*Specific heat, electrical and thermal conductivity measurements using  $3\omega$  method*

Usually, the thermal conductivity  $\kappa(T)$ , electrical conductivity  $\sigma(T)$ , and specific heat  $C(T)$  are measured separately using different instruments. However, by  $3\omega$  method (Ou et al., 2008; Allwood et al., 2005; Lu et al., 2001; Ou et al., 2007), the three parameters can be measured on a specimen simultaneously. Although the nanowire still exhibits metallic behavior in  $\rho(T)$ , the situation in thermal conductivity is changed drastically. The schematic diagrams of electrical connections are similar to the setup of resistance measurement. An example of thermal conductivity measurement is illustrated below.

To apply  $3\omega$  method for the measurement of sagging Ni-NW, a couple of restricted conditions have to be taken into account. In Fig. 16, the current path is consisting of current leads, junctions, and specimen, thus the total resistance of current loop can be represented by following formula:

$$R_t = R_{L1} + R_{J1} + R_{L2} + R_{Ni-NW} + R_{L3} + R_{J2} + R_{L4} \quad (4)$$

Since the mass ratio of leads to Ni-NW is about  $10^5$ , the estimated power density of leads and junction is ignorable as compared to that of Ni-NW, this consequence satisfies the restriction conditions of  $3\omega$  method. A junction-free design has been made to prevent the measurement error which could be caused by unexpected temperature variation of electrical contacts.

The  $3\omega$  signal across specimen of the sagging Ni-NW is represented by following approximation solution:

$$V_{3\omega} \approx \frac{4I^3 L R R'}{\pi^4 \kappa S \sqrt{1 + (2\omega\gamma)^2}}, \quad (5)$$

where the  $\kappa$  and  $\gamma$  are thermal conductivity and thermal time constant, respectively. To select appropriate ranges of frequency and magnitude of exciting current, a test run was performed at 300 K to ensure the condition of  $V_{3\omega} \propto I^3$  is held (Fig. 19). For the signal picking-up, a digital lock-in amplifier was selected to pickup the  $3\omega$  signal of  $V_{3\omega}$ . To ensure the observation of a true frequency dependence of  $V_{3\omega}$  the dc coupled input mode was selected with no filters was applied. In Fig. 20, the frequency dependencies of  $V_{3\omega}$  signal at 15, 85, 155, 225, and 295 K are fitted to the theoretical predication (the solid lines) of Eq. 5 to derive the magnitudes of thermal conductivity  $\kappa$ .

The thermal conductivity  $\kappa$  in the temperature region of 15-300 K is shown in Fig. 21. Thermal conductivity monotonically decreases as temperature drops. The  $\kappa(T)$  of Ni-NW showed a completely different temperature dependent trend and is much smaller when compared with the bulk (inset of Fig. 21) (White & Wood, 1959). The phenomena of the metallic electrical resistivity and decreasing thermal conductivity have been observed in disordered metallic systems of thin films, concentrated alloys and superlattices (Zhou et al., 2006; Zhang et al., 2006; Yang et al., 2006; Berman, 1976). Such behavior was explained by increased scattering of heat carrier with the structural defects and by the substantial contribution of the phonon thermal conductivity. In general, thermal conductivity  $\kappa$  is the summation of electronic  $\kappa_E$  and phonon  $\kappa_{PH}$ . If the WF (Wiedemann Franz) law holds, one can obtain  $\kappa_E$  from the data of  $\rho(T)$  through the relation  $\kappa_E = L_0 T / \rho$ . The calculated  $\kappa_E$  for  $T < 60$  K is larger than the experimental data  $\kappa_{total}$ , indicating the violation of the WF law in this temperature region. To estimate the phonon part of thermal conductivity  $\kappa_{PH}$  for  $T > 100$  K,  $\kappa_E$  was subtracted from experimental  $\kappa_{total}$ ; the result of  $\kappa_{PH}$  does not exceed 10 % of total thermal conductivity  $\kappa_{total}$ , and thus no considerable enhancement in the phonon part was observed at this temperature region.

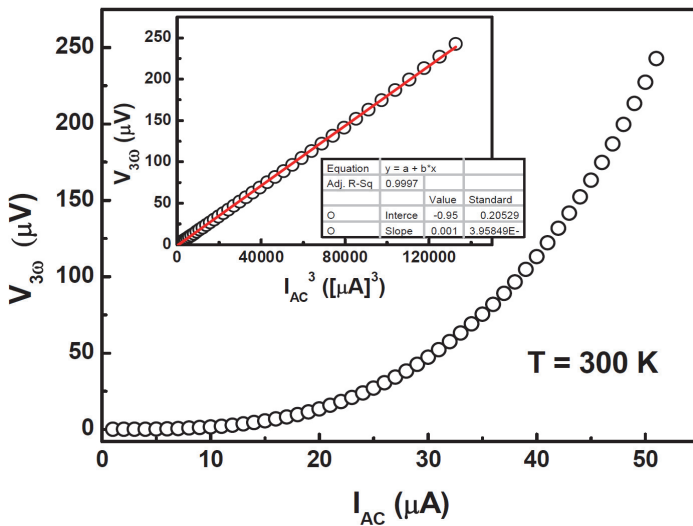


Fig. 19. The current dependence of 3<sup>rd</sup> harmonic signal at 300 K. The inset shows the linear dependence of  $V_{3\omega}$  versus  $I^3$ .

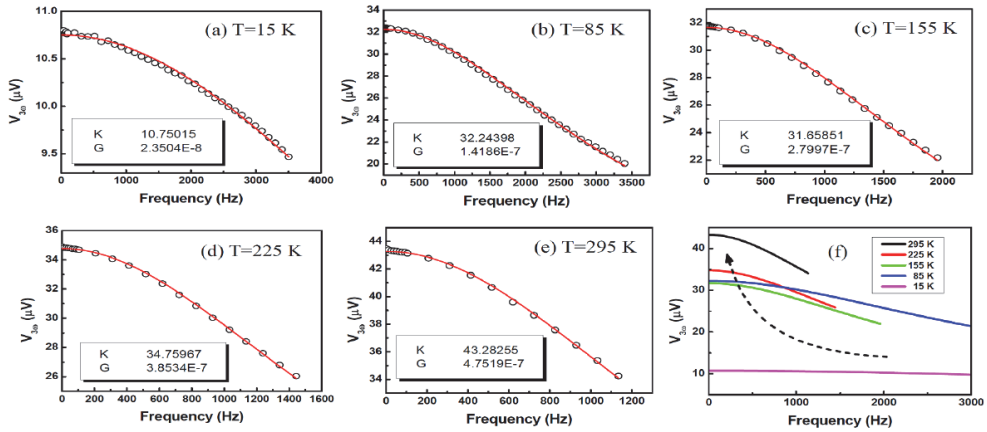


Fig. 20. The frequency dependence of 3<sup>rd</sup> harmonic signal. (a) to (e) are experimental data and curve fittings for the results of thermal conductivity  $\kappa$ . The frequency dependencies of  $V_{3\omega}$  signal for different measurement temperatures are displayed in (f) to show the trend as temperature changes.

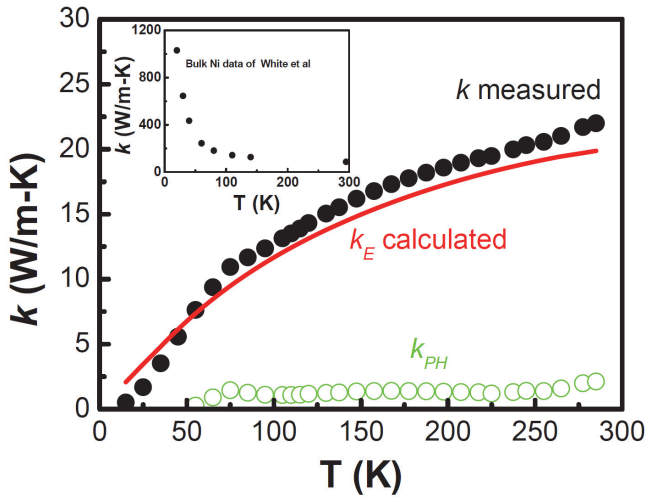


Fig. 21. The thermal conductivity  $\kappa(T)$  of the Ni-NW (solid circles), the calculated  $\kappa_E$  (solid line) and the  $\kappa_{PH}$  (open circles). Inset: the thermal conductivity  $\kappa(T)$  of the pure bulk Ni (White & Wood, 1959). (Reproduced with permission from Ou M. N. et al., *Appl. Phys. Lett.*, 92, 063101-063103. Copyright ©2008 from American Institute of Physics).

#### 4. Conclusion

In summary, a couple of nanowire fabrication methods, that can efficiently control growth condition, sample composition, size/diameter, and crystallization of nanowires, are

introduced. Furthermore the morphology, microstructures and crystallization of nanowires are characterized by SEM, TEM, XRD and EDX. The techniques for measurements of Seebeck coefficient, electrical conductivity and thermal conductivity for either nanowires array or a single nanowire are also illustrated thoroughly. Some novel physical properties of nanowires are revealed by the measurements. A typical example of a single sagging Ni-NW was used to illustrate the specimen preparation and measurement setups. These innovative techniques of sample fabrication, characterization and measurements provide new strategies to understand the intrinsic properties of nanowires. Especially these knowledge and technologies are applicable to improve the thermoelectric efficiency of materials on renewable energy applications.

## 5. Acknowledgments

Financial supported by the National Science Council of the Republic of China (Grant No. NSC 99-2120-M-001-001) is greatly acknowledged. We deeply appreciate to all of our colleagues and collaborators, their names appear in the cited literatures. We would like to thank Mr. T. C. Hsiung and Ms. Candy I Chen Tsai for their important contributions to the research effort.

## 6. References

- Allwood, D. A.; Xiong, G.; Faulkner, C. C.; Atkinson, D.; Petit, D. & Cowburn, R. P. (2005). Magnetic Domain-Wall Logic. *Science*, Vol. 309, pp. 1688-1692.
- Andricacos, P. C.; Uzoh, C.; Dukovic, J. O.; Horkans, J. & Deligianni, H. (1998). Damascene Copper Electroplating for Chip Interconnections. *IBM J. Res. Dev.*, Vol. 42, pp.567-574.
- Baily, S. A. & Emin, D. (2006). Transport Properties of Amorphous Antimony Telluride. *Phys. Rev. B*, Vol. 73, pp. 165211-165218.
- Berman, R. (1976). *Thermal Conduction in Solids*. Oxford University Press. USA.
- Bid, A.; Bora, A. & Raychaudhuri, A. K. (2006). Temperature Dependence of The Resistance of Metallic Nanowires of Diameter  $\geq 15$  nm: Applicability of Bloch-Gruneisen Theorem. *Phys. Rev. B*, Vol. 74, pp. 035426-035433.
- Borca-Tasciuc, D. -A.; Chen, G.; Prieto, A.; Martin-Gonzalez, M. S.; Stacy, A.; Sands, T.; Ryan, M. A. & Fleurial, J. P. (2004). Thermal Properties of Electrodeposited Bismuth Telluride Nanowires Embedded in Amorphous Alumina. *Appl. Phys. Lett.*, Vol. 85, pp. 6001-6003.
- Chen, C. L.; Chen, Y. Y.; Lin, S. J.; Ho, J. C.; Lee, P. C.; Chen, C. D. & Harutyunyan, S. R. (2010). Fabrication and Characterization of Electrodeposited Bismuth Telluride Films and Nanowires. *J. Phys. Chem. C*, Vol. 114, pp. 3385-3389.
- Frase, H. & Fultz, B. (1998). Phonon in Nanocrystalline Ni<sub>3</sub>Fe. *Phys. Rev. B*, Vol. 57, pp. 898-905.
- Fultz, B.; Ahn, C. C.; Alp, E. E.; Sturhahn, W. & Toellner, T. S. (1997). Phonon in Nanocrystalline <sup>57</sup>Fe. *Phys. Rev. Lett.*, Vol. 79, pp. 937-940.
- Ham, J.; Shim, W.; Kim, D. H.; Lee, S.; Roh, J.; Sohn, S. W.; Oh, K. H.; Voorhees, P. W. & Lee, W. (2009). Direct Growth of Compound Semiconductor Nanowires by On-Film Formation of Nanowires: Bismuth Telluride. *Nano Lett.*, Vol. 9, pp. 2867-2872.

- Hicks, L. D. & Dresselhaus, M. S. (1993). Thermoelectric Figure of Merit of A One-Dimensional Conductor. *Phys. Rev. B*, Vol. 47, pp. 16631-16634.
- Huang, Q.; Kellock, A. J. & Raoux, S. (2008). Electrodeposition of SbTe Phase-Change Alloys. *J. Electrochem. Soc.*, Vol. 155, pp. D104-109.
- Jin, C.; Zhang, G.; Qian, T.; Li, X. & Yao, Z. (2005). Large-Area Sb<sub>2</sub>Te<sub>3</sub> Nanowire Arrays. *J. Phys. Chem. B*, Vol. 109, pp. 1430-1432.
- Leimkuhler, G.; Kerkamm, I. & Reineke-Koch, R. (2002). Electrodeposition of Antimony Telluride. *J. Electrochem. Soc.*, Vol. 149, pp. C474-478.
- Li, D.; Wu, Y.; Kim, P.; Shi, L.; Yang, P. & Majumdar, A. (2003). Thermal Conductivity of Individual Silicon Nanowires. *Appl. Phys. Lett.*, Vol. 83, pp. 2934-2936.
- Liu, K.; Nagodawithana, K.; Searson, P. C. & Chien, C. L. (1995). Perpendicular Giant Magnetoresistance of Multilayered Co/Cu Nanowires. *Phys. Rev. B*, Vol. 51, pp. 7381-7384.
- Lu, L.; Yi, W. & Zhang, D. L. (2001).  $3\omega$  Method for Specific Heat and Thermal Conductivity Measurements. *Rev. Sci. Instrum.*, Vol. 72, pp. 2996-3003.
- Martin-Gonzalez, M. S.; Prieto, A. L.; Gronsky, R.; Sands, T.; Stacy, A. M. (2002). Insights Into The Electrodeposition of Bi<sub>2</sub>Te<sub>3</sub>. *J. Electrochem. Soc.*, Vol. 149, pp. C546-554.
- Michel, S.; Diliberto, S.; Boulanger, C. & Bolle, B. (2006). Effect of Electrochemical Deposition Conditions on The Crystallographic Texture of Bismuth Telluride Alloys. *J. Cryst. Growth*, Vol. 296, pp. 227-233.
- Osaka, T. (1999). Recent Development of Magnetic Recording Head Core Materials by Plating Method. *Electrochim. Acta*, Vol. 44, pp. 3885-3890.
- Ou, M. N.; Harutyunyan, S. R.; Lai, S. J.; Chen, C. D.; Yang, T. J. & Chen, Y. Y. (2007). Thermal and Electrical Transport Properties of A Single Nickel Nanowire. *Physica Status Solidi (b)*, Vol. 244, pp. 4512-4517.
- Ou, M. N.; Yang, T. J.; Harutyunyan, S. R.; Chen, Y. Y.; Chen, C. D. & Lai, S. J. (2008). Electrical and Thermal Transport in Single Nickel Nanowire. *Appl. Phys. Lett.*, Vol. 92, pp. 063101-063103.
- Ou, M. N.; Yang, T. J. & Chen, Y. Y. (2009). Anisotropic Magnetism and Magnetoresistance in Iron Nanowire Arrays. *Chin. J. Phys.*, Vol. 47, pp. 848-853.
- Reale, C. (1974). Conductivity Data for The Transition Metals Derived from Considerations on The Charge Transport in Thin Films. *J. Phys. F: Metal Phys.*, Vol. 4, pp. 2218-2222.
- Reich, D. H.; Tanase, M.; Hultgren, A.; Bauer, L. A. & Chen, C. S. (2003). Biological Applications of Multifunctional Magnetic Nanowires. *J. Appl. Phys.*, Vol. 93, pp. 7275-7280.
- Rowe, D. M. (1995). *CRC Handbook of Thermoelectric*. CRC Press: New York.
- Shim, W.; Ham, J.; Lee, K.; Jeung, W. Y.; Johnson, M. & Lee, W. (2009). On-Film Formation of Bi Nanowires with Extraordinary Electron Mobility. *Nano Lett.*, Vol. 9, pp. 18-22.
- Tritt, T. M. (1999). Thermoelectric Materials: Holey and Unholey Semiconductors. *Science*, Vol. 283, pp. 804-805.
- Tu, K. N. (1996). Cu/Sn Interfacial Reactions: Thin-Film Case Versus Bulk Case. *Mater. Chem. Phys.*, Vol. 46, pp. 217-223.
- Venkatasubramanian, R.; Siivola, E.; Colpitts, T. & O'Quinn, B. (2001). Thin-Film Thermoelectric Devices with High Room-Temperature Figures of Merit. *Nature*, Vol. 413, pp. 597-602.

- Weller, D. & Moser, A. (1999). Thermal Effect Limits in Ultrahigh-Density Magnetic Recording. *IEEE Trans. Magn.*, Vol. 35, pp. 4423-4439.
- White, G. K. & Wood, S. B. (1959). Electrical and Thermal Resistivity of the Transition Elements at Low Temperatures. *Philos. Trans. R. Soc. London, Ser. A*, Vol. 251, pp. 273-302.
- Yang, Y.; Zhu, J. G.; White, R. M. & Asheghi, J. (2006). Field-Dependent Thermal and Electrical Transports in Cu/CoFe Multilayer. *J. Appl. Phys.*, Vol. 99, pp. 063703-063707.
- Zhang, X. Y.; Zhang, L. D.; Chen, W.; Meng, G. W.; Zheng, M. J. & Zhao, L. X. (2001). Electrochemical Fabrication of Highly Ordered Semiconductor and Metallic Nanowire Arrays. *Chem. Mater.*, Vol. 13, pp. 2511-2515.
- Zhang, Q. G.; Cao, B. Y.; Zhang, X.; Fujii, M. & Takahashi, K. (2006). Influence of Grain Boundary Scattering on The Electrical and Thermal Conductivities of Polycrystalline Gold Nanofilms. *Phys. Rev. B*, Vol. 74, pp. 134109-134113.
- Zhou, Z.; Uher, C.; Xu, D.; Johnson, W. L.; Gannon, W. & Aronson, M. C. (2006). On The Existence of Einstein Oscillators and Thermal Conductivity in Bulk Metallic Glass. *Appl. Phys. Lett.*, Vol. 89, pp. 031924-031926.

# Role of Intrinsic Defects in Nanowires

Usha Philipose

*Department of Physics, University of North Texas  
United States of America*

## 1. Introduction

The properties of nanowires are distinctively different from those of bulk materials because they are affected by quantum confinement effect and large surface-to-volume ratios. A fundamental understanding of the intrinsic properties of nanowires, in terms of their structure, electronic and optical properties as well as a study of the nanowire surface is required to develop them for future device applications. The morphology and properties of the nanowires are strongly dependent on the synthesis process and growth parameters. Key to realizing the full potential of nanowires is the ability to synthesize uniform, defect free nanowires. Any deviation from stoichiometry leads to imperfections within the nanowire crystal lattice and affects its properties. Efforts to optimize growth conditions are spearheaded by investigations to identify and control native point defects inherent in semiconductors. Structural characterization using electron microscopy is usually the first step towards identifying the quality of the nanowire in terms of composition, morphology and defects like twinning and stacking faults. Optical characterization tools like Photoluminescence (PL) spectroscopy is useful for extracting information on band-to-band transition and other sub-band electronic transitions, thus providing information on any deviations from stoichiometry. However, it cannot provide a comprehensive view of every aspect of the optical properties of nanowires. Hence, complementary experiments like time-resolved PL, pump probe measurements, cathodoluminescence, absorption and reflection spectroscopy are often used. In this chapter, we will present a brief review of some of the techniques used in identifying and characterizing defects in semiconductor nanowires. Studies drawn primarily from the author's work, addressing the role of intrinsic point defects in nanowires and discussion of strategies for determining the type, energy and concentration of defects in nanowires will be presented in this chapter.

The presence of low energy luminescence bands in un-intentionally doped nanowires is evidence that intrinsic point defects (IPDs) play a significant role in the emission spectrum. IPDs in a compound semiconductor are vacancies, interstitials and antisites. In bulk semiconductors, IPDs are often studied by Optical Detection of Magnetic Resonance (ODMR) and Electron Paramagnetic Resonance (EPR) studies. However, the use of such studies on nanowires is only recent (Mal et al., 2010). It is important to understand the behavior of IPDs for the successful application of any semiconductor, since they control, directly or indirectly, doping, compensation, minority carrier lifetime, and luminescence efficiency. Semiconductor doping, in particular, can be adversely affected by IPDs, by causing self-compensation. For example, IPDs which act as donors may compensate the deliberately introduced acceptors. In group II-VI semiconductors like ZnO, specific native defects have long been believed to play

a very important role. As-grown ZnO, both in bulk and nanoscale, exhibits unintentional n-type conductivity, and its source is attributed to IPDs like oxygen and zinc vacancies as well as zinc interstitials. IPDs are also suspected to play an important role in the observed room temperature ferromagnetism in transition metal (TM) doped II-VI semiconductors through defect mediated coupling of the local d-electrons of the TM ions. There are also reports that nanoscale clusters of intrinsic ZnO defects containing ferromagnetically aligned spins are being confused with ferromagnetic Dilute Magnetic Semiconductors (Potzger & Zhou, 2009). This chapter will provide a review of experimental studies of IPDs in II-VI semiconductors and their influence on the optical and electronic properties of semiconductor nanowires. A brief description of a model based on chemical thermodynamics will be used to review the thermodynamics of intrinsic defects in nanowires and to show the dependence of IPDs on growth parameters. Using structural and optical characterization techniques, studies revealing a correlation between growth parameters, structural defects like stacking faults and twinning defects as well as the role of IPDs in determining the properties of nanowires will be presented.

The surface of nanowires also presents significant challenges as well as opportunities for affecting nanowire properties. On account of the large surface to volume ratio in nanowires, their surfaces can dominate their quantum confined properties. Hence, it is necessary to elucidate the fundamental relationships between nanowire interfaces with the environment and their electronic and optical properties. We will present a brief review of the efficacy of various surface passivation schemes. This chapter will thus review scientific advances made in the study of fundamental intrinsic properties of nanowires, namely an estimation and determination of type of defects in nanowires, with an aim to develop nanowires for viable applications.

## 2. Defect analysis using a thermodynamic model

The defect analysis presented in this section has been developed for ZnSe nanowires grown by Chemical Vapor Deposition (CVD), but the general analysis can be extended to most semiconductor materials. ZnSe is an important material for fabrication of optoelectronic devices. This direct band gap material should be characterized by high luminescence efficiency, but despite decades of research, emission is often dominated by low-energy luminescence bands caused by point defects which introduce energy levels within the band gap of ZnSe. The principle defects in a binary compound like ZnSe include vacancies on the sub-lattice of Zn ( $V_{Zn}^x$ ) and Se ( $V_{Se}^x$ ), interstitial atoms ( $Zn_i$ ) and ( $Se_i$ ), antistructural defects ( $Se_{Zn}$ ) and ( $Zn_{Se}$ ) (Se atom in the Zn sub-lattice and vice versa) and positively and negatively single- and double- charged vacancies ( $V_{Se}^+$ ,  $V_{Se}^{2+}$ ,  $V_{Zn}^-$  and  $V_{Zn}^{2-}$ ). There is no experimental evidence of antisite defects in ZnSe (Laks et al., 1992) and hence these defects have not been considered in this analysis. This work takes into account the neutral, the singly and doubly charged Zn vacancies and interstitials. The neutral Zn vacancy has a threefold-degenerate level in the band gap and the possible charged states are 1- and 2-, corresponding to the Zn vacancy levels acting as acceptor levels in undoped ZnSe. Similarly, the neutral Zn interstitial has two electrons occupying a single level in the band gap and the possible charge states are 1+ and 2+, and their levels act as donor states in the band gap of undoped ZnSe. The vacancies and interstitials of Zn having different charge states create different localized levels within the band gap and can also combine to form donor-acceptor pairs (DAP). Evidence of the existence of such DAPs has also been confirmed by photoluminescence (PL) measurements, discussed in greater detail in Section 3.

A vapor-liquid-solid (VLS) growth mechanism accounts for the formation of ZnSe nanowires and their formation follows the reaction:



The nanowire growth is driven by the chemical potential gradients between vapor, liquid and solid phase with growth taking place through a mass transfer across the liquid-solid interface. The system of nanowires is characterized by a temperature  $T$ , at which there are a certain number of intrinsic point defects in the crystalline nanowires. The concentration of Zn vacancies and interstitials,  $[V_{\text{Zn}}]$  and  $[Zn_i]$ , respectively, were estimated from (Laks et al., 1992; Reshchikov & Morkoc, 2005):

$$[V] = N_{\text{sites}} N_{\text{config}} \exp\left(\frac{S}{k}\right) \exp\left(-\frac{E_f}{kT}\right) \quad (2)$$

where,  $S$  is the entropy,  $E_f$  is the formation energy of the defect,  $N_{\text{sites}}$  is the number of sites in the lattice (per unit volume) where the defect can be incorporated (i.e., for ZnSe,  $N_{\text{sites}} = 2.2 \times 10^{22} \text{cm}^{-3}$ ),  $k$  is Boltzmann's constant,  $T$  is the absolute temperature and  $N_{\text{config}}$  is the number of equivalent configurations in which the defect can be incorporated. The vacancy formation reactions and the corresponding mass-action relations are given in Table 1. The concentrations of free electrons and holes are indicated by  $p$  and  $n$  and in reaction equations, free electrons and holes are indicated by  $e^-$  and  $h^o$ , respectively.

Reaction equations leading to the formation of vacancies and interstitials	Equations for equilibrium constants based on mass-action relation
$\text{Zn}_{(v)} + \frac{1}{2}(\text{Se}_2)_{(v)} = \text{ZnSe}_{(s)}$	$K_f = P_{\text{Zn}} P_{\text{Se}_2}^{1/2}$
$\frac{1}{2}(\text{Se}_2)_{(v)} = \text{Se}_{\text{Se}}^x + V_{\text{Zn}}^{2-} + 2h^o$	$K_v = \frac{[V_{\text{Zn}}^{2-}] p^2}{P_{\text{Se}_2}^{1/2}}$
$V_{\text{Zn}}^{2-} + h^o = V_{\text{Zn}}^-$	$K'_{\text{Zn}} = \frac{[V_{\text{Zn}}^-]}{[V_{\text{Zn}}^{2-}] p}$
$V_{\text{Zn}}^- + h^o = V_{\text{Zn}}^x$	$K^x_{\text{Zn}} = \frac{[V_{\text{Zn}}^x]}{[V_{\text{Zn}}^-] p}$
$V_{\text{Zn}}^{2-} + Zn_i^{2+} = 0$	$K_{fr} = [V_{\text{Zn}}^{2-}] [Zn_i^{2+}]$
$Zn_i^{2+} + e^- = Zn_i^+$	$K_i^+ = \frac{[Zn_i^+]}{[Zn_i^{2+}] n}$
$Zn_i^+ + e^- = Zn_i^x$	$K_i^x = \frac{[Zn_i^x]}{[Zn_i^+] n}$

Table 1. Equilibrium constants derived from reaction equations.

For the assumptions discussed above, the electrical neutrality condition is:

$$n + 2[V_{\text{Zn}}^{2-}] + [V_{\text{Zn}}^-] = p + 2[Zn_i^{2+}] + [Zn_i^+] \quad (3)$$

The Zn partial pressure ( $P_{\text{Zn}}$ ) and  $\text{Se}_2$  partial pressure ( $P_{\text{Se}_2}^{1/2}$ ) in the vapor phase are governed by the equation:

$$P_{\text{Zn}} P_{\text{Se}_2}^{1/2} = K_f \quad (4)$$

where  $K_f$  [in units of  $(Atm)^{3/2}$ ] is the equilibrium constant for sublimation of ZnSe, which is a constant at a given temperature. During growth, the compound ZnSe source provides a minimum total pressure  $P_{min}$  over the growing nanowire in the growth chamber, ensuring that it remained an equilibrium ZnSe solid phase. The required minimum partial pressure of Se,  $(P_{Se_2}^{1/2})_{min}$  was calculated using the approximation:

$$(P_{Se_2}^{1/2})_{min} \approx (K_f/2)^{1/3} \quad (5)$$

To calculate the concentration of the six defects ( $[V_{Zn}^{2-}]$ ,  $[V_{Zn}^-]$ ,  $[V_{Zn}^x]$ ,  $[Zn_i^+]$ ,  $[Zn_i^{2+}]$  and  $[Zn_i^x]$ ), as a function of  $(P_{Se_2}^{1/2})$ , equations in Table 1 were modified and expressed in terms of the equilibrium constants. The evolution chart of the defects and the possible transitions with increasing Se vapor pressure  $(P_{Se_2}^{1/2})$  is shown in Figure 1. The dependence of  $[V_{Zn}]$  and

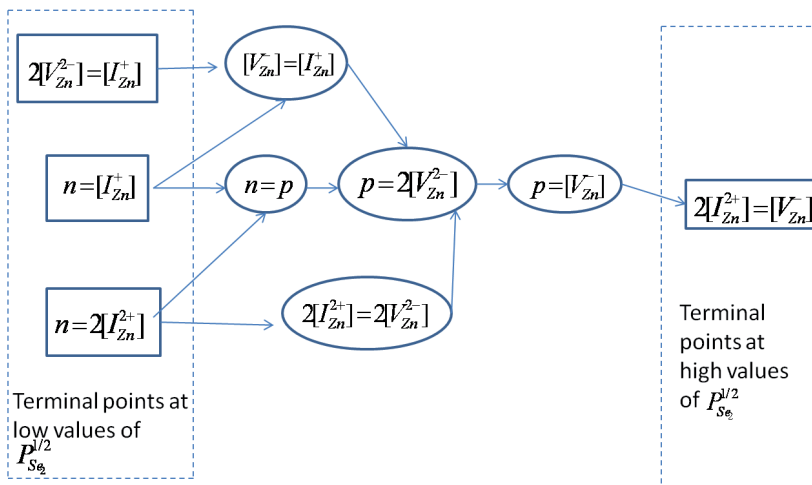


Fig. 1. Evolution chart of defects, where arrows refer to increasing  $(P_{Se_2}^{1/2})$ .

$[Zn_i]$  equilibrium concentrations on  $(P_{Se_2}^{1/2})$  was established using the mass-action laws and charge neutrality conditions (Gool, 1966). Figure 2 shows the approximate solution of this set of equations. The approximation implies that in the ranges of  $(P_{Se_2}^{1/2})$  pressure variation, three defect regimes ( $2[Zn_i^{2+}] = 2[V_{Zn}^{2-}]$ ,  $p = 2[V_{Zn}^{2-}]$ , and  $p = [V_{Zn}^-]$ ) of the nine regimes shown in Figure 1 are considered. The concentration of  $p$ ,  $[V_{Zn}^-]$ , and  $[V_{Zn}^x]$  increases with  $(P_{Se_2}^{1/2})$ . As  $(P_{Se_2}^{1/2})$  increases,  $p$  increases and its concentration dominates causing a transition to  $p = 2[V_{Zn}^{2-}]$  and finally at sufficiently high values of  $(P_{Se_2}^{1/2})$ ,  $p = [V_{Zn}^-]$  will take over. The net concentration of defects as a function of  $(P_{Se_2}^{1/2})$  is shown in Figure 3 for nanowires grown at 923 K. It can be seen that nanowires grown under stoichiometric conditions, close to  $(P_{Se_2}^{1/2})_{min}$  have a net vacancy concentration of the order of  $10^{17} \text{ cm}^{-3}$ . As the Se vapor pressure  $(P_{Se_2}^{1/2})$  increases, it can be seen that the net vacancy concentration increases significantly. The predictions of the defect model (Figures 2 and 3) can be validated by structural, optical and opto-electronic characterization, described in greater detail in the following sections.

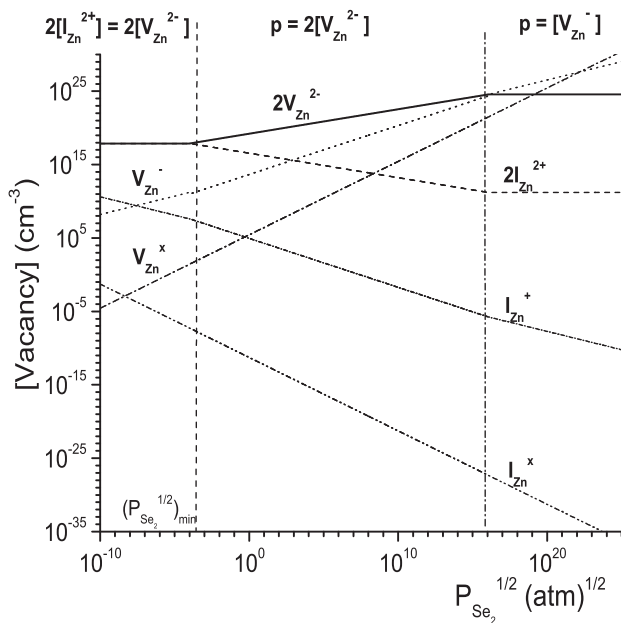


Fig. 2. Defect concentration as a function of Se vapour pressure ( $P_{Se_2}^{1/2}$ ) for nanowires grown at 923 K.

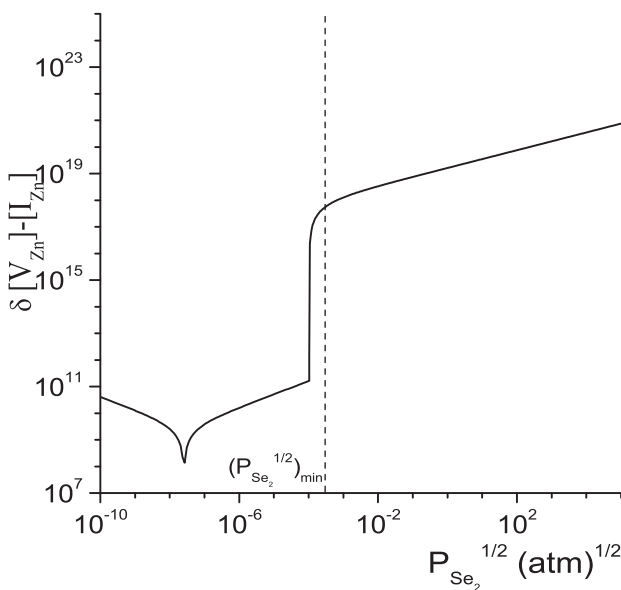


Fig. 3. Net defect concentration as a function of Se vapour pressure ( $P_{Se_2}^{1/2}$ ) for nanowires grown at 923 K.

### 3. ZnSe nanowire characterization

Nanowire morphology and properties are dependent on growth parameters such as temperature, pressure as well as stoichiometry of the component fluxes. A non-stoichiometric component flux enhances the generation of intrinsic point defects that in turn affects the structural, electronic and optical properties of the nanowires. In the case of ZnSe, an increase in the Se vapour flux was found to produce a high density of twinning defects. A brief review of structural, optical and opto-electronic properties of ZnSe nanowires and the dependence of these on growth conditions is presented.

#### 3.1 Structural characterization using electron microscopy

Microstructural analysis of ZnSe nanowires grown under optimized conditions (Philipose, P.Sun, Xu, Ruda, Yang & Kavanagh, 2007) show them to be structurally uniform and free from defects (Figure 4), although a few of the wires (especially those growing in the vicinity of the substrate edge) have planar defects.

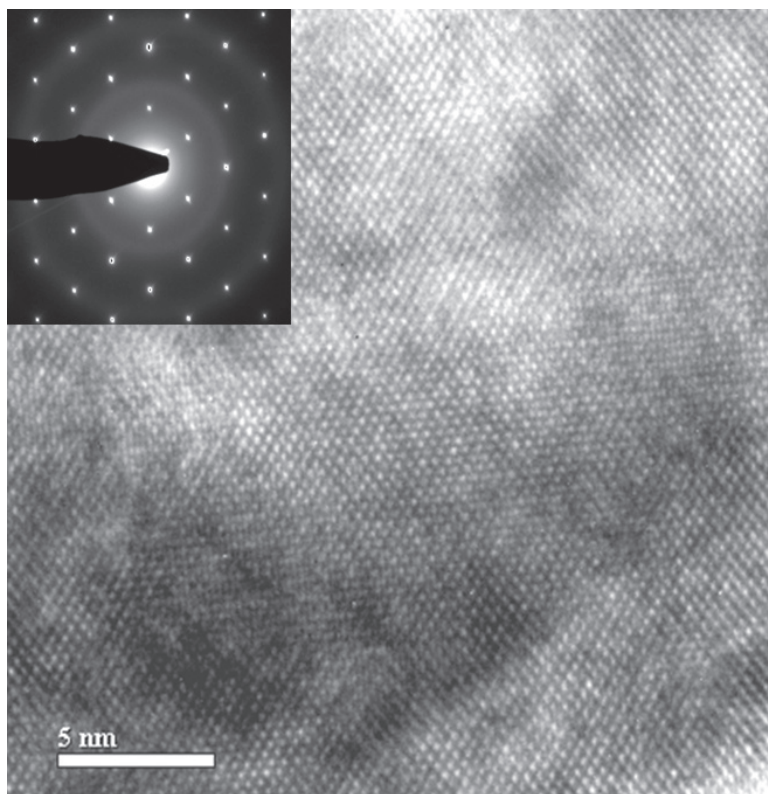


Fig. 4. Net defect concentration as a function of Se vapour pressure ( $P_{Se_2}^{1/2}$ ) for nanowires grown at 923 K.

The growth direction for these nanowires is [111]. The planar defects are twins with {111} twin planes, shown in Figure 5. Based on an analysis of numerous nanowires, it appears

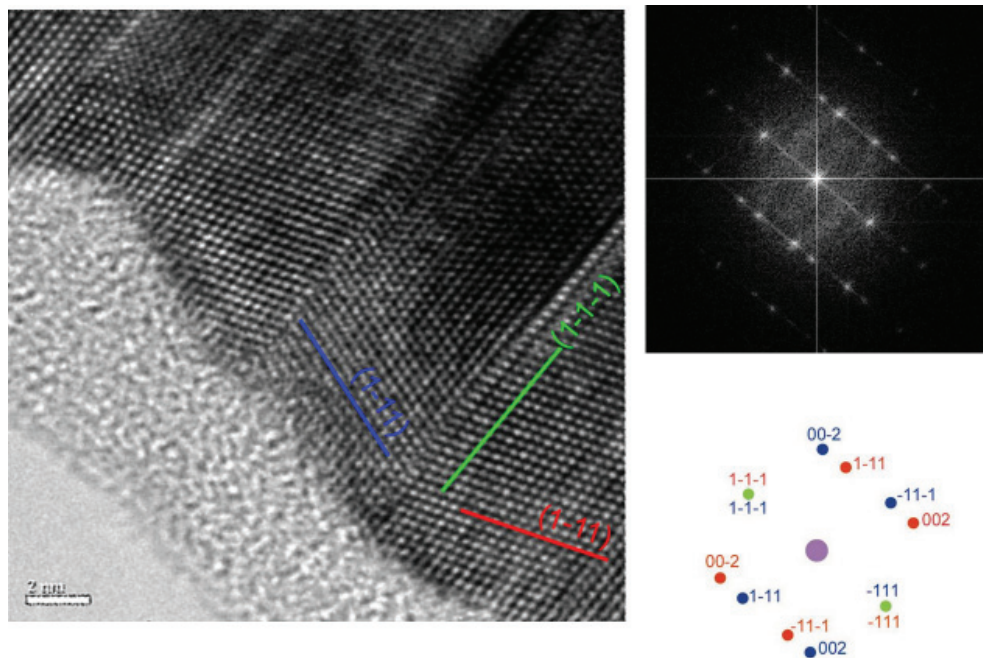


Fig. 5. HRTEM of non-periodic twins in a nanowire grown under Se rich conditions. SAED pattern and its Fourier transform are shown to the right. The drawing, with different colour spots, is indexed. The colour corresponds to colour of line in the HRTEM image.

that fluctuations in growth temperature, size and shape of Au catalytic droplet influence the formation of these defects. Thermal stress during the growth process, residual oxygen and vapor phase non-stoichiometry above the growing nanowires can all contribute to twinning. The high ionicity of ZnSe has also been discussed as a factor contributing to the propensity for this material to twin. In order to understand the dependence of growth direction on temperature, the nanowire has been considered as a column with side surfaces. The total energy of a nanowire includes contribution from the surfaces and from the bulk. Due to the large surface to volume ratio of the nanowires, an important factor controlling the growth orientation is the surface energy. In reference (Chan et al., 2006), the surface energies of the major facets of ZnSe crystal were estimated and though the values for different surfaces were almost comparable, the trend appears to be:  $\gamma_{111B} < \gamma_{100} < \gamma_{311} < \gamma_{110}$ . At low growth temperatures, the area of the side surfaces is relatively insignificant, and hence the contribution from the side surfaces can be ignored. In this case, the nanowires will prefer to grow along the [111] direction, due to the fact that the (111) interface has the smallest surface energy. At higher temperatures, the relative contribution from the side surfaces will be significant and preference is given by the system to the growth direction that will lower the total system energy. The relative importance of surface energy, substrate orientation and role of Au-alloy tip in controlling the growth process remains an open question. For compound semiconductors, the surface energy is not uniquely defined, but rather depends on the relative concentration of constituents through their chemical potentials. The presence of more than

one morphologically distinct nanostructure for a given growth condition suggests that several factors can be contributing to the growth process, with relatively small energy differences involved.

### 3.2 Optical characterization using photoluminescence spectroscopy

A typical room temperature photoluminescence (PL) spectrum of ZnSe nanowires has two characteristic emission peaks – a band edge (BE) emission peak at 2.68 eV (463 nm) and a broad deep defect (DD) emission peak in the region 1.8 – 2.4 eV (500 nm to 680 nm). The origin of the DD emission peak has been attributed to several recombination mechanisms: (i) donor-acceptor pairs (DAPs) involving Zn vacancies and Zn interstitials Philipose, Yang, Xu & Ruda (2007); (ii) DAP transitions caused by thermal exciton dissociation due to laser induced zinc vacancy (Martinez-Canton et al., 2005), etc.. In this section, we review the findings by Philipose et al., (Philipose, Yang, Xu & Ruda, 2007) in identifying the origin of the red luminescence band in ZnSe nanowires. To facilitate this study, the PL spectra of nanowires grown under three different growth conditions were obtained and is shown in Figure 6. The emission spectrum of nanowires grown under near stoichiometric conditions, when the Se vapor pressure is close to  $(P_{Se_2}^{1/2})_{min}$  (curve 2 in Figure 6) shows that the spectrum is comprised of two emission bands with a narrow band edge (BE) peak at 463 nm and a DD band extending from  $\sim 500$  nm to 680 nm. The BE emission peak intensity in some cases is stronger than the DD emission intensity centered at  $\sim 620$  nm. As the Se vapor pressure is increased ( $(P_{Se_2}^{1/2})$  is increased), the emission spectra (curve 3 in Figure 6) shows a complete disappearance of the BE emission peak and the PL spectrum is dominated by the DD emission peak. The amplitude of the BE emission is insignificant. These findings are consistent with the defect model predictions shown in Figure 3, that as  $(P_{Se_2}^{1/2})$  increases, the net vacancy concentration increases. Another interesting feature of the plot shown in Figure 3 is that as the partial pressure of Se vapor is reduced from  $(P_{Se_2}^{1/2})_{min}$ , there is a significant decrease in the net concentration of defects by several orders of magnitude. This was verified experimentally by growing ZnSe nanowires under Zn-rich conditions, i.e., when the partial pressure of Se is lower than  $(P_{Se_2}^{1/2})_{min}$ . The PL spectra (curve 1 in Figure 6) shows an enhanced BE emission with virtually no emission from the defect states. In comparison with curve 2 in Figure 6, there is an enhancement in the ratio of BE/DD emission by more than three orders of magnitude, in agreement with the predictions of the defect model.

### 3.3 Origin of the deep defect emission band in PL spectra

In PL spectroscopy, the simplest recombination process is a band-to-band recombination where a free electron from the conduction band recombines radiatively with a free hole from the valence band. Impurities or defects which introduce traps, donor or acceptor levels in the band gap provide alternate paths for recombination. When both the excited electron and hole are captured by different impurity centers and then the trapped electron and hole recombine radiatively, the process is a 'donor-acceptor' pair (DAP) recombination. Emission bands thus appear in the low energy region of the spectrum resulting from recombination of electron and hole pairs captured at acceptor and donor sites respectively. Recombination of this type reflects the energy difference between the donor and acceptor levels involved in the recombination process involving distant DAPs. The energy of the emission peak

corresponding to recombination of DAPs is given by the equation:

$$\hbar\omega_m = E_g - \left( E_d + E_a - \frac{e^2}{4\pi\epsilon\epsilon_0 R_m} \right) \tag{6}$$

where,  $\epsilon$  is the permittivity of ZnSe =  $8.8(\epsilon_0)$ ,  $\epsilon_0$  is the permittivity of free space =  $8.85 \times 10^{-14}$  F/cm,  $R_m$  is the distance between partners of the DAP and this determines the Coulomb interaction energy (the last term in equation 6),  $E_g$  is the energy band gap of ZnSe = 2.7 eV at room temperature; and  $E_d$  and  $E_a$  are the activation energies of the donors and acceptors. From equation 6, it is also evident that for small separation between donor and acceptor atoms, the energy of the DAP peak is substantially higher than that of the distant pairs. Hence, with DAP recombination, the actual spectral emission curve will depend on the opposing influence of pair distribution function and pair recombination transition probability — there are likely a large number of distant pairs, but their recombination probability will be low, while there will be few closely separated pair which will have a high recombination probability. In this case, the shape of the PL spectrum results from the opposing influence of

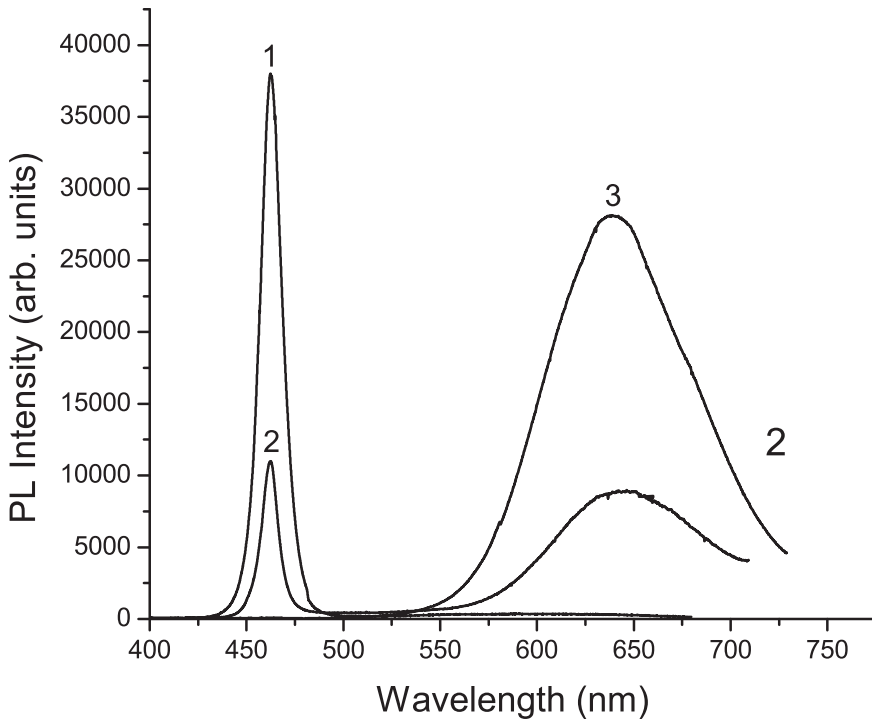


Fig. 6. Room temperature PL spectra of ZnSe nanowires grown under different growth conditions; **Curve 1:** When Se vapour pressure is less than  $(P_{Se_2}^{1/2})_{min}$ , the spectrum is dominated by BE emission; **Curve 2:** When Se vapour pressure is close to  $(P_{Se_2}^{1/2})_{min}$ , there is a significant decrease in the intensity of the BE emission and there is comparable DD emission; **Curve 3:** When the Se vapour pressure is greater than  $(P_{Se_2}^{1/2})_{min}$ , the PL spectrum shows strong DD emission and no emission from the BE states.

the DAP distribution function and the pair recombination transition probability. Studies on bulk ZnSe attribute the origin of the DD emission band (red luminescence band) to such DAP transitions. Vacancies and interstitials having different charged states ( $V_{Se}^+$ ,  $V_{Se}^{2+}$ ,  $V_{Zn}^-$ ,  $V_{Zn}^{2-}$ ,  $Zn_i$  and  $Se_i$ ) will thus introduce different localized energy levels within the band gap and also combine into donor-acceptor pairs (DAPs). The origin and mechanism of formation of the DD emission band in ZnSe nanowires is further explored to provide information on type, energy and concentration of the defects that contribute to it.

The broad defect band shown in Figure 6 is most likely formed by many closely spaced emission lines due to recombination of DAPs with large separation between them and the shape results from the opposing influence of the pair distribution function and the pair recombination transition probability. This emission band was for the first time treated quantitatively (for bulk ZnSe) in Reference (Zacks & Halperin, 1972) using experimental evidence and an expression was derived for the dependence of the peak energy of the DD band on excitation intensity. On increasing the excitation intensity, the peak of the broad DD emission band (corresponding to DAP recombination) shifts to higher energies. In the following section, a detailed study of the dependence of excitation intensity on DD emission for ZnSe nanowires is presented.

### 3.3.1 Dependence of peak position of DD emission band on intensity of laser excitation

To study this dependence, the excitation intensity was varied from about 0.07 mW to more than 2.5 mW for nanowires grown under high Se vapor pressure and for those grown under near stoichiometric conditions, and the shift of the peak position of the DD emission band was studied. Figure 7 shows the influence of excitation intensity,  $I_{ex}$ , on the DAP peak energy,  $h\nu_m$ . As can be seen in the figure, there is a shift in the DAP peak energy to higher energy values with increasing excitation intensity. According to Zacks and Halperin (Zacks & Halperin, 1972), the peak energy of the DAP emission ( $h\nu_m$ ) is related to the excitation intensity  $J$  by the following equation:

$$I_{ex} = D \left[ \frac{(h\nu_m - h\nu_i)^3}{(h\nu_B + h\nu_i - 2h\nu_m)} \right] \times \exp \left[ -2 \frac{(h\nu_B - h\nu_i)}{(h\nu_m - h\nu_i)} \right] \quad (7)$$

where  $I_{ex}$  is the excitation intensity,  $h\nu_m$  is the peak energy of the DAP transition spectrum, and  $h\nu_i$  is the emission energy for infinite R.  $h\nu_i$  is defined by the equation:

$$h\nu_i = E_g - (E_A + E_D) \quad (8)$$

The term  $h\nu_B$  is defined by the equation

$$h\nu_B = E_B + h\nu_i \quad (9)$$

where

$$E_B = e^2 / 4\pi\epsilon\epsilon_0 r_B \quad (10)$$

where,  $E_B$  is the binding energy of the DAP,  $r_B$  is the shallow impurity Bohr radius, and  $D$  is a constant. In the low excitation limit, the DAP peak energy approaches the value of  $h\nu_i$ . The values obtained experimentally (Figure 7) were used for calculating the parameters appearing in equation 7. Using the best-fit line, the value of  $E_B = 18 \pm 0.5$  meV is obtained for nanowires grown under high Se vapor pressure.

From equation 10, the value of  $r_B$  is estimated to be  $9.1 \pm 0.2$  nm for the shallow impurity Bohr radius in nanowires grown under high Se vapor pressure. The value of  $E_i$  is around 1.95 eV,

giving  $E_d$  of  $\sim 0.35$  eV and  $E_a$  of  $\sim 0.40$  eV. Using the value of  $r_B$ , the concentration of the minority defect species,  $[V]$ , can be calculated by using the equation:

$$[V] = \frac{3}{4\pi r_B^3} \quad (11)$$

Hence, the concentration of defects under high Se vapor pressure is  $3.1 \times 10^{17} \text{ cm}^{-3}$ , in excellent agreement with the defect analysis predictions described in Section 2.

The characteristic shift of the DAP peak energy with excitation intensity follows from the fact that at high excitation intensities, widely separated DAPs will be saturated because of their lower transition probability and hence a large fraction of DAPs with smaller radius will be excited. These will then decay radiatively due to their higher transition probability. Hence, an increase in the excitation intensity results in an increase in the relative intensity of PL emission from DAPs with smaller Bohr radius, leading to the observed shift in the DAP peak energy to higher energies as the excitation intensity increases.

Using the above analysis, as well as results obtained from PL measurements, the strong red DD emission in ZnSe is identified as due to a DAP recombination mechanism involving  $V_{Zn}$  as the acceptor species and  $V_{Se}$  or  $Zn_i$  as the donor species. In order to identify the second species in the DAP contributing to the broad DD emission at 1.95 eV and to confirm the presence of Zn vacancies, the as-grown nanowires were subjected to post-growth treatment.

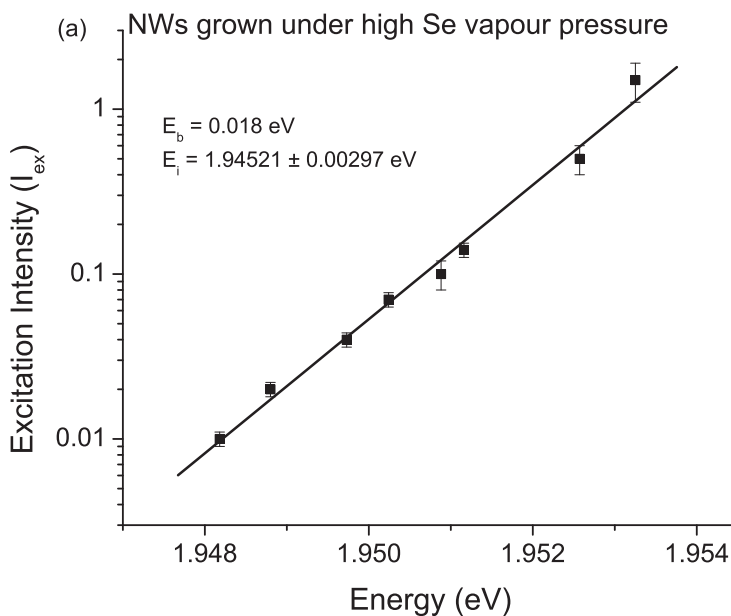


Fig. 7. Dependence of peak energy of the DAP recombination emission band on excitation intensity for growth under high Se vapour pressure.

### 3.3.2 Post-growth treatment of ZnSe nanowires to confirm the role of Zn vacancies in DD emission

In order to confirm the role of  $V_{Zn}$  in the DD emission, as-grown ZnSe nanowires were annealed at  $650^{\circ}\text{C}$  in a Zn-rich atmosphere under a constant flow of Ar gas. Figure 8 shows a comparison of the PL spectra for samples before and after Zn-vapor treatment for 30 minutes and 45 minutes, respectively. A considerable enhancement in the ratio of the BE

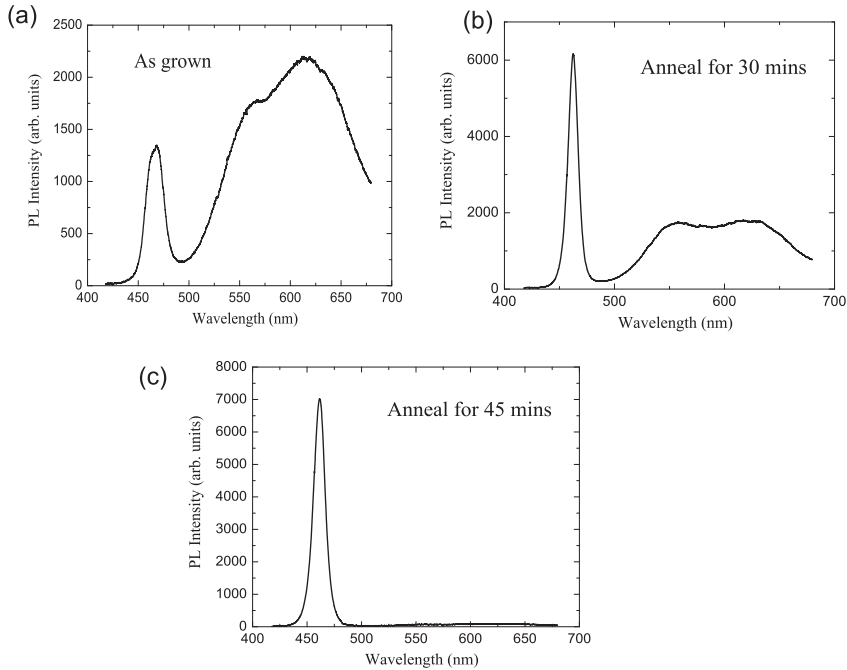


Fig. 8. PL spectra of ZnSe nanowires at room temperature: (a) as-grown nanowires; (b) after treatment in a Zn-rich atmosphere at  $650^{\circ}\text{C}$  for 30 minutes, and (c) after treatment in a Zn-rich atmosphere at  $650^{\circ}\text{C}$  for 45 minutes.

to DD emission intensity can clearly be seen as a result of the annealing process. This ratio increases with annealing time from  $\sim 0.6$  to 87 times. This enhancement may be explained by a reduction in the concentration of  $V_{Zn}$  owing to annealing in a Zn-rich atmosphere, and hence a reduction in the concentration of possible pairs contributing to DAP emission. The temporal dependence thus corresponds to the diffusion of Zn from the vapor into the nanowires. This process has a strong dependence on temperature as is shown in Figure 9. This temporal dependence of BE/DD intensity shows that Zn atoms migrate or 'self-diffuse' through the ZnSe crystal lattice by a mechanism involving vacancies or interstitials. Analyzing the temperature dependence of Zn diffusion from the vapor into the ZnSe nanowires (Figure 9), the activation energy is estimated to be 0.6 eV. Earlier reports on zinc diffusion in ZnSe (Rong et al., 1996) estimates the activation energy for interstitial diffusion to be  $\sim 0.6\text{--}0.8$  eV and that

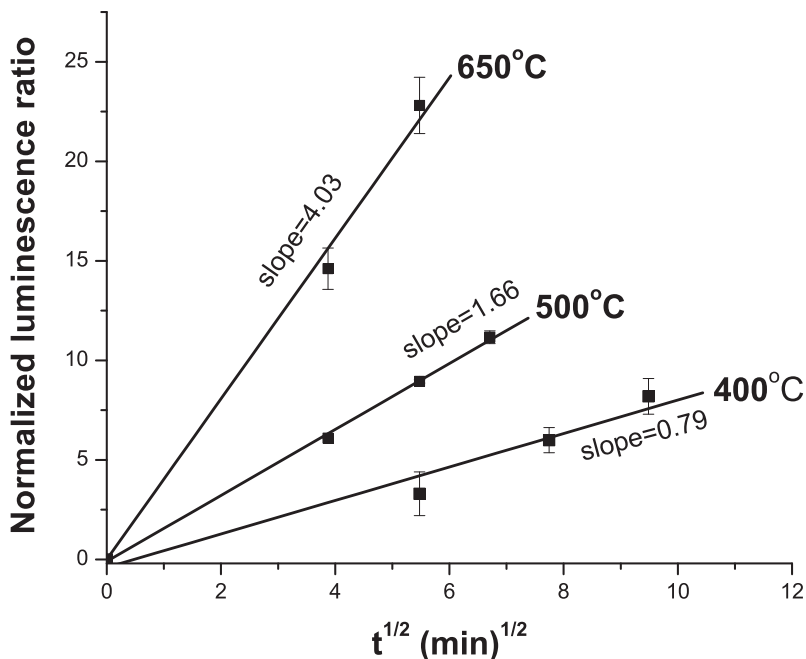


Fig. 9. Effect of temperature on ratio of BE to DD emission intensity of ZnSe nanowires. Nanowire diameters are in the range 80–90 nm.

for vacancy diffusion to be  $\sim 1.26$  eV (Watkins, 1976). The activation energy of 0.6 eV is hence considered suggestive of the fact that zinc interstitials are the mobile species in the diffusion mechanism. As the nanowires are annealed in Zn atmosphere, Zn interstitials diffuse into the vacancy sites and effectively reduces the concentration of DAPs responsible for the DD emission band.

### 3.3.3 Carrier dynamics in ZnSe nanowires

Studies on the ultrafast carrier dynamics can provide important insights into the role played by intrinsic point defects in the optical properties of nanowires. In Reference (Othonos et al., 2007), the authors present their results on transient absorption measurements for stoichiometric and defect-rich ZnSe nanowires, following ultrafast excitation above the band gap. Results of transient absorption measurements on ZnSe nanowires, excited at 400 nm is shown in Figure 10. When the nanowires were probed at wavelengths below the band gap, there was a sharp decrease in the absorption following the excitation pulse. This was followed by an exponential recovery within a few picoseconds. The opposite behavior is observed for probing wavelengths above the band gap. In this case, there is a sharp increase in absorption followed by a recovery to equilibrium. When probing at 450 nm, which is very close to the ZnSe band edge, the induced absorption has a very long recovery to its equilibrium value. This observation is explained on the basis that when a semiconductor is excited with photons

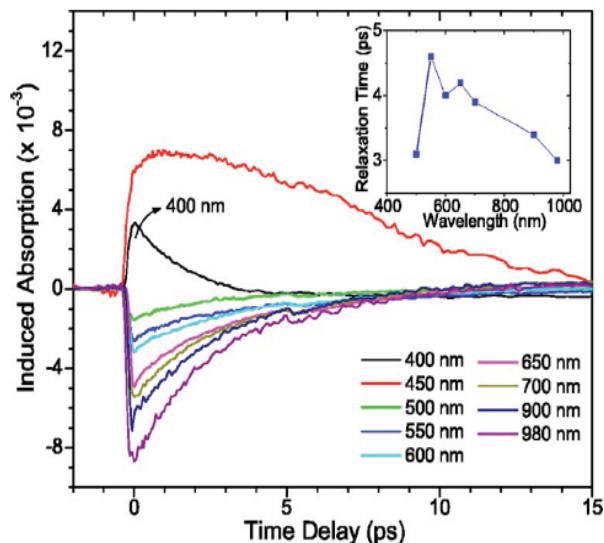


Fig. 10. Time-resolved induced absorption for near stoichiometric ZnSe nanowires. The sample is excited at 400 nm and probed using white light continuum generation. Inset shows the various relaxation rates for the different probing wavelengths.

of energy greater than its band gap, carriers generated within the conduction and valence band will relax to lower energy states within the bands or energy states below the bands originating from IPDs. These photogenerated carriers will contribute towards two competing effects; state filling (SF) and photoinduced absorption (PA). In the SF effect, the occupancy of energy states by the photogenerated carriers will result in a time dependent reduced linear absorption and thus enhanced transmission. In the PA effect, the probing beam will cause carriers occupying certain energy states to undergo secondary excitation to higher energy states resulting in an increase in linear absorption. The amplitude of this increase will depend on the coupling efficiency between the energy states and the number of carriers present in the lower coupled energy states. SF and PA are competing effects and can occur at the same time, thus affecting the intensity of the absorption signal, as is seen in Figure 10. In the stoichiometric ZnSe nanowires under discussion, the large concentration of defects inherent in this material accounts for the fact that SF effect is not observed when probed in the range from 450 – 500 nm. In this range, there is an increase in the temporal absorption due to secondary excitation of the photo-generated carriers. For probing wavelengths in the range of 500 – 550 nm, the transient absorption changes are very small, which could be due to the absence of energy states within this probed region or due to the competing effects of state filling and secondary excitation. When probing above 550 nm (below the band gap), the SF effects dominate and is attributed to the occupation of the IPD energy states causing an observed reduction in the absorption. The observed negative induced absorption will eventually return

to its equilibrium value as the photogenerated carriers move out of these energy states. The relaxation rate for these carriers out of the IPD states is estimated to be  $\approx 3 - 4$  ps.

#### 4. Electron transport mechanism in nanowires

Transport characteristics refer to the motion of electrons in response to an electric field. The two basic processes of current conduction are diffusion of carriers due to a gradient in carrier concentration, and drift of carriers due to the electric field. In 1D electron systems, drift and diffusion of electrons are equally important and any charge distribution relaxes according to the diffusion law with some effective diffusion coefficient enhanced due to the drift phenomena. During transport, the electrons always suffer scattering by impurities, crystal imperfections or with the lattice. In a nanowire, as the diameter of the wire decreases, electrons in the wire become increasingly confined. This affects the scattering of the electrons and causes a change in the electron transport mechanism. Electron transport can occur in the ballistic, diffusive or localized regimes, depending on the system size. In the localized regime, the system is highly disordered and the wave function becomes localized, i.e. the particle gets trapped and transport occurs by hopping. In the ballistic regime of transport, electrons can propagate through the material without scattering and current is determined by the ballistic motion of carriers in the electric field. In the diffusive regime, electrons suffer many scattering events. As the length scale ( $L$ ) of the wire is reduced to the mean free path ( $l$ ) of the electrons, the electron transport mechanism changes from diffusive to ballistic. Electrical conductivity of undoped nanowires is to a large extent controlled by the presence of impurity atoms and defects in the semiconductor crystal lattice. The localized electronic states related to these defects can limit the characteristics of the material by acting as scattering or recombination centers for the charge carriers.

##### 4.1 Transport properties of ZnSe nanowire array

ZnSe nanowire arrays for this study were fabricated by Au-catalyzed VLS mechanism. The nanowires in the array had diameters in the range of 80–150 nm and lengths of several micrometers. The estimated wire density in the array is  $\approx 10^6$  wires/ $mm^2$ . The voids between the wires were filled with 2% PMMA (poly-methyl-methacrylate) in Anisole, which serves as a dielectric. This ensures that the array of nanowires is encapsulated in a dielectric matrix which isolates individual nanowires and forms an insulating layer between the top and bottom electrodes. Au electrodes (1 mm x 1 mm) were evaporated on top of the encapsulated array of nanowires. The back contact to the nanowire array was established using the heavily doped Si substrate. Electrical characterization of the nanowire array was performed using an HP4140B meter at temperatures in the range of 90–400 K. The measured current-voltage (I-V) characteristics are shown in Figure 11. As can be seen, the I-V characteristics have a symmetric and essentially superlinear character with increasing bias. Superlinear I-V characteristics similar to those shown in Figure 11 have been observed in semiconductor nanowires by several groups. This non-linearity cannot be attributed to contact phenomena, for the samples discussed here, where the two contact materials are essentially different, while the I-V characteristic has a symmetric character. The top Au electrode is to the array of nanowires, while the bottom electrode is an indium contact established to the heavily doped substrate. The I-V characteristics are explained by wire non-uniformities (Philipose et al., 2006). In order to explain this observed phenomena, the conductivity of a single nanowire with carrier concentration varying randomly along the wire is considered:  $n = n(z)$  and, for simplicity, with a coordinate-independent mobility  $\mu$ . For relatively low carrier concentration

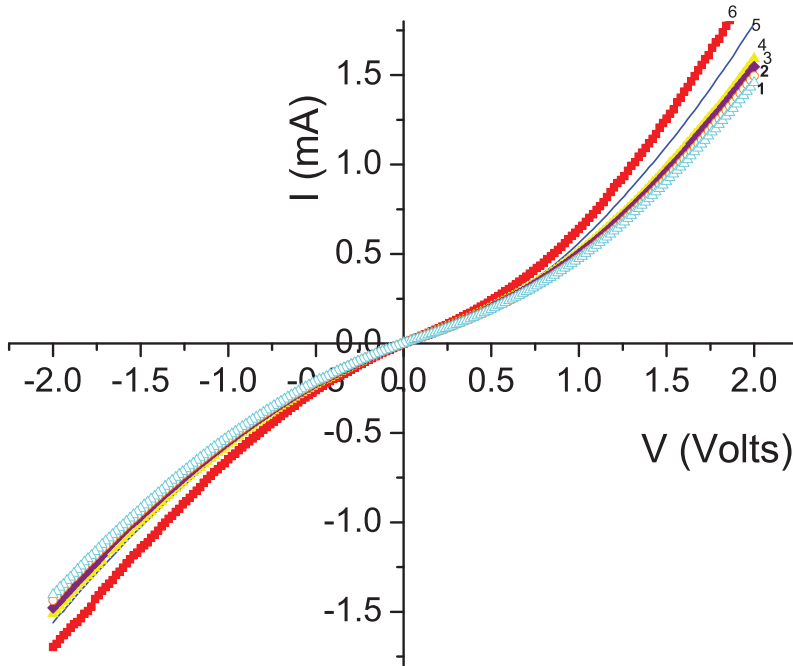


Fig. 11. Experimental current-voltage (I-V) characteristics at the temperatures  $T$  (in K): 90 (1); 140 (2); 200 (3); 250 (4); 350 (5); 400 (6)

samples, this is a reasonable assumption, based on the dependence of  $\mu$  on  $n$ . For a small applied voltage  $V$ , we may consider a wire as a series connection of segments with different conductivities, so that its total resistance is given by:

$$R_o = \frac{1}{e\mu} \int \frac{dz}{n(z)} \quad (12)$$

For the case of very large fluctuations in  $n$ ,  $R_o$  will be determined by the region with minimal  $n$ , or the so-called 'weakest link'. High electric fields applied to the nanowire array will distribute carriers in the sample more uniformly, and, if the contacts are not injecting, such that the total number of carriers does not change, then when  $V \rightarrow \infty$ , the distribution becomes uniform and the resistance tends to a limiting value:

$$R_1 = \frac{L^2}{e\mu} \left[ \int n(z) dz \right]^{-1} \quad (13)$$

where  $L$  is the wire length. For arbitrary  $n(z)$ ,  $R_o$  is always greater than  $R_1$  and the I-V characteristic has a superlinear character (Philipose et al., 2006). The above discussion is for a single nanowire, and the array comprises of many such nanowires contacted by two electrodes

and hence represents a parallel connection of many nanowires and what is measured in Figure 11 is the average conductivity of the nanowires. Details of the inhomogeneity in conductivity of the nanowires comprising the array and its temperature dependence is presented in Reference (Philipose et al., 2006).

A very important property distinguishing this model from other models, also giving a superlinear I-V characteristic (e.g., contact barrier), is the behaviour of differential conductivity  $dI/dV$ , which, being an increasing function of  $V$  at both  $V \rightarrow 0$  and  $V \rightarrow \infty$ , tends to constants of  $1/R_0$  and  $1/R_1$  respectively. The value of the differential conductance, determined from the measured I-V characteristics (Figure 12) shows the values of  $dI/dV$  obtained from the positive branches of the experimental curves of Figure 11 after smoothing. All the curves demonstrate a distinctive trend to saturation at  $V \rightarrow 0$  and  $V \rightarrow \infty$ , which confirms the hypothesis of inhomogeneity-related non-linearity of the I-V characteristic.

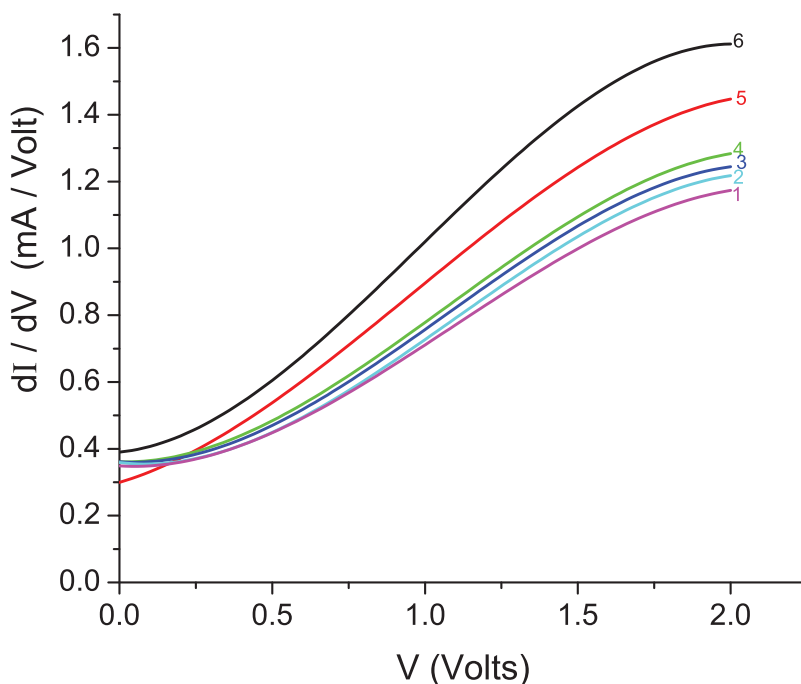


Fig. 12. Differential conductance ( $dI/dV$ ) for positive bias.

#### 4.2 Photoconductivity measurements on ZnSe nanowire array

Photocurrent measurements were performed on the nanowire array using a chopped halogen lamp source and scanning monochromator that covers the spectral range from 400 to 550 nm, with a lock-in amplifier. The spectral response of the ZnSe nanowire array (Figure 13) shows a threshold wavelength at about 463 nm, corresponding well to band edge emission for bulk ZnSe. The array under study was comprised of wires with diameters in the range of 80–150 nm, and due to their large diameters they should not be noticeably influenced by the size

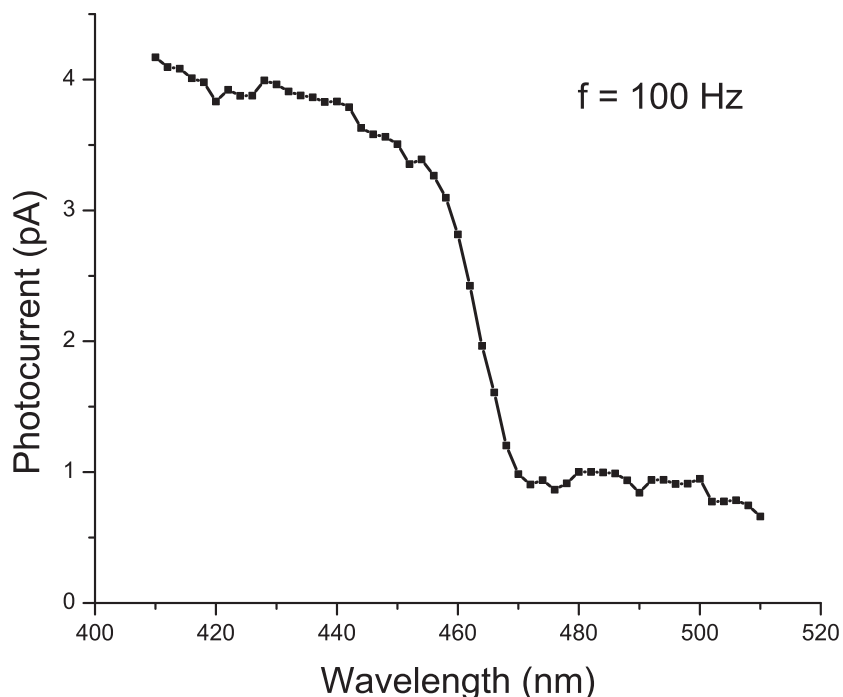


Fig. 13. Photocurrent as a function of wavelength for the ZnSe nanowire array.

quantization. The photoresponse of the ZnSe nanowire array also confirms that the nanowires are well contacted by the top and the bottom electrodes, as a photocurrent in proportion to the illumination flux is measured for these low excitation conditions. The frequency dependence of the photoresponse (Figure 14) shows that the amplitude of the photocurrent reduces with increasing modulation frequency. This dependence may be attributed to a process with characteristic time  $\tau = 3 \text{ ms}$ , presumably related to deep centre capture.

### 5. Surface damage caused to nanowires subjected to laser irradiation

In the optical characterization techniques discussed above, the nanowires were excited using focused laser light at room temperature and in air. It was observed that after prolonged exposure to the laser irradiation, there was a quenching of the NBE emission in the nanowires as shown in Figure 15. Possible factors that could be responsible for this phenomenon are sample heating by laser beam leading to photo-oxidation of the nanowires or radiation enhanced processes including laser-induced point defects generated at the surface of the nanowires. The large surface to volume ratio of the nanowires will enhance the effects of photo-induced adsorption of gases like oxygen on the nanowire surface. Chemical treatments which etch the surface oxide can remove this surface layer as shown in Figure 16, restoring the PL response to its original spectrum. The nanowires that were damaged by laser beam were first examined by SEM and its chemical composition was determined by EDXS. It was found

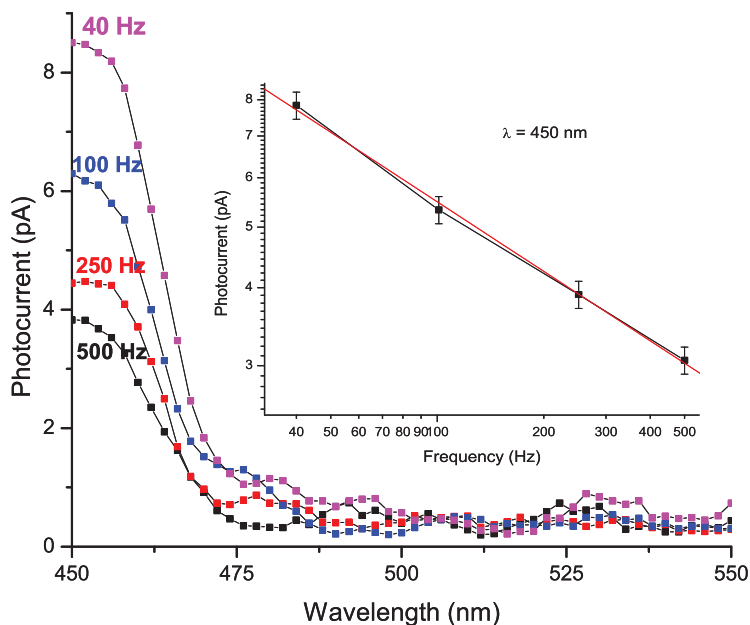


Fig. 14. Frequency dependence of photocurrent for the ZnSe nanowire array.

that the surface of the nanowire appeared roughened after exposure to the laser beam and also there was a higher concentration of oxygen detected at the surface. Hence the nanowires were treated with a solution of  $H_2SO_4:H_2O_2:H_2O$  in the proportion 1:25:1 to etch off the surface oxide layer and restore the intensity of the NBE emission. At this stage, it was not certain if laser induced photo-oxidation was the only modification to the surface of the nanowire after it was exposed to laser irradiation. There is the possibility of laser induced formation of IPDs in the bulk as well as in the surface layer of the nanowire. In order to confirm the dominating phenomenon responsible for the quenching of the NBE emission, the nanowires were exposed to the same intensity of laser radiation, but in an inert atmosphere to prevent photo-induced oxidation. It was found that there was no quenching of the NBE emission; thus confirming that surface photo-oxidation of the nanowires was the dominating phenomena responsible for NBE emission quenching.

## 6. Scanning photocurrent microscopy on nanowires

Scanning photocurrent microscopy (SPCM) is a technique that has been used successfully to quantify the intrinsic properties of nanowires such as its mobility and ascertain the carrier transport mechanisms in nanowires. It has also been used to determine the effect of surface passivation schemes on charge transport in semiconductor nanowires (Gu et al., 2006). A near-field scanning optical microscope (NSOM) is used to map the local photocurrent in individual nanowires contacted by electrodes and the response of the nanowires to local

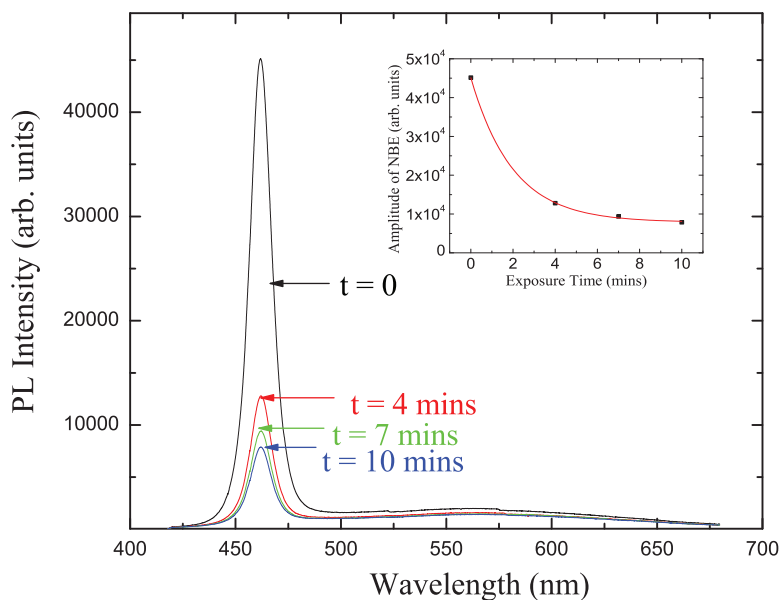


Fig. 15. Comparison of the room temperature PL spectra of ZnSe nanowires after laser illumination for 0 minutes; 4 minutes; 7 minutes; and 10 minutes. The inset shows the change in intensity with laser exposure time.

excitation is studied. Analysis of spatial variation and bias dependence on photocurrent enables determination of photocarrier transport and collection mechanisms. The resulting photocurrent image provides a two-dimensional map of the photocurrent versus NSOM tip position for a fixed electrode bias, as is reported by Y. Gu et al., (Gu et al., 2006). Analysis of the photocurrent profiles at different bias conditions can be used to determine the nature of electron and hole transport in the nanowire as well as a determination of its intrinsic properties.

### 6.1 Surface passivation of nanowires

The chemical and electronic stability of nanowire surfaces is important for its technological advancement. There are several strategies available for nanowire surface modification. Surface passivation can be achieved by the growth of an inorganic shell around the nanowire core or through organic functionalization. Several groups (Chang et al., 2006; Spencer et al., 2009) have reported on surface passivation achieved by the growth of  $SiO_2$  or  $Si_3N_4$  around a nanowire core made of either ZnO or ZnSe. In the case of ZnO, coated with  $SiO_2$ , the electrical properties were found to be influenced by the chemisorption of oxygen on the nanowire surface. Oxygen molecules absorbed at the defect sites of ZnO nanowires act as electron acceptors to form  $O_2^-$  ions, which then deplete the surface electron states and reduces channel

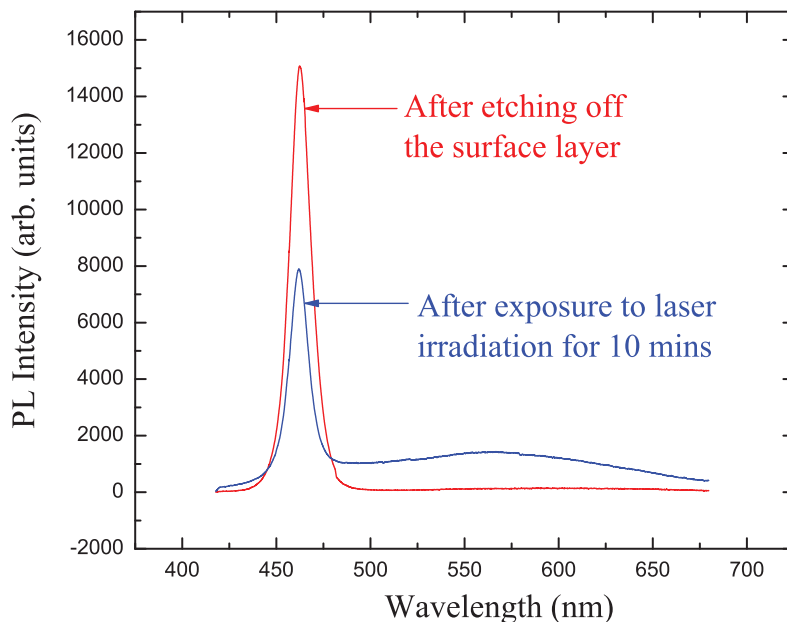


Fig. 16. Influence of etching on the PL intensity of ZnSe nanowires: After exposure to laser irradiation for 10 minutes (blue), and after etching (red).

conductivity. Hence, ZnO nanowire surfaces are passivated with a bi-layer of  $SiO_2/Si_3N_4$ , deposited by PECVD techniques serves as an effective passivating layer. Nanowire surfaces can also be passivated by Sulfur, in which case the nanowires are first etched using dilute HF acid, followed by temperature and time controlled treatment with  $(NH_4)_2S$  aqueous solution. Chloride- and hydride-terminated nanowires can similarly be produced by immersion in aqueous HCl or HF acid respectively.

## 7. Conclusion

Native point defects are always present in semiconductors and they notably affect the electrical and optical properties of the host material. The type and concentration of such defects in nanowires depend on the growth conditions. The optical and electronic properties of nanowires are defined to a large extent by these intrinsic point defects and a high density of defects is detrimental to the development of nanowires for device applications. The localized electronic states related to these defects degrades the characteristics of the material by acting as scattering or recombination centers for the charge carriers. Hence a detailed knowledge of the formation and nature of the defects is mandatory for the development of devices in high performance applications. There are several techniques for characterizing defects which

includes structural, optical and electronic characterization. This chapter presents a brief review of the various techniques used in identifying and quantifying defect concentrations in semiconductor nanowires with special emphasis on ZnSe nanowires.

## 8. References

- Chan, S. K., Cai, Y., Wang, N. & Sou, I. K. (2006). Control of growth orientation for epitaxially grown znse nanowires, *Applied Physics Letters* 88: 013108:1–3.
- Chang, P. C., Fan, Z., Chien, C., Stichtenoth, D., Ronning, C. & Lu, J. (2006). High performance zno nanowire field effect transistors, *Applied Physics Letters* 89(13): 133113:1–3.
- Gool, W. V. (1966). *Principles of Defect Chemistry of Crystalline Solids*, Arkin Publishing, Academic Press, New York.
- Gu, Y., Romankiewicz, J. P., David, J. K., Lensch, J. L. & Lauhon, L. J. (2006). Quantitative measurement of the electron and hole mobility lifetime products in semiconductor nanowires, *Nano Letters* 6(5): 948 – 952.
- Laks, D. B., de Walle, C. G. V., Neumark, G. F., Blochl, P. E. & Pantelides, S. T. (1992). Native defects and self compensation in znse, *Physical Review B* 45(19): 10965–10978.
- Mal, S., Nori, S., Jin, C., Narayan, J., Nellutla, S., Smirnov, A. I. & Prater, J. T. (2010). Reversible room temperature ferromagnetism in undoped zinc oxide: Correlation between defects and physical properties, *Journal of Applied Physics* 108(7): 073510:1–10.
- Martinez-Canton, A., Garcia-Rocha, M., Hernandez-Calderon, I. & Ortega-Martinez, R. (2005). Thermal quenching of the self-activated band of znse:cl thin films grown by molecular beam epitaxy, *Microelectronics Journal* 36(3-6): 527–530.
- Othonos, A., Lioudakis, E., Philipose, U. & Ruda, H. E. (2007). Ultrafast carrier dynamics in band edge and broad deep defect emission znse nanowires, *Applied Physics Letters* 91(24): 241113:1–3.
- Philipose, U., P.Sun, Xu, T., Ruda, H. E., Yang, L. & Kavanagh, K. L. (2007). Structure and photoluminescence of znse nanostructures fabricated by vapor phase growth, *Journal Of Applied Physics* 101: 014326:1–5.
- Philipose, U., Ruda, H. E., Shik, A., de Souza, C. F. & Sun, P. (2006). Conductivity and photoconductivity in undoped znse nanowire array, *Journal of Applied Physics* 99(6): 066106:1–3.
- Philipose, U., Yang, S., Xu, T. & Ruda, H. E. (2007). Origin of the red luminescence band in photoluminescence spectra of znse nanowires, *Applied Physics Letters* 90: 063103:1–3.
- Potzger, K. & Zhou, S. (2009). Non dms related ferromagnetism in transition metal doped zinc oxide, *Physics Status Solidi B* 246(6): 1147–1167.
- Reshchikov, M. A. & Morkoc, H. (2005). Luminescence properties of defects in gan, *Journal of Applied Physics* 97(6): 061301:1–95.
- Rong, F. C., Barry, W. A., Donegan, J. F. & G.D.Watkins (1996). Vacancies, interstitials, and close frenkel pairs on the zinc sublattice of znse, *Physical Review B* 54(11): 7779–7788.
- Spencer, T. L., Cisek, R., Barzda, V., Philipose, U., Ruda, H. E. & Shik, A. (2009). Orientation dependent nonlinear optical effects in znse nanowires, *Applied Physics Letters* 94: 233119:1–3.
- Watkins, G. D. (1976). Radiation effects in semiconductors, 31: 95.
- Zacks, E. & Halperin, A. (1972). Dependence of the peak energy of the pair-photoluminescence band on excitation intensity, *Physical Review B* 6(8): 3072–3075.

## **Part 4**

### **Metal Nanowires**



# Gold and Silver Nanowires for Fluorescence Enhancement

Krystyna Drozdowicz-Tomsia and Ewa M. Goldys  
*MQ BioFocus Research Centre, Macquarie University, NSW,  
Australia*

## 1. Introduction

One-dimensional (1-D) noble metallic nanoscale materials, particularly silver or gold have been attracting wide interest due to their unique optical, electronic, catalytic and mechanical properties. Recently significant interest has been devoted to ultrasensitive detection of trace analytes down to a single molecule level. Various strategies to lower the detection limit for fluorescence-based sensors include increasing the signal from fluorescent dyes that indicate the presence of a specific analyte. Metals such as gold and silver with nanometer scale dimensions (in the 1-100 nm range) exhibit a remarkable optical effect known as localised surface plasmon resonance (Hutter and Fendler 2001, Lakowicz et al 2002 and 2003, Geddes et al 2003a, Geddes et al 2003b, Liebermann and Knoll 2000, Tarcha et al 1998, Tarcha et al 1999, Sokolov et al 1998, Kummerlen et al 1993, Felidi et al 1999, Jensen et al 2000), which is due to resonant photons inducing coherent surface plasmon oscillations of their conduction band electrons. The confinement of the surface plasmon resonance to the nanoparticle dimensions can increase the amplitude of electromagnetic wave by as much as orders of magnitude. This strong electromagnetic field decays exponentially over a distance comparable with nanostructures size. Correspondingly, light intensity near such nanostructures (proportional to the square of the wave's amplitude) is also significantly increased. In such a way noble metal particles through plasmonic confinement, effectively focus resonantly coupled light. As a result, all radiative properties of molecules in proximity of such nanoparticles, such as light absorption, fluorescence, Rayleigh scattering and Raman scattering can be enhanced by orders of magnitude, when certain conditions are met. In particular, metal nanoparticles can modify the properties of close fluorophores. The presence of a nearby metallic nanoparticle can not only enhance fluorophore quantum yield but also stabilize adjacent fluorophores against photobleaching, further enhancing their utility in fluorescence sensing and imaging. However, when fluorophores are very close to the metal surface, the fluorescence quenching effect competes with these favorable effects<sup>2</sup> and it dominates within 5 nm from the surface of metallic particles. At larger distances, the enhancement starts to override the quenching and it reaches its maximum at about 10 nm from the metal surface (Kerker et al 1982, Gersten and Nitzan 1985). At larger metal-fluorophore separation, the enhancement effect progressively decreases. Early studies using colloidal silver or silver fractals deposited electrochemically on glass substrates showed substantial enhancement of fluorescence in the visible range (Geddes et al 2003a, 2003b, Sokolov et al 1998, Kummerlen et al 1993). Larger enhancements were created using more

precisely controlled, regular arrangements of noble metal nano-structures (Corrigan at all 2006, Corrigan et all 2005). Uniform arrays of nanostructures produced narrower resonances; allowing better control of the scattered light and optimization of spectral overlap between the metal particle plasmon resonances and absorption/emission of fluorescent molecules. Fluorescence intensities of up to 350 times of the original value on a bare glass surface had been observed for Ag nanoparticles on an “active” substrate (Guo et all 2008a, Guo at all 2008b) and even higher enhancement factors have been theoretically predicted.

Since last decade it has been anticipated that noble metal nanorods and nanowires offer exceptional potential to modify electromagnetic fields, on the basis of their apparent similarities to simple antennas. Indeed, Schatz et al (Hao and Schatz 2004) have theoretically calculated that isolated nanorods and nanowires show the highest electromagnetic (EM) field enhancement at their ends compared to other nanoparticle shapes, making them potentially attractive substrates for metal enhanced fluorescence (MEF), but very few reports to-date have reported relevant experiments. In our previous work (Goldys at all 2007) we showed that the nanowires were responsible for the fluorescence amplification factors of up to two orders of magnitude. Such amplification factors were induced by plasmon resonance in the nanowires but they were also due to the fact that these nanowires with high aspect ratio and sharp tips act as antennas for the radiating emission from fluorophores. Even higher enhancements can be expected for nanorods aligned end-to-end in one dimension. In such configuration large electromagnetic fields at the neighbouring nanorods can be coupled and used for sensing of single molecules.

In this chapter we explain unique, highly tuneable optical properties of gold and silver nanorods and briefly describe their synthesis. Further, we discuss functionalisation of silver and gold nanorods, designed to bind these nanorods to proteins labelled with fluorophores. These fluorophores are selected so that their excitation-emission characteristics provide the best overlap with plasmon resonances. These nanorods are then used to form well controlled arrays on glass substrates. Here we discuss various arrangements including glass substrates with thin continuous noble metal layer separated by a dielectric spacer from the nanorods. We also show various nanoantenna designs, modelled using Finite Element Method, which are able to efficiently couple light in and out of fluorophores.

## 2. Optical properties of metal nanorods and their effect on fluorescence enhancement

The extinction spectrum of metal nanoparticles consists of two components: scattering and absorption, whose relative contributions depends on size and shape of the nanoparticle. The scattering component is known to be responsible for fluorescence enhancement and the absorption component for fluorescence quenching. Another important parameter, the scattering quantum yield,  $\eta$ , was defined by El Sayed *et al.* (Lee and El-Sayed 2005) as the ratio of the scattering cross section  $\sigma_{\text{sca}}$  to the extinction cross section  $\sigma_{\text{ext}}$  of the nanoparticle:

$$\sigma_{\text{ext}} = \sigma_{\text{abs}} + \sigma_{\text{sca}} \quad (1)$$

$$\eta = \sigma_{\text{sca}} / \sigma_{\text{ext}} \quad (2)$$

Here the extinction cross section is obtained from the imaginary part of the nanoparticle polarizability  $\alpha$  and  $k$  is the wavevector of light ( $k=2\pi/\lambda$ ):

$$\sigma_{\text{ext}} = k \text{Im}(\alpha) \quad (3)$$

The scattering cross-section is also related to polarisability as:

$$\sigma_{\text{sca}} = \frac{k^4}{6\pi} |\alpha|^2 \quad (4)$$

The polarizability is defined through the relationship of the dipole moment  $p$  induced by the applied field  $E_0$

$$p = \alpha E_0 \quad (5)$$

In order for metal nanoparticles to strongly enhance fluorescence several conditions must be met. One of the most important is the spectral overlap of the resonant plasmon position in the metal nanoparticle with excitation/emission spectrum of the fluorophore (Chen et al 2007). The fluorescence enhancement also depends on nanoparticle geometry. This is because only the scattering component of the extinction spectrum of metal nanoparticles contributes to the fluorescence enhancement and its magnitude compared to the absorption component depends on size. For example, it starts to dominate for spherical nanoparticles larger than ~50 nm for silver and ~80 nm for gold. Another important aspect of the plasmon resonance is its linewidth as narrow resonances lead to higher enhancements and higher sensitivity to the local changes in dielectric constant of the environment, which can be also used for molecular sensing. When plasmon oscillations are generated in the metal nanoparticle, they are subject to a number of processes which dampen the collective oscillations and result in the plasmons decay. The plasmon resonance linewidth is inversely proportional to the lifetime of the plasmon and it provides a measure of this decay process. Damping can occur either through radiative or nonradiative processes. Radiative damping occurs when the oscillating dipole moment of the plasmon gives rise to photon emission. Nonradiative damping occurs when the plasmon excites intraband or interband electronic transitions within metal particle or through electron scattering processes at the surface of the nanostructure. Plasmon position and near-field electric fields created near metal particles can be additionally very strongly affected by nanostructure arrangement.

Metal nanostructures can enhance or quench fluorescence by modifying radiative and non-radiative emission rates of the fluorophore as a result of interactions of their plasmon resonances with absorption/emission bands of fluorophore. This effect is observed by changes in fluorophore quantum yield, and its lifetime. Nanorods have particularly favourable optical properties for fluorescence enhancement due to their high tunability of position of plasmon resonances, polarization sensitivity and their long dephasing times leading to strong, narrow spectral resonances.

### 2.1 Tunability of resonance

In 1912, Gans (Gans 1915) predicted that for very small ellipsoids, where the dipole approximation is satisfied, the surface plasmon mode splits into two distinct modes. This is a consequence of the surface curvature, which classically determines the restoring force or depolarization field that acts on the population of confined conduction electrons. He quantified the response as a function of the ellipsoid aspect ratio. For such oblate and prolate spheroid geometry analytical solutions have been found. In this case methods such as discrete dipole approximation (DDA) and numerical calculations such as T-matrix

method are commonly used. Schatz and co-workers have recently reviewed this computational approach (Kelly et al 2003) which can be successfully applied to nanorods, nanowires and nanocylinder structures as confirmed by very good agreement of the calculated and experimentally measured resonance spectra for such particles.

According to Gans's formula, the polarizability of an ellipsoidal metal particle along the  $x$  ( $y, z$ ) axis is given by:

$$\alpha_{x,y,z} = \frac{4}{3} \pi abc \frac{(\varepsilon_m - \varepsilon_0)}{\varepsilon_m + L_{x,y,z} (\varepsilon_m - \varepsilon_0)} \quad (6)$$

Here  $a$ ,  $b$  and  $c$  refer to the length of the ellipse along the  $x$ ,  $y$  and  $z$  axes ( $a > b = c$ ),  $\varepsilon_m$  is the dielectric function of metal,  $\varepsilon_0$  the dielectric constant of the medium at optical frequencies and  $L_{x,y,z}$  is the depolarization factor for the respective axis, which is given by:

$$L_x = \frac{1-e^2}{e^2} \left( -1 + \frac{1}{2e} \ln \frac{1+e}{1-e} \right); \quad (7)$$

$$L_{y,z} = \frac{1-L_x}{2} \quad (8)$$

Here,  $e$  is the rod ellipticity given by  $e^2 = 1 - (b/a)^2$  which can be also rearranged and expressed as a function of the aspect ratio  $R = b/a$ . For a sphere  $e = 0$  and  $L = 1/3$  and Equation /6/ becomes:

$$\alpha_0 = 3V \frac{\varepsilon_m - \varepsilon_0}{\varepsilon_m + 2\varepsilon_0} \quad (9)$$

where  $V$  is the nanoparticle volume. As it is clearly seen by comparing equations /6/ and /9/, for the same effective volume of the nanoparticle, the spectral tunability of the plasmon resonance for elliptical particle is much larger, and it is more sensitive to the aspect ratio than to the absolute particle size.

Finally the extinction of light is related directly to the polarizability by relationship in Equation /3/ and for an assembly of randomly oriented  $N$  ellipsoids the extinction coefficient  $\gamma$  can be calculated according to Gans formula.

$$\gamma = \frac{2\pi N V \varepsilon_0^{3/2}}{3\lambda} \sum_{x,y,z} \frac{\left(\frac{1}{L_{x,y,z}}\right) \varepsilon_{m2}}{\left(\varepsilon_{m1} + \frac{1-L_{x,y,z}}{L_{x,y,z}}\right)^2 + \varepsilon_{m2}^2} \quad (10)$$

where  $V$  is particle volume and  $\varepsilon_{m1}$  and  $\varepsilon_{m2}$  are real and imaginary components of dielectric function of metal nanoparticle and  $\lambda$  is the incident light wavelength.

For ellipsoidal nanoparticles the resonances for light polarized in the longitudinal (LE) direction (along the long axis of the particle) and in transverse (TE) direction are different, hence two peaks are observed in the absorption spectra for randomly oriented assembly of nanorods corresponding to LE and TE modes as calculated according to Equation /10/ and shown in Figure 1.

These relationships show that size and shape of the nanoparticle can control the plasmonic resonances, and thus by varying nanoparticle geometry it is possible to synthesize materials with tuneable extinction spectra. Gans's equations also predict that the LSPR position varies linearly with aspect ratio for small ellipsoids embedded in the same medium and that for the same aspect ratio nanoparticles their plasmon peak position will red shift, when the dielectric function of the surrounding medium increases. These attractive properties

motivated intense experimental efforts to develop controlled synthesis of metal nanorods summarised recently in several reviews (Huang et al 2009, Perez-Juste et al 2005).

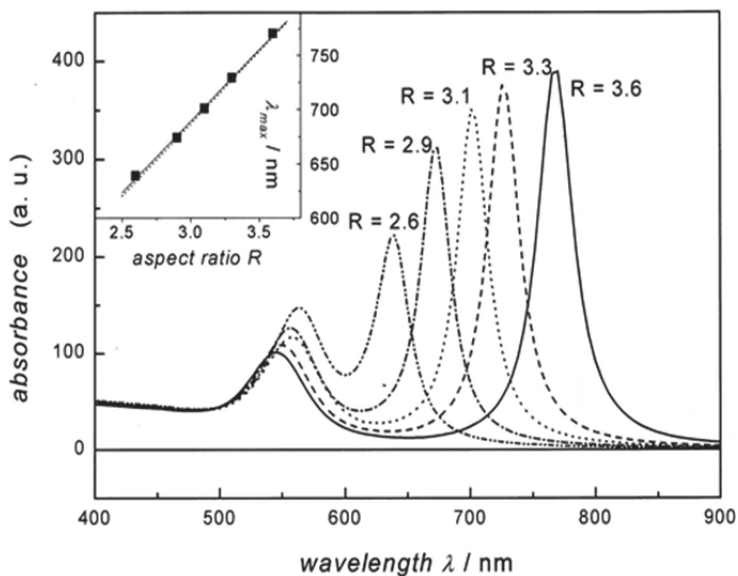


Fig. 1. Calculated absorption spectra of elongated ellipsoids with varying aspect ratios  $R$  using Equation /10/. The medium dielectric constant was fixed at a value of 4. The short wavelength peak corresponds to the transverse mode resonance, and the long wavelength one to longitudinal resonance which is very sensitive to the aspect ratio  $R$ . The inset shows a plot of the peak of the longitudinal plasmon band determined from the calculated spectra as a function of the aspect ratio. The solid line is a linear fit to the data points. (Reprinted from Reference Link at all 1999).

Figure 2 shows that by varying the aspect ratio of gold nanorods it is possible to adjust the plasmon resonance position in a broad spectral range (530 – 1200 nm), but the optimum scattering efficiency is reached for the nanorods with an aspect ratio of 3.4 (Figure 2 b) and for the rod diameter of 60 nm (Figure 2 c). The double peak character of extinction spectra for nanorods allows to predict that uniformly oriented ellipsoids and cylinders should exhibit strong, polarization-dependent optical spectra with tunability of enhancement for two different fluorophores.

Khlebtsov et al (Khlebtsov 2007) used T-matrix formalism to study the multipole resonances in long gold and silver nanorods whose shape was modeled by prolate spheroids and cylinders with flat or hemispherical ends. The particle diameters and aspect ratio were varied from 20 to 80 nm and from 2 to 20, respectively. They found that the parity of a given spectral resonance number  $n$  coincides with the parity of their multipole contributions  $l$ , where  $l$  is equal to or greater than  $n$ , and the total resonance magnitude is determined by the lowest multipole contribution. According to their calculations, multipole resonance wavelengths also obey a universal linear scaling behaviour when plotted versus the particle aspect ratio divided by the resonance number. This remarkable property of multipole resonances can be understood in terms of a simple concept based on plasmon standing waves excited in metal nanowires by an

electric field of incident light (Schider et al 2003). The refractive index sensitivity of the multipole resonance wavelength to a dielectric environment also exhibits linear scaling properties. Specifically, the relative shift of the resonance wavelength is proportional to the relative refractive index increment with a universal angular slope coefficient.

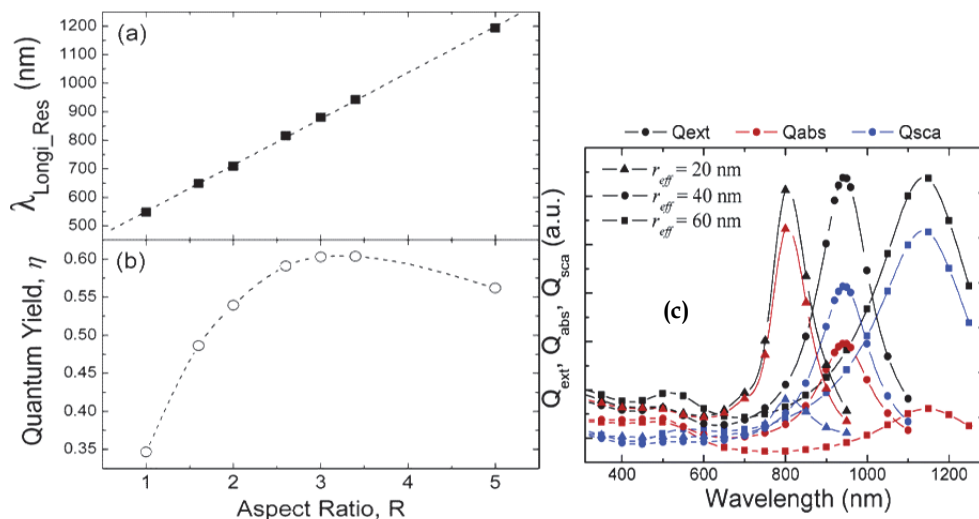


Fig. 2. (a) Dependence of the plasmon peak wavelength and (b) scattering quantum yield of the longitudinal surface plasmon resonance on the aspect ratio. Unlike resonance wavelength, which shows a linear relationship with the nanorod aspect ratio R, the scattering quantum yield increases with increasing R, reaching a maximum at 3.4, and begins to decrease from then on. (c) Relative contributions of light scattering and absorption to the total extinction efficiency for various rod diameters at a fixed aspect ratio of 3.4 for rods illuminated by light polarized in longitudinal direction. Reproduced from Ref. (Lee et al 2006).

## 2.2 Surface plasmon resonance linewidth and dephasing time

Sönnichsen (Sönnichsen et al 2002) and co-workers studied the dephasing of plasmons in single gold nanoparticles and their results are presented in Figure 3. They have found a pronounced reduction of the plasmon dephasing rate in nanorods compared to small nanospheres due to suppression of interband damping. In comparison to the same volume nanospheres, the examined rods showed also much weaker radiation damping. These findings explained higher light-scattering efficiencies and larger local-field enhancement factors for nanorods as compared with nanospheres; features that are especially beneficial for MEF applications.

Other authors (Novo et al 2006, Hu et al 2008) attempted to determine the optimum nanorod geometry that gives rise to the longest plasmon lifetimes by examining plasmon linewidths for nanorods of various width, but with identical aspect ratios. As expected, with the increase of the nanorod width the linewidth broadening was observed due to the increased radiation damping for larger volumes. However, such broadening was also observed for small nanorod width, due to increased surface scattering contribution. It was

found that the optimised nanorod diameter is in the range of 10-20 nm, leading to the narrowest plasmon spectra and the strongest near-field enhancements.

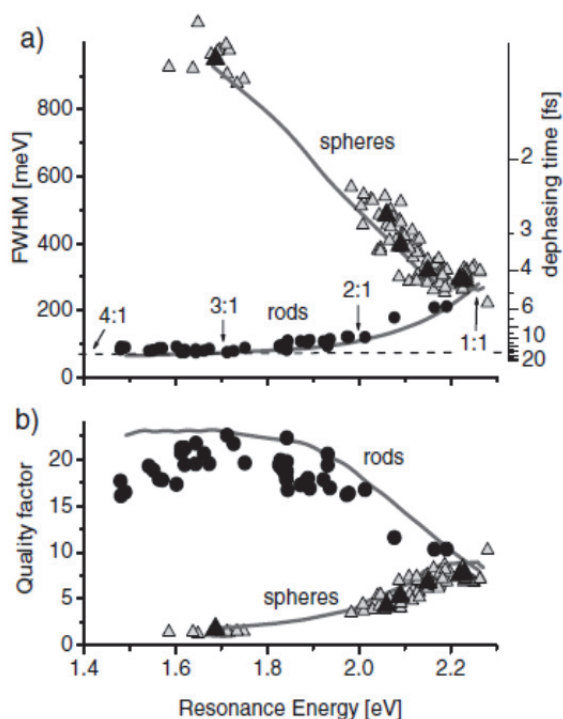


Fig. 3. (a) Measured linewidth ( $\Gamma$ ) of plasmon resonances in single nanorods (dots) and nanospheres (open triangles) as a function of resonance energy  $E_{\text{res}}$ . The right scale gives the dephasing times calculated from  $\Gamma$ . Black triangles: averages for spherical particles of the same nominal size (150, 100, 80, 60, 40, and 20 nm from left to right). Lines: theoretical simulations. Some selected aspect ratios  $b/a$  are indicated in the figure. (b) The same data plotted as quality factor  $Q = E_{\text{res}}/\Gamma$  which is expressed as a ratio of extinction intensity at resonance to FWHM of plasmon peak. Reprinted from Ref (Sonnichsen et al 2002).

### 2.3 Near field effect and coupling

Near field effect around nanoparticle depends on the particle type, size and shape. Silver is known to give more pronounced near field effects than gold due to less pronounced resonance damping by interband electron transitions, as it is known to have a higher energy separation between LSPR and interband absorption. High curvature nanoparticles give a strong field enhancement due to lightning rod-effect (Gersten 1980). Schatz and co-workers used DDA calculations (Hao et al 2004a, 2004b) to compare the electric field enhancement for nanoparticles of various shapes, showing that rods and spheroids with similar sizes and optimum aspect ratios of 3.4 produce similar enhancement in the range of  $>10^3$ , which are one order of magnitude larger than for spheres. The nanorod shows elevated electric fields (EF) at the ends of their long axis while the field is weakest at the centre of the rod and they were slightly higher than EF for spheroid of the same length and diameter as nanorod.

When plasmonic nanostructures are brought in close proximity to one another, their near-fields interact resulting in strong coupling. This effect was observed and most accurately quantified for electron lithographically produced gold and silver nanodisk pairs where clear trends were observed and confirmed by theoretical calculations. Coupled nanorods provide an attractive geometry, due to large oscillator strength and tunability of longitudinal plasmon mode. They were studied in various configurations: side-by-side, end-to-end and at various angles to each other (Funston et al 2009, Slaughter et al 2010). For two identical nanorods, the side-by-side geometry showed a blue-shift of the longitudinal mode and a red-shift of the transverse mode. The end-to-end geometry shows a red-shift of the longitudinal mode with a minor change in the transverse mode compared to the single nanorod spectra (see Figure 4 left). For different size nanorods arranged in the end-to-end geometry an additional antibonding dimer mode was observed on the blue side of the bonding mode peak (Figure 4 right).

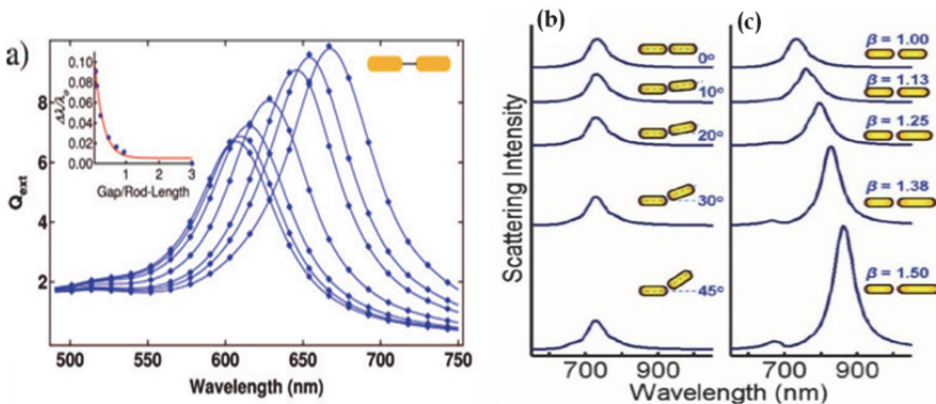


Fig. 4. Left: (a) Polarization averaged extinction of a pair of gold hemispherically capped rods with aspect ratio 2.0 interacting end-to-end as a function of interparticle separations 56.5, 42.4, 28.2, 14.1, 7.1, 5.3, and 3.5 nm with smaller separations more red shifted. Inset: Fractional shift of the longitudinal plasmon band as a function of interparticle distance scaled for rod length. The point at Gap/Rod-Length equal 3 represents the plasmon resonance of a fully decoupled rod with the same dimensions as those in the dimer. Reprinted from Ref (Funston et al 2009). Right: Integrated darkfield scattering spectra with varying angular offset for the pair of same size gold nanorods (b) and for a pair with increasing the length of the right rod starting from 80 x 30 nm in increments of 10 nm  $\beta$ =right rod length/left rod length (c). All spectra are normalized to the linear homo-dimer case. Reprinted from Reference (Slaughter et al 2010).

Su *et al* (Su et al 2003) demonstrated that the resonant wavelength peak of two interacting cylindrical particles is also red-shifted from that of a single particle because of near-field coupling. They found that the shift decays approximately exponentially with increasing particle spacing and becomes negligible when the gap between the two particles exceeds about 2.5 times the particle axis length. The change in plasmon position  $\Delta\lambda$  in respect to plasmon position without coupling  $\lambda_0$  follows a phenomenological equation:

$$\Delta\lambda/\lambda_0 = \kappa \exp^{-s/\tau D} \quad (11)$$

where  $\kappa$  is proportionality factor,  $s$  is the interparticle spacing,  $D$  is the diameter for cylindrical particles or length of long axis in the nanorods and  $\tau$  is the decay length with the value around 0.2. This equation emphasises that  $\Delta\lambda/\lambda_0$  is the same for all particles with the same  $s/D$  values. This behaviour, termed as “Universal Scaling Law”, is a result of interplay of nanoparticle polarizability, which varies as the cubic power of the nanoparticle size and the plasmonic near field coupling, which varies as the inverse cubic power of the distance. It is useful to predict the coupling response from a wide variety of nanostructures. The universal scaling behaviour makes it possible to predict plasmon position shifts upon coupling between homogenous metal particles but is not able to predict the exact plasmon position or near-field strength.

### 3. Nanorod fabrication

#### 3.1 Synthesis methods

Gold nanorods are most often prepared by a seed-mediated approach developed by Murphy's group in 2001 (Jana et al 2001a, 2001b, Murphy et al 2005) in which spherical 'seed' nanoparticles (4 nm diameter) are added to the growth solution containing gold salt, silver nitrate, ascorbic acid, and cetyltrimethylammonium bromide (CTAB) leading to the formation of gold nanoparticles having a rodlike morphology (Figure 5). Gold salt in the growth solution is slowly reduced in the presence of 'seed' particles while the growth-directing agent, CTAB, facilitates rod formation by preferentially binding to the side facets of the nanoparticle. The amount of silver nitrate additive is varied to alter rod length which is controlled by under-potential deposition of silver on the gold nanorod surface. Once synthesized, gold nanorod suspension is purified via centrifugation to remove excess CTAB, unreacted metal ions, and ascorbic acid. This step is important as failure to remove unreacted species will result in morphological changes over time and also to prevent cytotoxicity due to residual CTAB. The same method can be applied to produce silver nanorods. In this case the seed-mediated method uses silver 'seed' nanoparticles prepared by the reduction of silver by strong reducing agent such as sodium borohydride. Gold nanorods are very stable for all aspect ratios but low aspect ratio silver nanorods are usually unstable on the timescale of minutes in air and in light, tentatively attributed to a photo-oxidation process that releases  $\text{Ag}^+$ . However, silver nanowires that are 30 nm in diameter, but up to a dozen microns long, are very stable in these conditions.

In 2003, El-Sayed (Nikoobakt and El Sayed 2003) proposed two modifications to this method: replacing sodium citrate with a stronger CTAB stabilizer in the seed formation process and utilizing silver ions to control the aspect ratio of gold nanorods. This protocol includes two steps: 1) synthesis of seed solution by the reduction of an auric acid in the presence of CTAB with ice-cold sodium borohydride and 2) the addition of the seed solution to  $\text{Au}^+$  stock solution in the presence of CTAB which is obtained by the reduction of  $\text{HAuCl}_4$  with ascorbic acid. Silver nitrate is introduced to the gold solution before seed addition to facilitate the rod formation and to tune the aspect ratio. This method produces high yield gold nanorods (99%) with aspect ratio 1.5 to 4.5 and it avoids repetitive centrifugations. In order to grow nanorods with higher aspect ratios a co-surfactant bezyldimethylhexadecylammonium chloride (BDAC) is introduced to the original solution. By adding this surfactant it is possible to produce nanorods with aspect ratios up to 10 by changing silver concentration (Nikoobakt and El- Sayed 2003). With the Pluronic F-127 co-surfactant system nanorods with aspect ratios up to 20 were produced with good monodispersity (Iqbal et al 2007). In

both methods, the yield, monodispersity, size and fine details of gold nanorods shape are affected by multiple parameters such as seed concentration, size, structure, ascorbic acid and surfactant concentration, the use of other surfactants, additives, solvents and even the aging time.

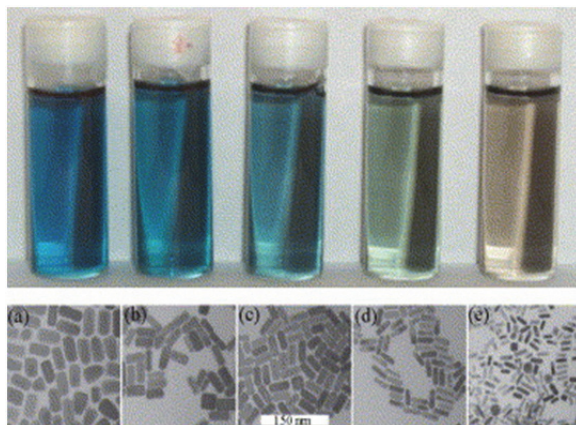


Fig. 5. The colour of gold rods and the respective micrographs. The colour changes take place for very small changes in mean aspect ratio. From Ref (Perez-Juste et al 2005).

Recently, polyol synthesis method developed by Xia and co-workers (Xia et al 2009) has been commonly used for the preparation of single-crystal Ag nanoparticles with uniform size and shape using polyvinylpyrrolidone (PVP) as a protecting agent (Willey et al 2007a, 2007b, 2005) (Figure 6). The same group synthesized Ag nanowires with higher aspect ratios by injection of ethylene glycol (EG) solutions of  $\text{AgNO}_3$  and PVP, added dropwise, at a constant solution temperature of  $160^\circ\text{C}$  (Chen et al 2007, Chen et al 2002). In the polyol process, the introduction of an exotic reagent is considered to be the key factor that leads to the formation of wire-like structures. In their experiments, Ag nanowires are generated using a self-seeding process and EG acts as both solvent and reducing agent, with addition of a trace amount of salt, such as  $\text{NaCl}$ ,  $\text{Fe}(\text{NO})_3$ ,  $\text{CuCl}_2$  and  $\text{CuCl}$  to assist one-dimensional growth. For the formation of silver nanowires, low precursor concentrations and slow addition rates are necessary. By controlling the injection rate, multiple-twined particle formed at the initial stage of the reduction process serve as seeds for the subsequent growth of silver nanowires. It was found that the morphologies and aspect ratios of Ag nanowires strongly depend on the molar ratio between the repeating unit of PVP and  $\text{AgNO}_3$ . When the molar ratio between PVP and  $\text{AgNO}_3$  was more than 15, the final product was essentially composed of silver nanoparticles. When the molar ratio decreased to 6, the resulting product contained mainly nanorods. Using this method, the authors demonstrated high throughput synthesis of Ag nanorods with well controllable aspect ratios (Iqbal et al 2007) and pentagonal silver nanorods Liang et al 2009).

Other methods for gold or silver nanorod synthesis include the electrochemical method (Pietrobon et al 2009, Goldys et al 2007) in which nanorods are grown in an electrolytic solution between two electrodes under controlled currents or template based methods (e.g. synthesis of particles confined within cylindrical membrane pores or synthesized around cylindrical particles). Template-related approaches have been performed with porous

anodic aluminum oxide membranes, carbon nanotubes or block copolymers (Nicewarner-Pena et al 2001). Other advanced fabrication methods such as electron-beam lithography (EBL) were also used to achieve high level of control over shape, position and arrangement of gold or silver nanorod structures (Yu et al 1997, Smythe et al 2007, Billot et al 2006). Assemblies of nanorods with long axis of the nanorods protruding from substrate were also obtained by oblique angle vacuum evaporation (Chaney et al 2005, Liu et al 2006). Examples of synthesised silver and gold nanorods are shown in Figure 5 and Figure 6.

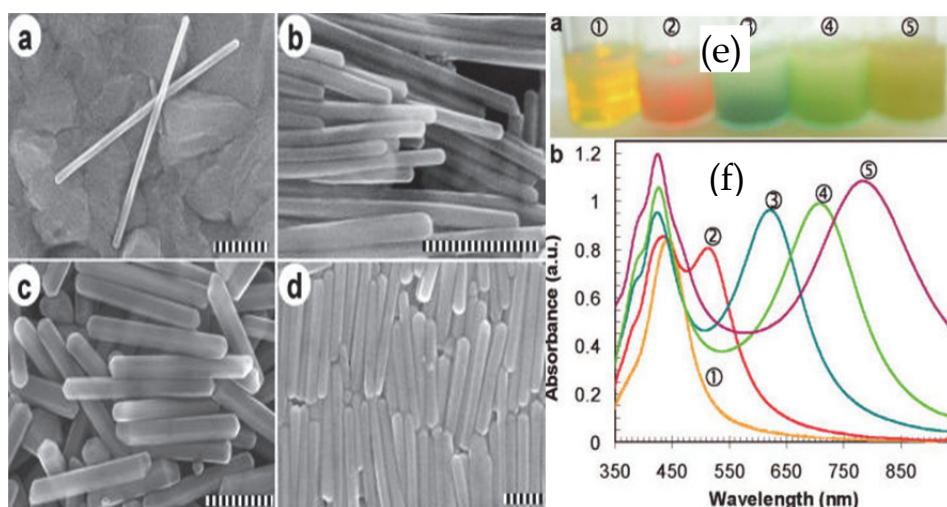


Fig. 6. Left: SEM images of longer pentagonal faceted silver nanorods with the aspect ratios of (a) 8.7 and (b) 10.2; as well as (c) and (d) longer  $2\mu\text{m}$  pentagonal faceted silver rods regrown from ca.  $0.5\mu\text{m}$  rods. The scale bar is 100 nm for (a) and (b) and  $2\mu\text{m}$  for (c) and (d). Right: Optical properties of synthesized pentagonal faceted silver nanorods. (e) Photographs of aqueous dispersions and (f) UV-vis spectra of pentagonal faceted silver nanorods with thickness of  $49.5 \pm 2.5\text{ nm}$  and length of (1)  $62 \pm 3\text{ nm}$ ; (2)  $75 \pm 3\text{ nm}$ ; (3)  $108 \pm 5\text{ nm}$ ; (4)  $142 \pm 7\text{ nm}$ ; (5)  $158 \pm 8\text{ nm}$ . From Ref (Pietrobon et al 2009).

### 3.2 Surface modification

Introduction of surface modification makes it possible to increase stability, facilitate surface chemistry, tune plasmonic properties and broaden practical applications of metal nanorods. For instance, by introducing silver coating on gold nanorods surface it is possible to increase metal enhanced fluorescence due to reduced plasmon damping and to provide a broader spectral range by controlling plasmon peak position. Silica coating can be used to control spacing from the metal surface, it prevents quenching due to FRET and induces red-shift of plasmon resonance position. Silver over-coating is usually carried out by the reduction of silver nitrate with ascorbic acid at base condition in the presence of gold nanorods and a stabilizing agent such as citrate, CTAB and PVP and the silver thickness is controlled by tuning the concentration of silver precursor. Silicon coatings are produced on silver or gold nanorods by dispersing nanorods in solution with 3-mercaptopropyl trimethoxysilane (MPTMS) or 3 mercaptopropyl triethoxysilane (MPTES) and adding aqueous sodium silicate (Obare et al 2001).

### 3.3 Bioconjugation

Biological detection methods based on fluorescence require controlled, specific binding protocols in which signal from fluorescent dye attached to signalling molecule is measured and quantified. To take advantage of the effect of MEF the biological molecule with fluorophore is either attached directly to the nanostructured metal surface or through another molecule using highly specific binding protocols. There is also a fast, growing interest in using gold nanorods in imaging applications of cells in both *in vivo* and *in vitro* due to their exceptional light scattering properties and relatively intense two-photon luminescence (Mohamed et al 2000).

One of the reasons that MEF has not been intensely explored for colloidal silver or gold nanorods is the fact that during their synthesis complex organic molecules such as CTAB or PVP remain on their surface and these molecules are not suitable for biological binding protocols without exchange or complex modifications. Conjugation of biomolecules to gold or silver nanorods can be divided into four different methodologies: direct ligand exchange, the use of biofunctional linker, surface coating and electrostatic absorption. Similarly to other types of gold or silver nanoparticles, thiol exchange is the most common way to replace the capping molecules, since the metal-sulfur bond is known to be stronger than bonds with alternative functional groups (i.e., amines, carboxylic acids, alcohols, and phosphors). Molecules, such as PEG (Grand et al 2003), DNA (Niidome et al 2006), or lipids (Yelin et al 2003) are firstly functionalized with an alkythiolated linker and then bound to gold nanorods through Au-S bonds in a prolonged (few hours) reaction. For complete exchange, sonication and heating might be required to remove CTAB while preventing the nanoparticles from aggregation. For some biomolecules, such as antibodies and proteins, thiolation is complicated by the fact that molecules are too large to reach the gold surface due to dense packing of the CTAB double layers. In this case, small biofunctional molecules such as 3-mercaptopropionic acid (MPA), 11-mercaptoundecanoic acids (MUDA) (Brown et al 2001, Dai et al 2008) and cysteamine (Li et al 2006) are suitable replacements. As most thiol molecules are not water-soluble, the use of organic solvents (such as ethanol and chloroform) and phase extraction are needed. This presents challenges for the modification of gold or silver nanorods as they easily aggregate in organic solvents. The easiest way to prevent this aggregation is to adsorb charged proteins, such as antibodies, by electrostatic forces. At pH higher than the isoelectric point (pI), the proteins are negatively charged, and therefore they can be directly adsorbed to metal nanorods via electrostatic attraction. However, the protein/rod ratio needs to be optimized to avoid the aggregation of the nanoparticles due to charge neutralization while ensuring high loading of the protein onto the nanorods.

Despite the fact that gold and silver nanorods produced by seed mediated methods are characterized by the most controllable and tunable LSPRs, more work is required to demonstrate their full potential for metal enhanced fluorescence.

## 4. Experimental examples of MEF on metal nanorods

Since the synthesis of gold nanorods with decent yield and monodispersity has been developed comparatively recently, only a few papers were published related to their application in MEF. Up to date, the majority of biological applications of metal nanorods is based on direct observation of changes in position of plasmon resonances upon binding with molecules, which can involve agglomeration, binding in end-to-end pairs or release of

molecules which fluorescence is otherwise quenched, or in imaging applications, utilizing their strong anisotropic light scattering properties. Imaging applications often use dark field microscopy to improve contrast and take advantage of excellent scattering properties of metal nanoparticles. As the scattering cross-section of gold nanoparticles is very high, they offer better visibility than fluorescent dye molecules and are therefore very well suited for biomedical imaging using reflectance confocal microscopy and for *in vivo* imaging using optical coherence microscopy. In the case of white light illumination using simple dark field microscopy, which is suitable for cellular imaging, the particles scatter strongly around the spectral position of surface plasmon resonance making them individually recognizable by their colour that is dependent on the particle size and shape. Applications involving modifications of fluorophore emissions in close proximity to metal nanorods are just only starting to appear in literature due to limitations in commercial availability of metal nanorods with functionalized surfaces for biological conjugations.

#### 4.1 Polarisation dependence

The geometry of nanowires and nanorods is clearly compatible with strong polarisation effects, and it is therefore surprising that this property in MEF has only just been demonstrated by Ming *et al.* (Ming *et al.* 2009). This group described strong excitation polarization dependence of the plasmon-enhanced fluorescence on single gold nanorods. The nanorods were encapsulated in a thin  $\sim 20$  nm silica shell, while the nanorods were about 90 nm long and 42 nm wide, with an aspect ratio of  $\sim 2.1$ . The authors showed that fluorescence from the organic fluorophores (Oxazine 725 perchlorate) embedded in a mesostructured silica shell around individual gold nanorods is enhanced by the longitudinal plasmon resonance of the nanorods. This enhancement is the greatest (by a factor of 56) when the excitation energy is matched to the longitudinal plasmon energy. The polarization dependence of the plasmon-enhanced fluorescence is due to the dependence of the averaged electric field intensity enhancement within the silica shell on the polarisation of the excitation beam. Under off-resonance excitation, the electric field intensity contour around a nanorod rotates away from the length axis as the excitation polarization is varied. As expected, the fluorescence enhancement factor increases as the longitudinal plasmon wavelength is tuned close to the excitation wavelength by varying nanorod length. Furthermore, the emission spectrum of the fluorophore is modified by the longitudinal plasmon resonance of the gold nanorods, a phenomenon attributed to the enhanced probability of fluorophore transition from the excited state to a specific vibrational ground state with the transition energy close to the plasmon resonance energy. The authors did not consider the possibility of strong coupling between fluorophores and plasmons, which is also able to produce similar spectral deformations. A linear correlation between the modified emission peak wavelength and the longitudinal plasmon wavelength was observed.

#### 4.2 Complex nanowire geometries.

It is not necessary for nanorods or nanowires to have uniform shapes in order to show attractive optical properties. Any elongated shape is capable of similar pattern of fluorescence enhancement as long as there is adequate electrical contact between nanowire subsections. This has been illustrated in the publication of He and Zhao (He and Zhao 2009). In this work novel silver chain-like triangular nanoplate assemblies (CTNAs) were synthesized via a solvothermal approach. The shape of CTNAs was determined by synthesis

parameters, including the concentration of PVP, reaction time and temperature. Each CTNA is a combination of one dimensional nanobelt and two-dimensional nanoplates. The edges of the nanoplates in the assembly are parallel to each other in order to lower surface energy. Interestingly, this novel nanostructure is able to show high enhancement factors in metal-enhanced fluorescence. Typically, 88- and 13-fold enhancement in the emission intensity of dye Rhodamine B were, respectively, achieved on the surface of silver colloids and silver coated-glass. The silver nanostructures were coated with PVP to ensure nanoscale separation between the metal and fluorophores. Our own studies (Goldys et al 2007) showed that electrochemically deposited silver structures with nanowires of 50–100 nm in diameter demonstrated high up to 57 times fluorescence amplification of conjugated to HSA protein, FITC fluorophore and strongly reduced fluorescence lifetimes. Both quantities depended on the structure thickness. With increasing thickness of the silver nanostructure the fluorescence amplification proportionally increased in correlation with strongly reduced fluorophore lifetimes. This thickness dependence was caused by fluorophore interaction with plasmon excitations in coupled nanowires extending over micrometer size regions. Thus the amplification was attributed to a combination of extended structure area and strong plasmonic coupling between nanowires which also helped to radiatively scatter via lighting rod effect the fluorescence emission. Another system (Drozdowicz-Tomsia et al 2010) investigated in our group contained complex elongated silver fractal nanostructures grown on silicon. Fluorescence of Deep Purple fluorophore in this structure showed uniform enhancements (average factor of 40) dominated by emission enhancement, and this was achieved by good correlation of fluorophore emission with plasmon position for such system.

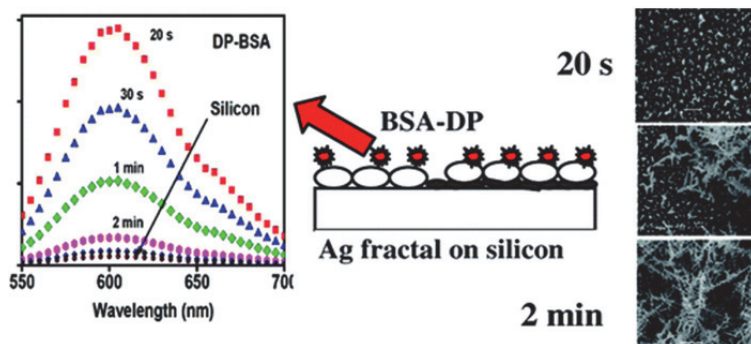


Fig. 7. Fluorescence enhancement study of BSA-Deep Purple (DP) fluorophore conjugate on silver fractal deposited by electroless deposition on silicon. Left: fluorescence spectra of DP for various silver growth times, middle: schematic of experimental sample, right: SEM images of silver fractals at various growth times. Reproduced from Ref (Drozdowicz-Tomsia et al 2010).

### 4.3 Nanorod-modified surfaces

The advantage of columnar geometry with nanorods coating the surface was realised as early as 2005 with the work by Aslan et al (Aslan et al 2005) who attempted to create a fast and inexpensive method of metal surface modification that would show at least some advantages of nanolithography. They developed two new techniques for the deposition of

silver nanorods onto conventional glass substrates. In the first method, silver nanorods were deposited onto 3-(aminopropyl)triethoxysilane (APTMS)-coated glass substrates simply by immersing the substrates in the silver nanorod solution. In the second method, spherical silver seeds that were chemically attached to the surface were subsequently converted and grown into silver nanorods in the presence of a cationic surfactant and silver ions. The size of the silver nanorods, ranging from tens of nanometers to a few micrometers, was controlled by sequential immersion of silver seed-coated glass substrates into the growth solution and by the duration of immersion. Atomic force microscopy and optical density measurements showed that the silver nanorods deposited onto the surface of the glass substrates were irregularly deposited. These new surfaces have been applied to MEF where they performed much better compared to traditional silver islands or colloid films, with amplification factors between 10 and 50.

The same idea has been explored in a more recent publication from Halas group (Bardhan et al 2009) who enhanced fluorescence of an infrared dye IR800 with gold nanorods and nanoshells. Fluorescent molecules emitting at wavelengths in the physiologically relevant "water window" (700-900 nm) are of particular interest due to large penetration depth of near infrared (NIR) light in most biological media and offer the potential for imaging at significant depths in living tissues. However, achieving bright fluorescent emission with photostable and biocompatible near-IR fluorophores has proven to be extremely difficult, prior to this work. Several interdependent processes are responsible for IR800 fluorescence enhancement, these include absorption enhancement, scattering enhancement, and radiative decay rate enhancement. In this report, the scattering efficiency of a nanoparticle appeared to provide the most important mechanism for improving the quantum yield of a fluorophore. Nanorods preferentially enhance the emission of the fluorophore by absorption enhancement, owing to the high-intensity near field resulting from the longitudinal plasmon resonance. However, due to the significant difference in scattering cross sections of nanoshells and nanorods, it is apparent that nanoshells increase the coupling efficiency of the fluorescence emission to the far field more efficiently than nanorods. This explains the 40-fold fluorescence enhancement observed for IR800 bound to nanoshells compared to the 9-fold enhancement for IR800 bound to nanorods. The radiative decay rate enhancement of the fluorophore is dependent on both the scattering efficiency as well as the absorption efficiency of nanoparticles. This explains why nanorods enhance the quantum yield of IR800 by 74% as well as considerably decrease the fluorophore's lifetime.

#### 4.4 Applications of nanorods in SERS

Surface-deposited nanorods have also been tested with respect to their surface-enhanced Raman scattering (SERS) properties (Guo et al 2009). These authors established the correlation of the shape and position of surface plasmon resonance with SERS properties of gold nanorods in dilute colloids. A series of gold nanorods with various aspect ratios was prepared via an improved seed-mediated technique. As discussed previously, increasing the aspect ratio finely tunes the position of the longitudinal plasmon mode of the nanorods in a wide spectral range. The subtle influence of surface plasmon resonance on SERS was then demonstrated by gradually tuning the plasmon wavelength across a fixed excitation line. The authors demonstrated that close overlap of surface plasmon and the excitation line maximizes the SERS enhancement. Tao et al. (Tao et al 2003) have earlier attempted to create a similar SERS surface by using a Langmuir-Blodgett method for silver nanorod

deposition. They assembled large area (over 20 cm<sup>2</sup>) monolayers of aligned silver nanowires that were 50 nm in diameter and 2-3 μm in length. Their nanowires had pentagonal cross-sections and pyramidal tips. They were close-packed and aligned parallel to each other. The resulting monolayers deposited on nanowires were tested for SERS with electromagnetic field enhancement factors of  $2 \times 10^5$  for thiol and 2,4-dinitrotoluene, and  $2 \times 10^9$  for Rhodamine 6G. Another example are the studies by Oyelere et al. (Oyelere et al 2007) who used nanorods to observe enhanced Raman bands from the nucleus of both cancer and non-cancer cells. In this study, the nucleus localization signal from binding peptide was conjugated to gold nanorods via a thioazide linker, and the incubation of the conjugates with cells led to preferential accumulation of the nanorods inside the cellular nucleus. Using a micro-Raman spectrometer with excitation at 785 nm, DNA backbone vibration and guanine Raman bands from a single cell were clearly observed. Normal and cancer cells showed fingerprint differences which could be useful for molecular cancer diagnosis. In the recent studies by Huang et al. (Huang et al 2007) the assembly of gold nanorods by cancer cells due to the binding of the anti-EGFR-conjugated rods to the over-expressed EGFR (epidermal growth factor receptor) on the cancer cell surface has given highly enhanced, sharp, and polarized SERS, while no SERS was observed from the majority of the normal cells.

#### 4.5 Applications of nanorods for resonant energy transfer

While metal nanostructures are known to extend the range of resonant energy transfer, there is very limited literature on the application of nanorods. Zhou et al. (Zhou et al 2010) reported efficient plasmon-mediated excitation energy transfer between the CdSe/ZnS semiconductor quantum dots (QDs) across silver nanorods array consisting of nanorods with lengths up to 560 nm. The sub-wavelength imaging and spectral response of the silver nanowire arrays with near-field point-source excitations have been also theoretically simulated. This nanowire array showed efficient exciton-plasmon conversion at the input side of the array through strong near-field coupling, directional guiding of waves and resonant transmission *via* half-wave plasmon modes of the nanowire array, making possible sub-wavelength imaging at the output side of the array. These advantages allow a long-range radiative excitation energy transfer with a high efficiency and good directionality.

#### 4.6 Nanowires on metal films

A number of recent works have been focusing on using metal nanowires with a columnar morphology protruding from metal films. These films have been produced by using oblique angle deposition (OAD) technique. (Latakhia and Messier 2005, Messier and Latakhia 1999). The growth mechanism is based on self-organized nucleation of nanoparticles and subsequent highly directional growth due to atomic shadowing of the nanoparticle flux reaching the substrate at a large, oblique angle with respect to the substrate normal. The OAD substrates have been recently used for surface enhanced Raman effect for virus detection (Shanmukh et al 2006). The application in MEF has been demonstrated only recently (Abdulhalim et al 2009). In this work metal enhanced fluorescence from porous, metallic sculptured thin films was demonstrated for sensing of bacteria in water. Enhancement factors larger than 15 were observed using structures made of silver, aluminium, gold, and copper with respect to their dense film counterparts. The structures used are assemblies of tilted, shaped, parallel nanowires prepared with

several variants of the oblique-angle-deposition technique. Comparison between the different films indicates that the enhancement factor is higher when the tilt is either small (30 deg) or large (80 deg); thus, the enhancement is higher when only a single resonance in the nanowires is excited.

Several mechanisms can contribute to the MEF from metallic OAD substrate, firstly such structures can act as reflective interfaces, secondly they constitute a porous material with high surface-to-volume ratio, and finally, metal nanorods enhance the local electromagnetic field and act as nanoantennas. The dipole-dipole coupling between neighbouring nanorods is also expected to play a role. The dipole-dipole interaction occurs when light incident on a nanorod induces across it an electric field that depends both on the shape of the nanorod and on the contributions from the neighboring nanorods. Near-field effects are important for internanorod distance much less than the wavelength while far-field effects can play a role for nanorods of larger size.

#### 4.7 Single nanorods and MEF

Recently, Fu, Zhang and Lakowicz (Fu et al 2010) used a single nanorod to enhance emission of fluorophore molecules coupled to one of its ends. Through covalent linkages of fluorophores at the preferred longitudinal axis of the nanorods, they were able to increase the overall optical signal for improved sensitivity. Their nanorods had an average aspect ratio of 6 (ca. 80 nm in length and 13 nm in diameter) and the longitudinal plasmon band at 980 nm. Functionalization of the nanorods was performed with biotin, however only on rod ends, owing to the difficulty of replacing CTAB molecules on the sides of the nanorods. Binding of thiol molecules to the end of the gold nanorod tips was mediated by streptavidin. The functionalized nanorods were incubated with a low concentration of oligonucleotides labelled with biotin and Cy5 (Biotin- 3'-AGG-TGT-ATG-ACC-GGT-AGA-AG-5'-Cy5, ca. 8 nm in length) to obtain hybrid nanocomplexes. This linker molecule has been optimized for best fluorescence enhancement. Much higher fluorophore emission rate has been clearly observed, approximately 40-fold greater than that observed in the absence of gold nanostructure. Additionally, polarization dependence of the excitation was demonstrated on a single Au nanocomplex excited at different directions. The emission intensity decreased abruptly as the excitation angle rotated 90° as for this orientation transverse plasmon excitations were excited in gold nanorods. These occur at much shorter wavelengths and out of resonance with fluorophore excitation/emission. The magnitude of the enhancement also depends on the location of the fluorophore around the particle and the orientation of its dipole moment relative to the metallic surface.

### 5. Theoretical simulations

Theoretical simulations of spontaneous emission of fluorophores coupled to nanoantennas were carried out by Giannini et al. (Giannini et al 2009). The modification of the corresponding radiative and nonradiative decay rates and resulting quantum efficiencies was calculated by means of the rigorous formulation of the Green's theorem surface integral equations. Resonant enhancement of the radiative and nonradiative decay rates of a fluorescent molecule was shown when coupled to an optical dimer nanoantenna. A numerical example was presented comprising two silver rectangular nanowires with the dimensions of each rectangle 20 x 200 nm, with a gap of 10 nm. Upon varying the dipole

position, it was possible to obtain preferential enhancement of radiative decay rates over the nonradiative counterpart, resulting in an increase of the internal quantum efficiency. For emitters positioned in the gap, quantum efficiency enhancements from the initial value of 1% to 75% was possible, however emitters that are originally more efficient can not be enhanced as much.

Kappeller *et al* (Keppeler et al 2007) studied locally enhanced optical fields created near tunable laser-irradiated metal nanostructures acting as local probes. Using three dimensional simulations with a commercial COMSOL Multiphysics software package based on the finite element method (FEM) they have shown electromagnetic fields near various optical antennas and optimized their geometry in order to obtain a strong enhancement in a selected frequency range and the results are shown in Figure 8 below. They compared three antenna designs: a) a self-similar antenna, which is consisting, of four overlapping gold nanospheres each smaller than the previous by scaling constant with tip of 10 nm radius, b) conical antenna, which has the same length and outside front and end curvatures as previous antenna and c) nanorod antenna, which has 200 nm length and 20 nm diameter.

According to their calculations the strongest lighting rod effect was observed for self-similar antenna, slightly weaker for conical antenna and the most complex for nanorod antenna where bright and dark modes were observed at different spectral resonance conditions. This suggests that strong lighting rod effect desirable for MEF can be achieved when the length of the nanorods is carefully tuned to emission of fluorophore.

## 6. Conclusions

Silver and gold nanorods have shown excellent optical properties suitable for a wide range of applications including MEF, SERS and resonant energy transfer. In this chapter we outlined the basic theory of optical properties of the nanorods, centred around their polarisability. We highlighted the opportunities they provide to tune plasmonic properties by varying the details of nanorod shape and size. For MEF applications the key parameters of relevance are the match of fluorophore emission and excitation to plasmonic characteristics, because at these wavelengths the near-field enhancement of the electromagnetic fields are maximised. The plasmon linewidth and plasmon dephasing time are also relevant as long dephasing times lead to increased fields. The effect of inter-particle coupling can also be exploited to maximise MEF, as well as the fact that complex geometries for example nanorods on a metal film may provide not only improved plasmon coupling but also better fluorescence out-coupling efficiency and high surface areas. Polarisation properties of aligned nanorods have been reported, but are yet to be exploited more fully. Theoretical work in this area is facilitated by the availability of commercial software packages such as COMSOL Multiphysics, but those attempting to use them should carefully match the simulated results with experiments, which still present a challenge. Further challenges remain in the areas of nanorod synthesis and post-processing discussed in the second part of this chapter. These include the understanding of nanorods chemistry, their functionalisation, controllable assembly and stability. Despite this (or perhaps because of this) we expect this area to continue rapid progress, stimulated by the increasing commercial availability of nanorods including their bioconjugates and a wide range of significant applications in biosensing and bioimaging.

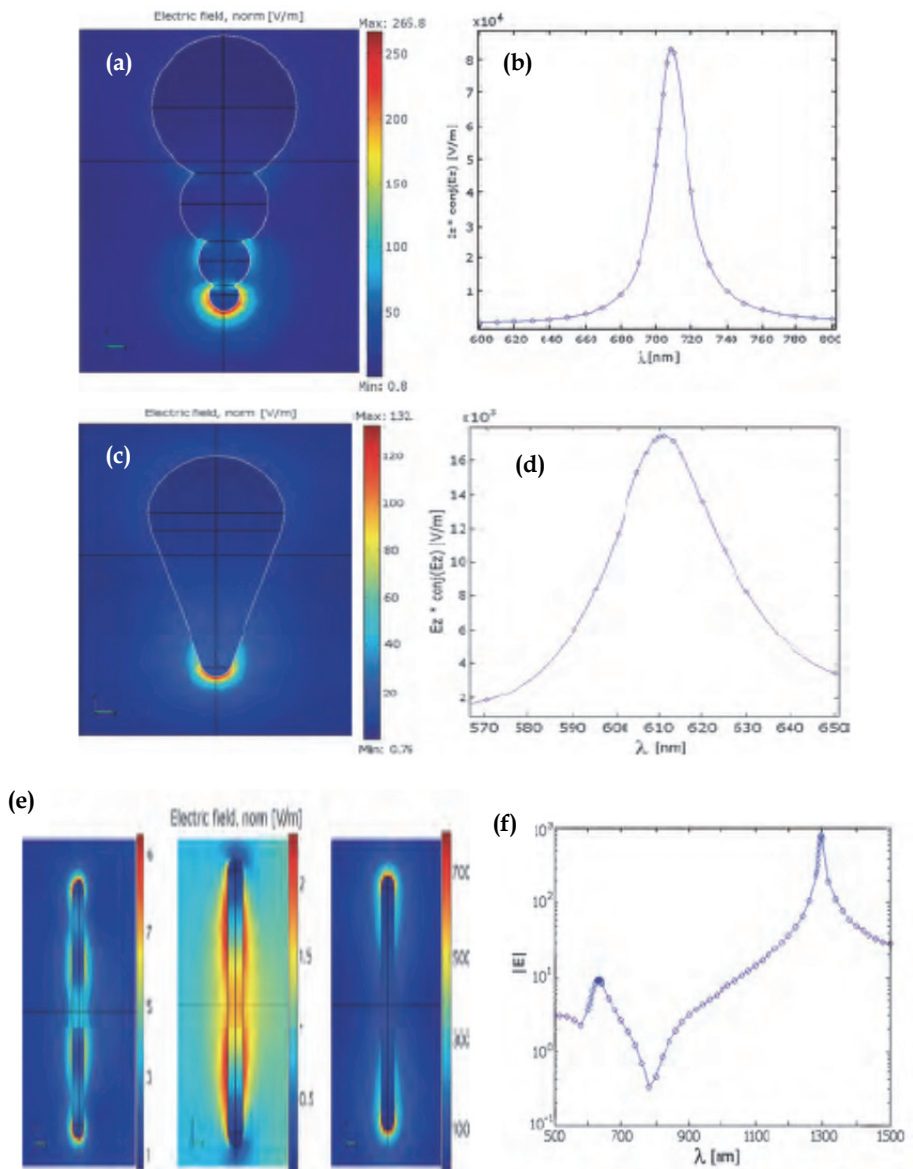


Fig. 8. Left: calculated field strength ( $|E|$ ) for the resonance conditions and right: corresponding resonance spectra for three different antenna designs: (a) self-similar antenna at resonance  $\lambda = 708$  nm, (c) conical antenna with resonance at  $610$  nm, (e) nanorod antenna with field distributions corresponding to the three extrema observed in resonance curve (f). For nanorod antenna electric field distribution (e) at  $\lambda \sim 1300$  nm (right) corresponds to the  $\lambda/2$  mode, the mode at  $\lambda \sim 650$  nm (left) is the  $3/2 \lambda$  mode and the 'dark' mode at  $\lambda \sim 780$  nm (centre) corresponds to the symmetric  $\lambda$ -mode. (Reproduced from Ref Keppeler et al 2007).

## 7. References

- Abdulhalim I.; Karabchevsky A.; Patzig C.; Rauschenbach B.; Fuhrmann B.; Eltzov E.; Marks R, Xu J., Zhang F.; and Lakhtakia A.; (2009) "Surface enhanced fluorescence from metal-sculptured thin films with application to biosensing in water" *App. Phys. Lett.*, 94, 063106.
- Aslan K.; Leonenko Z.; Lakowicz J. R.; and Geddes C. D.; (2005) "Fast and Slow Deposition of Silver Nanorods on Planar Surfaces: Application to Metal-Enhanced Fluorescence", *J. Phys. Chem. B*, 109, 3157-3162
- Bardhan R.; Grady N. K.; Cole J. R.; Joshi A.; and Halas N.J.; (2009) "Fluorescence Enhancement by Au Nanostructures: Nanoshells and Nanorods", *ACS Nano*, , 3, 744-752.
- Billot L.; Lamy de la Chapelle M.; Grimault A.-S.; Vial A.; Barchiesi D.; Bijeon J.-L.; Adam P.-M.; Royer P.; (2006) "Surface enhanced Raman scattering on gold nanowire arrays: Evidence of strong multipolar surface plasmon resonance enhancement" *Chem. Phys. Lett.*, 422, 303.
- Brown M.D.; Schatzlein A. G.; and Uchegbu I.F.; (2001) "Gene delivery with synthetic (non viral) carriers". *Int. J. Pharm.*, 229, 1-21.
- Chaney S. B.; Shanmukh S.; Dluhy R. A.; and Zhao Y. P.; (2005) "Aligned silver nanorod arrays produce high sensitivity surface-enhanced Raman spectroscopy substrates," *Appl. Phys. Lett*, 87, 031908.
- Chen Y.; Munehika K.; and Ginger D S.; (2007) "Dependence of Fluorescence Intensity on the Spectral Overlap between Fluorophores and Plasmon Resonant Single Silver Nanoparticles" *NanoLetters* 7, 690-696.
- Chen, J. Y.; Wiley, B. J.; & Xia, Y. N.; (2002) "One-dimensional nanostructures of metals: Large-scale synthesis and some potential applications". *Langmuir*, 2007, 23, 4120-4129 (b) Sun, Y. G. & Xia, Y. N. "Large-scale synthesis of uniform silver nanowires through a soft, self-seeding, polyol process". *Advanced Materials*, 14, 833-837.
- Corrigan, T. D.; Guo, S. H.; Szmazinski, H.; Phaneuf, R. J.; (2006) "Systematic study of the size and spacing dependence of Ag nanoparticle enhanced fluorescence using electron-beam lithography" *Appl.Phys. Lett.*, 88 (10), 101112.
- Corrigan, T. D.; Guo, S.; Phaneuf, R. J.; Szmazinski, H.; (2005) "Enhanced Fluorescence from Periodic Arrays of Silver Nanoparticles" *J. Fluoresc.*, 15 (5), 777-784.
- Dai, Q.; Coutts, J.; Zou, J.; Huo, Q.; (2008) "Surface modification of gold nanorods through a place exchange reaction inside an anionic exchange resin". *Chem. Comm.* 2858-2860.
- Drozdowicz-Tomsia K.; Xie F.; Goldys E.M.; (2010) "Deposition of silver dendritic nanostructures on silicon for enhanced fluorescence" *J Phys Chem C*, 114, 1562-1569
- Felidi, N.; Aubard, J.; Levi, G.; (1999) "Discrete dipole approximation for ultraviolet-visible extinction spectra simulation of silver and gold colloids" *J. Chem. Phys.* 111 (3), 1195-1208.
- Fu Y.; Zhang J.; and Lakowicz J. R.; (2010) "Plasmon-Enhanced Fluorescence from Single Fluorophores End-Linked to Gold Nanorods", *J. Am. Chem. Soc.* 132, 5540-5541
- Funston A. F.; Novo C.; Davis T. J.; Mulvaney P. (2009), "Plasmon Coupling of Gold Nanorods at Short Distances and in Different Geometries" *NanoLett.*, 9, 1651-1658.
- Gans R, (1915) "Über die Form ultramikroskopischer Silberteilchen" *Ann. Phys.*, 47, 270.
- Geddes, C. D.; Cao, H.; Gryczynski, I.; Gryczynski, Z.; Fang, J. Y.; Lakowicz, J. R.; (2003) "Metal-Enhanced Fluorescence (MEF) Due to Silver Colloids on a Planar Surface:

- Potential Applications of Indocyanine Green to in Vivo Imaging" *J. Phys. Chem. A*, 107 (18), 3443–3449.
- Geddes C. D.; Parfenov A.; Roll D.; Gryczynski I.; Malicka J.; Lakowicz J. R.; (2003) "Silver fractal-like structures for metal-enhanced fluorescence: Enhanced fluorescence intensities and increased probe photostabilities". *J. Fluorescence*, 13, 267-276.
- Gersten, J. I.; Nitzan A.; (1985) "Photophysics and photochemistry near surfaces and small particles" *Surf. Sci* 158, 165.
- Giannini V.; Sánchez-Gil J. A.; Muskens O. L.; and Rivas J. G.; (2009) "Electrodynamic calculations of spontaneous emission coupled to metal nanostructures of arbitrary shape: nanoantenna-enhanced fluorescence", *J. Opt. Soc. Am. B*, 26, 1569-1577.
- Goldys, E. M.; Drozdowicz-Tomsia, K.; Xie, F.; Shtoyko, T.; Matveeva, E.; Gryczynski, I.; and Gryczynski Z.; (2007) "Fluorescence amplification by electrochemically deposited silver nanowires with fractal architecture" *J. Am. Chem. Soc.*, 129 (40), pp 12117-12122.
- Grand J.; Kostcheev S.; Bijeon J.-L.; Lamy de la Chapelle M.; Adam P.-M.; Romyantseva A.; Le´rondel G.; Royer P.; (2003) "Optimization of SERS-active substrates for near-field Raman spectroscopy" *Synth. Met.* 139, 621.
- Guo, S. H.; Tsai, S. J.; Kan, H. C.; Tsai, D. H.; Zachariah, M. R.; Phaneuf, R. J.; (2008a) "The Effect of an Active Substrate on Nanoparticle-Enhanced Fluorescence" *Adv. Mater.* 20, 1424-1428.
- Guo, S. H.; Tsai, S. J.; Kan, H. C.; Tsai, D. H.; Zachariah, M. R.; Phaneuf, R. J. (2008b) "Spacer Layer Effect in Fluorescence Enhancement from Silver Nanowires over a Silver Film; Switching of Optimum Polarization" *Adv. Mater.* 20 (8), 1424-1428.
- Guo H.; Ruan F.; Lu L.; Hu J.; Pan J.; Yang Z.; and Ren B.; (2009) "Correlating the Shape, Surface Plasmon Resonance, and Surface-Enhanced Raman Scattering of Gold Nanorods", *J. Phys. Chem. C* 113, 10459-10464
- Hao, E.; Schatz, G. C.; (2004) "Electromagnetic field around silver nanoparticles and dimmers" *J. Chem. Phys.* 120, 357-366.
- He X.; Zhao X.; (2009) "Solvothermal synthesis and formation mechanism of chain-like triangular silver nanoplate assemblies: Application to metal-enhanced fluorescence (MEF)", *Applied Surface Science* 255, 7361-7368
- Hu M.; Novo C.; Funston A.; Wang H.; Staleva H.; Zou S.; Mulvaney P.; Xia Y.; Hartland G.V.; (2008) "Dark-Field Microscopy Studies of Single Metal Nanoparticles: Understanding the Factors that Influence the Linewidth of the Localized Surface Plasmon Resonance" *J. Mater. Chem.* 18, 1949.
- Huang X.; Neretina S.; and El-Sayed M.A.; (2009) "Gold Nanorods: From Synthesis and Properties to Biological and Biomedical Applications" *Adv. Mater.* 21, 4880-4910.
- Huang X.; El-Sayed I. H.; Qian w.; El-Sayed M. A.; (2007) "Cancer Cells Assemble and Align Gold Nanorods Conjugated to Antibodies to Produce Highly Enhanced, Sharp, and Polarized Surface Raman Spectra: A Potential Cancer Diagnostic Marker" *Nano Lett.* 7, 1591.
- Hutter E.; Fendler J. H.; (2004) "Exploitation of Localized Plasmon Resonance" *Adv. Mat.* 16, 1685-1706.
- Iqbal M.; Chung Y.; Tae G.; (2007) "An enhanced synthesis of gold nanorods by the addition of Pluronic (F-127) via a seed mediated growth process" *J. Mater. Chem.* 17, 335-342.

- Jana N. R.; Gearheart L.; Murphy C. J.; (2001) "Seed-mediated growth approach for shape-controlled synthesis of spheroidal and rod-like gold nanoparticles using a surfactant template" *Adv. Mater.* 13, 1389.
- Jana N. R.; Gearheart L.; Murphy C. J.; (2001) "Wet Chemical Synthesis of High Aspect Ratio Cylindrical Gold Nanorods" *J. Phys. Chem. B* 105, 4065.
- Jensen, T. R.; Malinsky, M. D.; Haynes, C. L.; Van Duyne, R. P. (2000) "Nanosphere Lithography: Tunable Localized Surface Plasmon Resonance Spectra of Silver Nanoparticles" *J. Phys. Chem. B* 104 (45), 10549-10556.
- Kappeler R.; Erni D.; Xudong C.; and Novotny L.; (2007) "Field Computations of Optical Antennas", *J. Comp. Theor. Nanosc.* 4, 686.
- Kelly K.L.; Coronado E.; Zhao L.L.; and Schatz G.C.; (2003) "The Optical Properties of Metal Nanoparticles: The Influence of Size, Shape, and Dielectric Environment" *J. Phys. Chem. B* 107, 668.
- Kerker, M.; Blatchford, C. G.; (1982) "Elastic scattering, absorption, and surface-enhanced Raman scattering by concentric spheres comprised of a metallic and a dielectric region" *Phys. Rev. B* 26, 4082.
- Khlebtsov B. N.; Khlebtsov N. G.; (2007) "Multipole Plasmons in Metal Nanorods: Scaling Properties and Dependence on Particle Size, Shape, Orientation, and Dielectric Environment" *J. Phys. Chem. C* 111, 11516-11527.
- Kummerlen, J.; Leitner, A.; Brunner, H.; Aussenegg, F. R.; Wokaun, A.; (1993) "Enhanced dye fluorescence over silver island films: Analysis of the distance dependence" *Mol. Phys.* 80 (5), 1031-1046.
- Lakhtakia A.; and Messier R.; (2005) "Sculptured Thin Films: Nanoengineered Morphology and Optics" *SPIE*, 2005, Bellingham, WA.
- Lakowicz, J. R. (2001) "Radiative decay engineering" *Anal. Biochem.* 298, 1.
- Lakowicz, J. R.; Shen Y, D'Auria, S.; Malicka J.; Fang J.; Gryczynski Z.; and Gryczynski I.; (2002) "Radiative decay engineering: Effects of Silver Island Films on Fluorescence Intensity, Lifetimes, and Resonance Energy Transfer" *Anal. Biochem.* 301, 261-277.
- Lee K. S.; El-Sayed M.A.; (2005) "Dependence of the Enhanced Optical Scattering Efficiency Relative to That of Absorption for Gold Metal Nanorods on Aspect Ratio, Size, End-Cap Shape, and Medium Refractive Index" *J. Phys. Chem. B* 109, 20331.
- Lee K. S.; El-Sayed M.A.; (2006) "Gold and Silver Nanoparticles in Sensing and Imaging: Sensitivity of Plasmon Response to Size, Shape, and Metal Composition" *J. Phys. Chem. B* 110, 19220.
- Li P. C.; Wei C. W.; Liao C. K.; Chen C. D.; Pao K. C.; Wang C. R. C.; Wu Y. N.; and Shieh D. B.; (2006) "Multiple targeting in photoacoustic imaging using bioconjugated gold nanorods," *Photons Plus Ultrasound: Imaging and Sensing 2006: The 7th Conference on Biomedical Thermoacoustics, Optoacoustics, and Acousto-optics, Proc. of SPIE*, vol. 6086, p. 60860M.
- Liang, H. Y.; Yang, H. X.; Wang, W. Z.; Li, J. Q.; Xu, H. X. (2009) "High-Yield Uniform Synthesis and Microstructure-Determination of Rice-Shaped Silver Nanocrystals" *J. Am. Chem. Soc.* 131, 6068- 6069.
- Liebermann, T.; Knoll, W.; (2000) "Surface plasmon field-enhanced fluorescence spectroscopy" *Colloid Surf. A* 171 (1-3), 115-130.

- Link S.; Mohamed M. B.; and El-Sayed M. A.; (1999) "Simulation of the Optical Absorption Spectra of Gold Nanorods as a Function of Their aspect Ratio and the Effect of the Medium Dielectric Constant" *J. Phys. Chem. B* 103, 3073-3077.
- Liu Y. J.; Fan J. G.; Zhao Y. P.; Shanmukh S.; and R. Dluhy R. A.; (2006) "Angle dependent surface enhanced Raman scattering obtained from a Ag nanorod array substrate," *Appl. Phys. Lett*, 89, 173134.
- Messaier R.; Latakhia A.; (1999) "Scalptured thin films II Experiments and applications" *Mater. Res. Innovations* 2, 217.
- Ming T.; Zhao L.; Yang Z.; Chen H.; Sun L.; Wang J.; and Yan C.; (2009) "Strong Polarization Dependence of Plasmon-Enhanced Fluorescence on Single Gold Nanorods", *Nano letters*, 11, 3896-3903.
- Mohamed M. B.; Volkov V.; Link S.; El-Sayed M. A.; (2000) "The 'lightning' gold nanorods: fluorescence enhancement of over a million compared to the gold metal" *Chem. Phys. Lett.* 317, 517-523
- Murphy C. J.; San T. K.; Gole A. M.; Orendorff C. J.; Gao J. X.; Gao J, Gou L.; Hunyadi S. E.; Li T.; (2005) "Anisotropic metal nanoparticles: synthesis, assembly, and optical applications". *J Phys Chem B* 109:13857-13870.
- Nicewarner-Pena, S. R.; Freeman, R. G.; Reiss, B. D.; He, L.; Pena, D. J.; Walton, I. D.; Cromer, R.; Keating, C. D.; Natan, M. J.; (2001) "Submicrometer Metallic Barcodes" *Science*, 294, 137
- Niidome T.; Yamagata M.; Okamoto Y.; Akiyama Y.; Takahashi H.; Kawano T.; Katayama Y.; Niidome Y.; (2006) "PEG-modified gold nanorods with a stealth character for *in vivo* applications" *J. Controlled Release*, 114, 343.
- Nikoobakht B.; El-Sayed M. A.; (2003) "Preparation and Growth Mechanism of Gold Nanorods (NRs) Using Seed-Mediated Growth Method," *Chem. Mater.* 15, 1957.
- Novo C.; Gomez D.; Perez-Juste J.; Zhang Z.; Petrova H.; Reismann M.; Mulvaney P.; Hartland G. V.; (2006) "Contributions from Radiation Damping and Surface Scattering to the Linewidth of the Longitudinal Plasmon Band of Gold Nanorods: A Single Particle" *Phys. Chem. Chem. Phys.*, 8, 3540.
- Obare S. O.; Jana N. R.; Murphy C. J.; (2001) "Preparation of Polystyrene and Silica-Coated Gold Nanorods and their use as Templates for the Synthesis of Hollow Nanotubes," *Nano Lett.* 1, 601.
- Oyelere A. K.; Chen B.; Huang X.; El-Sayed I. H.; El-Sayed M. A.; (2007) "Peptide-Conjugated Gold Nanorods for Nuclear Targeting" *Bioconjug. Chem.*, 18, 1490.
- P'erez-Juste J.; Pastoriza-Santos I.; Liz-Marzan L. M.; Mulvaney P.; (2005) "Gold nanorods: Synthesis, characterization and applications" *Coordination Chemistry Reviews* 249, 1870-1901.
- Pietrobon, B.; McEachran M.; and Kitaev V.; (2009) "Synthesis of Size-Controlled Faceted Pentagonal Silver Nanorods with Tunable Plasmonic Properties and Self-Assembly of These Nanorods" *ACS Nano*, 3, 21-26.
- G. Schider, J. Krenn R.; Hohenau A.; Ditlbacher H.; Leitner A.; Aussenegg F. R.; Schaich W. L.; Puscasu I.; Monacelli B.; and Boreman G.; (2003) "Plasmon dispersion relation of Au and Ag nanowires" *Phys. Rev. B*, 68, 155427.
- Shanmukh S. S.; Jones L.; Driskell J.; Zhao Y.; Dluhy R.; and Tripp R. A.; (2006) "Rapid and sensitive detection of respiratory virus molecular signatures using a silver nanorod array SERS substrate," *Nano Lett.* 6, 2630

- Slaughter L.S.; Wu Y.P.; Willingham B.; Nordlander P.; and Link S.; (2010) "Effects of symmetry breaking and conductive contact on the plasmon coupling in gold nanorod dimmers", *ACS Nano* 4, 4657-4666.
- Smythe E. J.; Cubukcu E.; Capasso F.; (2007) "Optical Properties of Surface Plasmon Resonances of Coupled Metallic Nanorods" *Opt. Express* 15, 7439.
- Sokolov, K.; Chumanov, G.; Cotton, T. M. (1998) "Enhancement of Molecular Fluorescence near the Surface of Colloidal Metal Films" *Anal. Chem.* 70 (18), 3898-3905.
- Sonnichsen C.; Franzl T.; Wilk T.; Plessen G. V.; Feldmann J.; (2002) "Drastic Reduction of Plasmon Damping in Gold Nanorods" *Phys. Rev. Lett.* 88, 077402.
- Su K. H.; Wei Q. H.; Zhang X.; Mock J. J.; Smith D. R.; Schultz S.; (2003) "Interparticle coupling effects on plasmon resonances of nanogold particles" *NanoLett.* 3, 1087.
- Tao A.; Kim F.; Hess C.; Goldberger J.; He R.; Sun Y.; Xia Y.; and Yang P.; (2003) "Langmuir-Blodgett Silver Nanowire Monolayers for Molecular Sensing Using Surface-Enhanced Raman Spectroscopy", *Nano letters*, 3, 1229-1233.
- Tarcha, P. J.; DeSaja-Gonzalez, J.; Rodriguez-Llorente, S.; Aroca, R. (1999) "Surface-Enhanced Fluorescence on SiO<sub>2</sub>-Coated Silver Island Films" *Appl. Spectrosc.* 53 (1), 43-48.
- Wiley B.; Sun Y.; Mayers, B. and Xia, Y. N. (2005). "Shape-controlled synthesis of metal nanostructures: The case of silver". *Chemistry-A European Journal*, 11, 454-463.
- Wiley B.; Sun Y, and Xia, Y. (2007) "Synthesis of silver nanostructures with controlled shapes and properties". *Accounts of Chemical Research*, 40, 1067-1076.
- Wiley B, Sun Y.; Chen J.; Cang H.; Li Z-Y.; Xingde L.; Xia Y. (2005) "Shape-controlled synthesis of silver and gold nanostructures". *MRS Bulletin*, 30, 356-361,
- Wiley, B.; Sun, Y.; Yu YY.; Chang S-S.; Lee C-L.; Wang C. C. R.; (1997). "Gold nanorods: electrochemical synthesis and optical properties". *J Phys Chem B* 101, 6661-6664.
- Xia, Y.; Xiong, Y.; Lim, B. & Skrabalak, S. E.; (2009) "Shape-controlled synthesis of metal nanocrystals: Simple chemistry meets complex physics" *Angewandte Chemie - International Edition*, 48, 60-103.
- Yelin D.; Oron D.; Thiberge S.; Moses E.; Silberberg Y.; (2003) "Multiphoton Plasmon-Resonance Microscopy" *Opt. Express* 11, 1385.
- Zhou Z.; Li M.; Yang Z.; Peng X.; Su X.; Zhang Z.; Li J.; Kim N.; Yu X.; Zhou L.; Hao Z.; and Wang Q.; (2010) "Plasmon-Mediated Radiative Energy Transfer across a Silver Nanowire Array via Resonant Transmission and Subwavelength Imaging" *ACS Nano*, 4, 5003-5010.

# On the Behavior of Ni Magnetic Nanowires as Studied by FMR and the Effect of “Blocking”

Carlos A. Ramos<sup>1</sup>, Ettore C. Vassallo Brigneti<sup>1</sup>,  
Emilio De Biasi<sup>1</sup> and Manuel Vázquez<sup>2</sup>

<sup>1</sup>*Centro Atómico Bariloche e Instituto Balseiro,  
Universidad Nacional de Cuyo, Rio Negro,*

<sup>2</sup>*Instituto de Ciencias de Materiales, CSIC, Madrid*

<sup>1</sup>*Argentina*

<sup>2</sup>*Spain*

## 1. Introduction

The development of nano-patterned membranes and nanowires (NW) is based on the interest in basic and applied research ranging from spintronics [Fert, 2008], chemical [Casanova *et al.*, 2008], biosensing [Orosco *et al.*, 2009; Pacholski *et al.*, 2006], semiconductor [Yang, *et al.*, 2010] and microwave applications [Darques *et al.*, 2009] among others [Ferain & Legras, 2009]. In particular, the study and applications of NWs has grown extensively during the last decades. One possibility to fabricate NWs is based on electron beam lithography leading to well defined structures of no less than ~100nm lateral size. In contrast with this technique there are other possibilities to generate nanoporous templates based on chemical or in physicochemical techniques [Pirota *et al.*, 2010]. One of these uses energetic heavy-ion particle beams impinging on a polymer membrane and subsequent chemical etching [Fert & Piroux, 1999]. Such membranes are commercially available with varying diameters and pore-density. Also a two-step anodization process [Masuda & Fukuda, 1995; Nielsch *et al.*, 2001] of aluminum leads to self-organized pores of amorphous anodized aluminum oxide (AAO) with a hexagonal order over relatively large regions (1-2 $\mu$ m). The pores align perpendicular to the substrate and remain separated from each other. These AAO templates can be prepared using different solutions and conditions of anodization, leading to varying diameters (20nm -110 nm), separation (65 - 500nm), and degree of order [Niesch *et al.*, 2001; Vázquez *et al.*, 2004]. These templates were used for growing by electrodeposition the Ni NWs that are the subject of this chapter.

Ferromagnetic NW can be approximated as uniformly magnetized single domains with reversal mechanisms that depend on the wire diameter [Hertel & Kirschner, 2004]. The magnetic characteristic of a NW array depends crucially on its effective anisotropy. The anisotropy measurement, its origin, and possible ways of modifying it, are of large interest in basic research and applications.

For the characterization of magnetic NWs arrays ferromagnetic resonance (FMR) is an excellent technique as it yields direct information about the uniform precession mode

which can be related to the average anisotropy magnitude [De La Torre Medina *et al.*, 2010; Encinas-Oropesa *et al.*, 2001; Ramos *et al.*, 2004a; 2004b]. Its variation on the sample that may be related to anisotropy fluctuations and/or to other relaxation routes. Other excitations, related to spin-waves or surface modes can also be studied by FMR in nanowires [Kraus *et al.*, 2011].

In the present chapter we deal with some of the relevant aspects associated to FMR studies of NW arrays. We will start describing briefly the preparation method, its structural characterization, the magnetic characterization (Scanning Electron Microscopy, SEM, Atomic Force Microscopy, AFM, and X-ray diffraction, dc Magnetometry, Magnetic Force Microscopy, MFM, and FMR). In this sense we will show how the magnetic anisotropy is extracted from the experiment, the information involved in the linewidth regarding alignment and order/disorder contribution.

Magnetic Nanoparticles (MNPs) manifest a crossover from superparamagnetic-regime to blocked-regime which is observed at low temperatures and low fields, when the magnetic anisotropy barrier becomes comparable with the thermal fluctuation energy within a time-interval of measurement [Brown, 1963]. As magnetic NWs have a magnetic anisotropy much larger than the thermal energy, they represent ideal systems to study FMR in “blocked” systems, in the same sense this word is used for MNPs. Indeed, all particles with a substantial uniaxial anisotropy should behave in a very similar way to this magnetic NW as long as they can be considered as single-domain, which is a characteristic of small MNPs. As there has been many publications pointing to the effect this “blocking” has on the FMR spectra in MNPs we will treat these concepts relating the NW magnetization and FMR of these model systems. In doing this we hope to contribute to understand the relation between “blocking” and its effect on the FMR spectra.

## 2. Sample preparation and characterization

Highly-ordered AAO membranes were prepared by two-step anodization process of a high purity Al foil [Masuda & Fukuda, 1995]. In this way it is obtained a self-organized nanostructured template with high density of uniform parallel cylindrical pores aligned perpendicular to the surface. Varying the anodizing conditions the pore diameters can be changed between roughly 10 and 200 nm. Except otherwise indicated the anodization of the samples presented here was performed in a 0.3 M oxalic acid solution at 2°C temperature under an applied potential of 40 V. A two-step anodization process allows us to obtain large scale polycrystalline array of the nanopores. (Fig. 1) The first anodization step in our samples lasted 24h (SNI) and 3h (SA) and is schematically drawn in Fig. 1b. This first AAO is eliminated by chemical etching of the AAO and the Al is exposed to a second anodization step performed for a few hours to produce the desired AAO template. The AAO obtained is then characterized by the presence of an array of self-ordered nanopores with a diameter of  $\sim 35$  nm arranged in a dense hexagonal lattice with a parameter  $\sim 105$  nm. The length of the nanopores, depends on the second anodization step duration. The AAO is then used as a template for the growth of the metallic NW by electrodeposition. However, the presence of an insulating alumina barrier-layer at the bottom of each nanopore prevents a direct deposition of material. Therefore, a suitable chemical process is used to reduce the thickness of the barrier-layer, resulting in the formation of dendrites, thus enabling the subsequent filling of pores with Ni by a pulsed-

electrodeposition method. Details regarding the electrodeposition conditions are given in the literature [Nielsch *et al*, 2000; 2001; Pirota *et al* 2004; Vázquez *et al*, 2004].

The pore filling-factor in the untreated AAO is close to 10% and can be increased by chemical treatments. Using pulsed electrodeposition these nanopores can be filled with a magnetic (Fe, Co, Ni) or non-magnetic metal. For this chapter we will deal with electrodeposited Ni NWs of typical lengths  $3\mu\text{m}$  (SNi) and  $1\mu\text{m}$  (SA). The typical aspect ratio (length/diameter) are close 80 (SNi) and 30 (SA). Ni NWs have a very small crystalline anisotropy as compared to the shape anisotropy which is, in magnetic field units, close 3 kOe for large aspect ratios (the shape anisotropy saturates rapidly for aspect ratios larger than 5[Cullity 1972]). This relatively small anisotropy field makes these samples very suitable for studying with FMR.

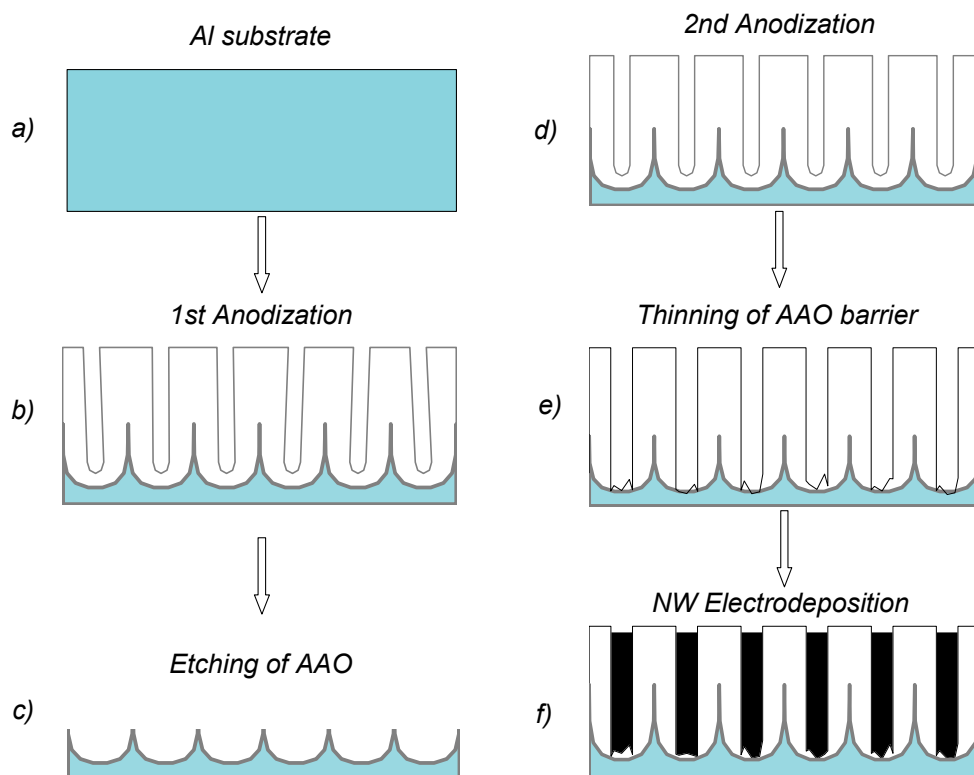


Fig. 1. Schematic representation of the Anodic Aluminum Oxide (AAO) template and the steps involved in the preparation of nanowires (after [Pirota *et al*, 2004]).

## 2.1 Structure

In Fig 2 we present the X-Ray diffraction scan of a Ni-electrodeposited NW array into a porous AAO membrane. We observe the crystalline Al peaks corresponding to the substrate and some broad and sharp peaks corresponding to the Ni NW. The nanoporous AAO

contributes to the broad background centred at  $2\theta \sim 25^\circ$ , indicating its amorphous structure. This AAO has not the structure or properties of the crystalline phases of  $\text{Al}_2\text{O}_3$ , such as the  $\gamma\text{-Al}_2\text{O}_3$  or the high-temperature phase of  $\alpha\text{-Al}_2\text{O}_3$ . Note that the Ni NWs are strongly textured along a generic  $[110]$  direction. This texture is also observed in NWs grown in AAO templates produced under sulphuric acid (with pore diameter  $\phi \sim 20\text{nm}$ ) and oxalic acid ( $\phi \sim 35\text{nm}$ ). We observed no preferential orientation for the AAO-template produced using phosphoric acid ( $\phi \sim 180\text{nm}$ ) [Vassallo Brigneti 2009]. This possibly indicates a correlation of pore diameter with preferential orientation.

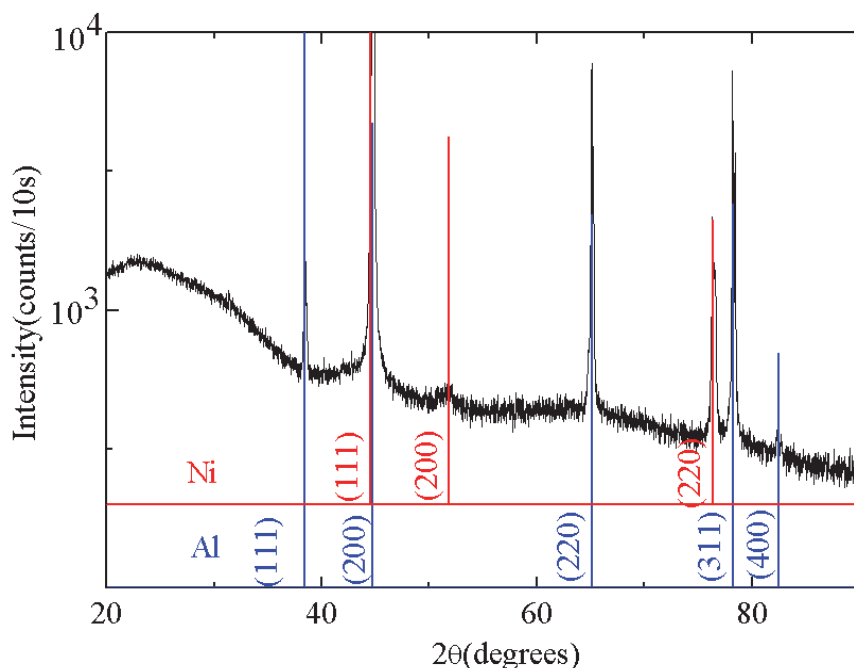


Fig. 2. XRD scan of a Ni NW array electroposited into an AAO membrane grown under oxalic acid. Most visible are the Al peaks from the substrate. The Ni NW grow with a  $\langle 110 \rangle$  preferential orientation.

## 2.2 Surface microscopy characterization

In Figure 3 we show some of the SEM, AFM and MFM images of the samples used in this work. As mentioned previously, this figure shows that the AAO self organize into crystals of  $1\text{-}2\ \mu\text{m}^2$  and the filling by the magnetic NW is almost perfect, to judged from the SEM image (top left) and MFM image (bottom right). Note the remarkable alignment of the AAO nanopores (up right) where a side view of the sample is presented. The detail of the AFM image (bottom left), as well as the SEM image, indicate some minor irregularities in the cylindrical shape of the NWs which is related with the hexagonal crystal deformation, as a

detailed study has shown [Vassallo Brigneti, 2009]. The MFM image, obtained in the remanent state after saturation (Fig 3a bottom right) shows the presence of some NWs clusters with reversed magnetization, seemingly due to the magnetic dipolar interaction between the wires (bright yellow in the image), yet most of the wires point on a preferential direction, which is consistent with the average magnetization in this system (see Fig. 4 below). The dark spots or clusters indicated the presence of NWs with reverse magnetization.

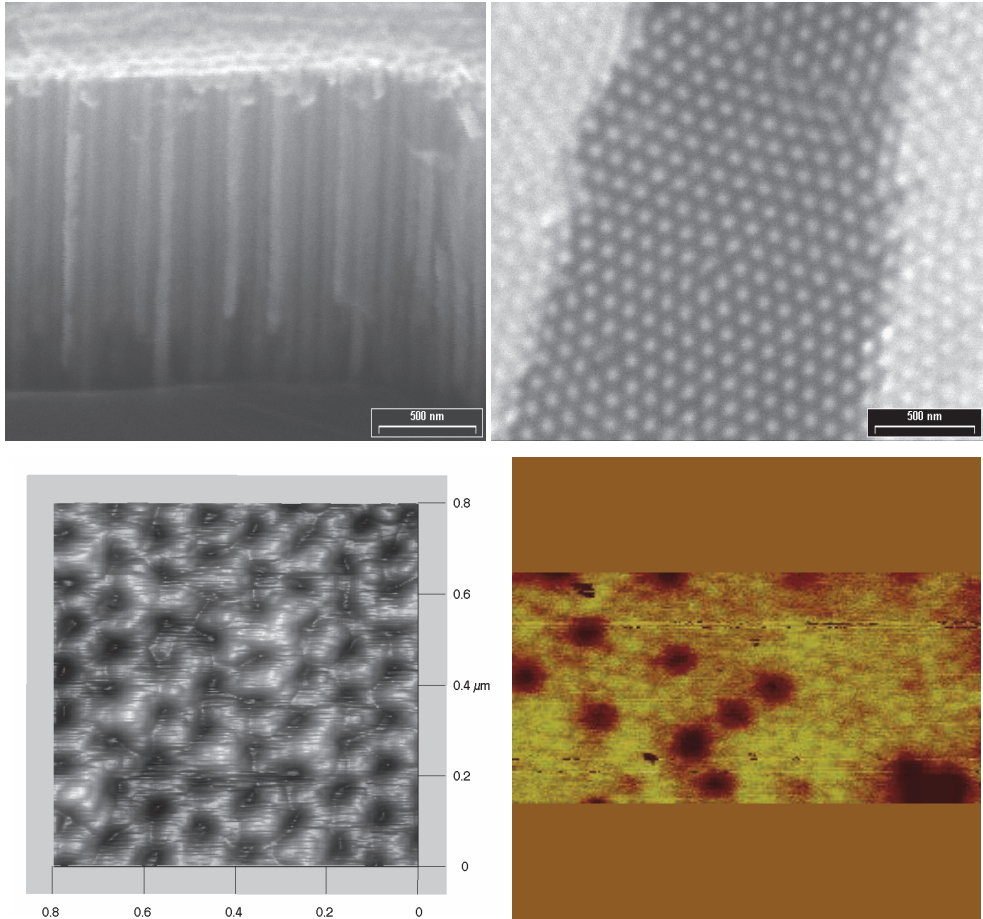


Fig. 3. (a) Top left : SEM top view of sample SNi. The clear dots are the Ni NWs. The hexagonal crystalline order extends through 1-2  $\mu\text{m}^2$ . Top right: side view of the columnar shape of the AAO matrix Bottom left: AFM image Bottom right: (MFM) image performed on the remanent state after saturation (obtained with a Nanoscope IV). The dark spots correspond to inversely polarized NWs. Only a small portion of the wires display inversion. From images like these we estimate the NW diameter,  $d \sim (37 \pm 4)\text{nm}$  and inter-wire separation  $S \sim (109 \pm 10)\text{nm}$ , derived from these quantities the filling factor of the NW is  $f = (\pi/2\sqrt{3}) (d/S)^2 = 0.106 \pm 0.015$ .

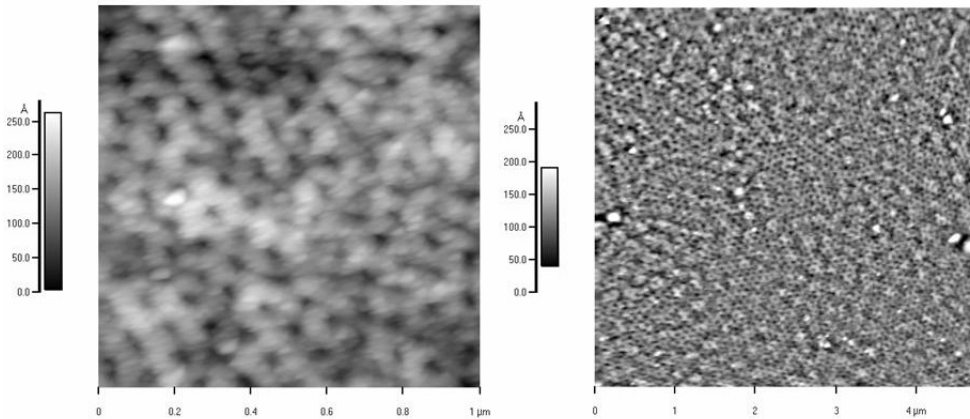


Fig. 3. (b) AFM scan of sample SA, fabricated under similar conditions but reducing the first anodization time to 3h instead of 72h (of sample SNi, Fig. 3a). Note that the hexagonal order is reduced and the disorder seems to increase as compared to sample SNi. From AFM images we estimate  $d = (31 \pm 7)\text{nm}$  and  $S = (92 \pm 14)\text{nm}$ , yielding  $f = 0.103 \pm 0.03$ .

### 2.3 Magnetic characterization by dc magnetization

The magnetization data was measured in a SQUID magnetometer and in a Lake Shore 7031 VSM.

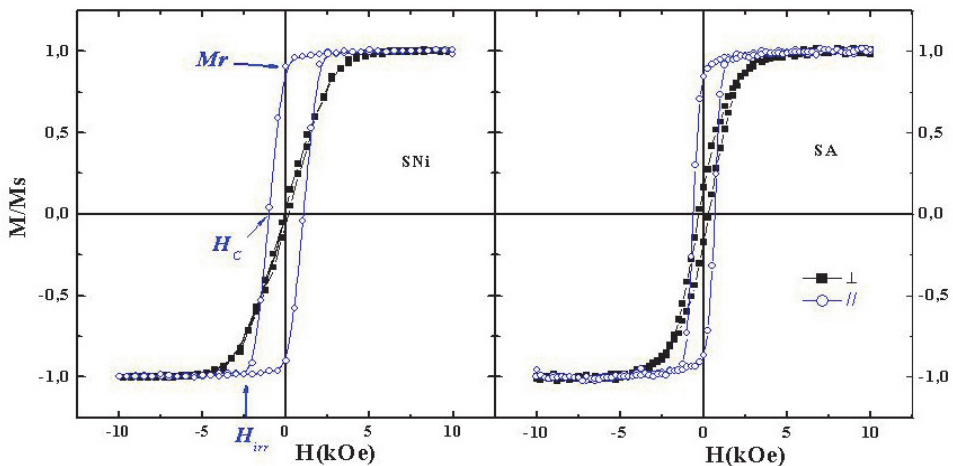


Fig. 4. Left: Magnetization of the Ni NW array under an applied field (sample SNi, Fig. 2 and 3) measured parallel (blue circles) and perpendicular (black squares) to the NW. The remanent magnetization ( $M_r$ ), coercive ( $H_c$ ), and irreversibility ( $H_{irr}$ ) fields are indicated. Right: same for sample SA.

Fig. 4 shows hysteresis loops measured on samples SNI and SA. In Fig. 4 we indicate  $H_C$ , the irreversibility field,  $H_{irr}$  (for  $|H| > |H_{irr}|$   $M$  is single-valued), and the remanent magnetization,  $M_r$ , which is close to 90% of saturation in these samples. This explains the large polarization observed in Fig. 3a by MFM after saturation. Ideally, in a uniaxial anisotropy system, the magnetization measured perpendicular to the easy axis should follow a linear behavior up to the saturation field, and this field should coincide with the anisotropy field,  $H_A$ . Observing Fig. 4 we notice that even though  $M(H \perp NW)$  follows an almost-linear behavior at low  $H$ , it departs significantly from this behavior at larger fields making it difficult to define a unique value for  $H_A$  from  $M(H \perp)$ . One of the interpretations of this effect resides on the fact that NWs, even though they can be well approximated as single-domains, do not behave internally as perfectly uniformly magnetized.

The departure from an ideal Stoner-Wohlfarth model [Brown, 1963] is due to the fact that the NWs can reverse the magnetization by inducing nucleating a vortex intermediate state or a transverse magnetization mechanism that implies a non-uniform reversal [Allende *et al.*, 2008; Hertel & Kirschner, 2004]. These mechanisms reduces the energy barrier which translates into a smaller  $H_C$  from what would be the uniform-reversal value ( $H_C = H_A$ ). Yet, in the saturated state it is possible to define an average anisotropy field,  $H_A$ . In this sense FMR is very helpful as it measures directly  $H_A$ . The anisotropy field determined using FMR for this sample [see below] is  $H_A = 2.0(2)$  kOe, double than the coercive field,  $H_C$ . In sample SA the measured  $H_A$  is also significantly larger than the coercive field.

#### 2.4 Magnetic resonance setup

The experiments were carried out in a Bruker ESP300 spectrometer at room temperature. As usual we use field modulation (10Oe-100kHz) to obtain the absorption derivative spectrum. The microwave field is perpendicular to the NW. We will present data on the bands operating at 1.2, 9.4 and 34 GHz, commonly known as L, X and Q-bands.

### 3. Ferromagnetic resonance and blocking in nanomagnetism

For over a decade there has been a growing interest in microwave response of magnetic NWs, stemming from basic and applied research [Boucher *et al.*, 2010; Darques *et al.*, 2009; Fert & Piraux, 1999]. One of the characteristic experiments in the microwave region (1-50GHz) is to study these nanostructured materials under a simultaneous presence of a uniform applied field,  $H$ , and an exciting microwave field usually applied perpendicular to  $H$ . The uniform field determines the natural precession frequency of the magnetization around the effective field which depends on:  $H$ , contributions due to shape anisotropy, dipolar interactions, crystal field, and magnetoelastic interactions. Ferromagnetic resonance (FMR) occurs when the microwave frequency matches the natural frequency of the magnetic system [Kittel, 2005]. The parameters that characterize a ferromagnetic system can be studied by measuring the power absorbed as a function of the microwave frequency and applied field,  $H$ . With the advent of vector analyzers (VNA) and microstrip exciting techniques microwave absorption can be studied conducted varying the frequency under a given  $H$ , or -as in the traditional FMR experiments- performed under a fixed frequency while sweeping  $H$ .

In apparent analogy with the FMR microwave absorption of nanoparticle systems stands the magnetic ac-susceptibility,  $\chi_{ac}$ , usually measured under  $H = 0$ . This technique has

been extensively used to study non-interacting nanoparticles [Dorman *et al.*, 1997], spin-glass [Lundgren *et al.*, 1983; Mydosh, 1993], and random-field [King *et al.*, 1986; Ramos *et al.*, 1988] systems as it yields information on the system dynamics. Performing  $\chi_{ac}$  as a function of temperature,  $T$ , in magnetic nanoparticle systems it is found that below a certain  $T$  the system is not able to respond to the alternating field, it is said that it “blocks”. This blocking temperature,  $T_B$ , depends logarithmically with the exciting frequency [Dorman *et al.*, 1997]. Yet, a *crucial* difference between  $\chi_{ac}$  and FMR is that the first technique is usually carried out at  $H = 0$  while FMR is not. The implications of this decisive difference have been overlooked and lead some authors to the conclusion that “blocking” occurs in FMR [Antoniak *et al.*, 2005; Berger *et al.*, 2001; Lubitz *et al.*, 2004; Sánchez *et al.*, 1999; Trunova *et al.*, 2009]. All these articles, dealing with magnetic nanoparticles, show that the ferromagnetic line broadens and its intensity decreases at low  $T$ , similarly to what is observed in  $\chi_{ac}$  for  $T < T_B$ . Below we present data supporting the idea that the loss of FMR intensity observed is consistent with an effective anisotropy increase as  $T$  is lowered, and that there is no evidence of blocking in FMR in the sense of the  $\chi_{ac}$ . We further explore the FMR response in the field region of magnetic hysteresis using one of the simplest nanomagnetic systems: single-domain magnetic NWs studied at three different exciting frequencies (1.2, 9.4 and 34.0 GHz) and as a function of the magnetic history of the sample.

### 3.1 Blocking in magnetic susceptibility

Magnetic systems possessing nearly degenerated energy minima are characterized by an extremely slow dynamics at low temperatures. This is evidenced in dc and ac susceptibility studies. Dispersed magnetic nanoparticles are among the simplest systems to study magnetic relaxation. Indeed, in these systems the magnetic relaxation depends on the anisotropy barrier,  $E_B$ , separating the two minima. For uniaxial anisotropy and zero applied field  $E_B = KV$ , where  $K$  is the uniaxial anisotropy energy per unit volume and  $V$  the particle volume. The characteristic time,  $\tau$ , a particle will take to flip its magnetic state from one minimum to the other will depend on this energy barrier and the thermal energy and is given by [Dorman *et al.*, 1997]:

$$\tau = \tau_0 \exp\left(\frac{E_B}{kT}\right) \quad (1)$$

where  $1/\tau_0 \approx 10^9 \text{ s}^{-1}$  corresponds to a typical attempt frequency for reversal,  $k$  is the Boltzmann constant and  $T$  the temperature. As  $\tau$  increases with decreasing  $T$ , for a given measuring time,  $\tau_m$ , there will be a temperature,  $T_B$ , at which the magnetic moment is no longer able to fluctuate between the two minima and will, therefore remain in one of them. This temperature,  $T_B$ , is called the “blocking temperature”. For a typical dc magnetization experiment  $\tau_m \approx 100\text{s}$ , and from Eq.(1) it follows the estimation  $25kT_B \approx KV$  that relates the zero-field anisotropy energy barrier with  $T_B$ .

Magnetization measurements as a function of temperature,  $M(T)$ , are performed under a small dc field. This procedure leads to clear differences of the magnetic moment measured below  $T_B$  depending on whether the sample is cooled below  $T_B$  under zero field (ZFC) or under a field-cooled (FC) condition, using in both cases the same small dc field for measuring. In ideal uniaxial-anisotropy nanoparticle systems the ZFC is characterized by a

much smaller magnetization at  $T \ll T_B$  than the corresponding FC state, up to  $T \approx T_B$  [De Biasi *et al.*, 2008].  $T_B$  depends on the magnitude of  $H$  and  $T_B(H) \rightarrow 0$  when the Zeeman energy equals the anisotropy barrier. For  $T < T_B$  these systems behave as ferromagnets and present magnetic hysteresis in the  $M(H)$  cycles. The maximum field for which the two branches merge defines the irreversibility field,  $H_{irr}$ , above which the system reaches an unambiguous magnetic state (see Figure 4).

### 3.2 FMR dispersion relation

In traditional FMR experiments the dc field is swept while keeping a constant microwave exciting frequency. While the field is swept the eigenfrequency of the system varies according to the Smit and Beljers dispersion relation [Smit & Beljers 1955, Morrish, 2001]:

$$\left(\frac{\omega}{\gamma}\right)^2 = \frac{(E_{\theta\theta}E_{\varphi\varphi} - E_{\theta\varphi}^2)}{(M_S \sin \theta)^2} \Bigg|_{\theta=\theta_0, \varphi=\varphi_0} \quad (2)$$

where  $\omega = 2\pi\nu$ ,  $\nu$  being the microwave frequency,  $\gamma = g\mu_B/\hbar$  is the gyromagnetic factor,  $M_S$  is the saturation magnetization,  $E_{\theta\theta}$ ,  $E_{\varphi\varphi}$ , and  $E_{\theta\varphi}$  are the second derivatives of the free energy ( $E$ ) with respect to the spherical angles ( $\theta$ ,  $\varphi$ ) evaluated at the magnetization equilibrium direction ( $\theta_0$ ,  $\varphi_0$ ), which is obtained from the free energy setting the first derivatives to zero ( $E_\theta = 0$  and  $E_\varphi = 0$ ).

This eigenfrequency reduces to:

$$\omega = (\gamma / M_S) \sqrt{E_{\theta\theta}E_{\varphi\varphi}} \quad (3)$$

evaluated at the equilibrium positions for the cases considered in this work. Eq (3) indicates that eigenfrequency is proportional to the geometric mean of the energy curvature along two perpendicular directions:  $\theta$  and  $\varphi$ . We hope to clarify this concept in the simplified model developed in the next sub-section.

### 3.3 Uniaxial anisotropy model

In order to show how the sample’s magnetic history affects the FMR, and compare this situation with the magnetic hysteresis cycle, we consider here a *uniformly magnetized system* with second order uniaxial anisotropy described by the free energy per unit volume,  $E$ :

$$E = -M_S H \sin \theta \cos(\varphi - \varphi_H) - K \sin^2 \theta \cos^2 \varphi \quad (4)$$

where  $H$  is the external magnetic field applied in the  $X$ - $Y$  plane,  $M_S$  and  $K$  are the magnetization and anisotropy energy per unit volume,  $\varphi$  is the magnetization angle away from the easy axis (considered parallel the  $X$ -axis) and  $\varphi_H$  is the angle  $H$  makes with the  $X$  axis. This particular arrangement, represented in figure 5, describes a general case of a uniaxial magnetic anisotropy under an applied field and has the advantage of being mathematically simpler (solving  $E_\theta = 0$ , yields  $\theta_0 = \pi/2$  in Eq. (2) as the magnetization equilibrium orientation).

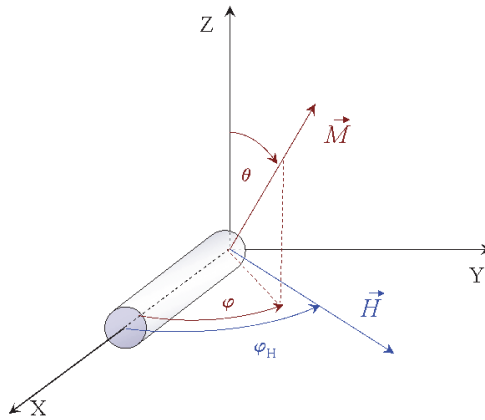


Fig. 5. Reference frame in which the NW axis coincides with the X direction. The magnetic field moves in the X-Y plane.

We will consider the application of  $H$  parallel or antiparallel to the anisotropy axis ( $\varphi_H = 0, \pi$ ). In this way the magnetic system can be in either one of two states for  $H < H_A$  ( $H_A = 2K/M_s$ ). In this simplified model the coercive field,  $H_C = H_A$ .

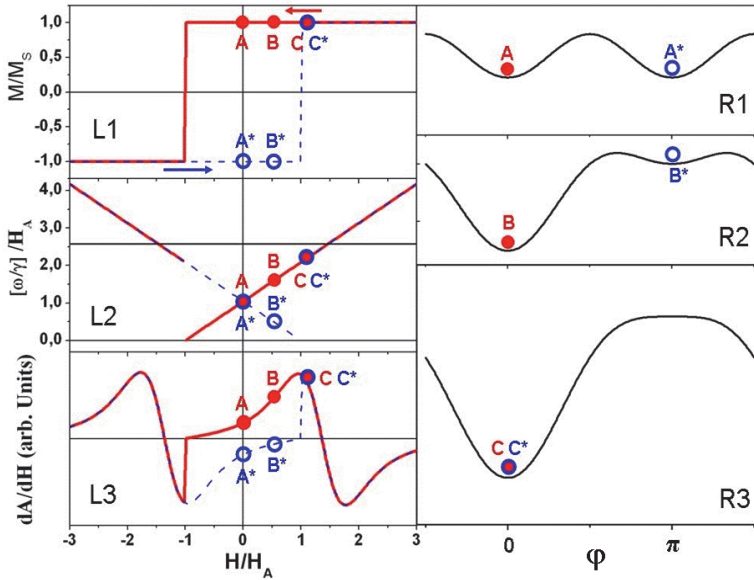


Fig. 6. R1-R3 energy landscape as a function of  $\varphi$  for  $\varphi_H = 0$  (Eq. 4). L1 hysteresis cycle. L2 dispersion relation (Eq. 3). In panel L3 we show the calculated absorption derivative for the conditions: initial magnetization pointing along the applied field ( $A \rightarrow B \rightarrow C$ ) in solid red line, and initial magnetization in the opposite sense ( $A^* \rightarrow B^* \rightarrow C^*$ ) in blue dash line.

In Figure 6 we represent the  $M(H)$  hysteresis loop (L1). Decreasing  $H$  from saturation (C→B→A) the magnetization will remain saturated in the positive direction down to the field  $-H = H_A$ , at which point it will reverse for  $-H > H_A$  (full red line). Similarly, increasing  $H$  from saturation in the negative direction (dashed blue curve) the magnetic state will follow the points  $A^*$ ,  $B^*$  and  $C^*$ . On the right panels R1-R3 we have plot the energy landscapes as a function of the magnetization direction,  $\varphi$ , for three different fields,  $H/H_A = 0, 0.5$  and  $1.1$  applied along the easy axis, corresponding to the points A, B, and C. For zero applied field the energy minima at  $\varphi = 0$  and  $\varphi = \pi$  are equivalent (Figure 5 - R1). The sequence R1-R2-R3 follows the points A-B-C of the hysteresis loop for the field applied along the easy axis. Looking at the sequence R1→R2→R3 we see that the curvature, given by  $E_{\varphi\varphi}$  increases for the equilibrium condition at  $\varphi = 0$  for increasing  $H$ . If the magnetization was initially opposite to  $H$  (points  $A^*$ ,  $B^*$ ), the energy curvature calculated at  $\varphi = \pi$  will *decrease* with increasing  $H$  up to the point at which there will be a single minimum, at  $H = H_A$ . Directly related with the energy curvature is the dispersion relation, drawn in Fig. 6 (L2) as full (red) and dash (blue) lines. The horizontal line in L2 corresponds to the microwave frequency, fixed in the traditional FMR experiment. The point at which the dispersion relation crosses this microwave frequency is the resonance field,  $H_R$ . Panel L3 shows the calculated microwave absorption derivative. To simulate the FMR spectra we used Netzelmann's equations [Netzelmann, 1990] with  $g = 2$  and  $\alpha = 0.3$ . Note that in Eq. 3 we have two possible equilibrium positions within the hysteresis cycle. Both equilibrium positions are, indeed, possible states. As shown in L2 when the magnetization is in the same sense as the applied field, the dispersion relation grows (full red line) with  $H$ , reaching the resonance condition at  $H_R = \omega/\gamma - H_A$  (for  $\omega/\gamma > H_A$ ). If, on the contrary, the sample is initially oppositely magnetized ( $A^*$ ) and the field is increased the dispersion relation *decreases* (following the curvature decrease observed in  $B^*$ , see R2), thus going away from the resonance condition (dash blue line in L2). The result, in the absorption spectrum calculated in L3, is the observation of a "tail", as though the absorption occurred at negative fields. This "tail" would continue to decrease in increasing  $H$  up to the irreversibility field at  $H = H_A$  and would jump to the "normal" absorption (red solid line) at larger fields. Note that L3 indicates absorption occurs even at  $H = 0$  within this simple model. This would be so as long as the exciting microwave frequency and the natural frequency are close to each other (measured in linewidths units).

In spite of the simplicity of the model it describes some of the most significant features observed. Only within the irreversibility region we could expect to see the effects of the sample magnetic history.

As shown in Figure 6-L2 there is a minimum frequency,  $\nu = \gamma H_A/2\pi$ , below which there will be no resonant microwave absorption, when  $H$  is applied near the parallel direction. This defines an anisotropy gap. If the anisotropy gap increases (as is found in superparamagnetic nanoparticle systems) we may expect, in some cases, to reach the condition in which  $H_A > \omega/\gamma$  and therefore the resonance condition would be lost for the parallel condition and for all directions close to the easy axis. The consequence would be a sudden intensity drop. Yet this effect cannot be related to the blocking: if it were so then experiments at higher frequencies would not be able to yield absorption signals, which is not what has been found in experiments [Ennas *et al.*, 1998].

Comparison of the measured magnetization loop along the easy axis (Fig. 4) with a Stoner-Wohlfarth hysteresis cycle of Fig. 6-L1 indicates that the total magnetization switches progressively. As observed in the magnetic state in Fig. 3 bottom right, these NWs are pointing either up or down, and the total magnetization is the result of the addition of all the NWs contribution. Thus, we can talk about the NW "population" at  $\varphi = 0$  and  $\varphi = \pi$ . Then, a phenomenological way to reproduce the measured hysteresis cycle is to consider that these populations change as a continuous function of the applied field. For this purpose we used a hyperbolic tangent of the applied field (offset by  $H_C$ ) and adjusted the transition width to best reproduce the experimental data. Having a function that describes correctly the hysteresis cycle we proceeded to model the FMR response based in the simple model outlined in this section with the basic ingredient that the population of each well (amount of magnetization pointing parallel or antiparallel to the applied field) is a function of the applied field, set to reproduce the hysteresis cycle. This is what we describe in sub-section 3.6 and compare with experiments.

### 3.4 FMR dispersion relation and angular variation in Ni NW arrays

Using the expression for the energy given by Eq. (4) and evaluating Eq. (2) at the equilibrium angles  $\theta_0 = \pi/2$  and  $\varphi = \varphi_0$  the following dispersion is obtained:

$$\left(\frac{\omega}{\gamma}\right)^2 = [H \cos(\varphi - \varphi_H) + H_A \cos^2 \varphi][H \cos(\varphi - \varphi_H) + H_A \cos 2\varphi] \quad (5)$$

where  $H_A = 2K/M_S$  is the anisotropy field. The observed angular variation at X band (9.4 GHz) of sample SNi is shown in Figure 7. The magnetic field that satisfies Eq. (5) is the resonant field.

For the particular conditions  $H//$  and  $\perp$  to the wires Eq. (5) adopts the expressions:

$$\frac{\omega}{\gamma} = H + H_A \quad (6)$$

for  $H_A > 0$  and  $H//$  easy axis

If  $H$  is applied with the magnetization pointing initially opposite then, for the limited region within the hysteresis cycle where the magnetization is reversed, Eq. 6 changes to  $(\omega/\gamma) = H_A - H$  as discussed previously in relation to Fig. 6-L2.

For the particular condition  $H\perp$  to the wires Eq. (5) adopt the following expressions:

$$\left(\frac{\omega}{\gamma}\right)^2 = (H_A^2 - H^2) \quad (7a)$$

for  $H < H_A$  and  $H\perp$  easy axis  
and

$$\left(\frac{\omega}{\gamma}\right)^2 = H(H - H_A) \quad (7b)$$

for  $H > H_A > 0$  and  $H\perp$  easy axis

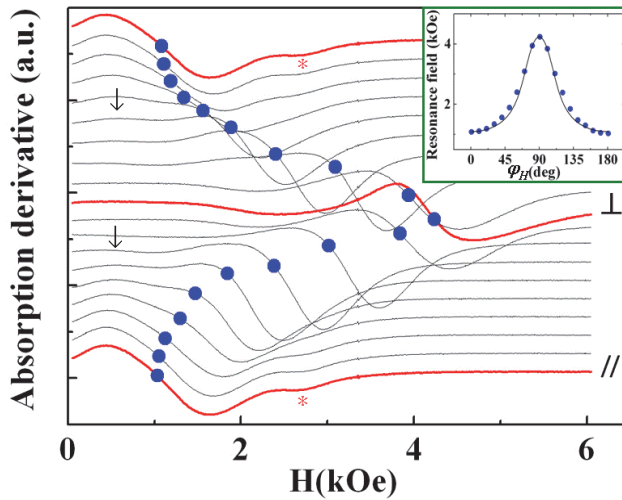


Fig. 7. Angular variation of sample FMR spectra obtained at 9.4 GHz (X-Band). The directions // and  $\perp$  indicate the conditions for which the field is applied parallel and perpendicular to the wires, respectively. The dots indicate the resonance field. Upper right inset: resonance field as a function of the externally applied field angle,  $\varphi_H$ . The full line is a non-linear least-square fit to the experimental data.

Using a non-linear least-square routine to fit the phenomenological parameters of Eq(6) from the observed angular variation, we obtained the following values for this sample:  $H_A = 1.99 \pm 0.08$  kOe and  $g = 2.19 \pm 0.04$ . The  $g$ -factor is consistent with the Ni bulk value  $g = (2.18-2.21)$  reported in the literature [Farle, 1998] and with previously reported values for Ni NWs [Ebels *et al.*, 2001; Ramos *et al.*, 2004a; 2004b]. Dipolar interactions among the wires decrease the effective anisotropy. Indeed, for the case of a homogeneous porous membrane filled with NWs, with filling factor  $f$ :  $H_A \approx 2\pi M_S (1-3f)$ , where  $M_S$  is the saturation magnetization per unit volume. In our case  $f = 0.106 \pm 0.015$  and for  $M_S = 485$  G we obtain  $H_A = 2.1 \pm 0.2$  kOe, consistent with the measured value (an isolated single domain NW would be expected to have  $H_A = 2\pi M_S = 3.0$  kOe, thus dipolar interactions seem to account for the experimentally measured  $H_A$ ).

Apart from this remarkable agreement there are some small features in the absorption derivative spectra that we consider now. In the main panel of Figure 7, signaled by “ $\downarrow$ ”, we have indicated a low-field absorption which is more clearly observed away from the parallel direction. This low-field absorption distorts the main line, particularly at intermediate angles between the // and  $\perp$  directions, thus we did not use these points in the fit (the range of 40-70 degrees away from the easy axis). Li *et al.* [Li *et al.*, 2005] claim that head-on domains as the ones responsible for this low-field line, particularly in the  $H \perp$  NW condition. An alternative explanation for the broad absorption observed in this direction is that a “tail” of the dispersion relation given in Eq. 7b would be the origin for this low-field “line”, particularly in the perpendicular direction (see Fig. 8). In Figure 9 we have drawn the dispersion relation for several angles, and particularly the dispersion relation given by Eq. 7b and 7a using the parameters measured for this sample. In order to test the hypothesis of a non-resonant contribution to the absorption that could come from the Eq. 7b, we have plot in Figure 9 the

calculated effect on the FMR spectrum for  $H < H_A$  (Eq. 7b) and for  $H > H_A$  (Eq. 7a) and compare this calculation with the experimental data. The agreement is remarkable despite the fact that the dispersion relation, does not soften down to  $\omega = 0$  [Encinas-Oropesa et al., 2001]. The fact that the dispersion relation does not soften down to reach  $\omega = 0$  in the hard direction may be connected to the shortcomings of describing all the magnetic spins in a NW as performing a uniform precession characterized by a single uniaxial anisotropy.

Another feature, indicated with an asterisk in the FMR spectra of Figure 7, is pointing to an absorption occurring at fields higher than the main resonance in the condition  $H//$  NWs. We speculate this absorption may be due to a mode localized near the NW ends. If so the intensity of this absorption should decrease with increasing NW length. While this is not apparent in the data of [Ramos et al., 2004a], it turns out that this higher-field absorption decays, in comparison with the main line, as  $1/L$ , where  $L$  is the NW length.

As mentioned previously maximum power absorption occurs when the eigen-frequency matches the exciting microwave frequency at the resonance condition (Fig. 8). This condition is met at  $H = H_R$ , the resonance field. As long as  $H_R > H_{irr}$ , the resonance spectrum does not depend on the magnetic sample history. In magnetic NW arrays in the region  $H < H_{irr}$  the microwave absorption may depend on the magnetic history [Ramos et al., 2007; De la Torre Medina et al., 2010] as explained in the previous subsection.

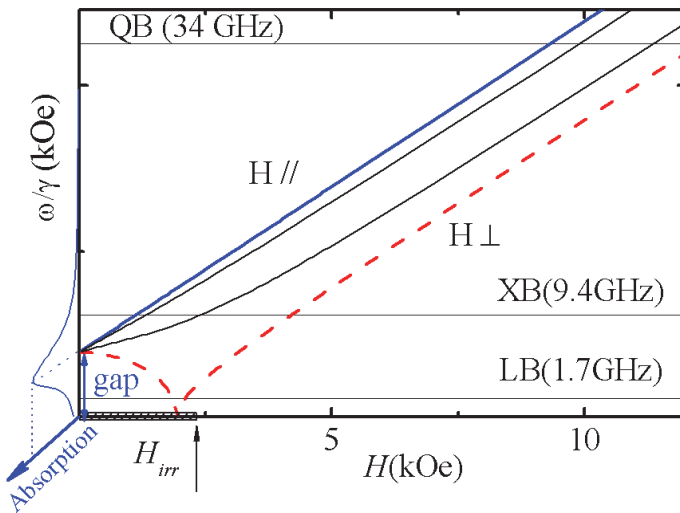


Fig. 8. Dispersion relation  $\omega/\gamma$  vs  $H$  of an ideal uniaxial ferromagnet, for  $H//$  easy-axis (straight blue line - Eq 6) and  $H\perp$  easy-axis (dashed red line, Eq. 7a,b). Two additional dispersion relations corresponding to  $H$  applied at 30 and 60 degrees off the easy axis are drawn as full black lines. The  $\omega/\gamma = H_A$  gap, at  $H = 0$ , is indicated by a vertical double-tip arrow. For  $H//$  easy-axis the resonance condition for 9.4 GHz (X-Band) is reached below the irreversibility field,  $H_{irr}$  (see Fig. 4). The  $\omega/\gamma$  corresponding to 1.2 GHz (L-Band), 9.4 GHz (X-Band) and 34 GHz (Q-Band) and  $g = 2.2$  are indicated as horizontal lines. We have also drawn a schematic Lorentzian line centered at the gap, corresponding to the absorption as a function of frequency for  $H = 0$ . This absorption profile was drawn considering a third axis coming out of the paper.

In Figure 8 we have marked a hysteretic region covering  $|H| < H_{irr} = 2.2\text{kOe}$ , indicated as a hatched rectangle on  $H$ -axis. Below  $H_{irr}$  a hysteretic behavior is observed in the magnetization data and in the FMR spectra LB and XB *only*. Changing the exciting frequency (L, X or Q band) we may choose situations in which the exciting frequency is below the gap (L-band), near the gap (X-band) and above it (Q-band).

A Lorentzian absorption profile is drawn in Fig. 8 centered at  $H = 0$ , the intensity of this Lorentzian is schematically shown as a third axis. For a fixed  $H$  as function of  $\omega/\gamma$  we expect to find an absorption similar to this shape, the position of the maximum changes with  $H$  following closely the dispersion relation, as has been experimentally observed [Encinas-Oropesa *et al*, 2001]. We observed absorption at  $H = 0$  at L-Band and at X-Bands as the line-width superimposes with the exciting frequency.

To simulate the FMR spectra in the case  $H \perp$  NW we consider a Lorentzian absorption centered at a field given by the dispersion relation. The field at which the dispersion relation reaches its minimum ( $H = H_A$ ) corresponds to the minimum of the absorption derivative. This simple model (Fig. 9: blue dash-line) follows well the observed experimental results (blue solid line). For simulating the  $H //$  NW spectrum we considered a low-intensity additional line centered near 2.5kOe, and the fact that a small portion of the NW are inverted near  $H = 0$ , as indicated by the remanent magnetization being 90% of its full value. This partial non-saturation explains, at least partially, the observation of a low-field peak (0.4 kOe) smaller than the high-field (1.6kOe) peak. We will return to the the simulation within the irreversibility region in 3.6.

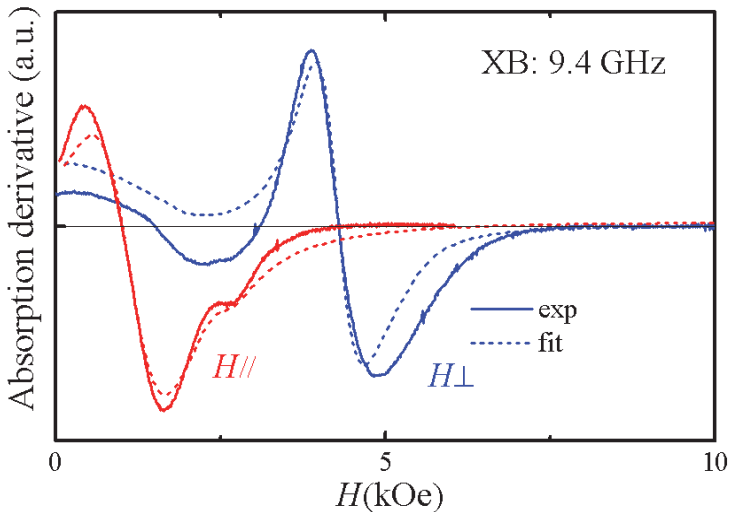


Fig. 9. FMR spectra of sample SNi (9.4 GHz) for  $H //$  and  $H \perp$  to the NWs. The main line position is well described by a single anisotropy field (Eq. 6 and 7). The dash lines are fits considering the dispersion relation with a suitable width. In both cases the zero-field absorption is well reproduced by this simple model.

Many of these low-field effects associated to the proximity of the anisotropy gap disappear when the sample is studied at higher frequencies. We show results of the data obtained at

34.0GHz on the two samples SNI and SA. One of the differences between SNI and SA is its local order, which is greater in sample SNI. In Fig 10 we show the measured angular variation and peak-to-peak line-width,  $\Delta H_{pp}$ .

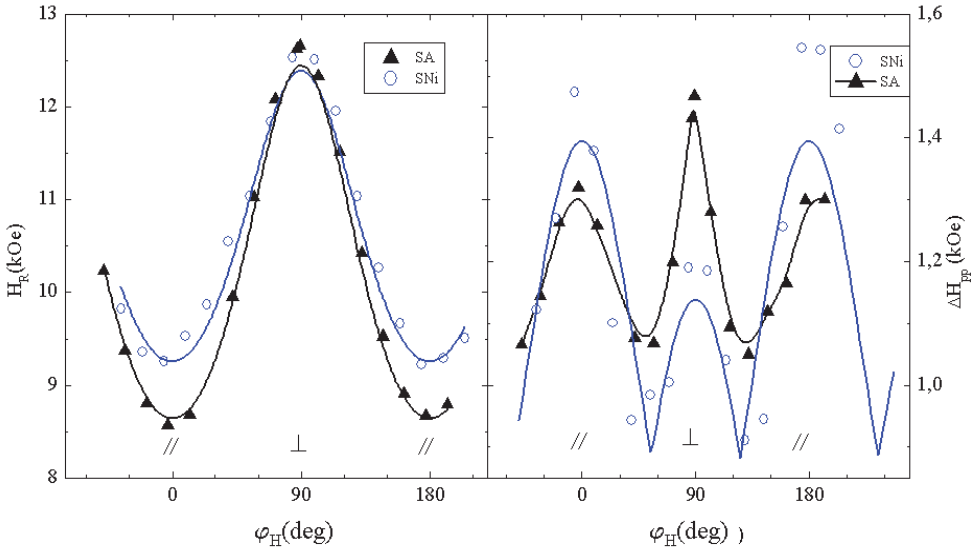


Fig. 10. Left: observed angular variation of the FMR spectra obtained at 34.0 GHz, for the samples reported. Right: observed angular variation of the line-width. This  $\Delta H_{pp}$  for SNI was fit to a model including variation of  $f$  and the NW angle orientation (blue line) The B-Spline fit to the data of SA is shown as a solid black line.

The fits of Eq. 5 to the data shown in the left panel of Fig. 10 yield  $g = (2.16 \pm 0.03)$  and  $(2.20 \pm 0.02)$  for sample SNI and SA respectively, and the effective anisotropy fields  $H_A = (2.1 \pm 0.2)$  kOe and  $(2.49 \pm 0.08)$  kOe for SNI and SA respectively. The  $g$ -value is consistent with the reported values for Ni. The larger value for the anisotropy field in sample SA may be related with a smaller filling factor suggested by the AFM images.

As these NWs have aspect ratios  $\sim 30$  and  $\sim 80$  for sample SA and SNI respectively, the self-demagnetizing factor along the wire length is negligible. The observed departure from the isolated value  $H_A = 2\pi Ms = 3.08$  kOe can be attributed to dipolar interactions, as has been clearly established previously [Ebels *et al.*, 2001; Encinas-Oropesa *et al.*, 2001; Ramos *et al.*, 2004a; 2004b]. There is no indication of tension along the wires, as characterized by X-Ray diffraction in Figure 2 [Vassallo Brigneti, 2009]. Even though the NW grow textured along the [110] direction the crystal field is small ( $\sim 0.2$  kOe), which cannot explain the relatively large linewidths observed in Fig 10 right panel. Ebels *et al.* suggest a Gilbert-damping contribution to  $\Delta H_{pp} \sim 0.4$  kOe independent of angle should be present. Other sources of line broadening can come from variations in the filling factor,  $f$ , and from NW misalignment with the AAO surface. This last option, however, can be discarded. Indeed, NW misalignment would produce a *maximum* at the angle of maximum variation of the resonance field with  $\phi_H$ . We performed a least square fit using a model that takes into account variations in  $\Delta f$ , as well as the NW angular deviation to  $\Delta H_{pp}$  and we obtained, for sample SNI:  $\Delta f/f = (18 \pm 6)$  %, an

angular dispersion of  $(0 \pm 3)$ deg, and a base-line-width of 0.87kOe. The blue line with sharp minima on the right corresponds to this fit [Vassallo Brigneti, 2009]. A similar discussion regarding this type of fit was also considered by Ebels et al, 2001.

A simple calculation indicates that the demagnetizing field when the sample is polarized along the NW, depends on the average filling factor,  $f$ , and not on the "local" disorder [Vassallo Brigneti, 2009]. More difficult to explain with variations in  $f$  alone is the absolute maximum observed in  $\Delta H_{pp}$  of sample SA in the condition  $H \perp$  NW. Previously we considered geometrical local disorder as the main cause for this increased linewidth observed in the perpendicular direction [Vázquez *et al.*, 2005]. More recently we have realized that consideration of local deformations from the ideal cylindrical shape of the NWs is very effective in producing large variations of the resonance field in the perpendicular direction, much more than in the parallel direction [Vassallo Brigneti, 2009]. This correlates the observed maximum at  $H \perp$  NW with the larger lattice disorder [Vassallo Brigneti 2009].

### 3.5 Consequences on the FMR applied to nanoparticles

In non-interacting superparamagnetic nanoparticle systems magnetization follows a  $(H/T)$ -scaling behavior. Thermal fluctuations decrease the effective uniaxial anisotropy field,  $H_{Aeff}$ . This  $H_{Aeff}$  increases as the  $T$  is reduced while preserving the uniaxial symmetry [De Biasi *et al.*, 2003; Dorman *et al.*, 1997; Pujada *et al.*, 2003; Raikher & Stepanov, 1994]. If we consider an initial anisotropy gap smaller than the exciting frequency (as in Figure 8 for X-Band and the gap shown), we may expect an increase of the effective anisotropy field as  $T$  is lowered [De Biasi *et al.*, 2003; Raikher & Stepanov, 1994] and the condition of a gap larger than  $\omega/\gamma$  is likely to be reached. As the anisotropy gap exceeds the microwave frequency the nanoparticles whose easy axes are close to the direction of the applied field will not longer reach the resonance condition. We concluded this is what happens in some nanoparticles at low temperature [DeBiasi *et al.*, 2004; 2005] that evidence an intensity drop as the effective anisotropy field becomes greater than  $\omega/\gamma$ . In previous works [Antoniak *et al.*, 2005; Berger *et al.*, 2001; Sánchez *et al.*, 1999] this intensity loss was associated with "blocking" in the sense that the magnetic system was not able to follow the microwave excitation frequency  $\nu \approx 10^{10}$  GHz (X band) below this "blocking" temperature. If that would be the case then, at the same temperature, the system would not be able to show any sign of resonance at a *higher* frequency, such as Q-band (35GHz), which is not the case (see also, [Ennas *et al.*, 1998]). In this work we use this ideal "blocked" Ni NWs to study the system at three different frequencies and as a function of the sample history.

In spite of the apparent restrictive case of ferromagnetic NW we want to emphasize that the consequences on the *line-shape* and resonance condition of other ferromagnets with large uniaxial anisotropy is straight forward [De Biasi *et al.*, 2003; Winkler *et al.*, 2004]. In these cases the FMR spectra could be satisfactorily accounted for as a collection of randomly-oriented uniaxial ferromagnets. This line-shape can be readily distinguished from paramagnetic phases [Winkler *et al.*, 2007; Likodimos & Pissas, 2007; Tovar *et al.*, 2008] that coexist in the material, such the case of mixed-valence manganites. Indeed, this phase coexistence seems to be the cause of the large magnetoresistance effects observed in these colossal-magneto-resistance materials (CMR).

### 3.6 FMR results in the irreversible region

In this section we present FMR results on sample S<sub>Ni</sub>, characterized in Fig 1- 4. The sample under study is made up of individual NWs subject to its own shape anisotropy, and dipolar

interactions among them. This sample is constituted of NW which can be approximated as single domain uniaxial ferromagnets which are “blocked” -in the sense of magnetic nanoparticles- and have the virtue of being aligned along the NW direction.

Two spectra types are shown in Figure 11: one in which the sample initial magnetization is polarized in the same direction as the field sweep ( $H//M_i$ , blue circles in Fig. 11, which we will call DP, for direct polarization), and a second experiment ( $H// -M_i$ , red triangles in Fig. 11, referred to as RP for reverse polarization) in which the sample is initially polarized in the reverse direction of the field sweep.

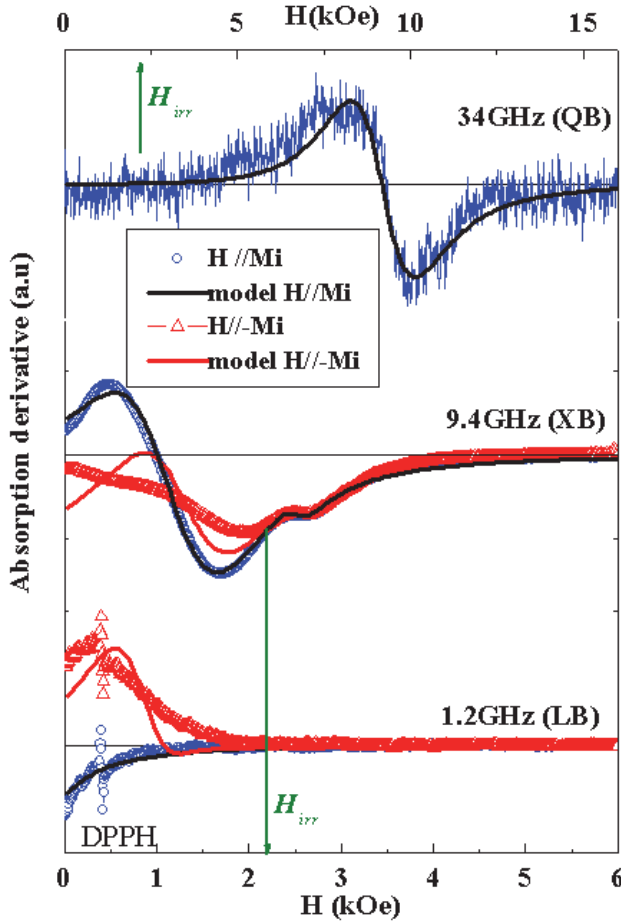


Fig. 11. FMR for sample SNI measured at three different frequencies, 34.0, 9.4 and 1.2 GHz, corresponding to Q, X and L-bands respectively. All data was obtained at room temperature in the condition  $H//NW$  after saturation in the same direction, and therefore the remanent magnetization is in the same direction as the field ( $H//M_i$ , blue circles) and the reverse initial magnetization ( $H// -M_i$ , open red triangles). The black (and red) full lines correspond to the model detailed in the text.

The RP was obtained using a compensating coil and reducing the field after saturation to  $(0.0 \pm 0.1)$  Oe, as measured by the Hall sensor that regulates  $H$ . Afterwards the sample was rotated by 180 degrees while the magnet was kept at  $H = 0$  and then the condition RP could be achieved. No significant changes were observed between DP and RP at 34GHz, particularly below  $H_{irr}$ , therefore we only plot the DP spectrum. A significant difference between DP and RP is observed below  $H_{irr}$  at 9.4 and 1.2 GHz. At  $H = H_{irr}$  DP and RP merge into a single signal. More remarkably, the signal is initially positive in the condition  $H//Mi$  at X band and *negative* under the same condition in L-Band. Particularly at L-Band it is very helpful to record simultaneously a DPPH g-marker, as it indicates the field and is an intrinsic calibration of the instrument *phase*, therefore indicates clearly that the initial signal is negative. The full lines correspond to a fit of the model described in association with Figure 6. The model consists of: 1) finding a phenomenological function to reproduce the measured total magnetization as the sum of independent contributions (populations) from different NWs whose magnetization projection can only be DP or RP as a function of  $H$ , 2) following the dispersion relation for the DP (RP) branch that corresponds to the full-line (dash-line) of Fig. 6-L2, with its population as a function of  $H$ ; 3) adding algebraically the two contributions centered at their natural frequencies.

The agreement is very good for L-Band, excellent in DP X-Band, and good in RP X-Band, considering the simplicity of the model. For Q-Band it indicates not difference between DP and RP should be expected, in accordance with experiment. Only coherent rotation has been considered in this model. Other mechanisms that could contribute to the microwave absorption in the irreversible region have not been taken into account.

#### 4. Conclusion

In this chapter we have reviewed some of the characteristics of Ni ferromagnetic nanowires grown by electrodeposition into AAO membranes of very good uniformity. A uniaxial anisotropy model was detailed and some results of FMR were shown to be consistent with small variations in the filling factors indicating dipolar interactions compete with the uniaxial character of the magnetic anisotropy. Furthermore, the measured filling factors indicate small variations in the magnetic anisotropy between samples could be associated with these subtle structural changes in the AAO matrix. We showed that a contribution to the FMR line-widths can be originated in fluctuations in the porosity or filling factors of the sample, particularly in the condition  $H//NW$ . On the other hand, local distortions from the cylindrical shape would affect more strongly the line-width in the perpendicular condition. The most important result of this work is that there is *no blocking in ferromagnetic resonance* in the way in which is normally used in AC susceptibility, essentially because FMR is not performed at  $H = 0$ . In many cases the applied field is higher than the irreversibility field (Fig. 4) and this condition defines a single energy minimum, therefore the system will be performing small oscillations around this minimum because the magnetization tends to relax extremely fast to the equilibrium position [Kittel, 2005]. What many researchers have believed (ourselves included in the past! [Sánchez *et al.*, 1999]) to be caused by “blocking” can be explained as being caused by the effective anisotropy field as a function of temperature growing larger than the characteristic exciting frequency,  $\omega/\gamma$ , and thus not being able to excite resonantly the material at any applied field. In this sense the Ni NW are

an excellent system to study the response far above (Q-Band), above and near (X-Band), and below (L-Band) the anisotropy field gap.

## 5. Acknowledgment

This work was partially supported by CONICET (PIP 2008-1333), ANPCyT (PICT 2007-832). CAR acknowledges the support of the Universidad Nacional de Cuyo (SeCTyP 06-C320)

## 6. References

- Allende, S. Altbir, D. Salcedo, E. Bahiana & M. Sinnecker, J. P., (2008) Propagation of transverse domain walls in homogeneous magnetic nanowires, *Journal of Applied Physics*, vol 104, No 1 (June 2008) pp 013907-1/6, ISSN: 0021-8979.
- Antoniak, C. , Lindner, J. & Farle, M. (2005), Magnetic anisotropy and its temperature dependence in iron-rich  $\text{Fe}_x\text{Pt}_{1-x}$  nanoparticles *Europhysics Letters* Vol 70, No 2 (March 2005) pp 250-256, ISSN: 0295-5075.
- Berger, R. , Bissey, J-C., Kliava, J. , Daubric, H. & Estournès, C. (2001), Temperature dependence of superparamagnetic resonance of iron oxide nanoparticles, *Journal of Magnetism and Magnetic Materials*, Vol 234, No 3 (September 2001) pp. 535-544, ISSN: 0304-8853.
- Boucher, V., & Ménard, D. (2010), Effective magnetic properties of arrays of interacting ferromagnetic wires exhibiting gyromagnetic anisotropy and retardation effects, *Physical Review B* Vol 81, No 17 (May 2010) pp 174404-1/21, ISSN: 0163-1829.
- Brown, J. W. (1963), Thermal fluctuations of a single-domain particle, *Physical Review* 130, No 5 (June 1963), pp. 1677-1686, ISSN: 0031-899X.
- Casanova, F., Chiang, C. E., Li, C-P., Roshchin, I. V. , Ruminski, A. M., Sailor M. J., and Schuller, I. K. (2008); Gas adsorption and capillary condensation in nanoporous alumina films *Nanotechnology*, Vol. 19, No.31 (June 2008) pp. 315709-1/6, ISSN: 0957-4484.
- Cullity, B. D., 1972, *Introduction to Magnetic Materials*, pp. 618-620. Addison Wesley. Reading, Massachusetts, USA, ISBN: 0-201-01218-9.
- Darques, M., Spiegel, J., De la Torre Medina, J., Huynen, I., & Piraux, L. (2009), Ferromagnetic NW-loaded membranes for microwave electronics *Journal of Magnetism and Magnetic Materials*, Vol. 321, No. 14 (July 2009) pp. 2055-2065, ISSN: 0304-8853.
- Darques, M., De la Torre Medina, J., Piraux, L., Cagnon L. & Huynen, I., Microwave circulator based on ferromagnetic NWs in an alumina template *Nanotechnology* Vol 21, No14 (March 2010) pp. 145208-1/4, ISSN: 0957-4484.
- De Biasi, E., Ramos, C. A. & Zysler, R.D. (2003), Size and anisotropy determination by ferromagnetic resonance in dispersed magnetic nanoparticle systems *Journal of Magnetism and Magnetic Materials*, Vol 262, No 2, (Jun 2003) pp. 235-241; Vol 278, No 1-2, (Jul 2004), pp 289. ISSN: 0304-8853.

- De Biasi, E., Ramos, C.A., Zysler, R.D., Romero, H. (2004), Ferromagnetic resonance in amorphous nanoparticles *Physica B*, Vol 354, No 1-4 (Dec 2004) pp. 286-289. ISSN: 0921-4526.
- De Biasi, E., Zysler, R. D., Ramos, C. A., Romero, H. & Fiorani, D. (2005) Surface anisotropy and surface-core interaction in Co-Ni-B and Fe-Ni-B dispersed amorphous nanoparticles *Physical Review B* Vol 71, No 10 (Mar 2005) pp. 104408-1/6, ISSN: 0163-1829.
- De Biasi, E., Zysler, R.D., Ramos, C. A. & Knobel, M. (2008), A new model to describe the crossover from superparamagnetic to blocked magnetic nanoparticles *Journal of Magnetism and Magnetic Materials*, Vol 320, No 14, (Jul 2008) pp. e312-e315. ISSN: 0304-8853.
- De La Torre Medina, J., Piraux, L., Olais Govea, J. M. & Encinas, A. (2010) Double ferromagnetic resonance and configuration-dependent dipolar coupling in unsaturated arrays of bistable magnetic NWs *Physical Review B*, Vol 81, No 14 (Apr 2010) pp. 144411-1/11, and references there in, ISSN: 1098-0121.
- Dorman, J.L., Fiorani, D. & Tronc, E. (1997), Magnetic relaxation in fine-particle systems *Advances in Chemical Physics* Vol 98 (Jan 1997) pp. 283-494, ISBN: 0-471-16285-X.
- Ebels, U., Duavil, J.-L., Wigen, P. E., Piraux, L., Buda, L. D., Ounadjela, K. (2001), Ferromagnetic resonance studies of Ni nanowire arrays, *Physical Review B*, Vol 64, No 14 (Sep 2001), pp.14421-1/6, ISSN: 1098-0121.
- Encinas-Oropesa, A., Demad, M., Piraux, L., Huynen, I. & Ebels, U. (2001) Dipolar interactions in arrays of nickel NWs studied by ferromagnetic resonance, *Physical Review B*, Vol 63, No 10 (February 2001) pp 104415-1/6, ISSN: 1098-0121.
- Ennas, G., Musinu, A., Piccaluga, G., Zedda, D., Gatteschi, D., Sangregorio, C., Stanger, J. L., Concas G. & Spano G. (1998), *Chemistry of Materials*, Vol(10), No 2, (Jan 1998), pp. 495-502, ISSN: 0897-4756.
- Farle, M. (1998), Ferromagnetic resonance of ultrathin metallic layers. *Reports of Progress in Physics*, Vol 61, No 7, (Jul 1998), pp. 755-826, ISSN: 0034-4885.
- Ferain, E., Legras, R. (2009), Templates for engineered nano-objects for use in microwave, electronic devices and biomedical sensing application, *Nuclear Instruments and Methods Physics Research B* Vol. 267, No. 6, (Mar 2009), pp. 1028-1031, ISSN: 0168-583X.
- Fert, A. (2008). Nobel Lecture: Origin, development, and future of spintronics. *Reviews of Modern Physics*, Vol. 80, No.4, (Oct-Dec 2008), pp. 1517-1530, ISSN 0034-6861.
- Fert, A., Piraux, L. (1999), Magnetic NWs *Journal of Magnetism and Magnetic Materials*, Vol. 200, No.1-3, (Oct 1999), pp. 338-358 ISSN: 0304-8853.
- Hertel, R., Kirschner, J. (2004), Magnetization reversal dynamics in nickel NWs, *Physica B* Vol 343 No 1-4, (January 2004) pp., 206-210. ISSN: 0921-4526.
- King, A. R., Mydosh, J. A., Jaccarino, V. (1986), ac Susceptibility Study of the d= 3 Random-Field Critical Dynamics, *Physical Review Letters* Vol 56, No 23 (Jun 1986) pp. 2525-2528. ISSN 0031-9007.
- Kittel, C., 2005, *Introduction to Solid State Physics*, 8<sup>th</sup> Edition, pp 379-383J. Wiley & Sons, Hoboken, NJ, USA, ISBN 0-471-41526-X

- Kraus, L., Infante, G., Frait, Z. & Vázquez, M., (2011), Ferromagnetic resonance in very thin wires (from micro- to nanowires), *Physical Review B*, Vol 83, No 17 (May 2011) pp 174438-1/11. ISSN 1098-0121.
- Li, T., Sui, Y., Huang, Z., Yang, S., Gu, B. & Du Y. (2005) , Spin-configuration-related ferromagnetic resonance in nickel nanowire array, *Journal of Physics: Condensed Matter*, Vol 17, No 23, (May 2005) pp. 3637-3645. ISSN: 0953-8984
- Likodimos, V., & Pissas, M. (2007), Phase coexistence and magnetic anisotropy in  $\text{La}_{1-x}\text{Ca}_x\text{MnO}_3$  ( $0 < x \leq 0.23$ ) studied via electron spin resonance *Physical Review B* Vol 76, No 2 (Jul 2007) pp. 024422-1/10pp. ISSN: 1098-0121.
- Lubitz, P. Rubinstein, M., Christodoulides, J. A. & Chrisey D. B. (2004), Source of anomalies in the temperature dependence of ferromagnetic resonance and susceptibility data in the FeAg heterosystem, *Journal of Applied Physics*, Vol 95, No 11 (June 2004) pp. 7124-7126. ISSN: 0021-8979.
- Lundgren, L., Svendlindh, P., Norblad, P. & Beckman, O. (1983), Dynamics of the Relaxation-Time Spectrum in a CuMn Spin-Glass, *Physical Review Letters*, Vol 51, No 10, (September 1983) pp. 911-914. ISSN: 0031-9007.
- Masuda, H., Fukuda, K. (1995), Ordered Metal Nanohole Arrays Made by a Two-Step Replication of Honeycomb Structures of Anodic Alumina *Science*, Vol. 268, No 5216, (June 1995), pp. 1466-1468 ISSN: 0036-8075.
- Morrish, A.H. (2001) *Physical Principles of Magnetism*, IEEE Press, Piscataway, New York, 2001. ISBN: 0-7803-6029-X.
- Mydosh, J.A. (1993), *Spin-glasses: an experimental introduction*, Taylor & Francis, London, Great Britain (June 1993). ISBN: 10- 0748400389.
- Niensch, K., Müller, F., Li, A.-P. & Gösele, U., (2000) Uniform Nickel Deposition into Ordered Alumina Pores by Pulsed Electrodeposition, *Advanced Materials*, Vol 12, No 8, (April 2000), pp 582-586, ISSN: 0935-9648.
- Niensch, K., Wehrspohn, R., Barthel, J., Kirschner, J., Gösele, U., Fischer, S. Kronmüller, H. (2001), Hexagonally ordered 100 nm period nickel NW arrays, *Applied Physics Letters* Vol 79, No 9, (August 2001), pp. 1360-1362. ISSN: 0003-6951.
- Orosco, M. M., Pacholski, C., Sailor, M. J. (2009) Real-time monitoring of enzyme activity in a mesoporous silicon double layer *Nature Nanotechnology*, Vol 4, pp. 255-258. ISSN: 1748-3387.
- Pacholski, C., Yu, C., Miskelly, G. M., Godin, D., and Sailor, M. J. (2006), Relective Interferometric Fourier Transform Spectroscopy: A Self-Compensating Label-Free Immunosensor Using Double-Layers of Porous  $\text{SiO}_2$  *Journal of the American Chemical Society*, Vol. 128, No 13, (Aug. 2006), pp. 4250-4252, ISSN: 0002-7863.
- Pirota, K.R., Knobel, M., Hernandez-Velez, M., Niensch K. & Vázquez, M. (2010) Magnetic Nanowires: fabrication and characterization, *Handbook of Nanoscience and Nanotechnology*, vol. II Eds. A. V. Narlikar and Y. Y. Fu (Oxford University Press, USA, 2010) chapter XXII, pp. 772-824, ISBN: 978-019-953305-3
- Pirota, K.R., Navas, D., Hernández-Velez, M., Niensch, K. & Vázquez, M. (2004) Novel magnetic materials prepared by electrodeposition techniques: arrays of nanowires and multi-layered microwires, *Journal of Alloys and Compounds* Vol. 369, No 1-2, (April 2004), pp 18-26, ISSN: 0925-8388

- Pujada, B.R., Sinnecker, E.H.C.P., Rossi, A. M., Ramos, C. A. & Guimarães, A.P.(2003). FMR evidence of finite-size effects in CoCu granular alloys *Physical Review B*. Vol 67, No 2 (January 2003) pp. 024402-1/6, ISSN: 0163-1829.
- Raikhher, Yu.L., Stepanov, V.I. (1994) Ferromagnetic resonance in a suspension of single-domain particles *Physical Review B* Vol 50, No 9 (September 1994) pp. 6250- 6259, ISSN: 1098-0121.
- Ramos, C. A., King, A. R. & Jaccarino, V. (1988), Determination of the crossover exponent in the random-field system  $Mn_xZn_{1-x}F_2$ , *Physical Review B* Vol 37, No 10 (April 1988), pp. 5483-5492 ISSN: 1098-0121.
- Ramos, C. A., Vázquez, M., Nielsch, K., Pirota, K., Rivas, R. B., Wherspohn, R. B., Tovar, M., Sánchez, R. D. & Gösele, U. (2004a). FMR characterization of hexagonal arrays of Ni NWs. *Journal of Magnetism and Magnetic Materials* Vol 272-276 (May 2004) pp. 1652-1653. ISSN 0304-8853.
- Ramos, C. A., Vassallo Brigneti, E. & Vázquez, M. (2004b). Self-organized NWs: evidence of dipolar interactions from ferromagnetic resonance measurements, *Physica B* Vol 354 (2004) pp. 195-197 ISSN: 0921-4526.
- Ramos, C. A., De Biasi, E., Zysler, R.D., Vassallo Brigneti, E. & Vázquez, M. (2007) 'Blocking' effects in magnetic resonance? The ferromagnetic NW case *Journal of Magnetism and Magnetic Materials*, Vol 316, No 2 (September 2007) pp. e63-e66 ISSN 0304-8853.
- Sánchez, R. D., Rivas, J., López Quintela, A. M., González Penedo, A. , García Bastida, A.J., Ramos, C. A., Zysler, R.D.& Ribeiro Guevara, S. (1999), Magnetization and EPR of Co clusters embedded in Ag nanoparticles, *Journal of Physics: Condensed Mater*, Vol 11, No 29, (1999) pp. 5643-5654, ISSN 0953-8984.
- Smit, J. & Beljers, H.G. (1955) Ferromagnetic resonance absorption in  $BaFe_{12}O_{19}$ , a highly anisotropic crystal, *Philips Research Reports* Vol 10, No 2 (April 1955)pp. 113-130, ISSN: 0031-7918.
- Tovar, M., Causa, M. T., Ramos, C. A. & Laura-Ccahuana, D. (2008) Phase separation in La-Ca manganites: magnetic field effects. *Journal of Magnetism and Magnetic Materials*, Vol 320, No 3-4 (February 2008) pp.523-527, ISSN: 0304-8853.
- Trunova, A. V., Linder, J., Meckenstock, R., Spasova, M., Farle, M., Ciuculescu, D., Amiens, C., Chaudret, B. & Respaud, M. (2009), Temperature dependent magnetic characterisation of core/shell  $Fe_{80}Rh_{20}$  nanoparticles, *Journal of Magnetism and Magnetic Materials*, Vol 321, No 20 (Oct 2009), pp 3502-3506 ISSN: 0304-8853.
- Vassallo Brigneti, E. C. (2009) Estudio de las propiedades estáticas y dinámicas de nanohilos magnéticos y películas nanoporosas, *Ph D. Thesis* (June 2009)pp 1-186, Instituto Balseiro, Universidad Nacional de Cuyo.
- Vázquez, M., Hernández-Vélez, M., Pirota, K., Asenjo, A., Navas, D., Velásquez, J., Vargas, P. & Ramos, C. (2004) Arrays of Ni NWs in alumina membranes: magnetic properties and spatial ordering *European Physics Journal B*, Vol 40 No 4, (June 2004) pp. 489-497, ISSN: 1434-6028.
- Vázquez, M., Ramos, C., Vassallo, E., Jaafar, M. & Asenjo, A. (2005), Combined Ferromagnetic Resonance and Magnetic Force Microscopy studies in arrays of magnetic NWs, *Transactions of the Magnetic Society of Japan* Vol 5, No 4 (2005) pp. 157-160, ISSN:1346-7948.

- Winkler, E., Causa, M. T., Ramos, C. A. & De Biasi, E., (2004) ESR phase competition study of  $\text{Pr}_{0.5}(\text{Ca}_{0.85}\text{Sr}_{0.15})_{0.5}\text{MnO}_3$  *Physica B*, Vol 354, No 1-4 (December 2004), pp 51-54. ISSN: 0921-4526
- Winkler, E., Causa, M. T. & Ramos, C. A. (2007), Ferromagnetic resonance study in  $\text{Pr}_{0.5}(\text{Ca}_{1-x}\text{Sr}_x)_{0.5}\text{MnO}_3$ , *Physica B* Vol 398, No 2, (September 2007) pp 434-437 ISSN: 0921-4526.
- Yang, P., Yan, R. & Fardy M. (2010), Semiconductor Nanowire: What's Next?, *Nano Letters* Vol 10, No 5, (April 2010) pp 1529-1536, ISSN: 1530-6984.

# Growth of Germanium Nanowires on a Flexible Organic Substrate

Lauren A. Klein<sup>1</sup>, Daniel D. T. Mastrogiovanni<sup>1</sup>, Aurelien Du Pasquier<sup>2</sup>,  
Tong Wang, Alan S. Wan<sup>1</sup> and Eric Garfunkel<sup>1</sup>

<sup>1</sup>*Department of Chemistry and Chemical Biology, Rutgers University, Piscataway,*

<sup>2</sup>*Department of Materials Science and Engineering, Rutgers University, Piscataway,  
New Jersey,  
USA*

## 1. Introduction

Germanium nanowires (GeNWs) have received extensive attention due to their potential use in electronic, optoelectronic, sensor and other applications. (Heath 2000; Wu and Yang 2000; Hanrath and Korgel 2002; Hanrath and Korgel 2004) (Greytak 2004) The small size, high aspect ratio, and high surface/volume ratio of Ge and other semiconducting nanowires also make them of great fundamental scientific interest. (Jing, Ni et al. 2006; Allen 2007) GeNWs grown via a vapor-liquid-solid (VLS) mechanism in a modified chemical vapor deposition (CVD) process are crystalline. (Dailey 2004) They can be patterned, functionalized, and/or made components of heterostructures for device applications. (Yun 2003; Hanrath and Korgel 2004; Dai 2005; Wang, Chang et al. 2005; Adhikari, Marshall et al. 2006; Pasquier, Mastrogiovanni et al. 2007) Germanium possesses a higher carrier mobility than silicon, as well as a lower nanowire growth temperature when grown using the VLS method (Adhikari, Marshall et al. 2007).

There would be a large market for flexible electronic and photonic devices if functionality and performance could approach that of conventional solid state devices at a reasonable cost. (Bradley, Gabriel et al. 2003; Bitetti, Marchetti et al. 2007) Polymer films hold great promise as a cost-efficient substrate for potential applications such as those of photovoltaics or display technologies, due in large part to their ease of manufacturing, low cost, and extensive past development.

Other complex materials combinations are being explored including integrating inorganic nanoparticles or small molecule organics with polymers. Two classes of methods for integrating semiconductor nanowires with flexible materials are: (i) transferring wires from a sacrificial growth substrate to a new material via contact printing or solution deposition (Bradley, Gabriel et al. 2003; McAlpine, Friedman et al. 2003; Saran, Parikh et al. 2004; Fan, Ho et al. 2008), and (ii) direct integration via solution growth or very low temperature VSS growth. (Gibson 2005; Lin 2005; Kang 2008) In the former method nanowires must first be grown on some other substrate and then harvested. However, for many large-scale applications direct growth would be highly preferable. Growing nanowires on the polymer substrates simplifies the processing of any devices through reduction of the number of

necessary steps, and thus becomes more cost-effective. Direct growth saves time, reduces the risk of damage to the nanowires during harvesting, and also securely fastens the wires to the substrate. The wires grown in this study were anchored to the polymer with sufficient integrity to withstand extensive flexing of the substrate, and were manufactured at standard VLS growth temperatures.

The relatively low decomposition temperatures of most polymers cannot survive the growth temperature used in most VLS nanowire processing. However, the growth temperatures of GeNWs, 300-400°C, does allow for direct growth on thermally stable polymers. Polyimides such as Kapton, are one class of polymers that offer promise. Recent advances in the thermal stability of polymers (to over 600°C) offer hope that flexible, and in some cases transparent, substrates can be manufactured to enable the extension of our methods to other nanowire/nanotube growth systems such as silicon nanowires or carbon nanotubes. (Ree, Kim et al. 1997; Maya, Lozano et al. 2005; Li, Liu et al. 2006; Choi, Chung et al.; Chung and Hsiao 2008; Wang, Yi et al. 2008)

## 2. Growth and processing methods

### 2.1 Polymer processing

In the near future, it is expected that an increasing amount of these materials will be made commercially available, though not many are on the market today. For the studies contained herein, Kapton (Dupont) and poly[(4,4'-hexafluoroisopropylidene) diphthalic anhydride-*alt*-3,6-diaminoacridine hemisulfate] (Sigma-Aldrich) are used. It is the relatively low growth temperature of germanium nanowires which makes growth on any polymer, even those listed above, possible. Both materials possess a glass-transition temperature just above the required growth range for germanium nanowires.

To prepare the fluorinated polyimide samples, poly[(4,4'-hexafluoroisopropylidene) diphthalic anhydride-*alt*-3,6-diaminoacridine hemisulfate] is dissolved in DMSO at a concentration of 10 mg/mL. The solution is subsequently drop cast onto a glass slide while simultaneously heating at 50 °C to expedite solvent removal. It should be noted that by this preparation method, the fluorinated polyimide samples are not flexible, but if bulk material were available, flexible substrates of fluorinated polyimide could easily be treated in the same manner as Kapton.

Germanium nanowires grow via a catalyzed mechanism, and the polymer substrates must first be coated with gold a thin gold film or gold particles. Gold deposition is achieved by one of two methods, either through sputter coating thin films on the surface, or through wet chemical treatment. Kapton sheets were sputter-coated with Au films roughly 2, 5, 10, and 50 nm thick. Exact thicknesses were determined using Rutherford Backscattering Spectroscopy (RBS). Polymer substrates cleaned with methanol to remove organic contaminants were exposed to a 0.1M solution of 3-aminopropyltriethoxysilane (APTES) in methanol for 24 hours. The sheets were removed, rinsed clean, and then blown dry with purified N<sub>2</sub>. The functionalized films were then submerged in commercial gold nanoparticle solutions (Ted Pella, Inc) with nanoparticle diameters ranging between 10 and 50 nm.

### 2.2 Germanium nanowire growth

The functionalized plastic substrates were confined to a specially designed stainless steel holder to prevent deformation of the polymer as higher temperatures were attained. For

growth on Kapton a stainless steel holder was required to keep the thin plastic sheets from deforming during growth. The stainless steel holder we used to secure the Kapton is shown in figure 1, below. As our growth temperatures approach the glass transition temperature of Kapton, if the film was not restrained, significant curling of the film would take place, undesirable for subsequent processing and studies. The holder measures 10cm x 1.8cm x 0.6cm.



Fig. 1. Stainless steel holder designed to accommodate Kapton samples

All processed substrates were placed in a hot-wall CVD reactor. Germane ( $\text{GeH}_4$ ) gas (5% in He, Voltaix) was flowed through the system at a rate of 20 sccm at partial pressures ranging from 1-3 Torr. Growth timing was varied between 5 and 30 minutes. Growth temperature was held at  $360^\circ$ . Processing temperatures in this range lead to conical wires, due to radial non-catalyzed CVD growth. A diagram of this procedure is shown in figure 2.

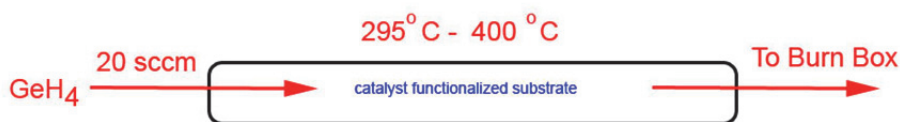


Fig. 2. Diagram of germanium nanowire growth scheme.

### 2.3 Post growth processing

Nanowire samples were placed in a 0.1M solution of 1-octanethiol for 24 hours immediately upon removal from the reactor. Alkanethiol solutions have been shown to form self-assembled monolayers on germanium substrates and are attractive chemicals to begin passivation studies with as they can be terminated with large number of functional groups which can be subsequently reacted to more fully functionalize a surface. (Hanrath and Korgel 2004; Wang, Chang et al. 2004; Wang, Chang et al. 2005) (Sang 2001)

### 3. Results

#### 3.1 Growth on polymer substrates

Germanium nanowires grown on Kapton and fluorinated polyimide samples produce a high yield of nanowires with good mechanical and chemical robustness. Wires produced in these growths are slightly tapered, due to uncatalyzed CVD deposition on the sides of the wire as growth proceeds.

A satisfactory mechanical robustness was observed when wires were anchored to a flexible material; the systems underwent considerable bending and flexing consistent with being handled in the lab and no detachment or damage to the wires was evident. Figure 3, below, represents one such system, imaged while the Kapton substrate was restricted in a bent position.

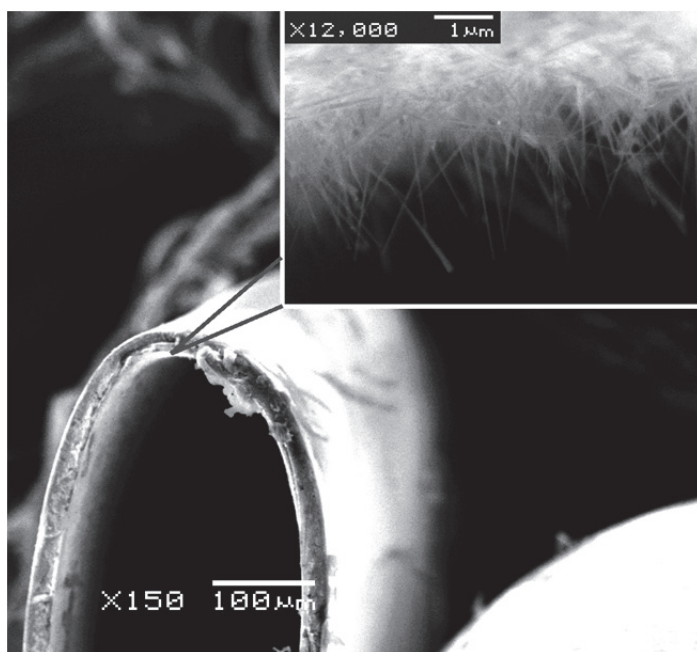


Fig. 3. Germanium nanowires grown on Kapton. Inset image shows wires from the height of the Kapton fold.

Figure 4 shows a side-view scanning electron micrograph of GeNWs on Kapton. These wires were grown at  $360^\circ$  for 15 minutes from 10nm Au colloid particles. Remaining catalysts can be observed at the tips of the wires. Tapering is clearly evident, most likely stemming from non-catalyzed radial CVD growth.

In Figure 5, a top-view image is shown of GeNWs grown on poly[(4,4'-hexafluoroisopropylidene) diphthalic anhydride-*alt*-3,6-diaminoacridine hemisulfate]. These wires were grown at  $360^\circ$  for 15 minutes from 10nm Au colloid particles. Excellent uniformity of the length and diameters of the wires is noted.

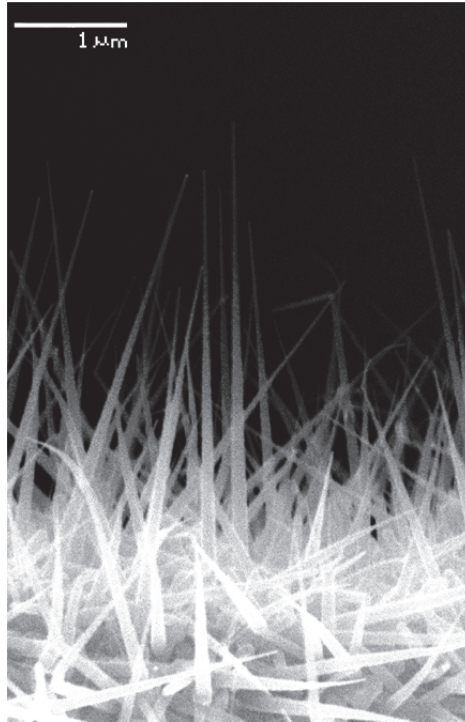


Fig. 4. Side view scanning electron micrograph images of GeNWs on Kapton.

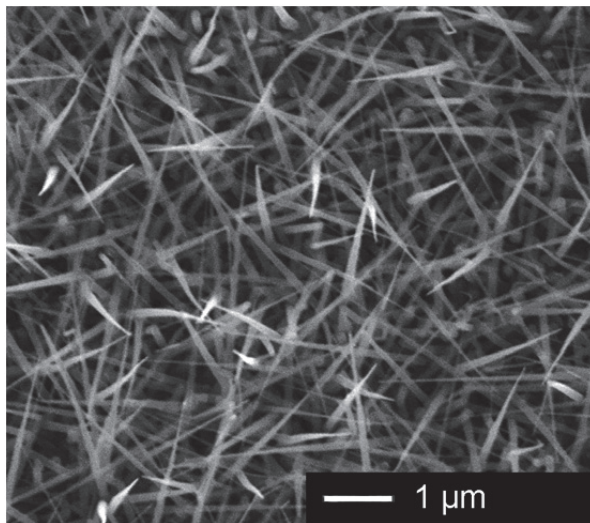


Fig. 5. Top view scanning electron micrograph image of GeNWs grown on poly[(4,4'-hexafluoroisopropylidene) diphthalic anhydride-*alt*-3,6-diaminoacridine hemisulfate].

### 3.2 Colloidal gold vs. sputtered gold films

The starting gold catalyst is critical to the nanowire formation. As described in the methods section above, both sputter-coated Au films and wet chemical deposition of colloidal gold particles were utilized as sources of gold. For most applications in nanotechnology it is uniformity in size and spatial distribution which is sought in these wires; variations in length and diameter lead to variations in electrical physical properties and physical. Thus, the ideal growth will produce wires as similar in length and diameter as possible.

To ensure uniformity of nanowire diameter across a single sample during growth, colloidal catalysts are preferred over sputter-coated films. As the eventual nanowire diameter is determined by the prepared colloid diameter, wires can be grown over large areas with precise control over their size. We used predominantly 10nm and 20nm colloids in these studies. The colloids, as purchased, have a rough concentration of about  $10^{11}$  nanoparticles/mL and will generally coat the substrates in a uniform manner when prepared as described above. Less dense areas can be prepared by diluting colloid solutions with distilled, deionized water.

In Figure 6, shown below, the wires were grown from 20 nm colloids under standard growth conditions as described above. One will note the general consistency among wire diameters. Prior to heating, the colloids are certified by Ted Pella to be within 18 and 22 nm in diameter. It is observed, however, that wires often differ from this initial diameter range by 10-20 nanometers. There are two reasons for this discrepancy. First, once exposed to air, wires typically grow a 5nm coating of native oxide,  $\text{GeO}_x$ , making them appear fatter in scanning electron micrographs.

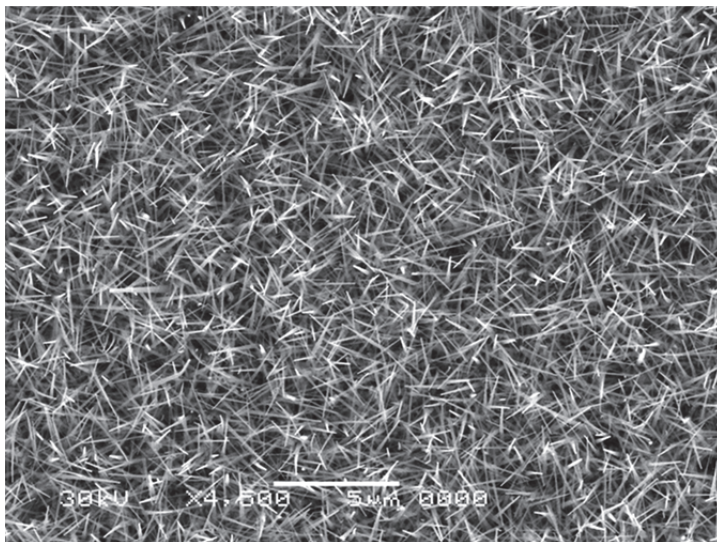


Fig. 6. Germanium nanowires grown from colloidal gold particles attached to the surface through the previously described wet chemical method. Wires are largely consistent in size and length.

Second, once heated, the gold becomes mobile on the substrate surface and can aggregate. Organic linker molecules used to hold the nanoparticles in place vaporize as soon as the

temperature reaches 213° C. Heating of the substrate must continue, however, until the bulk gold-germanium eutectic temperature is reached. During this period of time, the wires grown from 20 nm colloid particles may end up being closer to 40 nm in diameter, due to the combination of several original particles. There are, however, no such rules or generalizations which can be made for sputter-coated films.

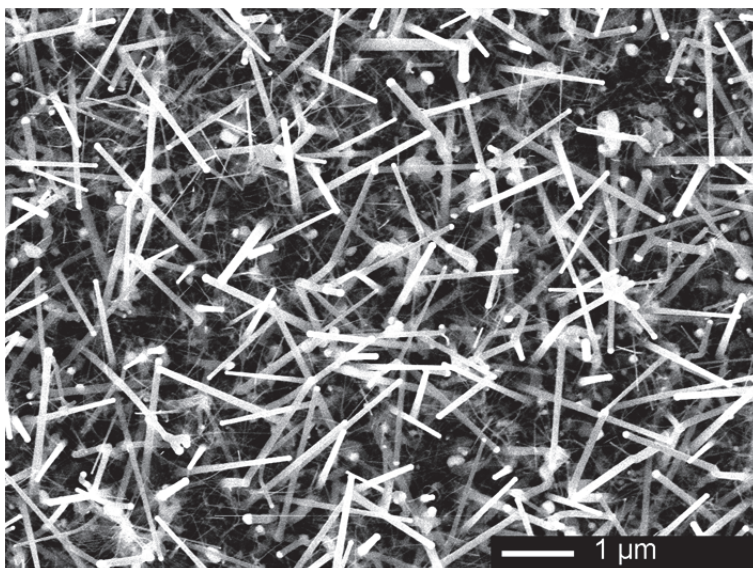


Fig. 7. Scanning electron micrograph of germanium nanowires grown on Kapton from 6.7 nm gold film. Note the non-uniform distribution of diameters present. Wires were grown under standard conditions.

Figure 7 is a characteristic image consistent with nanowire growth from a sputter-deposited gold film. The wires differ drastically in diameter, with fatter wires reaching several hundred nanometers in diameter and thinner wires maintaining diameters of 50 nm or smaller. As can be seen from a comparison of Figures 6 and 7, the nanowires grown from colloids are significantly more uniform than those that were grown from the sputter-coated films.

The growth on sputter-deposited films results from the diffusion and nucleation of the gold on the substrate surface. A discrete island or particle of gold is required to begin nucleation of the germanium nanowire. It is well known that when heated, thin gold films become mobile resulting in the balling up of the metal on the surface. It is this mechanism which makes it possible to grow wires from an initially contiguous film over the surface of a substrate. There are, however, specific limitations as to the deposited thickness of this film. Of the sputter-coated films, reasonable nanowire growth was observed for approximately 5-20 nm thick gold films, area averaged.

If insufficient gold is present, very poor growth is observed, resulting in few, if any, actual wires, as can be seen in Figure 8. For this exceptionally thin coating, it appears there is not enough gold to form the necessary nucleating islands. Wire-like masses are observed, but

they exist in the plane of the surface and are not free standing, resembling more amorphous germanium masses capped with gold than any useful nanowire structure.

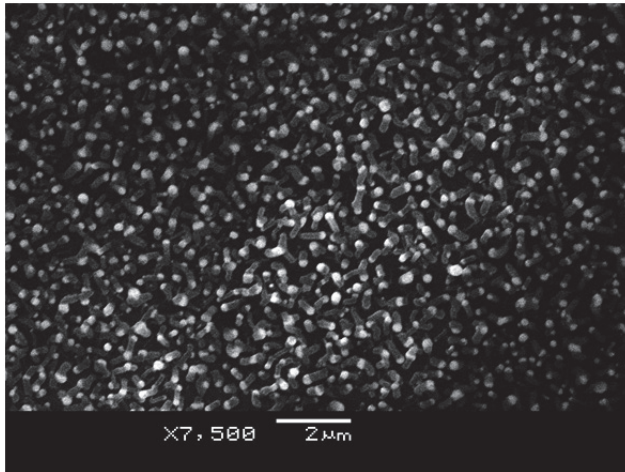


Fig. 8. Poor growth results from 2.8 nm gold film. "Wires" were grown under standard conditions.

If too much gold is present, an equally significant problem is encountered. Eventually, with the increase of thickness, one approaches a film which acts more closely to a bulk layer of gold. Balling-up and mobility across the surface is hindered, and catalyst islands do not form, making it impossible for nanowire nucleation to begin. As can be seen in Figure 9, no growth is observed under these conditions. If sputter coating is the only available method of functionalizing the substrate surface with the gold catalysts, it is preferable that the thickness of the deposited gold film is tightly controlled to approximately 10 nm.

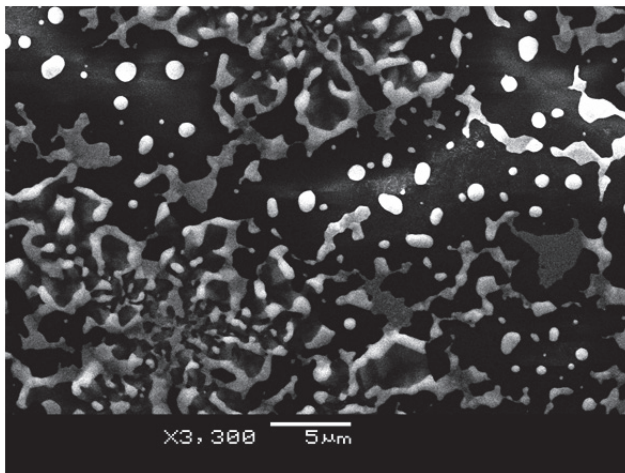


Fig. 9. Poor growth results from a 77 nm gold film.

The thicknesses of these films were confirmed through analysis by Rutherford Backscattering Spectroscopy (RBS) as shown in Figure 10.

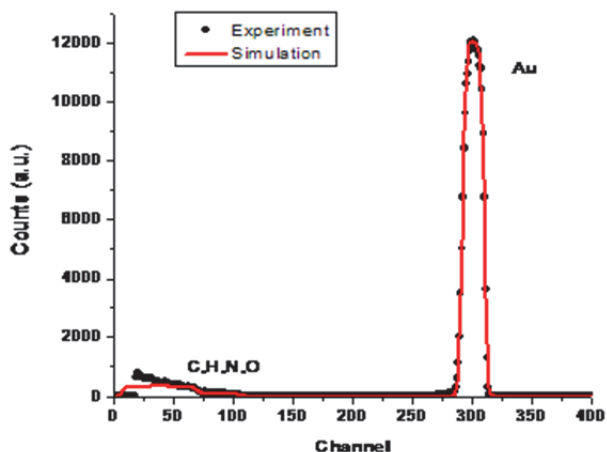


Fig. 10. (a)

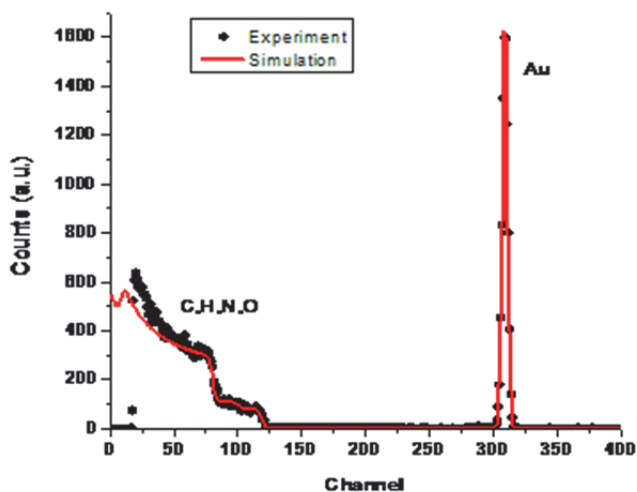


Fig. 10. (b)

Figure 10- RBS spectra confirming an area averaged Au thickness on Kapton. A) 77 nm B) 2.8 nm

### 3.3 AFM studies of Kapton

At a germanium nanowire growth temperature of 360°C (as used in part of this work), the growth temperature approaches the glass transition temperature of Kapton. It was necessary to determine if this would have any effect on the gold catalyst particles deposited

on the surface during the pre-treatment, particularly if the gold could become embedded within the polymer during the initial heating. In order to examine the location and morphology of the gold nanoparticle catalysts under growth conditions, atomic force microscopy (AFM) was employed. AFM images were obtained using a Digital Instruments MultiMode AFM with a Nanoscope IV controller operating in TappingMode. VISTA probes non-contact mode Si cantilevers with a spring constant of 0.40 N/m, resonant frequency of 300 kHz, and nominal tip radii of 10 nm were used.

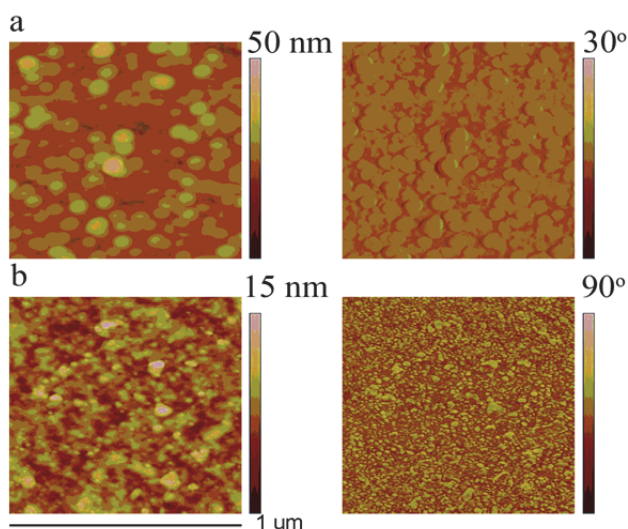


Fig. 11. AFM height (left) and phase (right) images of colloidal Au particles on a Kapton film (a) and plain Kapton film (b) after heating samples under conditions simulating nanowire growth. All images are  $1 \mu\text{m}^2$ .

Scans were performed on Kapton films treated with 3-aminopropyltriethoxysilane (APTES) and colloidal gold particles of 50 nm in diameter, as described in the methods section, and an untreated Kapton film as a control. Both samples were imaged before and after heating in  $\text{N}_2$  ( $360^\circ\text{C}$ , 15 min.) to mimic the conditions present during nanowire growth. Figure 11 reveals that gold remains in colloidal form on the surface of the polymer and does not appear to migrate into the bulk of the polymer.

Upon heating, the colloids do appear to aggregate and form particles roughly twice their initial diameter. As can be seen from Figure 11a, the colloids appear to be roughly 100 nm in diameter post-heating. Aggregation of the colloids is expected due to the increasing mobility of gold on surfaces at higher temperatures. This, in turn, is consistent with the typical observation of nanowires possessing diameters larger than the initial catalyst size.

#### 3.4 Treatment to remove nanowire oxide

Due to the poor electrical properties of the native oxide of germanium it is a significant problem which must be addressed with in order to utilize germanium nanowires to their full potential in electrical devices. The oxide must be prevented from growing or removed

after it has developed. Under ambient conditions, germanium surfaces undergo rapid oxidation to GeO followed by conversion to the thermodynamically more stable GeO<sub>2</sub>. This oxide can be removed through traditional processing methods such as treatment with a dilute aqueous HF solution. (Adhikari 2005) Our studies show that the germanium oxides are readily removed in a 2% HF solution for 1 minute with minimal damage to the GeNWs or the polymer substrate.

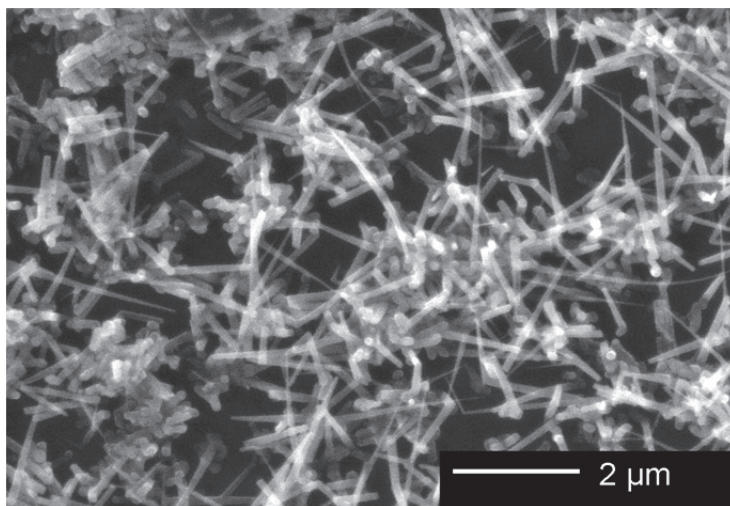


Fig. 12. Nanowires grown on a Kapton substrate retain their integrity after an HF dip.

The chemical robustness of the polymer substrate is key element if the eventual goal for such a system is printable electronics. Flexible polymer sheets and any deposited components must be able to withstand wet chemical processing to be of use. As can be seen in Figure 12, nanowires exposed to the HF treatment described above retain their structure and attachment to the Kapton surface.

### 3.5 Passivation

One method to passivate germanium involves capping the surface with organic thiols. Germanium nanowire samples grown on polymers were placed in a 0.1M solution of 1-octanethiol for 24 hours immediately upon removal from the reactor. To confirm the level of oxide on the surface, X-ray photoelectron spectroscopy was used. For the following spectra, data were collected using Al K $\alpha$  anode source with a cylindrical mirror analyzer. The FWHM of the C 1s peak (2.4 eV) was used as the FWHM for the deconvolution of the Ge 2p peaks. The C 1s is a single Gaussian and represents the energy resolution of the instrument at the pass energy utilized. Within the deconvolution of the Ge 2p 1/2, the peak with the lowest binding energy was assigned to that of bulk Ge. All spectra were shifted to ensure that this peak was centered at 1217.0 eV.

A comparison of passivated and non-passivated samples reveals a substantial decrease in the surface oxidation for samples that had been thiol passivated. Non-passivated samples possess a substantial oxide layer consisting primarily of GeO<sub>2</sub>, with a smaller contribution from GeO, as can be seen in Figure 13a. The passivated species also exhibit a small higher

binding energy shoulder consisting of a single peak attributed primarily to GeO, as can be seen in figure 13b. However, the contribution relative to the bulk germanium peak is greatly reduced from that of the non-passivated sample. The presence of GeO suggests that even the brief exposure of the sample to atmosphere while transferring from the growth chamber to the thiol solution is enough to partially oxidize the germanium. However, as previously mentioned, the stability of the polymer substrate is sufficient to remove this oxide coating prior to passivation, thus greatly reducing the presence of oxide.

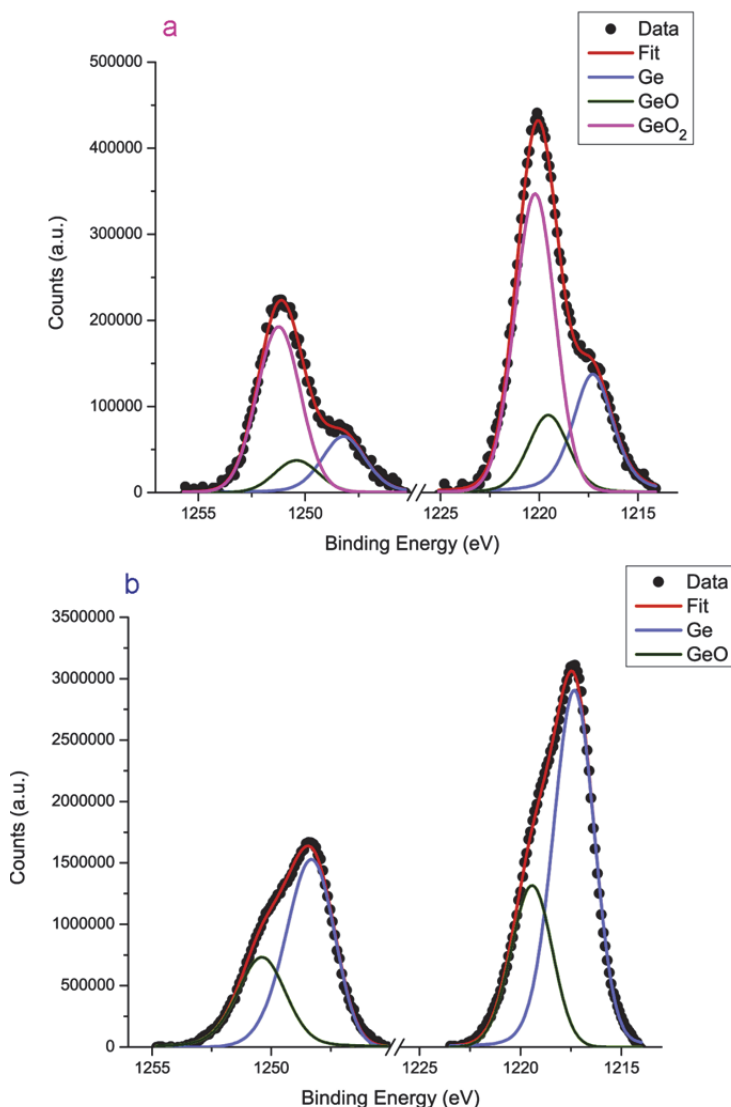


Fig. 13. XPS spectra of Ge 2p<sub>3/2</sub> and 2p<sub>1/2</sub> for non-passivated (a) and passivated (b) GeNWs

Passivation between processing steps, and passivation/packaging at the end of processing, are key in realizing device applications. The growth, processing, and passivation methods detailed in this work are all found to lead to a flexible and well-integrated GeNW-polymer hybrid film, of potential importance for a range of flexible applications such as batteries, solar cells, sensors, and transistors.

#### 4. Conclusion

In conclusion, we present results of GeNW VLS growth on flexible organic substrates. The nanowire attachment to the polymer substrates is robust and able to withstand flexing of the substrate. Post-growth processing to remove the oxide and to functionalize the nanowires (with or without the oxide present), can be applied without damaging the substrate. This work is of potential importance for a range of flexible applications such as batteries, solar cells, sensors and transistors. Direct growth of nanowires on flexible substrates simplifies processing and improves yield. We compare various methods of catalyst preparation from which nanowire growth can be initiated, and conclude that wet chemical methods to deposit colloidal gold particles on the substrate surface produces wires superior in uniformity than sputter coated gold films.

#### 5. Acknowledgements

The authors thank the National Science Foundation for financial support for this work. They acknowledge Ozgur Celik, Leszek Wielunski, and Robert Lorber for their valuable time and advice.

#### 6. References

- Adhikari, H., A. F. Marshall, et al. (2006). *Nano Lett.* 6(2): 318-323.
- Adhikari, H., A. F. Marshall, et al. (2007). *ACS Nano* 1(5): 415-422.
- Adhikari, H., Sun, S., McIntyre, P., and Chidsey, C.E.D (2005). *Applied Physics Letters* 87.
- Allen, P. B. (2007). *Nano Lett.* 7(1): 6-10.
- Bitetti, G., M. Marchetti, et al. (2007). *Acta Astronautica* 60(3): 166-174.
- Bradley, K., J.-C. P. Gabriel, et al. (2003). *Nano Lett.* 3(10): 1353-1355.
- Choi, H., I. S. Chung, et al. (2008). *Polymer*.
- Chung, C.-L. and S.-H. Hsiao (2008). *Polymer* 49(10): 2476-2485.
- Dai, H. (2005). *Angew. Chem. Int. Ed.* 44: 2-5.
- Dailey, J. W., Taraci, J., Clement, T., Smith, D.J., and Picraux, S.T. (2004). *J. Appl. Phys* 96.
- Fan, Z., J. C. Ho, et al. (2008). *Nano Lett.* 8(1): 20-25.
- Gibson, J., and Daghljan, C.P. (2005). *J. Appl. Phys* 97.
- Greytak, A. B., Lauhoun, L. J., Gudiksen, M.S., and Lieber, C.M. (2004). *Applied Physics Letters* 84.
- Hanrath, T. and B. A. Korgel (2002). *J. Am. Chem. Soc.* 124(7): 1424-1429.
- Hanrath, T. and B. A. Korgel (2004). *J. Am. Chem. Soc.* 126(47): 15466-15472.
- Heath, J. (2000). *J. Phys. Chem* 104(11864-11870).
- Jing, M., M. Ni, et al. (2006). *J. Phys. Chem. B* 110(37): 18332-18337.
- Kang, K., Lee, H., Kim, C., Yang, J., and Jo, M. (2008). *Advanced Materials* 9999.

- Li, H., J. Liu, et al. (2006). *Polymer* 47(4): 1443-1450.
- Lin, C., Liao, H., and Chen, S (2005). *Applied Physics Letters*(86).
- Maya, E. M., A. E. Lozano, et al. (2005). *Polymer* 46(25): 11247-11254.
- McAlpine, M. C., R. S. Friedman, et al. (2003). *Nano Lett.* 3(11): 1531-1535.
- Pasquier, A. D., D. D. T. Mastrogiovanni, et al. (2007). *Applied Physics Letters* 91(18): 183501.
- Ree, M., K. Kim, et al. (1997). *Journal of Applied Physics* 81(2): 698-708.
- Sang, W., Han, M., Carraro, C., and Maboudian, R., (2001). *J. Am. Chem. Soc.* 123.
- Saran, N., K. Parikh, et al. (2004). *J. Am. Chem. Soc.* 126(14): 4462-4463.
- Wang, D., Y.-L. Chang, et al. (2005). *J. Am. Chem. Soc.* 127(33): 11871-11875.
- Wang, D., Y.-L. Chang, et al. (2004). *J. Am. Chem. Soc.* 126(37): 11602-11611.
- Wang, L., B. L. Yi, et al. (2008). *J. Phys. Chem. B* 112(14): 4270-4275.
- Wu, Y. and P. Yang (2000). *Chem. Mater.* 12(3): 605-607.
- Yun, M. (2003). *Nanofabrication Technologies* 5220.

# Thermoelectric and Magnetic Nanowires

Yu-Biao Liu and Shao-Min Zhou

*Key Lab for Special Functional Materials of Ministry of Education,  
Henan University, Kaifeng,  
China*

## 1. Introduction

Approximately 90 per cent of the world's power is generated by heat engines that use fossil fuel combustion as a heat source and typically operate at 30–40 percent efficiency, such that roughly 15 terawatts of heat is lost to the environment (Hochbaum et al., 2008). Thermoelectric modules could potentially convert part of this low-grade waste heat to electricity (Lecher, 1905). In addition, it can also be used for thermoelectric cooler instead of Freon (succedaneum for Freon) and will not cause any environmental pollution (Thompson, 1932). According to solid state physics, semiconductor, semimetal, and some alloys are ideal thermoelectric material, and the efficiency of the thermoelectric materials depends on the thermoelectric figure of merit  $ZT$  ( $ZT=TS^2\sigma/\kappa$ ): a function of the absolute temperature ( $T$ ), of the Seebeck coefficient ( $S$ , or thermoelectric power), and of the electrical ( $\sigma$ ) and thermal conductivities ( $\kappa$ ) (Bucherer, 1900). Unfortunately, over the past ten decades it has been challenging to increase  $ZT$  for bulk thermoelectric materials, which are difficult to be used widely due to the low thermoelectric efficiency (Bell, 2008). Since the 1990s, Q1D nanostructures, particularly for NWs, have made great progress, in which many conventional materials have been made into the structural and morphology of NWs and then the unique properties appear (Masuda et al.,1997; Li et al., 1998; Ling et al., 1999; Gudixsen & Lieber, 2000; Wu et al., 2002; Gao et al., 2003; Lee et al., 2006; Zhou et al., 2008; Zhou et al., 2009; Zhou et al., 2010; Zhou et al., 2011). Under the one-dimensional, with improvement of the system of states near the Fermi energy density, the Seebeck coefficient of the system is improved. Simultaneously, with scaling down to a certain size, phonon scattering is enhanced without affecting the transmission of electronic. So thermoelectric NW shows a quite higher thermoelectric figure of merit  $ZT$  and the interest in thermoelectric NWs has been stimulated greatly by the discovery of its excellent thermoelectric properties (Ying, J. & Heremans,1998). In order to produce a variety of thermoelectric NWs, some new methods such as solvothermal and electro-deposition have been employed (Jin et al., 2004; Li, 2003; Li, 2006). Here we review the research status of NWs of thermoelectric materials, which include elements, alloys, and the development of thermoelectric super-lattice NWs will be also introduced. NW materials show excellent characteristics, which exhibit different property compared to bulk materials. In addition, as for magnetic NW section, it is found that magnetic NWs have a significant magnetic anisotropy and exhibit a large coercivity and a large remanence ratio when magnetization direction along NWs. Because of these unique low-dimensional properties,

magnetic NWs with straight shape are the best candidate to be applied for magnetic storage media with high density domain. In the past period time, a variety of magnetic NWs have been synthesized and characterized by nanotechnology, and here we also review the fabrication of the NW arrays of ferromagnetic metal, alloy, and heterogeneous ferromagnetic-nonmagnetic alloy. In the two section review, besides the method of nuclear track etching and thermal reduction, we highlight the common method of electro-deposition inside the anodic aluminum oxide template, with predomination of fast growth, simple device, and simplified operation, which has been employed for the synthesis of NW arrays. Several physical methods, especially microscopic techniques such as scanning electron microscopy (SEM), transmission electron microscopy (TEM), scanning tunneling microscopy (STM) and atomic force microscopy (AFM) are commonly used to characterize NWs. We present a comprehensive and up-to-date review of the thermoelectric and magnetic NWs wherein we discuss their synthesis along with their properties and potential applications.

## 2. Synthesis strategy

### 2.1 Thermoelectric nanowires

#### 2.1.1 Vapor phase synthesis

Gas phase reaction is a kind method for widely used to synthesis. Due to the special property of low-dimensional nanostructure, it is extensively used for producing NWs. The idea of synthesis is based on the vapor-liquid-solid (VLS) process, and the schematic diagram of the synthesis is shown in Fig 1 (Gudiksen & Lieber, 2000; Yang et al., 2002; Wagner & Ellis, 1964; Wu & Yang, 2001; Givargizov, 1975; Gao et al., 2003; Lee et al., 2006).

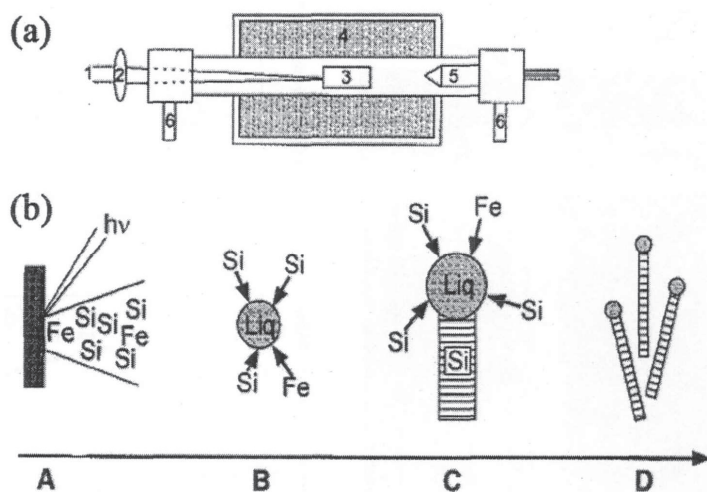


Fig. 1. Vapor-liquid-solid (VLS) process.

Under an inert gas, putting substrate in the appropriate place of temperature and leading to a certain amount of organic metal or the reaction gas source from against target by pulsed

laser semiconductor material. As the example of synthetic silicon NWs (Gudiksen & Lieber, 2000), in a temperature, the vapor of Si-Fe can form into the droplet nucleation undercooling. As more gas through, content of silicon in the droplet will be more and more and tends to saturation, and Si, exist in the droplets, is precipitated to a crystalline NWs (Wagner & Ellis, 1964). Combined with the technology of repeated precipitation or pulse deposition, the method based on vapor-liquid-solid mechanism has been used to produce super-lattice NWs. Yang's research group has successfully synthesized Single-Crystalline Si/SiGe Super-lattice NWs by using the hybrid pulse laser ablation/chemical vapor deposition (PLA-CVD) method (Yang et al., 2002). Fig 2 shows the single-crystalline Si/SiGe super-lattice NWs growth apparatus. Si wafer coated with a thin layer of Au was put inside a quartz furnace tube as substrate.

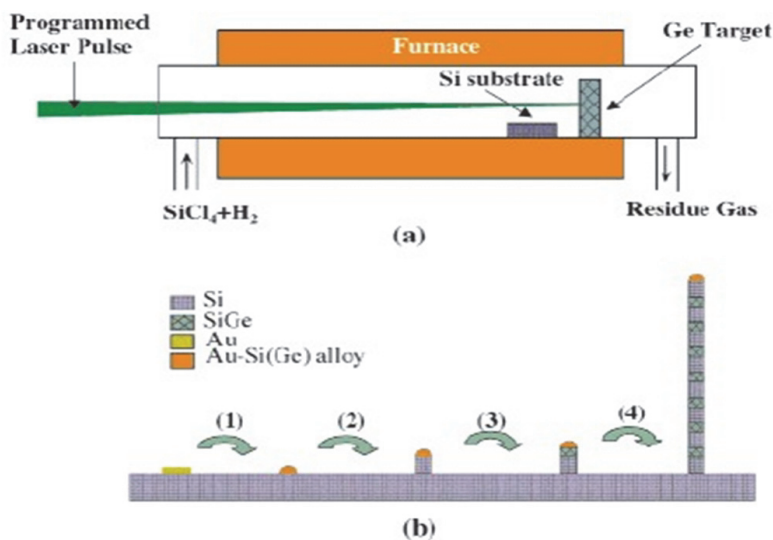


Fig. 2. Schematic illustration of the experimental setup (a) and vapor-liquid-solid sequential NW growth mechanism (b).

A gas mixture of  $H_2$  and  $SiCl_4$  was continuously introduced into the reaction tube. NW growth is based on the well-known vapor-liquid-solid (VLS) mechanism (Figure 2) with Au as solvent at high temperature (Wagner & Ellis, 1964; Wu & Yang, 2001; Givargizov, 1975). At a suitable temperature, an Au thin film forms a liquid alloy with Si and spontaneously breaks up into nanometer sized droplets (Figure 2 (1)). Si species continuously deposit into Au-Si alloy droplets where the Si NW growth is initiated upon super-saturation (Figure 2 (2)). During this growth process, if the laser is turned on, Ge vapor will be generated and both Ge and Si species will be deposited into the alloy droplets. The SiGe alloy then precipitates from the solid/liquid interface (Figure 2 (3)). By periodically turning the laser on and off (this sequence can be readily programmed), Si/SiGe super-lattice is formed on every individual NW (Figure 2 (4)) in a block-by-block fashion. Very recently, our research group (Zhou et al., 2011) reports on  $\beta-Zn_4Sb_3$  nanocantilevers and their thermoelectric properties. As shown in Fig. 3, the as-fabricated products have a cantilever morphology and a high ZT value

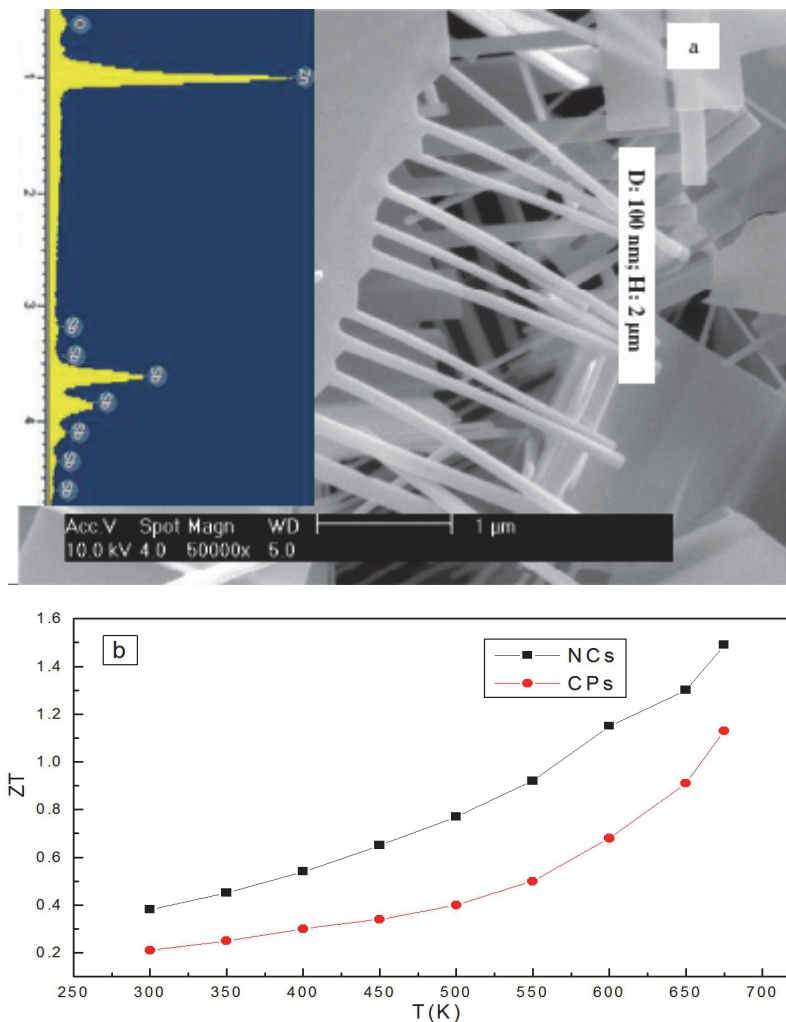


Fig. 3. A typical SEM image of  $\beta$ -Zn<sub>4</sub>Sb<sub>3</sub> nanocantilever (a) and thermoelectric figure of merit  $ZT(T)$  (b) of the as-produced  $\beta$ -Zn<sub>4</sub>Sb<sub>3</sub> nanocantilever (NCs, black) and  $\beta$ -Zn<sub>4</sub>Sb<sub>3</sub> conventional powders (CPs, red) as a function of temperature

### 2.1.2 Liquid phase synthesis

As a simple and convenient method, liquid phase reaction method is widely used to fabricate a tailored material by controlling the liquid environment of the crystal growth process without complex equipment. Gao et al. (Gao et al., 2003) have fabricated Bi NWs with 20–30 nm in diameter and 0.2–0.3 mm in length by solvothermal method. Although this method is simple, but mostly the structure of the synthesized NWs is very few, and this method is rarely employed for the synthesis of thermoelectric NW materials (Lee et al., 2006; Masuda et al., 1997; Li et al., 1998; Ling et al., 1999).

### 2.1.3 Electrochemical template synthesis

Electrochemical template method has been successfully used to the synthesis of thermoelectric NWs with various materials. In this technique, the template serves as a scaffold against which other materials with similar morphologies are synthesized. That is, the in situ generated material is shaped into a nanostructure with morphology complementary to that of the template. The nanoscale channels are filled using the electrochemical method. Until now, the most common templates are nanoscale channels within porous alumina and polycarbonate membranes. Unlike the polymer membranes with the broader and uneven distribution of pore size, fabricated by track etching, anodic alumina membranes (AAMs) containing a hexagonally packed 2D array of cylindrical pores with a uniform size are prepared using anodization of aluminum foils in an acidic medium. Porous alumina template pore size is controlled by adjusting the polarization voltage. However, when the voltage is too large, aluminum oxide template is easy to burn due to the lack of distribution of heat (Lee et al., 2006). Different acidic electrolytes have their own optimum aperture. It is found that sulfuric acid electrolyte is adapt to synthesize Alumina template with less than 50 nm in diameter (Masuda et al., 1997), oxalic acid electrolyte is adapt to synthesize Alumina template with 50 ~100 nm in diameter (Li et al., 1998), and phosphoric acid electrolyte is adapt to synthesize alumina template with 100 ~300 nm in diameter (Li et al., 1998) as shown in Fig 4.

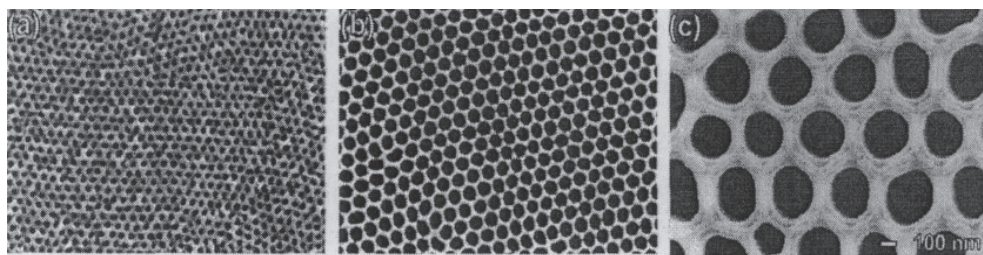


Fig. 4. Alumina templates of various apertures.

High-quality aluminum oxide template can be achieved by the method of reoxidation (Ling et al., 1999). The method of electro-deposition in anodic alumina membranes has been proved to be very effective and convenient to synthesize thermoelectric NWs. They first synthesized the NW arrays of the  $\text{Bi}_2\text{Te}_3$ , Bi-Sb-Te, and Bi-Te-Se thermoelectric material at room temperature (Prieto et al., 2001; Prieto et al., 2003; Martin-Gonzalez et al., 2003). To get uniform growth NW arrays of the various apertures, they made a depth work on the growth rate of NWs at the different temperatures. Li et al. modulate the growth of the  $\text{Bi}_2\text{Te}_3$  NWs with the different orientations by the method of pulse electrochemical deposition (Li et al., 2006), and the NW's diameter can also be modulated by controlling the cycle of the pulse plating and the concentration of the plating solution. In addition, the pulse plating template, based on the principle of that different ions have different potential, can be used to synthesis various thermoelectric super-lattice NWs, and the junctions with different lengths can be achieved by different plating time. So we can conclude that electrochemical template method provides a very reliable and controllable pathway for the synthesis of the thermoelectric NWs.

## 2.2 Magnetic nanowires

There are various methods for the preparation of magnetic NWs such as physical methods and chemical methods. However, the template method is widely used to fabricate magnetic NWs because of its unique advantages. The main application template include porous anodic aluminum oxide template (AAO), porous silicon templates, and track etched polymer membranes template.

### 2.2.1 Porous anodic alumina template

By the method of the electro deposition, the amount of metal deposition can be controlled by controlling the deposition time, and the aspect ratios of the NWs can be precisely controlled. Due to the way of driving metal ions, it can be divided into alternating current, direct current deposition, and pulsed power deposition. For the AC deposition, it is no need to separate the template form the Al matrix after the formation of ordered nanoporous, and various magnetic NW arrays can be fabricated by controlling the current, voltage, frequency and time parameters, after decreasing the thickness of the dense alumina film. As early as 1991, Mawlawi et al. (Aimawlawi et al., 1991) synthesized polycrystalline Fe NW arrays with diameter of 22 nm by ac electro deposition in porous anodic alumina template. While the operation process of ac electro deposition is simple and feasible, it can only be used to assemble single metal or alloys. The methods of DC or pulse electro-deposition can also be used to synthesize magnetic NW arrays. Alumina template is first stripped from the Al matrix, through-hole, and then the back of the template is coated metal film as a cathode by sputtering or vacuum coating. By controlling the voltage, current, temperature, and time conditions to prepare magnetic NWs, then the template is removed to obtain corresponding NWs. While it is a more complicated operation, various forms of magnetic nanophase materials such as multilayer magnetic NWs. Sol-gel method is a new fiber preparation technology, and can also be used to prepare magnetic NW arrays. It is that after a solution, Sol-gel and cure, Organometallic compounds or inorganic salts become oxides or other solid compounds by heat treatment. This method does not require special equipment, and the NW length can be controlled by impregnation times (Qin, 2006). For example, Otten et al (Otten et al., 2002) prepared NWs of cobalt ferrite using sol-gel method under different annealing speeds. Sol-gel template method has been used to fabricate highly ordered NW arrays of iron oxide (Liu et al., 2005). A large area of iron oxide NWs can be prepared by sol-gel template method, which suggests that it is easy to control conditions, reproducible, the process simple, and low cost. Chemical-deposition is known as electroless deposition or chemical plating. In order to prepare NWs, the metal is deposited into the channel or surface of the template by chemical reduction. Using  $\text{Co}_2(\text{CO})_8$  as precursor, Aranda et al (Aranda & Garcia, 2002) synthesize Co NWs in the AAO template and the polycarbonate template by chemical-deposition method.

### 2.2.2 Track etched polymer membranes template

Track etching polymer template preparation methods are as follows: Firstly, polymer film such as 6 ~10  $\mu\text{m}$  thick polycarbonate is bombard by fission fragments, and then the membrane damage is rusted into the nano-pore by chemical method. Polymer template has cylindrical nanopore with the pore size of 10~200 nm and the pore density of  $10^9\text{cm}^{-2}$ . While the pore canal of polymer template is not regular than that of anodic alumina template, polymer template, which has good flexibility, can maintain a long time in highly acidic conditions. So the applications of polymer template are more widely.

### 2.2.3 SBA-16 film

SBA-16 film, which is progressive development after the successful development of molecular sieve, is a highly ordered three-dimensional body-centered cubic film with a high degree of order of the pore structure and a average pore diameter of 8–9 nm.

## 3. Thermoelectric nanowires

### 3.1 Bi

Bismuth, as a semimetal with a very small band gap, provides a very attractive model system for studying low-dimensional physical phenomena due to its highly anisotropic Fermi surface, low carrier densities, small carrier effective masses, and long carrier mean free path (Dresselhaus et al., 2003; Zhang et al., 2000). The experiment results indicate that a semimetal-semiconductor transition in bismuth NWs when the wire diameter is decreased to a certain value (about 50 nm), which carried out by a novel vacuum melting and pressure injection technique (Zhang et al., 1998). The results of Fig. 5 indicate that these bismuth NWs undergo a semimetal-to-semiconductor transition due to two-dimensional quantum confinement effects.

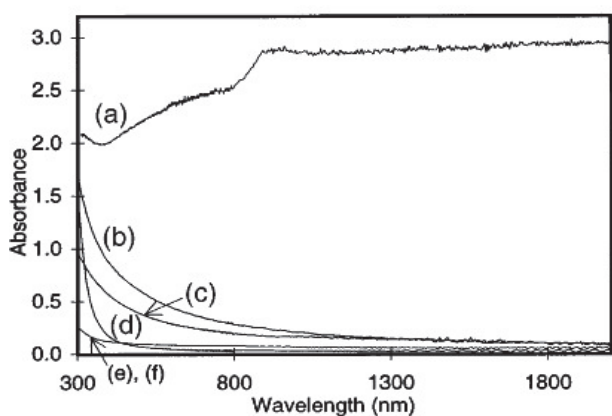


Fig. 5. The room-temperature optical absorption spectra of the Bi NW/anodic alumina composite films with average wire diameters of (a) 56 nm, (b) 23 nm, and (c) 13 nm, and the corresponding unfilled anodic alumina templates (d), (e), and (f).

Considerable effort has been devoted to synthesis Bi NWs and Bi NW arrays with diameters of 5–200 nm have been fabricated by liquid-phase pressure injection (Zhang et al., 1999), solution-phase process, vapor-phase deposition (Heremans et al., 2000), or electrochemical deposition (Liu et al., 1998; Piraux et al., 1999), until now, and various transport measurements have been performed to study classical and quantum finite-size effects.

### 3.2 Si

Researches of thermoelectric properties of silicon NWs, during all kinds of thermoelectric NWs, have made the most outstanding progress. Since the researcher discovered that there is large difference in mean free path lengths between electrons and phonons at room

temperature: 110 nm for electrons in highly doped samples and 300 nm for phonons in highly doped silicon materials (Ju et al., 1999). Consequently, incorporating structures with critical dimensions below 300 nm in Si should reduce the thermal conductivity without significantly affecting Seebeck coefficient because of scattering on phonon transmission. The first report of the thermal conductivities of individual single crystalline Si NWs was by Yang's research group (Li et al., 2003; Wu et al., 2002), who synthesized SiNWs by the vapor-liquid-solid method, in which Au clusters were used as solvent at high temperature. The Si and Au formed a liquid alloy and when the alloy became supersaturated with Si, Si NWs grew by precipitation at the liquid-solid interface. The Si NWs, which are synthesized by that method, are single crystalline. Thermal conductivity measurements of individual and 115 nm diam single crystalline Si NWs carried out using a micro-fabricated suspended device over a temperature range of 20–320 K as shown in Fig 6.

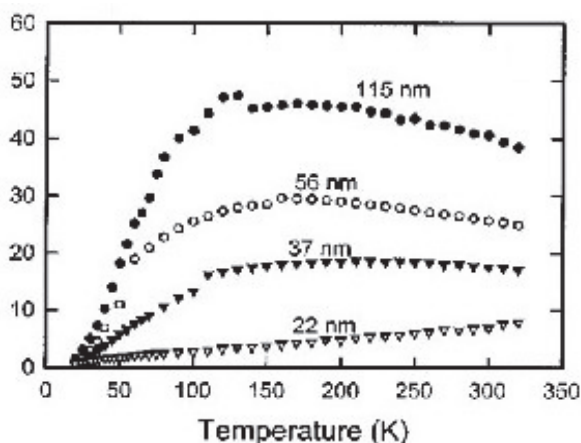


Fig. 6. Measured thermal conductivity of different diameter Si NWs. The number beside each curve denotes the corresponding wire diameter.

The thermal conductivity observed is more than two orders of magnitude lower than the bulk value. The strong diameter dependence of thermal conductivity in NWs is ascribed to the increased phonon-boundary scattering and possible phonon spectrum modification. Thermoelectric performance of rough silicon NWs had been made a detailed study by Hochbaum et al. (Hochbaum et al., 2008), who synthesized Wafer-scale arrays of Si NWs by an aqueous electroless etching (EE) method (Venkatasubramanian et al., 2001; Touloukian et al., 1970; Weber & Gmelin, 1991). NWs synthesized by this approach are vertically aligned and consistent throughout batches, and across large areas up to wafer-scale. Figure 7a (Venkatasubramanian et al., 2001) is a cross-sectional scanning electron microscope (SEM) image of one such array, and the inset shows a one-inch-square NW array. The NWs varied from 20 to 300 nm in diameter with an average diameter of approximately 100 nm, as measured from TEM micrographs (Fig 7b). The NWs are single crystalline, as shown by the selected area electron diffraction pattern (top inset) and high-resolution TEM image of the Si lattice of an EE NW in Fig 7c. In contrast to the smooth surfaces of typical vapour-liquid-solid (VLS)-grown, gold-catalyzed Si NWs (Fig 7d), these of the EE Si NWs are much rougher.

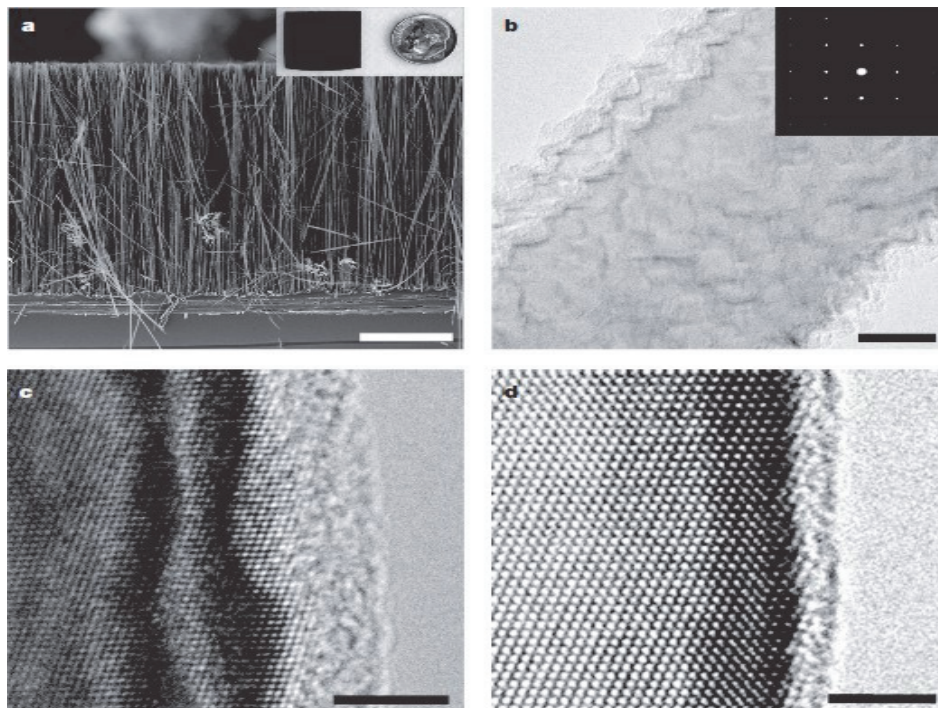


Fig. 7. (a) Cross-sectional SEM of an EE Si NW array; (b) Bright-field TEM image of a segment of an EE Si NW; (c) High-resolution (HR)TEM image of an EE Si NW; (d) HRTEM of a VLS-grown Si NW.

By the test of thermal conductivity of individual NWs, it has been shown that the magnitude of the  $k$  of EE Si NWs is five- to eight fold lower than VLS Si NWs of comparable diameters, which indicate that the roughness at the NW surface behaves like secondary scattering phases for  $k$  can be reduced by introducing scattering at additional length scales beyond the NW diameter. They founded that the peak  $k$  of the EE NWs is shifted to a much higher temperature than that of VLS NWs, and both are significantly higher than that of bulk Si, which peaks at around 25 K.

### 3.3 $\text{Bi}_{1-x}\text{Sb}_x$

Bulk  $\text{Bi}_{1-x}\text{Sb}_x$  alloys are among the best n-type low-temperature TE materials ( $20 < T < 220$  K), and the properties of the alloy change dramatically with composition. For alloys with 12% Sb, the dimensionless figure of merit,  $ZT$ , is 0.88 at 80 K. These properties of the alloy change dramatically with composition and the Bi-rich alloys have large TE efficiencies. New experimental and theoretical results suggest that the thermoelectric efficiencies of quantum-confined materials are enhanced compared with those of bulk materials, so it has been a resurgence of interest in the fabrication of  $\text{Bi}_{1-x}\text{Sb}_x$  NWs. The method of electro-deposition from dimethyl sulfoxide (DMSO) had been used for fabrication of dense arrays of crystalline  $\text{Bi}_{1-x}\text{Sb}_x$  ( $0 \leq x \leq 0.15$ ) NWs with 40-nm diameters by Prieto (Prieto, 2003). A representative X-ray diffraction pattern of the filled template is shown in Fig 8.

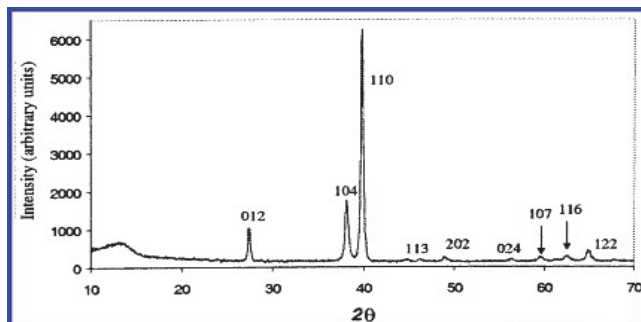


Fig. 8. XRD of 40-nm Bi-Sb NWs after the electrode layer has been removed mechanically.

The high intensity of the 110 peak shows that the wires are oriented and that the preferred wire axis is  $\langle 110 \rangle$ , which is different from the orientation obtained by pressure injection with the normal to  $\langle 012 \rangle$  parallel to the wire axis (Chien et al., 1998; Searson et al., 1998). They concluded that by tuning the solution concentrations and controlling the growth rate by controlling the potential, the composition, crystallinity, and morphology of the NWs can be tuned.

### 3.4 Bi-Te

During the past fifty years, the bismuth telluride ( $\text{Bi}_x\text{Te}_{1-x}$ ) based compounds have been a focus of extensive research because of their best thermoelectric performance near the room temperature and bismuth telluride alloys have remained the bulk materials with the highest ZT close to unity at  $T=300$  K (Mahan et al., 1997). In recent years, with the research that the properties of  $\text{Bi}_x\text{Te}_{1-x}$  alloys have a strong dependence on the Bi concentration and the discovery of evident improvement of the figure of merit in the quantum-confined systems compared to bulk materials,  $\text{Bi}_x\text{Te}_{1-x}$  NWs have been prepared by an electrochemical deposition method widely (Jin et al., 2004). Large scale and highly ordered thermoelectric  $\text{Bi}_x\text{Te}_{1-x}$  ( $0.4 \leq x \leq 0.7$ ) NW arrays were successfully fabricated by electrochemical deposition in AAM template (Wang et al., 2007). The structure of the NWs was characterized by X-ray diffraction and selected-area electron diffraction (SAED). Field emission scanning electron microscopy (FE-SEM) and transmission electron microscopy (TEM) results show that the NWs are smooth and uniform with the diameters of about 50 nm and lengths up to tens of micrometers. Energy dispersive spectroscopy (EDS) was used to check the exact stoichiometry of as-prepared samples. The results reveal that the atomic ratio between Bi and Te can be modulated effectively by controlling the concentration of the electrolyte solution. The synthesis of high quality  $\text{Bi}_x\text{Te}_{1-x}$  NWs with controllable  $x$  is significant for optimizing the thermoelectric performance. Shi et al. designed an experiment to measure the thermoelectric properties of individual  $\text{Bi}_x\text{Te}_{1-x}$  NWs prepared by an electrochemical deposition method, which suggested that the high ZT can be potentially obtained with an optimized atomic ratio (Zhou et al., 2005). A typical SEM image of a  $\text{Bi}_x\text{Te}_{1-x}$  NW trapped on the two suspended membranes of the measurement device as shown in Fig 8. Because of limited synthesis of  $\text{Bi}_x\text{Te}_{1-x}$  NWs with different compositions, the thermoelectric performance of the  $\text{Bi}_x\text{Te}_{1-x}$  NWs has not been systematically investigated. The focus of future research of  $\text{Bi}_x\text{Te}_{1-x}$  NWs is to make the dependence of the optimal conditions and thermal on properties composition clear.

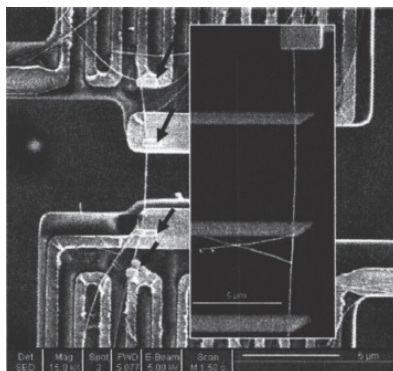


Fig. 9. SEM of a  $\text{Bi}_x\text{Te}_{1-x}$  NW trapped on the two suspended membranes of the measurement device.

### 3.5 $\text{Bi}_2\text{Te}_3$

Bismuth telluride are among the best known thermoelectric materials for the modern commercial application, which possess notable properties such as high anisotropic multi-valley Fermi surface, small value of the thermal conductivity, and optimal value of the carrier concentration at room temperature (RT). The thermoelectric figure of merit  $ZT$  of the  $\text{Bi}_2\text{Te}_3$  super-lattices was reported to have the value of 2.4 while the maximum  $ZT$  for the bulk bismuth telluride material is less than 1 at room temperature. Due to stronger spatial confinement, the bismuth tellurides NWs are expected to be better than the quantum well super-lattices. So the work of depth research of bismuth telluride NWs has been carried out. Until now, the method of synthesis of  $\text{Bi}_2\text{Te}_3$  NWs is few, but the method of template based on AAO is widely used and fairly mature for fabricating  $\text{Bi}_2\text{Te}_3$  NWs. The first report of the fabrication of Ordered  $\text{Bi}_2\text{Te}_3$  NW Arrays by electro-deposition was by Prieto et al. (Prieto et al., 2001), who had demonstrated the fabrication of dense, continuous  $\text{Bi}_2\text{Te}_3$  wires with uniform diameters of 40 nm by direct electro-deposition into an alumina template. The deposited wires are highly textured in the [110] direction as shown in Fig 10.

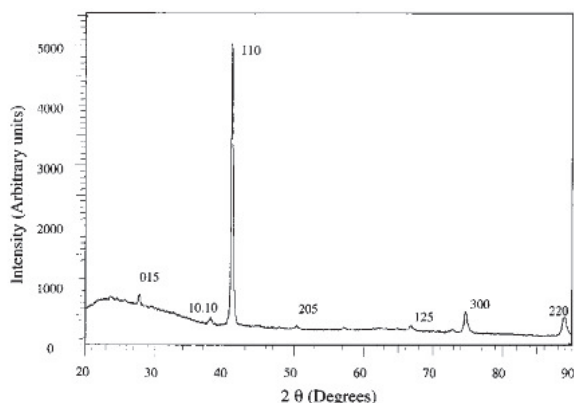


Fig. 10. Representative X-ray diffraction pattern of a filled 40 nm template.

Due to the good characteristics of the template for NW array fabrication, Sander et al. had chosen electro-deposition, and produced arrays of bismuth telluride ( $\text{Bi}_2\text{Te}_3$ ) NWs with diameters of  $\sim 25$ ,  $\sim 50$ , and  $\sim 75$  nm successfully using electrochemical deposition into porous anodic alumina templates. SEM confirms that the NW arrays are dense with a narrow distribution of NW diameters as shown in Fig 11.

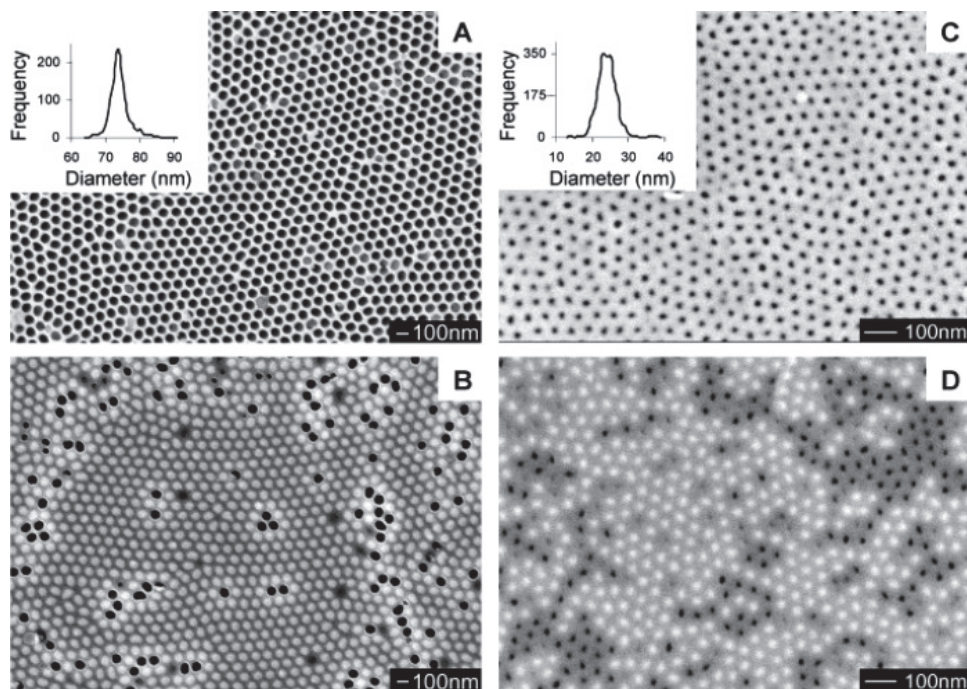


Fig. 11. (a) Empty template (b) array composite with average wire diameter of 75 nm (c) empty template (d) array composite with average wire diameter of 25 nm. The insets show pore diameter distribution for large (a) and small (c) diameter templates. Dark areas in these images are due to empty pores, whereas bright spots are due to the  $\text{Bi}_2\text{Te}_3$  NWs.

The latest theoretical studies show that electric field effect (EFE) is a powerful tool controlling the electrical properties of low dimensional structures. Bejenari et al. theoretically studied how the electric field effect can modify thermoelectric properties of intrinsic, n-type and p-type bismuth telluride NWs with the growth direction  $\langle 110 \rangle$  (Bejenari et al., 2010). After comprehensive analysis of various theories, the results of their calculations indicate that the external perpendicular electric field can increase the Seebeck coefficient of the bismuth telluride NWs with thicknesses of 7–15 nm by nearly a factor of 2 and enhance  $ZT$  by an order of magnitude. At room temperature,  $ZT$  can reach a value as high as 3.4 under the action of the external perpendicular electric field for realistic widths of the NWs. The obtained results may open up a way for a drastic enhancement of the thermoelectric figure of merit in a wide temperature range. The work of controlling the growth of bismuth telluride NWs and analysing the factors of oriented growth of bismuth telluride NW arrays have been carried out by the electrochemical deposition of the material

in the nanoporous of anodized alumina membranes (Miyazaki & Kajitani, 2001). The work and results of those researches lay the first stone for the measurement and optimization of bismuth telluride thermoelectric NWs.

### 3.6 Super-lattice nanowires

Theoretical calculations predict that further enhancement of the thermoelectric figure of merit can be achieved in super-lattice NWs (zero-dimensional) (Lin & Dresselhaus, 2003) rather than conventional NWs (1D) or super-lattice thin-films (2D), and thermoelectric super-lattice NWs are promising systems for the thermoelectric applications for this structure is believed to be better in reducing phonon transport and keeping high electron mobility (Hicks & Dresselhaus, 1993; Lin & Dresselhaus, 2003). Li et al. (Li, 2003) designed an experiment to measure the thermal conductivity of 58 and 83 nm diameter Si/SiGe single crystalline super-lattice NWs, which were synthesized by a hybrid pulsed laser ablation/chemical vapor deposition process based on vapor-liquid-solid mechanism. Figure 12a shows a TEM image of a Si/SiGe NW, and a SEM image of an 83 nm diameter Si/SiGe super-lattice NW bridging the two suspended pads is shown in Fig 12b.

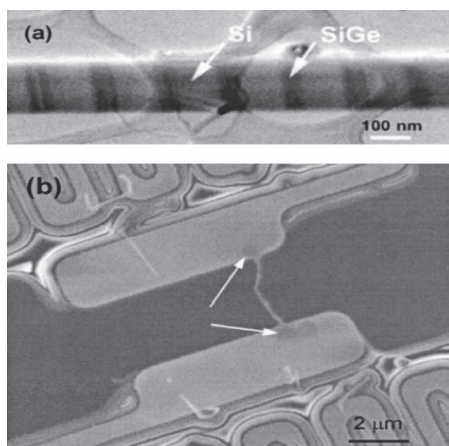


Fig. 12. (a) A transmission electron micrograph of a Si/SiGe super-lattice NW. (b) A scanning electron micrograph of an 83 nm Si/SiGe super-lattice NW bridging the two suspended heater pads. The arrows point to the carbon deposits.

The observed thermal conductivity shows similar temperature dependence as that of two-dimensional Si/SiGe super-lattice films. Comparison with the thermal conductivity data of intrinsic Si NWs suggests that alloy scattering of phonons in the Si-Ge segments is the dominant scattering mechanism in these super-lattice NWs. Yang et al. (Wu et al., 2002) had developed a hybrid pulsed laser ablation/chemical vapor deposition (PLA-CVD) process for the synthesis of semiconductor NWs with longitudinal ordered heterostructures, and have been successfully synthesized Single-crystalline NWs with longitudinal Si/SiGe super-lattice structure. Xue et al. reported a method for preparing super-lattice NW arrays in a single ethanol bath by using a pulsed electro-deposition technique (Xue et al., 2005). Here Bi/Sb super-lattice NW arrays had been fabricated by using this method and also four kinds of modulated structures of Bi/Sb super-lattice NWs with different periods had been

synthesized. This simple and efficient method can be expected to be used in other systems which can be electrodeposited. Heterostructured ZnSe-ZnTe quantum wires having axial heterojunctions are grown by the solution-liquid-solid (SLS) mechanism (Dong et al., 2007), and they found that the nature of the axial or radial heterostructure obtained is strongly influenced by the growth sequence and related synthetic conditions. Yoo et al (Yoo et al., 2007). electrodeposited  $\text{Bi}_2\text{Te}_3/(\text{Bi}_{0.3}\text{Sb}_{0.7})_2\text{Te}_3$  super-lattice NWs by using a template-directed method, where the composition and length of each segment was precisely controlled by adjusting deposition potentials and times Figure 13 shows SEM and TEM images of the NWs after removal of the polycarbonate template.

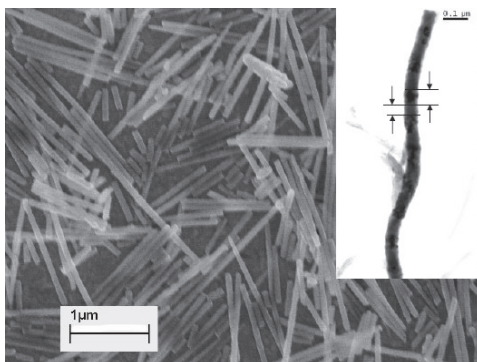


Fig. 13. Microstructure of the super-lattice BiSbTe NWs after removal of the polycarbonate template, the inset image was obtained by transmission electron microscopy (TEM).

The compositional modulation within the NWs was examined by electron dispersive X-ray spectroscopy (EDS) with the line-scanning method, where the intensity of the characteristic Bi La and Sb Ka peaks is plotted as a function of distance as shown in Fig 14.

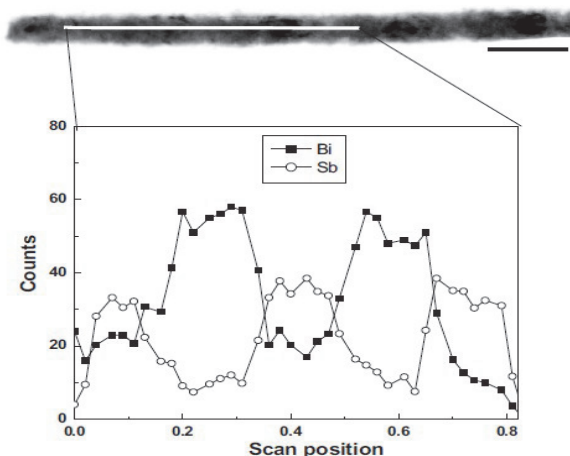


Fig. 14. Energy dispersive X-ray spectrometry (EDS) line scan, showing compositional oscillations of Sb and Bi in a BiSbTe super-lattice NWs.

Although there are several methods on the synthesis of thermoelectric super-lattice NWs, the test of thermoelectric properties is very lack, because the current thermoelectric super-lattice NW materials, which can be fabricated successfully, are also very small, and the corresponding methods and parameters are very complex.

## 4. Magnetic nanowires

### 4.1 Element

#### 4.1.1 Fe

Magnetic properties of Fe NWs had been studied by a number of groups, and Fe NWs had been fabricated in typical sizes range from 10 to 100 nm in diameter and from 0.1 and 1  $\mu\text{m}$  in length. There is a depth investigation in the behaviour of the coercivity of the Fe NWs. Figure 14 shows hysteresis loops for wires having a diameter of 9 nm and a length of 1  $\mu\text{m}$ ; the field is applied parallel and perpendicular to the wire axis. When the field is parallel to the wire axis (perpendicular to the film plane), the coercivity is about 2300 Oe (remanence ratio  $M_r/M_s = 0.96$ ), whereas the coercivity measured perpendicular to the wire axis (in the film plane) is about 300 Oe (remanence ratio 0.055).

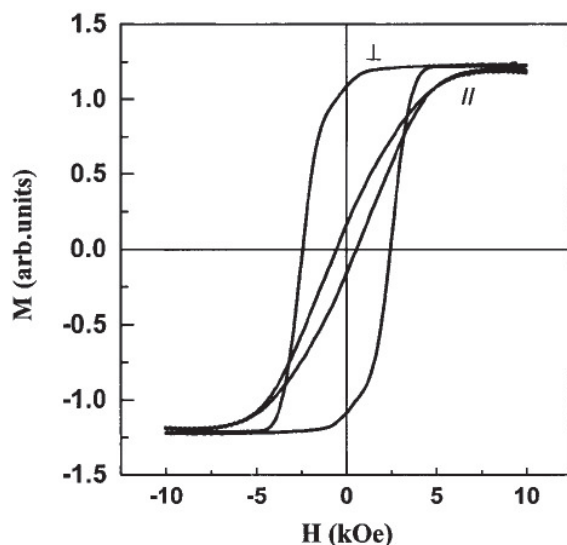


Fig. 15. Typical magnetic hysteresis loops for Fe NW arrays.

This indicates that the wires possess uniaxial anisotropy with the easy axis along the wire axis. The perpendicular anisotropy arises mainly from the shape anisotropy of the wires. The coercivity measured along the wire axis is 2100–2700 Oe for Fe (Menon et al., 2000; Huysmans & Lodder, 1988). Sugawara et al. fabricated Fe NWs by soaking the anodized film in phosphoric acid, and the diameter of Fe NWs is then controlled by the soaking time: varying from 9 to 19 nm for pore-widening times from 0 to 30 minutes (Sugawara et al., 1998). The variation of the coercivity as a function of pore diameter is shown in figure 16(a), and they find that  $H_c$  increases with increasing diameter until a maximum is reached at about 13 nm. The largest coercivity measured by Menon et al. is 2640 Oe for a diameter of 13

nm. Moskovits et al (Li et al., 1998; Li & Metzger, 1997) reported maximum values of 2220 Oe and 2240 Oe, respectively, both obtained for sulphuric-acid-anodized templates. So we can see that it is possible to control the magnetic properties of the wires by controlling the fabrication parameters for the dependence of  $H_c$  on the wire diameter. Some Fe samples were annealed in an attempt to cause grain growth and thus to influence the coercivity. Fig 16(a) shows that annealing at 100 °C, 200 °C and 300 °C enhances the coercivity for all NWs. However, annealing at even higher temperatures (400 °C) causes the coercivity drop to about 50 Oe, suggesting that the nanostructures are destroyed or oxidized. The oxidation is probably caused by the ions involved in the deposition process (Prieto et al., 2001). The value of the low-temperature coercivity ( $T = 5$  K) is higher than that of the room temperature coercivity with the same diameter of Fe NWs as shown in Fig 16(b). The coercivity also depends on the aspect ratio,  $l_w/d_w$  (wire length divided by wire diameter). Li et al. found that the coercivity of Fe NW increases gradually with increasing aspect ratio, but increases very little when the aspect ratio is larger than 10:1 (Li et al., 1998; Li & Metzger, 1997).

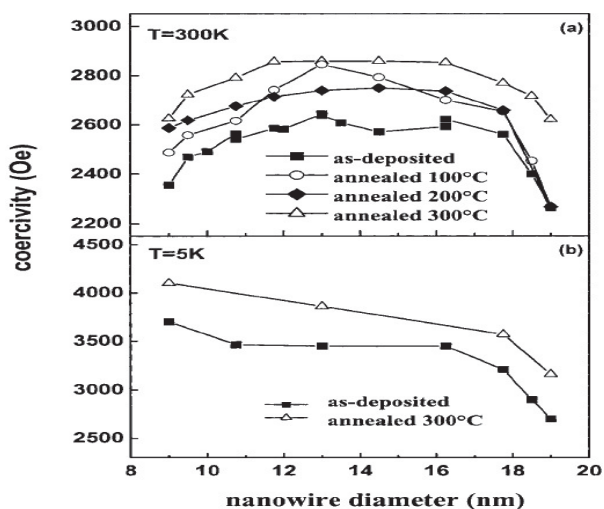


Fig. 16. (a)  $H_c$  as a function of NW diameter for as-deposited and annealed samples, and (b) diameter dependence at 5 K and 300 K.

Almawlawi et al. studied the coercivity of Fe NWs deposited into oxalic-acid-anodized alumites as a function of deposition time, pore-widening time and anodizing voltage. They found that the coercivity depends strongly on the aspect ratio and only weakly on the pore density (anodizing voltage)  $H_c$  decreases as the widening time increases.

#### 4.2 Co

Typical hysteresis loops for Co NWs in an anodic alumina template are similar to those of Fe NWs as shown in figure 15, and Zeng H et al. found that the coercivity measured in the perpendicular direction is as high as 2.6 kOe whereas the remanence ratio exceeds 0.9 emu/g (Zeng et al., 2000). Figure 17 shows coercivity and thermal activation volume as a function of the NW diameter ( $d_w$ ) and length ( $l_w$ ).

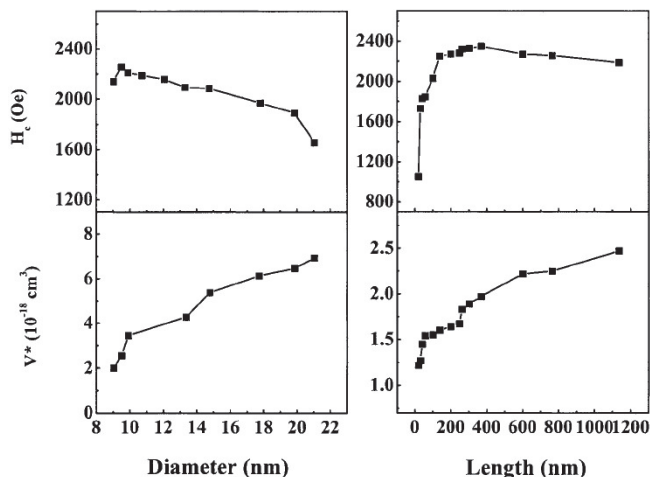


Fig. 17. Dependence of coercivity  $H_c$  and thermal activation volume  $V^*$  of Co NWs on wire diameter  $d_w$  and length  $l_w$ .

The thermal activation volume is used to investigate the energy barriers responsible for the magnetization reversal mechanism.  $V^*$  has been determined by exploiting the sweep-rate dependence of coercivity and magnetic viscosity measurements. It is shown that with increasing NW length,  $H_c$  increases steeply until a constant value of about 2300 Oe is approached, at a length of about 200 nm.  $V^*$  increases first rapidly but then gradually with  $l_w$ , but it is generally much smaller than the physical wire volumes. The effect of the applied magnetic field for the growth of Co NWs had been investigated by Chaure et al (Chaure et al., 2005). They demonstrated that the magnetic anisotropy axis and crystallographic texture can be controlled to some extent by applying an external field during electro-deposition of cobalt in a nanoporous alumina membrane. In Co NWs, electrodeposited in anodic alumina, Stijckers et al. observed a reversal magnetization that strongly depends on wire length ( $0.5 \leq L$  ( $\mu\text{m}$ )  $\leq 40$ ). This reversal magnetization is explained as competition between the demagnetizing fields and the dipolar interactions among wires. In order to check the general validity of these results, the method of electro-deposition in polycarbonate membrane pores had been used to produce arrays of cobalt NWs, with diameters in the range 100–400 nm and lengths of  $L < 6$   $\mu\text{m}$  by Kazadi Mukenga Bantua et al (Kazadi Mukenga Bantua et al., 2001). It can be concluded, from the measurements of hysteresis loops at room temperature, in the range of template pore diameters studied (100–200–400 nm), that the shortest wires have an easy axis of magnetization parallel to the axes of the wires, and the longest wires present a crossover towards perpendicular directions. This has been explained by a simple magnetostatic model, which corresponds to competition between the dipolar interactions, demagnetizing field, and the Co magnetocrystalline anisotropy. Very recently, our group (Zhou et al., 2011) reported wet chemical synthesis and magnetic properties of single crystal Co nanochains with surface amorphous passivation Co layers.

#### 4.3 Ni

Magnetic properties of nickel NWs had been investigated by several groups in recent years. In order to investigate the dependence of magnetic properties of nickel NWs on electro-

deposition process parameters (especially the pH and the temperature) and the electrical properties as a function of applied magnetic field in the presence of high frequency excitations. Rahman et al (Rahman et al., 2003) fabricated Nickel NWs through the pores of NCA of 200 and 20 nm nominal pore size using galvanostatic electro-deposition technique by applying a constant current density of  $10\text{mAcm}^{-2}$ . They made a study on the growth of NWs on the electrochemical cell parameters such as bath temperature, pH and time. It is found that bath temperature influences the preferred orientation of electrodeposited NWs regardless of pH of the electrolyte. By various kinds of property measurement, it is shown that the coercivity has a strong dependence on the pH of the electrolyte, and impedance change in the presence DC magnetic field did not show any considerable change in the impedance. This method, a combined technique of anodic anodization and direct current (DC) electrodeposition, had also been used by Lin et al., who successfully synthesized nickel NWs. Using an ordered porous alumina film as a template, it is found that the Ni NWs with different diameter and coercivity exhibit high perpendicular anisotropy. Based on an approach by Masuda and Fukuda, Nielsch et al. fabricated ordered porous alumina arrays with a sharply defined pore diameter by a two-step electrochemical anodization aluminum process, and homogeneously filled Ni into porous alumina templates by pulsed electro-deposition. The magnetic behavior of Ni NWs of 100 nm period arrays were characterized by magnetometry and magnetic force microscopy and the results show that stray field interactions of single domain NWs are entirely dependent on the NW diameter.

#### 4.4 Ferromagnetic alloys

##### 4.4.1 Fe-Ni

Fe-Ni alloys are the most common kind of soft magnetic, which have a series of physical properties with variational ratio of component. At an aim of superior magnetic properties such as higher coercivity and higher remanence ratio, Fe-Ni alloys NWs are prepared by a variety of components. The alloy NW arrays of  $\text{Ni}_{80}\text{Fe}_{20}$  had been fabricated using electro deposition in nanoporous alumina templates. By the analysis of magnetic properties, they observed higher coercivity of  $84349.5\text{ A/m}$  and higher  $M_r/M_s$  compared to a body material. Soft magnetic  $\text{Fe}_{26}\text{Ni}_{74}$  NWs of 18 nm diameter and various lengths, electrodeposited in the pores of anodic alumina, were synthesized by Khan et al. (Khan & Petrikowski, 2000), who made a depth research on its properties such as the room temperature magnetization, magnetoresistance and structural properties. NWs show perpendicular magnetic anisotropy, anisotropic crystallographic and magnetoresistance behavior with a coercivity of 967 Oe and a remanence value of 85%, and it should be noted that an electrodeposited  $\text{Fe}_{26}\text{Ni}_{74}$  layer (6  $\mu\text{m}$ ) on a copper substrate shows in-plane anisotropy and a coercivity of less than 1 Oe. It is found that the size dependence of the macro-magnetic properties is very interesting in  $\text{Fe}_{0.68}\text{Ni}_{0.32}$  NW arrays. In order to make a further study for this phenomenon, Liu et al. made an investigation on the effect of diameter on micro-magnetic properties of  $\text{Fe}_{0.68}\text{Ni}_{0.32}$  NW arrays (Liu et al., 2004). NW arrays of the alloy,  $\text{Fe}_{0.68}\text{Ni}_{0.32}$ , with different NW diameters had been fabricated by the electrochemical deposition method. XRD patterns of  $\text{Fe}_{0.68}\text{Ni}_{0.32}$  NW arrays with different diameters indicate that the  $\text{Fe}_{0.68}\text{Ni}_{0.32}$  NWs have a BCC structure with  $\langle 110 \rangle$  as the texture direction, which is parallel to the long axis of the NWs as shown in Fig 18. Mossbauer spectra are shown in Fig 19. The Mossbauer spectra of the NW arrays with smaller diameters show an absence of the second and fifth peaks, and then it emerge with increasing diameter. Hyperfine parameters extracted from the Mossbauer spectra show that the isomer shift and quadruple splitting are insensitive to

changes in the diameter. The FWHM and hyperfine field have evident changes when the NW diameters increase from 16 to 100 nm.

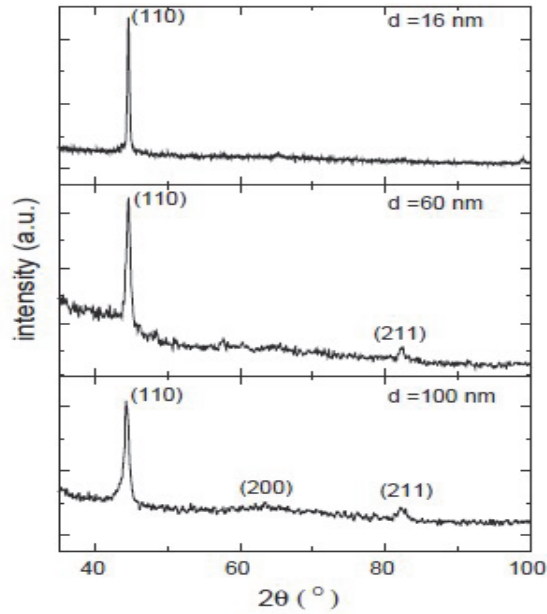


Fig. 18. XRD patterns for NW arrays of the alloy.

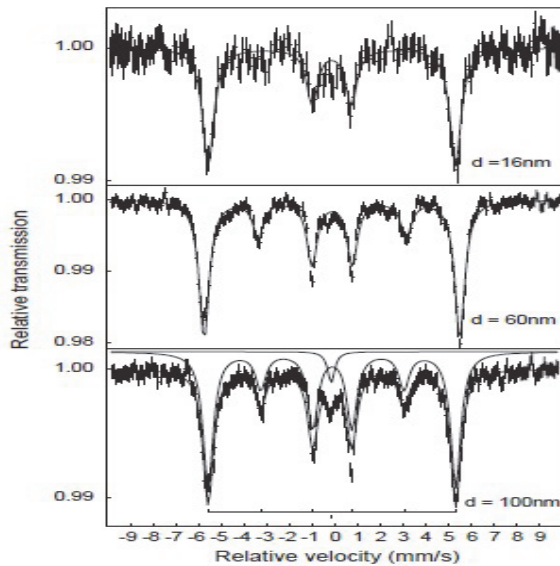


Fig. 19. Mossbauer spectra of  $\text{Fe}_{0.68}\text{Ni}_{0.32}$  NW arrays with different diameters.

#### 4.4.2 Co-Fe

Fodor et al. had an in-depth investigation on the crystallographic and magnetic properties of various concentrations of  $\text{Co}_{1-x}\text{Fe}_x$  alloys by electro-deposition in the alumina matrix produced by anodization in oxalic acid (Fodor et al., 2002). To obtain highly ordered pores a two-step anodization process was employed. Fig 20 shows that the crystalline structure of the NWs is concentration dependent and a transition from the cobalt hexagonal-closed-packed structure (hcp) to a face-centered-cubic structure (fcc) in the concentration range  $0 < x < 0.1$ . For an iron content greater than 15 at% the structure becomes body-centered-cubic (bcc). With magnetic measurements, it is suggested that the magnetic properties—coercivities and squareness of hysteresis loops—of the CoFe alloy NWs are improved over the properties of similar nanostructures composed of pure Co and Fe.

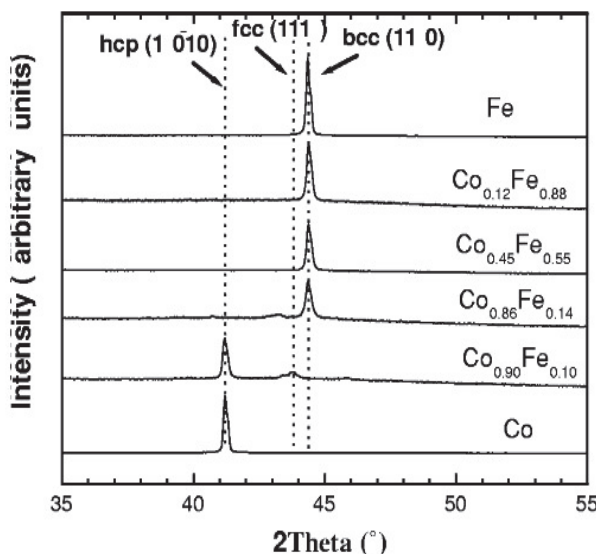


Fig. 20. X-ray diffraction pattern for  $\text{Co}_{1-x}\text{Fe}_x$  NWs arrays after removing the Al substrate.

The concentration dependence of the coercivity force along the NW axis appears to be related to the crystalline structure of the NWs and the coercivity reaches a maximum in the range in which the NWs crystallize in the body-centered-cubic structure. Khan et al. designed an experiment to fabricate the arrays of Co and  $\text{Co}_{90}\text{Fe}_{10}$  NWs (of diameters 18 and 78 nm) by electrochemical method (Khan & Petrikowski, 2002). They had investigated the structural and magnetic properties of the isolated, electrodeposited Co and Co-Fe NWs of 18 and 78 nm diameters. The arrays of 18 nm diameter show perpendicular magnetic anisotropy, and  $\text{Co}_{90}\text{Fe}_{10}$  shows enhanced  $H_c$  ( $\perp$ ) and  $M_r$  ( $\perp$ ) values compared to Co. The perpendicular magnetic anisotropy and the values of  $H_c$  ( $\perp$ ) and  $M_r$  ( $\perp$ ) decrease with increasing NW diameter and interwire distance.

#### 4.4.3 Co-Ni

As a soft magnetic material, Co-Ni alloys can be used as magnetic recording materials, and their magnetic properties can be greatly improved by changing components or adding other

trace elements. However, magnetic properties of the Co-Ni alloys film, which has a lot of research, are difficult to satisfy the condition of highly density perpendicular magnetic recording because of its small Hysteresis loop squareness ratio. Co-Ni NWs alloys are expected to exhibit a high degree of magnetic anisotropy and a higher hysteresis loop squareness ratio. Co-Ni NW arrays have been successfully fabricated by ac electro-deposition in porous anodic aluminum oxide template and have been studied for the relationship between magnetic properties and Co-Ni components. The result of magnetic measurement suggests that squareness ratio and coercivity of Co-Ni NW arrays can be modulated by changing the component of Co-Ni alloys. This kind of array film may become a promising high-density perpendicular magnetic recording material, because the Coercivity and hysteresis loop squareness of Co-Ni NW arrays are higher than that of Two-dimensional alloy film. Using AC electro-deposition, ultra small Co-Ni NWs with 8 nm diameters had been successfully fabricated by Zhang et al within nanochannel alumina templates (Zhang et al., 2004). The NWs possess an FCC structure and the corresponding SAED patterns showing that the NW possesses an FCC structure with the axis of the NW orientated along the [1 1 0] direction. The hysteresis loops of the samples with the external field perpendicular ( $\perp$ ) and parallel ( $\parallel$ ) to the sample plane from 5 to 350 K are measured. The magnetic behavior of the NWs shows strong temperature dependence. The coercivities increase greatly with the decrease in temperature. A coercivity as high as 2529 Oe has been obtained at 5 K.

#### 4.5 Heterogeneous ferromagnetic-nonmagnetic alloys

Since the magnetic properties of NW arrays are related to their element components and morphology, heterogeneous ferromagnetic-nonmagnetic alloy NW arrays systems are expected to exhibit better magnetic. The technique of electro-deposition in the pores of aluminium oxide membranes with quoted pore diameter 20 nm and length 60  $\mu\text{m}$  had been used to prepare AgCo and AgCoCu inhomogeneous alloy NWs by Fedosyuk et al (Fedosyuk et al., 1999). They had shown for the first time that it is possible to electro-deposit alloy NWs in which Ag is the predominant non-magnetic component, and that these NWs exhibit GMR. When  $\text{Ag}_{45}\text{Co}_{25}\text{Cu}_{30}$  NWs were annealed, the GMR increased significantly. Schwarzacher's group had studied the Co-Cu alloy NWs (Blythe et al., 2000) and Co-Ni-Cu/Cu multilayered NWs (Evans et al., 2000) electro-deposited into commercial anodic membranes. A gold layer had been evaporated on one side of the membrane to serve as a conducting electrode. The thickness or composition was controlled by the applied reduction potential. They found a large value of the current perpendicular to plane giant magnetoresistance (CPP-GMR) for Co-Ni-Cu (5.4 nm)/Cu (2.1 nm) multilayered NWs: 55% at room temperature and 115% at 77 K.

It is difficult to use the conventional dc reduction method to produce multi-layers or alloys of two metals with large different reduction potentials, such as Co and Cu or Fe and Pt. The new method of an alternating current between the alumina template and the suitable counterelectrode has been employed. Zheng et al. had succeeded in fabricating Fe/Pt multilayered NW arrays by alternating the alumite template between two chemical cells containing Fe and Pt ions using alternating current at a voltage of 20 V and a frequency of 250 Hz (Zheng et al., 2000). The thickness of individual layers is around 10 nm. They found that the multilayered Fe/Pt NWs exhibit an easy magnetization along the wire axis, which is probably due to shape anisotropy. Annealing studies led to either two phase or soft-phase phenomena. Future work will be aimed at studies as a function of layer thicknesses and at achieving higher coercivity and higher anisotropy.

Wang et al. had successfully fabricated ordered ferromagnetic-nonmagnetic alloy (Co-Cu, Co-Ag, and Fe-Ag) NW arrays embedded in the nanochannels of AAM by electro-deposition and studied their annealing temperature dependence of magnetic properties in detail (Wang et al., 2002). SEM and TEM observations reveal that those alloy NWs are uniform in diameter and ordered. Magnetic measurements show that the perpendicular coercivity ( $HC^{\perp}$ ) of those ordered NW arrays embedded in AAM increases dramatically as annealing temperature (TA) rises, reaches their maximum at one temperature, and then decreases sharply as TA rises further. However, there is not much change of the parallel coercivity ( $HC^{\parallel}$ ) for these alloy NW arrays in the same annealing conditions.

Yuan et al. fabricated perpendicular anisotropy ternary magnetic NW arrays for ultra-high-density magnetic recording. They fabricated Ni-W-P alloy NW arrays by electroless deposition in an anodic alumina membrane. The magnetic properties of Ni-W-P alloy NW arrays were characterized using a vibrating sample magnetometer. The hysteresis loops show that the easily magnetized direction of Ni-W-P NW arrays is parallel to the NW arrays and that it has obvious magnetic anisotropy as a result of the shape anisotropy. So we can see that electroless deposition opens up significant opportunities in the nanoscale fabrication of magnetic materials for ultra-high-density magnetic recording. In addition, our research group studied different magnetic nanowires (Zhou et al., 2008; Zhou et al., 2008; Lu et al., 2010; Zhou et al., 2010; Zhou et al., 2011).

## 5. Concluding remarks

As we all know, thermoelectric (Zhou et al., 2011; Yang et al., 2009; Eteessam-Yazdani et al., 2009; Sait & Ma, 2009; Narayanan et al., 2009; Hopkins & Beechem, 2010; Heatwole et al., 2009; Youssef & Elsibai, 2011) and magnetic (Zhou et al., 2011; Zhou et al., 2008; Zhou et al., 2008; Lu et al., 2010; Zhou et al., 2010; Zhou et al., 2011) materials have a very attractive prospect because of their special performance. Theory predicts that the properties of the thermoelectric and magnetic NWs may have a higher improvement compared to their bulk structure. In the earlier sections, we have discussed the synthetic strategies and properties of various thermoelectric and magnetic NWs, and the results of the experiment are generally agreement with the theoretical predictions. Clearly, there has been intense activity in this area demonstrating considerable success in preparing NWs in good quantities with a reasonable control on the dimensions. In order to improve the thermoelectric or magnetic properties of materials, there is little doubt that thermoelectric and magnetic NWs will be prepared in the future. New strategies will also be developed for the synthesis and manufacture of these materials.

## 6. Acknowledgments

This work was partially supported by the Program for Science & Technology Innovation Talents in Universities of Henan Province (No.2008 HASTIT002), Innovation Scientists and Technicians Troop Binstruction Projects of Henan Province (No.094100510015), and by the Natural Science Foundation of China under Grant No. 20971036.

## 7. References

- Aimawlawi, D.; Coombs, N. & Moskovits, M. (1991). *J. Appl. Phys.*, Vol. 70, P. 4421  
Aranda, P. & Garcia, M. J. (2002). *Magn. Mater.*, Vol. 249, P. 214

- Bejenari, I.; Kantser, V. & Balandin, A. (2010). *Phys. Rev. B.*, Vol. 81, P. 075316
- Bell, L. E.; (2008). *Science* Vol. 321, P. 1457
- Blythe, H.; Fedosyuk, V.; Kasyutich, O. & Schwarzacher, W. (2000). *J. Magn. Magn. Mater.*, Vol. 208, P. 251
- Bucherer, A.H.; (1900). *Ann. Physik*, Vol. 3, P. 204
- Chahre, N.; Stamenov, P.; Rhen, F. & Coey, J. (2005). *J. Magn. Magn. Mater.*, Vol. 290, P. 1210
- Dong, A.; Wang, F.; Daulton, T. & Buhro, W. (2007). *Nano Lett.*, Vol. 7, P. 1308
- Dresselhaus, M.; Lin, Y.; Rabin, O.; Jorio, A.; Souza Filho, A.; Pimenta, M.; Saito, R.; Samsonidze, G. & Dresselhaus, G. (2003). *J. Mater. Sci. Eng. C*, Vol. 23, P. 129
- Etessam-Yazdani, K.; Asheghi, M. & Hamann, H. (2009). *Nanosc. Microsc. Therm.*, Vol. 13, P. 203
- Evans, P. R.; Yi, G. & Schwarzacher, W. (2000). *Appl. Phys. Lett.*, Vol. 76, P. 481
- Fedosyuk, V.; Kasyutich, O. & Schwarzacher, W. (1999). *J. Magn. Magn. Mater.*, Vol. 198, P. 247
- Fodor, P.; Tsoi, G. & Wenger, L. (2002). *J. Appl. Phys.*, Vol. 91, P. 10
- Gao, Y.; Niu, H.; Zeng, C. & Chen, Q. (2003). *Chem. Phys. Lett.*, Vol. 367, P. 141
- Givargizov, E. (1975). *J. Crystal Growth*, Vol. 31, P. 20
- Gudiksen, M. S. & Lieber, C. M. (2000). *J. Am. Chem. Soc.*, Vol. 122, P. 8801
- Heremans, J.; Thrush, C.; Lin, Y.; Cronin, S.; Zhang, Z.; Dresselhaus, M. & Mansfield, J. (2000). *Phys. Rev. B.*, Vol. 61, P. 2921
- Heatwole, S.; Veeraragavan, A.; Cadou, C. & Buckley, S. (2009). *Nanosc. Microsc. Therm.*, Vol. 13, P. 54
- Hochbaum, A.; Chen, R.; Delgado, R.; Liang, W. & Yang, P. (2008). *Nature*, Vol. 451, P. 408
- Hopkins, P. & Beechem, T. (2010). *Nanosc. Microsc. Therm.*, Vol. 14, P. 51
- Huysmans, G. & Lodder, J. (1988). *J. Appl. Phys.*, Vol. 64, P. 2016
- Jin, C.; Xiang, X.; Jia, C.; Liu, W.; Cai, W.; Yao, L. & Li, X. (2004). *J. Phys. Chem. B.*, Vol. 108, P. 1844
- Ju, Y. & Goodson, K. (1999). *Appl. Phys. Lett.*, Vol. 74, P. 3005
- Kazadi Mukenga Bantua, A.; Rivas, J.; Zaragoza, G.; Lo'pez-Quintela, M. & Blanco, M. (2001). *J. Appl. Phys.*, Vol. 89, P. 615
- Khan, H. & Petrikowski, K. (2000). *J. Magn. Magn. Mater.*, Vol. 215, P. 528
- Khan, H. & Petrikowski, K. (2002). *Mater. Sci. and Eng. C.*, Vol. 19 P. 345
- Lecher, E. (1905). *Physikal. Zeitschr.*, Vol. 6, P.781
- Lee, W.; Ji, R.; Gosele, U. & Nielsch, K. (2006). *Nat. Mater.*, Vol. 5, P. 741
- Li, A.; Muller, F.; Birner, A.; Nielsch, K. & Gosele, U. (1998). *J. Appl. Lett.*, Vol. 84, P. 6023
- Li, D. (2003). *Appl. Phys. Lett.*, Vol. 83, P. 15
- Li, D.; Wu, Y.; Kim, P.; Shi, L. & Yang, P. (2003). *Appl. Phys. Lett.*, Vol. 83, P. 2934
- Li, F. & Metzger, R. (1997). *J. Appl. Phys.*, Vol. 81, P. 3806
- Li, F.; Zhang, L. & Metzger, R. (1998). *Chem. Mater.*, Vol. 10, P. 2470
- Li, L.; Yang, Y.; Huang, X.; Li, G. & Zhang, L. (2006). *Nanotechnology*, Vol. 17, P. 1706
- Lin, Y. & Dresselhaus, M. (2003). *Phys. Rev. B*, Vol. 68, P. 075
- Ling, A.; Muller, F.; Birner, A.; Nielsch, K. & Gosele, U. (1999). *Adv. Mater.* Vol. 11, P. 483
- Liu, J.; Yu, M. & Li, S. (2005). *Chin. J. Inorg. Chem.* Vol. 21, P. 429
- Liu, K.; Chien, C.; Searson, P. & Y. Kui. (1998). *Appl. Phys. Lett.*, Vol. 73, P. 1436
- Liu, Q.; Wang, J.; Yan, Z. & Xuel, D. (2004). *J. Magn. Magn. Mater.*, Vol. 278, P. 323
- Lu, M. & Zhou, S. (2010). *Phys. Lett. A*, Vol. 372, P. 2300
- Mahan, G.; Sales, B. & Sharp, J. (1997). *Phys. Today.*, Vol. 50, P. 42
- Martin-Gonzalez, M.; Prieto, A.; Gronsky, R.; Sands, T. & Stacy, A. (2003). *Adv. Mater.*, Vol. 15, P. 1003
- Masuda, H.; Hasegawa, F. & Ono, S. (1997). *J. Electrochem. Soc.*, Vol. 144, P. 127

- Menon, L.; Zheng, M.; Zeng, H.; Bandyopadhyay, S. & Sellmyer, D. (2000). *J. Electron. Mater.*, Vol. 29, P.510
- Miyazaki, Y. & Kajitani, T. (2001). *J. Crystal Growth*, Vol. 229, P. 542
- Narayanan, S.; Fedorov, A. G. & Joshi, Y. (2009). *Nanosc. Microsc. Therm.*, Vol. 13, P. 30
- Otten, C.; Lourie, O. & Yu, M. (2002). *J. Am. Chem. Soc.* Vol. 124, P. 4564
- Piroux, L.; Dubois, S.; Duvail, J.; Radulescu, A.; Demoustier-Champagne, S.; Ferain, E. & Legras, R. (1999). *J. Mater. Res.*, Vol. 14, P. 3042
- Prieto, A. (2003). *J. Am. Chem. Soc.*, Vol. 125, P. 2388
- Prieto, A.; Martin-Gonzalez, M.; Keyani, J.; Sands, T. & Stacy, (2003). *A. J. Am. Chem. Soc.*, Vol. 125, P. 2388
- Prieto, A.; Sander, M.; Martin-Gonzalez, M.; Gronsky, R.; Sands, T. & Stacy, A. (2001). *J. Am. Chem. Soc.*, Vol. 123, P. 7160
- Qin, R. (2006). *Chin. J. Micronoelectr. Techn. (Chinese)*, Vol. 43, P. 372
- Venkatasubramanian, R.; Siivola, E. & Colpitts, T. (2001). *Nature*, Vol. 413, P. 597
- Thompson, R.J. (1932). *Ind. Eng. Chem.* Vol. 24, P. 620
- Wagner, R. S. & Ellis, W. C. (1964). *Appl. Phys. Lett.*, Vol. 4, P. 89
- Wang, W.; Qu, J.; Lu, X.; Zhang, G.; Li, G. & Li, X. (2007). *Mater. Sci. Forum.*, Vol. 546, P. 2171
- Wang, Y.; Zhang, L.; Meng, G.; Peng, X.; Jin, Y. & Zhang, J. (2002). *J. Phys. Chem. B.*, Vol. 106, P. 2502
- Weber, L. & Gmelin, E. (1991). *Appl. Phys. A*, Vol. 53, P. 136
- Wu, Y.; Fan, R. & Yang, P. (2002). *Nano Lett.*, Vol. 2, P. 283
- Wu, Y.; Yan, H.; Huang, M.; Messer, B.; Song, J. & Yang, P. (2002). *Chem.-Eur. J.*, Vol. 8, P.1261
- Wu, Y. & Yang, P. (2001). *J. Am. Chem. Soc.*, Vol. 123, P. 3165
- Xue, F.; Fei, G.; Wu, B.; Cui, P. & Zhang, L. (2005). *J. Am. Chem. Soc.*, Vol. 127, P. 15348
- Yang, Y.; Hamann, H. & Asheghi, M. (2009). *Nanosc. Microsc. Therm.*, Vol. 13, P. 88
- Yoo, B.; Xiao, F.; Bozhilov, K.; Herman, J.; Ryan, M. & Myung, N. (2007). *Adv. Mater.*, Vol. 19, P. 296
- Youssef, H. & Elsibai, K. (2011). *Nanosc. Microsc. Therm.*, Vol. 15, P. 48
- Zhang, X.; Xu, L.; Dai, J. & Chan, H. (2004). *Phys. B.*, Vol. 353, P. 187
- Zhang, Z.; Gekhtman, D.; Dresselhaus, M. & Ying, J. (1999). *Chem. Mater.*, Vol. 11, P. 1659
- Zhang, Z.; Sun, X.; Dresselhaus, M.; Ying, J. & Heremans, J. (1998). *Appl. Phys. Lett.*, Vol. 73, P. 1589
- Zhang, Z.; Sun, X.; Dresselhaus, M.; Ying, J. & Heremans, J. (2000). *Phys. Rev. B*, Vol. 61, P. 4850
- Zeng, H.; Zheng, M.; Skomski, R.; Sellmyer, D.; Liu, Y.; Menon, L. & Bandyopadhyay, S. (2000). *J. Appl. Phys.*, Vol. 87, P. 4718
- Zheng, M.; Liu, Y.; Zeng, H.; Bandyopadhyay, S.; Kirby, R. & Sellmyer, D. (2000). *APS March Meeting*
- Zhou, J.; Jin, C.; Seol, J. & Shi, L. (2005). *Appl. Phys. Lett.*, Vol. 87, P.133109
- Zhou, S.; Li, N.; Wang, Y.; Lou, S.; Chen, X.; Yuan, H.; Liu, L. & Wang, P. (2011). *Nanosc. Microsc. Therm.*, Vol. 15, P. x
- Zhou, S.; Liu, L.; Lou, S.; Wang, Y.; Chen, X.; Yuan, H.; Hao, Y.; Yuan, R. & Li, N. (2011). *Appl. Phys. A*, Vol. 102, P. 367
- Zhou, S.; Lou, S.; Wang, Y.; Chen, X.; Liu, L. & Yuan, H. (2011). *Nanoscale Res. Lett.*, Vol. 6, P. 285.
- Zhou, S.; Wang, P.; Li, S.; Zhang, B.; Gong, H. & Du, Z. (2008). *Chin. Phys. Lett.*, Vol. 25, P. 4446
- Zhou, S.; Yuan, H.; Liu, L.; Chen, X.; Lou, S.; Hao, Y.; Yuan, R. & Li, N. (2010). *Nanoscale Res. Lett.*, Vol. 5, P. 1284
- Zhou, S.; Zhang, X.; Gong, H.; Zhang, B.; Wu, Z.; Du, Z. & Wu, S. (2008). *J. Phys.: Condens. Matter*, Vol. 20, P. 075217

# Nanowire Formation under Femtosecond Laser Radiation in Liquid

Yasuhiko Shimotsuma, Kiyotaka Miura and Kazuyuki Hirao  
*Kyoto University,  
Japan*

## 1. Introduction

The size and shape of nanoscale materials provide excellent control over many of the physical and chemical properties, including electrical and thermal conductivity, magnetic properties, luminescence, and catalytic activity (Lieber, 1998). In particular, the synthesis and morphological control of nanosized particles, which exhibit surprising and novel phenomena based on the unique property called the quantum size effect, are attractive to chemists and physicists (Alivisatos, 1996). In recent years, nanoparticles are widely used in many applications ranging from biosensing (Anker et al., 2008; Elghanian et al., 1997; Lin et al., 2006), plasmonic devices (Ferry et al., 2008; Maier et al., 2003), and multifunctional catalysts (Hu et al., 1999; Lu et al., 2004). There are a wide variety of techniques that are capable of creating nanoparticles with various morphology and production yield. These nanoparticle formation approaches are typically grouped into two categories: 'top-down' and 'bottom-up'. The first involves the breaking down of large pieces of bulk material into the required nanostructures. The second involves the building of nanostructures, atom-by-atom or molecule-by-molecule in a gas phase or solution. These two approaches have evolved separately and reached the limits in terms of feature size and quality, in recent years, leading to exploring novel hybrid approaches in combining the top-down and bottom-up methods. Colloidal chemists have gained excellent controlled nanosized particles for several spherical metal and semiconductor compositions, which has led to the discovery of quantum size effect in colloidal nanocrystals (Alivisatos, 1996). However, various bottom-up approaches for making morphologically controlled nanoparticles have been found; most of these solution methods are based on thermal process. On the other hand, top-down approaches have been developed for producing metal and semiconductor nanowires, nanobelts, and nanoprisms (Hu et al., 1999; Pan et al., 2001; Jin et al., 2001). In particular, the laser-induced ablation method has become an increasingly popular approach for making nanoparticles due to the applicability to various target materials in an ambient atmosphere (Jia et al., 2006a; Kawasaki & Masuda, 2005; Link et al., 1999; Sylvestre et al., 2004; Tamaki et al., 2002; Tull et al., 2006). Recently, various shape-controlled nanoparticles, such as nanowires (Morales & Lieber, 2008), nanotubes (Rao et al., 1997), and composite nanostructures (Zhang et al., 1998), have been fabricated by this technique. More recently, pulsed laser ablation in liquid has become profoundly intrigued for preparing nanoparticles from the viewpoint of the concise procedure and the ease of handling (Kawasaki & Masuda, 2005; Tamaki et al., 2002; Shimotsuma et al., 2007).

Besides, in recent decades, increasing interest has focused on the femtosecond laser field due to its unique characteristics based on the nonlinear optical effects deriving from ultrashort pulse width and high peak power density (Cavanagh et al., 1993; Stuart et al., 1995). Especially, by connecting the femtosecond laser technology with nanotechnology, an effective approach was provided to prepare and modify nanostructures in micro devices (Kabashin et al., 2003; Kanehira et al., 2005; ; Link et al., 2000; Muskens et al., 2006; Qiu et al., 2004; Shimotsuma et al., 2003, 2007). For example, the ripple nanostructures, which are aligned along the femtosecond laser polarization direction, have been observed on the surface of the metal and semiconductor caused by the interferences between the scattering incident femtosecond laser field and the surface plasmon-polariton waves (Jia et al., 2006a). We have recently reported the first experimental evidence of the periodic nanostructures embedded in silica glass after irradiation by a single focused beam of a femtosecond laser (Shimotsuma et al., 2003). This phenomenon can be interpreted in terms of interference between the incident laser light field and the generated bulk electron plasma waves, resulting in the periodic modulation of electron plasma concentration and the structural changes in transparent material. A great success has been achieved in forming zero dimensional nanoparticles by using intense ultrashort light pulses radiation. We have successfully fabricated a colourful micro-pattern composed of Au or Ag nanoparticles inside a glass matrix (Qiu et al., 2004; Shimotsuma et al., 2007). Podlipensky and co-workers reported the formation of anisotropic Ag nanoparticles in glass which were elongated in the direction parallel to the femtosecond laser polarization (Podlipensky et al., 2003). Link and co-workers reported the size and shape change of Au nanorods under both femtosecond and nanosecond laser irradiation in solution (Link et al., 1999). The limited prior exploration for preparing one-dimensional nanoparticles by a femtosecond laser was concentrated on their fabrication on the materials' surface. Jia et al. reported ZnSe nanowires' growth induced by the femtosecond laser. Yet the nanowires grew only on the ablation crater located on the surface of ZnSe wafer (Jia et al., 2006b). Mazur et al. reported the production of submicrometer-sized spikes that consisted of the silicon on the silicon wafer after irradiating a silicon surface with a femtosecond laser (Baldacchini et al., 2006; Shen et al., 2004). Thus it should be interesting to investigate the preparation and evolution of nanowires under intense ultrashort light fields, which might reveal the interaction between the photons and the excited plasmons (materials) in the nanoscale. In this Chapter, we present formation of one-dimensional metal Cu (Nakao et al., 2008; Shimotsuma et al., 2007) and ZnO (Lee et al., 2008, 2009) nanoparticles under femtosecond laser irradiation in liquid. It should be interesting to investigate the preparation and evolution of nanowires under intense ultrashort light fields, which reveals that the growth mechanism of Cu and ZnO nanowires could be a nucleation growth process (Chang et al., 2008; Wu et al., 2010).

## 2. Photofragmentation and evolution of metal Cu nanowire

In this section, the photofragmentation from Cu micro-flakes to nanowires and nanospheres via femtosecond laser radiation in alcohol solution was described. This phenomenon has provided the two distinct surface plasmon resonances based on the characteristic shape. The observed Cu nanowires of 50 nm diameter could be fragmented from the initial flakes as a result of the interference between the light field and the surface plasmon wave. By observing the morphology transformation of nanowires with time, the mechanism of Cu

nanowires growth with femtosecond laser irradiation in the solution was also presented. Interestingly, the growth of the Cu nanowires was influenced by the incident light polarization. Other starting materials, e.g. Cu microspheres, were also tested to fabricate nanowires under the same technique to verify the mechanism and procedure of nanowires' growth by another process. Furthermore, we demonstrate that the morphological control of Cu nanoparticles, dispersed in various alcohol solutions, under femtosecond laser irradiation. Beyond the basic understanding, such Cu nanowires have possible applications in the areas of plasmonic devices (Liu et al., 2008), surface-enhanced Raman scattering (SERS) (Sauer et al., 2006), and medicinal imaging (Desvaux et al., 2005).

### 2.1 Photo-conversion of Cu micro-flakes to nanowires

We used commercially available Cu micro-flakes produced by a chemical reduction method, which were 5  $\mu\text{m}$  in size and 100 nm thick. A small amount of the Cu flakes, 0.36 mg, was mixed with 4.5 mL of 99.5% alcohol solution in a rectangular quartz vessel of  $1 \times 1 \times 5 \text{ cm}^3$  with a vessel thickness of 1.25 mm. The laser radiation in Gaussian mode produced by a regenerative amplified mode-locked Ti:sapphire laser (Coherent Inc., 100 fs pulse duration, 1 kHz repetition rate) operating at a wavelength of 800 nm was focused via a microscope objective (Nikon; LU Plan Fluor,  $20\times$  0.40 N.A.) into the alcohol-suspended Cu micro-flakes placed on a magnetic stirrer. The typical beam waist diameter and laser energy fluence were estimated at  $\sim 4 \mu\text{m}$  and  $2.4 \times 10^3 \text{ J/cm}^2$ , respectively. The polarization of the laser light was set linear or circular by a half-wave or a quarter-wave plate placed in the incident beam before the focusing optics. A schematic of the experimental setup is shown in Fig. 1. Before

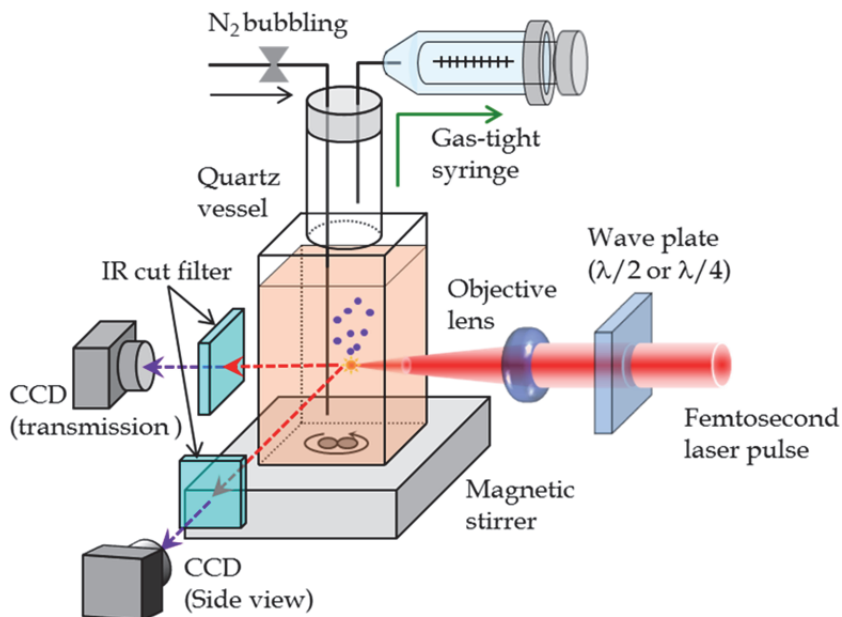


Fig. 1. Schematic of an experimental setup including gas trapping system during femtosecond laser pulse irradiation.

laser irradiation, the suspension was deaerated by bubbling nitrogen gas into it for 15 minutes. To keep as many Cu micro-flakes as possible suspended in the solution, the solution was continuously stirred with a magnetic stirrer during laser irradiation. The generated gas during laser irradiation was trapped in a gas-tight syringe at atmospheric pressure, and then analyzed by a gas chromatography (Shimadzu Corp., GC-2014). After laser irradiation, absorption spectra of the Cu suspension were measured by a spectrophotometer (JASCO, V-570). In order to analyze the nucleation site just after femtosecond laser irradiation, the suspension was immediately dropped onto a silicon substrate and the solvent was evaporated at room temperature. To reveal the growth mechanism of Cu particles, after laser irradiation, the suspensions were left at rest in a temperature-controlled bath having a constant temperature of 40 or 60 °C. The Cu particles after femtosecond laser irradiation were characterized by a field-emission scanning electron microscopy (JEOL, JSM-6700F), a transmission electron microscope (JEOL, JEM-2010F), and a field-emission electron probe micro analyzer (JEOL, JXA-8500F). All of the experiments were carried out at ambient temperature and pressure.

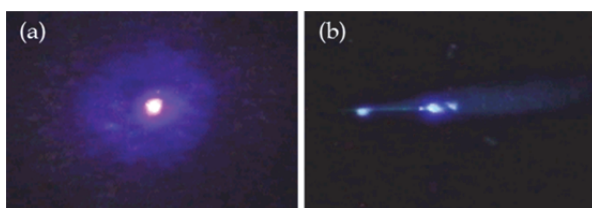


Fig. 2. CCD images of the focal spot during femtosecond laser irradiation into alcohol solution (methanol) along (a) and perpendicular (b) to the laser axis.

We observed the focal spot during femtosecond laser irradiation into alcohol solution along and perpendicular to the laser axis by using CCD camera (Fig. 2). These photos clearly indicate the generation of white-light filaments. It is well known that when a high intense femtosecond laser pulse is launched in gases (Braun et al., 1995; Corkum et al., 1986), liquids (Liu et al., 2002), and solids (Tzortzakakis et al., 2001), it self-focuses and self-transforms into a white-light emission during femtosecond laser filamentation. Filamentation is commonly explained in terms of a balance between two nonlinear effects: Kerr self-focusing inducing a change of the refractive index of the medium proportional to the laser intensity; plasma defocusing through multiphoton and/or tunnel ionization of the medium in the high-intensity zone.

The pulse width at the focus after propagating in the dispersion medium can be estimated by the following equation:

$$\Delta\tau_{out} = \sqrt{\Delta\tau_{in}^2 + \frac{4(\ln 2)^2 \lambda^6 L^2}{\pi^2 c^4 \Delta\tau_{in}^2} \left( \frac{d^2n}{d\lambda^2} \right)} \quad (1)$$

where  $\Delta\tau_{in}$ ,  $\Delta\tau_{out}$ ,  $\lambda$ ,  $L$ ,  $c$ ,  $d^2n/d\lambda^2$  are the input pulse width, the output pulse width, the wavelength, the propagation length in dispersion medium, the speed of light, and the second derivative of refractive index with respect to wavelength, respectively. From this equation, the input laser pulse width of 100 fs was stretched to 110 fs after propagating

through 10 mm in methanol (Fig. 3). Such elongation of pulse width in alcohol solution does not make any difference in nonlinear light-matter interaction.

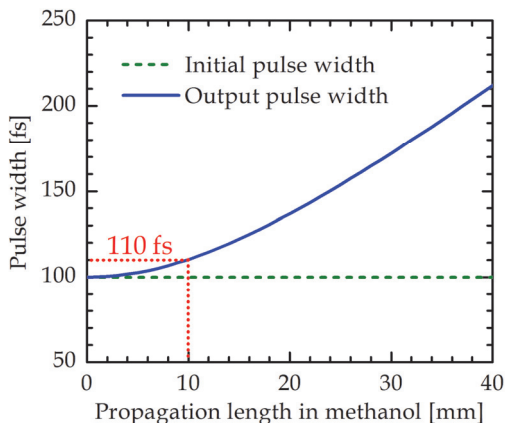


Fig. 3. Output pulse width after propagating in dispersion medium (methanol solution).

Fig.4 (a) shows the sequence of absorption spectra of the suspension, taken as a function of laser irradiation time. Minor absorption was observed for the dilute suspension of Cu microflakes in the wavelength region from 330 to 800 nm before the femtosecond laser irradiation while there were two apparent surface plasmon peaks in the absorbance ( $\lambda_{abs} = 380$  nm and 600 nm) during laser irradiation. The fluctuation of the surface plasmon peaks are considerably weaker as compared to the background interband transition that predominates

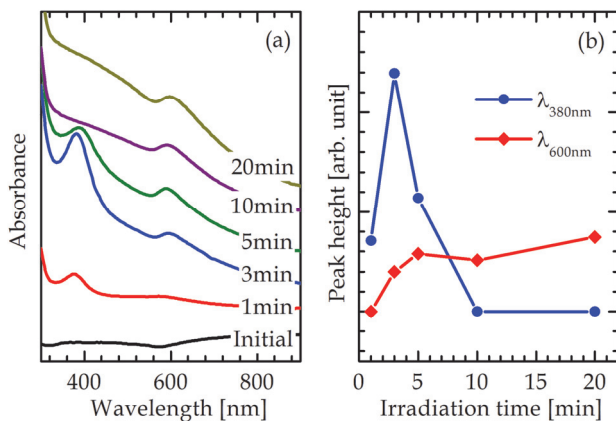


Fig. 4. (a) Sequence absorption spectra taken as a function of laser irradiation time at a pulse energy fluence of  $3.5 \times 10^3$  J/cm<sup>2</sup>. Each curve is shifted with respect to the next longer irradiation time. (b) Peak height profiles of the corresponding absorption at  $\lambda = 380$  nm and 600 nm as a function of laser irradiation time.

the high-energy wing ( $\lambda < 320$  nm) of the spectra (Kawasaki & Masuda, 2005). We also observed an increase in intensity of the surface plasmon absorption for the spherical particles at  $\lambda_{\text{obs}} = 600$  nm with a concomitant growth of a new peak at  $\lambda_{\text{obs}} = 380$  nm (Fig.4 (b)). Indeed, the surface plasmon absorption of 10 nm spherical Cu nanoparticles is located at 560 nm, which can be predicted by Mie theory with no free electron density correction (Lipinska-Kalita et al., 2005). After 10 min, the peak at 380 nm completely disappeared. In the case of long pulse laser irradiation, these unexplained peaks have not been observed (Kawasaki & Masuda, 2005).

Scanning electron images (SEIs), when correlated with the time-dependent absorption spectroscopic observations, show that the initial Cu micro-flakes (size:  $\sim 5$   $\mu\text{m}$ , thick:  $\sim 0.1$   $\mu\text{m}$ ) were converted to nanowires after the femtosecond laser irradiation between 1 and 5 minutes (Fig.5 (a) ~ (d)). During initial stages of the nanowires formation, both micro-flakes and nanowires can be seen (Fig. 5 (b)). The diameter of the nanowire increases with laser-irradiation time. The growth rate of the diameter of nanowires increases with the pulse repetition rate from 10.2 to 54.2 nm/min (Fig. 6 (a)). After 10 minutes irradiation, nearly all of the nanowires are converted to the nanospheres of 10 ~ 70 nm diameter (Fig. 5 (e), (f)). Detailed FE-SEM observations revealed that the diameters of Cu nanowire were about 62, 159, 270 nm for the number of light pulses of  $6 \times 10^4$ ,  $180 \times 10^4$ ,  $300 \times 10^4$ , respectively, and for the pulse energy of 0.4 mJ, corresponding to intensity of  $1.6 \times 10^{16}$  W/cm<sup>2</sup>. This indicated a linear dependence of the nanowire diameter on the number of light pulses (Fig. 6 (c)). During the nanowire growth stage, the lengths of nanowires slightly increased from 3  $\mu\text{m}$  and eventually were saturated to 6  $\mu\text{m}$  (Fig. 6 (b)). The extremely small Cu clusters could be also generated by the fragmentation of a portion of nanowire and consumed in this nanowire growth. Finally, nanospheres of 10 ~ 70 nm were formed by the fragmentation of nanowires along with the termination in growth of the nanowires. The Cu clusters were also formed from either fragmentation or dissolution of the nanospheres. The nanowires act as the sources of nanospheres and clusters. These data clearly show that the Cu nanospheres are dissociated from the initial flakes via

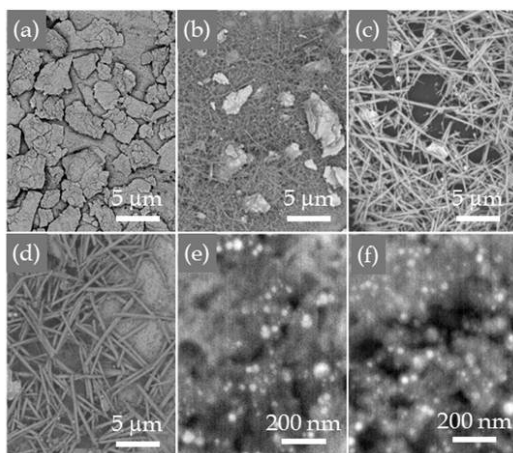


Fig. 5. SEIs indicating the morphology changes (a) before irradiation and after (b) 1, (c) 3, (d) 5, (e) 10, and (f) 20 minutes of the femtosecond laser irradiation.

nanowires formation. This photo-conversion is also indicated in the absorption spectral changes. Namely, the absorption peaking at  $\lambda_{abs} = 380$  nm could be assigned to the transverse surface plasmon resonance of Cu nanowires.

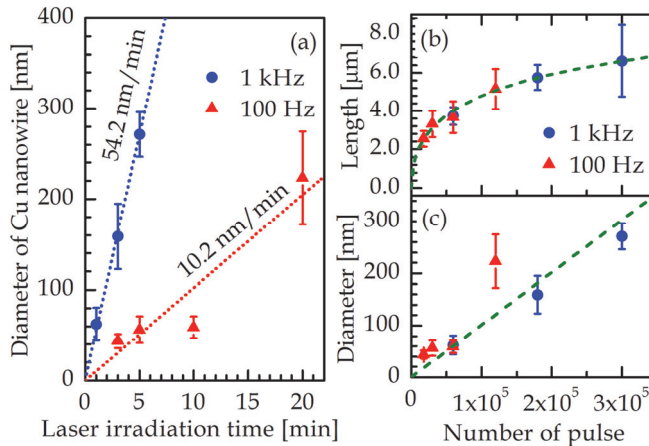


Fig. 6. (a) Diameter of the Cu nanowire as a function of laser irradiation time. (b) Length and (c) diameter of the Cu nanowire as a function of irradiated number of pulse with intensity of  $1.6 \times 10^{16}$  W/cm<sup>2</sup>.

To understand the mechanism of one-dimensional Cu nanoparticles under the intense ultrashort light pulses and to compare the results from different starting materials, other starting materials, e.g. Cu microspheres and Cu sheet, were also tested to fabricate nanowires and nanorods under the same experimental procedure (Fig. 7). A similar structural evolution process was found for the microspheres (Fig. 7 (a)), which was also firstly formation of the short nanorods on the surface of microspheres (Fig. 7 (b)), then the.

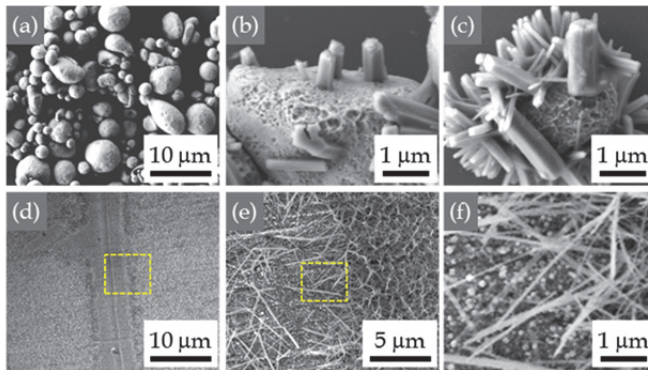


Fig. 7. SEIs of Cu microspheres before laser irradiation (a) and nanorods prepared with the different irradiation time: (b) 10 min and (c) 20 min. (d) SEI of Cu sheet after femtosecond laser scanning. The images in (e) and (f) are the high magnified images of the dotted regions in (d) and (e), respectively.

amount and length of the nanorods increased at the cost of the microspheres and finally the microspheres were reduced in size to the nanospheres with increasing laser irradiation time, as shown in Fig. 7 (c). This means that the nucleation growth mechanism of nanoparticles is the same with another materials evolving in the condition of intense ultrashort light pulses. This process could find wide applications for the preparation of one-dimensional nanoparticles. Indeed, we have also observed the growth of nanowire on the surface of Cu sheet after femtosecond laser irradiation (Fig. 7 (d) ~ (f)). Compared with the typical formation of Cu nanowires of 85 nm diameter from micro-flakes, it was nanorods with the average length and diameter of 1  $\mu\text{m}$  and 280 nm, respectively that formed in the methanol solution. In addition, it seemed that a slightly longer irradiation time (20 min) was needed for the transformation to the nanorods, indicating that higher laser energy was involved in the change to the nanorods from microspheres than that in the conversion from the micro-flakes to nanowires

## 2.2 Characterization of Cu nanowires

Fig. 8 (b), (c) show the typical SEIs of Cu nanowires, which were synthesized by femtosecond laser with an irradiation time of 5 min. It was clearly demonstrated that nanowires, with an average length of 1.0  $\mu\text{m}$  and an average diameter of 85 nm were formed via simple femtosecond laser irradiation. Comparing with the original Cu micro-flakes, shown in Fig. 8 (a), it is clear that almost all of micro-flakes transferred to the nanowire structure in the methanol after 5 min irradiation, indicating that femtosecond laser irradiation provided a highly effective way for the nanowires formation. Some small nanospheres attached to the edge of nanowires (Fig. 8 (c)) were thought to contribute to the growth of nanowires. Interestingly, many clumps consisting of needle-like nanowires along all directions were found in the images, which implied that one nucleation site was located in the centre and grew up to form the nanowires.

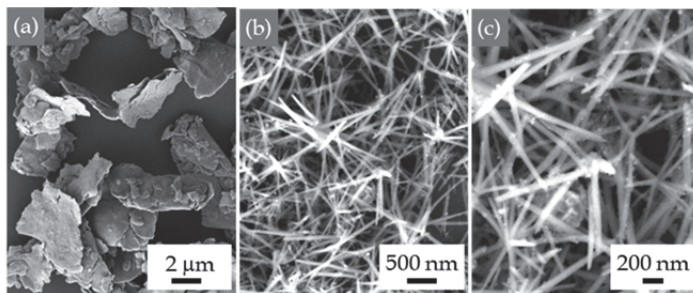


Fig. 8. Typical SEIs of Cu micro-flakes before femtosecond laser irradiation (a) and Cu nanowires observed after 5 min femtosecond laser irradiation. The images are shown in two different scales: (b) low- and (c) high-magnification image for the same area.

A detailed TEM analysis of Cu nanowires and nanospheres prepared in ethanol has been performed. Fig. 9 shows TEM observations of Cu nanowires after femtosecond laser irradiation for 3 minutes. Schematic diagrams of the analysis methods are also shown. The conventional observations indicate that the nanowires' surfaces are composed of polycrystalline  $\text{Cu}_2\text{O}$  (Fig. 9 (a), (b), (e)). Furthermore, the cross-sectional observations clearly demonstrate that nanowires are partially oxidized from the surface to a depth of

about 5 nm (Fig. 9 (d)). On the other hand, the inner part of the nanowires was composed of polycrystalline metallic Cu (Fig. 9 (c), (d), (f)). Indeed, the electron diffraction patterns of the inner and surface parts indicate that the observed areas were composed of metallic Cu (Fig. 9 (e)) and  $\text{Cu}_2\text{O}$  (Fig. 9 (f)), respectively.

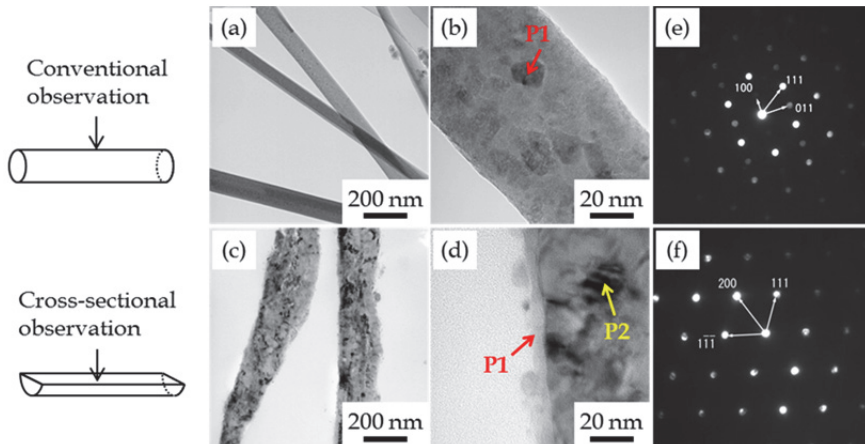


Fig. 9. TEM observations of Cu nanowires after femtosecond laser irradiation for 3 minutes. Schematic diagrams of the analysis methods are also shown on the left hand side. Two types of observations were carried out: conventional (a), (b) and cross-sectional (c), (d). The images are shown at two different scales: low magnification images (a), (c) and high magnification images (b), (d) for the same area. Arrows P1 and P2 in (d) show the analysis points of the electron diffraction patterns. The electron diffraction patterns at P1 and P2 are shown in (e) and (f), respectively.

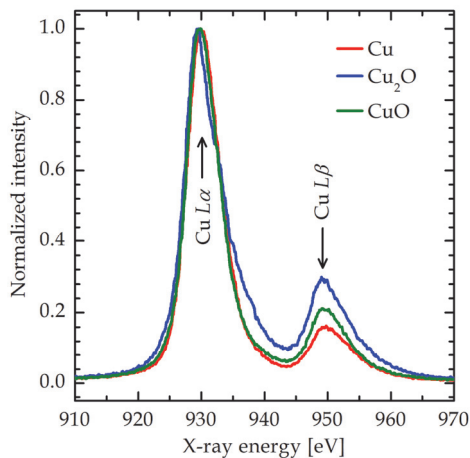


Fig. 10. Typical Cu  $L\alpha$  and  $L\beta$  X-ray fluorescence spectra of various copper oxide compounds.

In order to reveal the chemical state inside Cu nanowires, we carried out chemical state mapping of Cu on the cross-sectional surface by using a field-emission electron probe micro-analyzer (JEOL, JXA-8500F). The chemical state of copper by using EPMA can be determined from the difference in the peak intensity ratio of  $I_{L\alpha}/I_{L\beta}$  X-ray fluorescence spectra of Cu (Kawai et al., 1993). Typical X-ray fluorescence spectra of various copper oxide compounds and the peak intensity ratio of  $I_{L\alpha}/I_{L\beta}$  were shown in Fig. 10 and Table 1, respectively. Based on these relationships, we converted the spectral mapping into the chemical state mapping (Fig. 11). These observations revealed that the main chemical composition inside the nanowires was metallic Cu. The red, orange, and yellow regions in the chemical state mapping indicate the presence of Cu metal,  $\text{Cu}_2\text{O}$ , and CuO, respectively (Fig. 11 (b), (c)). Although the copper on the surface parts of nanowire was oxidized to  $\text{Cu}_2\text{O}$  and/or CuO, the chemical state inside nanowire was maintained as metal Cu, which corresponds to the foregoing TEM analyses. Based on these observations, we speculate that these Cu nanowires have electrical conducting properties.

Chemical state of Cu	Peak intensity ratio ( $I_{L\alpha}/I_{L\beta}$ )
Cu ( $\text{Cu}^0$ )	7.9
$\text{Cu}_2\text{O}$ ( $\text{Cu}^{1+}$ )	5.8
$\text{CuO}$ ( $\text{Cu}^{2+}$ )	4.3

Table 1. The peak intensity ratio of  $I_{L\alpha}/I_{L\beta}$  of various copper oxide compounds.

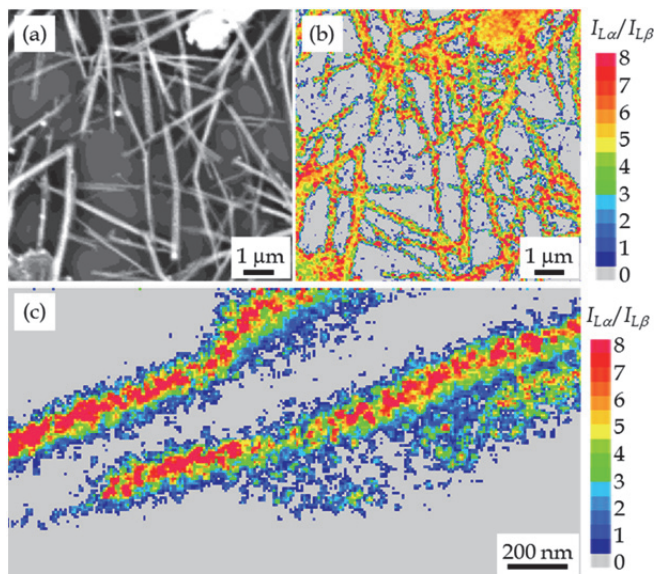


Fig. 11. Chemical state mapping on the cross-sectional surface of Cu nanowires. Backscattering electron image of the same area was also shown (a). The mappings are shown in two different scales: low-magnification (b) and high-magnification image (c) for the same area. Color bar indicates the peak intensity ratio of  $I_{L\alpha}/I_{L\beta}$  X-ray fluorescence spectra of Cu.

We have also confirmed that the nanospheres after long time laser irradiation in ethanol are composed of metallic Cu. Fig. 12 shows TEM observations of Cu nanospheres after femtosecond laser irradiation for 20 minutes in ethanol. A1 and A2 arrows in Fig. 12 (a) show the analysis points of the electron energy-loss spectroscopy (EELS). The EELS spectra near the C-K and Cu-L edges indicate that the Cu nanospheres are covered by a carbon layer (Fig. 12 (b), (c)). Results of the existence of the many metallic Cu nanospheres in the case of long time laser irradiation (Fig. 4 (e), (f)) indicate that these carbon layers, which could be produced by the photo-dissociation of the surrounding solvent molecules, act as a passivation layer preventing not only the aggregation and growth but also their oxidation. Through our experiments, it was found that the dispersed solvent was sensitive to the evolution of morphology of micro-flakes under laser irradiation. Methanol and ethanol were found to be suitable for producing the one-dimensional nanoparticles, such as nanowires and nanorods, while only spherical-like nanoparticles with diameters of about 40 nm were fabricated in the acetone and propanol solution. Moreover, there was no distinct change of the Cu nanospheres after storage in the methanol and ethanol solution for one month.

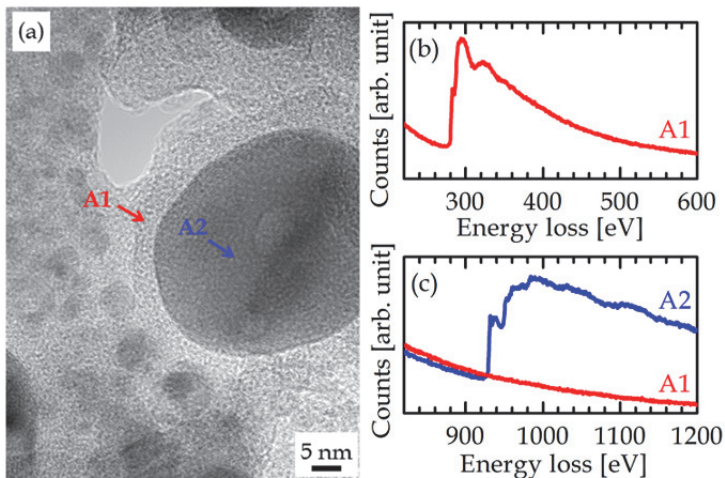


Fig. 12. (a) TEM observations of Cu nanospheres after femtosecond laser irradiation for 20 minutes in an ethanol. Arrows A1 and A2 in image show the analysis points of the electron energy-loss spectroscopy. The electron energy-loss spectra near C-K (b) and Cu-L edge (c) corresponding to the A1 and A2 arrows are also shown.

### 2.3 Morphology control factors of Cu nanoparticle

Fig. 13 shows the absorption spectra of the Cu micro-flakes dispersed in ethanol just after linearly or circularly polarized femtosecond laser irradiation for 5 minutes. The absorption spectra after a subsequent aging treatment at room temperature for 5 days are also shown. In each polarization case, absorptions peaking at 600 nm due to the surface plasmon resonance of Cu nanospheres are observed just after laser irradiation. An apparent difference in absorption spectra was observed after a subsequent aging treatment for 5 days. In the case of the circularly polarization, the maximum absorption was shifted to the short

wavelength region (Fig. 13 (b)). This is attributed to the fact that the partial oxidation of Cu nanospheres causes the blue shift (Tilaki et al., 2007). On the other hand, a particular absorption peaking at 380 nm was observed after linearly polarized laser irradiation and subsequent aging treatment (Fig. 13 (a)).

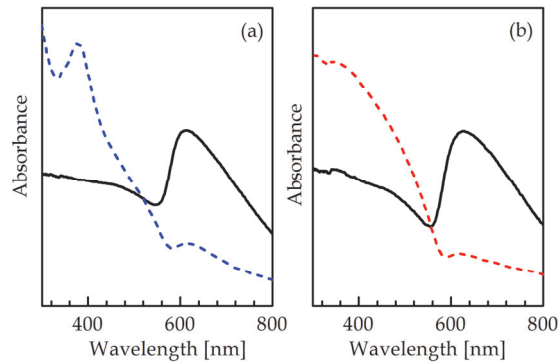


Fig. 13. Absorption spectra of the Cu micro-flakes dispersed in ethanol just after linearly (a) or circularly (b) polarized femtosecond laser irradiation for 5 minutes (solid line). The absorption spectra after subsequent aging treatment at room temperature for 5 days are also shown (broken line).

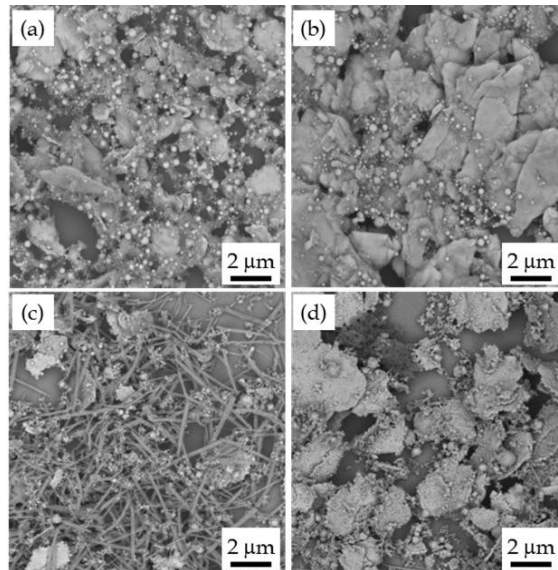


Fig. 14. SEIs of the Cu nanoparticles corresponding to the absorption spectra in Fig. 13. (a) just after linearly polarized laser irradiation and (c) subsequent aging treatment at room temperature for 5 days, (b) just after circularly polarized laser irradiation and (d) subsequent aging treatment at room temperature for 5 days, respectively.

Fig. 14 shows the SELs of Cu nanoparticles corresponding to the absorption spectra in Fig. 13. In each polarization case, the nanospheres and unreacted starting Cu micro-flakes are observed just after laser irradiation (Fig. 14 (a), (b)), while nanowires can be observed only after linearly polarized laser irradiation and a subsequent aging treatment (Fig. 14 (c)). On the other hand, in the case of circularly polarized laser irradiation, there is no observation of nanowires just after laser irradiation and the subsequent aging treatment (Fig. 14 (b), (d)). These results indicate that the absorption peaking at 380 nm may be due to the surface plasmon resonance of partially-oxidized Cu nanowires. Indeed, it is well-known that the surface plasmon resonance frequencies depend not only on the size but also the shape of particles (Yim et al., 2007).

Why are the nanowires not formed in the case of the circular polarization? In order to understand detailed mechanism of the Cu nanowire formation, we compared experimental results to the finite difference time domain (FDTD) calculation of surface plasmon polariton (SPP) wave propagating along the surface of the Cu nanosphere in an ethanol. Furthermore, the TEM observations of the fragmented Cu nanoparticles just after the linear polarized and the circular polarized femtosecond laser pulse irradiation for 5 minutes in ethanol were performed (Fig. 15 (a), (b)). The ethanol suspended Cu nanoparticle was immediately evaporated at room temperature in order to quench particle growth; therefore, these images may indicate the pre-grown Cu nanoparticle. The differences in the shape of these pre-grown Cu nanoparticles evidently depend on the laser polarization (Fig. 15 (a), (b)). Fig. 15 (c) and (d) show FDTD simulation results of electric field amplitude of the SPP wave excited by the linear polarized and the circular polarized light. In this simulation, we used an input

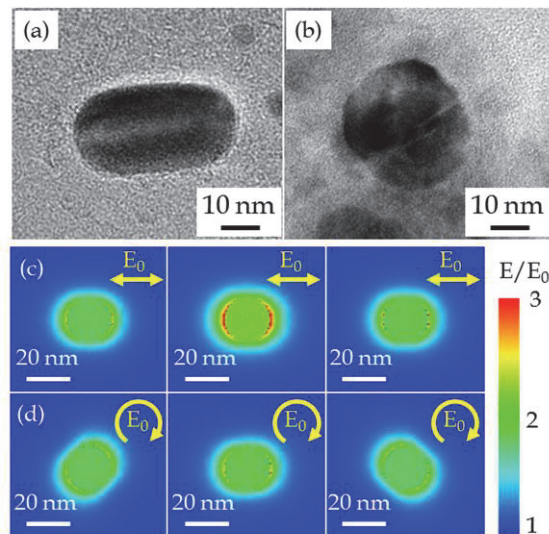


Fig. 15. TEM observations indicating of Cu nanoparticles just after the linear polarized (a) and the circular polarized (b) femtosecond laser pulse irradiation for 5 minutes in ethanol. FDTD simulation results of electric field amplitude of the SPP wave excited by the linear polarized (c) and the circular polarized (d) light are also shown. Each row in (c) and (d) from left to right corresponds to the time domain sequence.

electric field amplitude of  $E_0 = 2.4 \times 10^{11}$  V/m corresponding to the laser energy fluence of  $2.4 \times 10^3$  J/cm<sup>2</sup>, a wavelength of 800 nm, and a diameter of Cu nanosphere of 20 nm. In the case of linearly polarized radiation, the localized enhancement of the electric field along the light polarization can be expected (Fig. 15 (c)), while the region of the electric field enhancement rotates according to the circular polarization (Fig. 15 (d)). Such localized enhancement around the Cu nanosphere in the linear polarization induces an anisotropic distribution of the nonlinear photoionization of the Cu nanosphere, resulting in the anisotropic shape modifications.

Stalmashonak and co-workers have also reported that the laser induced shape modification of spherical Ag nanoparticles embedded in soda-lime glass was evoked by the surface plasmon assisted photoelectron emission of the electrons from the metal surface during femtosecond laser irradiation (Stalmashonak et al., 2009). They have also found that such transformation of the metal nanoparticles in glass, which takes place within a timescale of 1 ns, depends on the applied laser pulse intensity, and suggested that the directional memory is defined by the directed emission of hot electrons interacting with the laser field (Unal et al., 2009). Comparing experimental results with simulation results, the shape of the pre-grown Cu nanoparticle produced by the single laser pulse was defined by the laser polarization. Especially, Cu nanoparticles, which act as a nucleation site for Cu nanowire growth, were elongated in the direction parallel to the linear laser polarization. On the other hand, spherical Cu nanoparticles formed by irradiation with the circularly polarized pulses cannot grow into Cu nanowires. We have also confirmed that the one-dimensional growth of Cu nanoparticles occurs during the subsequent aging process.

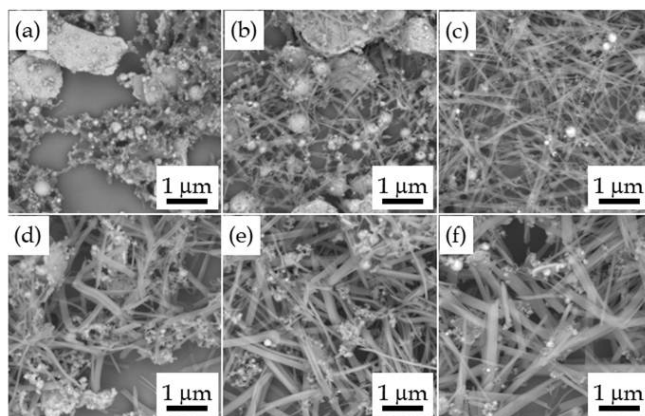


Fig. 16. SEIs of the Cu nanoparticles after linearly polarized femtosecond laser irradiation for 5 minutes and subsequent aging treatment at 40 °C (a) ~ (c) and 60 °C (d) ~ (f). Aging time was 12 hours (a), (d), 24 hours (b), (e), and 120 hours (c), (f), respectively.

Fig. 16 shows SEIs of the Cu nanoparticles after 5 minutes of the linearly polarized laser irradiation and subsequent aging treatment at 40 and 60 °C for several hours. These SEM observations reveal the diameter growth rate of Cu nanowires increases with the aging temperature (Fig. 16). In the initial stage during aging process at 40 °C, namely one-dimensional growth of Cu nanoparticles, nanoscale web-like aggregates of nanoparticles

were formed (Fig. 16 (a)). This phenomenon is similar to the formation of unusual aggregated structures composed of both crystalline and amorphous silicon nanoparticles by the femtosecond laser ablation in the presence of a background gas (Tull et al., 2006). These nanoscale web-like aggregates are expected to be evolved into Cu nanowires (Fig. 16 (a) ~ (c)). Indeed, the inner part of the Cu nanowires was composed of polycrystalline copper (Fig. 9). Detailed SEM observations indicated the diameter of Cu nanowires was variable as a function of the aging time. After the subsequent aging treatment for 120 hours, the diameters of Cu nanowires were eventually about 68 and 185 nm, and the lengths were about 7.5 and 3.5  $\mu\text{m}$  at the aging temperatures of 40 and 60  $^{\circ}\text{C}$ , respectively. This indicates that the aspect ratio of the Cu nanowires can be controlled by the change of the subsequent aging conditions. As described earlier, the shape of Cu nanoparticles was influenced by the surrounding solution. We have also investigated the effect on the growth of Cu nanoparticles by the surrounding solvent. Although the nanoparticles prepared by 3 minutes of laser irradiation in ethanol were almost wire-like, the fraction of nanospheres increased with the laser irradiation time (Fig. 17 (a), (d)). In contrast, the nanoparticles prepared by the same conditions of laser irradiation in methanol were observed to be cubic nanostructures (Fig. 17 (b)), while nanorods were formed in the case of the long time laser irradiation (20 minutes) (Fig. 17 (e)). Besides, in the case of long time laser irradiation in ethanol and methanol, many nanospheres still exist after a subsequent aging treatment for 5 days (Fig. 17 (d), (e)). However, the one-dimensional growth of the nanoparticles after laser irradiation and a subsequent aging treatment occurred in both the cases of ethanol and methanol but no morphological change was observed in the case of using propanol (Fig. 17 (c), (f)).

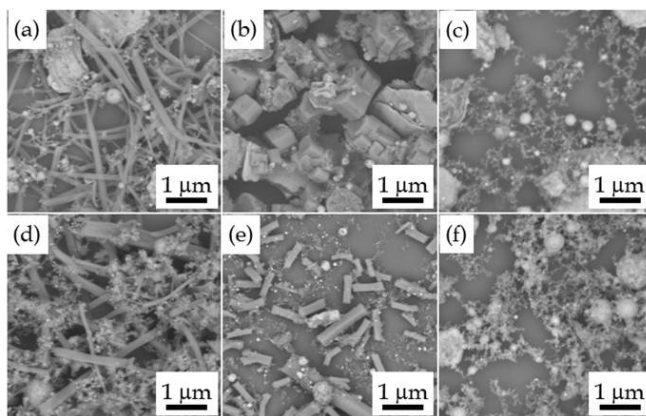


Fig. 17. SEIs of Cu nanoparticles after linear polarized femtosecond laser irradiation for 3 minutes (a) ~ (c) and 20 minutes (d) ~ (f) and a subsequent aging treatment for 5 days in ethanol (a), (d), methanol (b), (e), and propanol (c), (f), respectively.

We speculated that redox state associated with the hydrogen gas generation is also responsible for determining the shape of nanoparticles. To evaluate this assumption, the generated hydrogen gas was detected during laser irradiation. Fig. 18 indicates the hydrogen gas generation rate during femtosecond laser irradiation as a function of the standard enthalpy change of formation,  $\Delta_f H^{\circ}_{\text{liquid}}$ , of various alcohol solutions. Symbols of  $\bullet$ ,

▲, ■, and ▼ are experimental data of methanol, ethanol, butanol, and pentanol, respectively. Dotted line indicates a linear fit through the data points. From these results, the hydrogen gas generation rate was evidently proportional to the  $\Delta_f H^\circ_{\text{liquid}}$  of solvent molecules. In particular, methanol has the most profound inhibitory effect of oxidation. Additionally, an amorphous-like carbon was also produced by the dissociation of solvent molecules. The amount of this photo-dissociation of the solvent is increased with increasing the laser irradiation time and decreasing the length of carbon chain. Such an amorphous carbon could adhere to the surface of the growing Cu particles, and then act as a passivation layer which prevents not only the aggregation and growth but also the oxidation of pre-grown Cu nanoparticles.

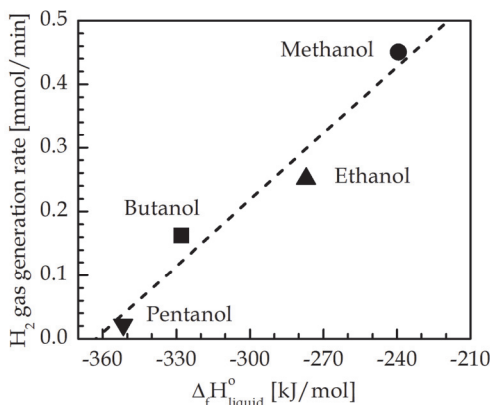


Fig. 18. Hydrogen gas generation rate during femtosecond laser irradiation as a function of the standard enthalpy change of formation,  $\Delta_f H^\circ_{\text{liquid}}$ , of various alcohol solutions. Symbols of ●, ▲, ■, and ▼ are experimental data of methanol, ethanol, butanol, and pentanol, respectively. Dotted line indicates a linear fit through the data points.

#### 2.4 Growth mechanism of Cu nanowires

The following explanation of the Cu nanowires' growth is proposed: when an intense femtosecond laser pulse is impinging onto the surface of a metal Cu, multiphoton ionization rapidly occurs without significant ablation. The SPP waves, with a large electric field parallel to the surface, are resonantly excited by light and propagate along the surface. The SPP waves could absorb the light wave via inverse Bremsstrahlung heating (Kupersztynch et al., 2004) and couple with the incident light wave only if it propagates in the plane of light polarization. This light-plasma coupling occurs at the flake surface over a narrow region with a depth of the order of the skin depth ( $d_p \ll \lambda$ ). Previous investigations suggested that either preimposed or self-generated deformations on the solid surface strongly affect laser energy absorption (Feurer et al., 1997). Evidence for small-deformations comes from the wide spreading of the reflected radiation observed in experiments (Zepf et al., 1998). The difference in the light-plasma coupling between linearly and circularly polarized laser pulses should be responsible for different morphology of nanoparticles. Numerical simulations suggested that electron oscillations may grow for a step density profile much faster than the typical time scale of ion motion, leading to an oscillatory "rippling" of the critical surface ( $n_e = n_c$ ) (Macchi et al., 2001).

Such rippling is generated as a result of interference between the light field and the SPP wave launched by initial random surface inhomogeneities. Positive feedback leads to exponential growth of the periodic surface structures oriented perpendicular to the light polarization, which become frozen within the material. The nanowires were also generated by the fragmentation of the initial flakes via interference between the light field and the electric field of the surface plasmon-polariton wave. Indeed, the nanowire formation could not be observed using a circularly polarized beam just after the laser irradiation (Fig. 14, 15). We propose the two successive steps of the Cu nanowire growth mechanism: (1) photofragmentation via interference between the incident light field and the electric field of the SPP wave and (2) nanoparticle growth in a certain direction. Small species of copper such as nanoclusters (and/or atoms) are fragmented from the initial Cu micro-flakes. This process corresponding to the nucleation is affected by the interaction between the electric field of the light wave and the electric field of the excited surface plasmon-polariton wave on the nanoscale. In fact, it is well-known that laser-ablation process of metal target under a liquid environment disperses many types of ablated material, which is called the plume, including small clusters, nanoparticles, free atoms, and ions. Such nanoclusters act as a nucleation site or a source for nanoparticle growth and aggregate into nanoparticles with a larger size compared to the nanoclusters. Self-aggregation of the nanoparticles suspended in the solvent should be prevented by hindering direct contact of the nanoparticles due to the interaction of solvent environment molecules and the surface of nanoparticles. Assuming femtosecond-laser irradiation into a continuous agitation of the suspension, the fragmented Cu nanoparticle with a radius of about 20 nm (Fig. 15) can move at least 86 nm within an interpulse time ( $\tau_{int}$ ) of 1 ms, which was estimated by the Brownian motion of suspended nanoparticles described by the Stokes-Einstein equation:

$$\langle \bar{x}^2 \rangle = \frac{\kappa_B T \tau_{int}}{3\pi\eta d} \quad (2)$$

where  $\kappa_B$ ,  $T$ ,  $\eta$ ,  $d$  are the Boltzmann constant, the temperature, the viscosity of solvent (methanol), and the diameter of the fragmented Cu nanoparticle, respectively. From this estimation, the Cu nanoparticles generated from the initial particles were produced by the single femtosecond laser pulse. Such nucleation site starts growing after the nanoclusters saturate in the solution. Increasing the irradiation time, with more and more nanoclusters being provided at the cost of the micro-flake, the short nanorods on the micro-flake surface keep growing to nanowires. After the micro-flakes are exhausted, no resource can seed the nanoclusters, and then the growth of the nanowires is stopped after consumption of the nanoclusters. At this stage, the laser energy will be absorbed by the nanowires themselves and the nanowires start to fragment into small nanorods and nanospheres due to the drive of the energy of minimization to a more stable morphology (Xiang et al., 2006). After a long irradiation time, nanospheres would become the main product in the methanol solution (Fig. 5 (e), (f)). A similar mechanism of growth was also observed for Se nanowires by using a sonication method (Gates et al., 2002). Although a part of the aggregates are oxidized to  $\text{Cu}_2\text{O}$ , most are kept the metallic state due to reducing environment provided by hydrogen gas generation and covering with the amorphous carbon layer which were photo-dissociated from the surrounding solvent molecules. By the competition between the oxidation to  $\text{Cu}_2\text{O}$  and the aggregation of metallic Cu nanoclusters, Cu nanoparticles grow one-dimensionally into nanowires which have core-shell structure. In fact, it is well known that in the case of  $\text{Cu}_2\text{O}$  crystals, as shown in Fig.19, the  $\text{O}^{2-}$  ions in the (001) facet are more

apt to hydrolyze, compared with those in the (111) facet, and the stacking along (001) directions therefore becomes energetically favorable (Chen et al., 2003).

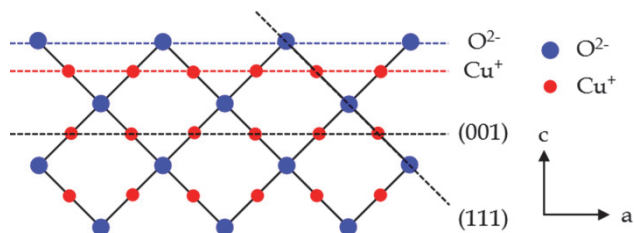


Fig. 19. Projection of the structure of Cu<sub>2</sub>O crystal along the [010] direction.

### 3. Photo-initiated growth of ZnO nanowire

Zinc oxide (ZnO) nanostructures have attracted immense attention as they offer a wide bandgap and a large exciton binding energy of 3.37 eV and 60 meV, respectively, at room temperature (Ohta & Hosono, 2004) and ultraviolet emission (Huang et al., 2001a; Kong et al., 2001; Lin et al., 2007). Various nanostructures such as nanowires (Huang et al., 2001b; Zhang et al., 2005), nanotubes (Zhang et al., 2002a), nanobelts (X. Y. Zhang et al., 2004), nanohelices, nanosprings and nanorings (Kong & Wang, 2003), nanonails (Kar et al., 2006) and nanodisks (Lin et al., 2007) have been successfully synthesized for various applications such as nanolaser (Huang et al., 2001a), gas sensor (Sberveglieri et al., 2007), biosensor (F. Zhang et al., 2004), field-effect transistor (Arnold et al., 2003), solar cell (Hosono et al., 2005) and field emission (Lee, et al., 2002). A number of physical and chemical synthesis processes have been studied for the growth of ZnO nanostructures. Some of the physical methods include the thermal evaporation and vapor transport approaches (Huang et al., 2001a; Pan et al., 2001), metal organic vapor-phase epitaxial growth (Park et al., 2002), molecular beam epitaxy (MBE) (Heo et al., 2002) and pulsed laser deposition (PLD) (Zhang et al., 2005), which are generally based on catalysed vapor-liquid-solid growth mechanism (Wagner & Ellis, 1964). In addition, the simple and low-cost chemical aqueous solution processing with hydrothermal treatments have also been thoroughly studied (Le et al., 2005; Yang et al., 2006; Zhang et al., 2002a; Zhang et al., 2002b; H. Zhang et al., 2004; X. Y. Zhang et al., 2004). However, all these processes require either high temperature, low pressure, complex procedures, extended growth period or the use of catalysts that could be embedded on the nanostructure tip, which are unfavourable conditions. In this section, a catalyst-free and surfactant-free synthesis process without the above-mentioned adverse conditions, comprising femtosecond laser irradiation to initiate heterogeneous nucleation in aqueous solutions at room temperature and pressure, followed by hydrothermal treatments at low temperatures for crystal growth, is demonstrated. This work exploits pulsed laser to induce nucleation for ZnO nanostructure growth, compared to previously reported laser processing as ablation tools (Zhang et al., 2005).

#### 3.1 ZnO nanorods and nanotubes formation

0.016 M zinc acetate dihydrate (Zn(CH<sub>3</sub>COO)<sub>2</sub>·2H<sub>2</sub>O) solution was first prepared at room temperature. 0.095 M ammonium hydroxide (NH<sub>4</sub>OH) was then added until pH 8 to create

an alkaline environment. By using the above mentioned experimental setup (Fig. 1), the mixture solution was then immediately irradiated with femtosecond pulses with a regeneratively amplified mode-locked Er-doped fiber laser (Cyber Laser Inc.), operating at 780 nm wavelength at 1 kHz repetition rate. The laser beam was focused via a microscope objective (Nikon; LU Plan Fluor, 20× 0.40 N.A.) with typical pulse width and pulse energy of 215 fs and 200  $\mu\text{J}/\text{pulse}$ , respectively, into a rectangular quartz vessel of  $1 \times 1 \times 3.5 \text{ cm}^3$  filled with the pH 8 solution. The vessel was placed on a magnetic stirrer and the solution continuously stirred to maintain homogeneity. Irradiation was performed for 60 minutes and the solution subsequently transferred into furnaces for heat treatments at 60 °C and 80 °C for 120 minutes before being cooled down to room temperature. The grown ZnO nanorods were analyzed by field emission scanning electron microscopy (JEOL, JSM-6705F) to study their morphologies. Samples were prepared by drop-casting the solutions onto silicon substrates and allowed to evaporate at room temperature. X-ray diffraction (XRD) pattern was collected using Rigaku Rint2500HF to study the crystal structure. Room temperature photoluminescence spectrum was obtained via a Horiba Jobin Yvon FluoroMax-P spectrometer with a Xenon lamp excitation source at 300 nm.

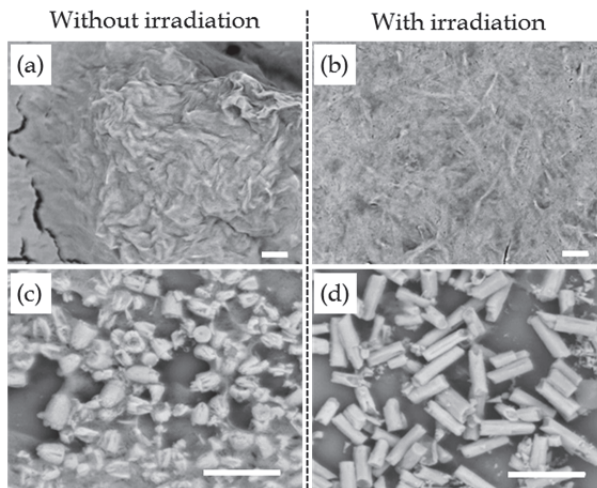


Fig. 20. SEIs of particles in pH 8 solutions without and with laser irradiation at pulse energy 200  $\mu\text{J}/\text{pulse}$  for 60 minutes, after hydrothermal treatments at 60 °C and at 80 °C (c), (d) for 120 minutes. Scale bars are 1  $\mu\text{m}$ .

Fig. 20 (a), (b) and (c), (d) show the SEIs for the pH 8 solutions without and with the laser irradiation process, after hydrothermal treatments at 60 °C and 80 °C, respectively, for 120 minutes. The results show that nanorods were grown only for the solution that underwent irradiation and subsequent treatment at 80 °C. This suggests that the femtosecond pulse irradiation plays a major role in the overall nanorod growth and also, the level of hydrothermal temperature is essential, affecting the solubility of the dissolved zinc species contributing to the ZnO crystal growth. This process shows significantly that no catalyst is required to initiate growth and no surfactant is necessary for preferential nanorod growth direction. Nanorods were grown after hydrothermal treatments for 120 minutes, compared

to previously reported aqueous-based methods requiring more than 10 hours (Yang et al., 2006; Zhang et al., 2002b; H. Zhang et al., 2004). The precipitate observed in Fig. 20 (c) was filtered from the solution, washed, dried at room temperature and analyzed to study the nanostructures in details.

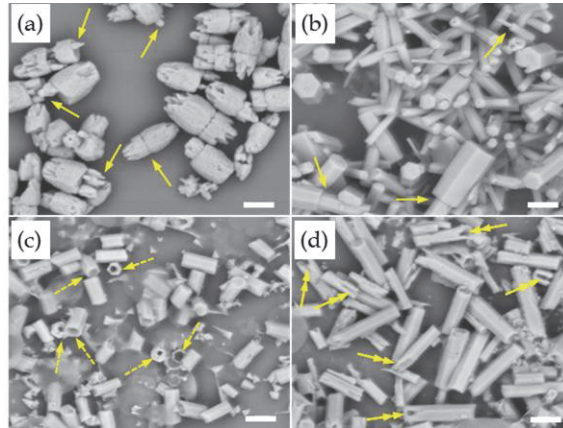


Fig. 21. SEIs for (a) filtered nanoparticles from as-prepared solution after hydrothermal treatment at 80 °C for 120 minutes, without laser irradiation, (b) an aggregation of nanorods and (c), (d) isolated individual nanorods, after irradiation at pulse energy 200  $\mu\text{J}$ /pulse for 60 minutes and hydrothermal treatment at 80 °C for 120 minutes. Scale bars are 400 nm.

The result, as seen in Fig. 21 (a), shows that without laser irradiation, random homogeneous nucleation could spontaneously occur, leading to the growth of poor quality rod-like nanostructures with rough and porous surfaces. In comparison, Fig. 21 (b) ~ (d) show that large hexagonal nanorods with flat tops and smooth surfaces, with diameters up to 200 nm and lengths up to 1  $\mu\text{m}$  were grown with laser irradiation, which appears to affect the morphology and quality of the nanostructures. We postulate that the femtosecond pulse irradiation initiates heterogeneous nucleation sites, due to induced solution inhomogeneity, acting as seeds for crystal growth into well-structured nanorods with smooth planes during the subsequent hydrothermal treatments where dehydration of the zinc complexation species to ZnO occurs. In addition, the zinc complexation species ions could interact with the laser light polarization and electric field, leading to specific growth directions. The level of hydrothermal temperature is critical and found to be 80 °C for optimal growth. Lower temperature is insufficient to dehydrate the zinc complexation species and no crystal growth is observed (Fig. 20 (b)) while higher temperature could result in the dissolution of the nanorods, leading to poor crystal quality. In Fig. 21 (a), (b), as indicated by arrows, there were instances where smaller secondary nanostructures grew on top of larger primary structures. This is due to additional ZnO nuclei attaching to the top flat surfaces of the primary nanostructures, thereby enabling secondary growth. Eventually, nanorods with lengths up to 1  $\mu\text{m}$  were produced. Other features could also be observed, where the dashed arrows in Fig. 21 (c) indicate nanotubes while the double-headed arrows in Fig. 21 (d) indicate lateral splits along the nanorod side planes. The top plane of the nanorod is the (0001) polar and metastable crystal plane, which could attract hydroxide ions ( $\text{OH}^-$ ). These

$\text{OH}^-$  ions attack the plane and erode the central parts of the nanorods, creating nanotubes. Prolonged exposure to  $\text{OH}^-$  ions could also cause the non-polar and stable crystal side planes to split (Yu et al., 2007).

Fig. 22 (a) shows the XRD pattern for the ZnO nanorods, dispersed on a glass substrate, where the diffraction peaks can be indexed to the ZnO hexagonal structure with  $a = 3.24 \text{ \AA}$  and  $c = 5.19 \text{ \AA}$ . Fig. 22 (b) shows the idealized (Li et al., 1999) (left) and the actual (right) growth habit observed in this work for the ZnO crystal. For ideal growth, the growth rates of different crystal directions are found to be  $V_{\langle 0001 \rangle} > V_{\langle 01\bar{1}0 \rangle} > V_{\langle 01\bar{1}1 \rangle} > V_{\langle 000\bar{1} \rangle}$ , with a tip at one end. The appearance of flat tops on the nanorods grown (Fig. 21 (b)) suggests that the growth rate of the (0001) crystal facet is relatively slower than ideal. At pH 8, when  $\text{NH}_4\text{OH}$  is added to  $\text{Zn}(\text{CH}_3\text{COO})_2 \cdot 2\text{H}_2\text{O}$ , the  $\text{Zn}(\text{NH}_3)_4^{2+}$  ammine complexation species is mainly formed as it prevented hydroxide formation and precipitation (Fratesi & Roventi, 1992). As the final growth unit for ZnO is  $\text{Zn}(\text{OH})_4^{2-}$  (Li et al., 1999),  $\text{Zn}(\text{NH}_3)_4^{2+}$  has to first decompose to  $\text{Zn}(\text{OH})_4^{2-}$  before dehydration to ZnO at elevated temperature. This intermediate decomposition requires heat, thereby suppressing crystal growth. Hence,  $\text{Zn}(\text{NH}_3)_4^{2+}$  acts as a buffer, slowly releasing the  $\text{Zn}(\text{OH})_4^{2-}$  growth unit prior to ZnO crystal growth. Furthermore, at pH 8, the nanorods tend to disperse and can be individually identified (Fig. 21) due to the weak basicity of  $\text{Zn}(\text{NH}_3)_4^{2+}$  and the presence of  $\text{NH}_3$  which prevent aggregation.

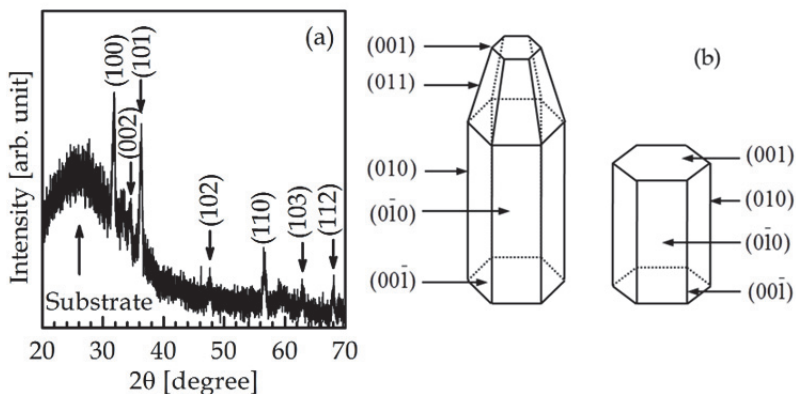


Fig. 22. (a) XRD pattern and (b) growth habits of ZnO nanorods.

Fig. 23 shows the room temperature photoluminescence of ZnO nanorods, with a broad UV emission peaking at  $\sim 380 \text{ nm}$  that is ascribed to the ZnO band-edge emission due to the recombination of free excitons (Huang et al., 2001b). The broad green emission observed beyond  $\sim 530 \text{ nm}$  is generally accepted as deep-level or trap-state emission due to radiative recombination of a photogenerated hole with an electron occupying the oxygen vacancy (Vanheusden et al., 1996). The broad spectrum and low intensity observed could be due to poor ZnO crystal quality caused by  $\text{OH}^-$  attack, the low intensity Xenon lamp source used or the random alignment of the nanorods, resulting in poor luminescence. In addition, coatings of organic solutions could be present on the nanorod surfaces, affecting the results and possibly giving rise to the peaks seen at  $450 \sim 470 \text{ nm}$ .

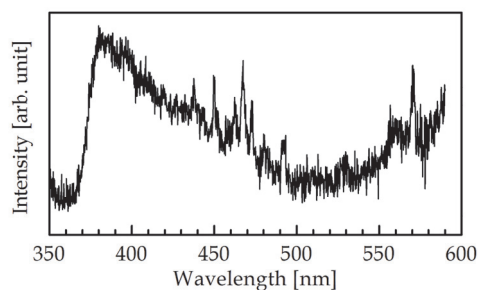


Fig. 23. Photoluminescence spectrum of ZnO nanorods measured at room temperature.

### 3.2 Role of femtosecond laser irradiation

In order to reveal the role and feasibility of femtosecond laser irradiation in the overall ZnO nanostructure growth process, we performed the following experiments by changing the femtosecond laser irradiation condition (pulse width, pulse energy, and pulse repetition rate). Aqueous mixture solutions of 0.016 M  $\text{Zn}(\text{CH}_3\text{COO})_2 \cdot 2\text{H}_2\text{O}$  (zinc acetate dihydrate) and 0.20 M  $\text{NH}_4\text{OH}$  (ammonium hydroxide) at a pH value of 11 alkaline environment were initially prepared and then immediately subjected to laser irradiation. The laser radiation in Gaussian mode produced by a regenerative amplified mode-locked Ti:sapphire laser (Coherent Inc., 100 fs pulse duration, 1 kHz or 250 kHz repetition rate) operating at a wavelength of 800 nm was focused by a microscope objective (Nikon; LU Plan Fluor, 20 $\times$  0.40 N.A.) to a spot size of  $\sim 2.4 \mu\text{m}$  diameter inside a rectangular quartz vessel of  $1 \times 1 \times 3.5 \text{ cm}^3$  filled with the pH 11 precursor solution. The quartz vessel was placed on a magnetic stirrer and continuously stirred to maintain homogeneity. Table 2 shows the laser irradiation conditions for the femtosecond pulse irradiation performed at the repetition rates of 1 kHz and 250 kHz. Immediately after the laser irradiation, the solutions were placed in ovens for hydrothermal treatments at 80  $^\circ\text{C}$  and 100  $^\circ\text{C}$  for 120 minutes for the ZnO crystal growth, before being cooled down to room temperature.

Sample	Pulse repetition rate [kHz]	Pulse energy $E_{\text{pulse}} [\mu\text{J}]$	Irradiation duration $t$ [min]	Total energy $E_T$ [kJ]
1a	1	50	120	0.36
1b	1	200	30	0.36
1c	1	400	15	0.36
2a	1	100	120	0.72
2b	1	200	60	0.72
2c	1	400	30	0.72
3a	1	200	120	1.44
3b	1	400	60	1.44
4a	1	300	120	2.16
5a	250	0.8	120	1.44
5b	250	1.6	60	1.44
5c	250	2.4	40	1.44

Table 2. Femtosecond laser irradiation conditions at 1 kHz or 250 kHz repetition rate.

Fig. 24 shows the SEIs of the nanostructures grown without and with laser irradiation (pulse energy,  $E_{pulse}$  200  $\mu\text{J}/\text{pulse}$ , irradiation duration 120 minutes, total irradiation energy  $E_T$  1.44 kJ and repetition rate 1 kHz), followed by hydrothermal treatments at 80  $^{\circ}\text{C}$  for 120 minutes. Without the laser irradiation, large flower-like structures comprising aggregated cone-shaped nanostructures can be observed, where their surfaces appear to be rough and porous. When the irradiation process was performed as one part of the synthesis process, ZnO nanowire growth can be observed. This shows that the ultrashort pulse laser irradiation plays a significant role in initiating heterogeneous nucleation sites for nanowire growth, compared to the random homogeneous nucleation process associated with hydrothermal growth without the laser irradiation. In a separate investigation, longer pulses of 860 fs were used for the laser irradiation process, instead of the 100 fs pulses used in this work in order to study the significance of ultrashort pulses for nanowire growth. For the study involving 860 fs (results not shown), short cone-tip nanostructures similar to Fig. 24 (b) were grown instead of thin elongated nanowires that were observed in this work.

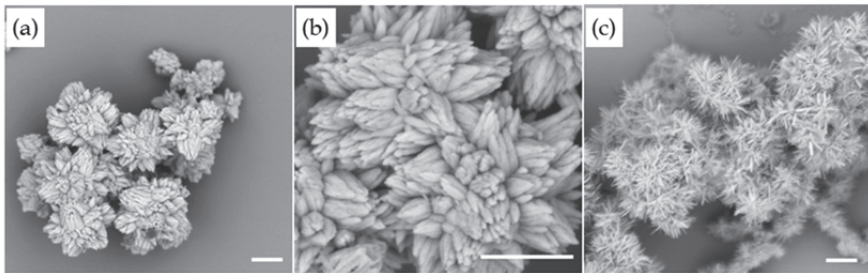


Fig. 24. SEIs of nanoparticles in pH 11 solutions after hydrothermal treatments at 80  $^{\circ}\text{C}$  for 120 minutes, (a), (b) without and (c) with initial laser irradiation at  $E_{pulse} = 200 \mu\text{J}/\text{pulse}$  for 120 minutes ( $E_T = 1.44 \text{ kJ}$ ) at 1 kHz repetition rate. The laser spot diameter was  $\sim 2.4 \mu\text{m}$ . Scale bars are 1  $\mu\text{m}$ .

The generally accepted reaction routes in aqueous ammonia solution at a high alkaline level are defined as below :



Upon mixing the starting reagents, the soluble complexation species of  $\text{Zn}(\text{OH})_4^{2-}$  were formed in a high alkaline environment (pH 11 in this work). Nucleation sites were then produced in the solutions via either random homogeneous nucleation or heterogeneous nucleation by the laser irradiation, which subsequently became aggregated. Acting as the growth units,  $\text{Zn}(\text{OH})_4^{2-}$  were then dehydrated to ZnO at elevated temperatures to construct the ZnO nanostructures. Fig. 25 summarizes the illustrated scheme for ZnO crystal growth. We postulate that the ultrashort pulse laser irradiation initiates heterogeneous nucleation seeds for subsequent crystal growth during the hydrothermal treatments. During the laser



fused together, possibly via oriented attachment (Pacholski et al., 2002), into larger nanowires. In Fig. 27, the results show that irradiation with  $E_{pulse} = 100 \mu\text{J}$  produced ZnO nanowires where individual nanowires could not be well-defined, as in the case for  $E_{pulse} = 50 \mu\text{J}$  in Fig. 26 (b). Increasing  $E_{pulse}$ , while maintaining  $E_T = 0.72 \text{ kJ}$  by reducing the irradiation duration, produced well-defined and individually separated nanowires. This again shows the critical role of  $E_{pulse}$  in initiating conducive nucleation sites for crystal growth. In Fig. 28, individual nanowires can be clearly observed for all samples as the threshold  $E_{pulse} = 200 \mu\text{J}$  required to initiate heterogeneous nucleation for favourable growth into ZnO nanowires was exceeded.

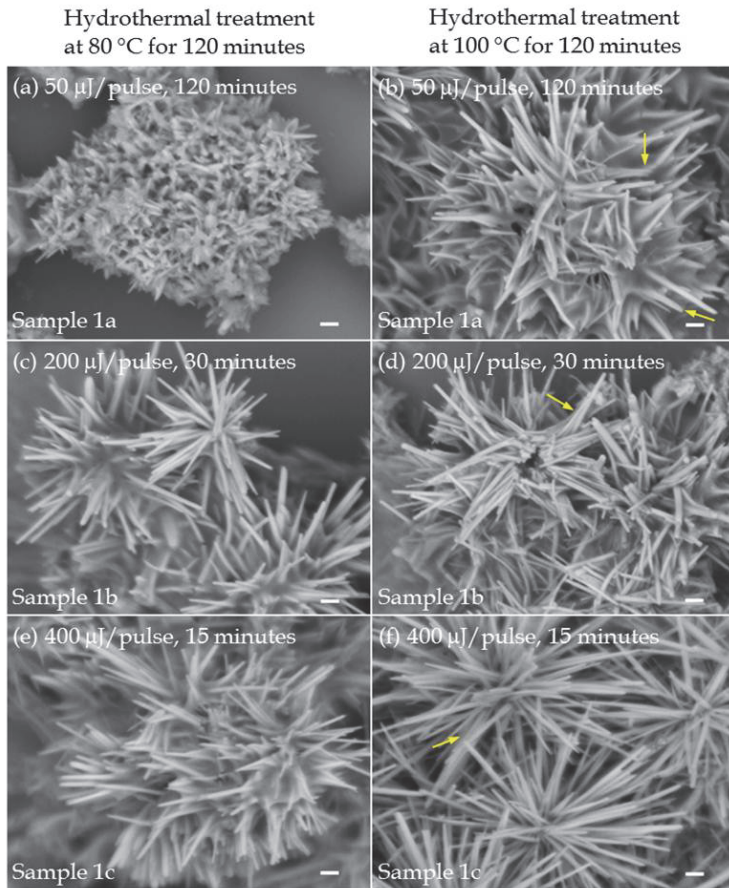


Fig. 26. SEIs for ZnO nanowires grown from ultrashort pulse irradiation at 1 kHz at (a), (b)  $E_{pulse} = 50 \mu\text{J}/\text{pulse}$  for 120 minutes, (c), (d)  $200 \mu\text{J}/\text{pulse}$  for 30 minutes, and (e), (f)  $400 \mu\text{J}/\text{pulse}$  for 15 minutes (similar  $E_T = 0.36 \text{ kJ}$ ), followed by hydrothermal treatments at  $80 \text{ }^\circ\text{C}$  for 120 minutes (left images) and at  $100 \text{ }^\circ\text{C}$  for 120 minutes (right images). Scale bars are 200 nm.

From the results in Fig. 26 ~ 28, it can be inferred that the pulse energy level,  $E_{pulse}$  is essential in initiating heterogeneous nucleation while the irradiation duration (and indirectly the total irradiation energy,  $E_T$ ) determines the density of nanowire growth due to the abundant nucleation sites initiated. In addition, these two factors together with the hydrothermal treatment temperature affect the morphology of the nanowires as the rates of dehydration and consumption of the zinc growth units for numerous crystal growth processes would be affected. Generally, based on the amount of zinc growth units available in the quartz vessel and depending on the laser processing parameters and hydrothermal treatments conditions, ZnO nanowires with diameter 10 ~ 40 nm and length up to 1.5  $\mu\text{m}$  can be grown.

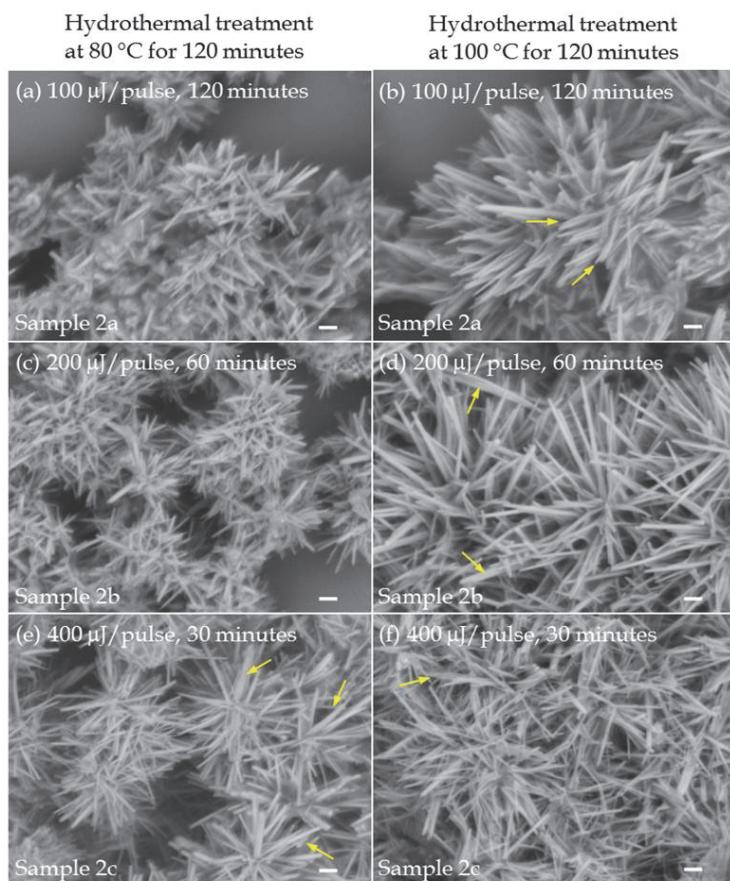


Fig. 27. SEIs for ZnO nanowires grown from ultrashort pulse irradiation at 1 kHz at (a), (b)  $E_{pulse} = 100 \mu\text{J}/\text{pulse}$  for 120 minutes, (c), (d)  $200 \mu\text{J}/\text{pulse}$  for 60 minutes and (e), (f)  $400 \mu\text{J}/\text{pulse}$  for 30 minutes (similar  $E_T = 0.72 \text{ kJ}$ ), followed by hydrothermal treatments at  $80 \text{ }^\circ\text{C}$  for 120 minutes (left images) and at  $100 \text{ }^\circ\text{C}$  for 120 minutes (right images). Scale bars are 200 nm.

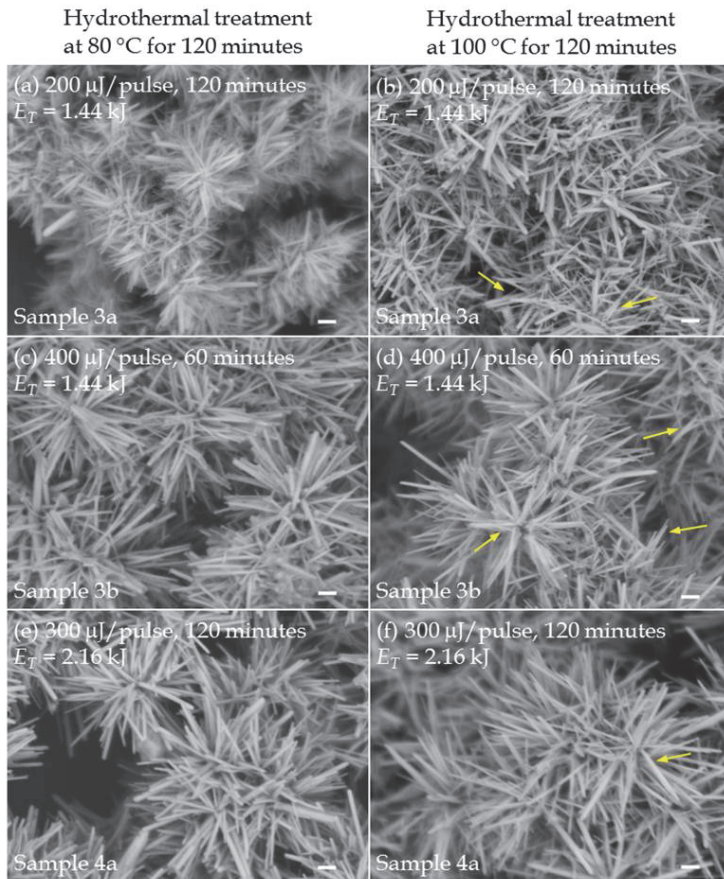


Fig. 28. SEIs for ZnO nanowires grown from ultrashort pulse irradiation at 1 kHz at (a), (b)  $E_{pulse} = 200 \mu\text{J}/\text{pulse}$  for 120 minutes and (c), (d)  $400 \mu\text{J}/\text{pulse}$  for 60 minutes (similar  $E_T = 1.44 \text{ kJ}$ ) and (e), (f)  $E_{pulse} = 300 \mu\text{J}/\text{pulse}$  for 120 minutes ( $E_T = 2.16 \text{ kJ}$ ), followed by hydrothermal treatments at 80 °C for 120 minutes (left images) and at 100 °C for 120 minutes (right images). Scale bars are 200 nm.

Fig. 29 summarises the results on ZnO nanowire synthesis after the laser irradiation at  $E_T = 1.44 \text{ kJ}$  at 250 kHz repetition rate for different  $E_{pulse}$  values and irradiation durations, followed by hydrothermal treatments at 80 °C and 100 °C for 120 minutes. For irradiation at  $E_{pulse} = 0.8 \mu\text{J}/\text{pulse}$  for 120 minutes, the ZnO nanostructures appear to have grown from random homogeneous nucleation similar to that of Fig. 24 (a), (b), suggesting that the low pulse energy had not been effective in initiating heterogeneous nucleation. For the laser irradiation at  $E_{pulse} = 1.6 \mu\text{J}/\text{pulse}$  for 60 minutes, the general shape of nanowires can be observed while the results for  $E_{pulse} = 2.4 \mu\text{J}/\text{pulse}$  for 40 minutes clearly show aggregations of ZnO nanowires. The difference in morphology and density of nanowires is most likely caused by the abundant nucleation seeds initiated by the higher pulse energy. At  $E_{pulse} = 1.6 \mu\text{J}/\text{pulse}$ , the soluble  $\text{Zn}(\text{OH})_4^{2-}$  species were consumed by less nucleation seeds, leading

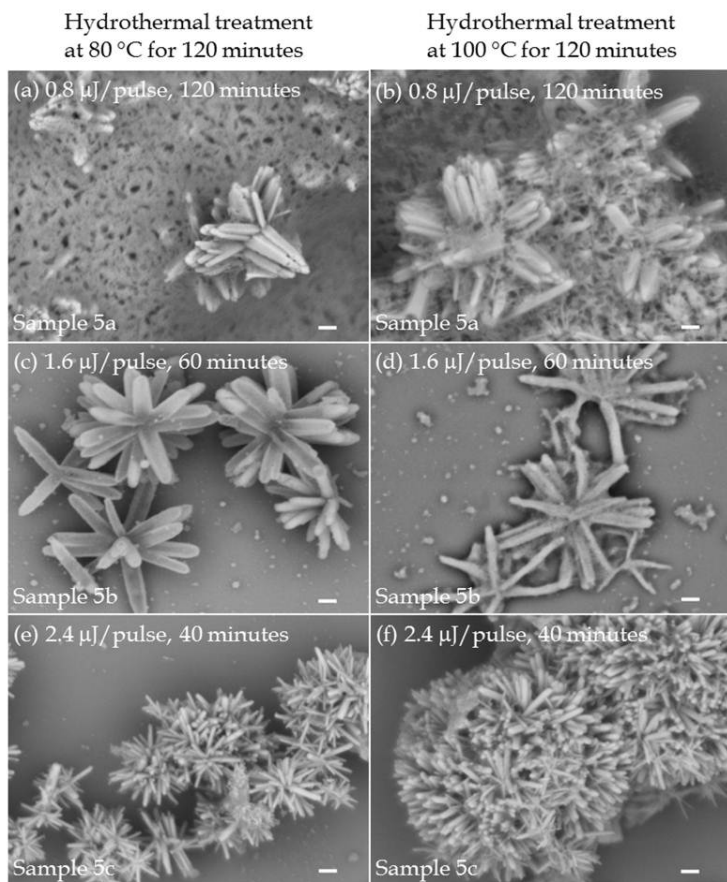


Fig. 29. SEIs for ZnO nanowires grown from ultrashort pulse irradiation at 250 kHz at (a), (b)  $E_{pulse} = 0.8 \mu\text{J}/\text{pulse}$  for 120 minutes, (c), (d)  $1.6 \mu\text{J}/\text{pulse}$  for 60 minutes and (e), (f)  $2.4 \mu\text{J}/\text{pulse}$  for 40 minutes (similar  $E_T = 1.44 \text{ kJ}$ ), followed by hydrothermal treatments at 80 °C for 120 minutes (left images) and at 100 °C for 120 minutes (right images). Scale bars are 200 nm.

to large nanowire dimensions. However, at  $E_{pulse} = 2.4 \mu\text{J}/\text{pulse}$ , the  $\text{Zn}(\text{OH})_4^{2-}$  growth units were consumed and distributed over a larger amount of nucleation sites for growth and thus reducing the dimensions of the nanowires grown. In addition, at  $E_{pulse} = 1.6 \mu\text{J}/\text{pulse}$ , the pulse energy might be too low to initiate stable heterogeneous nucleation so that two or more nucleation seeds might have merged to produce a larger seed and consequently the larger dimensions for the nanowires. This is highly likely due to the high frequency of pulses which initiate high amount of nucleation seeds in close proximity, thus enabling neighbouring seeds to merge to improve stability. This dependence of nanowire diameter on the size of the nucleation seeds is similar to the correlation between nanowire diameter and gold nanodot size, which acted as catalysts, observed by Fan et. al. (Fan et al., 2006). The high number of nucleation seeds near each other also enables them to produce large

aggregations of nanowires, as seen in Fig. 29 (f), compared to those grown from 1 kHz repetition rate laser irradiation. Finally, homogeneous nucleation might have also played a part in the growth process for Fig. 29 (c), (d), which has been shown to produce larger nanostructures compared to that grown purely from heterogeneous nucleation. These large differences in the results in Fig. 29 suggest that there is a certain threshold level for  $E_{pulse}$  to initiate nucleation sites in the solution. The results also agree with the results obtained via laser irradiation at the repetition rate of 1 kHz, which showed the significant role of  $E_{pulse}$ . In addition, comparing the results of Fig. 26 ~ 29 show that well-defined nanowires could be grown beyond  $E_{pulse} = 2.4 \mu\text{J}/\text{pulse}$  at 250 kHz repetition rate. However, at 1 kHz repetition rate,  $E_{pulse}$  beyond 200  $\mu\text{J}/\text{pulse}$  was required for well-defined ZnO nanowire growth. This difference in  $E_{pulse}$  level could be attributed to the thermal effect induced by irradiation at 250 kHz repetition rate.

Fig. 30 shows the illustrated temperature profiles expected in the sample solutions irradiated by 1 kHz and 250 kHz ultrashort pulses. The thermal diffusion time was estimated to be approximately 3  $\mu\text{s}$  using the thermal diffusion equation (Chartier & Bialkowski 1997), based on a laser spot radius of 1.22  $\mu\text{m}$  estimated by the Airy disc approximation (Vogel et al., 2005) and the heat diffusivity of water =  $1.38 \times 10^{-7} \text{ m}^2 \text{ s}^{-1}$  (Vogel et al., 2005). As seen in Fig. 30, the diffusion time is of the same order as the pulse interval for the 250 kHz pulses and hence thermal effect would be expected to build up within the localised laser spot volume and possibly contribute to the heterogeneous nucleation process. In contrast for the train of 1 kHz pulses, thermal effect was negligible as the heat induced by a single pulse would have completely dissipated by the time the next pulse arrived 1 ms later.

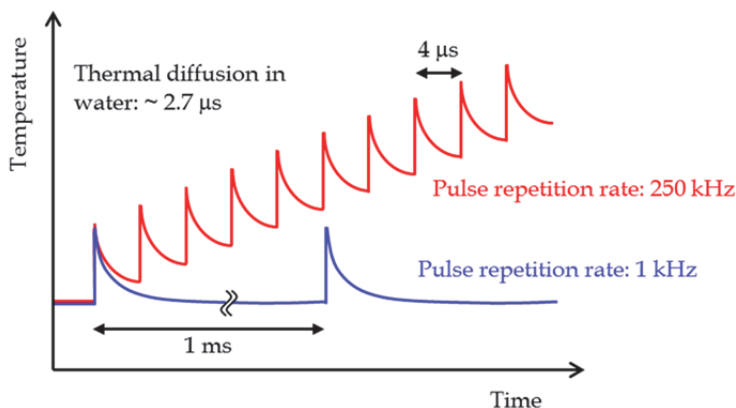


Fig. 30. Temperature profiles induced in the irradiated samples by femtosecond laser pulses at repetition rates of 1 kHz and 250 kHz.

### 3.3 Formation mechanisms of ZnO nanorods

In order to reveal the formation mechanisms of ZnO nanorods with the additional femtosecond laser irradiation process, we performed the following experiments. Aqueous mixture solutions of 0.02 M  $\text{ZnCl}_2$  and 0.032 ~ 0.200 M  $\text{NH}_4\text{OH}$  at pH value ranging from 8.5 to 10.5 alkaline environments were initially prepared. We used femtosecond laser pulses to focus in a liquid cell and efficiently transfer energy into the precursor solution. The initial

solution exhibits a slightly white turbidity decreasing with a pH increase because the formation of zinc ammonia complex, which was subjected to femtosecond pulse irradiation at room temperature. The laser radiation in Gaussian mode produced by a regenerative amplified mode-locked Er-doped fiber laser (Cyber laser Inc., 230 fs pulse duration, 1kHz repetition rate, pulse energy 0.5 mJ/pulse) operating at a wavelength of 780 nm was focused by an objective (Nikon; LU Plan Fluor, 20× 0.40 N.A.) into a rectangular quartz vessel of  $1 \times 1 \times 3.5 \text{ cm}^3$  filled with the precursor solution, which was placed on a magnetic stirrer and continuously stirred to maintain homogeneity. Irradiation was performed for 60 min and the solution subsequently transferred into furnace for heat treatments at 80 °C or 100 °C for 120 minutes before being cooled down to room temperature. Samples were prepared by drop-casting the solutions onto silicon substrates and allowed to evaporate at room temperature. The grown ZnO particles were analyzed by field emission scanning electron microscopy (JEOL JSM-6705F) to study their morphologies. X-ray diffraction (XRD) pattern was collected using Rigaku Rint2500HF to study the crystal structure.

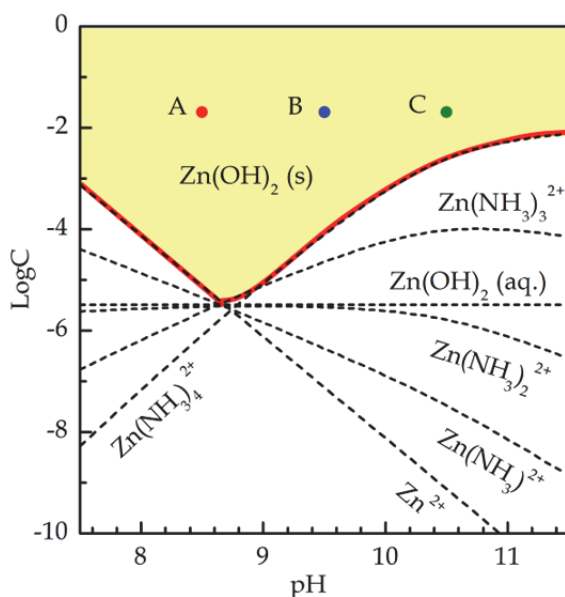
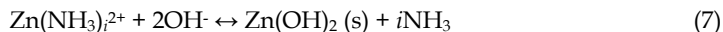


Fig. 31. Phase stability diagram for  $\text{Zn(OH)}_2\text{-NH}_3$  system at 25 °C as a function of pH. The points marked by A, B, and C represent the preparation conditions of precursor solution in this study. The dashed lines indicate the thermodynamic equilibrium between the various Zn(II) soluble species and the solid  $\text{Zn(OH)}_2$ . The red solid line represents the boundary of the solubility of the solid  $\text{Zn(OH)}_2$ .

It is well known that the solid phase stability of  $\text{Zn(OH)}_2$  in the precursor solution has been determined by the pH value and the concentration of Zn(II) soluble species (Yamabi & Imai, 2002). Fig. 31 shows the phase stability diagrams for the  $\text{Zn(OH)}_2\text{-NH}_3$  systems at 25 °C. The dashed lines indicate the thermodynamic equilibrium between the various Zn(II) soluble species, which are calculated by the following equilibrium equations (6) ~ (8).



Values of standard thermodynamic data and stability constant are taken from the literature (Goux et al., 2005; Hubert et al., 2007; Peulon & Lincot, 1998; Yamabi & Imai, 2002). The red solid line represents the boundary of the solubility of the solid  $\text{Zn}(\text{OH})_2$ . This diagram reveals that the solid  $\text{Zn}(\text{OH})_2$  is thermodynamically stable at a pH value ranging from 7 to 12 in the precursor solutions ( $[\text{Zn}^{2+}] = 0.02 \text{ M}$ ). Typical three precursor solutions with different pH values of 8.5, 9.5, and 10.5 were prepared in the present study.

Fig. 32 indicates XRD patterns of precipitates from mixed precursor solutions of  $\text{ZnCl}_2$  and  $\text{NH}_4\text{OH}$  at pH 8.5, 9.5, and 10.5 without (a) and with (b) the femtosecond laser irradiation for 60 minutes and the successive thermal treatment at  $80^\circ\text{C}$  for 120 minutes. The JCPDS standards of  $\text{Zn}_5(\text{OH})_8\text{Cl}_2 \cdot \text{H}_2\text{O}$ ,  $\text{Zn}(\text{OH})_2$ , and  $\text{ZnO}$  are also shown in Fig. 32.

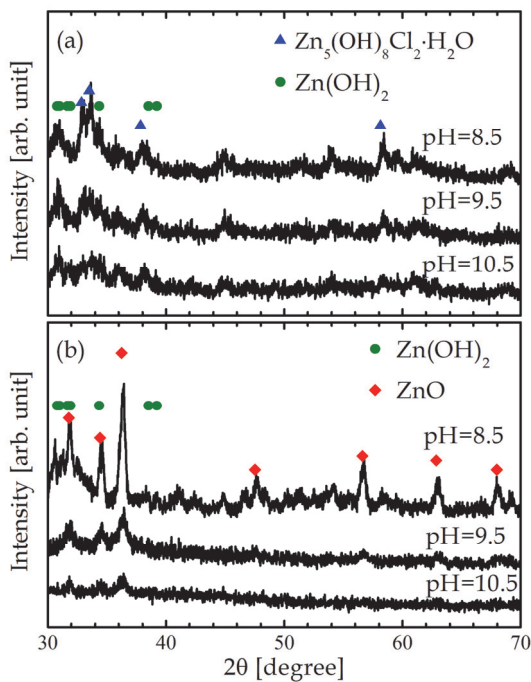


Fig. 32. XRD patterns of precipitates from mixed precursor solutions at pH 8.5, 9.5, and 10.5 without (a) and with (b) the femtosecond laser irradiation for 60 minutes and the successive thermal treatment at  $80^\circ\text{C}$  for 120 minutes. The JCPDS standards of  $\text{Zn}_5(\text{OH})_8\text{Cl}_2 \cdot \text{H}_2\text{O}$  ( $\blacktriangle$ ),  $\text{Zn}(\text{OH})_2$  ( $\bullet$ ), and  $\text{ZnO}$  ( $\blacktriangle$ ) are also shown.

The corresponding SELs are shown in Fig. 33. No apparent diffraction peaks of  $\text{ZnO}$  were observed in the case of the thermal precipitates from precursor solutions at every pH

condition without the laser irradiation (Fig. 32 (a)). These patterns were assigned to  $\text{Zn}(\text{OH})_2$  and  $\text{Zn}_5(\text{OH})_8\text{Cl}_2\cdot\text{H}_2\text{O}$ , suggesting that the precursor solutions could not become supersaturated at 80 °C with respect to the homogeneous ZnO nucleation. On the other hand, the apparent diffraction peaks attributed to ZnO were observed in the samples which the laser irradiation process was applied before thermal treatment at the same temperature (Fig. 32 (b)). This indicates that the photo-initiated heterogeneous nucleation could be induced by the femtosecond laser irradiation in the precursor solutions at room temperature. The SEIs in Fig. 33 evidently indicate that in contrast to the formation of the scale-like or amorphous precipitate after the thermal treatment at 80 °C for 120 minutes, the ZnO hexagonal nanorods with a diameter of 40 ~ 80nm, which slightly decreases with a pH increase, were obtained by applying the laser irradiation (Fig. 33 (d) ~ (f)). Based on these results, we speculated that the nucleations of ZnO nanorods were initiated by the local supersaturation via femtosecond laser pulse irradiation even at the room temperature.

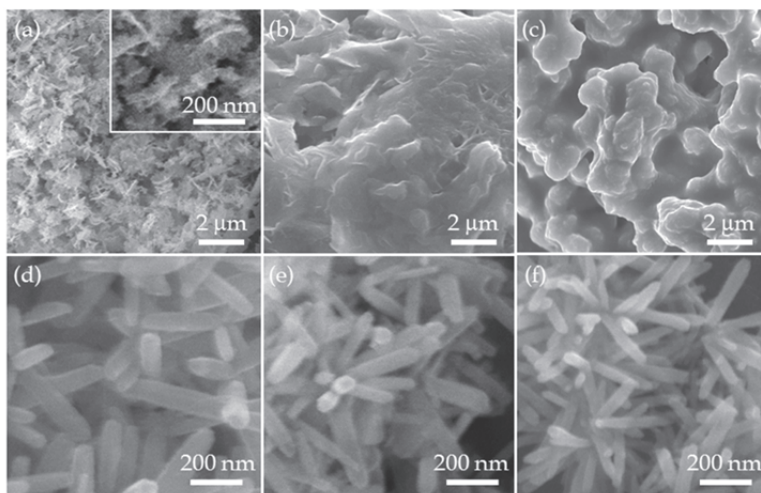


Fig. 33. SEIs of precipitates synthesized from mixed precursor solutions at pH 8.5 (a), (d), 9.5 (b), (e), and 10.5 (c), (f) by the thermal treatment at 80 °C for 120 minutes (upper row) and the additional femtosecond laser irradiation before the thermal treatment (lower row). Inset of (a) shows a high magnification image of scale-like particles.

In order to reveal the nucleation and growth mechanisms of ZnO nanorods with the additional femtosecond laser irradiation process, the heating temperature during the successive thermal treatment was changed to 100 °C. ZnO nanoparticles were precipitated with or without laser irradiation (Fig. 34). The shape of ZnO nanoparticles was changed from nanorods to flower-like with increasing the pH in the thermal treatment (Fig. 34 (a), (c)). In addition, the smaller ZnO nanoparticles resulting from secondary nucleation were observed at the pH of 9.5 (Fig. 34 (b)). It is well known that the flower-like ZnO nanostructures are formed via twinned ZnO nuclei along the (1122) planes in the system with higher supersaturation of  $\text{Zn}(\text{OH})_4^{2-}$  (Zhang & Mu, 2007). On the other hand, much smaller ZnO nanorods with a diameter of 20 ~ 70 nm were formed by the additional laser

irradiation compared to that of the thermal process regardless of pH, about 4 times thinner nanorods were especially formed at the pH of 8.5 (Fig. 34 (a), (d)). The size of ZnO nanorods obtained by the laser irradiation increased with an increase in pH (Fig. 34 (d) ~ (f)). Comparison of the effect of temperature on the size of ZnO nanorods between 80 °C and 100 °C with the laser irradiation indicates that the size decreases with increasing temperature at pH of 8.5 and 9.5, although the size increases with increasing temperature at pH of 10.5 (Fig. 33 (d) ~ (f), Fig. 34 (d) ~ (f)).

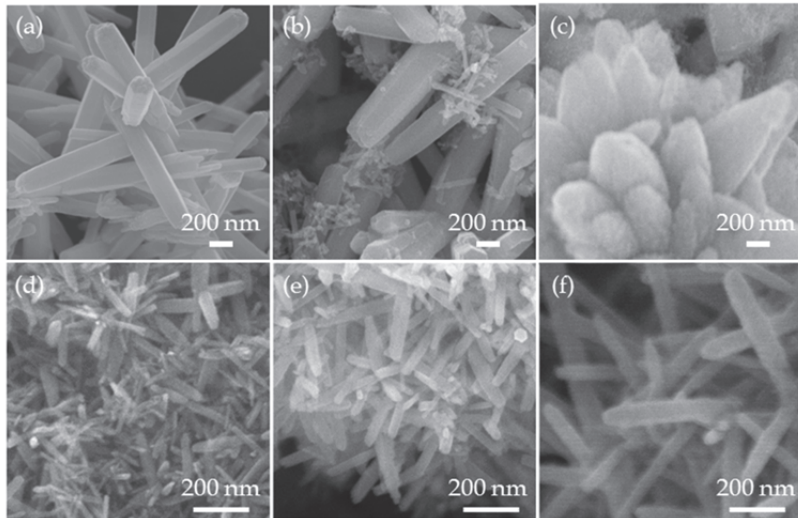
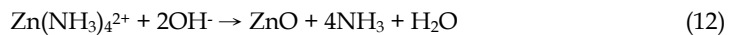


Fig. 34. SEIs of precipitates synthesized from mixed precursor solutions at pH 8.5 (a), (d), 9.5 (b), (e), and 10.5 (c), (f) by the thermal treatment at 100 °C for 120 minutes (upper column) and the additional laser irradiation before the thermal treatment (lower column).

Based on the difference in the shape and size of ZnO nanostructures with and without the femtosecond laser irradiation before the subsequent thermal treatment, we deduce the formation mechanism of ZnO nanorods below. The possible reactions in our experiments can be summarized in the following equations (9) ~ (12).



In the experimental pH region, we could consider the soluble species of the uncomplexed  $\text{Zn}^{2+}$  ions and the zinc-ammonia complex ions of  $\text{Zn}(\text{NH}_3)_4^{2+}$  at a much higher concentration of  $\text{NH}_3$ . In addition, the insoluble compounds of  $\text{Zn}(\text{OH})_2$  can be formed in this system. The calculated concentration of  $\text{Zn}(\text{NH}_3)_4^{2+}$  and solid  $\text{Zn}(\text{OH})_2$  in mixed precursor solutions are shown in Table 3.

pH	Zn(NH <sub>3</sub> ) <sub>4</sub> <sup>2+</sup> [mol/L]	Zn(OH) <sub>2</sub> (s) [mol/L]	ZnO nanorods	
			Diameter [nm]	Length [nm]
8.5	8.1 × 10 <sup>-7</sup>	9.1 × 10 <sup>-3</sup>	38 (7) <sup>a</sup>	164 (5) <sup>a</sup>
9.5	7.8 × 10 <sup>-5</sup>	9.1 × 10 <sup>-3</sup>	44 (5) <sup>a</sup>	233 (3) <sup>a</sup>
10.5	2.4 × 10 <sup>-3</sup>	6.6 × 10 <sup>-3</sup>	68 (24) <sup>a</sup>	515 (46) <sup>a</sup>

<sup>a</sup> The numbers in the parenthesis show the standard deviation for 20 samples.

Table 3. Calculated concentration of soluble and insoluble Zn(II) species and the corresponding the size of obtained ZnO nanorods.

The size of obtained ZnO nanorods produced by the femtosecond laser irradiation at 0.5 mJ for 60 minutes and the successive thermal treatment at 100 °C for 120 minutes are also shown. The amount of such precipitation depends on the pH and the concentration of NH<sub>3</sub> in the solution based on the solubility of Zn(OH)<sub>2</sub> and the dissociation constants of Zn(NH<sub>3</sub>)<sub>4</sub><sup>2+</sup>. At the pH of 8.5 and 9.5, the reaction of Eq. (9) is dominant and the equilibrium moves to right, namely the nuclei of ZnO are predominantly formed from Zn(OH)<sub>2</sub> by the laser irradiation. In contrast, a large amount of the soluble complexes ions of Zn(NH<sub>3</sub>)<sub>4</sub><sup>2+</sup> in addition to the precipitation could be consumed by the formation of ZnO nuclei during laser irradiation, because the reaction of Eq. (11) is dominant at the pH of 10.5. Indeed, the energy absorption by the focusing of femtosecond laser pulses was almost same of 66 % regardless of the pH, although the scattered light intensities at the pH of 8.5 and 9.5 was about 2.5 times higher than that at the pH of 10.5. During the subsequent thermal treatment after the laser irradiation, ZnO nuclei formed by the different reaction path grow into ZnO nanorods along the c-axis direction (Baruah & Dutta, 2009). In lower pH solution (pH 8.5), the smaller ZnO nanorods are formed by the secondary nucleation and growth during the hydrothermal process (Fig. 34 (d)). On the other hand, the larger nanorods could be obtained because ZnO nuclei formed by the laser irradiation grow dominantly during the thermal treatment. It is noted that the standard Gibbs free energy changes of Eq. (10) and (12) are -3.94 and -47.2 kJ/mol, respectively.

To discuss the dynamics of ZnO nuclei formation during the femtosecond laser irradiation, we measured the evolution of spectral extinction of the precursor solutions during the femtosecond laser irradiation (Fig. 35). The transmitted visible light was detected by a photonic multi-channel analyzer (Hamamatsu Photonics, PMA-11). The components of the extinction in Fig. 35 include the sum of light scattering and absorption by ZnO nuclei formed by the laser irradiation. Assuming that the visible absorption of ZnO is negligible, we could estimate the dynamics of the photo-initiated nucleation process based on the Rayleigh scattering theory. In the Rayleigh scattering regime, the scattered light intensity is inversely proportional to the fourth power of wavelength, indicating the shorter wavelength will scatter more than the longer wavelength. While the scattered light intensity in the lower pH solution was substantially constant (Fig. 35 (a)), in the higher pH solution, the scattered light intensity in the shorter wavelength region increases with an increasing in laser irradiation time (Fig. 35 (c)). The results clearly indicate that ZnO nuclei are produced from the liquid phase, i.e. Eq. (11) and (12), in the higher pH solution. On the other hand, the scattering light intensity does not change dramatically because solid Zn(OH)<sub>2</sub> already exists in the lower pH solution (Eq. (9) and (10)). Finally, ZnO nuclei produced through different reaction pathways grow into ZnO nanorods during the successive thermal treatment even in the higher pH solution.

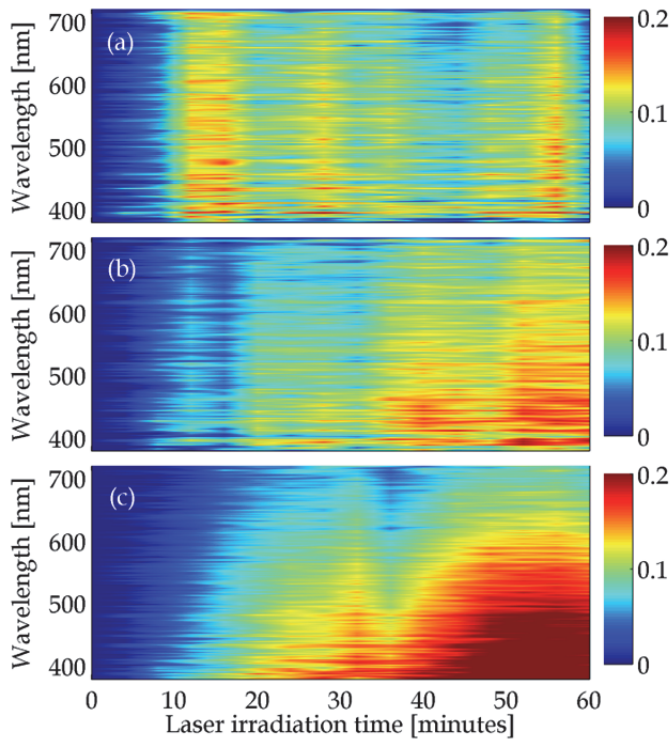


Fig. 35. Evolution of visible extinction spectra of the precursor solution at pH 8.5 (a), 9.5 (b), and 10.5 (c) during femtosecond laser irradiation. The components of the extinction include the sum of light scattering and absorption by ZnO nuclei formed by the laser irradiation.

In order to understand the origin of the observed phenomenon, the following explanation of the heating mechanism is proposed. Since the light intensity in the focus of the beam is of  $10^{16}$  W/cm<sup>2</sup>, the plasma is produced by multiphoton ionization in the focal volume. Once a high free electron density is produced by multiphoton ionization, the material has the properties of plasma and will absorb the laser energy via absorption mechanism of inverse Bremsstrahlung heating. Assuming that the electron temperature is proportional to the pulse energy, the electron temperature can be roughly estimated by a simple formula:  $Q = C_e VT_e$ , where  $Q (= \eta E)$  is the absorbed energy,  $\eta$  is the absorption coefficient,  $E$  is the pulse energy,  $V$  is the volume interaction,  $T_e$  is the electron temperature, and  $C_e$  is the electron heat capacity. Within the free electron gas model, The electron heat capacity can be approximately calculated by  $C_e(T_e) = \gamma T_e$ , where  $\gamma = \pi^2 n_e \kappa_B^2 / 2I_E$  (Lin et al., 2008), where  $n_e$  is the electron number density,  $\kappa_B$  is the Boltzmann constant,  $I_E$  is the ionization potential. The electron temperature is estimated to be 1.3 keV ( $\sim 1.5 \times 10^7$  K) by using the parameters in Table 4, which corresponds to the experimental results (Hatanaka et al., 2004).

Material	Water	-
Density, $\rho$	$1.0 \times 10^3$	[kg/m <sup>3</sup> ]
Molar weight, $M$	$1.8 \times 10^{-2}$	[kg/mol]
Ionization potential, $I_E$	6.5	[eV]
Laser wavelength, $\lambda$	$7.8 \times 10^{-7}$	[m]
Pulse width, $\tau_p$	$2.3 \times 10^{-13}$	[s]
Pulse energy, $E$	$5.0 \times 10^{-4}$	[J]
Absorption coefficient, $\eta$	0.2	-
Electron density, $n_e$	$1.0 \times 10^{20}$	[cm <sup>-3</sup> ]
Numerical aperture, $NA$	0.45	-

Table 4. Parameter for the calculation of the electron temperature.

Based on this calculation, not only the optical breakdown, bubble formation, but also the dissociation of the precursor solution could occur within the focal volume during the femtosecond laser irradiation. Such very high electron temperature decreases with an increase of the lattice temperature, then it reaches to the same temperature as lattice temperature with a time scale of several picoseconds. Assuming that the initial temperature of focal volume reaches  $\Delta T_0 = 3000$  K after the electron-phonon coupling, the thermal diffusivity can be calculated by the following equation. For simplicity, we used the thermal diffusivity coefficient of distill water ( $D_{th} = 1.43 \times 10^{-7}$  m<sup>2</sup>/s).

$$\Delta T(r, t) = \Delta T_0 \left( \frac{w_0}{\sqrt{w_0^2 + 4D_{th}t}} \right)^3 \exp\left( -\frac{r^2}{w_0^2 + 4D_{th}t} \right) \quad (13)$$

where  $\Delta T_0$  is the initial temperature just after the femtosecond single pulse irradiation,  $w_0$  is the laser beam waist,  $t$  is the time after the irradiation, and  $r$  is the distance from the focus. Fig. 36 indicates the calculated temperature distributions just after the femtosecond single

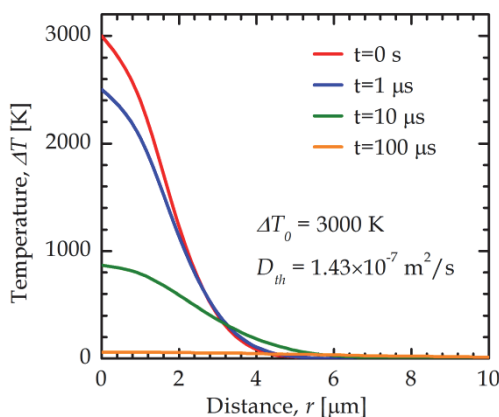


Fig. 36. Calculated temperature distributions just after the femtosecond single pulse irradiation as a function of the distance from focus. In this calculation, the time after the laser irradiation were changed from 0 s to 100  $\mu$ s.

pulse irradiation as a function of the distance from focus. In this calculation, the time after the laser irradiation were changed from 0 s to 100  $\mu$ s. Since the repetition rate of 1 kHz, i.e. the interpulse time of 1 ms in the experiments, these calculations apparently indicate that the heat induced by the first pulse can diffuse away from the focal region before the arrival of the successive pulse. Indeed, no apparent temperature change occurred after the femtosecond laser irradiation for 60 minutes. The ZnO nucleation induced by the femtosecond laser irradiation could occur at the instantaneous high-temperature region surrounding the focal volume in precursor solution at room temperature.

#### 4. Conclusion

In conclusion, we have successfully demonstrated the morphological control of Cu nanoparticles by femtosecond laser irradiation in an alcohol solution. Cu nanowires with a core-shell structure are formed depending on the surrounding solvent and laser irradiation time. The aspect ratio of the Cu nanowires can be controlled by a change of the subsequent aging conditions. The evolution of Cu nanowires from micro-flakes in the intense ultrashort light pulses, it was observed that first nanorods appeared on the micro-flake surface, then nanowires at the cost of initial microparticles and finally these were converted to nanospheres. The mechanism of nanowires' growth was suggested to be a nuclear growth mechanism, that is Cu atoms and/or nanoclusters, produced by the femtosecond laser irradiation, then grew into nanorods and finally nanowires. The uniaxial growth mechanisms of Cu nanowires are interpreted in terms of a competition between the oxidation to Cu<sub>2</sub>O and the aggregation of metallic Cu nanospheres. Another interesting phenomenon is the polarization-dependence of the formation of Cu nanowires, resulting from interference between the incident light field and the SPP wave. Apart from the fundamental importance of the observed phenomenon, as the first evidence of photofragmentation of Cu nanowires fabricated by the "top-down" approach, could be useful for an optical polarization control medium, an electro-conductive nanomaterial, and a probe for SPM.

Furthermore, ZnO hexagonal nanorods and nanowires were successfully synthesised from heterogenous nucleation initiated by femtosecond laser irradiation in aqueous solutions with subsequent hydrothermal treatments, without catalyst and surfactant. The laser irradiation process improves the morphology and quality of the nanorod crystal compared to porous rod-like structures when no irradiation was performed. Due to the localized high supersaturation of precursor solution, the size of the obtained hexagonal ZnO nanorods with femtosecond laser irradiation and the subsequent thermal treatment is about 4 times thinner than that obtained by the thermal treatment. The nanorods have diameters up to 200 nm and lengths up to 1  $\mu$ m, with flat tops due to the slow decomposition of Zn(NH<sub>3</sub>)<sub>4</sub><sup>2+</sup> to Zn(OH)<sub>4</sub><sup>2-</sup> stunting the crystal growth rates, before dehydration to ZnO. Exposure to hydroxide ions causes erosion of the nanorods, resulting in nanotubes and splits on the side planes. Studies involving various pulse energy levels and total irradiation energy at 1 kHz and 250 kHz repetition rates show that there exists the critical threshold pulse energy to induce heterogeneous nucleation favourable for growth into well-defined and individually separated nanowires. Furthermore, studies involving pH variation indicate that ZnO nucleus produced through different reaction pathways according to the pH value of the precursor solution. The size of the obtained hexagonal ZnO nanorods is variable according to the pH of the precursor solution. The ZnO nanorods and nanowires exhibit a broad UV emission peaking at 385 nm, with green emission due to defect states.

#### 4. Acknowledgment

The authors would like to thank Jianrong Qiu from Zhejiang University and Peter G. Kazansky from University of Southampton for helpful discussions. This research is partially supported by Grant-in-Aid for Scientific Research (B), Nippon Sheet Glass Foundation for Materials Science and Engineering (NSG Foundation), and MURATA Science Foundation and Engineering.

#### 5. References

- Alivisatos, A. P. (1996). Semiconductor Clusters, Nanocrystals, and Quantum Dots. *Science*, Vol.271, No.5251, (February 1996), pp. 933-937, ISSN 0036-8075
- Anker, J. N.; Hall, W. P.; Lyandres, O.; Shah, N. C.; Zhao, J.; Van Duyne, R. P. (2008). Biosensing with plasmonic nanosensors. *Nature Materials*, Vol.7, No.6, (June 2008), pp. 442-453, ISSN 1476-1122
- Arnold, M. S.; Avouris, P.; Pan, Z. W. & Wang, Z. L. (2003). Field-Effect Transistors Based on Single Semiconducting Oxide Nanobelts. *Journal of Physical Chemistry B*, Vol.107, No.3, (December 2003), pp. 659-663, ISSN 1520-6106
- Baldacchini, T.; Carey, J. E.; Zhou, M. & Mazur, E. (2006). Superhydrophobic Surfaces Prepared by Microstructuring of Silicon Using a Femtosecond Laser. *Langmuir*, Vol.22, No.11, (April 2006), pp. 4917-4919, ISSN 0743-7463
- Baruah, S. & Dutta, J. (2009). Hydrothermal growth of ZnO nanostructures. *Science and Technology of Advanced Materials*, Vol.10, No.1, (March 2009), pp. 013001-1-18, ISSN 1468-6996
- Braun, A.; Korn, G.; Liu, X.; Du, D.; Squier, J. & Mourou, G. (1995). Self-channeling of high-peak-power femtosecond laser pulses in air. *Optics letters*, Vol.20, No.1, (January 1995), pp. 73-75, ISSN 0146-9592
- Cavanagh, R. R.; King, D. S.; Stephenson, J. C. & Heinz, T. F. (1993). Dynamics of nonthermal reactions: femtosecond surface chemistry. *Journal of Physical Chemistry*, Vol.97, No.4, (January 1993), pp. 786-798, ISSN 0022-3654
- Chang, G.; Shimotsuma, Y.; Sakakura, M.; Yuasa, T.; Homma, H.; Oyama, M.; Miura, K.; Qiu, J.; Kazansky, P. G. & Hirao, K. (2008). Photo-conversion and evolution of one-dimensional Cu nanoparticles under femtosecond laser irradiation. *Applied surface science*, Vol.254, No.16, (June 2008), pp. 4992-4998 ISSN 0169-4332
- Chartier, A. & Bialkowski, S. E. (1997). Photothermal lens spectrometry of homogeneous fluids with incoherent white-light excitation using a cylindrical sample cell. *Optical Engineering*, Vol.36, No.2, (February 1997), pp. 303-311, ISSN 0091-3286
- Chen, Z. -Z.; Shi, E. -W.; Zheng, Y. -Q.; Li, W. -J.; Xiao, B. & Zhuang, J. -Y. (2003). Growth of hex-pod-like Cu<sub>2</sub>O whisker under hydrothermal conditions. *Journal of Crystal Growth*, Vol.249, No.1-2, (February 2003), pp. 294-300, ISSN 0022-0248
- Corkum, P. B.; Rolland, C. & Srinivasan-Rao, T. (1986). Supercontinuum generation in gases. *Physical Review Letters*, Vol.57, No.18, (November 1986), pp. 2268-2271, ISSN 0031-9007
- Desvaux, C.; Amiens, C.; Fejes, P.; Renaud, P.; Respaud, M.; Lecante, P.; Snoeck, E. & Chaudret, B. (2005). Multimillimetre-large superlattices of air-stable iron-cobalt nanoparticles. *Nature Materials*, Vol.4, No.10, (October 2005), pp. 750-753, ISSN 1476-1122
- Elghanian, R.; Storhoff, J. J.; Mucic, R. C.; Letsinger, R. L. & Mirkin, C. A. (1997). Selective Colorimetric Detection of Polynucleotides Based on the Distance-Dependent

- Optical Properties of Gold Nanoparticles. *Science*, Vol.277, No.5329, (August 1997) pp.1078-1081, ISSN 0036-8075
- Fan, H. J.; Fuhrmann, B.; Scholz, R.; Syrowatka, F.; Dadgar, A.; Krost, A. & Zacharias, M. (2006). Well-ordered ZnO nanowire arrays on GaN substrate fabricated via nanosphere lithography. *Journal of Crystal Growth*, Vol.287, No.1, (November 2006), pp. 34-38, ISSN 0022-0248
- Ferry, V. E.; Sweatlock, L. A.; Pacifici, D. & Atwater, H. A. (2008). Plasmonic Nanostructure Design for Efficient Light Coupling into Solar Cells. *Nano Letters*, Vol.8, No.12, (December 2008), pp. 4391-4397, ISSN 1530-6984
- Feurer, T.; Theobald, W.; Sauerbrey, R.; Uschmann, I.; Altenbernd, D.; Teubner, U.; Gibbon, P.; Förster, E.; Malka, G.; Miquel, J. L. (1997). Onset of diffuse reflectivity and fast electron flux inhibition in 528-nm-laser-solid interactions at ultrahigh intensity. *Physical Review E*, Vol.56, No.4, (October 1997), pp. 4608-4614, ISSN 1063-651X
- Fratesi, R. & Roventi, G. (1992). Electrodeposition of zinc-nickel alloy coatings from a chloride bath containing  $\text{NH}_4\text{Cl}$ . *Journal of Applied Electrochemistry*, Vol.22, No.7, (July 1992), pp. 657-662, ISSN 0021-891X
- Gates, B.; Mayers, B.; Grossman, A. & Xia, Y. (2002). A Sonochemical Approach to the Synthesis of Crystalline Selenium Nanowires in Solutions and on Solid Supports. *Advanced Materials*, Vol.14, No.23, (December 2002), pp. 1749-1752, ISSN 0935-9648
- Goux, A.; Pauporté, T.; Chivot, J. & Lincot, D. (2005). Temperature effects on ZnO electrodeposition. *Electrochimica Acta*, Vol.50, No.11, (April 2005), pp. 2239-2248, ISSN 0013-4686
- Hatanaka, K.; Miura, T. & Fukumura, H. (2004). White X-ray pulse emission of alkali halide aqueous solutions irradiated by focused femtosecond laser pulses: a spectroscopic study on electron temperatures as functions of laser intensity, solute concentration, and solute atomic number. *Chemical Physics*, Vol.299, No.2-3, (April 2004), pp. 265-270, ISSN 0301-0104
- Heo, Y. W.; Varadarajan, V.; Kaufman, M.; Kim, K.; Norton, D. P.; Ren, F. & Fleming, P. H. (2002). Site-specific growth of ZnO nanorods using catalysis-driven molecular-beam epitaxy. *Applied Physics Letters*, Vol.81, No.16, (August 2002), pp. 3046-3048, ISSN 0003-6951
- Hosono, E.; Fujihara, S.; Honma, I. & Zhou, H. (2005). The Fabrication of an Upright-Standing Zinc Oxide Nanosheet for Use in Dye-Sensitized Solar Cells. *Advanced Materials*, Vol.17, No.17, (July 2005), pp. 2091-2094, ISSN 0935-9648
- Hu, J. T.; Odom, T. W. & Lieber, C. M. (1999). Chemistry and Physics in One Dimension: Synthesis and Properties of Nanowires and Nanotubes. *Accounts of Chemical Research*, Vol.32, No.5, (February 1999), pp. 435-445, ISSN 0001-4842
- Huang, M. H.; Mao, S.; Feick, H.; Yan, H.; Wu, Y.; Kind, H.; Weber, E.; Russo, R. & Yang, P. (2001a). Room-Temperature Ultraviolet Nanowire Nanolasers. *Science*, Vol.292, No.5523, (June 2001), pp. 1897-1899, ISSN 0036-8075
- Huang, M. H.; Wu, Y.; Feick, H.; Tran, N.; Weber, E. & Yang, P. (2001b). Catalytic Growth of Zinc Oxide Nanowires by Vapor Transport. *Advanced Materials*, Vol.13, No.2, (January 2001), pp. 113-116, ISSN 0935-9648
- Hubert, B.; Naghavi, N.; Canava, B.; Etcheberry, A. & Lincot, D. (2007). Thermodynamic and experimental study of chemical bath deposition of  $\text{Zn}(\text{S},\text{O},\text{OH})$  buffer layers in basic aqueous ammonia solutions. Cell results with electrodeposited  $\text{CuIn}(\text{S},\text{Se})_2$  absorbers. *Thin Solid Films*, Vol.515, No.15, (May 2007), pp. 6032-6035, ISSN 0040-6090
- Jia, T. Q.; Zhao, F. L.; Huang, M.; Chen, H. X.; Qiu, J. R.; Li, R. X.; Xu, Z. Z. & Kuroda, H. (2006a). Alignment of nanoparticles formed on the surface of 6H-SiC crystals

- irradiated by two collinear femtosecond laser beams. *Applied Physics Letters*, Vol.88, No.11, (March 2006), pp. 11117-1-3, ISSN 0003-6951
- Jia, T. Q.; Chen, H. X.; Huang, M.; Wu, X. J.; Zhao, F. L.; Baba, M.; Suzuki, M.; Kuroda, H.; Qiu, J. R.; Li, R. X. & Xu, Z. Z. (2006b). ZnSe nanowires grown on the crystal surface by femtosecond laser ablation in air. *Applied Physics Letters*, Vol.89, No.10, (September 2006), pp. 101116-1-3, ISSN 0003-6951
- Jin, R.; Cao, Y. W.; Mirkin, C. A.; Kelly, K. L.; Schatz, G. C. & Zheng, J. G. (2001). Photoinduced Conversion of Silver Nanospheres to Nanoprisms. *Science*, Vol.294, No.5548, (November 2001), pp. 1901-1903, ISSN 0036-8075
- Kabashin, A. V.; Meunier, M.; Kingston, C. & Luong, J. H. T. (2003). Fabrication and Characterization of Gold Nanoparticles by Femtosecond Laser Ablation in an Aqueous Solution of Cyclodextrins. *Journal of Physical Chemistry B*, Vol.107, No.19, (April 2003), pp. 4527-4531, ISSN 1520-6106
- Kanehira, S.; Si., J.; Qiu, J.; Fujita, K. & Hirao, K. (2005). Periodic Nanovoid Structures via Femtosecond Laser Irradiation. *Nano Letters*, Vol.5, No.8, (August 2005), pp. 1591-1595, ISSN 1530-6984
- Kar, S.; Dev, A. & Chaudhuri, S. (2006). Simple Solvothermal Route To Synthesize ZnO Nanosheets, Nanonails, and Well-Aligned Nanorod Arrays. *Journal of Physical Chemistry B*, Vol.110, No.36, (August 2006), pp. 17848-17853, ISSN 1520-6106
- Kawai, J.; Nakajima, K. & Gohshi, Y. (1993). Copper L $\beta$ /L $\alpha$  X-ray emission intensity ratio of copper compounds and alloys. *Spectrochimica Acta Part B: Atomic Spectroscopy*, Vol.48, No.10, (August 1993), pp. 1281-1290, ISSN 0584-8547
- Kawasaki, M. & Masuda, K. (2005). Laser Fragmentation of Water-Suspended Gold Flakes via Spherical Submicroparticles to Fine Nanoparticles. *Journal of Physical Chemistry B*, Vol.109, No.19, (April 2005), pp. 9379-9388, ISSN 1520-6106
- Kong, X. Y. & Wang, Z. L. (2003). Spontaneous Polarization-Induced Nanohelices, Nanosprings, and Nanorings of Piezoelectric Nanobelts. *Nano Letters*, Vol.3, No.12, (August 2003), pp. 1625-1631, ISSN 1530-6984
- Kong, Y. C.; Yu, D. P.; Zhang, B.; Fang, W. & Feng, S. Q. (2001). Ultraviolet-emitting ZnO nanowires synthesized by a physical vapor deposition approach. *Applied Physics Letters*, Vol.78, No.4, (January 2001), pp. 407-409, ISSN 0003-6951
- Kupersztynch, J.; Raynaud, M. & Riconda, C. (2004). Electron acceleration by surface plasma waves in the interaction between femtosecond laser pulses and sharp-edged overdense plasmas. *Physics of Plasmas*, Vol.11, No.4, (April 2004), pp. 1669-1673, ISSN 1070-664X
- Le, H. Q.; Chua, S. J.; Koh, Y. W.; Loh, K. P.; Chen, Z.; Thompson, C. V. & Fitzgerald, E. A. (2005). Growth of single crystal ZnO nanorods on GaN using an aqueous solution method. *Applied Physics Letters*, Vol.87, No.10, (September 2005), pp. 101908-1-3, ISSN 0003-6951
- Lee, C. J.; Lee, T. J.; Lyu, S. C.; Zhang, Y.; Ruh, H. & Lee, H. J. (2002). Field emission from well-aligned zinc oxide nanowires grown at low temperature. *Applied Physics Letters*, Vol.81, No.19, (September 2002), pp. 3648-3650, ISSN 0003-6951
- Lee, E. T. Y.; Shimotsuma, Y.; Sakakura, M.; Nishi, M.; Miura, K. & Hirao, K. (2008). Photo-initiated growth of zinc oxide (ZnO) nanorods. *Materials Letters*, Vol.62, No.24, (September 2008), pp. 4044-4046, ISSN 0167-577X
- Lee, E. T. Y.; Shimotsuma, Y.; Sakakura, M.; Nishi, M.; Miura, K. & Hirao, K. (2009). Ultrashort Pulse Manipulation of ZnO Nanowire Growth. *Journal of Nanoscience and Nanotechnology*, Vol.9, No.1, (January 2009), pp. 618-626, ISSN 2078-0338

- Li, W.; Shi, E.; Zhong, W.; Yin, Z. (1999). Growth mechanism and growth habit of oxide crystals. *Journal of Crystal Growth*, Vol.203, No.1-2, (May 1999), pp. 186-196, ISSN 0022-0248
- Lieber, C. M. (1998). One-dimensional nanostructures: Chemistry, physics & applications. *Solid State Communications*, Vol.107, No.11, (August 1998), pp. 607-616, ISSN 0038-1098
- Lin, P. -F.; Ko, C. -Y.; Lin, W. -T. & Lee, C. T. (2007). Effects of processing parameters on ultraviolet emission of In-doped ZnO nanodisks grown by carbothermal reduction. *Materials Letters*, Vol.61, No.8-9, (April 2007), pp. 1767-1770, ISSN 0167-577X
- Lin, Y. -S.; Wu, S. -H.; Hung, Y.; Chou, Y. -H.; Chang, C.; Lin, M. -L.; Tsai, C. -P. & Mou, C. -Y. (2006). Multifunctional Composite Nanoparticles: Magnetic, Luminescent, and Mesoporous. *Chemistry of Materials*, Vol.18, No.22, (October 2006), pp. 5170-5172, ISSN 0897-4756
- Lin, Z.; Zhigilei, L. V. & Celli, V. (2008). Electron-phonon coupling and electron heat capacity of metals under conditions of strong electron-phonon nonequilibrium. *Physical Review B*, Vol.77, No.7, (February 2008), pp. 075133-1-17, ISSN 0163-1829
- Link, S.; Burda, C.; Mohamed, M. B.; Nikoobakht, B. & El-Sayed, M. A. (1999). Laser Photothermal Melting and Fragmentation of Gold Nanorods: Energy and Laser Pulse-Width Dependence. *Journal of Physical Chemistry A*, Vol.103, No.9, (March 1999), pp. 1165-1170, ISSN 1089-5639
- Link, S.; Burda, C.; Mohamed, M. B.; Nikoobakht, B. & El-Sayed, M. A. (2000). Femtosecond transient-absorption dynamics of colloidal gold nanorods: Shape independence of the electron-phonon relaxation time. *Physical Review B*, Vol.61, No.9, (March 2000), pp. 6086-6090, ISSN 0163-1829
- Lipinska-Kalita, K. E.; Krol, D. M.; Hemley, R. J.; Mariotto, G.; Kalita, P. E. & Ohki, Y. (2005). Synthesis and characterization of metal-dielectric composites with copper nanoparticles embedded in a glass matrix: A multitechnique approach. *Journal of Applied Physics*, Vol.98, No.5, (September 2005), pp. 054301-1-6, ISSN 0021-8979
- Liu, S. -D.; Cheng, M. -T.; Yang, Z. -J. & Wang, Q. -Q. (2008). Surface plasmon propagation in a pair of metal nanowires coupled to a nanosized optical emitter. *Optics Letters*, Vol.33, No.8, (April 2008), pp. 851-853, ISSN 0146-9592
- Liu, W.; Kosareva, O.; Golubtsov, I. S.; Iwasaki, A.; Becker, A.; Kandidov, V. P. & Chin, S. L. (2002). Random deflection of the white light beam during self-focusing and filamentation of a femtosecond laser pulse in water. *Applied Physics B: Lasers and Optics*, Vol.75, No.4-5, (October 2002), pp. 595-599, ISSN 0946-2171
- Lu, A. -H.; Schmidt, W.; Matoussevitch, N.; Bönnemann, H.; Spliethoff, B.; Tesche, B.; Bill, E.; Kiefer, W. & Schüth, F. (2004). Nanoengineering of a Magnetically Separable Hydrogenation Catalyst. *Angewandte Chemie International Edition*, Vol.43, No.33, (August 2004), pp. 4303-4306, ISSN 1433-7851
- Macchi, A.; Cornolti, F.; Pegoraro, F.; Liseikina, T. V.; Ruhl, H. & Vshivkov, V. A. (2001). Surface Oscillations in Overdense Plasmas Irradiated by Ultrashort Laser Pulses. *Physical Review Letters*, Vol.87, No.20, (October 2001), pp. 205004-1-4, ISSN 0031-9007
- Maier, S. A.; Kik, P. G.; Atwater, H. A.; Meltzer, S.; Harel, E.; Koel, B. E. & Requicha, A. A. G. (2003). Local detection of electromagnetic energy transport below the diffraction limit in metal nanoparticle plasmon waveguides. *Nature Materials*, Vol.2, No.4, (April 2003), pp. 229-232, ISSN 1476-1122
- Morales, A. M. & Lieber, C. M. (2008). A Laser Ablation Method for the Synthesis of Crystalline Semiconductor Nanowires. *Science*, Vol.279, No.5348, (January 1998), pp. 208-211, ISSN 0036-8075

- Muskens, O. L.; Fatti, N. D. & Vallee, F. (2006). Femtosecond Response of a Single Metal Nanoparticle. *Nano Letters*, Vol.6, No.3, (January 2006), pp. 552-556, ISSN 1530-6984
- Nakao, A.; Shimotsuma, Y.; Nishi, M.; Miura, K. & Hirao, K. (2008). Morphological control of nanoparticles by femtosecond laser irradiation. *Journal of Ceramic Processing Research*, Vol.9, No.4, (August 2008) pp. 425-429, ISSN 1229-9162
- Ohta, H. & Hosono, H. (2004). Transparent oxide optoelectronics. *Materials Today*, Vol.7, No.6, (June 2004), pp. 42-51, ISSN 1369-7021
- Pacholski, C.; Kornowski, A. & Weller, H. (2002). Self-Assembly of ZnO: From Nanodots to Nanorods. *Angewandte Chemie International Edition*, Vol.41, No.7, (April 2002), pp. 1188-1191, ISSN 1433-7851
- Pan, Z. W.; Dai, Z. R. & Wang, Z. L. (2001). Nanobelts of Semiconducting Oxides. *Science*, Vol.291, No.5510, (March 2001), pp. 1947-1949, ISSN 0036-8075
- Park, W. I.; Kim, D. H.; Jung, S.-W. & Yi, G. -C. (2002). Metalorganic vapor-phase epitaxial growth of vertically well-aligned ZnO nanorods. *Applied Physics Letters*, Vol.80, No.22, (April 2002), pp. 4232-4234, ISSN 0003-6951
- Peulon, S. & Lincot, D. (1998). Mechanistic Study of Cathodic Electrodeposition of Zinc Oxide and Zinc Hydroxychloride Films from Oxygenated Aqueous Zinc Chloride Solutions. *Journal of the Electrochemical Society*, Vol.145, No.3, (March 1998), pp. 864-874, ISSN 0013-4651
- Podlipensky, A.; Lange, J.; Seifert, G.; Graener, H. & Cravetchi, I. (2003). Second-harmonic generation from ellipsoidal silver nanoparticles embedded in silica glass. *Optics Letters*, Vol.28, No.9, (May 2003) pp. 716-718, ISSN 0146-9592
- Qiu, J.; Jiang, X.; Zhu, C.; Shirai, M.; Si, J.; Jiang, N. & Hirao, K. (2004). Manipulation of Gold Nanoparticles inside Transparent Materials. *Angewandte Chemie International Edition*, Vol.43, No.17, (April 2004), pp. 2230-2234, ISSN 1433-7851
- Rao, A. M.; Eklund, P. C.; Bandow, S.; Thess, A. & Smalley, R. E. (1997). Evidence for charge transfer in doped carbon nanotube bundles from Raman scattering. *Nature*, Vol.388, No.6639, (July 1997), pp. 255-259, ISSN 0028-0836
- Sauer, G.; Brehm, G.; Schneider, S.; Nielsch, K.; Choi, J.; Göring, P.; Gösele, U.; Miclea, P. & Wehrspohn, R. B. (2006). Surface-enhanced Raman spectroscopy employing monodisperse nickel nanowire arrays. *Applied Physics Letters*, Vol.88, No.2, (January 2006), pp. 023106-1-3, ISSN 0003-6951
- Sberveglieri, G.; Baratto, C.; Comini, E.; Faglia, G.; Ferroni, M.; Ponzoni, A. & Vomiero, A. (2007). Synthesis and characterization of semiconducting nanowires for gas sensing. *Sensors and Actuators B*, Vol.121, No.1, (January 2007) pp. 208-213, ISSN 0925-4005
- Shen, M. Y.; Crouch, C. H.; Carey, J. E. & Mazur, E. (2004). Femtosecond laser-induced formation of submicrometer spikes on silicon in water. *Applied Physics Letters*, Vol.85, No.23, (September 2004), pp. 5694-5696 ISSN 0003-6951
- Shimotsuma, Y.; Kazansky, P. G.; Qiu, J.; Hirao, K. (2003). Self-Organized Nanogratings in Glass Irradiated by Ultrashort Light Pulses. *Physical Review Letters*, Vol.91, No.24, (December 2003), pp. 247405-1-4, ISSN 0031-9007
- Shimotsuma, Y.; Sakakura, M.; Miura, K.; Qiu, J.; Kazansky, P. G.; Fujita, K. & Hirao, K. (2007). Application of Femtosecond-Laser Induced Nanostructures in Optical Memory. *Journal of Nanoscience and Nanotechnology*, Vol.7, No.1, (January 2007), pp. 94-104, ISSN 2078-0338
- Shimotsuma, Y.; Yuasa, T.; Homma, H.; Sakakura, M.; Nakao, A.; Miura, K.; Hirao, K.; Kawasaki, M.; Qiu, J. & Kazansky, P. G. (2007). Photoconversion of Copper Flakes

- to Nanowires with Ultrashort Pulse Laser Irradiation. *Chemistry of Materials*, Vol.19, No.6, (February 2007), pp. 1206-1208, ISSN 0897-4756
- Stalmashonak, A.; Podlipensky, A.; Seifert, G. & Graener, H. (2009). Intensity-driven, laser induced transformation of Ag nanospheres to anisotropic shapes. *Applied Physics B: Lasers and Optics*, Vol.94, No.3, (November 2009), pp. 459-465, ISSN 0946-2171
- Stuart, B. C.; Feit, M. D.; Herman, S.; Rubenchik, A. M.; Shore, B. W. & Perry, M. D. (1995). Laser-Induced Damage in Dielectrics with Nanosecond to Subpicosecond Pulses. *Physical Review Letters*, Vol.74, No.12, (March 1995) pp. 2248-2251, ISSN 0031-9007
- Sylvestre, J. -P.; Kabashin, A. V.; Sacher, E.; Meunier, M. & Luong, J. H. T. (2004). Stabilization and Size Control of Gold Nanoparticles during Laser Ablation in Aqueous Cyclodextrins. *Journal of the American Chemical Society*, Vol.126, No.23, (May 2004), pp. 7176-7177, ISSN 0002-7863
- Tamaki, Y.; Asahi, T. & Masuhara, H. (2002). Nanoparticle Formation of Vanadyl Phthalocyanine by Laser Ablation of Its Crystalline Powder in a Poor Solvent. *Journal of Physical Chemistry A*, Vol.106, No.10, (January 2002), pp. 2135-2139, ISSN 1089-5639
- Tilaki, R. M.; Irajizad, A. & Mahdavi, S. M. (2007). Size, composition and optical properties of copper nanoparticles prepared by laser ablation in liquids. *Applied Physics A: Materials Science & Processing*, Vol.88, No.2, (May 2007), pp. 415-419, ISSN 0947-8396
- Tull, B. R.; Carey, J. E.; Sheehy, M. A.; Friend, C. & Mazur, E. (2006). Formation of silicon nanoparticles and web-like aggregates by femtosecond laser ablation in a background gas. *Applied Physics A: Materials Science & Processing*, Vol.83, No.3, (June 2006), pp. 341-346, ISSN 0947-8396
- Tzortzakis, S.; Sudrie, L.; Franco, M.; Prade, B.; Mysyrowicz, A.; Couairon, A. & Berge, L. (2001). Self-Guided Propagation of Ultrashort IR Laser Pulses in Fused Silica. *Physical Review Letters*, Vol.87, No.21, (November 2001), pp. 213902-1-4, ISSN 0031-9007
- Unal, A. A.; Stalmashonak, A.; Seifert, G.; Graener, H. (2009). Ultrafast dynamics of silver nanoparticle shape transformation studied by femtosecond pulse-pair irradiation. *Physical Review B*, Vol.79, No.11, (March 2009), pp. 115411-1-7, ISSN 1098-0121
- Vanheusden, K.; Warren, W. L.; Seager, C. H.; Tallant, D. R.; Voigt, J. A. & Gnade, B. E. (1996). Mechanisms behind green photoluminescence in ZnO phosphor powders. *Journal of Applied Physics*, Vol.79, No.10, (February 1996), pp. 7983-7990, ISSN 0021-8979
- Vogel, A.; Noack, J.; Hüttman, G. & Paltauf, G. (2005). Mechanisms of femtosecond laser nanosurgery of cells and tissues. *Applied Physics B: Lasers and Optics*, Vol.81, No.8, (November 2005), pp. 1015-1047, ISSN 0946-2171
- Wagner, R. S. & Ellis, W. C. (1964). Vapor-Liquid-Solid Mechanism of Single Crystal Growth. *Applied Physics Letters*, Vol.4, No.5, (February 1964), pp. 89-90, ISSN 0003-6951
- Wu, N.; Shimotsuma, Y.; Nishi, M.; Sakakura, M.; Miura, K. & Hirao, K. (2010). Photo-initiation of ZnO nanorod formation by femtosecond laser irradiation. *Journal of the Ceramic Society of Japan*, Vol.118, No.1374, (February 2010), pp. 147-151 ISSN 1882-0743
- Xiang, Y.; Wu, X.; Liu, D.; Jiang, X.; Chu, W.; Li, Z.; Ma, Y.; Zhou, W. & Xie, S. (2006). Formation of Rectangularly Shaped Pd/Au Bimetallic Nanorods: Evidence for Competing Growth of the Pd Shell between the {110} and {100} Side Facets of Au Nanorods. *Nano Letters*, Vol.6, No.10, (September 2006), pp. 2290-2294, ISSN 1530-6984

- Yamabi, S. & Imai, H. (2002). Growth conditions for wurtzite zinc oxide films in aqueous solutions. *Journal of Materials Chemistry*, Vol.12, No.12, (September 2002), pp. 3773-3778, ISSN 0959-9428
- Yang, M.; Pang, G.; Jiang, L. & Feng, S. (2006). Hydrothermal synthesis of one-dimensional zinc oxides with different precursors. *Nanotechnology*, Vol.17, No.1, (January 2006), pp. 206-212, ISSN 0957-4484
- Yim, S. -Y.; Ahn, H. -G.; Je, K. -C.; Choi, M.; Park, C. W.; Ju, H. & Park, S. -H. (2007). Observation of red-shifted strong surface plasmon scattering in single Cu nanowires. *Optics Express*, Vol.15, No.16, (August 2007), pp. 10282-10287, ISSN 1094-4087
- Yu, K.; Jin, Z.; Liu, X.; Zhao, J. & Feng, J. (2007). Shape alterations of ZnO nanocrystal arrays fabricated from  $\text{NH}_3$   $\text{H}_2\text{O}$  solutions. *Applied Surface Science*, Vol.253, No.8, (October 2007), pp. 4072-4078, ISSN 0169-4332
- Zepf, M.; Tsakiris, G. D.; Pretzler, G.; Watts, I.; Chambers, D. M.; Norreys, P. A.; Andiel, U.; Dangor, A. E.; Eidmann, K.; Gahn, C.; Machacek, A.; Wark, J. S. & Witte, K. (1998). Role of the plasma scale length in the harmonic generation from solid targets. *Physical Review E*, Vol.58, No.5, (November 1998), pp. R5253-R5256, ISSN 1063-651X
- Zhang, F.; Wang, X.; Ai, S.; Sun, Z.; Wan, Q.; Zhu, Z.; Xian, Y.; Jin, L. & Yamamoto, K. (2004). Immobilization of uricase on ZnO nanorods for a reagentless uric acid biosensor. *Analytica Chimica Acta*, Vol.519, No.2, (August 2004), pp. 155-160, ISSN 0003-2670
- Zhang, H.; Yang, D.; Ma, X.; Ji, Y.; Xu, J. & Que, D. (2004). Synthesis of flower-like ZnO nanostructures by an organic-free hydrothermal process. *Nanotechnology*, Vol.15, No.5, (May 2004), pp. 622-626, ISSN 0957-4484
- Zhang, J.; Sun, L.; Liao, C. & Yan, C. (2002a). A simple route towards tubular ZnO. *Chemical Communications*, Vol.2002, No.3, (January 2002), pp. 262-263, ISSN 1359-7345
- Zhang, J.; Sun, L. D.; Yin, J. L.; Su, H. L.; Liao, C. S. & Yan, C. H. (2002b). Control of ZnO Morphology via a Simple Solution Route. *Chemistry of Materials*, Vol.14, No.10, (September 2002), pp. 4172-4177, ISSN 0897-4756
- Zhang, X. Y.; Dai, J. Y.; Ong, H. C.; Wang, N.; Chan, H. L. W. & Choy, C. L. (2004). Hydrothermal synthesis of oriented ZnO nanobelts and their temperature dependent photoluminescence. *Chemical Physics Letters*, Vol.393, No.1-3, (July 2004), pp. 17-21, ISSN 0009-2614
- Zhang, Y. & Mu, J. (2007). Controllable synthesis of flower- and rod-like ZnO nanostructures by simply tuning the ratio of sodium hydroxide to zinc acetate. *Nanotechnology*, Vol.18, No.7, (February 2007), pp. 075606-1-6, ISSN 0957-4484
- Zhang, Y.; Russo, R. E. & Mao, S. S. (2005). Femtosecond laser assisted growth of ZnO nanowires. *Applied Physics Letters*, Vol.87, No.13, (September 2005), pp. 133115-1-3, ISSN 0003-6951
- Zhang, Y.; Suenaga, K.; Colliex, C. & Iijima, S. (1998). Coaxial Nanocable: Silicon Carbide and Silicon Oxide Sheathed with Boron Nitride and Carbon. *Science*, Vol.281, No.5379, (August 1998), pp. 973-975, ISSN 0036-8075

# High-Bias Instability of Atomic and Molecular Junctions

Akira Sakai  
*Kyoto University*  
*Japan*

## 1. Introduction

Atom-sized contacts are appealing interconnects in atomic- and molecular-scale devices. Because these contacts are smaller than the mean free path of electrons, conduction electrons are rarely scattered when they pass through the contact. This absence of scattering events not only ensures high electron mobility but also achieves small energy dissipation at the contact. As a result, we can obtain in atom-sized contacts a huge current density that is unattainable for present-day microfabricated interconnects. A single-atom contact of Au, for example, is capable of sustaining a current density as high as  $8 \times 10^{10} \text{ A/cm}^2$  (Yanson et al., 1998), which is orders of magnitude higher than the current density realized in microelectronics devices. However, atom-sized contacts would eventually become unstable and break down when they are subject to sufficiently high biases or high currents. This stability limit of atom-sized contacts is of much value both in application and in academia. In electronics applications, the magnitude of allowable bias or current is a critical parameter because it directly determines the maximum rating of atom-sized contacts when they are incorporated into real devices. For atom-sized contacts, even a low voltage such as 3 V, commonly used in CMOS devices, can be regarded as a high bias which, in the case of an Au single-atom contact, would generate a current density that well exceeds the maximum value mentioned above. On the other hand, typical molecular FETs would operate under biases much higher than 3 V and hence achieve current densities far exceeding the maximum value. It is therefore practically quite important to know the stability limit of the atom-sized contacts under high-bias/current conditions.

The same stability problem also provides us a fertile ground of physical investigations. The high-bias/current instability of atom-sized contacts involves various microscopic processes which have not yet been fully worked out. When one applies a high bias to an atom-sized contact, hot electrons are injected from one electrode into the contact. Though the contact is smaller in size than the electronic mean free path, there still remains a non-zero chance for the hot electrons to interact with the lattice and partly transfer their kinetic energy, and/or momentum, to the contact atoms, often causing their vibrational heating and electromigration. At the downstream electrode, electrons dissipate their energy which diffuses out to the bulk through the lattice heat conduction. All these processes are individually well studied in macroscopic materials but little understood for ultrasmall conductors such as the atom-sized contacts. To obtain some insight on this topic of practical and academic interest, some

theories are currently emerging on the high-bias/current instability of atom-sized contacts, and systematic measurements are now called for to provide a solid database for further theoretical and experimental developments.

## 2. Contact lifetime

At the present time, microscopic theories have been proposed for specific high-bias problems, and there has been no general theoretical framework that can be universally used for analyzing various experimental data. A crude way for dealing with the stability problem is to consider the contact lifetime  $\tau$  and employ the following empirical formula, (Smit et al., 2004)

$$\tau = \tau_0 \exp\left(\frac{E(V, F)}{k_B T^*}\right), \quad (1)$$

where  $T^*$  is an effective contact temperature and  $E(V, F)$  is a stabilization energy of the contact at a bias voltage  $V$  and under a tensile force  $F$ . The latter is included in the stabilization energy because the atom-sized contacts are often produced by pulling apart macroscopic metal-metal contacts, as will be mentioned in the next section. Atom-sized contacts formed by such junction breaking always involve some internal tension, the strength of which is not negligible.

Within a linear approximation,  $E(V, F)$  can be written as,

$$E(V, F) = E_0 - \alpha V - \beta F \quad (2)$$

where  $E_0$  is the stabilization energy at  $V = 0$  and  $F = 0$ , and the coefficients  $\alpha$  and  $\beta$  represent the bias and the tensile-force sensitivity of  $E$ , respectively. Then we obtain,

$$\tau = \tau_0 \exp\left(\frac{E_0 - \alpha V - \beta F}{k_B T^*}\right). \quad (3)$$

This equation is purely empirical and has no rigorous theoretical basis for it. However, similar thermal-activation type formula has been widely used for describing the rate of atomic jumps during electromigration in nanocontacts, and Eq. 3 would thus be a reasonable first approximation for the lifetime of atom-sized contacts under high biases. According to Eq. 3, either  $V$  or  $F$  reduces  $E$  and tends to destabilize the contact. If one increases  $V$  while keeping  $F$  constant,  $E$  becomes comparable to thermal energy at  $V_b = (E_0 - \beta F - k_B T^*)/\alpha$ . This bias determines the break voltage of the contact. On the other hand, if one increases  $F$  at zero or low constant biases, the contact becomes unstable at  $F_b = (E_0 - \alpha V - k_B T^*)/\beta$ , which defines the maximum tensile strength of the contact.

Under high bias/current conditions, Joule heating of contacts is indeed non-negligible, and this is the reason why the effective temperature  $T^*$ , not the ambient temperature  $T$ , enters in Eqs. 1 and 3. In the case of atom-sized contacts, the contact overheating mainly depends on how fast the generated heat is carried away by the lattice thermal transport. Todorov and coworkers (Todorov et al., 2001) theoretically studied this heat generation/diffusion problem and proposed the following formula for  $T^*$ ,

$$T^{*4} = T^4 + \gamma(LV)^2 = T^4 + T_V^4, \quad T_V \equiv \gamma^{1/4} \sqrt{LV} \quad (4)$$

where  $L$  is a contact length and  $\gamma$  is a material-dependent constant which takes  $\gamma \sim 60 \text{ KV}^{-1/2}\text{nm}^{-1/2}$  for typical metals (Todorov et al., 2001). Because the contribution of the ambient temperature in Eq. 4 increases as  $T^4$ , the bias-dependent second term is negligible compared to the first term at room temperature, and hence we have  $T^* \sim T$ . On the contrary, the second term becomes dominant at liquid helium temperature where  $T^*$  increases with the bias as  $T^* \propto \sqrt{LV}$  (?).

The magnitude of  $T^*$  can be evaluated experimentally by measuring the frequency of the conductance two-level fluctuations (TLFs) often observed on the atom-sized contacts. This stochastic switching of the conductance is caused by the thermally activated jumps of an atom locating near the constriction, and the TLF frequency varies with the contact temperature. Tsutsui *et al.* (Tsutsui et al., 2006a) measured the TLF frequency of Au atom-sized contacts at 4 K under different biases and showed that their TLF data consistently fit to the  $\sqrt{V}$  dependence of  $T^*$ . According to their results, a contact at  $T = 4 \text{ K}$  under a bias of 1.0 V becomes heated up to  $T^* \sim 75 \text{ K}$ .

Compared to  $T^*$ , little has been known on the stabilization energy  $E_0$  and the coefficients  $\alpha$  and  $\beta$  in Eq. 3. Tsutsui *et al.* (Tsutsui et al., 2006b) analyzed the bias dependence of the conductance TLF frequency of noble metal contacts and obtained nearly the same value  $\alpha \sim 0.1 \text{ eV/V}$  for Au, Ag and Cu. Smit *et al.* (Smit et al., 2004) showed that their break voltage data on the single-atom contacts of Au and Pt can be consistently described by Eqs. 3 and 4. From the data fitting, they estimated  $E_0 = 0.738 \text{ eV}$ ,  $\alpha = 0.14 \text{ eV/V}$  and  $\beta = 0.49 \text{ eV/nN}$  for Au. On the other hand, Tsutsui *et al.* (Tsutsui et al., 2008) directly measured  $\tau$  of the Au single-atom contacts at room temperature. By fitting the observed data with Eq. 3, they obtained  $\beta \sim 0.1 \text{ eV/nN}$ . For metals other than Au, no experimental data are available at this time on  $\beta$  and  $E_0$ .

### 3. Conductance of atom-sized contacts of metals

Atom-sized contacts of metals are too small to be observed by conventional tools so that, except for some studies using high-resolution transmission-electron microscopy, we have no direct means to tell whether these ultras-small contacts are actually formed or not. Instead of direct observations, therefore, we usually measure the junction conductance  $G$  and use its magnitude as a convenient measure of the junction size. In the case of macroscopic conductors larger than the mean free path of electrons, a conductance  $G$  of a constriction can be expressed as  $G \propto 1/d$  (Agraït et al., 2003) where  $d$  is the constriction diameter. When  $d$  becomes smaller than the mean free path, the flow of free electrons through such a small constriction is physically analogous to the gas flow through a small orifice, and the gas conductance formula for a circular orifice of diameter  $d$  in the molecular flow regime can be transformed into that for the electronic conductance. This leads to the following conductance formula (Agraït et al., 2003),

$$G = \frac{2e^2}{16h}(k_F d)^2 = \frac{2e^2}{4\pi h}k_F^2 A, \quad (5)$$

where  $k_F$  is the electron Fermi wavelength and  $A = \pi d^2/4$  is the contact cross-sectional area. This is the Sharvin conductance formula which applies for conductors smaller than the electronic mean free path.

When  $d$  becomes even smaller and comparable to the Fermi wavelength, the contact electrons can no longer be regarded as free electrons but as valence electrons of contact atoms. In

this atomistic limit, the contact conductance is determined, roughly speaking, by how freely electrons can pass through the valence electronic states of the contact. If a contact has  $n$  valence states, its conductance can be written as,

$$G = \frac{2e^2}{h} \sum_n T_n = G_0 \sum_n T_n, \quad (6)$$

where  $T_n$  is the electron transmission probability of the  $n$ -th state, and  $G_0 \equiv 2e^2/h$  is the conductance quantum unit. More precisely, the conductance is determined by the transmission probability of the conductance channels which are a set of orthonormal states constituted from the valence states. This formula is usually referred to as the Landauer conductance formula. When  $T_n = 1$  for all states,  $G = n(2e^2/h)$  and the conductance becomes quantized in integer multiples of the conductance quantum.

In the quantum point contacts of two-dimensional electron gas, all electronic states are highly transparent, i.e.  $T_n = 1$ , and the number  $n$  of the contact states can be finely controlled by continuously varying the constriction width with a gate voltage. As a result, quantized steps in  $G$  in unit of  $G_0$  can be clearly observed. On the other hand, metal contacts cannot be continuously reduced in size because of the atomic discreteness of their lattices. The contact necking often proceeds discontinuously by repeating an elastic stretching followed by an abrupt relaxation or rearrangement of atomic configuration. Reflecting this discrete nature of the necking deformation, the conductance of a nanocontact often exhibits plateaus and steps when it is stretched by applying a tensile force. These stepwise changes in the conductance, however, have no relationship with the variation of the number  $n$  of transmission states in Eq. 6 and hence do not represent the quantized changes in conductance, except for some rare cases where the discrete reduction of the contact geometry precisely correlates to that of  $n$ . In most contacts, the conductance plateaus correspond to a formation of certain contact geometries that are more stable than others. Such stable contacts make a prolonged elastic deformation under a stretching force and often produce a long conductance plateau. Single-atom contacts of metals are the most stable contact because its failure involves the direct bond breaking. Consequently, single-atom contacts usually display a clear conductance plateau, the last plateau before the contact failure, and we can determine the single-atom conductance from the position of such a last conductance plateau. Also, we can know the formation of a single-atom contact by detecting this conductance plateau.

The electron transmission probability  $T_n$  in Eq. 6 varies with the valence characteristics of the state  $n$ . A general trend is that all  $s$  states and some  $sp$  states that extend along the contact axis show a high transmission, i.e.  $T_n \sim 1$ , while localized  $d$  states transmit electrons only partially (Cuevas et al., 1998). Monovalent noble metals such as Au, Ag, and Cu has one  $s$ -like valence state. As a result, the single-atom contact of these noble metals has a single conductance channel which shows  $T_n \sim 1$  and hence  $G \sim 1G_0$  according to Eq. 6. Experimentally, noble-metal contacts are known to exhibit a clear conductance plateau at  $1G_0$  when they are reduced to the size of atoms. The experimental results are thus in good agreement with Eq. 6, and it is now well established that the single-atom conductance of noble metals is  $1G_0$ . This does not necessarily guarantee that the  $1G_0$  contacts of noble metals are always a single-atom contact because larger contacts consisting two or more atoms may happen to show the  $1G_0$  conductance. However, such conductance coincidence scarcely

occurs, and one can usually identify the  $1G_0$  contacts of Au, Ag, and Cu as a single-atom contact.

#### 4. Fabrication method of atom-sized contacts

The break junction method is the most convenient and widely used one for producing atom-sized contacts of metals. This method utilizes the necking deformation of a metal contact to obtain atom-sized contacts. First, a macroscopic contact is formed between a pair of metal electrodes. Then, the electrodes are separated apart to stretch the contact, as schematically illustrated in Fig. 1.

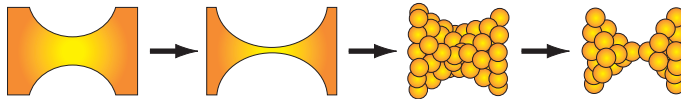


Fig. 1. Formation of an atom-sized contact by breaking a macroscopic contact.

The contact undergoes the necking deformation, shrinks in size, and becomes an atom-sized contact before it completely breaks up. As mentioned in the previous section, the conductance often exhibits plateaus in the course of necking deformation. Figure 2 represents a typical example of the temporal change in the conductance recorded during a breakup of an Au contact at 0.6 V. The last plateau appears at  $1G_0$ , and this  $1G_0$  plateau corresponds to the Au single-atom contact which has the  $1G_0$  conductance as explained in the previous section.

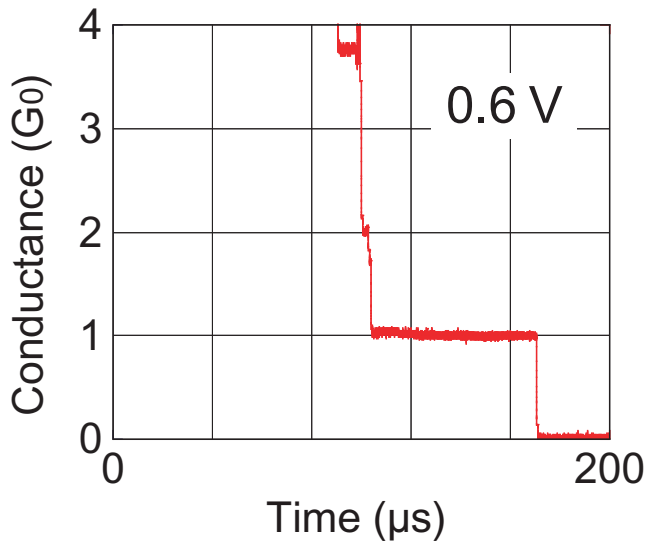


Fig. 2. Temporal change in the conductance of an Au contact during its breakup.

In the break junction method, the geometry of the electrodes and their initial macroscopic contact is irrelevant for the formation of atom-sized contacts, and a wide variety of macroscopic electrodes have been used so far in the past experiments. Figures 3 and 4 display two examples used for studying the high-bias instability of atom-sized contacts.

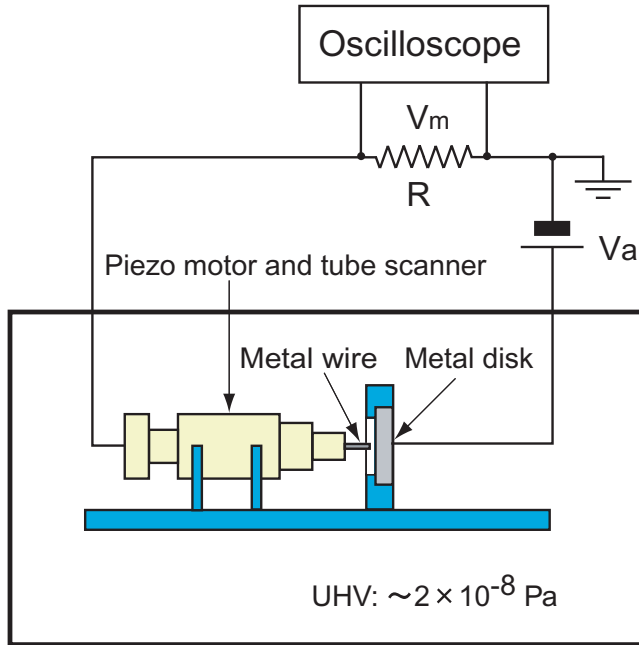


Fig. 3. An apparatus for fabricating wire-disk-type break junctions.

In a setup shown in Fig. 3, a metal wire and a metal disk serve as electrodes. A contact is made and broken by pressing and retracting the wire against the disk. A piezo tube scanner combined with a piezo motor is used for moving the wire and finely controlling its displacement. In Fig. 3, the contact conductance is measured by detecting the voltage drop  $V_m$  across a current-sensing resistor  $R$  connected in series with the contact. The conductance  $G$  is related to  $V_m$  through the following equation,

$$G = \frac{V_m}{R(V_a - V_m)}, \quad (7)$$

where  $V_a$  is an applied bias. In this measuring setup, the conductance nonlinearly depends on the measured voltage  $V_m$ , and the conductance resolution decreases at higher conductances. However, the use of an oscilloscope enables us to record fast transient behaviors of the conductance at and near the onset of instability. Some examples of such transient conductance traces will be shown in Sec. 5.1.

Figure 4 depicts the schematic of MCBJ (mechanically controllable break junction), which is another widely used method for fabricating atom-sized contacts. In the MCBJ, a thin-metal wire is glued at two points onto a flexible substrate. By bending the substrate by a piezo actuator, the wire is broken in the middle between the two fixed points, and each end of the broken wire serves as an electrode. The gap between the electrodes can be made open and closed by extending and retracting the actuator, respectively. Because the reduction ratio between the actuator displacement and the change in the gap distance can be made very large, the gap distance can be finely controlled by the actuator with a resolution of a few

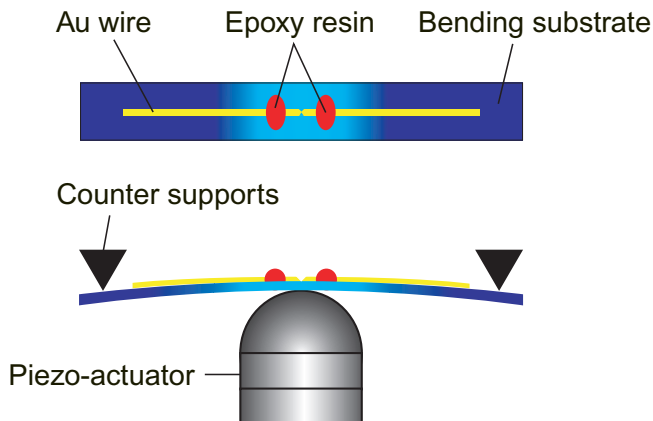


Fig. 4. Schematic of MCBJ (mechanically controllable break junction).

pm. This superior gap controllability of MCBJ, together with its high mechanical stability against disturbances from outside, makes MCBJ a superior method for fabricating atom-sized contacts and nanogapped electrodes for molecules.

### 5. Experiments on the high-bias /current instability of atom-sized contacts

Two experimental methods have been exploited for studying the high-bias instability of atom-sized contacts. In one method depicted in Fig. 5(a), a macroscopic contact is first prepared and placed under a constant bias voltage. Then, the contact is mechanically stretched to break it. As mentioned in the previous section, this contact stretching makes a necking deformation of the contact and often yields an atom-sized contact before the contact completely breaks up. As the contact necking proceeds, the contact cross section decreases and the current density increases accordingly. At some point during the deformation, the contact becomes unstable against its high current density and ruptures before it makes a mechanical fracture. By observing the threshold for such a contact failure, we can obtain information on the current-induced instability of atom-sized contacts. We will show in the next section experimental results on some metal contacts and explain how we can analyze the data to determine  $j_c$ , the threshold current density for the instability.

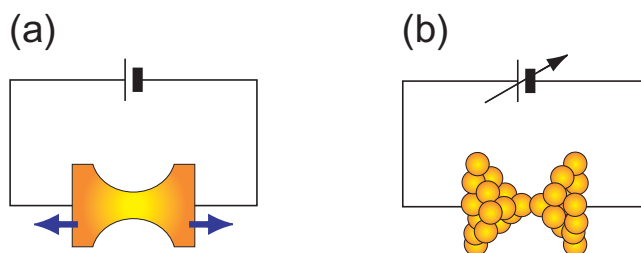


Fig. 5. Two methods for studying the high-bias instability of atom-sized contacts. In (a), a contact is mechanically stretched under high applied biases, whereas in (b), a single-atom contact is first produced and broken by applying a bias ramp.

In the method mentioned above, a contact usually fails before it shrinks to a single-atom. With this method, therefore, we are unable to study the instability of the single-atom contacts, and for studying single-atom contacts, another method shown in Fig. 5(b) is more suited. This method is basically an  $I - V$  measurement of a contact but the upper bound of the bias is extended beyond the contact stability limit. First, a single-atom contact is fabricated under low biases. With maintaining the contact in its single-atom state, the bias is set to increase until the contact ruptures. The voltage and current at the contact failure determines the break voltage and current of the single-atom contact. Although this method sounds quite simple and easy to carry out, it is by no means a trivial matter to hold a single-atom contact for some time long enough for applying the bias ramp. Experiments are particularly difficult at room temperature where single-atom contacts are usually short-lived as suggested by Eq. 3. This method was first applied to the single-atom contacts of Au by Kim Hansen in his doctoral thesis, who named it the current disruption method. Then, the same method has been employed by Smit *et al.* (Smit *et al.*, 2004) to determine the break voltage of Au and Pt single-atom contacts and chains at 4 K. All these previous measurements were performed at low temperatures to take an advantage of longer lifetime of single-atom contacts at cryogenic temperatures. In Sec. 5.2, we show our results on noble metals obtained at room temperature.

A noteworthy extension of this method is its application to molecular junctions where a single molecule is placed between a pair of nano-gapped electrodes. High-bias/current instability of various single-molecule junctions can also be investigated with the method shown in Fig. 5(b), provided that molecular bridges remain undestroyed until the onset of the high-bias instability. We carried out some experiments on junctions of thiol group molecules, and the results will be described in Sec. 5.4.

### 5.1 Current-induced instability

This section summarizes experimental results on the current-induced instability which happens in a metal nanocontact, the size of which is in nanometer scale but still larger than that of atoms. Experiments were carried out in ultrahigh vacuum at room temperature using the setup shown in Fig. 3.

As mentioned before, the current density in a contact increases with time when one breaks the contact by necking deformation under high biases. At some point in the course of contact necking, the contact becomes unstable and snapped off. This process can be monitored as shown in Fig. 6 where the time evolution of the conductance is depicted for Au, Ag, and Cu contacts under an applied bias of 2.0 V. Note that a conductance scale is quite nonlinear in the figure. Actually these plots are taken from oscilloscope traces, the vertical axis of which is not the conductance  $G$  but  $V_m$  in Eq. 7. As seen in Eq. 7, the conductance is a nonlinear function of  $V_m$ , and this nonlinearity between  $G$  and  $V_m$  largely distorts the vertical scale in Fig. 6, almost making it look like a logarithmic scale.

In all traces shown in Fig. 6, the conductance first decreases slowly and then becomes a bit accelerated. When the conductance reaches around several tens of  $G_0$ , it suddenly shows fluctuations and dives to zero. Because the vertical scale is nonlinear, the conductance fluctuations actually occur in large amplitudes. The onset of contact instability almost always accompanies such precursory conductance fluctuations. We first tried to characterize the instability by detecting the center of gravity of the conductance fluctuations, but some fluctuations are too short-lived to accurately determine the position of their gravity center. Alternatively, we detected the break conductance  $G_b$ , the last value of the conductance before

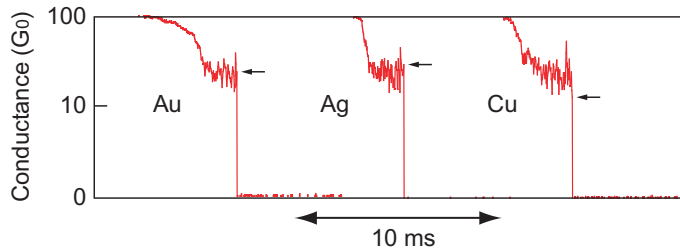


Fig. 6. Conductance traces of Au, Ag, and Cu contacts observed when they are stretched under an applied bias of 2.0 V. All contacts show significant conductance fluctuations before the contact failure. Arrows indicate the break conductance  $G_b$ , the last conductance value before the conductance jumps down. See text for the nonlinear conductance scale.

it jumps to zero. Each arrow in Fig. 6 indicates the break conductance of each contact. As seen in the figure,  $G_b$  is slightly off from the center of the fluctuations because, as seen in the case of Cu, the conductance sometimes jumps from the peak or the bottom of the fluctuation. Nevertheless, for many contacts,  $G_b$  serves as a reasonable parameter defining the onset of the instability.

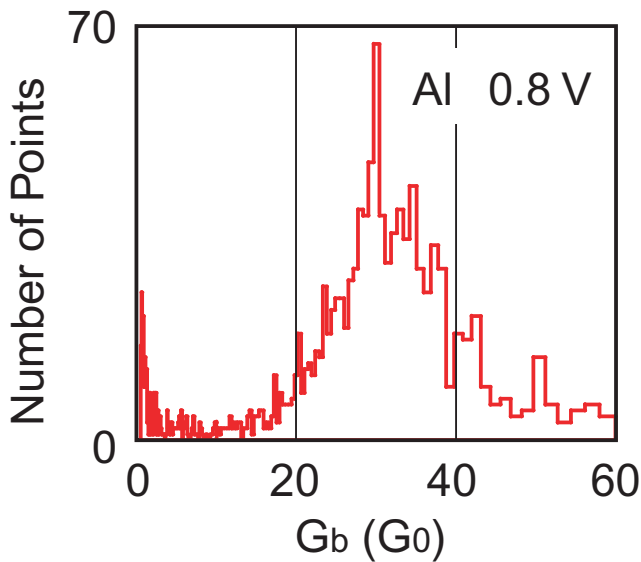


Fig. 7. Break conductance distribution for Al contacts obtained under an applied bias of 0.8 V.

We measured the break conductance for many contact breaks and constructed its histogram. An example of such break conductance histogram is shown in Fig. 7, this case for Al contacts at  $V_a = 0.8$  V. The histogram exhibits a broad distribution with a single maximum, the position of which is denoted by  $\hat{G}_b$ . Similar broad and single-peak distribution is also observed for other metals when  $V_a$  is sufficiently high. A common feature of these break conductance histograms of various metals is that the peak position  $\hat{G}_b$  changes with  $V_a$  and moves to the higher conductance side as  $V_a$  increases. Figure 8 shows a series of break conductance

histograms of Ag obtained under different  $V_a$ . Similar to that of Al shown in Fig. 7, the  $G_b$  distribution of Ag shows a single broad peak, the position of which is indicated by a stripe in each panel. Clearly, the peak position shifts to the higher conductance side as  $V_a$  increases. This means that a contact tends to break at a higher conductance under higher  $V_a$ .

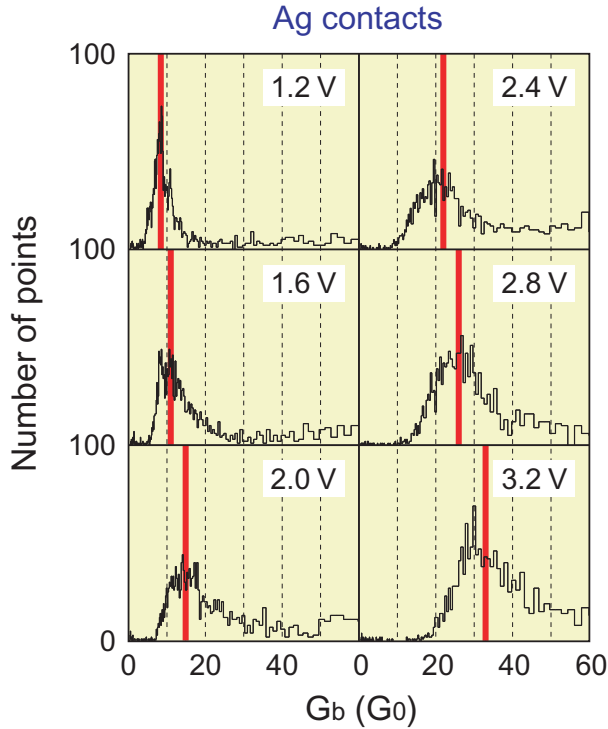


Fig. 8. Break conductance distribution for Ag contacts obtained under different applied biases. A strip marks the position of the distribution maximum, which shifts to the higher conductance side with increasing the applied bias.

To discuss this bias-induced shift of  $\hat{G}_b$  more quantitatively, we made a plot shown in Fig. 9 where the contact current  $\hat{I}_b$  corresponding to  $\hat{G}_b$  is plotted against  $\hat{G}_b$ . As seen in the figure, the data points nicely fit to a straight line passing through the origin. This means  $\hat{I}_b \propto \hat{G}_b$  or  $\hat{I}_b/\hat{G}_b = (\text{const.})$ . Figure 9 shows the example for Ag, but the same proportionality relationship between  $\hat{I}_b$  and  $\hat{G}_b$  can be found for noble metals, Au and Cu, and other metals such as Al (Minowa et al., 2005a), Zn (Suzuki et al., 2006), Pt (Minowa et al., 2005b), and Mo (Minowa et al., 2005b). The physical meaning of the observed proportionality between  $\hat{I}_b$  and  $\hat{G}_b$  can be understood if we notice that  $\hat{G}_b$  is in the range of the Sharvin conductance and thus proportional to the contact area  $A$  as shown in Eq. 5. Then,  $\hat{I}_b/\hat{G}_b = (\text{const.})$  can be rewritten as  $\hat{I}_b/A = (\text{const.})$ . Because  $j_c \equiv \hat{I}_b/A$  is the contact current density, this result indicates that there is a current density, specific to each metal, at which a contact becomes unstable and breaks up.

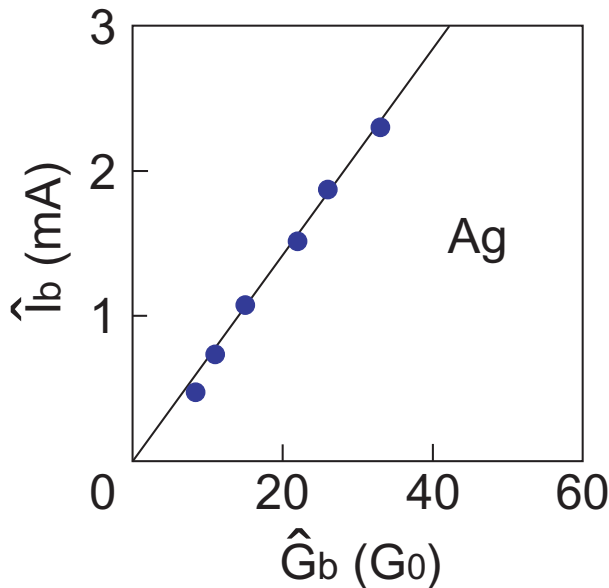


Fig. 9.  $\hat{I}_b - \hat{G}_b$  plot for Ag contacts. The slope of the straight line determines the current density for the contact instability.

Figure 10 summarizes the experimental  $j_c$  of five metals estimated from the slope of the  $\hat{I}_b - \hat{G}_b$  plot. In the figure,  $j_c$  is plotted against the melting temperature  $T_m$  of each metal. Though  $j_c$  of Au somehow deviates from others, a positive correlation is evident between  $j_c$  and  $T_m$ , i.e. metals of higher  $T_m$  show higher  $j_c$ . This result implies that the current-induced contact instability, and the marked conductance fluctuations shown in Fig. 6 as well, would be due to local contact melting. As seen in Fig. 10, the magnitude of  $j_c$  is in order of  $10\text{A}/\text{cm}^2$  which is three to four orders of magnitude higher than the current density flowing through interconnects in present-day microdevices. Significant Joule heating and local contact melting would thus be a plausible source of the observed contact failure. Another possibility is electromigration. Because the activation energy of electromigration empirically scales with  $T_m$ , electromigration can also account for the observed positive correlation between  $j_c$  and  $T_m$ . We, however, note that massive electromigration in atom-sized contacts would be effectively indistinguishable from local melting, and the distinction of two phenomena might be unnecessary. Whatever the instability mechanism is, the observed fast conductance fluctuations shown in Fig. 6 indicates that contact atoms would be quite mobile and nearly fluid-like at and near  $j_c$ .

A couple of remarks should be made on the magnitude and the meaning of  $j_c$ . First,  $j_c$  is estimated by applying the Sharvin conductance formula to the experimental  $\hat{I}_b - \hat{G}_b$  relationship. Its magnitude of  $j_c$ , therefore, depends on the validity of the Sharvin conductance formula. Ertz *et al.* (Ertz *et al.*, 2000) and Kizuka (Kizuka, 2008) carried out direct TEM observations of Au contacts simultaneously with the conductance measurements and showed that the Sharvin formula tends to underestimate the contact size. If  $A$  derived from Eq. 5 is smaller than the actual contact area, the true current density at the instability would

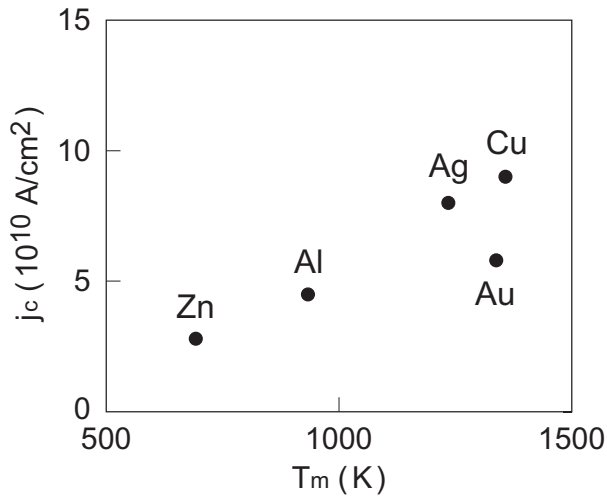


Fig. 10. Critical current density  $j_c$  for the contact instability is plotted against the melting point  $T_m$  of a metal. A linear correlation can be seen between  $j_c$  and  $T_m$ .

be lower than  $j_c$  shown in Fig. 10. For accurately determining  $j_c$ , we certainly need a reliable calibration formula that relates the conductance to the contact area. The Wexler conductance formula has been reported to yield better agreement with the TEM results than the Sharvin formula, but the Wexler formula contains a couple of fitting parameters, the values of which are unknown for most metals. Further accumulation of experimental data on the  $G - A$  relationship of various metals is highly awaited for the accurate estimation of  $j_c$ .

Another parameter in the Sharvin formula that affects the magnitude of  $j_c$  is the Fermi wavevector  $k_F$ . As mentioned in Sec. 3, the Sharvin formula assumes a situation where free electrons pass through a small orifice. The formula is therefore applicable to the "nearly free-electron" metals such as Au and Al but not necessarily to transition metals whose  $d$  and  $f$  electrons cannot be treated as free electrons. This makes it difficult to estimate  $j_c$  of most transition metals. Pt contacts, for example, exhibit linear  $\hat{I}_b - \hat{G}_b$  plot similar to that of noble metals. This result does not, however, yield  $j_c$  of Pt contacts because we cannot use the Sharvin formula for Pt to obtain the contact area. Again, the key issue is the lack of experimental  $G - A$  data on various metals.

A contact breaks when its conductance becomes  $\hat{G}_b$ , and  $j_c$  is the current density at  $G = \hat{G}_b$ . In this context,  $j_c$  can be considered as the critical current density for the current-induced contact break. It should, however, be noted that  $\hat{G}_b$  indicates the peak position of the break conductance distribution and represents the conductance at which a contact breaks with maximum likelihood. Because the distribution is not narrowly peaked at  $\hat{G}_b$  but broadly extended as seen in Fig. 7, a substantial number of contacts break at conductances other than  $\hat{G}_b$ . Thus,  $j_c$  is a statistical quantity and should be understood as the current density at which a contact breaks with maximum likelihood. Not all contacts break at  $j_c$  with 100% probability. A considerable fraction of contacts would survive the instability and shrink to smaller contacts, some of them even becoming single-atom contacts. These highly stable contacts might be the source of single-atom contacts occasionally formed under very high biases close to 2 V.

Under such high biases, the current-induced instability at  $j_c$  acts as a selection filter which discriminates stable contacts from marginal ones.

As mentioned in Sec. 2, the stability or the lifetime of an atom-sized contact depends not only the bias but also the internal force  $F$  appearing in Eqs. 2 and 3. In the break junction method, one cannot control the details of contact necking when a contact shrinks to a nanocontact. Thus, the produced atom-sized contacts would have a built-in tensile force of different strengths, and this wide dispersion in  $F$  would be the source of varied contact stability and the broad distribution of  $G_b$ . The same situation happens for the break voltage as we will show in the next section.

When the applied bias becomes sufficiently low, the current-induced instability no longer happens during the contact necking, and majority of the contacts shrink down to the size of atoms. The break of such atom-sized contacts takes place at certain preferred contact geometries and the break conductance distribution shows a couple of narrow peaks found at some specific values corresponding to the conductance of these preferred geometries (Fujii et al., 2005). Different from the  $\hat{G}_b$  peak, these peaks exhibit no shift with the bias. For  $V_a < 1.0$  V, the break conductance of Au exhibits a sharp peak at  $1G_0$  showing that most Au contacts break after they shrink to the single-atom contact. On the other hand, the same single-atom break becomes abundantly observed for Ag and Cu only at  $V_a < 0.1$  V and  $V_a < 0.3$  V, respectively. This comparison clearly indicates the superior high-bias stability of the single-atom contact of Au, which will be further discussed in the next section.

## 5.2 Break voltage

Under high applied biases, only the contacts of higher stability can survive the current-induced instability and become the single-atom contact. Experimental results on such instability-selected contacts would provide us biased information on the contact stability and cannot represent the high-bias/current stability of a majority of the single-atom contacts. To obtain proper information, it is therefore necessary to first produce single-atom contacts under low biases and then examine their stability by increasing the bias voltage and detecting the breakdown threshold. This is the experimental method depicted in Fig. 5(b).

As mentioned before, the first break-voltage measurement on a single-atom contact has been made by Hansen who used an Au-tip/Au-sample STM junction and produced the single-atom contacts of Au at 77 K in ultrahigh vacuum. By applying a fast voltage ramp, he could observe the contact disruption and measured the bias at the contact failure. He obtained the integral distribution of the break voltage and found that 90% of the Au single-atom contacts break at  $\sim 1.9$  V. Subsequently, Smit and coworkers (Smit et al., 2004) carried out a systematic study of the break voltage of Au and Pt single-atom contacts exploiting cryogenic MCBJ operated at 4 K, where atomic contacts and chains are stable almost indefinitely. Smit *et al.* could investigate not only the break voltage distribution but also its dependence on the atomic chain length. For the shortest single-atom chain, the break voltage distribution yields a mean break voltage  $\sim 1.2$  V and  $\sim 0.37$  V for Au and Pt, respectively.

Though these previous results obtained at low temperatures provide us a good measure of the break voltage of metal single-atom contacts, similar break-voltage experiments at room temperature are also needed for two reasons. First, for practical device applications, break voltage data at room temperature are more valuable, for example, for establishing the maximum rating of the single-atom contacts as device interconnects. Second, at room temperature, there would be less ambiguity in the contact temperature than at cryogenic

temperatures. As noted in Sec. 2, contacts can be significantly heated up at high biases when the ambient temperature is lower than the characteristic temperature  $T_V$  in Eq. 4. In experiments at 4 K, for example, the effective contact temperature at the break voltage of 1.2 V should not be 4 K but  $\sim 46$  K. On the other hand, at room temperature, the ambient temperature overwhelms  $T_V$  in Eq. 4, and the contact heating becomes negligible at 1.2 V. In return for these advantages, the single-atom contacts become short-lived at room temperature, and we have to carry out fast measurements for determining their break voltage.

Our procedures for measuring the break voltage of single-atom contacts are the following (Miura et al., 2009). First, a constant bias of 0.1 V is applied across a (contact) +  $R$  where  $R$  is a current-sensing resistor. When the contact is made open, the contact current decreases with reducing the contact size and reaches to a value corresponding to the single-atom conductance, which is  $1G_0$  for noble metals. If the single-atom state is stable for some time, the current remains constant and exhibits a plateau. Upon detecting such a  $1G_0$  current plateau, the bias is set to increase and the current increases accordingly. At a certain point, the contact ruptures and the current jumps down to zero. The break voltage can be obtained from the maximum applied bias before the contact failure. Figure 11 shows (a) the experimental setup and (b) a typical result of the break voltage measurement made, in this case, on an Au contact. Fabrication of single-atom contacts is made with the MCBJ method which has been briefly explained in Sec. 4. In Fig. 11(a), a block diagram of the conductance measuring circuit is also included. As in the experiment on the current-induced instability, a fast oscilloscope is used to monitor conductance transients at and near the contact breakdown. The conductance or the current can be obtained by measuring the voltage drop across  $R$ . The measured contact current is shown in the upper panel in Fig. 11(b). It decreases with time and, at point A in the figure, exhibits a plateau. This plateau appears at the current level corresponding to  $1G_0$  and hence signifies the formation of an Au single-atom contact. A trigger signal is generated at point A to start the bias ramp but delayed through a delay circuit before activating the bias source as shown in Fig. 11(a). As a result of this delay, the bias actually starts to increase at point B in the lower panel. The delay time is  $40\mu\text{s}$  for Au and Cu and  $10\mu\text{s}$  for Ag, Al, and AuAg alloys. This delay is needed to screen out marginal single-atom contacts. Upon starting the bias ramp, the contact current in the upper panel Fig. 11(b) increases linearly with time and suddenly drops to zero at point C which marks the contact breakdown. At a closer look, the contact current falls down not instantaneously but within a non-zero time interval, making it difficult to sharply define the point of breakdown. We therefore arbitrarily defined the breakdown point by the maximum of the  $I(t)$  curve. By taking into account the correction for the voltage drop across  $R$ , the break voltage is calculated as  $V_b = V_a - IR$  where  $V_a$  and  $I$  are their values at the current maximum.

Figure 12 summarizes the break voltage distribution measured for four metals at room temperature in ultrahigh vacuum. As for the break conductance shown in Figs. 7 and 8, a broad and single-peak distribution is commonly observed for the break voltage of four metals. The distribution of Cu appears relatively narrower, but its peak still covers a wide voltage range from 0.2 V to 1.4 V. In the case of Au, the break voltage distribution extends beyond 2 V. This is not the thermal broadening because a similar broad distribution is also observed for the break voltage of Au single-atom contacts at cryogenic temperatures. In Sec. 5.1, we pointed out that the wide distribution of the break conductance would be due to large fluctuations in the strength of the built-in tensile force  $F$  in Eqs. 2 and 3. The same fluctuations in  $F$  would also be responsible for the broadening of the break voltage distribution.

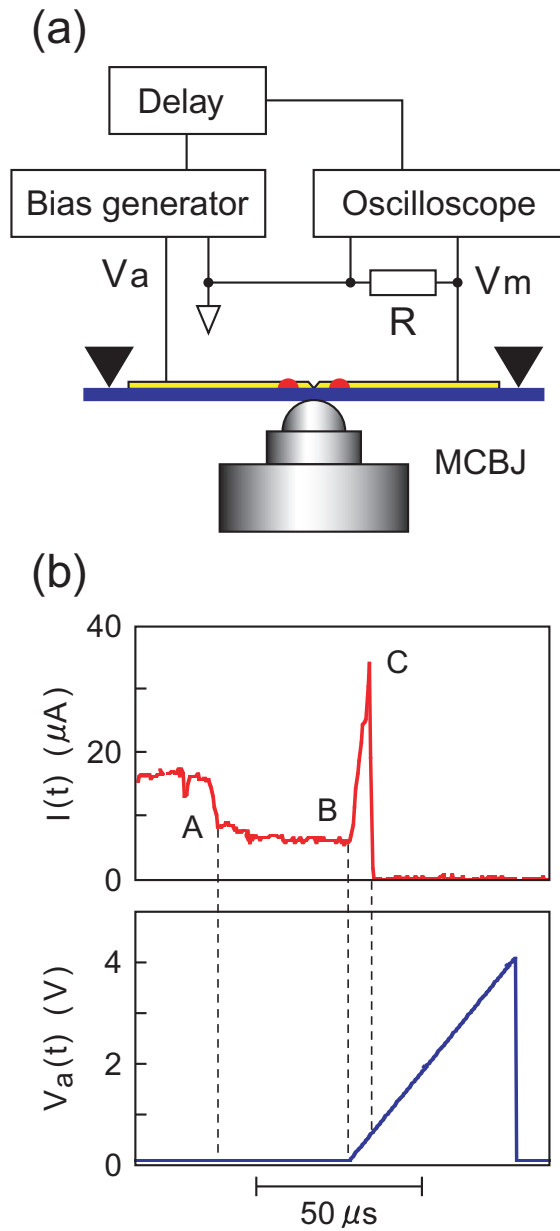


Fig. 11. Experimental setup (a) and typical temporal changes in the contact current and the bias voltage (b) in the break voltage measurements on an Au single-atom contact. See text for details.

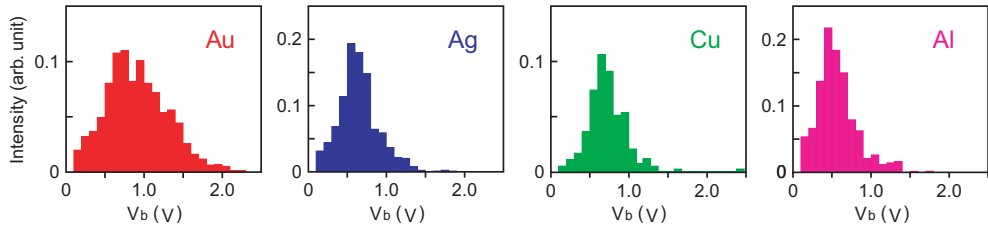


Fig. 12. Break voltage distribution obtained on single-atom contacts of Au, Ag, Cu, and Al at room temperature in ultrahigh vacuum.

The average break voltage is  $V_b(\text{Au}) = 0.93$  V,  $V_b(\text{Ag}) = 0.65$  V,  $V_b(\text{Cu}) = 0.69$  V, and  $V_b(\text{Al}) = 0.58$  V for Au, Ag, Cu, and Al single-atom contacts, respectively. This comparison simply indicates the superior high-bias stability of Au single-atom contacts over those of other metals. As we mentioned at the end of the previous section, the same conclusion is indirectly suggested from the break conductance data. The results of the break voltage experiment shown in Fig. 12 directly and quantitatively prove the high stability of the Au single-atom contact against high biases.

If we assume that the contact break occurs when  $E(V, F) \sim k_B T$  in Eq. 3, then  $V_b = (E_0 - \beta F - k_B T^*)/\alpha$  as we mentioned in Sec. 2. Thus, the observed higher  $V_b$  indicates larger  $E_0$  for the Au single-atom contact than that for Ag and Cu contacts, provided that  $\beta F$  would be the same for all metals. As mentioned in Sec. 2, Smit *et al.* (Smit *et al.*, 2004) report  $E_0(\text{Au}) = 0.738$  eV. No data are, however, available for  $E_0$  of other metals so that we cannot know whether  $E_0(\text{Au})$  is actually the largest or not. Some clues can, however, be obtained from the break force, i.e. the maximum tensile strength, of single-atom contacts. As for the break voltage, the break force can be expressed as  $F_b = (E_0 - \alpha V - k_B T^*)/\beta$ , and a larger  $E_0$  would yield a higher  $F_b$ . Again, the experimental value of  $F_b$  has been obtained only for two metals, Au and Pt, which show  $F_b(\text{Au}) \sim 1.5$  nN (Rubio-Bollinger *et al.*, 2001), and  $F_b(\text{Pt}) \sim 1$  nN (Kizuka & Monna, 2009), respectively. Fortunately, however, theoretical values are available for  $F_b$  of other metals (Bahn & Jacobsen, 2001; Pauly *et al.*, 2006). Though the magnitude of the calculated  $F_b$  does not necessarily conform well to the experimental values, all theories consistently predict higher tensile strength of Au and Pt single-atom contacts than that of Ag, Cu, and Ni. Thus, the observed higher  $V_b(\text{Au})$  is consistent with the results of these break force studies. It should, however, be noted that the estimation of  $V_b$  from  $E_0$  or  $F_b$  depends on the value of  $\alpha$  and  $\beta$  in Eq. 3, and the comparison of  $E_0$  and  $F_b$  of different metals would be meaningful only when these parameters little depend on metal species. As mentioned in Sec. 2, measurements of the conductance TLFs indicate that noble metals show nearly the same  $\alpha$  (Tsutsui *et al.*, 2006b). It thus seems not unreasonable to assume little variation of  $\alpha$  and  $\beta$  among metals, and the higher  $F_b$  of the Au single-atom contacts would be correlated with our observation of their higher  $V_b$ .

### 5.3 Break voltage of alloy contacts

In bulk alloys, foreign solute atoms usually act as a scattering center of electrons. Alloying, therefore, decreases the conductivity of host metals. This is, however, not the case of alloy single-atom contacts. The single-atom conductance of Au and Cu, for example, shows no substantial changes with the addition of Pd and Ni, respectively, up to a concentration as

high as 50 at% (Bakker et al., 2002; Enomoto et al., 2002). In the conductance histogram of AuPd and CuNi alloys, the single-atom peak of Au and Cu remains at  $1G_0$  and stays unshifted with alloying, though its intensity decreases nearly linearly with increasing the solute concentration. This result indicates that the single-atom conductance of alloy contacts is locally determined by the elemental species of an atom occupying the contact site. When a single Cu atom comes to the linking site, for example, the conductance becomes the single-atom conductance of Cu ( $G = 1G_0$ ), while it changes to that of Ni ( $\sim 1.3G_0$ ) when a Ni atom replaces the Cu atom. Such a conductance switching associated with the replacement of the contact atom has been actually observed on AuPt alloys (Heemskerk et al., 2002). Other alloy atoms locating nearby the contact site only make secondary contributions to the single-atom conductance.

Similar locality can thus be naturally expected for the break voltage of alloy single-atom contacts. Figure 13 shows the break voltage distribution obtained on the single-atom contacts of an Au-31at

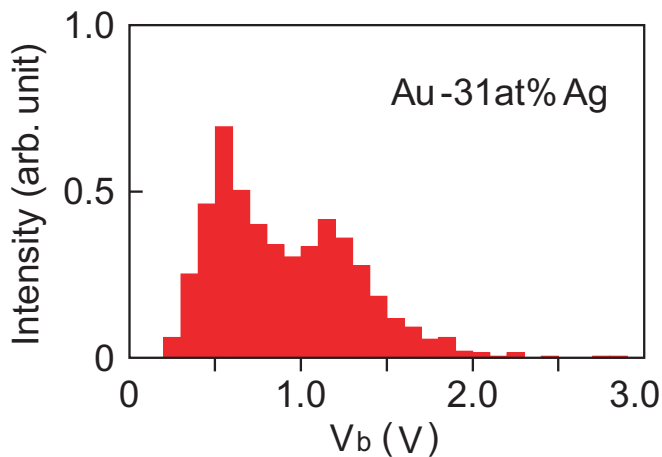


Fig. 13. Break voltage distribution obtained on single-atom contacts of an Au-31at%Ag alloy.

#### 5.4 Molecular junctions

Break-voltage measurements can be extended to single-molecule junctions or molecular links, where a single molecule, instead of a metal atom, bridges a pair of metal electrodes. Molecules in such junctions can be of full variety in species and in configurations and able to show various functionalities unobtainable by single metal atoms. As a result, single-molecule junctions are considered as a key active element in molecular devices, and a soaring number of theoretical and experimental studies have been made on various single-molecule junctions in the past decade.

Most of the previous studies are, however, concerned with the low-bias regime where the junction conduction is determined by the transmission function near the electrode Fermi level. However, many molecules have their HOMO and LUMO levels which do not necessarily locate near the Fermi level. As a result, the conduction through molecular junctions is usually made through the tail states of the HOMO and LUMO levels which are broadened by the

molecule-electrode coupling. To take various benefits of the resonant conduction through the HOMO and LUMO levels, one therefore has to apply high biases to encompass the HOMO and LUMO levels into the bias window. There is, however, no information as to how high biases one can apply to a single-molecule junction before it breaks down. A large number of  $I - V$  measurements have been made on various single-molecule junctions, and a few of them report the existence of a bias threshold beyond which a junction becomes unstable. However, such a high-bias threshold has been rarely studied in previous experimental investigations.

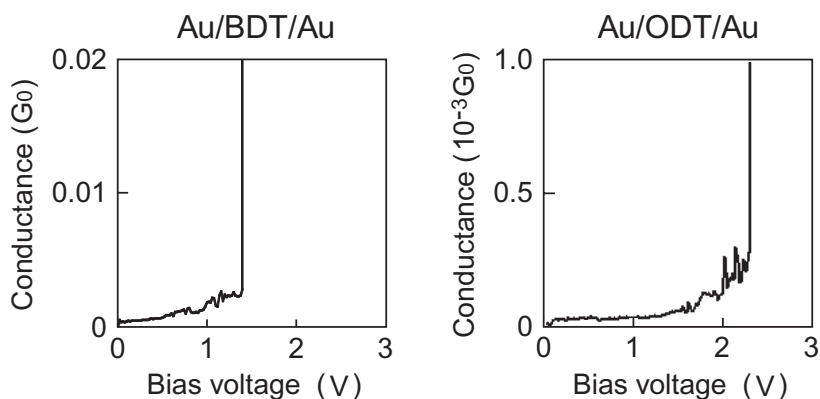


Fig. 14. High-bias instability observed on Au/BDT/Au and Au/ODT/Au single-molecule junctions at room temperature. The conductance jumps up at the instability.

Figure 14 shows a typical behavior of the molecular conductance when the bias surpasses the threshold (Hashimoto et al., unpublished; Teramae et al., 2008). Two conductance-voltage curves are shown for Au/benzenedithiol (BDT)/Au and Au/octanedithiol (ODT)/Au single-molecule junctions measured in Ar atmosphere at room temperature. The low-bias conductance of these junctions is  $0.01G_0$  and  $5 \times 10^{-4}G_0$ , respectively. In both  $G - V$  curves, the conductance first increases slowly with the bias and indicates positive nonlinearity in the  $I - V$  characteristics. At a threshold, the conductance jumps up, showing that the junction is coalesced. This high-conductance state remains until the junction is made open by mechanically pulling apart the electrodes.

The distribution of the threshold voltage  $V_{th}$  is shown in Fig. 15 (Hashimoto et al., unpublished; ?). For both Au/BDT/Au and Au/ODT/Au junctions, the distribution is broad and single-peaked, quite similar to the break-voltage distribution of single-atom contacts of metals shown in Fig. 12. It is also noted in the figure that the less conductive Au/ODT/Au junction shows higher threshold voltage compared to that of the Au/BDT/Au junctions.

This dependence of the threshold voltage on the (low-bias) junction conductance can be seen more clearly in Fig. 16 where the average threshold is plotted against the logarithm of the junction resistance  $\log R$ . Both Au/BDT/Au and Au/ODT/Au junctions are known to take a couple of junction states of different conductances, and the threshold data of these different states (three for Au/BDT/Au and two for Au/ODT/Au, respectively) are included in the plot. The resistances of Au/BDT/Au and Au/ODT/Au junctions differ by two orders of magnitude, but their threshold data lay on a single straight line.

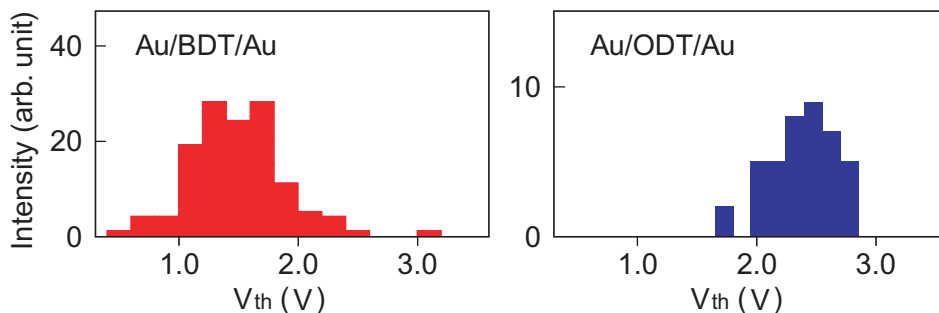


Fig. 15. Distribution of the instability threshold voltage obtained on Au/BDT/Au and Au/ODT/Au single-molecule junctions.

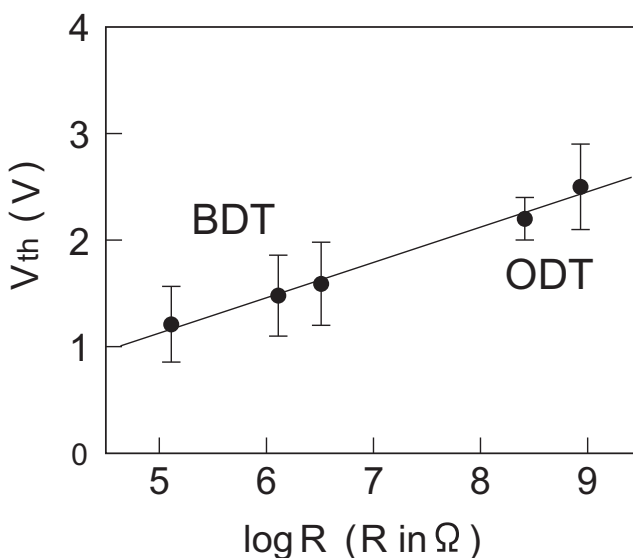


Fig. 16. Dependence the instability threshold on  $\log R$ .

As  $\log R$  of molecular junctions scales roughly linearly with the molecular length, or the electrode separation of the junction, the observed linear correlation between  $V_{th}$  and  $\log R$  indicates the existence of a critical field strength for the onset of the junction instability. Also, the observation that the  $V_{th}$  data of different molecular junctions lay on the same straight line indicates that a crucial parameter for the instability is not the species of bridging molecule but the magnitude of  $\log R$  or the electrode gap distance. This means that in the high-bias instability of single-molecule junctions, the molecule merely acts as an insulating material separating electrodes and defining its gap distance. Chemical properties of the bridging molecule little matter for the instability threshold. It should be noted that similar field-induced coalescence of electrodes is also observed in the high-bias breakdown of STM tunnel junctions (Mamin et al., 19908) and Au/alkane-SAM/Au junctions (Wold & Frisbie, 2001; Zhao & Uosaki, 2001).

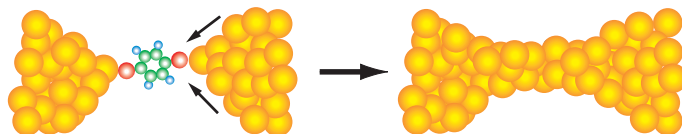


Fig. 17. Possible breakdown or collapse of electrodes at the high bias instability.

Because the junction conductance jumps up at the threshold as shown in Fig. 14, the electrodes are likely to become coalesced when the bias reaches the threshold, as schematically illustrated in Fig. 17. In such a case, the high-bias instability takes place not inside the molecule but at the electrodes. Thus, for improving the toughness of molecular junctions against high biases, one has to first select electrode materials more resistant to the high-bias collapse than Au.

### 5.5 Concluding remark

With recent developments in experimental techniques such as SPM and MCBJ, we can now routinely fabricate single-atom or single-molecule junctions, which are the smallest functional contact realizable in the world. We have already accumulated a large amount of knowledge on the conductance or the resistance of these ultrasmall junctions, and the mechanisms of their electronic conduction have been well documented. Still, we cannot answer a simple question how large electronic current one can flow through these junctions. Considering a huge number of studies devoted to atomic and molecular junctions, it seems quite strange that so few studies have been made on this academically interesting and practically important problem. Our experimental results described in this article have clarified some aspects of the high-bias/current instability for atom-sized contacts of a few metals and molecules, but there remain a large number of atomic scale junctions, the stability of which has been yet unexplored and awaits further experimental investigations. One noticeable characteristic, common to all three parameters  $G_b$ ,  $V_b$  and  $V_{th}$  studied in this work, is the appreciable broadening of their distribution. As we mentioned before, this broadening is likely due to fluctuations in the strength of the internal tensile force  $F$  acting on the breaking contacts. To make the distribution narrower and improve the accuracy of instability parameters, it would therefore be necessary to control the strength of  $F$  in each contact. High-bias experiments on such force-controlled contacts would provide us a direct test of Eq. 3 and give some useful insight about the microscopic origin of that empirical equation.

### Acknowledgements

The author would like to thank his former graduate students T. Minowa, A. Fujii, M. Tsutsui, Y. Teramae, and D. Miura for their carrying out various high-bias experiments described in this article. This work is partially supported by KAKENHI 17310072.

### 6. References

- Agraït, N.; Levy Yeyati, A. & van Ruitenbeek, J. M. (2003). Quantum properties of atomic-sized conductors. *Physics Reports* 377, 81-279.
- Bahn S. R. & Jacobsen, K. W. (2001). Chain formation of metal atoms *Physical Review Letters* 87, 266101(1-4).
- Bakker, D. J.; Noat, Y.; Yanson, A. I. & van Ruitenbeek, J. M. (2002). Effect of disorder on the conductance of a Cu atomic point contact. *Physical Review B* 65, 235416(1-5).

- Cuevas, J. C.; Levy Yeyati, A. & Martín-Rodero, A. (1998). Microscopic origin of conductance channels in atomic-size contacts. *Physical Review Letters* 80, 1066-1069.
- Enomoto, A.; Kurokawa, S. & Sakai, A. (2002). Quantized conductance in Au-Pd and Au-Ag alloy nanocontacts. *Physical Review B* 65, 125410(1-6).
- Erts, D.; Olin, D.; Ryen, L.; Olsson, E. & Tholen, A. (2000). Maxwell and Sharvin conductance in gold point contacts investigated using TEM-STM. *Physical Review B* 61, 12725(1-3).
- Fujii, A.; Tsutsui, M.; Kurokawa, S. & Sakai, A. (2005). Break conductance of noble metal contacts. *Physical Review B* 72, 045407(1-6).
- Hashimoto, S.; Kurokawa, S. & Sakai, A. *unpublished*.
- Heemskerk, J. W. T.; Noat, Y.; Bakker, D. J.; van Ruitenbeek, J. M.; Thijsse, B. J. & Klaver, P. (2003). Current-induced transition in atomic-sized contacts of metallic alloys. *Physical Review B* 67, 115416(1-5).
- Kizuka, T. (2008). Atomic configuration and mechanical and electrical properties of stable gold wires of single-atom width. *Physical Review B* 77, 155401(1-11).
- Kizuka T. & Monna K. (2009). Atomic configuration, conductance, and tensile force of platinum wires of single-atom width. *Physical Review B* 80, 205406(1-9).
- Mamin, H. J.; Guethner, P. H. & Rugar, D. (1990). Atomic emission from a gold scanning-tunneling-microscope tip. *Physical Review Letters* 65, 2418-2421.
- Minowa, T.; Kurokawa, S. & Sakai, A. (2005). Break Conductance of Al Nanocontacts. *Physica E* 29, 495-499
- Minowa, T.; Tsutsui, M.; Kurokawa, S. & Sakai, A. (2005). Break conductance of Pt nanocontacts. *Japanese Journal of Applied Physics* 44, 6321-6326.
- Miura, D.; Iwata, K.; Kurokawa, S. & Sakai, A. (2009). Break voltage of the  $1G_0$  contact of noble metals and alloys. *e-Journal of Surface Science and Nanotechnology* 7, 891-897.
- Pauly, F.; Dreher, M.; Viljas, J. K.; Häfner, M.; Cuevas, J. C. & Nielaba, P. (2006). Theoretical analysis of the conductance histograms and structural properties of Ag, Pt, and Ni nanocontacts. *Physical Review B* 74, 235106(1-21).
- Rubio-Bollinger, G.; Bahn, S. R.; Agraït, N.; Jacobsen, K. W. & Vieira, S. (2001). Mechanical properties and formation mechanisms of a wire of single gold atoms. *Physical Review Letters* 87, 026101(1-4).
- Smit, R. H. M.; Untiedt, C. & Ruitenbeek, J. M. (2004). The high-bias stability of monoatomic chains. *Nanotechnology* 15, S472-S478.
- Suzuki, R.; Mukai, Y.; Tsutsui, M.; Kurokawa, S. & Sakai, A. (2006). Conductance of atom-sized Zn contacts. *Japanese Journal of Applied Physics* 45, 7217-7223.
- Teramae, Y.; Horiguchi, K.; Hashimoto, S.; Tsutsui, M.; Kurokawa, S. & Sakai, A. (2008). High-bias breakdown of Au/1,4benzenedithiol/Au junctions. *Applied Physics Letters* 93, 083121(1-3).
- Todorov, T. N.; Hoekstra, J. & Sutton, A. P. (2001). Current-induced embrittlement of atomic wires. *Physical Review Letters* 86, 3606-3609.
- Tsutsui, M.; Kurokawa, S. & Sakai, A. (2006). Bias-induced local heating in Au atom-sized contacts. *Nanotechnology* 17, 5334-5338.
- Tsutsui, M.; Shoji, K.; Taniguchi, M. & Kawai, T. (2008). Formation and self-breaking mechanism of stable atom-sized junctions. *Nano Letters* 8, 345-349.
- Tsutsui, M.; Teramae, Y.; Kurokawa, S. & Sakai, A. (2006). Local heating in noble metal nanocontacts under high biases at 77 K. *Applied Surface Science* 252, 8677-8682.

- Wold D. J. & Frisbie, C. D. (2001). Fabrication and characterization of metal-molecule-metal junctions by conducting probe atomic force microscopy. *Journal of American Chemical Society* 123, 5549-5556.
- Yanson, A. I.; Rubio-Bollinger, G.; van den Brom, H. E.; Agraït, N. & van Ruitenbeek, J. M. (1998). Formation and manipulation of a metallic wire of single gold atoms. *Nature (London)* 395, 783-785.
- Zhao, J. & Uosaki, K. (2003) Dielectric properties of organic monolayers directly bonded on silicon probed by current sensing atomic force microscope. *Applied Physics Letters* 83, 2034-2036.

# Electron Diffraction and HRTEM Structure Analysis of Nanowires

José Reyes-Gasga, David Romeu and Alfredo Gómez-Rodríguez  
*Departamento de Materia Condensada, Instituto de Física, Universidad Nacional  
Autónoma de México, Apartado postal 20-364, 01000, México D.F.  
México*

## 1. Introduction

In this work an electron diffraction analysis and an electron microscope structure study of nanowires are presented. Nanowires, as one-dimensionally nanostructured materials, have become the focus of intensive research due to their great potential for use as building blocks in the fabrication of electronic, optoelectronic, and sensor devices with nanoscale dimensions. Therefore, the importance of studying and understanding the electron diffraction phenomena and their implications over their electron microscopy images is great.

It has been indicated that the silver nanowires are highly faceted at nanometric scales. A comprehensive electron diffraction study on the structure of nanowires, firstly in a general approach and then in the specific case of silver nanowires, will be presented in this chapter. The important role of twinning in determining the habit of the final morphology will also be discussed.

One interesting feature of silver, gold, and copper pentagonal cross-section nanowires, is their remarkable structure (Gao et al., 2003; Giersig et al., 2004; Hofmeister et al., 2002; Sun et al., 2002; 2003; Zhao et al., 2005). It has been proposed that this structure evolved from a multi-twin decahedral nanoparticle growing in the [110] direction by stabilizing more effectively the newly formed 100 facets than the 111 facets and their electron diffraction patterns present "forbidden" spots.

The pentagonal arrangement in the multiple twinned particles (MTP) is quite known. MTP nanoparticles of transition metals with face-centered cubic (FCC) lattice (Heinemann et al., 1979; Howie & Marks, 1984; Sun et al., 2002) have been reported. On the basis of these studies, the basic structure of a decahedral particle was described as the junction of five tetrahedral single crystals with twin-related adjoining faces along a common [110] edge in such a way that the [110] direction parallel to the five-fold axis is perpendicular to the  $\langle 110 \rangle$  direction of the edges, and that the normal vectors to all of them are parallel to  $\langle 100 \rangle$ . The theoretical angle between two [111] planes is  $70.5^\circ$ , so by joining 5 tetrahedrons, which are bounded by 111 facets, a gap of  $7.5^\circ$  is generated. Thus, to fill this gap some internal strain is necessary, giving place to dislocations and other structure defects (Heinemann et al., 1979; Howie & Marks, 1984; Sun et al., 2002). These defects have been observed in the TEM cross-sectional images of the mentioned penta-twinned nanowires (Chen et al., 2004).

When observing nanowires with the high-resolution transmission electron microscope (HRTEM) very often we observe a contrast that can be interpreted at first sight as coming

from some kind of an aperiodic array. Based on a five-twinned decahedron, it has been shown (Reyes-Gasga et al., 2006) that the HRTEM images of pentagonal cross-section nanowires can be interpreted as a moiré pattern contrast, and that their selected-area electron diffraction (SAED) patterns can be also completely generated through the same multi-twinned decahedron basis (Reyes-Gasga et al., 2006). However, up to today a completely satisfactory explanation of all the features present in the structure of these penta-twinned nanowires is lacking.

In this work the origin and structure analysis of the HRTEM contrast observed in nanowires will be also presented and it will be shown that they are closely related to a decahedron-base structure. To obtain the proper interpretation of the contrast presented by their HRTEM images, an understanding of the origin of these "forbidden" spots is necessary. We will, therefore, comment on the origin of these forbidden spots observed in the electron diffraction patterns of nanowires. The "forbidden" spots have been successfully indexed as corresponding to the first order Laue Zone (FOLZ) superimposed with the spots of the zero-order Laue zone (ZOLZ). Therefore, the HRTEM images presented a contrast produced by the interference of the zero-order Laue zone (ZOLZ) and FOLZ spots. The analysis of using of forbidden spots in the study of nanostructures has been successfully used in the interpretation of diffraction patterns of nanoparticles (Reyes-Gasga et al., 2008; Romeu & Reyes-Gasga, 2002) and it is also presented.

In order to do a comprehensible reading of this chapter, we include, among other, the following topics:

- A brief introduction to the electron diffraction phenomenon, including the Ewald sphere and the Laue zones.
- Diffraction patterns and images of twinning structures.
- A brief introduction to HRTEM image formation.
- Changes in the electron diffraction as a function of the sample size.
- Diffraction patterns and HRTEM images of nanowires.

## 2. Reciprocal lattices

Given three vectors  $\hat{a}$ ,  $\hat{b}$  and  $\hat{c}$  that span a lattice, we can always obtain another set  $\hat{a}^*$ ,  $\hat{b}^*$  and  $\hat{c}^*$  (called "reciprocal vectors") and defined through:

$$\hat{a} \cdot \hat{a}^* = \hat{b} \cdot \hat{b}^* = \hat{c} \cdot \hat{c}^* = 1 \quad (1)$$

$$\hat{a} \cdot \hat{b}^* = \hat{a} \cdot \hat{c}^* = \hat{b} \cdot \hat{c}^* = \hat{b} \cdot \hat{a}^* = \hat{c} \cdot \hat{a}^* = \hat{c} \cdot \hat{b}^* = 0 \quad (2)$$

The reciprocal vectors thus defined have several properties among which we may list:

a) The three reciprocal vectors are linearly independent (i.e. they are not coplanar) and span another lattice, called "reciprocal lattice".

Both sets  $\{\hat{a}, \hat{b}, \hat{c}\}$  and  $\{\hat{a}^*, \hat{b}^*, \hat{c}^*\}$  are bases for the three-dimensional Euclidean space. Given an arbitrary vector  $P$  there exist unique numbers  $x, y, z, x', y', z'$  and  $z'$  such that

$$P = x\hat{a} + y\hat{b} + z\hat{c} \quad (3)$$

$$P = x'\hat{a}^* + y'\hat{b}^* + z'\hat{c}^* \quad (4)$$

and, taking dot products, we can easily see that

$$P \cdot \hat{a}^* = x \quad (5)$$

$$P \cdot \hat{b}^* = y \quad (6)$$

$$P \cdot \hat{c}^* = z \quad (7)$$

$$P \cdot \hat{a} = x' \quad (8)$$

$$P \cdot \hat{b} = y' \quad (9)$$

$$P \cdot \hat{c} = z' \quad (10)$$

and

$$P = (P \cdot \hat{a}^*)\hat{a} + (P \cdot \hat{b}^*)\hat{b} + (P \cdot \hat{c}^*)\hat{c} \quad (11)$$

$$P = (P \cdot \hat{a})\hat{a}^* + (P \cdot \hat{b})\hat{b}^* + (P \cdot \hat{c})\hat{c}^* \quad (12)$$

b) the relationship between both sets of vectors can be cast in an explicit way:

$$\hat{a}^* = \frac{\hat{b} \times \hat{c}}{V} \quad (13)$$

$$\hat{b}^* = \frac{\hat{c} \times \hat{a}}{V} \quad (14)$$

$$\hat{c}^* = \frac{\hat{a} \times \hat{b}}{V} \quad (15)$$

where

$$V = \hat{a} \cdot \hat{b} \times \hat{c} \quad (16)$$

is the volume of the unit cell. In fact, an explicit evaluation shows that the volume  $V^*$  of the reciprocal lattice unit cell is given by

$$V^* = \hat{a}^* \cdot \hat{b}^* \times \hat{c}^* = \frac{1}{V} \quad (17)$$

c) consider a plane containing at least three non collinear lattice points (a "crystallographic plane"). Let  $P$ ,  $Q$  and  $R$  be three such points, a normal to the plane is given by

$$N = (Q - P) \times (R - P) \quad (18)$$

and upon expanding we see that  $N$  can be rewritten as

$$N = VG \quad (19)$$

for some  $G$  in the reciprocal lattice. The conclusion is that the normal to a crystallographic plane can always be taken to be a reciprocal lattice vector.

Furthermore, this implies that the vector equation for a crystallographic plane has the form

$$P \cdot G = z \quad (20)$$

where  $z$  is an integer.

d) conversely, given a reciprocal lattice vector  $G$  the plane

$$P \cdot G = z \quad (21)$$

(with integer  $z$ ) is a crystallographic plane (with some further qualifications as discussed below).

As a matter of fact we have that if  $P = h\hat{a} + k\hat{b} + l\hat{c}$  and  $G = u\hat{a}^* + v\hat{b}^* + w\hat{c}^*$  the corresponding plane equation is given by

$$hu + kv + lw = z \quad (22)$$

and we know (from number theory) that such an equation has integer solutions if and only if  $\text{gcd}(u, v, w) \mid z$  (by gcd we mean the greatest common divisor). In particular, notice that in the specific case  $z = 1$  there will be solutions if and only if  $\text{gcd}(u, v, w) = 1$  (the numbers  $u, v$  and  $w$  are relatively prime).

e) the Miller indices of the plane with normal  $G$  can be calculated easily. The plane will intersect the  $\hat{a}$  axis whenever there is a real number  $r$  such that  $P = r\hat{a}$  lies on the plane. Consequently  $P \cdot G = r\hat{a} \cdot G = z$  and

$$r = \frac{z}{\hat{a} \cdot G} \quad (23)$$

(provided  $\hat{a} \cdot G \neq 0$ , the case  $\hat{a} \cdot G = 0$  will be considered later). Similarly, the intersections with the  $\hat{b}$  and  $\hat{c}$  axes will be given by vectors  $Q = s\hat{b}$  and  $R = t\hat{c}$  that satisfy the conditions

$$s = \frac{z}{\hat{b} \cdot G} \quad (24)$$

$$t = \frac{z}{\hat{c} \cdot G} \quad (25)$$

The reciprocals of these intersections are

$$\frac{1}{r} = \frac{\hat{a} \cdot G}{z} \quad (26)$$

$$\frac{1}{s} = \frac{\hat{b} \cdot G}{z} \quad (27)$$

$$\frac{1}{t} = \frac{\hat{c} \cdot G}{z} \quad (28)$$

equations that can be considered as valid even when  $\hat{a} \cdot G$  or  $\hat{b} \cdot G$  or  $\hat{c} \cdot G$  is zero.

But if  $G = u\hat{a}^* + v\hat{b}^* + w\hat{c}^*$ , all this implies that

$$\frac{1}{r} = \frac{u}{z} \quad (29)$$

$$\frac{1}{s} = \frac{v}{z} \quad (30)$$

$$\frac{1}{t} = \frac{w}{z} \quad (31)$$

and the Miller indices of the plane are simply  $(uvw)$ .

A normal to the plane with indices  $u, v, w$  is the vector  $u\hat{a}^* + v\hat{b}^* + w\hat{c}^*$ , for this reason both the plane and the reciprocal lattice vector normal to the plane are labeled as  $(uvw)$ . Conversely, given a reciprocal lattice vector  $(uvw)$ , it is normal to a family of planes with Miller indices that can be obtained from  $u, v$  and  $w$  dividing them by their greatest common divisor (however, most of the time one simply assumes this divisor to be 1).

f) the distance between two consecutive lattice planes with indices  $u, v$  and  $w$  is precisely

$$d = |(uvw)|^{-1} \quad (32)$$

(the reciprocal to the reciprocal lattice vector size). Bear in mind that  $u, v$  and  $w$  are coprime, otherwise it might appear that there are lattice planes arbitrarily close to each other.

In order to prove this important result consider planes

$$P \cdot G = z \quad (33)$$

where  $G$  lies in the reciprocal lattice and  $z$  is an integer. Assume  $\text{gcd}(u, v, w) = 1$  so  $z$  can be any integer. Next, take the planes for which  $z = 0$  and  $z = 1$ . The distance between these planes is the length of the vector parallel to  $G$  going from the plane with  $z = 0$  to the plane with  $z = 1$ . This vector will be of the form

$$P = xG \quad (34)$$

but since

$$P \cdot G = 1 = x |G|^2 \quad (35)$$

we conclude that

$$x = \frac{1}{|G|^2} \quad (36)$$

and the distance is

$$|P| = |xG| = \frac{|G|}{|G|^2} = \frac{1}{|G|} \quad (37)$$

so the distance between planes  $(uvw)$  is

$$d = \frac{1}{|G|} \quad (38)$$

where

$$G = u\hat{a}^* + v\hat{b}^* + w\hat{c}^* \quad (39)$$

If  $\text{gcd}(u, v, w) \neq 1$

$$d = \frac{\text{gcd}(u, v, w)}{|G|} \quad (40)$$

g) the lattice that is reciprocal to the reciprocal lattice is the original lattice.

h) the rational index law, known long before the discovery of x-ray diffraction, states that crystallographic planes always have rational indices.

i) the angle between two crystallographic planes is the angle between the reciprocal lattice vectors that are normal to the planes. This entails the so called law of the constancy of angles: in every crystal only certain angles between planes can be found, they correspond to low index reciprocal lattice vectors.

### 3. Diffraction

The electrons leaving the electron gun are characterized by having very nearly the same energy  $E$ , which is typically of the order of some 100 *kev*. They travel forming a well collimated beam (beam divergences of the order of thousandths of radian) and the radiation may be very well represented as a plane wave of wavelength  $\lambda$ .

$\lambda$  and  $E$  are related by

$$E = \frac{h^2}{2m\lambda^2} \quad (41)$$

where  $h$  is Planck's constant and  $m$  is the electron mass. The momentum  $\vec{p}$  of the electron is given as  $h\vec{k}$  where  $\vec{k}$  is a vector of size  $|\vec{k}| = \frac{1}{\lambda}$  and has the same direction as the electron beam ( $\vec{k}$  is known as electron "wave vector"). From these relationships it follows that

$$E = \frac{h^2 |\vec{k}|^2}{2m} \quad (42)$$

For a given energy  $E$ , the possible values for  $\vec{k}$  lie on a sphere of radius  $\frac{1}{\lambda}$ . This sphere is known as Ewald's sphere.

The sample under study is hit by the incoming electrons, some of them leave the sample unaltered (transmitted beam) whereas some are elastically dispersed (diffracted beams). In this work we assume that the sample is crystalline and that the sample-radiation interaction is elastic (i.e. that the electrons don't change their energy).

The detection system is formed by a photographic plate or an electron detector. The record of the radiation scattered in various directions forms the "diffraction pattern".

#### 3.1 The diffraction grating

In order to understand the geometry of the diffraction phenomenon, first consider a simple one-dimensional row of identical atoms, figure 1.

Let  $\hat{a}$  be the vector generating this lattice. Consider neighboring atoms  $B$  and  $C$  and let the incident radiation have wave vector  $\vec{k}_0$ . Far from the row, as in elementary optics, what is observed depends on the phase difference between the rays leading to constructive or destructive interference. An observer far from the grating will see that the phase difference between rays from  $B$  and  $C$  is given by  $\delta$  where

$$\delta = |\vec{a}| (\cos(\alpha) - \cos(\alpha_0)) \quad (43)$$

If we call  $\vec{k}$  the wave vector after the grating, we have that

$$\delta = \lambda (\vec{k} - \vec{k}_0) \cdot \vec{a} \quad (44)$$

and, since in order to obtain constructive interference we must have

$$\delta = n\lambda \quad (45)$$

(with  $n$  being an integer) we have that the condition for constructive interference becomes

$$(\vec{k} - \vec{k}_0) \cdot \vec{a} = n\lambda \quad (46)$$

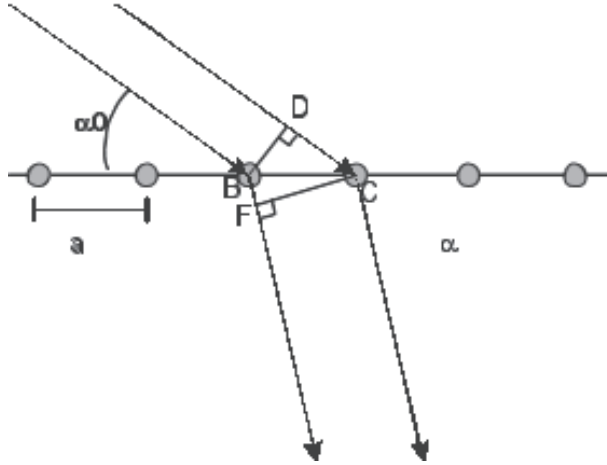


Fig. 1. Basic geometry of the one dimensional grid.

or

$$(\vec{k} - \vec{k}_0) \cdot \vec{a} = n \quad (47)$$

### 3.2 The three-dimensional crystal

A real three dimensional crystal can be thought of as a grid extending in three directions. Consequently if the crystal is generated by  $\hat{a}$ ,  $\hat{b}$  and  $\hat{c}$  the condition for constructive interference will be given by three equations similar to the previous one :

$$(\vec{k} - \vec{k}_0) \cdot \vec{a} = m \quad (48)$$

$$(\vec{k} - \vec{k}_0) \cdot \vec{b} = n \quad (49)$$

$$(\vec{k} - \vec{k}_0) \cdot \vec{c} = p \quad (50)$$

with  $m$ ,  $n$  and  $p$  being integers. These equations are known as "Laue equations".

### 3.3 The fundamental equation

If we now call  $\vec{g} = (\vec{k} - \vec{k}_0)$  and express this vector in terms of  $\hat{a}^*$ ,  $\hat{b}^*$  and  $\hat{c}^*$  we will have that

$$\vec{g} = x\hat{a}^* + y\hat{b}^* + z\hat{c}^* \quad (51)$$

where  $x$ ,  $y$  and  $z$  are three numbers to be determined. Multiplying this equation by  $\hat{a}$ ,  $\hat{b}$  and  $\hat{c}$  we have that

$$x = \vec{g} \cdot \hat{a} \quad (52)$$

$$y = \vec{g} \cdot \hat{b} \quad (53)$$

$$z = \vec{g} \cdot \hat{c} \quad (54)$$

so (using Laue's equations)

$$\vec{g} = m\hat{a}^* + n\hat{b}^* + p\hat{c}^* \quad (55)$$

The diffraction condition is that  $\vec{g}$  be a reciprocal lattice vector.

### 3.4 Ewald's construction

The basic geometry for diffraction is shown in figure 2. Here we have indicated the incident

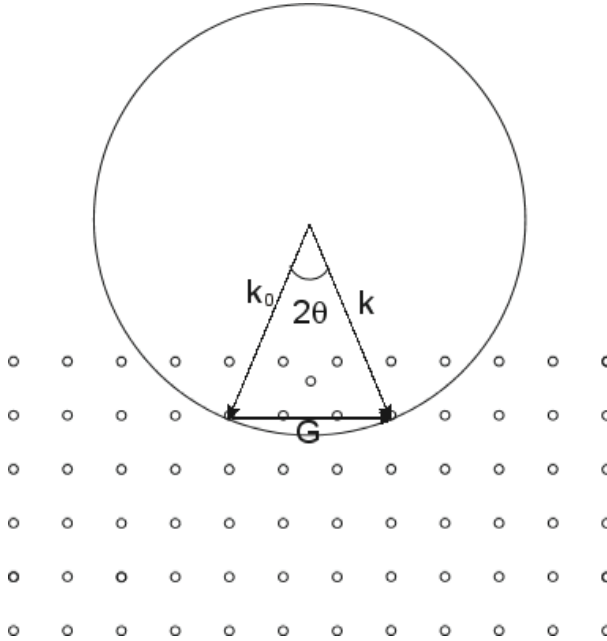


Fig. 2. Basic geometry for diffraction. The Ewald sphere is shown together with the diffraction condition.

and diffracted wave vectors ( $\hat{k}_0$  and  $\hat{k}$  respectively), both are on Ewald's sphere as they correspond to electrons with the same energy. The tip of vector  $\hat{k}_0$  has been placed at the origin of the reciprocal lattice and the tip of  $\hat{k}$  has been placed over a point  $\hat{g}$  in the reciprocal lattice to better illustrate that  $\hat{k} - \hat{k}_0$  is a reciprocal vector.

### 3.5 Bragg's law

There is a very simple way of visualizing the fundamental diffraction equation. In figure 3 we show schematically a family of planes that have a distance  $d$  ("interplanar distance").

Call  $\vec{g}$  the reciprocal lattice vector that is normal to these planes and, as we have already seen, it satisfies  $d = |\vec{g}|^{-1}$ . We also show (as arrows) the wave vectors  $\vec{k}_0$  and  $\vec{k}$  of the incident and diffracted waves. From the figure one can see that the angle  $\theta$  between  $\vec{k}_0$  and any plane is the same as the angle between  $\vec{k}$  and the planes. This angle is called "Bragg angle".

Since  $\vec{g} = (\vec{k} - \vec{k}_0)$ , taking the dot product of the equation with itself; we have that

$$|\vec{k}|^2 + |\vec{k}_0|^2 - 2\vec{k} \cdot \vec{k}_0 = |\vec{g}|^2 \quad (56)$$

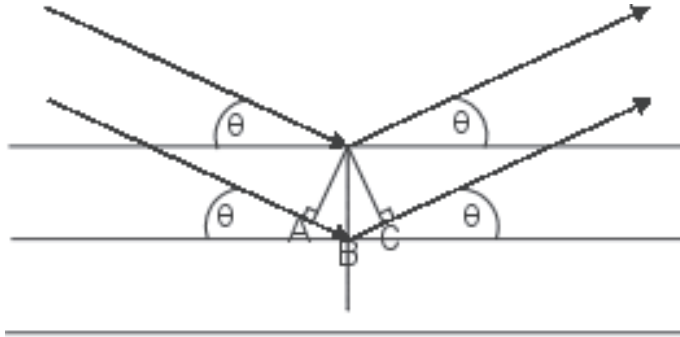


Fig. 3. Bragg’s construction. The crystallographic planes behave as mirrors that reflect the radiation producing interference.

or

$$2 | \vec{k} |^2 (1 - \cos(2\theta)) = \frac{1}{d^2} \tag{57}$$

where we have used the fact that the sizes of the incident and diffracted wave vectors are the same. Using a well known trigonometric identity for the cosine of the double of an angle we obtain

$$2d \sin(\theta) = \lambda \tag{58}$$

Now, here we have used a  $\vec{g}$  such that  $d = | \vec{g} |^{-1}$  but in the fundamental equation  $\vec{g}$  is any reciprocal lattice vector. For this reason we must modify the formula above to include all integer multiples of  $\vec{g}$ . Finally

$$2d \sin(\theta) = n \lambda \tag{59}$$

and this is the famous Bragg equation. In geometrical terms we can say that the crystal behaves like a family of mirrors, there being one such a family for every set of parallel crystal planes. Radiation is reflected specularly by each family( that is, with equal incidence and reflection angles). The only difference with respect to ordinary mirrors is that the beams are reflected (diffracted) only when they arrive at the mirror forming the “right” angle, that is, Bragg’s angle  $\theta$ .

### 3.6 Approximating Ewald’s sphere to a plane.

In practice, for electrons, the radius of the sphere ( $= \frac{1}{\lambda}$ ) is very large compared to the reciprocal lattice vectors. Consequently it is possible to approximate the sphere to a plane in a neighborhood of the origin of reciprocal space. If the incident wave vector is  $\vec{k}_0$  then the sphere resembles a plane with normal  $\vec{k}_0$  and going through the origin of the reciprocal lattice. Ordinarily we don’t give  $\vec{k}_0$  directly but rather its direction  $[hkl]$  in terms of the lattice. This vector is termed “zone axis”.

It is important to remark that this approximation is not a good one for x-rays because in this case the radius of Ewald’s sphere is comparable to the smallest reciprocal lattice vectors.

### 3.7 An example

Consider an FCC crystal and assume the beam is along the  $[001]$ . A reciprocal lattice point  $(uvw)$  will contribute to the diffraction pattern if it satisfies

$$[001] \cdot (uvw) = 0 \quad (60)$$

The smallest vectors satisfying this equation and that also satisfying the condition that all of the indices are even or all of them are odd are  $(200)$  and  $(020)$  so the diffraction pattern will consist of all the integer combinations of these vectors.

## 4. Higher order Laue zones

For a given zone axis  $[hkl]$  the planes

$$[hkl](uvw) = 0 \quad (61)$$

give, as indicated above, the diffraction pattern. But sometimes other reciprocal lattice planes also contribute to the pattern, and they are called "higher order Laue zones" (HOLZ). They may arise as a result of having a very thin crystal or as a result of having an incomplete number of layers in a given crystallographic direction. The ordinary case  $z = 0$  is termed "zeroth order Laue zone" or ZOLZ.

Whatever the physical origin of these "forbidden spots", their geometry can be calculated for cubic crystals in two equivalent ways:

1. Calculate the various reciprocal lattice planes by means of

$$[hkl](uvw) = n \quad (62)$$

where  $n$  is an integer. Then project the resulting points onto the zeroth-order Laue Zone  $[hkl](uvw) = 0$ . Here  $[hkl]$  is the direction of the incoming beam.

2. Calculate the lattice plane

$$(u'v'w')[h'k'l'] = 0 \quad (63)$$

where now  $(u'v'w')$  is a vector parallel to the incoming beam. Then calculate the (two-dimensional) lattice reciprocal to the lattice plane.

Both approaches give the same answer. The second method calculates a projection in reciprocal space that is reciprocal to a section in real space. Thus we have a particular instance of the well known section-projection theorem of Fourier theory.

In the previous equations we are using the convention that  $[hkl] = ka + kb + lc$  where  $a, b, c$  are lattice basis vectors and  $(uvw) = ua^* + vb^* + wc^*$  where  $a^*, b^*, c^*$  are the corresponding reciprocal lattice basis vectors.

However the second approach has several advantages:

- no need to solve for several values of  $n$ . In fact, all the values of  $n$  are taken into account.
- No need to calculate projections at all, ZOLZ indices being automatically provided.
- Lends itself to the simple interpretation to be discussed below.

The practical procedure can be briefly summarized as:

- If you know the beam is along the direction  $[hkl]$  then determine the vector  $(u'v'w')$  in the same direction (in the examples below this is very simple since a cubic lattice and its reciprocal lattice differ only in size).
- Determine basis vectors  $a$  and  $b$  for the section  $(u'v'w')[h'k'l'] = 0$  (a Diophantine equation to be solved by standard methods).
- The reciprocal lattice vectors  $a^*$  and  $b^*$  can be determined from

$$a^* = \frac{|b|^2 a - (a \cdot b)b}{|a|^2 |b|^2 - (a \cdot b)^2} \quad (64)$$

$$b^* = \frac{|a|^2 b - (a \cdot b)a}{|a|^2 |b|^2 - (a \cdot b)^2} \quad (65)$$

and all the integer combinations of them give all the allowed and forbidden spots.

#### 4.1 An example

For instance, in the FCC (112) zone the equation to solve is

$$(112)[hkl] = 0 \quad (66)$$

whose solutions can be determined in many ways, possibly the easiest is by inspection so

$$a = \frac{1}{2}[\bar{1}10] \quad (67)$$

$$b = [11\bar{1}] \quad (68)$$

and

$$a^* = 2a = (1\bar{1}0) \quad (69)$$

$$b^* = \frac{b}{3} = \frac{(11\bar{1})}{3} \quad (70)$$

(here we take advantage of the self reciprocity of cubic lattices). Notice that one of the points in the pattern is

$$a^* - b^* = \frac{(2\bar{4}1)}{3} \quad (71)$$

a “forbidden” spot actually being observed.

Diffraction spots (allowed or forbidden) are expected at

$$g = m(1\bar{1}0) + \frac{n(11\bar{1})}{3} \quad (72)$$

with  $m$  and  $n$  being integers.

## 5. Twinning

A twin is an aggregation of several crystals of the same species whose relative orientations follow well-defined laws. These orientations are related by symmetry operations which do not belong to the crystal class of the untwinned crystal, either by a rotation about an axis

$[uvw]$  or by reflection by a lattice plane  $(hkl)$ . The symmetry of the twin is generally higher than that of the untwinned crystal.

Two main kinds of twinning are distinguished, depending on whether the symmetry operation is: (a)  $180^\circ$  rotation about an axis, called the twin axis, or (b) a reflection across a plane, called the twin plane.

### 5.1 Mirrors

Let  $P$  be a vector and  $P'$  its image after reflection by a mirror that has  $N$  as a normal. Then it can be easily shown that

$$P' = P - \frac{P \cdot N}{|N|^2} N \quad (73)$$

For instance, in an FCC crystal, if  $N = (111)$  and the crystal is  $P = [100]$  oriented with respect to the incoming electron beam, the twin will be another crystal but oriented along  $P' = [100] - \frac{1}{3}[111] = \frac{1}{3}[2\bar{1}\bar{1}]$  or, simply  $[2\bar{1}\bar{1}]$ . In this way the diffraction patterns of the twins can be computed.

## 6. Effect of incomplete layers

Consider an FCC lattice. The smallest vectors in the  $(111)$  plane are

$$a = \frac{1}{2}[1\bar{1}0]$$

$$b = \frac{1}{2}[10\bar{1}]$$

(the  $\frac{1}{2}$  factor come from the fact that the standard unit cell is not primitive) and the lattice reciprocal to the 2 dimensional lattice spanned by  $a$  and  $b$  is the one spanned by

$$a^* = \frac{1}{2}[22\bar{4}] \quad (74)$$

$$b^* = \frac{1}{2}[2\bar{4}2] \quad (75)$$

so “kinematically forbidden” spots will appear.

In the lattice there are, however, other  $(111)$  planes, they are stacked in the sequence  $ABCABC\dots$ . A vector taking the  $(111)$  layer (A) to the next one (B) is given by  $c = [001]$ , and a vector taking it to the third layer (C) is  $d = [002]$ .

For this reason, the amplitude of a diffraction spot

$$\mu = \alpha a^* + \beta b^* \quad (76)$$

will be modulated by

$$\Psi = 1 + \exp[2\pi i(\mu \cdot c)] + \exp[2\pi i(\mu \cdot d)] \quad (77)$$

$$= 1 + \exp[2\pi i(\frac{-4\alpha + 2\beta}{3})] + \exp[2\pi i(\frac{-8\alpha + 4\beta}{3})] \quad (78)$$

and the amplitude will be zero when

$$-4\alpha + 2\beta \equiv 1 \pmod{3} \quad (79)$$

or

$$-4\alpha + 2\beta \equiv 2 \pmod{3} \quad (80)$$

and these equations rule out the forbidden spots when the stacking is complete, in the sense that it comprises a whole *ABCABC...* sequence.

## 7. Direct and reciprocal spaces

Any continuous function of space or time, no matter how complicated, can be expressed as a summation of a series of sine and cosine terms of increasing frequency. In other words, any continuous function of time or space can be described in terms of temporal or spatial frequencies, such as the number of cycles per unit time or the number of atomic planes per unit distance.

This duality in the possible representation of a function allows us to look at the physical property it describes in two different yet complementary spaces known as direct or physical and frequency spaces. In crystallography, these spaces are respectively given the names of real and reciprocal spaces. The latter has been described in detail in section 2 discussing the reciprocal lattice.

In order to gain some insight into the geometrical meaning of the Fourier transform, let us see how a simple sine wave  $f(t) = \sin(2\pi t)$  function is represented in both the direct and frequency spaces with the aid of figure 4.

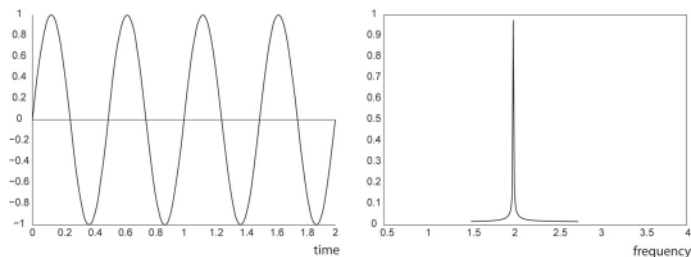


Fig. 4. A sine wave of unit amplitude and a frequency of 2 Hz represented in the time and frequency spaces.

On the left, fig. 4 shows 4 periods of the sine function with a frequency  $\nu = 2\text{Hz}$ , on the right the frequency space of the function, also called the power spectrum, is shown indicating that the function contains a single frequency of 2 Hz. We now add two more waves, one with a third of the amplitude of the original and a frequency 3 times larger (3rd harmonic) and another with an amplitude  $1/5$  of the original and a frequency 5 times larger (5th harmonic):

$$f(t) = \sin(2\pi\nu t) + \frac{1}{3}(\sin(2\pi 3\nu t)) + \frac{1}{5}(\sin(2\pi 5\nu t)) \quad (81)$$

and the time and frequency representations are shown in figure 5. Note that the shape of the new function no longer resembles a sine wave.

If we include the first 20 odd harmonics, a square wave pattern starts to emerge as shown in figure 6. This simple calculation already shows that in order to resolve rapid variations of a

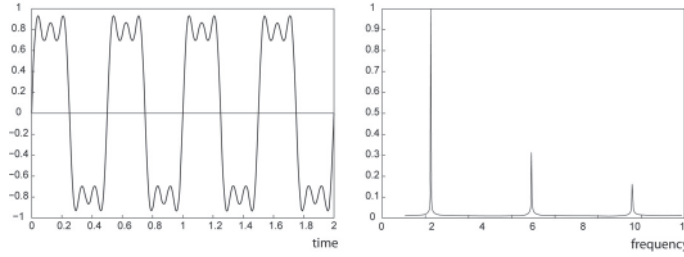


Fig. 5. The time and frequency space representations of a 2 Hz sine wave and its first two odd harmonics (equation 81).

function, such as the sharp edges of a square wave, we need higher frequencies. The higher the cut-off frequency, the better the approximation.

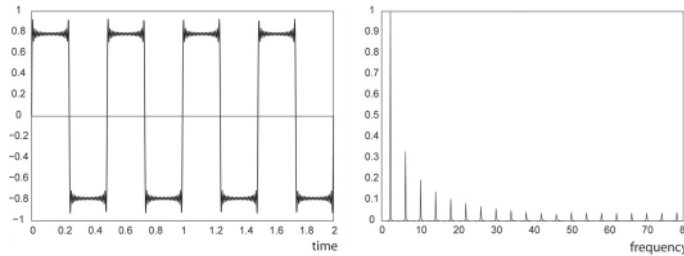


Fig. 6. The time and frequency space representations of the first 20 odd harmonics of a 2 Hz sine wave.

Since the sine is an odd function, i.e.  $\sin(a) = -\sin(-a)$ , only odd functions can be reproduced by combinations of them. We could use cosines instead of sines in the expansion, but being even functions, i.e.,  $\cos(a) = \cos(-a)$ , they allow only the reproduction of even functions. Since most functions are asymmetric (neither odd nor even) a combination of both sines and cosines is needed to reproduce arbitrary functions. As a result, a general function of time (or space) in one dimension can be expressed as

$$f(t) = a_0 + a_1 \cos(\omega t) + a_2 \cos(2\omega t) + \dots + b_1 \sin(\omega t) + b_2 \sin(2\omega t) + \dots \tag{82}$$

or, more succinctly:

$$f(t) = \sum_{i=0}^{\infty} a_i \cos(i\omega t) + \sum_{i=0}^{\infty} b_i \sin(i\omega t) \tag{83}$$

where  $\omega = 2\pi\nu$  and  $a_i, b_i$  are constants. In general, any non-periodic continuous function  $f(x)$  of a single variable  $x$  can be expanded as

$$f(x) = \sum_{i=0}^{\infty} F(u) e^{2\pi i x u} \tag{84}$$

where  $u$  is the temporal or spatial frequency variable and  $F(u)$  is given by

$$F(u) = \int_{-\infty}^{\infty} f(x) e^{-2\pi i x u} dx \tag{85}$$

In general,  $F(u)$  will be a complex quantity even though the original data are purely real. The meaning of this is that not only the amplitude of each frequency present is important, but also its phase relationship to the others.

Equation 84 is known as the Fourier transform of the function  $f(x)$  and equation 85 is the inverse transformation which is very similar except for the sign of the exponential term.

The time (or space) and frequency representations of a function are equivalent in the sense that besides size effects, they convey the same amount of information although they have very different meanings. For our purposes, the most important property of the Fourier transform is that it relates the direct or physical space containing a crystal lattice and the reciprocal space containing the reciprocal lattice and the kinematical diffraction pattern (see section 3).

For an infinite crystal, the direct and reciprocal lattices are given in terms of each other by the three dimensional form of equations 84 and 85. Since the size of real samples is always finite, this leads to important size and shape effects which become especially conspicuous in the case of nanoparticles. In what follows we shall briefly describe what these effects are in order to be able to properly interpret a micro-diffraction pattern

## 8. Size and shape effects

We have already seen that the higher the frequencies in Fourier (diffraction) space, the more detailed is the pattern in the physical space, the reason being that sharper features require smaller wavelengths to be reproduced. We shall further illustrate this property with the aid of fig. 7 which also serves to illustrate the effect the specimen shape has on its diffraction pattern. Figure 7 shows the Fourier transform of a function which equals one inside the black triangular region shown on the left hand side and zero elsewhere. Note that the Fourier transform has large spikes in the directions normal to the edges of the triangular region corresponding to the high frequency components needed to reproduce the sharp changes of the function at the boundaries of the triangle.

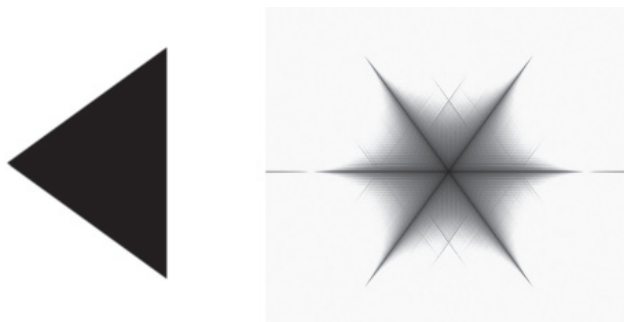


Fig. 7. Left: a triangular shape function which equals one inside the black triangle and zero outside. Right: its Fourier transform rescaled for clarity.

The size of the specimen modifies the size of the diffraction pattern spots. The easiest way to illustrate this is by calculating the Fourier transform of two waveforms of different length. Figure 8 shows the Fourier transform of the same function used in figure 5 (eq. 81) but using a different number of periods. Note that as the length of the waveform representing the size of a crystal increases, the width of the spectral components decreases. In the limit, for an infinite wave, the Fourier peaks become Dirac delta functions.

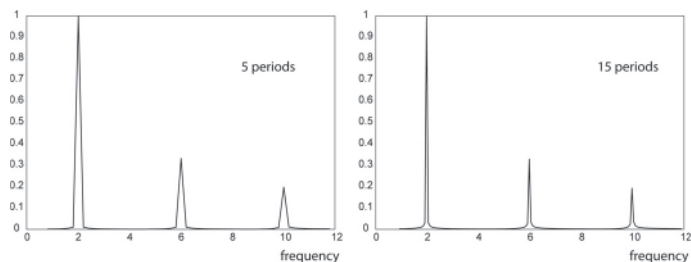


Fig. 8. Fourier transform of 5 and 15 periods of the function defined by equation 81

This effect is further illustrated in figure 9 which shows the kinematical diffraction pattern of two FCC nanoparticles of two different sizes. Note the spot size is smaller in the case of the larger particle and the diffraction lines which are normal to the faces of the nanoparticle.

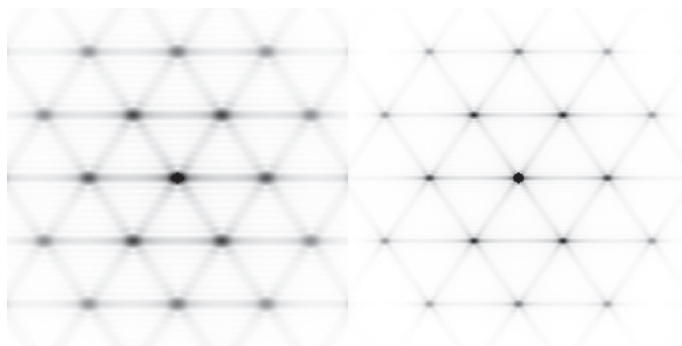


Fig. 9. Kinematical diffraction pattern (Fourier Transform) taken along the [011] direction) of two FCC nanoparticles composed of: left: 255 atoms and right: 1785 atoms.

## 9. The convolution theorem

The mathematical way to express the aforementioned size and shape effects is known as the convolution theorem. Succinctly, the theorem states that the Fourier transform of the product of two functions is equal to the mathematical convolution of their Fourier transforms. In other words, if  $f(x)$  and  $g(x)$  are integrable functions with Fourier transforms  $F(u)$  and  $G(u)$  respectively, then the Fourier transform of the product (denoted  $\widehat{fg}(u)$ ) is given by the convolution (denoted by  $*$ ) of the individual Fourier transforms.

$$\widehat{fg}(u) = F(u) * G(u) \quad (86)$$

The geometrical meaning of the convolution is simpler to express graphically. Figure 10 shows schematically the convolution of two graphic functions.

Since any nanoparticle of arbitrary size and shape can always be considered as an infinite crystal chopped by a "shape" function valued one inside the nanoparticle's volume and zero elsewhere, it turns out that its kinematical diffraction pattern will be the convolution of the Fourier transform of the crystal (the reciprocal lattice) with the Fourier transform of the shape. This is illustrated in fig.10 whose top three figures show from left to right the real space

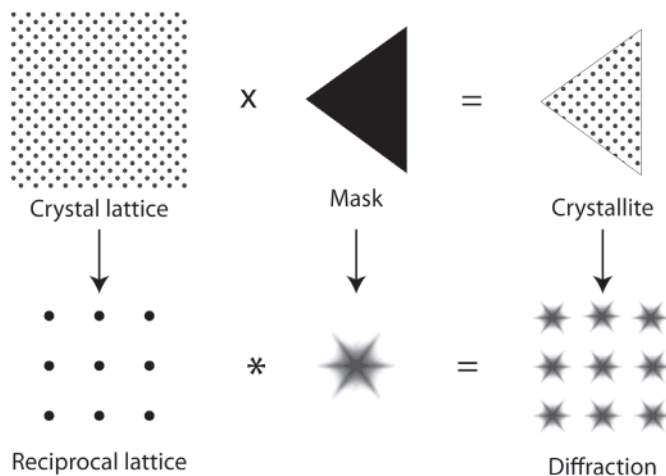


Fig. 10. Convolution of a set of reciprocal lattice points the Fourier transform of the triangular shape shown in fig. 7, representing schematically the reciprocal lattice of a small triangular bi-dimensional nanoparticle.

representation of a section of an infinite 2D crystal lattice, the masking function and the crystallite resulting from their multiplication. The corresponding Fourier transform i.e. the reciprocal space representation of each figure is shown below. Note that the effect of the convolution is to "stamp" each reciprocal lattice point with a copy of the Fourier transform of the shape function.

## 10. A brief introduction to HRTEM formation

The image formation in a conventional TEM and HRTEM microscope includes the microscope itself, the sample under study, the orientation relationship between the electron beam and the sample, and the objective aperture of the microscope. The contrast observed in the screen of the microscope depends on the aperture size and the diffraction (or reciprocal space) spot(s) going through it, and of course on the quality of the microscope. Thus, if the transmitted beam is the only one going through the objective aperture, we will observe the amplitude contrast in bright field mode (Fig. 11). In the case of a diffracted beam, a dark field image is observed. With more than one reflection, the quality of the microscope plays the main role: the "line" resolution requires that two beams go through the objective aperture, and the HRTEM requires the greatest number of reflections (Fig. 12). The most important point we must have in mind is that any reflection passing through the objective aperture is going to be included in the contrast of the obtained image, and once the image obtained any change can be done regarding the information of the sample under study. Figure 13 shows the HRTEM image of one of the particles shown in figure 12C. The insets show the periodicity of the image by the FFT (Fast Fourier Transform) spectra calculated with the Digital Micrograph software.

## 11. Pentagonal silver nanowires

The synthesis for silver nanowires has been reported elsewhere (Brust et al., 1995). Silver nanowires were synthesized by the polyol reduction of silver nitrate ( $\text{AgNO}_3$ ) in presence

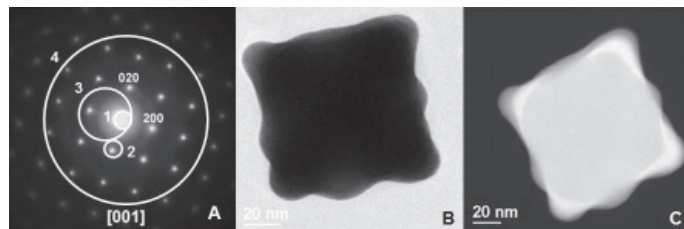


Fig. 11. A) Schematic representation of the size and position of the objective aperture in the focal plane of the objective lens for image formation in a TEM in different situations: bright field image (1), dark field image (2), line-resolution image (3) and high-resolution image (4). B) Bright field and C) dark field image of an Au particle.

of PVP. Scanning electron microscopy of the nanowires was conducted using the scanning electron microscope (SEM) Hitachi 4500F. Transmission electron microscopy was conducted in a HRTEM JEOL 2010F microscope equipped with Schottky-type field emission gun, ultra-high resolution pole piece ( $C_s = 0.5\text{mm}$ ), and a scanning transmission electron microscope (STEM) unit with high angle annular dark field (HAADF) detector operating at  $200\text{kV}$ . For digital image processing the Digital Micrograph (GATAN) software was used. To simulate the electron diffraction patterns, the SimulaTEM software (Gomez et al., 2010) was employed. Figure 14 shows the SEM images of the synthesized Ag nanowires where their pentagonal cross-section is presented.

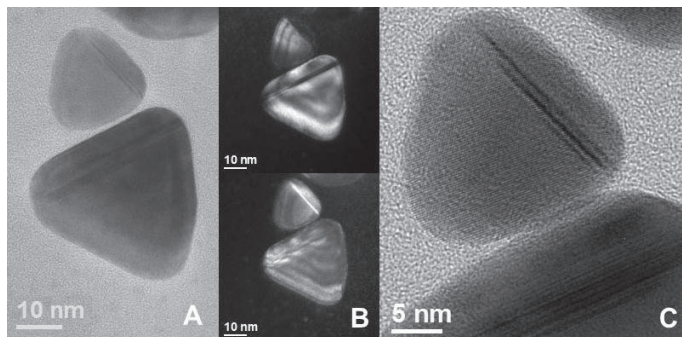


Fig. 12. Example of a bright field image (A), two dark field images using a different reflection in each case (B), and a high-resolution image (C) of Au nanoparticles.

## 12. Diffraction patterns and HRTEM images of pentagonal silver nanowires

Once in the HRTEM microscope, conventional bright field (Fig. 15A) and HRTEM (Fig. 15B) images and electron diffraction patterns of an Ag nanowire are obtained easily. Figure 16 shows the electron diffraction patterns of an individual pentagonal Ag nanowire when the electron beam goes through the directions indicated by (A) and (B) in the drawings, respectively. Because the pentagonal rotational periodicity, there is an angle of  $18^\circ$  between them. The analysis and indexation of these diffraction patterns indicate that they correspond to the overlapping of the  $[001]$  and  $[112]$  zone axes (Fig. 16A), and of the  $[111]$  and  $[110]$  zone

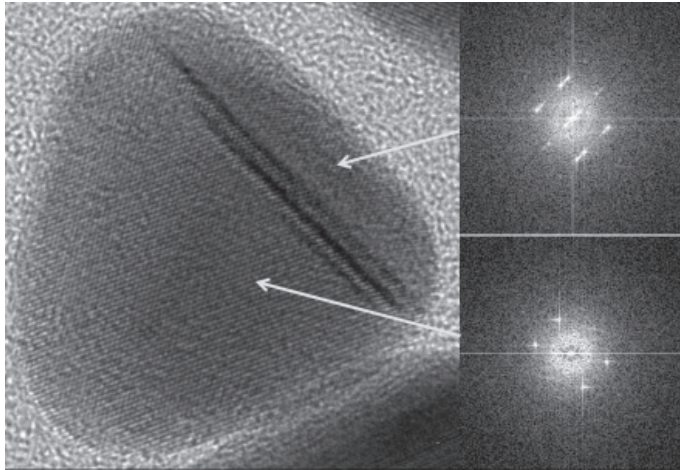


Fig. 13. Magnification of the high-resolution image shown in figure 2C. The insets show the FFT spectra calculated with the Digital Micrograph software where the periodicity obtained in each region of the Au nanoparticle is shown.

axes (Fig. 6B), of the silver FCC unit cell, respectively. The presence of an aperiodic sequence of diffraction spots, mainly in figure 16 A is of notorious relevance.

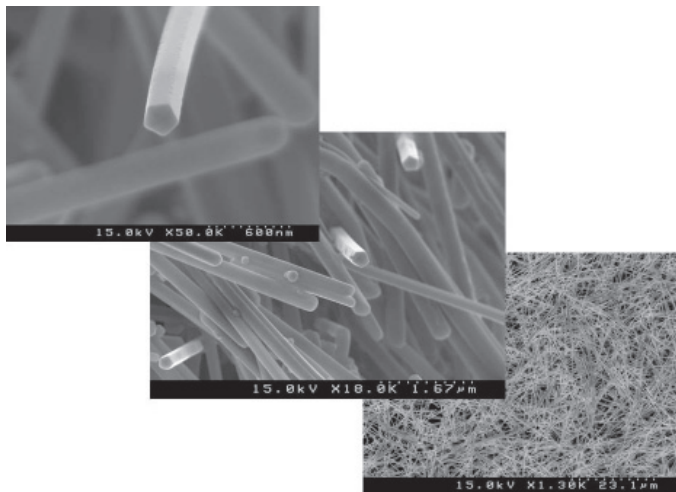


Fig. 14. SEM images of the synthesized Ag nanowires showing their pentagonal cross-section.

In order to understand the contrast observed in the HRTEM images of the pentagonal Ag nanowires is quite important to know their structure. A HRTEM image from the area close to the tip is shown in figure 17. The upper right inset shows the FFT from the indicated squared contrast, which corresponds to the [001] zone axis. The lower right inset shows the FFT from the region enclosed by the square in the HRTEM image. The analysis of this FFT indicates that

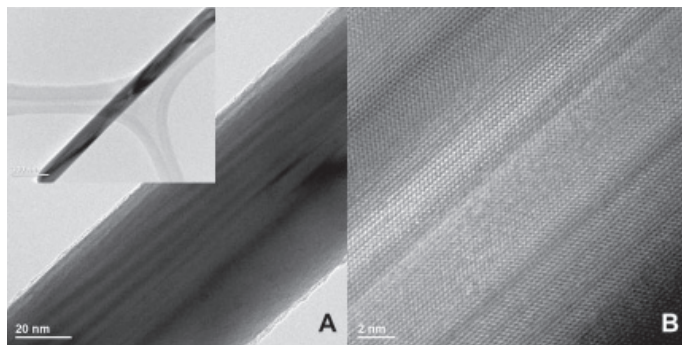


Fig. 15. TEM (A) and HRTEM (B) images of an Ag nanowire in its central region. The inset shows the TEM bright-field image of the nanowire at lower magnification.

it corresponds to the same overlapping diffraction pattern calculated in figure 16A, including the aperiodic sequence.

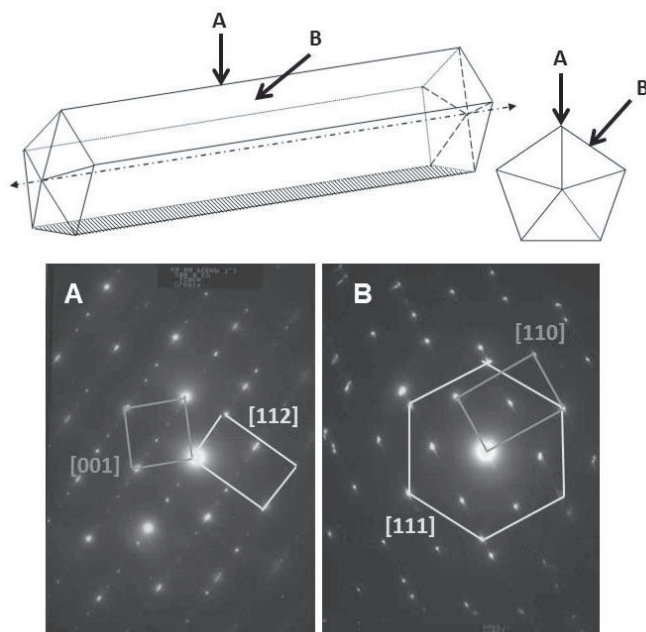


Fig. 16. Characteristic diffraction patterns of a pentagonal Ag nanowire when the electron beam goes through the directions indicated by (A) and (B) in the drawings, respectively. Their indexation indicates that they correspond to the overlapping of the [001] and [112] zone axes (A), and of the [111] and [110] zone axes (B). Note the existence of an aperiodic sequence of diffraction spots in (A).

### 13. Interpretation of the reflections observed in the diffraction patterns of pentagonal silver nanowires

Let us show that the observation of this aperiodic sequence of diffraction spots is produced by the nano-size-dimension of the nanowires in combination with double diffraction due to twinning. The nanometric size of the nanowire along its cross-section produces the enlargement of reciprocal spots, then it is easily deduced that some of the spots composing the diffraction pattern shown in figure 16 are in fact spots of not only to the Zero Order Laue Zone (ZOLZ), but also to the First Order Laue Zone (FOLZ). Schematic drawings of the fcc reciprocal space including the ZOLZ and the "upper" and "lower" FOLZ spots for both  $[001]$  and  $[112]$  zone axes and for both  $[110]$  and  $[111]$  zone axes are shown in figures 18 and 19, respectively. As the FOLZ spots are elongated, they intercept the Ewald sphere. The drawings in the corresponding squares of these figures show the generated pattern when the diffraction patterns, including their respective FOLZ spots, overlap according to the orientation relationships indicated in the diffraction patterns of figure 16. Note that many of the diffracted spots shown in figure 16 are reproduced.

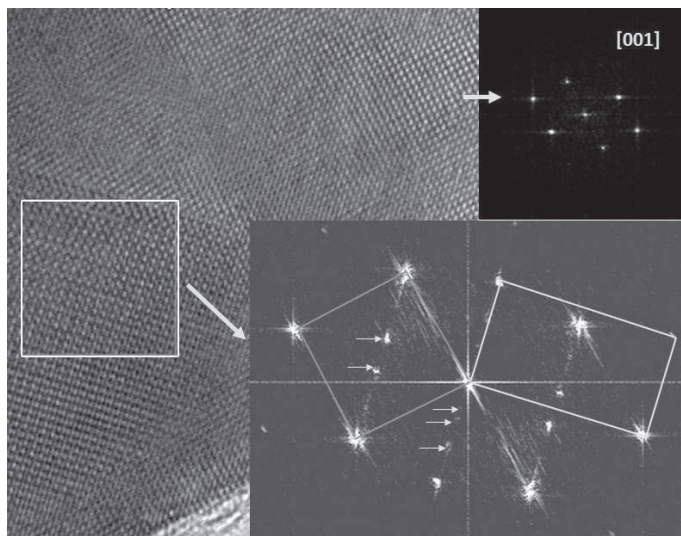


Fig. 17. HRTEM image from an area close to the tip of a pentagonal Ag nanowire. The upper right inset shows the FFT from the squared contrast; the lower right inset shows the FFT from the region enclosed by a square. Note the existence of the same spots as those in the diffraction pattern of figure 16A.

### 14. Final remarks

Reyes-Gasga et al. (Reyes-Gasga et al., 2006) have already proposed the structure of the Dh-NWs as a chain of decahedra joined along the vertex (which is parallel to the 5-fold symmetry). In this model, the Dh-NWs will be always growing along the  $[111]$  direction. Figure 20 shows the comparison among the experimental diffraction patterns shown in figure 16 (A) and (B) and the simulated diffraction patterns from an Ag decahedral (Ad and

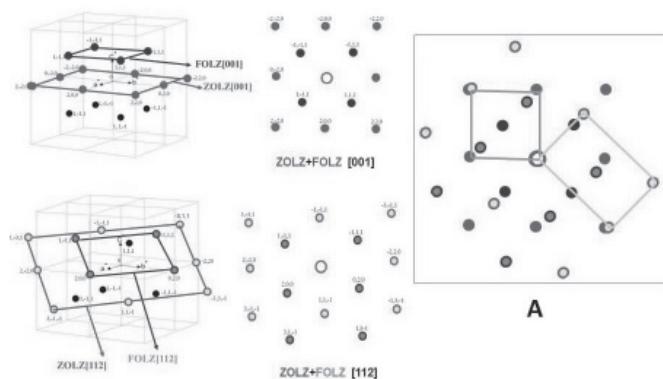


Fig. 18. . Schematic drawing of the fcc reciprocal space along the [001] and [112] zone axes including the ZOLZ and the "upper" and "lower" FOLZ spots. The patterns have been indexed accordingly. The square (A) shows the generated pattern when these patterns overlap according to the orientation relationships indicated in figure 16A.

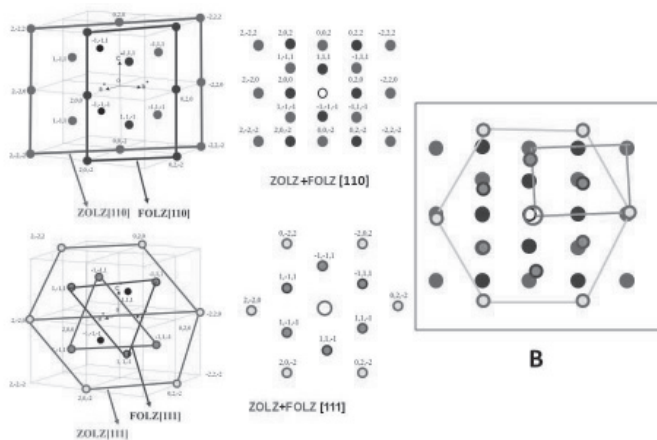


Fig. 19. Schematic drawing of the fcc reciprocal space along the [110] and [111] zone axes including the ZOLZ and the "upper" and "lower" FOLZ spots. The patterns have been indexed accordingly. The square (B) shows the generated pattern when these patterns overlap according to the orientation relationships indicated in figure 16B.

Bd) and an Ag elongated decahedron (Aed) and (Bed). Note that the aperiodic sequence observed in the experimental patterns is reproduced in the case of the decahedron, while the elongated model generates a different aperiodic sequence. This idea of the chain of decahedra joined along the vertex has been successfully used in the analysis and interpretation of diffraction patterns of Au nanoparticles (Reyes-Gasga et al., 2008; Romeu & Reyes-Gasga, 2002). However, observing the simulated patterns shown in figure 20, we conclude that there is still a lot of work to be done in this direction.

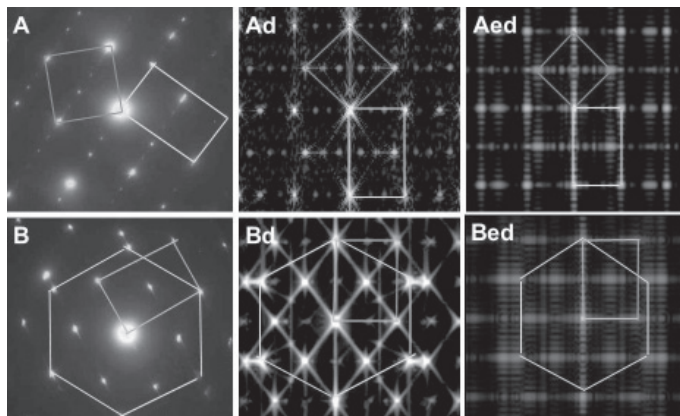


Fig. 20. Comparison among the experimental diffraction patterns shown in figure 16 (A) and (B) and the simulated diffraction patterns from an Ag decahedron (Ad and Bd) and an Ag elongated decahedron (Aed and Bed).

## 15. Acknowledgements

We are grateful to Prof. Dr. M. Jose Yacaman, Dr. J. L. Elechiguerra, and Dr. Xiaoxia Gao for supplying the samples used in this work and for their collaboration as coauthors of joint papers. We also thank S. Tehuacanero-Nuñez, P. Mexia-Hernández, R. Hernandez-Reyes, J. Cañetas and M. Monroy-Escamilla for their technical support in the elaboration of this work.

## 16. References

- Brust, M.; Fink, J.; Bethell, D.; Schiffring D. J. & Kiely, C. (1995). Synthesis and reactions of functionalized gold nanoparticles. *J. Chem. Soc. Chem. Comm.*, 1655, Issue 16. DOI: 10.1039/C39950001655.
- Chen, H.; Gao, Y.; Zhang, H.; Liu, L.; Yu, H.; Tian, H.; Xie, S. & Li, J. (2004). Transmission-electron-microscopy study on fivefold twinned silver nanorods. *J. Phys. Chem. B.*, Vol.108, No. 32, (August 2004), pp 12038-12043.
- Gao, Y.; Jiang, P.; Lui, D. F.; Yuan, H. J.; Yan, X. Q.; Zhou, Z. P.; Wang, J. X.; Song, L.; Liu, L. F.; Zhou, W. Y.; Wang, G.; Wang, C. Y. & Xie, S. (2003). Synthesis, characterization and self-assembly of silver nanowires. *Chem. Phys. Lett.*, Vol.380, No. 1-2, (October 2003), pp 146-149.
- Giersig, M.; Pastoriza-Santos, I.; & Liz-Marzán L. M. (2004). Evidence of an aggregative mechanism during the formation of silver nanowires in N,N-dimethylformamide *J. Mater. Chem.*, Vol.14, No. 4 (April 2004), pp 607-611.
- Heinemann, K.; Yacamán, M. J.; Yang, C. Y. & Poppa, H. (1979). The structure of small, vapor-deposited particles: I. Experimental study of single crystals and particles with pentagonal profiles. *J. Crystal Growth*, Vol.47, No. 2, (August 1979), pp 177-186.
- Hofmeister, H.; Nepijko, S. A.; Levlev, N. N.; Schulze, W.; & Ertl, G. (2002). Composition and lattice structure of fivefold twinned nanorods of silver. *J. Crystal Growth*, Vol.234, No. 4, (February 2002), pp 773-781.
- Howie A. & Marks, L. D. (1984). Elastic strains and energy balance for multiply twinned particles *Phil. Mag.*, A Vol.49, No. 1 (January 1984), pp 95-109.

- Reyes-Gasga, J.; Elechiguerra, J. L.; Liu, C.; Camacho-Bragado, A.; Montejano-Carrizales, J. M. & Yacamán, M. J. (2006). On the structure of nanorods and nanowires with pentagonal cross-sections. *J. Cryst. Growth*, Vol.286, No. 1, (January 2006), pp 162-172.
- Reyes-Gasga, J.; Gómez-Rodríguez, A.; Gao, X. & José-Yacamán, M. (2008). *Ultramicroscopy*, Vol.108, No. 9, (August 2008), pp 929-936
- Romeu, L.D. & Reyes-Gasga, J. (2011). Interpretation of the nano-electron-diffraction patterns along the five-fold axis of decahedral gold nanoparticles. *Microc.Microanal*, Vol.17, in press. DOI 10.1017/s1431927610094511.
- Sun, Y.; Gates, B.; Mayers, B. & Xia, Y. (2002). Crystalline silver nanowires by soft solution processing. *Nanoletters*, Vol.2, No. 2, (February 2002), pp 165-168.
- Sun, Y.; Mayers, B.; Herricks T. & Xia, Y. (2003). Polyol synthesis of uniform silver nanowires: a plausible growth mechanism and the supporting evidence. *Nanoletters*, Vol.3, No. 7, (July 2003), pp 955-960.
- Zhao, Q.; Qiu, J.; Zhao, C.; Hou L. & Zhu, C. (2005). Synthesis and formation mechanism of silver nanowires by a templateless and seedless method *Chem. Letters*, Vol.34, No. 1, (January 2005), pp 30-31.

# Charge and Spin Transport in Magnetic Nanowires

N. Sedlmayr<sup>1</sup>, J. Berakdar<sup>2</sup>, M. A. N. Araújo<sup>3</sup>, V. K. Dugaev<sup>4</sup> and J. Barnaś<sup>5</sup>

<sup>1</sup>*Fachbereich Physik, Technische Universität Kaiserslautern*

<sup>2</sup>*Department of Physics, Martin-Luther-Universität Halle-Wittenberg*

<sup>3</sup>*Department of Physics, Évora University, Évora  
CFIF, Instituto Superior Técnico, Lisbon*

<sup>4</sup>*Department of Physics, Rzeszów University of Technology, Rzeszów*

<sup>5</sup>*Department of Physics, Adam Mickiewicz University, Poznań*

<sup>1,2</sup>*Germany*

<sup>3</sup>*Portugal*

<sup>4,5</sup>*Poland*

## 1. Introduction

The large interest in magnetic nanowires is mostly related to their possible application in magnetoelectronics. It was established experimentally that the magnetic domain walls (DWs) in very thin magnetic wires can affect substantially their resistance up to 1000% or even more (Chopra & Hua (2002)), (Rüster et al. (2003)). On the other hand, the magnetic DWs in nanowires can be effectively controlled by weak external magnetic field and by electric current pulses. The latter effect of current-induced DW motion opens the way for various applications. One of the most impressive advances in this direction is the development of race-tracking memory devices for fast storage and reading of information (Parkin et al. (2008)). A review of the properties of magnetic nanowires with domain walls has been presented recently in Ref. (Kläui (2008)).

Several different phenomena have been in the scope of experimental and theoretical research, each of them being important for the use of magnetic nanowires in magnetoelectronics. The first one is the problem of transmission and reflection of electrons through the DW since this effect is mostly responsible for the magnetoresistivity. The other problem is related to the spin-transfer torque in magnetic nanowires and possible mechanisms of the current-induced DW motion. These mechanisms are responsible for effective current-induced control of the DW motion and correspondingly for current-induced variation of the resistance of magnetic nanowires. The third problem concerns the dynamics of the DWs motion since the dynamics are related to the possibility of fast current-induced control of the resistance.

In this Chapter we review our main results of theoretical investigations into charge and spin transport properties in magnetic nanowires, mostly using some simplified models. Solving the models one can understand better the underlying physical mechanisms of the spin and charge transport in magnetic nanowires, that can be also used in computer simulations, which should take into account real electronic and magnetic structure of a specific material.

The details of our calculations and more information on the methods can be found in Refs.: (Dugaev et al. (2002)), (Dugaev et al. (2003)), (Dugaev et al. (2004)), (Dugaev et al. (2005)), (Araújo et al. (2006)), (Dugaev et al. (2006)), (Araújo et al. (2007)), (Dugaev et al. (2007)), (Sedlmayr et al. (2009)) and (Sedlmayr et al. (2010)).

## 2. Reflection of electrons from the magnetic domain wall

Spin-polarized electrons moving in a magnetic nanowire are scattered not only from phonons, impurities and defects like in the case of nonmagnetic materials, but also from any spatial variation of magnetization, which leads to scattering with the variation of electron momentum and electron spin. This problem was considered theoretically first in Refs. (Cabrera & Falicov (1974,a)) and (Cabrera & Falicov (1974,b)).

In the case of very slow variation of magnetization, when the adiabatic approximation is applied, the electron wavefunction can be described semiclassically. For the scattering from DW the condition of semiclassical approximation is  $\lambda \ll L$ , where  $\lambda$  is the wavelength of electron and  $L$  is the width of DW. This condition is usually fulfilled in relatively thick microwires. We consider first this case, which provides relatively weak electron backscattering, so that the effect of DW reduces to a small correction to the conductance.

### 2.1 Transmission through a thick domain wall

#### 2.1.1 Model

Let us consider a ferromagnet with a nonuniform magnetization  $\mathbf{M}(\mathbf{r})$ . The one-particle Hamiltonian describing conduction electrons locally exchange-coupled to the magnetization  $\mathbf{M}(\mathbf{r})$  takes the form

$$H = -\frac{1}{2m} \psi_\alpha^\dagger \Delta \psi_\alpha - J \psi_\alpha^\dagger \sigma_{\alpha\beta} \cdot \mathbf{M}(\mathbf{r}) \psi_\beta, \quad (1)$$

where  $J$  is the exchange parameter,  $\psi_\alpha$  and  $\psi_\alpha^\dagger$  are the spinor field operators of electrons,  $\sigma = (\sigma_x, \sigma_y, \sigma_z)$  are the Pauli matrices, and we use the units with  $\hbar = 1$ . Hamiltonian (1) can be used to describe electrons interacting with a domain wall in ferromagnetic metals or in magnetic semiconductors. The domain wall is modeled by a magnetization profile  $\mathbf{M}(\mathbf{r})$ , and we assume  $|\mathbf{M}(\mathbf{r})| = \text{const}$ . Then we can write  $J\mathbf{M}(\mathbf{r}) = M\mathbf{n}(\mathbf{r})$ , where  $\mathbf{n}(\mathbf{r})$  is a unit vector field, and  $M$  is measured in the energy units including the parameter  $J$ .

The first step is to perform a local unitary transformation [Tatara & Fukuyama (1997)]  $\psi \rightarrow T(\mathbf{r}) \psi$ , which removes the nonhomogeneity of  $\mathbf{M}(\mathbf{r})$ , that is  $T(\mathbf{r})$  transforms the second term in Eq. (1) as  $\psi^\dagger \sigma \cdot \mathbf{n}(\mathbf{r}) \psi \rightarrow \psi^\dagger \sigma_z \psi$ . This transformation can be applied not only to a simple domain wall, but also to any other types of topological excitations in ferromagnetic systems, for instance helicoidal waves, skyrmions, and others. Applying this transformation to the kinetic part of Hamiltonian (1) one obtains

$$\psi^\dagger \Delta \psi \rightarrow \psi^\dagger (\nabla + \mathbf{A}(\mathbf{r}))^2 \psi, \quad (2)$$

where the gauge field  $\mathbf{A}(\mathbf{r})$  is given by  $\mathbf{A}(\mathbf{r}) = T^\dagger(\mathbf{r}) \nabla T(\mathbf{r})$ . This gauge field  $\mathbf{A}(\mathbf{r})$  is a matrix in the spin space.

Let us consider now a more specific case of a domain wall in a bulk system or a thick magnetic wire. We assume that the wall is translationally invariant in the  $x$ - $y$  plane:  $\mathbf{M}(\mathbf{r}) \rightarrow \mathbf{M}(z)$  and  $\mathbf{n}(\mathbf{r}) \rightarrow \mathbf{n}(z)$ . For such a simple domain wall one can parameterize the unit vector field  $\mathbf{n}(z)$  as

$$\mathbf{n}(z) = (\sin \varphi(z), 0, \cos \varphi(z)), \quad (3)$$

where the  $z$ -dependent phase  $\varphi(z)$  determines the type of a domain wall. In this case the gauge field assumes the form

$$\mathbf{A}(z) = \left( 0, 0, -\frac{i}{2} \sigma_y \varphi'(z) \right) \quad (4)$$

and the transformed Hamiltonian is

$$H = -\frac{1}{2m} \Delta + \frac{m \beta^2(z)}{2} - M\sigma_z + i\sigma_y \frac{\beta'(z)}{2} + i\sigma_y \beta(z) \frac{\partial}{\partial z}, \quad (5)$$

where  $\beta(z) = \varphi'(z)/2m$  describes the local perturbation.

For a slowly varying smooth function  $\varphi(z)$  (thick domain wall of width  $L$  centered at  $z=0$ ), the perturbation due to the domain wall is weak, and close to the center of the wall,  $|z| \ll L$ , the parameter  $\beta(z)$  can be treated as a constant. If we assume the domain wall in the form of a kink, then  $\varphi(z) = -(\pi/2) \tanh(z/L)$ , and the parameter  $\beta(z)$  is given by

$$\beta(z) = -\pi/4mL \cosh^2(z/L). \quad (6)$$

### 2.1.2 Semiclassical approximation

In bulk magnetic metals like Fe, Ni or Co, the width  $L$  of a magnetic domain wall is usually much larger than the electron Fermi wavelength  $\lambda_F$ . In such a case application of a semiclassical approximation can be justified (Cabrera & Falicov (1974,a); Cabrera & Falicov (1974,b)). The dominant perturbation from the domain wall is then described by the term with  $\beta(\partial/\partial z)$  in Eq. (5), since it is of order of  $\beta k_F$ . The term proportional to  $\beta^2$  is smaller, while the term including  $\beta'(z)$  is of the order of  $\beta/L$  and therefore can be neglected.

The Schrödinger's equation with Hamiltonian (5) has then the following semiclassical solutions ( $i = 1, 2$ )

$$\psi_i(\boldsymbol{\rho}, z) = \frac{\exp(\pm i \mathbf{q} \cdot \boldsymbol{\rho})}{[\varepsilon_i^2(z) + \beta^2(z) k_i^2(z)]^{1/2} k_i^{1/2}(z)} \begin{pmatrix} \mp i \beta k_i(z) \\ \varepsilon_i(z) \end{pmatrix} \exp \left[ \pm i \int_0^z k_i(z) dz \right]. \quad (7)$$

where  $\boldsymbol{\rho} = (x, y)$ ,  $\mathbf{q}$  is the momentum in the plane of the wall, the wavevector components normal to the wall (along the axis  $z$ ) are given by

$$k_{1,2}^2(z) = \kappa^2(z) + m^2 \beta^2(z) \pm 2m \left[ M^2(z) + \beta^2(z) \kappa^2(z) \right]^{1/2}, \quad (8)$$

and

$$\varepsilon_i(z) = \frac{k_i^2(z)}{2m} + \frac{m\beta^2(z)}{2} - M(z) - \frac{\kappa^2(z)}{2m}, \quad (9)$$

with  $\kappa(z)$  defined as  $\kappa^2(z) = 2m\varepsilon - q^2$ . Obviously, there is no reflection from the wall in the semiclassical approximation.

### 2.1.3 Scattering from the wall in Born approximation

For the case of not too thin domain wall, the term proportional to  $\beta(z) \partial/\partial z$  can be treated as a small perturbation and therefore the scattering from the wall can be evaluated within the Born approximation. The matrix elements of the  $(k_z \uparrow) \rightarrow (k'_z \downarrow)$  spin-flip scattering is given by

$$V_{k_z k'_z} = - \int_{-\infty}^{\infty} e^{-ik'_z z} \beta(z) \frac{d}{dz} e^{ik_z z} dz. \quad (10)$$

Using (6) and calculating the integral we find

$$V_{k_z k'_z} = \frac{i\pi^2 k_z (k'_z - k_z)L}{4m} \operatorname{csch} \left[ \frac{\pi(k'_z - k_z)L}{2} \right]. \quad (11)$$

Correspondingly, the probability of backscattering ( $k'_z = -k_z$ ) is

$$W_{back} \equiv 2\pi |V_{k_z, -k_z}|^2 = \frac{\pi^5 k_z^4 L^2}{2m^2} \operatorname{csch}^2(\pi k_z L). \quad (12)$$

For  $k_z L \gg 1$ , from the last equation we find

$$W_{back} = \frac{2\pi^5 k_z^4 L^2}{m^2} e^{-2\pi k_z L}. \quad (13)$$

Thus, the probability of the backscattering with simultaneous spin flip vanishes exponentially in the limit of  $k_F L \gg 1$ . The spin-conserving backscattering is determined by the term proportional to  $\beta^2$  in the Hamiltonian (5). In the first approximation this term can be neglected as it gives a smaller contribution than the one proportional to  $\beta(z) \partial/\partial z$ .

The question arises, whether the Born approximation gives correct results for the problem under consideration. There are two general conditions for its applicability:  $|U(z)| \ll 1/mL^2$  or  $|U(z)| \ll k/mL$ , where  $U(z)$  is the scattering potential. In the first case the Born approximation is good for arbitrary electron energy, whereas in the second one it is good only for fast electrons. Therefore, if we choose the limit  $k_F L \gg 1$ , then  $|U(z)| \sim \beta k_z \sim (k_z/mL)$ , and none of the conditions is satisfied. In the opposite case of a small domain-wall width,  $k_F L \ll 1$ , we have  $|U(z)| \sim 1/mL^2$  and the Born approximation is not justified again. Thus, the Born approximation can be used only for rough estimations. In the case under consideration,  $k_F L \gg 1$ , it just shows that the usual scattering from the wall is exponentially weak.

## 2.2 Reflection from a thin domain wall

### 2.2.1 Model and scattering states

Let us consider now a sharp domain wall assuming  $\mathbf{M}(z) = M_0 \mathbf{n}(z) = [M_0 \sin \varphi, 0, M_0 \cos \varphi]$ , where  $\varphi(z)$  varies from zero to  $\pi$  for  $z$  changing from  $z = -\infty$  to  $z = +\infty$ . When DW is laterally constrained, the number of quantum transport channels is limited. In the extreme case only a single conduction channel contributes. In such a situation, one can restrict considerations to a one-dimensional model, and write the Hamiltonian as

$$H = -\frac{1}{2m} \frac{d^2}{dz^2} - JM_z(z) \sigma_z - JM_x(z) \sigma_x. \quad (14)$$

Although this model describes only a one-channel quantum wire, it is sufficient to account qualitatively for some of the observations. Apart from this, it can be easily generalized to the case of a wire with more conduction channels.

In the following description we use the basis of scattering states. The asymptotic form of such states (taken sufficiently far from DW) can be written as

$$\chi_{R\uparrow}(z) = \begin{cases} \begin{pmatrix} e^{ik_{\uparrow}z} + r_{R\uparrow} e^{-ik_{\uparrow}z} \\ r_{R\uparrow}^f e^{-ik_{\downarrow}z} \end{pmatrix}, & z \ll -L, \\ \begin{pmatrix} t_{R\uparrow} e^{ik_{\downarrow}z} \\ t_{R\uparrow}^f e^{ik_{\uparrow}z} \end{pmatrix}, & z \gg L, \end{cases} \quad (15)$$

where  $k_{\uparrow(\downarrow)} = \sqrt{2m(E \pm M)}$ , with  $M = JM_0$ , and  $E$  denoting the electron energy. The scattering state (15) describes the electron wave in the spin majority channel incident from  $z = -\infty$ , which is partially reflected into the spin-majority and spin-minority channels, and also partially transmitted into these two channels. The coefficients  $t_{R\uparrow}$  and  $t_{R\uparrow}^f$  are the transmission amplitudes without and with spin reversal, respectively, whereas  $r_{R\uparrow}$  and  $r_{R\uparrow}^f$  are the relevant reflection amplitudes. It is worth to note that transmission from the spin-majority channel at  $z < 0$  to the spin-majority channel at  $z > 0$  requires spin reversal. The scattering states corresponding to the electron wave incident from  $z = -\infty$  in the spin-minority channel have a similar form. Furthermore, scattering states describing electron waves incident from the right to the left take a similar form, as well.

In a general case (for  $k_FL > 1$  or  $k_FL < 1$ ) the transmission and reflection coefficients can be calculated numerically, as described below. When  $k_FL \ll 1$ , then the coefficients can be calculated analytically. Upon integrating the Schrödinger equation  $H\psi = E\psi$  (with the Hamiltonian given by Eq. (14)) from  $z = -\delta$  to  $z = +\delta$ , and assuming  $L \ll \delta \ll k_{\uparrow(\downarrow)}^{-1}$ , one obtains

$$-\frac{1}{2m} \left( \left. \frac{d\chi}{dz} \right|_{z=+\delta} - \left. \frac{d\chi}{dz} \right|_{z=-\delta} \right) - \lambda \sigma_x \chi(z=0) = 0 \tag{16}$$

for each of the scattering states (for clarity of notation the index of the scattering states is omitted here), where

$$\lambda \simeq J \int_{-\infty}^{\infty} dz M_x(z). \tag{17}$$

Equation (16) has the form of a spin-dependent condition for electron transmission through a  $\delta$ -like potential barrier located at  $z = 0$ . To obtain it we also used the condition  $k_{\uparrow(\downarrow)}L \ll 1$ , which is opposite to the condition used in the semiclassical approximation. The magnitude of the parameter  $\lambda$  in Eq. (17) can be estimated as  $\lambda \simeq JM_0L$ .

Using the full set of scattering states together with the wave function continuity condition, one finds the transmission amplitudes

$$\begin{aligned} t_{R\uparrow(\downarrow)} &= t_{L\downarrow(\uparrow)} = \frac{2v_{\uparrow(\downarrow)}(v_{\uparrow} + v_{\downarrow})}{(v_{\uparrow} + v_{\downarrow})^2 + 4\lambda^2}, \\ t_{R\uparrow(\downarrow)}^f &= t_{L\downarrow(\uparrow)}^f = \frac{4i\lambda v_{\uparrow(\downarrow)}}{(v_{\uparrow} + v_{\downarrow})^2 + 4\lambda^2}, \end{aligned} \tag{18}$$

where  $v_{\uparrow(\downarrow)} = k_{\uparrow(\downarrow)}/m$  denotes the electron velocity in the spin-majority (spin-minority) channel. According to (18), the magnitude of spin-flip transmission coefficients can be estimated as (for simplicity we omit here the eigenstate indices)

$$|t^f|^2 \sim \left( \frac{\lambda v}{v^2 + \lambda^2} \right)^2 \sim \left( \frac{M\varepsilon_0}{\varepsilon_F \varepsilon_0 + M^2} \right)^2 (k_FL)^2, \tag{19}$$

where  $\varepsilon_F = k_F^2/2m$  and  $\varepsilon_0 = 1/mL^2$ . For  $k_FL \ll 1$  one finds  $\varepsilon_0 \gg \varepsilon_F$ . Thus, taking  $\varepsilon_F \sim M$ , one obtains

$$|t^f|^2 \sim \left( \frac{M}{\varepsilon_F} k_FL \right)^2 \ll 1. \tag{20}$$

Accordingly, a sharp domain wall can be considered as an effective barrier for the spin-flip transmission. On the other hand, the probability of spin conserving transmission is much

larger,  $|t/t^f|^2 \sim \varepsilon_F \varepsilon_0 / M^2 \gg 1$ . This means that electron spin does not follow adiabatically the magnetization direction when it propagates through the wall, but its orientation is rather fixed.

### 2.2.2 Resistance of the domain wall

To calculate the conductance of the system under consideration, one can start with the current operator  $\hat{j} = e \psi^\dagger(z) \hat{v} \psi(z)$ , where  $\hat{v}$  is the velocity operator, whereas  $\psi^\dagger(z)$  and  $\psi(z)$  are the electron field operators taken in the spinor form. Using the expansion of  $\psi(z)$  in the basis of scattering states (15) and carrying out quantum-mechanical averaging, one obtains the following formula for the current

$$j = -ie \sum_n \int \frac{dk}{2\pi} \int \frac{d\varepsilon}{2\pi} e^{i\varepsilon\eta} G_n(k, \varepsilon) \chi_n^\dagger(z) \hat{v} \chi_n(z), \quad (21)$$

where  $n$  is the index of scattering states ( $n = R \uparrow, R \downarrow, L \uparrow$ , and  $L \downarrow$ ) and  $\eta = 0^\pm$ . The matrix elements of the velocity operator  $\hat{v} = -(i/m) \partial/\partial z$  should be calculated in the basis of scattering states, and the retarded Green function  $G_n(k, \varepsilon)$  in Eq. (21) is diagonal in this basis. Using Eq. (21) in the limit of small deviation from equilibrium, one obtains the Landauer formula for conductance, which takes into account the spin up and down channels

$$G = \frac{e^2}{2\pi\hbar} \left( \frac{v_\downarrow}{v_\uparrow} |t_{R\uparrow}|^2 + |t_{R\uparrow}^f|^2 + \frac{v_\uparrow}{v_\downarrow} |t_{R\downarrow}|^2 + |t_{R\downarrow}^f|^2 \right), \quad (22)$$

where all the velocities and transmission coefficients are taken at the Fermi level.

For the thin domain wall,  $k_{F\uparrow(\downarrow)} L \ll 1$ , taking into account Eq. (15), one can write the conductance in the form

$$G = \frac{4e^2}{\pi\hbar} \frac{v_\uparrow v_\downarrow (v_\uparrow + v_\downarrow)^2 + 2\lambda^2 (v_\uparrow^2 + v_\downarrow^2)}{[(v_\uparrow + v_\downarrow)^2 + 4\lambda^2]^2}. \quad (23)$$

In the limit of  $v_\uparrow = v_\downarrow$  and  $\lambda \rightarrow 0$ , we obtain the conductance of a one-channel spin-degenerate wire,  $G_0 = e^2/\pi\hbar$ . In the regime of ballistic transport  $G_0$  is also the conductance of the system without the domain wall.

Variation of the conductance  $G$  with the wall width  $L$  (Fig. 1) was calculated from Eq. (22), with the transmission coefficients determined numerically. Thus, the results shown in Fig. 1, are valid for arbitrary value of  $k_F L$ . In the limit of  $k_F L \ll 1$ , the results shown in Fig. 1 coincide with those obtained from the formula (23).

The conductance of magnetic nanowire in the presence of a domain wall is substantially smaller than in the absence of the wall. Accordingly, the associated magnetoresistance can be large. For example, for  $p = 0.9$  in Fig. 1 the magnetoresistance is equal to about 70% (it corresponds to  $G/G_0 = 0.6$ ). It should be noted that in magnetoresistance experiments on magnetic nanowires, for which the inequality  $k_F L < 1$  is fulfilled, one can have more than one domain walls. Accordingly, the magnetoresistance effect can be significantly enhanced.

In the case of strong polarization ( $p > p_c$ ) the main contribution to the conductance is associated with the spin-flip transmission through the domain wall, and the conductance increases monotonously with the width of the domain wall.

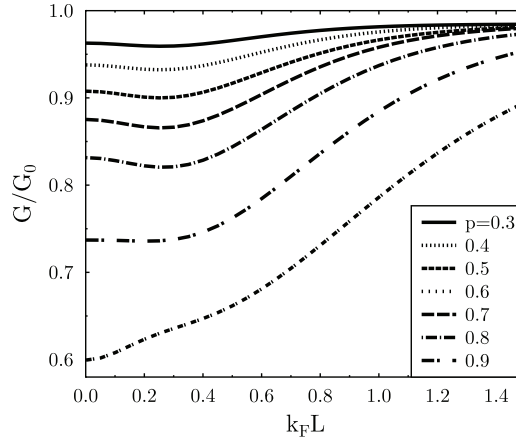


Fig. 1. Conductance of the domain wall as a function of DW width  $L$  in a magnetic quantum wire for different values of the parameter  $p = M/\varepsilon_F$ .

### 2.2.3 Spin current

When the electric current is spin polarized and when there is some asymmetry between the two spin channels, the flow of charge is accompanied by a flow of spin (angular momentum). The  $z$ -component of the spin current can be calculated from the following definition of the corresponding spin-current operator (it is defined here as number of spins per unit time)  $\hat{J}_z(z) = \frac{1}{2}\psi^\dagger(z) \{\sigma_z, \hat{v}\} \psi(z)$ , which leads to the following average value

$$J_z(z) = -i \sum_n \int \frac{dk}{2\pi} \int \frac{d\varepsilon}{2\pi} e^{i\varepsilon\delta} G_n(k, \varepsilon) \chi_n^\dagger(z) \sigma_z \hat{v} \chi_n(z). \quad (24)$$

After carrying out the calculations similar to those described above for charge current, one arrives in the linear response regime (limit of small bias voltage  $\mathcal{U}$ ) at the following formulas for the spin current  $J_z$ :

$$J_z(z < -L) = \frac{e\mathcal{U}}{2\pi\hbar} \left( \frac{v_\downarrow}{v_\uparrow} |t_{R\uparrow}|^2 + |t_{R\uparrow}^f|^2 - \frac{v_\uparrow}{v_\downarrow} |t_{R\downarrow}|^2 - |t_{R\downarrow}^f|^2 \right), \quad (25)$$

$$J_z(z > L) = \frac{e\mathcal{U}}{2\pi\hbar} \left( \frac{v_\downarrow}{v_\uparrow} |t_{R\uparrow}|^2 - |t_{R\uparrow}^f|^2 - \frac{v_\uparrow}{v_\downarrow} |t_{R\downarrow}|^2 + |t_{R\downarrow}^f|^2 \right). \quad (26)$$

Using Eq. (15) we find

$$J_z(z > L) = -\frac{8e\mathcal{U}}{\pi} \frac{\lambda^2 (v_\uparrow^2 - v_\downarrow^2)}{[(v_\uparrow + v_\downarrow)^2 + 4\lambda^2]^2} \quad (27)$$

and  $J_z(z < -L) = -J_z(z > L)$ . The magnetic torque due to spin transfer to the magnetic system within the domain wall is determined by the non-conserved spin current

$$T_z(\mathcal{U}) = \frac{16e\mathcal{U}}{\pi} \frac{\lambda^2 (v_\uparrow^2 - v_\downarrow^2)}{[(v_\uparrow + v_\downarrow)^2 + 4\lambda^2]^2}. \quad (28)$$

It should be noted that spin-flip scattering due to DW does not allow to separate spin channels like it was in the case for homogeneous ferromagnets. If we define now the spin conductance as  $G_z^s = J_z/\mathcal{U}$ , then one can write for  $z > 0$

$$G_z^s = -\frac{8e}{\pi} \frac{\lambda^2 (v_\uparrow^2 - v_\downarrow^2)}{[(v_\uparrow + v_\downarrow)^2 + 4\lambda^2]^2}. \quad (29)$$

Thus,  $G_z^s$  is negative for  $z > 0$  and positive for  $z < 0$ . In a nonmagnetic case we have  $v_\uparrow = v_\downarrow$

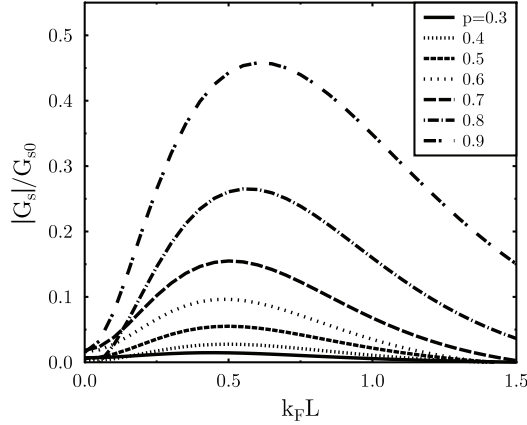


Fig. 2. Spin conductance of the wire with a domain wall as a function of DW width  $L$  for different values of  $p = M/\varepsilon_F$ .

and therefore  $G_s = 0$ . In the case considered here,  $G_s = 0$  when there is no DW in the wire. Let us introduce the spin conductance for one (spin-up) channel only,  $G_{s0} = e/2\pi$ . The relative spin conductance in the presence of DW,  $G_s/G_{s0}$ , calculated using Eq. (25) and with numerically found transmission coefficients, is shown in Fig. 2 as a function of the DW width  $L$  and for indicated values of the parameter  $p$ . It corresponds to the spin current outside the region of the domain wall. The spin current inside the wall is not conserved due to the spin-flip transitions.

The nonzero spin current in a one-channel wire with domain wall is due to a difference in spin-flip transmissions for spin-up and spin-down channels: the corresponding transmission coefficient turns out to be larger for faster (majority) electrons.

#### 2.2.4 Spin polarization due to domain wall

Spin dependent reflections from the wall lead to additional spin polarization of the system near the wall. The distribution of spin density created by the wall can be calculated using the basis of scattering states. The  $z$ -component of the spin density in the equilibrium situation ( $\mathcal{U} = 0$ ) is

$$S_z(z) = -i \sum_n \int \frac{dk}{2\pi} \int \frac{d\varepsilon}{2\pi} e^{i\varepsilon\eta} G_n(k, \varepsilon) \chi_n^\dagger(z) \sigma_z \chi_n(z). \quad (30)$$

The above formula contains a constant part corresponding to the spin density in the absence of DW, as well as the  $z$ -dependent part  $\delta S_z(z)$  created by the wall,

$$\begin{aligned}\delta S_z(z) &= \frac{1}{\pi} \int_0^{k_{F\uparrow}} dk r_{R\uparrow} \cos(2k_{\uparrow}z) - \frac{1}{\pi} \int_0^{k_{F\downarrow}} dk r_{R\downarrow} \cos(2k_{\downarrow}z), \quad (z < -L), \\ &= \frac{1}{\pi} \int_0^{k_{F\uparrow}} dk r_{L\uparrow} \cos(2k_{\uparrow}z) - \frac{1}{\pi} \int_0^{k_{F\downarrow}} dk r_{L\downarrow} \cos(2k_{\downarrow}z), \quad (z > L).\end{aligned}\quad (31)$$

>From (31) we infer that the spin density is an oscillating function of  $z$ . The spin dependent reflections from the wall create spatial oscillations of the electron spin density. These oscillations are similar to the Friedel oscillations of charge in a nonmagnetic metal. One should point out that in addition to the above calculated spin polarization, there is also a nonequilibrium spin polarization due to the current flowing through the system at  $\mathcal{U} \neq 0$  (Ebels et al. (2000)).

### 3. Spin quantum wells in magnetic nanowires

Let us consider now the magnetic nanowire with a magnetization profile exhibiting two domain walls at a distance  $2d$ . We assume that the magnetization  $\mathbf{M}(z)$  in both DWs varies within the  $x - z$  plane and the  $z$  axis is along the wire. Thus, now  $z$  is the easy axis, and the  $x - z$  plane is the easy plane. We study the case where the thickness and the width of the nanowire are smaller than the carrier Fermi wavelength so that only one size quantized level (a single one-dimensional subband) is populated. The Hamiltonian describing independent carriers along the wire in the presence of magnetization field  $\mathbf{M}(z)$  is given by Eq. (14).

We are interested in the case where the width  $2L$  of each DW is smaller than the carriers Fermi wavelength,  $k_F L \ll 1$  and particularly when  $k_F d \geq 1$  (otherwise the carriers are not influenced by the detailed topology of the DWs). For moderate carrier density the Fermi energy (chemical potential  $\mu$ ) is in one of the magnetically split subbands. This case corresponds to a full spin polarization of the electron gas. The electron wave functions are

$$\psi_k(z) = (e^{ikz} + r e^{-ikz}) |\uparrow\rangle + r_f e^{\kappa z} |\downarrow\rangle, \quad z < -d, \quad (32)$$

$$\psi_k(z) = (A e^{\kappa z} + B e^{-\kappa z}) |\uparrow\rangle + (C e^{ikz} + D e^{-ikz}) |\downarrow\rangle, \quad |z| < d, \quad (33)$$

$$\psi_k(z) = t e^{ikz} |\uparrow\rangle + t_f e^{-\kappa z} |\downarrow\rangle, \quad z > d, \quad (34)$$

where  $|\uparrow\rangle$  ( $|\downarrow\rangle$ ) is the spin-up (spin-down) component of the carrier states,  $k = [2m(\varepsilon + JM)]^{1/2}$ , and  $\kappa = [2m(JM - \varepsilon)]^{1/2}$ . The electron energy  $\varepsilon$  is measured from the midpoint in between spin-up and spin-down band edges. The non-spin-flip (spin-flip) transmission and reflection coefficients  $t$  and  $r$  ( $t_f$  and  $r_f$ ) as well as the constants  $A$ ,  $B$ ,  $C$  and  $D$  have to be deduced from the solutions of Schrödinger's equation and from the continuity requirements. Equations (32)-(34) describe spin-up carriers incoming from the left, being transmitted and reflected from the double DW structure into waves with the same or opposite spin polarizations with a subsequent decay of the spin-down part of the wave function.

To determine the unknown coefficients in Eqs. (32)-(34) we utilize the wave function continuity at  $z = \pm d$ , i.e.

$$\frac{1}{2m} \left( \frac{d\psi_k}{dz} \Big|_{z=-d+L} - \frac{d\psi_k}{dz} \Big|_{z=-d-L} \right) + \lambda \sigma_x \psi_k(-d) = 0, \quad (35)$$

where

$$\lambda \simeq J \int_{-d-L}^{-d+L} dz M_x(z) \simeq 2JML. \quad (36)$$

Similar equation holds for  $z = d$ . The boundary conditions at  $z = \pm d$  (eight equations for the spinor components) define all the coefficients.

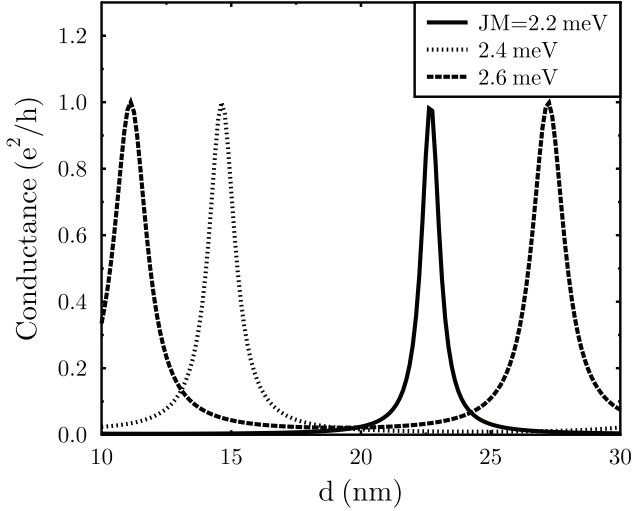


Fig. 3. Conductance as a function of the spin quantum well width for different values of the magnetization  $M$ .

For a physical insight into the results one can inspect the limiting case of  $\Delta = 4mJML = 0$ , where no spin-flip transitions occur at the DW. Correspondingly, only spin-up electrons tunnel through the barrier. Then the standard formula for barrier tunnelling

$$t = 2i\kappa e^{-2ikd} [2i\kappa \cosh(2\kappa d) + (k^2 - \kappa^2) \sinh(2\kappa d)]^{-1} \quad (37)$$

can be easily retrieved. The corresponding contribution to the conductance is very small, and for  $\kappa d \gg 1$  it can be completely neglected. The spin-down electrons are localized within the spin quantum well. One can find a symmetric solution with  $r_f = t_f$  corresponding to a localized state with the wave vector  $k$  and obeying the relation  $\tan kd = \kappa/k$ . The antisymmetric solution for such  $k$  (with  $r_f = -t_f$ ) satisfies the equation  $\tan kd = -\kappa/k$ . When the distance  $d$  between the DWs is varied the energetic positions of the size-quantized levels within the well are shifted. For certain values of  $d$  the energy of the localized states within the well coincides with the Fermi level. Thus, if the spin-mixing amplitude is finite (i.e.  $\Delta \neq 0$ ) we expect spin-up carriers to transverse resonantly the DWs. It is important to note that when  $\Delta \neq 0$ , the aforementioned localized spin-down states turn quasi stationary with a finite decay width  $\Gamma = 1/\tau \sim |t_f|^2$ , where  $\tau$  is the life time of these quasilocated states. The parameter  $|t_f|$  is controllable, e.g. by changing the parameters of the DWs.

In the regime of a linear response the conductance of the nanowire is determined by

$$G = \frac{e^2}{2\pi} |t(\varepsilon = \mu)|^2. \quad (38)$$

Using this relation one calculates the variation of the conductance  $G$  with the DWs distance  $2d$  for several values of the magnetization  $M$ . The conductance shown in Fig. 3 exhibits narrow resonance peaks corresponding to those values of  $d$  at which a quasi-discrete, size-quantized level coincides with the Fermi energy. The effective barrier created by the DWs is basically transparent at the conductance peak. The width of the resonance peaks is related to the life time  $\tau$  of the quasi-stationary spin-well states, and is determined by the spin-mixing mechanism mentioned above (and specifically by  $|t_f|$ ). The strength of spin mixing, and hence the width of the resonance peaks, can be controlled, e.g., by varying the width  $L$  of the DWs. Decreasing the spin-mixing parameter  $\Delta = 4mJML$ , the life time of the localized spin quantum-well states increases and the conductance resonance peaks become correspondingly narrower. The energetic positions of the quasi discrete levels depend also on the parameters  $\Delta$  and  $d$ . This results in a slight shift of the resonance positions when changing  $L$ . Experimentally the Fermi level position can be shifted by electrically gating the whole structure. In this case, the resonance conductance peaks occur as a function of the gate voltage for a fixed distance between the DWs.

The presented calculations are valid for  $d \ll L_e$ , where  $L_e$  is the decoherence length. Taking into account the decoherence effects, one expects that the double DWs resistance in this limit to be the sum of resistances of the individual DWs.

By gating the structure one can tune the Fermi energy and manipulate the spin density. For an experimental verification we note that spin-density modulations can be imaged with a sub nanometer resolution using spin-polarized scanning tunneling microscopy. The extreme sensitivity of the conductance to the inter-walls distance can be used to identify the relative position of the DWs.

## 4. Influence of electron-electron interactions

### 4.1 Thin domain walls

Now we consider quasi-one-dimensional magnetic nanowire with the domain wall taking into account the electron-electron interaction. This interaction is important at very low temperatures, and it can affect dramatically the charge and spin transport. We assume that the wire lies along  $z$  axis, and the domain wall is centered at  $z = 0$ . Its space modulation is described by  $\mathbf{M}(\mathbf{r})$ . Assuming  $\mathbf{M}(\mathbf{r})$  to lie in the  $xz$  plane, and the domain wall to be thinner than the Fermi wavelength, we write the single-particle Hamiltonian as

$$H_0 = -\frac{1}{2m} \frac{d^2}{dz^2} + V\delta(z) + JM_z(z)\sigma_z + \lambda\delta(z)\sigma_x, \quad (39)$$

where  $V$  is a potential scattering term that has been added for the sake of generality. The electron wavevector in each domain is related to the energy  $E$  by  $k = [2m(E \pm JM_0)]^{1/2}$ . The electron gas in the negative semi-axis ( $z < 0$ ) is predominantly  $\uparrow$ -spin. An electron incident from the left with the momentum  $k$  and spin  $\uparrow$  (or  $\downarrow$ ) can be transmitted to the positive semi-axis while preserving its spin, but the energy conservation requires the momentum to change from  $k$  to  $k_-$  (or  $k_+$ ), the latter being defined as a function of  $k$  as  $k_{\pm} = (k^2 \pm 4mJM_0)^{1/2}$ . If the transmission occurs with spin reversal, the momentum  $k$  is not changed.

Using the scattering states relevant to the problem, in the form of equation (15), one can easily find the scattering amplitudes for electrons incident from  $z = -\infty$ :

$$t_{\uparrow,\downarrow}(k) = \frac{2(v + v_{\mp} + 2iV)v}{(v + v_{\mp} + 2iV)^2 + 4\lambda^2} = r_{\uparrow,\downarrow}(k) + 1, \quad (40)$$

$$t_{\uparrow,\downarrow}^f(k) = \frac{4i\lambda v}{(v + v_{\mp} + 2iV)^2 + 4\lambda^2} = r_{\uparrow,\downarrow}^f(k), \quad (41)$$

where the velocities  $v_{\pm} = k_{\pm}/m$ . This is simply a generalization of equation (18) including now the potential scattering. These scattering amplitudes can be viewed as zero order with respect to the electron-electron interaction. Analogously one can determine the scattering states and amplitudes corresponding to the waves incident from  $+\infty$ .

The electron interactions are modeled by adding the following term to the Hamiltonian:

$$\hat{H}_{int} = g_{1,\alpha,\beta} \int \frac{dk_1 dq}{(2\pi)^2} a_{k_1,\alpha}^{\dagger} b_{k_2,\beta}^{\dagger} a_{k_2+q,\beta} b_{k_1-q,\alpha} + g_{2,\alpha,\beta} \int \frac{dk_1 dq}{(2\pi)^2} a_{k_1,\alpha}^{\dagger} b_{k_2,\beta}^{\dagger} b_{k_2+q,\beta} a_{k_1-q,\alpha}, \quad (42)$$

where the coupling constants  $g_1$  and  $g_2$  describe back and forward scattering processes between opposite moving electrons, respectively. We make use of field operators describing right ( $\hat{a}_{q\sigma}$ ) and left ( $\hat{b}_{q\sigma}$ ) moving plane-wave states. The Greek indices denote spin, and the summation over repeated indices is implied. Since the Fermi momentum depends on spin, we allow for the dependence of  $g$  on the spins of the interacting particles. We therefore distinguish between  $g_{1\uparrow}, g_{1\downarrow}, g_{1\perp}$  and  $g_{2\uparrow}, g_{2\downarrow}, g_{2\perp}$ . The forward scattering process between particles which move in the same direction will not affect the transmission amplitudes, although it will renormalize the Fermi velocity (Matveev et al. (1993)). This effect is equivalent to an effective mass renormalization, and the electrons with different spin orientations may turn out to have different effective masses.

The Hamiltonian terms (42) produce corrections, in first order of perturbation theory, to the scattering amplitudes, which we denote, for example, as  $\delta t_{\uparrow}^{(f)}, \delta r_{\uparrow}^{(f)}$ . If the bandwidth is  $D$ , and the energy of the scattered electron,  $\epsilon$ , approaches the Fermi level ( $\epsilon \rightarrow 0$ ) then these corrections diverge logarithmically as  $\log(|\epsilon|/D_0)$  (Matveev et al. (1993)) and are dealt with in a poor man's renormalization method, which works as follows. The bandwidth  $D$  is reduced step by step and such removal of states near the band edge is compensated by a renormalization of  $t_{\uparrow}$ . The problem of working out the first order perturbative corrections to the amplitudes is repeated for each new bandwidth with renormalized scattering amplitudes. Noting that  $t_{\uparrow} + \delta t_{\uparrow}$  remains invariant as  $D$  is reduced, one finds the following renormalization group differential equation:

$$dt_{\uparrow} + \frac{\partial \delta t_{\uparrow}}{\partial D} dD = 0,$$

and analogous equations for all the other scattering amplitudes. The bandwidth is progressively reduced from  $D_0$  to  $|\epsilon'|$  (which will eventually be taken as temperature  $|\epsilon'| = T$ ). Then the scaling equations for the transmission amplitudes can be found Araújo et al. (2006) and solved in the vicinity of some fixed points. The nature and location of fixed point are determined by some combination of initial coupling constants in (42). In our analysis they are the interaction parameters  $g_{\uparrow}, g_{\downarrow}$  and  $g_{\perp}$ , which are defined as follows:

$$\frac{g_{2\uparrow} - g_{1\uparrow}}{4hv_{F+}} = g_{\uparrow}, \quad (43)$$

$$\frac{g_{2\downarrow} - g_{1\downarrow}}{4hv_{F-}} = g_{\downarrow}, \quad (44)$$

$$\frac{g_{2\perp}}{2h(v_{F+} + v_{F-})} = g_{\perp}, \quad (45)$$

where  $v_{F-}$ ,  $v_{F+}$  are the Fermi velocities of spin minority and spin majority electrons, respectively.

For repulsive e-e interactions the system flows to fixed points where it is an insulator. The fixed point where  $|r_{\sigma}| \rightarrow 0$  is attained when  $2g_{\perp} - g_{\uparrow} - g_{\downarrow} > 0$ , in which case  $|r_{\uparrow}^f| \rightarrow \sqrt{v_{F+}/v_{F-}}$ . The reflection coefficient with spin reversal depends on temperature as:

$$\mathcal{R}_{\uparrow}^f(T) = \frac{v_{F-}}{v_{F+}} |r_{\uparrow}^f|^2 = \frac{\frac{\mathcal{R}_{\uparrow,0}^f}{1 - \mathcal{R}_{\uparrow,0}^f} \left(\frac{T}{D_0}\right)^{2(g_{\uparrow} + g_{\downarrow} - 2g_{\perp})}}{1 + \frac{\mathcal{R}_{\uparrow,0}^f}{1 - \mathcal{R}_{\uparrow,0}^f} \left(\frac{T}{D_0}\right)^{2(g_{\uparrow} + g_{\downarrow} - 2g_{\perp})}}, \quad (46)$$

where  $\mathcal{R}_{\uparrow,0}^f$  and is a constant equal to the reflection coefficient for non-interacting electrons.

It is easily seen that when  $2g_{\perp} - g_{\uparrow} - g_{\downarrow} > 0$ , then  $\mathcal{R}_{\uparrow}^f(T) \rightarrow 1$  as  $T \rightarrow 0$ . The domain wall becomes insulating. It reflects all incident electrons while reversing their spin. Therefore, such a DW may be considered as a perfect spin-flip reflector at zero temperature. In order to find the low  $T$  behavior of transmissions we put  $r_{\uparrow} = r_{\downarrow} = 0$  in the renormalization group equations and obtain  $|t_{\uparrow}| \sim |t_{\uparrow}^f| \sim |t_{\downarrow}^f| \sim T^{2g_{\perp}}$ .

In the regime where  $g_{\uparrow} + g_{\downarrow} - 2g_{\perp} > 0$  we have  $\mathcal{R}_{\uparrow}^f(T) \rightarrow 0$ ,  $\mathcal{R}_{\uparrow}(T) \rightarrow 1$ . So, the domain wall reflects all incident electrons while preserving their spin. For the transmission amplitudes we can obtain:  $|t_{\uparrow}| \sim T^{g_{\uparrow} + g_{\downarrow}}$ ,  $|t_{\uparrow}^f| \sim T^{2g_{\uparrow}}$ , and  $|t_{\downarrow}^f| \sim T^{2g_{\downarrow}}$ .

If  $g_{\uparrow} + g_{\downarrow} - 2g_{\perp} = 0$  then both  $\mathcal{R}_{\uparrow}^f(T)$  and  $\mathcal{R}_{\uparrow}(T)$  tend to finite values.

Zero temperature fixed points corresponding to the transparent domain wall can be achieved when the interaction constants are all negative, and that corresponds to an attractive electron-electron interaction. The reflection coefficients vanish under scaling as powers of temperature. If some of the interaction constants are positive and the others negative, the situation becomes more complex. We now describe several possible situations for the case  $V = 0$  in the Hamiltonian (39).

If  $g_{\uparrow}, g_{\downarrow} > 0$ ,  $g_{\perp} < 0$  then the system flows to the fixed point  $r_{\uparrow} = r_{\downarrow} = -1$  with all other amplitudes vanishing. The low- $T$  behavior of the transmission can be found as  $|t_{\uparrow}| \sim T^{g_{\uparrow} + g_{\downarrow}}$ ,  $|t_{\uparrow}^f| \sim T^{2g_{\uparrow}}$ , and  $|t_{\downarrow}^f| \sim T^{2g_{\downarrow}}$ . For  $r_{\uparrow}^f$ , one finds  $r_{\uparrow}^f \sim T^{g_{\uparrow} + g_{\downarrow} - 2g_{\perp}}$ , therefore we must have  $g_{\uparrow} + g_{\downarrow} - 2g_{\perp} > 0$  in order for  $r_{\uparrow}^f \rightarrow 0$ .

In the case of  $g_{\uparrow}, g_{\downarrow} < 0$ ,  $g_{\perp} > 0$  the system flows to the perfect spin-flip reflector fixed point  $|r_{\uparrow}^f| = \sqrt{v_{F+}/v_{F-}}$  with all other amplitudes vanishing.

In the case of  $g_{\uparrow} > 0$ ,  $g_{\downarrow} < 0$  and for negative or small positive  $g_{\perp}$ , the system flows to a fixed point where  $|t_{\downarrow}^f| = 1$ ,  $r_{\uparrow} = -1$ . The wall transmits all spin-down particles with a spin-flip and

reflects all spin-up particles. The exponents for the transmission amplitudes are  $|t_{\uparrow}| \sim T^{g_{\uparrow}}$  and  $|t_{\uparrow}^f| \sim T^{2g_{\uparrow}}$ .

When  $g_{\uparrow} < 0$  and  $g_{\downarrow} > 0$ , the situation is analogous to the previous one. For negative or small positive  $g_{\perp}$  the system flows to a fixed point where  $|t_{\uparrow}^f| = 1$ ,  $r_{\downarrow} = -1$  with all the other amplitudes vanishing. The wall transmits all spin-up particles with a spin-flip and reflects all spin-down particles. The exponents for transmission amplitudes are  $|t_{\uparrow}| \sim T^{g_{\downarrow}}$ ,  $|t_{\uparrow}^f| \sim T^{2g_{\downarrow}}$ .

Thus, we identified possible fixed points corresponding to (i) perfectly insulating wall (with or without complete spin reversal), and (ii) transparent wall. In any case, the electron-electron interaction changes completely the transport through the domain wall at sufficiently low temperatures and may in some cases suppress charge transport without suppressing spin current. These results may account for a huge magnetoresistance associated with a domain wall in ballistic nanocontacts.

#### 4.2 Thick domain walls

Electron-electron correlations play also role in the case of thicker domain walls (Sedlmayr et al. (2011)). Starting from equation (1), with an additional short range interaction  $H_I$  similar to equation (43), one can again make the gauge transformation, equations (2)-(5). This gauge transformation allows one to linearize the problem around the spin-split Fermi points and hence use the standard technique of bosonization. After this gauge transformation the interaction is left unaffected, the magnetization is locally rotated to a Zeeman term, and the kinetic energy operator introduces a new potential when it acts on the local rotation:

$$H = \sum_{\sigma} \int dz \psi_{\sigma}^{\dagger}(z) \left[ -\frac{1}{2m} \partial_z^2 - JM_s \sigma_{\sigma\sigma}^z - \mu \right] \psi_{\sigma}(z) + H_I + H_w \quad (47)$$

$$H_w = -\frac{1}{2m} \sum_{\sigma\sigma'} \int dz \psi_{\sigma}^{\dagger}(z) \left[ i\varphi'(z) \sigma_{\sigma\sigma'}^x \partial_z + \frac{i\varphi''(z)}{2} \sigma_{\sigma\sigma'}^x - \frac{1}{4} [\varphi'(z)] 2\delta_{\sigma\sigma'} \right] \psi_{\sigma'}(z). \quad (48)$$

$\psi_{\sigma}^{\dagger}(z)$  is a creation operator for an electron of spin  $\sigma$  at a position  $z$  in the wire. The gauge potential  $H_w$  can be approximated if we assume that the Fermi wavelength is much smaller than the domain wall width  $\lambda_F \ll L$ . In this case only the first term of equation (48) is relevant, the next two terms are of order  $(\lambda_F/L)^2$ . The next step is linearization via the ansatz  $\psi_{\sigma}(z) = e^{ik_{F\sigma}x} \psi_{\sigma+}(z) + e^{-ik_{F\sigma}x} \psi_{\sigma-}(z)$ , where  $k_{F\sigma} = \sqrt{2m(\epsilon_F \pm JM)}$ . The + and - indices denote the chiral right and left moving electrons respectively. The interaction  $H_I$  can be decomposed into spin parallel and spin perpendicular components which, when suppressing the spatial indices and defining the local density  $\rho_{\sigma\pm} = \psi_{\sigma\pm}^{\dagger} \psi_{\sigma\pm}$ , can be written as

$$H_2 = \sum_{\sigma,r=\pm} \int dz \left[ \frac{g_{2\parallel\sigma}}{2} \rho_{\sigma r} \rho_{\sigma-r} + \frac{g_{2\perp}}{2} \rho_{\sigma r} \rho_{\bar{\sigma}-r} \right], \quad (49)$$

$$H_4 = \sum_{\sigma,r=\pm} \int dz \left[ \frac{g_{4\parallel\sigma}}{2} \rho_{\sigma r} \rho_{\sigma r} + \frac{g_{4\perp}}{2} \rho_{\sigma r} \rho_{\bar{\sigma}r} \right] \quad (50)$$

$$H_1 = \sum_{\sigma,r=\pm} \int dz \left[ -\frac{g_{1\parallel\sigma}}{2} \rho_{\sigma r} \rho_{\sigma-r} + \frac{g_{1\perp\sigma}}{2} e^{2iz(k_{F\bar{\sigma}} - k_{F\sigma})} \psi_{\sigma r}^{\dagger} \psi_{\bar{\sigma}-r}^{\dagger} \psi_{\bar{\sigma}r} \psi_{\sigma-r} \right]. \quad (51)$$

Umklapp processes scattering two left movers into right movers and vice versa are always neglected here due to the non-commensurate nature of the Fermi wavevectors.

This fermionic model can now be bosonized (Penc et al. (1993)). Two adjoint bosonic fields are introduced which can be defined by the vertex operator

$$\psi_{\sigma r}(z) = \frac{1}{\sqrt{2\pi\alpha}} e^{-i\sqrt{\pi}[\theta_{\sigma}(z) - r\phi_{\sigma}(z)]}. \quad (52)$$

These bosonic fields satisfy  $[\phi_{\sigma}(z), \Pi_{\sigma}(z')] = i\delta(z - z')$  where  $\Pi_{\sigma}(z) = \partial_y \theta_{\sigma}(z)$ . Despite the absence of spin-charge separation, due to the spin-split bands, we will use the spin and charge representation as it conveniently represents the scattering terms. Defining  $\phi_{c,s}(z) = [\phi_1(z) \pm \phi_2(z)]/\sqrt{2}$  (and similar for the  $\theta_{c,s}(z)$  fields) gives us for the quadratic part of the bosonic Hamiltonian

$$H_q = \int dz \left[ [\partial_z \theta_c(z)] 2 \frac{v_c K_c}{2} + [\partial_z \theta_s(z)] 2 \frac{v_s K_s}{2} + [\partial_z \theta_c(z) \partial_z \theta_s(z)] v_a \right. \\ \left. + [\partial_z \phi_c(z)] 2 \frac{v_c}{2K_c} + [\partial_z \phi_s(z)] 2 \frac{v_s}{2K_s} + [\partial_z \phi_c(z) \partial_z \phi_s(z)] v_b \right]. \quad (53)$$

$K_s$  and  $K_c$  are the spin and charge Luttinger parameters.  $v_a$  and  $v_b$  describe the coupling between the spin and charge sectors. These parameters are functions of the interaction strengths and Fermi velocities. This quadratic Hamiltonian contains all of the quartic fermionic interaction terms except for  $g_{1\perp\sigma}$ .

The final bosonic Hamiltonian is  $H = H_q + H_{1\perp} + H_w^f + H_w^b$  where

$$H_w^f = \frac{k_{F\uparrow} + k_{F\downarrow}}{2m\pi\alpha} \int dz \frac{\text{sech}[z/L]}{L} \sin[\sqrt{2\pi}\theta_s(z)] \sin[z(k_{F\uparrow} - k_{F\downarrow}) + \sqrt{2\pi}\phi_s(z)] \quad (54)$$

$$H_w^b = \frac{k_{F\uparrow} - k_{F\downarrow}}{2m\pi\alpha} \int dz \frac{\text{sech}[z/L]}{L} \sin[\sqrt{2\pi}\theta_s(z)] \sin[-z(k_{F\uparrow} + k_{F\downarrow}) + \sqrt{2\pi}\phi_c(z)] \quad (55)$$

$$H_{1\perp} = \frac{2}{(2\pi\alpha)^2} \int dz \cos[2\sqrt{2\pi}\phi_s(z)] [g_{1\perp\uparrow} e^{-2iz(k_{F\uparrow} - k_{F\downarrow})} + g_{1\perp\downarrow} e^{2iz(k_{F\uparrow} - k_{F\downarrow})}]. \quad (56)$$

We have both forward and backward scattering terms,  $H_w^f$  and  $H_w^b$  respectively. We also find an oscillating sine-Gordon interaction term  $H_{1\perp}$ , describing "slow" Umklapp processes which are not averaged out. The normal modes of this  $SU(2)$  asymmetric model have no clear physical interpretation, in contrast to the non-spin split case in which they represent pure spin and charge modes. The Hamiltonian of equation (53) can be diagonalized to find the appropriate normal modes.

Standard renormalization group analysis on the scattering Hamiltonians  $H_1$ ,  $H_w^f$  and  $H_w^b$  yields the scaling equations of the form

$$\frac{dg_{1\perp\sigma}}{dl} = g_{1\perp\sigma} [2 - \gamma_1]. \quad (57)$$

$\gamma_1$ , and also the  $\gamma_{f,b}$  used below, are known, but rather complicated, functions of  $v_{F\sigma}$ ,  $g_{2\parallel\sigma}$ ,  $g_{2\perp}$ ,  $g_{4\parallel\sigma}$ ,  $g_{4\perp}$ ,  $g_{1\parallel\sigma}$ , and  $g_{1\perp\sigma}$  which can be found in the appropriate references. This first term is an irrelevant perturbation for any realistic microscopic model. Next we define the bare scattering coupling constants  $g_{f/b} \equiv k_{F\uparrow} \pm k_{F\downarrow}$ . For forward and backward scattering we find:

$$\frac{dg_{f,b}}{dl} = g_{f,b}[2 - \gamma_{f,b}]. \quad (58)$$

In this case we find a relevant forward scattering term. However, the backward scattering term can be either relevant or irrelevant depending on the particular microscopic model used. If backward scattering is relevant then we find the usual spin-charge gapped insulating behaviour of an impurity in a Luttinger liquid. However, if only the forward scattering is relevant the spin mode is gapped, but the charge mode remains ungapped (C1S0 phase). Physically, this means that electrons no longer undergo a change of spin on passing through the domain wall. The spin of the conduction electrons becomes locked.

Due to the extended nature of the domain wall we must consider a hierarchy of length scales, as well as the relevance of the renormalized operators. Let us define  $\lambda_{\pm} = (k_{F\uparrow} \pm k_{F\downarrow})^{-1}$ , which are the relevant lengthscales for the forward and backward scattering components. From the above considerations we have several possibilities. Firstly we can have backward scattering as either relevant or irrelevant. Secondly we must take into account the relative length scales. If  $\lambda_+ < L$  then at some stage of the renormalization process (i.e. when the appropriate length scale cut-off becomes of order  $\lambda_+$ ) the backward scattering terms will become small due to averaging over their oscillations. A similar case holds for the forward scattering with  $\lambda_+ \rightarrow \lambda_-$  in the preceding. For the case in which both the forward and backward scattering lengthscales are shorter than the domain wall length we end up in the completely adiabatic limit as one would expect. However we can also be in the opposite regime when both forward and backward scattering lengthscales are longer than the domain wall length in which case one need only consider the relevancy of the appropriate operators. Note that this is possible without requiring a delta function like domain wall profile. In addition we can of course be in the intermediate regime where the backward scattering is prone to this averaging out, but the forward scattering is not. As such the low temperature fixed point depends not only on the relevance of the operators, but also on the hierarchy of length scales, and leaves three possibilities: firstly a spin-charge insulator, secondly a spin gapped charge conducting phase, and thirdly a ferromagnetic Luttinger liquid with an adiabatically behaving domain wall.

## 5. Current-induced interaction of multiple domain walls

Now consider the Hamiltonian of a one-dimensional wire in a spatially non-uniform magnetization profile  $\mathbf{M}(z)$

$$H = \int dz \psi_{\alpha}^{\dagger}(z) \left[ -\frac{\partial_z^2}{2m} \delta_{\alpha\beta} - J \boldsymbol{\sigma}_{\alpha\beta} \cdot \mathbf{M}(z) \right] \psi_{\beta}(z), \quad (59)$$

and apply the local gauge transformation as described in Sec. 1. The transformed Hamiltonian can be presented as

$$H = \int dz \psi_{\alpha}^{\dagger}(z) \left[ -\frac{\partial_z^2}{2m} \delta_{\alpha\beta} + U_{\alpha\beta}(z) - JM\sigma_{\alpha\beta}^z \right] \psi_{\beta}(z) \quad (60)$$

where the DW-induced perturbation is

$$U(z) = -\frac{1}{2m} \left[ 2A \partial_z + (\partial_z A) + A^2 \right], \quad (61)$$

and  $A(z) = T^\dagger(z) \nabla_z T(z)$  is a gauge potential. For a wire with two DWs we can parametrize the magnetization profile by the angles  $\varphi(z)$  and  $\theta(z)$  (see Fig. 4)

$$\mathbf{n}(z) = (\cos \theta \sin \varphi, \sin \theta \sin \varphi, \cos \varphi), \quad (62)$$

$$\varphi(z) = \underbrace{\cos^{-1} \left( \tanh \left[ \frac{z}{L} \right] \right)}_{=-\varphi_1(z)} + \underbrace{\cos^{-1} \left( \tanh \left[ \frac{z-z_0}{L} \right] \right)}_{=-\varphi_2(z)}. \quad (63)$$

The angle  $\theta(z)$  describes the relative orientation between the wall pinned at  $z = 0$  and the other situated around  $z = z_0$ . We set  $\theta_1$  to zero at the first wall and  $\theta_2 = \theta_0$  around the second. For  $\theta_0 = \pi$  the walls are antialigned. For  $z_0 \leq L$  DWs may merge, hence we consider the case  $z_0 > L$  for which we may write  $U(z) \approx U_1(z) + U_2(z)$ , where ( $j = 1, 2$ )

$$U_j(z) = \frac{[\varphi'_j(z)]^2}{8m} + i\sigma^y \left[ \frac{\varphi''_j(z)}{4m} + \frac{\varphi'_j(z) \partial_z}{2m} \right] \cos \theta_j - i\sigma^x \left[ \frac{\varphi''_j(z)}{4m} + \frac{\varphi'_j(z) \partial_z}{2m} \right] \sin \theta_j. \quad (64)$$

This approach is generalizable to any number of DWs, which are sufficiently far apart. For  $k_F L \geq 1$ , i.e. when  $\mathbf{M}(z)$  hardly varies within  $k_F^{-1}$  (adiabatic DW), the terms in Eq. (64) proportional to  $\varphi''_j(z)$  are negligibly small and the perturbative approach is appropriate for treating the electron scattering from the DWs potential (Eq. (64)). In fact, it can be shown that this approach is justifiable even for  $k_F L = 1$ . Assuming  $\psi^0(z)$  to be the wave function of an independent electron with energy  $\varepsilon$  in the wire without the DWs, we find the first-order correction due to the perturbation  $U_1(z)$ , i.e. due to scattering from the first DW, as

$$\delta\psi_\varepsilon(z) = \int_{-\infty}^{\infty} dz' G_\varepsilon(z, z') U_1(z') \psi^0(z'). \quad (65)$$

The Green's function  $G_\varepsilon$  corresponds to the unperturbed Hamiltonian with  $U(z) = 0$ . It is diagonal in spin space with elements

$$G_{\varepsilon\sigma}(z, z') = -\frac{im}{k_\sigma} e^{ik_\sigma|z-z'|}, \quad (66)$$

where  $k_\sigma \approx k_\sigma^0 + \frac{i}{2\tau_\sigma} \frac{m}{k_\sigma^0}$  for lifetimes  $\tau_\sigma \gg \varepsilon_F^{-1}$ , and  $k_\sigma^0 = [2m(\varepsilon + \mu \pm JM)]^{1/2}$ . Hence

$$\delta\psi_{\varepsilon\uparrow}(z) = \int_{-\infty}^{\infty} dz' \begin{pmatrix} -\frac{i}{8k_\uparrow} e^{ik_\uparrow|z-z'|} [\varphi'_1(z)]^2 e^{ik_\uparrow z'} \\ -\frac{k_\uparrow}{2k_\downarrow} e^{ik_\downarrow|z-z'|} \varphi'_1(z) e^{ik_\uparrow z'} \end{pmatrix} \quad (67)$$

$$\delta\psi_{\varepsilon\downarrow}(z) = \int_{-\infty}^{\infty} dz' \begin{pmatrix} \frac{k_\downarrow}{2k_\uparrow} e^{ik_\uparrow|z-z'|} \varphi'_1(z) e^{ik_\downarrow z'} \\ -\frac{i}{8k_\downarrow} e^{ik_\downarrow|z-z'|} [\varphi'_1(z)]^2 e^{ik_\downarrow z'} \end{pmatrix} \quad (68)$$

for incoming electrons of spin up and down, respectively. The interaction energy of the two DWs due to the single scattered state  $\psi_{\varepsilon\sigma}(z) = \psi_{\varepsilon\sigma}^0(z) + \delta\psi_{\varepsilon\sigma}(z)$  is calculated as

$$\Delta E_\sigma = \int_{-\infty}^{\infty} dz \delta\psi_{\varepsilon\sigma}^\dagger(z) U_2(z) \delta\psi_{\varepsilon\sigma}(z). \quad (69)$$

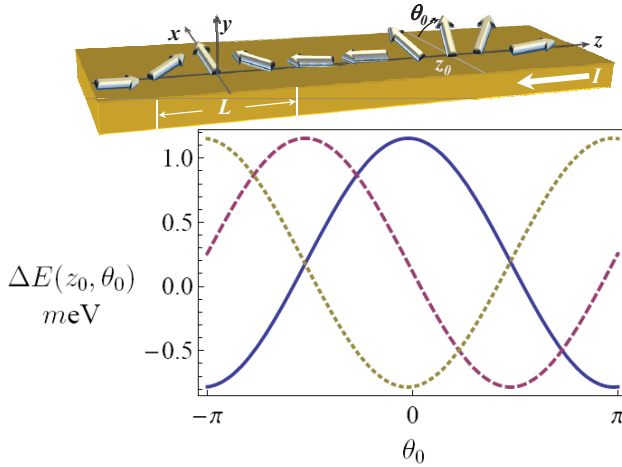


Fig. 4. Top panel: A schematics showing the DWs magnetization profile (thick arrows).  $L$  is the DW width,  $z_0$  and  $\theta_0$  are respectively the DW position and orientation with respect to the DW at  $z = 0$ ,  $I$  is the current. Lower panel: Interaction energy  $\Delta E(z_0, \theta_0)$  as a function of  $z_0$  and  $\theta_0$ . Solid curve is for  $z_0 = 3.67$  nm, the dashed is for  $z_0 = 4.13$  nm, and the dotted is for  $z_0 = 4.40$  nm.

Summing up the contributions of all scattering states in the energy range between  $\varepsilon_F$  and  $\varepsilon_F + e\Delta\phi/2$ , for an applied voltage  $e\Delta\phi/2 \ll \varepsilon_F$ , we obtain the current-induced coupling of the DWs as

$$\Delta E = \frac{e\Delta\phi}{\sqrt{2}\pi} \left( \frac{\Delta E_{\uparrow}}{v_{\uparrow}} + \frac{\Delta E_{\downarrow}}{v_{\downarrow}} \right), \quad (70)$$

where  $v_{\sigma} = k_{\sigma}^0/m$  is the velocity of electrons at the Fermi level.

Figure 4 shows the dependence of the coupling energy  $\Delta E$  as a function of distance  $z_0$  and relative angle  $\theta_0$  of the second DW. In the calculations we used the parameters:  $\lambda_F = 0.367$  nm (Fe),  $\tau_{\sigma}^{-1} = 10^{-9}\varepsilon_F$ ,  $L = \lambda_F$ ,  $JM = 0.2\varepsilon_F$ ,  $\varepsilon_F = 11.2$  eV, and  $e\Delta\phi = 0.01\varepsilon_F$  corresponding to an applied voltage of 112 meV. As we see, the interaction energy depends periodically on the DWs mutual angle  $\theta_0$  and distance  $z_0$ , which results in an oscillating motion of the DW along the axis  $z$  as well as an oscillating direction of DW polarization.

Now we focus on the effect of DW scattering on the electron spin density, leading to a nonequilibrium spin accumulation and to a spin torque acting on the wall. Subsequently, we study the dynamics of the DW related to the DW coupling. The spin-density due to the single transmitted wave of spin  $\sigma$  is

$$\mathbf{S}_{\sigma}(z) = \psi_{\varepsilon\sigma}^{\dagger}(z) T(z) \boldsymbol{\sigma} T^{\dagger}(z) \psi_{\varepsilon\sigma}(z), \quad (71)$$

and the total current-induced spin density is

$$\mathbf{S}(z) = \frac{e\phi}{2\pi} \left( \frac{\mathbf{S}_{\uparrow}}{v_{\uparrow}} + \frac{\mathbf{S}_{\downarrow}}{v_{\downarrow}} \right). \quad (72)$$

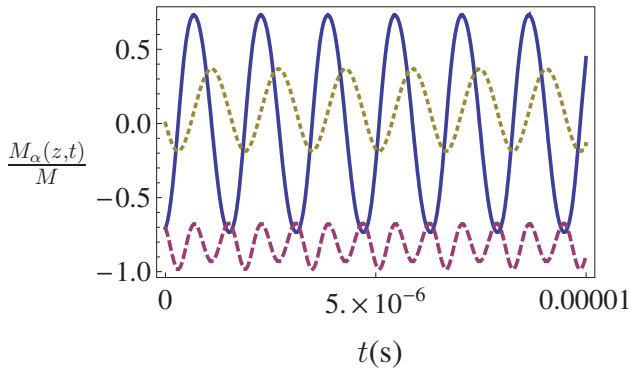


Fig. 5. The time dependence of the magnetization with the initial condition for the second wall to be at an angle of  $\theta_0 = \pi/4$  to the first wall. This is the solution to Eq. 74 with  $M \approx 5.56 \times 10^4 \text{ Am}^{-1}$ . The solid curve is the  $x$ -component, dashed the  $y$ -component, and dotted the  $z$ -component. Taken at the centre of the domain wall.

We find that the correction to the spin density follows the magnetization profile with additional Friedel oscillations, which are a superposition of two waves with periods  $k_{F\uparrow}^{-1}$  and  $k_{F\downarrow}^{-1}$ . The oscillations in the spin density are smaller in magnitude than the overall spin density profile. One can also calculate the current-induced torque acting on the second DW at  $z$  from

$$\Delta \mathbf{T}(z, z_0, \theta_0) = -\frac{\gamma J}{\sigma_{cs}} \mathbf{M}(z, z_0, \theta_0) \times \Delta \mathbf{S}(z, z_0, \theta_0), \quad (73)$$

where  $\gamma = g\mu_B$ ,  $g$  is the Landé factor and  $\mu_B$  is the Bohr magneton. The results of numerical calculations show that the force upon one of the DWs from the other one depends strongly on their relative polarizations.

Thus, the current through a magnetic nanowire containing DWs results in a DW interaction mediated by the scattered charge carriers. We developed a method for calculating the interaction energy and the consequences of this new coupling mechanism. The DWs interaction energy oscillates as a function of the DWs mutual orientation and distance. This has immediate consequences on how DWs rearrange upon applying a bias voltage and on the fundamental limit of the DWs packing density. In fact, different parts of the DW oscillate at different rates and in different ways: becoming more regular, smaller, and quicker away from the DW centre. This effect will be modified by the exchange interaction for longer domain walls, where there is an obvious limit to how much one can distort the domain wall before the energy costs becomes too high. The nonequilibrium DWs oscillations around the energy minima generates radiation with a frequency dependent on the applied bias voltage, DW length and scattering strength. These parameters are externally tunable for utilizing the interacting DWs as a versatile radiation source.

The effect of the modified spin density, which is the cause of the current induced interaction between the DWs, on the motion of the DW can be found using the standard Landau-Lifschitz equation (Lifschitz (1980)). To inspect the current-induced dynamics of the DW at  $z = z_0$ , we evaluate the accumulated spin density that acts on the DW at  $z = z_0$ . Thus for a relatively sharp domain wall which can be effectively treated as a magnetic moment we have only to

solve, at  $z = z_0$ :

$$\partial_t \mathbf{M} = -\frac{\gamma J}{\sigma_{cs}} \mathbf{M} \times \mathbf{S}[\mathbf{M}]. \quad (74)$$

As an initial condition we assume that the magnetization profile in the wire without electric current is described by Eq. (63). The results for the time dependence of the magnetization are shown in Fig. 5 for the centre of the DW,  $z = z_0$ . We should note that the relative orientation of the walls at the start of motion does play a role in the type of motion we see. Here we present it for an arbitrary configuration,  $\theta_0 = \pi/4$ . The DW motion is a result of the excess spin torque generated by the first DW, which is felt as an effective applied magnetic field. As such precession, as demonstrated in Fig. 5, is precisely what one would expect. The crucial point is that the characteristics of this precession depend upon the distance between, and relative orientation of, the two DWs.

The extension of our analysis to include the effects of magnetic anisotropy is straightforward, and constrains the motion in the appropriate direction. If one also wishes to consider the motion of a longer domain wall it is no longer possible to neglect the exchange interaction. In such a scenario one still finds distortion of the domain wall, but due to the extended nature of the spin density correction, it cannot produce any coherent motion. However, when one considers current induced motion (Zhang et al. (1980)) these spin density terms can allow for motion with smaller applied currents. This spin density takes on the role of an applied magnetic field, which is well known to ease the current induced motion of domain walls.

## 6. Conclusions

Using the presented models of electrons moving in a spatially varying magnetization field, one can study the properties of magnetic domain walls in magnetic nanowires. This allows for the calculations of charge and spin currents, current-induced spin torque, and current-induced interactions in magnetic nanowires. These are characteristics that strongly depend on the presence of domain walls. Our considerations were predominantly concentrated on very thin domain walls, where presence of a domain wall may affect very strongly the transmission of electrons in nanowires. Experimentally such thin domain walls can appear for instance in nanoconstrictions (Bruno (1999)). Domain walls in magnetic semiconductors with relatively low carrier density can be considered as thin because the electron wavelength in semiconductors  $\lambda$  is usually of the same order of magnitude or larger than the width of the walls.

## 7. Acknowledgement

This work is supported by the DFG through contract BE 2161/5-1 and SFB762, FCT Grant No. PTDC/FIS/70843/2006 in Portugal, Polish Ministry of Science and Higher Education as a research project in years 2011 – 2013 and by the Graduate School of MAINZ (MATCOR).

## 8. References

Araújo, M.A.N.; Dugaev, V.K.; Vieira, V.R.; Berakdar, J. & Barnaś, J. (2006) Transmission of correlated electrons through sharp domain walls in magnetic nanowires: a renormalization group approach. *Physical Review B*, Vol. 74, No. 22, (December 2006) 224429

- Araújo, M.A.N.; Berakdar, J.; Dugaev, V.K. & Vieira, V.R. (2007). Role of a spin-flip scatterer in a magnetized Luttinger liquid. *Physical Review B*, Vol. 76, No. 20, (November 2007) 205107
- Bruno, P. (1999). Geometrically constrained magnetic wall. *Physical Review Letters*, Vol. 83, No. 12, (September 1999) 2425-2428
- Cabrera, G.G. & Falicov, L.M. (1974). Theory of the residual resistivity of Bloch walls I. Paramagnetic effects. *Physica Status Solidi B*, Vol. 61, No. 2, (February 1974) 539-549
- Cabrera, G.G. & Falicov L.M. (1974). Theory of the residual resistivity of Bloch walls. II. Inclusion of diamagnetic effects. *Physica Status Solidi B*, Vol. 62, No. 1, (March 1974) 217-222
- Chopra, H.D. & Hua, S.Z. (2002). Ballistic magnetoresistance over 3000% in Ni nanocontacts at room temperature. *Physical Review B*, Vol. 66, No. 2, (June 2002) 020403(R)
- Dugaev, V.K.; Barnaś, J.; Łusakowski, A. & Turski, L. (2002). Electrons in a ferromagnetic metal with a domain wall. *Phys. Rev. B*, Vol. 65, No. 22, (June 2002) 224419
- Dugaev, V.K.; Berakdar, J. & Barnaś, J. (2003). Reflection of electrons from a domain wall in magnetic nanojunctions. *Physical Review B*, Vol. 68, No. 10, (September 2003) 104434
- Dugaev, V.K.; Berakdar, J. & Barnaś, J. (2004). Tunable conductance of magnetic nanowires with structured domain walls. *Physical Review Letters*, Vol. 96, No. 4, (February 2004) 047208
- Dugaev, V.K.; Barnaś, J.; Berakdar, J., Ivanov, V.I.; Dobrowolski, W. & Mitin, V.F. (2005). Magnetoresistance of a semiconducting magnetic wire with a domain wall. *Physical Review B*, Vol. 71, No. 2, (January 2005) 024430
- Dugaev, V.K.; Vieira, V.R.; Sacramento, P.D.; Barnaś, J.; Araújo, M.A.N. & Berakdar, J. (2006). Current-induced motion of a domain wall in a magnetic nanowire. *Physical Review B*, Vol. 74, No. 5, (August 2006) 054403
- Dugaev, V.K.; Vieira, V.R.; Sacramento, P.D.; Barnaś, J.; Araújo, M.A.N. & Berakdar, J. (2007). Current-induced spin torque on a domain wall in a magnetic nanowire. *International Journal of Modern Physics*, Vol. 21, Nos. 8 & 9, (April 2007) 1659-1663
- Ebels, U.; Radulescu, A.; Henry, Y.; Piraux, L. & Ounadjela, K. (2000). Spin accumulation and domain wall magnetoresistance in 35 nm Co wires. *Physical Review Letters*, Vol. 84, No. 5, (January 2000) 983-986
- Kläui, M. (2008). Head-to-head domain walls in magnetic nanostructures. *Journal of Physics: Condensed Matter*, Vol. 20, No. 31, (August 2008), 313001
- Lifshitz, E.M. & Pitaevskii L.P. (1980). *Statistical Physics Part 2: Theory of the Solid State* Butterworth-Heinemann, ISBN-10 0750626364, Oxford
- Matveev, K.A.; Yue, D. & Glazman, L.I. (2000). Tunneling in one-dimensional non-Luttinger electron liquid. *Physical Review Letters*, Vol. 71, No. 20, (November 1993) 3351-3354
- Parkin, S.S.P.; Hayashi, M. & Thomas, L. (2008). Magnetic domain-wall racetrack memory. *Science*, Vol. 320, (April 2008) 190-194.
- Penc, K. & Sólyom, J. (1993) One-dimensional Hubbard model in a magnetic field and the multicomponent Tomonaga-Luttinger model. *Physical Review B*, Vol. 47, No. 11, (1993) 6273-6292
- Rüster, C.; Borzenko, T.; Gould, C.; Schmidt, G.; Molenkamp, L.W.; Liu, X.; Wojtowicz, T.J.; Furdyna, J.K.; Yu, Z.G. & Flatté, M.E. Very large magnetoresistance in lateral ferromagnetic (Ga,Mn)As wires with nanoconstrictions. *Physical Review Letters*, Vol. 91, No. 21, (November 2003) 216602

- Sedlmayr, N.; Dugaev, V.K.; & Berakdar, J. (2009). Current-induced interactions of multiple domain walls in magnetic quantum wires. *Physical Review B*, Vol. 79, No. 17, (May 2009) 174422
- Sedlmayr, N.; Dugaev, V.K.; & Berakdar, J. (2010). Role of non-collinear magnetization: From ferromagnetic nanowires to quantum rings. *Physica Status Solidi B*, Vol. 247, No. 10, (August 2010) 2603-2609
- Sedlmayr, N.; Dugaev, V.K.; Berakdar, J.; Vieira, V.R.; Araújo, M.A.N.; & Barnaś, J. (2010). Spin and charge transport through non-collinear magnetic nanowires. *Journal of Magnetism and Magnetic Materials*, Vol. 322, Nos. 9-12 (May-June 2010) 1419-1421
- Sedlmayr, N.; Eggert, S. & Sirker, J. (2011). Electron scattering from domain walls in ferromagnetic Luttinger liquids. *cond-mat.str-el arXiv:1102.5446* (February 2011).
- Tatara, G. & Fukuyama, H. (1997). Resistivity due to a domain wall in ferromagnetic metal. *Physical Review Letters*, Vol. 78, No. 19, (May 1997) 3773-3776
- Zhang, S. & Li, Z. (2004). Roles of nonequilibrium conduction electrons on the magnetization dynamics of ferromagnets. *Physical Review Letters*, Vol. 93, No. 12, (September 2004) 127204

## **Part 5**

### **Organic and Inorganic Nanowires**



# Nanowires of Molecule-Based Charge-Transfer Salts

De Caro Dominique  
CNRS-LCC (*Laboratoire de Chimie de Coordination*),  
and *Université de Toulouse,*  
*Toulouse,*  
*France*

## 1. Introduction

As we approach the physical limits of conventional silicon-based electronics, there is a clear need for new types of materials that can deliver smaller and smaller devices. A strong candidate in this field is molecular electronics, which uses assemblies (via  $\pi$ - $\pi$  or van der Waals interactions) of individual molecules (organic or metallo-organic molecules). Organic or metallo-organic molecules should stack in one direction to provide a framework for possible band structure formation. Therefore, the repeat units should preferably have an overall planar geometry. The partial filling of the conduction band (*i.e.* the metallic state) should be ensured either by partial oxidation (mixed-valence salts) or by partial charge transfer (charge-transfer salts). Charge-transfer salts are formed when a number  $x$  of donor molecules D jointly donate an electron to a second type of molecule A, to form the compound  $D_xA$ ; owing to its charge, A is usually referred to as the anion molecule.

Charge-transfer based conductors (exhibiting a semiconducting behaviour, a metal-like conductivity, or a transition to a superconducting state) are more commonly prepared and studied as macroscopic single crystals (prepared by using slow diffusion in organic solution or electrocrystallisation techniques). Micrometer-sized crystals have nevertheless been obtained (Deluzet et al., 2002; Kobayashi et al., 2008; Mas-Torrent & Hadley, 2005). Charge-transfer conductors at the nanoscale have received broad attention in recent years because of their novel properties and potential applications for future electronic devices. However, nanowires of charge-transfer salts are still rare and only few examples have been reported. This chapter presents the most significant results in this area. The first part of this chapter will describe the preparation methods selectively leading to isolated nanowires or nanowire films of charge transfer compounds. The second part will be devoted to the spectroscopic studies of nanowires with a special emphasis on vibrational and photoelectronic techniques. The last part of the chapter will be the description of the physical properties of nanowires.

## 2. Preparation methods

Preparation methods can be divided into two main categories: vapour phase methods and solution-grown methods. When gas-phase reactions are involved, the most important

characteristic that the precursor molecules should fulfil to be used is their ability to be vapourised. The precursors must also be transported without decomposition from the vapourisation zone to the depositing zone. When a solution-grown technique is involved, soluble precursors are required.

## 2.1 Vapour phase techniques

Tetrathiafulvalene 7,7,8,8-tetracyano-*p*-quinodimethane (TTF·TCNQ, Fig. 1) is the main charge transfer compound which has been processed as nanowires using vapour phase methods. TTF·TCNQ is the archetype of charge transfer salts. In this compound, TTF and TCNQ molecules are in 1:1 ratio and form separate stacked donor (TTF) columns and stacked acceptor (TCNQ) columns. A partial charge transfer (of about 0.59 electron per molecule) between TTF and TCNQ transforms the molecular stacks into one-dimensional conductive paths *via* the formation of partially filled bands. As single crystals, TTF·TCNQ exhibits a metallic conductivity down to 60 K. Its room-temperature conductivity is of about  $600 \text{ S cm}^{-1}$  along the *b*-axis of the single crystal.

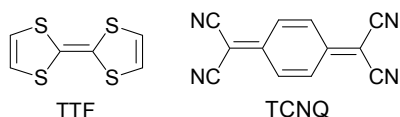


Fig. 1. Molecular structures for TTF and TCNQ.

TTF·TCNQ nanowires can be fabricated by the co-evaporation method in the absence or in the presence of an electric field (Sakai et al., 2003). Two independent crucibles (placed in a vacuum evaporation chamber) are loaded with TTF and TCNQ powders. The sublimation temperatures of the TTF (55 °C) and of the TCNQ (110 °C) are individually controlled. Moreover, a couple of parallel Au/Cr electrodes with a gap of 100  $\mu\text{m}$  are formed on a glass substrate. During the deposition process, the substrate is maintained at temperatures in the 40-45 °C range (deposition rate of about  $0.03 \text{ nm s}^{-1}$ ). In the absence of electric field, randomly oriented nanowires of TTF·TCNQ are formed on the glass substrate, particularly around the electrodes. In the presence of an applied electric field (35  $\text{kV cm}^{-1}$ ), highly oriented nanowires of TTF·TCNQ (aligned along the electric field) are observed. Using a gap of 20  $\mu\text{m}$  between the two Au/Cr electrodes and a low applied electric field (6  $\text{kV cm}^{-1}$ ), nanowires may connect the two electrodes.

We have developed an alternative route to TTF·TCNQ nanowires (growing from the edges of a microcrystal) using the chemical vapour deposition (CVD) technique (Wada et al., 2009). TTF·TCNQ nanowires are deposited from TTF and TCNQ, using a conventional hot-wall CVD apparatus. The vaporisation crucibles are charged with about 100 mg of each precursor. The substrates, (001)-oriented intrinsic Si wafers, are placed on top of a glass slide inside the CVD reactor. The precursors are vaporised from the crucibles at low pressures (about 850 Pa), and transported by He carrier gas (flow rate in the 60-80 standard  $\text{cm}^3 \text{ min}^{-1}$  range) through heated lines to the mixing zone, and then to the deposition zone (deposition time: 180 min). The lines and mixing zone are set at a higher temperature (170 °C) than the vaporisation zone (78 °C for TTF, and 145 °C for TCNQ) in order to avoid condensation of the starting compounds. The X-ray diffraction pattern recorded on nanowires deposited on (001)-oriented Si wafers only shows the (00 $l$ ),  $l = 2n$ , lines. This indicates a preferential

orientation of the nanowire films, *i.e.* the *ab*-plane parallel to the substrate surface. Fig. 2 shows that nanowires grow from random branching points on the initial TTF·TCNQ microcrystal. The dimensions of the nanowires are typically 100 nm in diameter and  $> 5 \mu\text{m}$  in length. Fig. 2 also evidence that nanowires grow in different orientations leading to a kind of “carnivorous plant”.

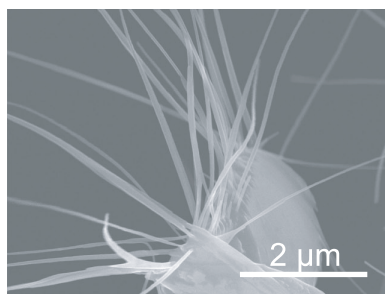


Fig. 2. Nanowires growing from random branching points on a TTF·TCNQ microcrystal

M(TCNQ) (M = Cu, Ag) nanowires can be prepared by organic solid-phase reaction that give good and simple control of the uniformity (Liu et al., 2005). The TCNQ powder is loaded in a ceramic crucible and then placed at the centre of a quartz tube that is inserted into a horizontal tube furnace. A copper or a silver foil is placed on top of the ceramic boat. The TCNQ molecule is then deposited on the surface of the foil (temperature in the 120-150 °C range) for formation of Cu(TCNQ) or Ag(TCNQ) nanowire films. Single Cu(TCNQ) nanowires exhibit a diameter of about 70 nm whereas those of Ag(TCNQ) exhibit a diameter of about 50 nm.

## 2.2 Solution-grown techniques

As described above, vapour phase methods require vaporizable precursors. These techniques are therefore restricted to only neutral molecules. Charge transfer salts are mostly prepared in organic solution, medium in which both neutral and ionic precursors are soluble. Moreover, a wide variety of charge transfer salts are obtained by electrochemical oxidation of the donor molecule in the presence of a supporting electrolyte. These systems are then not accessible to gas-phase techniques. In the first part of this paragraph, we will describe the preparation of nanowires of charge transfer salts for which there is a direct chemical reaction between the donor and the acceptor molecule. The second part of this paragraph will be devoted to the preparation of nanowires of charge transfer compounds in which the oxidation of the donor molecule is current-induced.

### 2.2.1 Nanowires of TTF·TCNQ and TTF[Ni(dmit)<sub>2</sub>]<sub>2</sub>

TTF·TCNQ can easily be prepared by slow addition of an organic solution of TTF into an organic solution of TCNQ. Electron micrograph images of the resulting powder show long micrometer-sized needles (typical sizes: 1-2  $\mu\text{m}$  wide and  $> 5 \mu\text{m}$  long). To constrain the growth as nanowires, two synthetic strategies have been developed: a two-phase method and a dipping process on an oxide conversion coating onto a stainless steel substrate.

TTF·TCNQ nanowires can be grown in organic solution using the two-phase method (Liu et al., 2007). TTF solutions are prepared by dissolving TTF in hexane and TCNQ solutions by

dissolving TCNQ in acetonitrile. The TCNQ solution is dripped into the TTF solution at various rates (in the  $1\text{--}500\ \mu\text{L s}^{-1}$  range) under stirring. The morphology and the state of dispersion of the nanowires is dripping-rate dependent: straight nanowires (at  $1\ \mu\text{L s}^{-1}$ ), helical nanowires (at  $20\ \mu\text{L s}^{-1}$ ), helical dendrites (at  $40\ \mu\text{L s}^{-1}$ ), and complicated helical dendrites (at  $500\ \mu\text{L s}^{-1}$ ). The faster growth rate along the *b*-axis is due to the  $\pi$ - $\pi$  stacking interaction for inducing the formation of TTF·TCNQ nanowires at the hexane-acetonitrile interface. However, using this two-phase technique, diameters lower than 100 nm is never observed.

We have developed an easy route to the formation of TTF·TCNQ nanowires exhibiting diameters lower than 80 nm, and well dispersed on a surface from which they can easily be removed (Savy et al., 2007). The substrate on which nanowires are formed is an oxide conversion coating onto stainless steel (stainless steel conversion coating, abbreviated SSCC). The SSCC substrates are prepared from austenitic stainless steel dipped in an aqueous sulphuric acid bath (0.2 % vol.) containing sodium thiosulfate ( $0.01\ \text{mol L}^{-1}$ ) at  $45\ ^\circ\text{C}$ . After an electrolytic activation ( $-1.5\ \text{V/SCE}$ ) for 2 min, the conversion coating grows by chemical treatment in the same bath. The resulting coatings are identified as magnetite and maghemite phases. They are known for showing advanced adsorption properties due to their fractal-like nanostructured surface. TTF·TCNQ nanowires are prepared by successive immersion of the SSCC substrate in acetonitrile solutions of TTF ( $10^{-2}\ \text{mol L}^{-1}$ ) and TCNQ ( $10^{-2}\ \text{mol L}^{-1}$ ). Adsorption of TTF is realised at first. Then, immersion of the TTF-containing oxide surface in the TCNQ solution results in the formation of TTF·TCNQ nanowires. Nanowires uniformly cover the substrate surface and a large amount of them bridge the cracks of the conversion coating (Fig. 3). Efficient adsorption of the TTF moiety onto the surface is not surprising because SSCC substrates are known to adsorb  $\pi$ -electron-rich planar molecules. Further formation of TTF·TCNQ as nanowires and not as a continuous film could be explained by the 1D-character of the charge transfer salt. Individual nanowires can be collected using a micropipette (diameter  $< 1\ \mu\text{m}$ ) gently scanned with a micro-manipulator inside the cracks of the conversion coating.

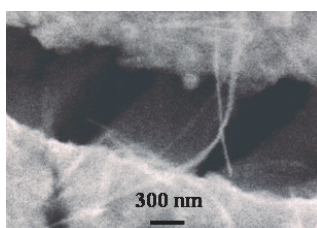


Fig. 3. TTF·TCNQ nanowires on a SSCC substrate.

Certain kind of metal complexes have been regarded as promising molecule-based conductors, because they combine a metal ion surrounded by ligands which exhibit a more or less extended  $\pi$  system. Among them and due to their remarkable coordination properties, dithiolene ligands have been intensively studied. TTF[Ni(dmit)<sub>2</sub>]<sub>2</sub> combine the TTF donor molecule and the [Ni(dmit)<sub>2</sub>]<sup>δ-</sup> acceptor bis-dithiolene complex (Fig. 4, the non integer  $\delta$  value, *i.e.*, the incommensurable character of the system will be discussed in part 3). It results from the reaction of the (TTF)<sub>3</sub>(BF<sub>4</sub>)<sub>2</sub> salt with [(*n*-C<sub>4</sub>H<sub>9</sub>)<sub>4</sub>N][Ni(dmit)<sub>2</sub>] in organic solution. The reaction leads to the formation of a 1:2 adduct where TTF and Ni(dmit)<sub>2</sub> species are partially oxidised. Within the final material, the charge transfer between the TTF

donor molecule and the Ni(dmit)<sub>2</sub> acceptor complex is found to be 0.80 from diffuse X-ray scattering experiments and band structure calculations. The structure of TTF[Ni(dmit)<sub>2</sub>]<sub>2</sub> consists of segregated stacks of TTF and Ni(dmit)<sub>2</sub> units. On single crystals, its room-temperature conductivity is about 300 S cm<sup>-1</sup> along the *b*-axis. The conductivity behaviour is metallic down to 4 K at ambient pressure. Moreover, this compound undergoes a complete transition to a superconducting state at 1.62 K under a hydrostatic pressure of 7 kbar.

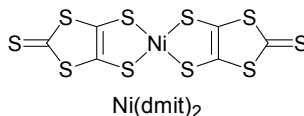


Fig. 4. Molecular structure for Ni(dmit)<sub>2</sub>.

The slow addition of an organic solution of [(*n*-C<sub>4</sub>H<sub>9</sub>)<sub>4</sub>N][Ni(dmit)<sub>2</sub>] in an organic solution of (TTF)<sub>3</sub>(BF<sub>4</sub>)<sub>2</sub> leads to TTF[Ni(dmit)<sub>2</sub>]<sub>2</sub> as long micrometer-sized needles (typical sizes: 1-2 μm wide and > 5 μm long). TTF[Ni(dmit)<sub>2</sub>]<sub>2</sub> nanowire films are prepared by successive immersion of the SSCC substrate in an acetonitrile solution of [(*n*-C<sub>4</sub>H<sub>9</sub>)<sub>4</sub>N][Ni(dmit)<sub>2</sub>] (3.54 g L<sup>-1</sup>) and in an acetonitrile solution of (TTF)<sub>3</sub>(BF<sub>4</sub>)<sub>2</sub> (2.04 g L<sup>-1</sup>) (Valade et al., 2002). The diameters of the nanowires lie from 50 to 250 nm (Fig. 5). By changing the order of immersion, *i.e.* (TTF)<sub>3</sub>(BF<sub>4</sub>)<sub>2</sub> first and then [(*n*-C<sub>4</sub>H<sub>9</sub>)<sub>4</sub>N][Ni(dmit)<sub>2</sub>], no nanowire is obtained on the SSCC surface. Tetraalkylammonium cations have a strong affinity for oxide surfaces. The adsorption of [R<sub>4</sub>N]<sup>+</sup> cations originates in their interaction with the dipoles of the oxide species. A hydrophilic surface, such as SSCC, also facilitates this adsorption. This could explain that [(*n*-C<sub>4</sub>H<sub>9</sub>)<sub>4</sub>N][Ni(dmit)<sub>2</sub>] is strongly anchored onto the SSCC substrate and reacts with (TTF)<sub>3</sub>(BF<sub>4</sub>)<sub>2</sub> to form TTF[Ni(dmit)<sub>2</sub>]<sub>2</sub> as nanowires.

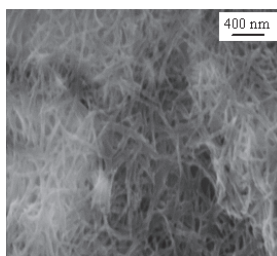


Fig. 5. TTF[Ni(dmit)<sub>2</sub>]<sub>2</sub> nanowires on a SSCC substrate.

### 2.2.2 Nanowire films prepared by the Langmuir-Blodgett technique

The Langmuir-Blodgett (LB) technique has been successfully applied to form nanowire films of charge transfer-based conductors (Miyata et al., 2003). The donor molecule is a didecyl derivative of a bis-tetrathiafulvalene substituted macrocycle (bis-TTF-(C<sub>10</sub>H<sub>21</sub>)<sub>2</sub>), and the acceptor molecule is the tetrafluorotetracyanoquinodimethane (F<sub>4</sub>TCNQ). A conventional LB trough is used for monolayer formation and LB film deposition. A KCl aqueous solution (0.01 mol L<sup>-1</sup>) is used as a subphase, and a mixture of chloroform/acetonitrile (9:1) is used as a spreading solvent. One equivalent of the bis-TTF-(C<sub>10</sub>H<sub>21</sub>)<sub>2</sub> molecule and two equivalent of F<sub>4</sub>TCNQ are combined in the spreading solution. Monolayers are transferred on freshly cleaved mica substrates by the vertical dipping method with the deposition speed of 10 mm

$\text{min}^{-1}$  at  $17\text{ }^\circ\text{C}$ . Atomic force microscopy images of transferred films exhibit nice extended nanowire network structures on mica surface. The majority of the nanowires (typical diameters: 70-100 nm) orient specific direction reflecting the lattice of mica surface. The orientation of six-fold symmetry should be due to the recognition of  $\text{K}^+$  array on mica surface by nanowires upon the deposition of monolayers.

### 2.2.3 Electrochemically-grown nanowires of charge-transfer salts

The electrochemical method is the most widely used technique to grow conductive molecular salts. During electrocrystallisation, compounds are intended to grow attached to the electrode surface, which is usually a platinum or a gold wire. However, it is clear that only conductive species may be considered, as the covered electrode should retain a high enough conductivity at any time during the process. An electrochemical synthesis may be conducted either under potentiostatic or galvanostatic conditions. The growth rate is highly important to control the size, the morphology, and the quality of crystals. For this reason, galvanostatic conditions are preferably applied for electrosynthesis of charge transfer salts. On platinum or gold wire-like electrodes, macroscopic needles or platelets of molecule-based conductors are commonly obtained. To constrain the growth as nanowires, two different strategies have been developed:

- The use of a pre-treated Si wafer, used as an anode,
- The use of an electrode functionalised by a membrane.

Flat metallic electrode (e.g. a Pt foil) have been used to grow thin films of charge transfer salts. However, in the conditions explored, nanowires have never been observed. We have developed the use of a semiconducting electrode, namely silicon, to process nanowire films (Savy et al., 2007). Silicon is the substrate of choice in the electronic domain. It is easily available, cheap, and has a high enough conductivity to be used as an electrode (conductivity of about  $5 \times 10^{-3}\text{ S cm}^{-1}$  at room temperature). A pre-treatment of the intrinsic silicon wafer is required to generate nanocavities, which will act as nanoflasks from which the growth as nanowires will be initiated. The pre-treatment consists in dipping the Si wafer in a mixture of  $\text{H}_2\text{SO}_4/\text{H}_2\text{O}_2$  (1:1 v/v) for 10 min. The Si wafer is then dipped in a mixture of  $\text{H}_2\text{O}/\text{HF}$  (9:1 v/v) for 10 min, and finally dipped in a mixture of  $\text{H}_2\text{SO}_4/\text{H}_2\text{O}_2$  (1:1 v/v) for 10 min. After these three aqueous treatments, the silicon wafer is rinsed (10 min) in the organic solvent in which the electrosynthesis will be carried out. The silicon surface thus obtained exhibits nanocavities (Fig. 6).

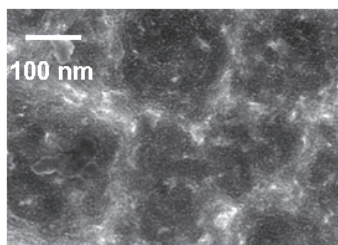


Fig. 6. Nanocavities on a treated intrinsic silicon wafer.

Charge-transfer salts combining an electron organic donor (D) and a  $[\text{M}(\text{dithiolate})_2]$  complex are grown as nanowires on the silicon electrode described above, used as an anode in a conventional electrochemical cell. The electrochemical reaction leading to  $\text{D}_n[\text{M}(\text{dithiolate})_2]_m$

charge-transfer salts, involves the oxidation of the donor in the presence of the  $[M(\text{dithiolate})_2]^-$  salt which plays the role of both the acceptor and the supporting electrolyte:

Electrochemical step:  $D \rightarrow D^+ + e^-$

Chemical step:  $n D^+ + m [M(\text{dithiolate})_2]^- \rightarrow (D^{+\delta/m})_n \{ [M(\text{dithiolate})_2]^{-\delta/n} \}_m$

TTF $[\text{Ni}(\text{dmit})_2]$  nanowires are electrodeposited on a pre-treated Si anode from TTF (3 mmol  $\text{L}^{-1}$  in acetonitrile) and  $[(n\text{-C}_4\text{H}_9)_4\text{N}][\text{Ni}(\text{dmit})_2]$  (1 mmol  $\text{L}^{-1}$  in acetonitrile) starting materials in a one-compartment electrochemical cell, under galvanostatic conditions (about 6  $\mu\text{A cm}^{-2}$ ). Nanowires obtained exhibit diameters in the 50-300 nm range (Fig. 7).

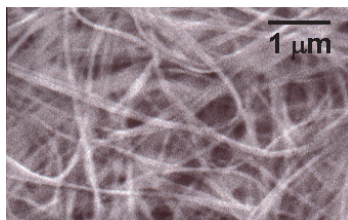


Fig. 7. TTF $[\text{Ni}(\text{dmit})_2]$  nanowires grown on a pre-treated intrinsic silicon wafer, used as an anode.

Another charge-transfer salt based on a metal bis(dithiolene) complex can be processed as a nanowire film onto Si substrates:  $(\text{Per})_2[\text{Au}(\text{mnt})_2]$  where Per stands for the perylene molecule,  $\text{C}_{20}\text{H}_{12}$  (Fig. 8). The interest of  $(\text{Per})_2[\text{M}(\text{mnt})_2]$  ( $M = \text{Fe}, \text{Co}, \text{Ni}, \text{Pd}, \text{Pt}, \text{Cu}, \text{Au}$ ) compounds resides upon the coexistence in the same system of delocalized electron chains (perylene molecules) and chains of localized spins, *via* the  $[\text{M}(\text{mnt})_2]^-$  units. Though diamagnetic ( $\text{Au}^{3+}$  square planar  $d^8$  configuration), the  $[\text{Au}(\text{mnt})_2]$ -based charge-transfer salt has been selected due to its high room-temperature conductivity value (700  $\text{S cm}^{-1}$  along the stacking  $b$  axis). Moreover, it can be easily studied by X-ray photoelectron spectroscopy (see paragraph 3) due to the presence of a relatively intense Au 4f line whose position is sensitive towards the formal oxidation number of the gold centre and towards electronic delocalization through mnt ligands.  $(\text{Per})_2[\text{Au}(\text{mnt})_2]$  nanowires are electrodeposited on a pre-treated Si anode from perylene (6 mmol  $\text{L}^{-1}$  in dichloromethane) and  $[(n\text{-C}_4\text{H}_9)_4\text{N}][\text{Au}(\text{mnt})_2]$  (1.5 mmol  $\text{L}^{-1}$  in dichloromethane) starting materials in a two-compartment electrochemical cell, under galvanostatic conditions (about 0.3  $\mu\text{A cm}^{-2}$ ). Electron micrographs reveal that the film coated on the Si surface consists of large-scale  $(\text{Per})_2[\text{Au}(\text{mnt})_2]$  nanowires (Fig. 9). Diameter of individual nanowires is in the narrow range of 35-55 nm.

One interest of processing a nanowire film onto an intrinsic silicon wafer is that it is not necessary to remove it from the surface to investigate the transport properties (resistivity *vs.* temperature for example). Silicon has a conductivity value (about  $5 \times 10^{-3} \text{ S cm}^{-1}$  at 25  $^\circ\text{C}$ ) which is lower than that of the deposited material itself. Electrical contacts can then be drawn on a nanowire film as prepared.

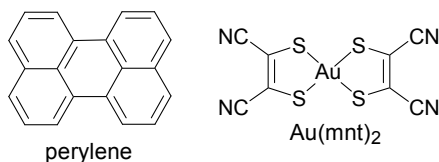


Fig. 8. Molecular structures for perylene and  $\text{Au}(\text{mnt})_2$

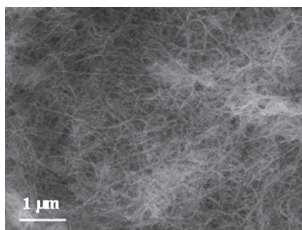


Fig. 9.  $(\text{Per})_2[\text{Au}(\text{mnt})_2]$  nanowires grown on a pre-treated intrinsic silicon wafer, used as an anode.

Nanowire of charge transfer salts can also be prepared by electrocrystallisation using a functionalised electrode: a porous anodic aluminium oxide (AAO) coated with a gold film, or a Si-supported multilamellar membrane. The use of the first type of electrode leads to nanowire arrays, whereas the second type of electrode leads to nanowire films.

1D nanostructured arrays of  $(\text{BEDT-TTF})_4[\text{H}_2\text{O}\cdot\text{Fe}(\text{C}_2\text{O}_4)_3]\cdot\text{C}_6\text{H}_5\text{NO}_2$  where BEDT-TTF stands for bis(ethylenedithio)tetrathiafulvalene (Ji et al., 2006) and  $[(\text{CH}_3)_4][\text{Ni}(\text{dmit})_2]_2$  (Cui et al., 2004) are grown on a AAO-coated gold electrode, the porous AAO acting as a template which serves as an ideal host for the synthesis of the material of sub-micrometer dimensions. The preparation of  $(\text{BEDT-TTF})_4[\text{H}_2\text{O}\cdot\text{Fe}(\text{C}_2\text{O}_4)_3]\cdot\text{C}_6\text{H}_5\text{NO}_2$  as nanowire arrays can be divided into two steps. The first step is electrocrystallisation in organic medium. The AAO template, coated on one side with a gold film serving as the anode, and a platinum sheet serving as the cathode, are immersed in the electrolyte solution that consists of BEDT-TTF,  $\text{K}_3[\text{Fe}(\text{C}_2\text{O}_4)_3]$ , 18-crown-6 ether (used to coordinate potassium cations), and nitrobenzene as a solvent. The nanowire arrays grow along the channels of the AAO template at a constant current density of  $1 \mu\text{A cm}^{-2}$  for 72 hours. In the second step, selective etching of the alumina template results in a freestanding  $(\text{BEDT-TTF})_4[\text{H}_2\text{O}\cdot\text{Fe}(\text{C}_2\text{O}_4)_3]\cdot\text{C}_6\text{H}_5\text{NO}_2$  charge-transfer salt nanowire array. The preparation of the mixed-valence compound  $[(\text{CH}_3)_4][\text{Ni}(\text{dmit})_2]_2$  follows a similar procedure (electrolyte solution:  $[(\text{CH}_3)_4][\text{Ni}(\text{dmit})_2]$ ,  $[(\text{CH}_3)_4]\text{ClO}_4$  as a supporting electrolyte, acetonitrile). The nanowires obtained fit perfectly the pore diameters of the AAO template (in the 32-49 nm range). These nanowire arrays are highly textured in the direction of higher conductivity. However, the preparation of the porous alumina template is not straightforward. Furthermore, the prepared AAO membrane has to be metallated to be used as a working electrode. We have preferred to use another type of template, *i.e.*, a Si-supported phospholipidic-based multilamellar membrane. These well-ordered multilamellar membranes (thickness  $\sim 2.5 \mu\text{m}$ ) are easily produced by spreading small drops of a lipidic solution on Si surfaces and letting the solvent (methanol/chloroform) evaporate slowly. The phospholipid used (DC8,9PC; Fig. 10) contains a zwitterion type headgroup and two long alkyl chains. Each alkyl chain has two conjugated carbon-carbon triple bonds which can polymerise by irradiating with a UV light. This template, used as a working electrode, preserves its lamellar structure in the electrolyte solution. This template-modified anode is advantageously used for growing a nanowire film of  $(\text{EDT-TTFVO})_4(\text{FeCl}_4)_2$  (EDT-TTFVO: ethylenedithiotetrathiafulvalenquinone-1,3-dithiomethide, Fig. 10). A solution of EDT-TTFVO ( $0.4 \text{ mmol L}^{-1}$ ) and  $[(\text{C}_2\text{H}_5)_4\text{N}]\text{FeCl}_4$  ( $15 \text{ mmol L}^{-1}$ ) is electrolysed in a two-

compartment electrochemical cell in a mixture of chlorobenzene/ethanol (9:1 v/v) at constant current density ( $0.15 \mu\text{A cm}^{-2}$ ) for 10 days. A nanowire film is obtained in which individual nanowires exhibit diameter  $\leq 20 \text{ nm}$  (Fig. 11). Using a Si-supported multilamellar membrane as electrode, growth as nanowires is conceivable as follows: EDT-TTFVO molecules migrate from the solution/membrane interface to the substrate surface *via* the channels delimited by the long alkyl chains. They are oxidized and produce the conducting salt by combination with  $\text{FeCl}_4^-$  ions, largely present at the vicinity of the hydrophilic silicon surface. As the growing salt is in contact with  $\text{FeCl}_4^-$  ions located in interheadgroup areas, the growth can continue but should adapt to nanometric size of the channels. Even when the growing salt reaches the membrane surface, the growth still continues towards the formation of long nanowires lying parallel to the membrane surface, as evidenced on Fig. 11.

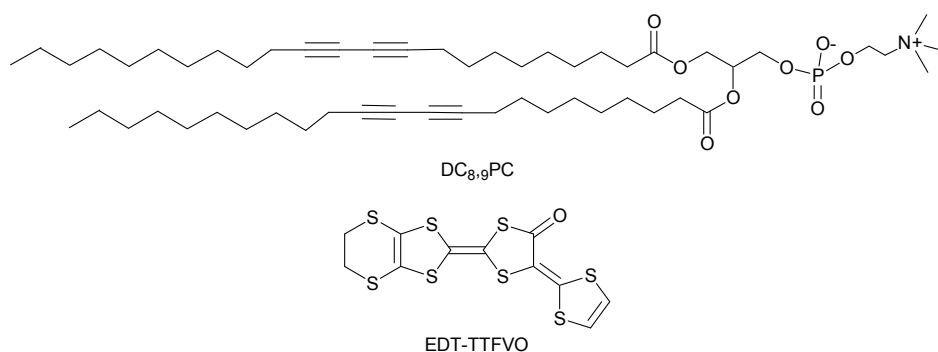


Fig. 10. Molecular structures for DC<sub>8,9</sub>PC and EDT-TTFVO.

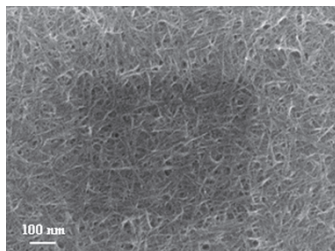


Fig. 11. Nanowires of  $(\text{EDT-TTFVO})_4(\text{FeCl}_4)_2$  electrochemically grown on a Si-supported multilamellar membrane, used as an anode.

### 3. Spectroscopic studies of charge-transfer salt-based nanowires

Infrared, Raman, and X-ray photoelectron spectroscopy are the most widely used techniques to characterize nanowires of charge transfer salts. The two first techniques allow the determination of the amount of charge transfer between the donor and the acceptor molecule. X-ray photoelectron spectroscopy provides both stoichiometry and formal charge borne by the moieties within the nanowires.

Infrared is particularly suitable for molecules bearing polar groups such as cyano groups (*e.g.* TCNQ, see Fig. 1). On the infrared spectrum of TTF·TCNQ nanowires (grown on Si using a vapour phase technique), a band attributed to the CN stretching mode ( $\nu_{\text{CN}}$ ) of TCNQ appears at  $2203\text{ cm}^{-1}$ . The vibration frequency of the CN groups of TCNQ is characteristic of the formal charge of TCNQ, thus of the charge transfer between TTF and TCNQ moieties. In the case of the nanowires, it corresponds to a TTF·TCNQ phase with a charge transfer of  $\rho = 0.57$ , consistent with that observed on single crystals ( $\rho = 0.59$ ).

Raman spectroscopy is particularly suitable to investigate polarisable molecules. It is a technique of choice for studying molecules exhibiting large delocalised  $\pi$  systems, which is the case for most of the molecules cited in this chapter. The Raman spectrum for TTF·TCNQ nanowires (grown on SSCC in acetonitrile) is shown on Fig. 12. In the  $1400\text{--}1600\text{ cm}^{-1}$  range, the Raman spectrum exhibits three lines, all related to C=C modes. The first line, exhibiting two maxima at  $1413$  and  $1418\text{ cm}^{-1}$ , corresponds to the  $\nu_4\text{ a}_g$  mode in TCNQ. Using the linear relation of the TCNQ  $\nu_4$  frequency *vs.*  $\rho$  (amount of charge transfer), we determine a degree of charge transfer ranging from  $0.65$  to  $0.60$ , in good agreement with  $0.59$  on single crystals. The second line ( $1512\text{ cm}^{-1}$ ) is due to the  $\nu_2\text{ a}_g$  mode in TTF. Its position is intermediate between neutral TTF ( $1555\text{ cm}^{-1}$ ) and TTF<sup>+</sup> ( $1505\text{ cm}^{-1}$ ). The third frequency ( $1600\text{ cm}^{-1}$ ) is assigned to the  $\nu_3\text{ a}_g$  mode in TCNQ, which is less sensitive to charge-transfer change ( $1602\text{ cm}^{-1}$  for neutral TCNQ and  $1595\text{ cm}^{-1}$  for TCNQ<sup>-</sup>). TTF·TCNQ nanowires grown on SSCC can then be written as:  $[\text{TTF}^{\delta+}][\text{TCNQ}^{\delta-}]$  with  $0.60 \leq \delta \leq 0.65$ .

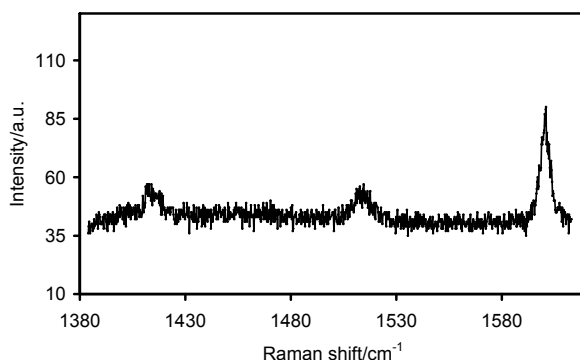


Fig. 12. Raman spectrum recorded on TTF·TCNQ nanowires grown on SSCC dipped in an acetonitrile solution of TTF and in an acetonitrile solution of TCNQ, respectively.

TTF[Ni(dmit)<sub>2</sub>]<sub>2</sub> (either grown on SSCC or electrodeposited on Si) are also investigated by Raman spectroscopy (Fig. 13). In the low frequency region (not shown on Fig. 13), bands at  $362$  (weak),  $496$  (strong) and  $510$  (medium)  $\text{cm}^{-1}$  are assigned to  $\nu_{\text{Ni-S}}$ ,  $\nu_{\text{C-S}}$  for TTF, and  $\nu_{\text{C-S}}$  for Ni(dmit)<sub>2</sub>, respectively. In the high frequency region ( $1300\text{--}1550\text{ cm}^{-1}$ ), two strong C=C stretching modes are observed at  $1436$  ( $\nu_3\text{ a}_g$  for TTF) and  $1511$  ( $\nu_2\text{ a}_g$  for TTF)  $\text{cm}^{-1}$ . The low intensity line at  $1475\text{ cm}^{-1}$  corresponds to the second overtone of the stretching  $\nu_{\text{C-S}}$  for TTF. The  $\nu_3\text{ a}_g$  mode for TTF is the most sensitive to the amount of charge transfer between the TTF donor and the Ni(dmit)<sub>2</sub> acceptor molecule, because it corresponds to a contribution of

about 71 % of the central C=C bond in the TTF moiety (highly symmetrical mode). Using the linear correlation between the  $\nu_3 a_g$  position *vs.* the degree of charge transfer ( $\rho$ ), a value of about  $\rho = 0.86$  can be extracted, in excellent agreement with that found on TTF[Ni(dmit)<sub>2</sub>]<sub>2</sub> single crystals ( $\rho = 0.80$ ). TTF[Ni(dmit)<sub>2</sub>]<sub>2</sub> nanowires can then be written as: [TTF<sup>0.86+</sup>][Ni(dmit)<sub>2</sub><sup>0.43-</sup>]<sub>2</sub>.

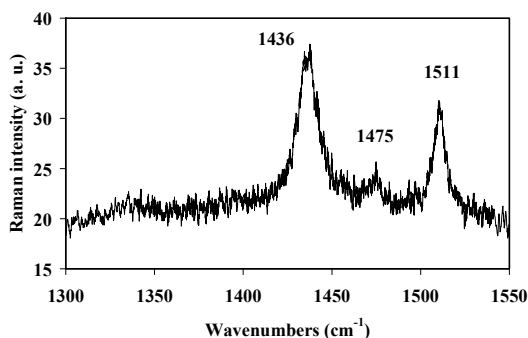


Fig. 13. Raman spectrum recorded on TTF[Ni(dmit)<sub>2</sub>]<sub>2</sub> nanowires (grown on SSCC or on silicon wafers).

Nanowires of metal bis(dithiolene) complexes-based charge transfer salts are also characterized by X-ray photoelectron spectroscopy (XPS). XPS is a powerful technique to investigate the stoichiometry (donor/acceptor) within the nanowire films. In TTF[Ni(dmit)<sub>2</sub>]<sub>2</sub>, the TTF and the Ni(dmit)<sub>2</sub> moieties both contain sulphur atoms (see Fig.1 and Fig. 4). However, their chemical environment is different. Taking into account the presence of 2 [Ni(dmit)<sub>2</sub>] and 1 TTF, 12 sulfur atoms are bound to two different sp<sup>2</sup> carbons (C-S-C), 8 sulfur atoms are bound to a nickel and a sp<sup>2</sup> carbon (C-S-Ni), and, finally, 4 sulfur atoms are bound to one sp<sup>2</sup> carbon (C=S). Atomic ratios are therefore 3:2:1. The X-ray photoelectron spectroscopy S2p line can be satisfactorily decomposed in three contributions (Fig. 14). According to their relative intensities, the most intense line, with a binding energy of 163.5 eV, corresponds to C-S-C bonds. Lines at 161.8 and 165.3 eV correspond to C-S-Ni and C=S bonds, respectively. The experimental intensity ratio between the C-S-C and C-S-Ni contributions is 1.4, in excellent agreement with the nominal 1.5 (3/2) value.

Nanowires of (Per)<sub>2</sub>[Au(mnt)<sub>2</sub>] are also studied by the XPS technique. Also the sulphur, nitrogen and gold have binding energies and lineshapes which are very sensitive to their formal charges. Fig. 15 shows the Au4f (a) and N1s (b) XPS lines measured on a Per<sub>2</sub>[Au(mnt)<sub>2</sub>] nanowire film, respectively. The binding energy of the Au4f<sub>7/2</sub> peak is 86.1 eV, which can be associated to a formal Au(III) oxidation state. The shape of the lines (essentially symmetric) together with their small Full Width at Half Maximum (FWHM), 0.8 eV, strongly suggest that the dominant contribution corresponds to Au(III) and that other non-zero oxidation states of gold contribute negligibly to the signal, *e.g.*, absence of mixed-valency. The N1s line is composed of a main peak located at 398.2 eV binding energy and a shoulder at *ca.* 401 eV. The lineshape is characteristic of the presence of the cyano group, with a main peak and a (shake-up) satellite. The satellite arises from the energy loss (about 3 eV) of electrons associated to the occupied-unoccupied CN-related states, a known feature previously evidenced in neutral TCNQ: the inset in Fig. 15 (b) shows the XPS spectrum of the N1s line of neutral TCNQ taken at high resolution in which the observation of the satellite is more evident.

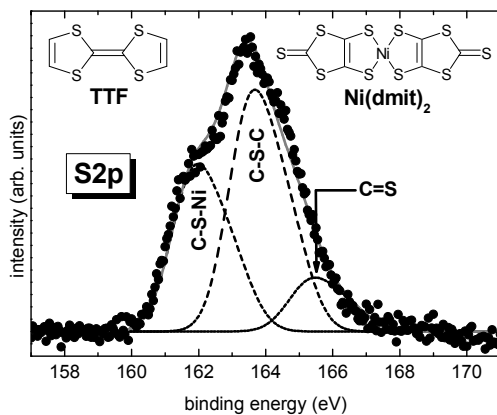


Fig. 14. S2p line in the XPS spectrum of TTF[Ni(dmit)<sub>2</sub>]<sub>2</sub> nanowires (grown on silicon wafers).

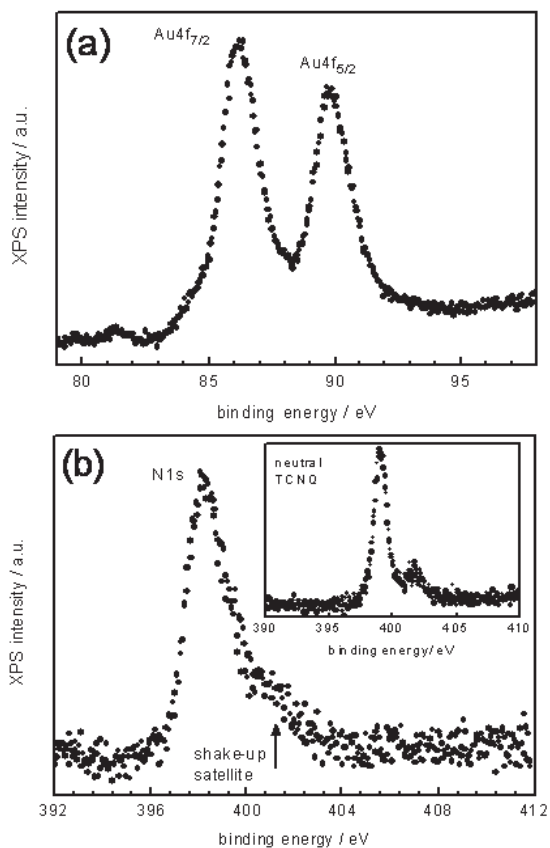


Fig. 15. Au4f (a) and N1s (b) lines in the XPS spectrum of (Per)<sub>2</sub>[Au(mnt)<sub>2</sub>] nanowires (grown on silicon wafers).

## 4. Physical properties of charge-transfer salt-based nanowires

### 4.1 Conductivity measurements

All charge-transfer salts described in this chapter are conducting materials as single crystals. At room temperature, their conductivity values range from 1 to about  $10^3 \text{ S cm}^{-1}$  along the molecular stacking direction. Conductivity measurements on single crystals are performed using the standard four-probe method: four electrical contacts are drawn on the single crystal using a conductive paste, such as gold, silver or graphite paste. Electrical current is passed between two of the contacts and the voltage created is measured between the other two contacts. The resistance can be calculated from the measured values of current and voltage. Knowing the dimensions of the single crystal and the distance between the electrical contacts, resistivity  $\rho$  (or conductivity,  $\sigma = 1/\rho$ ) values can be calculated. The same four-probe technique is successfully applied to measure the conductivity on nanowire films. Nanowire films of TTF·TCNQ (prepared by CVD), TTF[Ni(dmit) $_2$ ] $_2$  (electrochemically grown on Si), and (Per) $_2$ [Au(mnt) $_2$ ] (electrochemically grown on Si) all exhibit a semiconducting behaviour (conductivity  $\sigma$  increases with temperature). Room-temperature conductivities are 0.5, 9, and  $0.02 \text{ S cm}^{-1}$ , respectively. These values are at least one order of magnitude less those on single crystals. Within single crystals, the stacking axis is the direction of highest conductivity. The contributions of other directions due to random orientation of the nanowires on the surface, and the presence of inter-nanowire contacts which are presumably more resistive than the material itself, account for the lower conductivity value of the nanowire film *vs.* that of single crystals. For a semiconductor, the logarithm of the conductivity follows a linear relationship *vs.* the reciprocal temperature, the activation energy being extracted from the slope (Fig. 16). Activation energies in the 0.2-0.8 eV range are obtained for nanowire films of TTF·TCNQ, TTF[Ni(dmit) $_2$ ] $_2$ , and (Per) $_2$ [Au(mnt) $_2$ ].

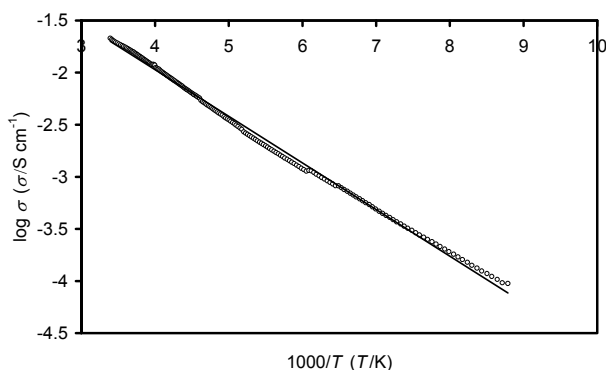


Fig. 16. Conductivity as a function of reciprocal temperature for electrodeposited (Per) $_2$ [Au(mnt) $_2$ ] nanowire films.

Very interesting conductivity investigations have been done on isolated TTF·TCNQ nanowires synthesized under an electric field (Phanindra Sai & Raychaudhuri, 2010). The TTF·TCNQ nanowires are prepared by the thermal evaporation method (using TTF·TCNQ powdered material as a source) on SiO $_2$  substrates, on which electrodes were prefabricated using

electron-beam lithography and the lift-off process. Recall that TTF·TCNQ single crystals exhibit a metal-like conductivity at high temperatures. However, the metal-like conductivity is suppressed by two successive Peierls transitions on the TCNQ and TTF stacks at 54 K and 38 K, respectively. A single TTF·TCNQ nanowire (vapour-phase grown in an electric field) shows a semiconductor-like behaviour. It does not show the metallic behaviour, as the stoichiometry of the nanowires does not remain 1:1 due to different vapour pressures of TTF and TCNQ molecules and these nanowires are generally TCNQ-rich. The temperature dependence of the resistivity is found to obey an activated behaviour. The plot of the logarithm of  $\rho$  versus  $T^{-1/2}$  clearly evidences change in slopes at 55 and 37 K, the region where the Peierls transition occurs. Moreover, the conductivity value on an isolated nanowire is about  $12 \text{ S cm}^{-1}$ , much lower than that for a single crystal along the  $b$  stacking direction ( $600 \text{ S cm}^{-1}$ ). This arises presumably from the disorder in the stacking sequences of TTF and TCNQ.

#### 4.2 Current-voltage curves on TTF·TCNQ isolated nanowires

Recall that TTF·TCNQ nanowires exhibiting diameters lower than 70 nm can be prepared on an oxide layer chemically grown on stainless steel (SSCC, *i.e.* stainless steel conversion coating). They can be removed from the substrate surface by moving a micropipette inside the cracks of the SSCC. Fig. 17 evidences a nanowire deposited on a copper grid covered by a carbon layer for transmission electron microscopy measurements, whereas Fig. 18 shows an atomic force microscopy image of an individual nanowire deposited on a silica surface.

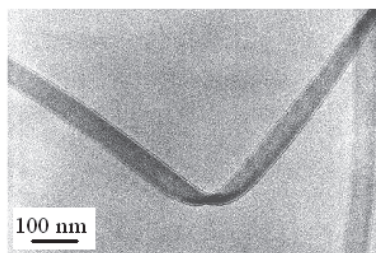


Fig. 17. Transmission electron micrograph of a TTF·TCNQ nanowire, grown by the dipping method.

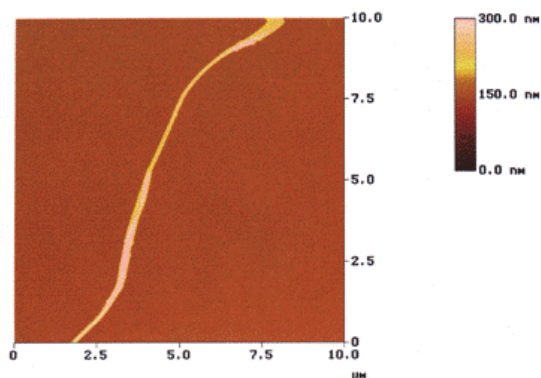


Fig. 18. Atomic force microscopy image of a TTF·TCNQ nanowire, grown by the dipping method.

To plot the current-voltage ( $I$ - $V$ ) response for TTF·TCNQ nanowires, they are placed between two electrodes of a metal-insulator-metal nanojunction fabricated on a silica surface. The non linearity of the  $I$ - $V$  curve (Fig. 19) is attributed to the non-ohmic character of the contacts which is possibly due to an imperfect interface between the electrodes and the nanowire. The existence of a tunnel junction at the electrode-TTF·TCNQ nanowire junction is therefore highly possible. Indeed, the observed gap of about 0.6 eV is compatible with values obtained by scanning tunnelling spectroscopy and photoemission measurements performed on TTF·TCNQ single crystals.

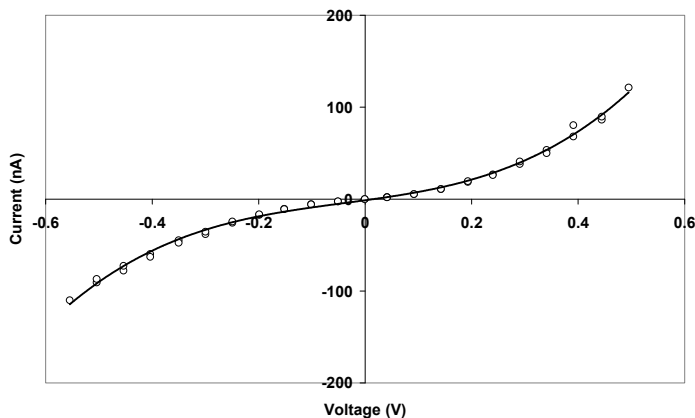


Fig. 19.  $I$ - $V$  curve on TTF·TCNQ nanowires.

As the nanowires are not parallel to the electrodes, the conductivity value deduced from the curve is dominated by the perpendicular conductivity. The conductivity found is about  $1 \text{ S cm}^{-1}$ , a value which is comparable to the conductivity value along the  $a$  axis on single crystals (recall that the conductivity value along the  $b$  axis is about  $600 \text{ S cm}^{-1}$ , the  $b$  axis being the molecular stacking axis). For TTF·TCNQ nanowires (prepared by the two-phase technique, Liu et al., 2007), in which the contacts are made on the side wall of a nanowire, the carriers need to overcome the energy barrier between TTF·TCNQ columns for current transport. So, the conductance of the nanowire in this configuration is very small. However, when the electrodes make a direct contact with the TTF·TCNQ tunnelling channel, the conductance of the nanowire is much higher (increasing intensity by a factor of about 4000).

## 5. Conclusion and perspective work

The interest of using molecule-based charge-transfer compounds for future electronic device applications is well established. Organic field effect transistors (OFETs) in which materials for source and drain electrodes are made of a TTF-based conductor, are currently studied. The TTF·TCNQ complex can also be used as an active component in the fabrication of new electrodes for amperometric detection of glucose. Charge-transfer conductors are usually prepared under mild conditions whereas commonly-used metals and semiconductors are elaborated by metallurgical procedures. Moreover, slight changes in the molecular structure on either the donor or the acceptor molecule can drastically influence the physical properties.

Methods described in this chapter allow the preparation of individual nanowires, bundles of nanowires, or nanowire films. Vapour-phase techniques can lead to nanowires whose diameters are well controlled. However, the experimental set-up can be relatively sophisticated (use of ultra high vacuum, presence of an electric field) and vapour-phase techniques can not be applied to ionic precursors (non-volatile precursors). Solution-grown methods are much easier to implement and can be applied to a large variety of precursors (neutral molecules, ionic species, compounds bearing a long-alkyl chain). Two-phase and dipping methods allow the formation of nanowires of TTF-based conductors exhibiting a narrow diameter distribution. Electrochemical techniques are the more promising methods. Indeed the application of a current is required to oxidize the majority of donor molecules. These electrochemical techniques require the use of a specific electrode on which the growth as nanowires can be initiated. Functionalised or nano-rough surfaces have then been developed. Nanowire films (made of randomly distributed nanowires) can be processed on a nano-rough intrinsic silicon electrode, used as an anode. Nanowire arrays (made of highly oriented nanowires) can be fabricated on electrodes functionalised by a nanoporous alumina membrane.

Individual nanowires and nanowire films have also been studied by spectroscopic methods, namely, infrared, Raman, and X-ray photoelectron spectroscopy. Such techniques have shown their potentiality in determining the amount of charge transfer between the donor and the acceptor molecule within nanowires. It has been shown that amount of charge transfer calculated on nanowires is similar to that on macroscopic single crystals.

Nanowires usually exhibit a semiconducting behaviour. However, calculated activation energies are relatively low, which is satisfactory taking into account the large number of inter-wire contacts and the presence of an imperfect interface between the nanowire and the electrode. However, a lot of work remains to be done in studying the transport properties of charge-transfer salts-based nanowires.

Finally, new synthetic challenges are offered to chemists: the preparation of nanowires, nanosticks or nanoparticles of molecule-based charge-transfer compounds embedded in a polymer matrix, dispersed in a micellar medium, or stabilized by an amphiphilic molecule. Poly(3,4-ethylenedioxythiophene), abbreviated PEDOT (Fig. 20), is a conducting polymer with small band gap allowing high optical transparency in the doped, conducting state (conductivity value of about  $5 \times 10^{-3} \text{ S cm}^{-1}$ ). To further increase the conductivity of the polymer material, it can be doped by adding a molecule-based salt, such as  $(\text{TTF})\text{A}_x$ , where A stands for a monoanionic species ( $\text{Cl}^-$ ,  $\text{Br}^-$ ,  $\text{ClO}_4^-$ ). For instance, we have recently prepared nanosticks of  $(\text{TTF})\text{Br}_{0.59}$  dispersed in a PEDOT matrix (Fig. 21). The PEDOT acts as a stabilizing agent around each  $(\text{TTF})\text{Br}_{0.59}$  nanostick and the conductivity value is increased to about  $0.25 \text{ S cm}^{-1}$  (Souque, 2011). We have also recently prepared nanoparticles of molecule-based charge-transfer salts which can, under certain conditions, organize as elongated nanostructures. For example, TTF-TCNQ nanoparticles organized in nanosticks or nanowires have recently been prepared (Souque, 2011). Acicular-shaped nanoparticles are prepared by adding a solution of TTF in a solution of TCNQ in the presence of a mixture of solvents, *i.e.*, acetonitrile/ionic liquid (imidazolium salt). Moreover, nanoparticle-made nanowires are obtained by mixing TTF and TCNQ solutions in the presence of a long-chain carboxylic acid (amphiphilic molecule), used as a stabilizing agent. Changing the nature and the amount of the amphiphilic molecule allows the formation of either isolated nanowires or nanodendrites structures.

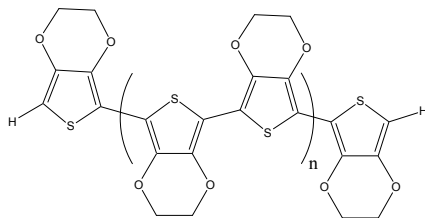


Fig. 20. Molecular formula for PEDOT.

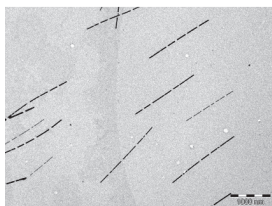


Fig. 21. Nanosticks of TTFBr<sub>0.59</sub> dispersed in a PEDOT matrix (bar = 1000 nm).

## 6. Acknowledgment

Pr. Dominique de Caro appreciates the contribution and collaboration of the following persons: Dr. L. Valade, Dr. C. Faulmann, Dr. H. Casellas and Dr. J. P. Savy (LCC-Toulouse, France); Dr. J. Fraxedas (CIN2-Barcelona, Spain); Dr. P. Auban-Senzier and Pr. C. Pasquier (LPS-Orsay, France); Pr. M. Almeida (Chemistry Department-Sacavém, Portugal); Pr. T. Sugimoto (Osaka University, Japan); Pr. T. Mori and Dr. H. Wada (Tokyo Institute of Technology, Japan). The author also thanks the Centre National de la Recherche Scientifique, the CNRS-AIST exchange program, and finally COST D14.

## 7. References

The order of references is that of citation in the text.

- Deluzet, A.; Perruchas, S.; Bengel, H.; Batail, P.; Molas, S. & Fraxedas, J. (2002). Thin single crystals of organic insulators, metals, and superconductors by confined electrocrystallization. *Advanced Functional Materials*, Vol. 12, No. 2, (February 2002), pp. 123-128.
- Kobayashi, K.; Koyama, H.; Ishikura, K. & Mitsui, T. (2008). Growth and observation of micro-organic crystals in two-dimensional glass nanovolume cell. *Applied Physics Letters*, Vol. 93, No. 14, (October 2008), pp. 143114/1-143114/3.
- Mas-Torrent, M. & Hadley, P. (2005). Electrochemical growth of organic conducting microcrystals of tetrathiafulvalene bromide. *Small*, Vol. 1, No. 8-9, (August 2005), pp. 806-808.
- Sakai, M.; Iizuka, M.; Nakamura, M. & Kudo, K. (2003). Fabrication and electrical characterization of tetrathiafulvalene-tetracyanoquinodimethane molecular wires. *Japanese Journal of Applied Physics*, Vol. 42, No. 4B, (April 2003), pp. 2488-2491.

- Wada, H.; de Caro, D.; Valade, L.; Ozawa, T.; Bando, Y & Mori, T. (2009). Thin-film phases of organic charge-transfer complexes formed by chemical vapour deposition. *Thin Solid Films*, Vol. 518, No. 1, (November 2009), pp. 299-304.
- Liu, H.; Zhao, Q.; Li, Y.; Lu, F.; Zhuang, J; Wang, S.; Jiang, L.; Zhu, D.; Yu, D. & Chi, L. (2005). Field emission properties of large-area nanowires of organic charge-transfer complexes. *Journal of the American Chemical Society*, Vol. 127, No. 4, (January 2005), pp. 1120-1121.
- Liu, H.; Li, J.; Lao, C.; Huang, C.; Li, Y; Wang Z. L. & Zu, D. (2007). Morphological tuning and conductivity of organic conductor nanowires. *Nanotechnology*, Vol. 18, No. 49, (December 2007), pp. 495704/1-495704/7.
- Savy, J. P.; de Caro, D.; Faulmann, C.; Valade, L.; Almeida, M; Koike, T.; Fujiwara, H.; Sugimoto, T.; Fraxedas, J; Ondarçuhu, T. & Pasquier, C. (2007). Nanowires of molecule-based charge-transfer salts. *New Journal of Chemistry*, Vol. 31, No. 4, (April 2007), pp. 519-527.
- Valade, L.; Casellas, H.; Roques, S.; Faulmann, C.; de Caro, D; Zwick, A. & Ariès, L. (2002). TTF[Ni(dmit)<sub>2</sub>]<sub>2</sub>: now as thin films and nanowires. *Journal of Solid State Chemistry*, Vol. 168, No. 2, (November 2002), pp. 438-443.
- Miyata, H.; Tatewaki, Y.; Akutagawa, T.; Hasegawa, T.; Nakamura, T; Christensen C. A. & Becher, J. (2003). Langmuir-Blodgett films of bis-tetrathiafulvalene substituted macrocycle and TCNQ derivatives. *Thin Solid Films*, Vol. 438-439, The 5<sup>th</sup> International Conference on Nano-molecular Electronics, (August 2003), pp. 1-6.
- Ji, H.; Hu, J.; Tang, Q.; Hu, W.; Song, W & Wan, L. (2006). Bis(ethylenedithio)tetrathiafulvalene charge-transfer salt nanotube arrays. *Advanced Materials*, Vol. 18, No. 20, (October 2006), pp. 2753-2757.
- Cui, G.; Xu, W.; Guo, C.; Xiao, X.; Xu, H; Zhang, D.; Jiang, L. & Zhu, D. (2004). Conducting nanopearl chains based on the dmit salt. *Journal of Physical Chemistry B*, Vol. 108, No. 36, (August 2004), pp. 13638-13642.
- Phanindra Sai, T. & Raychaudhuri, A. K. (2010). Observation of Peierls transition in nanowires (diameter ~ 130 nm) of the charge transfer molecule TTF:TCNQ synthesized by electric-field-directed growth. *Nanotechnology*, Vol. 21, No. 4, (January 2010), pp. 04703/1-04703/8.
- Souque, M. (2011). Nanostructured molecule-based conductors for space applications. *Ph.-D. Thesis*, Toulouse University: France (January 2011).

# Novel Pressure - Induced Structural Transformations of Inorganic Nanowires

Yang Song and Zhaohui Dong

*Department of Chemistry, University of Western Ontario  
Canada*

## 1. Introduction

Nanostructured materials in different morphologies such as dots, wires and belts are of fundamental importance because of their wide range of tunable electrical, optical and mechanical properties that the bulk materials do not possess. These properties that critically depend on the nano-structures predominantly determined by the synthetic approaches, however, can be substantially modified by compression (Chen et al., 2002; Chen & Herhold, 1997; Guo et al., 2008; He et al., 2005; Jacobs et al., 2001; Jiang & Gerward, 2000; Jiang et al., 1999; Jiang et al., 2001; Jiang et al., 1998; Park et al., 2008; Swamy et al., 2006; Tolbert & Alivisatos, 1994; Tolbert & Alivisatos, 1995; Wang et al., 2005; Wang et al., 2001). Investigations of the structures and phase transformations of nanomaterials under high pressures have received increasing attention simply because high pressure has proven to be a powerful driving force to produce new structures and, therefore, new nanomaterial properties (San-Miguel, 2006). The most interesting aspect of high-pressure studies on nanomaterials is the observation that compressed nanomaterials exhibit significantly different behaviours than their corresponding bulk counterparts, such as the size-dependent phase transformations observed for nano-scale CdSe (Tolbert & Alivisatos, 1994; Tolbert & Alivisatos, 1995), SnO<sub>2</sub> (He et al., 2005; Jiang et al., 2001) and TiO<sub>2</sub> (Swamy et al., 2006). In addition, morphology can play an important tuning role in the pressure-induced transformations of nanostructured materials. For instance, ZnS nanobelts have been found to exhibit a much wider stability region up to 6.8 GPa for the wurtzite phase, in strong contrast to bulk ZnS, which is much more stable in the sphalerite phase (Wang et al., 2005).

In this chapter, we focus our interests on one-dimensional inorganic nanostructured materials, such as nanowires, due to their wide range of applications. Table 1 summarizes all high-pressure studies on one dimensional inorganic nanomaterials so far. In particular, we will discuss the novel and unusual pressure behaviors of two inorganic nanowires with great technological importance: tin dioxide (SnO<sub>2</sub>) and gallium nitride (GaN). Our findings in these studies demonstrate the potential of using the combination of pressure and morphology as a powerful approach to tune the structures and properties of one-dimensional nanomaterials required for specific applications.

Material	Morphology	Dimension *	Pressure (GPa)	Characterization Method	Reference
ZnS	Nanobelt	$t$ : ~10 nm $w$ : ~1 $\mu\text{m}$ $l$ : 100 $\mu\text{m}$	0-11.4	X-ray diffraction	(Wang et al., 2005)
	Nanorod	$w$ : ~10 nm	0-19.4	Raman, Photoluminescence	(Li et al., 2007)
		$w$ : ~10 nm	0-37.2	X-ray diffraction	(Li et al., 2011)
BN	Nanotube	$d$ : 20-50 nm	0-16	Raman	(Saha et al., 2007; Saha et al., 2006)
		$d$ : ~ 50 nm	0-19.1	X-ray diffraction	(Muthu et al., 2008)
		$d$ : ~ 100 nm	0-34.6	FTIR	(Dong & Song, 2010)
ZnO	Nanowire	$w$ : 60-100 nm $l$ : tens of $\mu\text{m}$	0-21.5	Raman, X-ray diffraction	(Yan et al., 2009)
	Nanotube	$d$ : 10-70 nm	0-21.5	X-ray diffraction	(Hou et al., 2009)
SnO <sub>2</sub>	Nanowire	$w$ : 50-60 nm $l$ : several $\mu\text{m}$	0-37.9	Raman, X-ray diffraction	(Dong & Song, 2009)
	Nanobelt	$t$ : tens of nm $w$ : ~1 $\mu\text{m}$ $l$ : several $\mu\text{m}$	0-36.2	Raman, X-ray diffraction	(Dong & Song, 2009)
TiO <sub>2</sub>	Nanoribbon	$t$ : ~20 nm $w$ : 50-200 nm $l$ : tens of $\mu\text{m}$	0-30.9	Raman, X-ray diffraction	(Li et al., 2010)
GaN	Nanowire	$w$ : tens of $\mu\text{m}$ $l$ : < 100 nm	0-65	X-ray diffraction	(Dong & Song, 2010)

Table 1. Summary of high-pressure studies on one-dimensional inorganic nanomaterials.

\*  $d$ : diameter;  $w$ : width;  $l$ : length;  $t$ : thickness

## 2. Experimental details

### 2.1 Materials

SnO<sub>2</sub> nanobelts and nanowires were synthesized using chemical vapor deposition on silicon substrate, starting with SnO powders (99%, Alfa Aesar). The experimental details have been described elsewhere (Wang et al., 2007; Zhou et al., 2006). The morphologies and chemical composition of SnO<sub>2</sub> nanobelts and nanowires were examined by scanning electron microscopy (SEM) (Instrument model: Leo/Zesis 1540XB FIB/SEM) and energy dispersive X-ray spectroscopy. Fig. 1a and 1c show the dimensions and morphologies of the as-made SnO<sub>2</sub> nanobelts and nanowires. The nanobelts are several tens of nanometers thick, several micrometers long and a few hundred nanometers up to 1  $\mu\text{m}$  wide. The nanowires were 50-60 nm in diameter and several microns long.

The GaN nanowires were synthesized by passing ammonia through a mixture of Ga and Ga<sub>2</sub>O<sub>3</sub> at high temperature in the presence of Au nanoparticles as the catalysts. The experimental details were reported previously (Zhou et al., 2005). The nanowires were thoroughly characterized by SEM. The SEM images (Fig. 2) reveal that the GaN nanowires have wire-like structure with zigzag periodic units. Most of the wires have a length of tens to hundreds of microns and their thickness is several tens of nanometers.

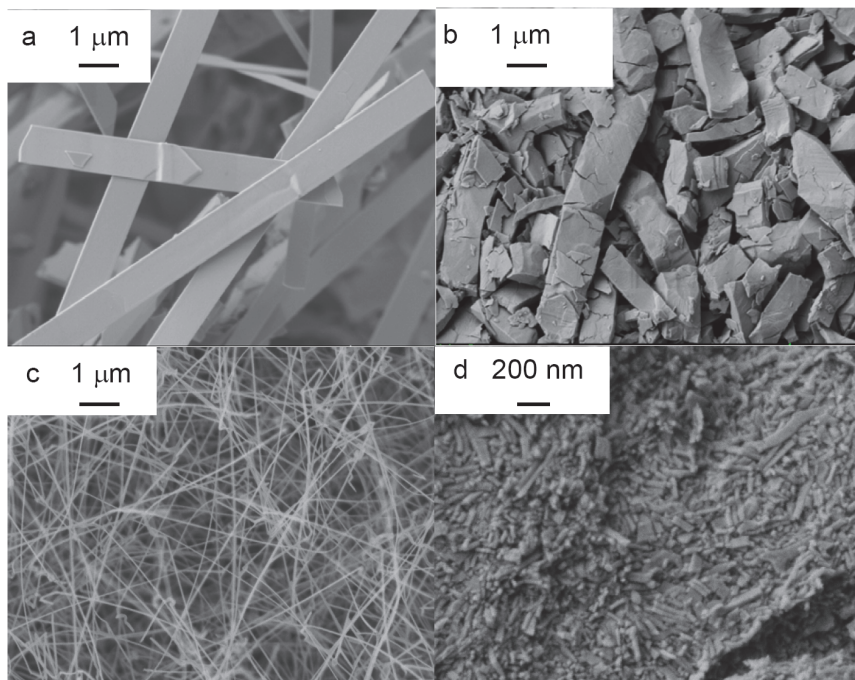


Fig. 1. SEM images of SnO<sub>2</sub> nanobelts before compression (a) and after decompression (b) as well as SnO<sub>2</sub> nanowires before compression (c) and after decompression (d) with scales shown in each panel. (From Dong & Song, 2009)

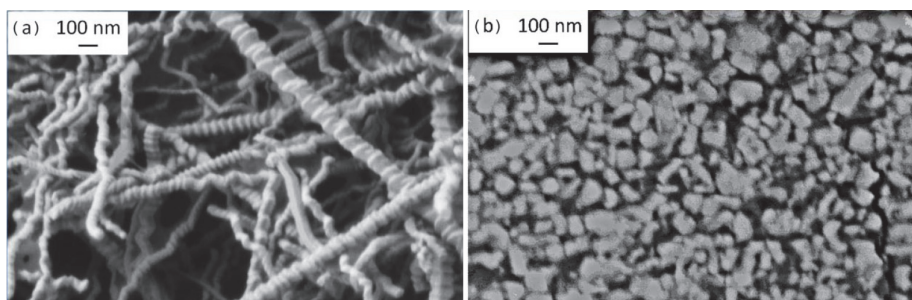


Fig. 2. SEM images of GaN nanowires before compression (a) and after decompression (b) with scales labeled in each panel. (From Dong & Song, 2010).

## 2.2 High pressure techniques

Diamond anvil cell (DAC) is a fundamental apparatus to achieve static high pressures. Recent rapid advances in the DAC technology have allowed the generation of extreme conditions in a broad P-T range with great controllability and accuracy (Hemley & Mao, 2002). The transparency of diamonds over a wide wavelength range allows the use of various optical techniques to examine the high-pressure behaviors of materials in situ. Over

the past a few decades, in particular, new emerging analytical probes including optical spectroscopy, synchrotron and neutron sources have enabled structural characterization of materials with unprecedented spatial, temporal and spectral resolutions (Hemley & Mao, 2002).

Fig. 3 shows a typical DAC apparatus where two brilliant cut diamonds are used as anvils to exert static pressure up to several million atmospheres (or several hundred GPa) with only moderate force. Such extreme pressures can be accurately determined by monitoring ruby fluorescence lines using the following relationship (Mao et al., 1978):

$$P = \frac{1904}{B} \left[ \left( 1 + \frac{\Delta\lambda}{694.24} \right)^B - 1 \right] \quad (1)$$

where  $P$  is the pressure in GPa,  $\Delta\lambda$  is the ruby  $R_1$  line shift in nm, and parameter  $B$  is 7.665 for quasi-hydrostatic conditions and is 5 for non-hydrostatic conditions.

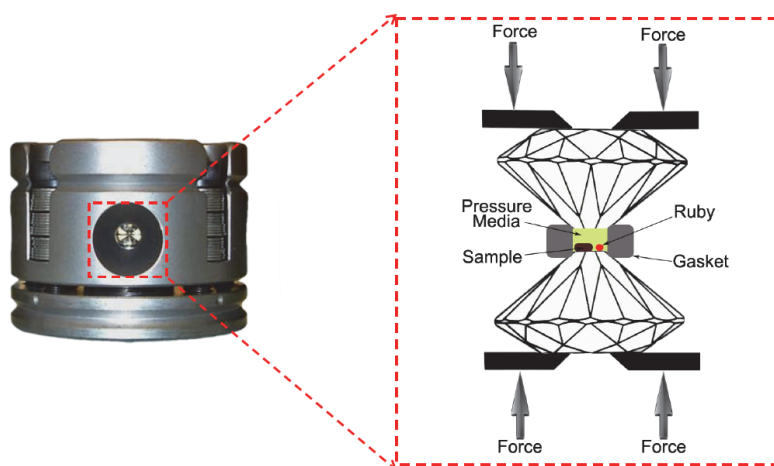


Fig. 3. Photo and schematics of a symmetric diamond anvil cell.

In the experiment for  $\text{SnO}_2$  nanomaterials, a symmetric DAC with a pair of type I diamonds and a 400-micron culet was used. A hole with a diameter of 150 microns was drilled on a stainless steel gasket and used as the sample chamber. A few ruby chips were loaded with the sample as the pressure calibrant. The samples were loaded without pressure transmitting medium (PTM) for Raman measurements, whereas silicon oil was used as the PTM for X-ray diffraction measurements. GaN nanowires were compressed up to 65 GPa using a symmetric diamond anvil cell (DAC) which consists of a pair of type I diamonds with 200  $\mu\text{m}$  culets and cubic boron nitride seats. The sample and a small ruby ball were enclosed in an 80- $\mu\text{m}$ -diameter hole in a tungsten gasket. Silicone oil was used as the PTM.

### 2.3 In situ Raman spectroscopy

Vibrational spectroscopies compatible with DAC apparatus, including Raman and Fourier Transform Infrared (FTIR) microspectroscopy have been widely used to characterize high-

pressure structures of materials in situ. In particular, Raman spectroscopy is a sensitive structural characterization probe providing rich information about molecular geometries, bonding properties, phase identities and transformations, lattice dynamics, and crystallinity of materials, etc. Raman measurements were performed on SnO<sub>2</sub> nanobelts using a customized Raman micro-spectroscopy system. A 488 nm line from an Innova Ar<sup>+</sup> laser (Coherent Inc.) was used as the excitation source and was focused to less than 5 μm on the sample by an Olympus microscope. The Rayleigh line was removed using a pair of notch filters. The scattered light was dispersed using an imaging spectrograph equipped with a 1800 lines/mm grating, achieving a resolution of 0.1 cm<sup>-1</sup>. The scattered light was then recorded using an ultrasensitive liquid-nitrogen-cooled, back-illuminated charge-coupled device (CCD) detector from Acton. The system was calibrated using neon lines with an uncertainty of ± 1 cm<sup>-1</sup>.

#### 2.4 Synchrotron X-ray micro-diffraction

Synchrotron light source in the high-energy hard X-ray region is an indispensable probe for DAC based materials characterizations. Such hard X-ray available in almost all synchrotron facilities worldwide enables in situ diffraction measurements on micron-sized materials under extreme P-T conditions with unparalleled accuracy for the elucidation of crystalline structures. For SnO<sub>2</sub> nanomaterials, the angle dispersive X-ray diffraction measurements were carried out at the X17C beamline at the National Synchrotron Light Source (NSLS) at Brookhaven National Laboratory (BNL). A high-energy, fixed-exit monochromator with Sagittally-bent double Si crystal Laue mode was used to optimize the high-energy synchrotron X-ray from 20 keV to 40 keV, with an incident X-ray wavelength of 0.4066 Å. A pair of Kirkpatrick-Baez (KB) mirrors consisting of Si crystals coated with Pt and a focal length of 100 mm was used to focus the white X-ray beam at a glancing angle of approximately 1 mrad. This focused a 180 μm×180 μm incident beam to a 25 μm (horizontal) × 25 μm (vertical) beam on the sample. A MAR CCD X-ray detector was used to collect the 2D Debye-Scherrer patterns. The goniometer geometry and other diffraction parameters were calibrated using CeO<sub>2</sub> standard diffraction. Each diffraction pattern was obtained during an average exposure time of 5 to 10 minutes. The two-dimensional Debye-Scherrer patterns were converted to one-dimensional diffraction patterns using Fit2D software and Rietveld refinements were performed using GSAS package.

The angle-dispersive X-ray diffraction measurements on GaN nanowires were performed at the undulator sector 16-ID-B, High-Pressure Collaborative Access Team (HPCAT), Advanced Photon Source (APS) of Argonne National Laboratory (ANL) using an incident wavelength of 0.3680 Å and beam size of 15 μm×10 μm. The procedures of data analysis for GaN nanowires are similar to those for SnO<sub>2</sub> nanomaterials.

### 3. SnO<sub>2</sub> nanobelts and nanowires under high pressures

#### 3.1 Properties, structures, and applications of SnO<sub>2</sub>

As an *n*-type semiconductor with a large band gap ( $E_g = 3.6$  eV at 300 K), SnO<sub>2</sub> has been studied extensively for applications in transparent conducting electrodes, lithium ion batteries and gas sensors (Watson et al., 1993). Specifically, because SnO<sub>2</sub> exhibits high sensitivity for detecting CO and NO<sub>x</sub> gases, vigorous studies on SnO<sub>2</sub>-based gas sensors

have been undertaken (Watson et al., 1993). In these studies, SnO<sub>2</sub> in orthorhombic structures was found to exhibit better sensitivity for specific gases than the tetragonal rutile-type structure (Arbiol et al., 2008; Sangaletti et al., 1997). However, natural SnO<sub>2</sub>, known as cassiterite, always exists as the rutile-type structure and it is generally difficult to obtain the orthorhombic phase directly from minerals (Chen et al., 2006). Therefore, finding new methods for producing SnO<sub>2</sub> with orthorhombic structures, such as by pressure tuning (Haines & Leger, 1997), is of particular interest in the sensor industry. In addition, studies suggest that nanostructured SnO<sub>2</sub> might exhibit significantly enhanced performance for certain gas-sensing applications than thick films or bulk materials (Wang et al., 2008). Therefore, many nanostructured SnO<sub>2</sub> of different morphologies, including nanoparticles, nanowires, nanorods and nanobelts, have been synthesized (Calestani et al., 2005; Calestani et al., 2005; Zhou et al., 2006) and their optical and electrochemical properties evaluated. Spectroscopic studies such as Raman measurements (Sun et al., 2003) and photoluminescence (Zhou et al., 2006) show that SnO<sub>2</sub> nanobelts exhibit unique optical properties that are different than those from bulk materials. These recent studies motivated us to undertake the high-pressure investigations on the behaviors of one-dimensional nanostructured SnO<sub>2</sub>, resulting in the observation of novel, and unexpected nano-effects.

### 3.2 Raman spectrum of SnO<sub>2</sub> nanobelts

Raman measurements were performed on SnO<sub>2</sub> nanobelts with selected spectra depicted in Fig. 4. SnO<sub>2</sub> nanobelts at ambient pressure had a regular rutile-type structure (space group P4<sub>2</sub>/mmn or  $D_{4h}^{14}$ , Z=2) and, therefore, the irreducible representation predicted the Raman active modes to be A<sub>1g</sub>, B<sub>1g</sub>, B<sub>2g</sub> and E<sub>g</sub>, with three bands observed at 473 cm<sup>-1</sup> (E<sub>g</sub>), 631 cm<sup>-1</sup> (A<sub>1g</sub>) and 773 cm<sup>-1</sup> (B<sub>2g</sub>), consistent with previous Raman measurements on nanostructured SnO<sub>2</sub> (Sun et al., 2003). Additional weak Raman bands at 500 cm<sup>-1</sup> and 692 cm<sup>-1</sup> can be assigned as A<sub>2u</sub> (TO) and A<sub>2u</sub> (LO) modes, both of which are IR active, whereas the band at 544 cm<sup>-1</sup> was a Raman forbidden B<sub>1u</sub> mode. These abnormal Raman bands are characteristic of SnO<sub>2</sub> nanobelts and are not observed in the Raman spectrum of bulk SnO<sub>2</sub> (Sun et al., 2003). Four additional Raman active modes were observed below 300 cm<sup>-1</sup> (not shown here), which can be attributed to the impurities of the substoichiometric Sn<sub>2</sub>O<sub>3</sub>/Sn<sub>3</sub>O<sub>4</sub> phases in the synthetic process (Wang et al., 2007). Interestingly, no strong Raman active modes were observed for the SnO<sub>2</sub> nanowires, which is in contrast to a Raman study by Zhou et al. (Zhou et al., 2006) on single crystalline SnO<sub>2</sub> wires. It is well known that the optical properties of nanomaterials, especially their Raman features, are very sensitive to a number of factors including size, morphology, synthetic route, purity, as well as short-range structures and environment (Gouadec & Colombari, 2007). As a result, different Raman measurements on the same materials (e.g., various metal oxides) but with different nano-parameters have been reported and analyzed extensively (Arora et al., 2007; Gouadec & Colombari, 2007). Upon compression, all SnO<sub>2</sub> nanobelts Raman modes exhibited a blue shift with decreasing intensities along with profile broadening. At the highest pressure, only the A<sub>1g</sub> mode was observed to have a significantly broadened profile (middle spectrum of Fig. 4). Upon decompression, the Raman profiles changed very gradually as the pressure decreased. As the SnO<sub>2</sub> nanobelts returned to ambient pressure (lower spectrum of Fig. 4), the E<sub>g</sub> and B<sub>2g</sub> modes were recovered but the bands remained broadened. These

observations indicate the partial reversibility of the SnO<sub>2</sub> nanobelts optical responses to compression and decompression, which is coincident with the pressure-induced morphology modifications. The SEM images obtained before compression (Fig. 1a), and after decompression (Fig. 1b), suggest that the belts are crushed to shorter sections that are thicker than the original belts before compression. In contrast, the SnO<sub>2</sub> nanowires exhibited more dramatic changes in morphology as a result of compression, i.e., the wire shapes were no longer recognizable (Fig. 1d).

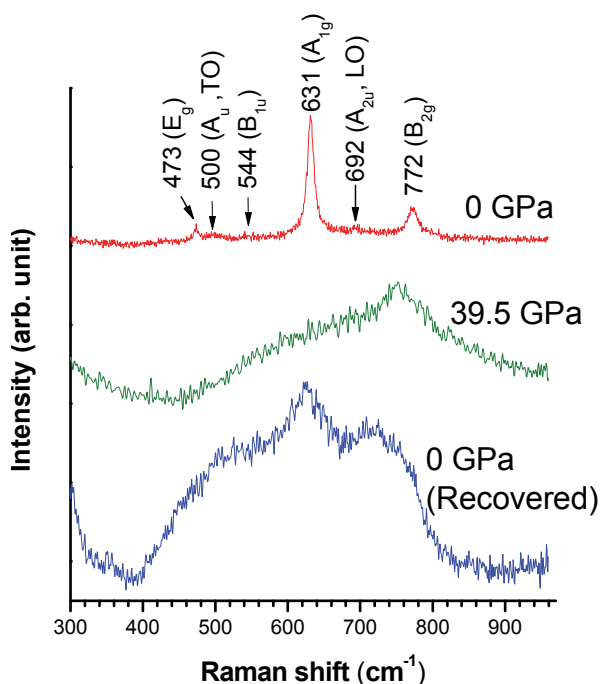


Fig. 4. Raman spectra of SnO<sub>2</sub> nanobelts in the spectral region of 300 to 1000 cm<sup>-1</sup> collected at ambient pressure (top), at 39.5 GPa (middle) and upon decompression (bottom). The assignments of the observed Raman modes are labeled above the ambient-pressure spectrum. (From Dong and Song, 2009)

### 3.3 X-ray diffraction of SnO<sub>2</sub> nanobelts

*In situ* high-pressure angle dispersive X-ray diffraction measurements were performed on SnO<sub>2</sub> nanobelts on compression up to 38 GPa followed by decompression. Representative diffraction patterns are depicted in Fig. 5. Fig. 6 shows the quantitative analysis of the nanobelts diffraction patterns at 14.8, 19.2 and 31.8 GPa and upon complete decompression (i.e., recovered). Starting at ambient pressure, the diffraction pattern of SnO<sub>2</sub> nanobelts indicates an excellent crystalline phase that adopts a rutile structure (P4<sub>2</sub>/mnm) that is the same as that for the bulk material (Haines & Leger, 1997), with cell parameters of  $a=4.7218\text{\AA}$  and  $c=3.1802\text{\AA}$ . All the diffraction patterns can be indexed with a single rutile-type phase

until compressed to near 15 GPa (Fig. 6a). The broadening of the (101), (200) and (211) reflections of the rutile phase suggests that an orthorhombic phase has formed (CaCl<sub>2</sub>-type structure with space group *Pnmm*). Rietveld refinement suggests that there was only a slightly modified cell parameter from the rutile structure:  $a=4.6543$  Å,  $b=4.5744$  Å and  $c=3.1483$  Å. This pressure-induced phase transformation was similar to that observed with bulk SnO<sub>2</sub> (Haines & Leger, 1997), but the transformation pressure was higher. SnO<sub>2</sub> nanobelts existed in this single phase up to 19.2 GPa beyond which new phase transformations were observed (Fig. 6b). The new reflections at  $2\theta$  of  $6.606^\circ$  and  $8.129^\circ$  were characteristic of a new orthorhombic  $\alpha$ -PbO<sub>2</sub> phase (*Pbcn*) at (110) and a cubic fluorite phase (*Pa* $\bar{3}$ ) at (111) directions, respectively. From 19.2 GPa to the highest pressure in the present study, SnO<sub>2</sub> existed as a mixture of these three phases (Fig. 6c). This observation is in strong contrast to the phases observed for bulk SnO<sub>2</sub> materials, in which both the CaCl<sub>2</sub>-type and  $\alpha$ -PbO<sub>2</sub> phases are reported to exist between 12 and 21 GPa (Haines & Leger, 1997). Upon decompression, the three-phase mixture was found to persist down to 7.5 GPa, when the cubic fluorite phase disappeared, with a subsequent back transformation to the rutile structure. Upon complete decompression, the SnO<sub>2</sub> nanobelts were composed of mixtures of rutile and  $\alpha$ -PbO<sub>2</sub> phases (Fig. 6d).

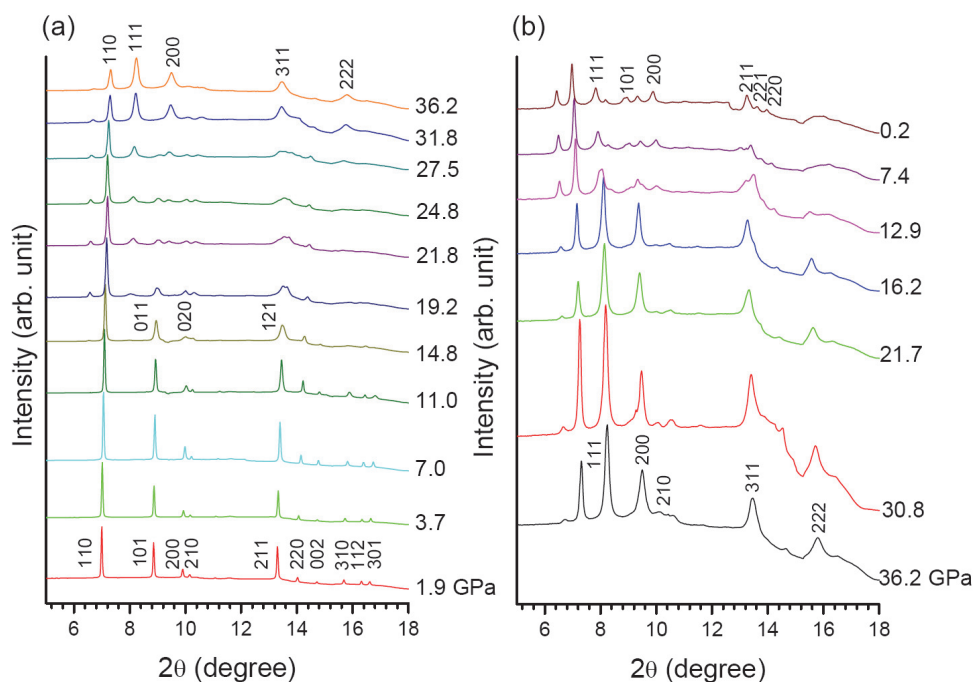


Fig. 5. X-ray diffraction patterns of SnO<sub>2</sub> nanobelts at selected pressures on compression (a) and decompression (b). Pressures in GPa are labeled along each pattern. The Miller indices are shown for the tetragonal structure at 1.9 GPa, the orthorhombic structure at 14.8 GPa and the cubic structure at 36.2 GPa on compression, and at 36.2 GPa and 0.2 GPa on decompression, respectively.

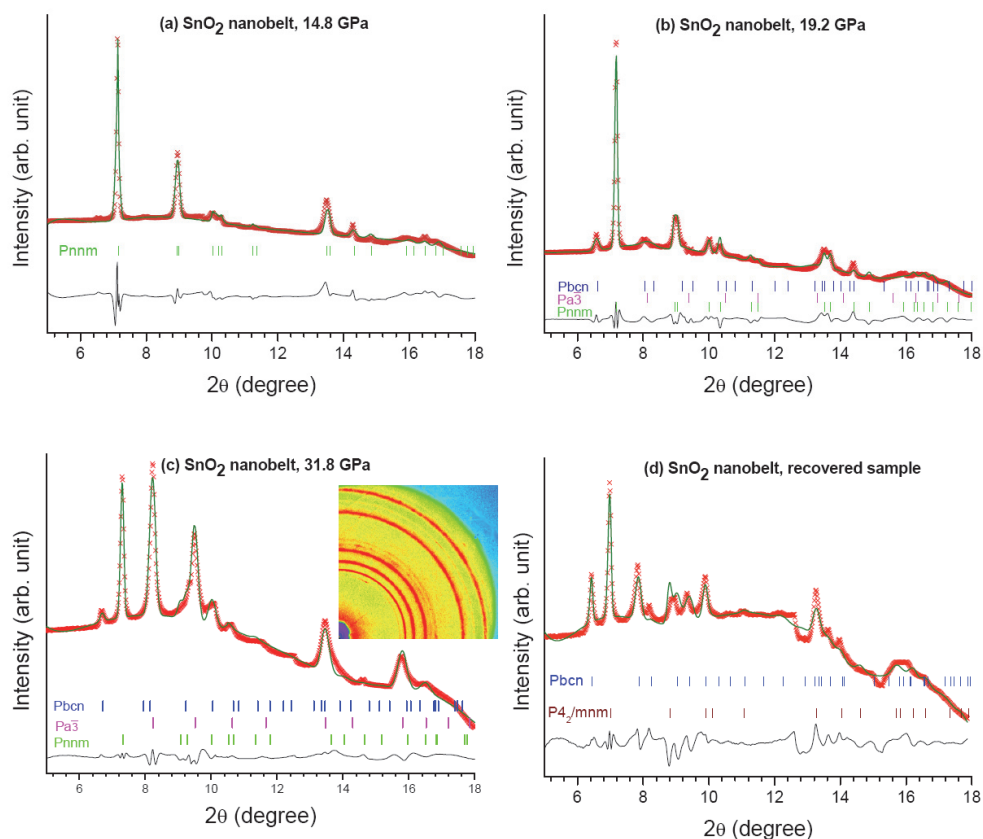


Fig. 6. Rietveld refinement of X-ray diffraction patterns of  $\text{SnO}_2$  nanobelts at 14.8 GPa (a), 19.2 GPa (b), 31.8 GPa (c) and from recovered sample (d). The inset in (c) shows the original 2D Debye-Scherrer patterns with one quadrant. The red cross is experimental X-ray intensity whereas the green solid line is the calculated diffraction pattern based on refinement with the black curve at the bottom showing the difference between the calculated and observed intensities. The vertical bars with different colors indicate the characteristic reflections of different phases labeled in the front.

### 3.4 X-ray diffraction of $\text{SnO}_2$ nanowires

The X-ray diffraction patterns  $\text{SnO}_2$  nanowires at selected pressures upon both compression and decompression are depicted in Fig. 7. The Rietveld refinement analysis for patterns at pressures of 14.8, 20.0 and 34.4 GPa and upon complete decompression is shown in Fig. 8. Upon compression and decompression, as can be seen,  $\text{SnO}_2$  nanowires exhibit unexpected

pressure responses that are different than those for nanobelts or bulk materials. Starting with the same rutile structure (e.g., Fig. 8a), transformation to a  $\text{CaCl}_2$ -type orthorhombic structure (Fig. 8b) was observed only when it was compressed to 17 GPa, which is a higher transition pressure than that for the nanobelts and much higher ( $\Delta P > 5\text{ GPa}$ ) than that for the bulk materials. When further compressed to 25 GPa, a fluorite-type phase was found to contribute to the overall diffraction pattern and coexisted with the  $\text{CaCl}_2$  type phase all the way to the highest pressure. A striking observation that the  $\alpha\text{-PbO}_2$  phase was missing in the entire compression region was noted as shown in the Rietveld refinement analysis of the diffraction pattern, which unambiguously suggests that the  $\text{SnO}_2$  nanowires are composed of only  $\text{CaCl}_2$ -type and fluorite-type phases at 34.4 GPa (Fig. 8c). Upon decompression, the  $\text{CaCl}_2$ -type phase transformed back to the rutile-type phase at 16 GPa, which is much earlier than that observed for either nanobelts or bulk materials. Further decompression results in more surprising transformations - the fluorite-type phase persists all the way to near-ambient pressure, whereas the  $\alpha\text{-PbO}_2$  phase that was missing during compression was observed when it was decompressed to 10.6 GPa and was recovered at ambient pressure (Fig. 8d).

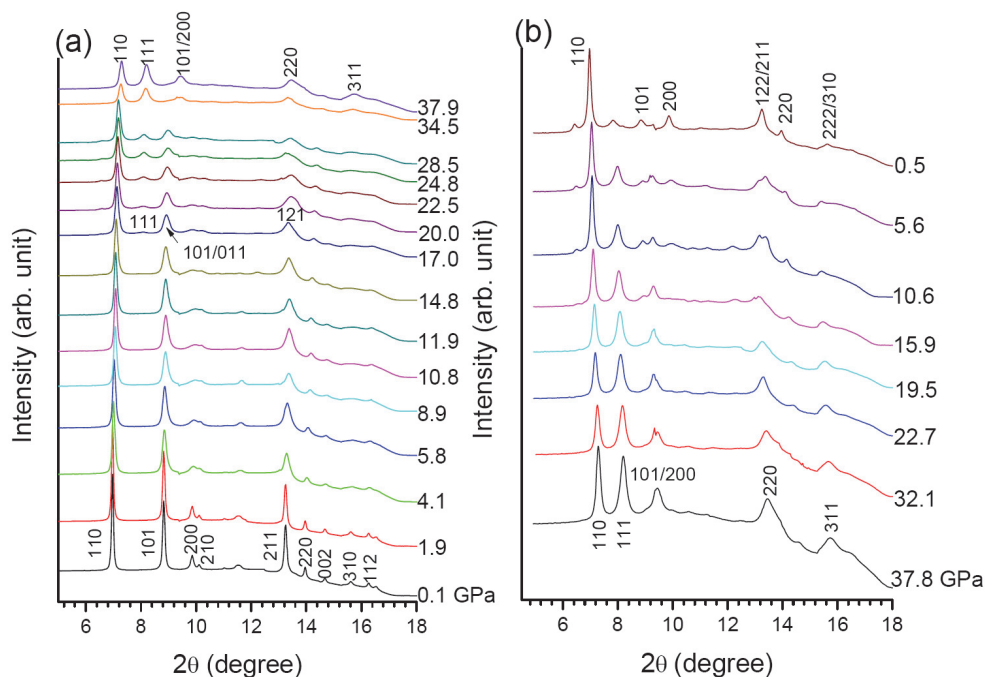


Fig. 7. X-ray diffraction patterns of  $\text{SnO}_2$  nanowires at selected pressures on compression (a) and decompression (b). The legends follow Fig. 5.

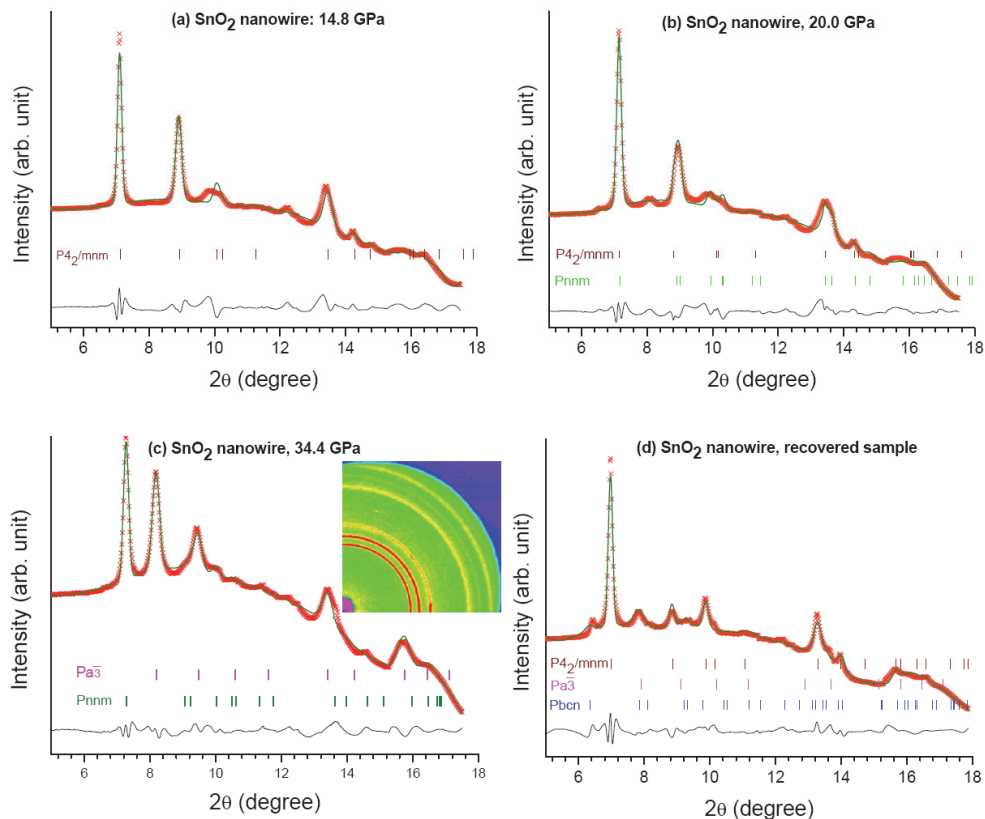


Fig. 8. Rietveld refinement of X-ray diffraction patterns of  $\text{SnO}_2$  nanowires at 14.8 GPa (a), 20.0 GPa (b), 34.4 GPa (c) and from recovered sample (d). The legends follow Fig. 6.

### 3.5 Equation of states

Rietveld refinement performed on all diffraction patterns indicated that the rutile and  $\text{CaCl}_2$ -type phases were the dominant phases both for nanobelts and nanowires, whereas the  $\alpha\text{-PbO}_2$  and fluorite phases contribute to the mixed phases only to a certain extent. Therefore, we fit the third-order Birch equation of state (EOS) based on only the dominant phases of nanobelts and nanowires (Fig. 9) to estimate the compressibility using (Birch, 1978):

$$P = \frac{3}{2}B_0 \left[ \left( \frac{V}{V_0} \right)^{-7/3} - \left( \frac{V}{V_0} \right)^{-5/3} \right] \times \left\{ 1 + \frac{3}{4}(B'_0 - 4) \left[ \left( \frac{V}{V_0} \right)^{-2/3} - 1 \right] \right\} \quad (2)$$

where  $V_0$  is the original cell volume at ambient pressure, and  $V$  is the cell volume at pressure  $P$ .  $B_0$  and  $B'_0$  are the bulk modulus and its first pressure derivative, respectively, at ambient pressure.

The bulk modulus and its first derivative were found to be  $B_0=169.3$  GPa and  $B'=8.4$  for the nanobelts whereas those for the nanowires were  $B_0=225.3$  GPa and  $B'=8.1$ , respectively. We note that the compressibility of the nanobelts was significantly higher than that for the bulk material ( $B_0=204$  GPa,  $B'=8.0$ ) (Haines & Leger, 1997), whereas the nanowires were less compressible.

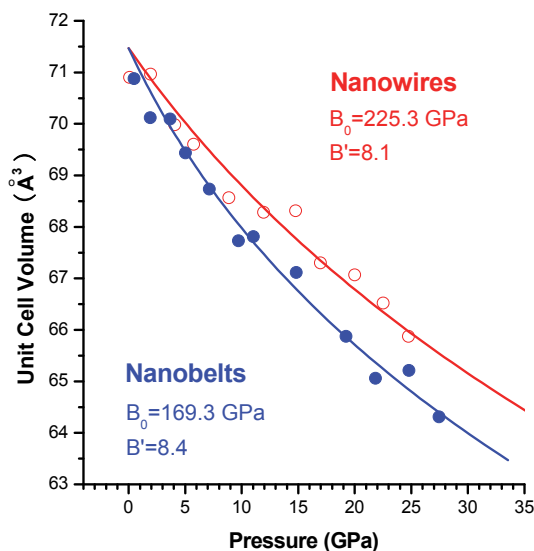


Fig. 9. Pressure-volume relations for  $\text{SnO}_2$  nanowires (open circles) and nanobelts (solid circles). The solid lines are fittings using 3<sup>rd</sup> order Birch equation of state (see text).

The size- and morphology-induced alteration of  $\text{SnO}_2$  compressibility characterized by bulk moduli can be understood in parallel with other nanomaterials.  $\text{CeO}_2$  nanoparticles exhibit a prominent enhancement of the bulk modulus compared with that for bulk materials (Wang et al., 2001; Wang et al., 2004), whereas no obvious difference in compressibility was observed for  $\text{ZnS}$  nanocrystals (Jiang et al., 1999). In contrast, the compressibility of  $\text{PbS}$  and  $\gamma\text{-Al}_2\text{O}_3$  (Chen et al., 2002) was found to increase with decreasing nanoparticle size. Furthermore, strongly contrasting compressibility was observed for  $\text{TiO}_2$  nanoparticles, i.e, the bulk modulus of the rice-shaped particles was reduced whereas that of the rod-shaped particles was enhanced by more than 50% relative to that of the bulk materials (Park et al., 2008). Therefore, multiple factors determine the mechanical properties of nanomaterials. In this case, by carefully examining  $\text{SnO}_2$  nanobelts at ambient pressure using SEM and Raman imaging (Wang et al., 2007), other tin oxides ( $\text{SnO}_x$ ) attached to the nanobelt surface could contribute to the defect in the  $\text{SnO}_2$  crystal lattice and may therefore decrease the stiffness. Compared with nanobelts,  $\text{SnO}_2$  nanowires carry much fewer or no defects and are more strictly one-dimensional in morphology, which may correlate with their general size-dependent compressibility (Wang et al., 2001). These arguments are corroborated by a previous comparative study of nanobelts and nanowires (Calestani et al., 2005).

### 3.6 Discussion

Fig. 10 summarizes the strongly contrasting pressure-induced phase transformations of SnO<sub>2</sub> nanobelts and nanowires compared with bulk materials. The differences in the pressure-induced phase transitions between nanostructured and bulk SnO<sub>2</sub> materials have been observed for other morphologies, primarily nanoparticles. However, contrasting results were reported by different groups - He et al. found that transition pressure increases with decreasing SnO<sub>2</sub> nanocrystal size (He et al., 2005), whereas Jiang et al. observed no obvious size-dependent transition pressure differences (Jiang et al., 2001). For other nanostructured materials such as oxides, sulfides or elements, transition pressure shifts have been found to go in both directions. The majority of these nanomaterials (e.g., CdSe (Tolbert & Alivisatos, 1994; Tolbert & Alivisatos, 1995), ZnS (Jiang et al., 1999) and PbS (Jiang & Gerward, 2000)) exhibit higher transition pressures than bulk materials do and their transition pressures also increase with decreasing nanocrystal size (Tolbert & Alivisatos, 1995). However, other nanocrystal oxides, such as  $\gamma$ -Fe<sub>2</sub>O<sub>3</sub> (Jiang et al., 1998) and CeO<sub>2</sub> (Rekhi et al., 2001), have reduced transition pressures. The general understanding of the 'size' effect in pressure-induced transformations is used to examine a thermodynamic function, i.e., the Gibbs free energy change ( $\Delta G$ ) with the major contributing factors: the ratio of the volume collapse ( $P\Delta V$ ), the surface energy differences ( $\Delta\gamma$ ) and the internal energy differences ( $\Delta U$ ) (Jiang, 2004; Wang et al., 2005). It is believed that enhanced transition pressures in nanomaterials indicate that surface energy differences are playing a dominant role, whereas reduced transition pressures might be associated with a compression process overwhelmed by volume collapse. The 'size' effect also seems to extend to one-dimensional nanomaterials such as ZnS nanobelts (Wang et al., 2005). Indeed, it was found that the reduced ZnS nanobelt thickness resulted in a higher transition pressure (Wang et al., 2005). Therefore, these principles can be adopted to explain some of the pressure-induced transformations observed in this study. The higher transition pressures observed both in nanobelts and nanowires indicate that there is a prominent surface energy effect on nanostructured SnO<sub>2</sub>. In particular, the onset pressures involving the rutile-to-CaCl<sub>2</sub> type transition are approximately 11.8, 15.0 and 17.0 GPa for bulk materials, nanobelts and nanowires, respectively. Because there is no significant change in the unit cell volume in this transition, the contribution of the first factor, i.e., the ratio of the volume collapse to the overall  $\Delta G$ , is negligible. Considering that the internal energy differences ( $\Delta U$ ) are typically small or negative (Jiang, 2004), the surface energy differences mainly are therefore believed to be responsible for the enhanced transition pressures for nanostructured SnO<sub>2</sub>. Gauging from the observed transition pressures, the surface energy differences in the nanowires were estimated to be 62.5% higher than in the nanobelts. Qualitatively, the significantly enhanced nanowire transition pressures can be interpreted by further 'reduced size' from nanobelts with reduced width and thickness. Indeed, the band widths of the nanowire reflections are slightly higher in the nanobelts in general, consistent with the size-induced broadening observed for other nanomaterials (Wang et al., 2004).

In addition to size effects, morphology has also proven to be an important factor for regulating nanomaterial structure and stability, either by early or delayed phase transitions (Wang et al., 2005). However, the drastically contrasting phase stability regions observed for different morphologies of SnO<sub>2</sub>, especially for the completely missing  $\alpha$ -PbO<sub>2</sub> phase, are

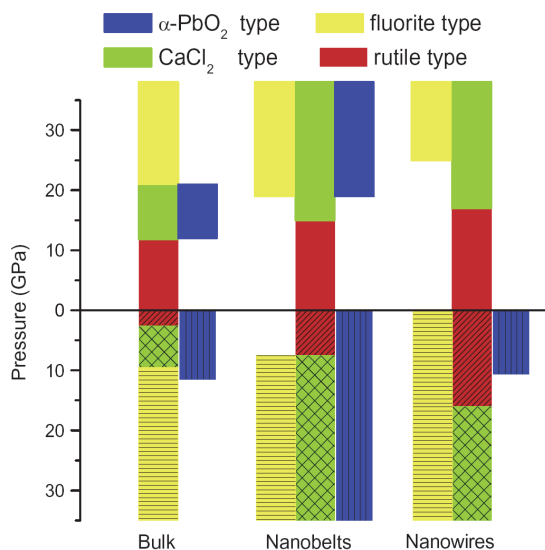


Fig. 10. Summary of pressure-induced phase transformations for SnO<sub>2</sub> nanobelts and nanowires upon compression (plain vertical bars) and decompression (hatched vertical bars) compared with those for bulk SnO<sub>2</sub> material. The different colors label different phases: rutile (red), CaCl<sub>2</sub> type (green), fluorite type (yellow) and  $\alpha$ -PbO<sub>2</sub> type (blue).

unprecedented. On the basis of the above principles, one may speculate that the  $\alpha$ -PbO<sub>2</sub> transition pressure might be significantly elevated (i.e.,  $\gg$  38 GPa), which requires further experimental and theoretical justification. However, such huge pressure increases may well induce other new SnO<sub>2</sub> phases to form (Shieh et al., 2006). Therefore, the  $\alpha$ -PbO<sub>2</sub> phase is likely a metastable phase that cannot simply be interpreted by thermodynamic principles alone. Furthermore, the observed prominent hysteresis, which was characterized by significantly different forward and backward transition pressures, is likely a consequence of different transformation barriers. While the stabilities of difference phases are only determined by thermodynamic functions, the actual transformation pressure may be predominantly governed by kinetics, which scales with the width of the hysteresis. It would therefore be interesting to investigate hysteresis and kinetics as a function of temperature. Indeed, the hysteresis for the nanocrystal CdSe transitions was found to narrow as temperature increased (Chen & Herhold, 1997). The combination of pressure, size, morphology, thermodynamics and kinetics has led to the formation of a multi-dimensional structure-property domain with extremely broad tunabilities. Our findings indicate that certain structures and/or phases can be switched 'on' or 'off' at selected pressure regions with selected morphologies via selected paths. Applying pressure to nanomaterials with different morphologies, therefore, has profound implications for producing controlled structures with desirable properties, such as those for gas sensors whose sensitivity has a preferential correlation to the orthorhombic  $\alpha$ -PbO<sub>2</sub>-type structure of SnO<sub>2</sub> (Arbiol et al., 2008). However, detailed transformation mechanisms, especially the origins of the surprising reversibility and metastability require further theoretical investigation.

## 4. GaN nanowires under high pressures

### 4.1 Properties, structures, and applications of GaN

Gallium nitride (GaN) is a wide band gap semiconductor (3.5 eV) of great technological importance due to its potential applications in high brightness blue/green light emitting diodes (LEDs) and room temperature blue laser (Nakamura et al., 1997). These applications usually require GaN in the wurtzite and zinc blende phases depending on the synthetic techniques (Lei et al., 1992). In addition, GaN is also characterized to have high hardness, low compressibility, high ionicity and high thermal conductivity. These properties make GaN a promising candidate for optoelectronic devices operating under extreme conditions such as at high pressure (Liu et al., 1999). At ambient condition, GaN crystallizes in a wurtzite (B4) structure with a space group of  $P6_3mc$  (Schulz & Thiemann, 1977). It is well established that GaN transforms to the rocksalt (B1) structure (space group  $Fm\bar{3}m$ ) at high pressure as suggested by recent theoretical and experimental reports (Cui et al., 2002; Jorgensen et al., 2003; Munoz & Kunc, 1991; Pandey et al., 1994; Perlin et al., 1992; Saib & Bouarissa, 2007; Ueno et al., 1994; Xia et al., 1993; Xiao et al., 2008). For instance, Perlin et al. identified such phase transformation at 47 GPa using Raman scattering and X-ray absorption spectroscopy (Perlin et al., 1992). By synchrotron energy-dispersive X-ray diffraction, Xia et al. reported the first observation of rocksalt phase at an onset pressure of 37 GPa (Xia et al., 1993). Additional later studies confirmed that GaN with different forms all underwent the wurtzite to rocksalt transformation on compression, however, with large discrepancies in transition pressures (e.g., 42-54 GPa for experimental results (Halsall et al., 2004; Perlin et al., 1992; Ueno et al., 1994) and 37-55 GPa for some theoretical studies (Abu-Jafar et al., 2000; Cai & Chen, 2007; Mujica et al., 2003; Munoz & Kunc, 1991; Pandey et al., 1996; Serrano et al., 2000)). GaN can also be synthesized in the nanocrystalline form, either as nanowires or as quantum dots (Jorgensen et al., 2003; Liu et al., 2003; Zhou et al., 2005). Compared to bulk GaN, nanostructured GaN exhibits attractive properties and thus enhanced performance for applications such as optoelectronic devices because of its excellent tunability as a direct band gap semiconductor (Qian et al., 2005). Therefore, studies on structural tuning of nano-GaN such as by the application of pressure in comparison with the bulk materials are of fundamental interests. To date, very few experiments were performed on nanostructured GaN at high pressure. Only Jorgensen et al. has investigated the phase transformations and compressibility of GaN nanocrystals in comparison with the bulk GaN using X-ray diffraction (Jorgensen et al., 2003). Here we discuss the *in situ* high-pressure X-ray diffraction measurements on one-dimensional nanostructured GaN in the form of zigzagged nanowires where interesting, abnormal pressure behaviors were observed.

### 4.2 GaN nanowires upon compression

Selected X-ray diffraction patterns of GaN nanowires collected upon compression to 65 GPa are shown in Fig. 11a. The X-ray diffraction pattern collected at near ambient pressure (i.e., 0.5 GPa) can be indexed with a hexagonal wurtzite structure ( $P6_3mc$ ) with cell parameters  $a=b=3.1916 \text{ \AA}$  and  $c=5.1733 \text{ \AA}$ , consistent with the previous X-ray diffraction measurement on GaN nanowires (Zhou et al., 2005). In contrast to the diffraction pattern of nanocrystalline GaN which is characterized with significantly broadened reflection profiles (Jorgensen et al., 2003), however, the narrow and sharp reflections for GaN nanowires here suggest an excellent crystalline phase that resembles bulk GaN. Upon compression, the

wurtzite phase was found to persist to 65 GPa indicated by the consistent indexing of the first six reflections associated with this phase. At 55 GPa, a new reflection appeared at  $10.4519^\circ$ , which can be indexed as (2 0 0) for the rocksalt phase, suggesting the onset of phase transformation. The phase transformation can be further evidenced by the depletion of the strong (1 0 0) reflection at the lowest  $2\theta$  angle and the dominant reflection (1 0 1) of wurtzite phase which coincides with reflection (1 1 1) of the rocksalt phase. We note that the phase transition pressure of 55 GPa is higher than that in most previous studies for bulk GaN (Ueno et al., 1994; Xia et al., 1993) but lower compared to that for nanocrystalline GaN which was found to be around 60 GPa (Jorgensen et al., 2003). Size and morphology dependent enhancement of transition pressures have been observed in other nanostructured materials (Dong & Song, 2009). Now it is the general understanding that the surface energy that plays an important role in nanostructures contributes to the enhanced transition pressures. The GaN nanowires in the current study had an initial wire-like morphology and converted to smaller nanoparticles on compression with an average size of 50-200 nm as shown in Fig. 2b, resulting an increase of surface area. Comparing with the particle size of nanocrystalline GaN (i.e., 2-8 nm) studied previously (Jorgensen et al., 2003), it can be inferred that surface energy of GaN increased from bulk to nanowires and to nanoparticles with decreasing sizes, giving the corresponding different transition pressures.

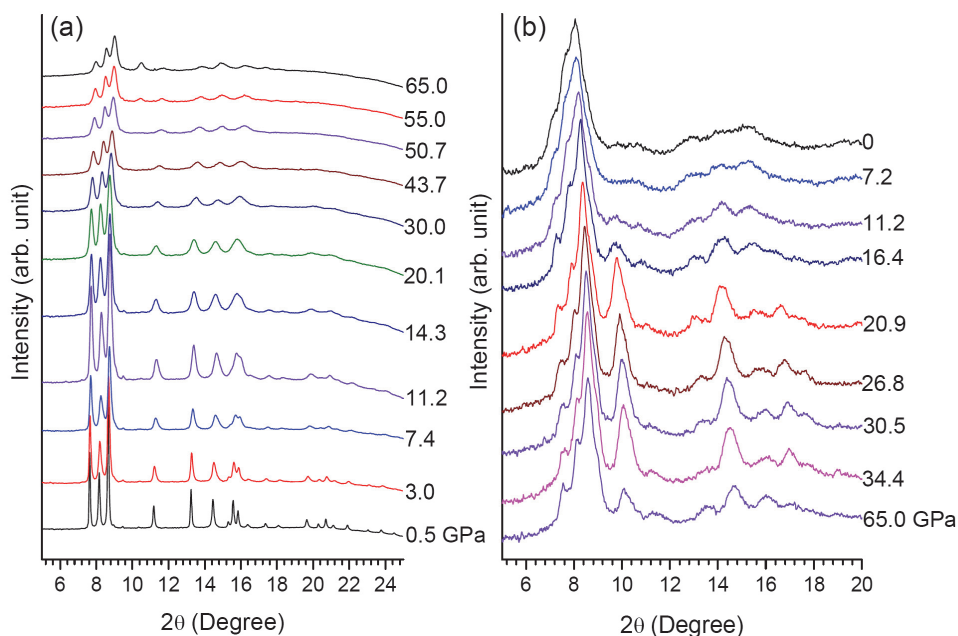


Fig. 11. Angle-dispersive X-ray diffraction patterns ( $\lambda=0.3680 \text{ \AA}$ ) of GaN nanowires at selected pressures upon compression (a) and decompression (b). The pressures in GPa are labelled along each pattern.

Another significant difference between this study and previous studies on bulk GaN is that the wurtzite-to-rocksalt transformation for GaN nanowires is far from complete even at 65 GPa. Quantitative Rietveld analysis of GaN nanowires diffraction pattern at 65 GPa shown

in Fig. 12a indicates that wurtzite and rocksalt phases co-exists at this pressure with respective abundance of 88% and 12%. In contrast, an abundance of near 100% for the rocksalt phase was reported for bulk GaN at a pressure less than 60 GPa in most of the previous studies. For example, Perlin et al. found that the wurtzite phase disappears at 54 GPa (Perlin et al., 1992), while Halsall et al. reported such a pressure to be 49 GPa (Halsall et al., 2004). The highest pressure for complete transformation to rocksalt phase for bulk GaN was reported to be 58.8 GPa (Cui et al., 2002) and 60.6 GPa (Ueno et al., 1994), respectively. Our observation is consistent with that for nanocrystalline GaN where the wurtzite to rocksalt phase transition was found incomplete even at 63.5 GPa (Jorgensen et al., 2003). Similar situations were also observed in other one-dimensional nanomaterials, such as in multi-wall boron nitride nanotubes (MW-BNNT) (Dong & Song, 2010). The required pressures for the hexagonal-to-wurtzite structural transformation to be completed are 23 GPa for bulk BN and > 35 GPa for MW-BNNTs, respectively, which can be understood from the topological and mechanical aspects of BNNT nanostructures (Dong & Song, 2010). In addition to the intrinsic properties of nanostructures, non-hydrostaticity may also contribute to the “sluggish” phase transformations. We realize that silicone oil used as the pressure transmitting media in this study, which forms a glass phase even at very low pressures (Ragan et al., 1996), is far from ideal. The non-hydrostaticity is manifested by the significant broadening of all reflections especially at high pressures as shown in the Debye-Scherrer 2D

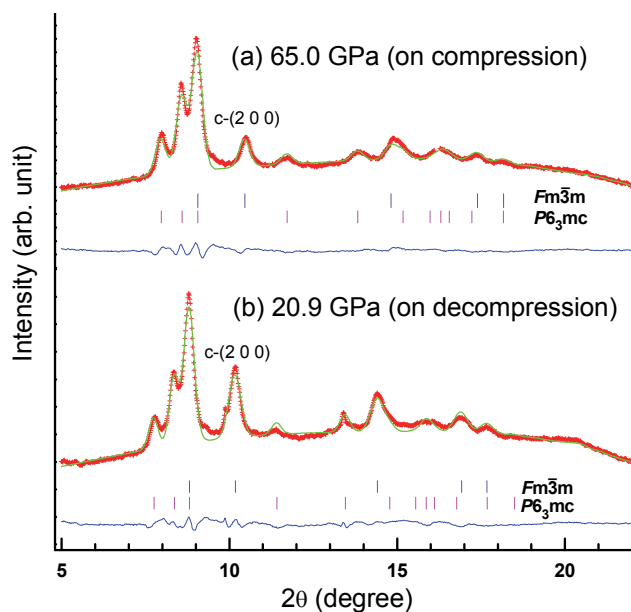


Fig. 12. Rietveld refinement of x-ray diffraction pattern at 65 GPa (a) and 20.9 GPa (b). The redcross is experimental X-ray intensity and the green line is the calculated diffraction patterns based on refinement with the blue curve at the bottom showing the difference between the calculated and observed intensities. The vertical bars denote the indexed reflections for each phase with the space groups labeled beside. The characteristic reflection for the cubic rocksalt phase is labeled as c-(2 0 0). (From Dong and Song, 2010)

diffraction patterns in Fig 13. For instance, the full width at half maximum (FWHM) of reflection (1 0 1) increased dramatically from  $0.09^\circ$  at 0.5 GPa to  $0.25^\circ$  upon compression 65 GPa. Furthermore, severe distortions in the Debye-Scherrer 2D diffraction patterns for reflections (1 0 0), (0 0 2) and (1 0 1) were observed in the high-pressure region (Fig. 13b), indicating pressure-induced enhancement of lattice strain. All these factors may interactively affect the phase stabilities and thus the transformation pressures.

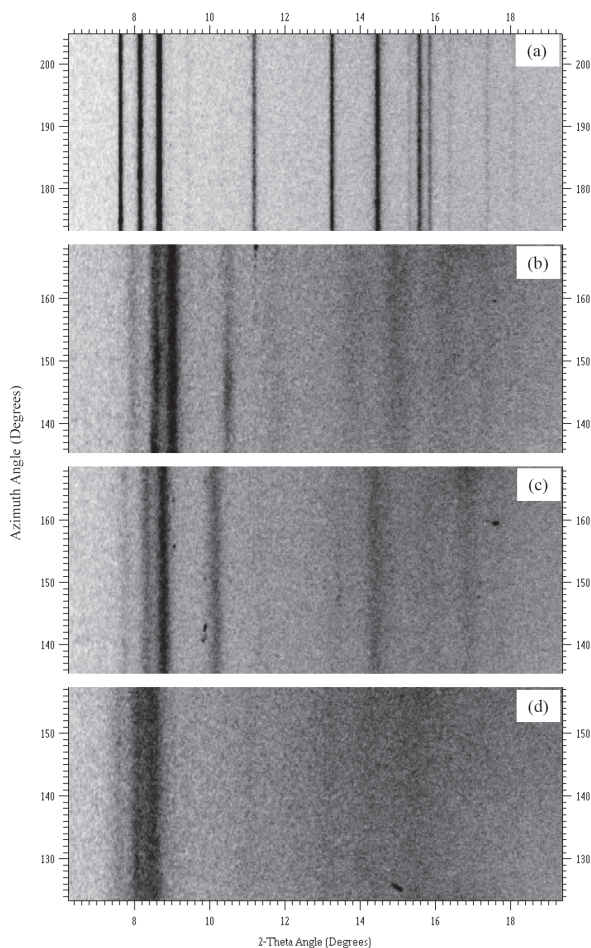


Fig. 13. Debye-Scherrer 2D X-ray diffraction patterns of GaN nanowires at ambient pressure (a), 65 GPa (b), 20.9 GPa upon decompression (c) and ambient pressure upon complete decompression (d).

### 4.3 GaN nanowires upon decompression

X-ray diffraction patterns of GaN nanowires at selected pressures upon decompression from 65 GPa to the ambient pressure are shown in Fig. 11b. An interesting yet unusual phase transformation was found during decompression. Upon releasing pressure from 65 GPa, the

highest pressure achieved in the current study, the abundance of rocksalt phase was found to increase significantly. For instance, Rietveld refinement (Fig. 12b) suggests that the fraction of rocksalt phase has increased upon releasing the pressure from 12 % at 65.0 GPa to 29% even at 20.9 GPa. Below 20.9 GPa, the rocksalt phase gradually transforms back to the wurtzite phase, but was retained even at very low pressures (e.g., <16.4 GPa) as indicated by the noticeable intensity of the (2 0 0) reflection as the dominant reflection of the rocksalt phase. The recovered phase at ambient pressure can be identified as a single wurtzite phase, but the significantly broadened diffraction pattern (Fig. 13d) suggests pressure-induced reduction of the grain size, consistent with the SEM image of the recovered GaN nanomaterial (Fig. 2b). All the previous studies found that B4-B1 phase transformation is reversible for both bulk GaN and nanocrystalline GaN (Cui et al., 2002; Halsall et al., 2004; Perlin et al., 1992) indicating that the wurtzite phase is thermodynamically stable in the low pressure region. However, the strongly contrasting, unprecedented decompression behavior of GaN nanowires exhibiting a large hysteresis suggests that the rocksalt phase is a metastable phase. Prominent hysteresis, which was characterized by significantly different forward and backward transition pressures, is likely due to different kinetic barriers that impede the sharp transitions often involving a metastable phase. Here, we note that this phase of GaN behaves similarly as one of the high-pressure phases (i.e.,  $\alpha$ -PbO<sub>2</sub> phase) for SnO<sub>2</sub> nanowires (Dong & Song, 2009).

#### 4.4 Equation of state

The unit cell parameters of GaN nanowires at different pressures are plotted in Fig. 14a with the unit cell volume against the pressure for the wurtzite phase plotted in Fig. 14b in comparison with previous studies. As can be seen, the unit cell parameters, the a/c ratio, and the corresponding P-V curve of GaN nanowires exhibit a noticeable discontinuity in the pressure region of 11-20 GPa. In the low pressure region (i.e., < 11 GPa), the equation of state (EOS) for GaN nanowires is almost identical for that of bulk GaN material. Above 11 GPa, obvious change in the P-V relation of GaN nanowires suggest a smaller compressibility or larger bulk modulus. Comparing with previously established EOS for bulk GaN ( $B_0=187$ -237 GPa) (Jorgensen et al., 2003; Ueno et al., 1994), and for nanocrystalline GaN ( $B_0=319$  GPa)(Jorgensen et al., 2003), the bulk modulus for GaN nanowires in the pressure region above 20 GPa is estimated to be in between, consistent with that an increase of the surface area may enhance the bulk modulus. This observation can be further understood from the fact the GaN nanowires break into nanoparticles when the external stress surpasses the yield strength at around 20 GPa, resulting in the size-induced enhancement of the bulk modulus. The correlation between the reduction of the particle size and the increasing bulk modulus has been found in other nanomaterials, such as AlN nanocrystals (Wang et al., 2004). A similar discontinuity was also found in the P-V curve for nanocrystalline CeO<sub>2</sub>.(Wang et al., 2004) However, a decrease in the bulk modulus of nanocrystalline CeO<sub>2</sub> was found above ~20 GPa, a pressure that was believed to signify the onset of a size-induced weakening of the elastic stiffness of nanocrystalline CeO<sub>2</sub>. Therefore, the discontinuity in the EOS for both nanocrystalline CeO<sub>2</sub> and GaN nanowires can be understood from the nano-size effect while the different shapes of the EOS curves may be associated with opposite pressure-induced changes in particle size. It is probable, too, that the P-V behavior observed in the region of 11-20 GPa is associated with the combined effect of the original nanowires and the yield-generated nanoparticles. The high yield strength observed in the GaN nanowires thus

further the understanding of the morphology-tuned improvement in yield strength and hardness in hard materials applications. Moreover, the choice of silicone oil as the pressure-transmitting medium may also contribute to the discontinuity observed in the P-V curve. An anomalous behavior inherent in silicone oil at  $\sim 12$  GPa, which is believed to be the result of phase transition (Chervin et al., 1995; Klotz et al., 2009), seems to have further complicated the abnormal behavior of GaN nanowires in the pressure region of 11-20 GPa. It would therefore be interesting to use better pressure transmitting media, such as helium, to study compressibility of GaN nanowires in a broader hydrostatic pressure region.

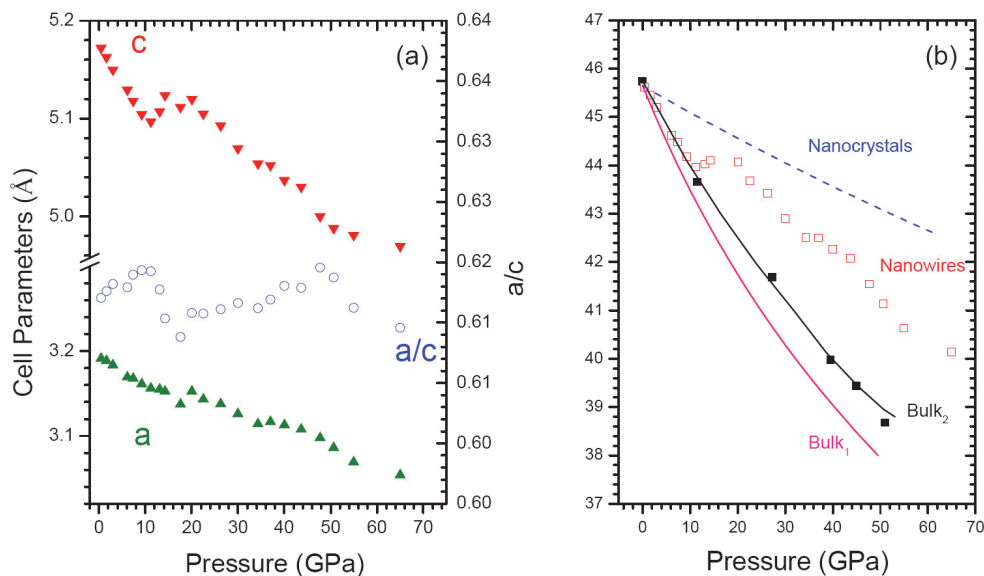


Fig. 14. Unit cell parameters of GaN nanowires as a function of pressure (a) and unit cell volume as a function of pressure for GaN nanowires (open squares) in comparison with that for bulk and nanocrystal GaN (b). Solid lines are fitted EOS curves for bulk GaN using bulk moduli of 187 GPa (bulk<sub>1</sub>) and 237 GPa (bulk<sub>2</sub>) from (Jorgensen et al., 2003) and (Ueno et al, 1994) respectively. The dashed line is fitted EOS curve for nanocrystalline GaN using bulk modulus of 319 GPa from (Jorgensen et al., 2003).

## 5. Summary

In summary, two one-dimensional inorganic materials with various morphologies and sizes were investigated under high pressures. In particular, pressure-induced structural evolutions in nanostructured SnO<sub>2</sub> in the form of nanobelts and nanowires were studied in diamond anvil cells using Raman spectroscopy, angle dispersive X-ray diffraction and SEM. We found that nanostructured SnO<sub>2</sub> exhibits drastically disproportionate high-pressure behaviors compared with bulk materials, which suggests that nanostructured SnO<sub>2</sub> has significantly different optical, chemical and mechanical properties. These morphology-induced differences for some of the phase transformations can be explained by surface energy differences as the dominant thermodynamics factor, while other phases are primarily mediated by kinetics.

These principles may serve as a general guideline for producing novel functional materials with desired stability and/or metastability that may yield promising industrial applications, particularly for semiconductor and chemical sensor uses.

For GaN nanowires, we have investigated high-pressure structures and properties of the first one-dimensional nanostructured GaN using angle-dispersive X-ray diffraction in situ. A wurtzite to rocksalt phase transformation is observed to start at 55 GPa and but is far from complete even at pressures up to 65 GPa. Upon decompression, the abundance of the rocksalt phase was found to increase and then decrease until ambient pressure, at which only the wurtzite phase was recovered, indicating a reversible transformation but with large hysteresis. A discontinuity in the EOS for GaN nanowires is found in the pressure region of 11-20 GPa. These abnormal pressure behaviors of GaN nanowires were compared with previous high pressure studies on bulk and nanocrystalline GaN and can be understood from the nano-size and morphology dependent thermodynamic and kinetic properties of GaN nanowires with the complication of the nonhydrostatic conditions.

## 6. Future perspectives

Despite that interesting high-pressure behaviors of the two inorganic nanowires were observed and analyzed, more in-depth understanding of these unusual behaviors at quantitative level is still needed. In strong contrast to the extensive high-pressure studies on zero-dimensional nanoparticles, only very few one-dimensional inorganic nanomaterials were investigated at high pressures up-to-date as outlined in Table 1. Therefore, further systematic studies on different inorganic 1D nanostructures with different dimensions under different compression conditions are needed. Additional experimental endeavor with more structural characterization approaches aided with theoretical modeling will help to understand and predict the structures, properties, and transformation mechanisms of these nanomaterials and to shed light on their new promising applications.

## 7. Acknowledgment

This work is supported by a Discovery Grant, a Research Tools and Instruments Grant from Natural Science and Engineering Research Council of Canada, a Leaders Opportunity Fund from Canadian Foundation for Innovation and an Early Researcher Award from Ontario Ministry of Research and Innovation. The authors acknowledge Prof. T. K. Sham for supplying the material, Drs. D. Shakhvorostov and C. Murli for experimental assistance, Drs. J. Hu and Y. Meng for technical assistance, and Drs. H. Liu and K. K. Zhuravlev for helpful discussions. The original experiments were performed at X17C beamline at the National Synchrotron Light Source at Brookhaven National Laboratory and at HPCAT (Sector 16), Advanced Photon Source, Argonne National Laboratory.

## 8. References

- Abu-Jafar, M.; Al-Sharif, A. I. & Qteish, A. (2000). FP-LAPW and pseudopotential calculations of the structural phase transformations of GaN under high-pressure. *Solid State Communications*, Vol. 116, No. 7, pp. 389-393.
- Arbiol, J.; Comini, E.; Faglia, G.; Sberveglieri, G. & Morante, J. R. (2008). Orthorhombic Pbcn SnO<sub>2</sub> nanowires for gas sensing applications. *Journal of Crystal Growth*, Vol. 310, No. 1, pp. 253-260.

- Arora, A. K.; Rajalakshmi, M.; Ravindran, T. R. & Sivasubramanian, V. (2007). Raman spectroscopy of optical phonon confinement in nanostructured materials. *Journal of Raman Spectroscopy*, Vol. 38, No. 6, pp. 604-617.
- Birch, F. (1978). Finite Strain Isotherm and Velocities for Single-Crystal and Polycrystalline NaCl at High-Pressures and 300-Degree-K. *Journal of Geophysical Research*, Vol. 83, No. NB3, pp. 1257-1268.
- Cai, J. & Chen, N. X. (2007). Microscopic mechanism of the wurtzite-to-rocksalt phase transition of the group-III nitrides from first principles. *Physical Review B*, Vol. 75, No. 13, pp. 12.
- Calestani, D.; Lazzarini, L.; Salviati, G. & Zha, M. (2005). Morphological, structural and optical study of quasi-1D SnO<sub>2</sub> nanowires and nanobelts. *Crystal Research and Technology*, Vol. 40, No. 10-11, pp. 937-941.
- Calestani, D.; Zha, M.; Zappettini, A.; Lazzarini, L.; Salviati, G.; Zanotti, L. & Sberveglieri, G. (2005). Structural and optical study of SnO<sub>2</sub> nanobelts and nanowires. *Materials Science and Engineering: C*, Vol. 25, No. 5-8, pp. 625-630.
- Chen, B.; Penwell, D.; Benedetti, L. R.; Jeanloz, R. & Kruger, M. B. (2002). Particle-size effect on the compressibility of nanocrystalline alumina. *Physical Review B*, Vol. 66, No. 14, pp. 144101.
- Chen, C.-C. & Herhold, A. B. (1997). Size dependence of structural metastability in semiconductor nanocrystals. *Science*, Vol. 276, No. 5311, pp. 398-401.
- Chen, Z.; Lai, J. K. L. & Shek, C.-H. (2006). Facile strategy and mechanism for orthorhombic SnO<sub>2</sub> thin films. *Applied Physics Letters*, Vol. 89, No. 23, pp. 231902.
- Chervin, J. C.; Canny, B.; Besson, J. M. & Pruzan, P. (1995). A Diamond-Anvil Cell for Ir Microspectroscopy. *Review of Scientific Instruments*, Vol. 66, No. 3, pp. 2595-2598.
- Cui, Q.; Pan, Y.; Zhang, W.; Wang, X.; Zhang, J.; Cui, T.; Xie, Y.; Liu, J. & Zou, G. (2002). Pressure-induced phase transition in GaN nanocrystals. *Journal of Physics: Condensed Matter*, Vol. 14, No. 44, pp. 11041-11044.
- Cui, Q.; Pan, Y.; Zhang, W.; Wang, X.; Zhang, J.; Cui, T.; Xie, Y.; Liu, J. & Zou, G. (2002). Pressure-induced phase transition in GaN nanocrystals. *Journal of Physics-Condensed Matter*, Vol. 14, No. 44, pp. 11041-11044.
- Dong, Z. & Song, Y. (2009). Pressure-induced morphology-dependent phase transformations of nanostructured tin dioxide. *Chemical Physics Letters*, Vol. 480, No. 1-3, pp. 90-95.
- Dong, Z. & Song, Y. (2010). Abnormal pressure-induced structural transformations of gallium nitride nanowires. *Applied Physics Letters*, Vol. 96, No. 15, pp. 151903.
- Dong, Z. & Song, Y. (2010). Transformations of Cold-Compressed Multiwalled Boron Nitride Nanotubes Probed by Infrared Spectroscopy. *Journal of Physical Chemistry C*, Vol. 114, No. 4, pp. 1782-1788.
- Gouadec, G. & Colombari, P. (2007). Raman Spectroscopy of nanomaterials: How spectra relate to disorder, particle size and mechanical properties. *Progress in Crystal Growth and Characterization of Materials*, Vol. 53, No. 1, pp. 1-56.
- Gouadec, G. & Colombari, P. (2007). Raman spectroscopy of nanostructures and nanosized materials. *Journal of Raman Spectroscopy*, Vol. 38, No. 6, pp. 598-603.
- Guo, Q. X.; Zhao, Y. S.; Mao, W. L.; Wang, Z. W.; Xiong, Y. J. & Xia, Y. N. (2008). Cubic to tetragonal phase transformation in cold-compressed Pd nanocubes. *Nano Letters*, Vol. 8, No. 3, pp. 972-975.

- Haines, J. & Leger, J. M. (1997). X-ray diffraction study of the phase transitions and structural evolution of tin dioxide at high pressure: Relationships between structure types and implications for other rutile-type dioxides. *Physical Review B*, Vol. 55, No. 17, pp. 11144-11154.
- Halsall, M. P.; Harmer, P.; Parbrook, P. J. & Henley, S. J. (2004). Raman scattering and absorption study of the high-pressure wurtzite to rocksalt phase transition of GaN. *Physical Review B*, Vol. 69, No. 23, pp. 235207
- He, Y.; Liu, J. F.; Chen, W.; Wang, Y.; Wang, H.; Zeng, Y. W.; Zhang, G. Q.; Wang, L. N.; Liu, J.; Hu, T. D.; Hahn, H.; Gleiter, H. & Jiang, J. Z. (2005). High-pressure behavior of SnO<sub>2</sub> nanocrystals. *Physical Review B*, Vol. 72, No. 21, pp. 212102.
- Hemley, R. J. & Mao, H. K. (2002). Overview of static high pressure science. Proceedings of the International School of Physics, "Enrico Fermi" Course CXLVII (High Pressure Phenomena), IOS Press, Amsterdam.
- Hou, D.; Ma, Y.; Gao, C.; Chaudhuri, J.; Lee, R. G. & Yang, H. (2009). Compression of a crystalline ZnO nanotube: An experimental exploration of the B4 to B1 transition mechanism. *Journal of Applied Physics*, Vol. 105, No. 10, pp. 104317-4.
- Jacobs, K.; Zaziski, D.; Scher, E. C.; Herhold, A. B. & Alivisatos, P. A. (2001). Activation Volumes for Solid-Solid Transformations in Nanocrystals. *Science*, Vol. 293, No. 5536, pp. 1803-1806.
- Jiang, J. Z. (2004). Phase transformations in nanocrystals. *Journal of Materials Science*, Vol. 39, No. 16-17, pp. 5103-5110.
- Jiang, J. Z. & Gerward, L. (2000). Phase transformation and conductivity in nanocrystal PbS under pressure. *Journal of Applied Physics*, Vol. 87, No. 5, pp. 2658-2660.
- Jiang, J. Z.; Gerward, L.; Frost, D.; Secco, R.; Peyronneau, J. & Olsen, J. S. (1999). Grain-size effect on pressure-induced semiconductor-to-metal transition in ZnS. *Journal of Applied Physics*, Vol. 86, No. 11, pp. 6608-6610.
- Jiang, J. Z.; Gerward, L. & Olsen, J. S. (2001). Pressure induced phase transformation in nanocrystal SnO<sub>2</sub>. *Scripta Materialia*, Vol. 44, No. 8-9, pp. 1983-1986.
- Jiang, J. Z.; Olsen, J. S.; Gerward, L. & Morup, S. (1998). Enhanced bulk modulus and reduced transition pressure in g-Fe<sub>2</sub>O<sub>3</sub> nanocrystals. *Europhysics Letters*, Vol. 44, No. 5, pp. 620-626.
- Jorgensen, J. E.; Jakobsen, J. M.; Jiang, J. Z.; Gerward, L. & Olsen, J. S. (2003). High-pressure X-ray diffraction study of bulk- and nanocrystalline GaN. *Journal of Applied Crystallography*, Vol. 36, No. 3, pp. 920-925.
- Klotz, S.; Chervin, J. C.; Munsch, P. & Le Marchand, G. (2009). Hydrostatic limits of 11 pressure transmitting media. *Journal of Physics D: Applied Physics*, Vol. 42, No. 7, pp. 075413.
- Lei, T.; Moustakas, T. D.; Graham, R. J.; He, Y. & Berkowitz, S. J. (1992). Epitaxial-Growth and Characterization of Zincblende Gallium Nitride on (001) Silicon. *Journal of Applied Physics*, Vol. 71, No. 10, pp. 4933-4943.
- Li, Q. J.; Liu, B. B.; Wang, L.; Li, D. M.; Liu, R.; Zou, B.; Cui, T.; Zou, G. T.; Meng, Y.; Mao, H. K.; Liu, Z. X.; Liu, J. & Li, J. X. (2010). Pressure-Induced Amorphization and Polyamorphism in One-Dimensional Single-Crystal TiO<sub>2</sub> Nanomaterials. *Journal of Physical Chemistry Letters*, Vol. 1, No. 1, pp. 309-314.

- Li, Z.; Liu, B.; Yu, S.; Wang, J.; Li, Q.; Zou, B.; Cui, T.; Liu, Z.; Chen, Z. & Liu, J. (2011). The Study of Structural Transition of ZnS Nanorods under High Pressure. *The Journal of Physical Chemistry C*, Vol. 115, No. 2, pp. 357-361.
- Li, Z. P.; Liu, B. B.; Li, X. L.; Yu, S. D.; Wang, L.; Hou, Y. Y.; Zou, Y. G.; Yao, M. G.; Li, Q. J.; Zou, B.; Cui, T. & Zou, G. T. (2007). Solvothermal synthesis of ZnS nanorods and their pressure modulated photoluminescence spectra. *Journal of Physics-Condensed Matter*, Vol. 19, No. 42, pp. 8.
- Liu, J.; Meng, X. M.; Jiang, Y.; Lee, C. S.; Bello, I. & Lee, S. T. (2003). Gallium nitride nanowires doped with silicon. *Applied Physics Letters*, Vol. 83, No. 20, pp. 4241-4243.
- Liu, Z. X.; Goni, A. R.; Syassen, K.; Siegle, H.; Thomsen, C.; Schottker, B.; As, D. J. & Schikora, D. (1999). Pressure and temperature effects on optical transitions in cubic GaN. *Journal of Applied Physics*, Vol. 86, No. 2, pp. 929-934.
- Mujica, A.; Rubio, A.; Munoz, A. & Needs, R. J. (2003). High-pressure phases of group-IV, III-V, and II-VI compounds. *Reviews of Modern Physics*, Vol. 75, No. 3, pp. 863-912.
- Munoz, A. & Kunc, K. (1991). High-Pressure Phase of Gallium Nitride. *Physical Review B*, Vol. 44, No. 18, pp. 10372-10373.
- Muthu, D. V. S.; Midgley, A. E.; Petruska, E. A.; Sood, A. K.; Bando, Y.; Golberg, D. & Kruger, M. B. (2008). High-pressure effects on boron nitride multi-walled nanotubes: An X-ray diffraction study. *Chemical Physics Letters*, Vol. 466, No. 4-6, pp. 205-208.
- Nakamura, S.; Senoh, M.; Nagahama, S.; Iwasa, N.; Yamada, T.; Matsushita, T.; Sugimoto, Y. & Kiyoku, H. (1997). Room-temperature continuous-wave operation of InGaN multi-quantum-well structure laser diodes with a lifetime of 27 hours. *Applied Physics Letters*, Vol. 70, No. 11, pp. 1417-1419.
- Pandey, R.; Causa, M.; Harrison, N. M. & Seel, M. (1996). The high-pressure phase transitions of silicon and gallium nitride: A comparative study of Hartree-Fock and density functional calculations. *Journal of Physics-Condensed Matter*, Vol. 8, No. 22, pp. 3993-4000.
- Pandey, R.; Jaffe, J. E. & Harrison, N. M. (1994). Ab-Initio Study of High-Pressure Phase-Transition in GaN. *Journal of Physics and Chemistry of Solids*, Vol. 55, No. 11, pp. 1357-1361.
- Park, S.-W.; Jang, J.-t.; Cheon, J.; Lee, H.-H.; Lee, D. R. & Lee, Y. (2008). Shape-dependent compressibility of TiO<sub>2</sub> anatase nanoparticles. *Journal of Physical Chemistry C*, Vol. 112, No. 26, pp. 9627-9631.
- Perlin, P.; Jaubertiecarillon, C.; Itie, J. P.; Miguel, A. S.; Grzegory, I. & Polian, A. (1992). Raman-Scattering and X-Ray-Absorption Spectroscopy in Gallium Nitride under High-Pressure. *Physical Review B*, Vol. 45, No. 1, pp. 83-89.
- Qian, F.; Gradecak, S.; Li, Y.; Wen, C. Y. & Lieber, C. M. (2005). Core/multishell nanowire heterostructures as multicolor, high-efficiency light-emitting diodes. *Nano Letters*, Vol. 5, No. 11, pp. 2287-2291.
- Ragan, D. D.; Clarke, D. R. & Schiferl, D. (1996). Silicone fluid as a high-pressure medium in diamond anvil cells. *Review of Scientific Instruments*, Vol. 67, No. 2, pp. 494-496.
- Rekhi, S.; Saxena, S. K. & Lazor, P. (2001). High-pressure Raman study on nanocrystalline CeO<sub>2</sub>. *Journal of Applied Physics*, Vol. 89, No. 5, pp. 2968.

- Saha, S.; Gadagkar, V.; Maiti, P. K.; Muthu, D. V. S.; Golberg, D.; Tang, C.; Zhi, C.; Bando, Y. & Sood, A. K. (2007). Irreversible pressure-induced transformation of boron nitride nanotubes. *Journal of Nanoscience and Nanotechnology*, Vol. 7, No. 6, pp. 1810-1814.
- Saha, S.; Muthu, D. V. S.; Golberg, D.; Tang, C.; Zhi, C.; Bando, Y. & Sood, A. K. (2006). Comparative high pressure Raman study of boron nitride nanotubes and hexagonal boron nitride. *Chemical Physics Letters*, Vol. 421, No. 1-3, pp. 86-90.
- Saib, S. & Bouarissa, N. (2007). Structural phase transformations of GaN and InN under high pressure. *Physica B: Condensed Matter*, Vol. 387, No. 1-2, pp. 377-382.
- San-Miguel, A. (2006). Nanomaterials under high-pressure. *Chemical Society Reviews*, Vol. 35, No. 10, pp. 876-889.
- Sangaletti, L.; Depero, L. E.; Dieguez, A.; Marca, G.; Morante, J. R.; Romano-Rodriguez, A. & Sberveglieri, G. (1997). Microstructure and morphology of tin dioxide multilayer thin film gas sensors. *Sensors and Actuators B: Chemical*, Vol. 44, No. 1-3, pp. 268-274.
- Schulz, H. & Thiemann, K. H. (1977). Crystal structure refinement of AlN and GaN. *Solid State Communications*, Vol. 23, No. 11, pp. 815-819.
- Serrano, J.; Rubio, A.; Hernandez, E.; Munoz, A. & Mujica, A. (2000). Theoretical study of the relative stability of structural phases in group-III nitrides at high pressures. *Physical Review B*, Vol. 62, No. 24, pp. 16612-16623.
- Shieh, S. R.; Kubo, A.; Duffy, T. S.; Prakapenka, V. B. & Shen, G. (2006). High-pressure phases in SnO<sub>2</sub> to 117 GPa. *Physical Review B*, Vol. 73, No. 1, pp. 014105.
- Sun, S. H.; Meng, G. W.; Zhang, G. X.; Gao, T.; Geng, B. Y.; Zhang, L. D. & Zuo, J. (2003). Raman scattering study of rutile SnO<sub>2</sub> nanobelts synthesized by thermal evaporation of Sn powders. *Chemical Physics Letters*, Vol. 376, No. 1-2, pp. 103-107.
- Swamy, V.; Kuznetsov, A.; Dubrovinsky, L. S.; McMillan, P. F.; Prakapenka, V. B.; Shen, G. & Muddle, B. C. (2006). Size-dependent pressure-induced amorphization in nanoscale TiO<sub>2</sub>. *Physical Review Letters*, Vol. 96, No. 13, pp. 135702.
- Tolbert, S. H. & Alivisatos, A. P. (1994). Size dependence of a first order solid-solid phase transition: the wurtzite to rock salt transformation in CdSe nanocrystals. *Science*, Vol. 265, No. 5170, pp. 373-376.
- Tolbert, S. H. & Alivisatos, A. P. (1995). High-pressure structural transformations in semiconductor nanocrystals. *Annual Review of Physical Chemistry*, Vol. 46, pp. 595-625.
- Ueno, M.; Yoshida, M.; Onodera, A.; Shimomura, O. & Takemura, K. (1994). Stability of the Wurtzite-Type Structure under High-Pressure - GaN and InN. *Physical Review B*, Vol. 49, No. 1, pp. 14-21.
- Wang, B.; Zhu, L. F.; Yang, Y. H.; Xu, N. S. & Yang, G. W. (2008). Fabrication of a SnO<sub>2</sub> nanowire gas sensor and sensor performance for hydrogen. *Journal of Physical Chemistry C*, Vol. 112, No. 17, pp. 6643-6647.
- Wang, F.; Zhou, X.; Zhou, J.; Sham, T.-K. & Ding, Z. (2007). Observation of single tin dioxide nanoribbons by confocal Raman microspectroscopy. *Journal of Physical Chemistry C*, Vol. 111, No. 51, pp. 18839-18843.
- Wang, Z.; Daemen, L. L.; Zhao, Y.; Zha, C. S.; Downs, R. T.; Wang, X.; Wang, Z. L. & Hemley, R. J. (2005). Morphology-tuned wurtzite-type ZnS nanobelts. *Nature Materials*, Vol. 4, No. 12, pp. 922-927.

- Wang, Z.; Saxena, S. K.; Pischedda, V.; Liermann, H. P. & Zha, C. S. (2001). In situ x-ray diffraction study of the pressure-induced phase transformation in nanocrystalline CeO<sub>2</sub>. *Physical Review B*, Vol. 64, No. 1, pp. 012102.
- Wang, Z. W.; Tait, K.; Zhao, Y. S.; Schiferl, D.; Zha, C. S.; Uchida, H. & Downs, R. T. (2004). Size-induced reduction of transition pressure and enhancement of bulk modulus of AlN nanocrystals. *Journal of Physical Chemistry B*, Vol. 108, No. 31, pp. 11506-11508.
- Wang, Z. W.; Zhao, Y. S.; Schiferl, D.; Zha, C. S. & Downs, R. T. (2004). Pressure induced increase of particle size and resulting weakening of elastic stiffness of CeO<sub>2</sub> nanocrystals. *Applied Physics Letters*, Vol. 85, No. 1, pp. 124-126.
- Watson, J.; Ihokura, K. & Coles, G. S. V. (1993). The tin dioxide gas sensor. *Measurement Science & Technology*, Vol. 4, No. 7, pp. 711-719.
- Xia, H.; Xia, Q. & Ruoff, A. L. (1993). High-Pressure Structure of Gallium Nitride - Wurtzite-to-Rock-Salt Phase-Transition. *Physical Review B*, Vol. 47, No. 19, pp. 12925-12928.
- Xiao, H. Y.; Gao, F.; Wang, L. M.; Zu, X. T.; Zhang, Y. & Weber, W. J. (2008). Structural phase transitions in high-pressure wurtzite to rocksalt phase in GaN and SiC. *Applied Physics Letters*, Vol. 92, No. 24, pp. 241909.
- Yan, X. Q.; Gu, Y. S.; Zhang, X. M.; Huang, Y. H.; Qi, J. J.; Zhang, Y.; Fujita, T. & Chen, M. W. (2009). Doping Effect on High-Pressure Structural Stability of ZnO Nanowires. *Journal of Physical Chemistry C*, Vol. 113, No. 4, pp. 1164-1167.
- Zhou, J. X.; Zhang, M. S.; Hong, J. M. & Yin, Z. (2006). Raman spectroscopic and photoluminescence study of single-crystalline SnO<sub>2</sub> nanowires. *Solid State Communications*, Vol. 138, No. 5, pp. 242-246.
- Zhou, X. T.; Heigl, F.; Murphy, M. W.; Sham, T. K.; Regier, T.; Coulthard, I. & Blyth, R. I. R. (2006). Time-resolved x-ray excited optical luminescence from SnO<sub>2</sub> nanoribbons: Direct evidence for the origin of the blue luminescence and the role of surface states. *Applied Physics Letters*, Vol. 89, No. 21, pp. 213109.
- Zhou, X. T.; Sham, T. K.; Shan, Y. Y.; Duan, X. F.; Lee, S. T. & Rosenberg, R. A. (2005). One-dimensional zigzag gallium nitride nanostructures. *Journal of Applied Physics*, Vol. 97, No. 10, pp. 104315.